DEMOCRATIC AND POPULAR REPUBLIC OF ALGERIA
Ministry of Higher Education and Scientific Research

University Oum El Bouaghi, Algeria

PROCEEDINGS

THE 1ST INTERNATIONAL CONFERENCE

ON ELECTRONICS, ARTIFICIAL INTELLIGENCE AND NEW TECHNOLOGIES

ICEAINT

ISBN: 978-9931-9728-1-5

Laboratory of Electronics and New Technologies –LENT-

Ain Beida, Algeria. December 8-9, 2021

University Larbi Ben M'hidi
University pole, Ain Beida. Algeria
Faculty of Sciences and Applied Sciences

ATRST
Thematic Agency of Research
in Science and Technology

Laboratory of Electronics and New Technologies –LENT-

The 1st International Conference on Electronics, Artificial intelligence and New Technologies

ICEAINT

8- 9 December 2021

SUMMARY

Track 1: Telecommunication	Page 01
Track 2: Artificial Intelligence	Page 100
Track 3: Control and System	Page 226
Track 4: Micro and Nanoelectronics	Page 336

Thematic Research Agency in Science and Technology – ATRST-

University Larbi ben M'hidi Oum el Bouaghi. Algeria

Laboratory of Electronics and New Technologies –LENT-

THE 1ST INTERNATIONAL CONFERENCE

ON ELECTRONICS, ARTIFICIAL INTELLIGENCE AND NEW TECHNOLOGIES

ICEAINT

09 - 08 December 2021

Online presentation is possible

ISBN: 978-9931-9728-1-5

The Electronics and New Technologies Laboratory (LENT) is organizing the first international conference on electronics, artificial intelligence and new technologies (ICEAINT'21), this will be held at the University of Larbi Ben M'hidi, Oum El Bouaghi. The conference will cover all the research activities of the laboratory; moreover, the conference will include different axes of electronics, computer science and new technologies likely to interest all researchers in these fields. The ICEAINT'21 aims to bring together academic researchers and industrial scientists to exchange new ideas, original research results and practical development experiences on all aspects dealing with the different themes of the conference.

Topics

Topic 1	Topic 2	Topic 3
Telecommunications and antennas	**Control, modelling and artificial intelligence**	**Micro and nanoelectronics**
– Wireless communications – Satellite and space communications – Cognitive radio networks – Wireless multimedia networks – Green wireless networks – 4G and 5G communication networks – Optical communication – Wireless network security and privacy – Antennas and wave propagation – LTE, LTE-Advanced, Wifi, and Wimax – Robotics and vision – Signal and image processing.	– Neural network and deep learning – Machine learning – Control of nonlinear systems – Fuzzy intervals and fuzzy systems – Robust control – Fuzzy control and intelligent systems – Adaptive and predictive control – Modeling and simulation – Identification and estimation – Renewable energy systems applications – Smart city – Embedded systems.	– Semiconductor devices – Thin solid films – Circuit theory and applications – Optoelectronics and photonic crystal – Solid-state electronics – Quantum electronics – Nanoelectronics and spintronics – Photovoltaic – Modeling and simulation, synthesis and verification of ICs – Electronic materials science and technology.

Registration fees

Participants : 5000 DA (Presentation) / 10000 DA (All Inclusive)
Students: 3000 DA (Presentation) / 8000 DA (All Inclusive)
Foreigners: 100 € (Presentation) / 200 € (All Inclusive)
~ Registration fees are to be sent or paid at arrival.

Deadlines

Submission deadline: 07 September 2021
Notification of acceptance: 07 October 2021
Camera ready: 14 October 2021
Conference dates: 08-09 December 2021

For more information, contact us at: ICEAINT@univ-oeb.dz

Website address : http://www.univ-oeb.dz/vrlex/en/2021/3717/

Paper Submission

Authors are invited to submit full-length papers (8 pages max) written in English, and formatted using the IEEE templates.

The papers should be submitted electronically in PDF format through the CMT platform:

https://cmt3.research.microsoft.com/ICEAINT2021

All papers will be double blind peer-reviewed. Acceptance will be based on quality, relevance, originality, and presentation. All papers submitted to the ICEAINT'21 must be previously unpublished

Honorary Chairs

Pr. Zohir Dibi, Rector of the University Larbi ben M'hidi of Oum El Bouaghi. Algeria

Pr. Chawki Mahfoudi, Dean of the faculty of Sciences and Applied Sciences, Ain Beida. OEB. Algeria.

Presidents of the Conference

Pr. Mohamed Lashab	University Larbi ben M'hidi of Oum El Bouaghi. Algeria
Pr. Kheireddine Lamamra	University Larbi ben M'hidi of Oum El Bouaghi. Algeria
Pr. Souheil Mouetsi	University Larbi ben M'hidi of Oum El Bouaghi. Algeria
Dr. Abderrahim Faycal Megri	University Larbi ben M'hidi of Oum El Bouaghi. Algeria

Organizing Committee

Dr. Ali Djebabla	University Larbi ben M'hidi of Oum El Bouaghi. Algeria
Dr. Abdessalem Barkat	University Larbi ben M'hidi of Oum El Bouaghi. Algeria
Dr. Farida Batat	University Larbi ben M'hidi of Oum El Bouaghi. Algeria
Dr. Hacen Belila	University Larbi ben M'hidi of Oum El Bouaghi. Algeria
Dr. Yamina Chiha	University Larbi ben M'hidi of Oum El Bouaghi. Algeria
Dr. Nawel Hamdi	University Larbi ben M'hidi of Oum El Bouaghi. Algeria
Dr. Nour El Houda Dehimi	University Larbi ben M'hidi of Oum El Bouaghi. Algeria
Dr. Wafa Ourzifi	University Larbi ben M'hidi of Oum El Bouaghi. Algeria
PhD student Akram Ghediri	University Larbi ben M'hidi of Oum El Bouaghi. Algeria
PhD student Boumediene Sadoun	University Larbi ben M'hidi of Oum El Bouaghi. Algeria
PhD student Djalel Baladji	University Larbi ben M'hidi of Oum El Bouaghi. Algeria
PhD student Houria Bayarassou	University Larbi ben M'hidi of Oum El Bouaghi. Algeria
PhD student Ouassim Boudja	University Larbi ben M'hidi of Oum El Bouaghi. Algeria

Scientific Committee

Pr. Bellaaj Najiba Mrabet
University of Sousse, Tunisia

Pr. Belmeguenai Aissa
University of Skikda, Algeria

Pr. Ben Salah Chokri
ISSAT of Sousse, Tunisia

Pr. Benatia Djamel
University of Batna, Algeria

Pr. Bouchemat Mohamed
University of Constantine 1, Algeria

Pr. Bououdene Sofiane
University of Khenchela, Algeria

Pr. Bourennane Mohamed
University of Stockholm, Sweden

Pr. Bouridane Ahmed
University of Northumbria,
United Kingdom

Pr. Boussaada Zina
ESTIA, French

Pr. Bouttout Farid
University of Bordj Bou Arreridj, Algeria

Pr. Bouzekri Hacen
University of Skikda, Algeria

Pr. Chemori Ahmed
University of Montpellier, French

Pr. Chibane Cherif
MIT, USA

Pr. Denidni Ahmed Tayeb
University of Quebec, Canada

Pr. Derouiche Nadir
University of Skikda, Algeria

Pr. Djemili Rafik
University of Skikda, Algeria

Pr. Fabrice Audépart
IUT - Aix-Marseille, French

Pr. Fertaki Tarek
University of Batna, Algeria

Pr. Hobar Farida
University of Oum El Bouaghi. Algeria

Pr. Hocini Abdessalem
University of M'sila, Algeria

Pr. Hima Abdelkader
University of El Oued, Algeria

Pr. Khaled Belarbi
ENPC, Algeria

Pr. Khechekhouche Abderrahmane
University of El Oued, Algeria

Pr. Khedrouche Djamel
University of M'sila, Algeria

Pr. Ladaci Samir
University of Constantine 3, Algeria

Pr. Lamamra Kheireddine
University of Oum El Bouaghi. Algeria

Pr. Lashab Mohamed
University of Oum El Bouaghi. Algeria

Pr. Lidjici Hamza
University of Laghouat, Algeria

Pr. Mahmoudi Said
University of Mons, Belgium

Pr. Mouetsi Souheil
University of Oum El Bouaghi. Algeria

Pr. M'sirdi Nacer Kouider
Polytech Marseille, French

Pr. Naamane Aziz
Polytech Marseille, French

Pr. Octavian Curea
ESTIA, French

Pr. Rechem Djamil
University of Oum El Bouaghi. Algeria

Pr. Soufi Yousef
University of Tebessa, Algeria

Pr. Sundarapandian Vaidyanathan
Vel Tech University, India

Pr. Zahir Ahmida
University of Skikda, Algeria

Pr. Xiaoling Wang
Beijing Information Science and Technology
University, China

Pr. Zamani Mehdi
Shahid Bahonar University of Kerman, Iran

Dr. Ait Kaki Abdelaziz
University of Oum El Bouaghi. Algeria

Dr. Amata Hadi
King Abdullah University of Science and
Technology, Kingdom of Saudi Arabia

Dr. Belattar Mounir
University of Skikda, Algeria

Dr. Belhani Ahmed
University of Constantine 1, Algeria

Dr. Benkara Salima
University of Oum El Bouaghi. Algeria.

Dr. Brik Fatima
University of Annaba. Algeria.

Dr. Dehimi Nour El Houda
University of Oum El Bouaghi. Algeria.

Dr. Djouablia Linda
University of Skikda, Algeria

Dr. Faycal Abderrahim Megri
University of Oum El Bouaghi. Algeria

Dr. Lamine Mohamed Talbi
University of Bordj Bou Arreridj, Algeria

Dr. Mokhtari Fouad
University of Quebec, Canada

Dr. Remeche Louardi
University of Oum El Bouaghi. Algeria

Dr. Salmi Saleh
University of Constantine 1, Algeria

Dr. Sayad Djamel
University of Skikda, Algeria

Dr. Semira Hichem
Emir Abdelkader University, Algeria

Dr. Zebiri Chemseddine
University of Setif, Algeria

Dr. Ziani Salim
University of Constantine 1, Algeria

Conference program summary ICEAINT'21

University Larbi Ben M'hidi, Oum El Bouaghi, Algeria

Wednesday 8th December 2021	
08h00 – 09h00	Registration and welcoming
09h00 – 09h45	Opening ceremony
09h45 – 10h30	Session of Keynote talk I
10h30 – 10h45	Coffee Break
10h30 – 11h00	Poster session
11h00 – 12h00	Oral/Online Session
12h00 – 13h45	Lunch
13h45 – 14h45	Session of Keynote Talk II
14h45 – 15h15	Coffee Break
15h15 – 17h00	Oral/Online Session
17h00	**End of the first day**

Thursday 9th December 2021	
09h30 – 10h30	Keynote Talk III
10h30 – 11h00	Coffee Break
11h00 – 12h00	Oral/Online Session
12h00 – 12h30	Speech session and closing ceremony
12h30	Lunch
End of the second day	

Wednesday 8th December 2021

08h00 – 9h00 Registration and welcoming

09h00 – 9h45 Opening ceremony:

- Chair of the conference

Director of the laboratory of research
Electronics and New Technologies:
Pr. Mohamed LASHAB

- Dean of the faculty of sciences and applied sciences: **Pr. Chawki MAHFOUDI**
- Rector of the University: **Pr. Zohir DIBI**

9h45 – 10h30: Session of Keynote talk I

Artificial Intelligence: An advanced approach in electrical power systems

Pr. Soufi YOUCEF
Department of Electrical Engineering, Laboratory of Electrical Engineering at the University Larbi Tebessi, Tebessa, Algeria

10h30 – 10h45 Coffee break

10h30 – 11h00: Poster session

Session chairs: Abdel Aziz AIT KAKI, Ahmed BELHANI

Track 1: Telecommunication	
ID: 77	**Linda DJOUABLIA,** N. H. ALIOUA, I. BOURAHLA, A. ZERMANE.
	Indoor communication scenario of electrical engineering departement - University of Skikda- based on RSS, frequency and path losses.
ID: 102	**Soumali CHAABANE,** Mounir BELATTAR.
	Design and Simulation of a microstrip band pass filter for C band
ID: 71	**Aziza ZERMANE,** Linda DJOUABLIA.
	A magnetically tunable planar band-stop filter using ferrite layer

Track 2: Artificial Intelligence	
ID: 117	**Abdesselam FERDI,** Said BENIERBEH, Youcef FERDI
	Five deep learning models for classification of chest X-ray images of COVID-19
ID: 90	**Soumia BEZZAZ,** Djamel BENMERZOUG, Kheireddine LAMAMRA.
	Business Intelligence Platform for Projects Related to the Internet of Things
ID: 115	**Naouel HAMDI,** Ouafi OURZIFI, Ali DJEBABLA
	A DSIM Control Using Artificial Neural Network Controller

Track 3: Control and System	
ID: 34	Badreddine ZEMMAL, **Saida MELLAL**, Issam HAMMA, Marwa MAIZI, Toufik ZIAR, Hichem FARAH and Adel OUANNAS.
	Simple criterions to achieve hybrid dislocated synchronization of two identical Chua's circuits
ID: 112	**Hassen BELILA,** Nasserdine BOUDJERDA, Ahsene BOUBAKIR, Imen BAHRI.
	Efficient STATCOM based on hybrid sliding mode control-proportional integral control and 48-pulse converter
ID: 43	**Abdesselam DEBBAH,** A.KERBOUA, R.KLAIAIA
	Control of reaction and thermo-acoustic instabilities of a combustion chamber

Track 4: Micro and Nanoelectronics	
ID: 59	**Roumaissa DERDOUR,** Mohamed Redha LEBBAL, Souheil MOUETSI.Abdesselam HOCINI, Boumediene SADOUN.
	Novel design of photonic crystal structure based on a coupled Microcavitywaveguides for all-optical and logic gates.
ID: 51	**Ahlam HARHOUZ,** Abdesselam HOCINI, Hadjira TAYOUB.
	Refractive index densor based on multiple fano resonances in plasmonic MIM waveguide coupled with oval resonator
ID: 93	**Fatima SAKER,** Remarche LOUARDI, Abdellah RAHMANI, Hassiba MOUALKIA
	Incorporation of CdS nanoparticles on mesoporous silicon substrate as application for detection systems
ID: 52	Chouaib CHETTAH, Khaled CHETTAH, **Ouarda BARKAT**
	Optical filters based on one dimensional dielectric photonic crystal defected by Magnetized cold plasma
ID: 99	**Abderraouf HOCINI,** Assia DAAS, Abdesselam HOCINI, Souheil MOUETSI
	Structure of the proposed RI biosensor (sensor with two functions)
ID: 18	**Mourad HEBALI,** Hocine Abdelhak AZZEDDINE, Menaouer BENNAOUM, Benaoumeur IBARI.
	A low-power and high sensibility of the smart CMOS(Si and 4H-SiC) temperature sensor in 130 nm technology.
ID: 39	**Hocine KARBOUA,** M'hamed BOULAKROUNE, Tarek FORTAKI.
	Effects of boron diffusion on Titanium silicide formation.
ID: 53	**Salim GHALEM,** Mohamed Redha LEBBAL, Mohamed BOUCHEMAT, BOUMAZA.Touria
	Magneto-optical properties of magnetic photonic crystal fiber of Cerium substituted Yttrium Iron Garnet medium (Ce -YIG) filled with magnetic fluid Fe3O4.
ID: 64	**Tliba TOUATI,** B. BENHAOUA
	Optical and structural properties of copper doped Zinc Oxide thin films prepared via spray pyrolysis method.

11h00 – 12h00: Oral Session

Room 1: Telecommunication

Session chairs: Djamel KHEDROUCHE, Linda DJOUABLIA

ID: 47	**Mounir BELATTAR,** Chaabane SOUMALI
	Analysis of asymmetrical composite right/left handed transmission line for broad band microwave devices
ID: 86	Fayza BOUSALAH, **A.RABAH**
	Design of directional planar antennas with circular polarizations for space applications
ID: 40	**Nassim BENADJINA,** Mohamed LASHAB, Djamel SLIMANI
	PAPR Reduction in OTFS by modified similar raised cosine mSRC pulse shaping
ID: 119	**Ahmed HALFAYA,** Mohamed LASHAB, Salah SALMI, Youcef SOUFI
	Microwave sensor for liquid mixture identification based on metamaterial based on double concentric elliptical complementary split ring resonator

Room 2: Artificial Intelligence

Session chairs: Sofiane BOUOUDEN, Ahmed BELHANI

ID: 41	**Belgacem FISSAH,** Hadj BELGHALEM, Messaoud DJADDOU, Belgacem MAMEN
	Predictive modeling of Young's modulus for alpha alumina using artificial neural network and multiple linear regression
ID: 124	**Hanane DEBBOU,** Abderrahim Fayçal MEGRI
	Use of Wavelet Transforms in Segmentation of Retinal Angiography Images
ID: 97	Rawnaq NAILI**,** Rania Chettab, **Mohamed Abdou Bouteldja,** Mohamed Badeche
	Temperature forecasting via neural networks based on time-series data
ID: 80	**Abdelghani TAKHA,** Mohamed Lamine TALBI, Ghania KHENICHET
	Generation of ECG synthetic signal using coupled ordinary differential equations and Hopf bifurcation
ID: 26	**Adel BENTOUMI,** Ahmed BELHANI
	Placement optimization in sensors network using a linear discernment analyses-based clustering for smart greenhouse.

Room 3: Control and System

Session chairs: Samir LADACI, Salim ZIANI

ID: 113	**Djalal BALADJI,** Kheireddine LAMAMRA
	Contribution on modeling and control of a wind power system based on fuzzy
ID: 116	**Mounira MEKKI,** Djamila CHERIFI
	Study and simulation of a photovoltaic solar panel connected to the electrical network
ID: 122	**Houria BAYARASSOU,** Abderrahim Faycal MEGRI, HACHEM BENNOUR
	Maximum Power Point Tracking for a PV System using Support Vector Machine

ID: 125	**Khelaifa FETHI,** Kheireddine LAMAMRA, Djaafar TOUMI
	Comparison of tow methods P&O and fuzzy logic controller for MPPT in the photovoltaic system

Room 4: Micro and Nanoelectronics

Session chairs: Abdesselam HOCINI, Hamza LIDJICI

ID: 38	**Nour El Houda DJEZZAR,** Kouider DRISS-KHODJA, Bouhalouane AMRANI
	Structural stability, electronic, and mechanical properties of new stable phases for the ternary alloy $Mg_xCd_{1-x}O$
ID: 04	**Assia DAAS,** Souheil MOUETSI, Abderraouf HOCINI, Abdesselam HOCINI, Fateh LARIOURI
	A new design of high-sensitive photonic crystal biosensor based on ring-shape holes for detecting glucose concentration
ID: 30	**Rafiaa KIHAL,** Hassiba RAHAL, Samia RAHAL, Abed Mohamed AFFOUNE
	Electrochemical synthesis of p-Cu_2O thin films on ITO-coated glass substrates for photovoltaic solar cells
ID: 98	**Asma BENCHIHEB,** Nedjoua BENCHIHEB, Yasmina SAIDI, Farida HOBAR
	Effects of doping profile and temperature on the solar cell performances
ID: 5	**Warda ELAGGOUNE,** Athmane MEDDOUR
	Systematic study of structural and magnetoelectronic properties of $Sr_{1-x}Ti_xS$ alloys for spintronic applications

12h00 – 13h45 Lunch

13h45 – 14h45: Session of Keynote Talk II

SDR: Past, Present, and Future

Pr. Cherif CHIBANE

Chief scientist of AuresTech. USA
Previously, he was a research scientist at MIT. USA

15h15 - 17h00: Oral/Online session

Room 1: Telecommunication

Session chairs: Mounir BELATTAR, Aziza ZERMANE

ID: 75	**Mohamed Amin RABAH,** Zohra SLIMANE, Kouther YAMANI, Kaoutar HACHEMI
	Design and analysis of 2×1 of new structure patch antenna array for RFID application

ID: 66	**Bouchera BOUGHERARA,** Amar HAMOUDA, Faycal GOUMIDANE, Amir KEBAILI, Roumaissa MESSAOUDI
	Improving the performance of the digital transmission line between Oum el Bouagui and Ain Mlila
ID: 58	Amar HAMOUDA, **Amina HAMLA,** Cheima DJEMIL
	Realization by simulation of an ultra-frequency carrier for digital transmission in advanced telecommunications
ID: 81	**Rahmouna EL BOUSLEMTI,** Faouzi SALAH BEL KHODJA, Abd el Kader SAYAH.
	A Microstript coupler with improving the characteristic transmission
ID: 55	**Mohamed SAHED**
	Non-coherent Radar CFAR detection based on ratios of consecutive order statistics for Pareto distributed clutter
ID: 19	**Bouchera BOUCHOUAREB,** Naam BOUHAFS
	Denoising ultrasound images and error estimate by non local means
ID: 14	El-Hadi Meftah, **Slimane BENMAHMOUD**, Riadh AJGOU
	RIS-assisted wireless communication from an energy and a spectral efficiency perspective
ID: 54	**Issam TIFOUTI,** Salah RAHMOUNI, Brahim MERIANE
	A Study of speckle noise reduction filters for SAR Images

Room 2: Artificial Intelligence

Session chairs: Soufi YOUCEF, Sofiane BOUOUDEN

ID: 28	**Zakaria TOLBA,** Makhlouf DERDOUR
	IoT lightweight cipher security investigation by machine Learning techniques
ID: 31	**Lila ZEMIHI,** Alkama SADIA, Elmoataz ABDERRAHIM
	Segmentation by Regions of Interest of Color Images Using SOM Neural Networks
ID: 91	**Lakhdar Nadjib BOUCETTA**, Bilal CHEMLOUL, Karima REBAI
	EMG-Based Hand gesture recognition for myoelectric prosthetic hand control
ID: 72	**Mehdi ROUISSAT,** Mohammed BELKHEIR, Hicham Sid Ahmed BELKHIRA
	A Modified Version Number Attack Against RPL Based Networks
ID: 76	**Fatima Zohra HAMLILI,** Mohammed BELADGHAM,Khelifi Mustapha,Oussama Dahmane
	Detection of Covid-19 in chest X-ray images using a Resnet-50
ID: 85	**Kaddour GHERFI,** Yazid LAIB dit leksir, Hocine BENDJAMA
	Suspect person localization using SVM of thermal vision image
ID: 78	**Djazila Souhila KORTI,** Foued DERRAZ, Zohra SLIMANE, Kheira LAKHDARI
	Enhanced approach for on-road obstacles detection using level-Set-YOLOv3 combination

Room 3: Control and system

Session chairs: Samir LADACI, Salim ZIANI

ID: 16	**Abdelghafour HERIZI,** Riyadh ROUABHI, Soufiane KRIM, Elkhier HACHI.
	Hybrid control using fuzzy sliding mode control of doubly fed induction machine
ID: 96	**Mohammed MEHIDI**
	Drone hand gesture control
ID: 9	**Amel BOULIFA,** Kamel GUESMI, Khansa BDIRINA
	Enhanced observed predictive control for linear systems
ID: 109	**Raid ZAIRI,** Salah SALMI
	Contribution to induction motor control for electric traction based on intelligent techniques
ID: 74	**Abdeslem KHELLOUFI,** Bilal SARI, Seif Eddine CHOUABA
	Stability enhancement of a single machine infinite bus system using H-infinity control
ID: 25	**Mendaz KHEIRA,** Amine ATTOU, Yamina BENHADDA, Houria BOUNOUA
	Effect of defective NPC three level inverter on speed artificial neural network control of Induction motor
ID: 29	**Saddam hocine DERROUAOUI,** Yasser BOUZID, Mohamed GUIATNI
	Reconfigurable multirotor control using fractional-Order P $I^{\lambda}D^{\mu}$ controller in the presence of uncertain geometric parameters
ID: 108	**Walid BENSALMI,** BELHANI Ahmed
	Design, simulation, sizing and optimization of hybrid renewable energy systems PV/Wind/Battery using PSO algorithm
ID: 42	**Adel DAHDOUH,** Lakhdar MAZOUZ, Brahim Elkhalil YOUCEF
	Performance enhancing of 3-phase UPQC using feedback linearisation based DPC Technique For Power Quality Improvement

Room 4: Micro and Nanoelectronics

Session chairs: Louardi REMACHE, Salima BENKARA

ID: 69	Ben kaci ZEDEK**, Hatem DJEDJIGA**, Mohamed MEGHERBI, Mohammed Said BELKAID
	Investigation of structural and optical properties of mixed phase nanoparticles titania synthesized by simple sol gel process
ID: 35	**Ahlem KOLLI,** Nacir GUECHI
	Pressure effect on structural, electronic and magnetic properties of the MAs (M = Cr, Mn) binary compounds: A first-principles study
ID: 15	**Asma KADRI,** Soumia BAHLOULI, Said HIADSI, Mokhtar ELCHIKH.
	Theoretical Investigation of Properties of Semiconductors Materials Based Rare Earth
ID: 37	**Salah Eddine Chouaib REFAS,** A.BOUAZZA, Y.BELHADJI, R.OTHMANI
	Influence of temperature and pressure on the atoms ejected path during thin films deposition

ID: 105	**Hocine BAHRI,** Souheil MOUETSI, Abdsselam HOCINI, Sven INGEBRANDT, Vivek PACHAURI, Hocine BEN SLAH
	A high-sensitivity biosensor based on metal–insulator–metal and rectangular resonator for biochemical detection

17h00 End of the first day.

Thursday 9 December 2021

9h30 – 10h30: Keynote Talk III

Reconfigurable antennas for multimode mobile handsets for 5G and beyond

Pr. Raed ABD-ALHAMEED
University of Bradford, UK

10h30 – 11h00 Coffee break

11h00 - 12h00: Oral session

Room 1: Telecommunication

Session chairs: Djamel KHEDROUCHE, Mounir BELATTAR

ID: 27	**Ahmed BELHANI,** Soumeya BOUMADJEN, Imène DJEBLI
	SDR based design of a system for meteorological image acquisition through NOAA satellite
ID: 70	**Hocine MERAH,** Belkacem MECHERI, Khaled TAHKOUBIT
	Energy efficiency comparison of IICM and clipping using real power amplifier
ID: 56	**Oulfa LAOUAR,** Nadir DEROUICHE, Imed AMAMRA
	Performance Comparison between Sum-Product and Bit-Flipping decoding Algorithms of Gallager's Construction for regular LDPC Convolutional Codes
ID: 61	**Seyf El-Islam DAIRA,** Mohamed LASHAB
	A compact circular Microstrip monopole antenna with rotated t-shaped slots and parasitic elements for UWB applications

Room 2: Artificial Intelligence

Session chairs: Sofiane BOUOUDEN, Salim ZIANI

ID: 123	**Fares ABDELHAKIM,** Abderrahim Fayçal MEGRI, Abdallah MERAOUMIA
	Enhancing Multimodal Biometric Frameworks Using Fuzzy Fusion at Matching Score Levels
ID: 48	**Chouaib SOUAIDIA,** Tawfik THELAIDJIA, Salah CHENIKHER
	Condition classification for bearing fault based on machine learning using GUI
ID: 101	**Samira ABDERREZAK,** Abdelhabib BOUROUIS
	Novel approach to estimate remaining useful life for condition based maintenance

ID: 3	**Hicham Talib BETAOUAF,** Hacene Rabab BOUKLI
	University Course and Examination Timetables Scheduling using a Multi-Agents System
ID: 87	**Mohammed BELKHEIR,** Mehdi ROUISSAT, Hicham Sid Ahmed BELKHIRA, Mohamed Achraf BOUKHOBZA, Mohamed Salim ABDOUN
	A new lightweight approach to mitigate the version number attack in RPL-based IoT networks

Room 3: Control and system

Session chairs: Samir LADACI, Ahmed BELHANI

ID: 121	**Bennour HACHEM,** Abderrahim Faycal MEGRI, Houria BAYARASSOU
	Supervisory Control for a robot manipulators using fuzzy interval
ID: 114	**Akram GHEDIRI,** Kheireddine LAMAMRA, Abdelaziz AIT KAKI
	Linear Quadratic-Based Computed-Torque Control of an Actuated Pendulum with Friction
ID: 10	**Khansa BDIRINA,** Kamel GUESMI, Lenda BELKACEMI, Djihad ELOTTRI
	Enhanced nonlinear sliding mode control
ID: 65	**Lakhdar DJAGHDALI**
	Torque Ripple Reduction of Induction Machine A Comparison between Two Approaches DTC-SVM
ID: 73	**Abdallah CHANANE,** Messaoud BELAZZOUG
	Novel approach for a ladder network model of the transformer winding high-frequency parameters identification based on FRA data

Room 4: Micro and Nanoelectronics

Session chairs: Abdesselam HOCINI, Hamza LIDJICI

ID: 83	**Salima BENKARA,** Nassima SEGHAIRI, Seddik BOUABIDA, Houda GHAMRI
	Influence of Synthesis Conditions and Al doping, on structural and optical properties of ZnO:SnO_2 thin film
ID: 107	**Kenza KAMLI,** HADEF Zakaria
	Tin disulphide properties optimisation for solar cells applications
ID: 45	**Lila MOKHTARI,** Hadjira BADAOUI, Mehadji ABRI, Bachir RAHMI, Farah LALLAM, Abdelbasset MOUNGAR
	All optical gate based on photonic crystal ring resonator
ID: 89	**Radouane DAIRA,** Madiha ZEROUALI, Bouzid BOUDJEMA
	Structural, electrical and optical properties of Fe-doped CuO deposited by spray pyrolysis technique
ID: 12	**Yamina BENHADDA,** Mokhtaria DERKAOUI, Kheira MENDAZ, Hayet KHARBOUCH
	Design and analyze of a monolithic square spiral planar micro-transformer

12h00-12h30: Speech session and closing ceremony

12h30 Lunch

End of the second day

Telecommunications and antennas

ISBN: 978-9931-9728-1-5

Indoor Communications scenario In The Electrical Engineering Departement Building -University of Skikda- Based on RSS, Frequency and Path Losses

L. Djouablia[1,2]; N.H. Alioua[1]; I.Bourahla[1]; A.Zermane[2,3]
[1]Faculty of technology, University 20 Aout 1955 - Skikda, Algeria.
[2]Laboratory LHS, Department of Electronic, Engineering sciences Faculty. University Constantine 1, Algeria.
[3] University of Batna2, Technology department, Algeria.
ln_djouablia@live.fr

Abstract— **This research work outlines a study of indoor propagation environment. The electrical engineering department building at SKIKDA university was taken as a model; it was designed and executed using the properties provided by the indoor simulation software "Wireless Insite". The study was performed at 2.4GHz, 5.2GHz and 30 GHz. Indoor propagation models must take into account obstructions inside the targeted building, the locations of access points, in addition to reflection, diffraction and scattering. However, study of the characteristics of multipath propagation based on parameters of delay propagation, path losses and received power RSS was carried out. Effects of building materials were taken into account by calculating the actual values of permeability and conductivity of each material. The results obtained for different parameters and cases show that the positioning of sensors, thickness and type of material of the walls, play a major role in the selection of the coverage range for indoor communication, another fundamental consideration was related to the specification of the transmitter antenna such as frequency, polarization, selection of an appropriate E and H plane and orientation of the antenna.**

Keywords—***Wireless insite software; RSS; Path losses, spread delay, frequency.***

I. INTRODUCTION

Wireless communication is reaching new heights due to its enormous business benefits. Wireless technology can provide network speed, flexibility and efficiency. It has become a powerful tool for the tech-savvy generation (new term for modern technology) because it can promote information sharing and increase productivity.

The explosive growth of wireless systems coupled with the proliferation of laptops and palmtops suggests a bright future for these networks, both as stand-alone systems and as part of the larger network infrastructure. However, many technical challenges remain robust, providing the performance needed in the design of wireless networks to support emerging applications [1].

One of the advantages of wireless technology is its ability to pass through obstacles (doors, walls, etc.) and cover the entire building with a stable signal. Indoor communications concerns all information or display media set up inside a building, which happens inside airports, stations, shopping centers or others.

The mobile propagation channel is particularly characterized by a strong influence of the surrounding clutter and objects around the transmitters and receivers in a wireless system. These obstructions primarily determine how the signal propagates along a specific path and therefore should not be underestimated. Thus, it is very important to identify the characteristics of these obstructions and their distribution, in order to account for these changes and variations in field strength. Indeed, the interior wireless design is very specific to the building; that is, each building has its unique characteristics which make the radio propagation different, and therefore the expected performance of the system will vary. However, an accuracy evaluation of the technology available to design an indoor wireless system should not be overlooked. For example, cellular operators may aim to be at the forefront of the latest technology, but this does not necessarily guarantee that system performance has been fully optimized. The use of

advanced technology does not guarantee that the indoor cellular system is well designed, but nevertheless represents a valuable infrastructure from which the performance of the system can be improved and optimized [2].
Wireless InSite is a commercial software used to predict channel parameters within indoor and outdoor environments. The software has been validated at 900 MHz and 1800 MHz [3] and at 2.4 GHz and 5 GHz [4,5]. Wireless InSite considers the effects of material electrical properties. It also allows the user to configure waveform, antenna types and the properties of the transmitter and receivers. In this study, a sinusoidal waveform is used for simulation at 2.4, 5.2 and 30 GHz of different access points (AP) indoor the electrical departement of university of Skikda, to seek the optimal AP sites. This paper aims to investigate the accuracy of results when applying real properties of concrete and wood component of the building using Wireless InSite.

II. THEORETICAL ASPECT AND DESIGN OF BUILDING

A 3D simulation model of the target building (the electrical engineering department of the University of Skikda), was designed and executed using the properties provided by the Wireless Insite software. The building has a ground floor and three floors with a height of 3 m for each floor and two auditoriums outside. We are going to take the building's ground floor as a target. This level includes four (4) offices, seven (7) classrooms, an archive room and a toilet as shown in figure.1. Construction materials include brick walls, ceiling, partitions between floors which are concrete, glass windows and wooden doors, with thicknesses (0.28, 0.30, 0.003, 0.045m) respectively. We will install transmitting antennas and receiving antennas in specific points of the level, which we will discuss later. We considered the sensitivity and effect of different building construction materials on wave propagation and telecommunications traffic indoors [6].

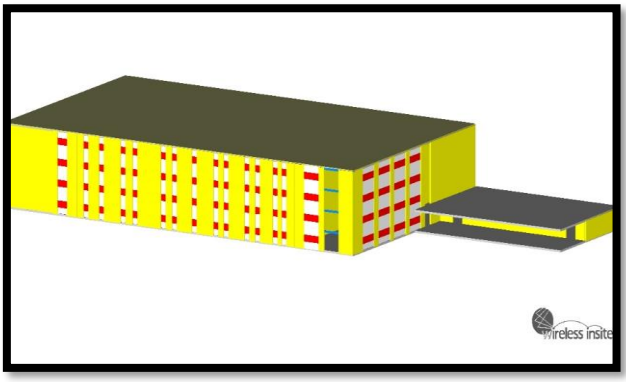

Figure 1: 3D view of the proposed target

An analytical calculation of the parameters η (permittivity) and σ (conductivity) of each constituent material must be carried out, or via the graphical interface GUI offered by Matlab (figure.2).

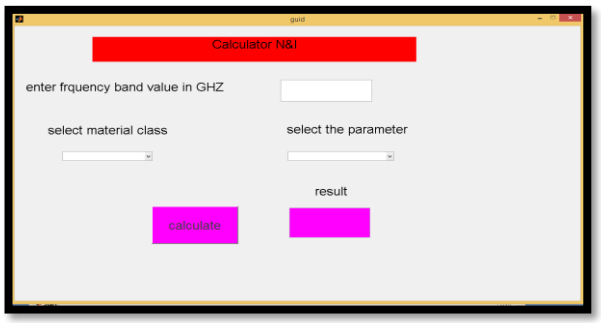

Figure 2: GUI window

In order to improve the accuracy of indoor propagation, valuable efforts have been made to study the effect of different building materials on different frequency bands, as reported in [7]. Additionally, wall measurements have been used to obtain an accurate characterization of a particular wall material in a target environment [6]. Two general representations followed by the WI software are necessary for this mission and known as the relative permittivity ε and conductivity σ. Relative permittivity represents the reflection of material influences on the electric field, which strongly depends on the selected frequency [8]. In most ray tracing simulators, the values given for different materials are approximate values which do not represent the actual measurement in a real environment and result in an inaccurate prediction of simulation results [9-10]. Each characteristic of matter can be represented by equation [7]:

$$\varepsilon = \eta' - \eta'' \quad (1)$$

where η' and η'' represent the real part and the imaginary part of the relative permittivity, respectively. For conductivity, it describes the imaginary part of relative permittivity. The conversion between them can be clarified in equation (2).

$$\sigma = \eta''\omega \quad (2)$$

ω is the angular frequency of the transmission carrier frequency in radians / sec. Accordingly, ε can be rewritten on the basis of a subsequent equation and as shown by equation (3) [11]:

$$\varepsilon = \eta' - j\frac{\sigma}{\omega} \quad (3)$$

and

$$\eta'' = 17.98\ \frac{\sigma}{f} \quad (4)$$

The values of σ and η' as a function of the frequency can be estimated, using the recommendations of the International Telecommunications Union (ITU) [12]:

$$\sigma = cf^d \quad (5)$$
$$\eta' = af^b \quad (6)$$

where a, b, c et d are constants of subsequent equations supplied by ITU for use when dealing with frequency-dependent materials problems.
Tables 1 summarize calculations results of the target materials constituent parameters.

Table 1 : Calculated values of conductivity σ and of relative permittivity η' of different target materials at 2.4 GHz. And 5.2 GHz.

Material	Material Thickness (m)	f= 2.4 GHz		f= 5.2 GHz	
		η'	σ	η'	σ
Concrete	0.30	5.31	0.00127	5.31	0.00238
Brick	0.28	3.75	0.038	3.75	0.038
Wood	0.045	1.99	0.053	1.99	0.12
glass	0.003	6.27	0.65	6.27	1.65

III. SIMULATION RESULTS AND DISCUSSIONS

In order to get accurate results, we created an omnidirectional antennas profile of Tx (transmitters) and Rx (receivers). Gain was fixed for both Tx and Rx at 2 dBi with vertical polarization, and an effective bandwidth of 20 MHz. A waveform profile must be formed, its properties which are the values of: carrier frequency, bandwidth and phase, are set in our case were respectively at 2.4 GHz, 20 MHz and zero. The creation and distribution of AP (access points) within the target must be chosen carefully. In our case, a total of seventeen (17) points were distributed in the middle of each room on the ground floor of the department. In addition, two points were distributed as waypoints along the corridors with a separation distance of 8 m and two points in the middle of the two amphitheatres with a height of 2 m above the ground, the transmission properties are specified and shown in figure.3.

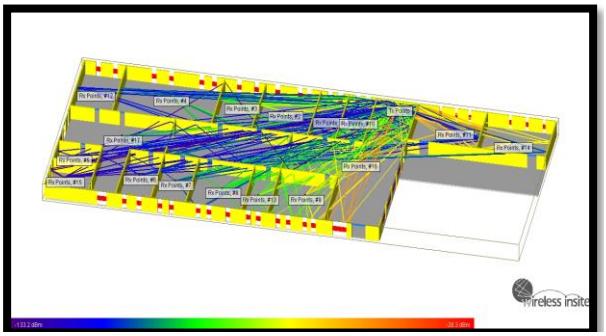

Figure 3: Signal propagation of 1 Tx and 17 Rx at 2.4GHz

The most important properties to consider are: power and transmission input height, which are 30 dBm and 2.8 m, respectively.
RSS, is the strength of a signal measured at the receiving antenna, it may give a better location approximation than proximity [13]:

$$RSS = \sum_{K=1}^{L} \overline{\left|\beta_k^d(t)\right|^2} \quad (7)$$

where β (t) is the arrival trajectories amplitude at a certain time, d is the distance and L is the number of trajectories between the transmitter and the receiver.
Tables 2 summarize results given by WI of RSS, number of propagations and delay spread of the received signal in the case of 1Tx and 17Rx.

Table 2**:** Propagation simulation results at 2.4 GHz with 1Tx and 17 Rx.

Tx	Nomber of propagation	RSS (dBm)	Average arrival time (s)	delay spread (s)
Rx1	10	-34.02	$3.515000e^{-008}$	$3.204200e^{-008}$
Rx2	10	-50.57	$6.941500e^{-008}$	$4.896000e^{-008}$
Rx3	10	-61.37	$1.143800e^{-007}$	$4.354600e^{-008}$
Rx4	10	-69.98	$1.256800e^{-007}$	$2.130200e^{-008}$
Rx5	10	-76.83	$2.211400e^{-007}$	$2.786200e^{-008}$
Rx6	10	-87.08	$2.178600e^{-007}$	$1.653700e^{-008}$
Rx7	9	-99.97	$2.685600e^{-007}$	$5.063700e^{-008}$
Rx8	3	-101.61	$2.720500e^{-007}$	$2.211200e^{-009}$
Rx9	8	-104.85	$2.404100e^{-007}$	$1.064300e^{-008}$
Rx10	9	-98.64	$2.213900e^{-007}$	$2.443000e^{-008}$
Rx11	10	-70.32	$1.680200e^{-007}$	$1.710900e^{-008}$
Rx12	10	-71.25	$1.553100e^{-007}$	$1.615600e^{-008}$
Rx13	10	-47.13	$1.307200e^{-007}$	$8.297300e^{-009}$
Rx14	10	-34.96	$4.310400e^{-008}$	$1.294700e^{-008}$
Rx15	10	-51.44	$1.029100e^{-007}$	$1.658400e^{-008}$
Rx16	10	-33.77	$6.514700e^{-008}$	$1.680600e^{-008}$
Rx17	10	-79.52	$2.293600e^{-007}$	$5.473800e^{-008}$

In another case we have placed three Tx in specific places. Keeping the 17 Rx in their locations, we operate each Tx separately to distinguish the best positions which give relatively optimal powers as shown in figure.4.

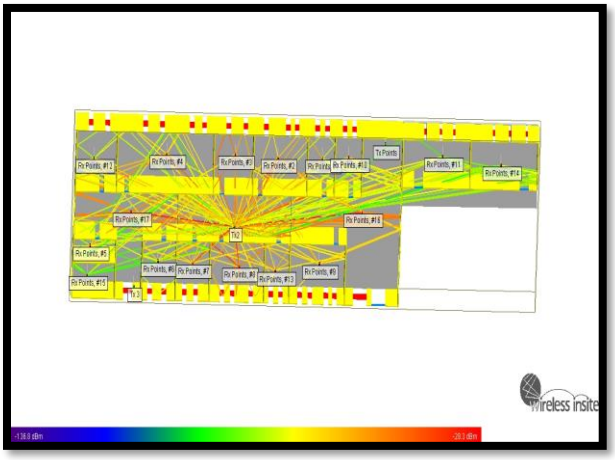

Figure 4: Signal propagation of 3 Tx and 17 Rx at 2.4GHz

Figure 5 and 6 show RSS total power and Tx2 trajectory losses plots versus distance with 3Tx at 2.4 GHz respectively. It can be observed that Tx2 position offers less losses for most of Rx compared to Tx1 and Tx3, this is due to the architectural nature of the targeted building, because the ground floor has a wide corridor open to all the teaching rooms, there are fewer obstacles for Tx2 than Tx1 and Tx3.

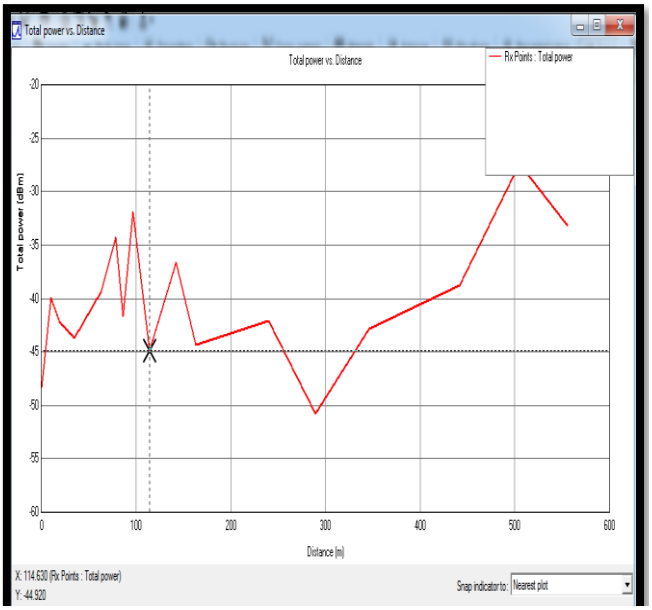

Figure 5: RSS total power plot versus distance for 3Tx at 2.4 GHz

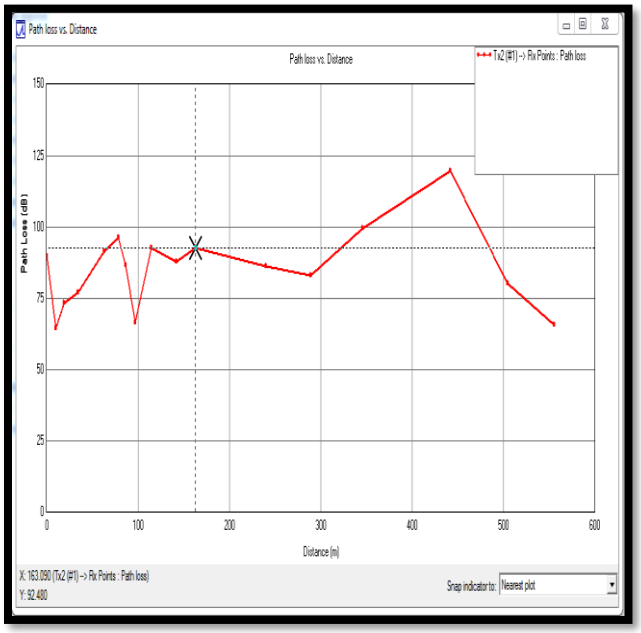

Figure 6: Tx2 trajectory losses for Tx2 at 2.4GHz

Some results obtained for different cases are summarized in Table 3. It can be confirmed that Tx1 position offers relatively high, but Tx2 position offers less path losses. Therefore, Tx3 position does not provide better coverage of all Rx. However, the same remarks were observed if we change transmission frequencies to 5.2 GHz and increasing to 30 GHz, keeping the same circumstances.

Table 3**:** Comparison of results for different cases at 2.4 GHz.

Tx		Rx	RSS (dBm)	Path losses (dB)
1Tx		Rx1	-34.02	87.82
		Rx2	-50.57	103.83
3Tx	Tx1	Rx1	- 48.1	79.37
		Rx2		97.12
	Tx2	Rx1		91.52
		Rx2		64.50
	Tx3	Rx1	-40.01	127.61
		Rx2		111.84

Table 4 summarize simulation results for received power RSS, for different transmission frequencies ranging from 2.4 GHz, 5.2 GHz and up to 30 GHz. It has been observed that the value of the path loss increases with increasing both frequencies and separation distance. For example, at 30 GHz, path loss was 134 dB. On the other hand, RSS decreases with the increase in frequency in our case.

Table 4**:** RSS and path losses comparison between 2.4 GHz frequencies; 5.2 GHz; 30 GHz.

Rx	**RSS (dBm)**			**Path losses (dB)**		
	2.4GHz	5.2GHz	30GHz	2.4GHz	5.2GHz	30GHz
Rx1	-34.02	-59.15	-72.93	87.82	88.75	102.21
Rx2	-50.57	-80.21	-90.16	103.83	107.41	127.95
Rx3	-61.37	-83.64	-103.93	117.29	116.35	134.31

IV. CONCLUSION

Through this research work, we investigated the field of indoor communications by doing a parametric study of the communications traffic inside the department of electrical engineering at university of Skikda, using performance of Wireless Insite simulator. It is important to mention that the thickness and type of wall material play a major role in the selection of the coverage range for indoor communication, and the degree of wave penetration as well as the location of the sensors. Another substantive consideration related to the specification of the transmitter antenna such as polarization, selection of the appropriate E and H plane and antenna orientation should be taken into account. The propagation characteristics of different radio frequencies such as 2.4 GHz, 5.2 GHz and 30 GHz were studied and compared in terms of path losses and the power received for indoor environment of the ground floor of the building targeted department. It was concluded that in the same millimeter band there is a smaller delay deviation if increasing frequency, but relatively low powers and high path losses, which will result in a preferable ability to improve the quality of internal communication by reducing the frequency. On the other hand, these results can add significant knowledge in the design of real buildings, including the selection of material types to achieve high performance of 5G.

V. REFERENCES

[1] Andrea Goldsmith, ‘’Wireless Communication ‘’, © Cambridge University Press, 2005.

[2] Alejandro Aragón-Zavala,”indoor Wireless Communications from Theory to Implementation”, Wiley, -09-08, 2017.

[3] Medeđović, P.; Veletić, M.; Blagojević, Ž. Wireless insite software verification via analysis and comparison of simulation and measurement results. Proceedings of the 35th International Convention MIPRO, Opatija, Croatian, 21–25; pp. 776–781, May 2012.

[4] Obeidat, H.A.; Obeidat, O.A.; Mosleh, M.F.; Abdullah, A.A.; Abd-Alhameed, R.A. Verifying Received Power Predictions of Wireless InSite Software in Indoor Environments at WLAN Frequencies. *Appl. Comput. Electromagn. Soc. J.* **2020**, *35*, 1119–1126, 2020.

[5] Dama, Y.A.S.; Abd-Alhameed, R.A.; Salazar-Quinonez, F.; Zhou, D.; Jones, S.M.R.; Gao, S. MIMO Indoor Propagation Prediction Using 3D Shoot-and-Bounce Ray (SBR) Tracing Technique for 2.4 GHz and 5 GHz. In Proceedings of the 5th European Conference on Antennas and Propagation (EUCAP), Rome, Italy, 11–15 April 2011; IEEE: New York, NY, USA; pp. 1655–1658, 2011.

[6] N. Qasem, “Enhancing Wireless communication system performance through modified indoor environments,” *Ph.D. dissertation*, Loughborough University Institutional Repository, 2014.

[7] D. Ferreira, I. Cui˜nas, R. F. Caldeirinha, and T. R. Fernandes, “A review on the electromagnetic characterization of building materials at micro-and millimeter wave frequencies,” In The 8th European Conference on Antennas and Propagation (EuCAP 2014). IEEE, pp. 145–149, 2014.

[8] Q. Liao, “Ray-tracing based analysis of channel characteristics and capacity improvement capabilities of spatial multiplexing and beam forming at 15 and 28 GHz,” Master thesis, Department of Electrical and Information Technology, Lund University 2016.

[9] S. Hur, S. Baek, B. Kim, J. Park, A. F. Molisch, K. Haneda, and M. Peter, “28 GHz channel modeling using 3d ray-tracing in urban environments,” In 2015 9th European Conference on Antennas and Propagation (EuCAP). IEEE, pp. 1–5, 2015.

[10] S. Hur, S. Baek, B. Kim, Y. Chang, A. F. Molisch, T. S. Rappaport, K. Haneda, and J. Park, “Proposal on millimeter-wave channel modeling for 5G cellular system,” IEEE Journal of Selected Topics in Signal Processing, vol. 10, no. 3, pp. 454–469, 2016.

[11] “Wireless InSite, Reference Manual, Version 2.6.3, REMCOM Inc., 315 S. Allen St., Suite 416 State College, PA 16801, November 2012., Jan. 2009.

[12] Recommendation ITU-R P.2040-1 “Effects of building materials and structures on radio wave propagation above about 100 MHz,”, pp. 22–23, July 2015.

[13] Alan Bensky,Short-range Wireless Communication: Fundamentals of Rf System Design and application ; 2019.

Design and Simulation of a Microstrip Band Pass Filter for C Band

Chaabane SOUMALI
Department of Electrical Engineering
University of Docteur Yahia Fares
Medea , Algeria
Soumali.chaabane@univ-medea.dz

Mounir BELATTAR
Department of Electrical Engineering
University of 20 August 1955
Skikda, Algeria.
belattar@univ-skikda.dz

***Abstract* - The objective of this work is to study and design a band pass filter based on microstrip technology for application in equipment of the fifth generation (5G) of cell phones in the C band. The presented process includes the estimation of filter parameters using analytical formulas, finding the corresponding low-pass prototype structure impedance and frequency scaling is performed to achieve a band pass filter. The pass-band filter is then implemented using end-coupled microstrip lines, the lengths of these lines and the gaps between them are obtained by using analytical formulas. The structure of this filter is simulated using Ansoft designer SV2.2 simulator. Good agreement between theoretical and simulated results is observed.**

Index Terms – Band pass filter, microstrip, end-coupled.

I. INTRODUCTION

Microwave filters are widely used in communication systems whose function is the frequency discrimination of the signal in order to select a frequency band containing the useful signal and to attenuate the frequencies around this band. Microwave filters can be classified into two categories localized element-based filters and distributed element-based filters. Localized elements are discrete elements which can be coils or capacitors while distributed elements are based on microstrip transmission lines and use lengths and widths to create their inductive or capacitive values [1].

The majority of communication systems operate on a frequency band therefore these systems incorporate a band pass filter usually just after the low noise amplifier as shown in the fig.1[2]. In this work the design of an end-coupled band-pass filter realized on microstrip technology is detailed and presented. The presented process begin by specifying the characteristics of the filter then the filter parameters estimation is done by using analytical formulas and finally the implementation of the filter is realized using end-coupled microstrip lines where the lengths and gaps are obtained from the filter parameters already estimated. The structure obtained of the filter on microstrip technology is simulated using Ansoft designer SV2 simulator [3], Scattering parameters of the filter are carried out.

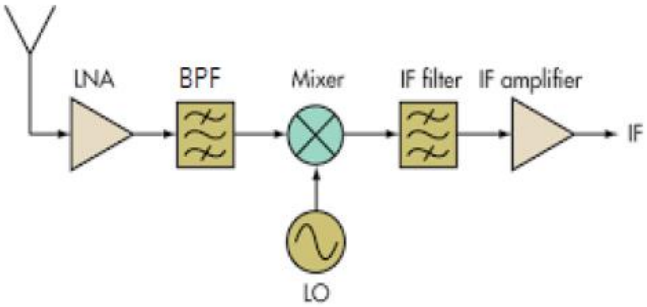

Fig. 1 Block Diagram of RF Receiver system

II. MICROSTRIP FILTER DESIGN STEPS

The design of microwave filters based on microstrip technology goes through various stages. The first is to specify the characteristics of the filter, then we establish the prototype of the low-pass filter then a translation to the desired frequencies and impedances is made and finally the lumped-element components replaced with distributed circuit elements for implementation at microwave frequencies.

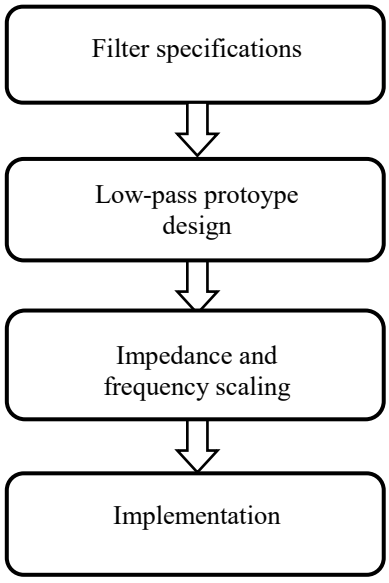

Fig. 2 Microstrip filter design steps.

A. *Specifications*

In this work we propose to study and simulate a band pass filter in microstrip technology for use in equipment of the fifth generation of cell phones, the specifications of which are as follows.

TABLE I
PARAMETERS OF THE FILTER

Parameter	Value
Order of the filter	3
Passband ripple	0.1 dB
Center Frequency	6 GHz
Operating Range	5.88-6.12 GHz
Source Impedance	50 Ω
Dielectric Constant	10.8
Thickness of substrate	1.27

B. *Low pass filter prototype values*

The first step is the design of a low-pass filter prototype with source impedance equal to 1 ohm and a cut off frequency equal to 1 rad/sec. the elements values are tabulated [4]

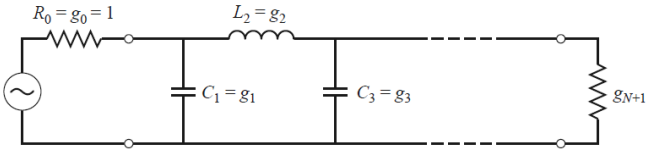

Fig. 3 Low-pass filter prototype

TABLE II
ELEMENT VALUES FOR EQUAL-RIPPLE LOW-PASS FILTER PROTOTYPES

n	g_1	g_2	g_3	g_4	g_5	g_6	g_7	g_8	g_9	g_{10}
1	0.3052	1.0								
2	0.8431	0.6220	1.3554							
3	1.0316	1.1474	1.0316	1.0						
4	1.1088	1.3062	1.7704	0.8181	1.3554					
5	1.1468	1.3712	1.9750	1.3712	1.1468	1.0				
6	1.1681	1.4040	2.0562	1.5171	1.9029	0.8618	1.3554			
7	1.1812	1.4228	2.0967	1.5734	2.0967	1.4228	1.1812	1.0		
8	1.1898	1.4346	2.1199	1.6010	2.1700	1.5641	1.9445	0.8778	1.3554	
9	1.1957	1.4426	2.1346	1.6167	2.2054	1.6167	2.1346	1.4426	1.1957	1.0

Then the values of our prototype will be:

TABLE III
ELEMENT VALUES FOR 3 ORDER FILTER PROTOTYPE

Parameter	Value	Element
g_1	1.0316	C_1
g_2	1.1474	L_2
g_3	1.0316	C_3
g_4	1	Z_L

C. *Scaling and conversion*

Once the element values are defined the scaling of impedance and frequency is realized to obtain the lumped model of the filter. The new elements values are determined by applying the next formulas [1].

$$L_k^{'} = \frac{R_0 L_k}{w_c} \quad (1)$$

$$C_k^{'} = \frac{C_k}{R_0 w_c} \quad (2)$$

The element values obtained of the low-pass prototype filter are summarized in the table.

TABLE IV
ELEMENT VALUES OF LOW-PASS FILTER PROTOTYPE

Parameter	Value
C_1	0.5475 pF
L_2	1.5225 nH
C_3	0. 5475 pF
Z_L	50 Ω

Once the lumped elements of the low-pass filter prototype are obtained, then the transformation to band-pass filter is done easily, by replacing the inductive element by a series LC resonant circuit and the capacitive element by parallel LC resonant circuit [4].

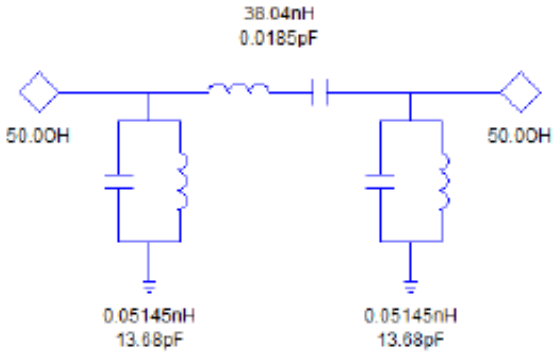

Fig. 4 Conversion of Low-Pass Filter to Band-Pass Filter

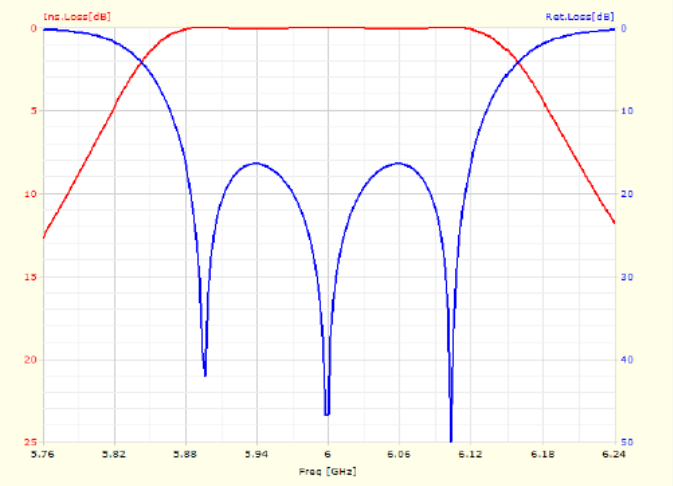

Fig. 5 Filter Design Wizard (FDW) Simulated result for insertion loss(S_{11}) and return loss(S_{21}) response

D. Implementation

The lumped-element filter generally work well at low frequencies, but two problems arise at higher RF and microwave frequencies. First, lumped-element inductors and capacitors are generally available only for a limited range of values, and can be difficult to implement at microwave frequencies. For these reasons the distributed element filter are suitable at high frequencies [1]. End-coupled microstrip lines are chosen to realize this filter fig.6

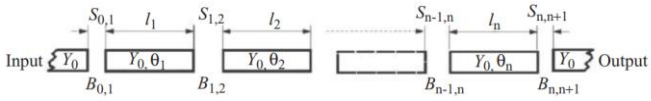

Fig. 6 General configuration of end-coupled microstrip band-pass filter.

For microstrip implementation, we use a substrate with a relative dielectric constant εr = 10.8 and a thickness h = 1.27 mm. The line width for microstrip half wavelength resonators is also chosen as W = 1.1 mm, which gives characteristic impedance Z_0 = 50 Ω on the substrate.

The $J_{j,j+1}$ are the characteristic admittances of J inverters and Y_0 is the characteristic admittance of the microstrip line.

The filter under consideration operates like the shunt-resonator type of filter whose general design equations are given as follows [4].

$$\frac{J_{0.1}}{Y_0} = \sqrt{\frac{\pi FBW}{2 g_0 g_1}} \tag{3}$$

Where g_o, g_1. . . g_n are the element of a ladder-type low-pass prototype with a normalized cutoff Ω_c=1, and FBW is the fractional bandwidth of band-pass filter.

For j=1 to n-1, we have

$$\frac{J_{j,j+1}}{Y_0} = \frac{\pi FBW}{2} \frac{1}{\sqrt{g_j g_{j+1}}} \tag{4}$$

$$\frac{J_{n,n+1}}{Y_0} = \sqrt{\frac{\pi FBW}{2 g_n g_{n+1}}} \tag{5}$$

Assuming the capacitive gaps act as perfect, series-capacitance discontinuities of susceptance $B_{j,j+1}$ given by

$$\frac{B_{j,j+1}}{Y_0} = \frac{\frac{J_{j,j+1}}{Y_0}}{1-(\frac{J_{j,j+1}}{Y_0})^2} \tag{6}$$

And

$$\theta_j = \pi - \frac{1}{2}\left[\tan^{-1}(\frac{2B_{j-1,j}}{Y_0}) + \tan^{-1}(\frac{2B_{j,j+1}}{Y_0})\right] \tag{7}$$

Where the $B_{j,j+1}$ and θ_j are evaluated at f_0.

By referring to the equivalent circuit of microstrip gap [4], the coupling gaps $s_{j,j+1}$ of the microstrip end-coupled resonator filter can be determined as to obtain the series capacitances that satisfy

$$C_g^{j,j+1} = \frac{B_{j,j+1}}{\omega_0} \tag{8}$$

Because the shunt capacitances C_p^{jj+1} are associated with the series capacitances C_g^{jj+1}, as defined in the equivalent circuit of microstrip gap, they are also determined once $C_g^{j,j+1}$ are solved for the required

The physical lengths of resonators are given by

$$l_j = \frac{\lambda g_0}{2\pi}\theta_j - \Delta_j^{e1} - \Delta_j^{e2} \tag{9}$$

Where $\Delta_j^{e1,e2}$ are the effective lengths of the shunt capacitances on the both ends of resonator j

$$\Delta_j^{e1} = \frac{\omega_0 C_P^{j-1,j}}{Y_0}\frac{\lambda g_0}{2\pi} \tag{10}$$

$$\Delta_j^{e2} = \frac{\omega_0 C_P^{j,j+1}}{Y_0} \frac{\lambda g_0}{2\pi} \qquad (11)$$

So the results are summarized in the next table.

TABLE V
MICROSTRIP LINE DIMENSIONS

Parameter	Value (mm)
h	1.27
W	1.1
l_1	8. 148
l_2	8.399
l_3	8.148
$S_{0,1}$	0.057
$S_{1,2}$	0.801
$S_{2,3}$	0.801
$S_{3,4}$	0.057

III. ANSOFT DESIGNER SIMULATION RESULTS

Ansoft designer SV2.2 is used to realize a physical band-pass filter using microstrip end-coupled lines where the dimensions are already calculated in last section.

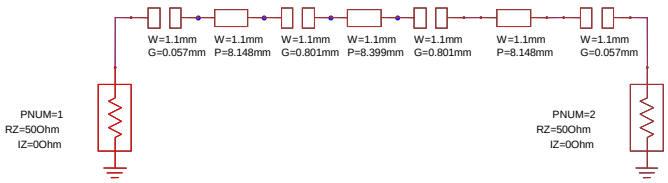

Fig. 7 Schematic of end-coupled micro strip band- pass filter

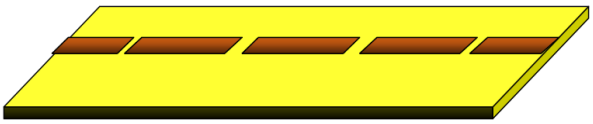

Fig. 8 Layout of end coupled microstrip band-pass filter.

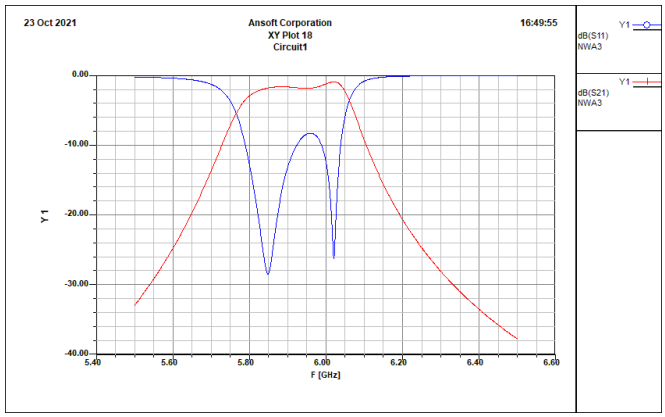

Fig. 9 Simulated Result for Insertion Loss(S_{11}) and Return Loss(S_{21}) Response of 3rd Order End-Coupled Microstrip Band Pass Filter

The simulated result for insertion loss and return loss response of 3rd order end-coupled microstrip band pass filter is shown in fig. 9. We observe that the insertion loss in the pass band is less than -2 dB and a return loss around -28 dB which are the characteristics of a good filter. However the filter design wizard simulated results as seen in fig.5 are -25 dB for return loss and -0.1dB for the insertion loss.

IV. CONCLUSION

A complete procedure to design a band-pass filter using Chebyshev low-pass filter approximation is reported. The procedure includes the filter specifications, finding the corresponding low-pass prototype filter, impedance and frequency scaling, transformation to get the structure of the band-pass filter and finally the implementation of the band-pass filter using end coupled microstrip lines. Then the structure of this filter is simulated using Ansoft designer V2.2. Obtained results seem good however a fabricated filter would be suitable to take some measure to validate the results.

REFERENCES

[1] D. M. Pozar, Microwave Engineering, United States of America: John Wiley & Sons, Inc., 2012.
[2] F. Gustrau, RF and Microwave Engineering, First ed., Chichester, UK: John Wiley & Sons Ltd., 2012.
[3] "Ansoft designer" SV2.2, Ansoft Corporation.
[4] Hong, J.-S., Microstrip Filters for RF/Microwave Applications, 2nd ed., Wiley, 2011.

About the Authors...

Chaabane SOUMALI He received the Ph.D degree in electronics from Batna University Algeria in 2018. His is currently an associate professor at the department of electrical engineering, university of Docteur Yahia Fares Medea Algeria. His research interests include microwaves, RF passive devices and wireless communication.

Mounir BELATTAR received the diploma of Engineer in Electronics in 1993 from the university Mentouri 1 of Constantine and the diploma of Magister in 1996 from the same university, and since 2012, he is assistant professor at the University 20 Août 1955 Skikda. Actually, he is the head of the master's telecommunication course, at the department of Electrical Engineering. His main research interests are non-uniform transmission lines, as broadband terminations, planar antennas, filters, and meta-materials.

A Magnetically Tunable Planar Band-stop Filter Using Ferrite Layer

Zermane Aziza

Department of common sciences and technologies, University Mustapha Benboulaid Batna2, Algeria.
Laboratory of High frequencies and Semiconductor (LHS), University Mentouri Constantine, Algeria

zermaneaziza@yahoo.fr

Djouablia Linda

Department of electrical engineering, University 20 Aout Skikda, Algeria.
Laboratory of High frequencies and Semiconductor (LHS), University Mentouri Constantine, Algeria

ln_djouablia@live.fr

Abstract **- A tunable metamaterial band-stop filter using magnetic material is presented in this paper with numerical results. Our filter is based on a 50 Ohms microstrip feed line, three metamaterial resonators and YIG layer. The feed is supplied with a variable magnetic bias in the range of 0-200KA/m, the central frequency of the filter varies from 10.10 GHz to 12.05GHz (up to 16% tuning) according to the applied magnetic bias, while achieving a maximum rejected bandwidth of 1.2 GHz.**

Index Terms -Microstrip filters, Metamaterial resonators, Tunable filters, YIG.

I. Introduction

Your goal is In recent years, tunable band-stop filters have been very useful to delete signal interference in receivers of frequency-tuned communications systems [1,2]. Several methods have been used to realize the tunability, micro electromecanical systems (MEMS) [3], BST varactor [4] and ferroelectric films [5]. Metamaterial resonators have been used in microwave filters, authors in [6,7] proposed the SRR (Split Ring Resonator) and CSRR (Complementary Split Ring Resonator) resonators.

In this work, the aim is to investigate in the design of a metamaterial microstrip band-stop filter with tunable properties. The proposed device is realized in microstrip technology with a YIG (Yttrium Iron Garnet) layer and metamaterial resonators (single-turn square planar resonator). The band-stop filter is simulated using the full wave commercial software HFSS. The obtained simulation results allow confirming the validity of the proposed tunable microstrip band-stop filter.

II. Design and Results with Alumina Substrate

Figure 1 shows the proposed metamaterial band-stop filter, it is composed of three single-turn square resonators and an adapted microstrip line. The metamaterial unit cell resonator used in this work was studied in Ref [8]. The proposed filter is in the microstrip technology based on Alumina substrate (Al_2O_3).

The resonators are located near the strip line to satisfy the excitation condition. They have the same dimensions and the same distance between them. The simplified electric equivalent circuit and the dimensions of the resonator are well detailed in [2].The used substrate have a relative permittivity close to 10, and thickness h=0.635mm.

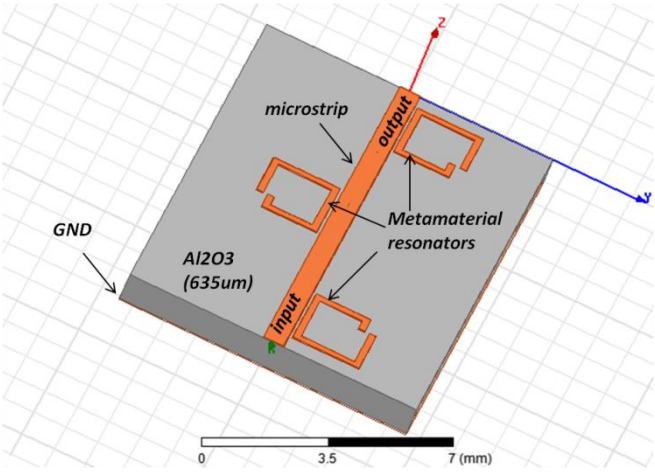

Fig. 1 Metamaterial microstrip band-stop filter.

The transmission coefficient of the proposed band-stop filter is presented in figure 2. The device has been analysed numerically using 3D finite element method based on the HFSS software.

The band-stop is centred around 9.80 GHz with a transmission level close to -20.09dB and a rejected band of 600MHz. This rejected band is three times wider than the rejected band obtained using a single resonator [2].

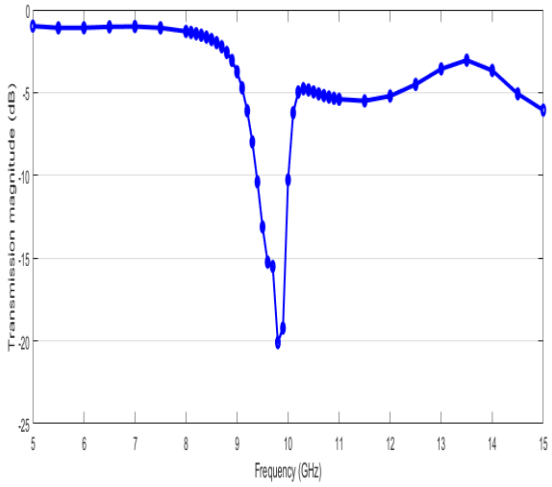

Fig. 2 Simulated transmission coefficient of the proposed band-stop filter.

III. Design and Results with YIG Substrate

In this part, by introducing Yttrium Iron Garnet (YIG) ferrite substrate into the previous structure (Figure 3), we propose and numerically demonstrate a magnetically tunable metamaterial microstrip band-stop filter.

The commercially available YIG has attractive microwave properties such as low loss tangent (tan $\delta \leq 2/10^{-4}$) at microwave frequencies and high dielectric strength. It has a relative dielectric permittivity close to 15, the saturation magnetization equal to 1780Gauss and a ferromagnetic resonance line with ΔH=20Oe. We suppose that the YIG is saturated and the internal bias field is uniform.

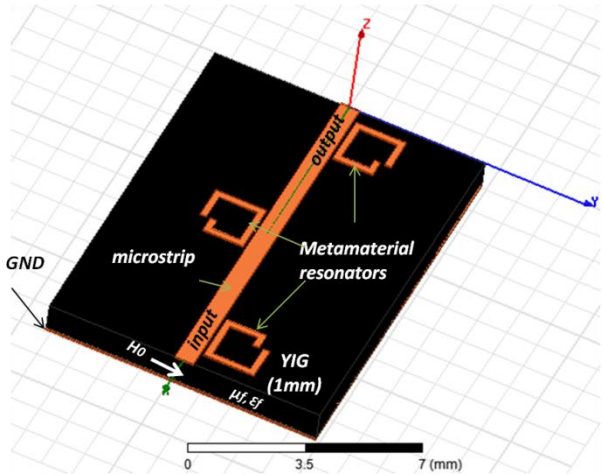

Fig. 3 Metamaterial microstrip band-stop filter over a YIG layer.

Based on the coordinate system shown in preceding figure, and according to the direction of the DC magnetic bias, the tensor permeability has the form of:

$$[[\overline{\overline{\mu_f}}]] = \begin{bmatrix} 1 & 0 & 0 \\ 0 & \mu_f & +jk \\ 0 & -jk & \mu_f \end{bmatrix} \quad (1)$$

Where:

$$\mu_f = 1 + \frac{\omega_0 \omega_M}{\omega_0^2 - \omega^2} \quad (2)$$

$$k = \frac{\omega \omega_M}{\omega_0^2 - \omega^2} \quad (3)$$

$\omega_M = \gamma \mu_0 M_s$, $\omega_0 = \gamma \mu_0 H_0$ and γ is the gyromagnetic ratio of the ferrite. μ_0 is the free space permeability. The damping factor is not taken into account.

Figure.4. shows a comparison of the results obtained for the stopband filter realized on Alumina substrate and the device realized on a YIG layer with a thickness h=1mm and without any bias field applied. We observe a sharper central frequency at 9.90GHz with better transmission levels, better and wider rejected band. The numerical results show a stopband, a central frequency around 10.10GHz with a transmission level of -25.04dB and a rejected band of 800MHz. The central frequency is greater than that the Alumina case. As the permittivity and the thickness are modified, the frequency is modified also.

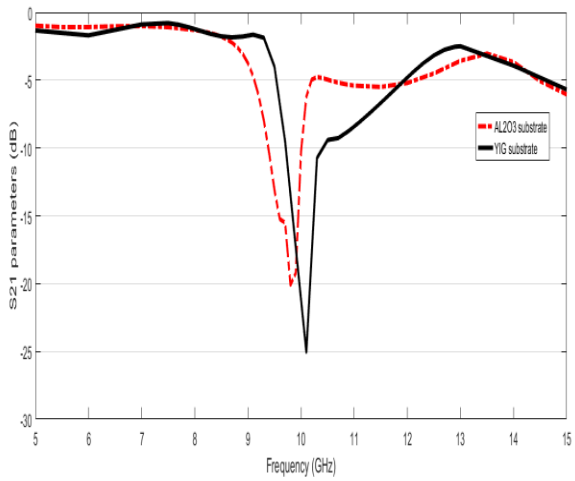

Fig. 4 Comparison of simulation results of the proposed band stop filter with Alumina substrate and the Band stop filter over a YIG substrate with no bias field.

To verify the tunable property of the proposed metamaterial microstrip band-stop filter on YIG substrate, the device has been analysed numerically using full wave simulations for different values of DC magnetic bias. In the case of the applied field of 50KA/m, the central frequency is equal to 10.30GHz,

at this frequency, a transmission level is about -21.45dB and a rejected bandwidth equal to 1000MHz. For the second values of the magnetic field (100KA/m), the band-stop filter resonates at 10.70 GHz with a transmission level close to -25.51dB and a rejected bandwidth equal to 1200MHz. In the case of the applied field equal to 200KA/m, the central frequency is shifted to 12.05 GHz with a transmission level equal to -20.96dB and a rejected bandwidth equal to 400MHz.

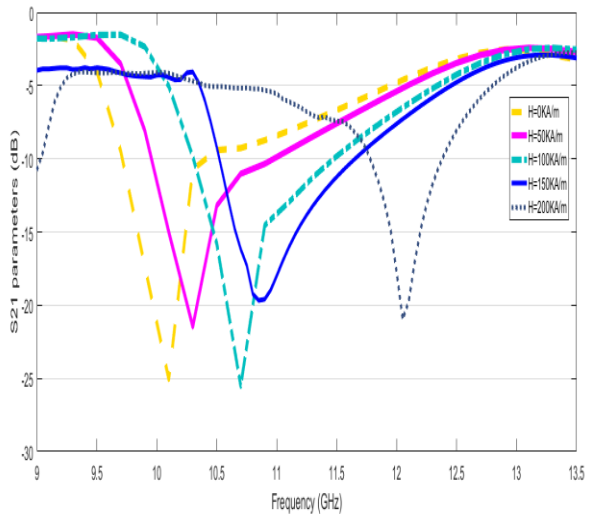

Fig. 5 Simulated results of the proposed metamaterial microstrip band-stop filter for different values of DC magnetic bias.

IV. Conclusion

In this paper, a planar metamaterial microstrip band-stop filter was proposed. The design is based on three metamaterials resonators and a 50 ohm microstrip line. The simulated S parameters of the proposed device is given and discussed. It is noted that the proposed filter is electrically small, simple and easy to realize compared to the conventional broadband BSFs.

The devices based on this concept can be very promising for microwave applications in planar technology. It provides a new way to design stop-band filters with small dimensions and simple structure. Moreover, the newly proposed filter is suitable for electrically small antenna applications.

References

[1] C.Rauscher: Varactor-Tuned active north filter with lower passband noise and signal distortion. IEEE Trans. Microwave Theory Tech. 49:8, pp.1431-1437. Aug (2001)

[2] A.Zermane, B.Sauviac, L.Djouablia and A. Benghalia: Tunability of metamaterial compact band-stop filters using YIG substrate. Journal of Electromagnetic Waves and Applications. Vol. 33, N°13, pp. 1726–1734. (2019)

[3] J. P. Carrier, T. Lisecand, and A. K. Skrivervik : Circuit model and design of silicon-integrated CRLH-TLS analogically controlled by MEMS. Microwave and Optical Technology Letters. Vol. 48, PP. 2496-2499.(2006)

[4] J. Nath, D. Ghosh, J. P. Maria, A. I. Kingon, W. Fathlbab, P. D. Franzon and B. Steer : An Electronically tunable Microstrip Bandpass Filter Using Thin-film Barium-Strontium-Titanate (BST) Varactors. *IEEE Trans. Microwave Theory Tech*. Vol. 53, N° 9, PP. 2707-2712. (2005)

[5] G. Houzet, X. Mélique, D. Lippens, L. Burgnies, G. Velu and J-C. Carru: Microstrip Transmission Line Loaded by Split Ring Resonators Tuned by Ferroelectric Thin Film. *Progress In Electromagnetics Research* C. Vol. 12. PP. 225-236. (2010)

[6] F. Falcone, F. Martin, J. Bonache, R. Marquès, T. Lopetegi, and M. Sorolla: Left handed coplanar waveguide band pass filter based on bilayer Split Ring Resonators. *IEEE Microwave Wireless Components Letters*.Vol. 14. PP. 10-12. Jan (2004)

[7] F. Falcone, T. Lopetegi, J. D. Baena, R. Marquès, F. Martin, and M. Sorolla: Effective negative Ɛ stopband microstrip lines based on complementary Split Ring Resonators. *IEEE Microwave and Wireless Components Letters*. Vol. 14. PP. 280-2892. Jan (2004)

[8] S. Nemer: Etude de motifs métamatériaux en forme de spirales circulaires ou rectangulaires. PhD thesis, Université Jean Monnet de Saint-Etienne, France (2010)

Analysis of Asymmetrical Composite Right/Left Handed Transmission Line for Broad band Microwave Devices

Mounir BELATTAR
Department of Electrical Engineering
University of 20 August 1955
Skikda, Algeria.
belattar@univ-skikda.dz

Chaabane SOUMALI
Department of Electrical Engineering
University of Docteur Yahia Fares
Medea , Algeria
Soumali.chaabane@univ-medea.dz

Abstract. *Metamaterials are artificial structures that can be designed to exhibit specific electromagnetic properties not commonly observe in nature . In this paper we use a new iterative method to evaluate the different parameter of asymmetrical composite right left handed transmission lines (CRLH TL). In order to define the scattering parameters of a given number of N CRLH TL unit cells mounted in cascade, an iterative method is proposed. Starting from the first unit ABCD parameter one can extract the whole cascade ABCD parameters, further the scattering parameter S of the cascade structure are easily extracted. Finally the CRLH-TL structure is simulated using the commercial software HFSS. Good agreement between our method and simulation results is observed.*

Keywords

CRLTH TL , metamaterials, scattering parameters,.

I. INTRODUCTION

The permittivity and the permeability of all materials are naturally positive; these materials are classified and named as right handed materials (RHMs). But now some artificial materials are produced to achieve negative permittivity and permeability, these artificial materials are classified and named as left handed materials (LHMs) .these materials with negative permittivity and permeability were firstly investigated theoretically by Russian Physicist Veselago [1]. in the beginning of 1990 Smith et al proposed and fabricated the first LHM using a periodic array of split-ring resonators (SSRs) combined with an array of straight conducting wires [2] using the theoretical work of Pendry [3,4]. Later transmission lines (TL) using LHM were proposed and realized [5]. However because of the parasitic effects occurred by the microstrip geometry which will result in right handed properties, a pure left handed transmission line (LH-TL) cannot be physically realized , then the LH-TL will be considered as a composite right left handed transmission line (CRLH-TL) [5].

The unit cell of CRLH-TL is generally composed of a series of inductor L_R and capacitor C_L, a shunt inductor L_L and capacitor C_R. The structure presents a band-pass filter, in the sense that it has left-handed (LH) high-pass with low frequency stop-band, and right-handed (RH) low-pass with high frequency stop-band. In regard of this, it is promising to apply CRLH-TL in microwave and millimeter wave devices for reducing physical length.

Generally analysis of the equivalent circuit of VRLH unit cell is done by using complex S-parameters at several distinct frequency points by full-wave simulation or by measurement, and the extraction of lumped elements in the equivalent circuit is achieved by converting *S* parameters of a CRLH TL unit cell to *ABCD* parameters [6, 7].

The use of equivalent circuit analysis is more efficient than the full-wave electromagnetic simulations for the case of CRLH-TL which is composed usually of cascaded periodic cells [8].

In our paper, a new recurrent method adapted to asymmetrical CLRH-TL model is used to obtain *ABCD* parameters of the equivalent circuit of N cascaded unit cells.

At first, the *ABCD* parameters are calculated in the case of a unit cell with respect to the series impedance *Z* and shunt admittance *Y*, and then the parameters in the case of two, three and more cells are obtained by recurrent relations, between i^{th} cell parameters and the equivalent ones of the (*i*-1) precedent cells [9]. After, the scattering parameters S are obtained using the relation between ABCD and S matrix [6].

In order to validate the results obtained by the proposed method, it is suggested to simulate a CRLH cell cascade by the HFSS simulator. We note a good agreement between the simulation results and those obtained by our method.

II. UNIT CELL MODEL OF CRLH-TL

The general CRLH TL model as shown in Fig. 1 contains an inductance L_R in series with a capacitance C_L and a shunt capacitance C_R in parallel with an inductance L_L. The components L_L and C_L govern the left-handed mode propagation properties, while L_R and C_R determine the right-handed mode propagation properties [8].

In electric equivalent unit cell, *Z* and *Y* are the impedance and admittance of the transmission line, respectively.

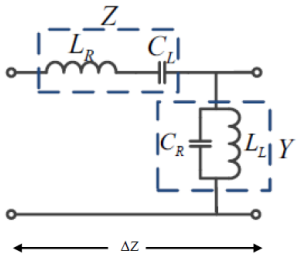

Fig. 1. Electric equivalent circuit of CRLH TL.

In the case of homogeneous CRLH TL, they are defined as:

$$Z(\omega) = j\omega L_R(1-\frac{\omega_{se}^2}{\omega^2}) \quad (1)$$

Where

$\omega_{se} = \frac{1}{\sqrt{L_R C_L}}$ is the series resonant pulsation.

While the admittance *Y(ω)* can be given by the following expression:

$$Y(\omega) = j\omega C_R(1-\frac{\omega_{sh}^2}{\omega^2}) \quad (2)$$

Where

$\omega_{sh} = \frac{1}{\sqrt{L_L C_R}}$ is the shunt resonant pulsation.

The characteristic impedance of the CRLH TL unit cell is given by:

Where Z_R is the RH (right hand)impedance given by:

$$Z_R = \sqrt{\frac{L_R}{C_R}} \quad (4)$$

Moreover, Z_L is the LH (left hand) impedance, which is given by:

$$Z_L = \sqrt{\frac{L_L}{C_L}} \quad (5)$$

As long as the frequency increases, the resonant circuit CRLH TL is increasingly dispersive, when the phase velocity is highly dependent on frequency, as a consequence, the CRLH TL has a double nature; at low frequencies is dominantly LH, and in contrast, in high frequencies the CRLH TL is dominantly RH [8].

Since the unit cell is smaller than quarter guided wavelength the CRLHTL is seen as homogeneous by electromagnetic waves [8].

III. Analysis of Cascaded Cells Structure

Considering a unit cell of a homogeneous CRLH TL as shown in Fig.1, and considering the *X* parameter used in this development to define *ABCD* parameters cell, defined as follows:

$$X = ZY + 1 \quad (6)$$

Then *ABCD* parameters of this cell are given as follows:

$$\begin{bmatrix} A & B \\ C & D \end{bmatrix} = \begin{bmatrix} X & (X-1)/Y \\ Y & 1 \end{bmatrix} \quad (7)$$

We first consider the propagation characteristics of the infinite loaded line shown in Fig. 2.

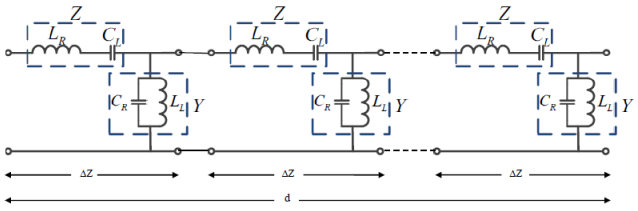

Fig. 2. CRLH transmission line of length d

Each unit cell of this line consists of a length *d*. If we consider the infinite line as being composed of a cascade of identical two-port networks, we can relate the voltages and currents on either side of the nth unit cell using the *ABCD* matrix:

$$\begin{bmatrix} V_n \\ I_n \end{bmatrix} = \begin{bmatrix} A & B \\ C & D \end{bmatrix} \begin{bmatrix} V_{n+1} \\ I_{n+1} \end{bmatrix} \quad (8)$$

In the case of two cells in cascade, we obtain the equivalent *ABCD* parameters as:

$$\begin{bmatrix} A_2 & B_2 \\ C_2 & D_2 \end{bmatrix} = \begin{bmatrix} X^2+X+1 & (X^2-1)/Y \\ (X+1)Y & X \end{bmatrix} \quad (9)$$

A new method is applied to define equivalent *ABCD* parameters of *i* cascaded cells, using the parameter *X* defined by equation (9) and based on a set of equations expressed as[9]:

$$A_i = (X+1)A_{i-1} - D_{i-1} \quad (10)$$

$$YB_i = XA_{i-1} - D_{i-1} \quad (11)$$

$$C_i = C_{i-1} + YA_{i-1} \quad (12)$$

$$D_i = A_{i-1} \quad (13)$$

In the previous relations A_i, B_i, C_i and D_i represent the elements of *ABCD* matrix and *i* represents then number of cascaded unit cells.

It is easy to remark that the previous equations are a relation two successive state (*i*-1) and (*i*).

Furthermore, this structure based on *N* cells satisfies the following relationships:

$$A_i = D_i + YB_i \quad (14)$$

$$A_i D_i - B_i C_i = 1 \quad (15)$$

Also, equations (12) and (13) are fulfilled in the same state of the i^{th} cell.

The network scattering parameters *S* are found by evaluating its *ABCD* parameters [6], using the iterative method explained previously.

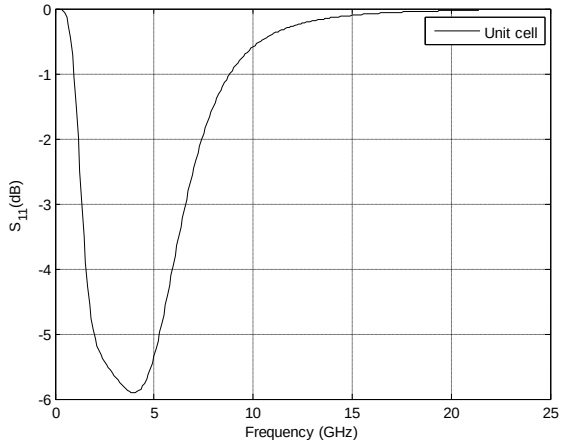

Fig. 3. Reflection coefficient in the case of a unit cell

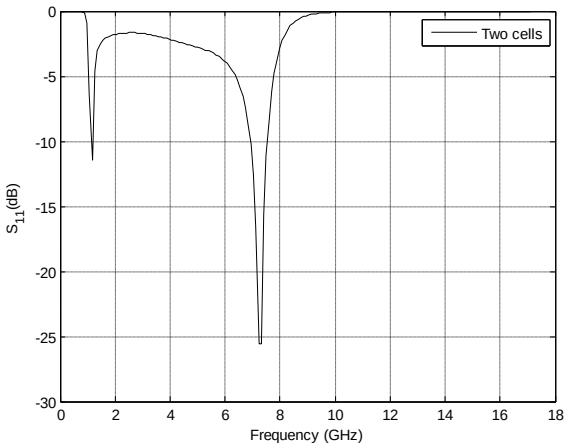

Fig. 4. Reflection coefficient in the case of two Cascaded cells

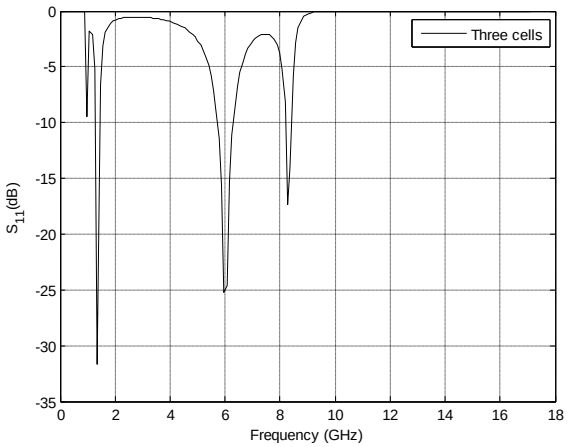

Fig. 5. Reflection coefficient in the case of three Cascaded cells

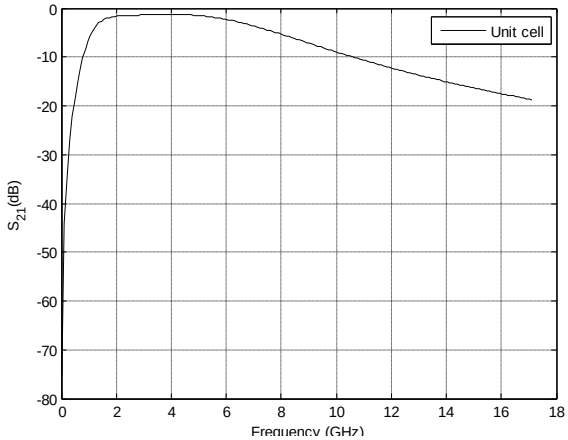

Fig. 6. Transmission coefficient in the case of a unit cell

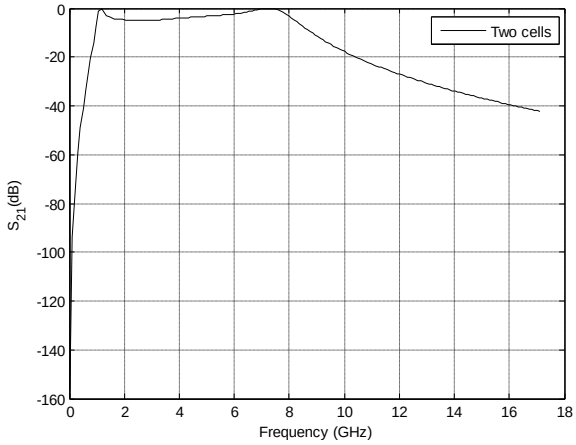

Fig. 7. Transmission coefficient in the case of two Cascaded cells

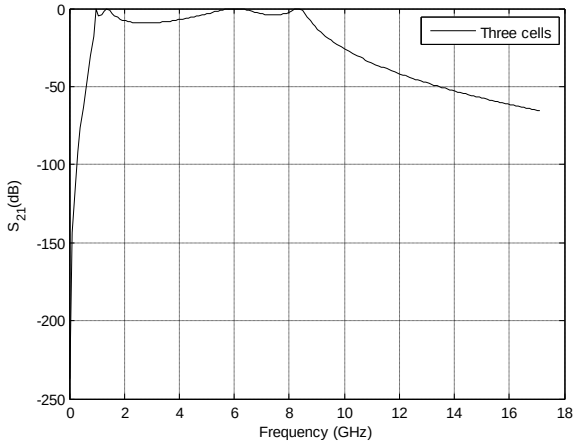

Fig. 8. Transmission coefficient in the case of three Cascaded cells

The variation of the reflection coefficient is shown in the fig.3-5 and that of the transmission coefficient is shown in fig.6-8, we note that the number of resonance frequency and the bandwidth increases as the number of cells in cascade increase.

IV. Simulation of the Asymmetrical CRLH-TL Structure

In this section we use HFSS simulator [10] to carry out the parameters of the proposed asymmetrical CRLH-TL structure based on interdigital capacitor (IDC) in series and vias to the ground plane at the stub ends in shunt as shown in Fig 9. The cascaded structure formed by two and three units of asymmetrical CRLH-TL is also analyzed.

In order to validate the results of the proposed method, we suggest to concept and simulate a circuit composed of one , two and three CRLH-TL cells designed on Rogers duroid 6006 substrate,

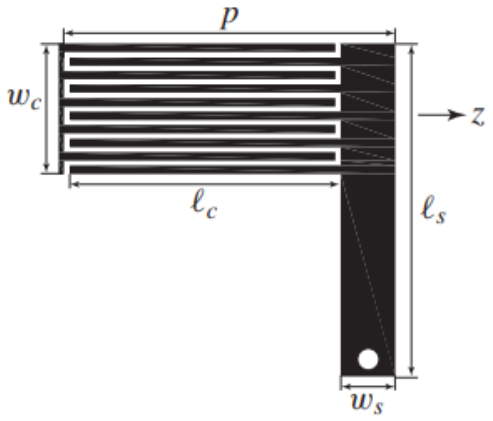

Fig.9. Microstrip implementation of the CRLH TL unit cell.

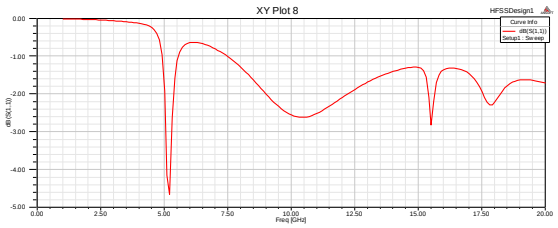

Fig. 10. Reflection coefficient obtained by HFSS in the case of a unit cell.

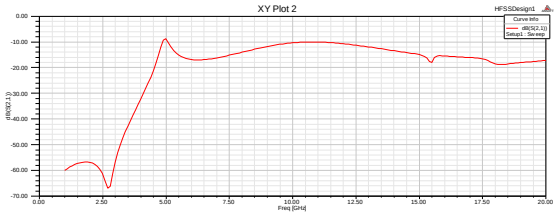

Fig. 11. Reflection coefficient obtained by HFSS in the case of two Cascaded cells.

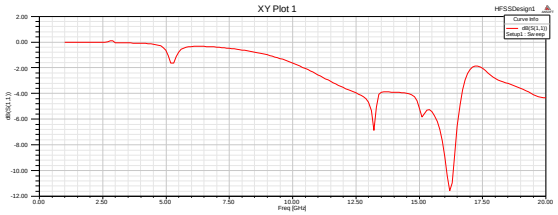

Fig. 12. Reflection coefficient obtained by HFSS in the case of three Cascaded cells.

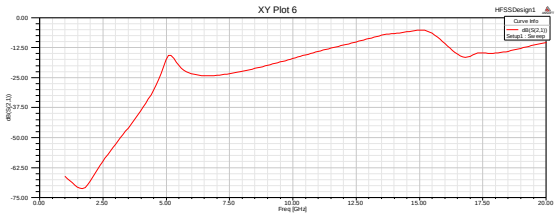

Fig. 13. Transmission coefficient obtained by HFSS in the case of a unit cell.

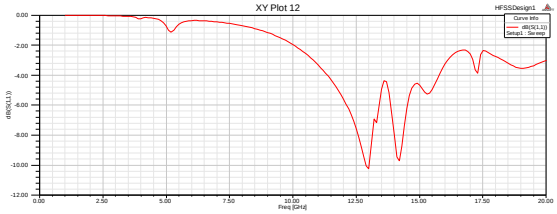

Fig. 14. Transmission coefficient obtained by HFSS in the case of two Cascaded cells

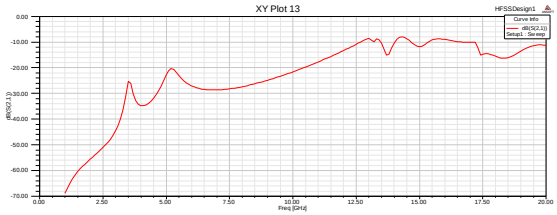

Fig. 15. Transmission coefficient obtained by HFSS in the case of three Cascaded cells

The results obtained by HFSS , shows good agreement with those obtained by the proposed method.

V. Conclusion

The progress in wireless communication and the rise in frequency in the fifth generation of cellular require components of reduced size; metamaterials play an important role in this field. The proposed method allows us to analyze the microwave circuits based on CRLH-TL in cascade, from the *ABCD* parameters of an elementary cell, the *ABCD* matrix of the overall circuit is obtained and from this result the matrix S is easily calculated. A CRLH-TL based circuit is designed and simulated using HFSS in order to validate the proposed method, a good agreement between the results of the simulation and those of the proposed method.

References

[1] VESELAGO,V. G. The electrodynamics of substances with simultaneously negative values of ε and μ, *Soviet Physics Uspekhi*, 1968,vol.10, no.4, pp.509-514.DOI:10.1070/PU1968v010n04ABEH003699

[2] R. Smith, W. J. Padilla, D. C. Vier, S. C. Nemat-Nasser, and S. Schultz, "Composite medium with simultaneously negative permeability and permivitty, " Phys.Rev.Lett.,84(18) :4184-4187,May 2000

[3] J. B. Pendry, A. J. Holden, D. J. Robbins, and W. J. Stewart, " Low Frequency Plasmons in thin wire structures," J. Phys. Condense Matter, vol. 10, pp. 4785–809, 1998.

[4] J. B. Pendry, A. J. Holden, D. J. Robbins, and W. J. Stewart, "Magnetism from Conductors and Enhanced Nonlinear Phenomena,"

IEEE Trans. Microwave Theory and Tech, vol. 47, no. 11, pp. 2075–2084, Nov. 1999.

[5] C. Caloz and T. Itoh, "Transmission line approach of left-handed (LH) materials and microstrip implementation of an artificial LH transmission line, " IEEE Trans. Antenas and Propaga., vol. 52, pp. 2701–2712, Dec. 2002.

[6] POZAR, D. M. *Microwave Engineering*.New York (USA): John Wiley& Sons, 2011. ISBN: 978-0470631553

[7] KOU, N., SHI, Y.,LI, L. New Equivalent Circuit Analysis and Synthesis for Broadband Composite Right/Left-Handed Transmission Line Metamaterials,*ACES Journal*,2006, no.8,vol.31, pp.884-893.

[8] BELATTAR, M.,LASHAB,M. Analysis of Metamaterial CRLH TL Antennas Parameters,*International Conference on Wireless Technologies, Embedded and Intelligent Systems (WITS'2019*), Morocco,2019, pp. 1–5.DOI: 10.1109/WITS.2019.8723817

[9] BELATTAR, M.,LASHAB,M.New Iterative Method for Analyzing Metamaterial CRLH TL Antennas Parameters,*International Conference on Advanced Electrical Engineering 2019 (ICAEE),* Algeria,2019,pp1-5.DOI: 10.1109/ICAEE47123.2019.9014770

[10] "High frequency structure simulator software package," HFSS v13, Ansoft Corporation.

About the Authors...

Mounir BELATTAR received the diploma of Engineer in Electronics in 1993 from the university Mentouri 1 of Constantine and the diploma of Magister in 1996 from the same university, and since 2012, he is assistant professor at the University 20 Août 1955 Skikda. Actually, he is the head of the master's telecommunication course, at the department of Electrical Engineering. His main research interests are non-uniform transmission lines, as broadband terminations, planar antennas, filters, and meta-materials.

Chaabane SOUMALI He received the Ph.D degree in electronics from Batna University Algeria in 2018. His is currently an associate professor at the department of electrical engineering, university of Docteur Yahia Fares Medea Algeria. His research interests include microwaves, RF passive devices and wireless communication.

Design of directional planar antennas with circular polarizations for space applications

F.BOUSALAH[1], A.RABAH[2]

[1]Department of telecommunications, Abou Bekr Belkaid University, Tlemcen, Algeria
bousalah.fayza@gmail.com
arabah6@gmail.com

Abstract

In this project, we propose a new patch antenna structure to establish an uplink with geostationary satellites operating in Ka band. The goal is to design this type of more directive antennas that work for this kind of applications while ensuring very high gain and good directivity with an acceptable reflection coefficient.

Keywords and phrases: Planar antenna, patch, circular polarization, high frequency 28GHz, Ka band, S-parameters, radiation pattern, CST WMS.

1 Introduction

The phased array antennas have, in recent years, been the subject of several researches, particularly in the field of applications such as satellite communication, which has enabled the discovery of many advantages of this type of antenna such as its beam capacity. Microstrip antennas [1] are widely used in array antennas due to their low cost and weight. They can also be easily printed on a dielectric substrate with photolithography techniques.[2]
The democratization of terrestrial satellite reception systems [3],[4] has also led to the proliferation of reception systems on the ground which have clearly contributed to the visual pollution caused particularly by antennas placed on roofs or in gardens and in balconies of buildings [5]. Beyond cost control, the notion of discretion and therefore integration into the urban landscape is becoming more and more essential. In recent years, the discretion criterion has taken on an importance rivaling the cost criterion in the direction of avoiding any public nuisance and to do this, new antenna solutions [6] with low visual impact have gradually emerged in recent years. This work is part of the research on miniature sub-array antennas. Our goal is to design and simulate a small array of antennas working in the ka frequency band at the 28Ghz resonant frequency for a space application. To do this, we rely on antenna theory to determine the geometric parameters of our proposed antenna using the CST MWS software as a simulation tool.

2 Characteristics and dimensions of the patch antenna

The different characteristics of the patch antenna are given by:
- Rectangular patch.
- Substrate: FR4 Lossy ($h = 1.6mm$, $\varepsilon r = 4.3$) with dielectric loss tangent, tan $\delta = 0.025$
- Resonance frequency: $fr = 28GHz$ (27.50GHz to 31GHz: band ka rising frequency).

Table 1 gives the dimensions of the patch antenna studied, (Sub: Substrate and PM: ground plane).

Table 1: Dimensions of the patch antenna.

Parameters	Description	Values (mm)
L	Longueur Sub et PM	11.29
W	Largeur Sub et PM	12.89
Hp	Epaisseur PM et patch	0.035
Lp	Longueur Patch	1.638
Wp	Largeur Patch	3.29
Hs	Epaisseur Sub	1.6
Lf	Longueur deligne	2.84
Wf	Largeur de ligne	1

3 Design and simulation of the patch antenna

Figure 3. ((a), (b), (c)), respectively represent the reflection coefficient, the standing wave ratio SWR and the gain of the initial antenna.

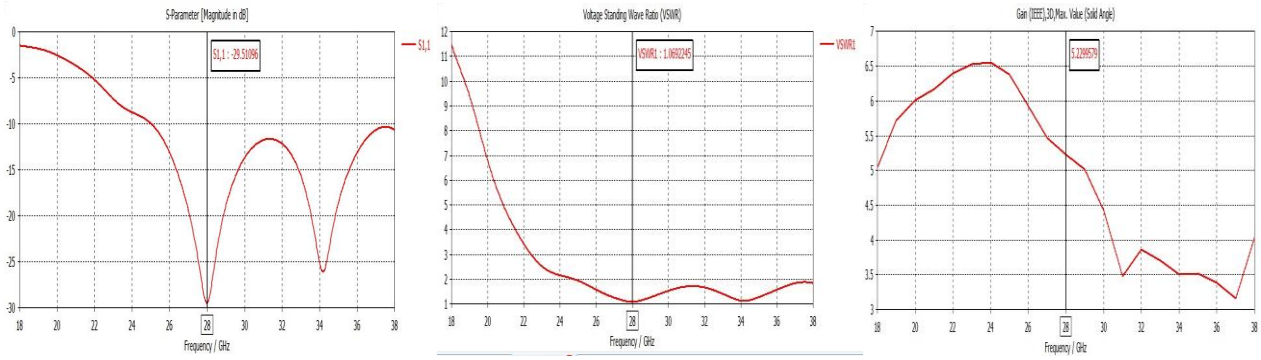

(a) **(b)** **(c)**

Figure 3: (a): Reflection coefficient. (b): Standing wave rate TOS. (c): Antenna gain.

A good adaptation is observed, since the reflection coefficient S11 is -29.51dB at the resonant frequency 28 GHz, with a maximum bandwidth of 1.795GHz (figure3.a). The standing wave ratio SWR <2 (figure3.b). The gain obtained from the antenna is 5.22dB at 28GHz.

Figures 4. ((a), (b), (c)) represent respectively the 2D and 3D polar radiation patterns of the antenna at the resonant frequency 28GHz.

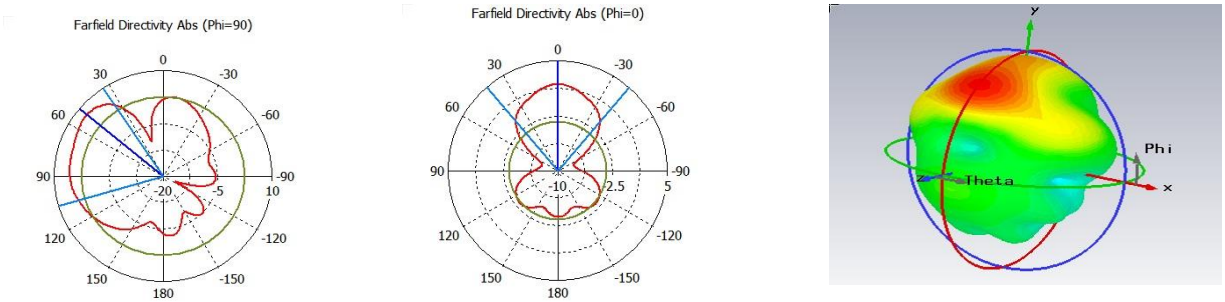

(a) **(b)** **(c)**

Figure 4 : (a) : 2D radiation pattern, plane H. (b) : 2D radiation pattern, E plane (c) : 3D radiation pattern.

We notice that the antenna presents an almost quasi-directional radiation in the plane E (φ= 0 °) and in the plane H (φ = 90 °), the latter are verified by the tracing of the radiation diagram in 3D.

4 Structure of a new design of the patch antenna

The proposed antenna structure as shown in figure 5, presents a star inserted in the middle of the triangular patch (an equilateral triangle), its three sides have the same length a = 1.305 mm, its three internal angles are 60 degrees, knowing that all the other parameters are the same as the initial antenna.

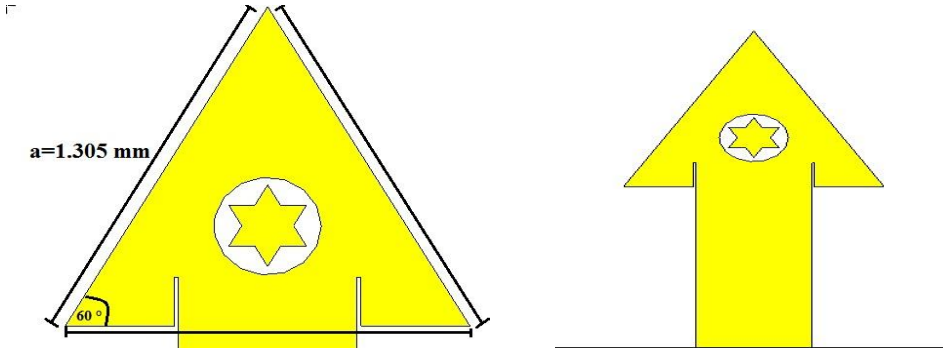

Figure 5: Geometry of triangular antenna.

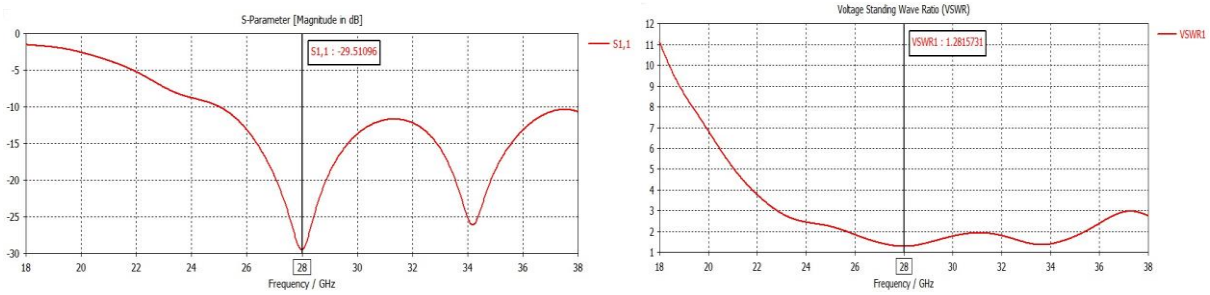

Figure 6: (a). Variation of coefficient S11 (dB) and (b): VSWR as a function of frequency (GHz).

The antenna has a maximum bandwidth of 5.246GHz with an S11 equal to -30dB at the resonant frequency (28GHz) in the interval (31.057-25.811) GHz, shown in (Figure 6.a). The standing wave ratio SWR <2 in the same bandwidth which gives a good adaptation of the patch antenna to the desired frequency as shown in (figure 6.b).
Figures 7 and 8 show the radiation pattern in 2D and 3D polar presentations, respectively. We notice that the antenna has directional radiation.

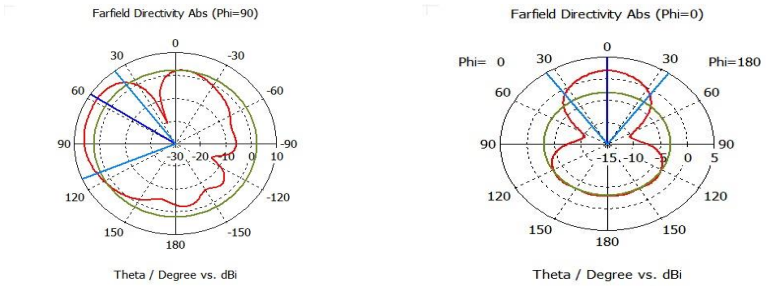

Figure 7: Radiation diagram in polar presentation phi = 0 and phi = 90.

The radiation pattern is concentrated in the upper part of the antenna (between the Y and Z plane), the gain value is 4.606dB and the maximum directivity is 6.562dB.

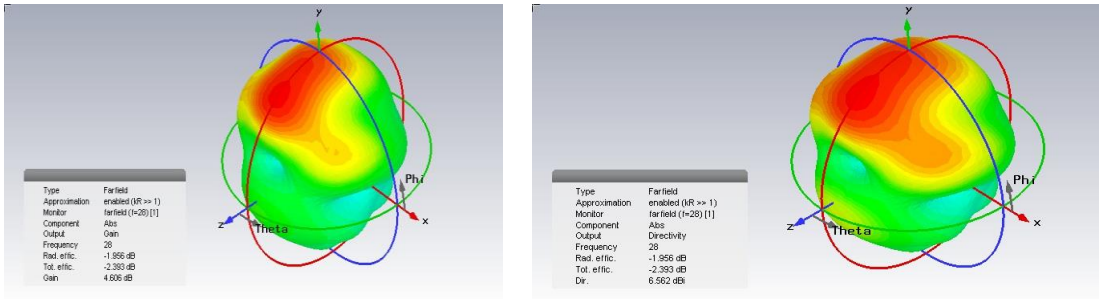

Figure 8: Patch antenna gain radiation and patch antenna directivity diagram.

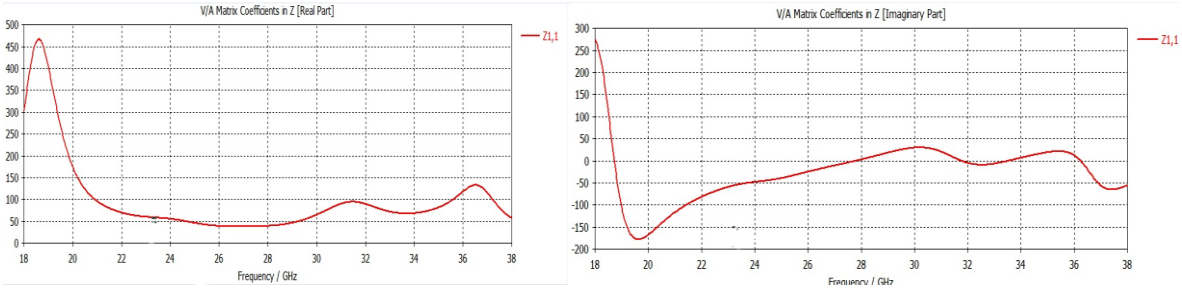

Figure 9: Antenna input impedance (real part) on the left, (imaginary part) on the right.

The efficiency of this antenna is given by the relation: $\varepsilon_R = \frac{G}{D} = \frac{4.606}{6.562} = 0.701 = 70\%.$

Table 2 shows the patch antenna parameters with a single element.

PARAMETRES	VALEURS
Return losses (S_{11})	$S_{11mín}$ = -18.17dB
Directivity	D = 6.562 dB
Gain	G = 4.606 dB
Radiation efficiency (ηrad)	ηrad = -1.956 dB

Total efficiency (ηT)	ηT = -2.393dB
Passe Band (BW)	BW = 5.246 GHz et S11 = -10 dB
Beam width (AW)	AW = 71.3°

Table 2: Basic parameters of the patch antenna at the 28GHz frequency.

6 Antenna arrays with 2 elements at the resonant frequency 28GHz

In our work, we choose the power divider as a T junction, because it is easy to model and compatible with the structure of 2 element antenna arrays as shown in figure 10.

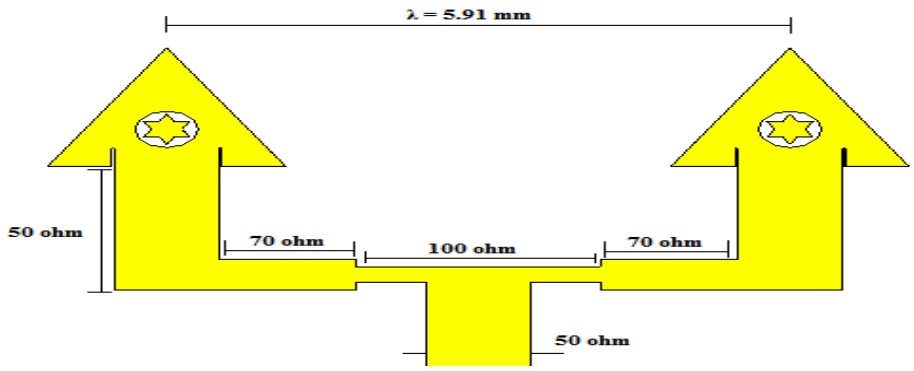

Figure 10: Network of antennas with 2 elements.

Table (3.3) shows the parameters of the T junction and their values.

Parameters	Larger (mm)	length (mm)
50 Ohm	1	2.84
70 Ohm	0.5	1.30
100 Ohm	0.255	2.31

Table 3: Parameters of the T junction.

Figure 14 ((a) and (b)) and (c)) shows the reflection coefficient, the standing wave ratio SWR and the 2-element antenna array gain, respectively.

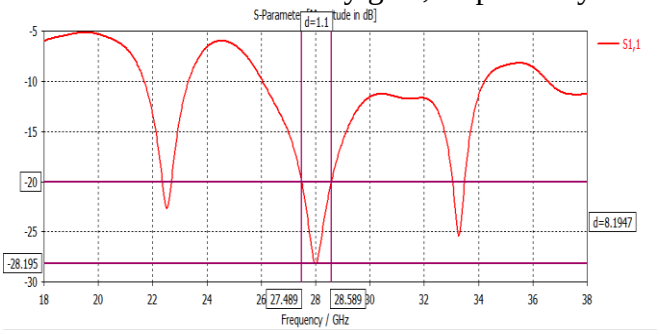

(a)

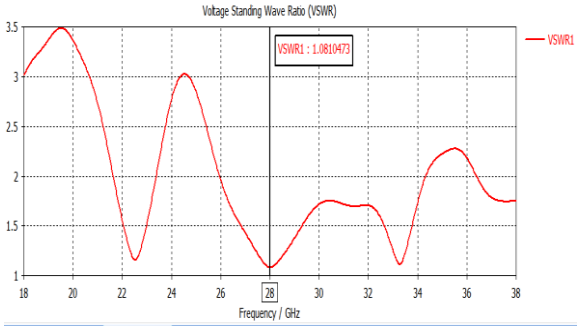

(b)

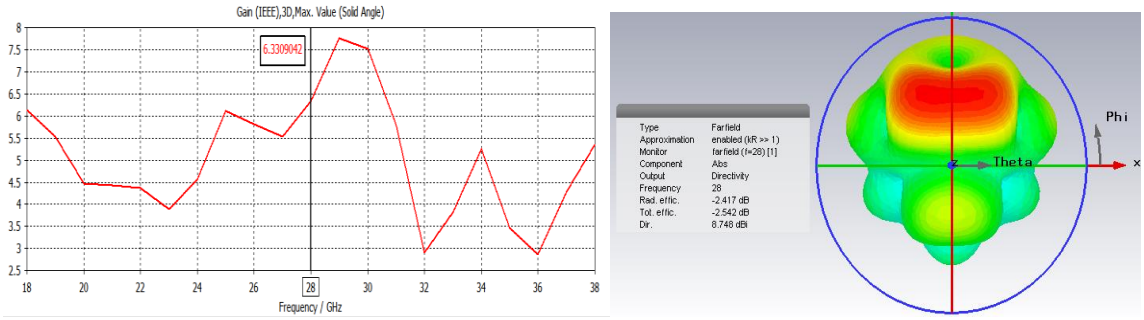

Figure 11: (a): Reflection coefficient. (b): Standing wave rate. (c): Gain. (d): Directivity radiation pattern. (2-element network).

Figure (11.a) shows a good match with a reflection coefficient S11 = -28.19dB at the resonant frequency 28GHz, with a bandwidth of 1.1GHz. We noted a TOS <2 (figure 19.b). The gain of the antenna obtained is 6.33dB (figure 19.b). The radiation pattern is concentrated in the upper part of the antenna (between the Y and Z plane), the maximum value of the directivity is 8.748dB (figure 19.d). Table (3.3) shows the parameters of the two-element antenna network.

Parameters	Values
Return loss (S11)	S11mín = -28.19 dB
Directivity	D = 8.748 dB
Gain	G = 6.33 dB
Radiation efficiency (ηrad)	ηrad = -2.417dB
Total Efficacity (ηT)	ηT = -2.542 dB
Passe Band (BW)	BW = 1100 MHz à S11 = -20 dB
Beam width (AW)	AW = 28.1°

Table 3: Basic parameters of a 2-element antenna network.

References

[1] C. A. Balanis, "Antenna Theory: analysis and design", 3rd edition, John Wiley & Sons, INC, ISBN: 0-471-66782-X, 2005.H.

[2] P. J. Soh, M. K. A. Rahim, A. Asrokin and M. Z. A. Abdul Aziz, “DE- SIGN, MODELING, AND PERFORMANCE COMPARISON OF FEEDING TECHNIQUES FOR A MICROSTRIP PATCH ANTEN- NA”, JurnalTeknologi, 47(D) Dis. 2007: 103–120.of

[3] Elbert, B. R, "Introduction to Satellite Communication ", Edition 3,2008.

[4] G. MARAL, M. BOUSQUET, ZHILI SUN, "satellite communication, Systems technique and technologies", Edition 6, 2020.

[5] Roddy, D, "Satellite Communications" Fourth Edition 2001 by The McGraw-Hill Companies

[6] Y. HUANG, and K. BOYLE, «Antennas from theory to practice», 1 stedn, England: John, 2008.

PAPR Reduction in OTFS by modified Similar Raised Cosine mSRC Pulse Shaping

Benadjina Nassim
Dept. of electrical engineering
Larbi Ben M'Hidi University
Oum El Bouaghi, Algeria.
nnassimm1983@yahoo.fr

Lashab Mohamed
Dept. of electrical engineering
Larbi Ben M'Hidi University
Oum El Bouaghi, Algeria.
lashabmoh@yahoo.fr

Slimani Djamel
Dept. of electronic
University of Setif 1
Setif, Algeria.
slimani.djamel@ymail.com

***Abstract*— In this letter, we analyze Peak-to-Average Power Ratio (PAPR) of orthogonal time-frequency space (OTFS) modulation with pulse shaping. We implemented modified similar raised cosine (mSRC) pulse shaping in the OTFS based System and compare it with rectangular and raised cosine (RC) pulse shaping. Simulations results show that the use of mSRC pulse shaping in OTFS based system reduces the PAPR significantly and achieves better performances maintaining BER performance compared to other pulses shaping.**

Keywords— OTFS, Peak-to-average power ratio (PAPR), Pulse Shaping PS, mSRC, delay-Doppler domain.

I. INTRODUCTION

Mobile communication systems are evolving from single carrier to orthogonal time frequency and space (OTFS) modulation [1].

Orthogonal time frequency and space (OTFS) modulation is a new type of modulation technique that can be used for low-latency wireless communication and high-quality data transmission [2, 3], it is a 2-dimensional modulation technique designed in delay-Doppler domain to efficiently handle the high Doppler sensitivity problem occurring in OFDM modulation and to achieve efficient data transfer in high-speed vehicular scenario. The main advantage of OTFS modulation is the use of orthogonal subcarriers. These are carriers at different frequencies which make it possible to send multiple streams of data simultaneously over the same signal bandwidth. Since OTFS modulation claims excellent performance and offers several advantages in doubly selective wireless channels, it seems to be one of those technologies that could change everything for next-generation communication systems.

However, OTFS is suffering from high PAPR problem for increasing number of symbols [4,6], it has been attracting considerable interest to study their PAPR characteristics for higher values of number of Doppler bins N. Several studies on PAPR of OTFS have been made in the literature [4-11].

Mathematical performance analysis of PAPR of OTFS has been presented in [4], where the authors derive an analytical upper bound on the PAPR, they demonstrated that this bound increases linearly with N and not with the number of delay bins M. Then, the effect of pulse shaping on the PAPR performance of OTFS system has been analyzed, they showed that Gaussian and raised cosine pulse shaping increases the PAPR of OTFS and OTFS can have better PAPR comparing to those of OFDM and GFDM. Authors in [5] proposed a novel interleaved time-frequency multiple access (ITFMA) scheme using OTFS on the uplink, this scheme was found to achieve good PAPR performance. In [11], the authors proposed a companding technique to reduce the PAPR of OTFS, but with slight degradation in BER performance. PAPR reduction method based on iterative clipping and filtering (ICF) was investigated in [12], this method found to reduce the PAPR with mild BER performance loss.

Reference [8] presents the first attempt to include pulse shaping in OTFS, the rectangular and prolate spheroidal pulse shaping were applied. The most first systems of OTFS have used a rectangular pulse shape [2,9-10]. Circular Dirichlet pulse shaped (CPS) is applied to reduce the out-of-band OOB power radiation in [11], the authors identified that this pulse shaped has a lower PAPR than conventional OTFS system.

To reduce high PAPR of OTFS signal in this paper, we use modified similar raised cosine (mSRC) pulse shaping which will reduce the PAPR of OTFS regarded to other existing pulses.

The similar raised-cosine (SRC) pulse was initially proposed in [12] and modified in [13] by adding a second design parameter β that provides an additional degree of freedom for a certain roll-off factor α, the mSRC corresponding time function is given by

$$p_{mSRC}(t) = \operatorname{sinc}\left(\frac{\beta t}{T_0}\right)\frac{1-2\cos\left(\pi\alpha\frac{t}{T_0}\right)}{(3\alpha t/T_0)^2-1} \qquad (1)$$

where, the parameter β is defined for all real numbers, α is the roll-off factor, T_0 is the symbol period. $t = nT_s$, where, n is the number of samples and T_s is the sampling frequency.

Fig. 1 represent the time domain function for modified similar raised cosine pulse shaping with α = 0.22 and different values of β.

II. UPLINK OTFS SYSTEMP

A. System Model

Each information symbols at the OTFS uplink transmitter are considered as points in two-dimensional delay-Doppler grid and are mapped to the time-frequency (TF) plane through the 2D inverse symplectic finite Fourier transform (ISFFT). The signal data obtained is then passed through a multicarrier modulation system. Then this signal is transformed to a time-domain signal and transmitted using Heisenberg transform. The output data of the Heisenberg transform are transmitted over the linear time-variant channel [4].

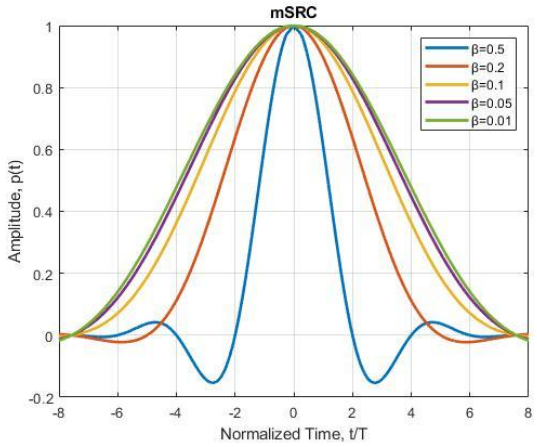

Fig. 1. Time function of mSRC pulse for α = 0.22 with β varies.

We consider $N \times T$ the total time duration of transmitted OTFS signal and $BW = M/T = M \times \Delta f$ the bandwidth occupied by the transmitted signal. The information symbols in delay-Doppler domain are represented using the notation $x[k,l], k = 0,1,\ldots,N-1, l = 0,1,\ldots,M-1$ and $x[k,l] \in A$, where A represents modulation data of one of various modulation schemes. Those modulation alphabet points are distributed to points in 2D delay-Doppler grid. These symbols are mapped to symbols in time-frequency plane by using a 2D transformation called inverse symplectic finite Fourier transform (ISFFT), that is given by

$$X_u[n,m] = \sum_{k=0}^{N-1}\sum_{l=0}^{M-1} x_u[k,l] e^{j2\pi\left(\frac{nk}{N}-\frac{ml}{M}\right)} \tag{2}$$

Then after passing the obtained TF signal via a multicarrier modulation system and a Heisenberg transformation, the time domain signal will get back from the time-frequency, which given by

$$s(t) = \sum_{n=0}^{N-1}\sum_{m=0}^{M-1} X[n,m] g_{tx}(t-nT) e^{j2\pi m\Delta f(t-nT)} \tag{3}$$

where $g_{tx}(t)$ represents the periodic prototype transmit pulse shape with total duration of $N \times T$. The discrete-time representation of (3) is obtained by applying sampling with $Fs = 1/Ts = BW$ sampling rate, that is given by

$$s(uT_s) = \sum_{n=0}^{N-1}\sum_{m=0}^{M-1} X[n,m] g_{tx}(uT_s-nT) e^{j2\pi m\Delta f(uT_s-nT)} \tag{4}$$

where $u = 0,1,\ldots,MN-1$. The Nyquist sampling with oversampling ratio = 1 for this description is considered. To represent the samples as $s(u), u = 0,1,\ldots,MN-1$ as an $N \times M$ matrix, assume $s(q,r)$ such that $u = r + qM$, where $r = 0,1,\ldots,M-1$ and $q = 0,1,\ldots,N-1$. Then by putting (2) in (4) with $u = r + qM$, the resulting equation is

$$(r+qM) = \sum_{n=0}^{N-1}\sum_{m=0}^{M-1}\sum_{k=0}^{N-1}\sum_{l=0}^{M-1} x[k,l] e^{-j2\pi\left(\frac{ml}{M}-\frac{nk}{N}\right)} g_{tx}([r + qM - nM]_{MN}) e^{j\frac{2\pi}{M}m(r+qM)} \tag{5}$$

In this, the mod-MN operation has represented by $[.]_{MN}$ confines the total duration of one frame transmission with in $N \times T$. The above equation can be further simplified as

$$s(r+qM) = \sum_{n=0}^{N-1}\sum_{m=0}^{M-1} x[k,l] \sum_{k=0}^{N-1} e^{\frac{j2\pi m}{M}(-l+r)} \sum_{l=0}^{M-1} g_{tx}([r + qM - nM]_{MN}) e^{j\frac{2\pi nk}{N}} \tag{6}$$

Now, defining $\mathcal{F} \triangleq \sum_{m=0}^{M-1} e^{\frac{j2\pi m}{M}(-l+r)}$, we note that

$$\mathcal{F} = \begin{cases} 0 & if\ r \neq l \\ M & if\ r = l \end{cases} \tag{7}$$

Substituting (7) in (6), we get

$$s(r+qM) = M \sum_{n=0}^{N-1}\sum_{k=0}^{N-1} x[k,r] e^{j\frac{2\pi nk}{N}} g_{tx}([r + qM - nM]_{MN}) \tag{8}$$

Observe that $\sum_{n=0}^{N-1} x[k,r] e^{j\frac{2\pi nk}{N}}$ is the n th ($n = 0,1,\ldots,N-1$) N-point IDFT of $x[k,r], k = 0,1,\ldots,N-1$, for a given r.

Denoting $\tilde{x}_r(n) = \sum_{n=0}^{N-1} x[k,r] e^{j\frac{2\pi nk}{N}}$, (8) can be written as

$$s(r+qM) = M \sum_{n=0}^{N-1} \tilde{x}_r(n) g_{tx}([r + qM - nM]_{MN}). \tag{9}$$

B. *Maximum Bound on OTFS PAPR*

Let's consider the samples of transmitted OTFS signal in equation (8). The Peak to Average Power Ratio of discrete OTFS time samples of transmit signal is defined as

$$PAPR = \frac{\max_{r,q}\{|s(r+qM)|^2\}}{P_{avg}} \tag{10}$$

where

$$P_{avg} = \frac{1}{MN}\sum_{r=0}^{M-1}\sum_{q=0}^{N-1} E\{|s(r+qM)|^2\} \tag{11}$$

The max bound of PAPR for the pulse shaped OTFS signal can be obtained as [4]

$$PAPR \leq \frac{M^2N^2 \max_{k,l}|x[k,l]|^2 B_1}{M^2N\sigma_a^2 B_2} \tag{12}$$

$$PAPR_{max} = \frac{N \max_{k,l}|x[k,l]|^2 B_1}{\sigma_a^2 B_2} \tag{13}$$

With $\sigma_a^2 = E\{|x[k,l]|^2\}$,

$$B_1 \triangleq \max_{r,q} \sum_{n=0}^{N-1} |g_{tx}([r + qM - nM]_{MN})|^2$$

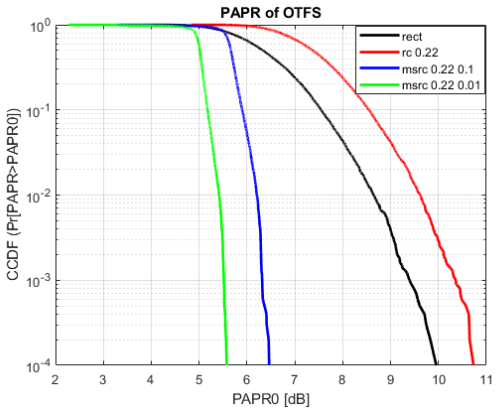

Fig. 2. CCDF of PAPR for pulse shaping OTFS with rectangular, RC, mSRC pulses and N=8, M=8, α = 0.22, and β = 0.1, 0.01.

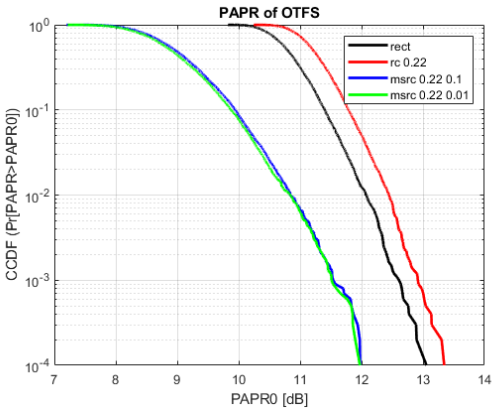

Fig. 3. CCDF of PAPR for pulse shaping OTFS with rectangular, RC, mSRC pulses and N=128, M=1024, α = 0.22, and β = 0.1, 0.01.

and,

$$\mathrm{B}_2 \triangleq \frac{1}{\mathrm{MN}} \sum_{\mathrm{n}=0}^{\mathrm{N}-1} \sum_{\mathrm{r}=0}^{\mathrm{M}-1} \sum_{\mathrm{q}=0}^{\mathrm{N}-1} |\mathrm{g}_{\mathrm{tx}}([\mathrm{r}+\mathrm{qM}-\mathrm{nM}]_{\mathrm{MN}})|^2$$

For rectangular pulse shape $\frac{\mathrm{B1}}{\mathrm{B2}} = 1$, therefore the maximum PAPR will be delimited as,

$$PAPR \leq \frac{M^2 N^2 \max_{k,l} |x[k,l]|^2}{M^2 N \sigma_a^2} \tag{14}$$

$$PAPR_{max} = \frac{N \max_{k,l} |x[k,l]|^2}{\sigma_a^2} \tag{15}$$

C. *CCDF (Complementary Cumulative Distribution Function) of OTFS PAPR*

The CCDF of PAPR of OTFS is given by [4]

$$P(PAPR \leq \lambda_0) \approx 1 - \left(1 - e^{\lambda_0}\right)^{MN} \tag{16}$$

where λ_0 is the threshold value when the probability that PAPR of OTFS transmitted signal per one frame not exceed.

III. RESULTS AND DISCUSSIONS

Figure 2 shows the comparison of simulated CCDF of PAPR of OTFS system with mSRC, RC and rectangular pulses using 16-QAM for M=8 and N=8, α=0.22, β=0.1,0.01, and the pulses are four times oversampled with a length of 8T. We observed that the use of mSRC pulse shaping reduces the PAPR of OTFS compared to rectangular and RC pulses. For example, the PAPR of OTFS with mSRC pulse shaped is 4 dB lower than that with rectangular pulse shaped for β=0.01 at a probability of 10^{-3} and 3 dB lower for β=0.1. We found that using β with small values improves the performance of PAPR of OTFS with mSRC pulse shaping.

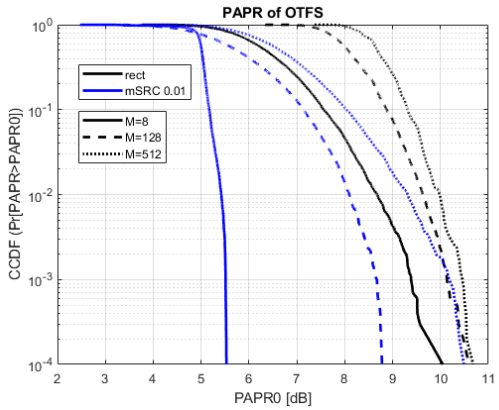

Fig. 4. CCDF of PAPR for pulse shaping OTFS with rectangular and mSRC pulses for N=8, α = 0.22, and β = 0.1, 0.01 when M varies.

Figure 3 shows the comparison of simulated CCDF of PAPR of OTFS system with mSRC, RC and rectangular pulses using 16-QAM for M=1024 and N=128, α=0.22, β=0.1,0.01 and the pulses are four times oversampled with a length of 8T. We observed that mSRC pulse shaping still reduces the PAPR of OTFS compared to rectangular and RC. But unlike for smaller value off N and M, the PAPR is 1dB lower with mSRC compared to rectangular pulse and the curve of PAPR with mSRC for β=0.01 is closer to that for β=0.1 (for N=8 and M=8, PAPR with mSRC for β=0.01 is almost 1dB lower at probability of 10^{-3} regarded to PAPR for β=0.1).

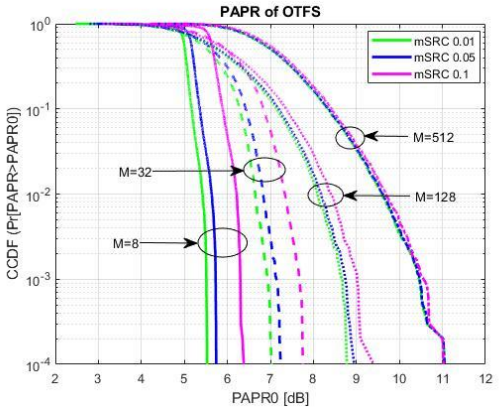

Fig. 5. CCDF of PAPR for pulse shaping OTFS with mSRC for N=8, α = 0.22 when M and β vary.

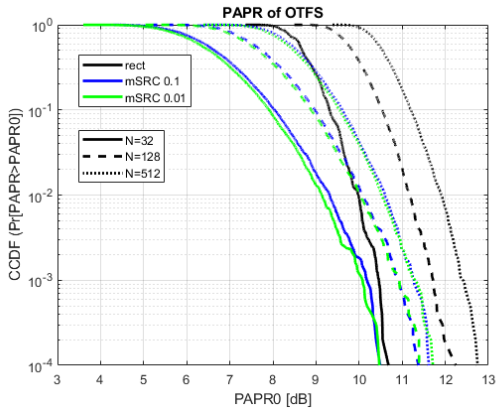

Fig. 6. CCDF of PAPR for pulse shaping OTFS with rectangular and mSRC pulses for M=512, α = 0.22 and β = 0.1, 0.01 when N varies.

Figure 4 shows the effect of mSRC pulses when M varies on the simulated CCDF of PAPR of pulse shaped OTFS system regarding rectangular pulse using 16-QAM for N=8 and α=0.22. For small values of M, there is a large distance between PAPR curves of mSRC and rectangular. When the values of M increase, this distance decreases.

Figure 5 shows the effect of β when M varies on the simulated CCDF of PAPR of pulse shaped OTFS system with mSRC using 16-QAM for N=8 and α=0.22. For small values of M, there is a large distance between PAPR curves for different values of β. When the values of M increase, this distance decreases until it vanishes so that changing the values of B does not affect the shape of PAPR.

Figure 6 shows the effect of β when N varies on the simulated CCDF of PAPR of pulse shaped OTFS system with mSRC and rectangular pulses using 16-QAM for M=512 and α=0.22. We note that when the values of N change, the variation of β does not affect the PAPR curves of mSRC, the curves are close to each other, but when N increases the distance of PAPR curves between the mSRC and rectangular pulses increases.

Figure 7 shows the comparison of simulated BER of pulse shaped OTFS system with mSRC pulse shaping and rectangular pulse for 16-QAM, M=32 and N=8, α=0.22, β=0.1,0.01. We observed that the BER curves of simulated pulse shaping is closer to the curve of original of OTFS.

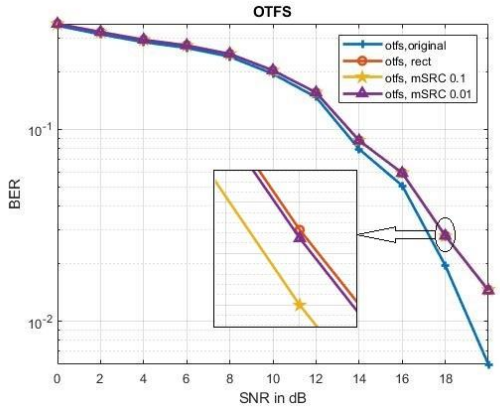

Fig. 7. BER performance of rectangular, mSRC pulse shaping OTFS based system with M = 32, N = 8, α = 0.22, and B= 0.1, 0.01.

IV. CONCLUSIONS

We proposed the use of modified similar raised cosine (mSRC) pulse shaping in OTFS based systems. This pulse shaping scheme was found to achieve better PAPR performance compared to other pulse shaping schemes presented in [4], where there is a reduction of PAPR about 4dB for $N = 8$ and $M = 8$ compared to rectangular pulse shaping.

REFERENCES

[1] C. An and H. Ryu, "Design and Performance Evaluation of Spectral Efficient Orthogonal Time Frequency Space System," 2019 IEEE 2nd 5G World Forum (5GWF), Dresden, Germany, 2019, pp. 249-252, doi: 10.1109/5GWF.2019.8911663.

[2] R. Hadani et al., "Orthogonal Time Frequency Space Modulation," 2017 IEEE Wireless Communications and Networking Conference (WCNC), San Francisco, CA, USA, 2017, pp. 1-6, doi: 10.1109/WCNC.2017.7925924.

[3] R. Hadani and A. Monk. (2018). "OTFS: A new generation of modulation addressing the challenges of 5G". [Online]. Available: https://arxiv.org/pdf/1802.02623.pdf

[4] G. D. Surabhi, R. M. Augustine and A. Chockalingam, "Peak-to-Average Power Ratio of OTFS Modulation," in IEEE Communications Letters, vol. 23, no. 6, pp. 999-1002, June 2019, doi: 10.1109/LCOMM.2019.2914042.

[5] R. M. Augustine and A. Chockalingam, "Interleaved Time-Frequency Multiple Access Using OTFS Modulation," 2019 IEEE 90th Vehicular Technology Conference (VTC2019-Fall), Honolulu, HI, USA, 2019, pp. 1-5, doi: 10.1109/VTCFall.2019.8891404.

[6] C. Naveen and V. Sudha, "Peak-to-Average Power Ratio reduction in OTFS modulation using companding technique," 2020 5th International Conference on Devices, Circuits and Systems (ICDCS), Coimbatore, India, 2020, pp. 140-143, doi: 10.1109/ICDCS48716.2020.243567.

[7] S. Gao and J. Zheng, "Peak-to-Average Power Ratio Reduction in Pilot-Embedded OTFS Modulation Through Iterative Clipping and Filtering," in IEEE Communications Letters, vol. 24, no. 9, pp. 2055-2059, Sept. 2020, doi: 10.1109/LCOMM.2020.2993036.

[8] P. Raviteja, Y. Hong, E. Viterbo and E. Biglieri, "Practical Pulse-Shaping Waveforms for Reduced-Cyclic-Prefix OTFS," in IEEE Transactions on Vehicular Technology, vol. 68, no. 1, pp. 957-961, Jan. 2019, doi: 10.1109/TVT.2018.2878891.

[9] P. Raviteja, K. T. Phan, Y. Hong and E. Viterbo, "Interference Cancellation and Iterative Detection for Orthogonal Time Frequency Space Modulation," in IEEE Transactions on Wireless Communications, vol. 17, no. 10, pp. 6501-6515, Oct. 2018, doi: 10.1109/TWC.2018.2860011.

[10] A. Farhang, A. RezazadehReyhani, L. E. Doyle and B. Farhang-Boroujeny, "Low Complexity Modem Structure for OFDM-Based Orthogonal Time Frequency Space Modulation," in IEEE Wireless Communications Letters, vol. 7, no. 3, pp. 344-347, June 2018, doi: 10.1109/LWC.2017.2776942.

[11] Tiwari S, Das SS (2019) Circularly pulse shaped orthogonal time frequency space modulation. Electron Lett. arXiv:1910.10457 ([cs.IT] 23 Oct 2019).

[12] N. C. Beaulieu and M. O. Damen, "Parametric construction of Nyquist-I pulses," in IEEE Transactions on Communications, vol. 52, no. 12, pp. 2134-2142, Dec. 2004, doi: 10.1109/TCOMM.2004.838739.

[13] Kamal, S., Azurdia-Meza, C.A. & Lee, K. Improved Nyquist-I Pulses to Enhance the Performance of OFDM-Based Systems. Wireless Pers Commun 95, 4095–4111 (2017). https://doi.org/10.1007/s11277-017-4044-3

Microwave Sensor for Liquid Mixture Identification based on Metamaterial based on Double Concentric Elliptical Complementary Split Ring Resonator

Halfaya Ahmed[1], Mohamed Lashab[1], Salah Salmi[2], Soufi Youcef[3],

[1] Larbi Ben M'hidi university, Oum el Bouaghi, laboratory (LENT), Algeria.
[2] Mentouri university, Constantine Algeria.
3Larbi Tebessi University, Tebessa, Algeria

Abstract—In this paper a Microstrip line coupled double concentric elliptical complementary split-ring **resonator** etched in the ground plane is used to create a sensor. The operating frequency of presented metamaterial sensor is from 1Ghz to 2 Ghz .The sensor is designed and simulated with the commercial software CST Studio Suite . The liquid sample's complicated dielectric permittivity affects the resonance frequency and bandwidth. We can build an empirical link between sensor resonance and sample permittivity using data collected from simulations. the resonance frequency is shifted from 1.50 down to1.49 Ghz. On the basis of variations in the resonance frequency and peak attenuation of the transmission response [l S21 l max] on resonance the sensor estimates the complex permittivity of a liquid. The proposed sensor is easily to fabricated and reusable resonator.

IndexTerms: sensor, microwave, split ring resonator, Q-factor, Metamaterials , permittivity, dielectric, liquid mixture, CST Microwave suite.

I. INTRODUCTION

New universally adaptable and reasonably priced sensor designs are highly sought after by modern industry. A wide range of monitoring and control systems should be compatible with these sensor approaches. Engineering's constant advancement and the growing demand for quick and efficient solutions. The treatment of the most diverse types of processes was made possible by the treatment of the most diverse types of processes. Sensors of various types are developed. In Biomedical [1,3], chemical [4,5] and other research fields have embraced low microwave sensors due to their high sensitivity and robustness, as well as their low cost. The concept of metamaterials has recently been used to create a new and alternative sensing platform [6]. They are artificially engineered materials based on sub-wavelength resonators that can manipulate electromagnetic waves, causing modifications to their properties that do not occur or may be difficult to obtain in nature [7,12].

Split-ring resonators (SRR) or complementary split-ring resonators (CSRR) are the main components of metamaterial microwave sensors, By simulating and analyzing the equivalent LC (inductance and capacitance), using the phenomenon of resonance , which are made using various techniques such as Antenna [13,14] ,measurement thickness of dielectrics [15], measurement of complex permittivity [11], for Strain Direction and Level Detection .Dielectric characterization [14]. They've also been used in microfluidic systems to characterize the liquid's dielectric properties [19,22] , to adjust the resonance frequency or transport the liquid or dissolved analyse into the sensor region, band stop filter [23],rotation sensor [24].

A double concentric elliptical complementary split-ring resonator (DECSRR) is used in this paper to generate a wider region of fringing electric field, thus increasing the effective interaction area with the sample. The proposed sensor calculates the complex permittivity of liquids based on variations in the resonance

frequency and the transmission response's peak attenuation during resonance. The following part introduces the suggested microwave sensor design and explains the changes to the (DECSRR) fundamental structure using an analogous circuit model.

This paper is presented as follow, the first section is dealing with theoretical aspect of the Double Concentric Elliptical Complementary Split Ring Resonator (DCESR). The second section is concerned with discussion of the results and finally conclusion.

II. Sensor design And theoretical study:

II. 1.Proposed Design of the Sensor :

The proposed sensor consists on Microstripline coupled double concentric elliptical complementary ring-resonator (DECSRR) as shown in figure.1.

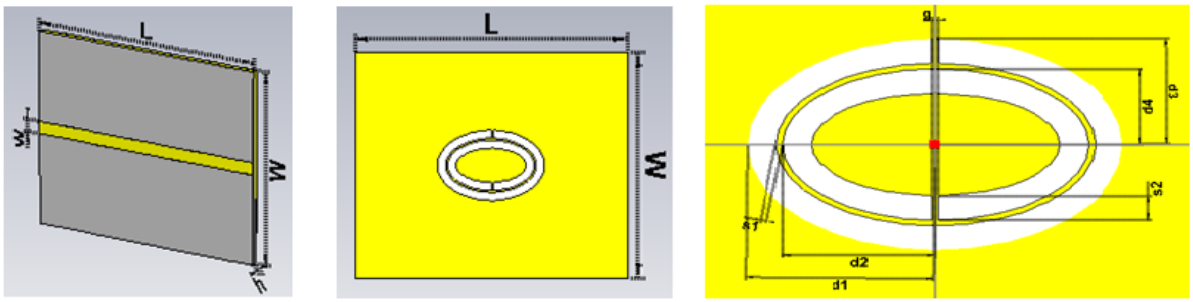

a) b) c)

Fig. 1. (a) 3D view of the sensor; (b) Ground plane with DECSRRs (c) DECSRRs with dimensions *L*= 30 mm, *W* = 25 mm, *h* = 0.787 mm, , *g* = 0.2 mm, *d1* = 5.9 mm, *d2* = 4.8 mm, *d3* = 1.95 mm, *D4* = 0.85 mm, *s1* = 0.2 mm, s2=0.9, *t* = 0.0175 mm, *w* = 1.6 mm.

The gadget was built on a Rogers RO3006 substrate with a relative permittivity of 6.5, and 0.0787 mm of thick. The ground plane and 50 Ω microstrip line copper metalization is 0.0175 mm .

II. 2 Theoretical study of the sensor:

The linked structure's equivalent lumped element circuit model is illustrated in Figure .2.(b); the equivalent circuit's resonance frequency may be determined using the following relationship[25] :

$$f_0 = \frac{1}{2\pi\sqrt{L_C(C+C_C)}} \qquad (1)$$

Fig. 2. (a) ECSRRs , (b) equivalent circuit model, , with L and C for the unit lengh inductance and capacitance of the microstrip transmission line and (RLC)c for DECSRRs.

The CST Microwave Suite simulates the DECSRRs sensor, with L and C for the unit length inductance and capacitance of the microstrip transmission line and (RLC)c for DECSRRs.

III. Results discussion:

The Table I displays the reference values measured by Bao et al. in 1995 [26] [28] are used in this paper. As shown in Figure 3, the suggested sensor exhibits a resonance at 1.54 GHz with a notch depth of –31.96 dB. According to the following relationship [26], the quality factor of the suggested sensor is 44, which can be computed as follows:

$$Q = R\sqrt{\frac{C+C_C}{L_C}} \qquad (2)$$

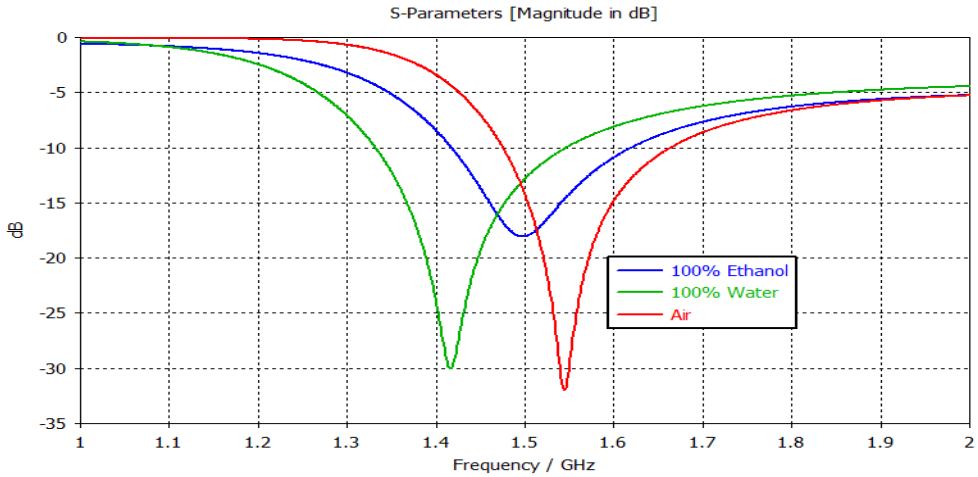

Fig.3, Simulation transmission response of the sensor in different conditions.

By adding liquid Ethanol on notice from Figure 3, that there is a displacement of the frequency of 0.05 GHz with respect to sensor loaded with air, the displacement is more interesting when the sensor is loaded with water, a difference if 0.15 GHz. The sensor has great sensitivity when the displacement is very wide, which means the error of measure is very low, this is the case in this sensor loaded with elliptical CSRRs

Table 1: References values of complex permittivity to binary mixtures water-ethanol [26] [28]

Water samples (%)	ϵ'	ϵ''	$\Delta\varepsilon'$	$\Delta\varepsilon''$
0	9	10	-38	-5
10	16.5	12.3	-30.5	-2.7
20	24	13.6	-23	-1.4
30	31.5	15.55	-15.5	0.55
40	39	15.6	-8	0.6
50	47	15	0	0
60	53	14.6	6	-0.4
70	61	12.8	14	-2.2
80	67	13.4	20	-1.6
90	72	10.6	25	-4.4
100	79.5	9	32.5	-6

.

For the first set of simulations, the volume fraction of water is increased from 0% to 100% with a step size of 10%, the sensor's resonant frequency and peak attenuation are calculated and are captured . The results of the resonance frequency and maximum attenuation are shown in fig 4(b) . The resonance frequency has been altered from 1.5 GHz to 1.49 GHz As the water volume portion increases from 0% (100%Ethanol) to 100% fig 4 (a)The frequency shift that corresponds to this is around 100 Mhz.

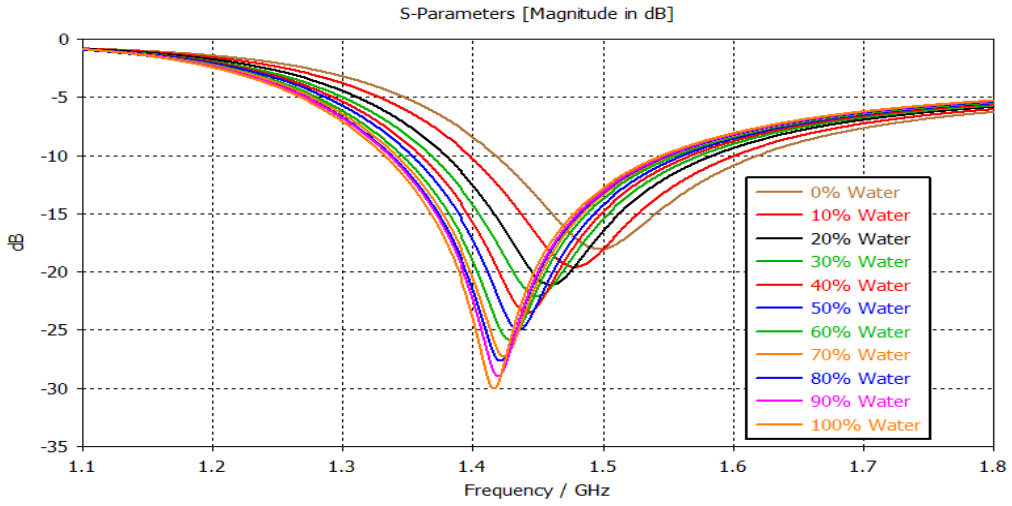

(a)

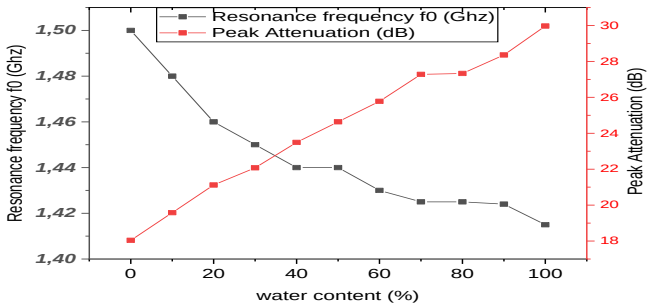

(b)

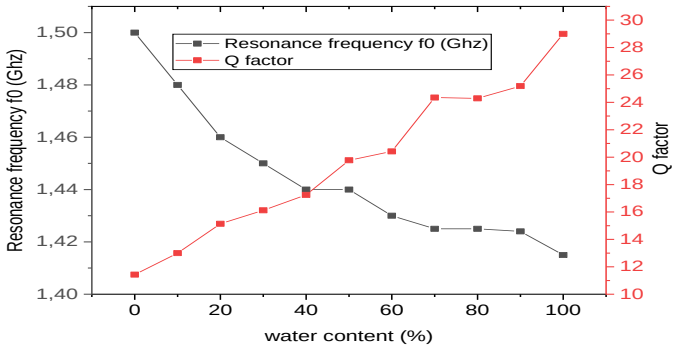

(c)

Fig. 4. (a) The Simulation transmission response of the water-ethanol test samples of the sensor from 0% to 1000% with the step size of 10%.
(b) resonance frequency and peak attenuation at different steps ,
(c) resonant frequeny and Qfactor simulated for different water-ethanol volume fractions.

Fig.4 (c) illustrates the resonance frequency and Q factor at various volume fractions of the binary water–ethanol mixture. When the quantity of water in the mixture is increased, the resonant frequency decreases and the Q factor increases.

IV. Conclusion:

In this paper A sensor structure designed by Double Elliptical concentrated (DECSRRs) is used, theoretical study is presented and simulation is done on CST. Obtained results from simulation indicate that the sensor presents very interesting displacement when loaded with ethanol and more interesting displacement when loaded with water. Future work can be extended for CRLH metamatrial structure for the sake of very high sensitivity.

References:

[1] Long Li, Zhen Jia, Feifei Huo, and Weiqiang Han "A Novel Compact Multiband Antenna Employing Dual-Band CRLH-TL for Smart Mobile Phone Application," *IEEE Antennas and Wireless Propagation Letters*, Vol. 12, 2013.
[2] Strangi, G., Sreekanth, K. V., & Elkabbash, M. (2017). "Hyperbolic Metamaterial-Based Ultrasensitive Plasmonic Biosensors for Early-Stage Cancer Detection," *Next Generation Point-of-Care Biomedical Sensors Technologies for Cancer Diagnosis*, 155–172. doi:10.1007/978-981-10-4726-8_7
[3]Korostynska, O., Mason, A., & Al-Shamma'a, A. (2014). "Microwave sensors for the non-invasive monitoring of industrial and medical applications," *Sensor Review*, 34(2), 182–191. doi:10.1108/sr-11-2012-72.
[4] Zhou H., Hu D., Yang C., Chen, C., Ji, J., Chen M., Chen Yu, Yang Y. ,Mu X. (2018). "Multi-Band Sensing for Dielectric Property of Chemicals Using Metamaterial Integrated Microfluidic Sensor,". *Scientific Reports*, 8(1). doi:10.1038/s41598-018-32827-y.
[5] Kim, H. K., Yoo, M., & Lim, S. (2015). "Novel ethanol chemical sensor using microfluidic metamaterial," *IEEE International Symposium on Antennas and Propagation & USNC/URSI National Radio Science Meeting*. doi:10.1109/aps.2015.7305068, 2015.
[6] Tung, N. T., & Tanaka, T. (2018). "Characterizations of an infrared polarization-insensitive metamaterial perfect absorber and its potential in sensing applications," *Photonics and Nanostructures - Fundamentals and* Applications, 28, 100–105. doi:10.1016/j.photonics.2017.12.004 , Oct 2008.
[7] V. Veselago, "The electrodynamics of substances with simultaneously negative values of ε and μ". *Sov. Phys. Usp*. **10**(4), 509–514 (1968)
[8] J. Pendry, A. Holden, D. Robbins, W. Stewart, "Magnetism from conductors and enhanced Nonlinear phenomena,". *IEEE Trans. Microw. Theory Tech*. **47**(11), 2075–2084 ,1999.
[9] Caloz, T. Itoh, "Application of the transmission line theory of left-handed (LH) materials to the realization of a microstrip LH line," *Proceedings of the IEEE Antennas and Propagation, Vol. 52, No. 5, May 2004.*

[10] C. Caloz, T. Itoh, "Electromagnetic Metamaterials," (*Wiley, Hoboken*, 2006).
[11]. G. Eleftheriades, K. Balmain, "Negative-Refraction Metamaterials," (*Wiley, Hoboken*, 2005).
[12] Reddy, G. B., & Kumar, D. S. (2018). "Miniaturization of microstrip slot antenna using SRR and CSRR Loading,". *3rd International Conference on Microwave and Photonics* (ICMAP). 2018
[13] Öznazı, V., & Ertürk, V. B. (2008). A comparative investigation of SRR- and CSRR-based band-reject filters: Simulations, experiments, and discussions. Microwave and Optical Technology Letters, 50(2), 519–523.
[14] Rahman, M., Khan, W. T., & Imran, M. (2018). Penta-notched UWB antenna with sharp frequency edge selectivity using combination of SRR, CSRR, and DGS. AEU - International Journal of Electronics and Communications, 93, 116–122.
[15] Li, H., & Jiang, Z. (2019). A CSRR and SRR Based Ultrawideband MIMO Antenna with Band-Notched Characteristics. 2019 IEEE International Symposium on Antennas and Propagation and USNC-URSI Radio Science Meeting.
[16] Zhang, Q., Khan, S. N., & He, S. (2009). Realization of left handedness through CSRRs and SRRs in microstrip line. Microwave and Optical Technology Letters, 51(3), 757–760.
[17] Yoo, M., & Lim, S. (2013). "SRR- and CSRR-loaded ultra-wideband (UWB) antenna with tri-band notch capability," *Journal of Electromagnetic Waves and Applications*, 27(17), 2190–2197. doi:10.1080/09205071.2013.837013.
[18] Chuma, E. L., Iano, Y., Fontgalland, G., Roger, L. L. B., & Loschi, H. (2020). "PCB-integrated Non-destructive Microwave Sensor for Liquid Dielectric Spectroscopy Based on Planar Metamaterial 11211Resonator. Sensors and Actuators A: Physical, 112112. doi:10.1016/j.sna.2020.
[19] Chudpooti, N., Silavwe, E., Akkaraekthalin, P., Robertson, I. D., & Somjit, N. (2018). "Nano-Fluidic Millimeter-Wave Lab-on-a-Waveguide Sensor for Liquid-Mixture Characterization," *IEEE Sensors Journal*, 18(1), 157–164. doi:10.1109/jsen.2017.2772348 .
[20] Chuma, E. L., Iano, Y., Fontgalland, G., & Roger, L. L. B. (2018). "Microwave Sensor for Liquid Dielectric Characterization based on Metamaterial Complementary Split Ring Resonator," *IEEE Sensors Journal*, 1-1. doi:10.1109/jsen.2018.2872859.
[21] Hassan, A., Lee, K., Bae, J., & Lee, C. H. (2017). "An inkjet-printed microstrip patch sensor for liquid identification. Sensors and Actuators A," *Physical*, 268, 141–147. doi:10.1016/j.sna.2017.11.028
[22] Bonache, J., Gil, M., Gil, I., Garcia-Garcia, J., & Martin, F. (2006). "On the electrical characteristics of complementary metamaterial resonators," *IEEE Microwave and Wireless Components Letters*, 16(10), 543–545. doi:10.1109/lmwc.2006.882400 .
[23] Haq, T., Ruan, C., Zhang, X., Kosar, A., & Ullah, S. (2019). "Low cost and compact wideband microwave notch filter based on miniaturized complementary metaresonator," *Applied Physics A*, 125(9). doi:10.1007/s00339-019-2923-z.
[24] Baena, J. D., Bonache, J., Martin, F., Sillero, R. M., Falcone, F., Lopetegi, T., Sorolla, M.(2005). "Equivalent-circuit models for split-ring resonators and complementary split-ring resonators coupled to planar transmission lines," *IEEE Transactions on Microwave Theory and Techniques*, 53(4), 1451– 1461. doi:10.1109/tmtt.2005.845211.
[25] Withayachumnankul, W., Jaruwongrungsee, K., Tuantranont, A., Fumeaux, C., & Abbott, D. (2013). "Metamaterial-based microfluidic sensor for dielectric characterization," *Sensors and Actuators A: Physical*, 189, 233–237. doi:10.1016/j.sna.2012.10.027.
[26] Zhou, K.; Zhou, C.-X.;Wu,W. "Resonance Characteristics of Substrate-Integrated Rectangular Cavity and Their Applications to Dual-Band andWide-Stopband Bandpass Filters Design," *IEEE Trans. Microwave. Theory Tech*. **2017**, 65, 1511–1524.
[27] Bao, J., Swicord, M. L., & Davis, C. C. (1996). "Microwave dielectric characterization of binary mixtures of water, methanol, and ethanol," *The Journal of Chemical Physics*, 104(12), 4441–4450. doi:10.1063/1.471197.

Design and Analysis of an Antenna Array Based on a New Structure for an RFID Application

Mohammed Amin RABAH
Algerian Space Agency
Satellite development center
Oran, Algeria
amine-ttl@live.fr

Zohra SLIMANE
Electrical Engineering Department
University of Ain Temouchent,
Ain Temouchent, Algeria
zoh_slimani@yahoo.fr

Kouther YAMANI
Electrical Engineering Department
University of Ain Temouchent
Ain Temouchent, Algeria
nessrinkawthar@gmail.com

Kaoutar HACHEMI
Electrical Engineering Department
University of Ain Temouchent
Ain Temouchent, Algeria

***Abstract*— This paper proposes a new design microstrip patch antenna for RFID application; by applying microwave frequency band. The chosen resonance frequency is about 2.45 GHZ. A new design of the patch antenna parameters is calculated using theoretical equations, then verified by a simulation and optimization on CST MWS® software .The obtained results from simulation two antenna array simulations present a good impedance matching, and significant gain for this application.**

Keywords—Antenna, CST, microwave, Patch, RFID, Reader,

I. INTRODUCTION

The RFID (Radio Frequency Identification) reader antenna[1-2] allows the activation of tags and the transmission of information to the reader. It is one of the essential identification elements of RFID [3] system and its miniaturization and evaluation are of a great interest. In this work we are interested in microwave[4]technology, more particular in the design of a new structure of a patch antenna array[5] that radiates at 2.45 GHz for a RFID reader. These antennas are constituted of a FR4 type substrate (εr = 4.3, thickness =1.6 mm).

The structure of this array allows us to have better performances comparing to a rectangular patch antenna; where the main contribution of this technique is to help increase the gain of this antenna network [6] . We present in this study, the reflection coefficient and the radiation pattern of this array obtained by simulation by the CST MWS® [7]. A discussion of the performances, improvements and perspectives of this antenna structure concludes this work.

II. GEOMETRY AND STRUCTURE OF PROPOSED ANTENNA

This geometry is inspired from hexagonal antenna presented in [8], where we use PEC (Perfect Electrical Conductor) as radiating patch as shown in Fig. 1.

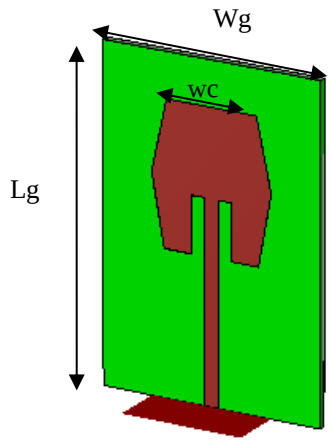

Fig. 1. Geometry of Antenna Design

TABLE 1: DIMENSION OF PATCH ANTENNA

Parameters	Dimensions (mm)
Substrate Length(Lg)	69.41
Substrate Width(Wg)	47.2
Patch Width(Wc)	9.75

The proposed patch antenna is designed with CST MWS®. Fig.2 shows the impedance matching result.

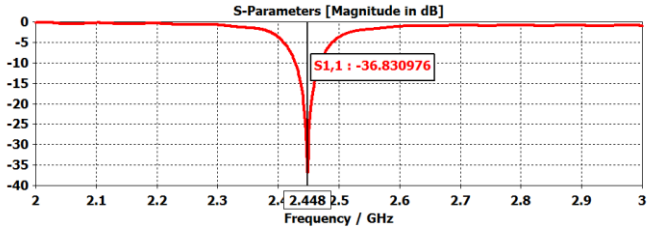

Fig. 2. The reflection Coefficient

From Fig.2, it is clear that hexagonal antenna has improved the performance of rectangular patch antenna work at the same resonance frequency. Where the value of return loss is less than -10 dB at 2.45 GHz, which means that a minimum return power can reflected at this frequency.

III. Simulation of an Array of Two Printed Antennas :

Fig.3 shows antenna array of two patch elements, separated by a distance d=0.6 mm, we opt for the parallel feeding method through a feed network in the form of a T-junction (power divider), where the characteristic impedance of the two microstrip lines is given as follows [9]:

$$Z0 = nZs \qquad (1)$$

The factor *n* is the number of microstrip transmission lines emanating from a node connected to a source generator. The characteristic impedance (Z1) of the two microstrip lines is given by Eq.1 as [9]:

$$Z1 = 2\,(50) = 100\,\Omega$$

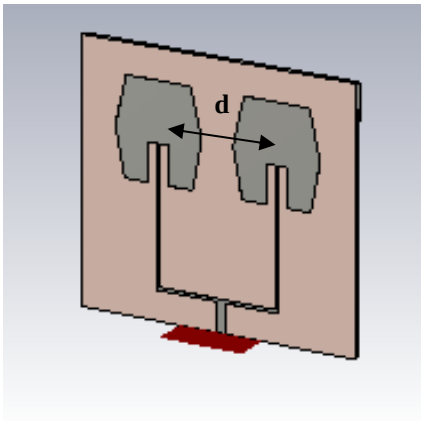

Fig.3. The patch Antenna Array

Reflection coefficient of the linear array of two patches is:

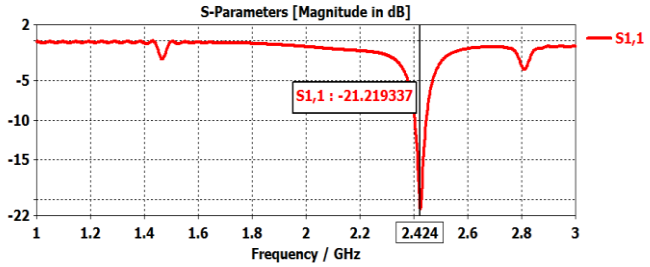

Fig.4. The Reflection Coefficient of a Two Elements Array Antenna

The Voltage Standing Wave Ratio of the linear array of two patches:

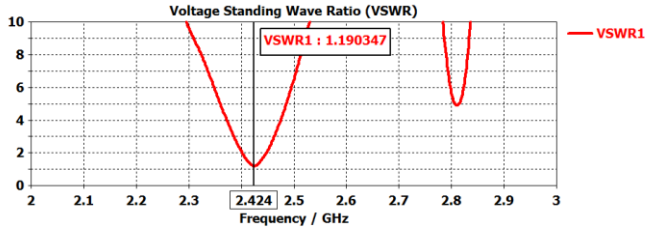

Fig.5. The VSWR Coefficient of Two Elements Array Antenna

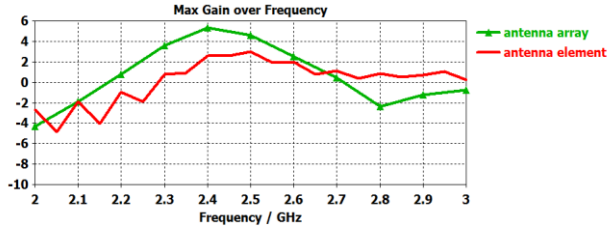

Fig.6. Gain Variation of Proposed Antenna Array

From Fig.6 we notice that the gain in a two parallel fed patches antenna array is improved compared to a single element antenna.

The 3D radiation pattern of a 2 patches array antenna reflects the value of the directivity, and on the polar plane graph which allows presenting the aperture of this antenna

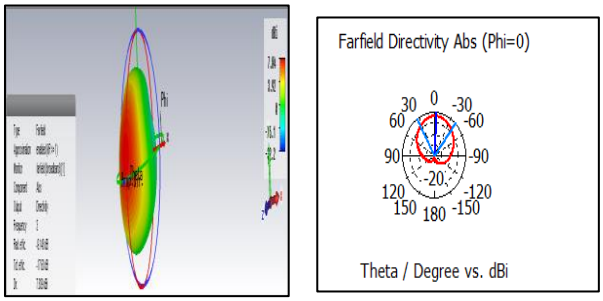

Fig.5.3D and Polar Directivity Radiation Pattern of a Patch Antenna

The obtained values from our proposed antenna are:

- The gain value is 5.14 dBi
- The directivity of this antenna is 7.83 dBi

- The aperture antenna is 75.8 deg.

It's very important to describe and present the reading range of RFID system; this parameter shows a distance of reading between the reader and the tag [11].

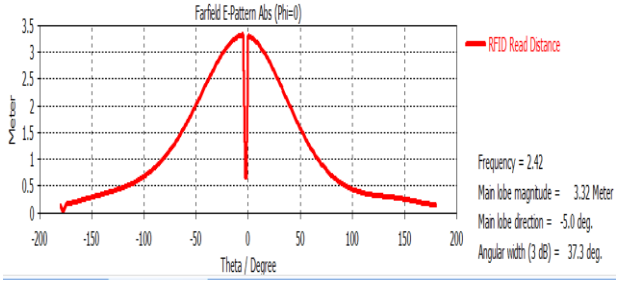

Fig.6.The RFID Reading Rang

TABLE.2.COMPARISON VALUES

	S11(dB)	VSWR(dB)	Gain(dB)	Directivity (dBi)
Single proposed patch antenna	-25.41	1.1133	2.79	6.142
Patch antenna array	-25.41	1.24	5.14	7.83

IV. CONCLUSION

we have simulated an antenna composed of two elements and the gain obtained is 5.14 dBi, this gain is improved by increasing the size of the network from 1 elements to 2 elements, in future works we will be interested in the realization of the antennas and the experimental validation antennas for RFID reader using network analyzer for measuring the reflection coefficient and the standing wave ratio.

REFERENCES

[1] Kaur, M.; Sandhu, M.; Mohan, N.; Sandhu, P.S,''RFID Technology Principles, Advantages,Limitations & Its Applications''. Int. J. Comput. Electr. Eng.vol., 3, pp.151–157, 2011
[2] P. Fuhrer, D. Guinard, and O. Liechti, "RFID: from Concepts to Concrete Implementation," Int. Conf. on Advances in the Internet, Processing, Systems and Interdisciplinary Research (IPSI'06), Marbella, Spain, February 2006
[3] Ren, A., Wu, C., Gao, Y., ''A robust UHF near-field RFID reader antenna'', IEEE Trans. Antennas Propag., Vol. 60, No.4, pp. 1690–1697, 2012
[4] M. G. Jeong and W. S. Lee, "A smart blood bag management system using a load-integrated U-shaped near-field RFID antenna array", IEEE Trans. Antennas Propag., vol. 67, No. 3, pp. 1837-1843, Mar. 2019.
[5] M. Abbak and I. Tekin, "RFID coverage extension using microstrip-patch antenna array [wireless corner]", IEEE Antennas Propag. Mag., vol. 51, no. 1, pp. 185-191, Feb. 2009.
[6] M. Manzani, A. Alù, F. Bilotti, and L. Vegni, "Polygonal Patch Antenna for Wireless Communication", IEEE transanctions on vehicular technology. Vol. 53, no. 5 (2004), pp. 1434- 1440,.
[7] Rütschlin, M. Tilmann,W ,"State of the art antenna simulation with CST STUDIO SUITE", in 9th European Conference on Antennas and Propagation (EuCAP) in Lisbon, Portugal 2015
[8] K. C Prakash, P. V Vinesh, R Vivek, Mohammad Ameen and K Vasudevan, "Circularly Polarised Hexagonal Patch Antenna With Polygonal Slot for RFID Applications",Journal of Communications Software and Systems, vol. 12, no. 2, pp. 122-128, 2016.
[9] Akaninyene B, Gabriel A. Igwue , Design and Simulation of Rectangular Microstrip Antenna Arrays for Improved Gain Performance International Journal of Networks and Communications 2019, 9(2): 73-81.
[10]Satya Sai Srikant, Rajendra Prasad Mahapatra''Read Range of UHF Passive RFID'', International Journal of Computer Theory and Engineering, Vol. 2, No. 3, pp.1793-8201, June, 2010
[11]

Simulation for the improvement of the performance of the digital transmission chain between Oum El Bouaghi and Ain Mlila

Boughrara Bouchra[1], Hamouda Amar[2], Goumidane Faycal[3], Kebaili Amir[1], Messaoudi Roumaissa[1]
[1]*Master applied physics, Department of SM, Faculty of Exact Sciences and Sciences of Nature and Life, University of Oum El Bouaghi, Algeria.*
[2]*MCB, Department RT, ISTA Ain Mlila, University of Oum El Bouaghi, Algeria.*
[3]*MCB, Department SM, Faculty of Exact Sciences and Sciences of Nature and Life, University of Oum El Bouaghi, Algeria.*

*Corresponding author, email : boughrarabouchra18@gmail.com

Abstract
The aim of this work is to study and precisely adjust the values of the parameters of the components used at the level of the transmitter, receiver and physical support modules of the digital transmission (optical fiber) using the OPTISYSTEM 7 simulator, in order to improve the quality and the binary error rate of the transmitted signal and subsequently the development of the performance of the transmission chain at a distance of 70 Km.
Keywords: *parameters, components, digital transmission, quality, performance*

I. Introduction

In view of the rapid changes in telecommunications services accessible to users, in particular enriched multimedia services such as very high-speed Internet, high definition TV, future access networks and home networks will soon have to be able to carry data streams of up to gigabit per second[1, 2, 3].

This demand for very high speeds goes far beyond the possibilities offered by current solutions based on coaxial cable (ADSL .....) [2].

The advantages of optical fiber as a transmission medium (high bandwidth, low propagation losses, immunity to electromagnetic waves) justify the important development of optical transmission systems over the last decade[3, 4].

Unfortunately the sensitivity to propagation defects increases with the flow rate, whether for linear effects due to chromatic dispersion (Chromatic Dispersion) or nonlinear effects essentially induced by the Kerr effect (dependence of the refractive index of the fiber of light intensity). Next-generation Optical Access Networks are intended to provide several services simultaneously on the common network. Access networks that can interconnect a larger number of users with symmetrical bandwidth of up to 10 Gbps per client will be required. The objective is to achieve the growing demand for QoS capacity, performance and quality of service, by exploiting the large bandwidth available on optical fiber. The challenge will be in exploiting the bandwidth of the fiber to the maximum to create a more structured network[5, 6].

Currently, copper access networks can transmit up to 30Mbit/s, provided you are close enough to the central, which is enough to simply surf the internet. With the arrival of new services, such as high-definition television, video on demand, remote data backup, remote monitoring, . . ., copper access networks do not have sufficient physical properties to meet the growing demand for throughput[6]. Optical access technologies have been developed to meet demands and offer users speeds ranging from 50Mbit/s to 1Gbit/s or even more in the future. The different access architectures proposed are the point-to-point (P2P), and the multipoint point or passive optical network (PON: Passive Optical Network) [7].

II. Theoretical study

II.1. Description of the transmission system Theoretical study

Our communication system is composed of three essential blocks : issuer, communication channel and receiver (see Figure 1)

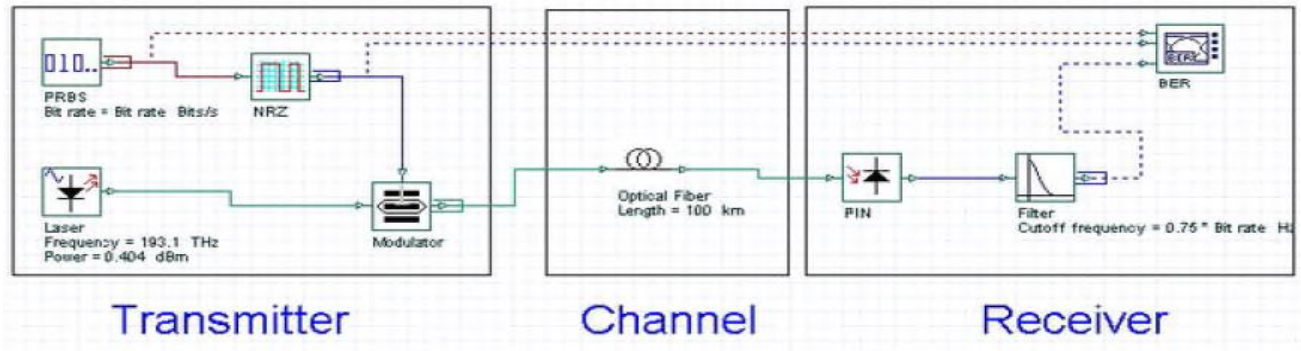

Figure 1 Optical Communication System Modules

II.2. Block 1

This block (see Figure 2) behaves to a transmission module, which consists of a laser diode produces a 193 THz carrier, a pseudo-random bit generator excites an RZ encoder which itself drives a Mach-Zehnder modulator.

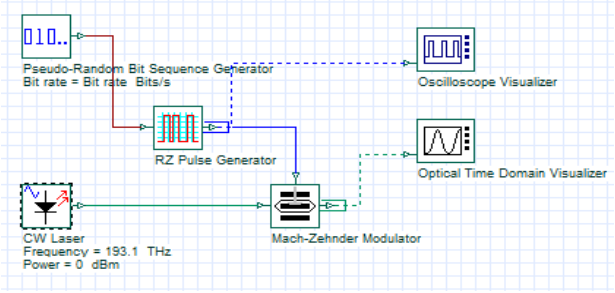

Figure 2 The transmission module

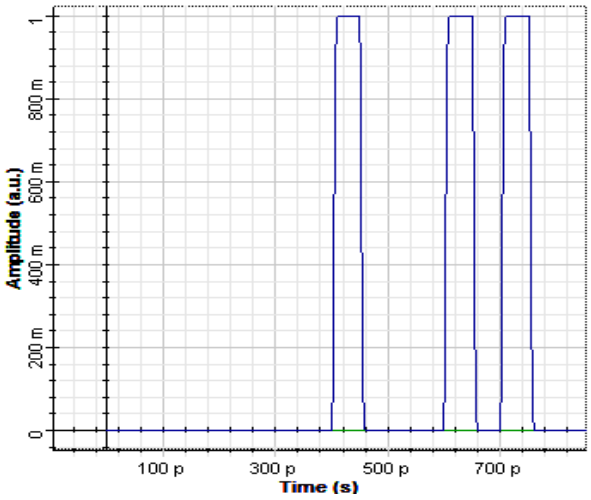

Figure 3 The signal at the output of the digital source (to be transmitted)

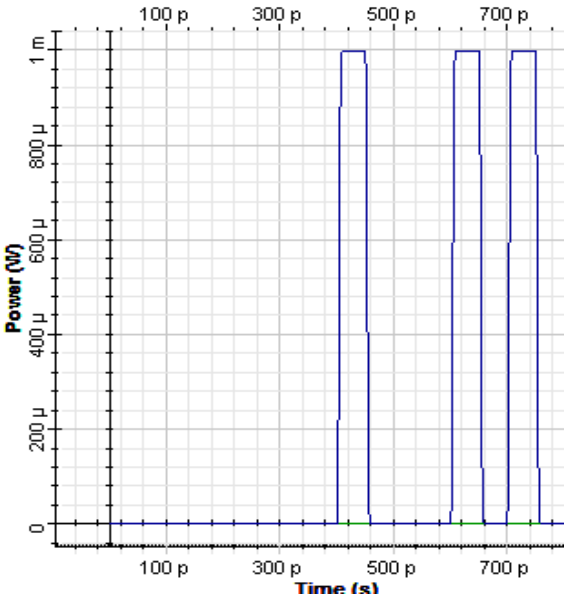

Figure 4. The signal at the output of the Mach-Zehnder Modulator

II.3 Block 2

This block has the physical digital transmission medium, which is an optical fiber type single mode (see Figure 5), the signal at the output of block 1, is amplified to recover the lost power within the Mach-Zehnder modulator, the signal at the output of the amplifier is injected into the optical fiber (block 2), the signal propagating through this type of support undergoes effects of the optical fiber (losses, chromatic dispersion, non-linear effects (Ker effect)) [8, 9, 10], The amplifier at the input of the optical fiber to recover losses at the Mach-Zehnder modulator, while qua the optical amplifier at the output of the fiber to recover losses in the optical fiber.

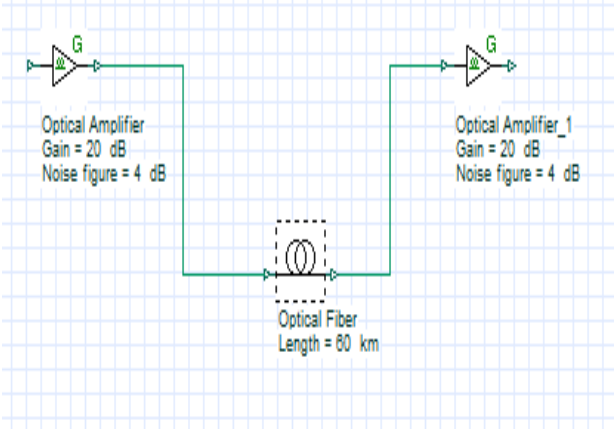

Figure 5. Block 2

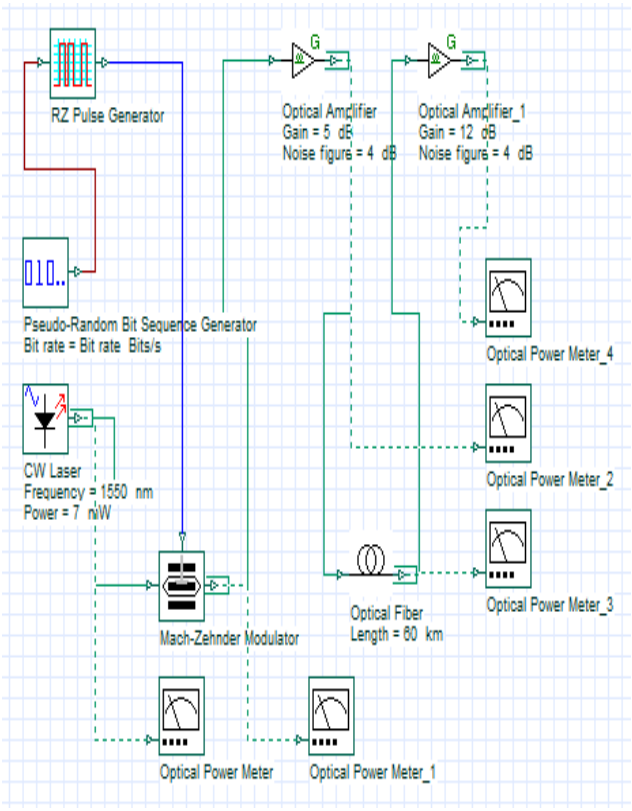

Figure 6. Power balancing.

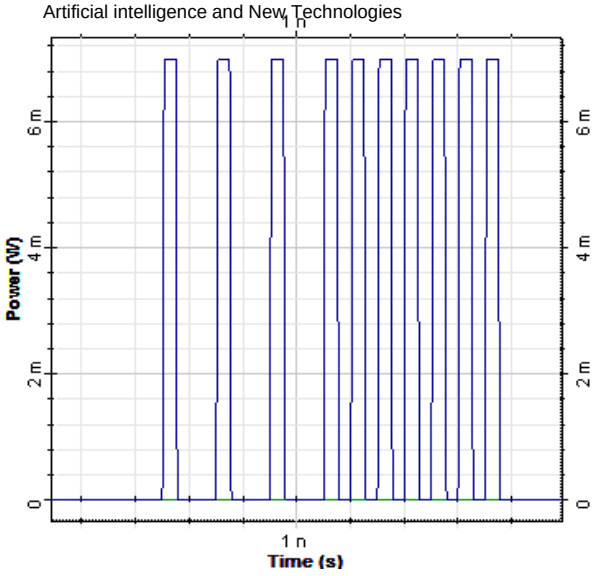

Figure 7. Time signal at the input of the fiber before amplification.

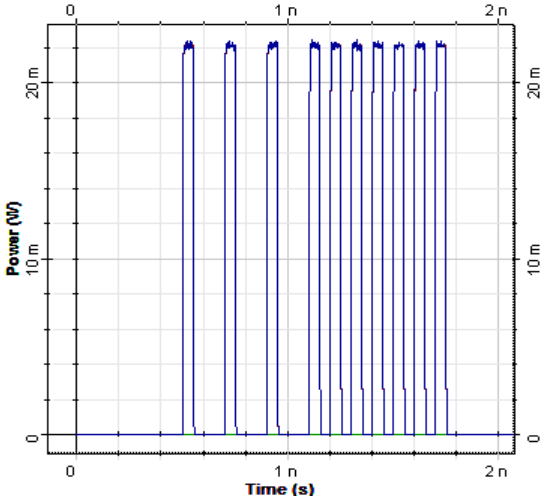

Figure 8. Time signal at the input of the fiber after amplification.

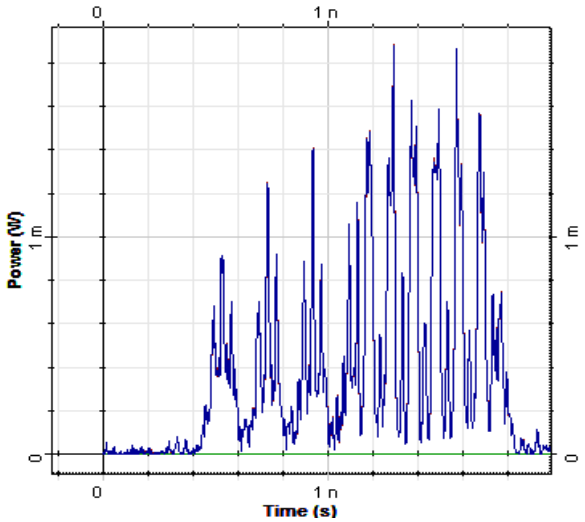

Figure 9. Time signal at the output of the fiber before amplification.

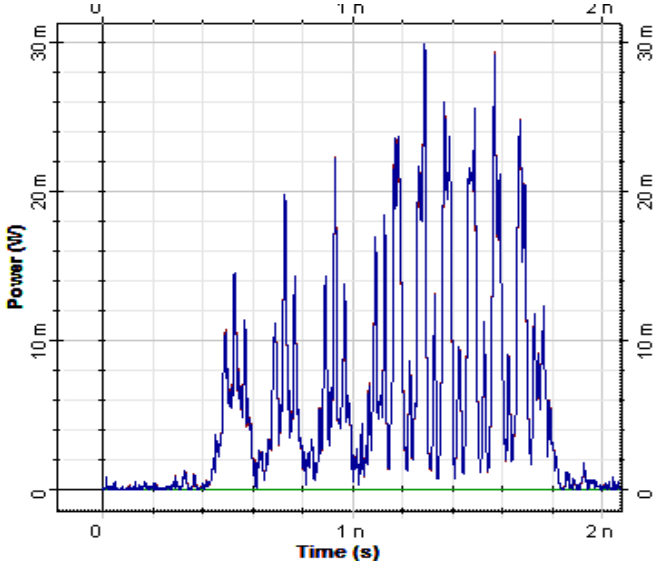

Figure 10. Time signal at the output of the fiber after amplification.

II. 4 Block 3

This block behaves to a PIN photodetector diode, is a component that transforms the light energy into an electrical energy of the same shape, this component is placed in series with a low-pass Bessel filter (see Figure 11).

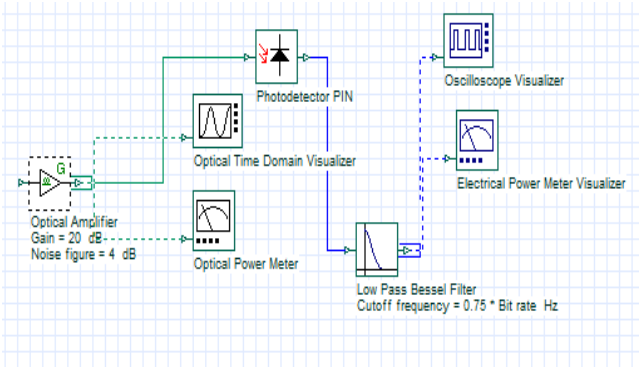

Figure 11. Block 3

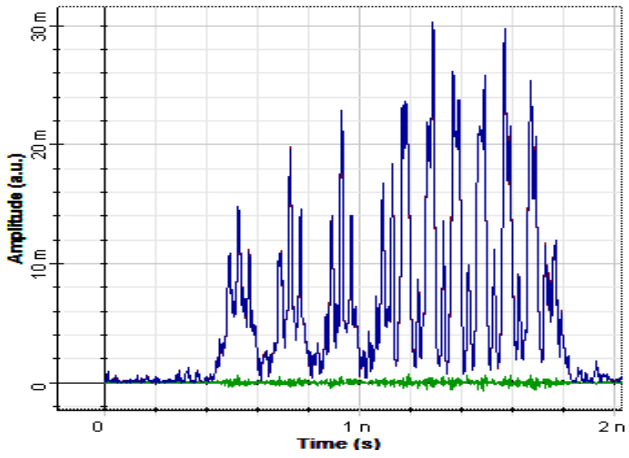

Figure 12. The time signal at the output of the PIN

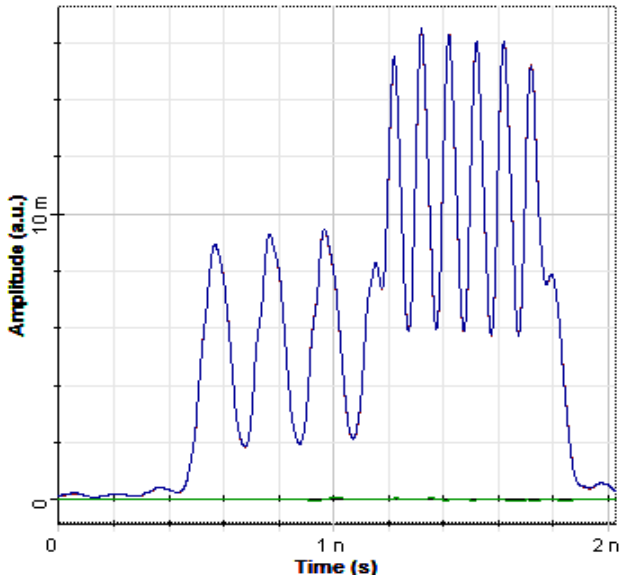

Figure 13. The time signal at the filter output

III. Digital simulation

Faced with the increasing complexity of the architectures and systems developed, simulation tools have acquired an important role. They are increasingly used to optimize the parameters involved in the realization of a system. They make it possible to predict results expected experimentally. They now also make it possible to use during a simulation, experimental elements such as signals recorded with measuring devices or curves characteristic of real components. In all that follows the simulation tool used is optisystem version 7[11, 12].

IV. Results and discussions

Despite the use of an optical amplifier at the output of one block to another or from one component to another in order to recover the power consumed (losses), we manage to balance the power but with amplitude jitters (see Figures 7 and 8).

At the level of block 2, it was possible to balance the optical power, but the length of the optical fiber influences the chromatic dispersion of order two which degrades the pulse (asymmetric distortion), (see Figures 9 and 10).

Also at block 2, the length of the fiber influences the modal dispersion of polarization (PMD), which causes the temporal jitter on the signal to be transmitted, (see Figures 12 and 13).

In addition at the level of the block 3 from Figures 12 and 13, one can notice the influence of the noise coming from the photo-detector diode PIN (Figure 12) before the filtering of the low-pass Bessel filter.

Because of these disadvantages mentioned above the use of optical fiber sections is necessary along the transmission line (see Figure 14).

The bit error rate analyzer gives us good signal quality recovered and an acceptable bit error rate (BER) (see Figures 15 and 16).

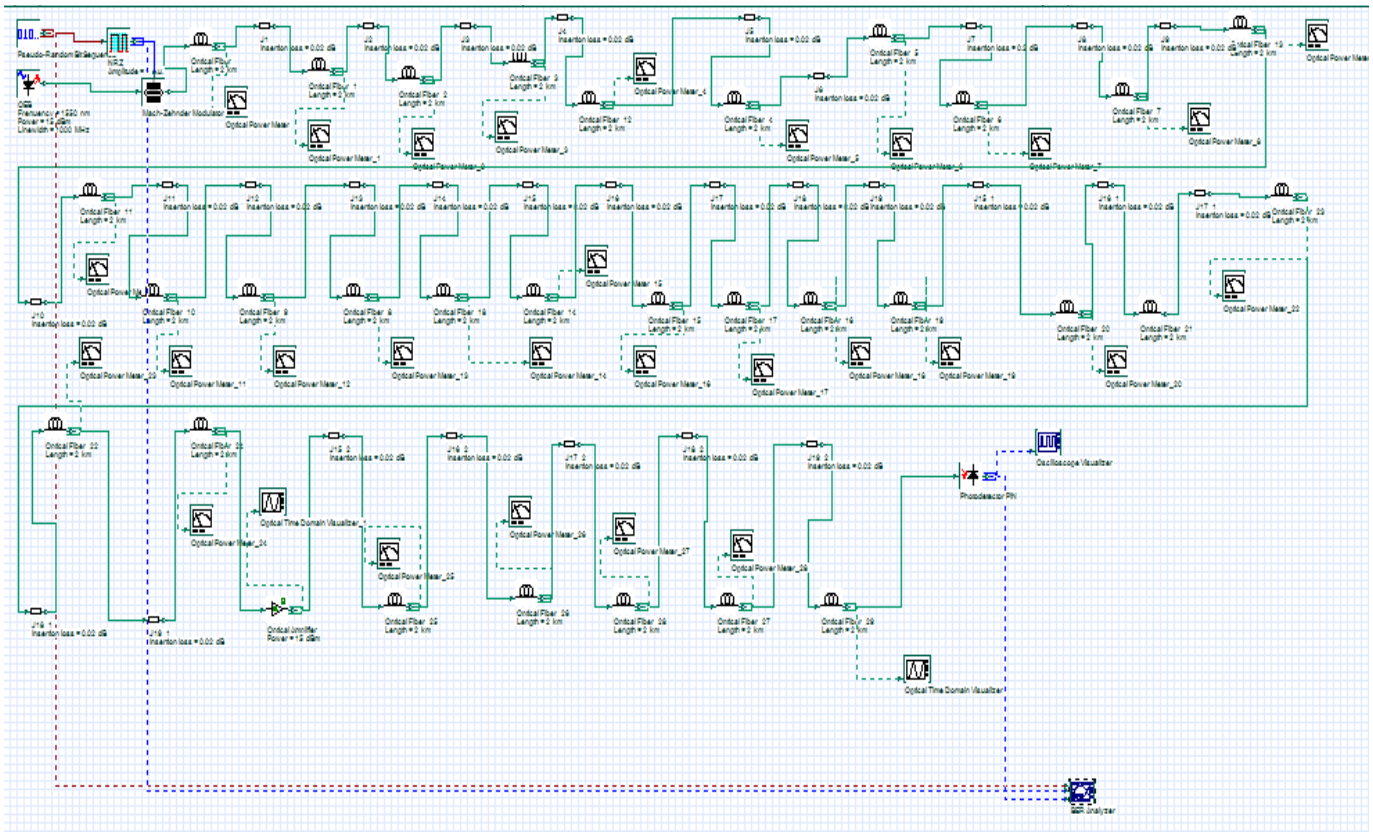

Figure 14. The actual chain of transmission

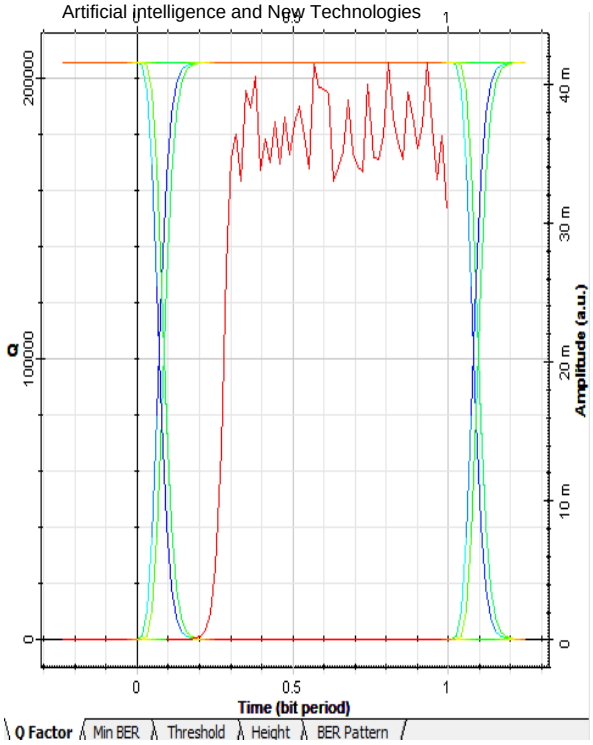

Figure 15. Quality of the recovered signal

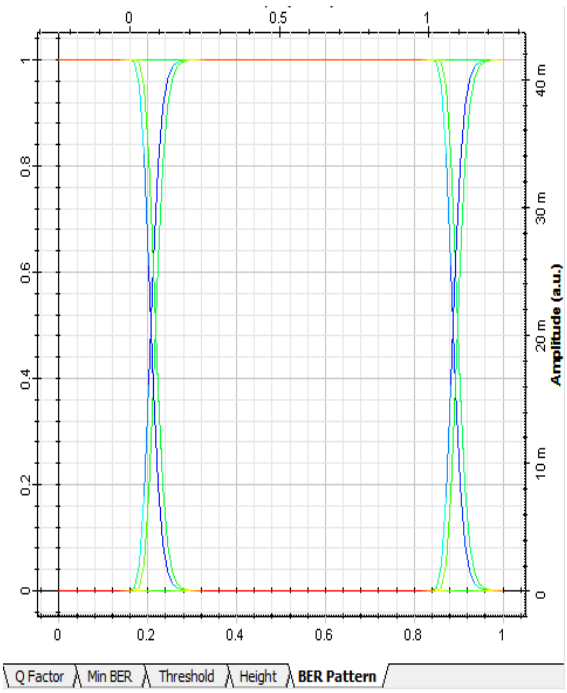

Figure 16. Transmission bit error rate

Conclusion

In order to transmit the growing mass of digital or analog information on the various networks and transmission chains with reliability and preserving a good quality of service. Indeed, this has necessitated the development of a communication system that is powerful and reliable enough to interconnect a constantly growing number of users across the globe.

To reduce the distortion of a signal across a transmission line, a compensating fiber must be inserted at the end of this optical link, but simulation results have shown that this cable causes a lot of losses that affect the distortion of the signal.

The final solution to improve signal quality is the addition of an amplifier and compensation cable, which is demonstrated by simulation.

References

[1] M. Dieng. Réseaux et systèmes de télécommunications dans une région périphérique du Sénégal: Ziguinchor en Casamance. Géographie. Université Michel de Montaigne - Bordeaux III, 2008. Français. fftel-00356029f

[2] H . BAKIS, Géographie des réseaux de communication et des télécommunications in NETCOM, n° 6, vol. 2, Avril 1992, pp. 309-395.

[3] H. LE BRAS, Étude des réseaux radio sur fibre dans le contexte des réseaux d'accès et privatifs, thèse de doctorat, UNIVERSITÉ PIERRE ET MARIE CURIE, 2008.

[4] F. Payoux, Étude des réseaux d'accès optiques exploitant le multiplexage en longueurs d'onde . Thèse doctorat, Ecole Nationale Supérieure des Télécommunications de Bretagne, 2006.

[5] P. Guignard, H. Ramanitra et L. Guillo, « Home Network based on CWDM Broadcast and Select technology », in European Conference on Optical Communication, 2007.

[6] F. Sanaei et P. Chu, « Passive all-optical bus network based on mode-selective coupling », in Global Telecommunications Conference, 1995. GLOBECOM '95., IEEE, vol. 2, p. 1007–1011 vol.2, 1995.

[7] FCC, « First report and order, revision of part 15 of the commission's rules regarding ultra-wideband transmission systems », document technique et docket 98-153, FCC, avril 2002.

[8] G. P. Agrawal, *"Nonlinear Fiber Optics"*. 2006.

[9] F. Bruyere, "Impact *of first and second order PMD in optical digital transmission systems*", Optical Fiber Technology, Vol.2, pp. 269-280, 1996.

[10] R. W. Boyd, *"Nonlinear optics". Academic press,* 3rd edition, 2008.

[11] Nishizawa N. & Goto T., 2006. Novel super-continuum fiber lasers and wavelength-tunable soliton pulses, SPIE Newsroom.

[12] Mohammadi S. O., Mozaffari S. & Shahidi M. M., 2011. Simulation of a transmission system to compensate dispersion in an optical fiber by chirp gratings,*International journal of the Physical Sciences*, Vol. 6(32), 7354-7360.

Contribution to the design of ultra-frequency carriers for digital transmission in advanced telecommunications

Hamouda Amar[1], Hamla Amina[2], Djemil Cheima[2]
[1] *MCB Department of Networks and Telecommunications, ISTA Ain Mlila, Univ-OEB, Algeria.*
Member of the Laboratory of Studies and Research of Instruments and Communications of Annaba (LERICA), Algeria.
[2] *Master's degree in Applied Physics, SM Department, Faculty of Exact Sciences and Natural and Life Sciences, Univ-OEB, Algeria.*
*Corresponding author, email : amarhamouda23@gmail.com

Abstract
Our goal of this work is the realization by simulation the production of a train of optical pulses in order to improve the factors that influence the parameters of the optical fiber material, which determine the flow of information and data to be transmitted, very high speed at very long distances by fiber or in the form of radio beams using dispersive and non-linear regimes by the OTDM technique, in order to improve the performance of the transmission chain, thus, the security and protection of the transmitted signal against noise, interference and distortion.
Keywords : optical pulses, the flow, high speed, non-linear, OTDM technique.

I. Introduction

At present, the most efficient and widespread technology is based on optic-fiber transmission systems. The latter offer a physical support with low attenuation, almost insensitive to electromagnetic noise, easy installation and high transmission capacities.

The starting point of telecommunications by optical fibers is undoubtedly the invention and development in the 60s of LASER [1, 2] which, by their compactness, their quasi-monochromatic and their high power, have the advantage of being able to be injected into a waveguide. The race to the ever further was then launched and was never to know an end. Fiber optics, as we currently use it, are the result of intensive research on new weakly dissipative waveguides.

Thanks to rapid advances in chemistry, very low loss coefficients of the order of 0.2dB/km around 1550 nm were reached in the 70s, bringing to 95% the amount of light conveyed after 1km of propagation. At the same time, the theoretical discovery of the optical soliton in 1973 by Hasegawa and Tappert [2], then of its experimental observation in 1980 by Mollenauer and his collaborators [2, 3] are landmarks in the history of telecoms. Indeed, researchers and industrialists were therefore able to propagate a pulse without deformation at the speed of light, over very long distances and with a wide bandwidth.

One of the main challenges of all-optical regeneration for future telecommunications networks is therefore to achieve a compact 2R regenerator that can remove the maximum noise from a signal whose rate can exceed 40 Gbits/s. For such speeds, electronics have reached their limits and are therefore no longer competitive. The use of an all-optical regeneration technique is therefore essential. A technique called Mamyshev [4, 5] is currently considered one of the most promising.

Digital transmission systems convey information between a source and a recipient using a physical medium such as cable, optical fiber or propagation over a radio channel. The signals transported can be either directly of digital origin, as in data networks, or of analog origin (speech, image ...) but converted into a digital form. The task of the transmission system is to convey information from the source to the recipient as reliably as possible [6].

With the rapid evolution of telecommunications services accessible to users, such as multimedia services enriched with very high-speed Internet, IPTV (Internet Protocol Television), video telephony, high-definition television and home networks. All these services will thus have to carry data streams reaching gigabit per second [6, 7].

II. Theoretical study

II.1. Block diagram of the generator

This generator consists of four blocks (modules) integrating electronics and optoelectronic functions, each of which has a well-defined role (see figure 1).

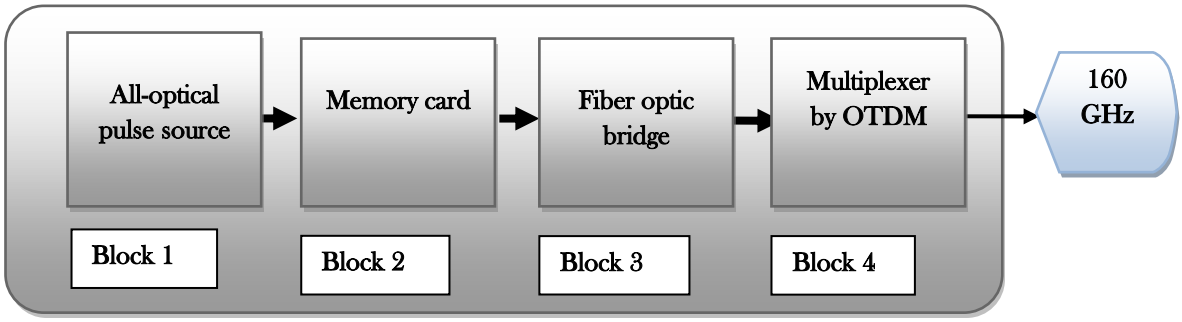

Figure 1. Descriptive diagram of the generator.

II.1.1. Block 1

This block (see Figure 2) represents a source of very high-speed picosecond optical pulses [8, 9].

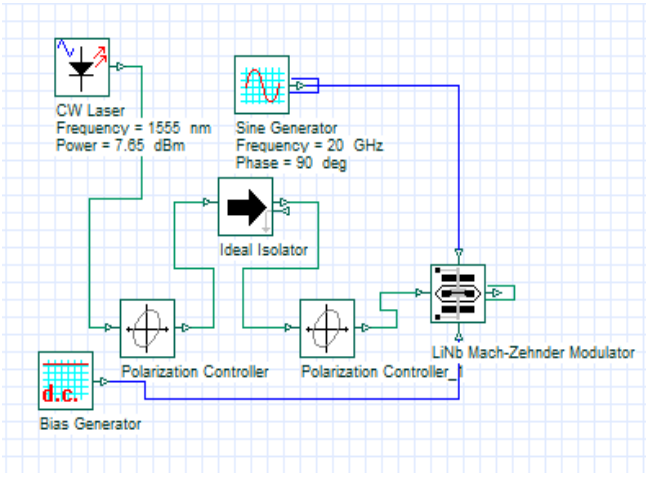

Figure 2 Source of picosecond optical pulses [8].

II.1.2. Block 2

This part incorporates a RAM-type memory card containing a program that specifies one of the three positions of the three optical fiber ends and the start-up (see figure 3).

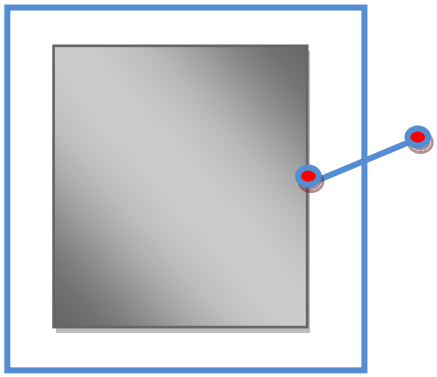

Figure 3. Memory card containing the program.

II.1.3. Block 3

This block contains two optical fibers in parallel (see Figure 4), the first of which had the property of imbalance between the effect of nonlinearity and chromatic dispersion of order 2[10, 11] and the effect of nonlinearity [12, 13, 14], so that the first is greater than the second, and vice versa in the second optical fiber.

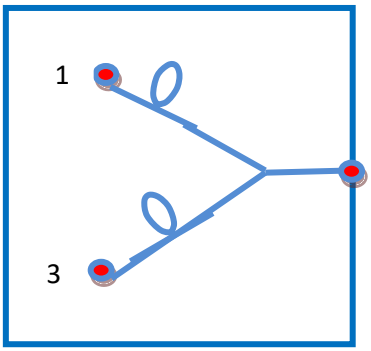

Figure 4. Fiber optic bridge.

II.1.4. Block 4

This block is a multiplexer (see figure 5) by the OTDM method [15, 16, 17] constitutes three stages, the temporal multiplexing is a method for multiplying the flow rate. It consists in interlacing several bit frames from offset sources. This technique is known as OTDM (Optical Time Division Multiplexing).

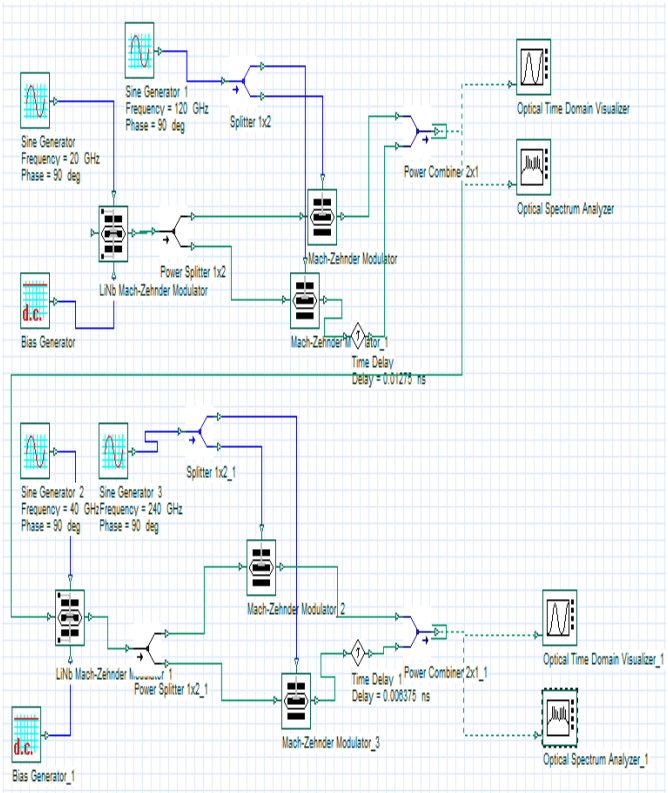

Figure 5. Multiplexer by the OTDM method.

II.2. Expressions of graders of the properties of optical fibers

II.2.1. Chromatic dispersion of order two

This phenomenon is considered harmful in the field of optical telecommunications, because it induces a temporal enlargement of the pulses (the information to be transmitted) during their propagation[18], which subsequently causes their overlap.

β_2, it is responsible for the temporal enlargement of the pulses also known as the dispersion coefficient of the group velocity GVD (Group Velocity Dispersion), it reflects the variation of the speed vis-à-vis the frequency[19, 20].

$$\beta_2 = \left(\frac{\partial^2\beta}{\partial t^2}\right)_{(\omega=\omega_0)} = \frac{1}{V_g^2}\frac{\partial V_g}{\partial \omega} = \frac{1}{c}\left[2\frac{\partial n}{\partial \omega} + \omega\frac{\partial^2 n}{\partial \omega^2}\right], \quad (1)$$

The chromatic dispersion or any short dispersion, denoted D, represents the deviation of the arrival time of two pulses of different central wavelengths of 1 nm and sent in a fiber of 1 km of lengths. This quantity can be expressed as a function of β_2, (in ps.nm^{-1}.km^{-1}).

$$D = -\frac{\pi}{\lambda^2}\,\beta_2\,, \qquad (2)$$

With C is the speed of light and λ is the wavelength.

L_D is the dispersion length, corresponding to the propagation distance at the end of which the initial pulse, of a temporal width at 1/e of T_0, has widened or spread by a factor $\sqrt{2}$.

It is important to know the length for which the effect of dispersion, of order 2, becomes important, or :

$$L_D = \frac{T_0}{|\beta_2|}, \qquad (3)$$

II.2.2. Kerr effect

This phenomenon of birefringence[21, 22] provoked, discovered by Kerr (in 1875), is known as the Kerr effect. This phenomenon has a remarkable feature, the Kerr coefficient is expressed by :

$$\gamma = \frac{\omega_0 . n_2}{c . A_{eff}}\,, \qquad (4)$$

Or ω_0: is the frequency of the carrier,
A_{eff}: corresponds to the effective area of the optical fiber.

$$\text{With } n_2 = \frac{2n_{NL}}{\varepsilon_0 cn}\,, \qquad (5)$$

n_2 represents the nonlinear index, n_{NL} the nonlinear refractive index.

We can define the L_{NL} parameter, as in the case of dispersive effects, the length of fiber for which nonlinear effects become important :

$$L_{NL} = \frac{1}{\gamma P_0}, \qquad (6)$$

P_0 is the peak power of the fundamental soliton (N = 1)[23] connected to the parameters of the optical fiber by the criterion $L_D = L_{NL}$.

Remark

The solitonic regime is carried out for :

$$L_D = L_{NL} \qquad (7)$$

We are talking about a purely non-linear regime for :

$$L_{NL} >> L_D, \qquad (8)$$

Is carried out purely dispersive regime for :

$$L_D >> L_{NL} \qquad (9)$$

II.2.3. Parameters of the optical fibers used

From equations (1,...,9), one can find the values and parameters of the components of the assembly (see Table 1 and Table 2).

Tab. 1 The properties and characteristics of the four optical fibers.

Optical fibers	Chromatic dispersion of order 2 (β)	Kerr effects (γ)	Fiber length (L)
Fiber 1	17 ps/(nm.Km)	1.7 $W^{-1}.Km^{-1}$	2.18 Km
Fiber 2	17 ps/(nm.Km)	1.95 $W^{-1}.Km^{-1}$	1.95 km
Fiber 3	17 ps/(nm.Km)	0.85 $W^{-1}.Km^{-1}$	1.44 km
Fiber 4	-100 ps/(nm.Km)	1.3 $W^{-1}.Km^{-1}$	1.4 km

Tab. 2 Values and parameters of the components of the simulated assembly.

component	parameter	symbol	value
Laser source	Longueur d'onde	L	1555 nm
	puissance	P	6.95 dBm
Mach-Zehnder 1 modulator	Tension d'extinction	zU_{ext}	23 v
	Tension de bias	V_b	9.5 v
Mach-Zehnder 2 modulator	Tension d'extinction	U_{ext}	29 v
	Tension de bias	V_b	4.68 v
EDFA 1 amplifier	Puissance de sortie maximale	$P_{s.max}$	13 dBm
EDFA 2 amplifier	Puissance de sortie maximale	$P_{s.max}$	28 dBm

II. 3. Generator memory card algorithm and program

The automation of this multi-speed generator is carried out according to a program from this algorithm (see alg. 1).

Alg. 1 Algorithm for multi-speed generator automation

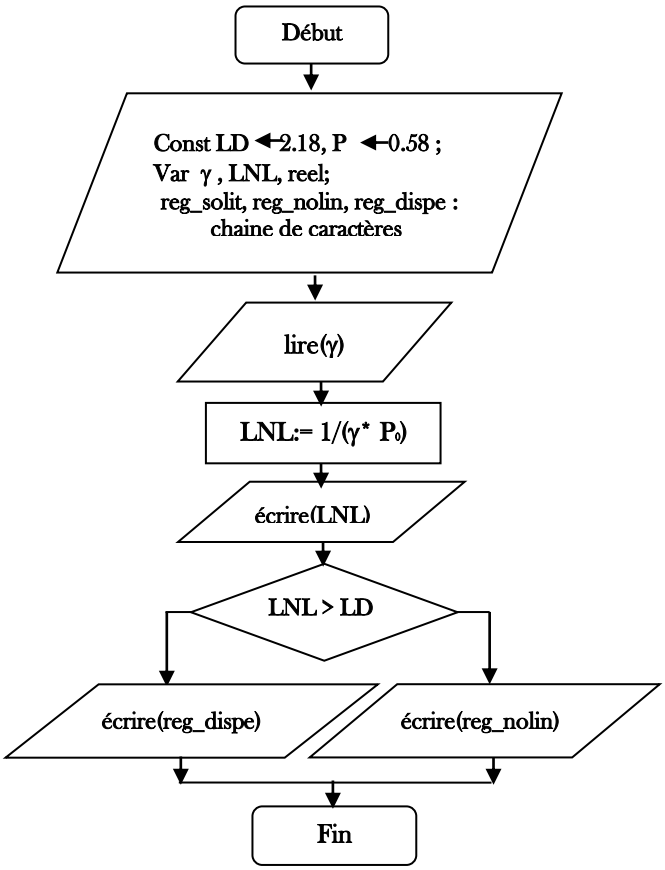


```
Program(multi_régimes)
Const
LD ← 2.18; P0 ←0.58;
var
γ , LNL : reel;
 reg_solit, reg_nonlin , reg_dispers : string;
Begin
Readln(γ);
LNL : =  1/(γ* P0);
Writeln(LNL) ;
If  LNL > LD then writeln(reg_nonlin);
   else
                        writeln(reg_dispers);
end,
end,
End.
```

III. Digital simulation

Faced with the increasing complexity of the architectures and systems developed, simulation tools have acquired an important role. They are increasingly used to optimize the parameters involved in the realization of a system. They make it possible to predict results expected experimentally. They now also make it possible to use during a simulation, experimental elements such as signals recorded with measuring devices or curves characteristic of real components. In all that follows the simulation tool used is the OPTISYSTEM version 7[24, 25].

IV. Results and Discussions

From the work[8] Simulation of an all-optical source flowing ultra-high-speed pulses (160 Gb/s), was carried out in solitonic regime according to the equilibrium condition between the dispersive effect and that of the nonlinearity within the main optical fiber (see Figures 6, 7 and 8), this is checked for the relationship ($L_D = L_{NLN}$).

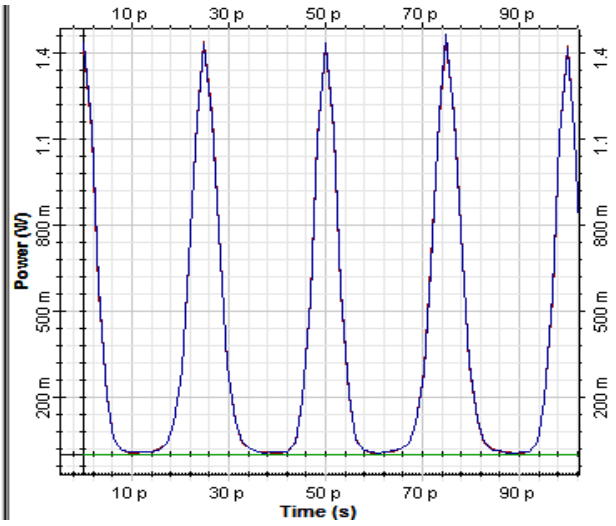

Figure 6. The pulse train at 40 Gb/s at the output of the generator according to condition [8].

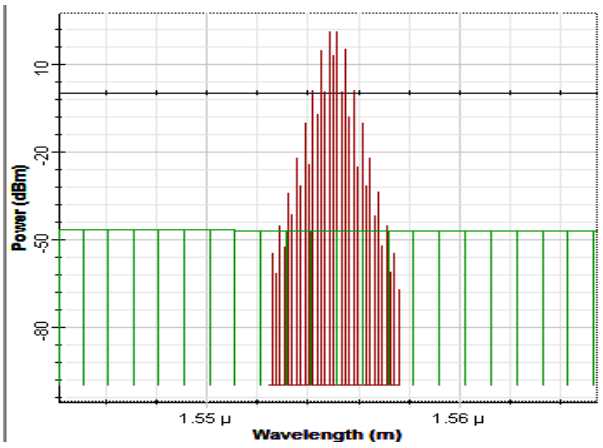

Figure 7. Spectrum of the signal at the output of the first block in solitonic regime[8].

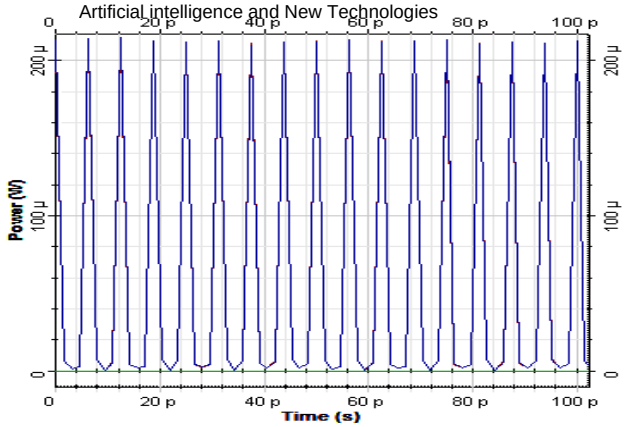

Figure 8. The pulse train at 160 Gb/s at the output of the generator according to the condition[8].

The replacement of this fiber by another that satisfies the condition ($L_D < L_{NLN}$) makes it possible to produce a train of light pulses in non-linear mode is the semilariton form (see figures 9 and 10), after multiplexing by the OTDM method [26, 27, 28], the self-modulation process was obtained (see figure 11).

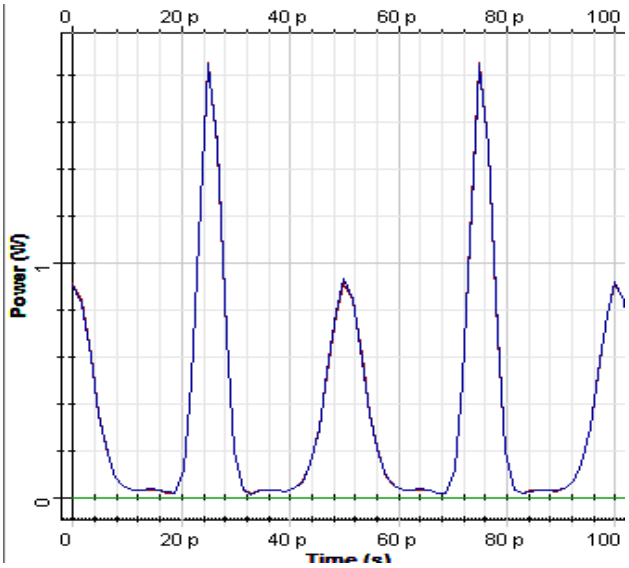

Figure 9. The pulse train at 40 Gb/s at the output of the generator according to the first condition.

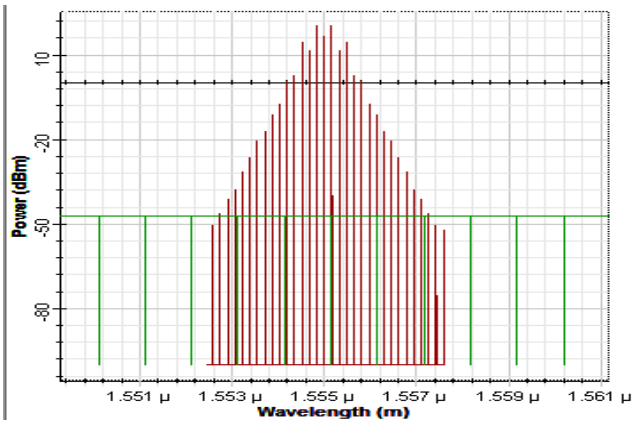

Figure 10. Spectrum of the signal at the output of the first block in non-linear mode.

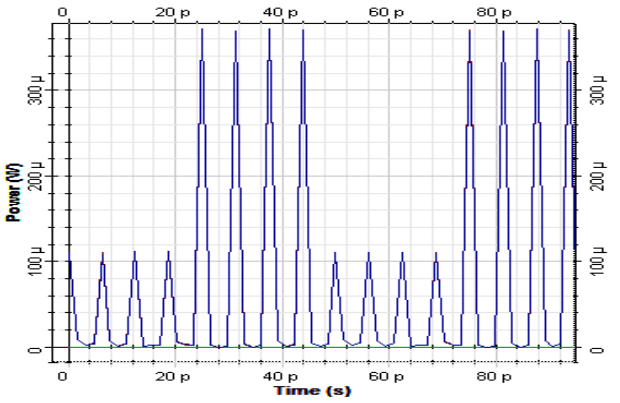

Figure 11. The pulse train at 160 Gb/s at the output of the generator according to the first condition.

Again the last fiber was changed by a third which verified the inverse of the previous condition ($L_D > L_{NLN}$), this provided a train of optical pulses in dispersive regime (see figures 12 and 13), the start of the train would be increased after passing through the multiplexer[29, 30] had become a self-modulated signal (see Figure 14).

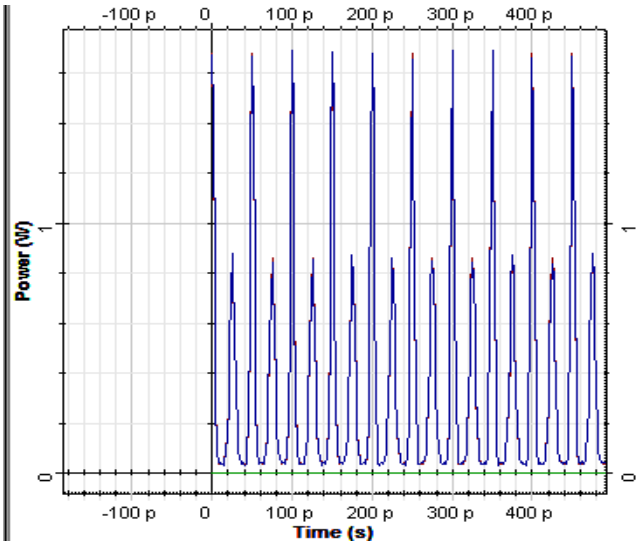

Figure 12. The pulse train at 40 Gb/s at the output of the generator according to the first condition

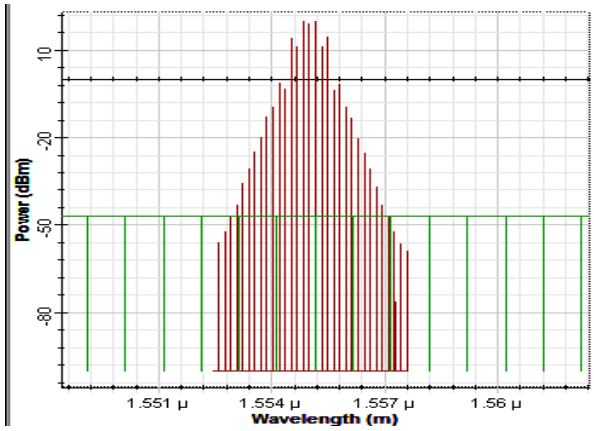

Figure 13. Spectrum of the signal at the exit of the first block in dispersive regime.

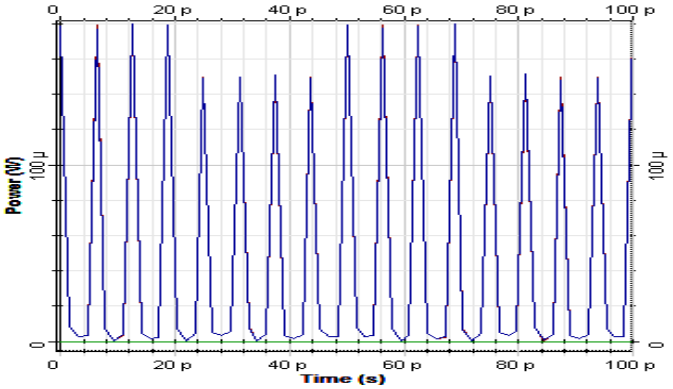

Figure 14. The pulse train at 160 Gb/s at the output of the generator according to the second condition.

The switching from one of the two optical fibers to the other is performed automatically according to a program recorded in the memory card inserted in the generator assembly (see figures 1 and 3).

V. Conclusion

This work based on the development and improvement of the generator [8], the latter consisted in carrying out the pulse train in solitonic regime by the balance between the effect of non-linearity and that of chromatic dispersion of order two within the optical fiber, two other fibers of the same types and properties were added, the first providing the train in nonlinear mode according to a very specific condition at the level of the equilibrium of the two effects within this optical fiber, the second fiber ensures the inverse of the previous condition to generate the pulse train in highly dispersive regime, the start of one of the two optical fibers is carried out thanks to a program in a memory card inserted in the assembly of the previous generator.

References

[1] T. H. Maiman, "*Stimulated optical radiation in Ruby masers*", Nature, vol. 187, pp. 493, 1960.

[2] A. Hasegawa and F. Tappert, "*Transmission of stationary nonlinear optical pulses in dispersive dielectric fibers, I. Anomalous dispersion*", Appl. Phy. Lett., vol. 23, pp. 142, 1973.

[3] L. F. Mollenaueur, R. H. Stolen, and J. P. Gordon, "*Experimental Observation of Picosecond Pulse Narrowing and Solitons in Optical Fibers*", Phys. Rev. Lett., vol. 45, pp. 1095-1098, 1980.

[4] P. V. Mamyshev, «*All-optical data regeneration based on self-phase modulation effect*», in *European Conference on Optical Communication, ECOC'98*, p 475- 476. Madrid, Spain, 1998.

[5] P.V. Mamyshev, S.V. Chernikov, and EM Dianov, *"Generation of fundamental soliton trains for high-bit-rate optical fiber communication lines"*, Journal of Quantum Electronics, IEEE, 27(10):2347–2355, 1991.

[6] http://www.enseirb.fr/~kadionik.

[7] V. Girondin, «*Etude et modélisation d'un modulateur à électro-absorption pour des applications de transmission radio sur fibre de signaux ULB aux fréquences centimétriques- Simulation système et caractérisation d'une liaison radio sur fibre à modulation externe*», Thèse de doctorat, Université Pierre et Marie Curie, 2016.

[8] A. Hamouda, K. Saouchi, 2017. Breves generator of pulses has different flow rates(40 Ghz, 80 Ghz and 160 Ghz), *journal of JNTM,* Vol. 7(01), p. 27-32.

[9] A. Hamouda, K. Saouchi, 2017. Simulation d'une source tout optique débitant des impulsions à ultra-haut débit (320 Gb/s), *Rev. Sci. Technol., Synthese,*Vol 35, p. 224-232.

[10] S. O. Mohammadi, S. Mozaffari and M. M. Shahidi, "*Simulation of a transmission system to compensate dispersion in an optical fiber by chirp gratings*", International journal of the Physical Sciences, 6(32), 7354-7360, 2011.

[11] D. Wake, C. R. Lima and P. A. Davies, «*Optical generation of millimeter-wave signals for fiber- radio systems using a dual-mode DFB semiconductor laser*», IEEE Transactions on Microwave Theory and Techniques, vol. 43, no. 9, p. 2270–2277, 1996.

[12] M. F. Ferreira, *"Nonlinear effects in optical fibers"*, volume 2. Wiley. com, 2011.

[13] T. Hirooka, S. Ono, K.-I. Hagiuda, and M. Nakazawa, *"Stimulated Brillouin scattering in dispersion-decreasing fiber withultrahigh-speed femtosecond soliton pulse compression"*, Opt. Lett., 30(4):364–366, 2005.

[14] T. Inoue, J. Hiroishi, T. Yagi, and Y. Mimura, *"Generation of in-phase pulse train from optical beat signal"*, Opt. Lett., 32(11):1596–1598, 2007.

[15] J. Fatome, S. Pitois, C. Fortier, B. Kibler, C. Finot, G. Millot, C. Courde, M. Lintz and E. Samain, 2010. Multiple four-wave mixing in optical fibers: 1.5–3.4-THz femtosecond pulse sources and real-time monitoring of a 20-GHz picosecond source, *Opt. Commun*, vol. 283, pp. 2425-2429.

[16] A. Takada and M. Saruwatari, 1988. 100Gbit/s optical signal generation by time-division multiplication of modulated and compressed pulses from gain-switched distributed feedback (DFB) laser diode, *Electronics Letters*, vol. 24(23), p.1406–1408.

[17] S. Wabnitz and N. Akhmediev, 2010 . Efficient modulation frequency doubling by induced modulation instability, *Optics Communications*, vol. 283(6), p. 1152–1154.

[18] G. P. Agrawal, 2001. Applications of Nonlinear Fiber Optics, Third edition. New York Academic press, 467 p.

[19] P. Béjot, B. Kibler, E. Hertz, B. Lavorel and O. Faucher, 2011. General approach to spatiotemporal modulational

instability processes, *Physical Review A*, Vol. 83(1), p. 138-145.

[20] R. W. Boyd, 2008. Nonlinear optics, Academic press, 3rd edition Paris. 173p.

[21] A. Hasegawa, 1984. Generation of a train of soliton pulses by induced modulational instability in optical fibers, *Opt. Lett.*, vol. 9(7), p. 288–290.

[22] A. Hasegawa and W. Brinkman, 1980. Tunable coherent IR and FIR sources utilizing modulational instability, *Journal of Quantum Electronics, IEEE*, vol. 16(7), p.694–697.

[23] K. Inoue, , 1992. Four-wave mixing in an optical fiber in the zero-dispersion wavelength region, *Journal of Lightwave Technology*, vol. 10(11), p. 1553–1561.

[24] N. Nishizawa and T. Goto, 2006. Novel super-continuum fiber lasers and wavelength-tunable soliton pulses, SPIE Newsroom.

[25] S. O. Mohammadi, S. Mozaffari and M. M. Shahidi, 2011. Simulation of a transmission system to compensate dispersion in an optical fiber by chirp gratings,*International journal of the Physical Sciences*, Vol. 6(32), 7354-7360.

[26] V. Kaman and J. E. Bowers, 2000. 120 Gbit/s OTDM system using electroabsorption transmitter and demultiplexer operating at 30GHz,*Electronics Letters*, Vol. 36(17), 1477-1479.

[27] Y. K. Chen, C. J. Hu, C. C. Lee, K. M. Feng, M. K. Lu, C. H. Chung, Y. K. Tu and S. L. Tzeng, 2000. Low-crosstalk and compact optical add-drop multiplexer using a multiport circulator and fiber Bragg gratings, IEEE Photonics Technology Letters, Vol. 12, 1394–1395.

[28] A. D Errico, C. Loiacono, M. Presi, G. Contestabile and E. Ciaramella, 2003. Widely tunable 40 GHz pulse source for 160 Gbit/s OTDM by simultaneous soliton generation and compression, In: European Conference and Exhibition on Optical Communication (ECOC) IEEE, p. 578-580.

[29] S. Trillo, S. Wabnitz, and T. A. B. Kennedy,1994. Nonlinear dynamics of dual-frequency-pumped multiwave mixing in optical fibers*, Physics. ReviewA*, Vol. 50(2), 1732–1747.

[30] C. Chluda, 2006. Bruit basse et moyenne fréquence des amplificateurs optiques distribués à effet Raman, PhD thes Multiplexeur par OTDM is on physics, university of Montpellier 2, France, 187p.

A Microstript Coupler With Improving the Characteristic Transmission

R. EL-BOUSLEMTI
Telecommunications and Digital Signal Processing Laboratory, Djillali Liabes University, Sidi Bel Abbes, Algeria.
ENPO, Maurice Audin
Oran, Algeria
rahmouna.elbouslemti@enp-oran.dz

F. Salah-Belkhodja
Telecommunications and Digital Signal Processing Laboratory, Djillali Liabes University, Sidi Bel Abbes, Algeria.
Djillali Liabes university
Sidi Bel Abbes, Algeria
fouzi.salahbelkhodja@univ-sba.dz

A. K. SAYAH
Laboratoire de Simulation, Commande, Analyse et Maintenance des Réseaux électriques
ENPO, Maurice Audin, Oran, Algeria
Abdelkader.sayah@enp-oran.dz

***Abstract*— In this paper, a new miniaturized microstrip coupler at the center frequency of 3.26 KHz is proposed. Meander line allowed for reducing the size of the component. The coupler demonstrates a coupling level of 2.29 dB, a reflection level of 25.39 dB and an isolation level as 42.41 dB. The meandered coupler have the compact sizes of 23×34.6 mm^2, and a characteristic impedance Z0 of 50.60 Ω. in order to validate our model, the compact coupler is designed and fabricated using microstrip technology on FR4 substrat. Good agreement is achieved between the simulated and measured results**

I. INTRODUCTION

The telecommunications was initially restricted to public and military services, later they became commonplace in recent years.

Driven by the enthusiasm of the public, wireless communications systems are experiencing tremendous growth worldwide, they became cheaper and faster and the microwave components became miniaturized. The use of directional couplers [1,2] has become commonplace in radio frequency systems and the modern optical communications systems. It therefore becomes important to present this "coupler" in the microwave research.

Directional and hybrid couplers are passive components that allow signals to be split or combined.

The perfect integration of the coupler in the design of RF and digital circuits requires the miniaturization of the device, which naturally leads to define the new design methodologies associated with new hardware and software tools which gives a novel enhanced and miniaturized coupler which is presented in [3-5].

This article presents a concrete case of realization of a directional coupler with meander transmission line in the microstrip technology.

This study led us to conceive, simulate, realize and characterize a compact meandered coupler.

The manipulation (electromagnetic simulations and measurements) guided us to determine the influence of the geometry on the transmission *characteristics* and to deduce all the parameters and rules of behavior.

Objectives of the study

- to highlight a design rule and a reliable process which aims to describe a geometric dimensioning
- To ensure a miniaturization of the component without having a performance degradation.

II. PARAMETERS CHARACTERISTICS OF A COUPLER

The concept of the planar transmission line was proposed from 1950, According to Pozar, from the 1960s, much thinner substrates began to be used, which promotes microstrip lines for microwave integrated circuits. Differents waveguide couplers were invented and characterized at the MIT Radiation Laboratory in the 1940s [6].

The concept of couplers in microstrip technology has been proposed since 1950, but it was not possible to achieve them effectively until 1960, when low-loss dielectrics arrived on the market [6]. Since then, research in this field has continued to intensify to exploit the many advantages of directional couplers:

A. Advantages:

- Simple to realize, suitable for two-layer circuits
- Simple connectivity,
- low-loss connector

Unfortunately, these components also have disadvantages ;

B. disadvantages

- Inhomogeneous propagation environments
- Sensitivy to electromagnetic disturbances
- Larger losses, only the substrate that is chosen
- Controlled phase shift

State space can be equivalent to the form showed Fig. 1 and the following functional form:

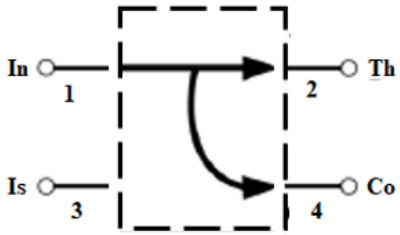

Figure 1. Functional definitions of a classical coupler with Input (In), through (Th), isolation (Is) and coupled port (Co).

Figure 2. Three types of COD directional couplers with Input, through, isolation and coupled port.

The simplest coupler to study is probably given in Fig. 2 which is defined by:

- **Its transmission characteristics**: S-parameters, S11 (reflection coefficient), S21 (isolation), S31 and S41 (characteristics transmission: coupled and through).
- **Its usage parameters:** the resonance frequency f1, its input impedance and its bandwidth B.
- **Its internal parameters:** The first step is the choice of the substrate and the conductor for which the characteristics to be known are:

✓ **For the substrate:** its relative permittivity and the dielectric losses of the substrate tan ∂, and its thickness h.

✓ **For the conductor:** its conductivity σ and its thickness t.

The baseline design of coupler consists to determine: the S-parameters, input impedance which must be adapted and the phase difference between the Coupler Output Ports of 90 degree.

In this article only one type feeding is presented. It's about an microstrip line excitation.

In order to formalize our design optimization, the following specification is provided:

- FR4 epoxy glass substrates (it is chosen for cost reasons): relative permittivity $\varepsilon_r = 4{,}6$, tan $\partial = 0{,}018$, h = 1,6*mm*
- The conductor: it is copper, $t = 35\ \mu m$.
- The type of excitation chosen is the Wave Port for simulation in HFSS.
- The resonance frequency is f1= 3.26 GHz.

The S31 and S41 (characteristics transmission: coupled and through) are given by:

$$S_{41} = \frac{\sqrt{1-k^2}}{\sqrt{1-k^2}.\cos(\theta)+j\,\sin(\theta)} \quad (1)$$

$$S_{31} = \frac{\mathrm{jk}\,\sin\vartheta}{\sqrt{1-k^2}.\ \cos\vartheta+\mathrm{j}\,\sin\vartheta} \quad (2)$$

The maximum amount of coupling between ports 1 and 3 (or between ports 2 and 4) occurs when [7] :

$$\theta = \beta l = \frac{\pi}{2} rads \quad (3)$$

Or

$$l = \frac{\pi}{2\beta} = \frac{\lambda_g}{4} \quad (4)$$

θ=βl denotes the electrical length of the coupler and β is the frequency bandwidth ratio of a directional coupler (single- or multisection) is defined in [7.

k is given by :

$$\mathrm{k} = \frac{Z_{0e}-Z_{0o}}{Z_{0e}+Z_{0o}} \quad (5)$$

where Z_{0e} and Z_{0o} denote the characteristic impedance of the even-mode and odd mode of symmetrical coupled lines respectively, which verify this condition [7] :

$$Z_{Oe}Z_{Oo} = {Z_O}^2 \quad (6)$$

We can write Z_{0e} /Z_{0o} in terms of a voltage coupling coefficient *k* as [7]:

$$\frac{Z_{Oe}}{Z_{Oo}} = \frac{1+k}{1-k} \quad (7)$$

If the coupling from port 1 to port 3 is given as *C* dB (where *C* is a positive quantity), then *k* is related to *C* as [7]:

$$k = 10^{-C/20} \quad (8)$$

The geometric parameters: given in the figure below:

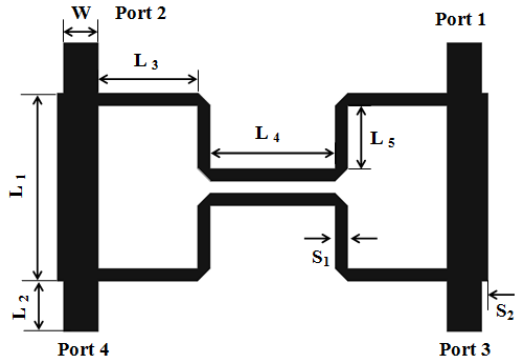

Figure 3. Geometry and dimension of the proposed coupler with:

L1=15mm; L2= 4mm; L3= 8mm; L4= 10mm; L5= 5mm; S1= 1mm; S2= 0.5mm; and W= 1.8mm.

Fig. 1 shows the schematic coupler design with dimension of the transmission-line sections.

The simulations were performed using the high-frequency structure simulator (HFSS) software who owns an electromagnetic simulator. It is based on Finite Element Method (FEM), also it requires the use of mesh patterns.

Figure 4. (left) Measurement setup: a network analyzer E5071C being used for *S*-parameter measurement, (right) component under test.

The coupler Measurement setup is shown on Fig 4. This stage of coupler measures validates the simulation steps. These measurements are made using Vector Network Analyzers E5071C being used for *S*-parameter.

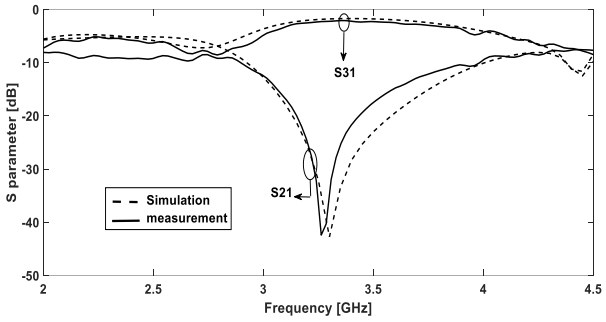

(a)

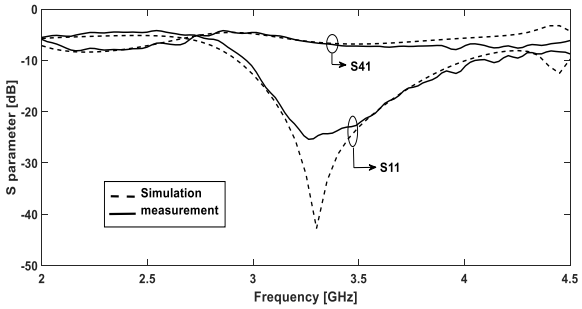

(b)

Figure 5. Simulated and measured *S*-parameters: (a) *S*31 and *S*21, and (b) *S*11 and *S*41.

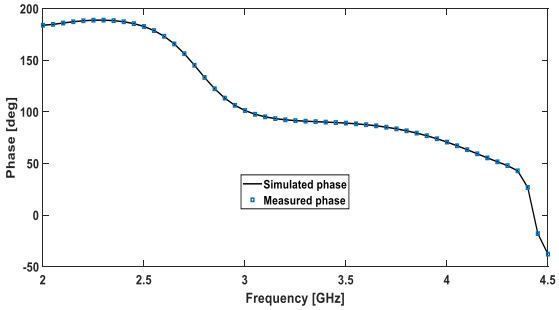

Figure 6. Measured phase difference between Port 3 and Port 4.

Fig 6 gives the measured responses of the coupler. The measurement results shows that the branch line coupler can operate at f = 3.26 GHz which are selected as the operating frequency.

The comparison of the performances of the proposed coupler is summarized in Table 1.

Table 1 Performance of Branch line meandered Coupler.

	Frequency GHz	S21 dB	S31 dB	S41 dB	S11 dB	Phase Diff	$\|S_{41}\| - \|S_{31}\| \leq \pm 1dB$
Simulation	**3.30**	**-33.04**	**-1.74**	**-6.45**	**-42.74**	**-90.87°**	**4.71**
Measurement	**3.26**	**-42.41**	**-2.29**	**-6.40**	**-25.39**	**-91.22°**	**4.11**

The frequency shifting may be caused by weld of SMA connectors.

At the center frequency of 3.26 GHz, the return loss S11 is -25.39 dB and the isolation S21 is -42.41 dB.

In the range of bandwidth, the insertions losses and S31 is -2.29 dB, it is under -3 dB and S41 is - 6.40 dB. Above all, the fabricated coupler only occupies 23×34.6 mm^2 which work at the center frequency of 3.26 GHz. Measured phase difference between Port 3 and Port 4 is 91.22° at operating bandwidth, shown in Fig. 6.

This study proves that we improved the transmission characteristic that can reach -1.74 dB. For miniaturization, the design and manufacture of the device operating in 3.30 GHz has been completed for WLAN applications.

we allowed ourselves to compare our work with that presented in [8]. this study was published in 2017. The following table shows the results of the comparison:

Table 2. Comparaison between our results and those published in [8].

Reference	[20]	This work
Operating frequencies (GHz)	2.52	3.26
Isolation (dB) -	> 20 dB	- 42.41
Insertion loss (dB)	-4.5	-2.29
Coupling loss (dB)	-2.8	-6.40
Phase difference	-92.8°	-91.86°
Perfect tramsission carachteristic	medium	better
Perfect impedance matching	No	Yes

we can notice that the results obtained in this work is better than those cited in [8].

III. CONCLUSION

In this paper, a new miniaturized compact coupler is proposed. The main purpose of this study is used meander transmission-line to replace the shunt arms of the classical coupler. The performance of the coupler was measured for 3.26 GHz operating frequency. The model of meander line was investigated for miniaturization.

The simulated and measured results are agreement which demonstrates th efficiency of numerical simulation using the HFSS. This work made it possible to highlight the feasibility of the realized microwave coupler

REFERENCES

[1] Michael Steer, "Microwave and RF design," A system approch, SciTech Publishing, Inc, 161–280, 2010.

[2] Samuel. Liao, Y., "Microwave Devices and Circuits", 3rd ed., Prentice Hall, Englewood Cliffs, USA: New Jersey 07632,1990, pp. 150-160.

[3] Maktoomi, M. A., Mohammad S. Hashmi, and Fadhel M. Ghannouchi, "A Dual-Band Port-Extended Branch-Line Coupler and Mitigation of the Band-Ratio and Power Division Limitations" : IEEE Trans on components, packaging and manuf tech, Vol 7,2017, pp. 1313-1323.

[4] H. Liu, S. Fang, and Z. Wang, "A Compact Trans-Directional Coupler With Wide Frequency Tuning Range and Superior Performance," IEEE Trans On Components, Packing and Manufacturing Technology, 2017.

[5] O. D. Gurbuz and G. M. Rebeiz, "A 1.6-2.3 GHz RF MEMS reconfigurable quadrature coupler and its application to a 360° reflectivetype phase shifter," *IEEE Trans. Microw. Theory Techn.*, vol. 63, no. 2, pp. 414–421, Feb. 2015.

[6] Pozar, D. M., "Microwave engineering",4rd ed., John Wiley & Sons, Inc, USA :Amherst, 2011, pp. 320–379.

[7] R. K. Mongia, I. J.Bahl, P. Bhartia and J. Hong, RF and Microwave Coupled-Line Circuits, 2nd ed., Norwood, MA 02062: Artech House, INC, 2007, pp. 111–200.

[8] Maktoomi M. A, Mohammad S, Hashmi, Fadhel M, Ghannouchi. A Dual-Band Port-Extended Branch-Line Coupler and Mitigation of the Band-Ratio and Power Division Limitations. IEEE Trans on components, packaging and manuf tech., 2017, 7: 1313-1323

Non-coherent Radar CFAR Detection Based on Ratios of Consecutive Order Statistics for Pareto Distributed Clutter

Mohamed SAHED
Laboratoire d'Analyse des Signaux et Systèmes (LASS), Department of Electronics
University Mohamed Boudiaf of M'sila
M'Sila, Algeria.
email: mohamed.sahed@univ-msila.dz
ORCID: https://orcid.org/0000-0002-0333-1177

***Abstract*—The Pareto distribution has been validated recently as a new statistical model for radar clutter backscattered from the sea surface for X-band high resolution maritime surveillance radar. Consequently, the derivation of the corresponding detection schemes has become of much interest, for operation under such clutter model, with the constant false alarm rate (CFAR) property. In this paper, a novel order statistic based CFAR detector operating in Pareto distributed clutter is introduced. This detector, which will be referred to us TGMR-CFAR, consists on using the trimmed geometric mean of ratios of consecutive order statistics obtained from samples of the sliding window. It is designed essentially to operate in a more realistic case, where nonhomogeneous clutter is considered. The author provides, here, a complete performance analysis for the TGMR-CFAR processor in homogenous and when interfering targets are present within the reference window. The exact expression of the false alarm probability of the proposed algorithms in a homogenous background is also presented. The detection performance of the TGMR-CFAR detector is investigated and compared with some exciting detectors by means of simulations.**

Keywords—Radar Signal Processing, Noncoherent CFAR Detection, Pareto Distributed Clutter, Order Statistics.

I. INTRODUCTION

The signal returns from radar targets are typically embedded in thermal noise and clutter, which is an unwanted backscatter from buildings, clouds, the sea, etc. Since the power of clutter and thermal noise is unknown at any given location, fixed thresholding techniques cannot be applied because they may result in an excessive number of false alarms. An attractive class of schemes that can be used to overcome the problem of clutter are the Noncoherent *constant false alarm rate* (CFAR) processing schemes which set the threshold adaptively based on local information of total noise power. Noncoherent CFAR detection is one of the main problems in practical radar signal processing systems. It was first examined by Finn and Johnson [1], where they proved that detection process could be formulated by maintaining the probability of false alarm (P_{FA}) constant in ideal situations. In this class of process, the received signal is passed into a serial shift register. The result of this is then passed again through a square-law envelope detector which converts the complex returns to amplitude or intensity measurements. For a typical CFAR detector, the square-law detected video range samples are then sent serially into a shift register (or a sliding window) of $M+1$ resolution cells. Hence, the detection threshold is set on a cell-by-cell basis using estimated local clutter power by processing a group of M reference cells surrounding a specific cell commonly called, the cell under test (CUT) (or simply test cell). We shall assume that the CUT is collocated in the middle of the sliding window, a customary assumption made in the literature. The cells surrounding the CUT are known as the clutter range profile (CRP) or reference range cells which comprise the reference window. The estimated clutter level in the reference window is then normalized by a constant, producing an adaptive threshold. The signal in the CUT is then compared to this threshold, and a target detection decision can be made. The same process is then repeated and applied to subsequent groups of data, which will be used to produce the updated estimate of the clutter power level [2, 3]. This procedure can be formulated mathematically in a statistical hypothesis testing problem. Suppose we denote by H_0 the hypothesis that the CUT does not contain a target (it instead contains only clutter). This is referred to as the null hypothesis. Let H_1 be the hypothesis that the CUT does contain a target signature plus clutter, which is known as the alternative hypothesis. Here, the target signal is combined coherently with clutter in the complex domain, and the modulus of the resultant complex measurement is taken. As the size of the reference window increases, the detection performance of a given CFAR scheme approaches that of the optimum detector which is based on a fixed threshold [3].

The statistical modeling of radar clutter was the key to any development of CFAR detection algorithms. As a result, modeling radar clutter statistics has become a very rich scientific subject over the past four decades. A variety of distributions have been proposed and reported in the literature in order to model clutter statistics, from Gaussian [3, 4], Lognormal [5] and Weibull [6], through to modern models such as the *K*, *K* plus Noise and Pareto distributions [7-10]. Recently, it has been demonstrated that the class of Pareto distributions is an excellent fit for X-Band high resolution radar clutter returns [11, 12]. Similar to the Gaussian model, the simplicity of the Pareto distribution has facilitated greatly

the development of a rich mathematical framework for the study of CFAR detection schemes [13-16]. In the same context, the present paper examines the development of a new CFAR detector operating in such distributed clutter.

Recent studies in the literature have shown that it is possible to produce CFAR detectors for Pareto distributed clutter by transforming the Gaussian intensity CFAR detectors. This can be accomplished by using the natural duality between the Exponential and Pareto distributions. The transformed schemes are significantly different in form compared to the traditional Gaussian processors extensively analyzed in the literature [2-4]. For each transformed scheme, the false alarm probability and the adaptive threshold are related through simple relationships which are linked inherently to the Gaussian detection case [13].

Furthermore, detection performance analysis reported in [13] showed that the existing detectors experienced serious shortcomings in nonhomogeneous (heterogeneous) clutter. Mainly, the geometric mean (GM) CFAR detector was shown to have the most consistent performance in homogenous clutter. However, it also experienced serious shortcomings when subjected to interference. Hence there is a need to investigate the construction of CFAR detectors that can accommodate interfering targets.

In this paper, we introduce and assess a new CFAR detector, which will be referred to us TGMR-CFAR. It consists on taking the product of *k*–1 ratios of any two consecutive ordered statistics of the reference cells to obtain the local clutter power estimate. A significant advantage of this contribution is that the proposed TGM-CFAR scheme is designed specifically to manage nonhomogeneous Pareto distributed background including multiple targets situation.

II. Pareto Distributed Clutter

The Pareto distribution has been validated as a new clutter intensity model for X-band high resolution maritime surveillance radar reverberation data [11, 12]. The validation of the Pareto model will not be provided here, since this has already been reported in the open literature. In addition to its appropriate statistical descriptions for the observed returns, the analytical simplicity of this intensity clutter model makes it more practical, especially for detection purposes, than other modern non-Gaussian distributions such as lognormal, Weibull and *K* models. Hence, the development and analysis of such detection processes has been facilitated by the elegant nature of the Pareto distributional model. As a result of the model's simplicity it has been possible to develop a rich mathematical framework for the study of CFAR detection schemes. A random variable, r.v., X is said to have a Pareto distribution with shape parameter $\alpha > 0$ and a scale factor $\beta > 0$, if its probability density function (PDF) is given by

$$f_X(x) = \frac{\alpha \beta^{\alpha}}{x^{\alpha+1}} \tag{1}$$

for $x \geq \beta$ and zero otherwise. The shape parameter governs the distribution's shape, while the scale parameter determines where its support begins. Hence such a random variable has support $[\beta, \infty[$. By integration of (1), the corresponding cumulative distribution function is given by

$$F_X(x) = \Pr(X \leq x) = 1 - \left(\frac{\beta}{x}\right)^{\alpha} \tag{2}$$

where $\Pr(\cdot)$ denotes probability.

To denote that the random variable X has a PDF similar to (1), we sometimes use the short notation $X \sim \text{Pa}(\alpha, \beta)$, throughout this paper.

The *r*th moments of $X \sim \text{Pa}(\alpha, \beta)$ are given by

$$\text{E}(X^r) = \alpha \beta^{\alpha} \int_{\beta}^{\infty} x^{-\alpha-1} dx = \frac{\alpha \beta^r}{\alpha - r} \tag{3}$$

provided that $\alpha > r$. Hence the mean is expressed as follow

$$\text{E}(X) = \frac{\alpha \beta}{\alpha - 1} \tag{4}$$

while its variance is

$$\text{Var}(\text{X}) = \text{E}(X^2) - (\text{E}(X))^2 = \frac{\alpha \beta^2}{(\alpha - 2)(\alpha - 1)^2} \tag{5}$$

showing that for finite first and second order moments, one requires $\alpha > 2$. This has been found to be the case for the real data sets acquired by the DSTO Ingara Radar [12].

It is worth observing that if Y has a standard Exponential distribution with unity mean (i.e, $f_Y(y) = e^{-y}$), then one can write the following relationship

$$X = \beta\, e^{Y/\alpha} \tag{6}$$

showing that Pareto and Exponential distributions have a natural association.

We now turn to the construction of CFAR schemes for the scenario under consideration. The key to this will be the application of (6).

III. Trimmed Geometric Mean of Ratios CFAR Detector

The trimmed geometric mean of ratios of consecutive order statistics (TGMR) CFAR processor is now introduced mathematically. Suppose we have a series of M independent and identically (iid) distributed Pareto clutter measurements, $X_1, X_2, \ldots, X_M$ and the statistic of the test cell is X_0 , which is considered independent of these measurements as well. Furthermore, let $X_{(1)}, X_{(2)}, \ldots, X_{(M)}$ be the corresponding order statistics (OS) and let $R_i = X_{(i)} / X_{(i-1)}$, $1 < i \leq M$, be the ratio of the two adjacent order samples $X_{(i-1)}$ and $X_{(i)}$. Hence, for the proposed TGMR-CFAR detector, the decision about the presence (hypothesis H_1) or the absence (hypothesis H_0) of a target in the CUT is made according to

$$X_0 \underset{H_0}{\overset{H_1}{\gtrless}} \beta \prod_{i=2}^{k} \left(\frac{X_{(i)}}{X_{(i-1)}} \right)^{(M-i+1)T} \tag{7}$$

where, X_0 is the statistic of the CUT, β is the scale parameter of the Pareto distribution, $X_{(i)}$ is the *i*-th largest statistic,

$k \le M$ is an OS index which is a scalar number and T is a fixed positive scale factor.

By application of the useful duality defined in (6) to each one of the random variables appeared in (7), it is straightforward to prove that the decision rule (7) is CFAR with respect to the shape parameter α. It may be noted also that the trimmed product of ratios $\prod_{i=2}^{k}(X_{(i)}/X_{(i-1)})^{M-i+1}$ is a geometric mean variant, hence the name Trimmed Geometric Mean of Ratios (TGMR) CFAR.

It is well known that the performance of different CFAR schemes in various environments may be evaluated with either the closed-form approach or the Monte-Carlo approach using probability distribution functions. The first approach, when mathematically tractable, is generally preferred since it is less time-consuming and yields more precise results. It is used here to analyze false alarm regulation for the TGMR-CFAR algorithm since it is possible to derive a simple closed-form expression for the P_{FA}. The key input to this closed-form approach is the elegant nature and the simplicity of the Pareto distribution function used to model radar clutter. As a result of that, it has been possible to develop a rich mathematical framework for the study of many CFAR detection schemes under the assumption of this model [13-15]. The probability of false alarm of the TGMR-CFAR is then derived as follow

$$P_{FA} = \Pr\left(X_0 > \beta \prod_{i=2}^{k} (X_{(i)}/X_{(i-1)})^{(M-i+1)T} \,\middle|\, H_0 \right) \tag{8}$$

By application of the useful duality defined in (6) to the random variables appeared in (8) and then by introducing the natural logarithm function to both sides of the inner inequality of (8), it follows straightforwardly that

$$\begin{aligned} P_{FA} &= \Pr\left(Y_0 > T \sum_{i=2}^{k} (M-i+1)(Y_{(i)} - Y_{(i-1)}) \,\middle|\, H_0 \right) \\ &= \Pr\left(Y_0 > TQ \,\middle|\, H_0 \right) \end{aligned} \tag{9}$$

which can be expressed in integral form as follow

$$P_{FA} = \int_0^{\infty} \left[\int_{Tq}^{\infty} f_{Y_0|H_0}(t \mid H_0) dt \right] f_Q(q) dq \tag{10}$$

where $Q = \sum_{i=2}^{k} (M-i+1)(Y_{(i)} - Y_{(i-1)})$ and $f_Q(q)$ is its corresponding PDF.

In addition, by using relationship (6), it can be easily shown that the conditional PDF of the modified test statistic Y_0 under hypothesis H_0 is

$$f_{Y_0|H_0}(t \mid H_0) = e^{-t} \tag{11}$$

Hence, it remains only to define the PDF of the statistic Q (i.e, $f_Q(q)$) in order to solve (10).

Lemma: *Let $Y_{(1)}, Y_{(2)}, ..., Y_{(M)}$ be the order statistics of iid random sample of size M from an Exponential distribution with unity mean. Moreover, let $V_i = Y_{(i)} - Y_{(i-1)}$, i = 1,2,...,M, be the difference between the two adjacent order statistics $Y_{(i)}$ and $Y_{(i-1)}$ with the convention $Y_{(0)} \triangleq 0$. Then the random variables V_i are independent and exponentially distributed with parameter $(M-i+1)$ for each $i = 1,2,...,M$ respectively. Hence, the PDF of V_i is given by*

$$f_{V_i}(t) = (M-i+1) e^{-(M-i+1)t} \tag{12}$$

for $t > 0$.

The proof of this lemma can be done in a similar way to that presented in [3], and hence is omitted here for brevity.

Corollary: *Let $Y_{(1)}, Y_{(2)}, ..., Y_{(M)}$ be the order statistics of an iid random variable distributed according to an Exponential law with unity mean. Moreover, let W_i, i = 1,2,...,M, be another random variable, defined by $W_i = (M-i+1) V_i$, then the random variables $W_1, W_2, ..., W_M$ are iid with standard Exponential distribution with unity mean. In other words, the PDF of W_i is given by*

$$f_{W_i}(t) = e^{-t} \tag{13}$$

for $t > 0$. This corollary can be proved straightforwardly by using random variables transformation rules. It is also argued in [3] that the random variables W_i's are independent since V_i's are independent.

Hence, it follows that the statistic Q, which is the sum of $k-1$ iid standard Exponential random variables, has a Gamma distribution with parameters $k-1$ and 1. Thus

$$f_Q(q) = \frac{1}{\Gamma(k-1)} q^{k-2} e^{-q} \tag{14}$$

By resolving (10), it follows that the P_{FA} of the TGMR-CFAR processor simplifies to

$$P_{FA} = (1+T)^{-k+1} \tag{15}$$

showing that the new decision rule defined in (7) is in fact a CFAR process. Hence, CFAR control can be achieved using (15), together with the detector (7).

The corresponding expression for the probability of detection P_D is given by

$$P_D = \int_0^{\infty} \left[\int_{Tq}^{\infty} f_{Y_0|H_1}(t \mid H_1) dt \right] f_Q(q) dq \tag{16}$$

Unlike the case of P_{FA} where closed-form approach was used; the calculation of the probability of detection P_D will be carried out by using Monte-Carlo approach. This is due to lack of closed-form expression for the distribution $f_{Y_0|H_1}(t \mid H_1)$ of the statistic of the test cell, Y_0, under the alternative hypothesis H_1.

IV. Simulation Results

It is now of interest to investigate the performance of the new TGMR-CFAR detector relative to that of the Ideal, GM-CFAR and OS-CFAR detectors [13-15]. This will be accomplished by generating simulated Pareto distributed

clutter, with shape parameter $\alpha = 4.7241$ and scale parameter $\beta = 0.0446$. These values have been selected because they have arisen from Pareto fit to X-band high-resolution high-grazing angle clutter data set [13, 14]. For consistency, the design P_{FA} is set to 10^{-4}, which allows for 10^6 Monte Carlo runs to be sufficient for estimation of the resultant probabilities of false alarm. A Swerling 1 fluctuation model is used throughout, to produce a synthetic target in the test cell and also to generate interfering targets in the reference cells [17]. The OS index selected to be $k = M - 2$ for the two considered processors OS and TGMR-CFAR. In order to provide an indication of detector performance, the P_D is plotted as a function of the signal-to-clutter ratio (SCR), which has been estimated using 10^6 Monte-Carlo runs.

Figures 1-3 show detection performance as a function of SCR, in the case of homogeneous clutter for different window size (M = 16, 24 and 32 respectively). Comparing these figures, we can conclude that the GM-CFAR detector has almost the best performance followed by the proposed TGMR-CFAR processor, while the OS-CFAR exhibits an extra detection loss compared to the TGMR-CFAR. For $M = 16$ the detection performance loss of all schemes is quite large compared with the ideal decision rule, but decreases considerably for increasing M (See Figures 2 and 3).

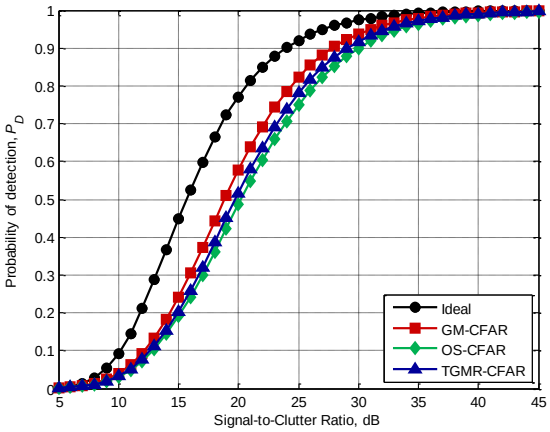

Fig. 1. Detection performance of Ideal, GM, OS and TGMR processors in homogenous clutter for M = 16.

The performance of the studied detectors becomes much more interesting when independent interfering targets are inserted into the reference cells (CRPs). In this case, we define the interference-to-clutter ratio (ICR) of the interfering target, and hence the remaining reference cells are supposed to have identical total power clutter. Next, the effect of these interfering target is investigated. In order to simulate such effects to test the robustness of the proposed detector, interfering targets are generated, as mentioned before, according to Swerling 1 model, with a fixed ICR and then inserted into a cell in the CRP and combined with the clutter in the complex domain. Detection performance is illustrated when each detector is subjected to only one interfering target, and then when each one of them is subjected to two interfering targets simultaneously. Here we observe a significant change in the performance when compared to the case of no interference discussed above. In Fig. 4, for a single interfering target, with an *ICR* = 20dB, the GM-CFAR performs very poorly, while the OS-CFAR experiences a slight CFAR loss. By contrast the proposed TGMR detector performs very well in this situation. When subjected to two interfering targets, the GM detector saturates as shown in Fig. 5, while the OS is slightly worse than the TGMR. Based upon these numerical simulations, it has been found that the proposed TGMR detector provides robust solution to interference, with acceptable CFAR loss relative to the ideal detector.

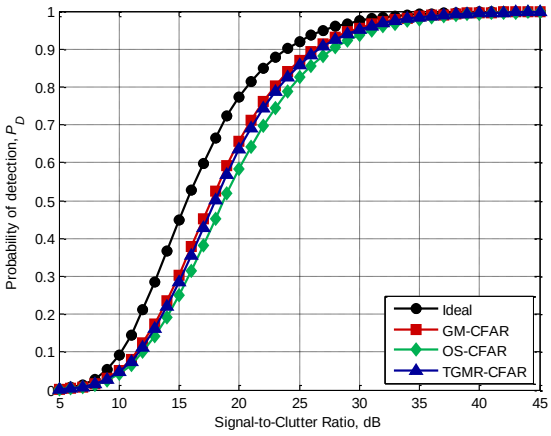

Fig. 2. Detection performance of Ideal, GM, OS and TGMR processors in homogenous clutter for M = 24.

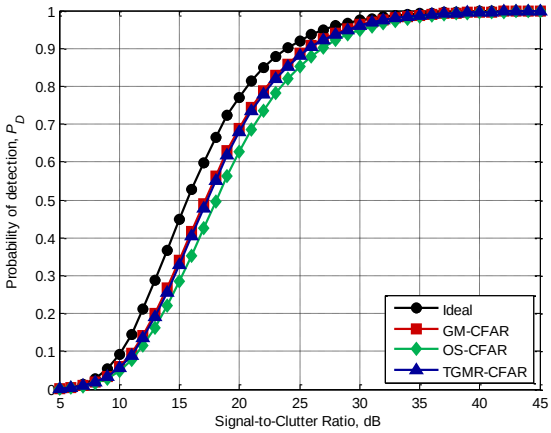

Fig. 3. Detection performance of Ideal, GM, OS and TGMR processors in homogenous clutter for M = 32.

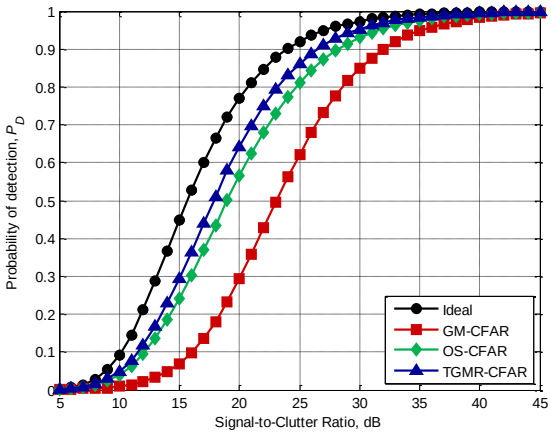

Fig. 4. Detection performance of Ideal, GM, OS and TGMR processors in the presence of one interferring target with *ICR* = 20dB and for M = 24.

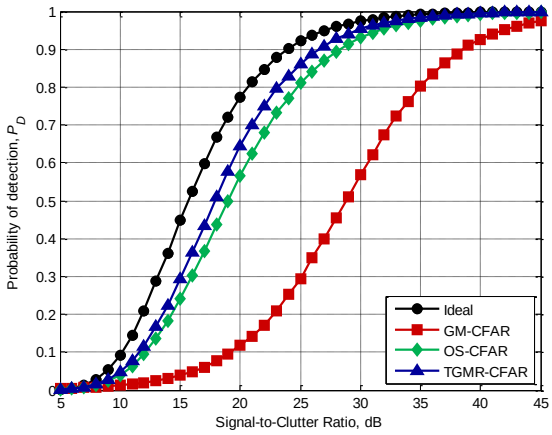

Fig. 5. Detection performance of Ideal, GM, OS and TGMR processors in the presence of two interferring targets with *ICR* = 20dB and for *M* = 24.

V. Conclusion

In this paper, we have considered the problem of Constant False Alarm Rate (CFAR) detection in homogeneous and heterogeneous Pareto clutter. Assuming Pareto distributed clutter, we have proposed the TGMR-CFAR detection scheme, which is based upon a trimmed geometric mean of ratios of consecutive OS. The corresponding expression of the probability of false alarm has been derived and given in closed-form. However, due to the lack of mathematical background, we have revealed that, at the present time, closed-form of its respective probability of detection could not be obtained. To alleviate such a problem and for comparison purposes, we have conducted Monte-Carlo simulations. Performance analysis carried out here showed that the GM-CFAR process worked very well in homogeneous clutter, especially for small size of the reference window *M*. However for increasing *M*, the performance of the proposed TGMR improved clearly and approach that of the GM. In the presence of interfering targets, the new CFAR processes worked very well in managing interference. This provided a significant improvement on the Pareto detection processes discussed in the literature.

References

[1] H. M. Finn, and R. S. Johnson, “Adaptive detection model with threshold control as a function of spatially sampled clutter-level estimates,” RCA Rev. vol. 29, pp. 414–464, 1968.

[2] G. Minkler and J. Minkler, “CFAR–the principles of automatic radar detection in clutter,” Magellan, Baltimore, 1990.

[3] P. P. Gandhi, and S. A. Kassam. “Analysis of cfar processors in nonhomogeneous background,” IEEE Transactions on Aerospace and Electronic Systems, vol. 24, n°4, pp. 427–445, Jully 1988.

[4] A. Farina, and F. A. Studer, “A review of CFAR detection techniques in radar systems,” Microwave Journal, vol. 29, pp. 115-1289, Sept. 1986.

[5] G. B. Goldstein, “False alarm regulation in log-normal and Weibull clutter,” IEEE Transactions on Aerospace and Electronic Systems, vol. 9, pp. 84–92, 1973.

[6] V. Anasstassopoulos, and G. A. Lampropoulos, “Optimal CFAR etection in Weibull clutter,” IEEE Transactions on Aerospace and Electronic Systems, vol. 31, pp. 52–64, 1995.

[7] S. Watts, “ Cell-averaging CFAR gain in spatially correlated K-distributed clutter,” IEE Radar, Sonar and Navigation, vol. 143, pp. 321–327, 1996.

[8] M. Sahed, A. Mezache, and T. Laroussi, “A novel [z log(z)]-based closed form approach to parameter estimation of *K*-distributed clutter plus noise for radar detection,” IEEE Transactions on Aerospace and Electronic Systems., vol. 51, no. 1, pp. 492–505, Jan. 2015.

[9] M. Sahed, and A. Mezache, “Closed-Form Fractional-Moment-Based Estimators for *K*-Distributed Clutter-Plus-Noise Parameters,” IEEE Transactions on Aerospace and Electronic Systems., vol. 53, no. 4, pp. 2094–200, Aug. 2017.

[10] M. Sahed, A. Mezache, and F. Soltani, “Closed-form estimators for the Pareto clutter plus noise parameters based on non-integer positive and negative order moments,” IET Radar, Sonar and Navigation, vol. 11, no. 2, pp. 359-369, 2017.

[11] M. Farshchian, and F. L. Posner, “The Pareto distribution for low grazing angle and high resolution X-band sea clutter,” In: IEEE Radar Conference Proceedings, pp. 789–793, 2010.

[12] G. V. Weinberg, “Assessing Pareto fit to high resolution high grazing angle sea clutter,” IET Electronics Letters, vol. 47, pp. 516–517, 2011.

[13] G. V. Weinberg, “Constant false alarm rate detectors for Pareto clutter models,” IET Radar, Sonar and Navigation, vol. 7, pp. 153-163, 2013.

[14] G. V. Weinberg, “Constant False Alarm Rate Detection in Pareto Distributed Clutter: Further Results and Optimality Issues,” Hikari Journal of Contemporary Engineering Sciences, Vol. 7, no. 6, 231 – 261, 2014.

[15] G. V. Weinberg, “Constant false alarm rate detection in Pareto distributed clutter : Further results and optimality issues,” Contemporary Engineering Sciences, vol. 7, vol. 6, pp. 231–261, 2014.

[16] M. Sahed, and A. Mezache, “Analysis of CFAR detection with multiple pulses transmission case in Pareto distributed clutter,” In: 4th International Conference on Electrical Engineering (ICEE), pp. 1–6, 2015.

[17] P. Swerling, “Probability of detection for fluctuating targets,” IRE Transactions on Information Theory, vol. 6, n°2, pp. 269–308, Avril 1960.

Denoising Ultrasound Images and Error Estimate by Non Local Means

Rachida Bouchouareb
Department of Network and telecommunications
Larbi Ben M'hidi University of Oum El-Bouag
Oum El-Bouaghi, ALgeria
Electrical engineering laboratory
University of Ouargla
Ouargla , ALgeria
rachidabouchouareb@gmail.com

Naam Bouhafs
Department of Electronic and Communication
University of Ouargla
Ouargla, Algeria
naamouargla@gmail.com

Abstract*—Image denoising is one of the main techniques in the field of computer graphic and computer vision. Non-local means method is one of the great useful methods which arouse tremendous research [1]. In this paper, we will study the utility of the Non Local Means method in denoising ultrasound images by error estimate. This method based on replacing a pixel by the average of similar pixels. But the most similar pixels to a given pixel can be also non adjacents. We can scan a big portion in search of all the pixels of the image that really resemble the pixel we want to denoise. [2]

Keywords—Denoising, Ultrasound Images, Non Local Means Method

I. INTRODUCTION

In the image processing literature, several methods have been proposed and used in image denoising methods have been proposed. We find as example methods using the spatial filtering, approaches based on PDEs variational [3, 4], other approaches using Markov random fields and methods based on multiscale transforms, like wavelet transform [5, 6, 7]. Each approach has its own assumptions, benefits, and limitations. However, many of these methods remove more and more noise from the details of the image. As a result, denoising algorithms continue to be developed to solve this problem. Among these methods, Non Local Means and the one we applied on ultrasound images [8]

II. NON-LOCAL MEANS THEORY

The algorithm of Non Local Means is used for image denoising, and it's different from « local means »filters where we calculate the mean value of all pixels surrounding the target pixel in aim to smooth the image. While, Non Local Means filters searches all the pixels that have similarities with the target one and take the mean value of these pixels. In this case, we have cleared image and less loss of detail compared with local means algorithm [9].

This approach is based on the self-similarity existing in the image it self; it is a question of finding similar pixels (patches) in the image, and then calculating their weighted average according to their similarity with the pixel denoised [10]. Fig 1 below presents an example of self-similarity.

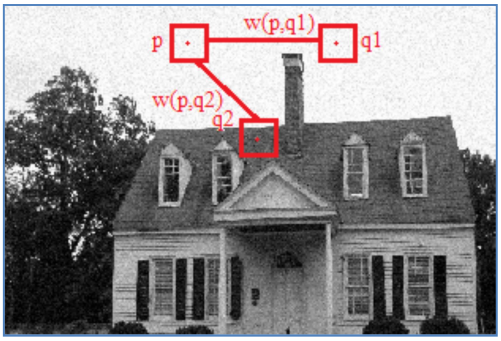

Fig. 1. Sel-fsimilarity in an image.

Neighborhoods Pixels of p and q1 are similar, but those for pixels p and q2 are not similar. For this reason, pixel q1 will have a big affect on the denoised value of p than q2 [10]

III. PRINCIPLE AND ALGORITHM OF THE METHOD

As shown by Buades et al, the principle of non-local averages (NL Means), is to take advantage of the remote information that can be found in images. This approach is based on the self-similarity existing in the image itself, so it is a question of finding the pixels (patches) similar in the image, then calculating their weighted average with their similarity with the pixel to denoise [11]

Let x (xεΩ):

s(x) the set of pixels similar to x(xεΩ). Thus :

$$u(x) = \sum_{y \wedge_x} w(x,y)v(y) \quad (1)$$

And

$$\sum_{y \wedge_x} w(x,y) = 1 \quad (2)$$

$$k(x,y) = e^{-\frac{||v(x)-v(y)||^2}{h^2}} \quad (3)$$

$$Z(x) = \sum_{y \wedge_x} k(x,y) \quad (4)$$

And

$$w(x,y) = \frac{k(x,y)}{\sum_{y \wedge_x} k(x,y)} = \frac{1}{Z(x)} k(x,y) \quad (5)$$

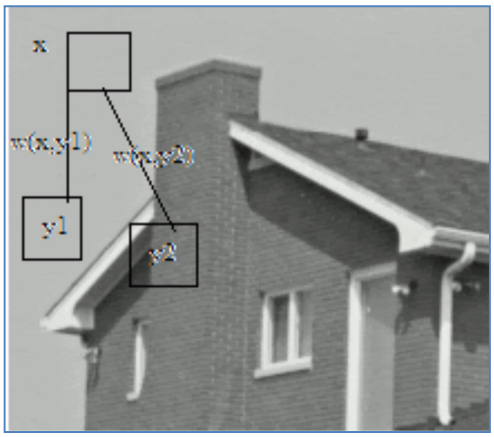

Fig. 2. Principle of the NL-Means algorithm

$$w(x,y) = \sum_{y\in\Omega_x} \frac{1}{Z(x)} e^{-\frac{\|v(x)-v(y)\|^2_{2,a}}{2h^2}} \quad (6)$$

Where $u(x)$ is the denoise value of a pixel x.
$v(y)$ The value to denoise at the point $y(y\epsilon\Omega_x)$
$k(x,y)$ The similarity between pixels x and y
$w(x,y)$ Weights
let $v: \Omega \to R$ tq $v = u + b$ noised image

u: Original image.

$\{b(x)\}_{x\epsilon\Omega}$ is the gaussien white noise with variance σ^2.

Spatial Denoising by the Non-Local means algorithm (NL-means) is classically written

$\forall x \in \Omega$, where the NL-means weights are written

$$NLM[v](x) = \sum_{y\in\Omega_x} \frac{1}{Z(x)} e^{-\frac{\|v(x)-v(y)\|^2_{2,a}}{2h^2}} v(y) \quad (7)$$

where $v(x)$ is the 7×7 patch centered in x in the image v that is, the grayscale.

$\{v(y)|y \in \Omega, \|x-y\|_\infty \leq 3\}$,

h a filtering parameter,

Z(x) a standardization coefficient

$\|.\|_{2,a}$ Euclidean norm weighted by a Gaussian of standard deviation "a" which defines the similarity between the patches

$\Omega_x = \{y \in \Omega \, | \|x-y\|_2 \leq d\}$ is the area of search for similarities and radius d [12]

IV. Results

In this study, we have used ultrasound image pixels. We load our image and transform it to gray level, where (N=256) is the number of pixels of two different grey level values, then we add White Gaussian Noise to obtain the denoised one.

For the Non Local Means method, we obtain the denoised image by changing the values of sigma of White Gaussian Noise when we add it to the original image (Fig 3). Than we applied NLM filter as shows the tables (I,II,III,IV).

We try to compare the results with those obtained by Gaussian, median and average filters as shown in the tables (V, VI).

The quality between the original image and the filtered is measured by the first parameter PSNR. Big value of PSNR means the quality of the image treated is good. It calculates the peak signal- to- noise ratio between two images by the following equation [13]:

$$PSNR = 10\log_{10}\left[\frac{255^2}{MSE}\right] \text{ dB} \quad (8)$$

MSE is the Mean Square Error, which is the square of the accumulated error between the original and filtered image. The lower value of MSE means quality is good. MSE is calculated by the equation:

$$MSE = \frac{1}{MN}\sum_{i=1}^{M}\sum_{j=1}^{N}(X(i,j) - Y(i,j))^2 \quad (9)$$
(6)

M and N are rows and columns of the input images, respectively

The mean square error (MSE) and peak ratio of signal to noise (PSNR) are the two error parameters used to compare the quality of image compression [14]

The second parameter is Structural Similarity (SSIM) is measure of similarity between two digital images.

The idea of SSIM is to measure the similarity of structure between the two images, rather than a pixel to pixel difference as for example the PSNR. The underlying assumption is that the human eye is more sensitive to changes in the structure of the image.

The SSIM metric is calculated on multiple windows of an image. The measurement between two windows x and y of size NxN is (7)

$$SSIM(x,y) = l(x,y).c(x,y).s(x,y) = \frac{(2\lceil_x\lceil_y+c_1)(2\lceil_x\lceil_y+c_2)(cov_{xy}+c_3)}{(\lceil^2_x+\lceil^2_y+c_1)(\lceil^2_x+\lceil^2_y+c_2)(\lceil_x\lceil_y+c_3)} \quad (10)$$

μ_x the average of x

μ_y the average of y

σ_x^2 the variance of x

σ_y^2 the variance of y

cov_{xy} is covariance of x et and y

$c_1 = (K_1L)^2, c_2 = (K_2L)^2$ et $c_3 = \frac{c_2}{2}$: Parameters to stabilize the equation, when the denominator is very low.

L is the dynamic of pixel values, ie 255 for 8-bit coded images

$k_1 = 0.01$ et $k_2 = 0.03$ by default

The value of SSIM is between 0 and 1, which indicates the correlation with respect to the source, 1 indicating a perfect correlation [15].

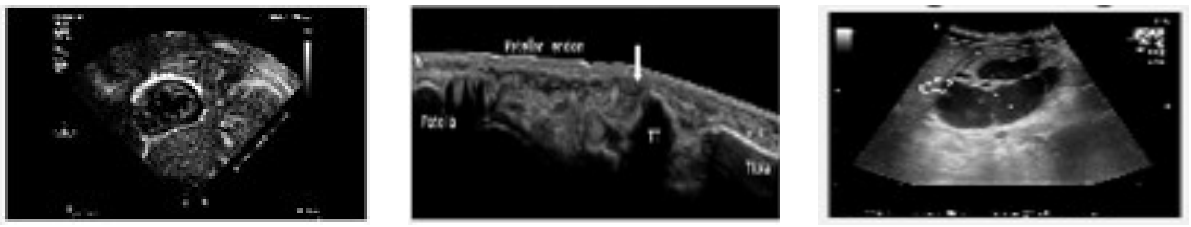

a b c

Fig. 3. Original Images a(stomach), b(the patellar tendon), c(Endoscopic Heterogeneous mass in the the gastric wall)

There is also the visual aspect as a third parameter: sometimes we get a high PSNR and SSIM near to 1 but the image is blurry which means there is a loss of detail.

In the following tables, the results obtained for different values of f (neighborhood window of the pixel), t (similarity window) and sigma, for the ultrasound image (a) of a stomach

TABLE I. PSNR AND SSIM FOR AN IMAGE DENOISED BY NLM METHOD FOR DIFFERENT SIGMA VALUES (F=2 T=5)

σ	PSNR (dB)	SSIM
0.001	38.7070	0.5996
0.0015	38.1607	0.5447
0.002	37.6332	0.5117
0.01	34.7745	0.2921
0.06	33.3832	0.1145
0.5	32.9653	0.0315

TABLE II. PSNR AND SSIM FOR AN IMAGE DENOISED BY NLM METHOD FOR DIFFERENT SIGMA VALUES (F=6 T=8)

σ	PSNR (dB)	SSIM
0.001	35.7043	0.5590
0.0015	35.6911	0.4985
0.002	35.6515	0.4662
0.01	35.2490	0.3265.
0.06	33.9151	0.1269
0.5	32.9830	0.0316

TABLE III. PSNR AND SSIM FOR AN IMAGE DENOISED BY NLM METHOD FOR DIFFERENT SIGMA VALUES (F=3 T=8)

σ	PSNR (dB)	SSIM
0.001	37.488	0.5861
0.0015	37.2072	0.5821
0.002	36.9725	0.4943
0.01	35.0997	0.3167
0.06	33.5062	0.1149
0.5	32.9498	0.0329

TABLE IV. PSNR AND SSIM FOR AN IMAGE DENOISED BY NLM METHOD FOR DIFFERENT SIGMA VALUES (F=3 T=12)

σ	PSNR (dB)	SSIM
0.001	36.9444	0.5859
0.0015	36.8426	0.5223
0.002	36.6679	0.4931
0.01	35.1133	0.3210
0.06	33.5524	0.1170
0.5	32.9262	0.0316

Interpretation

According to the results obtained when different sigma values were used in different windows, it is clear that the values of PSNR and SSIM are better in the case of sigma ≤0.002, F=2 and T=5 but in the case. From sigma = 0.06.the image remains noise whatever the size of the window, which is an inconvenient. As shown fig (4) in case of sigma=0.002and 0.01.

In the following tables (V, VI), a comparison has been presented between the PSNR and SSIM for the different types of filters (Gaussian, median and average) and the NLM method. An example is shown in fig (5) for sigma=0.06.

TABLE V. COMPARAISON BETWEEN THE VALUES OF PSNR FOR THREE FILTERS AND NLM METHOD

σ	0.001	0.0015	0.002	0.01	0.06	0.5
Gaussian Filter	38.4190	37.9282	37.4144	35.5195	34.699	35.0907
Median Filter	34.3692	34.3376	34.2861	34.1691	33.7409	33.2924
Avergae Filter	34.5473	34.5678	34.562	34.7678	35.6277	37.4081
NLM method	38.7070	38.1607	37.6332	34.7745	33.3832	32.9653

TABLE VI. COMPARAISON BETWEEN THE VALUES OF SSIM FOR THREE FILTERS AND NLM METHOD

σ.	0.001	0.0015	0.002	0.01	0.06	0.5
Gaussian Filter	0.5972	0.5150	0.4687	0.2896	0.1553	0.0488
Median Filter	0.7473	0.7236	0.6947	0.5326	0.3288	0.1438
Avergae Filter	0.4436	0.3876	0.3479	0.2121	0.1373	0.0643
NLM method	0.5996	0.5447	0.5117	0.2921	0.1145	0.0315

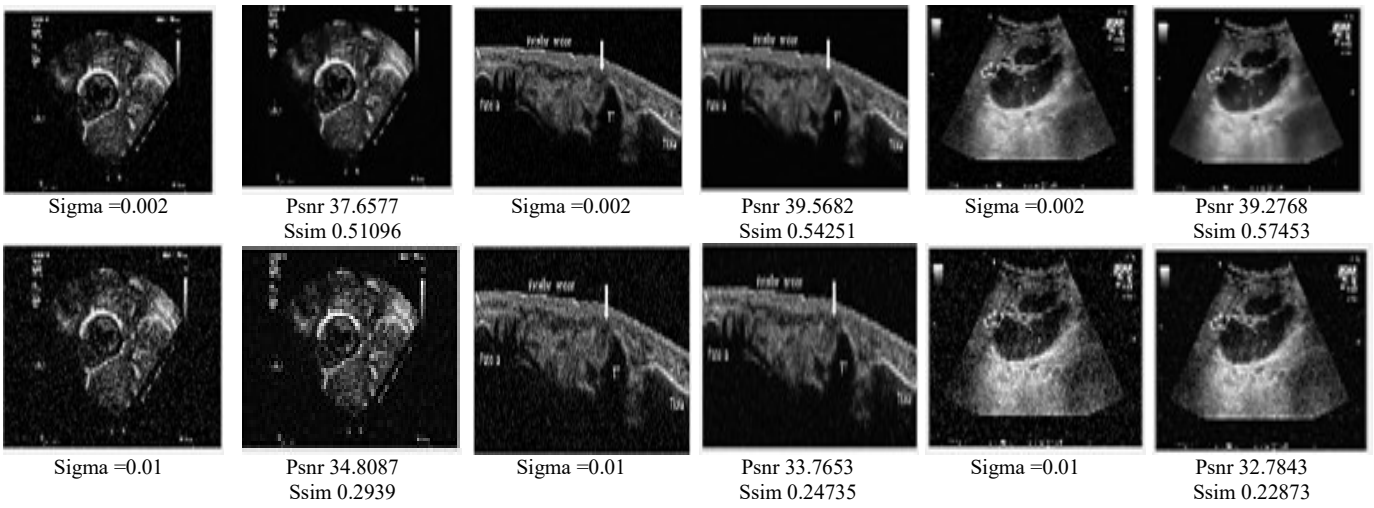

Fig. 4. Noised Image (0.002and 0.01) and filtered imaged by NL Means filter

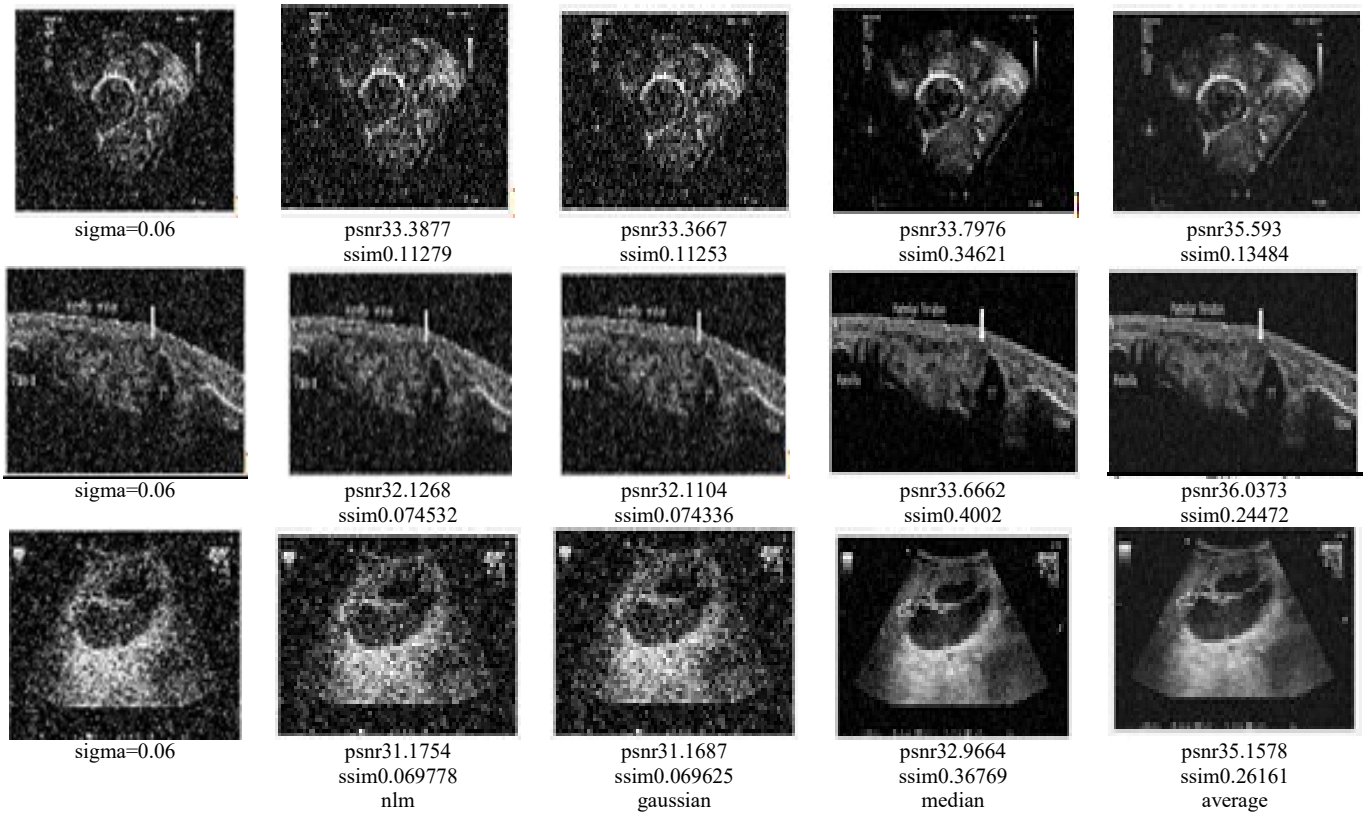

Fig. 5. PSNR and SSIM values obtanied by different filters

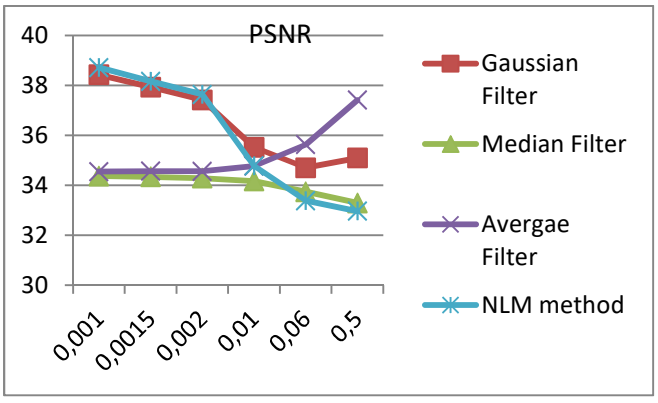

Fig. 6. PSNR values obtanied by different filters

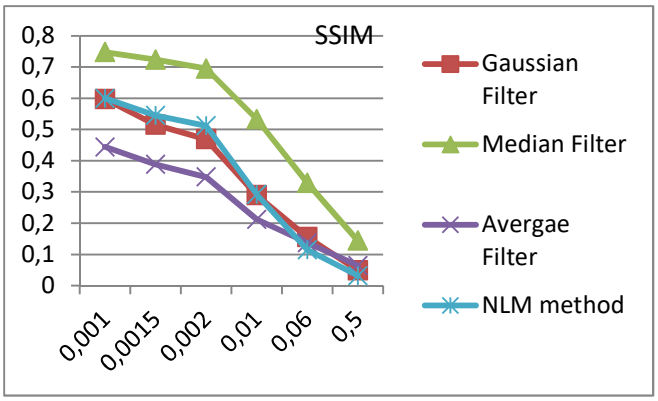

Fig. 7. SSIM values obtanied by different filters

Interpretation

In Fig. 5 and Fig. 6, The comparison shows that the PSNR and SSIM in the case of sigma <= 0.002 is best in the case of NLM Method than the other filters. For sigma>0.002 we get blurred image. We distinguished that the NLM method is very sensitive to noise and to the type of organ tissue (in case of ultrasound images).

V. CONCLUSION

We have seen in this paper the use of Non Local Means in reducing noise, which has a bad effect on medical imaging. This paper is organized in five sections. The first section, presents an introduction about different methods used in denoising images. Section 2 talks about Non Local Means Theory. Principle and Algorithm of this method are described in the Section3. In Section 4 we applied NLM on an ultrasound image denoised by White Gaussian Noise, and then we compared it with classic filters (Gaussian, Median and Average). Section 6 shows the conclusion of this study.

In this paper we have studied the use of NLM Method in denoising Ultrasound Images and we have demonstrated that NLM method is could offer better results

References

[1] L. Huang “Improved Non-Local Means Algorithm for Image Denoising” Journal of Computer and Communications, , 3, 23-29, 2015

[2] A. Buades1 , B. Coll2 , J. Morel3 “Non-Local Means Denoising” Published in Image Processing On Line on, 2011.

[3] T. Aksenova, A. Barachant, and S. Bonnet, “Spatial Filtering Optimisation in Motor Imagery EEG-Based BCI”, Neurocomp, 2008.

[4] W. Yijun, G. Shangkai, and G. Xiaorong, “Common Spatial Pattern Method for Channel selelction in Motor Imagery Based Brain-Computer Interface”, Engineering in Medicine and Biology Society, 2005.

[5] H. Attouch, G. Buttazzo and G. Michaille, “Variational Analysis in Sobolev and BV Spaces”, MPS-SIAM Series on Optimization, 2006.

[6] D. Azé, Dominique et J.B. Hiriart-Urruty, “Analyse variationnelle et optimisation: éléments de cours, exercices et problèmes corrigés”, Cépaduès-Éd., 2010

[7] A. Chambolle, “An Algorithm for Total Variation Minimization and Applications”, JMIV, 20 pp 89-97, 2004

[8] D BARRY. “Débruitage d’image par fusion de filtrage spatio-fréquentielle” Université de Montréal, 2018.

[9] B. Antoni “A non-local algorithm for image denoising”. IEEE Computer Society Conference on Computer Vision and Pattern Recognition. CVPR'05. pp. 60–65, 2005

[10] R. Shrivastav, V. Namdeo and T. Arjariya “Modified Non-Local Means De-noising With Patch and Edge Patch Based Dictionaries”International Journal of Engineering and Applied Sciences (IJEAS)ISSN: 2394-3661, Volume-2, Issue-6, June 2015

[11] A. Buades, B. Coll, and J Morel. “On image denoising methods.” Technical Report 2004.

[12] S.POSTEC, Jacques Froment, Béatrice Vedel. “Un algorithme de débruitage Non-Local Means espace-fréquence “. Université de Bretagne-Sud, Brest, France, 2013.

[13] R. Bouchouareb, N. Hedjazi, and D.Benatia “Denoising Medical Ultrasound Images and Error Estimate by Translation-Invariant Wavelets International”. Journal of Signal Processing, Image Processing and Pattern Recognition Vol.7, No.1, pp.193-202, 2014:

[14] R. Bouchouareb and D. Benatia. “Comparative Study between Wavelet Thresholding Techniques (Hard, Soft and Invariant-translation) in Ultrasound Images”. International Journal of Bio-Science and Bio-Technology Vol.6, No. 6, pp.29-38, 2014.

Z. Wang,; E.P. Simoncelli, A.C. Bovik. “Multiscale structural similarity for image quality assessment”. Conference Record of the Thirty-Seventh Asilomar Conference on Signals, Systems and Computers,. 2. pp. 1398–1402 Vol.2, 2004

A Study Of Speckle Noise Reduction Filters for SAR Images

TIFOUTI Issam[#1], MERIANE Brahim[#1], RAHMOUNI Salah[#1] and MOUSSAOUI abdelkrim[#2]
[1#]*Higher School for professors Of Technological education, Skikda, Algeria.*
[2#]*Laboratory of Electrical Engineering of Guelma (LGEG), University 8th May 1945 Guelma, Algeria.*
[1] issam86@yahoo.fr.

***Abstract*— Synthetic Aperture Radar (SAR) imaging systems can provide valuable sources of earth observation data for various applications. Speckle noise can reduce the image quality of synthetic aperture radar (SAR) and complicate image interpretation. Reduction of speckle noise is one of the most important processes to increase the quality of the image. Several filters are widely used to enhance the quality of images by despeckling it. This paper compares six different speckle reduction filters such as Lee Filter, Frost Filter, Kuan Filter, Wiener Filter, Median Filter and SRAD (Speckle Reducing Anistrophic Diffusion) Filter that are applied to the SAR image. The statistical measures SNR, PSNR, SSIM, MSE, RMSE are compared and the results are tabulated to determine the filter that is well suited for SAR images. Finally the best filter has been proposed based on the statistical and experimental results.**

***Keywords*— Synthetic Aperture Radar (SAR), Speckle noise, Speckle Filtering, Statistical measures.**

I. INTRODUCTION

Synthetic Aperture Radar (SAR) images employ active sensors that detect microwave radiation, which has longer wavelength than visible light that is detected in passive sensors, such as the optical sensor. Therefore, the surface of the Earth can be observed at high resolution, regardless of weather conditions and sun phenomena [1]. The active sensor of SAR images is also used with satellites or unmanned aerial vehicles (UAVs), as the development of the active sensor technology applied to SAR images enabled high-resolution target detection and identification. SAR images are widely used in applications of a variety of fields, such as the military, agricultural, weather forecasting, and environmental analysis, etc. [2]. Due to the advantages of SAR images and their various applications, research on the technology behind SAR images is being actively conducted around the world (image enhancement [3–5], image classification [6,7], image segmentation [8,9], etc.).

Synthetic aperture radar (SAR) is a coherent imaging system [10]. Each pixel in SAR images represents the coherent addition of scatterers from a corresponding resolution cell. These scatterers interfere, either constructively or destructively, depending on the phase of the scatterers. As such, the resulting images exhibit bright and dark pixels and are uneven, even for homogeneous regions.

This phenomenon is called speckle noise and it often reduces the quality of images and complicates image interpretation [10,11]. Mathematically there are two basic models of noise: Multiplicative noise and additive noise. Multiplicative noise is image dependent, complex to model and difficult to remove. Whereas additive noise is systematic in nature and can be easily modeled and hence reduced easily [12]. Speckle noise is a multiplicative noise. It occurs in all coherent imaging systems, such as SAR (Synthetic Aperture Radar), satellite images, medical ultrasonic and photographic images [13]. The aim of the noise reduction techniques is to remove speckle noise and retaining the important features of the images without destroying useful diagnostic information.

I.1 ADDITIVE NOISE

The so called additive noise (AN) model is commonly found in acquiring images from digital devices [14]. Most of the literatures principally process with this type of image formation models. Let $f[m,n]$ be the original image, $f'[m,n]$ be the noise assimilate version and $\eta[m,n]$ be the noise function which returns values coming from an arbitrary distribution. Then the additive noise is given by the equation

$$f'[m,n] = f[m,n] + \eta[m,n] \quad (1)$$

Typically, $\eta[m,n]$ is symmetric about zero. Additive noise is independent of the pixel values in the original image.

I.2 SPECKLE NOISE

There are different noise types in real world. Multiplicative noise is common beside additive noise. Quality of images may degraded while images acquisition, transmission, and storage. The noise of the original record equipment, external perturbation, the defects of the imaging system and the movement of objects also cause the image noise. According to the assumption that imaging system is linear translation invariance system [15]. Speckle or multiplicative noise is a signal dependent form of noise which magnitude is related to the value of the original pixel. The mathematical expression for a multiplicative noise model is given by

$$f'[m,n] = f[m,n] + \eta[m,n]f[m,n] \quad (2)$$

$$f'[m,n] = f[m,n] + [1 + \eta[m,n]] \quad (3)$$

II. SOURCES OF NOISE IN DIGITAL IMAGES

The main source of noise in digital image processing arises during the image acquisition or transmission process. In general, noise is measured by the percentage of the corrupted image pixel. Depending on how the image has been created, there are several causes to add noise in the original image. The causes are:

1) If the image is scanned from a photograph made on film, the film grain is a source of noise. Noise can also be introduced by the scanner itself, or be the result of damage to the film.
2) If the image is captured in a digital format directly, then the mechanism for collection (the data) may introduce noise.
3) Electronic transmission of image data can also make noise [16-17].
4) When the emitted light from the object cannot enter into the device lenses and that's why noise is introduced into the image if the device sensor is not properly opened . Light levels and sensor temperature are major factors in making a noise.
5) Dynamic range is a parameter which is used in mapping a 3D view in the image plane. If this range is small then more intensity is gathered on the pixels which also make the picture noisy and if the dynamic range is high then the light intensity is scattered into a wide region which makes the picture noisy [17].

III. DENOISING

Denoising is the process of reducing noise in the images [18]. Conceptually, Noise reduction techniques are very similar regardless of the image being processed, however a prior knowledge of the characteristics of an expected signal can mean the implementations of these techniques varies, greatly depending on the type of signal. Image denoising is often used in several domains like SAR and satellite images processing applications, where an image was infected with noise but needs to be enhanced before it can be making observations or used. For this type of application we must to know something about the degradation process in order to develop a model. The inverse process can be applied to the image to restore it back to the original form when we have a model for the degradation process. Image denoising finds applications in fields such as photography where noise is made up of lots of small points that are created, astronomy where the resolution limitations are intense and in medical imaging where the physical requirements for two high quality imaging are needed to analyze appropriate for images. So denoising is a technique to remove the undesirable information from an image to make it more appropriate for the next steps of the image processing [13].

IV. PROPOSED METHODOLOGY

Our work is based on the use of different techniques for the reduction speckle noise of SAR and satellite images. Several filters are used for speckle reduction, some filters are best adapted for some specific class of images. The proposed work is a comparative study on the performance of the several filters such as Lee Filter, Frost Filter, Kuan Filter, Weiner Filter, Median Filter and SRAD Filter in removing the speckle noise from the input images. Statistical parameters like SNR, PSNR, SSIM, MSE, RMSE are calculated for the output images obtained from the filters to assess the quality of the images used. The images corresponding to the best statistical value are shown and results are discussed.

V. METHODS FOR SPECKLE FILTERING

Divers methods are available for image denoising of images which are corrupted by speckle noise includes filtering techniques like Median Filter, Lee Filter, Frost Filter, Kuan Filter, Wiener Filter, and SRAD Filter.

V.1 MEDIAN FILTER

Median filter is one of the popular methods to be employed to reduce impulse noise level from corrupted images [19]. The median filter is a spatial nonlinear filter which removes pulse or spike noise by replacing the middle pixel value in the window with the median value of its neighbors in the window [20]. The median filter is very effective in retaining the image details since they do not depend on values which are significantly different from typical values in the neighborhood [21]. The median filter works on successive image window in a manner similar to that of the linear filters, but the method employed does not use a weighted sum. Pixels in each window are sorted into ascending order and the pixel value in the middle is selected as the new value for a particular pixel. Advantage of this filter is it preserves the edges [20]. Disadvantage is the long time needed for computation of the median value for sorting N pixels.

V.2 LEE FILTER

The Lee filter [22], developed by Jong-Sen Lee, is an adaptive filter which changes its characteristics according to the local statistics in the neighborhood of the current pixel. The Lee filter is able to smooth away noise in flat regions, but leaves the fine details such as lines and textures unchanged. The Lee filter is designed to eliminate speckle noise while preserving edges and point features in radar imagery [23]. Lee Filter is based on multiplicative speckle model [24], this model is first approximated by a linear model. Then the minimum mean square error criterion is applied to the linear model [25]. The resulting grey level value R for the smoothed pixel is

$$R = I_c * W + I_m * (1 - W) \quad (4)$$

Where

$$W = 1 - \frac{C_u^2}{C_i^2}, C_u = Sqrt\left(1/N_{look}\right), C_i = S/I_m \quad ,$$

I_c is the centre pixel of filter window. I_m = mean value of intensity within window, S = standard deviation of intensity within window, the C_u above is the estimated noise variation coefficient. C_i is the image variation coefficient. W is a weighting function.

V.3 FROST FILTER

Invented by Frost in 1982, is linear, convolutional filter used to remove the multiplicative noise from images [22]. Frost filter is an adaptive filtering approach based on local statistic about the target pixel. In homogenous regions frost filter acts as a mean filter and at edges filtering is inhibited completely. Despeckled pixel value is estimated by the weighting coefficient which decay from the filter centre when high contrast regions are filtered [26]. Thus despeckling is widely carried out by smoothing in homogeneous region, and lesser smoothing in regions with high contrast pixels and edges. The filter output is determined by

$$\hat{x_s} = \Sigma_{p\in\eta} k_p x_p \quad (5)$$

where x_p is noisy pixel of interest in the window k_p is given by

$$k_p = e^{(-KA_s^2 dis_{s,p})} / \Sigma_{p\in\eta} e^{(-KA_s^2 dis_{s,p})} \quad (6)$$

where K, damping coefficient, is selected such that $KA_s^2 \to 0$ at homogeneous regions and results in mean filter output and $KA_s^2 \to \infty$ (so large) at edges and results in less or no despeckling or smoothing.

$$A_s^2 = (1/|\eta_s|)\Sigma_{p\in\eta}(x_p - \bar{x_s})^2 / (x_p - \bar{x_s})^2 \quad (7)$$

Where

$\bar{x_s}$ is the mean value of the intensity within the filter window η_s

$$dis_{s,p} = \sqrt{(i-i_p)^2 + (j-j_p)^2} \quad (8)$$

(i_p, j_p) is the grid coordinates of pixel s and (i_p, j_p) is the grid coordinates of pixel p.

V.4 KUAN FILTER

It was developed by Kuan and Nathan and Kurlander in 1987 [22]. Kuan performs spatial filtering on each individual pixel in an image using the grey level values in a square window surrounding each pixel. The dimensions of the filter must be odd from 3x3 to 11x11 pixels. All pixels are filtered. In order to filter pixels located near edges of the image, edge pixels are replicated to give sufficient data. The resulting grey level value R for the smoothed pixel is: [25]

$$R = C_p * W + I * (1 - W) \quad (9)$$

Where,

$C_u = 1/N_{look}, C_i = Var/I, W = (1 - C_u/C_i)/(1 + C_u)$, i = Mean grey level in the filter window, C_p = central pixel in filter window, Var = Variance in filter window, N_{look} = Number of Looks.

V.5 WIENER FILTER

The aim of wiener filter is reduced the mean square error as much as possible [27]. The Wiener filter is designed by minimizing the MSE between the original image and filtered image. It can be applied to the image, adaptively, adaptation itself to the local image variance. When the variance is small, it performs more smoothing. When the variance is large, it performs low smoothing. Since the intensities of the pixels in the weld area follow a Gaussian distribution. The Wiener filter was selected for filtering of radiographic images of welds, because it is close to the matched filter in this case [28].

V.6 SRAD FILTER

SRAD is Speckle Reducing Anti Isotropic filter [29]. In the case of diffusion filtering the strength and direction of the diffusion are controlled by an edge detection function. It removes speckles by modifying the image via solving a Partial Differential Equation. It removes speckles and at the same time improves the edges. SRAD is proposed for speckled images without logarithmic compression. Just as lee and frost filters utilize the coefficient of variation in adaptive filtering, SRAD exploits the instantaneous coefficient of variation, which serves as edge detector in speckled images. The function produces high values at edges and presents low values in homogeneous regions. Thus it ensures the edge preserving and edge enhancing at the edges and mean preserving behavior in the homogeneous regions [30].

VI. ESTIMATION OF STATISTICAL PARAMETERS

To evaluate the performance of the proposed filters for removal speckle noise and to evaluate their comparative Performance. The parameters which are used in estimation of performance are Signal to Noise Ratio(SNR), Peak signal to noise ratio(PSNR), Mean Square Error(MSE), Root Mean Square Error(RMSE), Structural Similarity Index(SSIM).

VI.1 ESTIMATION OF SNR

SNR is a measurement of distortion. Especially in homogeneous regions, It exhibits the success of noise. It is calculated as:

$$SNR = 10\log_{10}\left(\frac{\sigma_g^2}{\sigma_e^2}\right) \quad (10)$$

where, σ_g^2 is the variance of the noise free image and σ_e^2 is the variance of error (between the original and denoised image). The value of SNR should be high for good quality image.

VI.2 ESTIMATION OF PSNR

PSNR is the ratio between maximum possible power of a signal and the power of corrupting noise that affects the reliability and quality of its representation. PSNR is calculated as

$$PSNR = 10\log_{10}\left(\frac{MAX^2}{MSE}\right) \quad (11)$$

Where MSE is mean square error and MAX is the maximum pixel value of image [31].

VI.3 ESTIMATION OF MSE

The MSE is the cumulative square error between the synthesized image and the original image defined by [32]:

$$MSE = \sum_{0}^{m-1}\sum_{0}^{n-1}\left\| f(i,j) - g(i,j)\right\|^2 \quad (12)$$

VI.4 ESTIMATION OF RMSE

RMSE is a good measure of accuracy. A lower value for RMSE means lesser error and this result in a high value of PSNR. RMSE is a frequently used measure of the differences between values actually observed and the values predicted by an estimator or a model [33]. Its formula is given by

$$RMSE = \sqrt{MSE} \quad (13)$$

VI.5 ESTIMATION OF SSIM

This parameter is used for measuring the similarity between two images. The index is a reference to measure of image quality based on an initial distorted image as reference. The measurement should provide a good approximation to perceive image distortion. This parameter is defined as follows:

$$SSIM = \frac{\left(2\mu_x\mu_y + C_1\right)\left(2\sigma_{xy} + C_2\right)}{\left(\mu_x^2 + \mu_y^2 + C_1\right)\left(\sigma_x^2 + \sigma_y^2 + C_2\right)} \quad (14)$$

Where μ_x the average of x, μ_y the average of y, σ_x^2 the variance of x, σ_y^2 the variance of y, σ_{xy} the covariance of x and y, $C_1 = \left(k_1 L\right)^2$, $C_2 = \left(k_2 L\right)^2$ two variables to stabilize the division with weak denominator, L the dynamic range of the pixel values (typically this is $2^{\text{bit per pixel}}$ -1) and k_1=0.01 and k_2=0.03 by default.

The resultant SSIM index is a value between -1 and 1, and value 1 is only accessible in the case of two identical sets of data or better image quality [34].

VII. ALGORITHM FOR FILTER SELECTION

The input images are corrupted with uniformly distributed multiplicative noise. With three different values of standard deviation (σ) of the noise. Noisy images are filtered by using six filters such as Median Filter, Lee Filter, Frost Filter, Kuan Filter, Wiener Filter, and SRAD Filter. After the filtering, the images are saved for estimation of statistical measures. Statistical parameters such as SNR, PSNR, MSE, RMSE and SSIM are calculated for the filtered images obtained from each filter and we obtain six sets of statistical parameters, each set corresponding to a specific filter. Filtered image and statistical parameters corresponding to the best result obtained are given in the output after the comparison of the results for images.

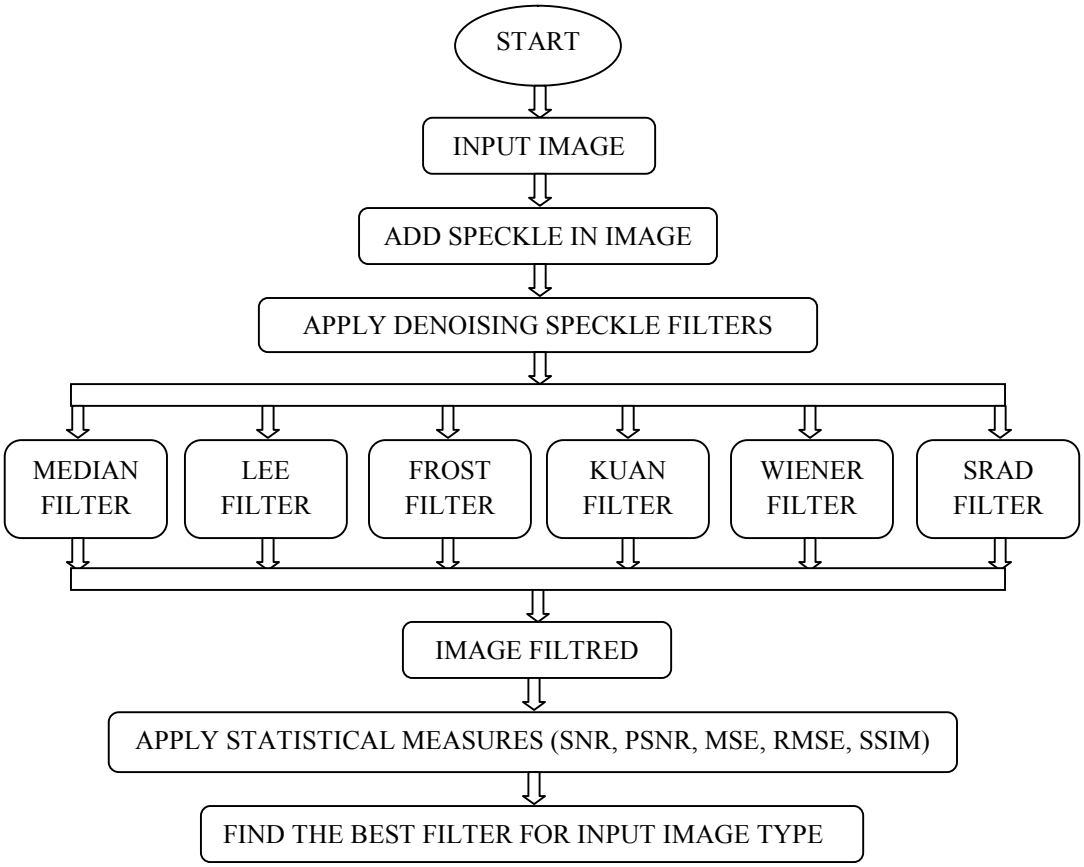

Fig. 1 Algorithm for Speckle noise reduction.

VIII. EXPERIMENTAL RESULTS

In this section we discussed the experimental results. These results have been obtained by applying reduction filters described above to SAR image., these image were filtered using Lee, Frost, Kuan, Wiener, Median and SRAD Filter, by using 3x3 windows size.

To compare the efficiency of each filter. Performance measurements of the reduction filters performed for each de-speckle image.

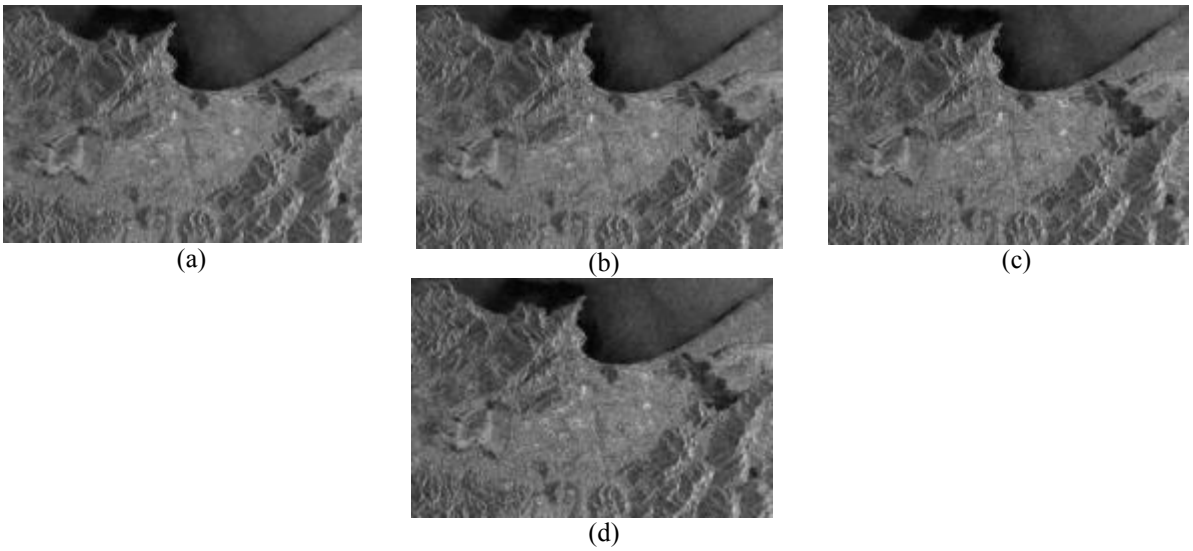

Fig. 2 (a) Original SAR Image (b) Noisy image with SD 0.01, (c) Noisy image with SD 0.02, (d) Noisy image with SD 0.03.

TABLE 1: RESULTS OF SAR IMAGE WITH STANDARD DEVIATION 0.01

FILTER	SSIM	SNR	PSNR	MSE	RMSE
LEE	0.9698	14.6065	26.5538	144.9090	12.0378
FROST	0.9158	15.9066	19.7958	686.9136	26.2090
KUAN	0.9155	16.2624	24.2879	244.1707	15.6260
WIENER	0.9479	17.6198	27.1892	125.1869	11.1887
MEDIAN	0.9231	16.1448	24.2921	243.9336	15.6184
SRAD	0.9153	16.5684	25.9815	165.3211	12.8577

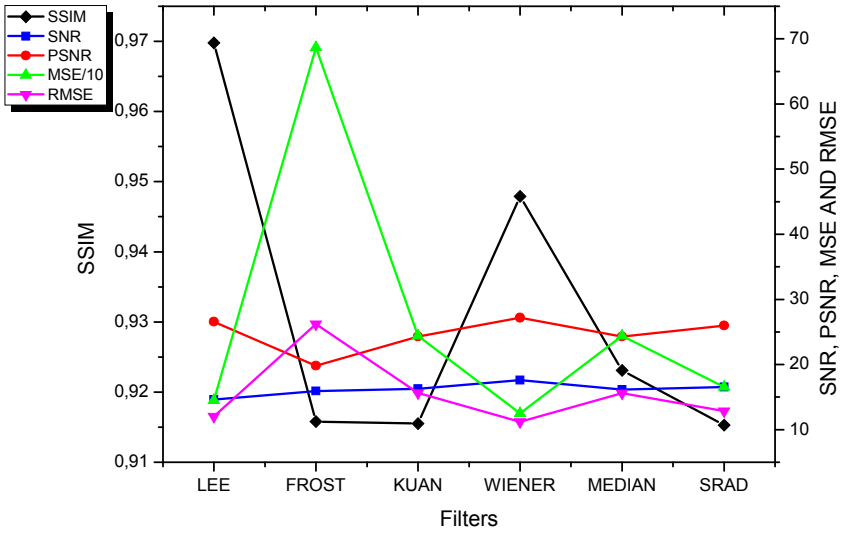

Fig. 3 Graph for SAR image with standard deviation 0.01

TABLE 2: RESULTS OF SAR IMAGE WITH STANDARD DEVIATION 0.02

FILTER	SSIM	SNR	PSNR	MSE	RMSE
LEE	0.9682	14.4279	26.4020	150.0668	12.2502
FROST	0.9125	15.8473	19.7756	690.1175	26.2701
KUAN	0.9154	16.1841	24.3347	241.5522	15.5419
WIENER	0.9432	17.3178	26.7524	138.4324	11.7657
MEDIAN	0.9177	15.6845	24.1048	254.6829	15.9588
SRAD	0.9170	16.4808	25.9349	167.1052	12.9269

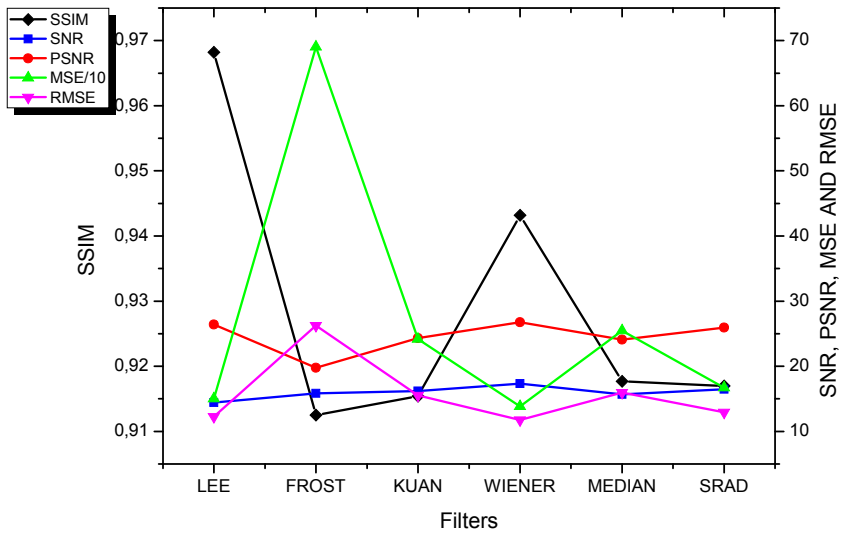

Fig.4 Graph for SAR image with standard deviation 0.02

TABLE 3: RESULTS OF SAR IMAGE WITH STANDARD DEVIATION 0.03

FILTER	SSIM	SNR	PSNR	MSE	RMSE
LEE	0.9669	26.2507	14.2973	155.3838	12.4653
FROST	0.9086	19.7533	15.7897	693.6705	26.3376
KUAN	0.9105	24.2738	16.1060	244.9628	15.6513
WIENER	0.9393	26.3738	17.1560	151.0430	12.2900
MEDIAN	0.9112	23.9210	15.4211	265.6959	16.3002
SRAD	0.9173	25.7858	16.2745	172.9399	13.1507

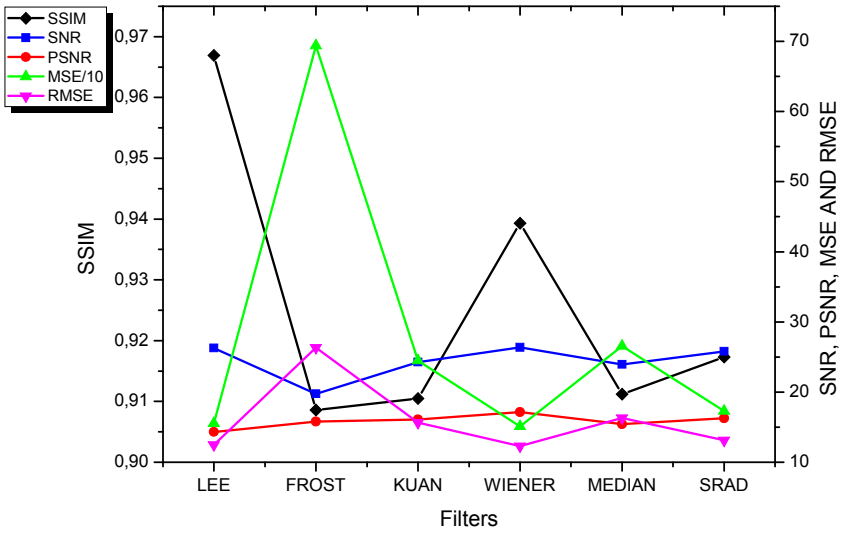

Fig.5 Graph for SAR image with standard deviation 0.03

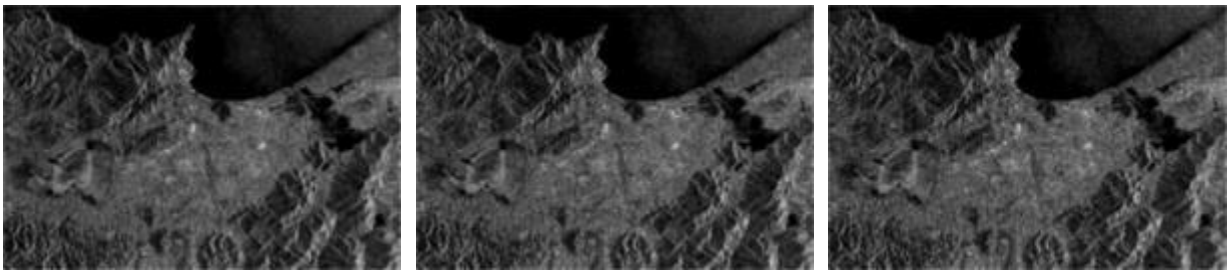

(a) (b) (c)

Fig. 6 Speckle noise reduction using Frost filter, (a) Denoised image for SD 0.01, (b) Denoised image for SD 0.02, (c) Denoised image for SD 0.03.

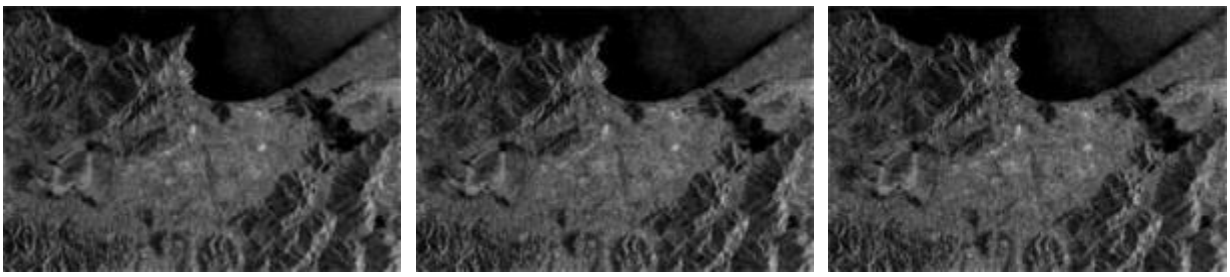

(a) (b) (c)

Fig. 7 Speckle noise reduction using Kuan filter, (a) Denoised image for SD 0.01, (b) Denoised image for SD 0.02, (c) Denoised image for SD 0.03.

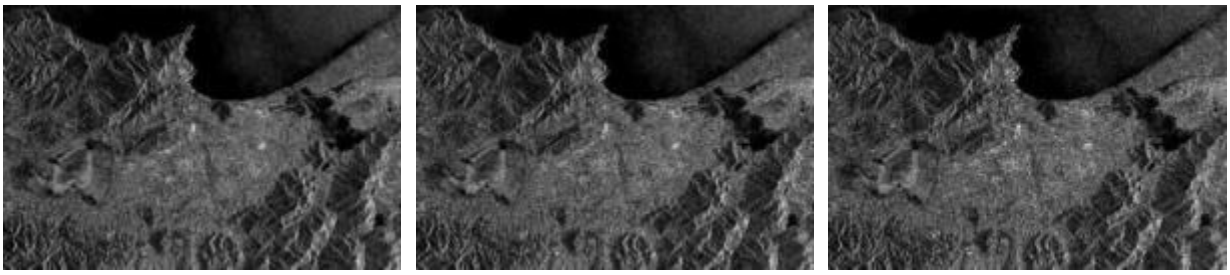

(a) (b) (c)

Fig. 8 Speckle noise reduction using Lee filter, (a) Denoised image for SD 0.01, (b) Denoised image for SD 0.02, (c) Denoised image for SD 0.03.

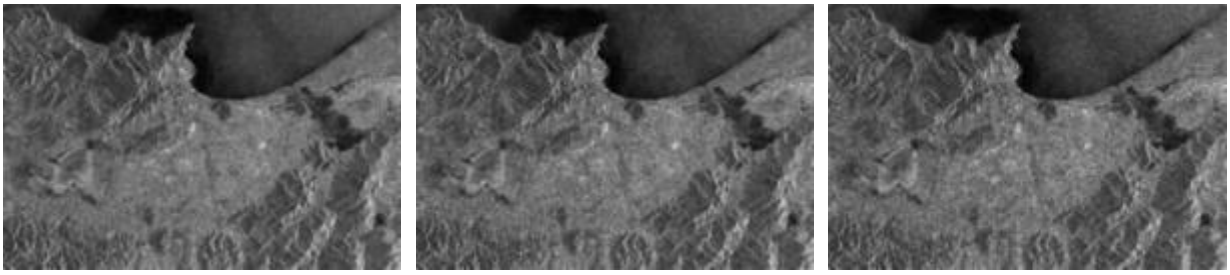

(a) (b) (c)

Fig. 9 Speckle noise reduction using Median filter, (a) Denoised image for SD 0.01, (b) Denoised image for SD 0.02, (c) Denoised image for SD 0.03.

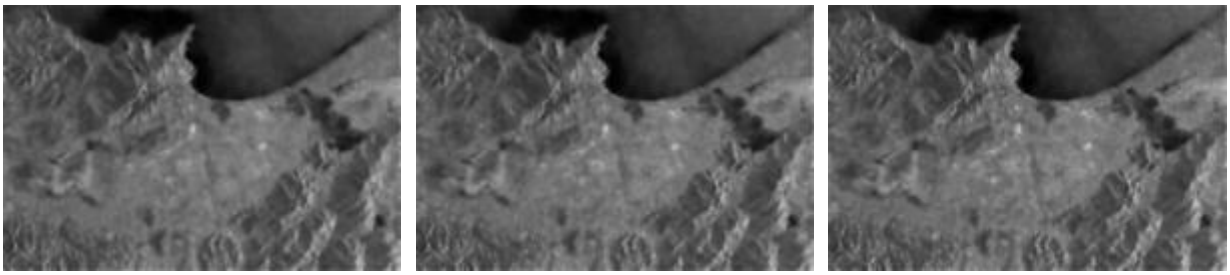

(a) (b) (c)

Fig. 10 Speckle noise reduction using SRAD filter, (a) Denoised image for SD 0.01, (b) Denoised image for SD 0.02, (c) Denoised image for SD 0.03.

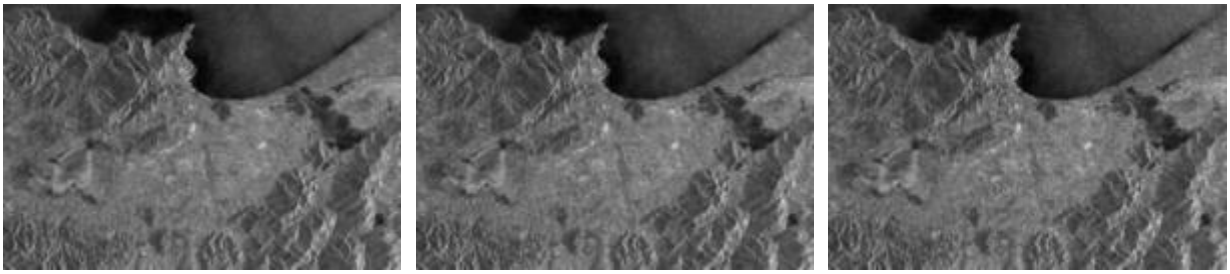

(a) (b) (c)

Fig. 11 Speckle noise reduction using Wiener filter, (a) Denoised image for SD 0.01, (b) Denoised image for SD 0.02, (c) Denoised image for SD 0.03.

By analyzing above results we can infer that Wiener and Lee give optimal result.

IX. CONCLUSION

The filter is used to reduce speckle noise and preserve image features like edges and so on. Hence we proposed an algorithm that takes the decision automatically, for SAR and satellite images, the

filter must be used, because this algorithm selects the best filter among the different filters used and which gives optimal results among the different results produced by different filtering techniques. We Studied six Different types of filters with different type of Standard Deviation of noise. Out of six filters used, Lee and Wiener Filter gives best results for SAR Images.

REFERENCES

[1] Yahya, N.; Karmel, N.S.; Malik, A.S. Subspace-Based Technique for Speckle Noise Reduction in SAR Images. *IEEE Trans. Geosci. Remote Sens*. 2014, 52, 6257–6271.
[2] Liu, F.; Wu, J.; Li, L.; Jiao, L.; Hao, H.; Zhang, X. A Hybrid Method of SAR Speckle Reduction Based on Geometric-Structural Block and Adaptive Neighborhood. *IEEE Trans. Geosci. Remote Sens*. 2018, 56, 730–747.
[3] Guo, F.; Zhang, G.; Zhang, Q.; Zhao, R.; Deng, M.; Xu, K. Speckle Suppression by Weighted Euclidean Distance Anisotropic Di_usion. *Remote Sens*. 2018, 10, 722.
[4] Yuan, Q.; Zhang, Q.; Li, J.; Shen, H.; Zhang, L. Hyperspectral image denoising employing a spatial-spectral deep residual convolutional neural network. *IEEE Trans. Geosci. Remote Sens*. 2018, 57, 1205–1218.
[5] Zhang, Q.; Yuan, Q.; Zeng, C.; Wei, X.; Wei, Y. Missing data reconstruction in remote sensing image with a unified spatial-temporal-spectral deep convolutional neural network. *IEEE Trans. Geosci. Remote Sens*. 2018, 56, 4274–4288.
[6] Yuan, Y.; Fang, J.; Lu, X.; Feng, Y. Remote sensing image scene classification using rearranged local features. *IEEE Trans. Geosci. Remote Sens*. 2018, 57, 1779–1792.
[7] Tu, B.; Zhang, X.; Kang, X.; Zhang, G.; Li, S. Density peak-based noisy label detection for hyperspectral image classification. *IEEE Trans. Geosci. Remote Sens*. 2019, 57, 1573–1584.
[8] Gemme, L.; Dellepiane, S.G. An automatic data-driven method for SAR image segmentation in sea surface analysis. *IEEE Trans. Geosci. Remote Sens*. 2018, 56, 2633–2646.
[9] Duan, Y.; Liu, F.; Jiao, L.; Tao, X.; Wu, J.; Shi, C.; Wimmers, M.O. Adaptive hierarchical multinomial latent model with hybrid kernel function for SAR image semantic segmentation. *IEEE Trans. Geosci. Remote Sens*. 2018, 56, 5997–6015.
[10] Wang, P.; Zhang, H.; Patel, V.M. SAR image despeckling using a convolutional neural network. *IEEE Signal Process. Lett*. 2018, 24, 1763–1767.
[11] Chierchia, G.; Cozzolino, D.; Poggi, G.; Verdoliva, L. SAR image despeckling through convolutional neural networks. *In Proceedings of the 2017 IEEE International Geoscience and Remote Sensing Symposium (IGARSS)*, Fort Worth, TX, USA, 23–28 July 2017; pp. 5438–5441.
[12] K. Bala Prakash, R.Venu Babu, B.VenuGopal,Image Independent Filter for Removal of Speckle Noise, *IJCSI International Journal of Computer Science*, Vol. 8, Issue 5, No 3, September 2011.
[13] Alenrex Maity, Anshuman Pattanaik, Santwana Sagnika, Santosh Pani, A Comparative Study on Approaches to Speckle Noise Reduction in Images, *International Conference on Computational Intelligence & Networks*, IEEE 2015.
[14] Noppadol Chumchob, Ke Chen, and Carlos Brito-Loeza, A New Variational Model for Removal of Combined Additive and Multiplicative Noise and a Fast Algorithm for Its Numerical Approximation , *International Journal of Computer Mathematics*, Vol. 90, No. 1, Jan 2013, 140-161.
[15] Bo Chen, Jin-Lin Cai, Wen-Sheng Chen, and Yan Li, A Multiplicative Noise Removal Approach Based on Partial Differential Equation Model , *Hindawi Publishing Corporation, Mathematical Problems in Engineering*, Volume 2012, Article ID 242043, 14 pages, doi:10.1155/2012/242043.
[16] Poorna Banerjee Dasgupta, Analytical Comparison of Noise Reduction Filters for Image Restoration Using SNR Estimation , *International Journal of Computer Trends and Technology (IJCTT)*, volume 17 number 3 – Nov 2014.
[17] Anindita Chatterjee, Dr. Chandhan Kolkata, Himadri Nath Moulick,Image Filtering Noise Removal with Speckle Noise, *International Journal of Advanced Research Foundation*, Volume 2, Issue 7, July 2015.
[18] Milindkumar V. Sarode, Dr. Prashant R. Deshmukh, Performance Evaluation of Noise Reduction Algorithm in Magnetic Resonance Images, *IJCSI International Journal of Computer Science*, Vol. 8, Issue 2, March 2011.
[19] Vicky Ambule, Minal Ghute, Kanchan Kamble, Shilpa Katre, Adaptive Median Filter for Image Enhancement, *International Journal of Engineering Science and Innovative Technology (IJESIT)*, Volume 2, Issue 1, January 2013.
[20] R. Sivakumar, Member IACSIT, M. K. Gayathri and D. Nedumaran, Speckle Filtering of Ultrasound B-Scan Images - A Comparative Study of Single Scale Spatial Adaptive Filters, Multiscale Filter and Diffusion Filters, *IACSIT International Journal of Engineering and Technology*, Vol.2, No.6, December 2010.
[21] KlogoGriffith S, GasonooAkpeko and Ampomah K. E. Isaac, On The Performance Of Filters For Reduction Of Speckle Noise In Sar Images Of The Coast Of The Gulf Of Guinea, *International Journal of Information Technology, Modeling and Computing (IJITMC)*, Vol.1, No.4, November 2013.
[22] Jyoti Jaybhay and Rajveer Shastri, A Study Of Speckle Noise Reduction Filters'', *Signal & Image Processing: An International Journal (SIPIJ)*, Vol.6, No.3, June 2015.
[23] A. Stella and Dr. Bhushan Trivedi, Implementation of Some Speckle Filters on Digital Image and OCT Image, *International Journal of Advanced Research in Computer Science and Software Engineering*, Volume 3, Issue 6, June 2013.
[24] Jappreet Kaur, Jasdeep Kaur and Manpreet Kaur, Survey of Despeckling Techniques for Medical Ultrasound Images, *Int. J. Comp. Tech. Appl*, Vol 2 (4), 1003-1007, IJCTA | JULY-AUGUST 2011.
[25] Suresh Velaga, Sridhar Kovvada, Efficient Techniques for Denoising of Highly Corrupted Impulse Noise Images, *International Journal of Soft Computing and Engineering (IJSCE)*, ISSN: 2231-2307, Volume-2, Issue-4, September 2012.
[26] R.Vijayarajan, S.Muttan, Cross Neighbourhood Kernel Filtering for Speckle Noise Removal in Ultrasound Images, *International Journal of Recent Technology and Engineering (IJRTE)*, ISSN: 2277-3878, Volume-1, Issue-2, June 2012.
[27] Akanksha Jain, Prateek Nahar, Performance Comparison of Two Image Denoising Algorithm at Different Noises'', *International Journal of Emerging Technology and Advanced Engineering*, Volume 3, Issue 12, December 2013.
[28] H. Kasban, O. Zahran, H. Arafa, M. El-Kordy and F. E. Abd El-Samie, S. M. S. Elaraby, Quantitative and Qualitative Evaluation for Gamma Radiographic Image Enhancement, *International Journal of Signal Processing, Image Processing and Pattern Recognition*, Vol. 5, No. 2, June, 2012.
[29] A.V. Meenakshi and V. Punitham, Performance of Speckle Noise Reduction Filters on Active Radar and SAR Images, *International Journal of Technology And Engineering System(IJTES)*, Jan –March 2011- Vol2.No1.
[30] Amira A. Mahmoud, S. EL Rabaie, T. E. Taha, O. Zahran, F. E. Abd El-Samie, Comparative Study of Different Denoising Filters for Speckle Noise Reduction in Ultrasonic B-Mode Images, *I.J. Image, Graphics and Signal Processing*, 2013, 2, 1-8.
[31] Arvinder Kaur & Prof. Sukhjeet Kaur Ranade, Review of Speckle Noise Reduction Techniques for Ultrasound Imaging, *Imperial Journal of Interdisciplinary Research (IJIR)*, Vol-2, Issue-9, 2016.
[32] Sandeep Kumar Agarwal and Prateek Kumar, Denoising of A Mixed Noise Color Image Through Special Filter, *International Journal of Signal Processing, Image Processing and Pattern Recognition*, Vol.9, No.1 (2016), pp. 159-176.
[33] Simarjeet Kaur, Rupinder Kaur, Balpreet Kaur, Image De-Noising Algorithms: A review, *International Journal of Computer Science & Engineering Technology (IJCSET)*, Vol. 7 No. 07 Jul 2016.

[34] Ardhi Wicaksono Santoso, Luhur Bayuaji, Lim Tien Sze, Habibah Lateh, Jasni Mohamad Zain, Comparison of Various Speckle Noise Reduction Filters on Synthetic Aperture Radar Image, *International Journal of Applied Engineering Research*, ISSN 0973-4562, Volume 11, Number 15 (2016) pp 8760-8767.

SDR based Design of a system for meteorological image acquisition through NOAA satellite

Ahmed BELHANI
Electronics department
Constantine university 1
Constantine, Algeria
ahmed.belhani@umc.edu.dz

Soumeya BOUMADJEN
Electronics department *
Constantine university 1
Constantine, Algeria
soumeya.boumadjen@student.umc.edu.dz

Imene DJEBLI
Electronics department
Constantine university 1
Constantine, Algeria
imen.djebli@student.umc.edu.dz

Abstract--- Software Defined Radio is a logical evolution, and convergence of digital radios and software technologies. It offers practical, effective, and inexpensive solutions. In this paper, we present SDR based design of a system for meteorological image acquisition through NOAA satellite. These satellites are equipped with a radiometer, which scans the earth in five channels; its scanner is able to map the clouds and vegetation, to measure the temperature and the humidity in the atmosphere and on the earth.

The idea behind this study is to create a database of meteorological parameters to serve all Algerian researchers

Keywords---. Software defined radio, SDR, RTL-SDR dongle, NOAA, Wxtoimg, SDRSharp, gr-gsm

I. INTRODUCTION

The concept of software-defined radio was emerged in the American defense sector, resulting from military research on multi-mode radios operating in VHF and UHF bands (US Air Force's ICNIA program), In 1979 [1].

In 1984, E-SYSTEMS, which called now ''Raytheon'', coined the term "radio software" in a corporate bulletin. It referred to a prototype digital base band receiver equipped with a set of processors that performed adaptive filtering for interference cancellation and demodulation of wideband signals [2].

After that, an RFI (Request For Information) on software defined radio for mobile telephony marked the starting point of increased activity in the field. In 1996, the MMITS (Modular Multifunctional Information Transfer System) Forum was launched, renamed in 1998 as the Software Defined Radio Forum, then as the Wireless Innovation Forum in 2009. Its objective is to promote and develop software radio technology, the deployment and use of open architectures for advanced wireless systems, also to stimulate and guide innovation and standards [3].

Software-defined radio has revolutionized the communications industry by providing a high level of flexibility. Despite the military origins of the SDR, today the radio equipment industries are investigating this trail, and changing their hardware architectures. The SDR became popular and applicable in various fields such as defense, mobile telecommunications, limited production devices and cognitive radio, broadcast radio, etc..

Due to its adaptability and flexibility, the software-defined radio mainly used in wars, such Americans JTRS program [4]. It considered a major element in the tactics of centered network conflict; it allows remote exchange at the battlefields, with the possibility of transmission in the HF to UHF bands, with a high rate using specific WNW waveforms (Wideband Networking Waveform). In the field of electronic warfare, this technology offers strategic support due to SCA (Software Communications Architecture) standards. During an attack, the Electronic Counter Measure (ECM) device receives, then transmits radio-electric transmissions to intercept and / or scramble the interchanged information in the environment, while taking into account the unforeseen improvement of military equipment, in order to protect his camp. This technology also allows the detection of the enemy by radar while controlling the electromagnetic spectrum by exploiting and / or preventing communication as well as the management of material equipment [5].

Software radio technology remains a choice for more innovation in the broadcasting field, known for its standard character. It also presents an alternative economic for telecommunication operators. Some companies use this technology because of its standards that define the interfaces of radio control equipment (RCE), based on digital links. This choice is justified by the possibility of putting the RCE on the top floor as well as in the basement [5].

According to Mitola, software radio is incorporated with model-based reasoning in this type of radio. This approach, called "cognitive radio" [3] improves and diversifies software radio and its functionalities, following a state of consciousness and using the information received by sensors, with a possibility of reconfiguration.

Moreover, SDR is used in the NASA Space Telecommunications Radio System (STRS), demonstrating

a partnership with the OMG and the SWG (Space Working Group) to create an independent platform model based on API (Application Programming Interface) to support special space equipment as well as certain functions [5].

In this paper we present the SRD utilization in meteorological image acquisition through the NOAA satellite. Every day, NOAA satellites send APT data to land with frequencies around 137 MHz. This data could be acquired by a system based on software-defined radio, using a PC and "RTL-SDR" attached to a suitable antenna for reception, and equipped with two software “SDRSharp” to record the APT signal, and “WXtoImg” to decode the signal into a metrological image

The paper is organized as follows. In section 2 we present The SDR concept and its development tools used in this work while, section 3 illustrates proposed architecture, where we detailed the antenna design and we describe the RTL-SDR dongle. Finally, a conclusion is presented in section 4.

II. AUTOMATIC PICTURE TRANSMISSION (APT)

Observation satellites are equipped with a scanning radiometer, a system comprising several sensors, lenses and mirrors controlled by motors. The radiometer scans the surface of the earth line by line and as it moves 120 lines are transmitted every minute forming a complete image. In figure, we observe from left to right: a synchronization band, a time marker, the image itself and a telemetry band. This succession is repeated twice, on the left the visible image and on the right the infrared image. Each time an image frame is received, the synchronization appears as lines vertical blacks to the left of the image while the telemetry data is presented as "corners" carrying calibration and other information. The markers are an alternation of black and white horizontal traces for the visible channel, white and black for the infrared channel, the synchronization is an alternation of vertical bands and the telemetry is an alternation of grayscale bands serving as a reference to decode the 'image [6]

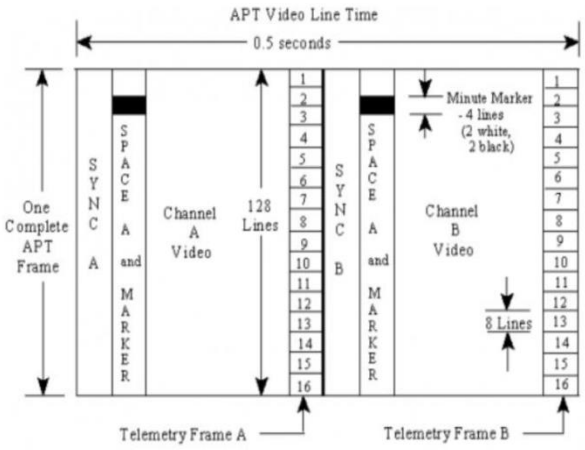

Fig. 1. APT format

III. SDR

A. Review

Generally, traditional radios consist of an integrated circuit transceiver developed using dedicated equipment. The main components used are mixers, amplifiers, filters, modulators/demodulators and converters [7]. In parallel with this approach, an innovative concept has appeared "Software Defined Radio" (SDR) which represents a radio communication system structurally different from traditional radios; it implements most of its features by software instead of a hardware implementation. The SDR Forum quotes: “The SDR is a radio in which some or all of the functions of the physical layer are defined by software” [8]. SDR consists of two subsystems: a hardware subsystem and a software subsystem. Its components include Digital Signal Processors (DSP), Field Programmable Gate Array (FPGA) and General Purpose Processors (GPP). Figure 2 illustrates Hardware /software division in software-defined radio.

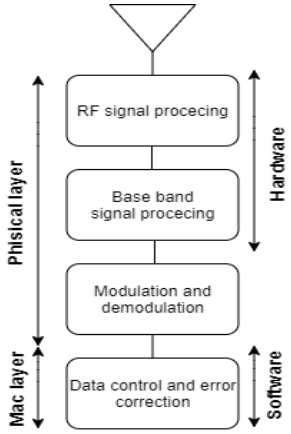

Fig. 2. Software/Hardware division in SDR [7]

B. Development tools

1) SDRSharp (SDR#) software

Currently, SDRSharp is the most popular SDR software, used with the RTL-SDR key (dongle). It is free, easy to set up and easy to use in radio reception to listen and view received signals.

The figure 3 illustrates its interface, which consists of four main windows:

1. Define demodulation mode and its parameters.
2. Adjust the desired frequency and volume.
3. View the spectrum in real time.
4. View the waterfall.

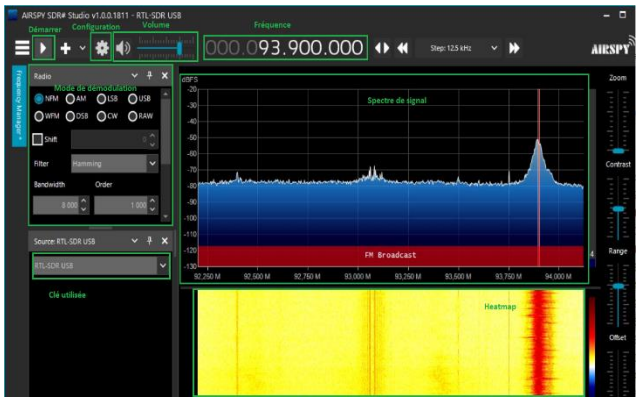

Fig. 3. Screen shoot of SDRSharp interface

2) Matlab/Simulink

Matlab/Simulink defines a hardware support package for RTL-SDR, with a library that contains different blocks compatible with the RTL-SDR dongle. The user is able to scan, and view in real time the signal's spectrum captured by the dongle and implement any type of digital signal processing under Matlab/Simulink.

The block of RTL-SDR Receiver shown in the figure 4 sets a direct communication with any RTL-SDR connected to the computer; it has many parameters such as frequency center, sample rate f, and tuner gain to adjust. In addition, a frequency correction value (ppm) can be sated to compensate for any hardware tolerance issues associated with the R820T

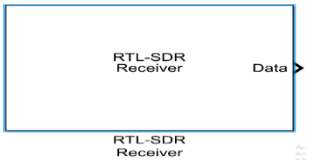

Fig. 4. RTL-SRD Receiver bloc

The figure 5 illustrates a GSM receiver designed on Matlab/Simulink using a RTL-SDR dongle. It is able to receive:

- FM radio with frequencies ranging from 88 MHz to 108 MHz.
- GSM for frequencies ranging from 800 MHz to 1000 MHz.

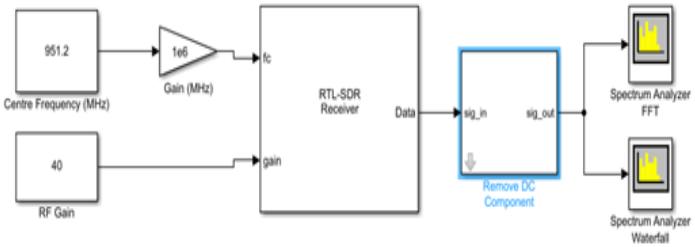

Fig. 5. GSM Receiver based on SDR

After running the simulation, the RTL-SDR's block receiver establishes a connection with the RTL2838U dongle, while setting the center frequency to 951.2 MHz and the RF gain to 40 dB.

The received signal is formed of 8 bits encrypted and encoded data stream, these samples are transmitted to the block "Remove DC Component" whose role is to find the average value of a data frame and remove the DC peak presented in the spectrum.

Then the signals pass through the two spectrum analyzer blocks. The first one configured to display a Fast Fourier Transform (FFT) of the received signal, which has a bandwidth of a sample rate of 2.4 MHz, defined by the RTL-SDR dongle. The spectrum analyzer (waterfall) configured to display the spectrogram using a short time Fourier transform.

The figures below illustrate some downlink GSM channels, captured at the 951.2 MHz frequency, as well as their waterfall.

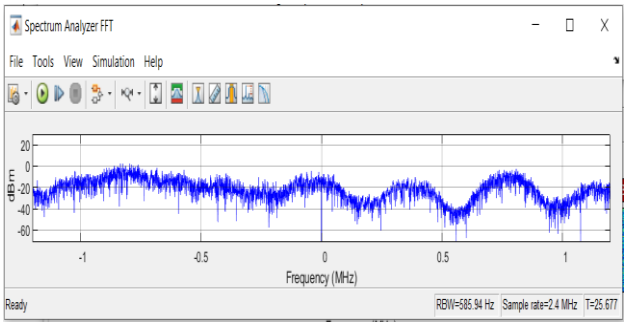

Fig. 6. Spectrum analyzer FFT for 951.2 MHz

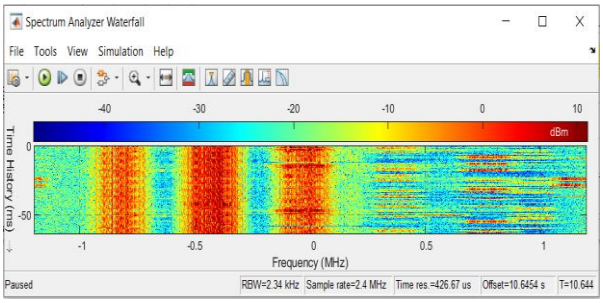

Fig. 7. Spectrum analyzer Waterfall for 951.2 MHz

3) gr-gsm

Matlab / Simulink only allowed us to visualize the GSM frequency spectrum, however with gr-gsm we can do flow capture, visualization, decoding, as well as data extraction.

To do this application, we used gr-gsm, which is a free project developed by Piotr Krysik, it is only available on Linux. Gr-gsm provides tools for receiving, decoding and decrypting GSM flow. It consists of the following five programs:

1. grgsm_scanner: used to scan the GSM band and display the surrounding BTS information.
2. grgsm_livemon: a graphical tool to monitor transmitted data on a given frequency in real time.
3. grgsm_channelize.py: useful when voice communication uses frequency hopping. It separates a broadband capture into several files, where each one contains an ARFCN (Absolute Radio-Frequency Channel Number).
4. grgsm_capture.py: requires only two arguments: frequency or ARFCN and an output file.
5. grgsm_decode: requires only two arguments: frequency or ARFCN and a capture file.

Figure 8 illustrates the diagram of the acquisition cycle and the steps of the GSM network investigation.

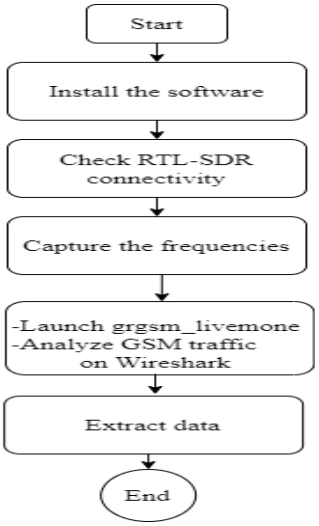

Fig. 8. GSM flow investigation flowchart

After installing the software and checking the connectivity between the dongle and the laptop, we start the scan in order to catch the frequencies used by the surrounding BTS (Base Transceiver Station) in real time. Figure 9 illustrates them, where each one is defined by channel number and power.

After that, we run grgsm_livemon in order to monitor transmitted data on a given frequency in real time. We have chosen the same frequency (951.2 MHz) used before on Matlab/Simulink to see the deferent.

The downlink transmitted data are presented by encrypted packets; their spectrogram is shown in the figure bellow.

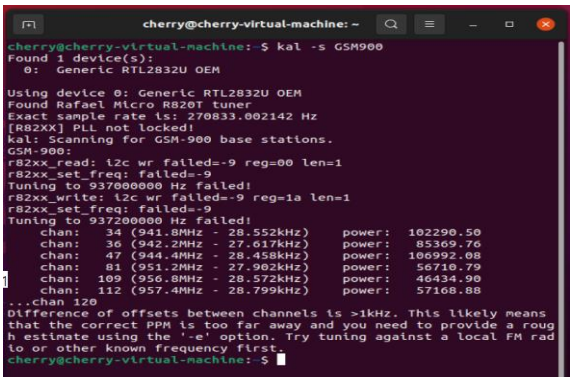

Fig. 9. Screenshot of surrounding frequencies

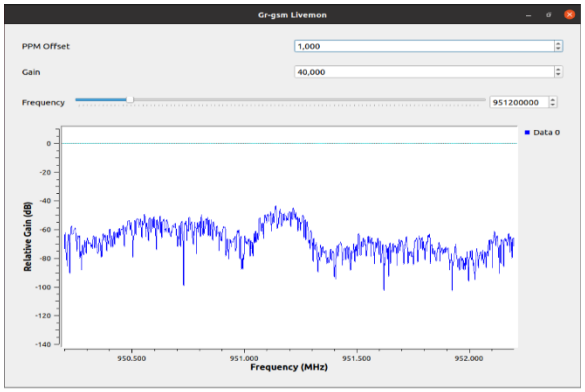

Fig. 10. Spectrum centered at 951.2 MHz

Finally, we launch Wireshark in order to extract cellular data, while grgsm_livemon sends data in the GSMTAP format over the UDP port, Wireshark runs automatically with a filter of GSMTAP packets. As a result, we could take out, slot number 0 , mobile country code (MCC) which equal 603, mobile network code (MNC) that identify the network of mobile operators represented by: 01,02,03 (Mobilis, Djezzy, Ooredoo), and absolute Radio-Frequency Channel Number (ARFCN) equal 47.

IV. PORPOSED ARCHITECTURE

A. *NOAA satellite*

The National Oceanic and Atmospheric Administration (NOAA) satellites are American meteorological satellites in polar orbit at an altitude of around 850 km, they transmit images continuously about 540 miles above the earth. The first NOAA satellite launched in 1970, and currently the NOAA 15, NOAA 18, NOAA 19 and NOAA 20 satellites are in service.

The satellites are equipped of a radiometer for monitoring cloud masses, to measure sea or continental surface temperatures, an infrared sounder providing atmospheric temperature and humidity profiles and a diffuso-meter for determining wind direction and speed over marine surfaces [8]. AVHRR (Advanced Very High

Resolution Radiometer) sweeps through six channels, distributed between the visible and the infrared, with a wavelength between 0.58 and 12.50 micrometers, with an instantaneous footprint of 1.1 km at the sub-satellite point. The scanner on this radiometer used to map vegetation and cloud formations and to measure temperature and humidity in the atmosphere and on earth [9].

The ATP signals of the NOAA satellites are in a sound format, we opted for the WXtoImg, which is a fully automated decoder for the APT weather satellite. The software supports recording, real-time decoding of satellite image data, map overlays, advanced color enhancements, image editing and visualization for many weather satellite receivers, communication receivers and scanners.

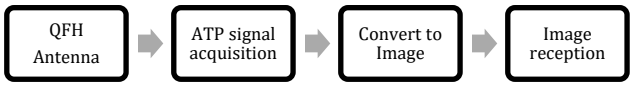

Fig. 11. WXtoImg operating principle

The reception of NOAA images is done through the two software. SDR-Sharp to receive the APT signal from NOAA satellites and transmit it to WXtoImg to decode it and then convert it into weather images

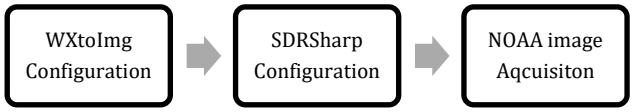

Fig. 12. Steps of NOAA image acquisition

Once the satellite positioned in our orbit, the decoding of the image begins automatically and the image will appear gradually. The decoding operation and the enhancement of its quality last about 15mn.

B. Antenna design

Quadrifilar Helicoidal antenna (QFH), is a good one for satellite waves reception, it is composed of two vertical loops arranged in a helix of 1/2 turn, and spaced around the perimeter of a common cylinder. These loops promote a right circular polarization (RHC) allowing to generate a current with a phase shift of 90 degrees. it uses different sizes of loops that make the current inductive in one and capacitive in the other with a general reactive nature [10].

We have chosen a model of a helical four-wire antenna, taking into consideration these parameters for its realization:

L: length of helical components of a half loop

$L_{ax:}$ Length of the cylinder axis.

R: radius of cylinder.

These dimensions depend of the value of λ and the frequency ≈ 137 MHz. In the table below, we mentioned the dimensions of the two loops and legs of QFH antenna as a function of λ [27].

TABLE I. DIMENSION OF QFH FOR 137 MHZ

Dimensions	Big loop	Small loop
Height	0.26λ	0.238λ
Diameter	0.173λ	0.156λ
Leg size	0.56λ	0.508λ

To design it we have used 2 meters 50 mm PVC pipe, 5 meter long 8mm copper tubing, 5 meters of 50 Ω coaxial cable and a junction box with four inputs.

.

Fig. 13. QFH antenna

C. RTL-SDR

RTL-SDR is an inexpensive software defined radio USB dongle that is able of receiving signals with good acquisition accuracy. This device used as a DVB-T (Digital Video Broadcast-Terrestrial) USB receiver based on the Realtek RTL2832U chip (demodulator chip) which is responsible of digital signal processing. The dongle is able to scan and receive a wide frequency spectrum ranging from 25 MHz to 1.75 GHz, Where the maximum sampling frequency is theoretically is 3.2 MHz.

V. RESULTS AND DISCUSSION

The received images are presented below; they are automatically enhanced by the WxtoImg software, depending on the quality of the ATP signal recorded. The images are composed of a color palette, whose vegetation appears greenish and the sea is colored blue, the ground in brown and the cloud masses in grey, however in figure 14 sea appears grey due to low reflectance in visible channels.

The quality can be improved by choosing an adequate emplacement for acquisition and also through a sophistical SRD USB dongle,

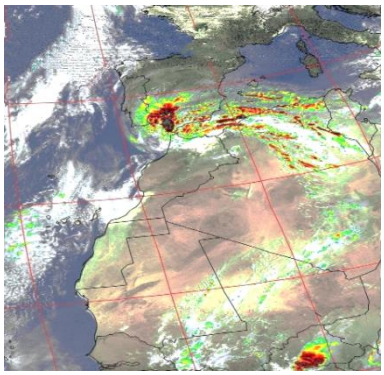

Fig. 14. Image NOAA 18 (28/06/21)

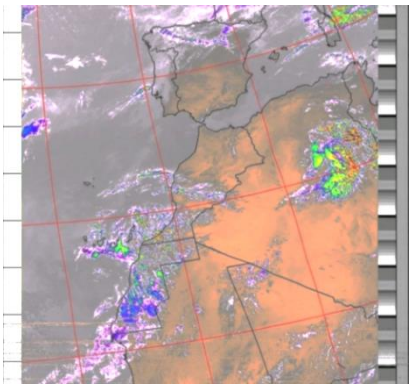

Fig. 15. Image NOAA 15 (28/06/21)

VI. CONCLUSION

In this work we have presented an architecture design of metrological images through NOAA satellite and using RTL-SDR dongle. The results show the reliability of system. However, the design can be improved and extended to an extraction of a metrological database through development of Python program

REFERENCES

[1] W. H. W. Tuttlebee, Éd., *Software defined radio: origins, drivers, and international perspectives*. West Sussex, England ; New York: John Wiley, 2002.

[2] P. Brisson et P. Kropf, « Global System for Mobile Communication (GSM) », p. 23.

[3] R. Lavoie, « A short history of software-defined radio (SDR) technology | Nutaq | Nutaq Technologies », oct. 10, 2013. https://nutaq.com/blog/short-history-software-defined-radio-sdr-technology, (consulted on June 24, 2021)

[4] M. S. Jean-Christophe, M. M. François, et M. P. Guy, « L'approche radio logicielle dans les systèmes de Nœud de Communication Aéroporté », p. 12.

[5] M. Nicolas, « Radio logicielle: analyse d'architectures matérielles et outils informatiques », p. 246.

[6] « Les satellites NOAA ». https://www.svom.eu/portfolio/les-satellites-noaa/, (consulted on June 24, 2021)

[7] D. Valerio, « Open Source Software-Defined Radio: A survey on GNUradio and its applications », p. 26.

[8] M. Fähnle, « Software-Defined Radio with GNU Radio and USRP/2 Hardware Frontend: Setup and FM/GSM Applications », p. 92.

[9] L. Thomas, « Réception et décodage d'images issues de satellites météorologiques en orbite polaire », p. 18, déc. 2020.

[10] « ESA - Eduspace FR - Accueil - NOAA - printer version », janv. 20, 2011. https://www.esa.int/SPECIALS/Eduspace_FR/SEMMX4S7NWF_2.html , (consulted on June 24, 2021)

[11] S. Mahmood, M. T. Mushtaq, et G. Jaffer, « Cost efficient design approach for receiving the NOAA weather satellites data », in 2016 IEEE Aerospace Conference, Big Sky, MT, USA, mars 2016, p. 1-6. doi: 10.1109/AERO.2016.7500854.

Energy efficiency comparison of IICM and Clipping using real power amplifier

Hocine Merah*, Belkacem Mecheri*, and Khaled Tahkoubit †
*Laboratoire Des Semi-conducteurs Et Matériaux Fonctionnels, Department of Electronics, Faculty of Technology
University of Amar Telidji, Laghouat, Algeria
Email: merah.hossein2@gmail.com, mecheribk@yahoo.fr
† LACOSI, USTO-MB University, 31000, Oran, Algeria.
Email: khaled.tahkoubit@univ-usto.dz

***Abstract*—Peak-to-Average Power Ratio (PAPR) is an important parameter in digital communications. Furthermore, 5G Communication Systems will be based on the new multicarrier modulation schemes. Hence, it is desirable to investigate the problems of PAPR in 5th generation communication systems. In this paper, first a detailed introduction of multicarrier modulation and PAPR problem are given. Than we compared two PAPR reduction methods : Iterative Invertible Clipping Method (IICM) and clipping with filtering method in terms of Error Vector Magnitude (EVM) for the same PAPR value. The simulation results shows that there is a gain of 1dB between the two methods.**

***Index Terms*—IICM, PAPR, 5G, PA, EVM.**

I. Introduction

Nowadays, wireless communication systems are more and more present in our daily life and they tend to replace the excessive use of cables. Although high-speed ADSL-type connections are increasing in number around the world, they do not provide the flexibility of use that a wireless radio network provides. To improve the quality of service they offer, researchers are preparing the arrival of the future generation called 5th Generation (5G) [1].

Orthogonal Frequency Division Multiplexing (OFDM) present in several telecommunication standards are today the modulation technique making it possible to best meet these requirements. digital modulators and demodulators associated with OFDM and MC-CDMA modulation have an acceptable digital complexity (logarithmic) for applications with low computing resources. The signals with multi-carrier modulations have a non-constant envelope, which creates a major difficulty when amplifying the power of multi-carrier systems.

To overcome this constraint, a parameter called the Crest Factor (CF) [2] is defined which makes it possible to identify and quantify this characteristic of multi-carrier signals. The crest factor is closely related to another entity commonly known in the literature, under the name of PAPR [2] and which establishes the relationship between the maximum power (maximum amplitude) and the average power of the signal.

The power amplifier (HPA) [3] is the means of giving the necessary power allowing the transmission of the signal towards the receiver without it being attenuated. It is therefore a key element in a communication chain insofar as it has a preponderant influence on the overall balance of the transmission chain in terms of energy consumption and in terms of the quality of the transmitted signal, the Bit Error Rate (BER) is evaluated according to the Signal to Noise Ratio (SNR). In fact, the power amplifier alone represents approximately two thirds of the energy consumption of a transmission chain on the transmitter side. It is therefore important to operate the amplifier with the greatest possible energy efficiency, especially for systems with low energy resources such as mobile terminals generally having low energy autonomy.

Among the techniques for reducing PAPR in OFDM system, we have retained the invertible clipping method with filtering, as already proposed by Ragusa [4]; this proposal aims to improve the classical technique [5] of PAPR reduction by introducing a clipping function with a smoother saturation. At the reception level, the application of the inverse of the clipping function is considered as a possible plausible solution to improve the performance of the BER. In fact, the inverse function compensates for some of the distortions (IESNL for Non-Linear Interference Between Symbols) introduced by clipping.

The proposed method adopted in this paper is called the Iterative Invertible Clipping Method (IICM) [6]. It uses a third degree polynomial to deliver the invertible clipping function, where the inverse function is obtained exactly by adopting the radical solution of the 3rd degree equation, hence better BER performance. In addition, the IICM method can reach higher degrees than Ragusa, using the iterative process. We will compare the IICM method clipping method with filtering in terms of EVM, for the same PAPR valus.

The remaining of this paper is organized as follows: In Section II, a brief presentation of both conventional clipping and IICM methods will be given. In Section III, we present the system model used for the comparison of the two techniques. Simulation results comparing the two approaches are shown in Section IV. Finally, the conclusion of this work is given in Section V.

II. System model

A. Waveform description

OFDM is an orthogonal multicarrier system based on a rectangular shaping filter and the Inverse Fast Fourier Transform

(IFFT). The n^{th} sample of the l^{th} OFDM symbol can be written as:

$$x(n) = \frac{1}{\sqrt{N}} \sum_{k=0}^{N-1} d_{k,l} e^{\frac{j2\pi kn}{N}}, \; n = 0, 1, \ldots, N-1, \qquad (1)$$

where $\boldsymbol{d}_m = \left[d_{0,l}, d_{1,l}, \ldots, d_{N-1,l}\right]$ is the emitted vector of complex M-QAM symbols, l is the index of the OFDM symbol, k is the index of the subcarrier, and N is the total number of subcarriers.

B. PA model

In this paper, a realistic PA model is used. The PA is a 2.6 GHz class-AB amplifier based on GaN transistor with a power gain of $19dB$, maximum output power of $56W$ and a power added efficiency (PAE) of 70% [7]. The AM/AM and PAE characteristics are shown in Fig.1

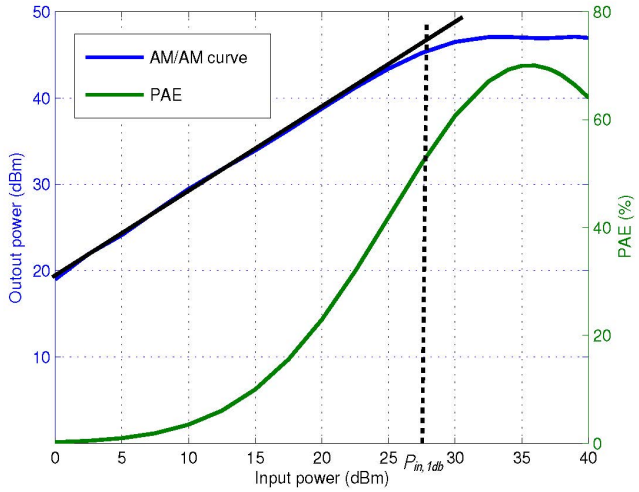

Fig. 1: Output power, PAE vs. input power of GaN PA [10].

III. Iterative Invertible Clipping Method and clipping techniques presentation

A. Clipping technique

Intuitively, this method is very simple to understand, because it consists of clipping the signal amplitude to a predetermined threshold to reduce the maximum amplitude of the signal at this threshold. This process therefore has the effect of reducing the power variation of the signal and consequently of reducing the sensitivity of the signal to non-linearities. The resulting signal, if it remains compatible, is degraded and will not have the nominal performance at reception. Moreover, since saturation is itself, in principle, a non-linear element, all the defects intrinsic to this type of element will be found here [9]. Numerous clipping methods have been developed, as shown by the works in [10], [11]. This technique was proposed at the beginning of the implementation of terrestrial OFDM (DVB-T), in the years 1997 [11]. Thus, a signal x will be clipped according to the following law:

$$f(x) = \begin{cases} x & |x| \leq A \\ Ae^{j\varphi(x)} & |x| > A \end{cases} \qquad (2)$$

where $y = f(x)$ is the resulting signal, A is the limiting amplitude or clipping threshold and $\varphi(x)$ is the phase of the signal x. This technique, like all distortion techniques, generates the three classic problems of a nonlinearity:

1) Side lobe rise from intermodulation products.
2) Generation of interference between non-linear symbols (provided that convolutional filtering is present).
3) Generation of noise in the useful band: noise with a particular structure because it corresponds to the different intermodulation products that fall into the useful band.

Point (1) can easily be treated by a frequency selective filter located just after the clipping. This filter has been proposed in [101], so we can say that it is part of the technique. This filter is necessary to decrease the ACPR, which measures the rise of the side lobes. For current OFDM standards, this filter does not really add complexity because it is defined in the standard to limit the channel band.

D.Guel in his PhD thesis [9] proposed a frequency filtering method based on digital filtering (FFT/IFFT) to deal with point (3). The articles of L.J Cumin [11] can be considered as the reference on this method. They analyze the effects of the 3 previous points on the power spectral density and on the BER. Of course, the latter is degraded by several dB because of the clipping noise in the band. In [12], K.R. Panta and J. Armstrong show that this problem is less important when the signal passes through a frequency selective channel. They show, in fact, that the error rate is mostly due to subcarriers that are highly affected by the channel, and in this case the contribution of the clipping noise on the BER is very small. Another analysis of this problem shows that the degradation in signal-to-noise ratio can be effectively mitigated by using a high performance code such as the combination of turbo code (TC) and low density parity check (LDPC) code [13].

B. Description of reversible clipping

The invertible clipping technique was recently proposed by S. Ragusa [4]. The main idea of this technique is to mask an unknown non-linearity by a known and more important non-linearity which is invertible on reception as shown in figure 2. It takes its origin in the studies of nonlinear automatics. It should be noted that the clipping is downward compatible if the inversion function is not performed on reception. Otherwise it results in a degradation of performance that must be taken into account.

1) Transmitter: As mentioned earlier, the invertible clipping function is performed separately on the components $I_{(b)}(n)$ and $Q_{(b)}(n)$ of the complex MC-CDMA signal $z_{(b)}(n)$, at the transmitter, using the following equations:

$$I_{(b)}^{clp}(n) = -\frac{1}{2R_I^2}\left(\left[I_{(b)}(n)\right]^3 - 3R_I^2\left[I_{(b)}(n)\right]\right) \qquad (3)$$

$$Q_{(b)}^{clp}(n) = -\frac{1}{2R_Q^2}\left(\left[Q_{(b)}(n)\right]^3 - 3R_Q^2\left[Q_{(b)}(n)\right]\right) \qquad (4)$$

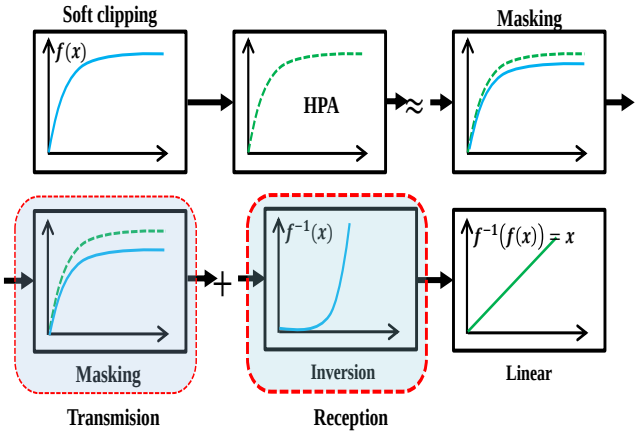

Fig. 2: Invertible clipping (masking of the power amplifier).

The clipped signal $z_{(b)}^{clp}(n)$ regenerated by two components (I/Q) for the bth symbol is given by the following relation:

$$z_{(b)}^{clp}(n) = I_{(b)}^{clp}(n) + jQ_{(b)}^{clp}(n) \tag{5}$$

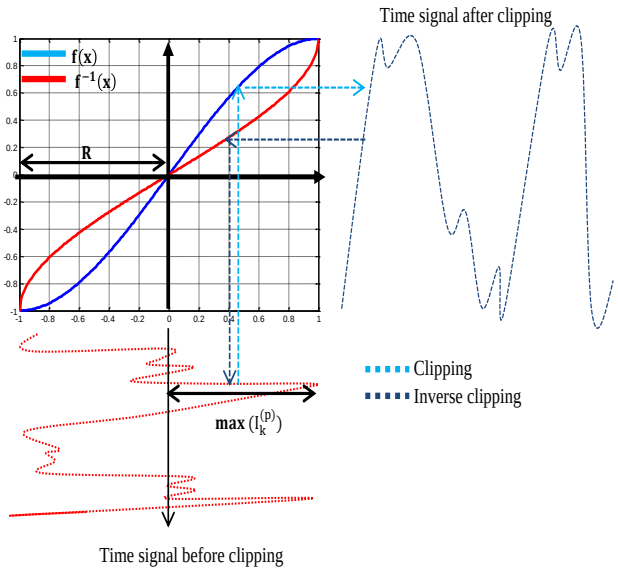

Fig. 3: Principle of the invertible iterative clipping method (example 3 iterations).

This method is repeated N_{iter} iterations; where: $z_{(b)}(n)$ and $z_{(b)}^{clp}(n)$ are replaced by $z_{(b)}^{j}(n)$ and $z_{(b)}^{j+1}(n)$, the initial signal is considered as $z_{(b)}^{0}(n) = z_{(b)}(n)$ to be able to execute the iterative process, for this purpose we named it the Iterative Invertible Clipping Method (IICM). Moreover, this method can reach higher degrees than S.Ragusa, as an example, we can reach an optimized sixth degree polynomial using only two iterations, while three iterations provide a ninth degree polynomial and so on. Figure 3 represents the principle of the Iterative Invertible Clipping Method (IICM).

2) FFT/IFFT-based digital filtering: Let $\widetilde{z}_{(b)}^{clp}(n)$ be the signal at the output of the FFT/IFFT, as shown in Figure 4, the filtering consists of an FFT operation followed by an IFFT operation. The FFT transforms the time samples $z_{(b)}^{ecr}(n)$ into frequency components $Z_{(b)}^{ecr}(k)$ of which those positioned on the out-of-band (OOB) carriers are set to zero, i.e. :

$$\widetilde{Z}_{(b)}^{clp}(k) = \begin{cases} Z_{(b)}^{clp}(k), & k \in \left[1; \frac{N}{2}\right] \cup \left[N\left(L-\frac{1}{2}\right); NL\right] \\ 0, & k \in \left[\frac{N}{2}+1; N\left(L-\frac{1}{2}\right)-1\right] \end{cases} \tag{6}$$

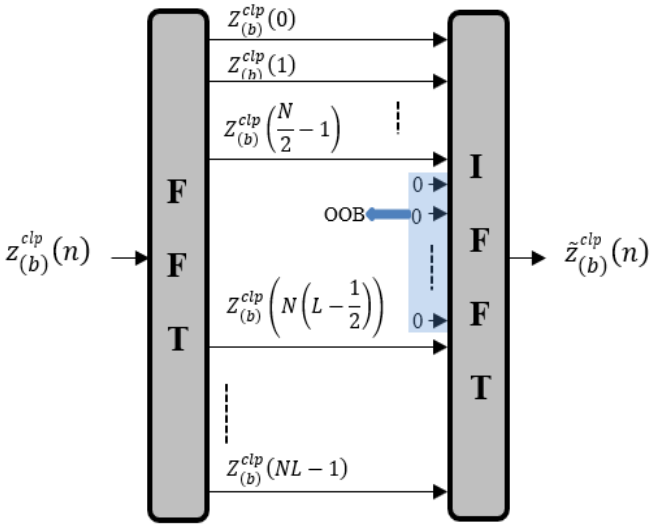

Fig. 4: Principle of the invertible iterative clipping method (example 3 iterations).

The frequency components $\widetilde{Z}_{(b)}^{clp}(k)$ are then transformed to the time domain by the IFFT. The $\widetilde{Z}_{(b)}^{clp}(k)$, however, must meet the specifications of the transmit mask. The resulting filter is time-dependent, and rejects discrete out-of-band frequency components. This means that it does not cause any distortion in the MC-CDMA signal band. Since the filter works symbol by symbol, it cannot cause any interference between symbols.

C. Iterative Invertible Clipping Method technique

This method was proposed in [6] known as IICM which uses a polynomial of degree 3 to derive the invertible clipping function, in improvement of that of Ragusa which uses a polynomial of degree 5. In addition, the Ragusa method uses an approximation in the inverse function, which can lead to degradation of the performance of the transmission system, unlike the proposed IICM method, the inverse function is used exactly.

The algorithm performing the IICM approach is summarized below.

It should be mentioned that the proposed algorithm is executed for MC-CDMA symbols.

In order to be able to easily follow the different steps of this algorithm, the digital filter FFT/IFFT has been designated by the function Ω.

Algorithm 1 Invertible iterative clipping (IICM).

1: Initialization : $b = 1$, $m = 1$
2: $R_I = max\,|I_b(n)|_{n=0,\ldots,NL-1'}$
3: $R_Q = max\,|Q_b(n)|_{n=0,\ldots,NL-1'}$
4: $I^{cl}_{(b)}(n) = -\frac{1}{2R_I^2}\left(\left[I_{(b)}(n)\right]^3 - 3R_I^2\left[I_{(b)}(n)\right]\right)$
5: $Q^{cl}_{(b)}(n) = -\frac{1}{2R_Q^2}\left(\left[Q_{(b)}(n)\right]^3 - 3R_Q^2\left[Q_{(b)}(n)\right]\right)$
6: $z^{cl}_{(b)}(n) = I^{cl}_{(b)}(n) + jQ^{cl}_{(b)}(n)$
7: $\tilde{z}^{cl}_{(b)}(n) = \Omega\left[z^{cl}_{(b)}(n)\right]$
8: $\tilde{z}^{cl}_{(b)}(n) = \tilde{I}^{cl}_{(b)}(n) + j\tilde{Q}^{cl}_{(b)}(n)$
9: $I_{(b)}(n) = \tilde{I}^{cl}_{(b)}(n)$ and $Q_{(b)}(n) = \tilde{Q}^{cl}_{(b)}(n)$
10: $m = m + 1$
11: **if** $m \leq N_{iter}$ **then**
12: go to 3
13: **else**
14: $z_{(b)}(n) = I_{(b)}(n) + jQ_{(b)}(n)$, $m = 1$
15: **end if**
16: $b = b + 1$
17: **if** $b \leq N_{sym}$ **then**
18: go to 1
19: **end if**
20: end

D. Improve EVM performance

Let the signal at the transmitter level be Y, with :

$$Y = [y_0, y_1, \ldots, y_{N-1}]^T \tag{7}$$

where T is the matrix transposon.

It can be also written as follows :

$$Y = I + JQ \tag{8}$$

Using the inverse function of the function used in the clipping we get the following

$$Y_{inv} = I_{inv} + JQ_{inv} = f^{-1}_{RI}(I) + jf^{-1}_{R_Q}(Q) \tag{9}$$

By entering the fft operation on the signal obtained, we find

$$x_{inv} = FFT\,\{Y_{inv}\} \tag{10}$$

Let the constellation points closest to the signal x_{inv} be $\hat{x}_{inv}$. We calculate the difference between them and write the result as a polynomial of degree P according to the following relationship

$$u = x_{inv} - \hat{x}_{inv} \tag{11}$$

For this, we follow the following steps :

- We calculate the IFFF of the signal u, we call it U, where :

$$U = IFFTu \tag{12}$$

- The real and imaginary part of the obtained signal are set, and we write the following

$$U = U_I + jU_Q \tag{13}$$

- We calculate the matrices H_I and H_Q as follows

$$H_I = [I^P, I^{P-1}, \ldots, 1] \tag{14}$$

$$H_Q = [Q^P, Q^{P-1}, \ldots, 1] \tag{15}$$

- We calculate the matrices M_I and M_Q according to the following

$$M_I = H_I^T.H_I \tag{16}$$

$$M_Q = H_Q^T.H_Q \tag{17}$$

- We calculate the coefficients of the polynomial according to the following relationship

$$A = [a_0, a_1, \ldots, a_P]^T = {M_I}^{-1}\left({H_I}^T U_I\right) \tag{18}$$

$$B = [b_0, b_1, \ldots, b_P]^T = {M_Q}^{-1}\left({H_Q}^T U_Q\right) \tag{19}$$

- Finally, the signal that has a better EVM can be obtained by

$$y'_{inf} = I'_{inf} + jQ'_{inf} = \left[f^{-1}_{R_I} + \sum_{i=0}^{P} a_i I^i\right] + j\left[f^{-1}_{R_I} + \sum_{i=0}^{P} b_i Q^i\right] \tag{20}$$

IV. Simulation results

The simulations are run in a Gaussian channel. The configuration is performed by using 256 subcarriers, the sampling frequency is 50 MHz, the duration of the guard interval taken equal to $0.8s$, i.e. 40 samples, the number of active subcarriers is 192, and consequently the occupied band is 37.5 MHz. The choice of the number of users depends on the length of the spreading codes used. In our case, we will consider orthogonal Walsh-Hadamard sequences. Indeed, the best properties of this family of codes have been demonstrated in the case of synchronous downlinks. The length L_c of these orthogonal sequences being in power of 2, we will consider in the case where L_c can take the value 16. Thus, each of the considered users can, according to the case, transmit 12 data per MC-CDMA symbol, the spacing between subcarriers is 195.3125 kHz.

As can be observed in Figure5 that the proposed method reduces the PAPR considerably after the first iteration, $N_{iter} = 2$. It can also be noticed that a gain of 6 dB at CCDF = 10^{-3} is obtained between the original OFDM signal (without PAPR reduction) and the IICM method with three iterations $N_{iter} = 3$.

To insure fair comparaison between the two methods in terms of EVM, it should have the same PAPR for both methouds. Figure 6 shows that the two compared method (Clipping and IICM) can have the same PAPR value equale to $9dB$ at CCDF=10^{-3}. The parameter to have this same PAPR value is, $N_{iter} = 2$ for IICM and $A = 0.21$ for conventional clipping.

For the same PAPR, Figure 7 present the EVM of the compared methods. We can see, IICM outperform conventional clipping by 0.06% at IBO=1dB. While, when setting the IBO

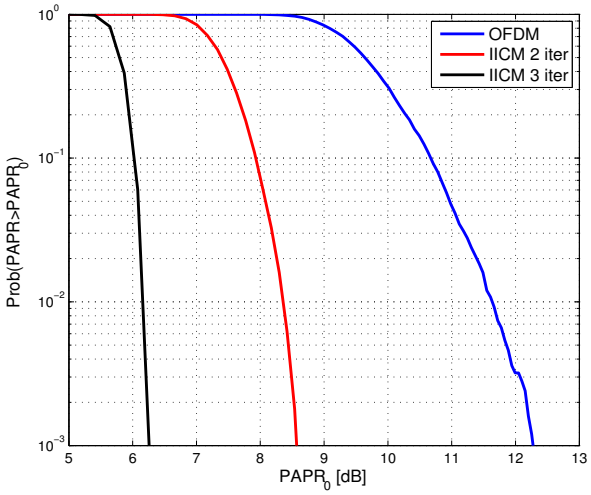

Fig. 5: PAPR reduction performance of the IICM methods for 2 iterations and 3 iterations

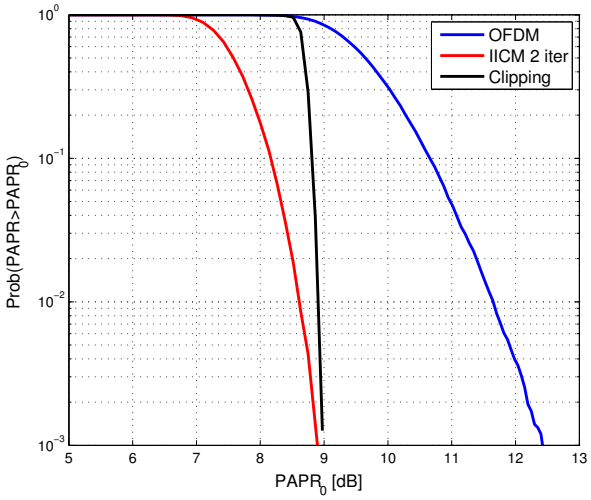

Fig. 6: Comparison of the PAPR reduction performance of the IICM methods, Clipping and the original OFDM signal

of the HPA used for IICM to $IBO_{clp} - 1$, we can see that the two methods have the same EVM, it is to say that there is a gain of 1dB between the two methods.

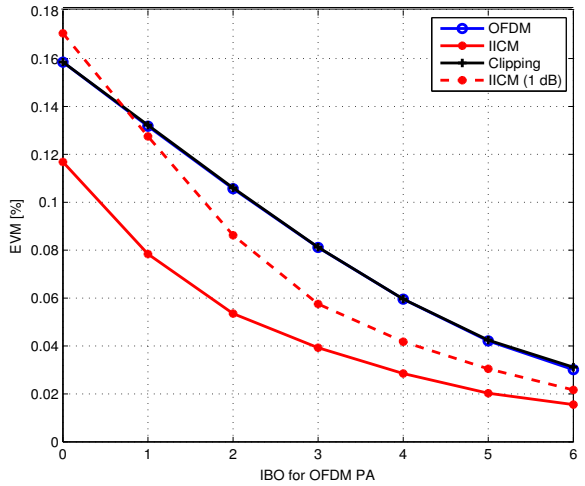

Fig. 7: Comapraison of the EVM of IICM, IICM 1dB, Clip-

V. Conclusion

In this paper we have presented a new PAPR reduction technique for OFDM signals that have strong amplitude fluctuations in a context of nonlinear amplification of these signals. This new technique relies on iterative invertible clipping based on more digital filtering (IFFT/FFT) in transmit before the power amplifier and on the inversion of this clipping function in receive. This allows us to mask the non-linearity of the HPA by that of the clipping in terms of PAPR reduction. Then, we campared the IICM method to conventional clipping in terms of EVM for the same PAPR reduction. The results shows that there is a gain of $1dB$ between the two methods, which is very important in point of view energy efficiency.

References

[1] Panwar, Nisha, Shantanu Sharma, and Awadhesh Kumar Singh. "A survey on 5G: The next generation of mobile communication." Physical Communication 18 (2016): 64-84.

[2] Wang, Yong, et al. "An efficient nonlinear companding transform for reducing PAPR of OFDM signals." IEEE Transactions on Broadcasting 58.4 (2012): 677-684.

[3] Singh, Amanjot, and Hardeep Kaur. "Non linearity analysis of high power amplifier in OFDM system." International Journal of Computer Applications 37.2 (2012): 37-41.

[4] Ragusa, Salvatore, et al. "Invertible clipping for increasing the power efficiency of OFDM amplification." ICT 2006. 2006.

[5] Li, Xiaodong, and Leonard J. Cimini. "Effects of clipping and filtering on the performance of OFDM." 1997 IEEE 47th Vehicular Technology Conference. Technology in Motion. Vol. 3. IEEE, 1997.

[6] Merah, Hocine, et al. "Iterative Invertible Clipping Method for PAPR Reduction in Wireless MC-CDMA Communication Systems." International Journal of Sensors Wireless Communications and Control 9.3 (2019): 372-387.

[7] Chen, Zeqiang, Ken Li, Kai Jin, Chenxi Huang, Peng Li, and Li Geng. "A 2.6 GHz Class-AB GaN Power Amplifier with Maximum Output Power of 56W Achieving 70% Power Added Efficiency." In 2018 1st Workshop on Wide Bandgap Power Devices and Applications in Asia (WiPDA Asia), pp. 328-331. IEEE, 2018.

[8] Y. W. Chang, T. -C. Tsai, J. -Y. Zhong, J. -H. Tsai and T. -W. Huang, "A 28 GHz Linear and Efficient Power Amplifier Supporting Wideband OFDM for 5G in 28nm CMOS," 2020 IEEE/MTT-S International Microwave Symposium, Los Angeles, CA, USA, 2020, pp. 1093-1096.

[9] Guel, Désiré. Étude de nouvelles techniques de réduction du facteur de crête à compatibilité descendante pour les systèmes multiporteuse. Diss. Rennes 1, 2009.

[10] Armstrong, Jean. "Peak-to-average power reduction for OFDM by repeated clipping and frequency domain filtering." Electronics letters 38.5 (2002): 246-247.

[11] Li, Xiaodong, and Leonard J. Cimini. "Effects of clipping and filtering on the performance of OFDM." 1997 IEEE 47th Vehicular Technology Conference. Technology in Motion. Vol. 3. IEEE, 1997.

[12] Panta, Kusha R., and Jean Armstrong. "Effects of clipping on the error performance of OFDM in frequency selective fading channels." IEEE Transactions on wireless communications 3.2 (2004): 668-671.

[13] Merah, Hocine, Mokhtaria Mesri, and Khaled Tahkoubit. "Significant Reduction Of Bit Error Rate in 5G-GFDM System Using Concatenated Turbo Code with Low Density Parity Check Code in Fading Channels." Journal of Electrical Systems 14.1 (2018): 118-129.

Performance Comparison between Sum-Product and Bit-Flipping decoding Algorithms of Gallager's Construction for regular LDPC Convolutional Codes

Oulfa LAOUAR
Laboratoire de Recherche en Electronique de Skikda(IRES)
Université de 20 Aout 1955
Skikda, Algeria
o.laouar@univ-skikda.dz

Nadir DEROUICHE
Laboratoire de Recherche en Electronique de Skikda(IRES)
Université de 20 Aout 1955
Skikda, Algeria
n.derouiche@univ-skikda.dz

Imed AMAMRA
Laboratoire de Recherche en Electronique de Skikda(IRES)
Université de 20 Aout 1955
Skikda, Algeria
i.amamra@univ-skikda.dz

***Abstract*—In this research, we present a performance evaluation and comparison, in terms of complexity and performance, of two decoding algorithms for regular LDPC convolutional codes with Gallager's construction. We define some characteristics of LDPC Convolutional ensembles that enable them to perform better with the Windowed decoder. The Belief Propagation decoding is used to discuss both Bit-Flipping and Sum-Product algorithms. We will focus at how these ensembles and codes perform over an AWGN channel using the BPSK modulation. Our simulation results using the sliding window decoding procedure shows that the Sum-product decoding algorithm outperforms the Bit-Flipping one.**

***Index Terms*— Belief Propagation (BP), Bit Error Rate (BER), Bit-Flipping (BF), Gallager's construction, LDPC Convolutional codes (LDPC-CCs), Sum-product (SP).**

I. INTRODUCTION

In the early 1960's Gallager [1] introduced Low-Density Parity-Check (LDPC) codes, which are one of the most important Forward Error Correcting (FEC) codes, which have been showing to perform well on a variety of channels.

Felstrom and Zigangarov [2] proposed the convolutional counterparts of LDPC block codes (LDPC-BC), namely LDPC Convolutional Codes (LDPC-CC). After that, a lot of attention has been attracted to these codes due to many additional advantages against the LDPC codes. LDPC-CC have a very flexible code length, comparable performance to LDPC-BC, simple encoding, more excellent error correction performance for the start bits of a frame, which contain some important information [3]. Like LDPC-BC, LDPC-CC are constructed by sparse parity-check matrices and are decoded iteratively, but on the other hand, a sliding window-based strategy can be used with the iterative message passing algorithms, as Belief Propagation (BP), which appeared to be very promising in terms of achieving low-error probabilities at high data rates. Iterative decoding with its different algorithms has attracted a lot of interest in recent years. The Message-Passing Algorithm (MPA) iteratively determines the A-Posteriori Probability (APP) of bits in the transmitted codeword provided the received word using the BP algorithm [4]. The concept behind BP decoding is to exchange uncertainties between correlated bits according to the encoder's or parity-check matrices (PCM) requirements.

In this paper, we present a review of Sum-Product algorithm (SP) [5], which is a common algorithm to understand a large number of widely varying algorithms, constructed in the fields of computer science and engineering. We compared its Bit Error Rate (BER) performance under several assumptions (equal decoding memory requirements and equal decoding code period) with Bit-Flipping algorithm (BF) [6] based BP which is proposed for decreasing the computational complexity.

The rest of the paper is organized as follows: We begin in section II by briefly introducing the LDP-CCs and their main parameters with a presentation of Gallager's construction method. In the next section III, we focus firstly on encoding steps of LDPC-CC, and then on the two different decoding BP algorithm methods (Sum-Product and Bit-Flipping) using the sliding-window strategy. The main part of the paper is section IV, where comparisons between the SP and BF decoding algorithms are presented, based on several criteria for Gallager's construction matrices. Finally, section V concluded the paper.

II. Fundamentals of LDPC-CCs

An LDPC Convolutional code (m_s, j, k) is defined by an infinite time-varying parity-check matrix $H_{[0,\infty]}$ which is periodically time-varying in practice. The code is given as the null space of $H_{[0,\infty]}$, or as a set of sequences satisfying the equation:

$$H_{[0,\infty]} v_{[0,\infty]}^{T} = 0^{T} \tag{1}$$

Both v and H are defined over $GF(2)$ in binary codes. The parity-check matrix of these codes with a rate $R = b/c$ $(b < c)$ is constructed by coupling the parity-check matrices of LDPC-BCs as follows:

$$H_{[0,\infty]} = \begin{bmatrix} H_0(0) & & & & & & \\ H_1(1) & H_0(1) & & & & & \\ \vdots & \vdots & \ddots & & & & \\ H_{m_s}(m_s) & H_{m_s-1}(m_s) & \cdots & H_0(m_s) & & & \\ & H_{m_s}(m_s+1) & H_{m_s-1}(m_s+1) & \cdots & H_0(m_s+1) & & \\ & & \ddots & & & \ddots & \\ & & H_{m_s}(t) & H_{m_s-1}(t) & \cdots & H_0(t) & \\ & & & & & & \ddots \end{bmatrix} \tag{2}$$

Where m_s refers for the parity-check matrix's syndrome former memory. Furthermore, the $H_i(t), i = 0,1,\ldots,m_s$ sub-matrices are binary $(c-b) \times c$ given by:

$$H_i(t) = \begin{bmatrix} h_i^{(1,1)}(t) & \cdots & h_i^{(1,c)}(t) \\ \vdots & & \vdots \\ h_i^{(c-b,1)}(t) & \cdots & h_i^{(c-b,c)}(t) \end{bmatrix} \tag{3}$$

The syndrome matrix $H_{[0,\infty]}$ in (2) ignores the irregularity at the beginning, if $H_i(t)$ are full rank for all time instances t. Starting from the $(m_s \cdot (c-b)+1)$-th row and $(m_s \cdot c+1)$-th column, $H_{[0,\infty]}$ has exactly k ones in each row and j ones in each column.

- Gallager's construction matrices:

In this paper, we construct regular matrices according to Gallager's method [1], which is defined as a matrix with column and row weights respectively d_v and d_c.

$$H = \begin{bmatrix} H_1 \\ H_2 \\ \vdots \\ H_{d_v} \end{bmatrix} \quad (4)$$

Gallager's method construct a parity-check matrix with the form defined in Eq.(4) that can be divided into d_v sub-blocks. The first sub-block H_1 is structured by forming a $h_{d_v} \times h_{d_c}$sub-matrix that consists of $d_c\left(h_{d_v} \times h_{d_c}\right)$ with column weight 1 and row weight d_c. However, the other sub-blocks are of random column permutation version of H_1. Figures 1 and 2 present Gallager's construction matrices used in Section IV for simulations.

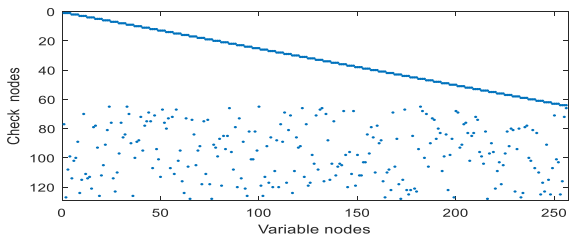

Fig. 1. Gallager's parity-check matrix of a code (256,2,4).

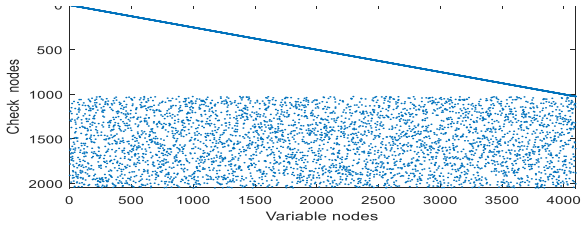

Fig. 2. Gallager's parity-check matrix of a code (4096,2,4).

III. Encoder and Decoder architecture

A data frame has a start and an end in most practical systems. Therefore, the LDPC-CC encoder and decoder must comply.

A. LDPC Convolutional Codes Encoder

Even if both of LDPC-BCs and LDPC-CCs encoders add redundancy to a stream of information bits, their implementation complexity is different. The implementation of an LDPC-CC encoder is usually much simpler than the implementation of an LDPC-BC encoder with identical characteristics.

The LDPC-CC encoder needs to know previous information bits as well as previous parity bits in order to generate the parity-bit $v(t)$. There is no need to implement a method of control to divide the input sequence into fixed-length blocks with LDPC-CCs encoders. At time t, the encoder output $v(t)$ is a function of the current input $u(t)$and even the encoder state.

The encoded sequence for a rate $1/2$ systematic LDPC-CC can be determined as follows:

$$v_1(t) = u(t) \quad (5)$$

$$v_2(t) = \sum_{i=0}^{m_s} h_1^{(i)}(t)\, u(t-i) + \sum_{i=1}^{m_s} h_2^{(i)}(t)\, v_2(t-i) \quad (6)$$

Figure 3 illustrates a regular LDPC-CC encoder of a rate $1/2$. The parameters α and β change with the period $T = m_s + 1$. A $'0'$ for α or β indicates disassociation, while a $'1'$ signifies association.

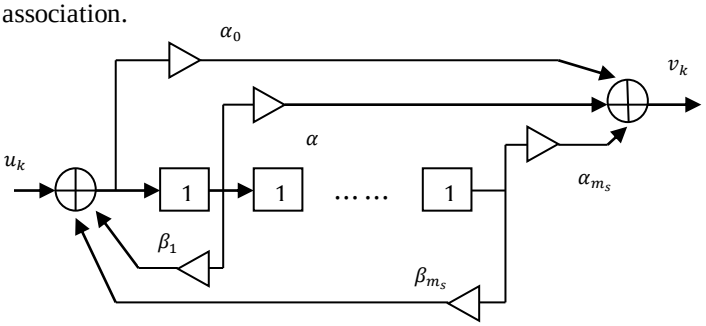

Fig. 3. LDPC-CC encoder for rate $R = 1/2$.

The figure shows that there are two outputs for each input u_k. The first output is systematic, which is u_k, while the second is the parity, which is v_k.

For a rate $R = 1/2$, if the last row $(c-b)$ of the sub-matrices $H_0(t)$ is linearly independent, and the first b symbols of $v(t)$ coincide with the information symbols, the LDPC-CC encoder is systematic [7] as follows:

$$v_t^{(1)} = u_t^{(1)}$$

B. LDPC Convolutional Codes Decoder

A soft-decision, iterative message-passing decoding algorithm is used by LDPC Convolutional codes. Messages containing probabilistic information are passed from one decoder processor to the next in a chain of similar processors using the message passing algorithm (MPA) due to the large values of the syndrome memory (m_s) that make the trellis representation of the LDPC-CC impossible which leads to the use of the iteration message passing decoding.

The Belief Propagation (BP) iterative algorithm, first introduced in [2], is usually used in the LDPC-CC decoding algorithm. The LDPC-CC decoding attempts to reconstruct the transmitted codeword from the possibly distorted received word by using the parity-check matrix H, which can be

ISBN: 978-9931-9728-1-5

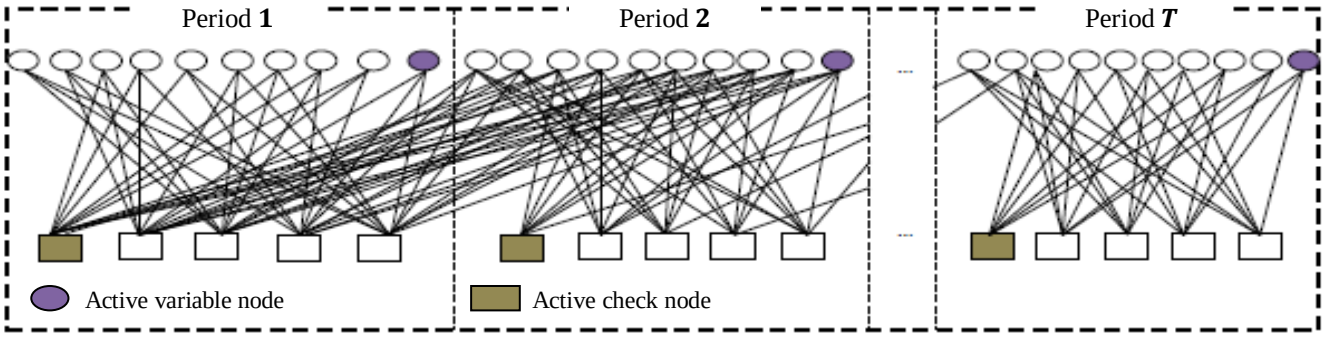

Fig. 4. Continuous decoding of LDPC-CC with T periods.

represented by an infinite Tanner graph, with columns corresponding to variable nodes (VNs) and rows corresponding to check nodes (CNs) as Figure 5 indicates:

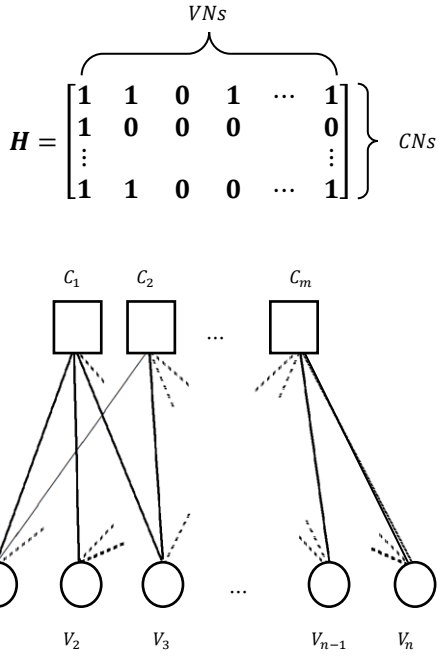

Fig. 5. General Tanner graph representation of the parity-check matrix H.

Continuous decoding of LDPC-CC with T periods, based on Tanner graph is presented in Figure 4.

The types of passed messages or those of operations performed at the nodes are used to classify different MPA [8]:

- BF decoding Algorithm:

For LDPC-CC, the BF algorithm is a hard decision MP algorithm that also works for LDPC-BC. Each check node sends a message to each linked bit node, declaring what value the bit is based on the check node's information. If the modulo-2 sum of equation (1) is zero, the check node determines that this equation is satisfied.

If the majority of received messages vary from the received values, the current value of the bit node is flipped. The BF algorithm's basic principle is that a codeword bit that appears in a large number of incorrect check equations is likely to be incorrect as well. Between the advantages of using this approach is that once a solution is found, additional iterations are avoided, and the inability to converge to a codeword is often detected.

Paper [6] proposed a new class of iterative BF decoding algorithm based on LDPC Convolutional codes, which improves Gallager's original BF algorithm [1] in terms of both coding gain and error correction speed. The BF algorithm works on the assumption that the greater the number of unsatisfied parity checks equations involving a specific bit, the more possible that bit is incorrect.

- SP decoding Algorithm:

The Tanner graph can be used to define an iterative decoder for LDPC-CCs. Messages are exchanged between the symbol nodes and the check nodes during all decoding iterations [5]. In this paper, an algorithm that is similar to Gallager's probabilistic iterative decoding algorithm known as the Sum-Product algorithm is presented.

The SP algorithm is a probabilistic soft decision message passing algorithm in which the messages represent each decision. The sum-Product algorithm is similar to the BF algorithm, except that the messages which represent each decision (whether the bit value is 0 or 1) are probabilities instead of bits. Since the input bit probabilities for the received bits were known in advance before running the LDPC-CC decoder, they are referred to as a priori probabilities [8], and the bit probabilities returned by the decoder are referred to as a posteriori probabilities. These probabilities are expressed as log-likelihood ratios (LLR) in sum product decoding as follows:

$$LLR(x) = \log\left(\frac{p(x=0)}{p(x=1)}\right) \quad (7)$$

For AWGN channel, $y_i = x_i + n_i$ is the $i\,th$ received sample, where n_i are independent and normally distributed as $N_0/2$, and N_0 is the noise density which its estimated value is necessary in practice.

- Windowed Decoding (WD) for BF and SP algorithms:

For LDPC Convolutional codes, Belief Propagation decoding algorithms are usually used. However, like block code decoding, these algorithms' iterations cannot continuously use the messages of recently joined variable nodes within the next iteration windows, limiting decoding performance. The windowed scheme is proposed for LDPC-CC decoding [9], and it is verified that it can achieve good performance. The fusion of two different iterative decoders is considered: the conventional BP decoder (Bit-Flipping and Sum-Product) and the variant Windowed Decoder.

The VNs connected to the same parity-check equations are

constrained by the code's convolutional structure. This property can be used to perform continuous decoding of the received stream using a "Window" that slides along the bit sequence. This structure allows parallelization of the MP decoder's iterations across multiple processors operating in different Tanner graph regions.

Long LDPC-C codes decoded with BP can have a high latency and require a large memory. The advantage of limiting BP decoding to a window is that it reduces decoding latency, complexity and memory use. The LDPC-CC parity matrix has a nonzero diagonal band structure represented with the gray area, as seen in Figure 6. Therefore the BP decoding can be constrained in a window, and the condition [10]:

$$(w+1) \leq W \leq L \tag{8}$$

must be satisfied for the window size W with L copies of an LDPC-CC and coupling width w.

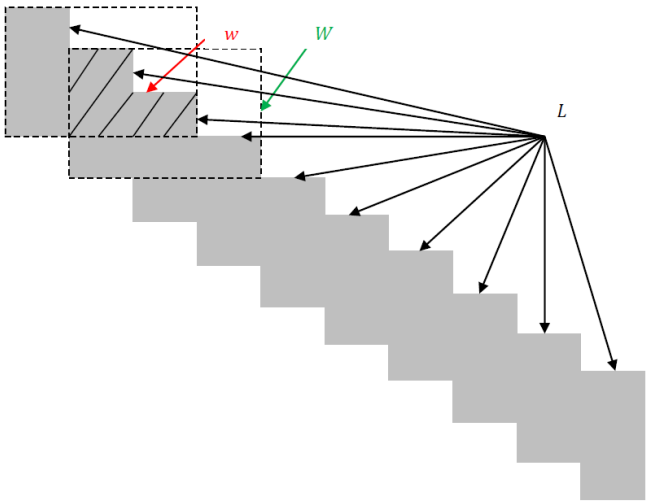

Fig. 6. WD of LDPC-CC where $L = 10, w = 2$ and $W = 3$.

The procedure is then repeated until the entire codeword is decoded.

Although an LDPC-CC's Tanner graph has an infinite number of nodes, the distance between two variable nodes connected to the same check node is limited by the code's memory. This allows continuous decoding using a decoder that slides a finite window along the received sequence.

In this paper, after receiving the partial codeword, the WD starts BP decoding through a partial Tanner graph of the codeword and slides along the diagonal band with an overlap between the windows.

Example: Considering the regular full-rank parity-check matrix:

$$H = \begin{bmatrix} 0 & 1 & 1 & 0 & 1 & 0 & 1 & 1 & 1 & 0 \\ 0 & 1 & 1 & 1 & 0 & 1 & 0 & 0 & 1 & 1 \\ 1 & 1 & 1 & 0 & 0 & 1 & 1 & 1 & 0 & 0 \\ 1 & 0 & 0 & 1 & 1 & 0 & 0 & 1 & 1 & 1 \\ 1 & 0 & 0 & 1 & 1 & 1 & 1 & 0 & 0 & 1 \end{bmatrix}$$

With size $M \times N = 5 \times 10$, of a rate-$1/2$ block code. As indicated above, we cut the parity-check matrix into two parts (red and black), where each cutting pattern is such that we repeatedly move $c = 2$ columns to the right and $b = 1$ row down. After achieving this diagonal cut, we copy and paste the two parts $(L = 3)$ following the unwrapping method presented in [11] to obtain the matrix shown in Figure 7:

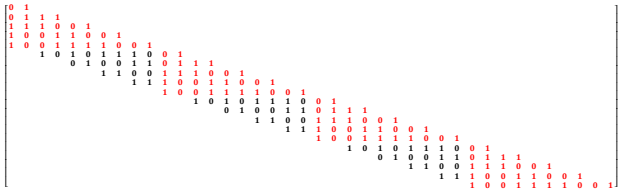

Fig. 7. Deriving a rate $R = 1/2$ periodically time-varying convolutional code from a rate-$1/2$ block code of length 10.

The received codeword using random $u(t)$ is as follows:

$$V = [\underbrace{0\,0\,0\,0\,0\,0\,0\,0\,0\,0}_{V_0}\,\underbrace{0\,1\,0\,1\,1\,0\,0\,1\,0\,1}_{V_1}\,\underbrace{0\,0\,0\,0\,1\,1\,1\,1\,1\,1}_{V_2}\,\underbrace{0\,1\,1\,1\,1\,0\,0\,0\,1\,0}_{V_3}]$$

Applying the WD on the first part of the LDPC-CC matrix:

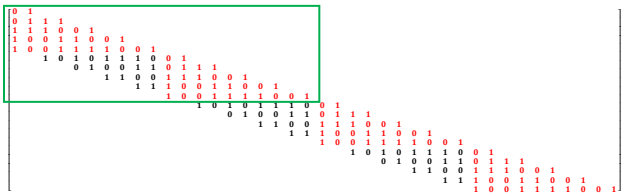

Fig. 8. WD applied on $[V_0 V_1]$.

The WD then slides to the next sub-vector to decode it as follows:

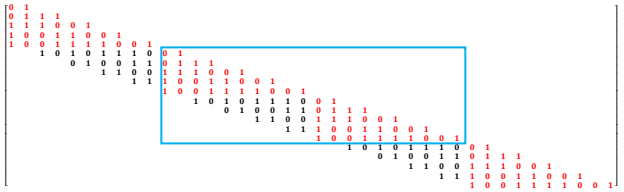

Fig. 9. WD applied on $[V_1 V_2]$.

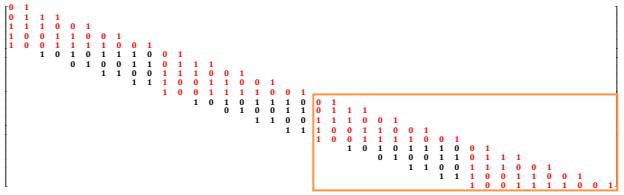

Fig. 10. WD applied on $[V_2 V_3]$.

As Figure 11 shows, the WD is then slides with overlap of M rows and N columns between windows :

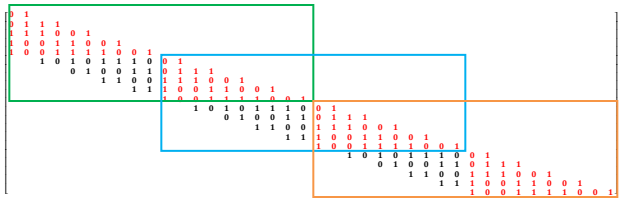

Fig. 11. WD applied on V.

The WD terminates and outputs the current sub-decoding vector's result once the BER of the sub-vector is 0 or the number of iterations achieves the limit. It is clear for each

iteration; the previous sub-vector is re-decoded with the present sub-vector, which increases the decoding performance.

IV. Simulation Results

This section examines the performance of regular LDPC-CC for Gallager's construction matrices shown in Figure 1 and 2. As well as, the performance curves of WD-BF and WD-SP under AWGN channel are presented in Figure 12.

To compare BER performance of a rate$-1/2$, the corresponding LDPC-BCs with block length $N = 256, N = 4096$ are chosen respectively for constructing LDPC-CCs of periods $(T = 128, T = 2048)$ under the same processor complexity decoding, where the LDPC-CCs are decoded using a sliding-window BF and SP algorithms.

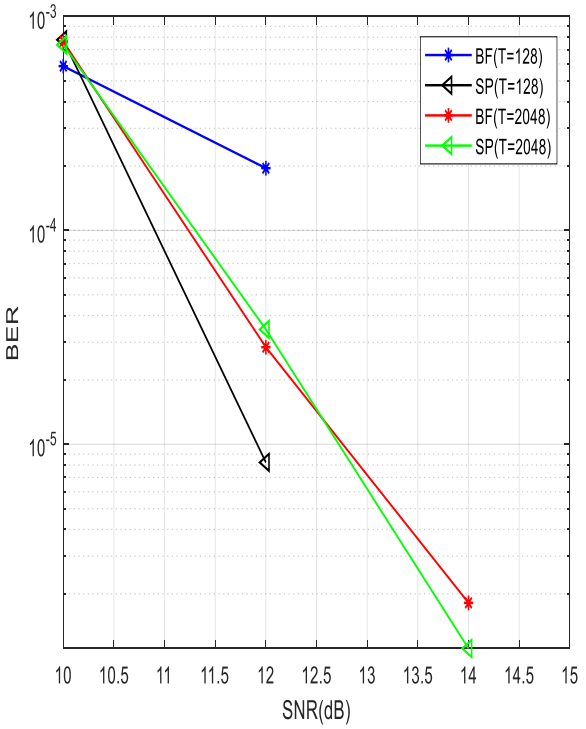

Fig. 12. Performance Comparison between WD-BF and WD-SP of Gallager's Construction.

As can be observed for $T = 128$, a BER of 2×10^{-4} and 8×10^{-6} at $12dB$ are obtained using WD-BF and WD-SP respectively. Also for $T = 2048$, a BER of 1.8×10^{-6} and 10^{-6} at $14\,dB$ are obtained using WD-BF and WD-SP respectively. From which we can say that WD-SP outperforms the corresponding WD-BF for the same period.

Also, it has been shown that BER values for $T = 2048$ are more reduced than those for $T = 128$, and the corresponding SNR is increased. Which means that by increasing the period, we can attend a better BER values.

V. Conclusion

Performances of both WD-BF and WD-SP Belief propagation decoding algorithms for LDPC-CC are evaluated in terms of Bit Error Rate (BER).

Sum-Product decoding of LDPC-CCs retains many of the desirable features of Bit-Flipping decoding, and LDPC-CC with large constraint length v_s can be decoded using a sliding window message passing decoder. For each iteration, the sliding-window decoder takes from the previous decoding window a sub-vector overlapping with the present window, in order to decode it for the second time. This strategy is responsible for increasing decoding performance.

Sum-Product decoders are excellent algorithms for practical communication conditions due to their excellent BER performances. Simulation results show that the WD-SP algorithm for regular LDPC-CC outperforms the WD-BF algorithm with comparable processor complexity for moderate constraint length codes.

REFERENCES

[1] R. G. Gallager, "Low-Density Parity-Check Codes". Cambridge, MA: MIT Press, 1963.
[2] A. Jimenez-Felstrom¨ and K. Sh. Zigangirov, "Time-varying periodic convolutional codes with low-density parity-check matrix," IEEE Trans. Inform. Theory, vol. IT-45, pp. 2181–2191, Sept. 1999.
[3] Y. Chen, C. Zhou, Y. Huang, and X. Zeng, "An efficient multirate LDPC-CC decoder with layered decoding algorithm," in IEEE International Conference on Communications (ICC), June 2013.
[4] J. Hagenauer, E. Offer, and L. Papke, "Iterative decoding of binary block and convolutional codes," IEEE Trans. Inform. Theory, vol. 42, pp. 429–445, Mar. 1996.
[5] M. Lentmaier, A. Sridharan, K. S. Zigangirov, and D. J. Costello, Jr., "Terminated LDPC convolutional codes with thresholds close to capacity," in Proc. IEEE Int. Symp. Inf. Theory, Adelaide, Australia, Sep. 2005, pp. 1372–1376.
[6] X. S. Zhou, B. F. Cockburn and S. Bates., "Improved Iterative Bit Flipping Decoding Algorithms for LDPC Convolutional Codes", IEEE Pacific Rim Conference on Communications, Computers and Signal Processing, Canada, 2007.
[7] A. E. Pusane, K. Sh. Zigangirov, and D. J. Costello, Jr., "Construction of irregular LDPC convolutional codes with fast decoding", Proc. IEEE Int. Conf. on Communications, Istanbul, Turkey, June 2006.
[8] R. Lakshmi, G. Vijitha., "The Performance of LDPC Convolutional Codes-A Quantitative Analysis", in IJIRCCE, vol. 3, Issue 6, pp. 5402-5403, June 2015.
[9] A. R. Iyengar, M. Papaleo, P. Siegel, J. Wolf, A. Vanelli-Coralli, and G. Corazza, "Windowed decoding of protograph-based LDPC convolutional codes over erasure channels," IEEE Trans. Inf. Theory, vol. 58, no. 4, pp. 2303–2320, Apr. 2012.
[10] S. Mo, L. Chen, Improved sliding window decoding of spatially coupled low-density parity-check codes, in: Proc. 2017 IEEE Inf. Theory Work. (ITW), Kaohsiung, Taiwan, 2017, pp. 126–130.
[11] A. E. Pusane, R. Smarandache, P. O. Vontobel, and D. J. Costello, Jr., "Deriving good LDPC convolutional codes from LDPC block codes," IEEE Trans. Inf. Theory, vol. 57, no. 2, pp. 835–857, Feb. 2011.

Novel approach for a ladder network model of the transformer winding high-frequency parameters identification based on FRA data

Abdallah Chanane[1], Messaoud Belazzoug[1]

[1]Laboratoire des systèmes électriques et télécommande, Faculté de Technologie, Université Blida1, BP 270, route de Soumaa, Blida, Algeria.
chanane.abdallah@gmail.com,m_belazzoug@yahoo.fr
Corresponding author: chanane.abdallah@gmail.com
chanane.abdallah@univ-blida.dz

Abstract
The identification of the high-frequency ladder network model (LNM) parameters for the transformer winding is the way to confirm its actual condition. This paper aims to present the application of one of the latest approach algorithms, namely, Particle Swarm Optimization with Invasive Weed Optimization (PSO-IWO) method for the identification of the high frequency LNM parameters for the transformer winding. The physical realizability of the LNM is ensured and it is based on the frequency response analysis FRA data and some terminal measurements of a transformer winding. The results are agreement and indicate that the identified model, is superior in terms of representing the physical behavior of the transformer winding in high frequency.

Keywords
Identification, Transformer winding, Diagnosis, equivalent circuit, PSO-IWO

Introduction

Power transformer is one of the most expensive equipment in a power system. Transformers practice excessive faults during exploitation, and this disturb the quality and the continuity of service. For this motive, diagnosis is necessary. Several procedures have been developed for diagnosis such as vibration analysis [1], [2], transfer function (TF) [3], [4] and frequency response analysis (FRA) [5], [6].

The FRA is one of the best technique that can detect even the slightest changes in the transformer winding [7], [8]. Even so, pertaining FRA practice requires consistent interpretation methods including finite element modelling (FEM), mathematical models, analytical approaches, numerical indices and TF as reported in [6], [8], [9].

Nowadays, intelligent algorithms have been used to identify the LNM and to offer a global solution, such as genetic algorithm, particle swarm optimization, crow search and simulated annealing algorithms [10], [11] bacterial swarming [12], neural network [13], Grey Wolf [14] and bat algorithm [15]. In this paper, a novel approach is applied to identify the high-frequency parameters transformer winding using the PSO-IWO algorithm. The proposed algorithm uses the IWO method as a local search tool to improve the convergence and the characteristics of PSO in fast calculation. The proposed LNM is mutually coupled and physically realizable. Identification of the model parameters is presented and the results are validated through a case study of a transformer winding.

1. Proposed LNM

The transformer winding can be modeled by considering a mutually coupled LNM with N-section as shown in the Figure 1. The parameters of the LNM are defined as follows: N is the number of sections, r is the resistance per section, C_g is the capacitance to the ground per section, C_s is the series capacitance per section, L_s is the self-inductance and M_{1N} is the mutual inductances between different cells.

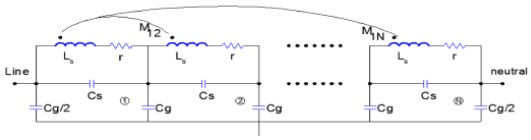

Fig. 1 *Equivalent circuit of a transformer winding*

- Capacitance matrix:

The total shunt capacitance (C_{geff}) and the ground capacitance per section (C_g) are, respectively, estimated according to the equations (1) and (2) [4], [14]:

$$C_{geff} = C_s . Q^2 / N \quad (1)$$

$$C_{gi} = C_g / N \quad (2)$$

Where: Q is the voltage distribution constant.

The equivalent capacitance of the LNM (C_{eq}) is estimated according to equation (3):

$$C_{eq} = \frac{C_{gi}}{2} + \frac{1}{\frac{1}{C_s} + \frac{1}{C_{gi} + \frac{1}{\frac{1}{C_s} + \cdots}}} \quad (3)$$

- Inductance matrix

One of the physical properties of the transformer winding is that the magnetic coupling decreases when the distance between the discs increases [4], [6]. Consequently, the self and the mutual inductances could be limited between two bounds (upper and lower bounds) as given in equations (4) and (5):

$$0.1\ L_{ij} < M_{ij} < 0.9\ L_{ij} \quad (4)$$

$$0.10M_{ij} < M_{ij+1} < 0.99M_{ij}\ ,\ i, j = 1\ \ldots.\text{where}, i \neq j$$

$$\text{and}\ \ L_{ij} > M_{12} > \ldots > M_{ij} \quad (5)$$

The total equivalent inductance of the model winding could be expressed as per equation (6):

$$L_{eq}(\text{estimated}) = NL_i + 2\sum_{i=1}^{N-1}(N-1)M_{i,i+1} \quad (6)$$

2. Proposed PSO-IWO method

2.1 PSO Algorithm

This algorithm is one of the stochastic algorithms [16]. By the way, novel concepts were developed such as the convergence rate and the selected parameters as reported in [17], [18], [19]. The position of the particle is calculated according to the individual's best and the group's best experience of the particle swarm. Each particle represents an achievable solution to the problem [18], [19].

2.2 IWO algorithm

The IWO is a stochastic algorithm inspired from the colonization of invasive weeds [20]. The algorithm starts randomly, then, members of the population produce seeds based on their comparative fitness in the population. The convergence rate and the selected parameters are reported in [20].

3.3 Hybrid PSO-IWO algorithm to identify the LNM

For a better solution quality, two algorithms are combined, in which, fully-guided movements for each iteration good exploration are ensured by PSO and IWO method respectively. This choice avoids some drawbacks such as being trapped in local optima or converging to global optima in a long time.

Reference value [4]	Frequency peaks (F_{Pi})						ΔF_{Pi}
	1st	2nd	3nd	4nd	5nd	6nd	
	40.48	142.58	249.42	346.41	414.34	473.73	
PSO-IWO	40.77	142.30	249.20	346.00	414.20	473.00	0.5917
CSA[11]	40.1	142.30	248.5	344.70	414.20	477.6	2.8100
Reference value [4]	Frequency Troughs(F_{Ti})						ΔF_{Pi}
	1st	2nd	3nd	4nd	5nd	-	
	105.19	224.79	334.44	410.09	472.42	-	
PSO-IWO	104.9	224.5	334.00	409.50	471.00	-	0.9830
CSA[11]	104.9	223.8	332.7	409.5	475.6	-	2.0400

$$\Delta F_i = \frac{\sum \text{Reference values} - \sum \text{Estimated values}}{\sum \text{Reference values}} \text{x100}$$

Table. 2 Comparison of the reference and the estimated frequencies

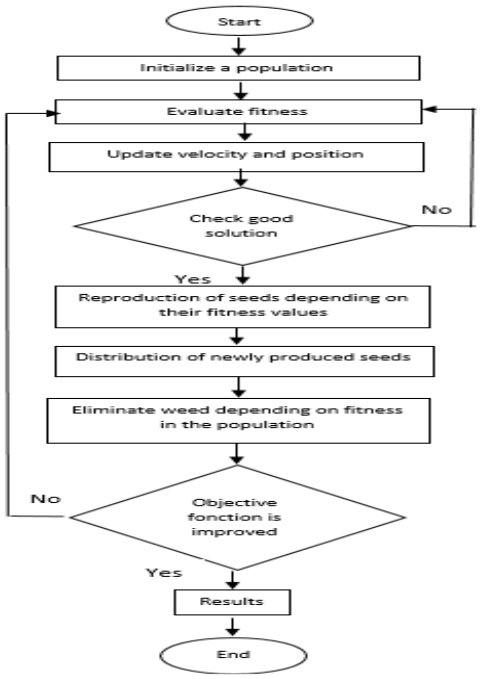

Fig. 2. *Flowchart of the PSO-IWO algorithm*

3. Implementation of the PSO-IWO to identify the LNM Parameters

FRA measurements were performed on the model of winding [4], in which the physical parameters are given as follow; the total inductance and effective capacitance were equal to 6.98mH and 5.6nF respectively. The total resistance was equal to 8Ω. An iterative algorithm was used to estimate the parameters of the involved electrical equivalent circuit. Finally, the FRA signature is obtained through the synthesized electrical equivalent circuit [4]. To identify the LNM of the transformer winding, the obtained results are compared to with those obtained by [11].

Parameters	Reference value (reprinted from [4])	PSO-IWO	CSA[11]	Deviation from the reference (%) $DEV = \frac{100}{N} \times \lvert\frac{Reference - identified}{Reference}\rvert$	
				PSO-IWO	CSA
Ls (mH)	0.4310	0.4310	0.4307	0.0	0.01
M1 (mH)	0.2392	0.2390	0.2390	0.013	0.138
M2 (mH)	0.1435	0.1430	0.1429	0.056	0.068
M3 (mH)	0.0947	0.0945	0.0949	0. 011	0.035
M4 (mH)	0.0612	0.0613	0.0610	0.026	0.053
M5 (mH)	0.0496	0.0497	0.0492	0.033	0.133
C_s (nF)	0.600	0.601	0.59	0.026	0.276
C_{eq}(nF)	0.8819	0.8824	0.8765	0.00	0.101
α	7.48	7.47	7.54	0.0223	0.021
L_{eq}(mH)	7.0385	7.0316	7.0292	0.0163	0.021

Table. 1 Comparison of the reference and the identified parameters of the LNM

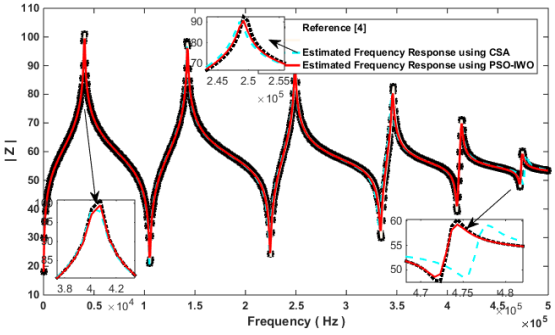

Fig. 3. *FRA curves of the model winding*

Discussion:

The proposed Ladder Network Model presents the physical behavior of the transformer winding. The proposed PSO-IWO method present serval advantages, mainly:

- The best exploration and exploitation search. Thereby, the global best solution always directed to a better position, as the algorithm proceeds.
- A luxurious, time-efficient and a flexible computation is verified, the effectiveness of PSO-IWO was tested by the Crow Search Algorithm.

conclusion

This paper has presented a novel approach based on PSO-IWO to identify the parameters of a Ladder Network Model of a transformer winding. The case study presented in previous sections suggest the capability of the PSO-IWO method for the construction of the LNM of a transformer winding. Through the case study, it has shown that the proposed PSO-IWO is good in terms of accuracy and effectiveness, since the proposed method is compared with other reported in the literature. The obtained results are very promising and prove the efficiency and the high solution quality.

Acknowledgment

The authors would like to thank the Directorate General for Scientific Research and Technological Development, Algeria (Direction Générale de la Recherche Scientifique et du Développement Technologique "DGRSDT", Algerie), for the resources provided for scientific research and development.

References

[1] Hong, K., Huang, H. and Zhou, J. (2015), "Winding condition assessment of power transformers based on vibration correlation", IEEE Transactions on Power Delivery, Vol. 30 No. 4, pp. 1735-1742.

[2] Seo, J., Ma, H. and Saha, T.K. (2017), "A joint vibration and arcing measurement system for online condition monitoring of onload tap changer of the power transformer", IEEE Transactions on Power Delivery, Vol. 32 No. 2, pp. 1031-1038.

[3] Mukherjee, P. and Satish, L. (2012), "Construction of equivalent circuit of a single and isolated transformer winding from FRA data using the ABC algorithm", IEEE Transactions on Power Delivery, Vol. 27 No. 2, pp. 963-970.

[4] Ragavan, K., Satish, L.: 'Localization of changes in a model winding based on terminal measurements: experimental study', *IEEE Trans. Power Deliv.*, 2007, **22**, (3), pp. 1557–1565

[5] Alsuhaibani, S., Khan, Y., Beroual, A. and Malik, N.H. (2016), "A review of frequency response analysis methods for power transformer diagnostics", Energies, Vol. 9 No. 11, p. 879

[6] Pramanik, S. and Satish, L. (2011), "Estimation of series capacitance of a transformer winding based on frequency-response data: an indirect measurement approach", IEEE Transactions on Power Delivery, Vol. 26 No. 4, pp. 2870-2878.

[7] Liu, Y., Ji, S., Yang, F., *et al.*: 'A study of the sweep frequency impedance method and its application in the detection of internal winding short circuit faults in power transformers', *IEEE Dielectr. Electr. Insul. Soc.*, 2015, **22**, (4), pp. 2046–2056

[8] Samimi, M., Tenbohlen, S.: 'FRA interpretation using numerical indices: state-of-the-art', *Electr. Power Energy Syst.*, 2017, **89**, pp. 115–125

[9] Liu, S., Liu, Y. A L. H. and Lin, F. (2016), "Diagnosis of transformer winding faults based on FEM simulation and on-site experiments", IEEE Transactions on Dielectrics and Electrical Insulation, Vol. 23 No. 6, pp. 3752-3760.

[10] Chanane, A., Bouchhida, O., Houassine, H.: 'Investigation of the transformer winding high-frequency parameters identification using particle swarm optimisation method', *IET Electr. Power Appl.*, 2016, **10**, (9), pp. 923–931

[11] Chanane, A., Houassine, H. and Bouchhida, O. (2019), "Enhanced modelling of the transformer winding high frequency parameters identification from measured frequency response analysis", IET Generation, Transmission and Distribution, Vol. 13 No. 8, pp. 1339-1345.

[12] Shintemirov, A., Tang, W. A T. W. and Wu, Q. (2010), "Improved modelling of power transformer winding using bacterial swarming algorithm and frequency response analysis", Electric Power Systems Research, Vol. 80 No. 9, pp. 1111-1120.

[13] Zambrano, G., Ferreira, A. and Caloba, L. (2006), "Power transformer equivalent circuit identification by artificial neural network using frequency response analysis", IEEE Power Engineering General Meeting, Montreal, Canada, No. 11, pp. 1-6.

[14] Abdallah Chanane, M. Belazzoug, ' On accuracy of a mutually coupled ladder network model high-frequency parameters identification for a transformer winding using gray wolf optimizer method', Computer Science Compel-the International Journal for Computation and Mathematics in Electrical and Electronic Engineering Vol. 40 No. 1, pp. 40-50.

[15] Sahnoune Chaouche, M., Houassine, H., Moulahoum, S., *et al.*: 'BA to construction of equivalent circuit of a transformer winding from frequency response analysis measurement', IET Electric Power Applications, vol-12, pp-728-736.

[16] Kennedy, J., Eberhart, R.C.: 'Particle swarm optimization'. Proc. IEEE Int. Conf. on Neural Networks IV, Perth, Australia, 1995, pp. 1942–1948

[17] Trelea, I.: 'The particle swarm optimization algorithm, convergence analysis and parameter selection', Inf. Process. Lett., 2003, **6**, (85), pp. 317–325

[18] Shi, Y., Eberhart, R.C.: 'Empirical study of particle swarm optimization'. Proc. of the Congress on Evolutionary Computation, Washington D.C., USA, 1999, pp. 1945–1950

[19] Clerc, M., Kennedy, J.: 'The particle swarm explosion, stability, and
convergence in a multidimensional complex space', IEEE Trans. Evol.Comput., 2002, **6**, pp. 58–73

[20] Mehrabian, A.R., Lucas, C.:' A novel Numerical Optimization Algorithm Inspired from Weed Colonization', Ecological Informatics, 2006,(1), pp. 355-366.

Artificial intelligence

Five Deep Learning Models for Classification of Chest X-Ray Images of COVID-19

Abdesselam FERDI
Electronics Department
Frères Mentouri Constantine 1 University
Constantine, Algeria
abdesselam.ferdi@gmail.com

Said BENIERBAH
Electronics Department
Frères Mentouri Constantine 1 University
Constantine, Algeria
said_benierbah@umc.edu.dz

Youcef FERDI
National Higher School of Biotechnology
Constantine, Algeria
youcef.ferdi@gmail.com

***Abstract*—In recent years, deep learning algorithms have acquired a great popularity in many fields including medical imaging to achieve different tasks such as image segmentation, classification, detection, and retrieval tasks. Although reverse transcription polymerase chain reaction test (RT-PCR) is considered to be the gold standard for COVID-19 screening, deep learning algorithms may help radiologists to automatically diagnose this disease by processing chest X-ray (CXR) and chest CT images. This paper proposes a comparative study of five deep learning models for classification of CXR COVID-19 images. The five selected models are pre-trained networks, namely, ResNet-50, InceptionResNet-v2, Inception-v3, MobileNet-v2, and GoogleNet. The models were evaluated using CXR COVID-19 and normal images from publicly available datasets. The obtained classification results show that the GoogleNet model achieves the highest classification performance with a validation accuracy of 95.69%.**

Keywords—COVID-19 · Deep Learning · Convolutional Network · Chest X-ray image · Medical Image Processing

I. INTRODUCTION

The COVID-19 is an infectious disease caused by a virus called severe acute respiratory syndrome coronavirus 2 (SARS-CoV-2). The outbreak has been first identified in Wuhan, China, in December 2019. Since then, the number of infected people is increasing rapidly and, unfortunately, some patients develop difficulty in breathing and require hospitalization. To help combatting the spread of this worldwide pandemic, researchers are working on developing accurate detection and early treatment of infected patients. The reverse transcription polymerase chain reaction test (RT-PCR) is the gold standard for diagnosis of COVID-19. However, this method is not always available because of the possible short supply of test kits and the strict environment requirements for accomplishing screening [1]. Some studies have also shown false positives in PCR testing.

Another fast and effective method for COVID-19 screening is based on chest X-ray (CXR) and chest computed tomography (CT) images analysis. COVID-19 diagnosis systems based on radiological imaging techniques have been considered as a good complement to RT-PCR tests because of the clinical signs of most COVID-19 patients, which suffer from lung infection. In addition, these methods have several advantages such as speed, availability, and accessibility. Medical images are acquired and analyzed by radiologists who look for visual findings associated with lung infections caused by the virus. Visual medical images analysis is time-consuming, and the findings may be observed in other lung infections, such as Influenza (H1N1) and SARS [2]. Figure 1 shows an image example of a normal case and a COVID-19 case.

Deep learning is widely used in many disciplines such as computer vision, medical imaging, and bioinformatics. In medical imaging, deep learning techniques have been used to achieve image segmentation, classification, detection, and retrieval tasks [3-9]. In the context of COVID-19, deep learning is used to help radiologists to interpret radiographic images faster and more accurately to detect COVID-19 cases, in order to fight against its spread. Recently, many deep learning models has been proposed to detect patients infected with COVID-19 using both CXR and chest CT images [3-9]. Deep learning based COVID-19 diagnosis systems are developed either from existing pre-trained models with transfer learning or as customized networks. Most of deep learning models used for COVID-19 detection are based on convolutional neural networks (CNNs) architecture. These include GoogleNet, Inception or Xception, VGGNet, ResNet, AlexNet, MobileNet, and ShuffleNet. Recently, some papers dealing with reviewed studies of deep learning based COVID-19 diagnosis systems have been published [3-9]. Their results for COVID-19 detection from various datasets of CXR and CT images mostly collected from internet sources have been reported. Metrics commonly used to assess the performance of deep learning models are accuracy, sensitivity, specificity, precision, F1-score, and area under the curve (AUC). According to these studies, promising performance has been achieved by the developed systems, but improvements still need to be proposed regarding the datasets of medical images and the design of optimized deep learning algorithms to reduce computational cost and overcome the problem of small amount of data.

In this paper, five deep learning models are fine-tuned by replacing the last layers with new layers adapted to the datasets. Although previous works have dealt with this topic, the aim of the proposed work is to compare these models on new datasets with a larger number of COVID-19 images.

The rest of the paper is organized as follows. Section II provides a literature survey on the most recent works dedicated to the application of deep learning technology to COVID-19 diagnosis. Transfer learning, dataset, image preprocessing, classification models, parameters settings, and metrics are described in Section III. The obtained results are discussed in Section IV. The paper ends with a conclusion and opens up prospects for new research.

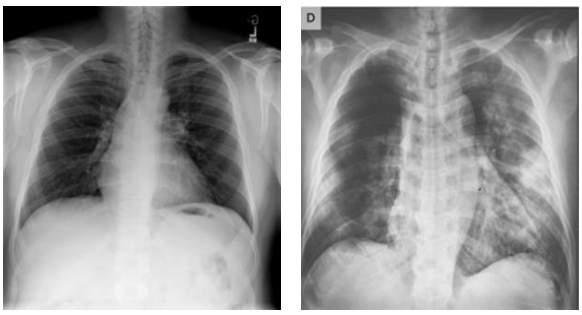

(a) (b)

Fig. 1. Examples of a) normal and b) COVID-19 CXR images [2]

II. LITTERATURE SURVEY

Very recently, several works on the application of deep learning models to COVID-19 classification in CXR and chest CT images have been proposed. In this section, we list some of these works. H. X. Bai et al. [3], compared the performance of radiologists in detection of COVID-19 from other pneumonia with and without AI assistance. The model was trained using 1186 chest CT images. On independent testing, this model achieved an accuracy of 87%, a sensitivity of 89%, and a specificity of 86%. K. El. Asnaoui et al. [4], presented a comparative study of seven different models for classification of COVID-19 pneumonia in CXR and CT images. These models were trained using 6087 images. The Inception-ResNet-v2 provided the highest accuracy of 92.18%. U. Ozkaya et al. [5], compared the proposed method as fusing and ranking deep features with three different pre-trained models. 150 CT images were used to train these models to classify COVID-19 cases. The proposed method shows best results with 98.27% accuracy. I. D. Apostolopoulos and T. A. Mpesiana [6], evaluated the classification performance of five different CNNs using transfer learning. To train the models to distinguish COVID-19 from common pneumonia, a collection of COVID-19, normal, and common bacterial and viral pneumonia images was selected. The MobileNet-v2 is the better model with an accuracy and a specificity of 96.78% and 96.46% respectively. A. Narin et al. [7], proposed five pre-trained CNNs for the classification of COVID-19 pneumonia. To train the models, 341 COVID-19, 2800 normal, 1493 viral pneumonia, and 2772 bacterial pneumonia X-ray scans are used. The performance results shows that the ResNet-50 provides the highest classification performance with 99.7% accuracy. E. E.-D. Hemdan, et al. [8], evaluated seven different pre-trained CNNs to classify COVID-19 in X-ray images. The models are trained and tested on 50 chest X-ray images. The VGG19 and DenseNet models showed better and similar classification performance with f1-scores of 0.91 and 0.89 for COVID-19 and normal, respectively. M. Chieregato et al. [9], developed a hybrid machine learning/deep learning model to classify patients in two classes (non-ICU and ICU: Intensive Care Unit admission) using 558 CT images. The proposed method reached a probabilistic AUC of 0.949.

III. METHODS

In this Section, transfer learning, dataset, image preprocessing, classification models, parameters settings, and metrics are described.

A. Transfer Learning

Transfer learning is the enhancement of the learning of a new task by the transfer of knowledge from another similar task that has already been learned. In neural networks, this is done by using parts of the previously trained network in the new one. This operation is, particularly, important when the new task is using a smaller number of training images [10]. In pre-trained CNNs, the convolutional layers extract image features that the last learnable layer and the final classification layer use to classify the input image. To fine-tune the network to classify CXR images into two classes (COVID-19 and normal) using transfer learning, we replace the last layers with three new layers adapted to the new dataset.

B. Dataset

In this study, we used *COVID-19 Radiography Database* [2]. This is a dataset of 13808 CXR images of normal and COVID-19. It contains 3616 COVID-19 positive cases along with 10.192 Normal, 6012 Lung Opacity, and 1345 Viral Pneumonia images. All the images are in PNG format of size 299×299 pixels. Only the COVID-19 and Normal images are selected.

C. Images preprocessing

The selected images has been resized into 224×224 pixels and 299×299 pixels in Jpeg format. The dataset has been randomly divided into two independent sets with 80% for training and 20% and validation. The k-fold cross-validation method is used, where the value of k is 5.

D. Classification models

Five models are used to classify CXR images into two classes: COVID-19 and normal. These models are pre-trained networks, namely, ResNet-50 [11], Inception-ResNet-v2 [12], Inception-v3 [13], MobileNet-v2 [14], and GoogleNet [15]. These models are trained on over millions of images in the dataset ImageNet, and can classify images into 1000 classes. The main characteristics of these networks are given in Table I. These networks are fine-tuned with transfer learning by replacing the last learnable layer with three new layers of GlobalAveragePooling2D and two fully connected layers with the number of outputs equal to 1024 and 2 respectively.

TABLE I. MAIN CHARACTERISTICS OF THE MODELS.

Network	Depth	Parameters (Millions)	Image Input Size
ResNet-50	50	25.6	224×224
Inception-ResNet-v2	164	55.9	299×299
Inception-v3	48	23.9	299×299
MobileNet-v2	53	3.5	224×224
GoogleNet	22	7.0	224×224

E. Performance evaluation

To evaluate the performance of the different algorithms used to classify CXR images into two classes, three criteria are calculated, namely, Accuracy, Sensitivity, and Specificity. In terms of positives and negatives, they are defined as:

$$\text{Accuracy (ACC)} = (TP+TN)/(TP+TN+FP+FN) \quad (1)$$

$$\text{Sensitivity (SN)} = TP/(TP+FN) \quad (2)$$

$$\text{Specificity (SP)} = TN/(TN+FP) \quad (3)$$

where TP is the true positive in case of COVID-19 case and TN is the true negative in case of normal case, while FP and FN are the incorrect false positive and false negative predictions for COVID-19 and normal cases.

F. Parameters Settings

The work has been carried out in MATLAB R2021a on a computer equipped with an Intel® Core ™ i7-7800X CPU @ 3.50 GHz processor with 64 GB of RAM and RTX 2080 TI GPU. For models training, we used the Adam optimizer as the optimizer with an initial learning rate of 0.0005, 50 epochs, and mini-batch size of 32.

IV. RESULTS COMPARISON AND DISCUSSION

The obtained results of our implementation of the five models are presented here in the form of:

- Training progress curves for fold-5. These are shown in figures 2 to 6.
- Table of the computed performance metrics. These are presented in Table Ⅱ.
- Confusion matrices. These are shown in figure 7.

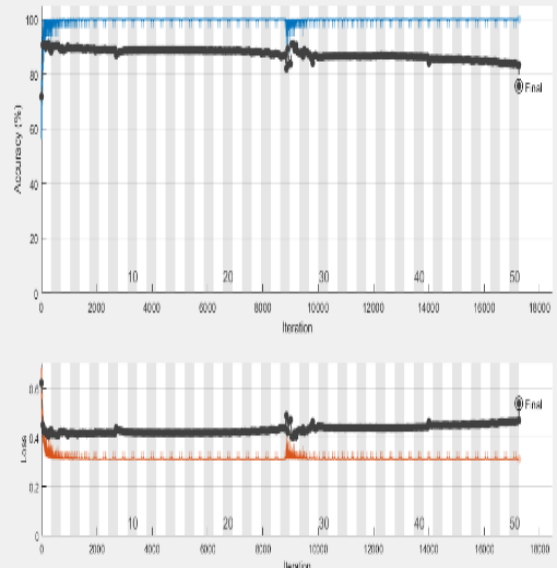

Fig. 2. Training progress curve of the ResNet-50 model.

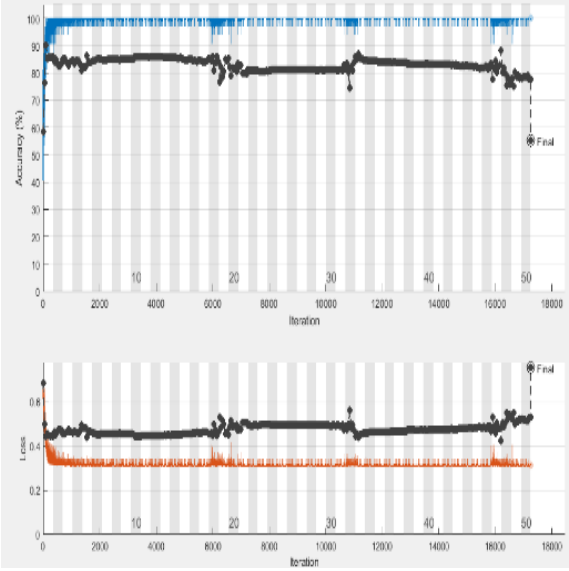

Fig. 3. Training progress curve of the InceptionResNet-v2 model.

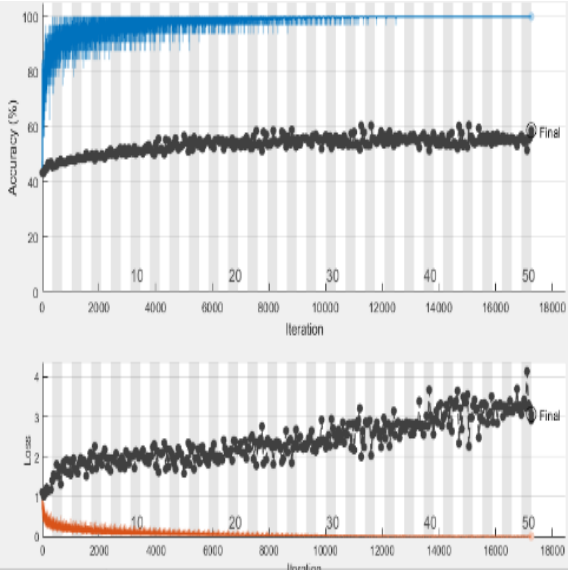

Fig. 4. Training progress curve of the Inception-v3 model.

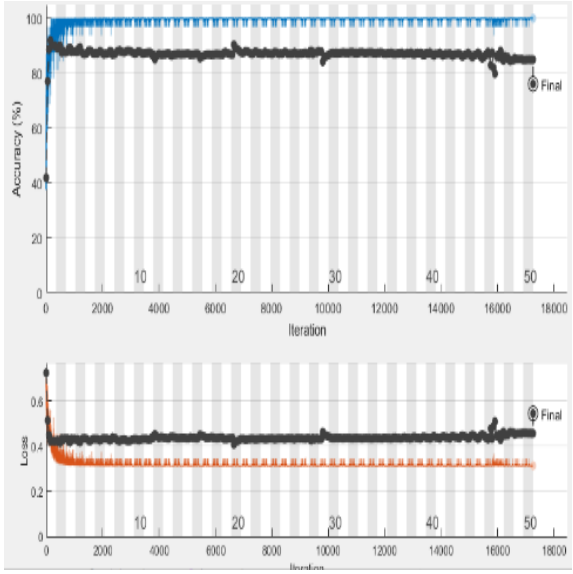

Fig. 5. Training progress curve of the MobileNet-v2 model.

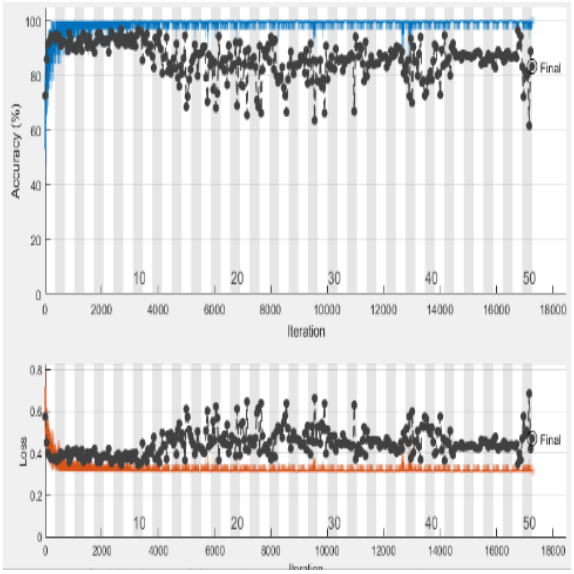

Fig. 6. Training progress curve of the GoogleNet model.

During the training of the models, MATLAB R2021a software can display a progression figure of four curves representing, in the upper part, the training and validation accuracy in blue and black respectively, and in the lower part the loss curves in training and validation in orange and black respectively , depending on the number of iterations (epochs). Figures 2 to 6 show the training progress curves for fold-5 of ResNet-50, Inception-ResNet-v2, Inception-v3, MobileNet-v2, and GoogleNet respectively. We can see from these figures that the highest training accuracy is obtained with the GoogleNet model. The second is ResNet-50 model which is more efficient than MobileNet-v2, Inception-v3, and Inception-ResNet-v2 models. We can also see that the validation loss decreases in five models during the training stage. In figure 4, we can observe that the validation loss values of the Inception-v3 model increase and approaches 3.

Table II shows the values of the three performance criteria given by the implementation of the five models. As can be observed from Table II, The results obtained using the GoogleNet model outperform those obtained from ResNet-50, MobileNet-v2, Inception-v3, and Inception-ResNet-v2 models in accuracy and sensitivity with 95.69% of validation accuracy.

The confusion matrices of COVID-19 and normal validation results of the models for fold-5 are shown in figure 7. The confusion matrix measures the quality of a classification model, with rows representing output classes, and columns representing target classes. The GoogleNet model classified 690 of COVID-19 as true positive and classified 33 images as false positive. In normal case, 1612 images are classified as true negative and 426 images as false negative. The ResNet-50 model classified 704 of COVID-19 as true positive and classified 19 images as false positive. In normal case, 1383 images are classified as true negative and 655 images as false negative.

TABLE II CLASSIFICATION PERFORMANCE RESULTS OBTAINED FROM THE FIVE MODELS.

Models/Folds		Acc	SN	SP
ResNet-50	Fold-1	0.995	0.994	0.995
	Fold-2	0.995	0.992	0.996
	Fold-3	0.992	0.9861	0.9941
	Fold-4	0.9964	0.9917	0.998
	Fold-5	0.7559	0.518	0.9864
	Mean	**0.9469**	**0.8964**	**0.9939**
InceptionRes-Net-v2	Fold-1	0.9848	0.9736	0.9887
	Fold-2	0.9967	0.9917	0.9985
	Fold-3	0.9804	0.9912	0.9769
	Fold-4	0.9942	0.9836	0.998
	Fold-5	0.5516	0.3665	0.9808
	Mean	**0.9015**	**0.8613**	**0.9886**
Inception-v3	Fold-1	0.993	0.994	0.993
	Fold-2	0.99	0.975	0.996
	Fold-3	0.9942	0.9944	0.9941
	Fold-4	0.9971	0.9917	0.999
	Fold-5	0.5867	0.3797	0.978
	Mean	**0.9122**	**0.8669**	**0.992**
MobileNet-v2	Fold-1	0.985	0.988	0.984
	Fold-2	0.99	0.978	0.994
	Fold-3	0.992	0.9861	0.9941
	Fold-4	0.9884	0.9765	0.9926
	Fold-5	0.7606	0.523	0.9866
	Mean	**0.9432**	**0.89**	**0.99**
GoogleNet	Fold-1	0.983	0.983	0.983
	Fold-2	0.99	0.985	0.993
	Fold-3	0.9837	0.9788	0.9854
	Fold-4	0.9898	0.9833	0.9922
	Fold-5	0.8338	0.6183	0.9799
	Mean	**0.9569**	**0.9097**	**0.9867**

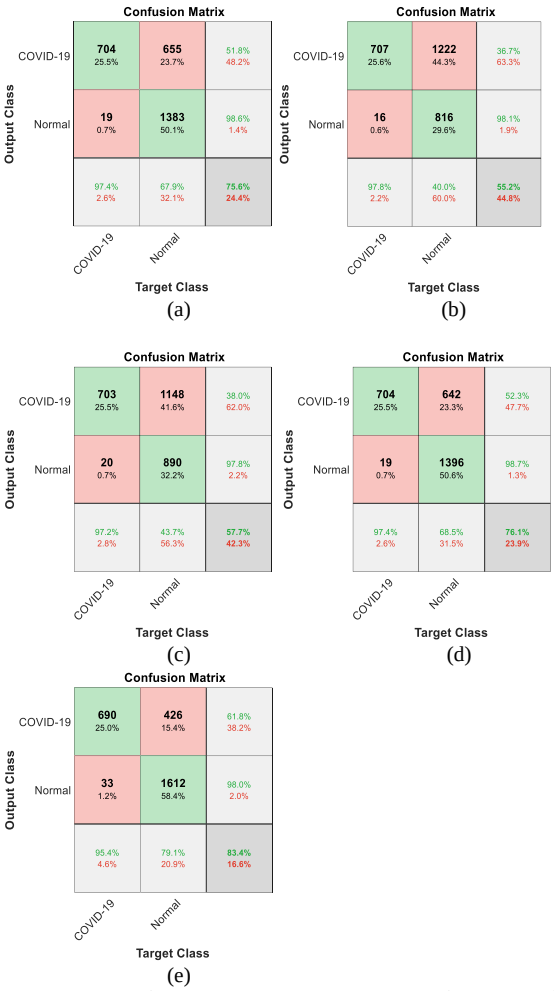

Fig. 7. The confusion matrices obtained using the five models for fold-5 results: a) ResNet-50, b) Inception-ResNet-v2, c) Inception-v3, d) MobileNet-v2, e) GoogleNet.

V. CONCLUSION AND FUTURE WORK

This paper described a comparative study of five deep learning models for CXR COVID-19 images from publically available dataset. These models were used to automatically classify the COVID-19 CXR images into two classes. Among the five models tested, GoogleNet have yielded the highest validation accuracy of 95.69%.

In our future work, we will tackle the problem of generalizing the proposed model to wider range of practical scenarios in order to facilitate diagnosis of more types of diseases from CXR and CT images.

REFERENCES

[1] C. Chen, G. Gao, Y. Xu, L. Pu, Q. Wang, L. Wang, W. Wang, Y. Song, M. Chen, L. Wang, F. Yu, S. Yang, Y. Tang, L. Zhao, H. Wang, Y. Wang, H. Zeng, and F. Zhang, "Sars-cov-2-positive sputum and feces after conversion of pharyngeal samples in patients with COVID-19," Annals of Internal Medicine, 2020.

[2] COVID-19 RADIOGRAPHY DATABASE, https://www.kaggle .com/tawsifurrahman/covid19-radiography-database. Accessed June 15, 2021.

[3] H. X. Bai, "Ai augmentation of radiologist performance in distinguishing COVID-19 from pneumonia of other etiology on chest ct," Radiology, 2020.

[4] K. E. Asnaoui and Y. Chawki, "Using x-ray images and deep learning for automated detection of coronavirus disease," J. Biomol. Struct. Dyn., 2020.

[5] U. Ozkaya, S. Ozturk, and M. Barstugan, "Coronavirus (COVID-19) classification using deep features fusion and ranking technique," Springer, 2020.

[6] I. D. Apostolopoulos and T. A. Mpesiana, "COVID-19: Automatic detection from x-ray images utilizing transfer learning with convolutional neural networks," Phys. and Eng. Sci. in Med., Jul. 2020.

[7] A. Narin, C. Kaya, and Z. Pamuk, "Automatic detection of coronavirus disease (COVID-19) using x-ray images and deep convolutional neural networks," Pattern Analysis and Applications, 2021.

[8] E. E.-D. Hemdan, M. A. Shouman, and M. E. Karar, "COVIDX-Net: a framework of deep learning classifiers to diagnose COVID-19 in x-ray images," arXiv, 2020, [accessed 15-June-2021]. [Online]. Available: https://arxiv.org/abs/2003.11055.

[9] M. Chieregato, F. Frangiamore, M. Morassi, C. Baresi, S. Nici, C. Bassetti, C. Bnà, and M. Galelli, "A hybrid machine learning/deep learning COVID-19 severity predictive model from CT images and clinical data," arXiv, 2021. [accessed 20-June-2021]. [Online]. Available: https://arxiv.org/pdf/2105.06141.

[10] S. J. Pan and Y. Qiang, "A survey on transfer learning," IEEE Transactions on knowledge and data engineering, 2009.

[11] K. He, X. Zhang, S. Ren, and J. Sun, "Deep residual learning for image recognition," Proceedings of the IEEE conference on computer vision and pattern recognition, 2016.

[12] C. Szegedy, S. Ioffe, V. Vanhoucke, and A. A. Alemi, "Inception-v4, inception-resnet and the impact of residual connections on learning," in Thirty-first AAAI conference on artificial intelligence, 2017.

[13] C. Szegedy, V. Vanhoucke, S. Ioffe, J. Shlens, and Z. Wojna, "Rethinking the inception architecture for computer vision," in Proceedings of the IEEE conference on computer vision and pattern recognition, 2016.

[14] M. Sandler, A. Howard, M. Zhu, A. Zhmoginov, and L. C. Chen, "Mobilenetv2: Inverted residuals and linear bottlenecks," in Proceedings of the IEEE conference on computer vision and pattern recognition, 2018.

[15] C. Szegedy, W. Liu, Y. Jia, P. Sermanet, S. Reed, D. Anguelov, D. Erhan, V. Vanhoucke, and A. Rabinovich, "Going deeper with convolutions," in Proceedings of the IEEE Conference on Computer Vision and Pattern Recognition, 2015.

Business Intelligence Platform for Projects Related to the Internet of Things

Bezzaz Soumia
University Larbi Ben M'hidi
Oum Elbouaghi, Algeria
bezzaz.soumia@univ-oeb.dz

Benmerzoug Djamel
Information Systems and Software Technologies
University Constantine 2
Constantine, Algeria
djamel.benmerzoug@univ-constantine2.dz

Lamamra Kheireddine
Electronics and New Technologies Laboratory (LENT)
University Larbi Ben M'hidi
Oum Elbouaghi, Algeria
lamamra.kheireddine@univ-oeb.dz

***Abstract* —**

The exponential growth in the number of connected objects is evidence of a particularly impactful trend in the digital world, driven by the uses of the general public. This innovative technological trend will also have a strong impact on companies, bringing changes to the management of the large amount of data that comes from connected objects. To ensure better management of this data, we have proposed a business intelligence platform called tGRC (Governance, Risk Management and Compliance related to IoT) as a suitable solution for this area.

We believe that this platform is much more important for connected objects because of the heterogeneity of objects, the more or less controlled access to their data and the way their data can be used. Moreover, it is essential that a significant part of the tasks is effectively automated in order to guarantee homogeneous operations when making decisions in compliance with the rules and controlling the risks.

Keywords: Internet of Things, Business Intelligence, tGRC (Governance, Risk Management and Compliance)

I. INTRODUCTION

Increasingly, the Internet of Things (IoT) is invading our daily lives. Connected objects make our lives easier in the rainy domain.

Today, the Internet of Things (IoT) is experiencing accelerated development since the Covid-19 health crisis, the confinement and the new lifestyle habits of users.

The IoT will never stop; billions of objects connected to the Internet will collect data and be at the origin of a flood of information. The problems that arise are the management of this large mass of data collected by these billions of connected objects, the processing of events and computing power, and also the security and confidentiality of personal data.

In order to overcome these problems, we will adapt as a solution the tGRC approach that simplifies the management of the network as well as the management of the huge amount of data from connected objects to meet the needs.

The expected goal is to have a tGRC platform, which can support all decision-making processes from the extraction of data from the database to the dissemination of reports, with the aim of offering decision support and allowing managers to have an overview of the activities processed.

II. INTERNET OF THINGS

The Internet of Things (IoT) refers to all sensors and objects – excluding smartphones and tablets – connected to the Internet to inform the user of the status of the device with which they are associated. But the concept is not limited to the hardware – the device – it also includes connectivity, which depends on the uses to best transmit the data, as well as the software to perform the analysis of this data on a cloud platform.

Connected objects are deployed as well to the general public, to allow the user to manage his home or health, and to manufacturers to optimize their business processes. [1]

A. What is a connected object?

It is an electronic device that can communicate with a smartphone, a touchscreen tablet, a watch, a computer or a television. Communicating means that it can send and receive information, through a wireless, Bluetooth or Wi-Fi link. [2]

According to Thierry Fabing, Deputy Digital Director, AXA France:

"Objects connected to the Internet network which, on the one hand, are objects that have already existed for a long time but are now becoming intelligent and are able to interact and which, on the other hand, are more recent objects in full swing through the contribution of connectivity".

Connected devices (IoT)) rose to (20.35 billion in 2017 from 15.41 billion in 2015 and are expected to reach 51.11 billion by 2023, given the huge surge in investment by technology providers through continuous research and development. To use this increasing number of connected devices and machine-to-machine connection in the manufacturing industry, the need for control and monitoring should become more important; this can be attributed to the increase in devices and systems connected and controlled by the network. [3]

B. connected objects and the Covid-19 crisis

The Covid-19 crisis and the confinement have had an unprecedented impact on society and the economy. Consumer behaviors and expectations have evolved. The adoption of digital technology to overcome the constraints of confinement has accelerated and not only to allow teleworking.

According to the third barometer, French people and Connected Objects, conducted in September 2020 by IFOP

for Boulanger, French people no longer consider connected objects for their security utility or to save time, but as real objects for the improvement of the quality of life. The IoT is closer and more "human".

"There is a shift in the image of connected objects from performance to comfort, timeshare quality and entertainment. The connected object makes it possible to reclaim one's home. Beyond the Covid effect, it is indeed a sustainable trend that seems to be setting in motion. The French are refocusing on their homes and anticipating the increasing time they will spend at home, whether through the deployment of teleworking, or the relocation of leisure activities within the home," says Claire Verbrugge, Marketing Director at Boulanger.

According to the figures, 17% of French people bought a connected object during the confinement. Nearly half of French people who bought a connected object during the confinement did so to improve the comfort of their home, 36% to keep in touch with their relatives. [4]

To ensure effective management of the large amount of data recovered by these connected objects, Business Intelligence (BI) techniques are necessary.

III. BUSINESS INTELLIGENCE (BI)

Business Intelligence refers to the set of technologies that allow companies to analyze data for the benefit of their decision-making. The term Business Intelligence (BI) refers to applications, infrastructures, tools and practices that provide access to information, and to analyze information to improve and optimize the decisions and performance of a company. In other words, business intelligence is the technology-driven process of analyzing data to uncover information that can be used to help business leaders and other end users make more informed decisions. [5]

A. Restitution tool and data analysis

To facilitate access to information for all users according to their business profiles and to extract decision elements to boost overall responsiveness in the company, some tools have been made available to decision-makers, including:

1) Dashboard: in business intelligence dashboards are used in companies to allow the visualization of raw data that aims to make them more accessible and understandable. This visualization gives meaning to this data by using different visual representations and different types of data prioritization.

A good dashboard sheds light at a glance on trends, performance and the path to travel to achieve the objectives that the company has set itself, and reduce any risk taking. [6]

2) Reporting: Reporting is "the set of reports allowing a company to monitor its activity and allows it to evaluate itself through the periodic creation of reports and analytical reports of its activity. These reports are often intended for the manager or the executive body."

The purpose of these regular reports and balance sheets is to make a punctual point on the company's strategy and thus make it possible to evaluate the means implemented. But they also provide decision support for the strategic and economic choices of the company.

B. OBJECTIVES OF BI

The reasons why companies use a decision-making system are common despite the variety of their fields of activity:

• Easy and fast accessibility to information.

• Consistency of information: system data is credible and of high quality.

• Adaptation to changes: Existing data should generally remain unchanged. When technology or needs change, data must be changed by making all users of the system aware.

• Presentation of information on time: Information must be available at the right time in order to react quickly.

• Protection and security of information: the system must allow access control to this confidential information.

• Conversion of the mass of data into a business value: the system, through analysis tools, makes it possible to identify a value that helps in decision-making.

• BI applications facilitate end-user access to information and enable the extraction of data needed for decision-making. [7]

The dashboard is a management tool, reporting is a control tool. some large companies have felt the need to detect and correct risks, also to protect confidential data and especially to have a means of helping to make major strategic decisions.

To do this, business leaders have adopted in-depth initiatives of Governance, Risk Management and Compliance, which is the concept (GRC).

BI centralizes the information and knowledge generated by the GRC approach that provides companies with an in-depth view of all aspects of corporate governance, risk management and compliance to provide a holistic view of business activity as well as decision-making support.

IV. WHAT IS GRC?

GRC is a synchronized approach to three areas, avoiding duplication of effort and ensuring the effectiveness of the approaches used.

GRC refers to an overall governance management strategy, enterprise risk management and regulatory compliance. To better understand, GRC should be seen as a structured approach to aligning IT with business objectives, while effectively managing risk and meeting compliance requirements.

A well-planned GRC strategy has many benefits: improved decision making, optimal IT investments, elimination of silos and reduced fragmentation between divisions and departments, to name a few. GRC can help you align your IT activities with your business goals, requirements, effectively manage risk and stay on top of compliance. [8]

In 2019, there were eight billion connected objects in the world, according to US research firm 451 Research, which predicts that number will be 13.8 billion devices by 2024. [1]

Behind connected objects lies an even larger universe: that of data. And while there are undoubtedly challenges in

designing connected hardware, it is in the data that the real potential of the IoT lies.

To ensure that this data is managed and that these networks of objects function properly, it seems more promising to us to integrate these functionalities into a more general framework of governance, risk management and compliance, which is the tGRC approach.

V. THE TGRC APPROACH

The definition of tGRC follows the principle of classic GRCs, adding the specific features of loTs and adding, in particular, the loT project management part in the governance part and diagnosis and corrective maintenance in the risk management part. In addition, it only integrates processes that can be automated.

GRC + IoT + BI = tGRC

Here is a more precise definition of the three dimensions of tGRC:

A. Governance

Governance concerns the management of the Internet of Things project, and also defines the modes and tools for monitoring the system during its operation in real time, as well as the adequate metrics to evaluate the indicators for strategic decision-making and reporting by BI tools, for example. This level also implements automatic mechanisms for readjusting the system to meet predefined risk levels and compliance with standards and regulations.

B. Risk

Defines how to manage technical or management risks. This dimension must be able to identify, assess, analyze and respond to the various risks involved.

C. Compliance

Ensures the alignment of the IoT project with the various regulations and standards, the respect of the law, the security rules, the privacy rules, the internal rules of the organization. In this dimension, business rules are defined.

VI. BI AND THE TGTR APPROACH

Business Intelligence centralizes the information and knowledge generated by the tGRC approach, which provides companies with an in-depth view of all aspects of corporate governance, risk and compliance to offer a global view of the company's activity and support for decision-making.

This tGRC approach is fed by data processed by a business intelligence platform and feeds the same platform with risk and compliance analysis results and guidance from the governance side.

To illustrate the integrated tGRC approach, we opted for a real case study in the context of "Algerian Water" organization.

VII. PRESENTATION OF THE HOST ORGANIZATION « ADE »

A. Knowing the ADE

The **Algerian Water** (ADE) is a national public establishment of an industrial and commercial nature with legal personality and financial autonomy. It was created by the executive decree n° 01-101 of 27 Moharram 1422 corresponding to April 21, 2001. The establishment is placed under the supervision of the Minister in charge of water resources, and its head office is located in Algiers.

B. Missions

The establishment is responsible for:

Within the framework of the national development policy: to ensure the implementation of the national drinking water policy throughout the national territory, through the management of production, transport, treatment, storage, conveyance, distribution and supply of drinking and industrial water as well as the renewal and development of the related infrastructures.

In this respect, it is responsible, by delegation:

The standardization and monitoring of the quality of distributed water; initiating any action aimed at saving water, particularly by improving the efficiency of transfer and distribution networks; introducing any water conservation technique; the fight against wastage by developing information, training, education and awareness-raising actions for users, the design, with the public education services, of school programs disseminating the culture of water saving; to plan and implement the annual and multi-year investment programs. [9]

VIII. STUDY OF THE EXISTING SITUATION

In order to have the right information and come up with a clear study of the existing of the ADE, we worked in collaboration with the following sources:

- The person in charge of the follow-up of the water quality (in charge of quality of the center).
- The director of the Laboratory of analysis and quality control (Oum El bouaghi).

A. Critique of the existing

The problems posed at the level of the ADE are:

- The storage of information

The problem of data storage exists in this organization, since these data are transmitted to the company by agents on sheets, and for the storage the employees use programs like EXCEL tables. This situation becomes unnecessary with the evolution of the strategies.

- Procedure: Management of non-conformities

In case of non-conformity, ADE follows the following procedure:

- The head of the center or the sector of the incriminated place must come on site to note the degree of water pollution on the network or at the customer's place.
- The head of the concerned center must isolate the network as soon as a health risk is noticed.
- The center manager must inform the unit manager, the Laboratory.

- The Center shall take corrective action and request a retest from the Laboratory.
- The Center shall take steps to inform of the restriction of water use for domestic purposes only and specify the alternative means for drinking water that will be implemented. This information is done by posting or door-to-door.
- The center informs the commune by fax or simple letter.
- As soon as the analyses indicate the return of the conformity of the water, the decision to put the network back into service is taken by the Head of the Center.
- The center must inform its subscribers of the return to service of the network.

It can be seen that these provisions are followed in an operational way (classic, traditional).

B. The Proposed Solution

After seeing the difficulties that ADE encounters, connected objects represent the most adaptable solution to this domain. For this reason, we think that the integrated tGRC approach is much more important for connected objects because of the heterogeneity of the objects, the more or less controlled access to their data and the way their data can be used. Moreover, it is essential that a significant part of the tasks are effectively automated in order to guarantee homogeneous operation when making decisions in compliance with the rules and by controlling the risks. When tens of billions of objects will be deployed, some data that must remain confidential will be accessible. It would be essential to have automatic tools that would enable networks of objects that meet specific needs.

We are convinced of the need to develop this type of tools for the IoT and we think that tools such as tGRC associated with business intelligence tools with a connected object that can measure or detected the concentration of one of the parameters in the water has been proposed to facilitate one of the activities of the procedure for managing a non-conformity of this organization, are good candidates to ensure these tasks, In order to concretize this approach for this area and to prove the automation of some tasks of this organization by the tGRC platform, and to ensure effective management of the recovered data.

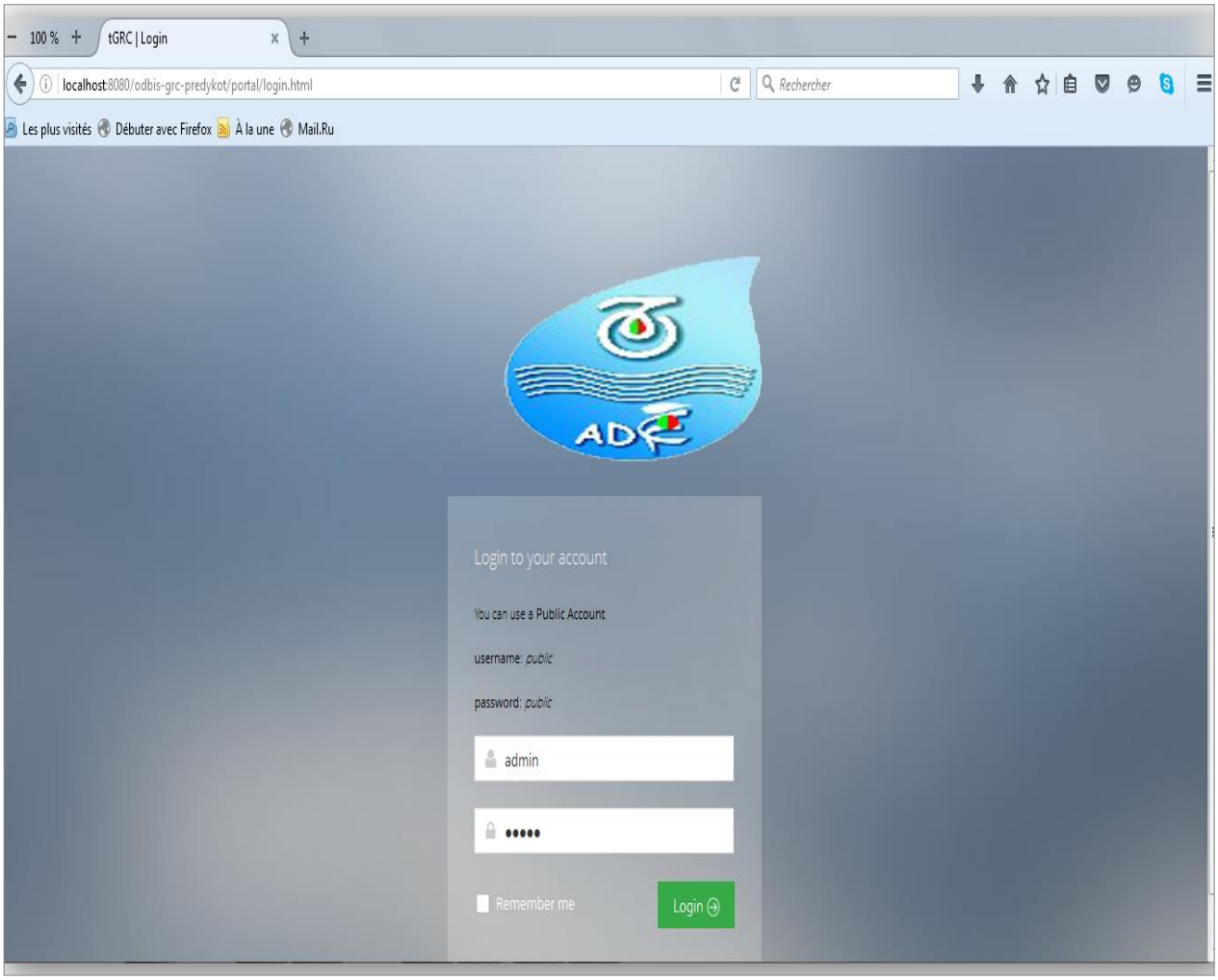

Fig. 1. system authentication page

C. *System objectives*

tGRC gives users an overview of the current situation of the targeted problems. It can be the starting point for a data overview. Users do not have to search for information through pages of useless data that are not meaningful. Instead, through certain predefined parameters, the data is logically organized and displayed through different types of graphs and tables on the dashboards. Users can make informed and evidence-based decisions based on the information on the dashboard, as the dashboard can identify and show the data calculated by the right parameters directly. Overall, the dashboard steering is like a compass, which allows users to analyze large amounts of complex data with visual and graphical reports. In addition, the dashboard direction also provides features such as data source management, define management, dashboard management and report data management. Users can create their own data source to connect to their databases. After that, they can define the dataset. This way, users can retrieve the data they are interested in through SQL queries.

Finally, users can create their own dashboard with their defined data. Data tables and different types of charts are supported by the dashboard. In addition, users can download reports with the reporting module and export these reports in different types of formats, including Word, Excel, pdf, power point and so on.

One of the goals of this project was to design a business intelligence platform that helps decision makers and managers make decisions based on the data received and interpreted in the form of a graph in what is called a Dashboard.

D. *Dashboard management*

- **Add a table:** Click on the "New table" button to add a table to this dashboard. Choose a dataset and the columns you are interested in. Then click on the "Preview" button to preview the table. Save the table. If you can't save check the table name field, as required. Click "show" to verify the table.
- **Add a chart:** click on the "New Chart" button to add a chart, we can add different types of charts

Choose a dataset, the category field and the value field you are interested in. Preview the chart and save it. If you can't save it, check the name of the graph, as required.

- **Edit the dashboard.**
- **Delete the dashboard.**
- **Previewing the dashboard:** To allow decision makers to view the data received from a connected object permanently and make decisions you should take a look at the dashboard by going to the "Governance" menu and choosing "Dashboard", the page below will be displayed:

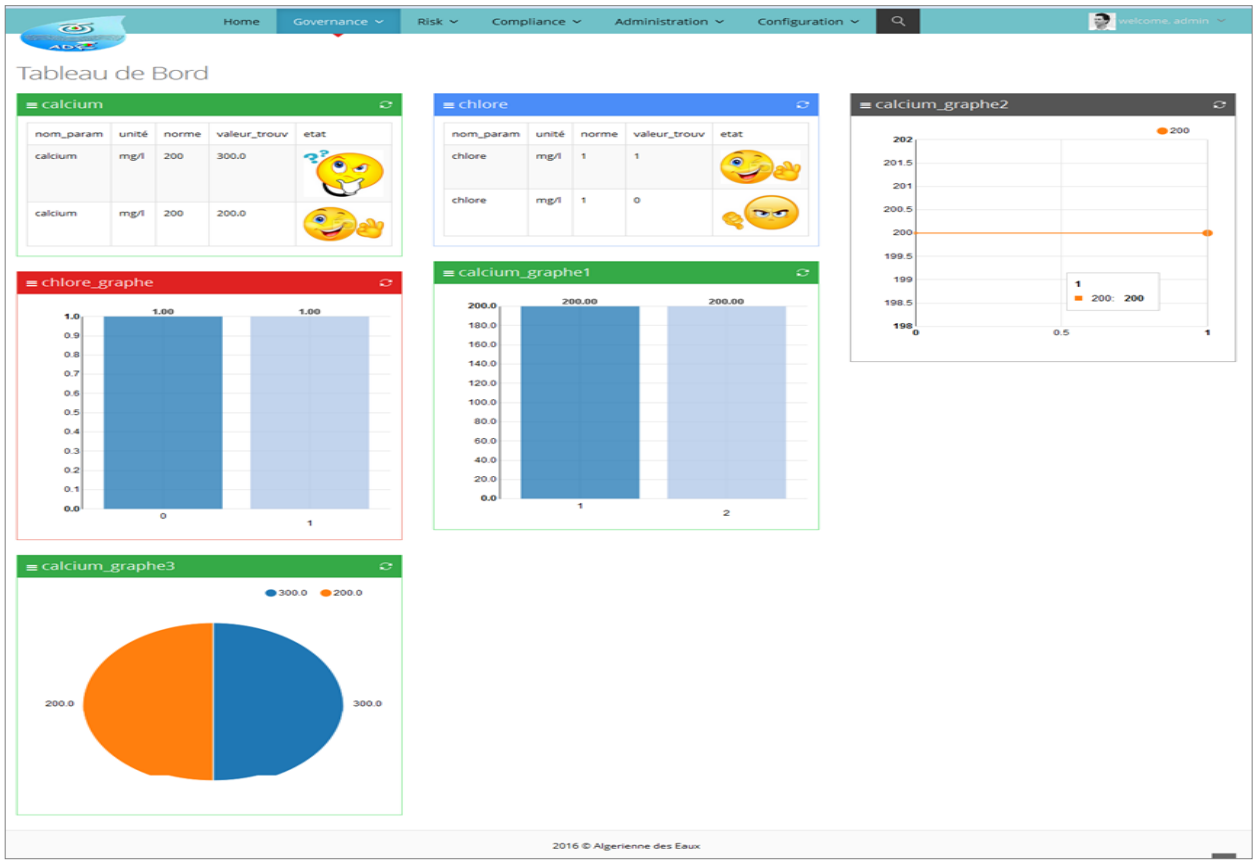

Fig. 2. An example of a dashboard on the tGRC platform

These smileys are presented as indicators to show that the result is good or not.
This platform is also designed to use another business intelligence tool which is reporting.
From this page you can do the following:

Download the report: click on the "Browse" button or drop the file on the empty area to download a new report.
After choosing a report, it will be downloaded automatically. And it will be presented in the following list.
View the report: you can click on the "view" button to display the report.
You can also click on the export button to export the report in Word, power point or PDF format.
Delete a report: in the list of reports, click on the "delete" button, a dialog box will appear to confirm the deletion.

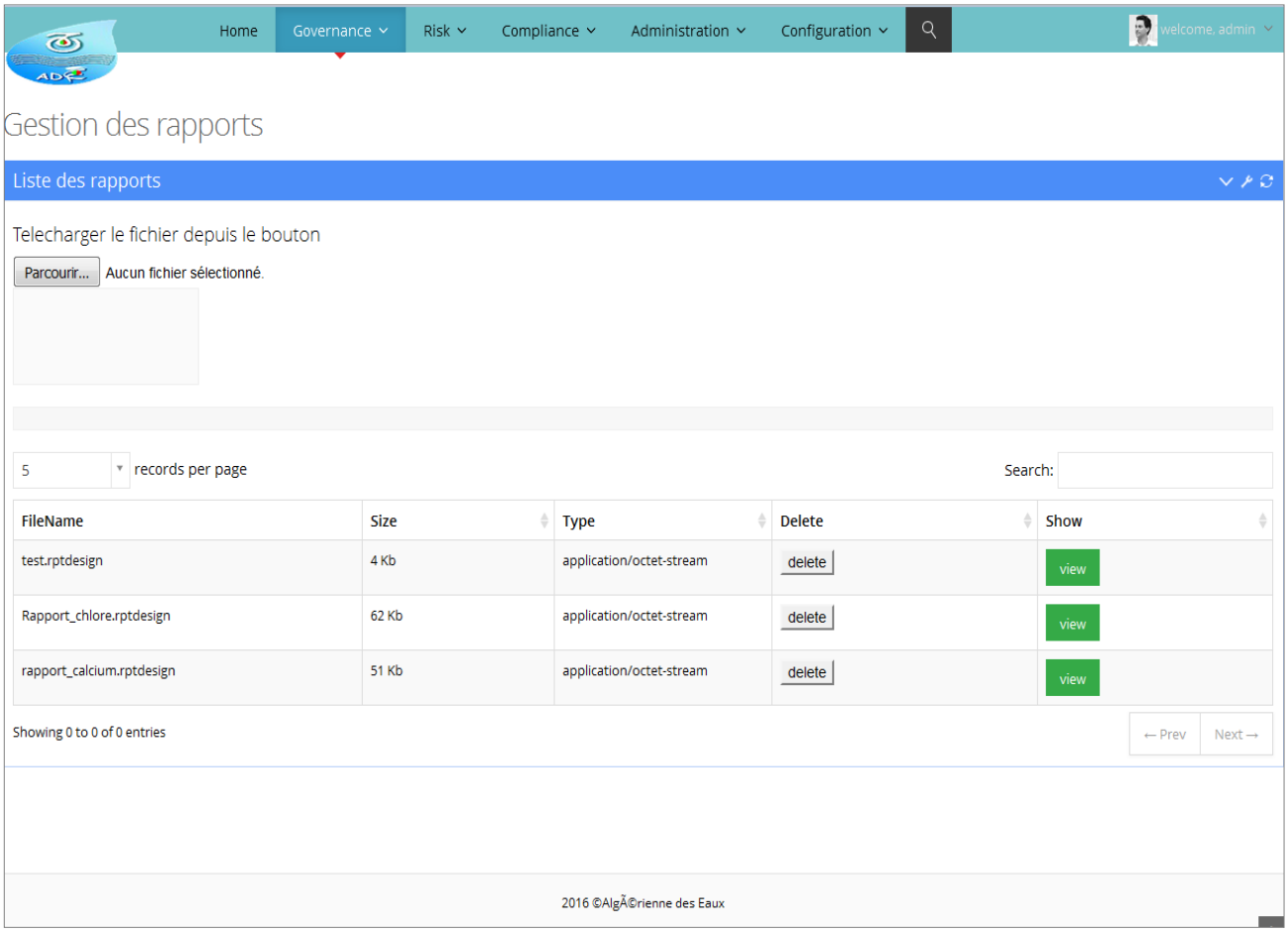

Fig. 3. An example of a report on the tGRC platform

IX. CONCLUSION:

Internet of Things (IoT) technology has tremendous and growing potential to connect objects, visualize data and interact with connected people in an efficient way. Recognizing this, a large volume of data is being generated which is constantly increasing.

The tGRC (Governance, Risk and Compliance for IoT) approach offers a better management and processing of this mass of data, with the aim of simplifying the decision-makers to have useful information that can help them to pilot more efficiently, and help them to take strategic decisions and react quickly, through the services offered by the Business Intelligence (BI) techniques

Several research and implementation perspectives are emerging from this work. Indeed, the realization of our tGRC approach has allowed us to identify several work perspectives:

- Exploiting Big Data techniques to manage and secure the large amount of information disseminated by connected objects.
- Exploiting Cloud Computing technology to migrate our application as a Cloud service (SaaS: Software as a Service).

Our work will always be open to criticism and suggestions that could readjust it, especially to improvements that could be brought to it by further studies. Our ultimate hope is that it will help users and that this study will be a model for others.

REFERENCES

[1] JDN: https://www.journaldunet.com/ebusiness/internet-mobile/1492599-iot/ published on 22 July 2020

[2] The DGCCRF. *objets connectés : les risques à connaitre* on 21/12/2020

[3] Cody Garrison. *La croissance dans le monde dynamique et tendances du Marché prevision 2024.* August 2021

[4] Mourad Krim , Journaliste and report IT . *Les Français, les objets connectés et la crise : une consommation utile et éthique*. 2020

[5] By Bastien L. *Business Intelligence ou informatique décisionnelle : définition et outils.* January 2021.

[6] By Kilian Bazin. *10 étapes pour faire un tableau de bord.* 2021.

[7] Mrs. Khouri Selma and Miss. Lanasri Dihia, mémoire Master of Science in Computer Science, « Étude de la conception des projets BI selon les principes Agiles », 2015.

[8] Cédric GASPARD. *Comprendre la GRC.* Synetis Parole d'expert©. April 2019.

[9] L'Algérienne des Eaux (ADE). Available on-line at: https://www.ade.dz/index.php/presentation/presentation

A DSIM Control Using Artificial Neural Network Controller

Naouel HAMDI , Ouafa OURZIFI , Ali DJEBABLA

Laboratory of Electronics and New Technology (LENT) University of Oum El Bouaghi, Algeria

Abstract. *This paper presents a vector control indirect (IFOC) of double –star induction machine (DSIM) based on artificial neural network (ANN). Double star induction machine are used in high-power applications because they are characterized by efficiency and their ability to power splitting. The objective of this work is the comparison between the CVI indirect vector control with the PI regulator and the CVI indirect vector control with the artificial neural network regulator (ANN) MULTI-LAYER (MLP) found us that the tuning by the neural networks is good and robust in comparison of the PI. Simulation results through MATLAB/Simulink are using for both controls, the results obtained showed a very satisfactory behavior of this machine*
.

Keywords: vector control indirect (IFOC), doubly stator induction machine (DSIM), Artificial neural network (ANN).

NOMENCLATURE

DSIM doubly stator induction machine
MLP The Multilayer Perceptron
ANN artificial neural networks
CVI control vector indirect
PI proportional integrator
V_{sd}, V_{sq} *d*- and *q*-axis components of the stator voltage.
V_{rd}, V_{rq} *d*-and *q* -axis components of the rotor voltage.
i_{sq}, i_{sq} *d*- and *q*-axis components of the stator current .
i_{rd}, i_{rq} *d*- and *q*-axis components of the rotor current.
R_s Stator phase resistance.
R_r Rotor phase resistance.
M_{sr} Mutual inductance between the stator and rotor.
L_s Stator inductance.
L_r Rotor inductance.
P Number of poles of the induction machine.
ω_s Stator pulsation.
ω_r Rotor pulsation.
C_{em} **Electromagnetic torque.**

1. Introduction

Nowadays, many industry segments need doubly star induction motors are one of widely used motor. Due to their advantages in power segmentation, reliability, and minimized torque pulsations. Such segmented structures are very attractive for high-power applications since they allow the use of lower rating power electronic devices at a switching frequency higher than the one usually used in three-phase AC machine drives. This machine has been used required in many applications, such as pumps, fans, compressors, rolling mills, cement mills, mine hoists[10].
In recent years, the multiphase machines, five-phase and six-phase induction are the most considered in the literature. The present study is focused on the doubly star Induction motor. This type of machine is composed by two three-phase windings shifted by 30 degrees and a standard simple squirrel-cage rotor [11].
In order to ensure an effective control of DSIM, several methods have been proposed [12]. An alternative solution is the use of indirect vector Oriented Control (IFOC) is modern technique for high-performance control of MLI inverter fed DSIM. To achieve a variable speed operation a power electronics inverter can be used.

The indirect vector control theory is the base of a special control method for doubly star induction motor drives. With this theory doubly star induction motors can be controlled like a separately excited DC motor. This method enables the control of field and torque of the DSIM independently (decoupling) by manipulating the corresponding field oriented quantities [13].

With the aim of improving the performance of traditional IFOC-based electrical drives, artificial neural network control is increasingly attracting the attention of many scientists to the configuration and design of the artificial neural network controller for control. The proposed neural network controller has been successfully simulated on a simulink model. The performance of ANN compared to conventional PI.
This paper is structured as follows: In Section II the model of the DSIM is presented, a suitable transformation matrix is used to develop a simple dynamic model. We will describe the indirect Field Oriented control.
In section III the control vector strategy for this system is proposed. In section IV, the controllor ANN is proposed.
At the end, in section V we shows simulation results for a comparison between the performances of controller ANN field oriented control DSIM with those obtained from conventional PI controller under various conditions operation

2. MATHEMATICAL MODEL OF THE DSIM

A . Three-phase model of MASDE on real axes

The schematic representation of the double star asynchronous machine in electrical space is given in the following figure (1)
The doubly star induction machine represented by two stators windings : As1, Bs1, Cs1 and As2, Bs2, Cs2 which are displaced by $\alpha = \frac{\pi}{6}$ electrical angle .and the rotor windings (Ar, Br, Cr) are sinusoidal distributed and have axes that are displaced apart by $\frac{2\pi}{3}$
The customary assumptions are adopted [2]:
1. Motor windings are sinusoidal distributed.
2. The saturation of magnetic circuit is neglected.
3. The two stars have same parameters.
4. The flux path is linear.
The windings of the DSIM are shown in Figure 1

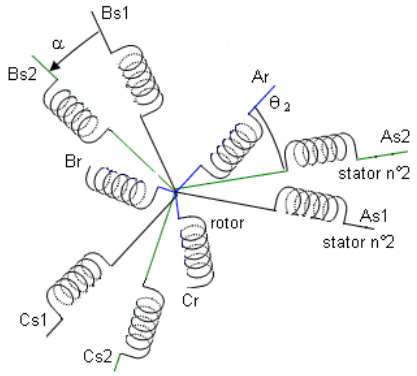

Figure 1. Doubly stator winding representation

The voltage equations for stator and rotor circuits for model of the DSIM motor have the following matrix form [4]:

$$\begin{cases} [V_{abc,s1}] = [R_{s1}][I_{abc,s1}] + \dfrac{d}{dt}[\psi_{abc,s1}] \\ [V_{abc,s2}] = [R_{s2}][I_{abc,s2}] + \dfrac{d}{dt}[\psi_{abc,s2}] \\ [V_{abc,r}] = [R_r][I_{abc,r}] + \dfrac{d}{dt}[\psi_{abc,r}] \end{cases} \quad (1)$$

With:
$[V_{abcs1}], [V_{abcs2}], [V_{abc,r}]$: stato and rotor voltages
$[I_{abc,s1}], [I_{abc,s2}], [I_{abc,r}]$: stator and rotor currents
$\psi_{abc,s1}$, $\psi_{abc,s2}$, $\psi_{abc,r}$:flux stator and rotor
$[R_{s1}]$, $[R_{s2}]$, $[R_r]$:Resistance matrices stator and rotor

B.Two-phase model

Park's transformation [6] is based on the transformation of a three-phase system of axes (a, b, c) into an equivalent two-phase system of axis (x, y) and vice versa, with the creation of a rotating electromagnetic field with magneto motive forces figure(2).

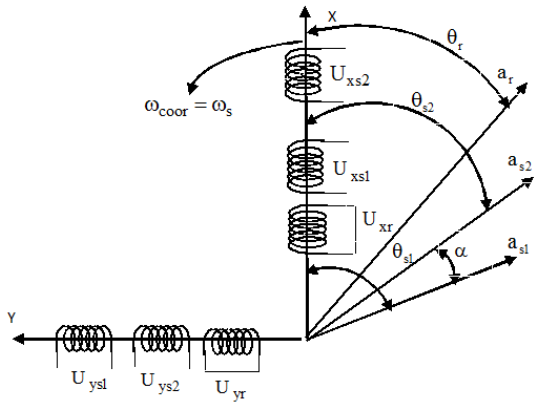

Figure 2: Schematic representation of the DSIM PARK model

Park's transformation [7] is based on the transformation of a three-phase system of axes (show Figure 2). The schematic representation of the DSIM PARK model (a, b, c) into an equivalent two-phase system of axis (x, y) and vice versa, with the creation of a rotating electromagnetic field with magneto motive forces.

$$\begin{cases} V_{xs1} = R_{s1} i_{xs1} + \dfrac{d\psi_{xs1}}{dt} - \omega_s \psi_{ys1} \\ V_{xs2} = R_{s2} i_{xs2} + \dfrac{d\psi_{xs2}}{dt} - \omega_s \psi_{ys2} \\ V_{ys1} = R_{s1} i_{ys1} + \dfrac{d\psi_{ys1}}{dt} + \omega_s \psi_{xs1} \\ V_{ys2} = R_{s2} i_{ys2} + \dfrac{d\psi_{ys2}}{dt} + \omega_s \psi_{xs2} \\ 0 = R_r i_{xr} + \dfrac{d\psi_{xr}}{dt} - \omega_{gl} \psi_{yr} \\ 0 = R_r i_{yr} + \dfrac{d\psi_{yr}}{dt} + \omega_{gl} \psi_{xr} \end{cases} \quad (2)$$

With:
$V_{s1,xy}$, $V_{s2,xy}$:Stator voltages *xy* components
$I_{s1,xy}$, $I_{s2,xy}$, $I_{r,xy}$:Stator and Rotor currents xy components
$\psi_{s1,xy}$, $\psi_{s2,xy}$, $\psi_{r,xy}$: Stator and Rotor flux xy components.
The relation flux and current are :

$$\begin{cases} \psi_{xs1} = L_{s1} i_{xs1} + L_m (i_{xs1} + i_{xs2} + i_{xr}) \\ \psi_{xs2} = L_{s2} i_{xs2} + L_m (i_{xs1} + i_{xs2} + i_{xr}) \\ \psi_{ys1} = L_{s1} i_{ys1} + L_m (i_{ys1} + i_{ys2} + i_{yr}) \\ \psi_{ys2} = L_{s2} i_{ys2} + L_m (i_{ys1} + i_{ys2} + i_{yr}) \\ \psi_{xr} = L_r i_{xr} + L_m (i_{xs1} + i_{xs2} + i_{xr}) \\ \psi_{yr} = L_r i_{yr} + L_m (i_{ys1} + i_{ys2} + i_{yr}) \end{cases} \quad (3)$$

Where:
Lm: Cyclic mutual inductance between stator 1, stator 2 and rotor.
Ls1,s2,r: the inductance of a stator 1, stator 2 and rotor respectively.
Ls1+Lm , Ls2+Lm, Lr+Lm: the total inductance of a stator 1, stator 2 and rotor respectively.
The electromagnetic torque and the mechanical equations can be written as:

$$C_{em} = \frac{3}{2} P \frac{L_m}{L_m + L_r} [\psi_{xr}(i_{ys1} + i_{ys2}) - \psi_{yr}(i_{xs1} + i_{xs2})] \quad (4)$$

$$J \frac{d\Omega}{dt} = C_{em} - C_r - k_f \Omega \quad (5)$$

3 . VECTOR CONTROL OF THE DSIM FLUX STRATEGY

The technique of vector control is based on a control law leading to a characteristic adjustment similar that of a DC machine with separate excitation. The vector control with rotoric flux oriented concerns.
The constraint of the rotor flux orientation can be written as, $\psi_{rq} = 0$ and $\psi_{rd} = \emptyset_r$, which consider that the assumption of the constant stator flux [5].
The expressions of the rotoric currents may be given as:

$$i_{dr} = \frac{1}{l_m + l_r} [\psi_r - l_m (i_{ds1} + i_{ds2})] \quad (6)$$

$$i_{qr} = \frac{-l_m}{l_m + l_r}\left(i_{qs1} + i_{qs2}\right) \quad (7)$$

$$\psi_{ds1} = \hbar_1 i_{ds1} + l_r \sigma i_{ds2} + \sigma \psi_r^* \quad (8)$$

$$\psi_{qs1} = \hbar_1 i_{qs1} + l_r \sigma i_{qs2} \quad (9)$$

$$\psi_{ds2} = \hbar_2 i_{ds2} + l_r \sigma i_{ds1} + \sigma \psi_r^* \quad (10)$$

$$\psi_{qs2} = \hbar_2 i_{qs2} + l_r \sigma i_{qs1} \quad (11)$$

where

$$\sigma = \frac{l_m}{l_m + l_r} \quad (12)$$

$$\hbar = l_{s1,s2} + \sigma l_r \quad (13)$$

We have

$$\psi_r^* = l_m\left(i_{ds1} + i_{ds2}\right) \quad (14)$$

$$i_{qr} = \frac{-\omega_g^* \psi_r^*}{R_r} \quad (15)$$

After replacement we find

$$\begin{cases} V_{ds1}^* = R_{s1} i_{ds1} + l_{s1} \frac{d}{dt} i_{ds1} - \omega_s^*\left(l_s i_{qs1} + T_r \psi_r^* \omega_{gl}^*\right) \\ V_{qs1}^* = R_{s1} i_{qs1} + l_{s1} \frac{d}{dt} i_{qs1} + \omega_s^*\left(l_s i_{ds1} + \psi_r^*\right) \\ V_{ds2}^* = R_{s2} i_{ds2} + l_{s2} \frac{d}{dt} i_{ds2} - \omega_s^*\left(l_{s2} i_{qs2} + T_r \psi_r^* \omega_{gl}^*\right) \\ V_{qs2}^* = R_{s2} i_{qs2} + l_{s2} \frac{d}{dt} i_{qs2} + \omega_s^*\left(l_{s2} i_{ds2} + \psi_r^*\right) \end{cases} \quad (16)$$

4 .CORRECTEUR WITH ARTIFICIAL NEURAL NETWORKS

The corrector with neural networks was originally proposed to identify the critical point of a system to be controlled.

The motivation was, by automating the measurement procedure, increase safety and reduce the experimental time required compared to conventional controllers.

A . definition

An artificial neural networks (ANN) (is a set of formal neurons (simple computing units, processor nodes) associated in layers (or subgroups) and operating in parallel. In a network, each subgroup does an independent treatment of the others and transmits the result of its analysis to the next subgroup. The information given to the network will therefore be propagated layer by layer. From the input layer to the output layer, passing either through none, one or more intermediate layers (known as hidden layers). It should be noted that depending on the learning algorithm, it is also possible to propagate information backwards ("back propagation"). Usually (except for the input and output layers), each neuron in one layer is connected to all neurons in the previous layer and the next layer. ANNs have the capacity to store empirical knowledge and make it available for use. The processing skills (and therefore the knowledge) of the network will be stored in the synaptic weights, obtained by adaptation or learning processes [5].

B.operation of ANN

The functioning of an ANN is based on the formal neuron which calculates the sum of its inputs and then this value passes through the activation function to produce its output (fig3).

As a rule, the calculation of the value of this function can behave in two stages [8]:

A linear combination of inputs:

$$v = \sum_{i=1}^{n} w_i x_i + b \quad (17)$$

The output of the neuron is

$$y = f(v) = f\left(\sum_{i=1}^{n} w_i x_i + b\right) \quad (18)$$

When input signals (x_i), Les (w_i) are called synaptic weights, (b) is called bias.

(f): is the activation function of the neuron (step, sigmoid, Gaussian ...).

Next in the backward phase, the error of each neuron is calculated, which is essentially: Target - Actual Output [1].

$$E(k) = \frac{1}{N} \sum_{n=1}^{k} \left(d_i(k) - y_i(k)\right)^2 \quad (19)$$

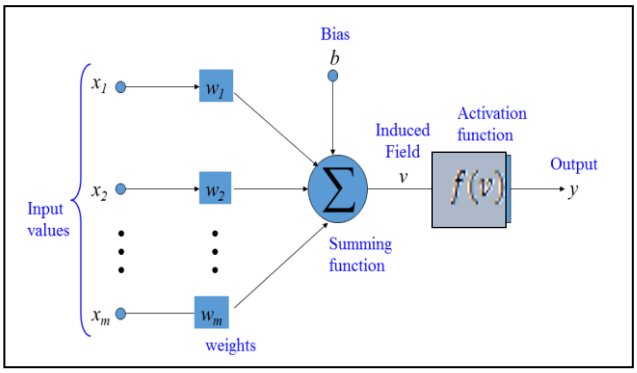

Fig.3: Model of an artificial neuron

C. The Multilayer Perceptron MLP

A Learning algorithm performs the adaptation of bias and weights of the network to minimize the error between the input vector and the neural output vector (fig4). The criterion of error minimization is:

$$e = \sum_i (d_i - x_i)^2 \quad (20)$$

The learning algorithm used in our work is that of the error backpropagation because the latter is best suited to the learning of typMLP neural networks [3].

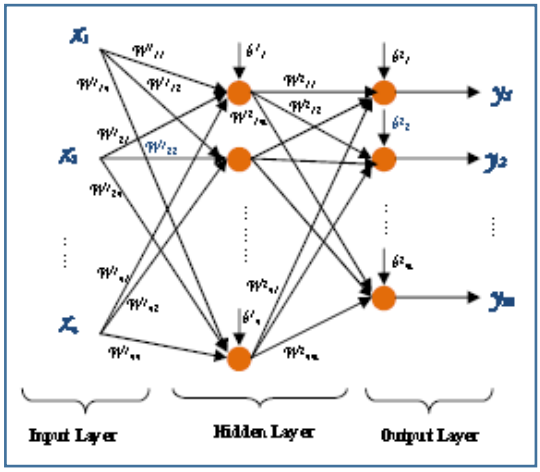

Fig.4:Example of a Multi-Layer perceptron network.

5. SIMULATION RESULTS

In order to know the best DSIM control technique, a comparative study is essential between the two previously mentioned controls (classical CVI-PI, and CVI -neuronal). The following figure shows the comparison between them:
The test: Wr = 300rad / s; Cr = 14N.m at time t = [1.5, 2.5] s.

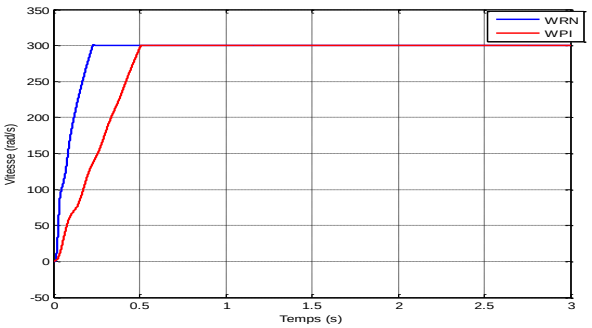

Fig-5: Comparison between CVI-NN and CVI-PI speeds.

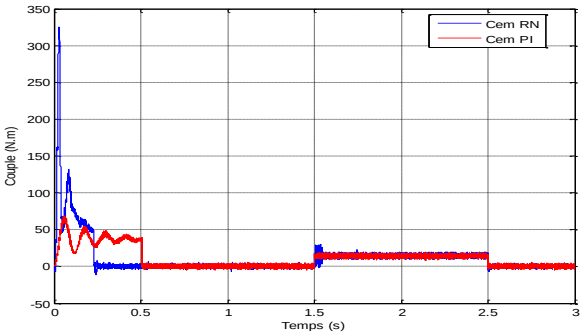

Fig-6: Comparison between the torque of the CVI –PI and CVI-NN

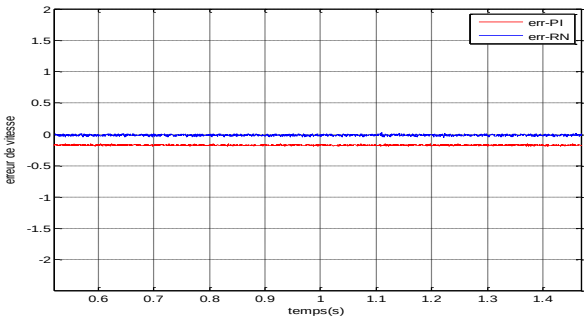

Fig-7 Speed error between CVI-PI and CVI-RN.

The figures show the comparison of dynamic speed response and electromagnetic torque and speed error for indirect vector control by neural regulation and classical PI regulator
We notice that the response time is faster and the speed follows the reference speed well in the case of CVI-NN in an instant t = 0.28sec On the other hand the CVI-PI in an instant t = 0.51sec
We also notice that the torque with the NN regulators at the start time of the large oscillations, but quickly returned to the value close to zero in a short time (t = 0.28sec). on the other hand in the CVI-PI of the oscillations until time (t = 0.51sec). Moreover after stabilization, the shape of the electromagnetic couple shows that follows the resistive couple. with great precision and a fast reaction.
In figure (7) (the error) shows the comparison of the speed error for CVI-RN and CVI-PI. It is noted that the error in speed of the neural regulation (CVI-NN) is almost non-existent, which indicates that the speed of rotation follows the reference speed well. the opposite for the speed error of the control by PI (CVI-PI) equal to 0.2. This indicates the divergence between the rotational speed and the reference speed, which means that there is an improvement in tracking accuracy and a decrease in error for indirect vector control by neural regulation.

CONCLUSION

This work has been the subject of the application of indirect vector control of the double star asynchronous machine based on neural regulation, the main objective being torque and speed regulation. In this context, we first presented a theoretical reminder on the double star machine.
The various simulations made show that the regulation system gives good static and dynamic performance.
From this fact, we conclude that the speed and torque adjustment by ANN regulator brings remarkable improvements compared to the vector control with PI regulator. Because the ANN regulator offers good static and dynamic performance with a time of shorter response and without overshoot.

Appendix

Parameter's of DSIM

Pn= 4,5 kW
Vn= 220 V
In = 6.5 A
Rs1= 3,72 Ω
Rs2= 3,72
Rr = 2,12 Ω
Ls1= 0,022H
Ls2= 0,02H
Lr= 0,006 H
Lm = 0,3672 H
J = 0,0625 kg.m2
Kf= 0,001 N.m.s/rad
f = 50 Hz
P = 1

References

[1] Souha Boukadida, Soufien Gdaim, Abdellatif Mtibaa, "direct torque control for asynchronous machine using artificial neural networks", 14th international conference on Sciences and Techniques of Automatic control & computer engineering - STA'2013 Sousse, Tunisia, December 20-22, 2013

[2] Lallouani Hellali, Saad Belhamdi «speed control of doubly star induction motor (DSIM) using direct field oriented control (DFOC) based on fuzzy logic controller (FLC) » .Advances in modelling and analysis G Vol 73,No4 December 2018,pp128-136Journal

[3] Gning Ndeye « robust control of double star pmsg using artificial neural network » , 2019 IEEE 2nd International Conference on Renewable Energy and Power Engineering

[4] R. Moghe, D. Divan, D. Lewis, and J. Schatz, "Turning Distribution Feeders into STATCOMs," *IEEE Trans. Ind. Appl.*, vol. 53, no. 2, pp. 1372–1380, 2017, doi: 10.1109/TIA.2

[5] O. ASSAS, « Classification floue des images », Thèse de Doctorat de l'université de Batna, Algérie, Décembre 2013 *IEEE Access*, vol. 5, pp. 16684–16692, 2017, doi: 10.1109/ACCESS.2017.2749119

[6] E. Merabet « Amélioration des Performances de Régulation d'une Machine Asynchrone Double Etoile par les Techniques de l'Intelligence Artificielle ». Thèse de

doctorat, Université de Batna. 2013.. 548

[7] G.SALLOUM, ''contribution à la commande robuste de la machine asynchrone a doublé alimentation'', docteur de l'institut national polytechnique de Toulouse, 2007

[8] Gupta K, Bhatnagar P. « Chapter 2 –Basics of multilevel inverters. In:Multilevel Inverters Conventional and Emerging Topologies and their » Control;2018. pp. 21-42

[9]]Kirankumar B, Reddy YV,Vijaya kumar M. « Multilevel inverter with space vector modulation: Intelligence direct torque control ofinduction motor ». IET Power Electronics 2017;10:1129-1137

[10] Hadiouche D, Razik H, Rezzoug « AOn the modeling and design of dual stator windings to minimize circulating harmonic currents for VSI Fed AC machines ». IEEE Transactions on Industry Applications 40(2): 506-515. . (2004).

[11]] Tir Z, Soufi Y, Hashemnia MN, Malik OP, Marouani K. « Fuzzy logic field oriented control of double star induction motor drive ». Electrical Engineering 5: 1-9. (2016).

[12] Tir Z., Malik OP, Eltamaly AM. « Fuzzy logic based speed control of indirect field oriented controlled double star induction motors connected in parallel to a single six-phase inverter supply ». Electric Power Systems Research 134: 126-133(2016).. https://doi.org/10.1007/s00202-016-0377-

[13] Hadiouche D, Razik H, Rezzoug A. (2000). Study and simulation of space vector PWM control of double-star induction motors. In: Proc. of the VII IEEE International Power Electronics Congress, Acapulco, Mexico: 42-47..

Predictive modeling of Young's modulus for alpha alumina using artificial neural network and multiple linear regression

Belgacem Fissah
dept. of Mechanical Engineering
Larbi Tébessi University
Tebessa, Algeria
belgacem.fissah@univ-tebessa.dz

Hadj Belghalem
dept. of Mechanical Engineering
Larbi Tébessi University
Tebessa, Algeria
hadj.belghalem@univ-tebessa.dz

Messaoud Djaddou
dept. of Mechanical Engineering
Larbi Ben M'Hidi University
Oum el Bouaghi, Algeria
djeddou.messaoud@gmail.com

Belgacem Mamen
dept. of Civil Engineering
University Abbes Laghrour
Khenchella, Algeria
belgacem.mamen@univ-khenchela.dz

***Abstract*— In the present work, we have constructed a predictive model for one of the important mechanical properties in the study of the mechanical and thermal behavior of materials, this property is Young's modulus. The samples on which the experiments to determine the above property of alumina (α-Al2O3) were performed were made by Spark Plasma Sintering (SPS). The experimental results were exploited using the radial basis function (RBF) neural network model and multiple linear regression (MLR) to predict and construct the mathematical model. A comparison was made of the multiple linear regression model with the radial basis function (RBF) neural network model. Then, the two proposed models were compared with the experimental results. The study obtained showed good agreement between the experimental results and the proposed RBFNN models. But the MLR models were modest in predicting the studied mechanical property.**

Keywords*— *Alumina, Spark Plasma Sintering (SPS), Neural network (RBF), Multiple linear regression (MLR).

I. INTRODUCTION

Across the behavioral science disciplines, multiple linear regression (MLR) is a standard statistical technique in the researcher's toolbox. An extension of simple linear regression, MLR allows researchers to answer questions that consider the roles that multiple independent variables play in accounting for variance in a single dependent variable. Artificial neural network (ANN) is one of the most important research areas related to the science of biology, electronics, computer science, mathematics, and engineering. It has wide application in solving complex multidimensional nonlinear problems, nonlinear mapping between several variables, and regularity synthesis from experimental data [1]. With the advancement of computational tools and ceramic materials science in recent years, the study of mechanical and thermal behavior of ceramic materials can be done based on knowledge and experience with these materials, using artificial neural network techniques. Several studies have been conducted on the study of mechanical parameters. In 2006, Necat Altinkok [2] applied the BP-ANN model to predict the tensile strength, hardness, and density of different metal matrix composites (MMCs). In 2020, D. Merayo et al constructed an artificial neural network (ANN), capable of making predictions on material density and Young's modulus with an average confidence of more than 99% and 98%, respectively whose topology and connections were improved to accelerate the training and predictive power of ANN [3].

The purpose of this study is to build a predictive model of the mechanical parameter Young's modulus due to its influence on the mechanical and thermal behavior, by developing a multiple linear regression (MLR) model and a radial basis function (RBF) neural network model. This paper describes how the MLR and RBF techniques work to develop the predictive model of a ceramic material (alumina). The mechanical parameter models are discussed using ANOVA statistical methods. To verify the presence of the desired input-output relationship, the multiple collinearity test was performed using the Pearson correlation test.

Finally, the ability of a radial basis function (RBF) neural network model to statistically predict the mechanical parameter of alumina was evaluated using the values of the correlation coefficient (R^2), mean absolute percentage error (MAPE), and root mean square error (RMSE) . which were calculated by Equations 1, 2, and 3.

$$R^2 = 1 - \left(\frac{\sum_{i=1}^{n}(t_i - o_i)^2}{\sum_{i=1}^{n}(o_i)^2}\right) \quad (1)$$

$$MAPE = \frac{1}{n}\left[\frac{\sum_{i=1}^{n}|t_i - o_i|}{\sum_{i=1}^{n} t_i} \times 100\right] \quad (2)$$

$$RMSE = \sqrt{\frac{1}{N}\sum_{i=1}^{N}(t_i - o_i)^2} \quad (3)$$

Where *t* is the predicted value and *o* is the output value and *n* is the total number of *t* and *o* value pairs.

II. DATABASE

In this study, the data received from [4]. They were used to build the multiple linear regression models (MLR) and to train and test the artificial neural network (ANN) models. Sintering temperature (T), holding time (t), relative density (D), and grain size (Gs) were used as input parameters to determine the mechanical parameters of alumina developed by the SPS (spark plasma sintering) method.

A scanning electron microscope (SEM) is commonly used to examine the grain distribution of the samples. Figure 1 shows, for example, the effect of temperature on grain size.

The bulk density of the sintered samples was determined according to Archimedes' principle.

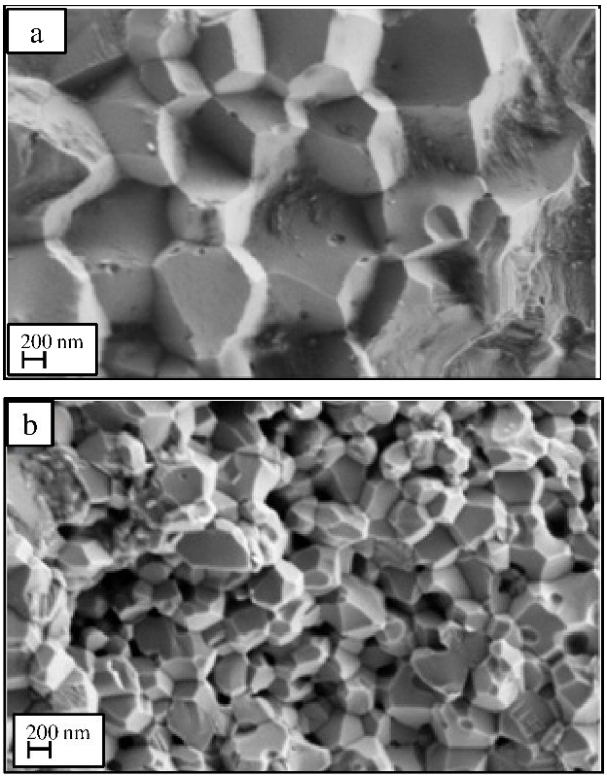

Fig. 1. Effect of processing parameters on grain size (a) and (b) effect of temperature.

Figures 2, 3 show the variation of the mechanical parameter studied in this paper as a function of density and grain size.

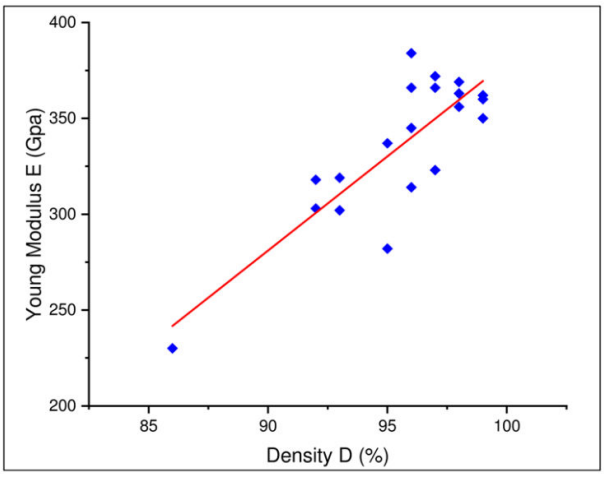

Fig. 2. variation of Young's modulus as a function of density

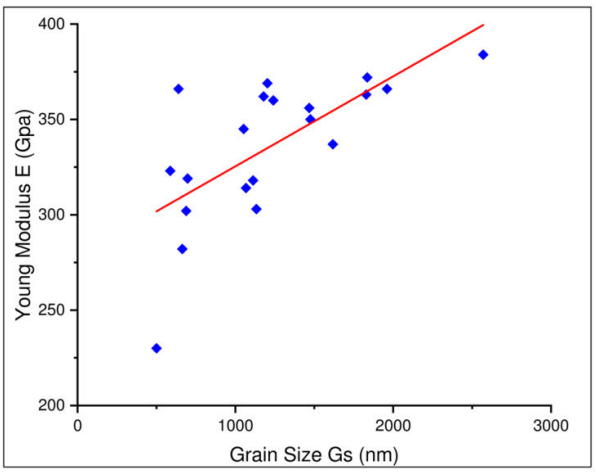

Fig. 3. variation of Young's modulus as a function of grain size

III. MULTIPLE LINEAR REGRESSION MODEL (MLR)

Regression analysis is a statistical tool widely applied in several engineering fields to model the relationship between a response variable and one or more independent variables. This modeling technique includes the statistical and mathematical approach and experimental investigations [5]. The basic multiple regression model of a dependent (response) variable Y on a set of k independent (predictor) variables can be expressed as [6]:

$$\begin{cases} y_1 = \beta_0 + \beta_1 x_{11} + \cdots + \beta_k x_{1k} + e_1 \\ y_2 = \beta_0 + \beta_1 x_{21} + \cdots + \beta_k x_{2k} + e_2 \\ \vdots \\ y_n = \beta_0 + \beta_1 x_{n1} + \cdots + \beta_k x_{nk} + e_n \end{cases} \quad (4)$$

In compacted form, equation (4) becomes :

$$y_i = \beta_0 + \beta_1 x_{i1} + \beta_2 x_{i2} + \cdots + \beta_k x_{ik} + e_i$$

Pour $i=1, 2, \ldots n$ (5)

Where y_i is the value of the dependent variable Y for the i^{th} case, x_{ij} is the value of the j^{th} independent variable X_j for the i^{th} case, β_0 is the intercept of the regression surface, each β_j, $j=1,2 \ldots k$, k is the slope of the regression surface concerning the variable X_j and e_i is the random error component for the i^{th} case.

IV. MODEL OF NEURAL NETWORKS WITH RADIAL BASIS FUNCTION (RBF)

The RBF network in it's simplest form is a back propagation neural network with three layers. The first layer corresponds to the inputs of the network, the second is a hidden layer consisting of a number of nonlinear RBF activation units, and the last corresponds to the final output of the network with a linear function. The activation functions in RBFNs are classically implemented as Gaussian functions [7]. Each layer is completely connected to the next (Fig.6). The output of the hidden layer of the network of the i^{th} activation function ϕ_i can be calculated using equation (6):

$$\emptyset_i(\|x - \mu_i\|) = exp\left(-\frac{\|x-\mu_i\|^2}{2\sigma_j^2}\right) \quad (6)$$

Here, $x = [x_1, \ x_2, \cdots \ x_n]$ is the input vector, $\|.\|$ is the Euclidean norm, μ_i and σ_j are the center and width of the hidden neuron j respectively.

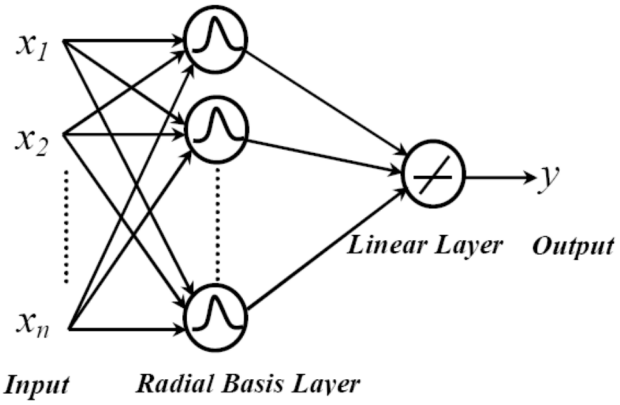

Fig. 4. Structure of the RBF neural network.

The equation characterizing the output of the RBF neural network is described by Equation (7):

$$y_i = \sum_{i=1}^{n} \omega_i \emptyset(\|x - \mu_i\|) + \omega_0 \quad (7)$$

Where μ_i the activation function centers ϕ, ω_j the synaptic weights of the network, ω_0 the bias.

V. Resultat and Discussion

A. Multiple Linear Regression Results

To find out the relationship between Young's modulus (E) and physical parameters such as density (D) and grain size (Gs) under certain experimental conditions of pressure (P), temperature (T), and time (t), the multiple linear regression model was used in which the physical and processing parameters were considered as explanatory variables and Young's modulus (E) as the dependent variable. The obtained mathematical model is studied for its statistical reliability according to the significance of the model coefficients. The statistical significance of each coefficient was checked by the probability value (P-value), and the Fisher value (F-value). A low P-value ($P \leq 0.05$) indicates statistical significance for the source on the corresponding response (i.e., $\alpha = 0.05$, at the 95% confidence level); this indicates that the resulting model is considered statistically significant, which is desirable, as it demonstrates that the terms in the model have a significant effect on the response, and higher F-values for each coefficient suggest greater significance for that term in the model [8].

The fitness of the model is measured with the R^2 value and the accuracy of the predictions is measured with the mean absolute percentage error (MAPE), which is calculated using equation (2). If the calculated MAPE is less than 10%, it is interpreted as an excellent accurate forecast, between 10% and 20% good forecasts, between 20% and 50% acceptable forecasts, and more than 50% inaccurate forecasts. An R^2 value of 0.9 or more is very good, a value greater than 0.8 is good, and a value of 0.6 or more may be satisfactory in some applications [9].

The results from the regression model showed that there was a significant relationship between and the explanatory variables. The explanatory variables explain variations in E ($R^2 = 0.845$) showing that the strength of the relationship between E and the explanatory variables is good. Referring to the value of F and its significant value P (Tab.1), we can conclude that the model is valid and that there is a correlation between E and the explanatory variables.

Thus, the results obtained give the following model equation:

$$E = 21 \times 10^{-3}T - 2{,}06t - 154 \times 10^{-3}P + 24 \times 10^{-3}G_s + 9{,}05D - 565{,}59 \quad (8)$$

To verify the existence of the mentioned relationship, a multi-collinearity test was performed, the table (Tab.2) shows the Pearson correlation coefficients between the explanatory variables and Young's modulus where the correlation coefficient was positive between Young's modulus, temperature, holding time, grain size and density. The highest correlation was for density at 0.829, followed by grain size at 0.682 and temperature at 0.610, in statistical terms, at the 0.05 significant level. The correlation coefficient with pressure and hold time was low with values of 0.146 and 0.223, respectively. The coefficients for hold time and pressure were not statistically significant.

TABLE I. ANOVA RESULTS FOR YOUNG'S MODULUS

Model	R	R^2	Variation of F	Sig. Variation of F
	0,919	0,845	15,234	0,000

TABLE II. PEARSON CORRELATION COEFFICIENTS BETWEEN EXPLANATORY VARIABLES AND YOUNG'S MODULUS.

Var. explicatives	Coef. correlation	Sig. stat
Temperature (T)	0.610	0.002
Time (t)	0.223	0.173
Pressure (P)	0.146	0.269
Grains (Gs)	0.682	0.000
Density (D)	0.829	0.000

B. Modeling using neural networks (RBF)

The model was tested with different combinations of neurons in the hidden layer and it was found that the 5-17-1 model gave a better value for MAPE, RMSE, and for the correlation coefficient R^2 (Table.3).

The experimental data are grouped into training data and test data. The training data is used to train the RBFNN and the test data is used to validate the RBFNN.

Based on the prediction using the RBF model, the comparison between the predicted results and the experimental results is shown in Figure 5. As shown in Figures 5 and 6, the curves between the experimental results and the prediction results for the RBF model reveal that the RBF model has an advantage in terms of prediction accuracy and fit accuracy (99.6%).

In addition, the direct comparison of the predicted results with the experimental results is displayed using a line graph

(Fig. 6). Therefore, the RBF model produces more accurate Young's modulus prediction results.

TABLE III. PERFORMANCE PARAMETERS OF THE PREDICTED YOUNG'S MODULUS.

	Predicted YOUNG'S Modulus Performances Parameters		
	Train	Test	ALL
RMSE	1.6087	3.3051	2.0627
MAPE(%)	0.1973	0.5891	0.2757
R^2	0.999976	0.9877	0.9982

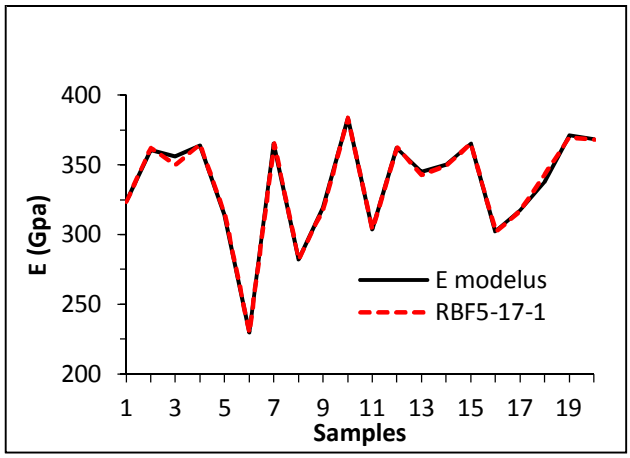

Fig. 5. Comparison between predicted and experimental results of Young's modulus.

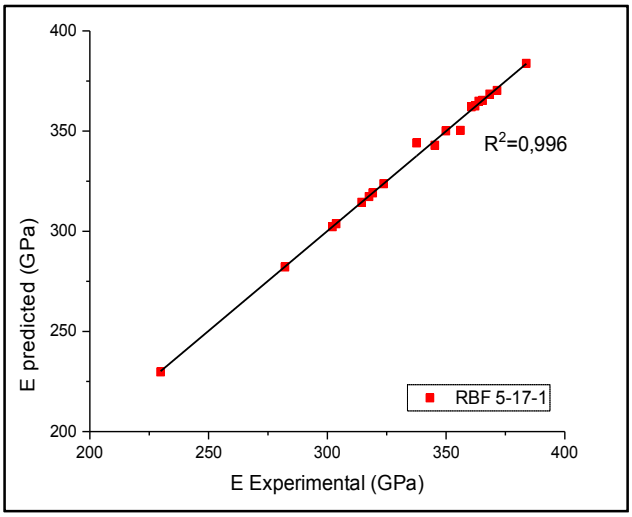

Fig. 6. Experimental and predicted values of Young's modulus.

C. *Comparison of results between RBFNN and MLR*

The MLR and RBFNN model predictions were compared to the experimental results for Young's modulus.

Figure 7 shows a comparison of the experimentally measured Young's modulus values and the predicted values using the MLR and RBFNN models.

It was clearly observed that the measured Young's modulus values were well correlated with the Young's modulus values predicted by RBFNN is acceptable compared to the Young's modulus values predicted by the MLR model. The minimum and maximum deviations was found for the MLR model of 0.15 and 15.28%, respectively. While the minimum and maximum deviations for the RBF model is 0 and 2.09%, the percentage error value determines the validity of the RBFNN calculation.

From the above, it is clear that the RBFNN models are suitable for predicting the Young's modulus of brittle materials especially on the studied alumina material within very acceptable error ranges. While the MLR models did not provide acceptable predictive results.

The proposed RBFNN models predict results closer to the experimental mechanical property values than the MLR models.

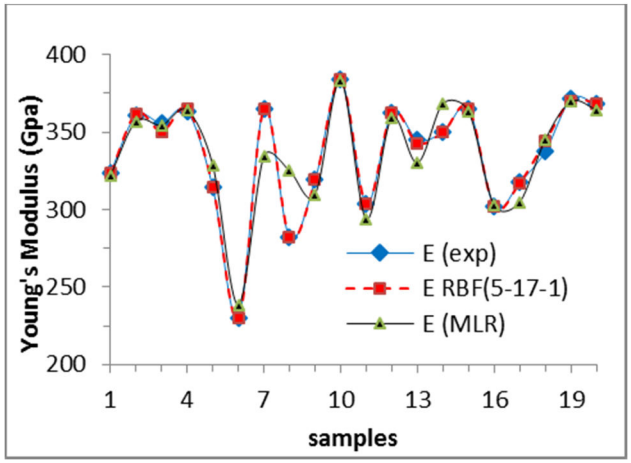

Fig. 7. comparison of predicted (MLR, RBF) and experimental results of Young's modulus.

VI. CONCLUSION

This study describes a comparative analysis of two modeling methods, namely the artificial neural network (RBFNN) and the multiple linear regression (MLR) method to predict the effect of physical properties (density, grain size) and processing parameters (temperature, pressure, and holding time) on Young's modulus of alumina.

The RBFNN model was based on 5 inputs (physical properties, processing parameters) and one output (Young's modulus) with a hidden layer of 17 neurons, and was trained using a back propagation algorithm.

Model performance was compared in terms of the predictive accuracy of the experimental results. It was found that the artificial neural network (ANN) model provided a good predictive potential for the mechanical property studied, predicting this property better than the MLR model.

REFERENCES

[1] C.Z. Huang, L. Zhang, L. He, J. Sun, B. Fang, B. Zou, Z.Q. Li, and X. Ai, "A study on the prediction of the mechanical properties of ceramic tool based on an artificial neural network," Journal of Materials Processing Technology, vol. 129, 2002 , pp. 399-402.

[2] N.Altinkok, "Use of Artificial Neural Network for Prediction of Mechanical Properties of Particulate-reinforced Al–Si10Mg Alloy Composites Prepared by using Stir Casting Process," Journal of Composite Materials, Vol. 40(9), 2006, pp. 779-796.

[3] D. Merayo, A. Rodríguez-Prieto, and A. M, "Camacho, Prediction of physical and mechanical properties for metallic materials selection using big data and artificial neural networks,"

[4] [4] H. Belghalem, M. Hamidouche, L. Gremillard, G. Bonnefont, and G. Fantozzi, "Thermal shock resistance of two micro-structured alumina obtained by natural sintering and SPS," Ceramics International, vol. 40, 2014, pp. 619–627.

[5] G.R. Anstis, P. Chantikul, B.R. Lawn, and D.B. Marshall, "A critical evaluation of indentation techniques for measuring fracture toughness by direct crack measurements," Journal of the American Ceramic Society, vol. 64 (9), 1981, pp.533–538.

[6] U. M. R. Paturia, H. Devarasettia, and S. K. R. Narala, "Application Of Regression And Artificial Neural Network Analysis In Modelling Of Surface Roughness In Hard Turning Of AISI 52100 Steel," Materials Today: Proceedings, vol. 5, 2018, pp. 4766–4777.

[7] E. Ostertagová, "Modelling using polynomial regression, Procedia Engineering, vol. 48, 2012, pp. 500 – 506.

[8] H. Faris, I. Aljarah, and S. Mirjalili, "Handbook of Neural Computation, Evolving Radial Basis Function Networks Using Moth–Flame Optimizer," CHAPTER 28, pp.537-550.

[9] A. Benkhelladi , H. Laouici , and A. Bouchoucha, "Tensile and flexural properties of polymer composites reinforced by flax, jute and sisal fibres," The International Journal of Advanced Manufacturing Technology , 2020,.

[10] G. Satyanarayanaa, G. Swami Naidub, and N. Hari Babu, "Artificial neural network and regression modelling to study the effect of reinforcement and deformation on volumetric wear of red mud nanoparticle reinforced aluminium matrix composites synthesized by stir casting," Boletín de la sociedad española de cerámica y vidrio, vol. 57, 2018, pp. 91–100.

[11] M. Cao , N. Alkayem , L.Pan , and D. Novák, Chapter 13, "Advanced Methods in Neural Networks-Based Sensitivity Analysis with their Applications in Civil Engineering," pp.335-352.

Use of Wavelet Transforms in Segmentation of Retinal Angiography Images

DEBBOU Hanane

Laboratory of Electronics and New Technologies

Deoartement of Electrical Engineering University of Oum El Bouaghi, Algéria

debbou.hanane@univ-oeb.dz
debhanane@hotmail.com

MEGRI Abederrahim Fayçal

Laboratory of Electronics and New Technologies

Department of Electrical Engineering University of Oum Elbouaghi, Algeria

f.megri@univ-oeb.dz
f_megri@yahoo.fr

GHENNAM Souhaila

Laboratory of signal processing

Department of Electrical Engineering University of Bejaia, Algeria

Souhaila.ghennam@univ-bejaia.dz
ghsouhi@yahoo.fr

Abstract

Medical imaging plays a very important role in the non-invasive visualization of anatomical components in humans. In this work we focus on the retinal fundus by studying retinal angiography images. An algorithm for the extraction of the vascular tree has been developed, based on the enhancement by means of the Shrearlet transform, then on the decomposition by the continuous wavelet transform via the Morlet wavelet to finally proceed to a segmentation based on the thresholding on histogram.

I. Introduction

The rapid development of medical imaging technologies is revolutionizing medicine. Medical imaging provides scientists and physicians with vital information about the human body and is playing an increasingly important role in the diagnosis and treatment of diseases. Among the medical imaging, we count the retinal imaging which today is more and more concerted to diagnose pathologies affecting the retina and other diseases. The objective of our work is to detect the retinal vascular tree from a retinal angiography image and to extract it by segmentation, in order to eventually provide diagnostic assistance. Given the variability in terms of size, intensity and orientation of retinal vessels, we plan to approach this extraction via wavelet transformation, as it is a multi-resolution approach, which will allow us to explore the vessels under different scales. We will adopt the classical wavelet transform in its different aspects, as well as another variant which is the Shearlet transform.

II. The wavelet transform

The wavelet transform, which appeared at the beginning of the 80's [1], is a signal processing tool allowing the analysis of local properties of complex signals on several time (or space) scales. Indeed, and as in the present work, the objective is to segment retinal vessels of various sizes (large or fine), in this case, under different scales, the wavelet transform could be well suited to this task.

A. *The wavelet*

A wavelet is an oscillating function (which explains the word 'wave') of zero mean, often noted $\psi(t)$, possessing a certain degree of regularity and whose support is finite (hence the name 'wavelet') [2]. The fact that the support is finite, we say that the wavelet is localized.

From this single function $\psi(t)$which is called the mother wavelet, we construct by translation of b and dilation of a a family of functions $\psi_{a,b}(t)$ which are the basic atoms:

$$\left\{\boldsymbol{\psi_{a,b}(t)} = \frac{\mathbf{1}}{\sqrt{\boldsymbol{a}}}\boldsymbol{\psi}\left(\frac{\boldsymbol{t-b}}{\boldsymbol{a}}\right)\right\}_{(\boldsymbol{a},\boldsymbol{b})\in \boldsymbol{R_0^+}\times \boldsymbol{R}} \qquad (1)$$

B. *2D Discrete Wavelet Transform*

In The Discrete Wavelet Transform (DWT) the translation parameters b and dilation a of the wavelet will be discretized as follows: $a = 2^j, b = k2^j$ for $(j,k) \in Z^2$. And from now on we will place a function, called the scale function noted φ which is to local approximations; it is associated with ψ which is to details. [3].

We then define the basic atoms of the wavelets, as well as the basic atoms of the scaling function:

$$\boldsymbol{\psi_{j,k}(t)} = \mathbf{2}^{\frac{-j}{2}}\boldsymbol{\psi}\left(\mathbf{2}^{-j}\boldsymbol{t}-\boldsymbol{k}\right), \quad \boldsymbol{for} \ \ (\boldsymbol{j},\boldsymbol{k}) \in \boldsymbol{Z^2} \ (2)$$

$$\boldsymbol{\varphi_{j,k}(t)} = \mathbf{2}^{\frac{-j}{2}}\boldsymbol{\varphi}\left(\mathbf{2}^{-j}\boldsymbol{t}-\boldsymbol{k}\right), \quad \boldsymbol{for} \ \ (\boldsymbol{j},\boldsymbol{k}) \in \boldsymbol{Z^2} \quad (3)$$

Thus the computation of the coefficients of the approximation $\boldsymbol{\beta_{j,k}}$ and the details $\boldsymbol{\alpha_{j,k}}$ at a resolution j and translated from k, is done by :

$$\boldsymbol{\alpha_{j,k}} = \int_{-\infty}^{+\infty} \boldsymbol{s(t)}\,\boldsymbol{\psi_{j,k}(t)dt} \qquad (4)$$

$$\boldsymbol{\beta_{j,k}} = \int_{-\infty}^{+\infty} \boldsymbol{s(t)}\,\boldsymbol{\varphi}_{\boldsymbol{j,k}}\boldsymbol{(t)dt} \qquad (5)$$

And at reconstruction, the signal s(t) is restored from the approximation A_J at the last resolution J and the detail set D_j at all resolutions $j \leq J$ as follows:

$$\mathbf{s(t)} = \boldsymbol{A_J} + \sum_{\boldsymbol{j\leq J}} \boldsymbol{D_j} \qquad (6)$$

Where $A_j = \sum_{k\in Z} \beta_{j,k}\, \varphi_{j,k}(t)$
And $D_j = \sum_{k\in Z} \alpha_{j,k}\, \psi_{j,k}(t)$.

1. Implementation of the DWT-2D

There are mainly two fast decomposition-reconstruction algorithms for the discrete wavelets transform 2D DWT:

- Mallat algorithm: DWT with decimation
- Hole Algorithm: DWT without decimation

Both use appropriate filters to obtain the approximation coefficients and the detail coefficients in the three orientations (vertical, diagonal and horizontal). These filters are computed from the wavelet function and its associated scale function.

2. Decomposition filters:

For a wavelet ψ, the associated scaling function φ satisfies a fundamental relationship which is the following equation:

$$\frac{1}{2}\varphi\left(\frac{1}{2}\right) = \sum_{n\in Z} a_n\, \varphi(t-n) \qquad (7)$$

Due to the fact that φ is compactly supported, the sequence $(a_n)_{n\in Z}$ would therefore be of finite number and could be viewed as the coefficients of a finite impulse response (FIR) low-pass filter ω .

From this ω filter, four FIR filters are defined [3]:

2 for the decomposition:

- LoD low-pass filter, to calculate the coefficients of the approximation $\beta_{j,k}$
- HiD high-pass filter, to calculate the coefficients of the details $\alpha_{j,k}$

2 for the reconstruction :

- LoR low-pass filter, to reconstruct the A_j approximation

  high-pass filter HiR, to reconstruct the details D_j

3. Mallat algorithm :DWT-2D with decimation

a) Decomposition

The decomposition procedure according to this algorithm is shown in Figure 1.

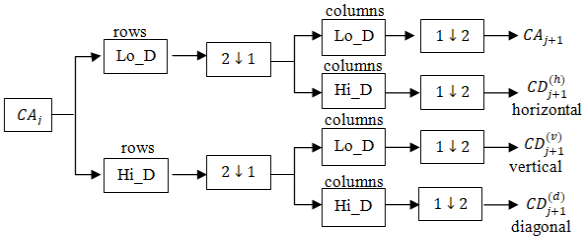

Figure 1. Basic step for DWT-2D decomposition with decimation, where $\mathbf{1}\downarrow\mathbf{2}$ represents the decimation of the rows (preservation of even index rows), and $\mathbf{2}\downarrow\mathbf{1}$ represents the decimation of columns (conservation of even index columns).

b) Reconstruction

The reconstruction of an approximation cA_j (if j=0, A_0 is the final rendered image) from the approximation cA_{j+1} and the set of details at resolution $j+1$, can be summarized in a figure 2.

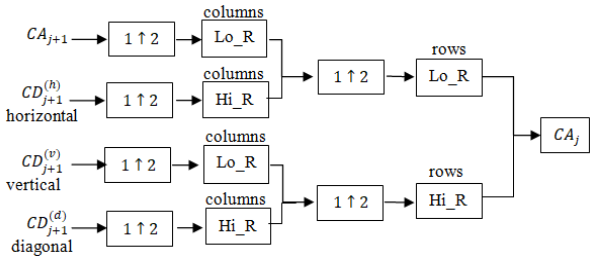

Figure 2. Basic step for DWT-2D reconstruction with decimation

4. Algorithm with holes: DWT-2D without decimation

✓ Decomposition

In the present algorithm, the image is not decimated and keeps its original size. Indeed, at a given resolution j, and to analyze 1 point among the 2^j points, it is the filter that will be oversampled by adding $2^j - 1$ zeros between two coefficients. This addition of zeros is assimilated to an addition of holes, hence the name by hole algorithm.

This algorithm is illustrated in figure 3.

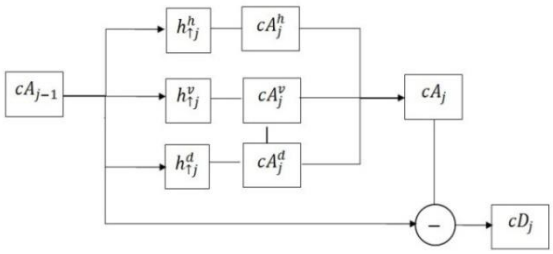

Figure 3. 2D decomposition algorithm without decimation.

✓ Reconstruction

Reconstructing an approximation cA_{j-1} (si j=1, cA_0 is the final rendered image) from the set of approximations cA_j and details at resolution j, this algorithm can be summarized in Figure 4.

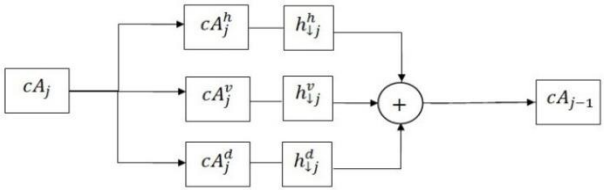

Figure 4. 2D reconstruction algorithm without decimation.

The three convolution results are summed to finally obtain the approximation cA_{j-1} at resolution $j-1$, according to the following equation:

$$\boldsymbol{cA_{j-1}} = \frac{\mathbf{1}}{\mathbf{3}} \sum_{\boldsymbol{p=h,v,d}} \boldsymbol{cA_j^p} * \boldsymbol{h_{\downarrow j}^p} \qquad (8)$$

C. 2D Continuous Wavelet Transform

The 2D continuous wavelet transform (CWT-2D) is done by computing correlation of the 2D signal $f(x,y)$ (such as

an image) with a wavelet $\psi_{a,b,\theta}(x,y)$ that depends not only on the scale parameters a and translations b, but also on a third parameter θ of rotation [4].
It is defined by:

$$\boldsymbol{\psi_{a,b,\theta}(x,y) = \frac{1}{\sqrt{a}}\psi\left(R^{\theta}\left(\frac{x-b}{a},\frac{y-b}{a}\right)\right)} \quad (9)$$

With R^{θ} is a rotation (change of reference frame) matrix:

$$R^{\theta} = \begin{bmatrix}\cos\theta & \sin\theta \\ \sin\theta & -\cos\theta\end{bmatrix}$$

And the calculation of the coefficients $C_f(a,b,\theta)$ of the 2D wavelet transform [4], is done according to:

$$\boldsymbol{C_f(a,b,\theta) = \iint_{-\infty}^{+\infty} f(x,y)\psi^{*}_{a,b,\theta}(x,y)\ dx\,dy} \quad (10)$$

III. The shearlet transform

The Shearlet transform, introduced in 2005 by Labate, Lim et al [5], is like the discrete wavelet transform, it uses a decomposition by means of filters extracted from wavelets and scale function, but unlike it, it is anisotropic, and even better according to [19], it is adapted to the detection of curvilinear shapes, such as retinal vessels, hence our interest in approaching this approach in the segmentation of retinal vessels.

A. The Shearlets

Shearlets as well as discrete wavelets are constructed from generating functions (wavelets) that can be modified with a certain scaling operator, they are scaled anisotropically by means of a shear that orients the wavelet in different orientations [5]. Figure 5 shows the approximation of a curvilinear curve using isotropic bases (wavelets) and anisotropic bases (shearlets). It is clear, that the latter is better suited to approximate curvilinear forms.

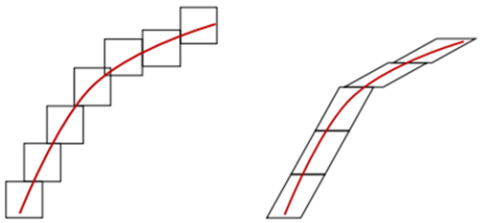

(a) (b)

Figure 5. (a) Approximation of a curve by means of an isotropic basis. (b) Approximation of a curve by means of anisotropic basis [23].

The construction of a Shearlet requires a combination of :

- a scaling operator based on a parabolic scaling matrix $A_a$of the form [6]:

$$\boldsymbol{A_a = \begin{pmatrix} a & 0 \\ 0 & a^{1/2}\end{pmatrix} = \mathbf{diag}\left(\mathbf{a}\ , \mathbf{a^{1/2}}\right);} \quad (11)$$

  Where a is a scaling factor.
- a shear operator, allowing orientation changes. This operator is represented by the shear matrix S_s given by [6]:

$$\boldsymbol{S_s = \begin{pmatrix} 1 & s \\ 0 & 1\end{pmatrix};} \quad (12)$$

Where s is a shear factor.

- a translation factor t to move the shearlet on the 2D plane.

In view of this combination, the shearlet function is expressed as [7]:

$$\boldsymbol{\psi_{a,s,t}(x) = a^{3/4}\psi\left(A_a{}^{-1}S_s{}^{-1}(x-t)\right)} \quad (13)$$

Where $\psi \epsilon L^2(\mathrm{R}^2))$ is a generating function. The shearlets $\psi_{a,s,t}$ would therefore emerge by expansion, shear and translation of the ψ function.

B. Continuous Shearlet Transformation

For a number of scale, shear and translation values, a continuous Shearlet system can be generated by:

$$\boldsymbol{SH_{con}(\psi) = \left\{\psi_{a,s,t}(x) = a^{3/4}\psi\left(A_a{}^{-1}S_s{}^{-1}(x-t)\right) \,/\, a \in R^{+}, s \in R, t \in R^2\right\}} \quad (14)$$

The Shearlet transformation $\mathrm{TSH}_{\psi}(f)$ of a function $f \in L^2(R)$ would be defined by [8]:

$$\boldsymbol{\mathbf{TSH}_{\psi}(f)(\mathbf{a},\mathbf{s},\mathbf{t}) = \iint_{-\infty}^{+\infty} f(x,y)\psi^{*}_{a,s,t}(x,y)dx\,dy} \quad (15)$$

It is used to calculate correlation (degrees of similarity) between the function f and the Shearlet ψ.

C. Discrete Shearlet transformation

A discrete version of the Shearlet system can be obtained by discretizing the set of parameters associated with the continuous Shearlet system, as follows:

$$\begin{cases} \text{the scale factor :} & \mathrm{a} \to 2^{j} \\ \text{the shear factor :} & \mathrm{s} \to k \quad \mathrm{j,k} \in Zet\ \mathrm{m} \in Z^2 \\ \text{the translation parameter :} & \mathrm{t} \to \mathrm{m} \end{cases}$$

Thus, the scale and shear operators become: $A_a \to A_{2j}$ et $S_s \to S_k$

The discrete shearlet system would therefore be [9] :

$$\boldsymbol{SH_{disc}(\psi) = \left\{\psi_{j,k,m}(n) = 2^{3j/4}\psi\left(S_k A_{2j}\,(n-cm)\right)\right\}} \quad (16)$$

where : $\mathrm{n} \in Z^2$ discrete spatial coordinates of the image, and $c \in R_+^2$ is a sampling constant.

Therefore, the calculation of the discrete Shearlet transformation will be as follows:

$$\boldsymbol{TSH_{\psi}(f)(j,k,m) = \iint_{-\infty}^{+\infty} f(x,y)\psi^{*}_{j,k,m}(x,y)dx\,dy} \quad (17)$$
$$\boldsymbol{f \in L^2(R^2)}$$

D. Vascular structure enhancement using the Shearlet transform

The intuitive idea behind this approach is that, since the coefficients of the Shearlet transform are closely related to the curvilinear structures whether major or minor, a complete representation of the retinal vascular tree could be obtained by inverse calculation of the coefficients of the Shearlet transform. This inverse calculation, in this case inversion of equation (3.5), is done as follows [5]:

$$\boldsymbol{f} = \mathbf{TSH}_{\psi}^{-1}\{\mathbf{TSH}_{\psi}\{\boldsymbol{f}\}(\mathbf{a},\mathbf{s},\mathbf{t})\} = \mathbf{TSH}_{\psi}^{-1}\{\langle \boldsymbol{f}, \boldsymbol{\psi}_{a,s,t}\rangle\} = \sum_{\psi \in SH} \langle \boldsymbol{f}, \boldsymbol{\psi}_{a,s,t}\rangle . \boldsymbol{S^{-1}}\boldsymbol{\psi}_{a,s,t} \qquad (18)$$

But as, the number of coefficients of the Shearlet transformation could be important, especially since some coefficients could correspond to slender structures, other than retinal vessels, We will retain only the high coefficients, really representing the curvilinear structures of the vessels, This trimming of the coefficients, will give an enhancement of the curvilinear structures according to the following equation [5]:

$$\boldsymbol{f_n} = \sum_{i \in I} \langle \boldsymbol{f}, \boldsymbol{\psi_i}\rangle . \boldsymbol{S^{-1}}\boldsymbol{\psi_i} \qquad (19)$$

Where I is the set of indices i, associated with the n highest coefficients among the set of all coefficients $\langle f, \psi_{a,s,t}\rangle$.

IV. The DRIVE data base

The Drive image database includes 40 colour fundus images, 7 of which have pathologies. The images are acquired using the fluorescence angiography modality by means of a Canon RC5 with a 45 degree field of view (FOV, Fieled Of View). They are recorded in JPEG format, with a size of 768 * 584 pixels. The image base is divided into two sets, 20 images for training and the rest for testing. It also includes manually segmented images of the vascular network, performed by two experienced ophthalmologists [10].

V. Application on retinal images

step 1. Reading of the image of the bottom of the retina from the DRIVE base. It is a color image of RGB type. (figure 6.a)

step 2. Transformation into a gray level luminance image, or conservation of the green channel only (because it is more contrasted). (figure 6.b)

Figure 6. Image read from the DRIVE database, (a): original image, (b): grayscale image.

step 3. Noise smoothing pre-processing by median filtering of size $[3 \times 3]$. The background of the image becomes more homogeneous and the vessel contours smoother.

step 4. As in the calculation of the various discrete or continuous TO, we proceed to a calculation of convolution with wavelets or filters, to avoid the effect of edge at the level of the disc of the retina, we replace the null values outside the disc of the retina by a value which recalls the contents inside the disc. The choice is carried on the average value of the values inside the disc.

To make this calculation, we need the FOV (Field Of View) mask found in the DRIVE database, and according to the expression :

$$val_{ave} = average(I_{image}(FOV == 255))$$

step 5. Invert the image to make the vessels bright, and the background dark.

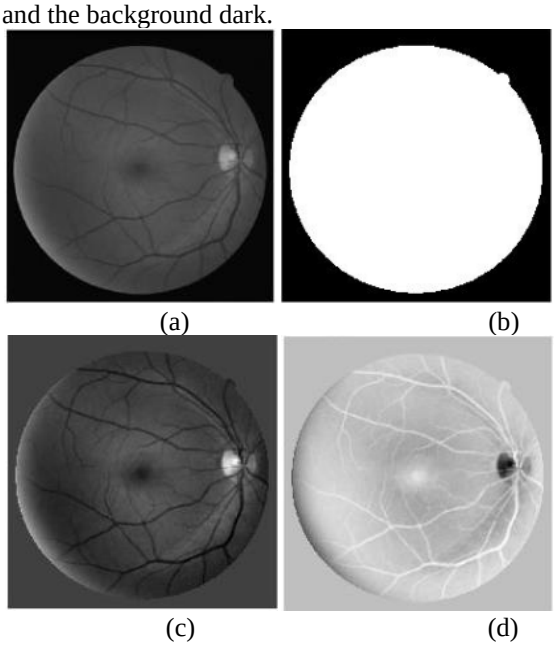

Figure 7. Preprocessed image, (a): filtered image, (b): the FOV mask, (c): edge effect removal, (d): intensity reversed image.

These 5 steps are common to the algorithms that will be discussed in the following.

A. Application of the Wavelet Transform Algorithm with decimation

For the wavelet transform algorithm with decimation we will use the procedure exposed in section Ⅱ.B.3.

step 6. Creation of the decomposition filters. To do this, we must first choose the appropriate onelette whose shape corresponds to the profile of the blood vessels, in order to better enhance the vascular shapes. The wavelets: 'Daubechies 4 or 5', 'Symplet 6 or 8', 'Coiflet 2 or 3', meet this requirement. In the following we will use the wavelet 'Daubechies 5', shown in figure 8.

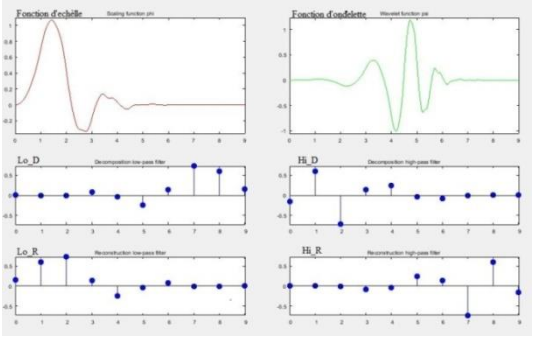

Figure 8. Wavelet 'Daubechies 5', represent the function of Db5 and scale with the 4 associated filters.

step 7. DWT-2D image decomposition with decimation, on 4 levels $(j = 1{:}\,4)$,with the 4 associated filters, according to the procedure explained in section II.B.3, and the results are shown in Figure 9. It is clear that the vessels are enhanced on the detail images.

step 8. To obtain an image where the vessels are enhanced, we will keep only the detail images of levels 2 to 4, because level 1 is too noisy. The sum of all the details at scales 2 to 4, gives us the final image of the enhanced vessels, shown in figure 10.(a).

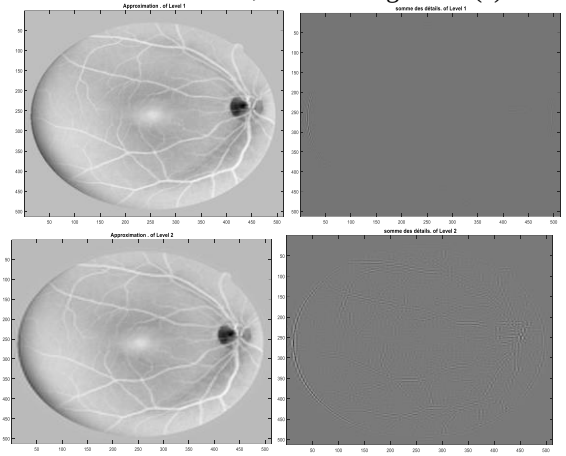

Figure 9.Image decomposed by the wavelet 'Daubichies 5', the left column represents the aproximations and the right column represents the sum of the details (horizontal, vertical and diagonal) for the different scales from 1 to 4.

step 9. Segmentation by the histogram thresholding method, and whose optimal threshold is calculated according to the Otsu method (implemented in Matlab). The result is shown in figure 10.(b).

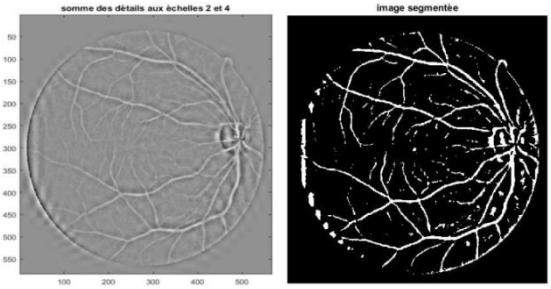

(a) (b)

Figure 10. Image segmentation based on the 2D DWT algorithm.

On the segmented image, we notice that the segmented vessels show discontinuities, and the thin vessels are almost non-existent, this is due to the loss of information during decimation.

B. Application of the Wavelet Transform Algorithm without Decimation

For the wavelet transform algorithm without decimation we will use the procedure outlined in section II.B.4. The algorithm of the transformation without decimation is similar to that of the transform with decimation, the only difference is that at the decomposition we do not decimate the approximation but we oversample the matched filter by inserting zeros.

step 6. The decomposition filters are designed from the filter $h = [1\ 2\ 4\ 6\ 4\ 2\ 1]$, shown in figure 11, the different decomposition filters

$$\boldsymbol{h_{Horizontal} = [1\ 2\ 4\ 6\ 4\ 2\ 1]} \quad (20)$$
$$\boldsymbol{h_{vertical} = transpose(h)} \quad (21)$$
$$\boldsymbol{h_{diagonal} = diag(h)} \quad (22)$$

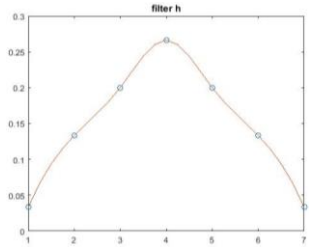

Figure 11. decomposition filter.

step 7. Wavelet decompositions on 4 levels, the horizontal, vertical and diagonal approximations at level j are obtained by convolving the level $j-1$ approximation with the filters above. While the details of level j are obtained by subtracting, from the approximation of level $j-1$, the sum of the resulting approximations of the convolution. At each level $j > 1$ we oversample the 3 filters. Figure 12 shows the results of this step.

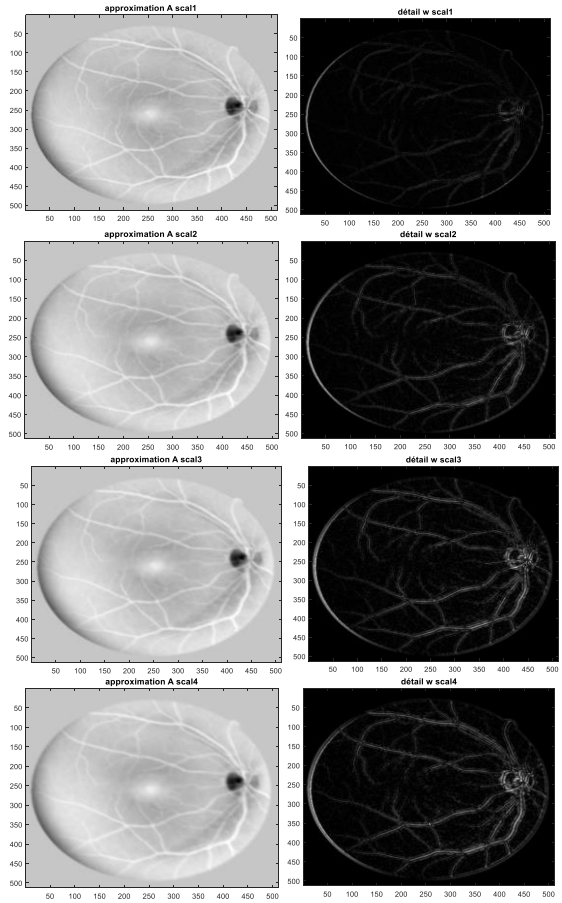

Figure 12. Image decomposed by an h filter, the left column represents the approximations and the right column represents the sum of the details (horizontal, vertical and diagonal) for the different scales from 1 to 4.

step 8. Calculation of the image of the enhanced vessels by summing the details of levels 2 to 4, without level 1 because it is too noisy. Figure 13.(a), shows the result of this step.

step 9. Segmentation by the histogram thresholding method, and whose optimal threshold is calculated according to the Otsu method. The result is shown in figure 13.(b).

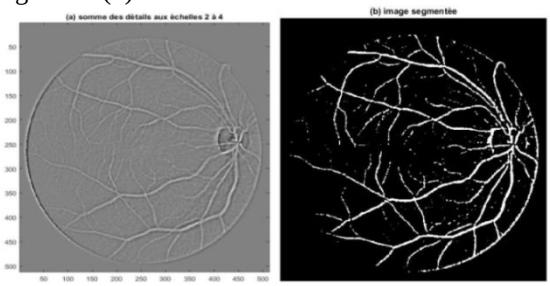

(a) (b)

Figure 13. Image segmentation based on the hole algorithm (a): sum of details at scales 2 to 4, (b): segmented image.

If we compare the results obtained with the 2D DWT algorithm with decimation (figure 10.b) with those obtained with the hole algorithm (figure 13.b), we notice that in the latter there is an appearance of some fine vessels and a decrease in false detections caused by the non-homogeneity of the retina background.

C. Morlet wavelet-based segmentation algorithm

step 6. Generation of the wavelet according to equation (11). The image is correlated with this wavelet, on several scales, and for each scale on several directions, according to equation (3), with b=0 (the calculation is centered on each pixel). Some results of the decomposition are shown in figure 14.

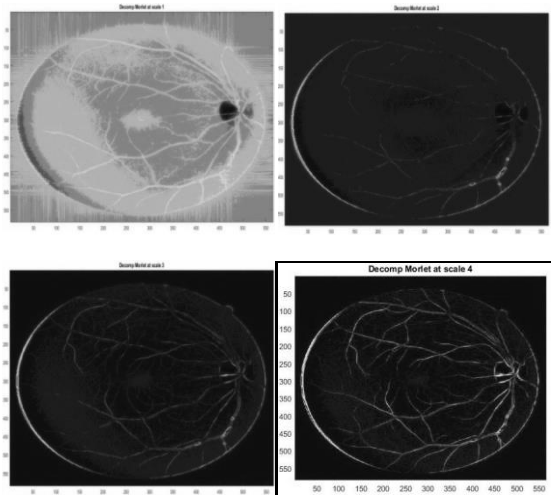

Figure 14. Morlet wavelet decomposition, scale 1 to 4.

step 7. Production of the image where the blood vessels are enhanced.

-On each scale, and for any point of the image, we retain the maximum response on all directions.

$$M_f(a) = \underbrace{\max}_{\theta} C_f(a,\theta)$$

-And for any point in the image, we retain the maximum response on the set of scales. the angle maxima of the coefficients for the different scales and directions.

$$F_f = \underbrace{\max}_{a} M_f(a)$$

The result is shown in Figure 15.a.

step 8. Segmentation by the histogram thresholding method, and whose optimal threshold is calculated according to the Otsu method The result is illustrated in figure 15.b.

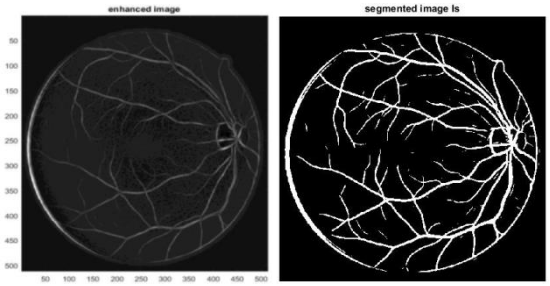

(a) (b)

Figure 15. Morlet wavelet-based image segmentation (a): enhanced image, (b): segmented image

On the segmented image (15.b) we can see a decrease in false detections by comparing the results obtained with the 2D DWT algorithm with decimation (figure 10.b) and those obtained with the hole algorithm (figure 13.b). There is a clear improvement in the segmentation of large vessels and including fine vessels.

D. The segmentation algorithm via the Shearlet Transform

step 3. In the ToolBoxShearlet V3.11, to generate the Shearlet system, the Cohen-Daubechies-Feauven wavelet is used as a generating wavelet. [11]
A 4 scale decomposition was chosen: $a = 2^j\big|_{j=0:3} = [1,2,4,8]$. A shear for k= [1, 1, 3, 3]. (Choice imposed by the ToolBox, due to the fact that the size of the shear vector must be the same as that of the scale vector).

step 4. The decomposition of the image on the shearlet SH_{disc} system, according to equation (18), and then an approximation corresponding to the broadest coefficients is selected according to equation (20). The selection of the wide coefficients is done by thresholding operation. This approximation corresponds to the enhanced image, and is represented in figure 16.b.

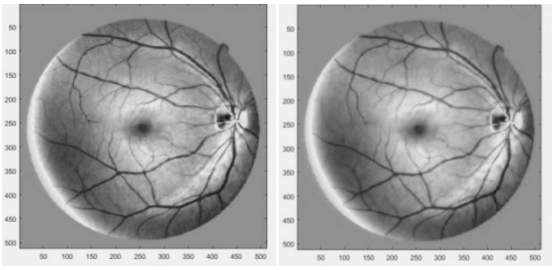

(a) (b)

Figure 16. Image Enhanced retinal image by shearlet decomposition: (a) the original image, (b) the enhanced image.

We notice that in the enhanced image that the vascular structures are more highlighted (enhanced) and have higher intensities than in the original image. In addition, and the background of the retina is completely smoothed.

Segmentation of the enhanced image by thresholding on histogram, as for the segmentation algorithms developed previously. But this time, the CWT-Morlet is applied beforehand to enhance the Gaussian profile of the blood vessel intensity. The results are shown in figure 17.

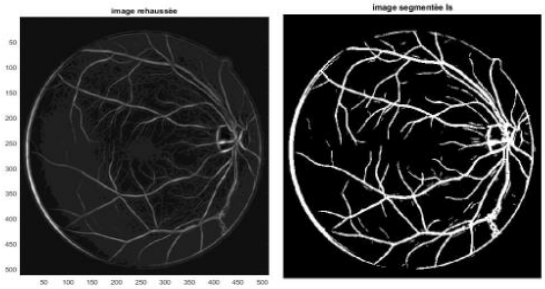

Figure 17. Image segmentation by the shearlet transform: (a) CWT-Morlet enhancement of the image in Figure 3.5.b, (b) segmented image.

We note:

A clear improvement of the segmentation compared to the previous algorithms, because appearance of fine vasculatures absent in the 1st ones. This improvement is due to the basic shape of Shearlet, which by shearing can approximate all curvilinear shapes of any elongation and in any orientation, and thanks to the change of scale, it can approximate vessels of any width.

Also, much less false detections, due to the non-homogeneity of the retinal background. This improvement is due to the approximation enhancement procedure that keeps only the wide coefficients of the Shearlet transformation. Since the geometric structures of the background do not correspond to the elongated shape of the base of the Shearlet. The coefficients of the Shearlet transform related to the background would be small and will be removed in the approximation enhancement procedure.

VI. Performance Measurement

A. Presentation of the performance measures of an algorithm

The performance is evaluated by comparing the image segmented by the algorithm with a reference image, segmented manually by a professional, and contained in the database.

The performance of the algorithm is quantified significantly by :

1. Sensitivity (se):

Indicates the ability of the algorithm to correctly detect retinal vessels, according to the following equation [01]:

$$\boldsymbol{se} = \frac{\boldsymbol{TP}}{\boldsymbol{TP} + \boldsymbol{FN}} \qquad (23)$$

Where TP (true positives): the number of vessel points correctly detected in the retinal images.

And FN (false negatives): the number of points as non-vessels detected.

2. Specificity (sp):

Indicates the ability of the algorithm to distinguish all non-vascular structures, according to the following equation [01]:

$$\boldsymbol{sp} = \frac{\boldsymbol{TN}}{\boldsymbol{TN} + \boldsymbol{FP}} \qquad (24)$$

Where FP (false positives): the number of non-vascular points detected as vessels.

And TN (true negatives): the number of correctly detected non-vessel points.

3. Accuracy (acc):

Measures the ratio of correctly classified pixels (both vessel and non-vessel) to the total number of pixels in the image field of view, according to the following equation [01]:

$$\boldsymbol{acc} = \frac{\boldsymbol{TP} + \boldsymbol{TN}}{\boldsymbol{TP} + \boldsymbol{TN} + \boldsymbol{FP} + \boldsymbol{FN}} \qquad (25)$$

4. La ROC (Receiver Operating Characteristic) :

This is a characteristic curve for the functioning of the receiver, it plots the fraction of the true positive rate (TVP) against the false positive rate (TFP), where :

-The TPV indicates the ratio of the points correctly classified as vessels to the total number of vessel points in the reference image.

$$\boldsymbol{TVP} = \frac{\boldsymbol{TP}}{\textbf{total number of vessel points in the reference image}} \qquad (26)$$

- The TFP indicates the ratio of points incorrectly classified as vessels to the total number of non-vessel points in the reference image.

$$\boldsymbol{TFP} = \frac{\boldsymbol{FP}}{\textbf{total number of non} - \textbf{vessel points in the reference image}} \qquad (27)$$

B. Performance evaluation of the proposed segmentation method

The performance of the proposed retinal vessel segmentation method using the Shearlet transform, after application to all images in the DRIVE database, is shown

in Table 1. In addition, the ROC curve is shown in Figure 19.

Image	Sensitivity	Specificity	Accuracy
01	0,911	0,9039	0,9049
02	0,7989	0,9491	0,9266
03	0,7506	0,936	0,909
04	0,7088	0,9376	0,9071
05	0,7643	0,9544	0,9286
06	0,7113	0,9339	0,9025
07	0,7521	0,9443	0,9189
08	0,6062	0,9542	0,9104
09	0,7946	0,9174	0,903
10	0,7561	0,9606	0,9362
11	0,7133	0,9191	0,8924
12	0,7281	0,941	0,9144
13	0,717	0,9327	0,9021
14	0,8031	0,9388	0,9228
15	0,8019	0,9472	0,9321
16	0,7727	0,9339	0,9128
17	0,7377	0,8988	0,8789
18	0,7565	0,9437	0,9222
19	0,8456	0,9301	0,9199
20	0,8204	0,9141	0,9041
mean	0,7625	0,9345	0,9124

Tableau 1. Performance measures.

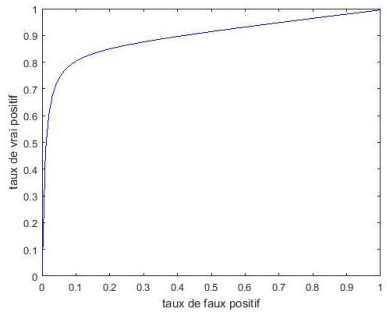

Figure 18. ROC characteristic curve

VII. Conclusion

In the present work we have set ourselves the challenge of developing a method that can segment the retinal vascular tree, taking into account the variability, in terms of size, intensity and orientation of the retinal vessels.

We managed to produce 2 segmentation algorithms based on the discrete wavelet transform with and without decimation, whose results were not up to our expectations, because this transform is anisotropic, and a 3rd algorithm based on the continuous wavelet transform, delivering convincing results but with enough false detections.

We also established a segmentation algorithm based on the Shearlet transform, which allows to enhance the curvilinear structures, such as blood vessels, associated with the continuous wavelet transform by means of the Morlet wavelet to better highlight the gray level profile of the vessels, to finally allow a better segmentation and the results obtained are more than convincing.

In order to compare the last algorithm developed with the retinal vessel segmentation methods cited in the literature, we calculated its performance in terms of sensitivity (0.7625), specificity (0.9345), accuracy (0.9124) and area under the ROC curve (0.8941).

Finally, we recommend, in order to improve the performance of the algorithm and get as close as possible to the expert segmentation, to perform a post-processing on the final image to reduce false detections, to use other segmentation methods, such as the active contour, or to perform a pre-processing to correct the non-homogeneous illumination of the retinal angiography image.

VIII. Bibliographic reference

[1] Chetan L Srinidhi, P Aparna, Jeny Rajan. Recent Advancements in Retinal Vessel Segmentation. DOI 10.1007/s10916-017-0719-2, 2017.

[2] C.Charles, Introduction aux ondelettes. Université de Liège, 2011.

[3] Michel Misiti, Yves Misiti et all, Les ondelettes et leurs application, LAVOISIER, 2003, Paris.

[4] Jo˜ao V. B. Soares, Jorge J. Retinal Vessel Segmentation Using the 2-D Morle.Wavelet and Supervised classification.2006].

[5] *ShearLab 3D. Manual. v1.0. August the 29th, 2013.*

[6] Gitta Kutyniok, Demetrio Labate, Editors, Shearlets Multiscale Analysis for Multivariate Data, Birkhäuser, 2012, Springer New York Dordrecht Heidelberg London.

[7] Kai Hu, Aiguo Song et all, An Image Filter Based on Shearlet Transformation and Particle Swarm Optimization Algorithm, Volume 2015, Article ID 414561, 9 pages.

[8] Sören Häuser, Fast Finite Shearlet Transform: a tutorial, February 8, 2012.

[9] Gitta Kutyniok , Wang-Q Lim, and Gabriele Steidl, Shearlets: Theory and Applications, 2014 WILEY-VCH Verlag GmbH & Co. KGaA,Weinheim.

[10] DRIVE: digital retinal images for vessel extraction, http://www.isi.uu.nl/Research/ Databases/DRIVE , 2004.

[11] www.shearlab.org

[12] Elaheh Imani, Malihe Javidi et all, Improvement of retinal Blood vessel detection using morphological component analysis, 2015 Elsevier Ireland Ltd.

Temperature Forecasting via NeuralNetworks Based on Time-Series Data

Rawnaq Naili[1], *Rania Chettab*[1], *Mohamed AbdouBouteldja*[2], Mohamed Badeche[2*].

[1]Software and Information Systems Technologies (TLSI) Department, University of Constantine 2 - AbdelhamidMehri, Algeria.

[2]LIRE Laboratory, University of Constantine 2 - AbdelhamidMehri, Algeria.

[*] Corresponding address: mohamed.badeche@univ-constantine2.dz

***Abstract*—**in this paper, we presentdeep neural network architectures and use themintime series weather forecasting. We started with a MLP (Multi-Layer Perceptron) architecture, then we used CNN (Convolutional Neural Network) architecture, and moving on to LSTM (Long-Short Term Memory), to finally making a hybrid architecture of CNN and LSTM. Eight years (2009-2016) of hourly meteorological data were used to train each model and the results show that neural network could be a good way to predict future temperatures.

***Keywords*—**Artificial neural networks, Temperature forecasting, Time series, MLP, CNN, LSTM, Time series forecasting.

I. INTRODUCTION:

Weather forecasting is the prediction of the state of the atmosphere for a given location using the application of science and technology. It is nowadays an incredibly complex technical feat, and only the most powerful computers can handle the ever-increasing amount of information collected. [6] And when talking about weather forecasting, temperature prediction is one of the major concerns in the domain of meteorology. [5]

The current wideavailability of massive weather observation datamotivated researchers to explore pattern hidden in thelarge dataset and make weather prediction. The adventof information and computer technology in the lastdecade also support the research of weather forecastingto get more accurate results.[13]. Moreover, the best and most used technique that could handle the huge amount of collected data is time series forecasting.

Time series forecasting is the use of certain model to forecast future values based onpast observed values, and thus can be understood as a method for predicting future values by understanding past values [9].

Numerical weather forecasts use atmospheric models to predict future weather conditions based on current weatherconditions [10, 11, 12]. Unlike numerical weather prediction, time series forecasting uses a model to predictfuture values based on past values.

The prediction of time series data in meteorology can help in decision-making processes carried out by organizations responsible for the prevention of disasters. [4]

II. DATA COLLECTION:

1. Raw data :

The dataset contains weather conditions recorded at the Weather Station at the Max Planck Institute for Biogeochemistry in Jena, Germany, over several years. In this dataset, 14 different quantities (including air temperature, atmospheric pressure and humidity) were recorded every 10 minutes (see Table 1). [7]

FEAUTURE	UNIT
PRESSURE	Mbar
TEMPERATURE	C°
T POT	K
T DEW	C°
RH	%
VP MAX	Mbar
VP ACT	Mbar
VP DEF	Mbar
SH	g/kg
H2OC	Mmol/mol
RHO	g/m**3
WV	m/s
MAX WV	m/s
WD	Deg

Table 1: Features recorded in the dataset

The original data goes back to 2003, but in our case we used a subset, from 2009 to 2016 (both inclusive). In addition, we used a further reduced version in which recordings are kept for every hour.

The graph below represents the variation of the temperature in the chosen weather data:

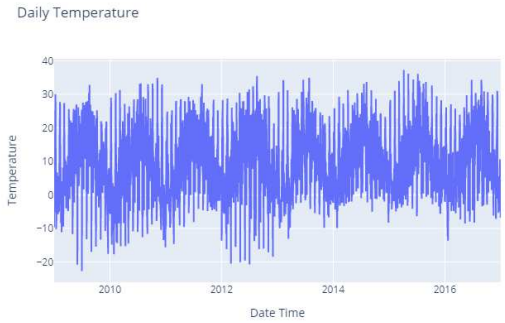

Figure 1: Temperature variation (2009 - 2016)

We divided the chosen weather data into two successively selected groups, the training group, corresponding to the first 75% of the dataset, and the test group, corresponding to 25% of the rest of the dataset so that the generalization capacity of network could be checked after training phase.

2. Data pre-processing:

As a rule of thumb, whenever we use a neural network, we should normalize or scale our data. For it helps in fastertraining of models.

The goal of normalization is to change the values ofnumeric columns in the dataset to a common scale,without affecting differences in the ranges of values orlosing any information.

The preprocessing that we carried out here isnormalizing data using MinMaxScaler. Which does exactly what we mentioned before.

For each value in a feature, MinMaxScalersubtracts the minimum value in the feature and then divides by the range. The range is the difference between the original maximum and original minimum.

The default range for the feature returned by MinMaxScaler is 0 to 1.

MinMaxScaler preserves the shape of the original distribution and does not change the information embedded in the original data.

For measuring the error made by the neural network, we used the Mean Absolute Error (MAE) :

$$mae = \frac{1}{n}\sum_{j=1}^{n} | y_j - \hat{y}_i |$$

Where:

- y_j is the true value.
- $\hat{y}$ is the predicted value.
- n is the total number of test sample.

III. RECURRENT NEURAL NETWORKS:

Neural networks have seen big interest lately, and they are being successfully appliedin various domains, especially when it comes to solve prediction, classification, or control problems.

They are defined as an interconnected of simpleprocessing element whose functionality is based on thebiological neuron which is a unique piece ofequipment that carries information or a bit of knowledge andtransfers to other neuron in the chain of networks. Artificialneuron imitates these functions and their unique process oflearning [3].

In our case, we used three different architectures of artificial neural networks.

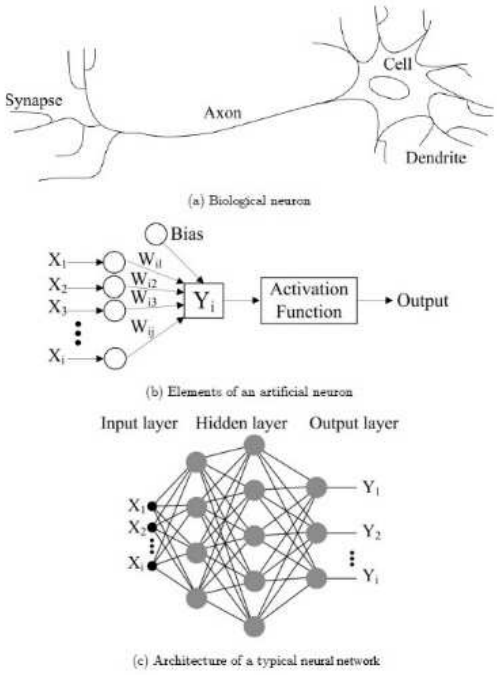

Figure 2: Neural network architecture [8]

1. MULTI-LAYER PERCEPTRON (MLP):

The multi-layer perceptron is the first kind ever of artificial neural networks, it has many layers, the first layeris the input layer, the last one is the output layer, themiddle layers are called hidden layers, and each layer includes several neurons. The neurons in MLP have thecharacteristics of inter-layer full connection and intra-layerconnectionless. (Figure 2)

Following this architecture, we developed a sequential model of one input layer, successively followed by a dense hidden layers with a ReLu activation function (used to decide whether a neuron can be activated or not), and one last dense layer of one neuron that represents the output of this model.

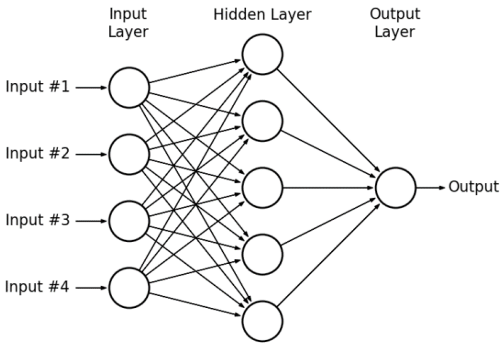

Figure 3: Multi-Layer Perceptron Network

2. CONVOLUTIONAL NEURAL NETWORK (CNN):

Convolutional neural networks are generally associated with computer vision applications. Their architecture is specifically adapted to carrying out complex visual analyzes. It is defined by a three-dimensional arrangement of neurons, instead of the standard two-dimensional network. The first layer of these neural networks is called "Convolutional Layer". Each neuron in this layer only processes information from a small part of the visual field. The convolutional layers are followed by rectified or ReLU layer units, which allows CNN to process complicated information.

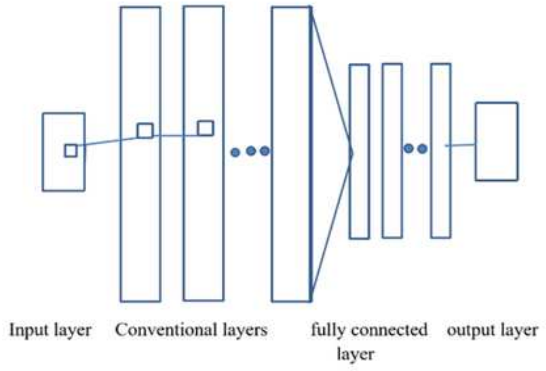

Figure 4: CNN architecture

Although traditionally developed for two-dimensional image data, CNNs can be used to model univariate time series forecasting problems, in our case it is temperature prediction. For that, we developed sequential model composed of one input layer, one convolutional hidden layer with a ReLu activation function. This layer is used to extract the relationship between the values of the 14 different features fed as input and to see if they have a useful impact to precise predictions.And then a pooling layer that is used to distill the output of the convolutional layer to the most salient elements.

The convolutional and pooling layers are followed by a fully connecteddense layer that interprets the features extracted by the convolutional part of the model.

A flatten layer is used between the convolutional layers and the dense layer to reduce the feature maps to a single one-dimensional vector.

3. LONG-SHORT TERM MEMORY (LSTM):

The developed RNN model is based on one of the neural network architecture named LSTM (Long short-Term Memory).

LSTM is a network that is composed of cells (LSTM blocks) linked to each other. Each LSTM block contains three types of gate: Input gate, Output gate, and Forget gate, respectively, which implement the functions of writing, reading, and resetting on the cell memory. [1]

The presence of these gates, allows LSTM cells to remember information for an indefinite time; in fact, if the following Input gate is the activation threshold, the cell will retain the previous state, and if the current state is enabled, it will be combined with the input value. As the name suggests, the Forget gate resets the current state of the cell, and the Output gate decides whether the value in the cell must be carried out or not. [1]

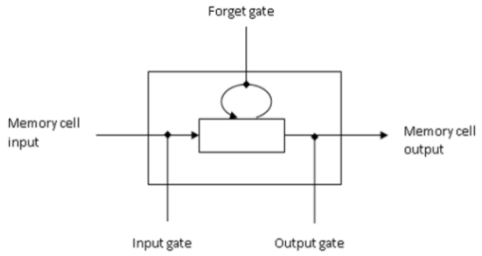

Figure 5: Block diagram of an LSTM cell [1]

The reason behind using it is that it is free from the problem of vanishing gradients, and offers excellent results and performance;also, it is ideal for prediction and classification of temporal sequences.[1]

Following this background we developed a sequential modelcomposed of multiple layers: one input layer and one single LSTM layer with ReLu activation function, and to make it more robust; it was followed by a dense layer with only one neuron that predicts the future temperature value.

4. CNN-LSTM:

In this section, we developed a hybrid architecture of the two previous models, started with the convolutional and the pooling layers of the developed CNN; and ended by the LSTM layer with a ReLu activation function of the

LSTM model, which replaced the fully connected dense layer in this model.

In addition, the flatten layer is used between the convolutional layers and the LSTM layer as before.

In each of the four architectures, we trained the model using all the 14 features, in order to forecast only the temperature.

When compiling the model, and to optimize the algorithm, we used the Adam optimizer, which realizes the benefits of both AdaGrad and RMSProp. Adaptive Gradient Algorithm maintains a per-parameter learning rate that improves performance on problems with sparse gradients. Root Mean Square Propagation that also maintains per-parameter learning rates that are adapted based on the average of recent magnitudes of the gradients for the weight.[2]

IV. TOOLS USED:

- *Pandas* - Open source data structuring and analysis tool.
- *Keras* - An open source neural network library in Python.
- *NumPy* - Used for scientific computing in Python.
- *Matplotlib* - Python library for visualization of data.
- *TensorFlow* - Python library used for dataflow programming.

V. RESULT AND DISCUSSION:

The optimal structures for the developed model in every part for obtaining minimum prediction error are shownbelow:

MLP	Number of 1st denselayer's neurons	100
	Batch size	32
	Number of epochs	10
	MAE	**0.64**
CNN	Number of dense layer's neurons	50
	Batch size	32
	Number of epochs	10
	MAE	**1.03**
LSTM	Number of dense layer's neurons	50
	Batch size	32
	Number of epochs	10
	MAE	**0.60**
CNN-LSTM	Number of dense layer's neurons	50
	Batch size	32
	Number of epochs	10
	MAE	**0.61**

Table 2 :Optimal structures' configurations

The graph below represents the results of the MLP's optimal structure's configuration:

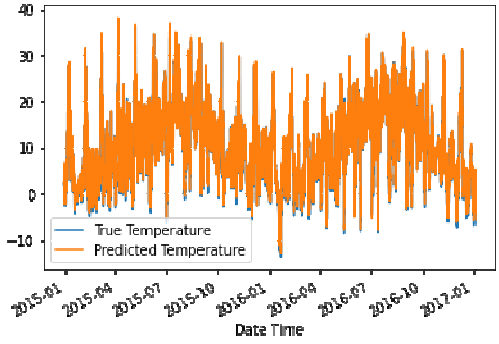

Figure 6: MLP predictions

For the CNN, these are the results:

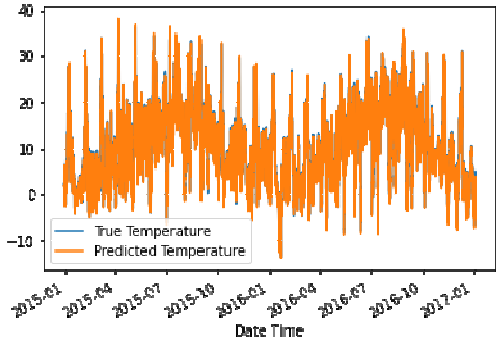

Figure 4: CNN predictions

And these are the results of the LSTM model:

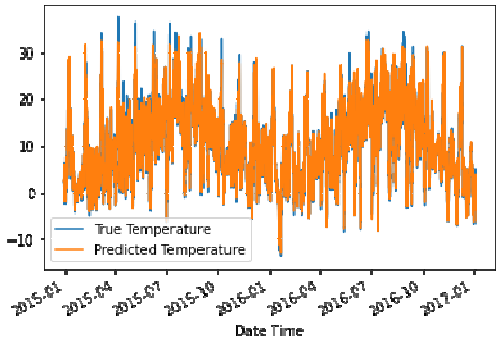

Figure 7: LSTM predictions

Lastly,the results of the CNN-LSTM model are:

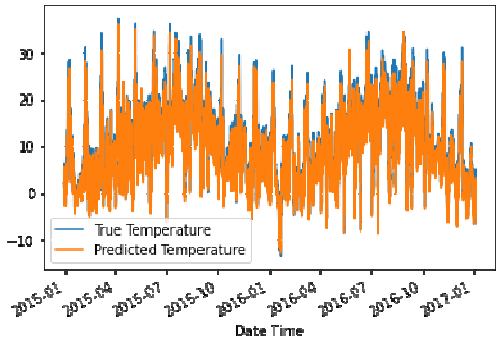

Figure 8:LSTM model predictions

VI. CONCLUSION:

The results of this paper show that the MAE values obtained were as small as possible, which suggest that neural networks generally and LSTM specifically could be a good way to relate on to predict temperature of general weather conditions. In addition, numerical weather forecastscan be used with these models to make such reasonable and accurate predictions and help the weather decision making systems in case of alerts or warning.

REFERENCES:

[1] Deep Learning with TensorFlowby Giancarlo Zaccone, Md. Rezaul Karim, Ahmed Menshawy, April 2017.

[2] Neural networks and deep learningby Aurélien Géron, March 2018.

[3] L. Fausett, Fundamental of Neural Networks, New York , Prentice Hall.A well-written book, with very detailed worked examples to explainhow the algorithm function, 1994.

[4] Modise Wiston and Mphale KM (2018) Weather Forecasting: From the Early Weather Wizards to Modern-day Weather Predictions. JClimatol Weather Forecasting 6: 229. doi:10.4172/2332-2594.1000229.

[5] METEOROLOGICAL APPLICATIONS.Meteorol. Appl. 15: 431–445 (2008).Published online 9 July 2008 in Wiley InterScience(www.interscience.wiley.com) DOI: 10.1002/met.83

[6] Weather forecasting article by Encyclopaedia Britannica, Inc17 January 2019. Encyclopaedia Britannica. https://www.britannica.com/science/weather-forecasting.

[7] Weather time series dataset recorded by the Max Planck Institute for Biogeochemistry

[8]GORDAN, Meisam; RAZAK, Hashim Abdul; ISMAIL, Zubaidah and GHAEDI, Khaled. Recent Developments in Damage Identification of Structures Using Data Mining. Lat. Am. j. solids struct. [online]. 2017, vol.14, n.13 [cited 2020-05-30], pp.2373-2401. Available from: <http://www.scielo.br/scielo.php?script=sci_arttext&pid=S1679-78252017001302373&lng=en&nrm=iso>. ISSN 1679-7825. https://doi.org/10.1590/1679-78254378.

[9]Raicharoen, T., Lursinsap, C., &Sanguanbhokai, P. (2003). Application of critical support vectormachine to time series prediction. International Symposium on Circuits and Systems (Vol.5,pp.V-741-V-744 vol.5). IEEE

[10] Barker, D., Huang, X. Y., Liu, Z. Q., Auligné, T., Zhang, X., &Rugg, S., et al. (2012). Theweather research and forecasting model's community variational/ensemble data assimilationsystem: wrfda. Bulletin of the American Meteorological Society, 93 (6), 831 - 843.

[11] Shen, F., Min, J., &Xu, D. (2016). Assimilation of radar radial velocity data with the wrf hybridetkf–3dvar system for the prediction of hurricane ike (2008). Atmospheric Research, 169, 127-138.P.G. Clem, M. Rodriguez, J.A. Voigt and C.S. Ashley, U.S. Patent 6,231,666. (2001).

[12] Xu, D., Min, J., Shen, F., Ban, J., & Chen, P. (2016). Assimilation of mwhs radiance data fromthe fy□3b satellite with the wrf hybrid□3dvar system for the forecasting of binary typhoons.Journal of Advances in Modeling Earth Systems, 8 (2).

[13] AfanGalih Salman *et al.* / Journal of Computer Science 2018, 14 (7): 930.938 DOI: 10.3844/jcssp.2018.930.938

Generation of ECG synthetic signal using coupled ordinary differential equations and Hopf bifurcation

1st Abdelghani Takha
Electronics, Department
ETA Laboratory,
bourdj bou arreridj, Algeria
takha.abdelghani@gmail.com

2nd Mohamed lamine TALBI
Electronics, Department
ETA Laboratory,
bourdj bou arreridj, Algeria
mltalbi@yahoo.fr

3rd Ghania KHENICHET
Electronics, Department
ETA Laboratory,
bourdj bou arreridj, Algeria
ghaniakhenichet1992@gmail.com

***Abstract*— In this study, we present a modeling technique for producing a synthetic ECG signal with realistic PQRST morphology and prescribed heart rate dynamics including various cardiac arrhythmias. The proposed model is based on the use of three coupled ordinary differential equations, where the two first equations depend on Hopf bifurcation. The fourth-order Runge–Kutta method is used to solve numerically the model.**

The results of numerical simulation show that, a wide variety of synthetic ECG can be generated, including normal and arithmetic heartbeat; a visual examination of arithmetic ECG signals taken from the MIT database was utilized to recommend acceptable values for the model's parameters.

.

Keywords— Dynamical model, Hopf bifurcation, synthetic electrocardiogram signals, cardiac arrhythmias

I. INTRODUCTION

The ECG (electrocardiogram) is a diagram which records the heart's electrical activity. Electrodes on the surface of the body are inserted in the ECG to capture these electrical cardiac currents [1]. A typical ECG consists of five major waves, which are typically referred to as (P, QRS and T). When the atrial depolarizes, the P wave is produced, followed by the QRS complex and the T wave [2].

Signal modeling is one of the most commonly utilized methods, ECG modeling can be used in a variety of ways, depending on the application [3], There are several studies in literature on synthetizing ECG signals by using mathematical modeling. McSharry et al.[4] use dynamic model to generate synthetic ECG signals based on coupled ordinary differential equations, both are responsible for introducing the cycle limit, the three equations have a push up and down as the P, Q, R, ,S and T waves. Li and Ma [5] proposed a data flow graph method based on piecewise curve to model ECG signals. Sameni et al. [6] proposed a 3-D dynamic model to generate ECG and ECG noise model., Clifford et al. in [7] proposed a method based on a three-dimensional vectorcardiogram (VCG) formulation to generate the normal and abnormal heartbeats. Roonizi et al. [8] proposed an approach for modeling the morphology of electrocardiogram (ECG) signals. Pascalin et al [9] generate several cardiac arrhythmias based on McSharry mathematical model and compared with a real cardiac arrhythmias.

In this study, we propose to modify the model of McSharry et al by using a novel Hopf bifurcation in the first two equations to create a new model for synthetic ECG. We believe that, such approach leads to generate a wide range of synthetic ECG signals that can provide us with some clinically significant information about human heart health.

II. MATHEMATICAL MODELING OF SYNTHETIC ECG

A. McSharry model

The dynamical model of McSharry is given by:

$$\begin{cases} \dot{x_1} = \alpha x_1 - \omega x_2 \\ \dot{x_2} = \alpha x_1 + \omega x_2 \\ \dot{x_3} = \sum_{i\in\{P,Q,R,S,T\}} a_i \Delta\theta_i \exp\left(-\frac{\Delta\theta_i^2}{2b_i^2}\right) - (x_3 - z_0) \end{cases} \quad (1)$$

with $\alpha = 1 - \sqrt{x_1{}^2 + x_2{}^2}$, $\Delta\theta_i = (\theta - \theta_i) \bmod 2\pi$, $\theta = \operatorname{atan2}(x_1, x_2)$, ω is the angular velocity as it moves around the cycle limit. The baseline wander was introduced by coupling the baseline value in (1) to the respiratory frequency using

$$z_0(t) = A \sin(2\pi f2\, t) \quad (2)$$

Where A = 0.15 mV.

McSharry et al used for generate healthy ECG signal the typical parameters as shown in Table I.

TABLE I: PARAMETERS OF THE ECG MODEL USED IN (1)

Index(i)	P	Q	R	S	T
Time (secs)	-0.2	-0.05	0	0.05	0.3
θ_i	-1/3 π	-1/12 π	0	1/12 π	1/2 π
a_i	1.2	-5.0	30.0	-7.5	0.75
b_i	0.25	0.1	0.1	0.1	0.4

B. The proposed model

To create our model, we propose to replace the two first equation of the McSharry model by the Hopf bifurcation [10], defined in equation (3)

$$\begin{cases} \frac{dx_1}{dt} = -(g + x_1{}^2 + x_2{}^2)x_1 - \omega x_2 \\ \frac{dx_2}{dt} = -(g + x_1{}^2 + x_2{}^2)x_2 - \omega x_1 \end{cases} \quad (3)$$

The new model is defined as:

$$\begin{cases} \dot{x_1} = -(g + {x_1}^2 + {x_2}^2)x_1 - \boldsymbol{\omega} x_2 \\ \dot{x_2} = -(g + {x_1}^2 + {x_2}^2)x_2 - \boldsymbol{\omega} x_1 \\ \dot{x_3} = \sum_{i \in \{P,Q,R,S,T\}} a_i \Delta\theta_i \exp\left(-\frac{\Delta\theta_i^2}{2b_i^2}\right) - (x_3 - z_0) \end{cases} \quad (4)$$

with $\Delta\theta_i = (\theta - \theta_i) \bmod 2\pi$, $\theta = \operatorname{atan2}(x_1, x_2)$,

We fixe values of the parameters g = -1.

ω is the angular velocity as it moves around the cycle limit.

The most widely used methods of integration for ordinary differential equations is the Runge-Kutta method, we use these algorithm (fourth-order Runge–Kutta) for solving the equations (4).

The equations (4) can be written as :

$$\frac{d\vec{X}}{dt} = \vec{f}(t, x) \quad , x(t_0) = x_0 \quad (5)$$

Where $\vec{X}\begin{pmatrix} x_1 \\ x_2 \\ x_3 \end{pmatrix}$ and

$$\vec{f}(t, x) = \begin{pmatrix} \dot{x_1} = x_1 - \boldsymbol{\omega} x_2 - (x_1^2 + x_2^2)x_1 \\ \dot{x_2} = \boldsymbol{\omega} x_1 + x_2 - (x_1^2 + x_2^2)x_2 \\ \dot{x_3} = \sum_{i \in \{P,Q,R,S,T\}} a_i \Delta\theta_i \exp(-\frac{\Delta\theta_i^2}{2b_i^2}) - (x_3 - z_0) \end{pmatrix}$$

Runge-kutta 4th order formula :

$$\vec{x}_{n+1} = \vec{x}_n + \frac{h}{6}[\vec{k}_1 + 2\vec{k}_2 + 3\vec{k}_3 + \vec{k}_4] \quad (6)$$

$$t_{n+1} = t_n + h$$

with h the time step , h=1/f_s and f_s is the sampling frequency .

The $\vec{k}_1, \vec{k}_2, \vec{k}_3$ and $\vec{k}_4$ are defined as :

$$\vec{k}_1 = \vec{f}(t_n, \vec{x}_n) \quad (7)$$

$$\vec{k}_2 = \vec{f}\left(t_n + \frac{h}{2}, \vec{x}_n + h\frac{\vec{k}_1}{2}\right) \quad (8)$$

$$\vec{k}_3 = \vec{f}\left(t_n + \frac{h}{2}, \vec{x}_n + h\frac{\vec{k}_2}{2}\right) \quad (9)$$

$$\vec{k}_4 = \vec{f}(t_n + h, \vec{x}_n + h\vec{k}_3) \quad (10)$$

The flow chart of the Runge-Kutta method and processes in ECG synthetic are shown in fig1

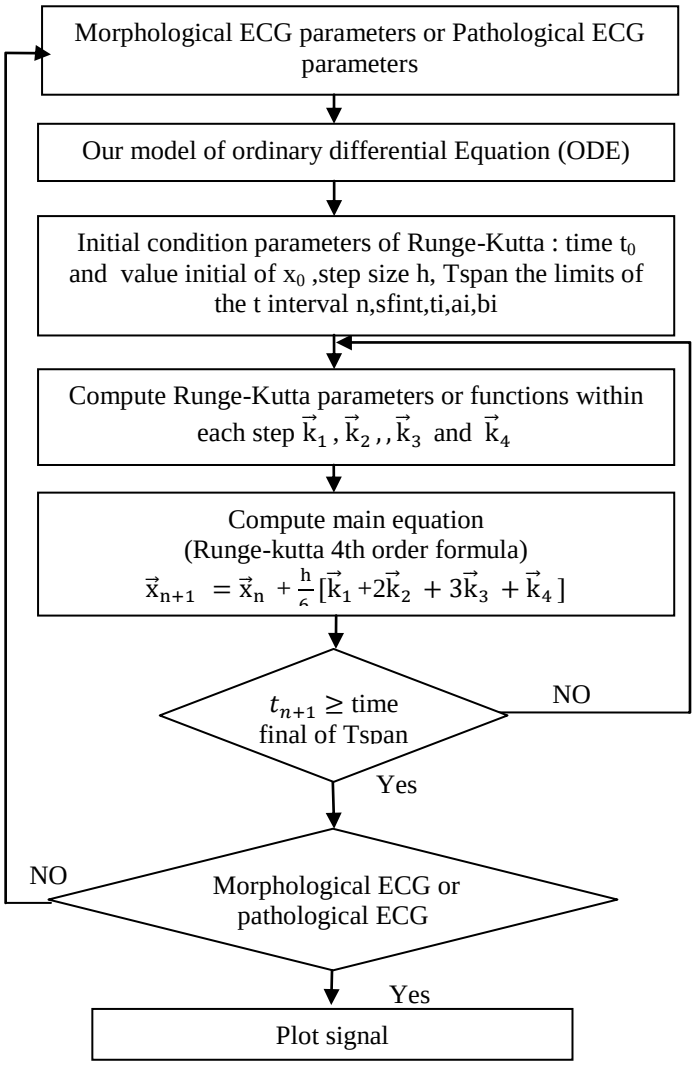

Fig1 ECG sybthetic (morphological and pathological) flow chart of the Runge-kutta 4th order

III. RESULTS AND DISCUSSION

To resolve equation (4) and as mentioned above, the fourth-order Runge–Kutta is use with fixed step size of $\Delta t = \frac{1}{f_s} = 0.0039$ s and an initial starting point equal to
x_0 = [1, 0, 0.04].

In order to evaluate the ability of our model to generate reel synthetic ECG signal, a healthy and unhealthy ECG signal has been taken from the MIT database [11]. We compared generated signals by our model with those obtained from the MIT database.

To this end, visual analysis is used to suggest suitable values for our mathematical model parameters are suggested for each type of arrhythmia.. Fig 2.a shows the normal ECG signal generated with our model. and Fig 2.b shows the normal ECG signal taken from MIT database [11]. Tables 2,3,4,5,6,7,8 and 9 summarize the difference between the model created using parameter values and those taken from the MIT database.

Table 2: parameters values for the proposed model for producing sinus bradycardia ECG signal.

Index(i)	P	Q	R	S	T
Time(s)	-0.2	-0.05	0	0.05	0.3
$\theta_i\,(rad)$	$\frac{-\pi}{3}$	$\frac{-\pi}{12}$	0	$\frac{\pi}{12}$	$\frac{\pi}{2}$
a_i	1.2	-5.0	30	-7.5	0.75
b_i	0.25	0.1	0.1	0.1	0.4
ω	$\mathbf{\frac{15\,\pi}{10}}$				

Table 3: parameters values for the proposed model for producing junctional bradycardia ECG signal.

Index(i)	P	Q	R	S	T
Time(s)	-0.2	-0.05	0	0.05	0.3
$\theta_i\,(rad)$	$\mathbf{\frac{-4\,\pi}{5}}$	$\frac{-\pi}{12}$	0	$\frac{\pi}{12}$	$\frac{\pi}{2}$
a_i	1.2	**1.0**	30	-7.5	0.75
b_i	0.25	0.1	0.1	0.1	0.4
ω	$\mathbf{\frac{4\,\pi}{3}}$				

Table 4: parameters values for the proposed model for producing tachycardia ECG signal.

Index(i)	P	Q	R	S	T
Time(s)	-0.2	-0.05	0	0.05	0.3
$\theta_i\,(rad)$	$\frac{-\pi}{3}$	$\frac{-\pi}{12}$	0	$\frac{\pi}{12}$	$\frac{\pi}{2}$
a_i	1.2	-5.0	30	-7.5	0.75
b_i	0.25	0.1	0.1	0.1	0.4
ω	$\mathbf{4\,\pi}$				

Table 5: parameters values for the proposed model for producing flutter ECG signal.

Index(i)	P	Q	R	S	T
Time(s)	1.2	**1**	**-10**	**-7.5**	**0.075**
$\theta_i\,(rad)$	$\frac{-\pi}{3}$	$\frac{-\pi}{12}$	0	$\frac{\pi}{12}$	$\frac{\pi}{2}$
a_i	**5.0**	**15.0**	15.0	**15**	**5.0**
b_i	0.25	0.1	0.1	0.1	0.4

Table 6: parameters values for the proposed model for producing atrial extrasystole ECG signal.

Index(i)	P	Q	R	S	T
Time(s)	-0.2	-0.05	0	0.05	0.3
$\theta_i\,(rad)$	$\mathbf{\frac{-3\,\pi}{4}}$	$\frac{-\pi}{12}$	0	$\frac{\pi}{12}$	$\frac{\pi}{2}$
a_i	**-1.2**	-5.0	30	-7.5	0.75
b_i	0.25	0.1	0.1	0.1	0.4

Table 7: parameters values for the proposed model for producing ventricular extrasystole ECG signal.

Index(i)	P	Q	R	S	T
Time(s)	-0.2	-0.05	0	0.05	0.3
$\theta_i\,(rad)$	$\frac{-\pi}{3}$	$\frac{-\pi}{12}$	0	$\frac{\pi}{12}$	$\frac{\pi}{2}$
a_i	**0.5**	**1.0**	**-30.0**	**0.2**	**1**
b_i	0.25	0.1	0.1	0.1	0.4

Table 8: parameters values for the proposed model for producing left branch ECG signal.

Index(i)	P	Q	R	S	T
Time(s)	-0.2	-0.05	0	0.05	0.3
$\theta_i\,(rad)$	$\frac{-\pi}{3}$	$\frac{-\pi}{12}$	0	$\frac{\pi}{12}$	$\frac{\pi}{2}$
a_i	**-1.2**	**0.0**	**-30**	-7.5	0.75
b_i	0.25	0.1	0.1	0.1	0.4

Table 9: parameters values for the proposed model for producing right branch ECG signal.

Index(i)	P	Q	R	S	T
Time(s)	-0.2	-0.05	0	0.05	0.3
$\theta_i\,(rad)$	$\frac{-\pi}{3}$	$\frac{-\pi}{12}$	0	$\mathbf{-0.4\pi}$	$\mathbf{0.4\pi}$
a_i	1.2	-5.0	30	**0**	**-0.3**
b_i	0.25	0.1	0.1	0.1	0.4

DISCUSSION

For all the studied cases, we observe that by using suitable parameters, the proposed model permits to generate an excellent ECG for cardiac arrhythmias similar to those taken from the MIT database.

For example, in fig.3 our model allows the generation of sinus bradycardia with a low heart rate (the rate is below than 50 Bpm); and in fig.5 the model can generate sinus tachycardia with heart rate upper than 100 Bpm.

In fig.4 we observe that, we can control the presence/absence of P or superimposed P wave with QRS complex (junctional bradycardia). The fig.6 illustrate flutter ECG signal when the frequency is greater than or equal to 300 Bpm ($\omega > 10\pi$). Atrial extrasystole is generated by the proposed model and illustrated in fig.7, where a negative P-wave is created. fig8 illustrate the ventricular extrasystole and fig.9 and fig.11 illustrate the Left branch block.

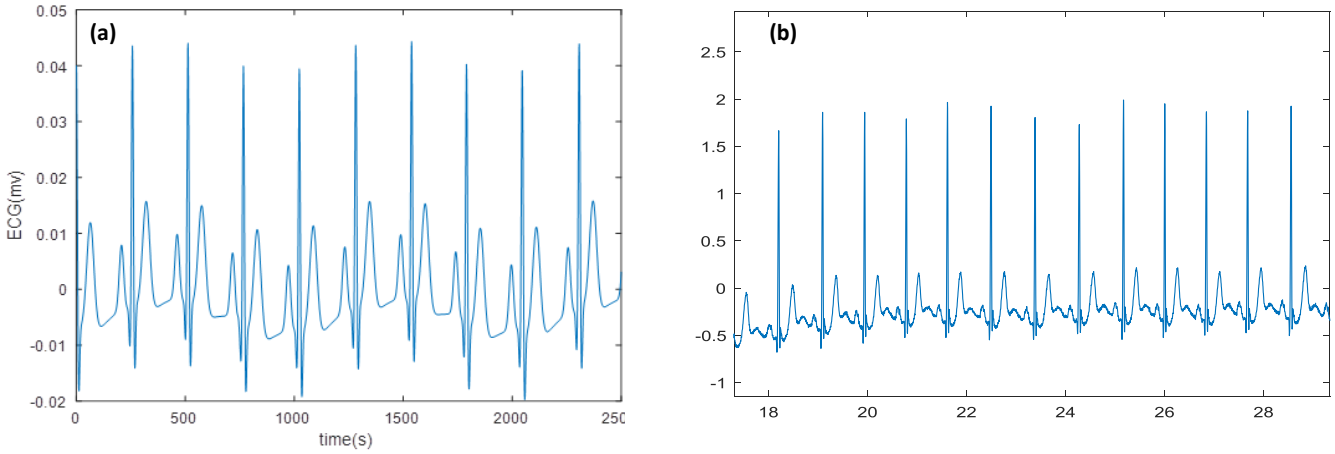

Fig. 2 Normal ECG signal: (**a**) generated by our model and (**b**) taken from MIT database (lead MLII) .

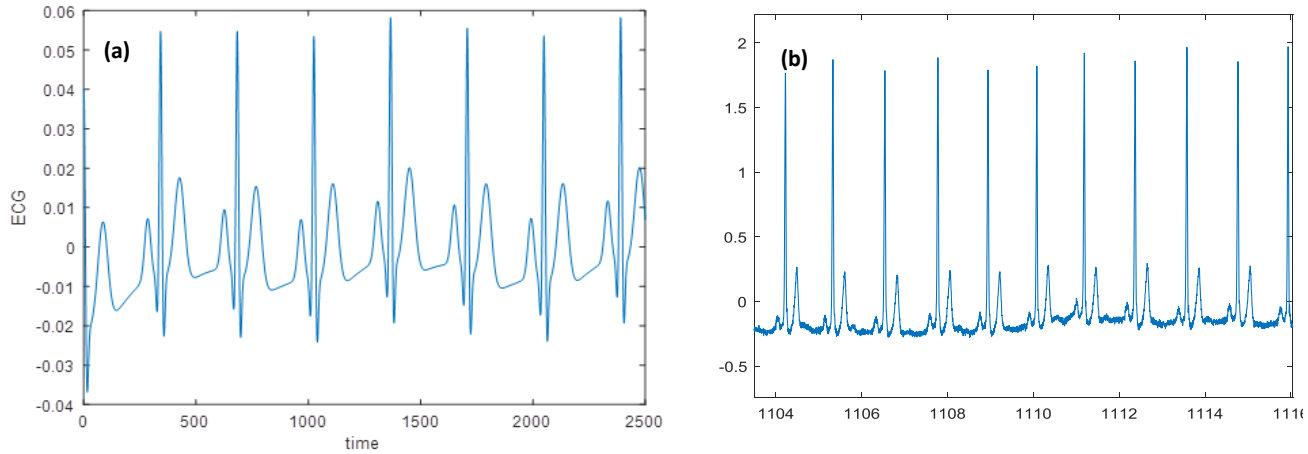

Fig. 3 Sinus bradycardia ECG signal :(**a**) generated by our model and (**b**) taken from MIT database (lead MLII) .

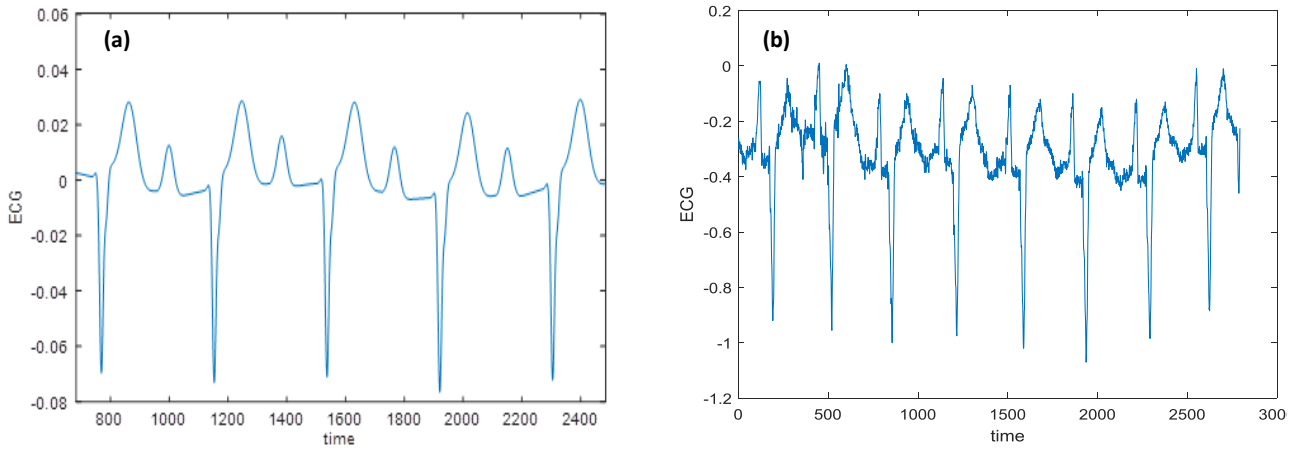

Fig. 4 Junctional bradycardia ECG signal **:** (a) generated by our model and (b) taken from MIT database (lead MLII) .

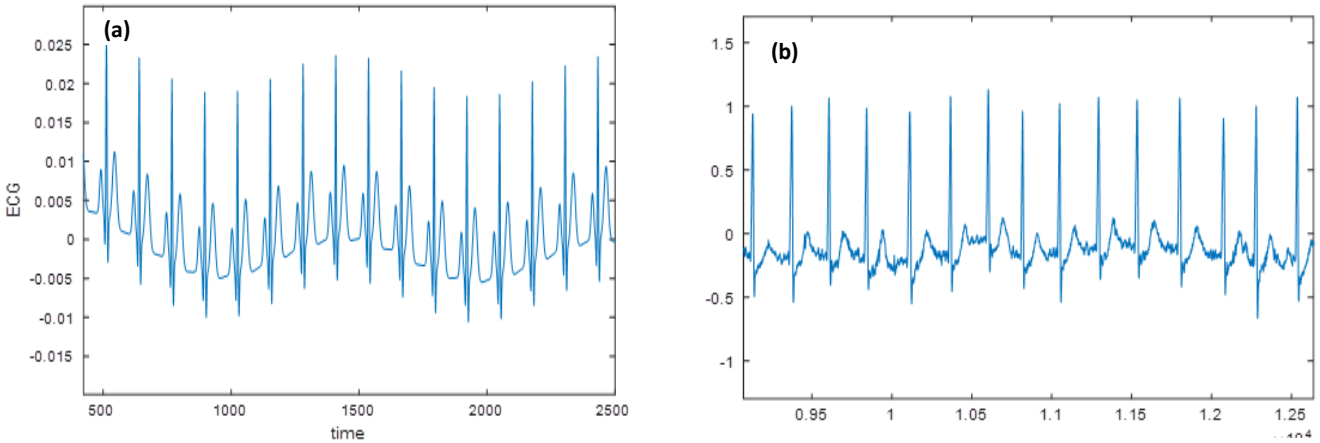

Fig. 5 Tachycardia ECG signal: (**a**) generated by our model and (**b**) taken from MIT database (lead MLII) .

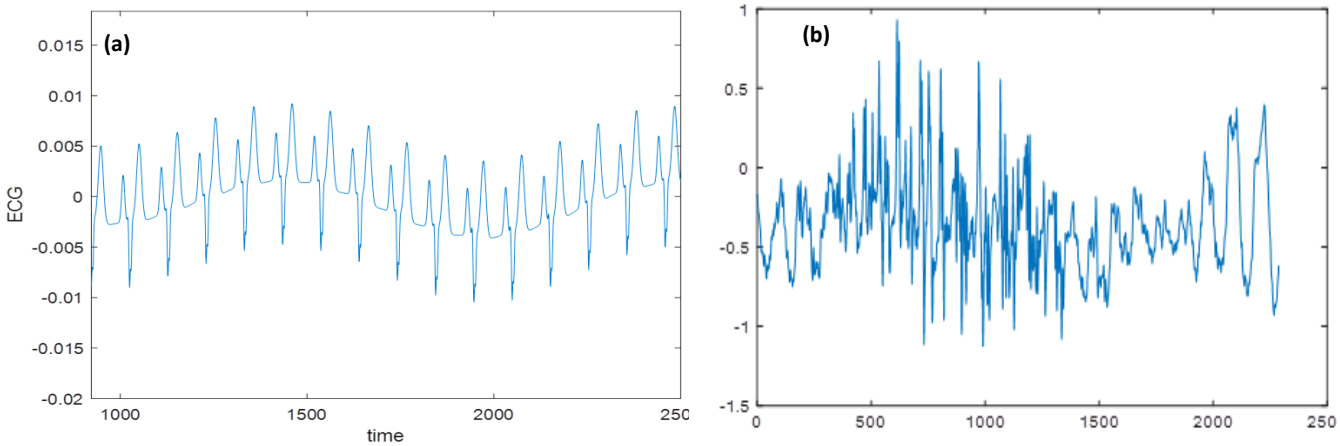

Fig.6 Flutter ECG signal **:** (**a**) generated by our model and (**b**) taken from MIT database (lead MLII) .

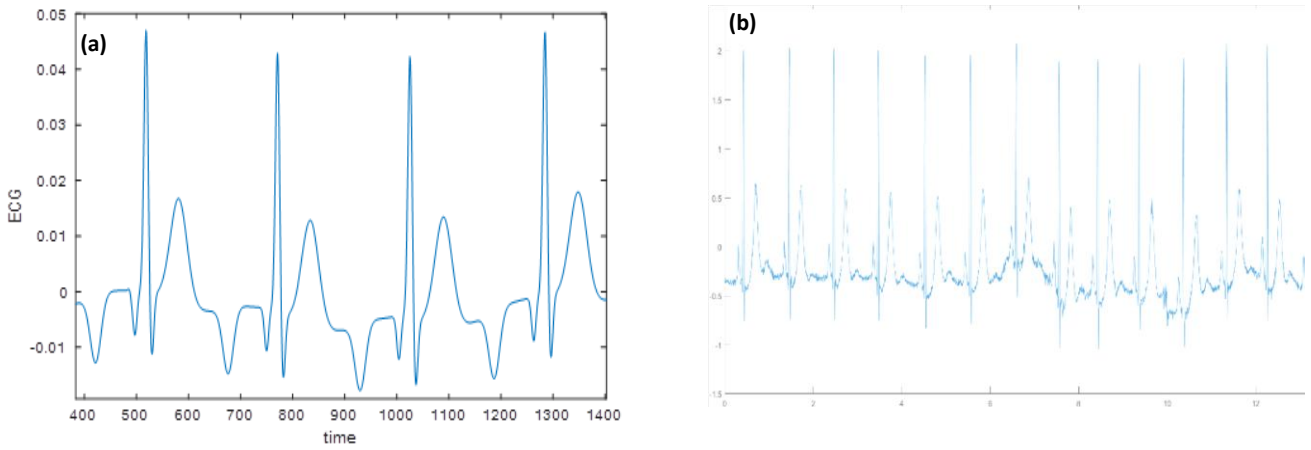

Fig. 7 Atrial extrasystole ECG signal : (**a**) generated by our model and (**b**) taken from MIT database (lead MLII) .

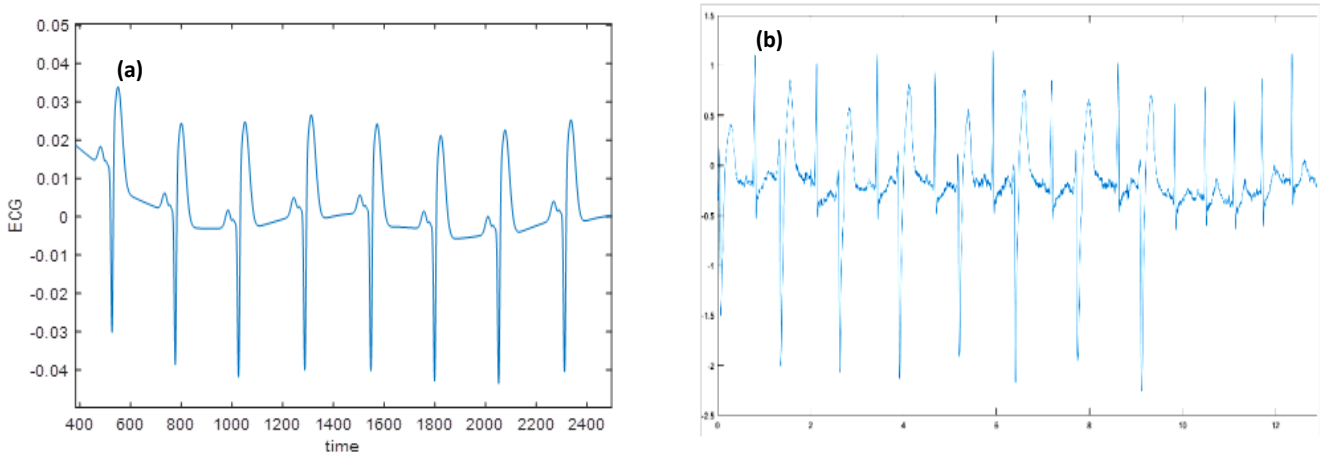

Fig. 8 Ventricular extrasystole ECG signal : (**a**) generated by our model and (**b**) taken from MIT database (lead MLII) .

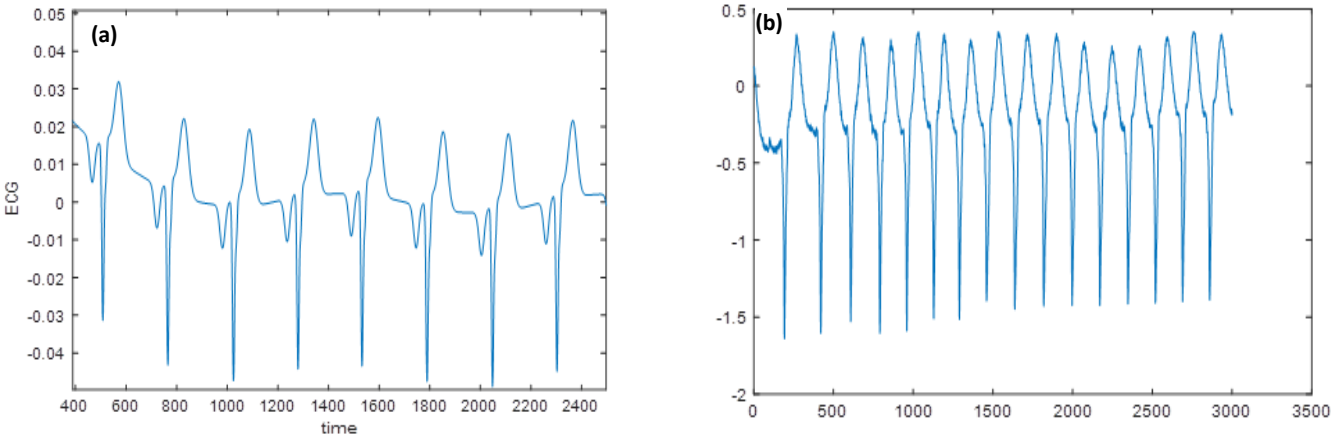

Fig. 9 Left branch block ECG signal : (**a**) generated by our model and (**b**) taken from MIT database (lead MLII) .

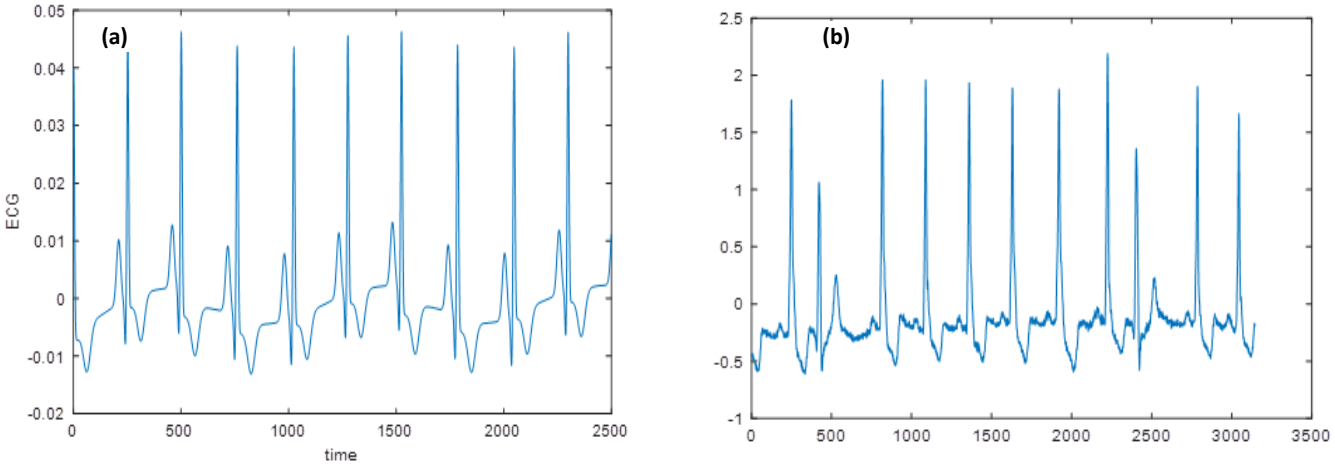

Fig. 10 Right branch block ECG signal : (**a**) generated by our model and (**b**) taken from MIT database (lead MLII) .

IV. CONCLUSION

In this paper, we propose a new model for synthetic ECG generation, this model is based on the McSharry and the use of Hopf bifurcation in the first two equations. The proposed model allows the generation of normal and pathological ECG signal.

The results from numerical simulation show that there is a great similitude between the generated ECG signal and the reel ECG taken from the MIT.

REFERENCES

[1] Ary L. Goldberger, MD, Clinical electrocardiography,seventh edition.elsevier.2006

[2] L. Khansa, A. Naït-Ali, Parametrical modeling of a premature ventricular contraction ECG beat:comparison with the normal case, Comput. Biol. Med. 37(2007) 1–7

[3] Mohamed Lamine Talbi, Philippe Ravier, Detection of PVC in ECG signals using fractional linear prediction, biom. Sig. Cont. 23(2016) 42–51.

[4] McSharry PE, Clifford GD, Tarassenko L, Smith LA, A dynamical model for generating synthetic electrocardiogram signals. IEEE Trans Biomed Eng 50(2003):289–294

[5] Z. Li , M. Ma , ECG modeling with DFG, in: Proceedings of the 27th IEEE Annual Conference Engineering in Medicine and Biology (2005) pp. 2691–2694 .

[6] R. Sameni , G.D. Clifford , C. Jutten , M.B. Shamsollahi , Multichannel ECG and noise modeling: Application to maternal and fetal ECG signals, EURASIP J. Adv. Signal Process. 1 (2007) 043407 .

[7] G.D. Clifford , S. Nemati , R. Sameni , An artificial vector model for generating abnormal electrocardiographic rhythms, Physiol. Meas. 31 (5) (2010) 595 .

[8] E.K. Roonizi , R. Sameni , Morphological modeling of cardiac signals based on signal decomposition, Comput. Biol. Med. 43 (10) (2013) 1453–1461 .

[9] Pascalin Tiam Kapen, Serge Urbain Kouam Kouam, Ghislain Tchuen, A comparative study between normal electrocardiogram signal and those of some cardiac arrhythmias based on McSharry mathematical model, Aus. Phy & Eng. Sci in Medi.132456-019- 007522-7

[10] H. J. Korsch & H. J. Jodl, Chaos, Springer, 1998.

[11] https ://www.physionet.org. Accessed 08 Nov 2018

Placement optimization in sensors network using a linear discernment analyses-based clustering for smart greenhouse.

BENTOUMI Adel
Department of Electrical Engineering
Laboratory of Electronics and New Technologies –LENT-
University of Larbi Ben M'hidi, Oum El Bouaghi
Oum El Bouaghi, Algeria
bentoumi.adel@univ-oeb.dz/Bentoumi.adel@outlook.com

BELHANI Ahmed
Department of electronics
Université Frères Mentouri - Constantine 1
Constantine, Algeria
ahmed.belhani@umc.edu.dz

***Abstract*—The location of the sensors is generally determined based on the experience of greenhouse producers and designers. To monitor accurately the interior environment of a greenhouse, the installation locations of sensors must be carefully chosen. In this study, we propose a linear discriminant analysis (LDA) which chooses an optimal configuration of sensors for a particular application from a whole set of Networks. The proposed method finds the direction w via the LDA such that when data are projected onto this direction, The scheme aims to split the large network into irregular subareas, regarded as blocks. In each of such blocks, the nodes measurements are as uniformly correlated as possible in placement from each cluster.**

Keywords: IoT, Sensors, Clustering, OSP, Smart greenhouse, LDA.

I. INTRODUCTION

Smart agriculture or smart farming is regarded as an important axis and priority that can be developed and implemented to ensure the food safety.

Based on information and communication technology (ICT) capabilities and IoT, environmental parameters can be measured and communicated in order to supervise and control internal parameters microclimate (example: greenhouse) like temperature, humidity, CO_2 under some constraints like solar radiation, UV, CO_2 concentration and wind speed.

In large greenhouses it is difficult to control the internal environment in a consistent and appropriate manner using information technology and communication (ICT) , , so a communication between sensors must be guaranteed by IoT in order to ensure a best control and supervision quality, furthermore, the sensor placement must be optimized in smart agriculture system.

The arrangement of the sensors is a crucial factorthat must be given proper attention, this arrangement creates a layout notion that means a physical topology. Due to the dynamic nature of greenhouse environment where parameters vary spatially and temporally [1], the plant will grow over time and eventually affect the performance of the sensors. A large greenhouse itself contains many microclimatic zones. It can have heterogeneous areas where parameters differ from surrounding areas and the global environment within a single greenhouse. These microclimates exist both horizontally and vertically in a greenhouse. Thus, monitoring the parameters requires inconsistent deployment of sensors. Irrigation and fertilization methods can also affect the sensors location decision. The arrangement of the sensors in a greenhouse has been broadly categorized as horizontal and vertical arrangement [1].

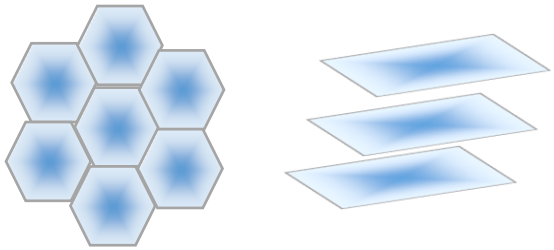

Fig. 1.Tessellations.

Several techniques and methods are used to place the sensors, Javier López et José [2]. the sensors formed a grid of 12 measuring stations was distributed along the greenhouse to record data. Each station is composed of 9 sensors, placed at 0.23 m, 0.93 m and 1.56 m from the ground, (air temperature, black globe temperature, air velocity and relative humidity -117 sensors at all). In addition, another measurement station was placed outside the greenhouse to measure the outdoor climatic conditions.

Konstantinos and P.Ferentinos [3] have adopted the sensors nodes strategy, with sensors are placed symmetrically at the level of the canopy (plant) (1.5 m high) and second four nodes «in caisson» are placed at the four corners of the 20 m by 8 m greenhouse, 3 lanes from the sides, at a height of about 1.8 m. The main goal of the experiments was to investigate the accuracy and reliability of measurements as influenced by sunlight inside the greenhouse.

Marco Mancuso and Franco Bustaffa [1] have proposed asensor network as a grid of wireless nodes organized in a 20 by 50 meters greenhouse of

tomatoes. 6 nodes were used and arranged in two rows 12,5 m apart. The mutual distance between the row nodes is 6.5 m.. The nodes are placed at the bottom of the field with an average height of 0,25 m. A similar configuration developed by Ferentinos and Tsiligiridis [2] they made and implemented to cover larger greenhouses a network of 30 by 30 units using 900 sensors placed on all junctions' blocks.

For Min-Sheng Liao and Shih-Fang Chen [3], the wireless imaging platform based on the IoT is built using 12 wireless camera modules, each of which includes a 5-megapixel sensor camera . The IoT-based environmental monitoring system consists of 12 nodes of wireless sensor and gateway.

Because all crops grow vertically, either upwards or downwards, the sensors are not deployed at ground level, resulting in a vertical arrangement system. The vertical arrangement is of particular importance for greenhouse climate control. The growth and foliage of the crops significantly affect the communication range of the sensor, so the vertical layout seems to be one of the most important solutions. This survey classifies all variants of vertical arrangements in a typical greenhouse, while other authors suggested placement the sensors. K. Mesmoudi and A. Soudani [4] used the model to monitor parameters at the canopy level and above the canopy level of the crop. In another variant of vertical layout, the sensors were positioned on the ground and only the coordinators were placed at a highier level or in the center in the case of a single coordinator Marco Mancuso and Franco Bustaffa [1]. Hybrid of both layouts can also prove to be quiet promising in both the monitoring accuracy and the number of sensors, cropping and the measured parameter is an important factor. Although the topology of the grid seems simple to deploy, it can be about deployment at the periphery and wasting nodes sometimes in a greenhouse environment.

Overlap is a serious problem in the layout of the square grid, few environmental parameters do not change in a few meters in a greenhouse.

Thus, for the measurement of parameters such as temperature, humidity and brightness, the grid layout does not work optimally. For parameters with a range of variability of few meters such as soil temperature, soil moisture, soil pH the grid layout is suitable but requires more sensors [5].

In this work, the main goal is to design an efficient clustering and energy optimization network and placement of sensors to estimate the optimal number of clusters. We illustrate an optimal algorithm for clustering the sensor nodes such that each cluster (which has a master) is balanced and the total distance between sensor nodes and master nodes is minimized. Then, we conceive an efficient clustering scheme, based on Linear Discriminant Analysis (LDA) technique thus exploiting the correlation between clusters.

The remainder of this paper is organized as follows, Section II describes the deferent methods of optimal sensors placement. Section III we explain LDA optimization approach for clustering layout senors and the problem statement where the adopted scenario and the considered assumptions will be presented. Section IV we present sensor layout based on LDA approach for a smart greenhouse and we present the simulation results and discussions, section V offers our conclusion and future work.

II. Sensor Placement Optimiszation Methods

The issue of optimal sensor placement (OSP) in modal testing has attracted considerable attention over the decades. A large body of research has been published contributing to two basic components in determining OSP: the endpoint, which involves a specified performance modal test requirements, and the solution strategy, which explains how to find the best OSP for requirement given by Sang-yeon Lee and In-bok Lee [6].And the optimization which was performed using two methods: placement of the sensor based on error and placement based on entropy. Locations of the sensors for which the monitored data was close to the reference, i.e., the mean data of all measurement locations, were selected. Sensor locations influenced by external weather conditions in poor environmental control were selected. Using these methods, to determine optimal sensor locations to represent the entire facility environment and to detect areas with significant changes in air temperature.

Rainald Lohner and Fernando Camelli [7] The method considers the general problem of sensor placement. Assuming a given number of sensors, each version scenario leads to a sensor input. The data recorded from all possible release scenarios at all possible sensor locations identifies the optimal sensor locations. Clearly, if a single sensor is to be placed, it should be at the location that has recorded the greatest number of rejections. This argument can be used recursively by removing from any further consideration all versions already recorded by previously placed sensors.

new approach developed by M. Arnesano and G.M. Revel [8], based on index measurement performance, to help the HVAC engineers optimize air temperature monitoring, in terms of number of sensors and placement in large spaces. The methodological workflow consists essentially of two main steps:

-Generation of a data set characterizing the horizontal distribution of air temperature in space, which is a key climatic condition that must be measurable physically, virtually or both.

-Optimization of the number and placement of sensors along the perimeter of space.

Khairul and Mohd N [9] proposed another method that is more practical to implement for wired and wireless light sensors in small and large buildings, as well as for new buildings and renovation projects.

- Formulation of a new model for calculating the dimming levels of the LED luminaire, which is also incorporated into the PSO algorithm.

Three contributions related to the lighting control strategy are presented as follows:

-Development of a new method for placing light sensors in terms of numbers and positions using the particle swarm optimization algorithm (PSO) to minimize costs (ie, sensors and electrical energy);

-The proposed method offers superior performance in terms of computational effort and optimal solution (i.e., the number and position of light).

Worden and A.P. Burrows [10], choose a defect detection and classification approach using neural networks and combinatorial optimization methods. Given the existence of an effective defect detection procedure, place the sensors for optimum detection efficiency, a neural network is used to locate and classify defects and a variety of methods are applied to determine an optimal (or almost optimal) sensor distribution.

Ting Hua Yi1 and Guang Dong [11] they propose the optimal placement of the triaxial sensor which plays a crucial role in three-dimensional modal identification. To efficiently find the optimal configuration of the triaxial sensor with the proposed three-dimensional optimal criterion, the hierarchical wolf algorithm (HWA) is developed by mimicking the swarm intelligence embedded in the wolf pack.

Dongmin Guo and David Zhang [12] propose a linear discriminant analysis (LDA) based sensor selection technique (LDASS) which chooses an optimal configuration of sensors for a particular application from a whole set of available configurations. The proposed method finds the direction **w** via the LDA such that when data are projected onto this direction, the samples from two classes are as separate as possible. It is found that after projection, the difference of means of the two distinct sample classes can be expressed as the linear combination of the responses of all the sensors in the system, and **w** can be regarded as the weight vectors for these sensors which indicate the contribution weight of each sensor.

For this work we will use a linear discriminant analysis (LDA) to determine the placement of sensors and their cluster in the network.

.

TABLE I. Method of optimal sensor placement

Reference	Domain	Strategies sensors placement		Hauteur	Parameters of measurement	Approach
		Fixe	*Optimal*			
[1]	greenhouse	X		0.25m	-Temperature -Relative humidity	-WSN Réseaux de capteurs sans fil
[13]	Greenhouse		X		-WSN	-Genetic algorithms
[6]	Greenhouse		X	0.9 m	-Temperature	-Error-based method.
						-Entropy-based method
[7]	Building		X		- Contamination	Computational Fluid Dynamics (CFDs) model simulation
[8]	Salle de sport		X		-Temperature	-Zonal model -The mean deviation. -The standard deviation.
						-The outliers period.
						-The Z index.
[9]	Building		X		-La lumière	- Particle swarm optimization (PSO) algorithm.
[10]	Materials		X		-Default detection	- Réseaux de neurones -Méthodes d'optimisation combinatoire
[14]	Greenhouse	X			-Solar radiation - Temperature	Computational Fluid Dynamics (CFDs) model simulation
[15]	Greenhouse	X			-Solar radiation - Temperature	The thermal energy stored in plants and soil is transferred to the greenhouse environment through respiration, convection and radiation, the curtain and roof reduce losses through the upper walls.
[16]	Greenhouse	X		0.23m 0.93m	-Temperature -Ultraviolet	ISO7726 obligation for favorable conditions of humans works.
				1.56m	-humidity	
					-Speed of Wind	
[11]	Génie civil		X		-Position	-L'algorithme de loup hiérarchique (HWA)

III. LDA Optimization Approach For Cluastring Lyaout Senor

The linear discriminant analysis (LDA) is a fundamental data analysis method originally proposed by R. Fisher [17] in 1936 ,for discriminating between different types of Cluster that can be used for supervised or unsupervised learning [18]. It consists in finding the projection hyperplane that minimizes the interclass variance and maximizes the distance between the projected means of the classes. The LDA can determine the optimum direction of projecting ω, such that when projecting onto ω, the samples from two different classes are as separate as possible and the samples from the same classes are as close as possible. The intuition behind LDA. Data samples in two dimensions are projected in a Lower dimension space Fig 2 (line ω). The line has to be chosen so that the projection maximizes the "separability" of the projected samples.

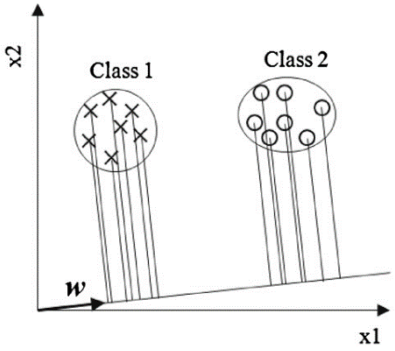

Fig. 2. Data from two classes that are projected onto ω [1].

For Network we consider a large-scale wireless sensor network WSN composed by a large number of sensors, noted *N*, randomly deployed over the monitored area to collect environmental information such as temperature, humidity and solar radiation, as well as soil moisture, which are generally highly correlated both in space and time domains.

For large scale networks, the gathered data volume and needed memory for storage are huge, to reduce the amount of data transmission and then energy consumption, we seek to use a clustering that partitions the considered network into sub-networks, regarded as subareas, by exploiting the inherent data spatial correlation. We here consider WSN with locally uniformly correlated data. After clustering, the network will be partitioned into sub-areas such that the sensor readings in the same spatially contiguous sub-network are uniformly spatially correlated even if the spatial data correlation throughout the network is non-uniform.

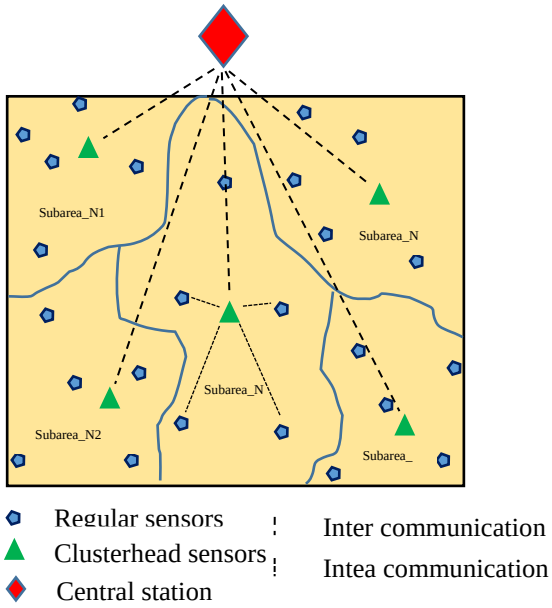

Fig. 3.Network model description.

In the example shown in Fig 3, the network comprises 5 irregular sub-areas with random distribution of nodes. Each region equipped with N_i sensor nodes, where $i = 1, 2., 5$, is presented by a blue line boundary thus designating region with a different uniform data correlation.

A. Assumptions

In our framework, we make the following assumptions:

- The *N* sensor nodes are supposed randomly distributed in a squared monitored area.
- Provided that a sensor may operate as a cluster head transmitting at an appropriate signal range (CH sensor) which allows the communication with the remote base station, or it may operate as a ‘‘regular sensor’’ (RS sensor)
- All sensor nodes know their own geographic location.
- The length unit is defined as the distance between the positions of two neighboring sensor nodes in the horizontal or vertical dimension
- The network topology and the data correlation stay unchanged over the required processing period. In our scenario, sensor nodes are partitioned into clusters, and each cluster has an aggregator node (local sink), represented.

B. Balanced k-Clustering

There are several sophisticated clustering methodologies in the literature of WSNs towards energy saving[19] . However, our work tackles the energy saving issue through the optimization of energy aware clustering in sensor networks nodes. A simple approach of clustering sensors in regular operating modes with their closest CH sensor is adopted for clusters design in the network. The balanced clustering formulation can overcome this drawback by having an upper/lower bound on the size of each cluster, we transform the balanced k-clustering problem to a min-cost flow instance. This instance, can be solved optimally using existing techniques, we use in our work pre-sort with K-means methods [20] for clustering. Suppose we are given N points and we want to group them into k clusters. For the sake of simplicity, we assume that N is a multiple of k. We want to obtain a strictly balanced solution, i.e., each cluster has to contain exactly N/K sensors. After that we apply LDA for optimization methodology for self-organizing, and for validation K optimal Classes we apply five cluster validity Metrics indices for clustering performance evaluation,

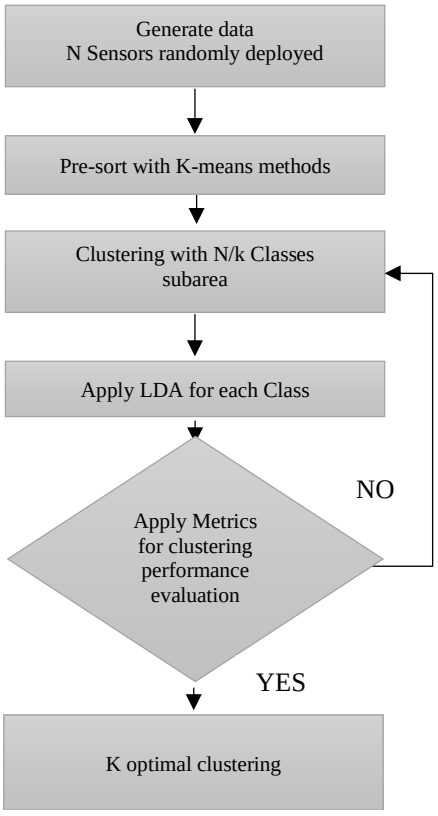

Fig. 4. The working flowchart of Approach K optimal clustering.

Fig 5. demonstrates an example of clustering effect on communication energy consumption. In this figure, black filled points indicate master nodes while the empty circles represent the sensor nodes. Assuming the capacity constraint of 3 for each master node, two sample clustering options, namely AB and C-D have been shown. The total square of distances between master nodes and sensors in clustering A-B is 65 unit, while it is 117 units for clustering C-D. Considering the relation of energy dissipation and this simplified metric (total square of distances), LDA and optimization problem.

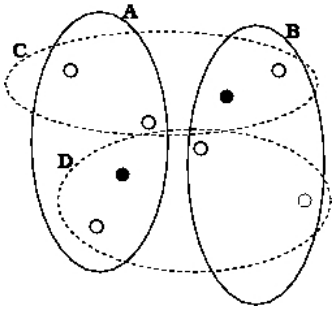

Fig. 5.Partitioning the nodes into clusters A and B leads to a solution dissipating less communication energy compared to clusters C and D [18].

C. Data expression

Assume that we have N sensors samples. They are labeled as classes C_1, C_2,..,C_k, respectively. Each subarea consists of Ni sensors, i.e., S1,.., S_{Ni}, where Ni= N/K our system. each sensor is represented by a discrete by three coordinates 3D (X,Y,Z)(where dimensional d = 3 in our case the ith sensor from class C_1, So the training set including Ni sensors subarea C_1 is expressed as

$$\begin{bmatrix} S_1^1 \\ \vdots \\ S_{Ni}^1 \end{bmatrix} = \begin{bmatrix} x_1^1 & y_1^1 & z_1^1 \\ \vdots & \vdots & \vdots \\ x_{Ni}^1 & y_{Ni}^1 & z_{Ni}^1 \end{bmatrix} \quad (1)$$

Where $S_i^k = [x_i^k \quad y_i^k \quad z_i^k]$ it is sensor i in Cluster k With coordinate (x,y,z).

Same as Eq. (1), the subarea set consisting of Ni sensors from class C_2 is expressed as

$$\begin{bmatrix} S_1^2 \\ \vdots \\ S_{Ni}^2 \end{bmatrix} = \begin{bmatrix} x_1^2 & y_1^2 & z_1^2 \\ \vdots & \vdots & \vdots \\ x_{Ni}^2 & y_{Ni}^2 & z_{Ni}^2 \end{bmatrix} \quad (2)$$

Hence, the sensors set from the whole area can be written as

$$X^T = \begin{bmatrix} S_1^1 \\ \vdots \\ S_{Ni}^1 \\ S_1^2 \\ \vdots \\ S_{Ni}^2 \\ \vdots \\ \vdots \\ S_1^k \\ \vdots \\ S_{Ni}^k \end{bmatrix} = \begin{bmatrix} x_1^1 & y_1^1 & z_1^1 \\ \vdots & \vdots & \vdots \\ x_{Ni}^1 & y_{Ni}^1 & z_{Ni}^1 \\ x_1^2 & y_1^2 & z_1^2 \\ \vdots & \vdots & \vdots \\ x_{Ni}^2 & y_{Ni}^2 & z_{Ni}^2 \\ \vdots & \vdots & \vdots \\ \vdots & \vdots & \vdots \\ x_1^k & y_1^k & z_1^k \\ \vdots & \vdots & \vdots \\ x_{Ni}^k & y_{Ni}^k & z_{Ni}^k \end{bmatrix} \quad (3)$$

where $N = Ni.K$ is the total number of sensors.

D. Find out the optimum direction by LDA

Given the sensors introduced in Section 1,

$$Y = \omega^T.X \quad (4)$$

Where $\omega = \begin{bmatrix} \omega_{11} & \omega_{12} & \omega_{13} \\ \omega_{21} & \omega_{22} & \omega_{23} \\ \omega_{31} & \omega_{23} & \omega_{33} \end{bmatrix}$

is the projection of X onto ω,
ω is the $3 * 3$ dimensional matrix
Y is the $3 * Ni$ dimensional matrix given by

$$Y = [Y_1^1, \dots, Y_{Ni}^1; Y_1^2, \dots, Y_{Ni}^2; Y_1^3, \dots, Y_{Ni}^3] \quad (5)$$

Each entry of row in Y represents projection of a sensor, or $Y = [\mathrm{LDA1}, \mathrm{LDA2}, \mathrm{LDA3}]$.

Where $LDA_i = [\omega_{11}X(1) + \omega_{21}X(2) + \omega_{31}X(3)]$.

And- $X(1)$ row number 1 of matrix X.
-$X(2)$ row number 2 of matrix X.
-$X(3)$row number 3 of matrix X.

The means of the sensors with the two different subareas after projection are denoted by μ_1 and μ_2.

$$\mu_1 = \frac{1}{Ni}\sum_{i=1}^{Ni} S_i^1 \quad (6)$$

$$\mu_2 = \frac{1}{Ni}\sum_{i=1}^{Ni} S_i^2 \quad (7)$$

The means of entire area are denoted by μ. Thus, we have

$$\mu = \mu_1 + \mu_2 + \cdots + \mu_k \quad (8)$$

After projection, we would like the samples with different placement to be well separated, which implies that the means of the classes with different places should be as far apart as possible and the sensors with the same placements are scattered in as small a region as possible. As we know, the LDA determines the ω by maximizing,
According to Fisher's [17] intuition it is desired to find a hyperplane in order to maximize the distance between the means of the two classes and at the same time to minimize the variance in each class. Mathematically this can be described by maximization of Fisher's criterion:

$$J(\omega) = max \left\| \frac{\omega^T Sb\ \omega}{\omega^T Sw\ \omega} \right\| \quad (9)$$

where Sb_i is the between classes scatter of subarea i .

$$Sb_i = (\mu_i - \mu))(\mu_i - \mu)^T \quad (10)$$

The between scatter matrix Sb is defined as

$$Sb = \sum_{i=1}^{k} Sb_i \quad (11)$$

Furthermore, Sw_i is the Within class scatter matrix of subarea i.

$$Sw_i = \left(S_1^i - \mu_i\right))(S_1^i - \mu_i)^T \quad (12)$$

And Within scatter matrix is expressed as

$$Sw = \sum_{i=1}^{k} Sw_i \quad (13)$$

This optimization problem can have infinitely many solutions That is for a solution ω all the vectors $c\ \omega$ give exactly the same value. If, without loss of generality, we replace the denominator with an equality constraint in order to choose only one solution. Then the problem becomes:

$$\max_{\omega} \|\omega^T Sb\ \omega\| \quad (14)$$

$$\text{If } \omega^T Sw\ \omega = 1 \quad (15)$$

The Lagrangian associated with this problem is:

$$\mathcal{L}_{LDA}(x, \lambda) = \omega^T Sb\ \omega - \lambda(\omega^T Sw\ \omega - 1) \quad (16)$$

where λ is the Lagrange multiplier that is associated with the constraint equation (15). Since S_b is positive semidefinite the problem is convex and the global minimum will be at the point for which

$$\frac{\delta \mathcal{L}_{LDA}(x,\lambda)}{\delta x} = 0 \Leftrightarrow Sb\ \omega - \lambda\ Sw = 0 \quad (17)$$

The optimal ω can be obtained as the eigenvector that corresponds to the greatest eigenvalue of the following generalized eigensystem

$$Sb.\omega = \lambda.Sw.\omega \quad (18)$$

E. Raisonment algorithm

Algorithm 1 summarizes the complete LDA selection procedure.

Algorithm 1

Input: N sensors $[\boldsymbol{S_1} \quad \dots \quad \boldsymbol{S_N}]$.

1) Partition with k subarea by $K=N.N_i$ and with k means (we compute k with divide N/Ni and Ni is variable with number of clusters it is satisfied $K=N.N_i$).
2) Compute Sb et Sw matrix.
3) Compute the eigenvector $\boldsymbol{\omega}$ by the LDA.
4) Sort eigenvector with decreasing order of eigenvalues in matrix $\boldsymbol{\omega}$.
5) Calcule projection basis $= \boldsymbol{\omega^T}.\boldsymbol{X}$.
6) Standardization of Y with Z index $\boldsymbol{Z_{i=1,k}} = \frac{Y_i - \mu}{\sqrt{Var(Y_i)}}$
7) Calcule the decision boundary with divide the means of each adjacent two subareas in one dimensional linear combination.

8) Apply Metrics for clustering performance evaluation Check if the classification accuracy if not go to step 1
9) Output: K optimal clustering.

IV. Sensor Layout Based On LDA Approach For A Smart Greenhouse

A. Greenhouse

Wireless Sensors can form a dense network and provide the possibility for continuous monitoring of relevant parameters in a dense grid for a reasonable price, providing a decision support system (DSS) for delivering insight into possible treatments, field-wide or for specific parts of a field.Challenges for the implementation of a wireless network are on one hand due to the fact that large-scale greenhouses have large distributed areas, high variance of temperature and humidity. Thus, it is difficult to lay wires and power supplements. On the other hand, the workload of wired equipment installation and maintenance is heavy. So, in large-scale greenhouses, transmitting signals with wires is not suitable. Finally, the network made up of wireless sensor nodes has some good characters such as mobility, reliable stability and good maintainability. However, in order to attain the desired results, the variables with an indirect influence on the climate also need to be modeled fig 6. in this work we model with Computational Fluid Dynamics (CFD) model developed by ANSYS fluent the solar radiation and the soil heat, for a tomato greenhouse of 10 by 50 meters.

B. Cluster generation

We consider a WSN field composed of N sensor nodes randomly distributed in a large square monitored area with irregular topology. For uniform correlation regions generation, we use the K means to divide the whole network into K contiguous subareas. In each block, there are Ni, sensor nodes whose data are assumed to be uniformly correlated.
The clustering approach proposed is based on LDA . As mentioned before, the network state is assumed to be stationary over a long period of time. After collecting the data from sensors, the sink calculates the data matrix as given in (3) and computes its Eigenvalue Decomposition (EVD).
Then, the matrix ω is constructed from the 3 main eigenvectors of the data matrix.
The WSN is clustered into K subareas, since the number of clusters K is not available in practice, it must be estimated. The optimal number K of clusters is of great importance as it fixes the amount of inter and

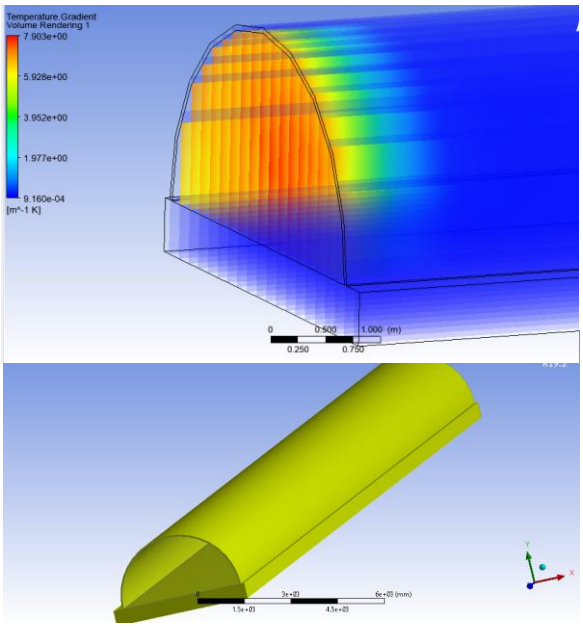

Fig. 6. Greenhouse CFD model

intra-cluster communications. To estimate K, we propose the exploiting the spatial data correlation local uniformity by using LDA technique.
Where $\omega \in R^{3*3}$ is the projection matrix with orthonormal columns formed by the sorted eigenvectors of the equation (18) (in decreasing order of eigenvalues), Y can be considered in one dimensional degree by using dimensionality redaction of LDA when neglecting the d-2;
Therefore, we propose estimating the number of subarea K (corresponding to the clusters number). For this purpose, we recover the optimal K that minimizes LDA reconstruction error or mean square error (MSE), expressed, for the assumed K as

$$MSE(K) = E\left\{\left\|S_i^k - Y_i^K\right\|^2\right\}_{i\,=\,1,2,..,K} \qquad (19)$$

Where Y_i^K is the reconstructed signal using LDA for an assumed K subarea, given by equation (4). this way, we evaluate the error MSE for each possible value of K ranging from 1 to N by using $k = N.N_i$. The optimal number of clusters, Kopt lowest value of MSE.

C. Metrics for clustering performance evaluation

The performance of clustering approaches is evaluated in terms of the validity indices, variance analysis and the global silhouette value. More precisely, five cluster validity indices [21], as expressed in the following, have been evaluated.

1) Calinski-Harabasz

$$CH_{index} = \frac{\frac{1}{K-1}\sum_{l=1}^{K}\|Z_l - Z\|^2}{\frac{1}{N-1}\sum_{l=1}^{K}\sum_{i=1}^{Ni}\|x_l - Z_l\|^2} \qquad (20)$$

- N_i number of points in the ith cluster.
- z: the centroid of the entire data set.
- z_i: represents the ith cluster centroid.

2) Sum of Squared Error (SSE)

the variance analysis is evaluated in terms of the Sum of Squared Error (SSE) given by

$$SEE = \frac{1}{N}\sum_{l=1}^{K}\sum_{i=1}^{Ni}\left\|Y_{ij} - \bar{C}_i\right\|^2 \qquad (21)$$

- Yij is the jth element in C_i .
- $\bar{C}_i$ is the mean measure of Ci nodes.

3) Davies-Bouldin (DB)

$$DB = \frac{1}{K}\sum_{i=1}^{k}\max_{j,j\neq i}\left(\frac{S_i+S_j}{d'_{ij}}\right) \qquad (22)$$

With

- $S_i = \frac{1}{N_i}\sum_{x\in C_i}\|x - z_i\|$
- $d'_{ij} = \|z_i - z_j\|$: distance between clusters C_i and C_j respective centroids.
- z_i: represents the ith cluster centroid.

4) Dunn's (V_D)

$$v_D = \min_{1\leq i\leq K}\left(\min_{1\leq j\leq K, j\neq i}\left(\frac{\delta(C_i,C_j)}{\max_{1\leq l\leq K}\Delta(C_i)}\right)\right) \qquad (23)$$

- $\delta(C_i, C_j) = \min_{x\in C_i, y\in C_j}(d(x,y))$ set distance between C_i and C_j .
- $\Delta(C_i) = \max_{x,y\in C_i,}(d(x,y))$ the diameter of C_i.

5) Global silhouette

for the global silhouette evaluation, we compute the silhouette score over clusters, which corresponds to the mean of silhouette coefficient for each sample calculated using the mean intra-cluster distance and the mean nearest-cluster distance.

$$S_{sil} = \frac{1}{K}\sum_{l=1}^{K}\frac{1}{Ni}\sum_{i=1}^{Ni} S_{sil}(i) \qquad (24)$$

- $S_{sil}(i) = \frac{b(i)-a(i)}{\max(a(i),b(i))}$
- $a(i) = \frac{1}{N_i-1}\sum_{x\in C_i, y\in C_j} d(x,y)$ be the mean distance between x and all other data points in the same cluster.
- $b(i) = \min_{k'\neq k}\frac{1}{N_i}\sum_{x\in C_i, y\in C_j} d(x,y)$ the mean dissimilarity of point x to some cluster C_k as the mean of the distance from x to all points in C_i (where $C_k \neq C_i$).

The objective here is to minimize the values of DB, SSE and maximize the indices values of CH, v_D and the global silhouette value to achieve proper clustering best value which is 1 [22], [23].

D. Evaluation of optimal number of clusters in greenhouse

In order to effectively detect the number of clusters K, we use the dimensionality reduction through LDA technique application. In this approach, we consider a large WSN with N = 30 sensor nodes that are partitioned into $k = N.N_i$ uniform correlation and spatially contiguous subarea. Fig. 7 displays the error MSE(K) as a function of the supposed sparsity level (K). We can see that MSE(K) minimum value with K =2. This means first that LDA captures the useful information through the one independent dominant component, thus showing the effectiveness of LDA application for clusters number detection.

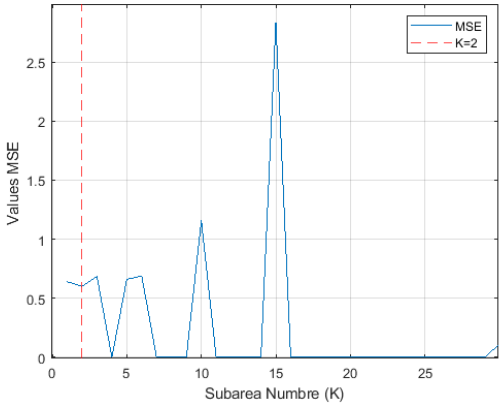

Fig. 7. MSE evaluation as a function of the supposed sparsity level (K).

Also, in order to estimate Kopt, we use method is called the Elbow [21] and the validity indices are evaluated for different values of K as shown in Fig 8,9,10,11&12 In such study, the number of clusters that maximizes CH index, global silhouette value is taken as Kopt. We notice the effectiveness of such proposed metrics as they lead to Kopt = 2.

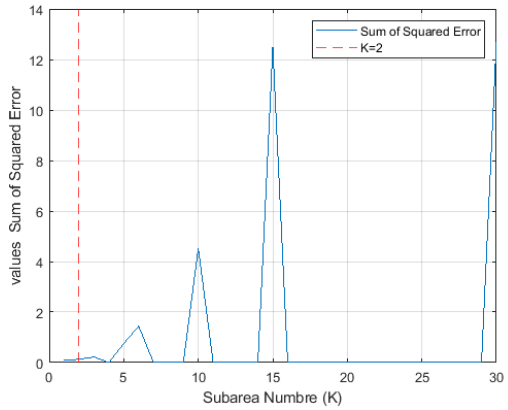

Fig. 8. Validity indices, SSE versus the clusters number (K).

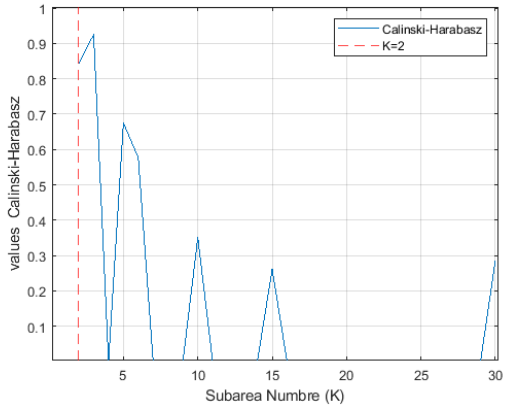

Fig. 9. Validity indices, Calinski-Harabasz versus the clusters number (K).

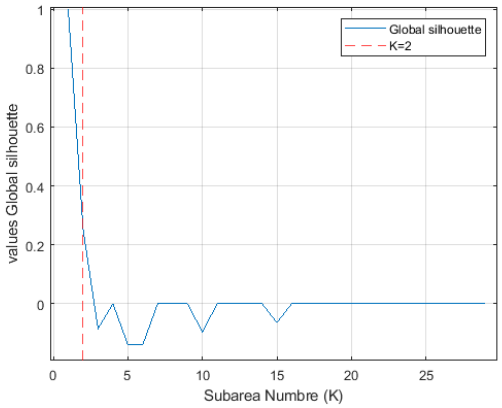

Fig. 11. Validity indices, Global silhouette versus the clusters number (K).

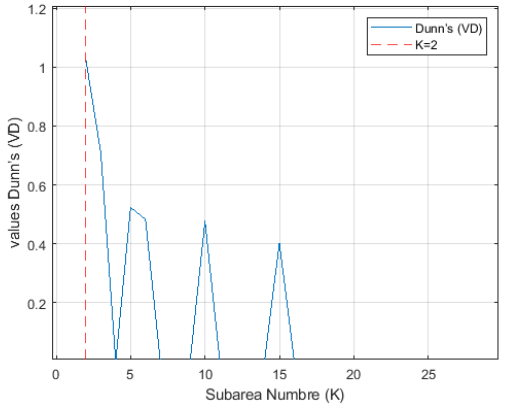

Fig. 10. Validity indices, Dunn's versus the clusters number (K).

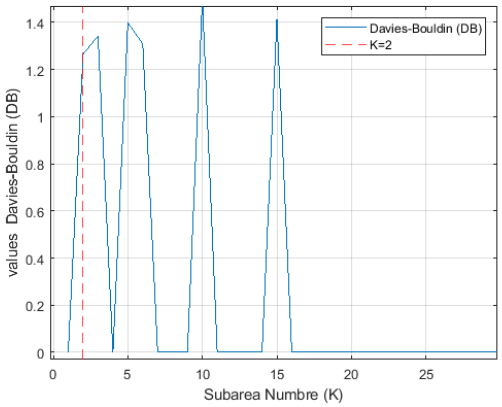

Fig. 12. Validity indices, Davies-Bouldin (DB) versus the clusters number (K).

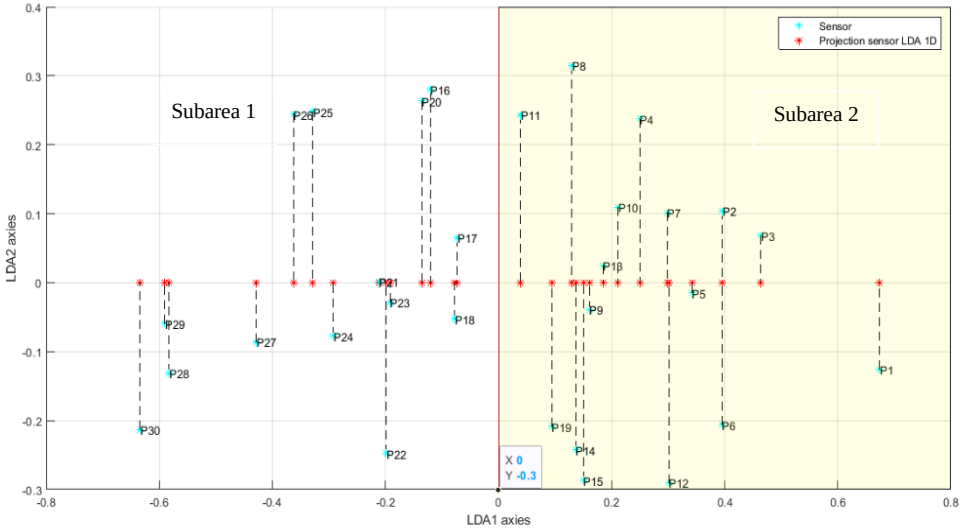

Fig. 13. Optimal partition K=2, Projection Data of sensors in LDA bias with line decision boundary

For finding the projection hyperplane that minimizes the interclass variance and maximizes the distance between the projected means of the classes. The LDA can determine the optimum direction of projecting ω, such that when projecting onto ω, Table II show the variation within and between scatter for each K are considered when setting K to Kopt =2 the samples from two different subarea are as separate as possible and the sensors from the same classes are as close as possible Var=0.08 and sbet =273.2.
Var: interclass variance /Sbet: between scatter

TABLE II. Within and between scatter for each K

	K=1	K=2	K=3	K=5	K=6	K=10	K=15	K=30
Var	0.03	**0.08**	0.13	0.31	0.38	0.92	2.85	1.07
Sbet	1.59e-29	**273.2**	226.9	168.1	140.6	92.24	63.20	32.25

Data samples in two dimensions are projected in a Lower dimension space present in Fig 13 the line has to be chosen so that the projection maximizes the "separability" of the projected samples.
The obtained results K=2 show that the proposed LDA-based clustering achieves the lowest SSE rates compared to others as shown In Fig. 7 Also, our approach realizes the best performance by reaching the higher global silhouette value as well as v_D and CH rates as seen in Fig 9,10 & 11.

V. CONCLUSION

This paper proposes a method for obtaining the optimal sensor configuration in a system. Placement and best clustering When seeking the best direction, for LDA, Experiments show that this approach could significantly increase the classification accuracy and energy management.
This clustering approach aims to divide the large network into irregular subareas, regarded as blocks, in each of which the measurements nodes are as uniformly correlated as possible. This heterogeneity is exploited for estimating the number of possible clusters number in the network. The best we obtained Kopt=2.
Some improvements such as using the Quadratic Discriminant Analysis (QDA) could be investigated in the future to achieve better results for boundary lines.

REFERENCES

[1] M. Mancuso and F. Bustaffa, 'A wireless sensors network for monitoring environmental variables in a tomato greenhouse', in *2006 IEEE International Workshop on Factory Communication Systems*, Jun. 2006, pp. 107–110. doi: 10.1109/WFCS.2006.1704135.

[2] K. P. Ferentinos, N. Katsoulas, A. Tzounis, T. Bartzanas, and C. Kittas, 'Wireless sensor networks for greenhouse climate and plant condition assessment', *Biosyst. Eng.*, vol. 153, pp. 70–81, Jan. 2017, doi: 10.1016/j.biosystemseng.2016.11.005.

[3] M.-S. Liao *et al.*, 'On precisely relating the growth of Phalaenopsis leaves to greenhouse environmental factors by using an IoT-based monitoring system', *Comput. Electron. Agric.*, vol. 136, pp. 125–139, Apr. 2017, doi: 10.1016/j.compag.2017.03.003.

[4] M. Kamel *et al.*, 'Modèle de bilan énergétique d'une serre agricole sans couvert végétal', vol. 11, pp. 1–51, Jan. 2008.

[5] S. Lee, I. Lee, U. Yeo, R. Kim, and J. Kim, 'Optimal sensor placement for monitoring and controlling greenhouse internal environments', *Biosyst. Eng.*, vol. 188, pp. 190–206, Dec. 2019, doi: 10.1016/j.biosystemseng.2019.10.005.

[6] R. Löhner and F. Camelli, 'Optimal placement of sensors for contaminant detection based on detailed 3D CFD simulations', *Eng. Comput.*, vol. 22, no. 3, pp. 260–273, Jan. 2005, doi: 10.1108/02644400510588076.

[7] M. Arnesano, G. M. Revel, and F. Seri, 'A tool for the optimal sensor placement to optimize temperature monitoring in large sports spaces', *Autom. Constr.*, vol. 68, pp. 223–234, Aug. 2016, doi: 10.1016/j.autcon.2016.05.012.

[8] Khairul Rijal Wagiman, Mohd Noor Abdullah, Mohammad Yusri Hassan, Nur Hanis Mohammad Radzi, 'A new optimal light sensor placement method of an indoor lighting control system for improving energy performance and visual comfort', *Building Engineering*, 2020.

[9] K. Worden and A. P. Burrows, 'Optimal sensor placement for fault detection', *Eng. Struct.*, vol. 23, no. 8, pp. 885–901, Aug. 2001, doi: 10.1016/S0141-0296(00)00118-8.

[10] T.-H. Yi, G.-D. Zhou, H.-N. Li, and C.-W. Wang, 'Optimal placement of triaxial sensors for modal identification using hierarchic wolf algorithm: Optimal placement of triaxial sensors using HWA', *Struct. Control Health Monit.*, vol. 24, no. 8, p. e1958, Aug. 2017, doi: 10.1002/stc.1958.

[11] D. Guo, D. Zhang, and L. Zhang, 'An LDA based sensor selection approach used in breath analysis system', *Sens. Actuators B-Chem. - Sens. ACTUATOR B-CHEM*, vol. 157, pp. 265–274, Sep. 2011, doi: 10.1016/j.snb.2011.03.061.

[12] K. P. Ferentinos and T. A. Tsiligiridis, 'Adaptive design optimization of wireless sensor networks using genetic algorithms', *Comput. Netw.*, vol. 51, no. 4, pp. 1031–1051, Mar. 2007, doi: 10.1016/j.comnet.2006.06.013.

[13] A. Saberian and S. M. Sajadiye, 'The effect of dynamic solar heat load on the greenhouse microclimate using CFD simulation', *Renew. Energy*, vol. 138, pp. 722–737, Aug. 2019, doi: 10.1016/j.renene.2019.01.108.

[14] A. Abene, M. Mefoued, L. Maacha, and V. Dubois, 'Modélisation thermique d'une serre agricole chauffée par l'énergie géothermale', in *Revue des énergies renouvelables*, 2007, pp. 207–215. Accessed: Jul. 27, 2021. [Online]. Available: http://pascal-francis.inist.fr/vibad/index.php?action=getRecordDetail&idt=20792914

[15] J. López-Martínez, J. L. Blanco-Claraco, J. Pérez-Alonso, and Á. J. Callejón-Ferre, 'Distributed network for measuring climatic parameters in heterogeneous environments: Application in a greenhouse', *Comput. Electron. Agric.*, vol. 145, pp. 105–121, Feb. 2018, doi: 10.1016/j.compag.2017.12.028.

[16] 'Ronald Aylmer Fisher', *Wikipédia*. Jun. 29, 2021. Accessed: Jul. 30, 2021. [Online]. Available: https://fr.wikipedia.org/w/index.php?title=Ronald_Aylmer_Fisher&oldid=184222594

[17] P. Xanthopoulos, P. M. Pardalos, and T. B. Trafalis, 'Linear Discriminant Analysis', in *Robust Data Mining*, P. Xanthopoulos, P. M. Pardalos, and T. B. Trafalis, Eds. New York, NY: Springer, 2013, pp. 27–33. doi: 10.1007/978-1-4419-9878-1_4.

[18] S. Ghiasi, A. Srivastava, X. Yang, and M. Sarrafzadeh, 'Optimal Energy Aware Clustering in Sensor Networks', *Sensors*, vol. 2, no. 7, Art. no. 7, Jul. 2002, doi: 10.3390/s20700258.

[19] 'K-moyennes', *Wikipédia*. Sep. 09, 2020. Accessed: Jul. 30, 2021. [Online]. Available: https://fr.wikipedia.org/w/index.php?title=K-moyennes&oldid=174559088

[20] 'Performance evaluation of some clustering algorithms and validity indices | IEEE Journals & Magazine | IEEE Xplore'. https://ieeexplore.ieee.org/abstract/document/1114856 (accessed Aug. 02, 2021).

[21] Z. Jellali, L. N. Atallah, and S. Cherif, 'Principal Component Analysis based Clustering Approach for WSN with Locally Uniformly Correlated Data', in *2019 15th International Wireless Communications Mobile Computing Conference (IWCMC)*, Jun. 2019, pp. 174–179. doi: 10.1109/IWCMC.2019.8766477.

[22] U. Maulik and S. Bandyopadhyay, 'Performance evaluation of some clustering algorithms and validity indices', *IEEE Trans. Pattern Anal. Mach. Intell.*, vol. 24, no. 12, pp. 1650–1654, Dec. 2002, doi: 10.1109/TPAMI.2002.1114856.

IoT lightweight cipher security investigation by machine learning techniques

Zakaria Tolba
Laboratory of Mathematics, Informatics and Systems (LAMIS)
University of Larbi Tebessi
Tebessa , Algeria
zakaria.tolba@univ-tebessa.dz

Makhlouf Derdour
Laboratory of Mathematics, Informatics and Systems (LAMIS)
University of Larbi Tebessi
Tebessa , Algeria
m.derdour@yahoo.fr

***Abstract*—The standard Use of Internet of Things (IoT) technology is increasing dramatically and is present in every field of our modern lives. In most IoT systems, the information encryption and decryption of sensitive data are completely implemented by the used terminals which merely limit its specific functionality in the secure transmission of sensitive information. Where the development of lightweight ciphers adequately addresses the limitations of the modest size, small storage memory, low consumption of energy, and weaker computing power.**

Cryptanalysis work published on IoT encryption may be impractical or convincingly demonstrate apparent limitations to generalized. Because they frequently require a considerable amount of critical time, known plain texts, and large storage memory, they are generally performed without the restriction of keyspace, or only the small round variants are attacked. This work proposes deep learning (DL) model-based approach for a successful attack that discovers the plain text from the ciphertext one, the proposal DL-based cryptanalysis is shown to represent a promising step towards and an automated test to verify the security of emerging IoT ciphers.

the results are given and communicated to precisely demonstrate the effective performance of the attack.

***Index Terms*—Tensorflow , Deep learning , neural networks , Cryptanalysis , lightweight cipher , attack , Internet of Things.**

I. Introduction

Nowadays the world marks the contemporary era of IoT, where all data travel from personal device to another along with personal and confidential information. This specific information ordinarily requires private security. Cryptography, this modern art of scientifically investigating the sophisticated techniques for properly securing sensitive information either in communication networks or in proper storage data [1].
The famously used cryptograms like AES [11] and DES [3] critically require an important number of necessary resources for their successful implementation, these cryptograms are unfeasible in the specific IoT devices [17] [6] [9] [18] because of the potential limitations of various performance metrics. Lightweight cryptography occupied a principal role in handling devices that have typically limited memory space to overcome these fundamental limitations.
Lightweight block ciphers operate correctly for IoT on a specific block of sophisticated data for fixed-length specific bits and a symmetric key with a profound transformation. In general cases, these profound transformations in common remain elementary operations with bits, like possible substitution and permutation networks (SPN) or private Feistel networks.
Lightweight ciphers efficiently are mostly symmetric ciphers, made lightweight in practical terms of modest size, small storage, local memory, potential limited energy, and processing time, it's popularly used in smart healthcare sensors, intelligent wireless multimedia surveillance networks (SWMSN), radio-frequency identification tags (RFID), self-driving vehicles (SDV), drones surveillance systems (DSS) modern cars, biochip remote farm animals surveillance, cyber-physical systems (CPS), the intelligent transportation system (STS), and smart industry 4.0 monitoring system, etc.
Cryptanalysis is an audit step that leads designers to develop more robust cryptographic algorithms and adequately assess algorithms' overall impressive performance. However, The fundamental problem is that cryptanalysis of these ciphers can be impractical or convincingly demonstrate apparent limitations to be generalized. Because they frequently require a large amount of considerable time, known plain texts, and big storage memory, they are typically performed without the arbitrary restriction of keyspace, or only the reduced round variants are typically attacked.
This practical work proposes a deep learning (DL) model-based approach for a successful attack on KATAN 32 Bit that discovers the plain text from cipher text one, it's representing a promising step towards a more efficient and automated test to verify the security of emerging ciphers. We directly attack the encryption independently of the private key or the used number of rounds utilizing the TensorFlow platform in a google collaboratory notebook environment that runs in the cloud and stores the results on Google Drive.

II. IoT Lightweight Ciphers Implementation Techniques

IoT lightweight ciphers are implemented by two following techniques:

A. Hardware Implementation:

In this apparent case, the algorithms are efficiently implemented in specific hardware [2], the practical efficiency of the

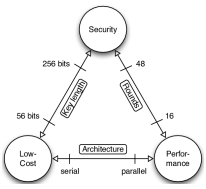

Fig. 1. Trade-off between Security,Performance and Cost of IoT devices

primitive is adequately evaluated by the following metrics:
– Gate Equivalents (GEs) which define the physical memory area ordinarily required to efficiently implement the algorithm primitive. The impressive performance will be excellent if the specific area is lesser.
– The latency traditionally remains the proper time instantly conducted by the hardware circuit to efficiently produce the specific output. It is correctly valued in necessary seconds. The remarkable performance will be more satisfactory if latency is lower.
– Energy consumption efficiently is the economic power consumed by the specific hardware circuit, The economic performance is good for the low power consumption .

B. Software Implementation:

The lightweight algorithm can also be implemented in specialized software [6], mainly for practical use on micro controllers. In this specific type of successful implementation, the performance metrics which will in common be properly evaluated correctly are the Random Access Memory (RAM) usage, program length, and throughput.
–The throughput efficiency represents the measurable quantity of the authentic message being properly processed per time unit. It is valuated as bps. the optimal performance will be more impressive if the private message is typically processed highly.
– Random Access Memory (RAM) usage related to the reasonable amount of necessary information carefully scripted to the proper storage IoT specialized device.
– Program length represents the determinate quantity of necessary information ordinarily required to validate the economic performance without typically depending on its essential input .

The figure 1 highlights the necessary trade-off between Cost, Performance, and marketable private security. The impressive performance of lightweight cryptography is critically evaluated by the used metrics like latency, energy consumption, throughput, and typically waits for the proper time.

III. RELATED WORK

The practical use of machine learning in modern cryptography is not new but successful works in cryptanalysis have scarcely recently emerged. The most famous use case of machine learning is distinguishing or reasonably the identification of encryption algorithms typically based on ciphertext data only.
These published papers have been efficiently implemented to objectively analyze specific data encrypted by modern block ciphers such as AES, 3DES, Blowfish, and Camellia . Cryptanalysts have also attempted to use efficiently deep learning straightforwardly - performing decryption of ciphertexts without any practical knowledge of the private key. This is equivalent to training a machine learning model to emulate or mimic an encryption algorithm for a static private key. For this specific purpose [2] implemented unsupervised learning with deep neural networks to typical cryptanalysis substitution ciphers such as the Vigenere and Shift ciphers.

After that, Mishra et al. investigated whether neural networks can be intentionally used to correctly predict the chosen plaintext of PRESENT block cipher from any particular round [7]. Xiao et al. reasonably described a blackboard security evaluation approach to accurately measure the considerable strength of proprietary ciphers without the necessary knowledge of the encryption algorithms themselves [12].
They precisely quantified the effective strength of a modern cipher by measuring how difficult it was objectively for a neural network to mimic the cipher algorithm. Their published results instantly showed that the marketable security of the modern cipher used for key less entries in modern cars appropriately named Hitag2 was weaker than 3 DES. In [8] Cipher mimicking has also been explored. The academic researchers optimized a deep neural network to decrypt ciphertexts of 64-bit DES.
Perov convincingly demonstrated that using deep-learning techniques could accurately distinguish the ciphertexts of round-reduced ciphers from arbitrary sequences [13].
A deep learning model was used indoors [14] to positively predict the desired outputs of a quantum random number generator.

Gohr properly introduced what was considered functionally the first successful application of machine learning from the comparative perspective of conventional cryptanalysis. A successful machine learning-based differential distinguisher in a side-channel attack was adequately developed and properly used to typically attack the lightweight block cipher Speck32/64 reduced to 11 rounds.

deep learning has also been applied to traditionally perform and objectively evaluate the linear cryptanalysis on DES based on linear expressions [15].
[16] recently proposed machine learning classifiers that can correctly classify differential trails as secure or insecure based on differential private data. Many practical experiments were performed impressively on GFS ciphers. Their published papers satisfactorily showed that the well-trained models were able to generalize to modern ciphers that the developed models have not seen in the past. Finally [17] attempted key recovery attacks on block ciphers, Simon and Speck, using deep learning for side-channel attacks. their published work was successful in properly recovering encryption secret keys for full-round Simon32/64 and Speck32/64 only when the key space of the modern cipher was traditionally restricted to text-

based keys.

IV. TensorFlow and TensorBoard Framework

TensorFlow intellectually represents an ethical Open Source framework that ideally allows us to gently apply machine learning and efficiently perform various complex calculations on decentralized data.TensorFlow was adequately developed to promote open science and creative experimentation with federated learning, a machine learning method by which a shared global model is operated by a considerable number of voluntarily participating clients who maintain their training data locally.

TensorFlow not merely allows independent developers to accurately simulate the federated learning algorithms properly included on their developed models and private data but also to test new algorithms. The fundamental components generously provided by TensorFlow can be intentionally used to implement correctly not intended for training, such as aggregate analyzes .

TensorBoard provides the visualization and tooling needed for machine learning experimentation like tracking and visualizing metrics such as loss and accuracy and visualizing the model graph and viewing histograms of appropriate weights, biases, or other tensors as they change over time. TensorBoard's Graphs dashboard in common remains an effective tool for comprehensively examining any TensorFlow model. It ideally allows the brief view of a conceptual graph of the appropriate model's structure and ensures, it matches the intended design. we can also view an op-level graph to instantly interpret how TensorFlow recognizes our comprehensive program. Comprehensively examining the op-level graph can give insight as to how to voluntarily revise your developed model. For a notable example, we can redesign our developed model if typically training is progressing slower than reasonably expected.

V. Methodology and Results

We have carefully selected to experiment with the fully connected deep neural network architecture in our regression task. After experimenting with various neural network architectures like Deep believe neural networks (DBN), Auto encoders, RNN, LSTM and CNN and MPLs, we found that the fully connected neural network performed consistently for our prediction problem. In notable addition, a fully connected neural network does not require any fundamental assumption to the input, therefore making it flexible to be correctly applied in our problem.

A fully connected neural network consists of a series of fully connected layers, where each neuron is connected to all neurons in the following layer. Figure 3 illustrates the fully connected neural network that was used in our experiments.

A. PROBLEM FRAMING

The global goal of the proposed work is to train neural network models to predict the plaintext from the ciphertext one. Using supervised learning, we framed the problem as a regression task because the goal is to predict the Block cipher consisting of non-negative integers. Practical experiments were performed professionally for both KATAN 32 bit cipher. The ultimate goal of a cryptanalyst is to minimize the distinguisher model from a different block cipher data inputs .

B. Datasets processing

By properly using the Katan 32 bit ciphers for proof-concept experiments, we could typically generate large datasets within a practical amount of considerable time. KATAN block cipher is highly compact and achieves indeed more minimal size with a visible footprint of 802 GE compared to PRESENT cipher. It's a hardware-oriented block cipher, with a specific kind of fundamental Feistel structure and uses a simple key scheduling mechanism. It properly includes three distinct variants of 32 bit, 48 bit, or 64-bit block sizes with a key length of 80 bits and 254 possible rounds of active operations. The software implementation is ordinarily found to be inefficient. The cipher eagerly consumes too much potential energy and has low throughput.

We efficiently generated datasets of 1 470 000 samples profitably using Python lightweight cryptography tools in the google collaboratory environments for the training step and 245 000 samples for the model validation.

C. NEURAL NETWORK ARCHITECTURE

In all of the following experiments, we utilized fully connected neural networks. We initially performed hyperparameter tuning to positively identify the optimal number of layers, number of neurons per layer, loss function, optimizer, number of epochs, and batch size for the regression task.

Scientifically based on our practical experiments, we carefully selected a neural network with seven hidden layers. The specific number of neurons per distinct layer differs typically depending on the specific layer. For Katan 32 bit ciphers, there are 32 neurons in the input layer (equivalent to the specific number of input features), seven hidden layers with 24,20,16,12,16,20,24 neurons each, and an output layer with 32 neurons to represent the predicted plaintext as depicted in Figure 4. The remaining hyper parameters properly used in our remarkable experiments are summarized below:

- Weights initialization : Glorot Uniform .
- Optimizer: SGD for Stochastic gradient descent Optimizer.
- learning rate = 0.001 .
- Activation Function: Rectified Exponential linear unit (RELU) .
- Epochs: 3000 epochs .
- Batch Size: 64 .
- Trainable parameters: 3 748 , None Trainable parameters: 0 .

```
Model: "sequential"
_________________________________________________________________
Layer (type)                 Output Shape              Param #
=================================================================
dense (Dense)                (None, 32, 32)            64
_________________________________________________________________
activation (Activation)      (None, 32, 32)            0
_________________________________________________________________
dense_1 (Dense)              (None, 32, 24)            792
_________________________________________________________________
activation_1 (Activation)    (None, 32, 24)            0
_________________________________________________________________
dense_2 (Dense)              (None, 32, 20)            500
_________________________________________________________________
activation_2 (Activation)    (None, 32, 20)            0
_________________________________________________________________
dense_3 (Dense)              (None, 32, 16)            336
_________________________________________________________________
activation_3 (Activation)    (None, 32, 16)            0
_________________________________________________________________
dense_4 (Dense)              (None, 32, 12)            204
_________________________________________________________________
activation_4 (Activation)    (None, 32, 12)            0
_________________________________________________________________
dense_5 (Dense)              (None, 32, 16)            208
_________________________________________________________________
activation_5 (Activation)    (None, 32, 16)            0
_________________________________________________________________
dense_6 (Dense)              (None, 32, 20)            340
_________________________________________________________________
activation_6 (Activation)    (None, 32, 20)            0
_________________________________________________________________
dense_7 (Dense)              (None, 32, 24)            504
_________________________________________________________________
activation_7 (Activation)    (None, 32, 24)            0
_________________________________________________________________
dense_8 (Dense)              (None, 32, 32)            800
_________________________________________________________________
activation_8 (Activation)    (None, 32, 32)            0
=================================================================
Total params: 3,748
Trainable params: 3,748
Non-trainable params: 0
_________________________________________________________________
```

Fig. 2. The fully connected deep neural network Trained model

- Error function: Mean squared error $MSE = \frac{1}{n}\sum_{i=1}^{n}\left(y_i - \hat{y}_i\right)^2$.
- accuracy function : R-squared defined by : $R^2 = 1 - \frac{UnexplainedVariation}{TotalVariation}$.

The R-squared value R^2 is always between 0 and 1 inclusive , An R^2 of 1 indicates that the regression predictions perfectly fit the data.

Our work is a regression problem the accuracy of the model is defined with these additional metrics:

– Cosine proximity ,Root Mean squared error , Absolute squared error . Figure 2 illustrates the Graph dependencies for the trained model.

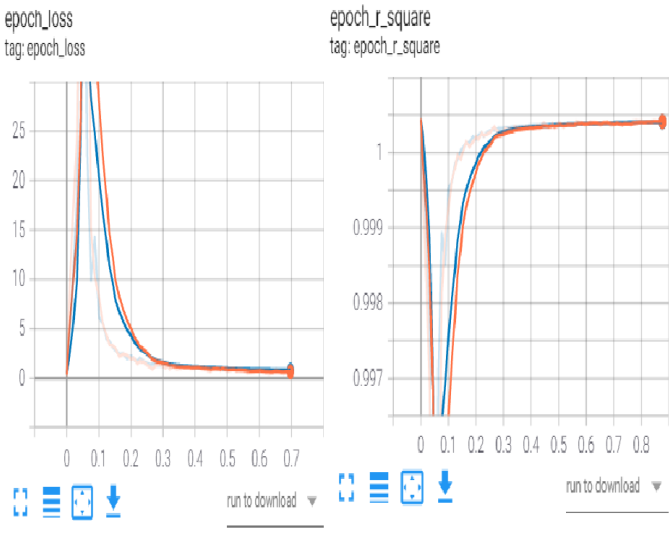

Fig. 3. The experimental results for training and validation.

D. EXPERIMENTAL RESULTS

We have operated the Keras checkpoint named Call Backs to typically save the most satisfactory results after every iteration and to saving the weight and bias of our trained model, After 3000 epoch iterations in 11 hours and 43 minutes, the most impressive results are properly obtained in the 2759 epoch.
Error function: Mean squared error = 0.0087.
accuracy function = 0.89.

The high R-squared value typically ranging from 0.89 also indicates there is an effective relationship between predicted plaintext and the ciphertext. The results are illustrated in the following figure 4.

VI. CONCLUSION

In this illustrated paper,we properly investigate the feasibility of the proposed attack simulation using cloud tools , our work is properly established as a deep learning supervised model to IoT lightweight block cipher security analysis. Our work represent a regression task where we tentatively proposed a deep learning approach to KATAN 32 bit lightweight block cipher security analysis. Exclusively, we typically train fully connected deep neural network models to accurately predict the plaintext from the chosen-ciphertext one. the fully connected deep neural networks are improved using TensorFlow Framework in a Google Cloud environment. We properly investigate the economic feasibility of the proposed attack using cloud tools. in the future works, we plan to extend this work for more larger Block cipher size like KATAN 48 bit and 64 bit , and for more promising step towards a more efficient and automated test to verify the security of emerging lightweight block and stream ciphers .

REFERENCES

[1] R. B.-R. C. and T. LJ and U., "The Electronic Communications Privacy : The Challenge of Applying Ambiguous Statutory Language to Intricate Telecommunication Technologies," Hein On line Act of 1986 .

[2] A. Gomez, S. Huang, I. Zhang, B. Li, M. Osama, and L. Kaiser, "Unsupervised Cipher Cracking Using Discrete GANs," in International Conference on Learning Representations, 2018.

[3] W. Wu and L. Zhang, "LBlock: A Lightweight Block Cipher," in Applied Cryptography and Network Security. Springer Berlin Heidelberg, 2011, pp. 327–344.

[4] K. V. Pradeepthi, V. Tiwari, and A. Saxena, "Machine Learning Approach for Analysing Encrypted Data," in 2018 Tenth International Conference on Advanced Computing (ICoAC). IEEE, dec 2018.

[5] W. Zhang, Y. Zhao, and S. Fan, "Cryptosystem Identification Scheme Based on ASCII Code Statistics," Security and Communication Networks, vol. 2020, pp. 1–10, dec 2020.

[6] F. Yu, X. Gong, H. Li, and S. Wang, "Differential cryptanalysis of image cipher using block-based scrambling and image filtering," Information Sciences, vol. 554, pp. 145–156, apr 2021.

[7] G. Mishra, S. V. S. S. N. V. G. K. Murthy, and S. K. Pal, "Neural Network Based Analysis of Lightweight Block Cipher PRESENT," in Harmony Search and Nature Inspired Optimization Algorithms. Springer Singapore, aug 2018, pp. 969–978.

[8] A. Mundra, S. Mundra, J. S. Srivastava, and P. Gupta, "Optimized deep neural network for cryptanalysis of DES," Journal of Intelligent and Fuzzy Systems, vol. 38, pp. 5921–5931, 2020.

[9] G. Bansod, N. Raval, and N. Pisharoty, "Implementation of a New Lightweight Encryption Design for Embedded Security," IEEE Transactions on Information Forensics and Security, vol. 10, no. 1, pp. 142–151, jan 2015.

[10] A. Jain and G. Mishra, "Analysis of Lightweight Block Cipher FeW on the Basis of Neural Network," in Harmony Search and Nature Inspired Optimization Algorithms. Springer Singapore, aug 2018, pp. 1041–1047.

[11] A. Bogdanov, L. R. Knudsen, G. Leander, C. Paar, A. Poschmann, M. J. B. Robshaw, Y. Seurin, and C. Vikkelsoe, "PRESENT: An Ultra-Lightweight Block Cipher," in Cryptographic Hardware and Embedded Systems - CHES 2007. Springer Berlin Heidelberg, pp. 450–466.

[12] Y. Xiao, Q. Hao, and D. D. Yao, "Neural Cryptanalysis: Metrics, Methodology, and Applications in CPS Ciphers," in 2019 IEEE Conference on Dependable and Secure Computing (DSC). IEEE, nov 2019.

[13] A. Perov, "Using Machine Learning Technologies for Carrying out Statistical Analysis of Block Ciphers," in 2019 International Multi-Conference on Engineering, Computer and Information Sciences (SIBIRCON). IEEE, oct 2019.

[14] N. D. Truong, J. Y. Haw, S. M. Assad, P. K. Lam, and O. Kavehei, "Machine Learning Cryptanalysis of a Quantum Random Number Generator," IEEE Transactions on Information Forensics and Security, vol. 14, no. 2, pp. 403–414, feb 2019.

[15] B. Hou, Y. Li, H. Zhao, and B. Wu, "Linear Attack on Round-Reduced DES Using Deep Learning," in Computer Security – ESORICS 2020. Springer International Publishing, 2020, pp. 131–145.

[16] T. R. Lee, J. S. Teh, J. L. S. Yan, N. Jamil, and W.-Z. Yeoh, "A Machine Learning Approach to Predicting Block Cipher Security," in Cryptology and Information Security Conference. Universiti Putra Malaysia, 2020.

[17] J. So, "Deep Learning-Based Cryptanalysis of Lightweight Block Ciphers," Security and Communication Networks, vol. 2020, pp. 1–11, jul 2020.

[18] E. Biham and A. Shamir, "Differential cryptanalysis of DES-like cryptosystems," Journal of Cryptology, vol. 4, no. 1, pp. 3–72, jan 1991

Segmentation by Regions of Interest of Color Images Using Self-Organizing Maps Neural Networks*

*Note: Sub-titles are not captured in Xplore and should not be used

1st Zemihi Lila
dept. automatic
University of Mouloud Mammeri
Tizi-Ouzou, Algeria
z_automatique@live.fr

2nd Alkama Sadia
dept. automatic
University of Mouloud Mammeri
Tizi-Ouzou, Algeria
sadia_alkama@yahoo.fr

3rd Elmoataz Abderrahim
dept.Computer Science
University of Caen Basse Normandy
Caen, France
abderrahim.elmoataz-billah@unicaen.fr

***Abstract*—In many image processing applications, regions of interest are analyzed in order to extract the relevant information contained in the image. In this paper, we propose to segment regions of interest of a color image where the regions can be segmented into different number of classes. The Kohonen Self-Organizing Maps (SOM) algorithm, which is an unsupervised neural network, is used for this purpose. After, the neurons of the organized map are regrouped into clusters by using a new procedure based on the ascending hierarchical clustering which takes into account the connectedness of the neurons of the topological Kohonen map. The number of neurons groups obtained corresponds to the number of clusters in the region of interest; it can be different for each region.**
Experiments on different kinds of color images showed the efficiency of the proposed segmentation method.

***Index Terms*—Image Segmentation, Kohonen Self-Organizing Maps, Region of Interest.**

I. Introduction

Nowadays, the use of images has become indispensable in various sectors such as medicine, biology, remote sensing, etc. Images processing and analysis have become a rapidly expanding field of research. Segmentation is an important step in image processing as it conditions the interpretation of the results. Numerous image segmentation approaches have been developed [2]–[4], [6].

In this work, we propose an approach based on SOM neural networks. The proposed approach consists of two steps. The first step consists of training the SOM neural networks (Kohonen topological organizing maps) which have the ability to detect similarities, regularities and correlations between big data, grouping them into classes. The second step is to perform a grouping of the neurons using an ascending hierarchical classification [1] that we have modified for the purpose of our work and whose details are given in section III in the paper.

We propose in this work to segment the image not in the classical way by using all the pixels to obtain a segmentation result for the whole image but to work in regions of interest. Indeed, an image has often one or more regions that represent useful information for a user and a background that generally provides no information. The regions of interest may also have different interests for a user. For example, in one region he wants to have all the details while for others a coarse segmentation may be sufficient.

In this work, we propose a tool that allows the user to choose the number of regions of interest and the fineness of the segmentation for each region. To do so, we start in Section II by detailing the principle of Kohonen's self-organizing maps. In Section III, we explain the neurons grouping method we have developed. In Section IV, we will discuss the approach adopted and interpret the obtained results. We end the paper with a conclusion and some perspectives.

Identify applicable funding agency here. If none, delete this.

II. Kohonen self-organizing maps

A. Definition

Self-Organizing Maps (SOM) or topological are artificial neural networks whose learning takes place in an unsupervised manner. They were first developed in 1981 by Tenvo Kohonen [1], [8], [9]. This model has largely demonstrated its capabilities in performing discretization, classification, clustering, quantization and visualization tasks on multidimensional data

B. Concept and principle

The neural model of self-organizing maps proposed by Tenvo Kohonen has a main role which is to project the space of multidimensional observations (data) onto a discrete space of low dimension (generally 2). This space, which is called the map, will be noted φ. The projection allows the extraction of a set of vectors called neurons or prototypes $W = [w_{1i}, ..., w_{ni}]$. They are positioned in such a way that they preserve the topological form and neighbourhood relations of the observation space, i.e. data that are close in the input space will have close representations in the output space and will be classified in the same class or in neighboring classes [5] (see Fig. 1).

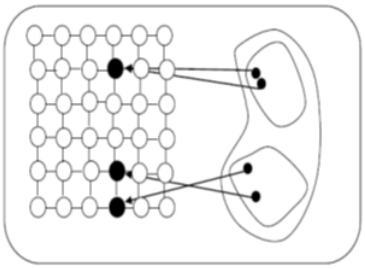

Fig. 1: Neighboring neurons on the map represent fairly "close" objects in the input data space.

The Kohonen network is therefore composed of two layers of neurons, an input layer and an output layer. The input layer is used to present the observations, which are in our case the pixels of the color image,$Y = \{y_i, i = 1, 2, ...3\}$. The output layer (also called adaptation layer) is composed of a lattice of neurons where each of them is connected to all the elements of the input layer and these neurons are organized according to a certain topological structure.

In this work we use a rectangular neighborhood topology with a 2D architecture which consists of interconnecting each neuron to its adjacent neighbors in the row and column to which it belongs (see Fig. 2).

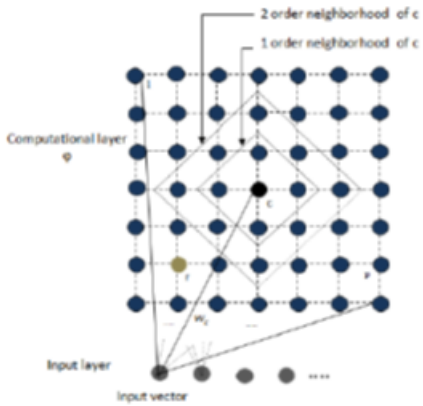

Fig. 2: Representation of a 2D topographic map of Kohonen.

The structure of this topology induces the distances $\delta(c, r)$ that link the winning neuron c to the other neurons r in the map φ. The neuron index $c \in \varphi$ is a winning neuron if its neuron vector w_c is closest to the input vector $y \in Y$.

The distances $\delta(c, r)$ allow us to vary the relative influence of different neurons. This importance is quantified by the neighborhood function $V(\delta(c, r))$ which forces neurons in the neighborhood of c to move their neuron vectors closer to the input vector y. A neuron which is closer to the winning neuron will have a smaller displacement. So the neighborhood function $V^T(\delta(c, r))$ decreases as the distance $\delta(c, r)$increases.

Several neighborhood functions can be used [1].The function used in this paper is the Gaussian one, given by equation 1 and illustrated in Fig. 3

$$V(\delta) = \exp \frac{|\delta|}{T} \tag{1}$$

This function is parameterized by a factor T to take into account the size of the neighborhood (see Fig. 3).

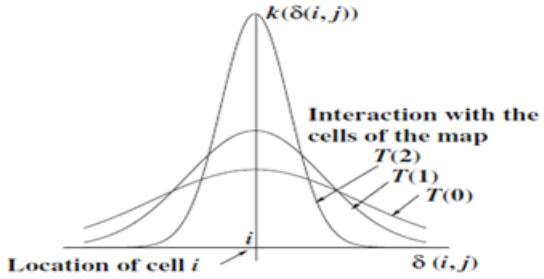

Fig. 3: Gaussian neighborhood function.

C. SOM learning

The objective of a SOM algorithm is to adapt the values of the weights of the neurons of the self-organizing map to the topology of the input space. This is done by minimizing the cost function noted J which is described by the following formula:

$$\mathcal{J}_{som}^T(\mathcal{F}, W) = \sum_{y_i \in Y} \sum_{c \in \varphi} V^T(\delta(c, \mathcal{F}(y_i)))\|y_i - w_i\|^2 \tag{2}$$

The minimization of this function is performed by successive iterations where each of these iterations realized in two phases:

- Competition (or affectation) phase: all the neurons of the grid (map) compete to determine the winning neuron corresponding to the neuron closest to the input vector. The affectation function used by Kohonen is given by :

$$\mathcal{F}(y_i) = argmin_c\|y_i - w_c\|^2 \tag{3}$$

- Adaptation phase: once the winning neuron is found, its neighboring neurons update their weights according to the function:

$$w_c^t = w_c^{t-1} - \mu^t V^T(\delta(c, \mathcal{F}(y_i)))(w_c^{t-1} - y_i) \tag{4}$$

Where μ^t represents the step size of the gradient which decreases according to the iterations t. In this work the gradient step function used is given by the following equation [2].

$$\mu^t = \frac{1}{\sqrt{t}} \tag{5}$$

The Kohonen algorithm is given as follows [1], [7] :

- **Initialization phase**
  - choose the structure, size of the map and the initial neurons (randomly).
  - set the values of T_{max} and T_{min} and the number of iterations N_{iter} , let $t = 0$.
- **t iterative step**
  - choose an observation y_i (usually randomly).
  - calculate the new value of T by applying the formula:
    $T = T_{max} \cdot (\frac{T_{min}}{T_{max}})^{\frac{t}{N_{iter}-1}}$
  - For this parameter perform the following two phases:
    * Affectation phase: affect the observation y_i to the neuron $\mathcal{F}_t(y_i)$ defined by the relation (3).
    * Minimization phase: change the values of W^t by the relation (4).
- **t=t+1**,Repeat the step 2 iteratively until $t = N_{iter}$

III. GROUPING OF NEURONS

The segmentation of color images is the main objective of this paper. Therefore, we have proposed an unsupervised method which consists in a two-level classification. Indeed, each subset of observations is associated in the first level to a neuron of the map via the SOM algorithm. Once the self-organization of the map is completed, it must be completed by a second phase which consists in labeling each neuron of the map in order to obtain the required number of classes.

The labeling can be done by grouping these neurons as best as possible. We propose to group these neurons using a method based on the hierarchical ascending classification method [1].

Due to the topology of the map used in our work, it is not always possible to group neurons or groups of neurons that have a minimum vector distance. In order to group them together, they must also be neighbors in the topological map. We will use an example corresponding to a map containing 3x3 neurons to describe the clustering procedure (see Fig. 4). For an easier illustration, each neuron will be represented by a scalar value instead of a vector containing three values corresponding to the color components of the image.

Thus we can observe in Fig. 4.a a representation of a topological map of size 3x3 with neuron values between 0 and 1. In order to perform the first grouping, all distances between neurons i (i ranging from 1 to 9) and neurons j (j ranging from 1 to 9) of the map are computed. The measure used is a Euclidean distance. The results are displayed in Table Ia.

The minimum distance shown in this table is 0.01, which is achieved between the neurons N1 and N9. This minimum distance will not allow these two neurons to be grouping because they do not verify the neighborhood condition. In fact they are not neighbors (4 neighbors).

We then look for the smallest distance that verifies the neighborhood condition of the neurons in the map. In this example, this is the distance 0.05 measured between the referents N1and N2.

These two neurons will then be grouped together. This grouping is noted N1-N2 and its value is calculated using the following formula:

$$wg_j = \frac{1}{ng_j} \sum_{i \in g_j} w_i \tag{6}$$

where:

g_j is the set of indices of the neurons contained in grouping number j

wg_j is the weight of grouping j

ng_j is the number of neurons in grouping j

w_i is the weight of neuron i

This first grouping will then have a weight : $wg_1 = 0.52$.

A new distance table is calculated (see Table1.b) to determine the next grouping to be performed. And so on, the process is iterated until the desired number of classes is obtained (see Fig. 4 and Table I).

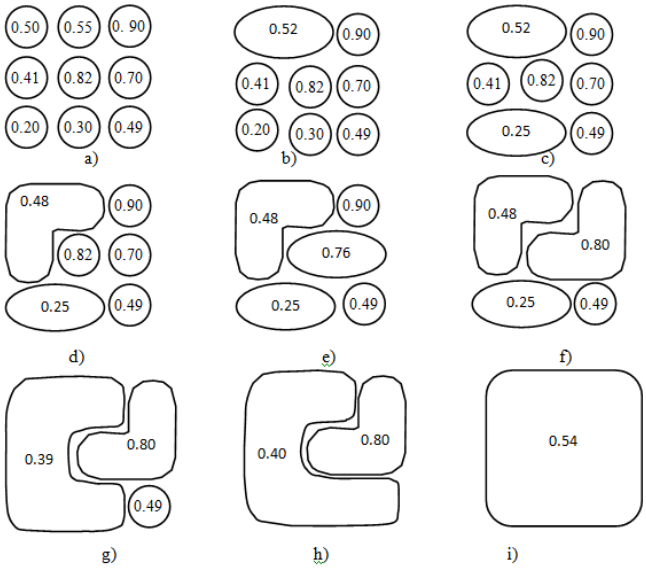

Fig. 4: Example showing the different stages of neurons grouping.

a) Example of a Kohonen map of size 3x3 after self-organization b) Map after the 1st grouping. c) Map after the 2nd grouping. d) Map after the 3rd grouping. e) Map after the 4th grouping. f) Map after 5th grouping. g) Map after 6th grouping. h) Map after the 7th grouping. i) Map after the 8th grouping

TABLE I: Tables of distances between groupings of neurons for the example of Fig. 4.

(a) Distance table for the choice of the first grouping

	N1	N2	N3	N4	N5	N6	N7	N8	N9
N1	0	0.05	0.4	0.09	0.32	0.2	0.3	0.2	0.01
N2		0	0.35	0.14	0.27	0.15	0.35	0.25	0.06
N3			0	0.49	0.08	0.20	0.7	0.6	0.41
N4				0	0.41	0.29	0.21	0.11	0.08
N5					0	0.12	0.62	0.52	0.33
N6						0	0.5	0.4	0.21
N7							0	0.10	0.29
N8								0	0.19
N9									0

(b) Distance table for the choice of the second grouping

	N1-N2	N3	N4	N5	N6	N7	N8	N9
N1-N2	0	0.38	0.11	0.3	0.18	0.32	0.22	0.03
N3		0	0.49	0.08	0.20	0.7	0.6	0.41
N4			0	0.41	0.29	0.21	0.11	0.08
N5				0	0.12	0.62	0.52	0.33
N6					0	0.5	0.4	0.21
N7						0	0.10	0.29
N8							0	0.19
N9								0

(c) Distance table for the choice of the 3rd grouping

	N1-N2	N3	N4	N5	N6	N7-N8	N9
N1-N2	0	0.38	0.11	0.3	0.18	0.27	0.03
N3		0	0.49	0.08	0.2	0.65	0.41
N4			0	0.41	0.29	0.16	0.08
N5				0	0.12	0.57	0.33
N6					0	0.45	0.21
N8						0	0.24
N9							0

(d) Distance table for the choice of the 4th grouping

	N1-N2-N4	N3	N5	N6	N7-N8	N9
N1-N2-N4	0	0.42	0.34	0.22	0.23	0.01
N3		0	0.08	0.2	0.65	0.41
N5			0	0.12	0.57	0.33
N6				0	0.45	0.21
N7-N8					0	0.24
N9						0

(e) Distance table for the selection of the 5th grouping

	N1-N2-N4	N3	N5-N6	N7-N8	N9
N1-N2-N4	0	0.42	0.28	0.23	0.01
N3		0	0.14	0.65	0.41
N5-N6			0	0.51	0.27
N7-N8				0	0.24
N9					0

(f) Distance table for the selection of the 6th grouping

	N1-N2-N4	N3-N5-N6	N7-N8	N9
N1-N2-N4	0	0.32	0.23	0.01
N3-N5-N6		0	0.55	0.31
N7-N8			0	0.24
N9				0

(g) Distance table for the selection of the 7th grouping

	N1-N2-N4-N7-N8	N3-N5-N6	N9
N1-N2-N4-N7-N8	0	0.32	0.01
N3-N5-N6		0	0.31
N9			0

(h) Distance table for the selection of the 8th grouping

	N1-N2-N4-N7-N8-N9	N3-N5-N6
N1-N2-N4-N7-N8-N9	0	0.4
N3-N5-N6		0

After the organization of the topological map and the grouping of neurons into nc classes, the image pixels are then assigned to the different classes. Each pixel is assigned to the class that is closest to it, i.e. to the grouping of neurons whose weight is closest to its value.

IV. Tests and results

Our goal is to segment the color images with a different fineness (different number of classes) for different regions of interest. Indeed, for example, in the medical field, the doctor only examines a part (region) of the image. This is the part where the disease is located. It is this part that is of interest and for which a fine segmentation must be carried out, whereas for the background it is not necessary to carry out segmentation with several classes because it does not provide any useful information (coarse segmentation). The approach adopted to carry out this segmentation is developed below.

A. Adopted approach

The choice of regions of interest and the number of classes for each region is made by the user according to the analysis to be carried out and the objective sought. To better understand the approach adopted, we illustrate its implementation using the image shown in Fig.5 which contains four regions of interest.

Fig. 5: Example of an image to be segmented into regions of interest .

For this image we want to segment the four regions corresponding to a ball and three players, and consider the rest as a background. The first task is to select the four regions of interest manually. The selection is made by delimiting these regions with the mouse. The boundary can have any shape. In the case of the image in Fig. 5, we perform the selection of the regions and the delimitation is shown in green in Fig. 6

Fig. 6: Image of Figure 5 with manually selected regions .

The next task is to set the desired number of classes for each region. In the case of this example we choose 8 classes for region 1, which corresponds to the player on the right side, 8 classes for region 2, which corresponds to the player in the center of the image, 2 classes for region 3, which corresponds to the ball, and 9 classes for the player on the left side of the image. For the background, which contains no useful information, we set the number of classes to 1. The result of the proposed segmentation is shown in the figure below.

Fig. 7: Segmented image.

B. Segmentation results

In this section we will apply the segmentation developed in the previous sections to test images from the Berkeley [11] and Kaggle [10] databases.
To better illustrate the results, we present in the following the segmentations obtained on images with one and several regions of interest.
In Fig. 8, we show the results of the segmentation on images with a single region of interest. Indeed, the image presents often only one object of interest for a user. For example, in the case of traffic cameras, the interest is to read the registration numbers of vehicles that have committed a traffic violation as in the case of Fig. 8.1.a. In the medical field, to establish a diagnosis on the skin lesion, the doctor only focuses on the lesion and ignores the rest of the image as in the case of Fig. 8.2.a.
It also happens that the image presents several regions of interest for the user (see Fig. 9).
For example, in the medical field, several regions of the skin may have lesions, as in the case of the images in Figs. 9.1 and 9.2, where the skin has 2 and 3 lesions respectively.
In the sports field, to identify athletes, it is necessary to read the numbers of their bibs as in the case of Fig. 9.4 where the 3 regions of interest correspond to the 3 bibs.

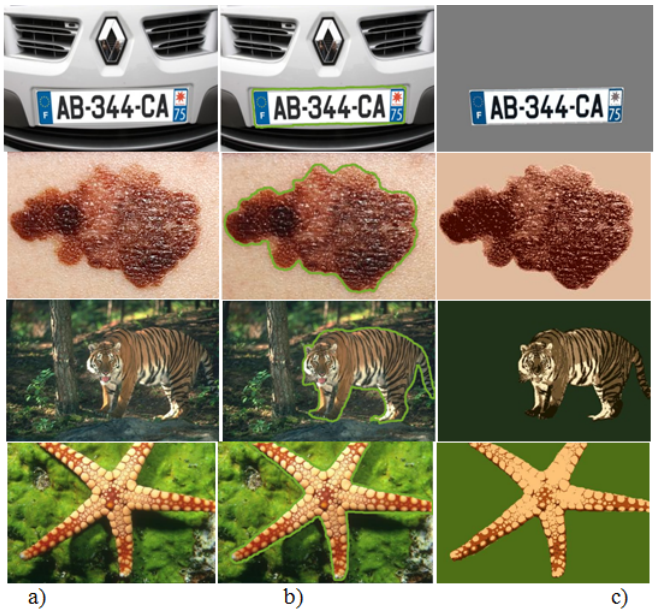

Fig. 8: Result for test images with a single region of interest. a) Original images, b) Images with a selected region, c) Segmented images.

For each manually selected region in the images of Fig. 8 and Fig. 9, we set the number of classes according to tables II and III, knowing that the regions are numbered from left to right in the images with several regions.

TABLE II: Number of classes of the manually selected regions of the images in Fig. 8

image number	nc
8.1	5
8.2	15
8.3	4
8.4	3

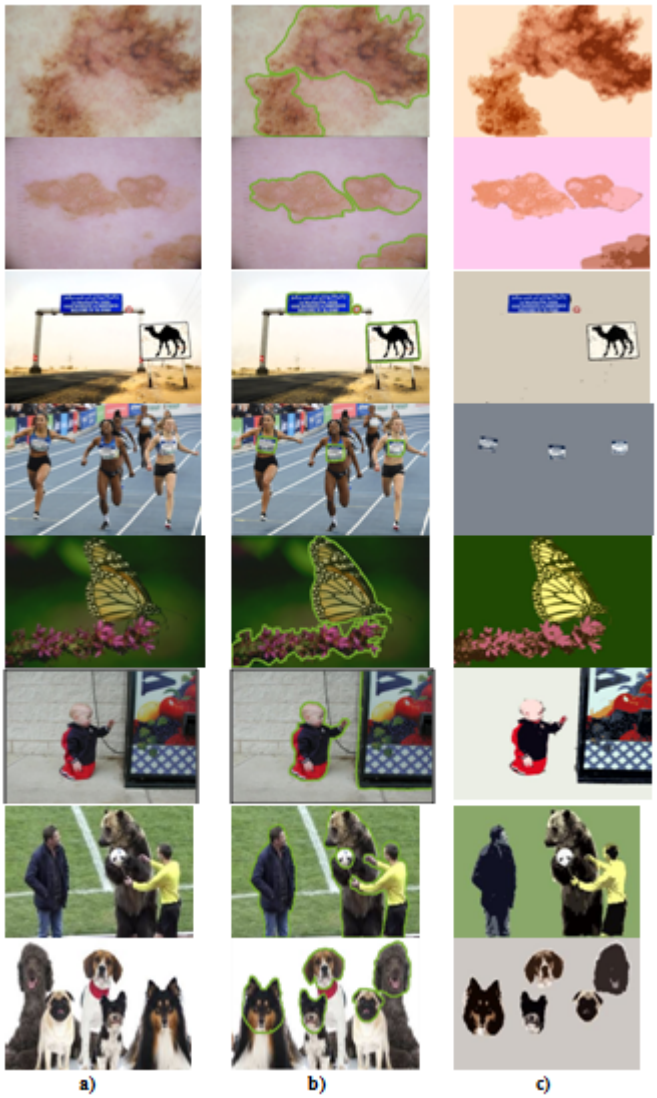

Fig. 9: Result for test images with several regions of interest. a)Original images, b) Images with several selected regions, c) Segmented images.

TABLE III: Number of classes of the manually selected regions of the images in Fig. 9

image number	nc Region1	nc Region2	nc Region3	nc Region4	nc Region5
9.1	5	10	/	/	/
9.2	3	4	2	/	/
9.3	2	3	2	/	/
9.4	5	5	5	/	/
9.5	3	5	/	/	/
9.6	4	7	/	/	/
9.7	3	7	2	3	/
9.8	6	4	5	5	3

The results of the segmentation of images 8.1.a, 8.2.a, 8.3.a and 8.4.a in Fig. 8 with the numbers of classes given in Table II are given in images 8.1c, 8.2c, 8.3c and 8.4c in the same figure. In this figure, each image shows one region of interest. The results of the segmentation of images 9.1.a, 9.2.a, 9.3.a, 9.4.a, 9.5.a, 9.6.a, 9.7.a and 9.8.a in Fig. 9 with several regions of interest are shown in images 9.1.c, 9.2.c, 9.3.c, 9.4.c, 9.5.c, 9.6.c, 9.7.c and 9.8.c of the same figure with the numbers of classes given in Table III. We can see, for example, that in the case of Fig. 8.1, the vehicle number plate is well segmented and reading it becomes easier. An automatic or semi-automatic system can more easily use the image in Fig. 8.1.c to recognize the numbers and letters on the plate. Indeed, the information to be processed in this image is greatly reduced compared to the case where the whole segmented image is used. The number of classes we have chosen in this example (which is 5) is more than sufficient since all the details of this plate are found in the segmented image. In the case of the following images in Fig. 8, the number of classes for the regions of interest is chosen according to the details we wish to have. In the case of the starfish (Fig. 8.4), three classes are sufficient to detect the epidermal growths (i.e. pedicellar) covering the central disc and the five arms of the star. In the case of image 8.3, we have performed the segmentation of the tiger with four classes corresponding to the black stripes, the white fur, the light brown fur and the dark brown fur (or shaded regions). We can see that the segmentation is well done. For image 8.2, we opted for a larger number of classes (15 classes) because in the medical field detail is important for diagnosis. The different nuances are clearly visible, although the number of color levels is greatly reduced. It also happens, in the medical field, that the skin presents more than one lesion, which is the case of images 9.1 and 9.2 of Fig. 9 which present two and three lesions. We have therefore selected respectively two and three regions of interest and the number of class assigned for each region is given in Table III. These numbers are of course chosen according to the details we wish to have of the lesions. We note that, for these two cases, the results of the segmentations are satisfactory. Indeed they allow us to visualize and read easily the different nuances in the lesions. In image 9.3 of Fig 9, the regions of interest are the three road signs. The segmentation is performed with a reduced number of classes for each sign (2, 3 and 2 (see Table. III)) and the result is satisfactory since the letters, numbers and the pictures are clear. The same is true for the other images in Fig. 9 where the number of regions of interest is between two and five and where the segmentation provides images with a reduced number of information while designing the information useful for the application domain. Indeed, for example, in the case of Fig. 9.8, the heads of the dogs are the five regions of interest and the result of the segmentation given by image 9.8.c allows identifying the family of each of them.

V. Conclusion

The main objective of this work is to allow a user to choose the regions on the image to be processed that have an interest for his application. We allow him to delimit as

many regions as he wishes and give him the possibility to perform segmentations with a different number of classes from one region to another. To achieve these objectives, we implemented the SOM algorithm, which is one of the artificial neural networks. The learning is performed in an unsupervised manner. We then developed a technique for grouping the neurons of the map to obtain the desired number of classes for each region of interest. Tests carried out on images from different domains of use and presenting one or more regions of interest have shown the effectiveness of the proposed method.

REFERENCES

[1] S. Alkama, Y. Chahir and D. Berkani, "Label maps fusion for the marginal segmentation of multi-component images," Neural Network World, vol. 25, pp. 405–426, 2015.
[2] K. Qin, K. Xu, F. Liu and D. Li, "Image segmentation based on histogram analysis utilizing the cloud model," Computers & Mathematics with Applications," vol. 62, pp. 2824–2833, 2011.
[3] O. Severino and A. Gonzaga," A new approach for color image segmentation based on color mixture," Machine vision and applications,vol. 24, pp. 607–618, 2013
[4] H. Min, X. F. Wang, D. S. Huang, J.Jin, H. Z. Wang and H. Li, "Level set method for image segmentation based on moment competition," Journal of Electronic ,vol. 24, 033020 ,2015.
[5] S. khedairia and M. T. Khadir, "Impact of clustered meteorological parameters on air pollutants concentrations in the region of Annaba, Algeria," Atmospheric research, vol. 113, pp. 89-101, 2012.
[6] R. Gothwal,S. Gupta,D. Gupta and A. K. Dahiya," Color image segmentation algorithm based on RGB channels," Proceedings of 3rd International Conference on Reliability, Infocom Technologies and Optimization, pp. 1–5, IEEE, India, 2014.
[7] G . Dreyfus, J. M. Martinez,M. Samuelides,M. B. Gordon,F. Badran,S. Thiri and al. Hérault, "Réseaux de neurones ," Vol. 39, Paris: Eyrolles, 2002.
[8] T. KOHONEN, Self organization and associative memory, Springer , Heidelberg ,1984.
[9] T.KOHONEN, Self Organizing Maps, 3rd. ed. Springer, 2000.
[10] Kaggle dataset, https://www.kaggle.com/datasets, last accessed 2021/01/25.
[11] Berkeley dataset,https://www2.eecs.berkeley.edu/Research/Projects/CS/vision/bsds/, last accessed 2021/01/25.

EMG-Based Hand gesture recognition for myoelectric prosthetic hand control

BOUCETTA Lakdhar Nadjib , CHEMLOUL Bilal , REBAI Karima
Electrical Engineering and Computer Science Department, ENST, Algiers-Algeria

Email: l_boucetta@enst.dz , b_chemloul @enst.dz , Karima.rebai@enst.dz

Abstract **– The work presented in this paper aims to contribute to the development of a deep learning-based approach to recognize hand movements using surface electromyography signals (sEMG). This will be used subsequently for the incarnation of these movements using a prosthetic hand.**

The developed classification mechanism combines the proprieties of the convolutional neural network (CNN) known by its ability to extract EMG signal features with the properties of the Long short-term memory (LSTM) cells that extract and learn sequential properties of the time series phenomena. The developed approach could achieve an accuracy rate of 98.8% using the "sEMG for Basic Hand movements Data Set" dataset. To our knowledge, the obtained result is one of the highest accuracy values among all researches done using this dataset.

To develop a complete prosthetic hand system, a prosthetic hand prototype was designed. It was controlled by the hand recognition unit in order to embody the six movements (cylindrical, hook, lateral, palmar, spherical, and peripheral) available in the dataset used.

Index Terms**–Hand gesture recognition, sEMG signals, Deep learning, Convolutional neural networks (CNN), Long Short- Term Memory (LSTM), Prosthetic hand.**

I. INTRODUCTION

For decades, millions of people have suffered from limb amputations like hands. This often caused a functional disability and psychological issues that deprived them to perform many essential vital functions.

Faced with this intractable situation, it was necessary to search for solutions to replace the amputated organs with artificial ones that would help them perform their daily tasks.

With the development of the technology, the efficiency of prosthetic limbs has increased to witness the peak of its development in the current era with the development of many control technologies that allow prosthetic limbs to be obtained with a greater number of movements, a larger functional area, greater comfort, and a more natural appearance.

Myoelectric prostheses are one of the most effective prosthesis technologies created for people with upper limb amputations. They are externally powered artificial limbs dominated by electrical signals generated by muscles called Electromyogram signals (EMG). Controlling schemes of myoelectric hand prostheses can be split into two categories: non-pattern recognition and pattern recognition-based methods. The non-pattern recognition methods (e.g., on/off controllers and/or finite state machines) provide pre-defined control commands based on a sequence of muscle contractions. In this work, the pattern recognition-based approach or the so-called pattern recognition control will be discussed.

The pattern recognition-based control is the extensively studied myoelectric control strategy, in which it is assumed that there is a set of distinguishable and repeatable patterns in EMG signals during different types of movements. The patterns are learned by pattern recognition algorithms that consist of two major steps: feature extraction and classification. Depending on these two steps, the classification of the surface electromyography signals (sEMG) can be done using one of the following three methods:

- Conventional approach: Features extraction and classical classifier.
- Hand-crafted features in deep learning algorithms.

- End to end approach.

II. RELATED WORKS

The classification of EMG signals can be done with different approaches, as mentioned previously. In this section, we will present the two last approaches as they are based on deep learning techniques.

In recent years, deep learning has emerged as one of the most popular Artificial Intelligence techniques, yielding state-of-the-art results for a range of supervised and unsupervised tasks. It is part of a more prominent family of machine learning methods dealing with algorithms inspired by the structure and function of the brain called Artificial Neural Networks (ANN). The superior performance of deep learning resides in the ability to incorporate the feature extraction step, i.e., the ability to extract high-level features from raw data using statistical learning on large datasets. This approach produces effective representations of the input space, based on powerful discriminative features, different from the traditional techniques based on non-deep ML, built on hand-crafted features or rules designed by expert researchers.

This considerable increase in the popularity of deep learning has provided a new perspective to analyze sEMG signals for hand gesture recognition. Currently, classify hand gestures using deep learning can be made using two methods. The first one is based on the separation between feature extraction and classification stages. This method is not widely used because deep architectures have the enough capacity to learn good feature representations on their own.

Typically, the most architecture used in the **Hand-crafted features with deep learning algorithms** approach is the Multilayer Perceptron (MLP) [1]. This architecture does not have the sufficient capacity to learn features such as Convolutional Neural Network (CNN) or Recurrent Neural Network (RNN). For this, it requires a set of input extracted characteristics. Zhang et al. [1] proposed a real-time hand gesture recognition model using sEMG. A feed-forward artificial neural network (ANN) was used for this purpose with a sliding window approach to segment data during feature extraction. The proposed model achieved an average recognition rate of 98.7%.

The second approach is the end-to-end learning of the relationship between raw inputs and classes, which is the most progressive approach in the last years. This approach bypasses the intermediate steps used in traditional pipeline designs. Many researchers used the convolutional neural network (CNN) for myoelectric pattern recognition purposes. In [2], authors compare the success rate of four different CNN architectures applied on the UCI dataset [3], with different signal inputs (raw signals, Fourier transform of the signal; the root means square, and the Empirical mode decomposition (EMD)). In another study [4], Ulysse Côté-Allard et al. proposed the application of a convolutional neural network (CNN) augmented using transfer learning techniques for two datasets of 18 and 17 participants recorded using the Myo armband device. The proposed CNN architecture achieved an average accuracy of 97.81% on seven hand/wrist gestures of the second data set.

In another way, some researchers proposed to consider the sequential character of the EMG signal and developed approaches that exploit Recurrent Neural Network (RNN) or Long Short-Term Memory (LSTM). M. Simão et al. [5] proposed the use of an LSTM recurrent neural network to classify gestures of [6]. They were able to recognize hand gestures with an accuracy greater than 90%.

Xia et al. proposed in [7], the development of a CNN-LSTM architecture to classify the surface electromyography signals (sEMG), this architecture was composed of successive convolution, pooling, and LSTM layers. It is essential to notice that the inputs of this model are time-frequency vectors. This architecture achieved an accuracy rate of 90%. In another work, Nahid et al. [8] proposed a comparative study of classifying different hand gestures of two well-known surface Electromyogram (sEMG) data sets, Rami Khusaba EMG repository and UCI Machine Learning Repository [3] using transfer learning and CNN-LSTM neural network architectures. The combination of CNN and LSTM has achieved state-of-the-art accuracy for these data sets, 99.72% for the UCI Machine Learning Repository and 99.83% for the Rami Khusaba EMG repository.

In the light of these studies, it was decided to develop an architecture that combines the Convolutional Neural Network layers (CNN) and Long Short-Term Memory layers (LSTM) since it incorporates the ability to extract features provided by CNN layers and also the ability to learn the given time-dependent features provided by LSTM layers.

The particularity of our proposed architecture compared to most works cited above which use the CNN-LSTM architecture resides in the use of one-dimensional convolutional layers instead of the two-dimensional ones as done in [7], [8], this choice is motivated by the fact that inputs are of a one-dimensional nature. The second particularity is the wrapping of the CNN layers in time distributed layers, which allow applying the same layer to several inputs and produce one output per input to get the result in time. This will be useful as these CNN layers are followed by LSTM layers, which are known for their ability to process time-series data.

III. Materials and Methods

A. EMG Data Collection

In this work, and due to our inability to provide an adequate amount of data to train the CNN-LSTM architecture, it was decided to use the **"sEMG for Basic Hand movements Data Set".**

This open-source dataset is got from UC Irvine Machine Learning Repository (UCI) [3]. It contains signals of different people grapping different objects. Three surface EMG electrodes attached to the forearm are used for getting signals, two of them in Flexor Capri Ulnaris and Extensor Capri Radialis and the reference electrode in the middle, in order to gather information about the muscle activation. For the data collection, five healthy subjects (two males and three females) of the same age approximately (20 to 22-year-old) were asked to perform six movements each for about 6 seconds with 30 trials [3]. The following movements are the most commonly used in daily life:

1. Spherical (S): for holding spherical tools.

2. Tip (T): for holding small tools.

3. Palmar (P): for grasping with palm facing the object.

4. Lateral (L): for holding thin, flat objects.

5. Cylindrical (C): for holding cylindrical tools.

6. Hook (H): for supporting a heavy load.

The data were collected at a sampling rate of 500 Hz, using as a programming kernel the National Instrument's (NI) LabVIEW [3]. The signals were band-pass filtered using a Butterworth band-pass filter with low and high cutoff 15Hz and 500Hz respectively and a notch filter at 50Hz to eliminate line interference artifacts.

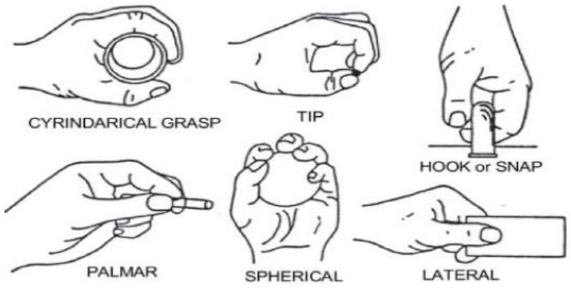

Fig. 1. Gestures performed in **"sEMG for Basic Hand movements Data Set," [3]**

B. Preprocessing

To focus only on segments where the muscle is contracted, we applied the sliding window approach. This approach serves to decompose the signal into segments where possible muscle activities of value for feature extraction might exist. This improves the classification performance.

The windowing technique is divided into types: adjacent and overlapping windowing. The signal is divided into windows, with the end of the previous window is associated with the following window in the adjacent windowing technique. In the overlap windowing, pieces of the past and next window are overlapped, as illustrated in ***fig. 2***.

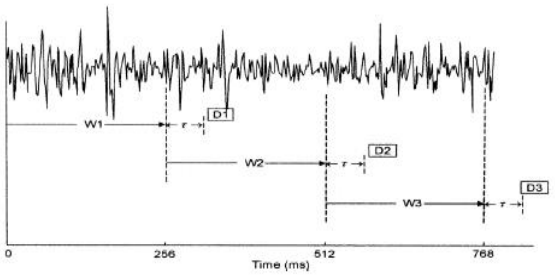

Fig. 2. Signal windowing

In this study, signals were segmented with a 300 ms window and 60 ms of overlap between windows. In the end, a data matrix of 89991x150x2 was got, so 89.991 window samples were generated with a data length of 150.

After splitting the dataset into a set of 300 ms windows, the final step of processing was devoted to organizing this data into training, validation, and testing sets. The training samples represent 75% of the dataset, while the remaining 25% was divided into

the validation and test samples with proportions of 10% and 15%, respectively.

C. Classification using the CNN-LSTM architecture

The architecture proposed in this work is a hybrid architecture containing convolution layers used for extracting features from the sEMG signal, combined with recurrent layers that support sequence prediction.

The model ***(fig.3)*** is made up of two one-dimensional convolutional layers (1D-CNN), where each one is followed by a max-pooling layer. The number of filters used in convolutional layers is 96, with a kernel size of 3. The approach used to implement this model consists of dividing each window of 150-time steps into subsequences of 30-time steps, allowing the CNN layers to process them using the time-distributed layer.

The entire convolutional layers are wrapped in the Time Distributed layer, which applies the same layer to several inputs and produces one output per input to get the result in time; this allows the same CNN model to read in each of the five subsequences of the window.

The feature vectors extracted by convolutional layers will then be the input of two stacked recurrent networks, where the first one is a many-to-many LSTM layer with 80 nodes. As for the second, it is a many-to-one LSTM layer with 64 nodes. Dropout layers with the probability of 0.3 and 0.25 follow each of the LSTM layers, respectively. In the end, there is a fully connected layer containing 32 nodes, followed by a Softmax layer with six nodes that correspond to the number of classes.

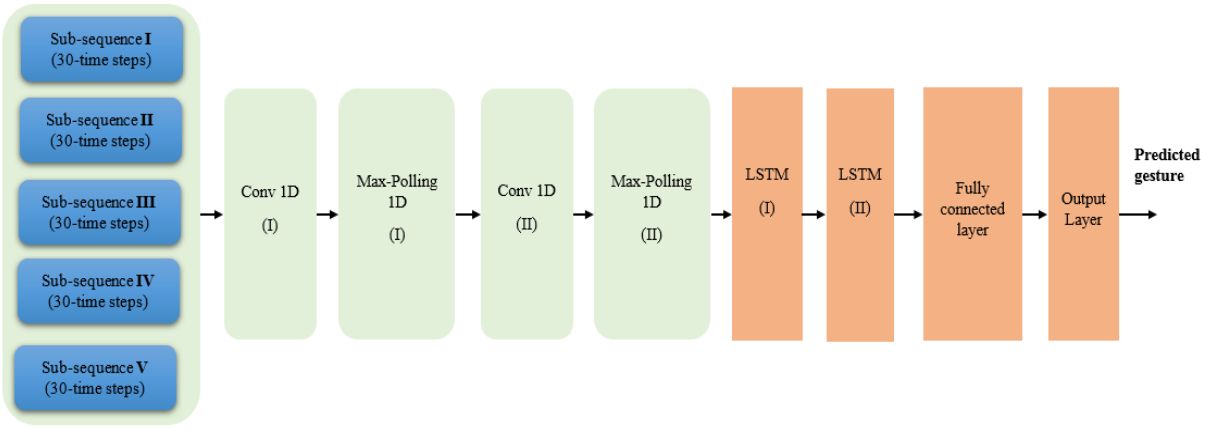

Fig. 3. CNN-LSTM architecture proposed

IV. EXPERIMENT AND RESULTS

In deep learning applications, even after finding the appropriate architecture, it is still necessary to look for optimal hyper-parameters that improve the algorithm's performance. Generally, there are several possible techniques to achieve this, such as performing a grid search where several combinations of parameters are tested and comparing the results. The approach used in this paper is based on testing the model with only one parameter at a time and keep the others parameters constants. This gave us the advantage of seeing the effect of each parameter on model learning. At the end of each test, the hyper-parameter value provided the best result is kept for the subsequent tests.

In most cases, the process of searching for optimal hyper-parameter values begins with testing the architecture with random parameter values. This allowed us to get an idea of the model's performance to improve it in the phase of hyper-parameter tuning.

For this, the first step made was to test the CNN-LSTM model with parameters indicated in ***Table I***.

Table I. The initial hyper-parameter values used for the model training

Activation function	Tanh
Optimizer	Adam
Learning rate	0.001
Number of epochs	100
Batch size	16

To assess the model's performance during the training phase, we check after each epoch if there is an improvement in the validation accuracy. If so, then weights and biases will be stored. At the end of 100 epochs, the model that provides the best validation accuracy will be used for the test phase. This can be seen as a kind of early stopping.

The model evaluation comes out with the following accuracy curve ***(fig.4)*** and the confusion matrix ***(fig.5)***.

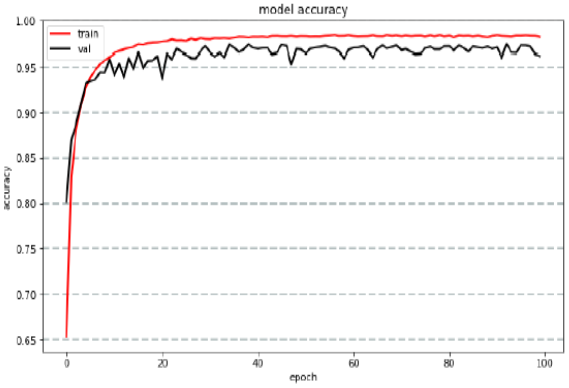

Fig. 4: Model accuracy curve using the training and validation data.

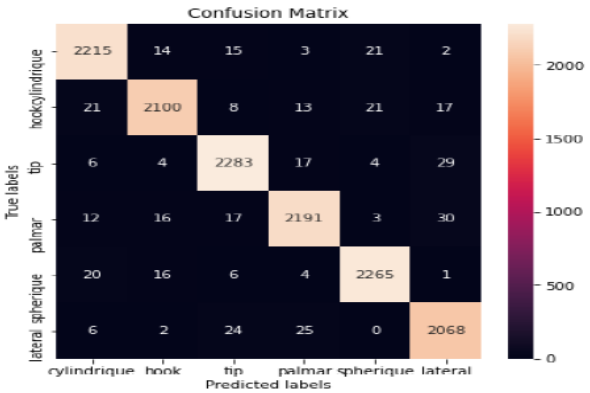

Fig. 5. Confusion matrix

From the resulting accuracy curve, we note that the CNN-LSTM model tested using arbitrary parameter values gave satisfactory results. The accuracy was 98.38% during the training phase and 97.2% in the testing phase.

In addition, we can also observe from the confusion matrix that the classification errors are almost evenly distributed across all classes, which means that the classification has no bias in favor of a class.

Despite the promising results achieved, it remains possible to improve the accuracy values, reduce the loss error, and reduce the training period. This is through testing the model with different hyper-parameter values to get the optimal model.

For this, four hyper-parameters were tested namely, the activation function, learning rate, number of epochs, and batch size.

A. Final structure

The final structure of the developed CNN-LSTM model is the same as that presented in ***fig.6***.

As a final evaluation of the results, the CNN-LSTM model was again trained using the best set of parameters shown in ***Table II***.

Table II: Hyper-parameters used in the final model

Activation function	Relu
Optimizer	SGD
Learning rate	0.2
Number of epochs	100
Batch size	128

Results obtained after the evaluation of this model are represented by the accuracy curve ***(fig.6)*** and the confusion matrix ***(fig.7)***.

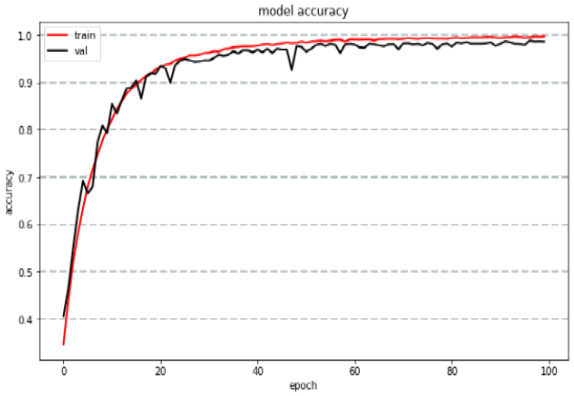

Fig. 6. Model accuracy curve in the train and validation phase

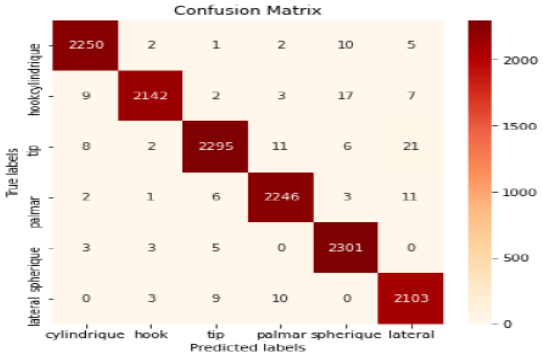

Fig. 7. Confusion matrix

The model evaluation comes out with an accuracy of 98.8%, which is an excellent result. By looking at ***fig. 6*** and ***fig. 7***, some observations can be extracted. At first, the accuracy values in the training and validation phases are very close, which confirms the absence of the overfitting problem. The second remark to note from the confusion matrix is that the classification errors are almost equally distributed in all classes, which confirms the above observation regarding the unbiasedness of the model for any of the classes.

V. HAND PROSTHESIS SYSTEM

Prosthetic hands are artificial devices designed for hand amputees to provide them with certain functions of human hands. Depending on the application of these prostheses and some other criteria, there are several types of control. Perhaps the most important and widely used is one that uses the EMG signal.

In the previous section, a mechanism was developed for the recognition of hand gestures based on the CNN-LSTM model. Subsequently, the embodiment of these hand movements using a myoelectric prosthesis.

The final project architecture comprises five units **(*fig.8*):** Data unit, hand gesture recognition unit, control unit, actuation unit, and also the printed prosthetic hand. In the data unit, data can be either signals captured in real-time from the patient limb using an EMG sensor, or pre-existing signals, as done in this project. The hand gesture recognition unit is a sub-system that classifies hand gestures based on EMG signals provided by the previous unit; this unit was described previously.

The control unit receives the classification result of the EMG signal and sends the corresponding command signal to the actuation unit. This latter consists of four servo motors. According to the command signal provided by the control unit, servo motors move to certain angles, pulling the printed prosthetic hand's fingers to a specific position to form the required gesture. Figure ***(fig.8)*** shows system architecture and its units.

To avoid confusion, we will use the expression **"Printed prosthetic hand"** to refer only to the mechanical structure. In contrast, we will refer to the system comprising (control unit + actuator unit + printed prosthetic hand) by the expression **"prosthetic hand"**.

Figures ***(a-f (fig.9))*** show the different movements performed by the developed prosthetic hand.

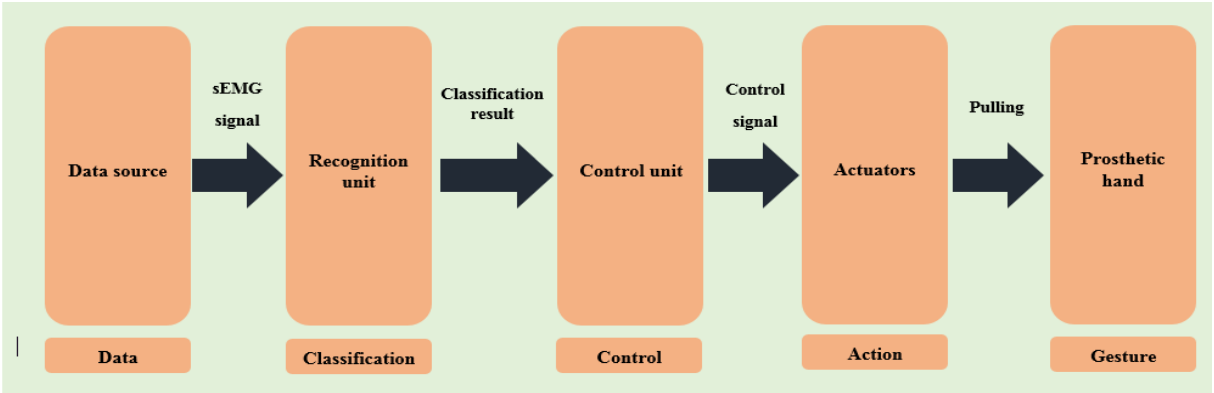

Fig. 8. Hand prosthesis system

(a): Cylindrical gesture

(b): Hook gesture

(c): Tip gesture

(d): Palmar gesture

(e): Spherical gesture

(f): Lateral gesture

Fig. 9. Hand gestures realization

VI. Discussion

When developing a control mechanism for a prosthetic hand based on gesture recognition techniques, two major objectives must be met: achieving high accuracy in the shortest possible time. The test of the complete system represented by the classification algorithm (CNN-LSTM) and the prosthetic hand system showed excellent results, with an overall accuracy of 98.8%, and the ability to classify each movement with approximately equal accuracy. On the other hand, the classification algorithm took 0.08 seconds to classify the 150 ms EMG signal, which is a good value. This value can be improved if more powerful calculation tools are used.

The test of the prosthetic hand system allowed us to compare the movements performed by the natural hand with those of the prosthetic hand. This comparison showed satisfactory results in the latter's ability to embody the desired gestures, although some shortcomings were recorded, mainly due to the structure of the hand which lacks some of the characteristics of the natural hand, making it very difficult to embody certain gestures.

Regarding the time needed for the prosthetic hand to embody these movements, this time varied with the movement performed, but in general, the average time was equal to 2 seconds. This value is considered reasonable given the characteristics of the electrical and mechanical components used.

VII. Conclusion

In this paper, we proposed to develop a hand gesture recognition system using sEMG signals to control a prosthetic hand. This recognition algorithm is based on deep learning techniques that combine the convolutional neural network and the recurrent neural network, which have shown promising results in this type of application. Where the first one is effective in feature extraction and is robust against the noise that overwhelms this type of data. While the LSTM cells can represent features of time dependencies. The developed CNN-LSTM model was tested on the dataset **sEMG for Basic Hand movements Data Set**, which resulted in obtaining a high classification accuracy of 98.8%, this value is one of the highest accuracy values obtained among all researches done using this dataset. This hand gesture recognition model was used subsequently to control a prosthetic hand prototype. Although these satisfactory results, different aspects can be investigated in the future:

- Integrating an sEMG acquisition unit into the system to produce a myoelectric prosthetic hand.

- Improving the model performances either by using the current architecture itself or by developing another architecture while considering the properties of the EMG signal.

- Improving the functional side of the prosthetic hand by increasing the number of degrees of freedom.

VIII. REFERENCES

[1]. Zhang, & Yang, Jaemo & Qian, Jinwu, "Real-Time Surface EMG Pattern Recognition for Hand Gestures Based on an Artificial Neural Network", (2019), DOI: 19. 3170. 10.3390/s19143170.

[2]. Bakırcıoğlu, Kaan & ÖZKURT, Nalan, "Classification of Emg Signals Using Convolution Neural Network". International Journal of Applied Mathematics Electronics and Computers, (2020), DOI: 10.18100/ijamec.795227.

[3]. Sapsanis, Christos, Tzes, Anthony & Georgoulas, sEMG for Basic Hand movements. UCI Machine Learning Repository, (2014).

[4]. U. Côté-Allard, C. L. Fall, A. Campeau-Lecours, C. Gosselin, F. Laviolette, and B. Gosselin, "Transfer learning for sEMG hand gestures recognition using convolutional neural networks", IEEE International Conference on Systems, Man, and Cybernetics (SMC), (2017), DOI: 10.1109/SMC.2017.8122854.

[5]. M. Simão, P. Neto, O. Gibaru, "EMG-based online classification of gestures with recurrent neural networks", Pattern Recognition Letters, (2019), DOI: 10.1016/j.patrec.2019.07.021.

[6]. Simão, Miguel, Neto, Pedro, & Gibaru, Olivier. UC2018 DualMyo Hand Gesture Dataset (1.0-alpha) [Dataset].Zenodo,(2018),https://doi.org/10.5281/zenodo.1320922

[7]. Xia P, Hu J, Peng Y, "EMG-Based Estimation of Limb Movement Using Deep Learning with Recurrent Convolutional Neural Networks". Artif Organs, (2017), DOI: 10.1111/aor.13004. Epub.

[8]. N. Nahid, A. Rahman, and M. A. R. Ahad, "Deep Learning-Based Surface EMG Hand Gesture Classification for Low-Cost Myoelectric Prosthetic Hand," 2020 Joint 9th International Conference on Informatics, Electronics & Vision (ICIEV) and 2020 4th International Conference on Imaging, Vision & Pattern Recognition (icIVPR), (2020), DOI: 10.1109/ICIEVicIVPR48672.2020.9306613.

A Modified Version Number Attack Against RPL Based Networks

Mehdi ROUISSAT
Department of Electronics
Nour Bachir University Center. El-Bayadh, Algeria
STIC Laboratory, University Abou bekr Belkaid, Tlemcen, Algeria.
mehdi.m.rouissat@gmail.com

Mohammed BELKHEIR
LTTNS Laboratory, University Djilali Liabes, Sidi Bel Abbes, Algeria
LIMA Laboratory, Nour Bachir University Center. El-Bayadh, Algeria
belkheir_m@yahoo.fr

Hicham Sid Ahmed Belkhira
Department of Electronics
Nour Bachir University Center. El-Bayadh, Algeria
belkhira.hichem@gmail.com

***Abstract*—Routing Protocol for Low Power and Lossy Networks (RPL) has been proposed to efficiently manage the different functions of the network layer for wireless sensor networks when providing Internet connectivity. RPL has been designed for constrained devices and networks. Owing to their constrained power, memory, and processing, RPL-based networks are exposed to a wide range of security attacks that mainly include control message tampering. In this paper, we present a new modified Version Number attack, called Decreased Version Number Attack (DVNA), where the idea behind it is that the version number is decreased instead of increased as in the traditional version number attack. The aim of the attack is to initialize continually the trickle timer of the malicious node's neighbors, which leads to unnecessary exchange of control messages, therefore exhausts the resources of the nodes and reduce the network lifetime. The obtained results show an increase of up to 71% in the exchanged control messages and an increase of up to 47.77 % in energy consumption.**

Keywords—RPL, Security, DVNA, resources, version number

I. INTRODUCTION

Due to the constraint of Internet of Things (IoT) devices, routing is one of the most researched fields nowadays. Routing Protocol for Low Power and Lossy Networks (RPL), introduced by Internet Engineering Task Force (IETF) [1], is adequate and widely used with the power, memory, and processing constrained devices, where it became the standard for routing in many IoT networks, while providing effective routing service. Routing security was an integral part of RPL's design with several, but optional, security mechanisms available [1.2].

RPL is an IPv6 proactive distance-vector routing protocol for lossy wireless networks [1]. It arranges and organizes the nodes in the network into an inverted treelike topology known as Destination Oriented Directed Acyclic Graphs (DODAGs) [3]: a network of nodes connected without loops and where the traffic is rooted at a single destination called the root node or sink node [3]. The DODAG construction depends on the used Objective Function (OF), which defines essential configurations such as the used routing metrics, how the rank of the nodes is calculated (the rank represents its distance to the root node based on the routing metrics defined by the OF), and how to select the preferred parent in the DODAG [2].

Much work in both academia and industry has shown that RPL provides a promising routing solution for a wide range of network types [4], Nevertheless, security is particularly challenging in RPL based networks, not only because of the sensors limitation in terms of resources but because of their open, mobile and unattended deployment.

Some security mechanisms have been already considered in basic RPL. However, they can be useful and effective only against external attack, in other words they are unable to protect the network from internal attacks, like abnormal behavior of nodes that exhibit an egoistic conduct and control message tampering attacks. Therefore, RPL can be exposed to a wide variety of security attacks [5]

Some of the existing attacks aim to waste the resources of the motes, by making legitimate nodes performing unnecessary processing in order to exhaust their resource. [6]. Version Number attack is a well known attack against the resources, it leads to a repetitive recreation of the network by provoking global repairs, this is done by illegitimately increasing the version number by the malicious node.

In this paper we propose a modified Version Number Attack, in which the attacker node does not provoke global repairs, as the traditional version number attack acts, it provokes the initialization of the trickle timers of each mote listening to the attacker mote's DIO messages. In the next sections the impact of the proposed attack in terms of control over head and energy is introduced.

The rest of this paper is organized as follows. Section II introduces RPL protocol, section III presents the reference network that presents the base of our comparisons, in Section IV we present the proposed attack and highlight its impact. Finally, Section IV concludes the work and presents several directions for further work.

II. RPL PROTOCOL DESCRIPTION

RPL is a standardized routing protocol for the IoT. It was designed for power, memory, and processing constrained devices and networks. The design of RPL is a combination of multiple DODAGs networks, each of which considers many nodes connected to a DODAG sink. To create and maintain the DODAG graph and routing operation, RPL use several ICMPv6 control messages [5]:

A. Control messages

RPL Internet Control Message Protocol (ICMP) are used to created and maintained the DODAG, the most used messages are :

- DODAG Information Solicitation (DIS) : it is a broadcasted message used by nodes wishing to join a network to solicit DIO messages,
- DODAG Information Object (DIO) : are initially multicast by the DODAG root to create a new DAG. This message contains information to allow nodes discovering a RPL instance, compute their own ranks based on the objective functions (OF), select a preferred parent, and maintain the graph.. The rate at which these DIO messages are broadcasted is determined by the trickle algorithm [7]. Essentially, the longer a DODAG has been stable, the fewer the number of DIO transmissions.
- Destination Advertisement Object (DAO): is sent up the DODAG to form downwards routes to parents. [8,9]. They are sent by each node to spread and advertise routing tables with prefixes of their children as well as their addresses and prefixes to their parents [4].

B. *Version Number*

The version number is one of the important fields in DIO messages. It is incremented only by the root each time a rebuilding of the DODAG is necessary (also called global repair), to ensure that all nodes in the DODAG are up-to-date with the routing state [10], this value is propagated unchanged down the DODAG graph. An older value indicates that the node has not migrated to the new DODAG graph and cannot be used as a parent node [11].

However, there is no default mechanism to check the integrity of the version number by the nodes. A malicious node may modify this value and share it in its own DIO messages in order to harm the network [10].

Version number attack is an indirect attack against the resources of the network, where an attacker can makes other nodes generate an important overload for the network through illegitimately incrementing the version number associated with a topology, thereby forcing an unnecessary rebuild of the whole DODAG graph, which can negatively impact the energy consumption of the nodes, and therefore the network lifetime.

C. *Trickle timer algorithm*

As the generation and the forwarding of the different control messages incurs additional energy consumption, and in order to achieve optimal messages exchange between nodes, RPL uses trickle timer algorithm to assign the main interval for each node in the network through dynamically adjusting the transmission windows, which allow an exchange of information in a highly robust, energy efficient, simple, and scalable manner [12].

When the network is stable, the trickle timer interval is large. However, upon detection of inconsistencies, the trickle timer is reset, and more DIO messages are sent by the nodes.

The transmission window is controlled using an exponentially incremented interval. After the convergence of the network, the need for DIO messages decreases and thus the trickle timer algorithm is used to control the number of messages and the period of sending messages reaches its maximum.

The 'RPL_DIO_INTERVAL_MIN' value and the 'RPL_DIO_INTERVAL_DOUBLINGS' value define the DIO trickle timer, and are used to calculate respectively, the minimum and the maximum interval between DIO messages, [13], these values are defined by the sink and shared to all nodes through DIO messages.

The minimum interval of the trickle timer between DIO messages is given by:

$$I_{min} = 2^{n1} \quad (1)$$

Where "n1" presents the RPL DIO INTERVAL MIN, the default value in Contiki is 12. If n = 12, means:

$$I_{min} = 2^{12} = 4096 \text{ ms} \approx 4 \text{ s} \quad (2)$$

which is the initial and the minimum interval between two successive DIO sent by a given node.

On the other hand, the maximum interval between two successive DIO for a given node is used in the case where the network is stable, it is based on I_{min} and $I_{doubling}$.

$$I_{max} = I_{min} * 2^{n2} \quad (3)$$

Where n_2 is RPL DIO INTERVAL DOUBLINGS, the default value in Contiki is 8, based on that :

$$I_{max} = 4096 * 2^8 = 1048576 \text{ ms} \approx 17{,}5 \text{ min} \quad (4)$$

The configuration of the trickle timer through I_{min} and I_{max} is critical for the design of the network, in order to wisely use the energy of the nodes, especially in low power and lossy networks. Large used intervals improve energy efficiency but lead to low responsiveness while lower intervals improve responsiveness on at the cost of energy consumption and lifetime of the network. [14]

One of the well known issues that face LLNs is limited energy, the design of RPL protocol takes energy consumption seriously into consideration and proposes methods to minimize and limit its usage, where is addressed by the trickle timer [12], which mainly aims to minimize the unnecessary exchanged of control messages within the network. An attack that provokes the initialization of the trickle timer may affect the quality of the communication and the network lifetime.

III. REFERENCE NETWORK

We used RPL implementation in the Contiki OS to implement a given network, in a normal case, and under attack, using Cooja simulator. In our simulations, each node is created as a Z1 node.

Figure 1, shows the reference network in the normal cases where all the nodes are running a legitimate code, including node 20, which presents the malicious node in the next section.

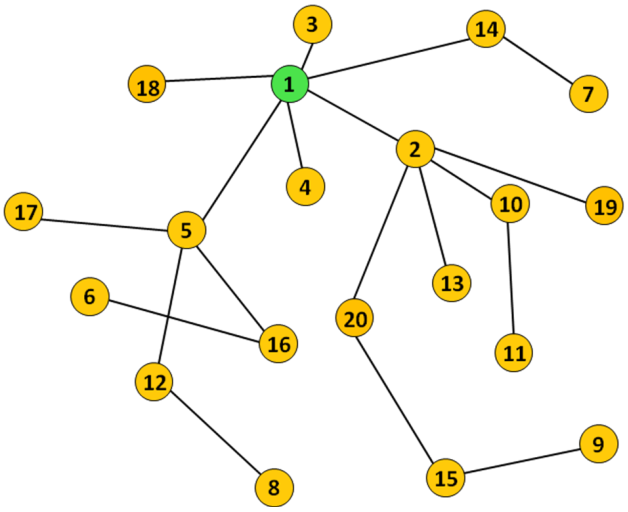

Fig. 1. Reference Network

It should be noticed that in this case the node 20 has two motes attached to it, which are node 15 and node 9.

A. *Control overhead in the normal case*

Table 1 shows the different control messages exchanged by all the nodes in 10 minutes of simulation, on the one hand, and by node 20 on the other hand. These gathered data is used as a benchmark to compare and show the behavior of the network in the case of an attack.

TABLE I. PROCESSED DIO AND DAO MESSAGES IN THE NORMAL CASE

	Sent / Generated		Transferred	Received	
Mote	**DIO**	**DAO**	**DAO**	**DIO**	**DAO**
All	244	150	138	818	291
20	12	6	15	57	17

B. *Energy consumption in the normal case*

Figure 2, shows the consumed energy by the different nodes. The nodes show different levels of consumption, based on their positions in the network, in terms of hops toward the root, number and distances to children and number and distances to neighbors. Where the nodes 18 and node 3 show the minimum consumption because they are close to the root and do not assure any forwarding task.

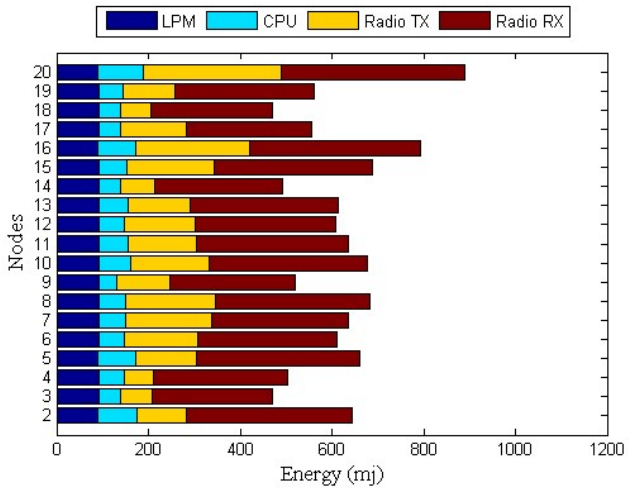

Fig. 2. Energy consumption by the different nodes in the normal case

IV. DECREASED VERSION NUMBER ATTACK

In the case of the proposed modified attack, DVNA "Decreased Version Number Attack", the malicious node decreases the version number of the topology by one in its DIO messages, while being up to date of the current version number of the network.

The goal behind this version number falsification is to create an inconsistency in the network and instability in the trickle timer of the malicious node's neighbors. The nodes initialize theirs timers upon detecting an old version in the network. The malicious node takes advantage of this feature and share a dynamic falsified value equal to the current topology version number minus 1. This dynamism in the chosen value is used to hide the malicious behavior of the attacker.

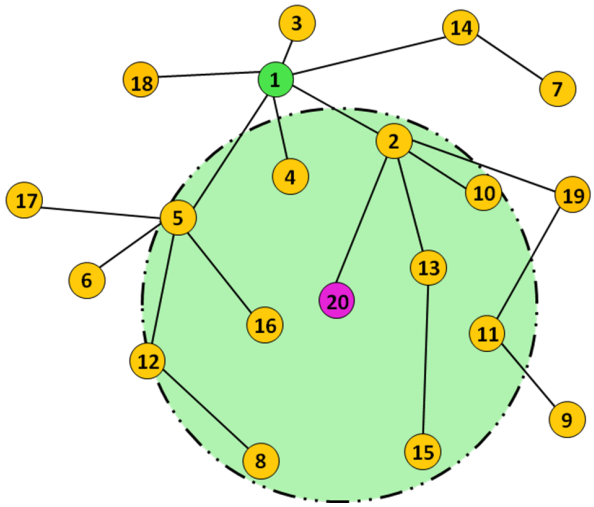

Fig. 3. Network Topology after the attack

Figure 3 illustrates the network topology after the attack. It can be seen that the node 20 does not has any children connected to it, this is due to the fact that nodes choose parents with newest version number, while node 20 is pretending to has an old version. The malicious node can be chosen as best parent and have children connected to it only in the case where it is the only available neighbor.

A. *Control overhead in the case of the attack*

The exchanged control messages before and after the attack are shown in table 2.

TABLE II. PROCESSED DIO AND DAO MESSAGES IN THE NORMAL CASE AND AFTER THE ATTACK

	Sent / Generated		Transferred	Received	
	DIO	**DAO**	**DAO**	**DIO**	**DAO**
	All the nodes				
normal	244	150	138	818	291
DVNA	377	256	317	1635	579
	Node 20				
normal	12	6	15	57	17
DVNA	12	17	1	153	4

The table 2 shows an increase in the control overhead after the attack, where the number of sent DIO messages jumped from 244 to 377, which presents an increase of 55%, and an average of 37 DIO message sent per minute. On the other hand the number of sent DAO messages jumped from 150 to 256, which presents an increase of 71%.

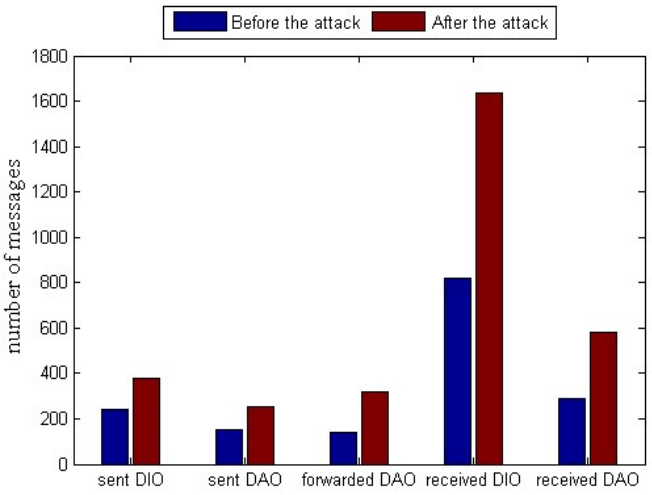

Fig. 4. Number of exchanged messages before and after the attack

The number of forwarded DAO messages shows the most important increase from 138 to 317 messages which presents an increase of 130 %. The results of table 2 are illustrated in figure 4, where it can show a noticeable increase in the received DIO messages which increase consequently the consumed energy, as is shown in the next section.

B. *Energy consumption in the case of the attack*

The consumed energy by the different nodes in terms of LPM, CPU, TX and RX are shown in figure 5.It can be seen that the conducted attack leads to global increase in the consumed energy.

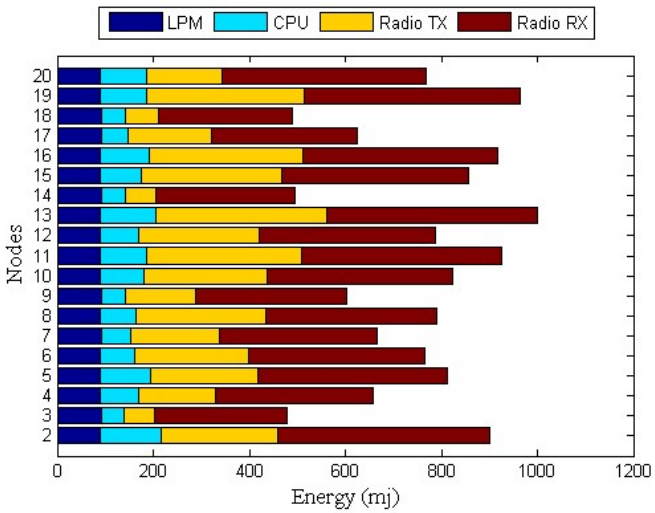

Fig. 5. Energy consumption by the different nodes in the case of the attack

Figure 6 details the differences in energy consumption in the two cases. The figure shows that the node 20 is the only node that shows a decrease in the consumed energy, this is due to the fact that its trickle timer had net been initialized since it is not receiving an old version number, moreover it is not assuring any forwarding task as it has no nodes connected to it, unlike the normal case.

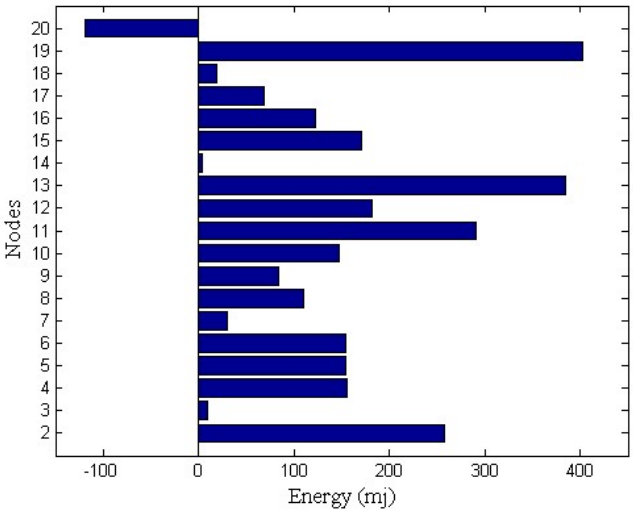

Fig. 6. Difference in energy consumption before and after the attack

Figure 6 also illustrates that the remaining nodes show different behaviors, where the node 19 is the most affected node where it shows an increase by 400 mj, which presents an increase by 72 %. This increase for node 19 is mainly because the transmitting mode, where the consumed energy jumped from 114 mj to 328 mj which present an increase by 188 %. This logic can be applied to all the remaining nodes.

In order to clarify this latter point, figure 7 shows the total consumed energy by all the nodes in terms of LPM, CPU, TX and RX before and after the attack.

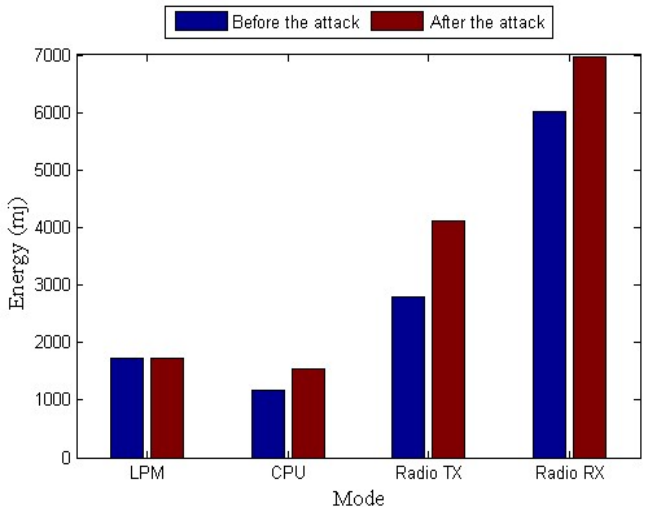

Fig. 7. Total consumed energy by all the nodes before and after the attack

Figure 7 aims to show the mode that demonstrates the most noticeable increase in energy consumption. The change in the total consumed energy by all the nodes in terms of LPM, CPU, TX and RX are respectively -0.63 %, 30.93 %, 47.77 % and 15.68 %. These obtained results confirm the impact of the attack in the energy consumed in the transmitting mode, where an increase of 47.77 % is shown, which allows us to describe the attack as successful.

V. CONCLUSION

In this paper, we presented a modified version number attack, called DVNA, which aims to exhaust the network resources. The basic idea of the attack is to force the victim nodes to initialize their trickle timers, which lead to an unnecessary generated, forwarded and listen to traffic.

According to the obtained results, the attack can be described as successful, where it reaches the goal behind it. The network under attack shows an important increase in the control overhead, by about 71 %, on the other hand the total consumed energy shows an increase of 74.77%. This destructive impact limits the nodes lifetime and consequently the network's.

In the proposed attack, the malicious node follows the default increase in its trickle timer, that starts with a minimum and stops at a maximum once the network is stable. Using small fixed interval may be more harmful and damaging to the network, this will be the subject of our future work, beside the focus on how to detect and mitigate such attack.

REFERENCES.

[1] T. Winter *et al.*, "RPL: IPv6 Routing Protocol for Low Power and Lossy Networks," Internet Requests for Comments, RFC Editor, RFC 6550, March 2012, https://ietf.org/doc/*rfc6550*/

[2] A Raoof, A Matrawy, CH Lung, "Secure Routing in IoT: Evaluation of RPL's Secure Mode under Attacks", 2019 IEEE Global Communications Conference (GLOBECOM), 1-6.

[3] J. Granjal, E. Monteiro, and J. Silva "Security for the Internet of Things: A Survey of Existing Protocols and Open Research Issues," *IEEE Comm. Surveys and Tutorials*, vol. 17, no. 3, pp. 1294–1312, 2015.

[4] S. Yasser Hashemi , F. Shams Aliee, "Dynamic and comprehensive trust model for IoT and its integration into RPL", The Journal of SupercomputingVolume 75Issue 7July 2019 pp 3555–3584

[5] F. Ahmed, Y. Ko, "Mitigation of black hole attacks in Routing Protocol for Low Power and Lossy Networks", Security and Communication Networks, vol. 9, pp. 5143–5154, 2016

[6] S. Mohammad Hossein Mirshahjafari & B. Shahgholi Ghahfarokhi "Sinkhole+CloneID: A hybrid attack on RPL performance and detection method", Information Security Journal: A Global Perspective, 28:4-5, (2019) 107-119,

[7] .Winter, T., Thubert, P., Brandt, A., Hui, J., Kelsey, R., Levis, P., Pister, K., Struik, R., Vasseur, J., Alexander, R.: RPL: IPv6 Routing Protocol for Low-Power and Lossy Networks. IETF RFC 6550 (March 2012)

[8] P.A Levis, N. Patel, D. Culler, S. Shenker, "Trickle: A Self Regulating Algorithm for Code Propagation and Maintenance in Wireless Sensor Networks". In: 1st Symposium on Networked Systems Design and Implementation (NSDI), San Francisco, CA (March 2004)

[9] M. A Boudouaia., A. Ali-Pacha, A. Abouaissa, & P. Lorenz." *Security Against Rank Attack in RPL Protoco"l.2020. IEEE Network, 34(4), 133–139.*

[10] A. Mayzaud, A. Sehgal, R. Badonnel, I. Chrisment, J. Schönwälder, "A Study of RPL DODAG Version Attacks". *8th IFIP International Conference on Autonomous Infrastructure, Management and Security (AIMS)*, Jun 2014, Brno, Czech Republic. pp.92-104

[11] A. Mayzaud, R. Badonnel, I. Chrisment, " A Taxonomy of Attacks in RPL-based Internet of Things", International Journal of Network Security, ACEEE a Division of Engineers Network, 2016, 18 (3), pp.459 - 473.

[12] P. Levis, T. Clausen, J. Hui, O. Gnawali, and J. Ko, "The Trickle Algorithm," *Internet Engineering Task Force, RFC 6206*, 2011

[13] H. Lamaaz., N. Benamar, "RPL Enhancement Based FL-Trickle: A Novel Flexible Trickle Algorithm for Low Power and Lossy Networks". *Wireless Pers Commun* 110**,** 1403–1428 (2020).

[14] H. Kharrufa, H. Al-Kashoash, A. Kemp. *"RPL-Based Routing Protocols in IoT Applications: A Review." IEEE Sensors Journal 19 (2019): 5952-5967.*

Detection of Covid-19 in chest X-ray images using a Resnet-50

Fatima-Zohra Hamlili
Department of Electrical Engineering
Faculty of Technology
University Tahri Mohammed
Bechar, Algeria
hamlili.fatima@univ-bechar.dz

Mohammed Beladgham
Department of Electrical Engineering
Faculty of Technology
University Tahri Mohammed
Bechar, Algeria
beladgham.mohammed@univ-bechar.dz

Khelifi Mustapha
Department of Electrical Engineering
Faculty of Technology
University Tahri Mohammed
Bechar, Algeria
khelifi.mostepha@univ-bechar.dz

Oussama Dahmane
Department of Electrical Engineering
Faculty of Technology
University Tahri Mohammed
Bechar, Algeria
dahmane.oussama@univ-bechar .dz

***Abstract*— Covid-19 is a serious illness that has affected millions of individuals worldwide, it has been declared as a pandemic by the World Health Organization (WHO) on 11th March 2020. One critical element in combating COVID-19 is the capacity to identify infected individuals early and place them under special care. Chest computed tomography (CT) and chest X-ray are two medical imaging methods widely used to identify lung infection. This study presents a deep convolutional neural network (DCNN) based on a pre-trained deep CNN model Residual Network (Resnet-50) that can distinguish COVID-19 from two other classes (normal and pneumonia) by using 4-fold cross validation. The dataset used consists of 317 frontal x-ray images of COVID-19, 5836 pneumonia, and 1203 normal chest x-ray images.**

The experimental results demonstrate that the proposed model is effective at identifying COVID-19 from normal and pneumonia cases, with average accuracy, precision, and sensitivity cases of 97.3 %, 98.1 %, and 95.1%, respectively.

Keywords—COVID-19, Chest X-ray images, Classification, Deep-learning, Pre-trained deep CNN model

I. INTRODUCTION

Covid-19 is a severe disease where millions of people are infected by this dangerous virus around the world. The outbreak of COVID-19 started in Wuhan, China in December 2019, and it quickly spread throughout the world in a few months [1]. This virus causes significant symptoms in humans such as fever (98%), cough (76%), and myalgia or fatigue (44%) [2]. The coronavirus (CoV) belongs to a large family of viruses that cause diseases such as the Middle East Respiratory Syndrome (MERS-CoV) and the Severe Acute Respiratory Syndrome (SARS-CoV) [3]. On March 11,2020 ,when the number of COVID-19 cases in 114 countries exceeded 118,000 cases, with over 4,000 deaths, WHO declared a Coronavirus is a pandemic [4]. Chest radiography imaging (CXR and CT scan images) is very important and standard tools for the alternative means of COVID-19 testing [5]. CXR images are one of the popular and useful methods for detecting COVID-19 and monitoring disease progression [6] because it is widely available, faster and cheaper than CT images [7].

Deep learning has been one of the fastest developing fields in computer and data science in recent years. In the area of medical imaging, deep learning (DL) has many more successes in terms of analysis and interpretation. DL solves the problem of diagnostic COVID-19 where their accuracy in the prediction of the disease is the same and sometimes even greater than an average radiologist [8]. Deep Convolutional Neural Networks (DCNN) are among the deep learning approaches that have showed significant promise in medical image classification and have therefore been widely adopted by the research community [9].

In this paper, we present an approach for differentiating COVID-19 from two other classes normal and pneumonia chest X-ray images using a DCNN model based on the Residual Network architecture with 50 layers (ResNet-50) [10].Our method has been evaluated in multi-class (normal (healthy), COVID-19 and pneumonia) classifications. We then compared the results with other literature research. The model can enable doctors to diagnose a chest X-ray (CXR) infection with COVID-19.

To evaluate the framework in a robust and effective way, a number of evaluation metrics such as multiclass accuracy, F1-scores [11], sensitivity, specificity [12], precision, and confusion matrix has been used. The values of these metrics have been determined on different ratios of training and test samples considering a number of layers in deep model.

The rest of the paper is organized as follows: Section II presents related works. Section III reports the materials and methodology. Section VI provides the experimental results and discussion, performance evaluation, and the result comparison of our proposed approach with existing approaches, and finally, the conclusion of the paper residues in section V.

.

II. RELATED WORKS

Deep learning (DL) techniques on chest X-ray for COVID-19 classification have been actively used by researchers from all over the world, with over 40,000 studies published [13], including the work presented in [14], in which the authors proposed the DarkNet model for classifying X-ray images into two classes (COVID vs. No-Findings) and three classes (COVID vs. No-Findings vs. Pneumonia). The model obtained 98.08 % and 87.02 % accuracy in binary and multi-class classification, respectively. Horry et al. [15] evaluated the effectiveness of five (5) pre-trained CNNs in identifying COVID-19 from X-ray images: VGG16/VGG19 Resnet50, Inception V3, and Xception. Wang and Wong [13] created COVID-Net, an algorithm that detects COVID-19 from two other classes, normal and pneumonia (bacterial and viral), with an accuracy of 83.5%.In the work [16], a deep learning network of 101 layers (ResNet-101) was used, and it obtained an accuracy of 77.3 %. The Optimized Convolutional Neural Network (OptCoNet) proposed in [17] is divided into two components: optimized feature extraction and classification. Using a publicly accessible dataset of COVID-19, normal, and pneumonia images, the model was evaluated and compared with different classification approaches. OptCoNet achieved an accuracy of 97.78 %.

Furthermore, the authors of [18] proposed a novel approach called Decompose, Transfer, and Compose (DeTraC) address to classify COVID-19 from chest X-ray images, with an accuracy of 95.12 %. To identify COVID-19-infected patients based on X-ray images the authors of proposed a model in [19] that combined a pre-trained CNN model with a support vector machine (SVM). The proposed approach in [20] consists of three pre-trained CNN models: DenseNet201, Resnet50V2, and Inceptionv3. The model was used to classify Covid-19 patients based on CXR images; it achieved an accuracy of 95.7 %. Khan et al. [21] developed a Deep Convolutional Neural Network model (CoroNet) based on exception architecture that has been pre-trained to identify COVID-19 infection from chest X-ray images, with an overall accuracy of 89.6% . In [22], the performance of four pre-trained convolutional models (ResNet18, ResNet50, SqueezeNet, and DenseNet121) for detecting COVID-19 from Chest X-ray images was evaluated using a dataset including 224 COVID-19, 700 pneumonia, and 504 normal X-ray images. The majority of these networks achieved a sensitivity of 98 %.

The researchers in [23] developed a novel algorithm called Domain Extension Transfer Learning (DETL), which used a pre-trained deep convolutional neural network to classify datasets into four categories (normal, pneumonia, other diseases, and Covid – 19). Their model achieved an accuracy of 90.13 %. Narin et al. [24] evaluated the performance of five convolutional neural network-based models (ResNet50, ResNet101, ResNet152, InceptionV3, and Inception-ResNetV2) to predict COVID-19 patients automatically using chest X-ray images .The dataset used including four categories : normal, COVID-19, bacterial, and viral pneumonia patients. They obtained a performance accuracy of 99.7 % with model ResNet50.

Moreover, the performance of -stats of-the-art convolutional neural network architectures was evaluated in [25]. The authors determined that vgg19 is the best classification model, with an accuracy of 98.75 % in 2-class classifications and 93.48 % in 3-class classifications respectively. Punn and Agarwal [26] tested the performance of six pre-trained convolutional (baseline ResNet, Inception-v3, Inception ResNet-v2, DenseNet169, and NASNetLarge) on binary classification (as normal and COVID-19 cases) and multiclass classification (as COVID-19, pneumonia, and normal cases) from CXR images.

Following the results, the authors conclude that NASNetLarge performed better, especially in the binary classification of COVID-19 samples. The authors of [27] evaluated the performance of pre-trained convolutional neural networks for identifying COVID-19 infection from chest X-ray images. The experimental results show that VGG16 and VGG19 obtained a better accuracy of 95 %.

III. MATERIALS AND METHODOLOGY

The dataset used in this study will be introduced in this part, followed by the approved preprocessing and data augmentation methods. Finally, the architecture of the deep convolutional neural network (DCNN) suggested in this research will be described.

A. Chest x-ray dataset

In our study, we collected datasets from two different sources. The first dataset is normal and pneumonia x-ray images obtained from the source Kaggle repository “Chest X-Ray Images (Pneumonia)” [28], and it contains 1583 normal, 2780 bacterial pneumonia, and 1493 viral pneumonia cases with a total of 4273 images. The second dataset from the open-source GitHub repository shared by Dr. Joseph Cohen et al. [29], which was largely assembled from websites such as (Radiological Society of North America (RSNA), Radiopaedia, the Italian Society of Medical, and others). It includes 317 frontal x-ray images of COVID-19 positive patients.

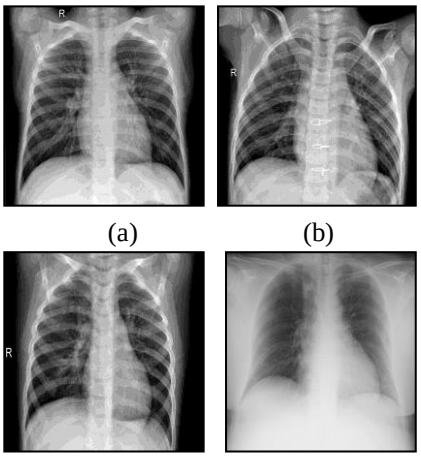

Fig .1. Samples of chest radiography images (a) Normal (b) Bacterial pneumonia (c) Viral pneumonia (d) COVID-19.

A. *Preprocessing*

In this work, a preprocessing step was employed, which comprised several techniques for enhancing the quality of the original images and eliminating undesirable characteristics in order to increase the efficacy of training the classifier. In the first stage, all x-ray images were converted to grayscale and scaled to 224×224×3 pixels. The datasets used in this experiment were acquired from several hospitals. Most images in these datasets have poor quality and low contrast; thus, in the final step, we used an enhancement technique that includes a method called Contrast Limited Adaptive Histogram Equalization (CLAHE) and a wavelet image de-noising algorithm for increasing contrast and changing the brightness level of an image to make it look better.

Adaptive histogram equalization (CLAHE): Contrast limited adaptive histogram equalization (CLAHE) is an effective contrast enhancement approach because it improves textural characteristics and resolvable details based on the contrast or intensity of the pixels [30]. The CLAHE procedure is divided into two phases. To begin, the input images are divided into a number of sub-images (tiles) of about similar size [31]. This division results in three distinct sets of regions: corner region (CR), border region (BR), and inner region (IR) . Second, the histogram of each group is generated [32]. The difficulty of enhancing contrast in CLAHE may be solved by providing the boundary value on the histogram , is determined using Equation (1).

$$\beta = \frac{M}{N}\left(1 + \frac{1}{\alpha}(S_{max} - 1)\right) \quad (1)$$

Where

- β is the clip limit
- M and N are the number of pixels and gray-levels in each region, respectively.
- The parameter α is a clip factor (0-100) [33].

1) Denoising algorithm : The de-noising approach works by first decomposing the image into wavelets using the Daubechies (db3) transform, and then determining soft threshold values, is provided in Equation (2).

$$Soft(w,T) = \begin{cases} sgn(w)(|w| - T)_+ & : |w| \geq 0 \\ 0 & : |w| < 0 \end{cases} \quad (2)$$

The thresholding results discriminate between undesired coefficients and those containing important image components, and it is over smoothing in the reconstructed image.

The Bayes technique was then used to apply wavelet shrinkage based on the idea of thresholding the wavelet coefficient. The Bayes threshold, t_B, is shown in Equation (3).

$$t_B = \frac{\sigma^2}{\sigma_s} \quad (3)$$

Where σ^2 represents the noise variance and σ_s represents the signal variance without noise.

The variance of the signal σ_s is computed in Equation (4).

$$\sigma_s = \sqrt{max(\sigma_w^2 - \sigma^2, 0)} \quad (4)$$

However, the noise and the signal are independent of one another; they may be approximated as follows:

$$\sigma_w^2 = \sigma_s^2 + \sigma^2 \quad (5)$$

The additive noise variance can be calculated as illustrated in Equation (6).

$$\sigma_w^2 = \frac{1}{n^2}\sum_{x,y=1}^{n}(w^2(x,y)) \quad (6)$$

- *n* represents the number of sub-band
- $w_{X,Y.}$ means wavelet coefficients

Finally, using the Inverse transform, the image was de-noised (wavelet reconstruction).

Fig. 2. Illustrates the results of each technique that was used in the preprocessing step.

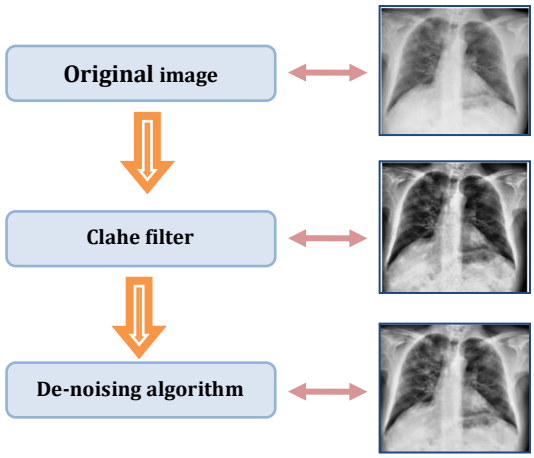

Fig.2. Schematic representation of preprocessing steps to obtain the final images for the dataset.

In this study, data augmentation techniques were used after the preprocessing stage to expand the number of samples in the constrained database by producing additional labeled images without changing the semantic meaning of the images. The transformations used in this research include horizontal flip, rotation (10%), and translation (10% in x and y dimensions).

B. *Proposed deep convolutional neural network (DCNN)*

Transfer learning (TL) has been more popular in medical imaging applications in recent years since it is a good feature extractor. Among the many deep learning models, ResNet-50 based on a residual network created by He et al. [10] was used in the proposed deep convolutional neural network (DCNN).

DCNN is composed of a base network and a classification network. The base network is a deep transfer learning model (Resnet-50) that is used to generate feature values for each image. It consists of 16 residual bottleneck blocks, each of which is composed of a convolutional layer, batch normalization, and rectified linear regularization unit (ReLU). The convolution layer sizes in each block are 1x1, 3x3, and 1x1 with feature maps (64, 128, 256, 512, and 1024) while the classification network in DCNN replaces the fully connected layer of the ResNet-50 to classify COVID-19 chest x-ray images from two other categories (Normal and Pneumonia). This stage comprises three sets of fully connected layers and three sets of dropout layers. The sizes of the two initial sets of fully connected layers in this architecture were chosen to be 200 and 300, respectively, while the size of the last depends on the number of categories in the dataset.

Dropout ratios of 0.12, 0.2, and 0.15 have been chosen. The dropout layer in the design helps to alleviate the overfitting problem and enhance model performance. In addition, in the final layers of the proposed model, the Softmax activation function is used to classify the images into three classes. A deep convolutional neural network (DCNN) is shown schematically in Fig. 3.

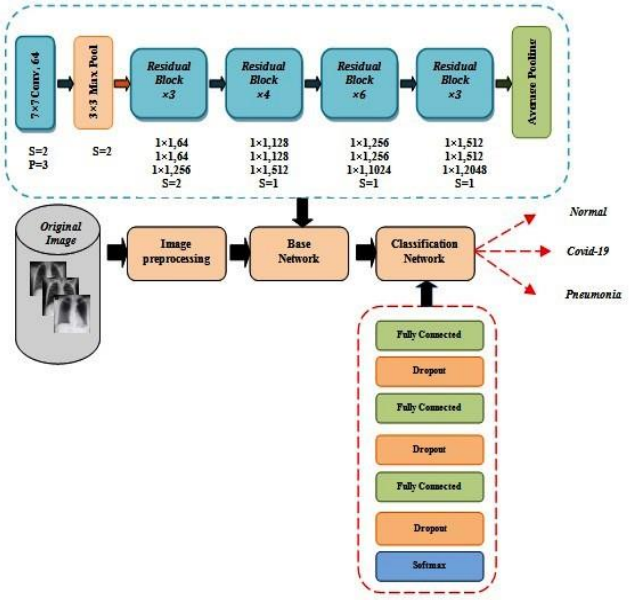

Fig.3. A schematic of the DCNN model used to predict normal (healthy), COVID-19, and pneumonia patients.

IV. RESULTS AND DISCUSSION

A. Training

The effectiveness of our algorithm was tested by using X-ray images to detect and classify COVID-19 confirmed patients into two categories: normal and pneumonia. 317 COVID-19 images, 1583 normal images, and 4273 pneumonia cases were used to train the model. The system was trained using a different set of images from the dataset using K-fold cross-validation (K=4), which could give us a better assessment of our performance.

This type of validation involves dividing the data set into four equal-sized pieces, using one part as the test set and the remainder as the training set each time. The suggested model was run on a computer with 8 GB RAM and an Intel (R) Core (TM) i5-4460 CPU running on Windows 10 using MATLAB 2020a (64 bit). CXR images were used to evaluate the suggested model for multi-class classification (Normal, Covid-19, and pneumonia). For 35 epochs, we fine-tuned our model. The loss function is optimized using the ADAM optimizer with a learning rate of 0.0001 and a batch size of 25.

B. Evaluation Metrics

The metrics of measurement Acc_m, $Sens_m$, $Spec_m$, $Prec_m$, and $F1\text{-}score_m$ are used to assess the success of multi-class classification, as illustrated in Equation (7) to Equation (11). Represents the multiclass accuracy, sensitivity, specificity, precision, and F1-scores measure.

$$Acc_m = \frac{TPn + TPc + TPp}{\text{total samples}} \times 100 \quad (7)$$

$$Sens_m = \frac{TPc + TPp}{TPc + TPp + FNc + FNp} \times 100 \quad (8)$$

$$Spec_m = \frac{TPn}{FPc + TPn + FPp} \times 100 \quad (9)$$

$$Prec_m = \frac{TPc + TPp}{TPc + FPc + TPp + FPp} \quad (10)$$

$$F_{1\text{-}Scorem} = 2 \times \frac{Prec_m \times Recall_m}{Prec_m + Recall_m} \quad (11)$$

Where:

- TPc signifies correctly classified COVID-19 cases.
- TPp means correctly classified pneumonia cases.
- TPn defines correctly classified normal cases.
- FPc indicates healthy cases classified as COVID-19.
- FPp indicates healthy cases classified as pneumonia.
- FNc and FNp mean COVID-19 and pneumonia cases classified as normal cases.

C. Results

The performance of our proposed model for identifying outputs in three-class classification (COVID-19 vs. Normal vs. Pneumonia) has been tested for each fold and is shown in Fig.4 as a separate Confusion matrix (CM). Table. I summarizes the findings of the performance measures sensitivity, specificity, precision, F1score, and accuracy, as well as their averages. The average values for sensitivity, specificity, precision, F1-score, and accuracy are 95.1%, 98.1%, 95%, 94.9%, and 97.3%, respectively.

TABLE I. PERFORMANCE RESULTS OF PROPOSED MODEL IN 3-CLASS CLASSIFICATION TASK.

Folds	**Performance Metrics (%)**				
	Sensitivity	***Specificity***	***Precision***	***F1 score***	***Accuracy***
Fold 1	95.5	98.4	95.7	95.5	97.7
Fold 2	93.9	97.8	94.2	94.1	96.8
Fold 3	95.2	98.6	97.2	96.0	97.7
Fold 4	95.7	97.4	92.9	94.0	97.0
Average	**95.1**	**98.1**	**95.0**	**94.9**	**97.3**

Fig.4.Confusion Matrices of multi-class classification task (a) Fold 1 CM (b) Fold 2 CM (c) Fold 3 CM (d) Fold 4 CM.

The suggested deep CNN outperforms other techniques according to the results in Table II. Basu et al. [23] established a new technique for the identification of Covid – 19 of four grades (normal, pneumonia, other diseases and Covid–19) known as Domain Extension Transfer (DETL). They obtained 90% accuracy. The efficacy of different neural networks pretrained was examined by Punn and Agarwal [26]. They find that the NASNetLarge has fared better, with binary class accuracy of 98 % and multi class accuracy of 96 %.

TABLE II. COMPARISON OF THE PROPOSED APPROACH WITH PREVIOUS WORK

Authors	***Architecture***	***Accuracy 2-class (%)***	***Accuracy 3-class (%)***
Khan et al. [21]	CoroNet	99	89.6
Ozturk et al. [14]	DarkNet	87.02	98.08
Wang and Wong.[13]	Covid-Net	92.4	NA
Goel et al. [17]	OptCoNet	NA	97.78
Sethy et al. [19]	ResNet50 + SVM	95.38	NA
Punn and Agarwal [26]	NASNetLarge	98	96
Apostolopoulos and Mpesiana [25]	VGG19	98.75	93.48
Our proposed model	**DCNN**	**NA**	**97.3**

Ozturk et al. [14] presented the DarkNet model, a Convolutional Neural Network (CNN), to detect X-ray images using two classification scenarios: binary (COVID vs. No-Findings) and multi-class (COVID vs. No-Findings vs. Pneumonia). They achieved an accuracy of 98.08 % in 2-class classification and 87.02 % in 3-class classification. Markis et al. [27] investigated the effectiveness of pre-trained convolutional neural networks in identifying the various classes (covid, pneumonia, normal). The classification performance showed that VGG16 and VGG19 offered the highest overall accuracy of 95%. Das et al. [20] developed a method for classifying Covid-19 patients from CXR images by combining three pre-trained CNN models, DenseNet201, Resnet50V2, and Inceptionv3, and obtained an accuracy of 95.7 %.

V. CONCLUSION

In this work, we present a deep convolutional neural network (DCNN) model for automatically distinguishing COVID-19 from two other classes of chest X-ray images: normal and pneumonia. The proposed system is based on the Residual Network architecture (ResNet-50) with 50 layers. According to the experimental findings, our developed model obtained a maximum accuracy of 97.3 %. Preprocessing and data augmentation were employed to increase model performance. The model's performance was evaluated using the benchmark performance metrics of accuracy, F1 scores, precision, recall, and specificity. In addition to the literature research, it was observed that the proposed DCNN model outperforms the other models in the identification of COVID-19 from normal and pneumonia x-ray images. This system may assist medical doctors in making decisions about COVID-19 patients based on chest X-ray images.

REFERENCES

[1] K. H.Shibly, S. K. Dey, M.T.Islam , and M. M. Rahman, "COVID faster R–CNN: A novel framework to Diagnose Novel Coronavirus Disease (COVID-19) in X-Ray images;" Informatics in Medicine Unlocked, vol. 20, 2020.

[2] A. Makris, I. Kontopoulos, and K. Tserpes, "COVID-19 detection from chest X-Ray images using Deep Learning and Convolutional Neural Networks," SETN 2020: 11th Hellenic Conference on Artificial Intelligence, pp. 60-66, Sep 2020.

[3] S.S. Thejeshwar, C . Chokkareddy, and K. Eswaran, "Precise Prediction of COVID-19 in Chest X-Ray Images Using KE Sieve Algorithm," medRxiv Preprint, 2020.

[4] N. S. Punn and S. Agarwal., "Automated diagnosis of COVID-19 with limited posteroanterior chest X-ray images using fine-tuned deep neural networks," IEEE Transactions on Industrial Electronics, pp. 2689–2702, October 2020.

[5] S. Minaee , R.Kafieh, M.Sonka, S.Yazdani, and G.Jamalipour, "Deep-COVID: Predicting COVID-19 From Chest X-Ray Images Using Deep Transfer Learning," Medical Image Analysis, vol.65, October 2020.

[6] L.O. Hall, R. Paul, D. B. Goldgof, G. M. Goldgof, "Finding COVID-19 from Chest X-rays using Deep Learning on a Small Dataset, " arXiv preprint arXiv: 2004.02060,2020.

[7] E. Goldstein et al., "COVID-19 classification of X-ray images using deep neural networks, " Eur Radiol ,May 2021.

[8] M. F.Hashm, S. Katiyar, A. G .Keskar, N. D. Bokde, and Z. W. Geem, "Efficient Pneumonia Detection in Chest Xray Images Using Deep Transfer Learning, " Diagnostics, vol.10, ,June 2020.

[9] E. Rezende, G.Ruppert, T. Carvalho, F. Ramos, and P. d. Geus, "Malicious Software Classification using Transfer Learning of ResNet-50 Deep Neural Network, " 16th IEEE International Conference on Machine Learning and Applications (ICMLA),2017.

[10] [K. He , X.Zhang , S. Ren , and J. Sun, “Deep residual learning for image recognition,” IEEE Conference on Computer Vision and Pattern Recognition (CVPR), pp. 770-778, June 2016.

[11] Marina Sokolova et al., "Beyond Accuracy, F-Score and ROC: A Family of Discriminant Measures for Performance Evaluation," Australasian joint conference on artificial intelligence. Springer, Berlin, pp. 1015–1021, 2006.

[12] R. Parikh et al., "Understanding and using sensitivity, specificity and predictive values," Indian Journal Ophthalmol, pp.45-50, 2008.

[13] L. Wang, Z.Q. Lin ,and A. Wong, “COVID-Net: a tailored deep convolutional neural network design for detection of COVID-19 cases from chest X-ray images, ” Scientific Reports, November 2020.

[14] T. Ozturk, M. Talo, E. A. Yildirim, U.B. Baloglu, O. Yildirim, and U. R. Acharya, “ Automated detection of COVID-19 cases using deep neural networks with X-ray images, ” Computers in Biology and Medicine, vol.121,April 2020.

[15] M. J . Horry et al., “X-Ray Image based COVID-19 Detection using Pre-trained Deep Learning Models, ” engrXiv. April ,2020. *(doi:10.31224/osf.io/wx89s).*

[16] M. Z. C.Azemin, R. Hassan, M. I. M.Tamrin,and M.A. M. Ali, “COVID-19 Deep Learning Prediction Model Using Publicly Available Radiologist-Adjudicated Chest X-Ray Images as Training Data: Preliminary Findings, ” International Journal of Biomedical Imaging, vol. 2020, Aug 2020.

[17] T. Goel , R. Murugan ,S. Mirjalili ,and D. K. Chakrabartty “ OptCoNet: an optimized convolutional neural network for an automatic diagnosis of COVID-19, ” Appl Intell , pp.1351–1366, Sep 2020.

[18] A. Abbas, M. M. Abdelsamea , and M. M. Gaber, “Classification of COVID-19 in chest X-ray images using DeTraC deep convolutional neural network, ”Appl Intell , pp. 854–864, Sep 2020.

[19] P. K. Sethy, S. K. Behera, P. K. Ratha, and P. Biswas, “Detection of coronavirus Disease (COVID-19) based on Deep Features, ” 2020 Preprints:2020030300.

[20] A. K. Das, S. Ghosh, S. Thunder, R. Dutta, S. Agarwal , and A. Chakrabarti , “Automatic COVID-19 Detection from X-Ray images using Ensemble Learning with Convolutional Neural Network, ” Pattern Anal Applic , pp.1111–1124, March 2021.

[21] A. I. Khan, J. L. Shah , and M. M. Bhat, “CoroNet: A deep neural network for detection and diagnosis of COVID-19 from chest x-ray images, ” Computer Methods and Programs in Biomedicine, vol.196, Nov 2020.

[22] S. Minaee, R. Kafieh ,M. Sonka, S. Yazdani, and G. J. Soufi, “Deep-COVID: Predicting COVID-19 from chest X-ray images using deep transfer learning, ” Medical Image Analysis, vol.65, July 2020.

[23] S. Basu, S. Mitra and N. Saha, “Deep Learning for Screening COVID-19 using Chest X-Ray Images, ” IEEE Symposium Series on Computational Intelligence (SSCI), pp. 2521-2527, 2020.

[24] A. Narin , C. Kaya , Z. Pamuk , “Automatic Detection of Coronavirus Disease (COVID-19) Using X-ray Images and Deep Convolutional Neural Networks, ” Pattern Anal Applic , pp. 1207–1220 ,May 2021.

[25] I.D. Apostolopoulos and T.A. Mpesiana, “Covid-19: automatic detection from X-ray images utilizing transfer learning with convolutional neural networks,” Physical and Engineering Sciences in Medicine, pp.635–640, april 2020.

[26] N . S. Punn and S. Agarwal , “Automated diagnosis of COVID-19 with limited posteroanterior chest X-ray images using fine-tuned deep neural networks, ” Appl Intell ,pp. 2689–2702, October 2020.

[27] A. Makris, I. Kontopoulos, K. Tserpes, COVID-19 detection from chest X-Ray images using Deep Learning and Convolutional Neural Networks," SETN 2020: 11th Hellenic Conference on Artificial Intelligence, pp. 60-66, Sep 2020.

[28] Chest X-rayimages (pneumonia). *(https://www.kaggle.com/paultimothymooney/chest-xray-pneumonia)*

[29] Joseph Paul Cohen, Paul Morrison and Lan Dao COVID-19 image data collection, 2020. arXiv: 2003.11597 *(https://github.com/ieee8023/covid-chestxray-dataset)*

[30] P. Singh, R. Mukundan ,and R. D. Ryke , “Feature Enhancement in Medical Ultrasound Videos Using Contrast-Limited Adaptive Histogram Equalization, ” J Digit Imaging ,pp. 273–285, Feb 2020.

[31] S. B. Patil , and B. P. Patil, “Retinal fundus image enhancement using adaptive CLAHE methods, ”Journal of Seybold Report,2020,vol.15, pp. 3476-3484.

[32] N. Salem, H. Malik, and A. Shams, “Medical image enhancement based on histogram algorithms, ” Procedia Computer Science, 2019,vol. 163 ,pp.300–311.

[33] F. M. Hana, and I. D. Maulida, “Analysis of contrast limited adaptive histogram equalization (CLAHE) parameters on finger knuckle print identification, ” 2021 J. Phys.: Conf. Ser. 1764 012049.

Suspect Person localization Using SVM of Thermal Vision Image

Kaddour Gherfi[1], Yazid laib dit leksir[2], Hocine bendjama[1], Zoheir mentouri[1]
[1]Research Center in Industrial Technologies CRTI, BP 64,
Cheraga, 16014 Algiers, Algeria.
[2]Université Constantine 1, Route Ain El-bey, Constantine 25011, Algérie.
kaddour.gherfi@gmail.com

***Abstract*— This article presents a study of the localization of suspect person, by infra-red thermography in a complicated zone or there are several different obstacles of different temperature, which gives difficulties to make a precise diagnostic of natures of the mobile things, for that the mathematical methods of classification and localization are, apply of the infra-red images. The results of detection obtained by these mathematical methods are presented and discussed.**

***Keywords*—localization, thermal image, SVM.**

I. INTRODUCTION

In the last years the non destructive testing (NDT) became important research domain in the industrial field, especially for the localization of the objects, Among the nondestructive testing methods there are ultrasonic technique [1], magnetic particle technique [2], eddy current technique [3], ray technique [4] and infrared thermography who the more used in NDT domain, however it is limited in certain cases [5].

When there are very small variations in the temperature, it is necessary to make special treatments of the infra-red images, because the infra-red camera does not make the classification and precise localization of the images. In this paper support vector machine (SVM) and neural networks are applied for classification and localization of person.

Neural networks ensure a simulation of how to organize information as a human brain. They are already used in various fields, as well as, pattern reorganization, data mining, target detection, and fault diagnosis [6], [7]. The network model consists of three layers: the input layer, the hidden layer, and the output layer.

Support vector machine (SVM) has been widely used in several domains, especially for detection and localization of objects; it's a binary supervised method.

This paper will investigate the application of infrared thermography technique as a detect method for suspected person in defense and protection domain and apply two different post-processing techniques, namely neural network and Support Vector Machine (SVM). This two techniques gives more detailed for infrared images.

II. DEFECT CLASSIFICATION METHOD

A. Neural Networks

Neural networks are structures based on the human brain, the research began in this domain of the connection started with presentation in 1943 by W. MCCulloch and W. Pitts of a simple model of biological neuron commonly called formal neuron, the representation of this neuron is shown by the following figure:

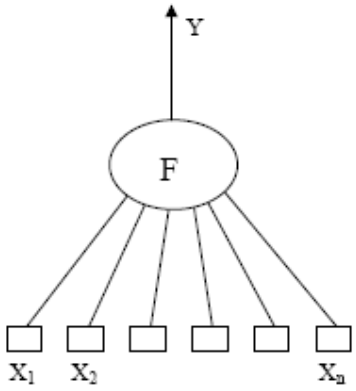

Fig. 1. Artificial neuron.

The neuron then carries out three operations on its inputs:

- Weighting: multiplication of each input by a parameter called connection weight,
- Summation: summation of the balanced inputs is carried out.
- Activation: passage of this sum in a function, called activation function.

Each neuron receives a variable number of inputs from upstream neurons. Each of these inputs is associated with a weight w which represents the strength of the connection. Each elementary processor has an output, which then branches out to feed a variable number of downstream neurons. Each connection is associated with a weight.

The calculated value is the output of the neuron which is transmitted to the following neurons.

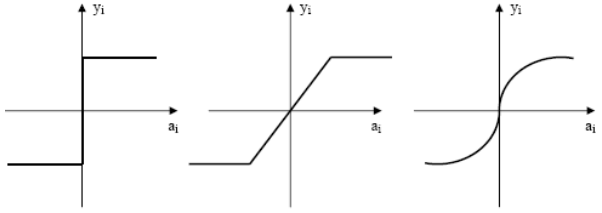

Threshold function Linear function by parts Sigmoid function

Fig.2. Different types of transfer function for the artificial neuron.

The function F is called activation function (figure 1.2).It can be a function with threshold, a linear or not linear function.

The sigmoid function is presented as a continuously derivable approximation of the linear function of activation by parts or of the threshold function. It has the advantage of being regular, monotonous, continuously derivable, and limited between 0 and 1:

$$f(x) = \frac{1}{1+\exp(-x)} \quad (1)$$

The most used of neural networks are the networks which contain three types of layers:

Input layer: the neurons of this layer receive the values of input of the network and transmit them to the hidden neurons.

Hidden layers: each neuron of this layer receives the information from several preceding layers, carries out the summation balanced by the weights, then transforms it according to its activation function which is in general a sigmoid function. Thereafter, it sends this response to the neurons of the following layer.

Output layer: it does the same role as the hidden layers, the only difference between these two types of layers is that the output of neurons of the output layer is not related to any other neuron.

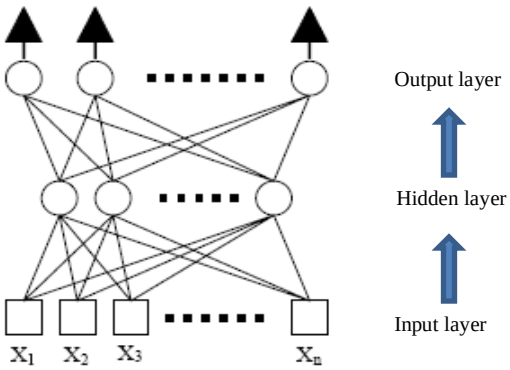

Fig.3. Neural networks with n inputs, one layer with N_c hidden neurons and N_0 output neurons.

B. Support Vector Machine (SVM)

Among the cores methods, based on statistical theory of training of Vladimir Vapnik, SVM constitute the most known form. SVM is a method of binary classification by supervised training; it was introduced by Vapnik in 1995. This method is a recent alternative for classification. It based on the existence of a linear classifier in a suitable space. Since it is a problem of classification with two classes, this method calls to a data file of training to learn the parameters from the model. It is based on the use of function known as core (kernel) which allows an optimal separation of the data, it are based on a solid mathematical theory contrary to the neural networks method. It was developed with the opposite direction of the development of the neural networks.

For two given classes of examples, the objective of SVM is to find a classifier that will separate the data and maximize the distance between these two classes. With SVM, this classifier is a linear classifier called a hyperplane.

In the following diagram, we determine a hyperplane that separates the two sets of points.

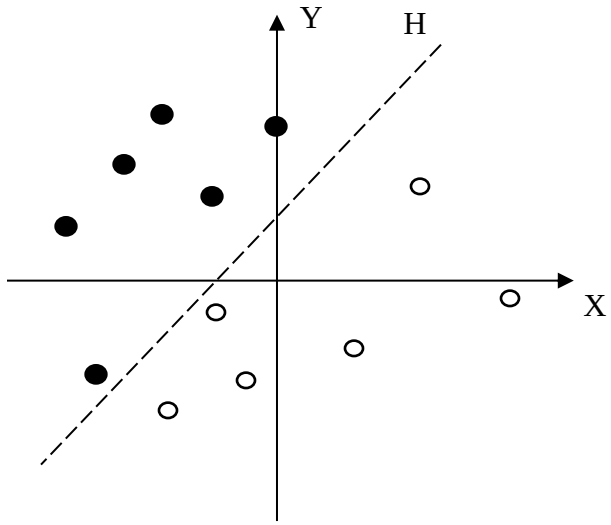

The closest points, which are the only used for the determination of the hyperplane, are called support vectors.

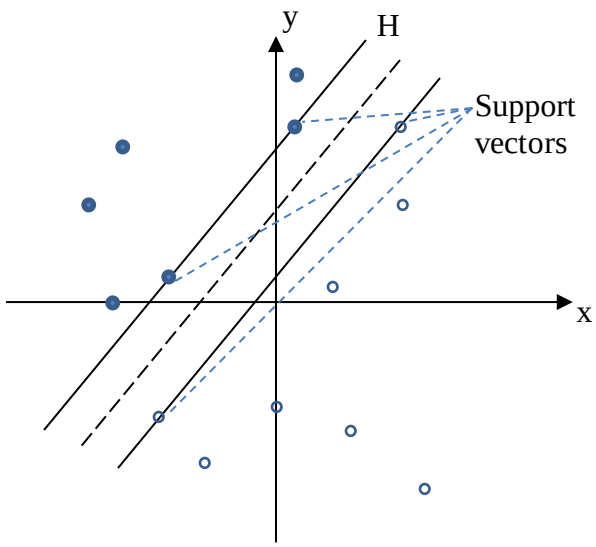

It is obvious that there is a multitude of valid hyperplanes but the remarkable property of SVM is that this hyperplane must be optimal. We will therefore search among the valid hyperplanes, the one that passes "in the middle" of the points of the two classes of examples. Automatically, this is like looking for the "safest" hyperplane. Indeed, suppose that an example has not been described exactly, a small variation will

not modify its classification if its distance to the hyperplane is large. Formally, this amounts to looking for a hyperplane whose minimal distance to the training examples is maximal.

We call this distance "margin" between the hyperplane and the examples. The optimal separating hyperplane is the one that maximizes the margin. As we try to maximize this margin, it called separators with a large margin.

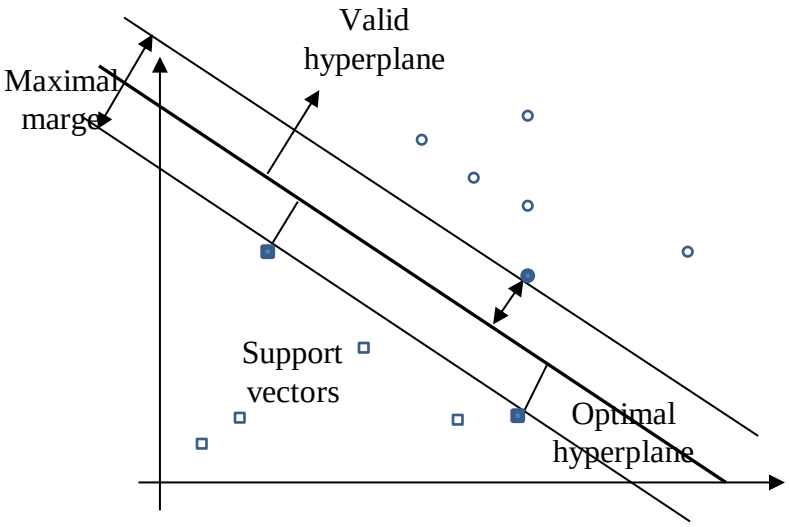

III. RESULTS AND DISCUSSION

Fig.4. Infrared image of suspect person.

Fig.5. Classification of image by neural networks method.

Fig.6. Localization or contour detection
of suspect person by neural networks method.

Fig.7. Classification of image by SVM method.

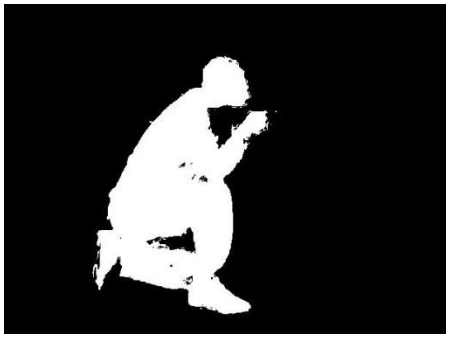

Fig.8. Localization or contour detection
of suspect person by SVM method.

Fig.9. Infrared image of two suspect persons.

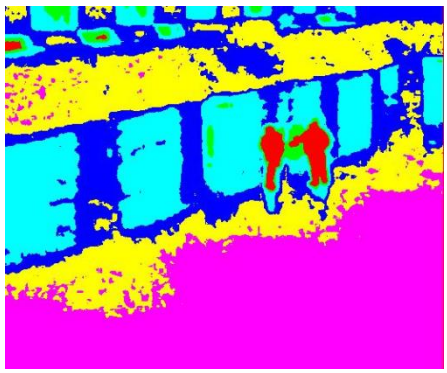

Fig.10. Classification of image by neural networks method.

Fig.11. Localization or contour detection of two suspect persons by neural networks method.

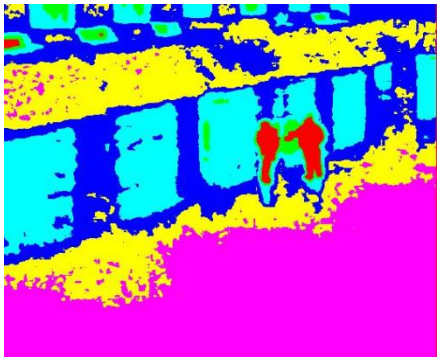

Fig.12. Classification of image by SVM method.

Using an infrared camera and a special software we analyse thermal images for detecting anomalies areas, in this study we will present the results obtained using some classification methods, and we choose a method for localization persons.

After applying the tow supervised methods, it can be seen in figures 5, 7, 10, 12, that there is a good classification, because there are a precise classification in all figures.

Fig.13. Localization or contour detection of two suspect persons by SVM method.

IV. Conclusion

Localization suspects persons (figures 6, 8, 11, 13) by its thermal image is a difficult task, this is due to characteristics of thermal images. In this paper we have presented two techniques for classification thermal images, neural networks and SVM methods. The results have shown that the two techniques are gives a best classification in infrared images.

The SVM approach proposed in this study allows localization of suspect persons before any dangerous of these persons, gives global information of the number, nature and situation of these persons.

From these results we can conclude that the SVM method gives a good result in classification and localization like the neural networks method. The two proposed methods in this paper, allows the control or survey procedure easy and safe, gives more details of image nature.

References

[1] Yang B , Huang Y , Cheng L . Defect detection and evaluation of ultrasonic infrared thermography for aerospace CFRP composites. Infrared Physics & Technology, 60:166-173, 2013.

[2] Wu J , Zhu J , Xia H , et al. DC-biased Magnetization Based Eddy Current Thermography for Subsurface Defect Detection. IEEE Transactions on Industrial Informatics, 1-1, 2019.

[3] Min H, Zhang L, Li J, et al. Methods for suppression of the effect of uneven surface emissivity of material in the moving mode of eddy current thermography. Applied Thermal Engineering, 118(Complete):612-620, 2017.

[4] Lashkia V . Defect detection in X-ray images using fuzzy reasonin. Image and Vision Computing, 19(5):261-269, 2001.

[5] Konishi, S., Kawakami, K., Taguchi, M., Inspection method with infrared thermometry for detect void in subway tunnel lining. Procedia Eng. 165, 474–483. 2016.

[6] Awodele O, Jegede O. Neural networks and its application in engineering. Informing Science & IT Education Conference Proceedings, vol. 542. p. 83–95. 2009.

[7] Dai X, Duan Y, Hu J, Liu S, Hu C, He Y, Chen D, Luo C, Meng J. Near infrared nighttime road pedestrians recognition based on convolutional neural network. Infrared Phys Technol, 97:25–32. 2019.

Enhanced Approach for On-road Obstacles Detection using Level-Set-YOLOv3 Combination

1st Djazila Souhila KORTI
Department of Telecommunication
Belhadj Bouchaib University
Ain-Temouchent, Algeria
souhilakorti@gmail.com

2nd Foued DERRAZ
Department of Telecommunication
Abou Bekr Belkaid University
Tlemcen, Algeria
fdrz70@gmail.com

3rd Zohra SLIMANE
Department of Telecommunication
Belhadj Bouchaib University
Ain-Temouchent, Algeria
zoh_slimani@yahoo.fr

4th Kheira LAKHDARI
Department of Telecommunication
Abou Bekr Belkaid University
Tlemcen, Algeria
kblakhdari@gmail.com

***Abstract*—Automatic detection and classification of on-road obstacles is an integral part of Intelligent Transport Systems (ITS). It increases road safety by providing valuable information about the environment where the vehicle navigates using on-board sensors, and can intervene in risky situations. However, it is a difficult task to achieve due to multiple variability conditions presenting in the real urban scenes. These latter can perform partial occlusion, multi-view angles, multi-scale objects, different lighting conditions, etc. In order to solve these problems, we describes in this paper a system for automatic detection and classification of on-road obstacles. The system is achieved by combining the Level-Set segmentation technique and the YOLOv3 algorithm that uses Darknet-53. The YOLOv3 used in our work was pre-trained with COCO dataset, on 80 categories of common objects. We started by fine tuning the model, to detect three types of on-road obstacles: Car, Person, and Bycicle, with KITTI dataset, which contains scenes from public roads. Then we used the segmented RGB images from KITTI, for training and testing the performance of the model. The proposed model with combination of Level-Set and YOLOv3 is compared to a simple YOLOv3 model without any preprocessing. The results demonstrate the effectiveness of the model with combination in detecting small size, overlapping objects with high precision of about 87%.**

***Index Terms*—ITS, on-road obstacles, object detection, object classification, Level-Set, YOLOv3.**

I.I NTRODUCTION

With the increasing number of accidents and fatalities on the roads each year, the development of Intelligent Transport Systems (ITS) has received a great deal of attention [1][2][3][4]. ITS should maintain a driver's safety and comfort during the navigation to the required destination, by integrating different systems that can react to any external environmental changes and make automatic decisions. However, a detection and recognition system of on-road obstacles such as pedestrian, cyclist, roadsides, traffic sign, etc. is an essential element for the development of ITS[5][6]. Such a system will enable providing real time information about the external environment where the vehicle navigates from on-board sensors, and intervene in risky situations. Several types of sensors have been used, the most known are RADAR[7], LiDAR[8], and cameras[9]. With the high complexity and dynamism of the external environment, many issues are encountered and must be overcome[10]. For example:

- Road obstacles are subject to partial occlusion.
- Road obstacles have many representations in the geometric and textual sense, which make their identification difficult.
- Road obstacles can be detected from different angles and at different distances, which usually causes confusion for the recognition system.

To handle these issues, several methods were proposed using deep learning (DL), as a powerful technique for extracting and learning feature representations automatically from data. Prabhakar *et al.*[10] used Faster R-CNN for the detection and classification of road obstacles. The results show that the proposed system is invariant to obstacle's shape and view. Guan *et al.*[11] Proposed a real time decision fusion framework for the detection and recognition of vehicles. LiDAR's and camera's data were fused and fed to the You Only Look Once version 3 (YOLOv3) for training. The results shows that the system achieves high accuracy precision for both day and night driving scenes. Bouti *et al.*[12] proposed a two-stage method for the detection and recognition of road signs captured by a camera. For the first stage, they used Histogram of Oriented Gradient (HOG) and Support Vector machine (SVM) for the detection part. The second stage consist of using a modified LeNet model for the classification part. Zhou *et al.*[13] Proposed to use a set of detectors that can capture partial occlusion patterns from different body parts.

The results shows that training jointly these part detectors can improve the performance for detecting occluded pedestrians. However, the final decision is still made by integrating multiple part scores, which makes the whole procedure more complex and hard to train. Malbog *et al.*[14] applied a Mask Region-Based CNN and instance segmentation to detect pedestrian's crosswalk. The model was trained using image data gathered from camera, and an accuracy of 97% was achieved. Heng *et al.*[15] Proposed a real time segmentation method to road signs recognition by using You Only Look at Coefficient (YOLACT). However, YOLACT performance is deteriorating for different situations such as lighting, weather, and different angle on the traffic signs. Chang *et al.*[16] Proposed to use a simple segmentation algorithm and a CNN model to classify occluded vehicles. For the occlusions with more than two vehicles, the performance of the proposed method deteriorates in terms of precision.

Aiming at the above problems, we used a two-stage method for the detection and the classification of on-road obstacles. We first realized a segmentation using level-set technique. Then the segmented data was fed to the pre-trained neural network YOLOV3, which will predict for the segmented objects their corresponding labels using rectangular bounding boxes. The proposed method is able to overcome the topology problems, allowing the detection of non-rigid objects such as human with different postures, occluded, and different scales objects.

The following contents are arranged as follows: section II describes the entire process of the proposed on-road obstacles detection and classification system. Experimental results to assess the performance of the proposed system are presented in Section III. Section IV concludes the paper and present an outlook on further possible future works and improvements.

II. METHODOLOGY

A. System Design

The system flow chart for our detection and classification of on-road obstacles, is depicted in Fig. 1. Our system uses a pre-trained YOLOv3 with COCO (Common Objects in Context) dataset to initialize the weights. We have realized two experiences. For the first one, all layer weights were trained with KITTI dataset, to tune the model to detect only three object classes. It includes Car, Person, and Bicycle. For the second one, a segmentation using the Level-Set technique was first realized, to identify every pixel, belonging to each object. The segmentation step allowed us to overcome the overlapping and confusion issue and detect each object distinctly. Finaly, the model was trained and tested on these segmented data.

B. Datasets

- COCO dataset : COCO, is a large-scale object detection, segmentation, and captioning dataset[18]. COCO includes images of complex everyday scenes. Therefore, it is based on 200.000 images, and 330.000 labeled images of 80 object categories.
- KITTI dataset: KITTI dataset[19], contains 7481 finely annotated images of driving scenes, with 80 object classes. Among these classes, only frequent objects (car, truck, pedestrian, cyclist, bicycles and seated people) are labeled independently, all other classes are labeled as "Others" or "Don't Care".

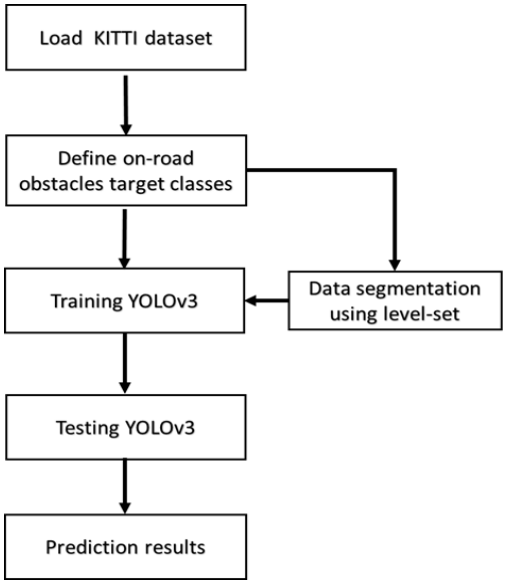

Fig. 1. System flow chart.

C. Level-Set method

The Level-Set method was proposed by Osher *et al.*[20]. It is a powerful numerical technique for image segmentation and analysis. The basic idea is to represent a curve $\boldsymbol{C}$ as the zero level of a higher dimensional level set function (LSF) $\phi(x, y)$ as mentioned in (1).

$$C = \{x \in \Omega | \phi(x, y) = 0\} \tag{1}$$

With the curve as the boundary, the whole surface can be divided into an internal region and an external region of the curve. Define a Signed Distance Function (SDF) on the surface as shown in (2).

$$\phi(x, y) = \pm dist(x, C) \tag{2}$$

Where, the value of ***dist*** is the shortest distance between the point of x on the surface and the curve.ϕ is positive on the inside and negative on the outside of the curve.

The curve evolution can then be formally defined as (3)

$$\frac{\partial C(t)}{\partial t} = V\overrightarrow{N} \tag{3}$$

This can also be expressed by the evolution of the level set function $\phi(x, y)$ as shown in (4).

$$\frac{\partial \phi}{\partial t} = V|\nabla_{\phi}| \tag{4}$$

Where $\overrightarrow{N}$ is the unit vector in the inward normal direction of the curve, and V the speed function that controls the motion of the curve along its normal direction.

The evolution of the LSF is performed iteratively. For $t \in \{0, 1, ..., T-1\}$, the T-step iterative update is represented in (5).

$$\phi_{t+1}(x,y) = \phi_t(x,y) + \Delta t \frac{\partial \phi_t}{\partial t} \quad (5)$$

Where Δt is the time step, $\frac{\partial \phi_t}{\partial t}$ is the update term, $\phi_0(x,y)$ is the initial LSF, and $\phi_T(x,y)$ is the corresponding output after T evolution steps.

D. YOLOv3 architecture

YOLOv3[21], is an improved version of YOLO[22], and YOLOv2[23]. The defining feature of this network is its ability to combine three phases in one-step: (i) Object detection, (ii) Classification, and (iii) Localization.

Compared to previous versions, YOLOv3 is a multi-label classification, and a multi-scale detection tool, based on the principle of regression instead of classification. The whole detection process is performed in a single evaluation of the image, which make the model very fast. The network structure of YOLOv3 consists of two main blocs, a deeper and robust feature extractor, called Darknet-53, and a multi-scale detector.

- Darknet53[21]: Darknet53 network is formed by 53 convolutional layers for features extraction and dimension reduction as shown in Fig.2. The architecture was improved by adding five residual blocs. These blocs are built of shortcut connections that are necessary for the gradient descent. The feature extraction process uses the Feature Pyramid Network (FPN) mechanism[24] to extract features maps at three different scale.
- Multi-scale detector: is a convolutional network, which uses the extracted multi-scale feature maps. Each map is divided into grids, and different bounding boxes are predict for each grid. For each box YOLOv3 predicts four attributes: Width (w), Height (h) and Cartesian position (x and y) of the box inside the image. A score confidence $\boldsymbol{c}$ indicates whether this box contains an object, and a class probability $\boldsymbol{p}$ to indicate to which class this box belongs. If $\boldsymbol{c}<\alpha$, where α is a given confidence threshold, then the bounding boxes with the least confidence score are removed. On the other hand, if $\boldsymbol{c} \geq \alpha$, then the box is associated with the object type. Finally the Non-Maximum Suppression (NMS) algorithm[25], is used to eliminate the overlapping boxes for the same object, and only the box with the high score confidence is kept.

E. Implementation

- System specifications :
  The algorithm used for our obstacle detection and classification system was written using Python. The model training and testing were implemented on a computer with the following specifications: Ubuntu 18.04, i7-7700 64-bit, 16 GB RAM, 256 GO SSD. The implementation extensively makes use of the libraries: OpenCV[26], Pytorch[27] and TensorFlow[28]. In our implementation, the dataset labels were modified so it includes only three classes, Car, Person, and Bicycle. KITTI labeling format was formatted, so it matches with YOLOv3 as following: [<object-class><x><y><w><h>], where a class takes value between 0 to 2, which means Car, Person, Bicycle, respectively.
  The experimentations were executed using two model's architectures: the YOLOv3 model on its own and also combined with a first step of segmentation using the Level-Set method.

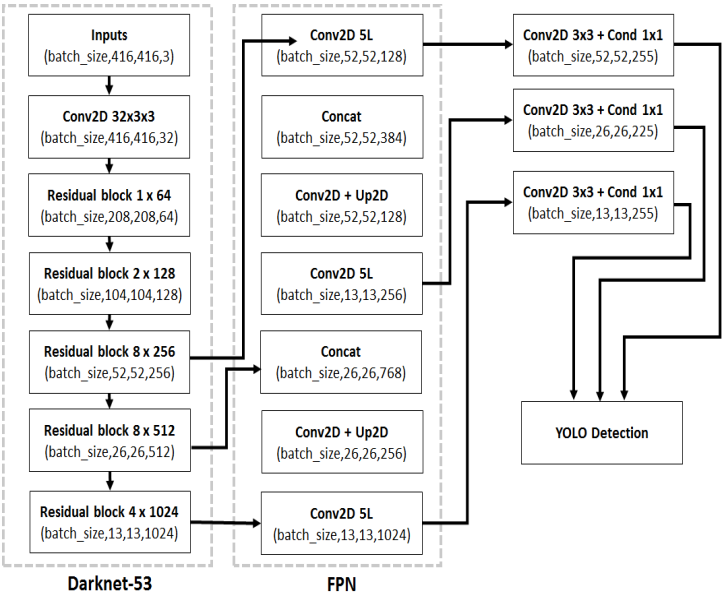

Fig. 2. YOLOv3 architecture.

- YOLOv3 model :
  The pre-trained weights of YOLOv3 with COCO dataset were uploaded as initial weights for this first model (Fig. 3). We adapted the weights of this pre-trained model to our tree-class detection problem, by training all the layers using KITTI dataset. The model receives inputs images of 416×416 pixels (RGB images), where each one is divided to 13×13 cells. 9 bounding boxes are generated from each cell. The score predicted for each box takes a value from 0 to 1, which indicates whether the box contains an object or not. The learning rate was chosen to be 0.001. The momentum and weight decay were set to 0.9 and 0.0005, respectively.

- Level-Set-YOLOv3 model: For this second model (Fig. 4), the input images were first segmented using the Level-Set method. We started by setting an initial contour on the different objects of interest automatically. Next, we have initialized the Level-Set function to the signed distance function of the initial contour. Finally we used T=10 iterations, to update the contour until convergence. The training and the testing process remain the same as the first experience.

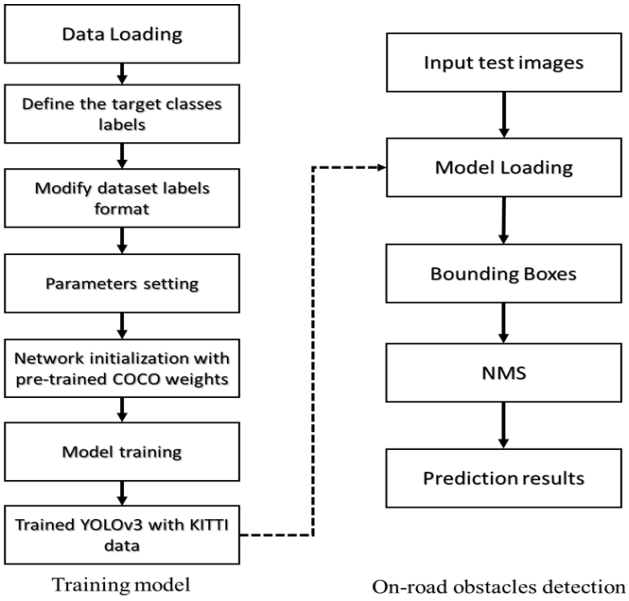

Fig. 3. The bloc diagram of the YOLOv3 model.

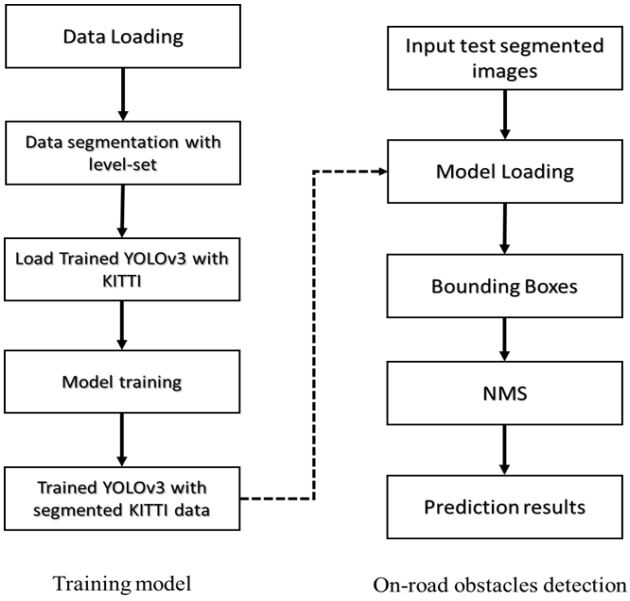

Fig. 4. The bloc diagram of the Levelset-YOLOv3 model.

III. RESULTS

The system was tested using 300 images from KITTI test dataset. The scoring threshold for classification was set 0.5, and the NMS for the detection boxes overlapping was set 0.5. To verify the effectiveness of the conducted experiments on the trained YOLOv3, Precision, is used as evaluation parameter as shown in (6).

$$Precision = \frac{T_p}{T_p + F_p} \tag{6}$$

Where, T_p and F_p refers to True Positive (correct detections), and False Positive (incorrect detections), respectively. For the first experience, the model achieves a precision of 68.01% with a detection speed of 30 seconds per frame (CPU computation time). One of the limitations observed during the experiments is the low accuracy for the detection of low contrast objects when only the YOLOv3 is used. The system failed to recognize the distant persons, with different lighting conditions.

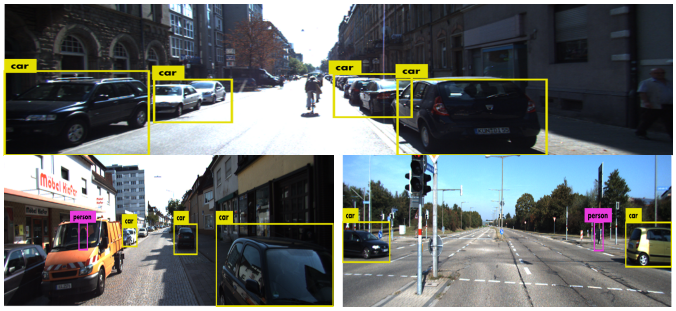

Fig. 5. The bloc diagram of the Levelset-YOLOv3 model.

With the combination of Level-Set with YOLOv3, a precision of 87% was achieved, with a detection speed of about 35 seconds per image (CPU computing time). The results show the ability of the Level-set to adapt to different topologies with no requirement of any knowledge of their shapes. This advantage allowed the model to recognize person's with different postures at different scales. The model was able to detect distinctly the overlapping objects with accuracy.

Despite its simplicity, the results show the feasibility of combining a fast YOLO detector with a segmentation technique, in order to enhance the model's performance to detect small, overlapping objects in order to handle complicated recognition tasks.

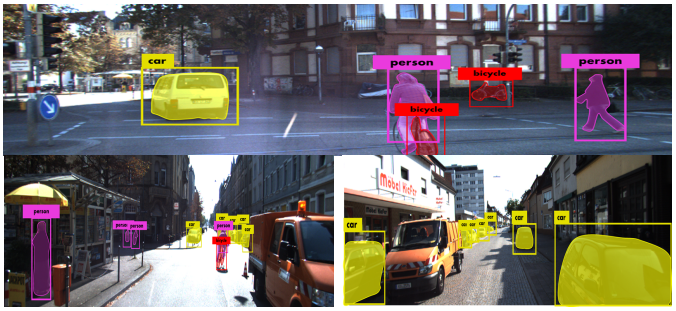

Fig. 6. Prediction results with Level-Set-YOLOv3 on testing images.

IV. CONCLUSION

Due to the increasing numbers of road accidents, the development of intelligent systems is required for making driving safer and more reliable. Facing the complex traffic scenes, such as occluhaved, different lighting conditions, multi-view angles and far distances, a vision-based system for on-road obstacles detection and classification was implemented in this paper. We have realized two experiences. For the first one, the pre-trained YOLOv3 model with COCO dataset was fine

tuned to detect only three object classes with KITTI dataset. However, the results have shown that the algorithm produced more false negatives in small objects detection. To enhance the model's performance we have realized a second experience, during which we have added a segmentation step. The data were first segmented using the Level-Set method, then fed to the tuned YOLOv3 model for training and testing. The Level-Set method showed its ability to represent contours of complex topologies, and handle topological changes, such as persons with different postures.

Despite its simplicity, the experimental results have shown that the proposed Level-Set-YOLOv3 combination has achieved substantial performance improvement, which makes the model able to detect small, overlapping objects with high precision. As perspectives, we propose to integrate the segmentation part into the YOLOv3 model directly. Which means train the model to do both segmentation and prediction simultaneously, with a wider number of target classes. We also propose to create our own dataset, run the model on a GPU, and test its performance for real-life applications.

REFERENCES

[1] M. N. Ahangar, Q. Z. Ahmed, F. A. Khan, and M. Hafeez, "A survey of autonomous vehicles: Enabling communication technologies and challenges," Sensors (Switzerland), vol. 21, no. 3, pp. 1–33, 2021, doi: 10.3390/s21030706.

[2] V. Sharma, L. Kumar, and S. Sergeyev, Recent Developments and Challenges in Intelligent Transportation Systems (ITS)—A Survey. Springer Singapore, 2021.

[3] S. Telang, A. Chel, A. Nemade, and G. Kaushik, Intelligent transport system for a smart city, vol. 308. Springer International Publishing, 2021.

[4] T. K. Chan and C. S. Chin, "Review of autonomous intelligent vehicles for urban driving and parking," Electron., vol. 10, no. 9, 2021, doi: 10.3390/electronics10091021.

[5] D. Gangwani and P. Gangwani, Applications of Machine Learning and Artificial Intelligence in Intelligent Transportation System: A Review, no. January. Springer Singapore, 2021.

[6] L. S. Iyer, "AI enabled applications towards intelligent transportation," Transp. Eng., vol. 5, p. 100083, 2021, doi: 10.1016/j.treng.2021.100083.

[7] A. Palffy, J. Dong, J. F. P. Kooij, and D. M. Gavrila, "CNN Based Road User Detection Using the 3D Radar Cube," IEEE Robot. Autom. Lett., vol. 5, no. 2, pp. 1263–1270, 2020, doi: 10.1109/LRA.2020.2967272

[8] V. Ponnaganti, M. Moh, and T. S. Moh, "Utilizing CNNs for Object Detection with LiDAR Data for Autonomous Driving," Proc. 2021 15th Int. Conf. Ubiquitous Inf. Manag. Commun. IMCOM 2021, 2021, doi: 10.1109/IMCOM51814.2021.9377361.

[9] R. D. Brehar, M. P. Muresan, T. Marita, C. C. Vancea, M. Negru, and S. Nedevschi, "Pedestrian Street-Cross Action Recognition in Monocular Far Infrared Sequences," IEEE Access, vol. 9, pp. 74302–74324, 2021, doi: 10.1109/ACCESS.2021.3080822.

[10] X. Yu and M. Marinov, "A study on recent developments and issues with obstacle detection systems for automated vehicles," Sustain., vol. 12, no. 8, 2020, doi: 10.3390/SU12083281.

[11] G. Prabhakar, B. Kailath, S. Natarajan, and R. Kumar, "Obstacle detection and classification using deep learning for tracking in high-speed autonomous driving," TENSYMP 2017 - IEEE Int. Symp. Technol. Smart Cities, pp. 3–8, 2017, doi: 10.1109/TENCONSpring.2017.8069972.

[12] L. Guan, Y. Chen, G. Wang, and X. Lei, "Real-time vehicle detection framework based on the fusion of lidar and camera," Electron., vol. 9, no. 3, 2020, doi: 10.3390/electronics9030451.

[13] A. Bouti, M. A. Mahraz, J. Riffi, and H. Tairi, "A robust system for road sign detection and classification using LeNet architecture based on convolutional neural network," Soft Comput., vol. 24, no. 9, pp. 6721–6733, 2020, doi: 10.1007/s00500-019-04307-6.

[14] C. Zhou and J. Yuan, "Multi-label Learning of Part Detectors for Heavily Occluded Pedestrian Detection," Proc. IEEE Int. Conf. Comput. Vis., vol. 2017-October, pp. 3506–3515, 2017, doi: 10.1109/ICCV.2017.377.

[15] M. A. Malbog, "MASK R-CNN for Pedestrian Crosswalk Detection and Instance Segmentation," ICETAS 2019 - 2019 6th IEEE Int. Conf. Eng. Technol. Appl. Sci., pp. 2–6, 2019, doi: 10.1109/ICETAS48360.2019.9117217.

[16] S. S. Heng, A. U. bin Shamsudin, and T. M. M. Said Mohamed, "Road Sign Instance Segmentation By Using YOLACT For Semi-Autonomous Vehicle In Malaysia," pp. 406–410, 2021, doi: 10.1109/icce50029.2021.9467206.

[17] J. Chang, L. Wang, G. Meng, S. Xiang, and C. Pan, "Vision-based occlusion handling and vehicle classification for traffic surveillance systems," IEEE Intell. Transp. Syst. Mag., vol. 10, no. 2, pp. 80–92, 2018, doi: 10.1109/MITS.2018.2806619.

[18] G. T. U. A. Colleges et al., "Microsoft COCO," Eccv, no. June, pp. 740–755, 2014.

[19] A. Geiger, P. Lenz, C. Stiller, and R. Urtasun, "Vision meets robotics: The KITTI dataset," Int. J. Rob. Res., vol. 32, no. 11, pp. 1231–1237, 2013, doi: 10.1177/0278364913491297.

[20] S. Osher and J. A. Sethian, "Fronts propagating with curvature-dependent speed: Algorithms based on Hamilton-Jacobi formulations," J. Comput. Phys., vol. 79, no. 1, pp. 12–49, 1988, doi: 10.1016/0021-9991(88)90002-2.

[21] J. Redmon and A. Farhadi, "YOLO v.3," Tech Rep., pp. 1–6, 2018, [Online]. Available: https://pjreddie.com/media/files/papers/YOLOv3.pdf.

[22] J. Redmon, S. Divvala, R. Girshick, and A. Farhadi, "You only look once: Unified, real-time object detection," Proc. IEEE Comput. Soc. Conf. Comput. Vis. Pattern Recognit., vol. 2016-December, pp. 779–788, 2016, doi: 10.1109/CVPR.2016.91.

[23] J. Redmon and A. Farhadi, "YOLO9000: Better, faster, stronger," Proc. - 30th IEEE Conf. Comput. Vis. Pattern Recognition, CVPR 2017, vol. 2017-January, pp. 6517–6525, 2017, doi: 10.1109/CVPR.2017.690.

[24] X. Li, T. Lai, S. Wang, Q. Chen, C. Yang, and R. Chen, "Weighted feature pyramid networks for object detection," Proc. - 2019 IEEE Intl Conf Parallel Distrib. Process. with Appl. Big Data Cloud Comput. Sustain. Comput. Commun. Soc. Comput. Networking, ISPA/BDCloud/SustainCom/SocialCom 2019, pp. 1500–1504, 2019, doi: 10.1109/ISPA-BDCloud-SustainCom-SocialCom48970.2019.00217.

[25] N. O. Salscheider, "Featurenms: Non-maximum suppression by learning feature embeddings," Proc. - Int. Conf. Pattern Recognit., pp. 7848–7854, 2020, doi: 10.1109/ICPR48806.2021.9412930.

[26] https://opencv.org/about/

[27] https://pytorch.org/

[28] https://www.tensorflow.org/

Enhancing Multimodal Biometric Frameworks Using Fuzzy Fusion at Matching Score Level

Abdelhakim Fares[1], Abderrahim Fayçal Megri[1] and Abdallah Meraoumia[2]

[1]Laboratory of Electronics and New Technologies (LENT), Electrical Engineering Department
University of Larbi Ben M'hidi, Oum El-Bouaghi, ALGERIA
[2]Laboratory of Mathematics, Informatics and Systems (LAMIS),
University of Larbi Tebessi, Tebessa, ALGERIA.

Email: Fares.abdelhakim@univ-oeb.dz, f.megri@univ-oeb.dz, ameraoumia@univ-tebessa.dz

***Abstract*—Multimodal biometric systems aim to achieve the best performance in persons recognition, by combining more than one biometric modality so that the combination is done using the fusion principle. In fact, although different levels of fusion are available, score-level fusion is the most commonly used. Indeed, in this process and before combining, the heterogeneous scores provided by the different biometric subsystems must be normalized. In this paper and in order to cancel the scores normalization step, a fuzzy fusion strategy has been proposed. Our experimental results, using a PolyU finger-knuckle-print database, show that the proposed fusion scheme improves the results compared to the Z-score normalization method followed by the min and max classical combining arithmetic rules.**

***Index Terms*—Biometrics, Multimodal biometrics, Data fusion, fusion at score level, Fuzzy logic.**

I. Introduction

BIOMETRICS is the process of automated individuals identification based on their physical characteristics (fingerprint, iris, palm, ear, etc.) and/or their behavioral characteristics (gait, signature, voice, keystroke, etc.). Indeed, these characteristics must meet certain conditions to be valid for being used as distinctive biometric traits [1]: *i)* Universality which means everyone has the concerned characteristics, *ii)* Uniqueness which indicates that these characteristics can't be the same for two or more persons, *iii)* Permanence is another factor, which means that the characteristics must be invariant over time, and finally, *iv)* Measurability, which means that these characteristics can be collected and analyzed.

Unfortunately, despite the advantages of unimodal biometric systems over traditional systems (password, ID cards, etc.), it can suffer from several limitations which can considerably degrade their performance. For example, some person lack some modalities due to a disability [2], and the facial traits of real twins are very similar [3]. In addition to the aforementioned, sensor errors caused by different sources (*e.g.* noise, sensor physic characteristic changes, digitization errors) can significantly affect the unimodal biometric system. In order to overcome these limitations, information from several biometric modalities can be combined and consolidated (synthesis) for better system performance [4, 5]. However, there are five possible scenarios for the sources of information that can be considered in a multimodal biometric system: multiple sensors for the same biometric, multiple instances (multiple prints of different fingers), multiples snapshots, multiple feature extraction/matching, and finally different biometric traits (*e.g.* fingerprint and Iris). The multimodal biometric system is the result of the fusion of several unimodal biometric systems, which requires the processing of multiple information. As shown in Fig. 1, the processing process can be performed simultaneously (parallel mode, Fig. 1.*(a)*) or successively (serial mode, Fig. 1.*(b)*).

In a multimodal biometric system, the fusion can be performed in four different levels [6, 7, 8]: at the sensor level, at the feature extraction level, at the score level or at the decision level. Thus, sensor-level fusion directly combines information from sensors (raw data). The use of this level is relatively low because it requires homogeneity between the data to be combined. Feature-level fusion combines different biometric feature vectors obtained from various processing and analysis phases [9]. This level has the advantage that most of the computations can be done on a single fused feature. Fusing at the matching score level refers to the combination of different scores provided by different classifiers (subsystems). Combination at this level is preferred due to the ease of combining the matching scores and the low computational complexity [10]. Finally, decision-level fusion is the combination of decisions obtained from each subsystem [11]. This level of fusion is often used for its simplicity. This is because each unimodal biometric subsystem provides a binary decision in the form of *yes* or *no*, and the system must make a final decision based on this series of *yes* and *no*.

In the biometrics literature, fusing at matching score seems to be the effective fusion level because of its simplicity as well as the promising results obtained, which allows it to become the most useful level in multimodal biometrics [10]. In this technique, each biometric system operates independently and then their results are combined to obtain a scalar score that is later used for decision making. Many techniques are used to combine scores obtained from biometric subsystems, but the most effective method is known as the rule-based [10], in which simple rules are used (such as sum, minimum, maximum). Indeed, the scores provided by the different biometric systems are generally heterogeneous, of different nature and scales depending on the classifier used (for example if an SVM classifier is used, more the distance is important from margin lines more the score is important, unlike in a KNN classifier, more the distance is important more the score is small). In addition, the scores belonging to different ranges

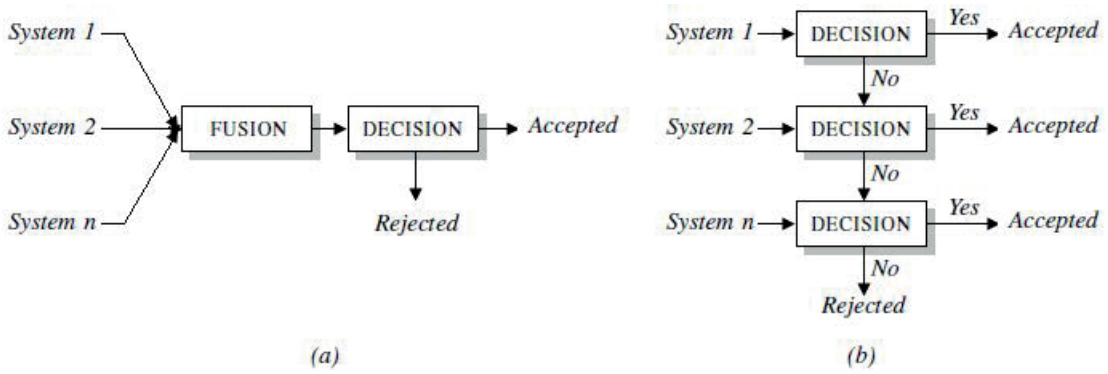

Fig. 1. Processing of multiple information. *(a)* Parallel architecture, and *(b)* Serial Architecture

of values, leads to a statistically different distribution of the scores [10]. The score fusion step must therefore be preceded by a normalization step, which consists in transforming the heterogeneous scores into a common domain before any combining process. In addition to the fact that the normalization step increases processing time, it may not effectively improve system performance. Thus, in order to efficiently combine the scores, we have proposed in this paper an efficient method based on fuzzy logic to directly fuse the matching scores of subsystems without normalization process.

The rest of this paper is organized as follows: Section 2 briefly describes the relevant work. In section 3, we present and discuss in detail the proposed method. This section includes a brief overview of the two hand-crafted feature extraction methods, namely Four Patch Local Binary Patterns (FP-LBP) and Gabor Filtering. Section 4 deals with the experimental results in which a popular Finger-Knuckle-Print (FKP) database is used. Finally, the conclusion and future work are presented in section 5.

II. Related works

Biometric technologies have proven their effectiveness in various security systems, leading many sectors to include this technology in many applications that require a high-security level, but despite this, their use still poses many security and privacy challenges, and therefore the researchers made a great effort to improve the level of security thanks to the multimodality principle. Thus, by consulting the biometric literature, several approaches and attempts have been presented with the aim of improving score level fusion techniques. *A. Ben khalifa et al.* [10] have proposed an adaptive score normalization coupling of face, palmprint and fingerprint modalities before score fusion. In fact, they conclude that the system performance is strongly dependent on the normalization technique. In addition, an adaptive multimodal biometric system using various modalities has also been proposed by *A. Kumar et al.* [12], in which Particle Swarm Optimization (PSO) method was used to optimize the matching score fusion. *S. Aratbez et al.* introduced a new multibiometric fusion scheme based on optimized and weighted functions [13]. Also, *A.P. Yazdanpanah et al.* [14] have proposed a multimodal system based on face, ear and gait with fusion at matching score level using classical arithmetic rules, such as the weighted sum and weighted product approaches.

Artificial Intelligence (AI) is used to describe the many technologies and applications that reproduce human intelligence. Currently, available AI systems are in their infancy, but technology promises to change almost every aspect of our life over the next few decades. As one of the main categories of AI, fuzzy logic has proven to be impressive, so it has been used effectively in many multimodal biometric schemes, but it is still too early to judge its effectiveness. *V. Aarohi et al.* [15] used fuzzy rules in score level fusion to enhance cloud access security, by combining face and fingerprint modalities. In this study, the authors show the simplicity and effectiveness of fuzzy rules in score level fusion. In [16], *H. Benaliouche and al.* fuse the iris and the fingerprint at the matching score level using fuzzy logic schemes. In these two previous works, authors conclude that fuzzy logic is a soft and simple way and gives enhanced results.

III. Proposed method

The proposed architecture in this paper (see Fig. 2) improves the security level in the biometric systems schemes. Our method uses a multi-algorithm scenario, *i.e.* the same biometric modality is analyzed in two different ways to extract the discriminating biometric features. Each biometric subsystem (unimodal biometric system) uses one of the extracted feature vectors to identify the person, and then the two obtained scores are combined to obtain a single score (multimodal biometric system) which is used to make the final decision to reject or accept the concerned person.

A. Feature extraction

The efficient extraction of the salient features of an image is an essential task in any pattern recognition system. Therefore, the extracted features must adequately represent the overall information contained in the image, because the good results are directly related to the uniqueness and the variability of these features, which make it possible to distinguish different patterns [17]. In the image, various features can be extracted and then used as a distinctive vector, but texture-based feature extraction methods have proven to be effective due to the high degree of discrimination of the resulting feature vectors. In our work, we used two efficient and well-known hand-crafted feature extraction methods in the field of texture analysis, namely Local Binary Pattern (LBP) and Gabor Filtering (GF). We give hereafter a brief overview of these two methods.

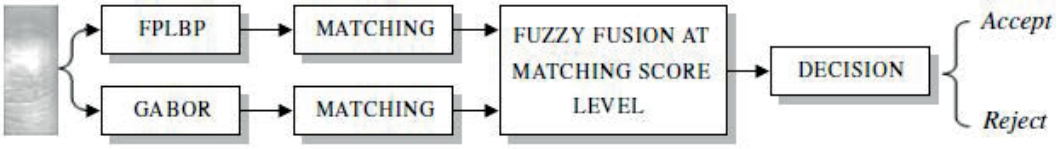

Fig. 2. Proposed multi-algorithmic based multimodal biometric system

1) Four Patch Local Binary Patterns : Given the growing interest in the use of images in machine vision applications, several methods were used to analyze and therefore understand the content of images. One of the most effective methods is the LBP operator that was first proposed by *Ojala et al.* [18] for the texture classification. The basic idea of this method is to define the structure of an image by subdividing it into sliding windows, in which for a given window all the central neighbors are calculated by subtracting the central value from all the pixel values, after whereby the resulting negative-values are coded as 0, while zero and positive-values are coded as 1, formally, the LBP operator can be defined as follows [19]:

$$\text{LBP}_{P,R}(p) = \sum_{p=0}^{P-1} \mathcal{S}(q_p - q_c)2^p \tag{1}$$

Where q_c is the central pixel, P and R denote respectively the number of neighboring pixels and the Radius. The function $\mathcal{S}(x)$ is equal to 0 if x is negative, and to 1 otherwise. the binary code is obtained by concatenating all the codes clockwise, and converting them to a decimal value, finally the center of the window is updated to this decimal value. In Fig. 3.*(a)* we give an example to illustrate the process of calculating the LBP operator for a given pixel. It is clear that the LBP value of each pixel is between 0 and 255, which is similar to the pixel intensity in a gray-scale image. Finally after having calculated all the LBP operators for all the pixels, a feature vector is generated in the form of a histogram.

Due to the efficiency of the LBP technique in image analysis, many researchers have tried to improve it, which has led to the emergence of many variants, in which FP-LBP (introduced by Wolf et al in 2008) is one of the effective extensions of LBP. The new variant changes the scale of LBP to provide other categories of local information [20]. In this approach, two rings are examined for a considered pixel at the origin. Patches of size $n \times n$ spread out consistently over each ring, as shown in Fig. 3.*(b)*. The number of bits in the binary code will be half of the patches in each ring. The FP-LBP is generated by relating two center symmetric patches in the outer ring with two center symmetric patches in the inner ring. The binary code is determined based on which of the two pairs of patches in each ring is closest.

Mathematically, the FP-LBP variant is defined for a center pixel P with coordinate C, a set S of patches of size $w \times w$ distributed uniformly out evenly on each ring of radius r_1 and r_2, respectively, as follows:

$$\text{FP-LBP}_{r_1,r_2,S,w,\alpha}(p) = \sum_{i}^{S/2} f[d(C_{1,i}, C_{2,i+\alpha \mod S}) - d(C_{1,i+S/2}, C_{2,i+S/2+\alpha \mod S})] \times 2^i \tag{2}$$

where $d(\bullet,\bullet)$ the distance between two patches and f is defined as $f(x) = 1$ if $x > \tau$, otherwise 0. The value of τ is set slightly greater than zero. Finally, the resulting response is divided into non-overlapping regions and a histogram is calculated for each region. The histograms are normalized to the unit-rank and concatenated into a single vector to represent the entire image feature.

2) Gabor filtering: The Gabor filter was proposed as a feature extraction method in the field of image analysis and computer vision [21] by the British physicist *Gabor* (the one-dimensional (1D) Gabor function) in 1946. Shortly afterwards and because of the promising results of this method, *Daugmann* [22] proposed the 2D Gabor function in 1980. Gabor filters are characterized by a good time-domain and frequency-domain transform presentation so that it can capture local structure information corresponding to spatial frequency (scale), spatial location and direction selectivity.

The Gabor filter is a combination of a Gaussian kernel, with standard deviations (σ_x, σ_y), and an illumination function which is a sinusoid, at a center frequency (μ_0, ν_0). This filter is sensitive to contours, therefore to differences in illumination (contrast) and not to the absolute value of luminance. In dimension 2, in the spatial domain, the impulse response of this filter is defined as a sine wave modulated by a Gaussian kernel (see Fig. 4).

$$\mathcal{G}(x,y) = e^{2j\pi(\mu_0 x + \nu_0 y)} \times e^{-(\frac{(x-x_0)^2}{\sigma_x^2} + \frac{(y-y_0)^2}{\sigma_y^2})} \tag{3}$$

The Gabor function has a real and imaginary component that represents orthogonal directions. To obtain the feature vector $(\mathcal{V})$, the input image $(\mathcal{I})$ must be filtered with the Gabor filter $\mathcal{G}$, as follows:

$$\mathcal{V} = \mathcal{F}(\hat{\mathcal{I}}) = \mathcal{F}(\mathcal{G} * \mathcal{I}) \tag{4}$$

where the $*$ symbol denotes 2D convolution process and $\hat{\mathcal{I}}$ is the output filtered image. The function $\mathcal{F}$ denotes the method used to extract the feature vector from the filtered image, such as the histograming or the binary conversion.

B. Fuzzy Logic based score level fusion

In the fusion process, the individual scores are combined to form a single score which is then used to make the final decision. In order to ensure that the combination of scores from different modalities is consistent, the scores must first be transformed into a common domain called the normalization of scores. Indeed, the normalization step consists of transforming heterogeneous scores into a common domain, in this paper the *Min-Max* and *Z-scores* methods are used, these are the most commonly used score normalization techniques [23].

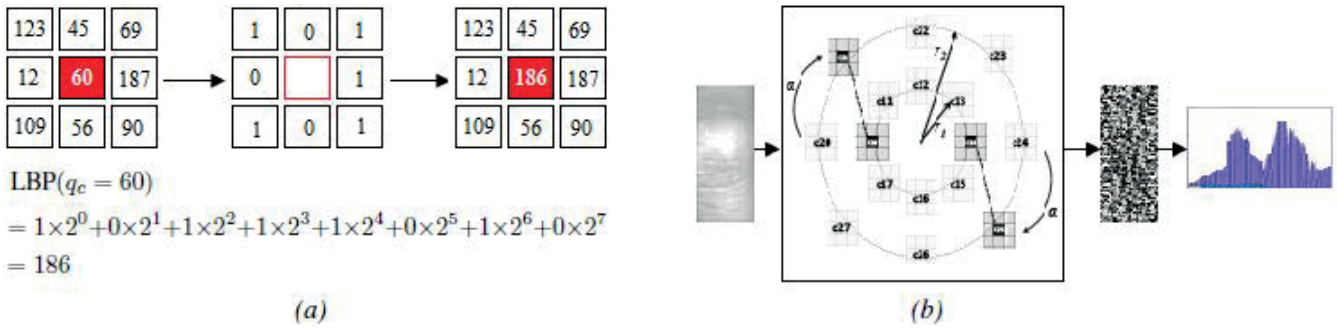

Fig. 3. Texture analysis using LBP. *(a)* LBP operator calculation, and *(b)* FP-LBP based image feature extraction

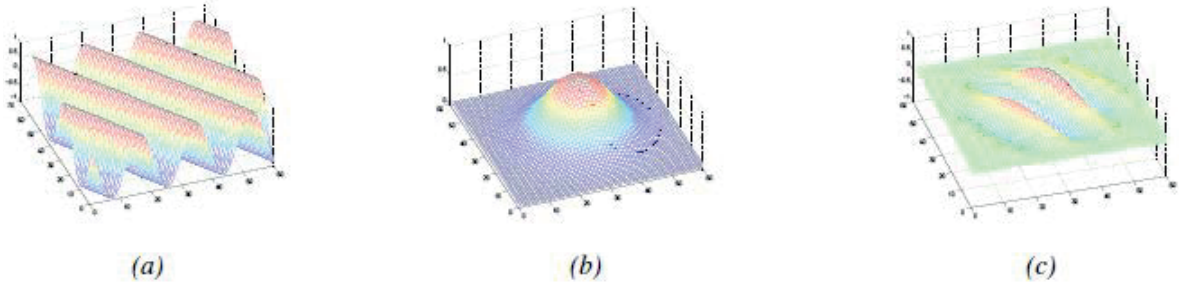

Fig. 4. 2D Gabor filter composition. *(a)* 2D sinusoid oriented with respect to the horizontal axis, *(b)* Gaussian kernel, and *(c)* corresponding Gabor filter

The *Min-Max* technique is known as the simplest normalization technique. In fact, for a given vector $S = (s_1, s_2, \cdots s_k, \cdots, s_n)$, the normalized scores are given as follows:

$$S_k^N = \frac{s_k - \rho_{\min}}{\rho_{\max} - \rho_{\min}} \tag{5}$$

Where $\rho_{\max}$ and $\rho_{\min}$ are respectively the maximum and minimum values of the raw scores (S). The *Min-Max* technique has the spectacular advantage of confining all the normalized scores in a common interval [0, 1], on the other hand this method is very sensitive to the presence of outliers, therefore this method is not very robust.

The *Z-score* is calculated using the arithmetic mean and standard deviation of the raw data. In this case, the normalized scores are given by:

$$S_k^N = \frac{s_k - \mu(S)}{\sigma(S)} \tag{6}$$

Where μ and σ are respectively the mean and the standard deviation of the set of scores (S). The *Z-score* technique generates positive client scores and negative impostor scores [10], on the other hand, it is not very sensitive to outliers because it is based on mean and standard deviation values.

The score combination approaches are very simple methods and aim to obtain a final score S_f from the N available scores (if N biometric subsystems are combined). Indeed, the most used methods are the minimum, the maximum, the sum, the weighted sum and the product. In this paper, we only use the first two methods to combine the *Z-scores* normalized results.

The Fuzzy Logic based score level fusion is based on decision switching between geniune and imposters based on strict breakpoints, which can affect system performance. On the other hand, Fuzzy Logic (FL) aims to design a low cost and robust solution [24, 12], for "partial truth" or "degrees of truth" problems. It exploits the tolerance for imprecision and uncertainty, considering truth values between 0 and 1. In addition, fuzzy rules show a large margin of simplicity and elasticity, which allows the fuzzy designer to easily obtain the best and adequate solution for his problem. In this work, FL is used to fuse the scores provided by the FP-LBP and Gabor filters based biometric unimodal system using FKP modality.

1- The fuzzy variables for the two systems (FP-LBP scores and Gabor filtering scores) are defined using trapezoidal membership functions (see Fig. 5.*(a)*).

2- The output fuzzy variable is defined as "Score Fusion" also using trapezoidal member functions.

3- For both input and output, 3 fuzzy sets are used to present the 3 regions: Bad, Average and Good.

The trapezoidal membership function is represented by:

$$\mu(x) \begin{cases} 0 & (x \le a) \\ \frac{x-a}{b-a} & (a \le x \le b) \\ 1 & (b \le x \le c) \\ \frac{d-x}{d-c} & (c \le x \le d) \end{cases} \tag{7}$$

Fuzzy *if-then* rules are defined in Fig. 5.*(b)*.

IV. Experiment Result

In this work, the proposed method will be evaluated using FKP images provided by Hong Kong Polytechnic University (PolyU) [25]. This database contains 7920 images collected from 165 persons. Each person provides 48 images of four different fingers, with an average of 12 images each of the Left Index Finger (LIF), Left Middle Finger (LMF), Right Index Finger (RIF), and Right Middle Finger (RMF).

In order to limit the set of tests, only multimodal/unimodal biometric systems based on the LIF modality were evaluated.

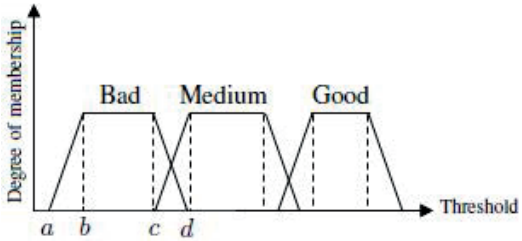

(a)

		Gabor filter		
		Bad	**Med**	**Good**
FP-LBP	**Bad**	Bad	Med	Good
	Med	Med	Med	Good
	Good	Med	Good	Good

(b)

Fig. 5. Fuzzy rules. *(a)* Trapezoidal membership functions, and *(b)* Fuzzy *if-then* rules

In addition, the systems to be examined use one of two feature extraction methods (FP-LBP and Gabor filtering). In our experimental tests, five samples will be randomly selected for enrolment, and the remaining samples (seven samples) for identification tests. Thus, a total of 95865 match scores can be obtained, in which 1155 matching scores are genuine experiments and 94710 matching scores are impostor experiments. Thus, in our study, the experimental results will be divided into two parts. In the first part, the performance of FP-LBP/Gabor based unimodal biometric identification systems are tested and evaluated. In the second part, we will focus on multimodal biometric identification systems, in which various fusion techniques (classical and Fuzzy fusion techniques) will be examined and compared.

A. Unimodal biometric system performance

To perform a fair assessment, all methods were implemented using the same methodology. This part is also divided into two sub-parts so that the first deals with FP-LBP-based biometric identification systems, while the second deals with Gabor-based biometric identification systems.

1) FP-LBP based unimodal biometric system: The FP-LBP-based feature extraction method is based on various parameters, including patches size, a set of patches (S), two rings of radii r_1 and r_2, and an α patch along the circle. Several tests can be performed to select these parameters, but in our work we have limited our tests only to selecting the best patch size. In our series of tests, we attempted to determine the value of the patch size among three predefined values (3×3, 5×5 or 7×7) while the remaining parameters of the FP-LBP based feature extraction method were taken from the predefined values (r_1 = 2, r_2 = 8, S = 8, α = 1). In general, as a first remark on all the obtained results, we can note that FP-LBP allows to obtain better unimodal biometric identification performance, which generally exceeds 99.50%, but the best value was 98.99% using a patch size 5×5.

Fig. 6.*(a)* clearly shows the system performance in terms of Equal Error Rate (EER). In fact, an excellent error equal to 1.10% can be obtained at a security threshold (T_o) equal to 0.289. In crisps logic framework scores less than threshold will be considered as impostors, whereas if the score is high than threshold the system accept the user as genuine. This functional period, around the threshold, represents the area of uncertainty that will be fuzzified. This experimental result is very satisfactory because it will also be combined with the second feature extraction method and thus increase the security level of the biometric identification system in order to achieve the best case (EER $\rightsquigarrow$ 0.00%).

2) Gabor filtering based unimodal biometric system: This method also depends on several parameters, mainly the standard deviations and the center frequency (orientation). Therefore, in order to assess the effectiveness of the identification system, it is first necessary to choose these parameters. Note that, as in the previous experiments, we examined only one parameter, which is the orientation, and selected the best value from a set of predetermined values ($[0^o, 30^o, 45^o, 60^o, 90^o]$). Indeed, this sub-part consists in studying the effect of orientation on the performance of the identification system, so the EER of system at all orientations was measured.

In our tests, all the obtained results show that with the exception of the Gabor orientation of 90^o, which gives a poor performance, the remaining Gabor orientations work best, in which excellent EER not exceeded 1.50% can be obtained. Thus, the obtained results demonstrate that the orientation of 0^o gives the best biometric system performance with an EER equal to 1.25% at the threshold of 0.284, as shown in Fig. 6.*(b)*, for this, this area will be fuzzified.

B. Multimodal biometric system performance

Although the developed unimodal biometric systems give very acceptable identification results, this does not exclude the possibility of accepting unauthorized persons or rejecting authorized persons. For this and in order to improve the performance of the proposed unimodal systems, we can fuse the two feature vectors (extracted by FP-LBP and Gabor) to obtain a multimodal biometric system.

To evaluate the performance of the proposed fusion method, we compared the results obtained from the fuzzy fusion method with those based on two classical methods using simple rules, namely the maximum scores and the minimum scores. Of course, before the score fusion step, a score normalization step will be applied (*Z-scores* and *Min-Max* normalization methods). Thus, Table 1 summarizes the EER of multimodal biometric systems obtained by the different fusion methods (*Z-scores*/min, *Z-scores*/max, *Min-Max*/min, *Min-Max*/max and *fuzzy* fusion method). To clarify, in Fig. 7.*(a)* we have plotted the Receiver Operating Characteristic (ROC) curves of all cases in order to compare the system performance under all the fusion methods studied.

From Table 1 and Fig. 7.*(a)*, we can clearly see the superiority of the classical method, in particular *Min-Max*/Min and *Min-Max*/Max over the fuzzy fusion method. In general,

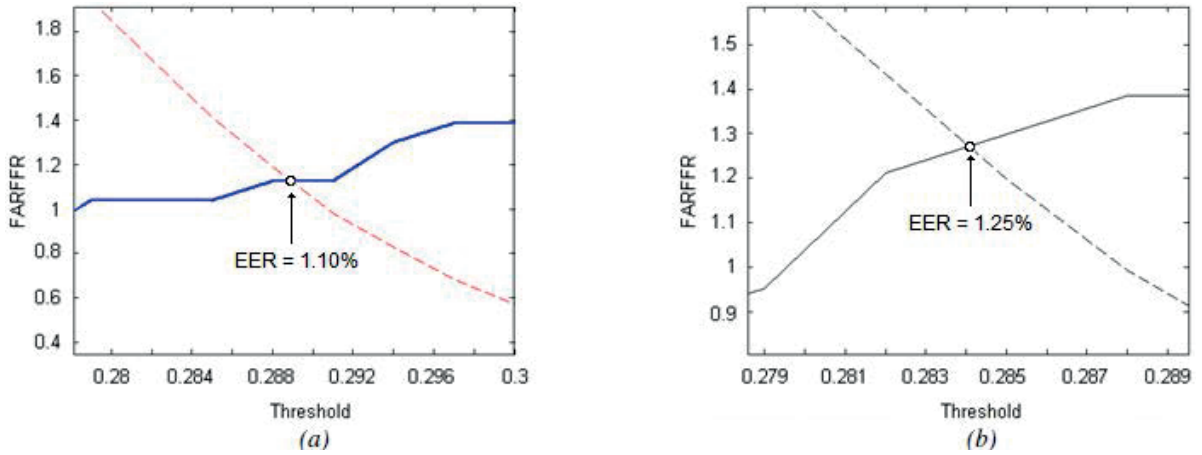

Fig. 6. Unimodal biometric system performance. *(a)* FP-LBP based unimodal biometric system, and *(b)* Gabor filtering based unimodal biometric system

Table 1: Equal Error Rate (EER)

Normalization/Fusion	EER [%]
Z-score/Min-Score	0.90
Z-score/Max-Score	0.75
Min-Max/Min-Score	0.33
Min-Max/Max-Score	0.17
Fuzzy Fusion	0.43

Table 2: Genuine Acceptance Rate (GAR) at FAR=1%

Normalization Techniques	Fusion Techniques		
	Min-Score	Max-Score	Fuzzy Fusion
Z-score	99 ,22%	99 ,57%	/
Min-Max	99.14%	100.00%	/
/			99,65%

the fusion process improves the unimodal system performance in all cases. Thus, an improvement of about 18%, 31%, 70%, 84.5% and 60.9% was obtained compared to the FP-LBP-based unimodal biometric identification system for *Z-score*/Min, *Z-score*/Max, *Min-Max*/Min, *Min-Max*/Max, and Fuzzy Fusion method, respectively. Similarly, an improvement of about 28%, 40%, 73.6%, 86.4% and 65.6% was obtained compared to the FP-LBP-based unimodal biometric system for *Z-score*/Min, *Z-score*/Max, *Min-Max*/Min, *Min-Max*/Max, and Fuzzy Fusion method, respectively.

As earlier mentioned, the *Min-Max* normalization method is very sensitive to outliers, therefore, different techniques will be evaluated after adding random outliers to the score matrices. Thus, after adding the outliers, the biometric system performance was re-evaluated and the results obtained are shown in Fig. 7.*(b)*. From this figure, the sudden degradation in system performance can be observed in the case of Min-Max. Also, unlike the *Z-scores* which show a slight degradation, the fuzzy fusion shows a slight improvement.

V. Conclusion and Further Work

Multimodal systems are strongly dependent on the chosen normalization and fusion techniques; the effectiveness of the system is determined by the overlap between the two distributions genuine and impostor. To separate these two classes, Boolean logic-based methods switch values observing strict breakpoints, which cannot deal clearly with confusion zone. Fuzzy logic is a very robust and simple implementation tool for managing the systems behavior in the uncertainty area. Thus, in this paper, we exploit fuzzy logic to improve the performance of multimodal systems based on fusion at the score level. Fortunately, the proposed method does not require any scores normalization process, and therefore, it avoids a lot of errors, difficulties and extra-calculation. The experimental results show that the fuzzy fusion method provides better results in the presence of outliers compared to the classical normalization (*Z-score* and *Min-Max* normalization techniques) followed by min and max fusion rules. The flexibility offered by fuzzy logic makes it efficient and easy to study and describe biometric systems especially in the area of uncertainty. In future work, we plan to use this technique with other classifiers such as Random Forest Tree (RFT) and Radial Basis Function (RBF). We are also trying to extend the proposed approach to other fusion levels, such as the sensor, feature and decision levels.

References

[1] J. M. Carvalho, S. Bras, J. Ferreira, S. C. Soares, and A. J. Pinho, "Impact of the Acquisition Time on ECG Compression-Based Biometric Identification Systems", Pattern Recognition and Image Analysis, Cham, pp. 169-176, 2017.
[2] P. Sanjekar and J. Patil, "An Overview of Multimodal Biometrics", Signal & Image Processing: An International Journal (SIPIJ) Vol, vol. 4, pp. 57-64, 2013.
[3] K. Vengatesan, A. Kumar, V. Karuppuchamy, R. Shaktivel, and A. Singhal, "Face Recognition of Identical Twins Based On Support Vector Machine Classifier", Third International conference on I-SMAC (IoT in Social, Mobile, Analytics and Cloud) (I-SMAC), Palladam, India, pp. 577-580, 2019.
[4] A. Jain, K. Nandakumar, and A. Ross, "Score normalization in multimodal biometric systems", Pattern Recognition, vol. 38, no. 12, pp. 2270-2285, 2005.
[5] Q. Tao and R. Veldhuis, "Hybrid fusion for biometrics: Combining score-level and decision-level fusion", pp. 1-6, 2008.
[6] A. Ross and A. Jain, "Information Fusion in Biometrics", Journal of Pattern Recognition Letters, vol. 24, pp. 2115-2125, 2003.

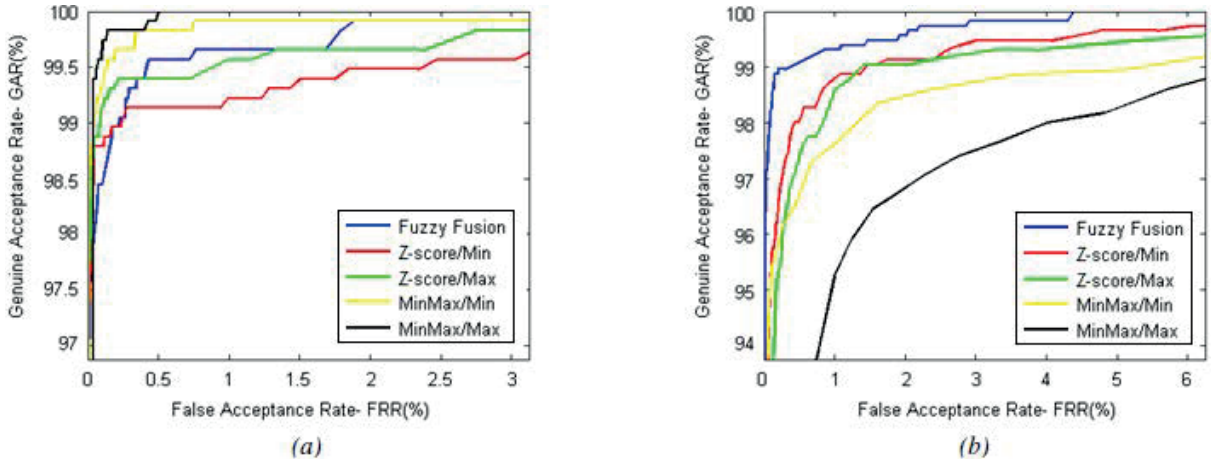

Fig. 7. Multimodal biometric system performance. *(a)* Multimodal system performance under different fusion methods, and *(b)* Multimodal system performance under different fusion methods in case of outliers

[7] H. Purohit and P. K. Ajmera, "Optimal feature level fusion for secured human authentication in multimodal biometric system", Machine Vision and Applications, vol. 32, no. 1, p. 24, 2020.

[8] M. I. Ahmad, W. L. Woo, and S. Dlay, "Non-stationary feature fusion of face and palmprint multimodal biometrics", Neurocomput., vol. 177, no. C, pp. 49-61, 2016.

[9] A.Mondal and A. Kaur, "Comparative study of feature level and decision level fusion in multimodal biometric recognition of face ear and iris", Int. J. Comput. Sci. Mob. Comput. (IJCSMC) , pp.822-842. 2016.

[10] A. B. Khalifa, S. Gazzah, and N. E. BenAmara, "Adaptive Score Normalization: A Novel Approach for Multimodal Biometric Systems", vol. 7, no. 3, p. 10, 2013.

[11] 14- R. Dwivedi, "Score-level fusion for cancelable multi-biometric verification', Pattern Recognition Letters", vol. 126, Apr. 2018.

[12] M. Hanmandlu, A. Kumar and V. K. Madasu, "Fusion of Hand Based Biometrics using Particle Swarm optimization", Fifth International Conference on Information Technology: NewGenerations (ITNG), pp. 783-788, 2010.

[13] S. Artabaz, L. Sliman, K. Benatchba, and M. Koudil, "Optimized multi-biometric enhancement analysis", IET Biometrics, vol. 10, no. 3, pp. 326-341, 2021.

[14] 17- A. Yazdanpanah, K. Faez and R. Amirfattahi, "Multimodal Biometric System using Face, Ear and Gait Biometrics", 10th International Conference on Information Sciences SignalProcessing and their Applications (ISSPA), Kuala Lumpur, pp. 251-254, 2010.

[15] A. Vora, C. Paunwala, and M. Paunwala, "A Score Level Fuzzy Rule based Multi-Biometric Framework for enhancing security of cloud access scenario", IEEE International Conference on Advanced Networks and Telecommunications Systems (ANTS), GOA, India, pp. 1-5, 2019.

[16] 19- H. Benaliouche and M. Touahria, "Comparative Study of Multimodal Biometric Recognition by Fusion of Iris and Fingerprint", The Scientific World Journal, vol. 2014, pp. 1-13, 2014.

[17] Mohammed Saigaa, Salim Chitroub & Abdallah Meraoumia, "An effective biometric identification system using enhanced palm texture features", Evolving Systems, (In press), 2021.

[18] T. Ojala, M. Pietikinen, T. Maenpaa, "Multiresolution gray-scale and rotation invariant texture classification with local binary patterns", IEEE Trans. Pattern Anal. Mach. Intell., Vol. 24, No. 7, pp. 971987, 2002.

[19] A. Attia, A. Moussaoui, C. Mourad, and Y. Chahir, "Finger-Knuckle-Print Recognition System based on Features-Level Fusion of Real and Imaginary Images", ICTACT Journal on Image and Video Processing, vol. 8, 2018.

[20] L. Nanni, A. Lumini, and S. Brahnam, "Survey on LBP based texture descriptors for image classification", Expert Systems with Applications, vol. 39, no. 3, pp. 3634-3641, 2012.

[21] Y. Zhang, W. Li, L. Zhang, X. Ning, L. Sun, and Y. Lu, "Adaptive Learning Gabor Filter for Finger-Vein Recognition", IEEE Access, vol. 7, pp. 159821-159830, 2019

[22] J. G. Daugman, "Two-dimensional spectral analysis of cortical receptive field profiles", Vision Research, vol. 20, no. 10, pp. 847-856, 1980.

[23] A. Jain, K. Nandakumar, and A. Ross, "Score normalization in multimodal biometric systems", Pattern Recognition, vol. 38, no. 12, pp. 2270-2285, 2005.

[24] 25- R Timothy J, "Fuzzy logic with engineering applications", Wiley India Edition, 3rd edition, 2008.

[25] The Hong Kong Polytechnic University (PolyU), available at: http ://www.comp.polyu.edu.hk/∼biometrics/.

Condition classification for bearing fault based on machine learning using GUI

Chouaib SOUAIDIA
LABGET Laboratory
Department of Electrical Engineering
Faculty of Science and Technology
Larbi Tebessi University
Tebessa, Algeria
chouaib.souaidia@univ-tebessa.dz

Tawfik THELAIDJIA
LABGET Laboratory
Department of Electrical Engineering
Faculty of Science and Technology
Larbi Tebessi University
Tebessa, Algeria
tawfik.thlaidjia@univ-tebessa.dz

Salah CHENIKHER
LABGET Laboratory
Department of Electrical Engineering
Faculty of Science and Technology
Larbi Tebessi University
Tebessa, Algeria
salah.chenikher@univ-tebessa.dz

***Abstract* –** In this paper, a new method based on a graphical user interface is developed for bearing fault diagnosis. The suggested method consists of using statistical parameters for feature extraction. Then the classification task is guaranteed using two classifiers namely: neural networks and random forest. The suggested approach is tested based on the bearing dataset provided by the Case Western Reserve University, Bearing Data Center. To facilitate the exploitation of the proposed approach a GUI has been developed. The obtained results show the effectiveness and the simplicity of the proposed approach for bearing fault diagnosis.

Keywords: *Rolling Bearing, Fault Diagnosis, ANN, Random forest, Feature Extraction, Classification Algorithms.*

I. INTRODUCTION

Rotating machines are necessary and familiar in the industry. Rolling bearing is the crucial component that directly influences the running condition of the industrial process [1]. Statistics show that more than two-thirds of electrical motor failures are due to rolling bearing damages [2]. Besides, the failure of this mechanic component may cause a catastrophic breakdown of the system and as consequence an expensive maintenance cost [3]. To avoid this shortcoming researchers should be focused on bearing fault diagnosis.

In this paper, a pattern recognition technique is used for bearing fault diagnosis. It is based on key steps: feature extraction and condition classification [4].

Diversity of data analysis techniques have been used by researchers, namely time-domain analysis [6–8], frequency domain analysis [9, 10], and time-frequency domain analysis [11]. Among these features, statistical parameters such as Root mean square (RMS), kurtosis, crest factor, average amplitude, minimum value, standard deviation, and Impulse Factor have been successfully used for feature extraction. These statistical parameters are useful due to their sensitivity to any change that occurs on the vibration signal [4].

Researchers have employed many artificial intelligence techniques for bearing fault classification such as fuzzy logic [12], expert system [12], random forest techniques, neural network (NN) [6, 7, 14, 15], neuro-fuzzy system [8], genetic algorithm (GA) [6, 15]and support vector machine (SVM) [7, 13]. neural networks and random forest techniques are important classification methods, due to their efficiency and accuracy.

The aim of this work is not only to propose an approach for fault diagnosis but also to develop a graphical user interface (GUI) based on MATLAB to ensure simple exploitation by the user.

This paper is organized as follows. In section 2, the feature extraction technique is presented. Then, neural networks and random forest techniques are discussed in section 3. The used dataset is given in section 4. In section 5, the obtained results are analyzed and discussed.

II. FEATURE EXTRACTION

Features extraction plays an important role in data analysis and classification. It allows extracting useful information from signals. Extracting effective parameters may increase the reliability of fault diagnosis. In this paper, seven (7) time-domain features were extracted from vibration signals. The considered parameters are the minimum (Min), the impulse factor (IMF), the crest factor (CRF), standard deviation (SD), the root-mean-square (RMS), the peak to a peak value

(PPV), and the kurtosis (Kur). All these features are given by their expressions as follows:

Peak value: [23]

$$x_p = maximum\ (x) \quad (1)$$

minimum value: [22]

$$Min = minimum\ (x) \quad (2)$$

peak to a peak value (PPV): [22]

$$PPV = maximum(x) - minimum\ (x) \quad (3)$$

root mean square (RMS): [22]

$$x_{RMS} = \sqrt{\frac{\sum_{i=1}^{K}|x_i|^2}{K}} \quad (4)$$

standard deviation (SD): [22]

$$\sigma = \sqrt{\frac{\sum_{i=1}^{K}(x(i)-\bar{x})^2}{K-1}} \quad (5)$$

the crest factor (CRF): [23]

$$CRF = \frac{x_p}{x_{RMS}} \quad (6)$$

impulse factor (IMF): [23]

$$IMF = \frac{x_p}{\frac{1}{K}\sum_{i=1}^{K}|x_i|} \quad (7)$$

kurtosis (KUR) : [23]

$$KUR = \sqrt{\frac{\sum_{i=1}^{K}(x(i)-\bar{x})^4}{K*(\sigma^2)}} \quad (8)$$

Where:

x represents the vibration signal in the time domain.

σ represents the Standard Deviation

K the length of a signal

III. MACHINE LEARNING METHODS

A. ARTIFICIAL NEURAL NETWORKS

Artificial neural networks (ANNs) are biologically inspired computational networks. ANN has the capability of establishing the relationship between the input and output patterns. [17]. It can be configured for a specific application, such as pattern recognition or data classification, through a learning process [18].

Among different topologies, the feed-forward network is probably the most popular; the basic multilayer feed-forward network contains one input layer, one output layer, and several hidden layers [19], [20].

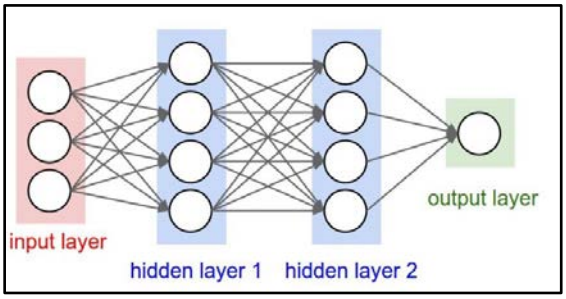

Fig. 1. feed-forward neural network [21]

The sigmoid activation function is used in ANN. It is given by equation 8. The activation function confines the amplitude neuron output to some finite value and introduces non-linearity in the network.

$$Z(x) = \frac{1}{1+e^{-x}} \quad (9)$$

An ANN model consists of two phases: the learning or training phase and the testing phase. The dataset is divided into two parts; the first one which contains 75% of data is used for ANN training and the rest is employed for testing purposes.

B. RANDOM FOREST

random forest classifier is a tree-based machine learning algorithm that consists of many individual decision trees that operate as an ensemble or group. It uses averaging to improve the predictive or classification accuracy. It can be used both for classification and regression and the more trees it has, the more robust a forest is.

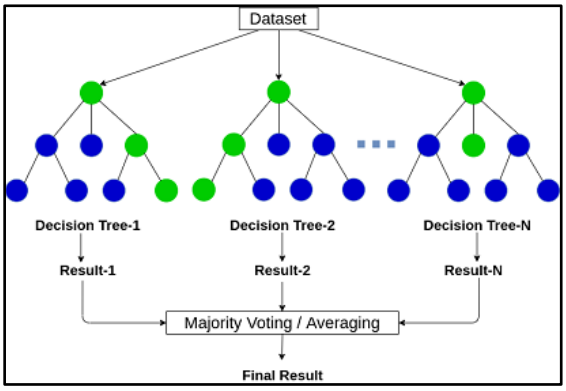

Fig. 2. random-forest Classifier [24]

Random-forest works based on four main steps:

1. Selecting random samples from a given dataset.
2. Creating a decision tree for each sample and get a prediction result from each decision tree.

3. Performing a vote for each predicted result.
4. Finally, selecting the prediction result with the most votes as the final prediction.

IV. DATASET & GUI

A. *THE DATASET*

The dataset is provided by the Case Western Reserve University Bearing Data Center is used for this study [25].

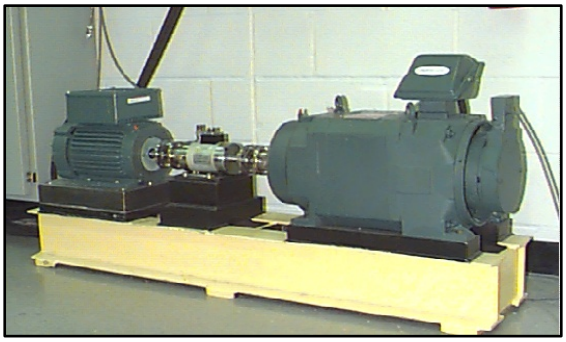

Fig. 3. The test stands (Source: Case Western Reserve University Bearing Data Center website) [25]

As shown in Fig. 3, the test stand consists of a 2 hp motor (left), a torque transducer/encoder (center), a dynamometer (right), and control electronics (not shown).

The following seven bearing conditions are considered in this work:

- Bearing with ball fault of 0.1778 mm (BF1)
- Bearing with ball fault of 0.5334 mm (BF2)
- Bearing with inner race fault of 0.1778 mm (IF1)
- Bearing with inner race fault of 0.5334 mm (IF2)
- Bearing with outer race fault of 0.1778 mm (OF1)
- Bearing with outer race fault of 0.5334 mm (OF2)
- Healthy bearing (HTY).

The dataset used in this study contains 280 samples, each category contains 40 signals.

B. *GUI*

The developed GUI allows doing the following operations:

1. Choose the dataset folder using the button 'Browse'.
2. Select the desired classifier namely: the feed-forward neural network or the random forest.
3. When the user selects a feed-forward neural network, he can choose the number of hidden layers and the number of epochs as shown in Fig. 7. On the other hand, when the user selects the random forest classifier, he can choose the number of trees as illustrated in Fig. 11.
4. Train the selected classifier once only using the button 'NEW'.
5. Calculate the test using the button 'validate'.
6. The user can check a random signal to which class it belongs by clicking on the check button, it also allows to visualize the values of statistical parameters of the selected signal.

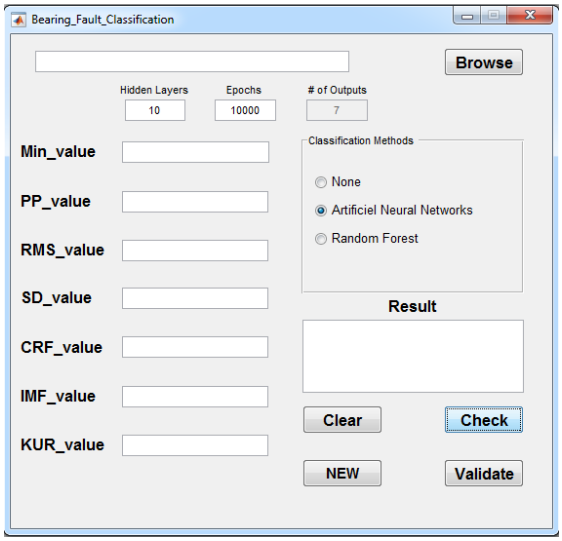

Fig. 4. The developed graphical user interface for classification

This GUI uses the extracted feature as a dataset, in our study the rows are the 280 bearing conditions and columns are the 7 extracted features (statical parameters).

TABLE I. GUI DATASET FORMAT

	Min	PPV	RMS	SD	CRF	IMF	KUR
BF1	-0.520	0.977	0.136	0.136	7.139	8.884	2.877
BF2	-0.411	0.995	0.118	0.117	8.402	10.81	3.580
IF1	-1.172	2.738	0.290	0.289	9.433	13.15	5.588
IF2	-2.347	5.287	0.516	0.515	10.24	15.02	7.185
OF1	-3.212	6.705	0.678	0.677	9.882	16.31	7.621
OF2	-5.427	11.49	0.627	0.627	18.31	36.86	22.40
HTY	-0.272	0.495	0.076	0.075	6.507	8.123	2.891

V. OBTAINED RESULTS

A. *ANN RESULTS:*

After feature extraction, the first classifier based on a feed-forward neural network is employed to classify samples. Fig. 5 illustrates the suggested method for fault diagnosis based on a feed-forward neural network.

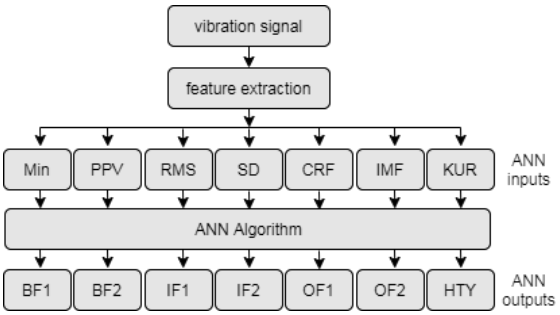

Fig. 5. The suggested method for fault diagnosis is based on a feed-forward neural network.

The inputs of ANN are the seven statistical parameters [Min; PPV; RMS; SD; CRF; IMF; KUR and the outputs are the bearing states: [BF1; BF2; IF1; IF2; OF1; OF2; HTY] as shown in Table II.

TABLE II. DESIRED OUTPUTS OF ANN

Bearing state	Desired Outputs						
ball fault of 0.1778 mm (BF1)	1	0	0	0	0	0	0
ball fault of 0.5334 mm (BF2)	0	1	0	0	0	0	0
inner race fault of 0.1778 mm (IF1)	0	0	1	0	0	0	0
inner race fault of 0.5334 mm (IF2)	0	0	0	1	0	0	0
outer race fault of 0.1778 mm (OF1)	0	0	0	0	1	0	0
outer race fault of 0.5334 mm (OF2)	0	0	0	0	0	1	0
Healthy bearing (HTY).	0	0	0	0	0	0	1

Feed-forward neural network suffers from the main shortcoming which is the correct choice of its architecture. After several experiments, the architecture of the considered feed-forward neural networks is presented in Table III.

TABLE III. THE ARCHITECTURE OF THE CONSIDERED FEED-FORWARD NEURAL NETWORK

Number of hidden layers	10
Maximum number of epochs	10000
Mean square error	10^{-10}

The feed-forward neural network training contains 7 Inputs, 10 Hidden Layers, and 7 outputs as presented in Fig. 6.

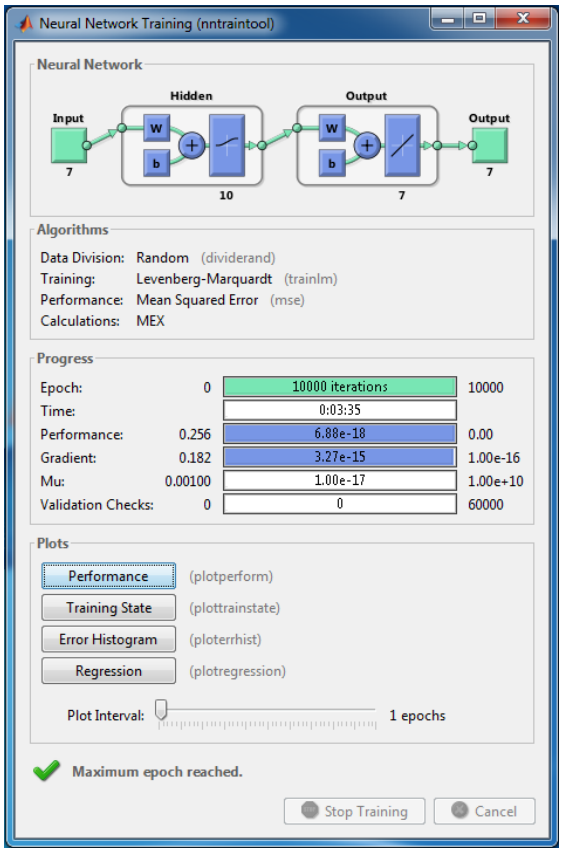

Fig. 6. The feed-forward neural network training

The test accuracy of the optimal feed-forward neural network has reached 100%.

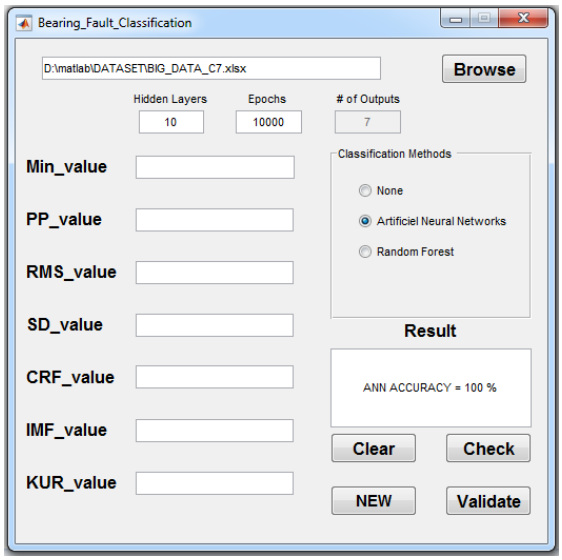

Fig. 7. Accuracy rate based on feed-forward neural network

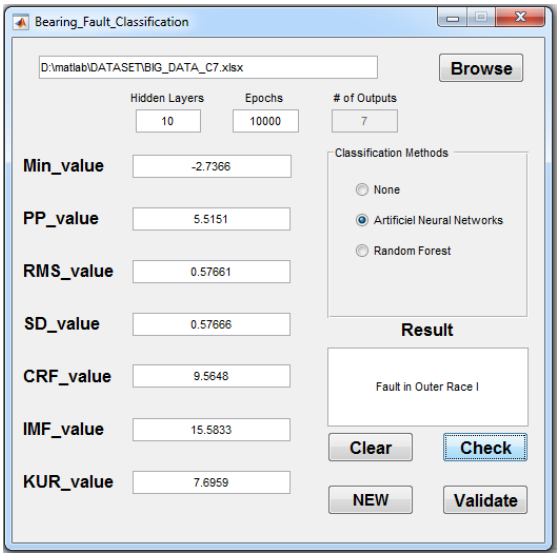

Fig. 8. An example of testing a bearing with Outer Race fault (OF1).

B. *RANDOM FOREST RESULTS:*

In the case of the random forest classifier, several experiments have been done using a variable number of trees. The obtained results demonstrate that test accuracy is heavily depending on the right choice of the number of trees. Fig. 10 gives the varying error rate according to the number of trees. From Fig. 10 it can be seen that the error rate decrease when the number of trees increases, then it will be established when the number of trees is equal to or greater than 10.

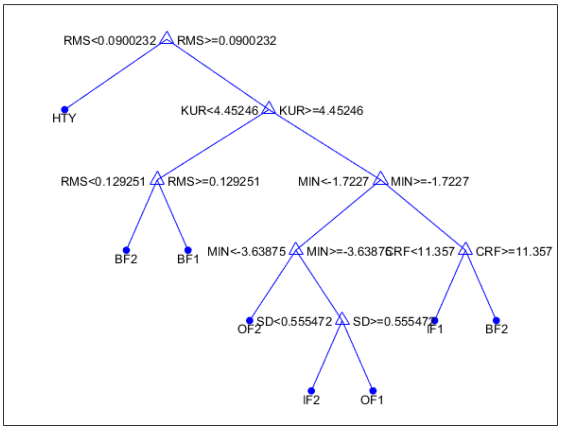

Fig. 9. Classification Tree

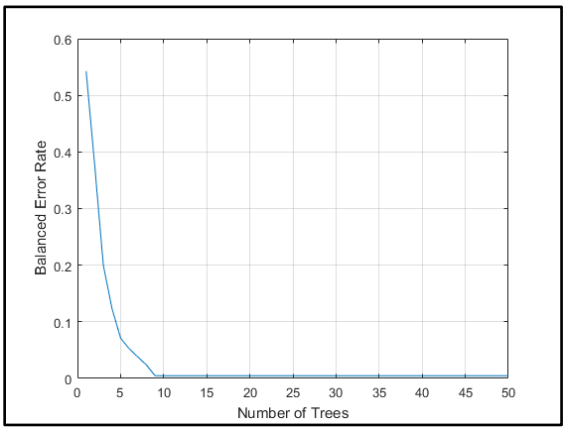

Fig. 10. Varying of the error rate according to the number of trees

The test accuracy obtained using 50 trees is equal to 98.5714%. Fig. 11 shows the developed graphical user interface (GUI) for bearing fault diagnosis.

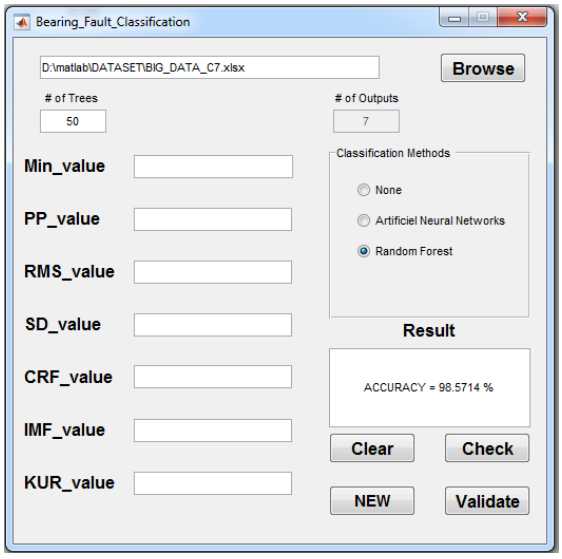

Fig. 11. Accuracy rate based on random forest.

VI. CONCLUSION

In this study condition classification using a graphical user interface has been developed for fault diagnosis. The proposed approach employed statistical parameters for feature extraction. Then, two classifiers namely: feed-forward neural network and random forest algorithm ensure the classification task. As the results showed that deep neural networks are more accurate than random forests. Using the GUI for training and testing classifiers facilitates the operation for several faults diagnosis without a programming background. The obtained results demonstrate the good performance of the suggested approach for bearing fault diagnosis.

REFERENCES

[1] A. Heng, S. Zhang, A. C. C. Tan, and J. Mathew, "Rotating machinery prognostics: State of the art, challenges, and opportunities," Mech. Syst. Signal Process., vol. 23, no. 3, pp. 724739, 2009.

[2] Bonnett, A.H., Yung, C.: Increased efficiency versus increased reliability. IEEE Ind. Appl. Mag. 14(1), 29–36 (2008).

[3] W. A. Smith and R. B. Randall, "Rolling element bearing diagnostics using the Case Western Reserve University data: A benchmark study," Mech. Syst. Signal Process., vols. 6465, pp. 100131, Dec. 2015.

[4] Sharma, Aditya, et al. “Feature Extraction and Fault Severity Classification in Ball Bearings.” Journal of Vibration and Control, vol. 22, no. 1, Jan. 2016, pp. 176–192, doi:10.1177/1077546314528021.

[5] T. Thelaidjia, S. Chenikher, and A. Moussaoui, "An Effective Approach for Severity Fault Diagnosis of Rolling Bearings," 2019 1st International Conference on Sustainable Renewable Energy Systems and Applications (ICSRESA), Tebessa, Algeria, 2019, pp. 1-6, DOI: 10.1109/ICSRESA49121.2019.9182688.

[6] Wu, D., Wang, H., Liu, H., He, T., Xie, T.: Health monitoring on the spacecraft bearings in high-speed rotating systems by using the clustering fusion of normal acoustic parameters. Appl. Sci. 9(16), 3246 (2019).

[7] Samanta, B., Al-Balushi, K.R.: Artificial neural network-based fault diagnostics of rolling element bearings using time-domain features. Mech. Syst. Signal Process. 17(2), 317–328 (2003).

[8] Kankar, P.K., Sharma, S.C., Harsha, S.P.: Fault diagnosis of ball bearings using machine learning methods. Expert Syst. 1876–1886 (2011).

[9] Marichal, G., Artes, M., Garcia-Prada, J.: An intelligent system for faulty-bearing detection based on vibration spectra. J. Vib. Control 17(6), 931–942 (2011).

[10] Khadersab, A., Shivakumar, S.: Vibration analysis techniques for rotating machinery and its vibration analysis effect techniques for rotating on bearing faults machinery and its effect on bearing faults costing models for capacity optimization in industry 4. 0: trade-off between used capacity and operational efficiency. Procedia Manuf. 20, 247–252 (2018).

[11] Nikolaou, N.G., Antoniadis, I.A.: Rolling element bearing fault diagnosis using wavelet packets. NDT& E Int. 35, 197–205 (2002).

[12] Liu, T.I., Singonahalli, J.H., Iyer, N.R.: Detection of roller bearing defects using expert system and fuzzy logic. Mech. Syst. Signal Process. 10, 595–614 (1996).

[13] Jenkins, C.D.: Bearing fault detection and wear estimation using machine learning. Los Alamos National Lab (LANL), Los Alamos (2019).

[14] Alguindigue, I.E., Loskiewicz-Buczak, A., Uhrig, R.E.: Monitoring and diagnosis of rolling element bearings using artificial neural networks. IEEE Trans. Ind. Electron. 40(2), 209–217 (1993).

[15] Jack, L.B., Nandi, A.K.: Genetic algorithms for feature selection in machine condition monitoring with vibration signals. IEEE Proc. Vis. Image Signal Process. 147(3), 205–212 (2000).

[16] Sawaqed, L.S., Alrayes, A.M. Bearing fault diagnostic using machine learning algorithms. ProgArtifIntell 9, 341–350 (2020). https://doi.org/10.1007/s13748-020-00217-z

[17] W. Li, A. Monti, and F. Ponci, "Fault Detection and Classification in Medium Voltage DC Shipboard Power Systems with Wavelets and Artificial neural networks," in IEEE Transactions on Instrumentation and Measurement, vol. 63, no. 11, pp. 2651-2665, Nov. 2014, DOI: 10.1109/TIM.2014.2313035.

[18] Gs, Vijay &Pai, P. &Sriram, N. S.. (2010). Artificial Neural Network based Condition Monitoring of Rolling Element Bearing.

[19] D. E. Rumelhart and J. L. McClelland, Parallel Distributed Processing. Cambridge, MA, USA: MIT, 1986.

[20] R. P. Lippmann, “An introduction to computing with neural nets,” IEEE ASSP Mag., vol. 4, no. 2, pp. 4–22, Apr. 1987.

[21] Building A Deep Learning Model using Keras | by EijazAllibhai | Towards Data Science.

[22] "IEEE Standard for Transitions, Pulses, and Related Waveforms," in IEEE Std 181-2011 (Revision of IEEE Std 181-2003), vol., no., pp.1-71, 6 Sept. 2011, DOI: 10.1109/IEEESTD.2011.6016198.

[23] MathWorks R2021, Copyright 1993-2004 The MathWorks, Inc. Available: https://www.mathworks.com/help/predmaint/ug/signal-features.html

[24] Dr. ABHISHEK SHARMA, A Simple Analogy to Explain Decision Tree vs. Random Forest, May 12, 2020, Accessed on: December 28, 2020 [Online]. Available: https://www.analyticsvidhya.com/blog/2020/05/decision-tree-vs-random-forest-algorithm

[25] Case Western Reserve University Bearing Data Center Website http://www.eecs.case.edu/laboratory/bearing/download.htm

Novel approach to estimate Remaining Useful Life in Condition Based Maintenance

Samira Abderrezek
ReLa(CS)^2 Laboratory
University of Oum El Bouaghi P.O. Box 358
04000 Oum El Bouaghi, Algeria
s.abderrezek@centre-univ-mila.dz

Abdelhabib Bourouis
ReLa(CS)^2 Laboratory
University of Oum El Bouaghi P.O. Box 358
04000 Oum El Bouaghi, Algeria
bourouis.abdelhabib@univ-oeb.dz
ORCID: 0000-0002-4592-4042

***Abstract*—Deep learning is an efficient tool for Remaining Useful Life (RUL) estimation, which is crucial for intelligent prognosis and Condition-Based Maintenance (CBM) strategies. To achieve this task, Bidirectional long short-term memories have been preferred for their ability to identify patterns of temporal sequences independently, and Convolutional Autoencoder is performed in extracting features. To benefit from the advantages of these two deep learning models, this paper proposes their hybridization. We investigate the best configuration by varying the values of the hyperparameters and evaluating their impact on the new model's performance. Finally, it is compared with other similar models in order to study the effectiveness of the approach.**

***Index Terms*—Condition-based maintenance; Remaining Useful Life (RUL), Bidirectional Long-Short Term Memory neural network, Convolutional auto-encoder neural network, C-MAPSS dataset**

I. Introduction

Intelligent prognostics and machine health management technologies have shown promising application capabilities in many industries, also called condition-based maintenance (CBM). By monitoring the installation conditions, CBM can maximize operational availability, reduce maintenance costs, and improve the reliability and security of the system. It involves the evaluation of machines' performance degradation by estimating their Remaining Useful Life (RUL). The RUL of an asset is defined as time left from the current time to the end of its useful life [1]. It is the prediction of the remaining time during which a system can perform its planned function. Generally, RUL has a significant influence on decision-making [2].

According to Lee and al in [3] RUL prediction approaches' are regrouped in Model-based approaches, data-driven approaches, and hybrid prognostic approaches. Model-based approaches require prerequisites of in-depth knowledge of the physical systems, which is not generally available in practice. Data-driven approaches, on the other hand, can model degradation characteristics based on historical sensor data. In recent years, many efficient data-based algorithms have been proposed, in particular: learning models such as neural networks, support vector machine (SVM), and hidden Markov models. Deep learning networks are emerging as a highly effective structures for pattern recognition, which can improve performance in the current intelligent prognostics. It is characterized by the deep network architecture where multiple layers are stacked in the network to fully capture the representative information from raw input data [4]. High-level abstractions of data can be modeled well with the help of complex deep structures, leading to more efficient feature extraction than shallow networks. Deep learning methods have gained great interest and achieved significant results in many fields, including image recognition [5] and speech recognition [6]. Since the raw data obtained from machinery health monitoring share similar high dimensionality with those in image processing researches, deep learning architecture has excellent potential in Prognosis Health Monitoring (PHM) and RUL estimation.

Data describing Condition-Based Maintenance (CBM) parameters are categorized as time series types. Time series prediction problems are a complex type of predictive modeling, which unlike predictive modeling of regression, also add the complexity of a dependency of sequence between input variables. A powerful type of artificial neural network (ANN) designed to handle sequence dependence is called recurrent neural networks (RNN). Bidirectional LSTM (BiLSTM) is a variant of RNN used in several recent works. It has given promising results, especially in capturing the hidden long-term temporal dependencies among time sequence signals. Another type of deep learning model is the Convolutional Neural Network (CNN) and the Autoencoder (AE). They have improved their performance in the domain. Mainly they can extract the essential local features from sequential data. Taking advantage of their characteristics, we have chosen to use them in a hybrid ANN for RUL estimation.

The rest of this paper is organized as follows: Section II presents recent related works. Section III presents the proposed model architecture, Section IV describes the dataset used for evaluating the models, the data pre-processing, the evaluation metrics, and the approach description. Finally, section V concludes this paper and discusses future work for the RUL estimation task.

This work is implemented using HPC resources of UCI-UFMC (Unit de Calcul Intensif) of University FRERES MENTOURI CONSTANTINE university and HPC of Batna2 university

II. Related work

Bidirectional LSTM, CNN, and Autoencoder networks have been the subject of several recent works. They have been used alone or in hybridization with other deep algorithms, and they have been improved their performances in the RUL estimation domain.

Recently, CNN was successfully introduced in RUL prediction for its strong capability in local feature extraction [7], [8], [9]. For example, in work presented in [10], a Deep Convolutional Neural Network (DCNN) alone is proposed for prognosis. It used the time window approach for sample preparation to achieve better feature extraction by the DCNN. The raw data collected with normalization is directly used as the proposed network inputs without any prior expertise on prognosis and signal processing, which facilitates the application of the proposed method.

Another architecture applied a CNN first and then uses LSTM for estimating RUL in [11]. A method of data augmentation is applied to improve the performance of the proposed approach. Another instance of this category combines CNN and LSTM in parallel [12]. While in a second paper [13], they integrated three fully noisy deep learning architectures, Noisy CNN and Noisy Bi-directional Gated Recurrent Unit (GRU) paths are designed in parallel, and their concatenated output is fed into the Noisy fusion center.

Authors in [14], designed a deep learning model combining CNN for extracting robust local features from the sequential input, and then Bi-directional LSTM is adopted to encode temporal information on the sequential output of CNN. In [15], authors used an LSTM Encoder-Decoder architecture in only the first Commercial Modular Aero-Propulsion System Simulation (C-MAPSS) dataset, obtaining an unsupervised health index to determine RUL.

A variational encoder-decoder is proposed in [16]. It is based on visual data analysis to predict when an in-service machine will fail. A deep Convolutional Variational AutoEncoder is used for automatically extracting performance degradation feature from multiple sensors. Furthermore, an encoder-decoder model has been proposed in [17]. The BiLSTM and CNN are used in the encoder, and fully connected networks are used to decode feature information.

A RUL prediction method for electric valves has been presented in [18]. Hybridization used a Convolutional Auto-Encoder for extracting deeper features and an LSTM for efficiency in dealing with time-series data. The authors designed a parallel structure between the outputs of the Convolutional Auto-Encoder and the original data to enrich features fed into the LSTM.

III. Description of the proposed approach architecture

The previous noticed works inspire the idea of our proposition in section II. It aims to combine the advantages of three different techniques through their integration so that the results can be aggregated to improve prediction performance. Convolutional Auto Encoder is used to extract principal significant features from the original signal and is also used for data dimension reduction. BiLSTM is used as a tool that models time series and captures bidirectional features long-term dependencies, since the time series of the study domain has a characteristic of dynamic instability and long-term dependencies. That's the reason for proposing a model which couples the convolutional autoencoder neural network (CAENN) and the Bidirectional neural network (BiLSTM NN) for aero turbofan engines in this paper. And so, the hybrid architecture has the advantage of giving high estimation accuracy and low computing burden. Our purpose in this work is to propose a hybrid model combining a set of the most successful Neural Network classes, which are Convolutional Autoencoder (CAE) and Bidirectional LSTM neural network in a hybrid solution that constitutes the most promising category of RUL estimation [19]. The first challenge is to perform the tuning of hyperparameters and the study of the effect of each one on the model performance to find the best alternative. The approach is finally compared with some algorithms in the literature and validated using the NASA C-MAPSS dataset.

Its components are:

1) **Convolutional AutoEncoder deep neural network**
   An autoencoder is a type of neural network used to learn efficient code in an unsupervised manner [20]. It consists of an encoder and decoder. The encoder learns to compress the input data into a short code, whereas the decoder learns to decompress the code into a set of data that closely matches the input data [21]. It could extract hidden features from input data and reconstruct original data with these features. It can be applied not only for dimension reduction but also for further classification, and prediction [22]. The authors, in [23], observed that the combination of Autoencoder with CNN could improve model accuracy.
   As an encoder in our model, we use two convolutional 2D layers. After each one, a maxpooling layer is used, where the central concept is the size reduction of the feature maps by selecting the maximum value for each patch of the feature map. Hence, reducing the number of model parameters and simplifying the computational complexity of the network, as well as helps in avoiding the over-fitting issue [24]. Then as a decoder, two convolutional 2D layers are used, and after each one, an upsampling layer (UpSampling2D) doubles the dimensions of the input. We have chosen $10, 10, 10, 10, 5, 2$ as filters, and $(10, 1), (10, 1), (10, 1), (10, 1), (10, 1), (1, 1)$ as kernel sizes. Zero padding is used to keep the feature map through the network and also (2,1) as kernels for each maxpooling and upsampling layers.
2) **Bidirectional LSTM deep neural network**
   BiLSTM is used in the proposed model to capture the bidirectional temporal dependencies between features. BiLSTM results in two LSTM layers instead of one on the input sequence. One access information in the

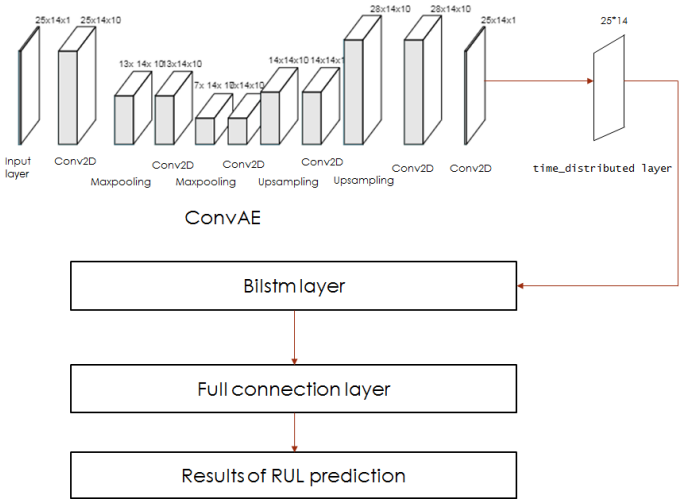

Fig. 1. CAEBi-Architecture

forward direction, and the other access it in the backward direction, which can provide additional context to the network and lead to faster and more complete learning of the problem.

Our model comprises one Bidirectional LSTM layer, followed by a dropout layer to avoid overfitting. Finally, a fully connected layer (dense layer) is applied to map the output of the Bidirectional LSTM model to the desired output size, which is equal to 1 and provided by the linear activation function.

The whole model structure is illustrated in Figure 1. The CAENN is applied firstly to perform downsampling of data to minimize its size and complexity and enhance the model generalization and learning capacity. By extracting hidden features from input data, it could easily then use them to reconstruct original data by oversampling it. Then, a distributed flatten layer is connected to the network output to hybridize with the BiLSTM network. After that, the data is introduced to the BiLSTM NN for deepening the characteristics of the information given by the CMAPSS data sources and establishing the nonlinear relationship between the multivariable's time-series and RUL. Finally, a fully connected dense layer is connected to the output of the model.

IV. Experiments and Discussion

A. Dataset description

The performance of the proposed model is evaluated using the public and widely used in the literature NASA C-MAPSS dataset [25]. It contains simulated data produced using a model-based simulation program developed by NASA.

The dataset comprises 4 subsets of multi-variate temporal data that simulate the condition monitoring data of turbofan engines under different operating conditions and failure modes. In this paper, the first sub-dataset FD001 is used. It contains 100 training engines, 100 test engines, one operating condition, one failure mod, 20630 training samples, 13 095 test samples, 21 sensors, and three operating indicators [26].

FD001 is a multiple high-dimensional consecutive time-series data. The training set records condition-monitoring data of turbofan engines from the normal condition at the beginning to complete failure at last. The condition-monitoring data of the test set ends at some point before failure occurs. The goal is to predict the number of remaining operational cycles of turbofan engines in the test set.

Only 14 sensor data are chosen here as the input data of the network, like in [10] where is discarded some sensor values because they do not vary throughout the entire engine life cycle. The picked columns are 2, 3, 4, 7, 8, 9, 11, 12, 13, 14, 15, 17, 20 and 21.

B. Data pre-processing

1) Normalization: For an equal contribution of all features, under all conditions of operation, normalization with the min-max method is applied to a range of [-1, 1] using Equation 1 [12].

$$x_{norm}^{i,j} = \frac{2 \times x^{i,j} - x_{min}^{i,j}}{x_{max}^{j} - x_{min}^{j}} - 1, \forall i, j \tag{1}$$

Where $x^{i,j}$ denotes the i^{th} origin data point of the j^{th} sensor, and $x_{norm}^{i,j}$ norm is the normalized value of $x^{i,j}$. x_{max}^{j} and x_{min}^{j} denote respectively the maximum and minimum values of the original measurement data of the j^{th} sensor [10].

2) Time window processing: The data is processed with a sliding time window approach of size $N_f = 25$ and stride of 1. The sliding window means that the first input sample to the network takes measurements from cycles 1-25, the second 2-26, and so forth for each fleet unit. The RUL label for a sample is then simply the total number of cycles the engine can operate, minus the cycle where the window ends. [10].

Following the standard procedure adopted by other researchers, the maximum horizon of prediction for RUL (R_{early}) was limited to 125 cycles, which has an impact on the model accuracy and makes models more stable.

C. Evaluation Metrics

In order to assess the performance of the proposed prognostic model, the following functions are used.

1) **Root mean squared error (RMSE):**
RMSE is the most widely used metric for regression tasks and a performance indicator to determine the accuracy of the estimated RUL. It is given by:

$$RMSE = \sqrt{\frac{\sum_{i=1}^{n} e_i^2}{n}} = \sqrt{\frac{\sum_{i=1}^{n} (\hat{y}_i - y_i)^2}{n}} \tag{2}$$

Where n is the total number of samples in the test set and $e_i = \hat{y}_i - y_i$ is the error between the estimated RUL values $\hat{y}$, and the actual RUL values y for each engine within the test set. The errors are first squared before

TABLE I
AVERAGE TEST AND TRAIN LOSS RESULTS WITH DIFFERENT TIME WINDOW SIZES.

TWindow Size (WS)	Train				Test			
	MSE	MAE	RMSE	R^2	MSE	MAE	RMSE	R^2
15	360.14	15.21	16.87	0.80	263.99	11.91	14.78	0.84
20	345.89	15.02	18.10	0.76	270.94	11.65	16.16	0.81
25	239.19	12.38	13.94	0.85	190.55	10.19	13.13	0.87
30	292.21	13.43	15.12	0,82	241.46	11.50	13.35	0.86

averaging, which poses a high penalty on significant errors [27].

2) Regression score function(R^2) The scoring function is a performance measure defined by the PHM community in "The 2008 PHM data challenge competition" [26]. It is given by :

$$R^2(y, \bar{y}) = 1 - \frac{\sum_{i=1}^{n} (y_i - \hat{y}_i)^2}{\sum_{i=1}^{n} (y_i - \bar{y})^2} \quad (3)$$

where $\bar{y} = \frac{1}{n} \times \sum_{i=1}^{n} y_i$ and $\sum_{i=1}^{n} (y_i - \hat{y}_i)^2 = \sum_{i=1}^{n} {e_i}^2$

3) Mean squared error(MSE) Given n models of the data set, for the ith example, let p_i be the predicted value and a_i the real value. The MSE of the tested dataset is [28] :

$$MSE = \frac{\sum_{i=0}^{n} (a_i - p_i)^2}{n} \quad (4)$$

4) Mean absolute error(MAE) Robust to outliers and does not penalize the errors, S_i the predicted value of the i_th sample, and is the corresponding true value, then the mean absolute error (MAE) estimated on is defined as [29]:

$$MAE(y, \hat{y}) = \frac{1}{n_{samples}} \times \sum_{i=1}^{n_{samples}-1} |y_i - \hat{y}_i| \quad (5)$$

D. Hyper Parameter tuning

Our objective in this section is to thoroughly investigate all the hyperparameters of the model architecture that deliver the best recognition accuracy for the C-MAPSS dataset. The number of epochs here is fixed to 20.

1) Time window size parameter effect: When using deep learning models for RUL predicting, a sliding time window approach is widely employed to convert condition monitoring data stream into input samples for supervised learning. Specifically, the time window approach takes features in previous time steps as input variables, while RUL labels in the next time step as the output variable [30].

Table I shows the results obtained from the proposed CAE Bidirectional framework using values of window sizes (WS) of 10 to 30. The values of metrics function for $WS = 25$ are clearly better than the other WS values. Results obtained from larger window sizes are more efficient. A larger time window size can cover more raw information, which is the basis for further extraction features [10]. This value will be adopted in the rest of the paper.

TABLE II
EFFECTS OF LEARNING RATES.

LR	Train				Test			
	MSE	MAE	RMSE	R^2	MSE	MAE	RMSE	R^2
0.001	310.10	14.59	16.09	0.81	259.36	12.82	16.59	0.80
0.0001	249.03	12.89	14.28	0.85	218.34	10.95	13.23	0.87
0.00001	**236.89**	**12.43**	**13.87**	**0.86**	**174.34**	**10.09**	**11.59**	**0.90**

TABLE III
EFFECTS OF BATCH SIZE VALUES.

Batch Size	Train				Test			
	MSE	MAE	RMSE	R^2	MSE	MAE	RMSE	R^2
512	236.89	12.43	13.87	0.85	174.34	10.09	11.59	**0.90**
128	171.48	9.20	10.91	0.90	174.93	**9.20**	**11.29**	0.89
100	121.90	7.85	9.41	0.93	**168.59**	9.43	12.62	0.88
64	159.60	8.82	10.57	0.91	214.12	11.09	13.37	0.84

2) Effects of learning rate and batch sizes: The learning rate controls the update rate of weights in response to the estimated gradient at the end of each batch. It can significantly impact the trade-off between how quickly or how well the model learns the problem. Results in table II show that the small values of learning rate (0.00001) give better performance. Table III also shows that 128 as the value of batch size gives the best performance of the model.

3) Effects of activation function and optimizer: By using different activation functions with different optimizers, we notice that the Hyperbolic Tangent Function **Tanh** for hidden layers with "linear" activation function for the dense layer and "Adam" optimizer give the best results (Table IV).

The "Tanh" activation function has a very similar structure to the "Sigmoid" function, but it is always preferred when optimization is easier. It is frequently used in hidden layers of an ANN, as its values lie between -1 to 1. Hence, the mean of the hidden layer comes out close to 0, which helps to center data by bringing the mean close to 0. This makes learning for the next layer much more effortless and means that it will be more efficient because it has a broader range for faster learning and grading. Its inconvenience over ReLU is the problem of gradients at the ends of the function [31].

4) Effects of layers and unit numbers of BiLSTM: Table V and Table VI, show that one BiLSTM layer is enough to give best results with unit number equal to 300.

TABLE IV
EFFECTS OF ACTIVATION FUNCTION AND OPTIMIZER.

Activation Function	Optimizer	Train				Test			
		MSE	MAE	RMSE	R^2	MSE	MAE	RMSE	R^2
Tanh	**adam**	**171.48**	**9.20**	**10.91**	**0.90**	**174.93**	**9.20**	**11.29**	**0.89**
	rmsprop	160.69	8.79	10.44	**0.90**	204.53	9.78	15.02	0.82
	adadelta	141.76	7.74	9.43	0.93	245.01	10.81	17.87	0.72
ReLU	**adam**	206.85	10.43	12.18	0.88	190.22	9.91	12.44	0.88
	rmsprop	257.74	12.34	14.16	0.81	268.98	11.92	13.93	0.83
	adadelta	411.32	16.79	18.09	0.72	318.04	13.23	16.16	0.81
Sigmoid	**adam**	1750.23	37.19	38.41	/	1765.44	36.04	40.59	/
	rmsprop	1648.17	35.05	39.46	/	1750.99	37.27	38.47	/
	adadelta	1750.64	37.24	38.45	/	1651.23	35.03	39.50	/
Leaky ReLU	**adam**	127.76	8.12	9.54	0.92	**161.11**	9.38	13.19	0.86
	rmsprop	104.68	6.94	8.30	0.95	235.18	10.29	15.98	0.77
	adadelta	76.57	6.05	7.63	0.96	281.31	11.66	14.59	0.82

TABLE V
EFFECTS OF BILSTM LAYERS.

Layers	Train				Test			
	MSE	MAE	RMSE	R^2	MSE	MAE	RMSE	R^2
1	**162.02**	**8.98**	**10.64**	**0.90**	**142.90**	**8.41**	**10.36**	**0.91**
2	146.35	8.38	10.01	0.92	153.38	8.95	12.95	0.87
3	176.50	9.35	10.92	0.89	171.67	9.34	12.62	0.87
4	201.57	10.28	12.03	0.85	172.73	9.24	11.81	0.89
5	198.03	10.52	12.18	0.85	169.57	9.46	11.89	0.89

TABLE VI
EFFECTS OF BILSTM UNIT NUMBER.

Unit Number	Train				Test			
	MSE	MAE	RMSE	R^2	MSE	MAE	RMSE	R^2
128	171.48	9.20	10.91	0.88	174.93	9.20	11.29	0.89
256	162.66	9.02	10.65	0.87	182.95	9.67	11.31	0.89
300	**162.02**	**8.98**	**10.64**	0.87	**142.90**	**8.41**	**10.36**	**0.91**
350	155.87	8.71	10.41	0.89	141.30	8.55	12.13	0.89
400	191.47	9.95	11.70	0.85	192.10	9.96	11.90	0.88

5) Effects of number of layers, filters, and kernel sizes of Convolutional Auto Encoder: Results in Tables VII, VIII and IX, show that for different values of filters and kernel sizes, the values of $(10, 10)(10, 10)(10, 10)(10, 10)(10, 5)(1, 2)$ give the best performance. Furthermore, six layers of Convolutional 2D are the best.

6) Effects of validation split values: Results in Table X show that for different values of validation split, the value of 0.15 gives the best performance.

E. Final results for FD001 sub-dataset

Final results for FD001 with 20 epochs after the tuned hyperparameters are for training: MSE=166.66, MAE = 9.40, RMSE = 12.22 and R^2 = 0,85. For test: MSE=149.25, MAE=8.86, RMSE=10.07 and R^2=0.91.

Figures 2, 5 and 4 illustrated detailed comparisons between the predicted RUL values and the actual values during the whole life of engine units. It is observed that the prediction error is decreasing with usage, and units can be predicted precisely. There is more useful degradation information in the late stage than in the early stage.

Therefore, the experimental results demonstrate that the piece-wise linear degradation function is suitable for this problem. As shown in figure 3, the training RMSE and the validation RMSE decrease with the epoch in the training process. Besides, the loss value tends to be constant in the late stage. It is found that the training loss has the same trend of change as the validation loss. Therefore, there is no overfitting problem in the training process, and the selection of training hyperparameters is suitable for this problem.

TABLE VII
EFFECTS OF FILTERS.

Filters	Train			Test			
	MSE	MAE	RMSE	MSE	MAE	RMSE	R^2
10	142.71	8.31	9.91	146.35	8.92	10.15	0.91
16	155.76	8.67	10.28	171.01	9.35	12.81	0.87
32	218.97	10.59	12.38	239.39	11.45	14.34	0.84
64	132.26	8.04	9.72	182.92	9.73	13.32	0.86

TABLE VIII
EFFECTS OF KERNELS.

Kernels	Train			Test			
	MSE	MAE	RMSE	MSE	MAE	RMSE	R^2
10	142.71	8.31	9.91	146.35	8.92	10.15	0.91
6	178.64	9.55	11.16	159.88	8.94	10.27	0.90

TABLE IX
EFFECTS OF CAE LAYERS.

CAE Layers	Train			Test			
	MSE	MAE	RMSE	MSE	MAE	RMSE	R^2
7	162.02	8.98	10.64	**142.90**	**8.41**	10.36	0.91
6	**142.71**	**8.31**	**9.91**	**146.35**	**8.92**	**10.15**	**0.91**
5	173.89	9.39	11.00	162.05	8.90	10.36	0.90

TABLE X
EFFECTS OF VALIDATION SPLIT VALUES.

VS	Train				Test			
	MSE	MAE	RMSE	R^2	MSE	MAE	RMSE	R^2
0,05	159.57	8.96	10.6	0,89	169.02	9.16	12.56	0.87
0,1	**142.71**	**8.31**	**9.91**	**0,93**	**146.35**	8.92	10.15	**0.91**
0,15	**166.66**	**9.40**	**12.22**	**0,85**	149.25	**8.86**	**10.07**	**0.91**

F. Comparison of similar approaches using C-MAPSS dataset

A comparison with other similar and recent approaches presented in table XI shows that the model gives encouraging results.

V. CONCLUSION

In this paper, a model based on Convolutional Autoencoder and BiLSTM neural network for RUL estimation of C-MAPSS data is proposed. The model has the capacity of feature extraction and data reduction of CAENN and the skill of time series prediction and bidirectional temporal features extraction of BiLSTM NN.

The accuracy of the RUL prediction model exceeds 91%, while RMSE and MAE are limited to 10.07 and 8.86, respectively.

The proposed method is suitable for predicting the RUL of C-MAPSS data. Future research interests exist in optimizing different parameters of the model with a suitable meta-heuristic method. A parallel architecture is also another interesting way and maybe another network hybridization in searching for a high-efficiency model. Attention mechanism and Ensemble learning also can be applied to improve accurately predicting RUL. Furthermore, extend the study to all the other sub-datasets.

TABLE XI
RMSE COMPARISON ON C-MAPSS DATASET.

Approach	**FD001**
CNN BiLSTM [32]	10.74
LSTM [33]	16.14
BD-LSTM [34]	15.42
LSTM [34]	18.07
BD-RNN [34]	20.04
CNN [7]	18.45
MLP [34]	20.84
RVR [7]	23.79
SVR [7]	20.96
MLP [7]	37.56
DCNN [10]	12.61
LSTM [10]	13.52
RNN [10]	13.44
DNN [10]	13.56
NN [10]	14.80
[35]	12.18
Parallel LSTM CNN [12]	13.017
Noisy Parallel CNN BiGRU and FC (NPBGRU) [13]	10.44
Deep separable convolutional network (DSCN) [36]	10.95
Double channel CNN and bidirectional LSTM [37]	12.58
Gated graph neural networks (GNNs) [38]	12.14
BiLSTM MultiscaleCNN [39]	12,75
CAE with BDGRUBDLSTM [40]	9.51
CNNBDGRU [40]	11.085
The proposed method	**10.15**

TABLE XII
ABBREVIATIONS USED IN THIS MANUSCRIPT.

Adam	Adaptive Moment Estimation
ANN	Artificial Neural Network
BiLSTM	Bidirectional LSTM Neural network
CAE	Convolutional Auto Encoder
CNN	Convolutional Neural Network
C_MAPSS	Commercial Modular Aero Propulsion System Simulation
DCNN	Deep Convolutional Neural Network
DL	Deep Learning
DNN	Deep Neural Network
LSTM	Long Short-Term Memory
MAE	Mean Absolute Error
MLP	Multi Layer Perceptron
MSE	Mean Squared Error
DBN	Deep Belief Network
Relu	Rectified Linear Unit
RMSE	Root Mean Square Error
RMSProp	Root Mean Square Propagation
RNN	Recurrent Neural Network
R_2	R^2 correlation
RUL	Remaining Useful Life
Tanh	Hyperbolic Tangent Activation Function

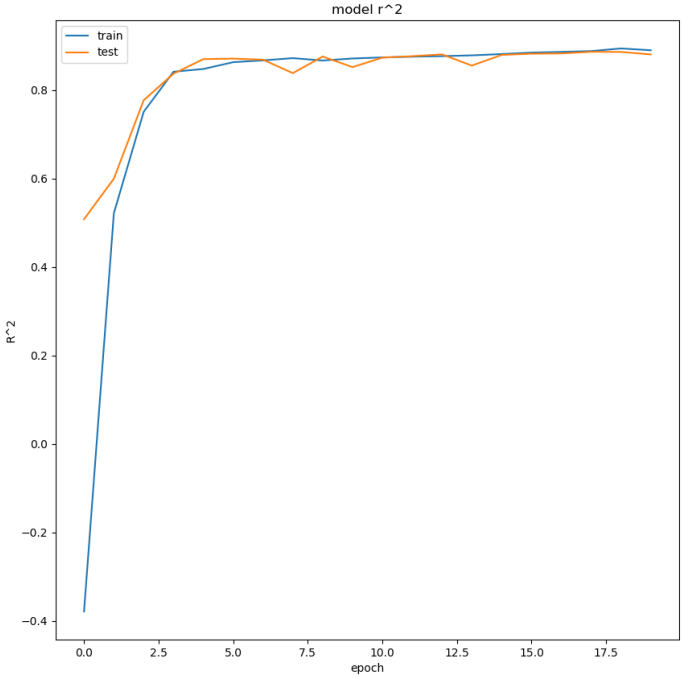

Fig. 2. R^2 values: comparison between predicted and actual RUL values for testing engines.

REFERENCES

[1] X.-S. Si, W. Wang, C.-H. Hu, and D.-H. Zhou, "Remaining useful life estimation–a review on the statistical data driven approaches," *European journal of operational research*, vol. 213, no. 1, pp. 1–14, 2011.

[2] D. R. Obando, "From deterioration modeling to remaining useful life control: a comprehensive framework for post-prognosis decision-making applied to friction drive systems," Ph.D. dissertation, Université Grenoble Alpes, 2018.

[3] J. Lee, F. Wu, W. Zhao, M. Ghaffari, L. Liao, and D. Siegel, "Prognostics and health management design for rotary machinery systems—reviews, methodology and applications," *Mechanical systems and signal processing*, vol. 42, no. 1-2, pp. 314–334, 2014.

[4] E. M. Brakni, "Réseaux de neurones artificiels appliqués à la méthode électromagnétique transitoire infinitem," Ph.D. dissertation, Université du Québec en Abitibi-Témiscamingue, 2011.

[5] Wikistat, "neural network and introduction to deep learning— wikistat," 2016, available Janury 21st 2016, 17pages, pdf format. [Online]. Available: https://www.math.univ-toulouse.fr/besse/Wikistat/pdf/st-m-hdstat-rnn-deeplearning.pdf

[6] F. Chollet, *Deep Learning mit Python und Keras: Das Praxis-Handbuch vom Entwickler der Keras-Bibliothek*. MITP-Verlags GmbH & Co. KG, 2018.

[7] G. S. Babu, P. Zhao, and X.-L. Li, "Deep convolutional neural network based regression approach for estimation of remaining useful life," in *International conference on database systems for advanced applications*. Springer, 2016, pp. 214–228. [Online]. Available: https://doi.org/10.1007/978-3-319-32025-0_14.

[8] J.-R. Jiang and C.-K. Kuo, "Enhancing convolutional neural network deep learning for remaining useful life estimation in smart factory applications," in *2017 International Conference on Information, Communication and Engineering (ICICE)*. IEEE, 2017, pp. 120–123. [Online]. Available: https://doi.org/10.1109/ICICE.2017.8478928.

[9] J. Zhu, N. Chen, and W. Peng, "Estimation of bearing remaining useful life based on multiscale convolutional neural network," *IEEE Transactions on Industrial Electronics*, vol. 66, no. 4, pp. 3208–3216, 2018. [Online]. Available: https://doi.org/10.1109/TIE.2018.2844856.

[10] X. Li, Q. Ding, and J.-Q. Sun, "Remaining useful life estimation in prognostics using deep convolution neural networks," *Reliability Engineering & System Safety*, vol. 172, pp. 1–11, 2018. [Online]. Available: https://doi.org/10.1016/j.ress.2017.11.021

[11] L. Jayasinghe, T. Samarasinghe, C. Yuenv, J. C. N. Low, and S. S. Ge, "Temporal convolutional memory networks for remaining useful life estimation of industrial machinery," in *2019 IEEE International Conference on Industrial Technology (ICIT)*. IEEE, 2019, pp. 915–920, online available: http://arxiv.org/abs/1810.05644.

[12] A. Al-Dulaimi, S. Zabihi, A. Asif, and A. Mohammadi, "A multimodal and hybrid deep neural network model for remaining useful life estimation," *Computers in Industry*, vol. 108, pp. 186–196, 2019.

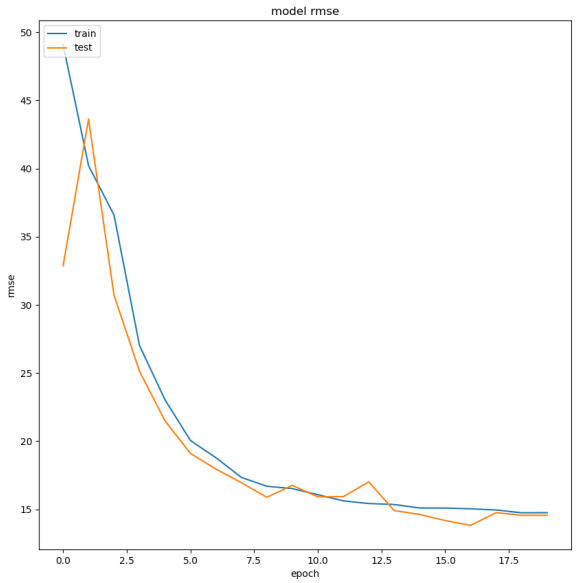

Fig. 3. RMSE values: learning curve of FD001 in the training and test processes.

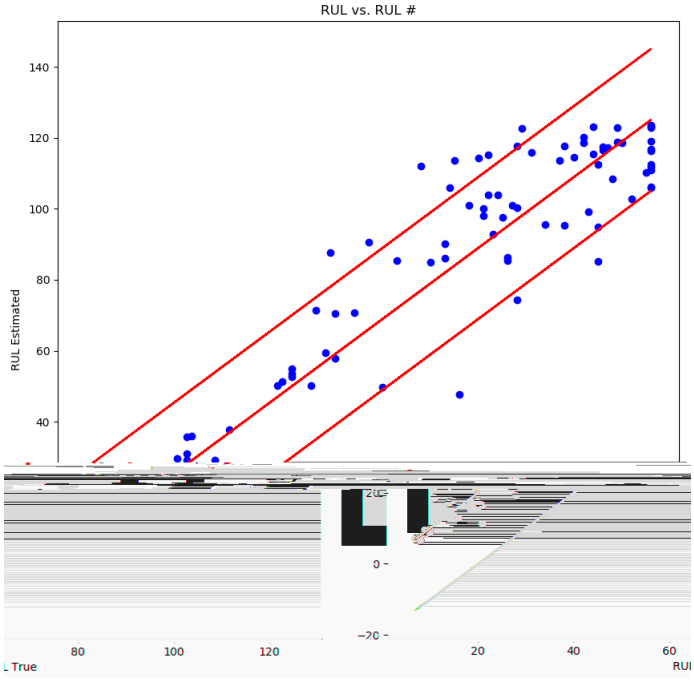

Fig. 4. Comparison between predicted and actual RUL values for testing engines.

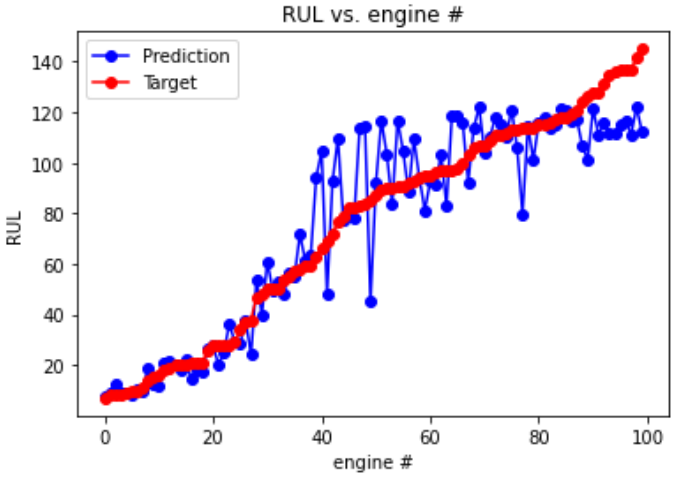

Fig. 5. RUL predictions for the testing engins in FD001

[13] A. Al-Dulaimi, A. Asif, and A. Mohammadi, "Noisy parallel hybrid model of nbgru and ncnn architectures for remaining useful life estimation," *Quality Engineering*, vol. 32, no. 3, pp. 371–387, 2020.

[14] R. Zhao, R. Yan, J. Wang, and K. Mao, "Learning to monitor machine health with convolutional bi-directional lstm networks," *Sensors*, vol. 17, no. 2, p. 273, 2017.

[15] P. Malhotra, V. TV, A. Ramakrishnan, G. Anand, L. Vig, P. Agarwal, and G. Shroff, "Multi-sensor prognostics using an unsupervised health index based on lstm encoder-decoder," *arXiv preprint arXiv:1608.06154*, 2016.

[16] R. Zemouri, Z. Al Masry, I. Remadna, S. L. Terrissa, and N. Zerhouni, "Hybrid architecture of deep convolutional variational auto-encoder for remaining useful life prediction," in *Proceedings of the 30th European Safety and Reliability Conference and the 15th Probabilistic Safety Assessment and Management Conference*, F. D. M. Piero Baraldi and E. Zio, Eds., Copyright c ESREL2020-PSAM15 Organizers. Venice, Italy: Research Publishing Services, Singapore, 2017, pp. 3591–3598. [Online]. Available: https://www.rpsonline.com.sg/proceedings/esrel2020/html/4876.xml

[17] H. Liu, Z. Liu, W. Jia, and X. Lin, "A novel deep learning-based encoder-decoder model for remaining useful life prediction," in *2019 International Joint Conference on Neural Networks (IJCNN)*. IEEE, 2019, pp. 1–8. [Online]. Available: https://doi.org/10.1109/IJCNN.2019.8852129

[18] H. Wang, M.-j. Peng, Z. Miao, Y.-k. Liu, A. Ayodeji, and C. Hao, "Remaining useful life prediction techniques for electric valves based on convolution auto encoder and long short term memory," *ISA transactions*, vol. 108, pp. 333–342, 2021. [Online]. Available: https://doi.org/10.1016/j.isatra.2020.08.031.

[19] A. Al-Dulaimi, S. Zabihi, A. Asif, and A. Mohammadi, "Hybrid deep neural network model for remaining useful life estimation," in *ICASSP 2019-2019 IEEE International Conference on Acoustics, Speech and Signal Processing (ICASSP)*. IEEE, 2019, pp. 3872–3876.

[20] G. E. Hinton and R. R. Salakhutdinov, "Reducing the dimensionality of data with neural networks," *science*, vol. 313, no. 5786, pp. 504–507, 2006.

[21] W. Yu, I. Y. Kim, and C. Mechefske, "Remaining useful life estimation using a bidirectional recurrent neural network based autoencoder scheme," *Mechanical Systems and Signal Processing*, vol. 129, pp. 764–780, 2019.

[22] C. Yin, S. Zhang, J. Wang, and N. N. Xiong, "Anomaly detection based on convolutional recurrent autoencoder for iot time series," *IEEE Transactions on Systems, Man, and Cybernetics: Systems*, 2020.

[23] J. Masci, U. Meier, D. Cireşan, and J. Schmidhuber, "Stacked convolutional auto-encoders for hierarchical feature extraction," in *International conference on artificial neural networks*. Springer, 2011, pp. 52–59.

[24] R. Zhao, R. Yan, Z. Chen, K. Mao, P. Wang, and R. X. Gao, "Deep learning and its applications to machine health monitoring," *Mechanical Systems and Signal Processing*, vol. 115, pp. 213–237, 2019.

[25] Y. Liu and N. G. R. Center, *User's guide for the commercial modular aero-propulsion system simulation (C-MAPSS)*, ser. NASA technical memorandum. National Aeronautics and Space Administration, Glenn Research Center, 2012. [Online]. Available: https://books.google.dz/books?id=MhGXnQAACAAJ

[26] A. Saxena, K. Goebel, D. Simon, and N. Eklund, "Damage propagation modeling for aircraft engine run-to-failure simulation," in *2008 interna-*

tional conference on prognostics and health management. IEEE, 2008, pp. 1–9.

[27] D. Mishra. Regression: An explanation of regression metrics and what can go wrong. [Online]. Available: https://towardsdatascience.com/regression-an-explanation-of-regression-metrics-and-what-can-go-wrong-a39a9793d914

[28] C. Staudemeyer, Ralf Omlin, "Evaluating performance of long short term memory recurrent neural networks on intrusion detection data," in *CM International Conference Proceeding*, ser. 218, 2013.

[29] R. C. Staudemeyer and C. W. Omlin, "Evaluating performance of long short-term memory recurrent neural networks on intrusion detection data," in *Proceedings of the South African Institute for Computer Scientists and Information Technologists Conference*, 2013, pp. 218–224.

[30] T. Xia, Y. Song, Y. Zheng, E. Pan, and L. Xi, "An ensemble framework based on convolutional bi-directional lstm with multiple time windows for remaining useful life estimation," *Computers in Industry*, vol. 115, p. 103182, 2020.

[31] C. Nwankpa, W. Ijomah, A. Gachagan, and S. Marshall, "Activation functions: Comparison of trends in practice and research for deep learning," *arXiv preprint arXiv:1811.03378*, 2018.

[32] I. Remadna, S. L. Terrissa, R. Zemouri, S. Ayad, and N. Zerhouni, "Leveraging the power of the combination of cnn and bi-directional lstm networks for aircraft engine rul estimation," in *2020 Prognostics and Health Management Conference (PHM-Besançon)*. IEEE, 2020, pp. 116–121.

[33] S. Zheng, K. Ristovski, A. Farahat, and C. Gupta, "Long short-term memory network for remaining useful life estimation," in *2017 IEEE international conference on prognostics and health management (ICPHM)*. IEEE, 2017, pp. 88–95.

[34] Y. Zhang, R. Xiong, H. He, and M. G. Pecht, "Long short-term memory recurrent neural network for remaining useful life prediction of lithium-ion batteries," *IEEE Transactions on Vehicular Technology*, vol. 67, no. 7, pp. 5695–5705, 2018.

[35] H. Yang, F. Zhao, G. Jiang, Z. Sun, and X. Mei, "A novel deep learning approach for machinery prognostics based on time windows," *Applied Sciences*, vol. 9, no. 22, p. 4813, 2019.

[36] B. Wang, Y. Lei, N. Li, and T. Yan, "Deep separable convolutional network for remaining useful life prediction of machinery," *Mechanical Systems and Signal Processing*, vol. 134, p. 106330, 2019.

[37] C. Zhao, X. Huang, Y. Li, and M. Yousaf Iqbal, "A double-channel hybrid deep neural network based on cnn and bilstm for remaining useful life prediction," *Sensors*, vol. 20, no. 24, p. 7109, 2020.

[38] J. Narwariya, P. Malhotra, V. TV, L. Vig, and G. Shroff, "Graph neural networks for leveraging industrial equipment structure: An application to remaining useful life estimation," *arXiv preprint arXiv:2006.16556*, 2020.

[39] Y. Jiang, Y. Lyu, Y. Wang, and P. Wan, "Fusion network combined with bidirectional lstm network and multiscale cnn for remaining useful life estimation," in *2020 12th International Conference on Advanced Computational Intelligence (ICACI)*. IEEE, 2020, pp. 620–627.

[40] I. Remadna, L. S. Terrissa, S. Ayad, and N. Zerhouni, "Rul estimation enhancement using hybrid deep learning methods," *International Journal of Prognostics and Health Management*, vol. 12, no. 1, 2021.

@

Abou bakr Belkaid
University
@

***Abstract*— Scheduling is one of the important topics conducted over the years in several studies. One part of the schedule is known as university timetables. The most universities are faced with this NP-hard problem. The timetabling process must be performed on a regular basis for every academic semester and is daunting and time consuming. The aim of this research was to create an integrated method for creating a timetable of university courses in our department using a multi-agent approach and genetic algorithms. This method allows faculty members and department heads to plan, monitor, screen, and edit all events related to their classes. The timetable is created collaboratively and cooperatively by three agents: Capture Agent, Processing Agent, and Distributing Agent. Several simulations were conducted to assess system performance by evaluating the human and material constraint satisfaction rate.**

Keywords*— Course timetable scheduling, Multi-agent, Intelligent agents, Genetic algorithms

-
-
-

A. Problem definition

-
-
-

B. Related works

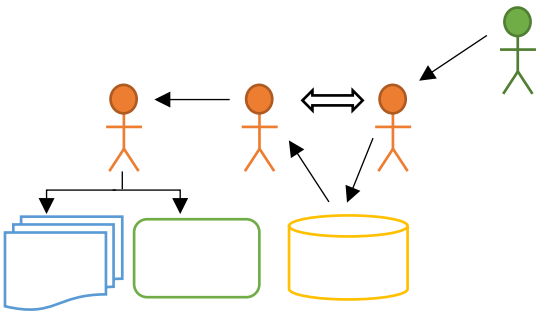

1) Capture Agent (CA)

2) Processing Agent (PA)

3) Distributing Agent (DA)

A. System Components

1) Head of Department Module

-
-
-
-
  -
  -

2) Faculty member Module

B. System Architecture

C. Timetable Development Process

1) Teachers allocation subprocess

a) Algorithm of CA:

2) Rooms and timeslots allocation subprocess

b) Algorithm of DA:

c) Algorithm of PA:

3) Timetable Development Algorithms

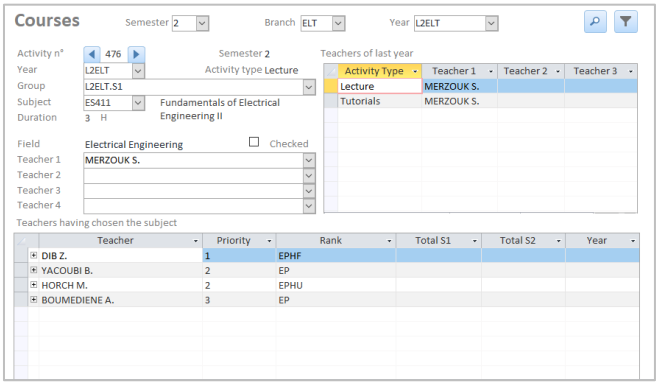

D. Examination Scheduling

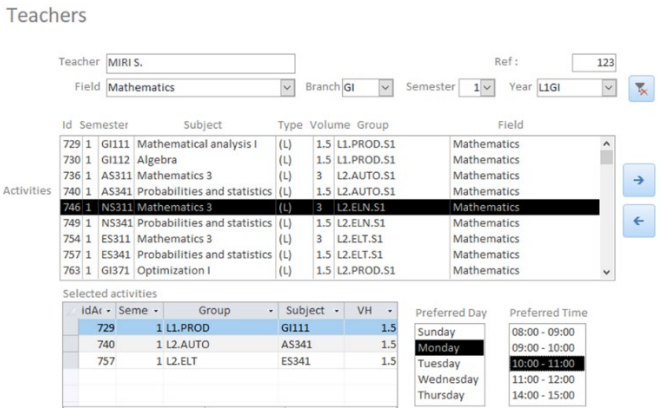

E. Tools and Technologies

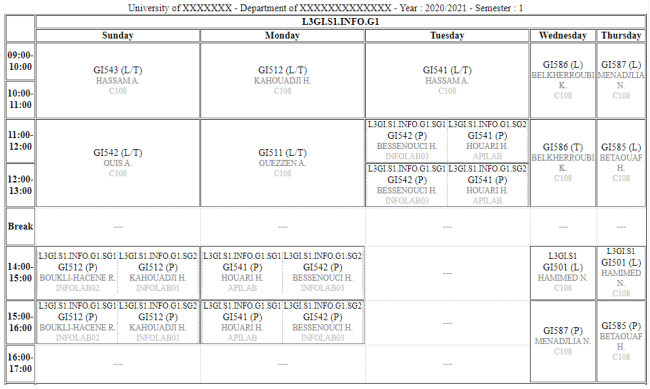

University of Tlemcen - Department of Electrical and Electronic Engineering - Year : 2020/2021 - Semester : 1

	KADDOURI N.				
	Sunday	**Monday**	**Tuesday**	**Wednesday**	**Thursday**
09:00-10:00	---	L2ELT.S1.ELT.G1 ES321 (L/T) B304	---	L2AUTO.S1.AUTO.G1 AS321 (L/T) B302	---
10:00-11:00	---		---		---
11:00-12:00	---	L2ELT.S1.ELT.G2 ES321 (L/T) B308	---	---	---
12:00-13:00	---		---	---	---
Break	---	---	---	---	---
14:00-15:00	---	---	---	L2AUTO.S1.AUTO.G1.SG1 AS343 (P) LFELN1	L2AUTO.S1.AUTO.G1.SG2 AS343 (P) LFELN1
15:00-16:00	---	---	---		
16:00-17:00	---	---	---	---	---

Characteristics	**Department size**		
	Small	***medium***	***Large***
	100	**97.53**	**96.05**

University of XXXXXXX - Department of XXXXXXXXXXXX - Year : 2020/2021 - Semester : 1

	APILAB				
	Sunday	**Monday**	**Tuesday**	**Wednesday**	**Thursday**
09:00-10:00	---	---	L3GI.S1.AUTO.G1.SG2 HOUARI H. GI541 (P)	---	---
10:00-11:00	---	---		---	---
11:00-12:00	---	---	L3GI.S1.INFO.G1.SG2 HOUARI H. GI541 (P)	---	---
12:00-13:00	---	---		---	---
Break	---	---	---	---	---
14:00-15:00	L3GI.S1.AUTO.G1.SG1 HOUARI H. GI541 (P)	L3GI.S1.INFO.G1.SG1 HOUARI H. GI541 (P)	---	---	---
15:00-16:00			---	---	---
16:00-17:00	---	---	---	---	---

Proceedings of the 5th International Conference on the Practice and Theory of Automated Timetabling (PATAT-2004)

International Conference on Intelligent Technologies and Applications

IEEE/ACS Internation Conference on Computer Systems and Applications (AICCSA)

International Workshop on Systems, Signal Processing and their Applications, WOSSPA

A new lightweight approach to mitigate the version number attack in RPL-based IoT networks

Mohammed BELKHEIR
LTTNS Laboratory, University Djilali Liabes, Sidi Bel Abbes, Algeria
LIMA Laboratory, Nour Bachir University Center. El-Bayadh, Algeria
belkheir_m@yahoo.fr

Mehdi ROUISSAT
Department of Electronics
Nour Bachir University Center. El-Bayadh,
STIC Laboratory, University Aboubek Belkaid, Tlemcen, Algeria.
Mehdi.m.rouissat@gmail.com

Hicham Sid Ahmed Belkhira
Department of Electronics
Nour Bachir University Center. El-Bayadh, Algeria
belkhira.hichem@gmail.com

Mohamed Achraf Boukhobza
Department of Electronics
Nour Bachir University Center. El-Bayadh, Algeria
bzaachraf@gmail.com

Mohamed Salim Abdoun
Department of Electronics
Nour Bachir University Center. El-Bayadh, Algeria
abdouns33@gmail.com

***Abstract*— In the recent few years, the cybersecurity challenge stood out to the research community with the drastic evolution of IoT networks. The present article deals with the version number attack, a major security concern for IoT networks using RPL as routing protocol. Although a number of techniques have been proposed to mitigate this kind of attack, the main challenge of the proposed technique remains to contemplate the limited capabilities of the embedded devices composing the network in terms of computing, storage and energy. This makes decentralized heavy algorithms and cryptographic solutions not suitable to cope with the inherited resources of nodes and the network core routing operations.**

The main purpose of our present work is to implement a new lightweight approach aiming to reduce the destructive effect of the version number attack, whereby the node takes into consideration only the version number received from its preferred parent and ignores other versions of its neighborhood. This leads to propagate the same version number value of the root node over the entire network and ensures the network integrity, by reducing the repeated global repair process caused by falsified values of the version number.

The proposed method is implemented under Contiki 3.0 operating system and simulations are performed using COOJA for different scenarios while changing the intruder node position in the network. The obtained results obviously depict that our proposed method yields better aftermath, where the energy saving is between 10% and 50%, depending on the intruder position, while the control overhead is between 2% and 50%.

Keywords*— *IoT, RPL, DODAG, Version number, DIO, COOJA

I. INTRODUCTION

Nowadays, the networking domain undergoes a massive evolution by implementing new trend of wireless networks able to receive, process and transmit data. Such a well-known network is The Internet of Things (IoT) [1], where the main purpose is to gather data from different environments and relay it to the internet for further computing and decisions. The market witnesses the wide spread of this technology in various domains of our lives like healthcare, energy industries, wearable technologies, automotive, military…etc [2]. An IoT network is essentially composed by small smart devices called sensors that are expected to collect data from a supervised environment. These sensors are connected to a sink playing the gateway role to the internet for a real-time supervision and process [3]. The network connectivity of an IoT in the lower layers is assured by implementing well-known technologies such as IPV6, 6LoWPAN, IEEE802.15.4 [4]. Despite the advantages brought by this trend of networks, many concerns remain in challenge such as the inter-connectivity, the topology changing and the security issues [5].

In this paper we are focusing on the security concern, whereas IoT networks witness a drastic scalability evolution from a closed network, to a decentralized wide area network composed by a millions of devices. Statistics held by [6] reveal that the number of the connected IoT devices is expected to outstrip the 50 billion in 2030. Likewise, the inter-connectivity poses an enormous security challenge against external threats, especially when the IoT is integrated to the new internet platforms as cloud computing or Big Data systems. However, the proposed secure mechanisms should take into consideration the network constraints, especially the limited computing, storage and energy characteristics of the IoT-enabled devices, even though they are based on Artificial Intelligence algorithms or cryptographic solutions [7].

The main purpose of our present work is to propose a lightweight technique for reducing the tampering effect of the version number attack in RPL-based IoT networks. Therefore, the rest of the paper is organized as follows: At first, in section (II) we give a brief description of the RPL routing protocol and its global repair mechanism based on the version number. After that, in section (III) we describe how an intruder node can perform a version number attack and its malicious effect by exhausting the network resources. In the section IV, we explain our proposed method and its outperformed action to lessen the version number attack affect, while simulating different scenarios of an IoT network. Finally, the conclusion resumes our work and highlights the efficiency of our proposed approach.

II. RPL AND THE DODAG VERSION NUMBER

A. RPL protocol description

RPL (Routing Protocol for Low Power and Lossy Networks) has been designed by IETF as routing protocol for constrained networks, named LLNs (Low power and Lossy Networks). RPL specification is defined by IETF in the RFC6550 [8]. The RPL is based on the IPV6 protocol, where the topology adopted is mesh/tree, forming thereby an acyclic graph named DODAG (Destination Oriented Directed Acyclic Graphs) built from the root which represents the data sink of the graph and plays the gateway role of the network. For the core routing operation and managing the DODAG, RPL defines four control messages: DIS, DIO, DAO and DAO-ACK messages [9], as depicted by figure 1.

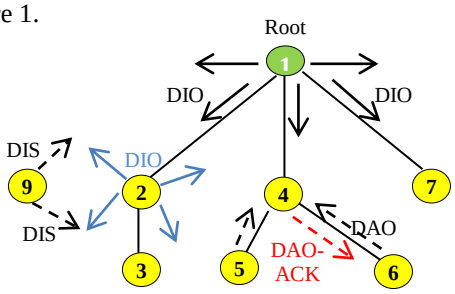

Fig.1. RPL Topology and control messages

The DIO message (DODAG Information Object) represents a reply to a DIS message (DODAG Information Solicitation) which is sent by a node to request DODAG information in order to join the network. The DIO message vehicles DODAG parameters as: DODAG ID, Version Number, Rank value and MOP (Mode of Operation) that allow each node to joining the DODAG. The latters are updated where a topology changing ensues, by using a trickle timer algorithm. The aim of the trickle timer is to ensure a fewer transmission of DIO messages to save nodes resources and reduce the control overhead. In addition, RPL implements an Objective Function (OF) that allow nodes performing upwards paths to the root and selecting their parents according to specific parameters [10].

The DODAG version number is an important parameter to establish a DODAG topology and maintain its integrity. This 8-bit integer value is initiated by the root node and broadcast via DIO messages (by default the version number value is 240) [11]. Once a topology change occurs, the root triggers a RPL mechanism called "global repair" by incrementing the current version number. Thus, receiving nodes compare the existing version number with their own, if the new value is higher; nodes should reset their trickle timer in order to recalculate their new willingness parameters (Rank) to rebuild the DODAG.

B. Version number attack

Since RPL has no mechanism to keep the root version number unchanged through the entire network [12], a malicious node can easily counterfeit the value and propagate it via its DIO messages to its neighborhood. Consequently, a receiving node initiates a *"local repair"* process by leaving its preferred parent and selecting a new parent among its parent list, based on the rank value. Then, the receiving node resets its trickle timer and broadcast this new version to their neighbors as well. Therefore, every node in the network should perform the same process aforesaid. Upon this new version received by the root, the latter triggers a "global repair" process, by incrementing the current version and broadcast it again via DIO messages to its neighborhood. This continually upsetting behavior is well-known as a "version number attack", and it causes a harmful volatility problem in the network. This unpredictable state affects the routing process by creating loops, making the established routes unavailable and forcing the unnecessary rebuilt of the DODAG. Thus, nodes should consume more their processing resources and generate an extra control traffic to rebuild their repositories which leads to exhausting their intrinsic resources.

C. The proposed DIO message process

At first, we should notice that RPL allows nodes to trust any version number received by DIO messages from their neighbors, even from their children. Therefore, our present work is focusing on guaranteeing that the same version number is disseminated downward to the entire network, in order to avoid loops and a subsequent global repair triggering.

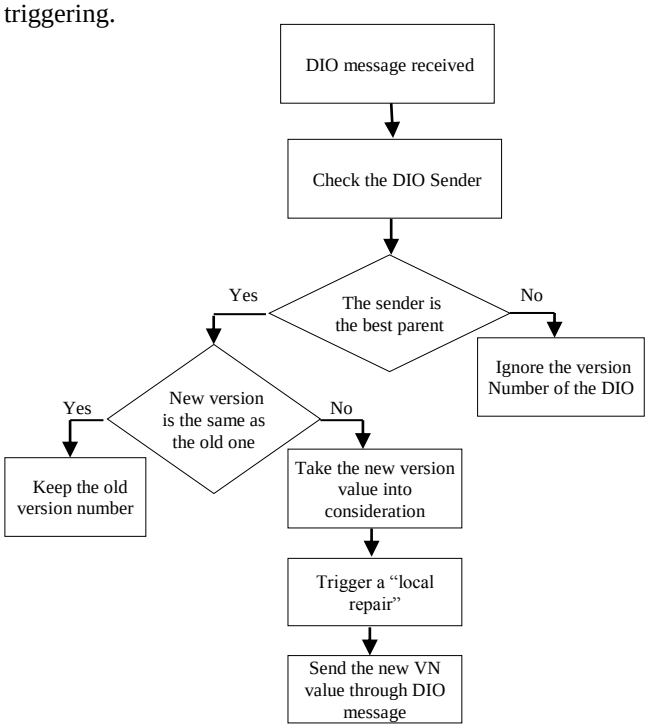

Fig.2. The proposed process of DIO message

Therefore, the node must take into consideration only the version number received from its best parent, and ignores any version number from its children set. The proposed DIO process is depicted by the figure 2, in which

we ensure the avoidance of the coexisting different version number values.

In the following section we illustrate how this process is implemented, and we analyze the positive effect of our approach for different scenarios of the version number attack.

III. SIMULATIONS AND ANALYSIS

Simulations are performed using COOJA under Contiki 3.0, operating system, a widely known OS for IoTs [13], whereas "Wireshark" tool is used to analyze the traffic over the network.

In all our performed simulations, we used Z1 motes[14], where characteristics are summarized in Table 1.

TABLE I. SIMULATION PARAMETERS

Parameter		Value
OS		Contiki 3.0
Traffic Analysis		Wireshark (1.7.2)
Power analysis		Powertrace
Z1 mote	µController	MSP430F2617 – 16 bits RISC
	CPU Frequency	16 MHz
	Transceiver	CC2420 (IEEE.802.15.4), 2.4 GHz
	RAM	8KB with 92KB (flash memory)
	Voltage	3V
	TX Current	17.4 mA
	RX Current	18.8 mA
	LPM Current	0.426 mA
RTimer		32768 ticks per second
Measurement interval		10 seconds
Simulation Time		10 Mn

A. *Reference Network*

At first, we build a reference network composed by 7 nodes and 1 sink as root.

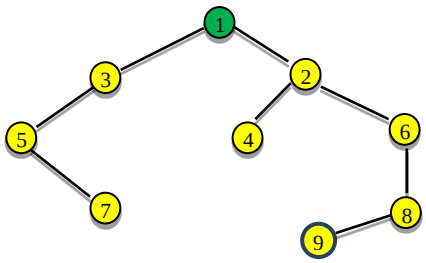

Fig.3 The reference network topology

After three minutes of simulation, the network has converged as illustrated by figure 3, where nodes 2 and 3 are directly connected to the sink (1). Node 2 connects node 4 and 6, and node 3 connects only node 5. Node 6 connects node 8 and the latter is a parent for the node 9. Nodes 4,7,9 are considered as leaves nodes. In this case, all the nodes are considered as legitimate and there is no harmful behavior.

by the following, simulations results of the reference network will be used as a benchmark to highlight the effect of the version number attack, and then the aftermath of our proposed approach.

B. *Version number attack effect*

The version number attack is implemented by adding a malicious behavior on node (Id 9), as illustrated by figure 4.

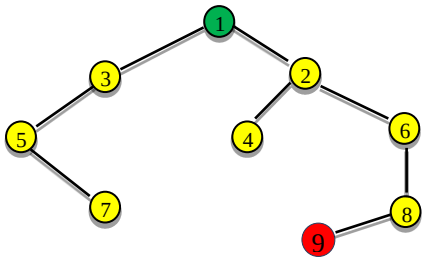

Fig.4 Version number attack with node 9 acting as malicious

To implement the attack in COOJA, the file containing the DIO processing *"Contiki 3.0_core_net_rpl_rpl-icmp.c"*, is modified as follows:

```
/* DAG Information Object */
pos = 0;
buffer = UIP_ICMP_PAYLOAD;
buffer[pos++] = instance->instance_id;
buffer[pos++] = dag->version++;
```

The last instruction shows that the malicious node continually increments its current version number and inserts it within its outgoing DIO message. Upon receiving this counterfeit version by the neighboring nodes, they reset their trickle timer and broadcast the new value as well. When the root detects this unauthorized increment, it directly triggers the global repair mechanism which produces an instable state of the network. In this upsetting case, simulations reveal that the network after 30 mn the convergence didn't converge compared to the normal case where the DODAG is built just after 3 mn of simulation. This explains the hurtful effect of the malicious node leading the network to an instable state.

C. *Network lifetime analyzis*

In order to evaluate the network lifetime, we calculate the consumed energy by means of a tool named "Powertrace" under COOJA. Powertrace collects data power based on number of ticks, and the formula (1) allows calculating the residual energy by node [15]:

$$Energy\ (mj) = \frac{Energest_{Value} \cdot Current \cdot Voltage}{RTIMER_{Second}} \quad (1)$$

Where:

- $Energest_{Value}$: Difference between the number of ticks in two time intervals
- $Current$: Consumed current in each operating state of the node (in mA)
- $Voltage$: Consumed voltage by the node (in Volts)

- $RTIMER_{Second}$: Number of ticks per seconds (see Table 1)

Figure 5 illustrates the obtained results of the consumed energy by each node in the reference network after ten minutes of simulation

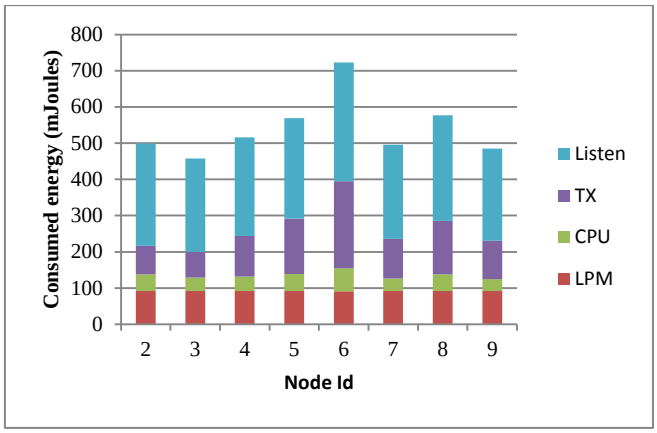

Fig.5 Energy consumed during 10 Mn of simulation in case of the reference network

As shown by figure 5, the residual energy depends on how long each mode the mode is operating [16]. The four usual modes are:

- LPM: low power mode or sleep mode
- CPU: processing Mode
- Radio Listen: includes the listening, the receiving, and the idle states
- Radio Transmit: refers to the TX mode

Figure 6 depicts a comparison between the total energy consumed by each node in the case of the attack with respect to the reference network.

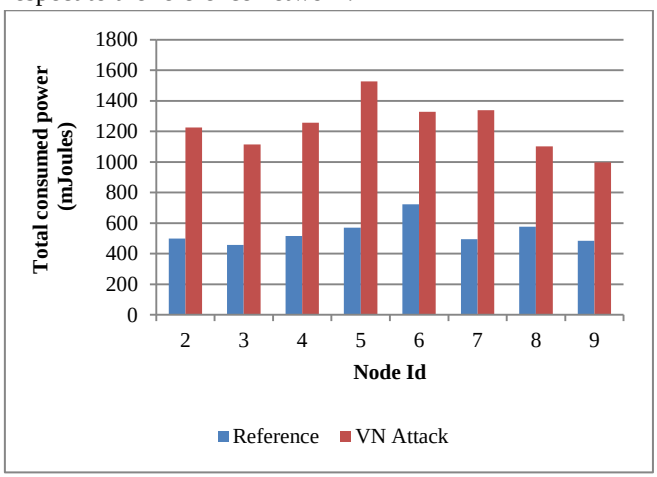

Fig.6 Energy consumption comparison (Reference network Vs Attack case)

It can be noticed that the energy consumed in the reference network case is between [485 mJ, 722mJ], while in the case of attack the interval is [998 mJ, 1526mJ]. Thus, the surge of the energy consumption between the two cases is about 227%, which is very important. This is mainly caused by the nodes activity which increased in the case of the version number attack, where the behavior of the intruder node forces nodes to send more control packets in order to accomplish the network convergence and to maintain the topology consistency. Nodes exchange unnecessary traffic to perform their repositories among their neighborhood which increases the sending, receiving and forwarding tasks of a node.

In addition, the energy gap between nodes in the case of the attack is about 528 mJ with respect to the reference network where the gap is about 237 mJ. This important gap may induce the extinction of some active nodes so earlier than others and leads to create holes in the network, even if the dead node is gaining a good position in the DODAG. Thus, the version number attack has an intrinsic effect by exhausting nodes resources, and an extrinsic effect related to the core networking activity by disrupting established routes and creating holes in the network.

D. Control overhead analyzis

The control overhead is an essential parameter to analyze the effect of the version number attack. It refers to the number of control packets broadcast over the entire network to establish and maintain the topology. The higher the control overhead is for a given network, the lower is its efficiency leading to exhausting the nodes resources. The control overhead is calculated using the following formula:

$$Control\ Overhead\ = \sum_1^n DIS + \sum_1^n DIO + \sum_1^n DAO \qquad (2)$$

Where n is the number of nodes in the network.

After ten minutes of simulations, the control overhead results are shown by the figure 5.

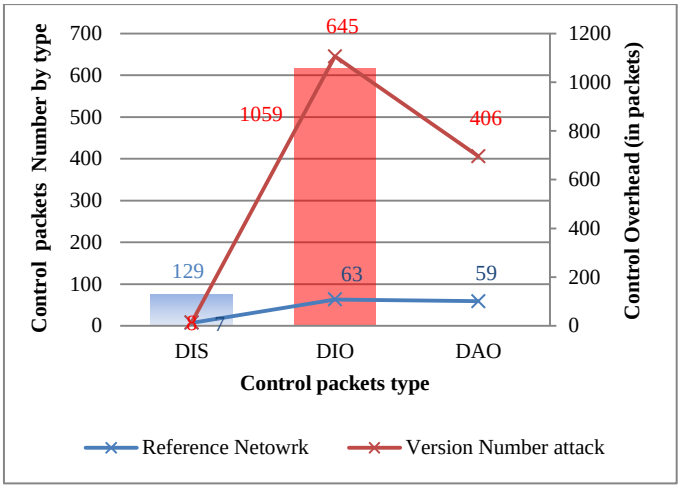

Fig.7 Control overhead comparison between the reference network and the network under attack

We notice that the control overhead in the case of the attack is 1059 packets, with the respect of the reference network where it is 129 packets; therefore it has increased 8 times more. Moreover, there are more DIO messages exchanged than other control messages, which explains the harmful behavior of the malicious node (Id 9), where it continually increments the version number and broadcast it to its neighborhood. Thus, every node receiving the new

value resets its trickle timer and broadcast the new version via DIO messages, which explain the increase of the control overhead.

E. Implementation of the proposed approach

In order to implement our new process illustrated by figure 2, the file *"Contiki 3.0_core_net_rpl_rpl-icmp.c"* is updated by adding the following code:

```
possible_version = buffer[i++];  // A temporary variable
....
instance = rpl_get_instance(dio.instance_id);
dag = instance->current_dag;
if(uip_ipaddr_cmp(&from , rpl_get_parent_ipaddr
(instance->current_dag->preferred_parent)) )
// if the DIO is received from the parent so do as follows
  {
  dio.version = possible_version;          // take the VN
  }
  else  {
  dio.version = dag->version ; // Don't take the VN
  }
...
```

Consequently, that the node performing the DIO process is taking into consideration the version number received only from its parent and ignoring other coming version number from its neighborhood.

To demonstrate the efficiency of the new proposed DIO processing, we consider 3 scenarios (figure 6), while changing the malicious node ranking in the DODAG. In the first scenario the intruder acts as a leaf node and it is connected to node 8. However, in the 2nd scenario the intruder has a good position where it is a parent of 1 node (node 8), then it is placed to be a neighbor of the root in the 3rd scenario.

In what follows we analyze the energy consumed and the control overhead by keeping the same simulation parameters, in order to better highlight the aftermath of our proposed approach.

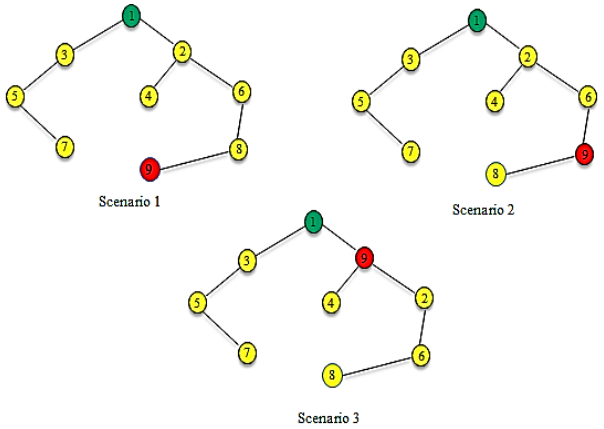

Fig.6 The three analyzed scenarios for our proposed approach

The energy computation result is shown by figure 7 for the three simulated scenarios.

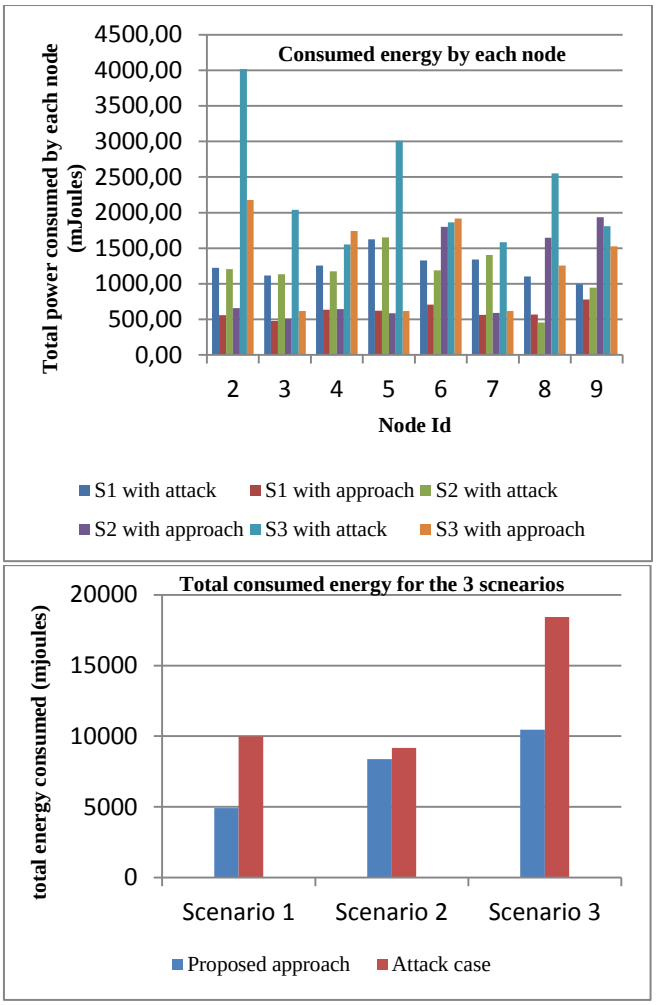

Fig.7 Energy consumption analysis for the three scenarios

It's obviously illustrated by the two plots of the figure 7 that the total energy consumed is much higher in case of the attack, and it decreases where we implement our method. This saving is about 50% for scenarios 1&3, and 10% for scenario 2. In addition, in the case of our approach, the increase in the total energy is regular, which confirms that the new process performs a deterministic behavior in the network, compared to the version number attack case. This deterministic behavior leads to avoid holes and preserve the network lifetime. Therefore, our proposed method acts better for each simulated scenario and is more efficient to mitigate the damage caused by the attacker node.

Let's see how our proposed approach is carrying out in terms of the control overhead for the three simulated scenarios. The figure 8 shows the control overhead evolution in the case of the attack (red color) and after implementing our method (blue color). We can observe that the control overhead increases in the two cases, starting from scenario 1 to scenario 3.

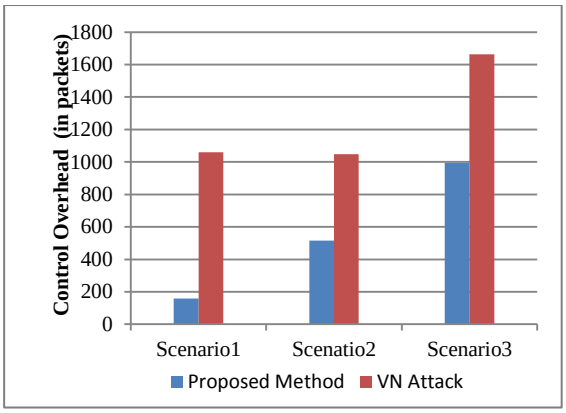

Fig.8 The Control overhead analysis for the three simulated scenarios

This depends on the intruder rank in the DODAG, where it was a simple leaf node in scenario 1 to having a good position being the root's neighbor. In the scenario 1, the harmful action of the attacker (Node 9) is directly eliminated by its parent (Node 8), according to our proposed method. Thus, it ignores the falsified version number being carried out by the intruder DIO messages. However, for scenarios 2 and 3, where the intruder is placed in a good position as a parent for other nodes (node 8 for scenario 2 and nodes 2,4,6,8 for scenario 3), it disseminates the falsified version number to its children and forces them to continually resetting their trickle timer to broadcast the falsified version number. Thus, the control overhead increases as long as the malicious node climbs the DODAG.

Simulation results depicts that the average value of the decrease is about 700 messages, which explains the important efficiency brought by our method. Based on the percentage difference analysis, the efficiency of our approach is about 148% for the scenario 1, 68% for scenario 2 and 50% for scenario 3. So, our approach acts better especially for the scenario 1 where the intruder is acting as a simple leaf node. The difference of the control packets for this scenario is about 900 messages. This is mainly due to our approach, where the parent ignores the falsified version number coming from the intruder child.

IV. Conclusion and Future Work

In this paper, by modifying the DIO processing of a node, we proposed and presented a new lightweight approach for mitigating the version number attack in an IoT network. The aim of our method is to allow the version number propagating downward the DODAG, where the node takes into consideration only the version number received from its preferred parent and ignores any other version from its neighborhood.

Simulations have been conducted for different scenarios, while changing the intruder node position in the network, where the obtained results obviously depict the aftermath of our proposed method in terms of the network lifetime and the control overhead. The energy saving is between 10% and 50%, depending on the malicious node position, while the control overhead is between 2% and 50%. These results demonstrate that our proposed method acts better to mitigate the harmful effect of the version number attack in a RPL-based IoT network.

As a future work, we expect to enhance the accurate action of our proposed process by delaying the reset of the trickle timer to allowing each node to gather a set of version number values in order to select the trusted one from its neighborhood.

References

[1] S. Rachit, Bhatt and P.R Ragiri, “Security trends in Internet of Things: a survey”. SN Appl. Sci, Vol3, 121, Jan. 2021. https://doi.org/10.1007/s42452-021-04156-9

[2] V. Hassija, V. Chamola, V. Saxena, D. Jain, P. Goyal and B. Sikdar, "A survey on IoT security: Application areas, security threats, and solution architectures," in IEEE Access, vol. 7, pp. 82721-82743, 2019, doi: 10.1109/ACCESS.2019.2924045.

[3] F. Al-Turjman, “Artificial Intelligence in IoT”. Transactions on computer intelligence and computational Intelligence. 2019. Springer.

[4] M. A. Boudouaia, A. Ali-Pacha, A. Abouaissa and P. Lorenz, "Security Against Rank Attack in RPL Protocol," in IEEE Network, vol. 34, no. 4, pp. 133-139, August 2020.
doi: 10.1109/MNET.011.1900651.

[5] H. Touqeer, S. Zaman, R. Amin, H. Mudassar, F. Al-Turjman and M. Bilal, “Smart home security: challenges, issues and solutions at different IoT layers”. J Supercomput. May 2021. https://doi.org/10.1007/s11227-021-03825-1

[6] https ://www.statista.com/statistics /47126 4/iot-number-ofconnected-devices-world wide/. (Accessed July 2021)

[7] M. Kuzlu, C. Fair and O.Guler, “Role of Artificial Intelligence in the Internet of Things (IoT) cybersecurity. Discover Internet of Things, 1, 7. Februay 2021. https://doi.org/10.1007/s43926-020-00001-4

[8] T. Winter, P. Thubert, A. Brandt, J. Hui, R. Kelsey, P. Levis, K. Pister, R. Struik, J.P. Vasseur, R. Alexander, “RFC 6550: RPL IPv6 routing protocol for low-power and lossy networks”. https://tools.ietf.org/html/rfc6550, 2012. Accessed 2 April 2021.

[9] S.W. Min, SH. Chung, H.J. Lee and Y.V. Ha, “Downward traffic retransmission mechanism for improving reliability in RPL environment supporting mobility”. International Journal of Distributed Sensor Networks. vol 16, issue 1, Februay 2020. https://doi.org/10.1177/1550147720903605

[10] A. Lamaazi and N. Benamar, “A comprehensive survey on enhancements and limitations of the RPL protocol: A focus on the objective function”. Ad Hoc Networks, Vol 96, January 2020. https://doi.org/10.1016/j.adhoc.2019.102001

[11] Z. Almusaylim, N. Jhanjhi, and A. Alhumam, “Detection and mitigation of RPL rank and version number attacks in the Internet of Things: SRPL-RP”. Sensors. Vol 21: 5997, October 2020. https://doi.org/10.3390/s20215997

[12] S, Bhatt and PR Ragiri, “Security trends in Internet of Things: a survey”. SN Applied Sciences, vol 3 (121). Janaury 2021. https://doi.org/10.1007/s42452-021-04156-9

[13] S. Mittal, SK. Nagdeo and J. Mahapatro, "Performance Study of IoT enabled Wireless Body Area Network in Contiki Platform”. IEEE Global Conference for Advancement in Technology (GCAT), pp. 1-5, October 2019. doi: 10.1109/GCAT47503.2019.8978467

[14] Z1 datasheet. www.zolertia.com. (Accessed April 2021)

[15] S. Cakir, S. Toklu and N. Yalcin, "RPL Attack Detection and Prevention in the Internet of Things Networks Using a GRU Based Deep Learning". IEEE Access, vol. 8, pp. 183678-183689, 2020, doi: 10.1109/ACCESS.2020.3029191

[16] N.N. Hadaya and S.A. Alabady, “ Improved RPL protocol for Low-Power and Lossy Network for IoT environment”. SN Computer Science., vol 2 (341), June 2021. https://doi.org/10.1007/s42979-021-00742-1

Control and system

Simple Criterions to Achieve Hybrid Dislocated Synchronization of Two Identical Chua's Circuits

Badreddine Zemmal [$1] ,Saida Mellal[#&2], Issam Hamma[^3] , Marwa Maizi[$4] , Toufik Ziar[#$*], Hichem Farah[#$6] and Adel Ouannas [@7].

[$] *Sciences of matter Department, S.S.N.V Faculty, Larbi Tebessi University of Tébessa, 12000, Algeria.*
[&]*Sciences of matter Department, S.T Faculty, Abbas Laghrour University of Khenchela,40000, Algeria.*
[#] *Materials & active devices laboratory LCAM, Larbi Ben M'hidi University of Oum El Bouaghi, Algeria.*
[^] *Sciences of matter department, Akli Mohand Oulhad university of Bouira, 10000, Algeria.*
[@]*Department of Mathematics and Computer Science, Larbi Ben M'hidi University of Oum El Bouaghi, Algeria.*

*corresponding author: Email: toufik.ziar@univ-tebessa.dz

[1]zemmal2@yahoo.fr,[2]mellalsaida95@gmail.com, [3]isshamdoct096@gmail.com, [4]marwamaizi252016@gmail.com, [6]farhichem@gmail.com, [7]ouannas_adel@yahoo.fr

Abstract—**This paper presents simple criterions to achieve synchronization scheme between two chaotic systems combining tow classical synchronizations i.e the hybrid synchronization (HS) and the dislocated synchronization(DS) , the novelty of the proposed scheme named hybrid dislocated synchronization (HDS synchronization for short) is that it is much more simple to perform. Two mathematical theorems present the necessary and sufficient conditions under which (HDS) synchronization can be achieved. To show the effectiveness of our approach, numerical example of the (HDS) synchronization of two identical Chua's circuits is executed**.

Keywords— **Chua circuit, synchronization, chaos, Lyapunov stability, simple criterion**.

I. INTRODUCTION

The concept of synchronization of chaotic systems was presented to the scientific community first by Yamada and Fujisaka [1] followed by the work of Pecora and Carroll [2],[3] . Synchronization chaos is a way to explain the sensitive dependence on initial conditions [4]-[6]. It was established that the synchronization of two or more chaotic systems shows the tendency of these systems coupled together to closely follow the same trajectory. The output of the slave system is asymptotically the output of the master system i.e. the output of the master system controls the output of the slave system.

Synchronization of chaotic systems was generalized by the discovery of several types such as generalized synchronization [7],[8], phase synchronization [9], projective synchronization [10], generalized projective synchronization [11]-[14] and anti-synchronization [15],[16]. When synchronization and anti synchronization coexist at the same time, in chaotic systems, the synchronization is called hybrid synchronization [17]-[20]. Several schemes to ensure the control and synchronization of chaotic systems were demonstrated on the basis of their potential applications in areas such as design chaos generators, secure communication [21]-[23]. So far, a variety of impressive approaches have been proposed for the synchronization of chaotic systems as the method of OGY [24] , sampled feedback synchronization method [25], the method of time delay feedback [26], adaptive design method [27], the sliding mode control method [28], the active control method [29] and back-stepping control design [30]. The paper is organized as follows. In Section 2, a presentation of general form of the dynamical chaotic systems used followed by some useful definitions relevant to classical synchronization and the detailed theoretical study of the presented synchronization scheme. In Section 3, after a brief presentation of Chua's circuit and a reinvestigation of its sensibility to the initial conditions changes as a chaotic circuit, a numerical application of the proposed scheme of two identical chaotic Chua's circuits is executed. In Section 4, conclusion concludes the paper.

II. MAIN RESULTS

A. Systems Presentation

In this section we present the synchronization scheme named hybrid dislocated synchronization involving two types of synchronization: the hybrid synchronization and the dislocated synchronization. We use a general form of 3D autonomous continuous dynamical chaotic system which can be applied to present a wide class of well-known chaotic systems.
Consider two 3D autonomous continuous dynamical chaotic systems (1) and (2) as master system and slave system respectively.

$$\begin{cases} \dot{x}_1 = a_{11}x_1 + a_{12}x_2 + a_{13}x_3 + d_1 \\ \dot{x}_2 = a_{21}x_1 + a_{22}x_2 + a_{23}x_3 + d_2 \\ \dot{x}_3 = a_{31}x_1 + a_{32}x_2 + a_{33}x_3 + d_3 \end{cases} \quad (1)$$

$$\begin{cases} \dot{y}_1 = a_{11}y_1 + a_{12}y_2 + a_{13}y_3 + \acute{d}_1 + u_1 \\ \dot{y}_2 = a_{21}y_1 + a_{22}y_2 + a_{23}y_3 + \acute{d}_2 + u_2 \\ \dot{y}_3 = a_{31}y_1 + a_{32}y_2 + a_{33}y_3 + \acute{d}_3 + u_3 \end{cases} \quad (2)$$

where $(x_1,x_2,x_3)^T$ and $(y_1,y_2,y_3)^T$ are the states of the master system and the slave system, respectively, $a_{ij} \in \mathbb{R}^{3\times3}$ are constants determined by the linear part of the autonomous continuous dynamical chaotic systems , $(d_i)_{1\leq i\leq 3}$, $(\acute{d}_i)_{1\leq i\leq 3}$ are non linear functions and u_i; i= 1; 2; 3; are synchronization controllers to be determined.

B. Hybrid Synchronization (synchronization and anti synchronization):

The error system of hybrid synchronization is defined as follows

$$e_{hi} = x_i \pm y_i \ ; \ i = 1,2,3 \quad (3)$$

One can see in (3) that there are several configurations in our study we take only one configuration the following

$$\begin{cases} e_{h1} = x_1 - y_1 \\ e_{h2} = x_2 + y_2 \\ e_{h3} = x_3 - y_3 \end{cases} \quad (4)$$

To estimate the control functions, we can easily subtract (2) to (1).

C. Dislocated Synchronization:

The error system of dislocated synchronization is defined as follows

$$e_{di} = x_i \pm y_j, i = 1,2,3; j = 1,2,3 \quad (5)$$

With at least one configuration $i \neq j$.

In (5) there are several configurations in our study we take only the following configuration

$$\begin{cases} e_{d1} = x_1 - y_3 \\ e_{d2} = x_2 - y_2 \\ e_{d3} = x_3 - y_1 \end{cases} \quad (6)$$

D. Hybrid Dislocated Synchronization (HDS)

The errors system of the hybrid dislocated synchronization (HDS) is defined as follows

$$\begin{cases} e_1 = x_1 - y_3 \\ e_2 = x_2 + y_2 \\ e_3 = x_3 - y_1 \end{cases} \quad (7)$$

In order to define the threshold for chaos synchronization, one needs to define controllers u_i; i =1; 2; 3; which stabilize the synchronization errors (7), then the aim of synchronization is to make $\lim_{n\to\infty}\|e_i(t)\| = 0 \ \ i = 1;2;3$ where $\|.\|$ is Euclidean norm.
The error system (7) between the master system (1) and the slave system (2), can be derived to obtain error dynamical as

$$\begin{cases} \dot{e}_1 = a_{11}x_1 + a_{12}x_2 + a_{13}x_3 + d_1 - a_{31}y_1 - a_{32}y_2 - a_{33}y_3 - \acute{d}_3 - u_2 \\ \dot{e}_2 = a_{21}x_1 + a_{22}x_2 + a_{23}x_3 + d_2 + a_{21}y_1 + a_{22}y_2 + a_{23}y_3 + \acute{d}_2 + u_2 \\ \dot{e}_3 = a_{31}x_1 + a_{32}x_2 + a_{33}x_3 + d_3 - a_{11}y_1 - a_{12}y_2 - a_{13}y_3 - \acute{d}_1 - u_3 \end{cases} \quad (8)$$

The error dynamical system (8) can be written as

$$\begin{cases} \dot{e}_1 = a_{11}e_1 + a_{12}e_2 + a_{13}e_3 + Q_1 - u_3 \\ \dot{e}_2 = a_{21}e_1 + a_{22}e_2 + a_{23}e_3 + Q_2 + u_2 \\ \dot{e}_3 = a_{31}e_1 + a_{32}e_2 + a_{33}e_3 + Q_3 - u_1 \end{cases} \quad (9)$$

With

$$\begin{cases} Q_1 = (a_{13} - a_{31})y_1 - (a_{12} - a_{32})y_2 + (a_{11} - a_{33})y_3 + d_1 - \acute{d}_3 \\ Q_2 = (a_{21} + a_{23})(y_1 + y_3) + d_2 + \acute{d}_2 \\ Q_3 = (a_{33} - a_{11})y_1 - (a_{32} + a_{12})y_2 + (a_{31} - a_{13})y_3 + d_3 - \acute{d}_1 \end{cases} \quad (10)$$

Theorem 1 The master system (1) and the slave system (2) are globally hybrid dislocated synchronized under the following controllers

$$\begin{cases} u_1 = Q_3 + a_{31}e_1 + a_{32}e_2 + (a_{33} + \|a_{33}\|)e_3 \\ u_2 = -Q_2 - a_{21}e_1 - (a_{22} + \|a_{22}\|)e_2 - a_{13}e_3 \\ u_3 = Q_1 + (a_{11} + \|a_{11}\|)e_1 + a_{12}e_2 + a_{13}e_3 \end{cases} \quad (11)$$

Proof 1 the error dynamical system can be described as

$$\begin{cases} \dot{e}_1 = -\|a_{11}\|e_1 \\ \dot{e}_2 = -\|a_{22}\|e_2 \\ \dot{e}_3 = -\|a_{33}\|e_3 \end{cases} \quad (12)$$

We construct the candidate Lyapunov function in the form

$$V(e(t)) = \frac{1}{2}\sum_{i=1}^{3} e_i^2(t) \quad (13)$$

We obtain

$$\dot{V}(e(t)) = -\|a_{11}\|e_1^2 - \|a_{22}\|e_2^2 - \|a_{33}\|e_3^2 \leq 0$$

Thus, from the Lyapunov stability theory that is the zero solution of the errors system (7) is globally asymptotically

stable and therefore, systems (1) and (2) are globally dislocated hybrid synchronized. That completes the proof of theorem 1.

Theorem 2 There exist a suitable control matrix L ∈ $\mathbb{R}^{3\times3}$ to realize the dislocated hybrid synchronization between the master system (1) and the slave system (2).

Proof 2 The error dynamical system can be written in the compact form as

$$\dot{e}(t) = Ae(t) + \mathrm{Q} + U \tag{14}$$

Where

e (t) = $(e_1(t),e_2(t),e_3(t))^T$; $A = (a_{ij})_{3\times3}$; Q = (Q_1;Q_2;Q_3) et U = (-u_3; u_2;-u_1)

Let the vector controller be

$$U = -Le(t) - \mathrm{Q} \tag{15}$$

where L is the control matrix.

The error dynamics becomes

$$\dot{e}(t) = (A - L)e(t) \tag{16}$$

Construct the Lyapunov function candidate in the following form

With $V(e\,(t)) = e^{\mathrm{T}}(t)\,e(t)$

We obtain

$$\dot{V}(t) = \dot{e}^T(t)e(t) + e^T(t)\dot{e}(t)$$

$$\dot{V}(t) = e^T(t)(A-L)^T e(t) + e^T(t)(A-L)e(t)$$

$$\dot{V}(t) = e^T(t)[(A-L)^T + (A-L)]e(t)$$

If the control matrix L is chosen such that $(A - L)T + (A - L)$ is negative definite matrix, then we get $\dot{V}(t) < 0$. Thus, from the Lyapunov stability theory, that is the zero solution of the error system (7) is globally asymptotically stable and therefore, systems (1) and (2) are globally dislocated hybrid synchronized.

III. Numerical examples

A. *Chua Circuit Presentation*

In this section we present Chua's circuit as introduced by [31]. The famous chaotic circuit consists of two linear capacitors C_1 and C_2, a linear inductor L, two linear resistors R and R_0, and a piecewise-linear negative resistor called Chua's diode. Chua's circuit is described by the following dynamical state system:

$$\begin{cases} C_1\frac{dv_1}{dt} = G(v_2 - v_1) - Gg(v_1) \\ C_2\frac{dv_2}{dt} = G(v_1 - v_2) + i_3 \\ L\frac{di_L}{dt} = -v_2 - R_0 i_3 \end{cases} \tag{17}$$

where v_1, $v_2$and i_L are voltage across C_1, voltage across C_2 and current through L respectively with $G = 1/R$

and

$$g(v_1) = -G_b v_1 - \frac{1}{2}(G_a - G_b)\{|v_1 + E| - |v_2 - E|\}. \tag{18}$$

$g(v_1)$ is the voltage-current characteristic of the non linear resistor (Chua diode),E is the breakpoint voltage of the Chua's diode and G_a , G_b are slops in the inner and outer regions of the voltage-current characteristic as shown in fig.1(b) with corresponding circuit shown in Fig.1(a).

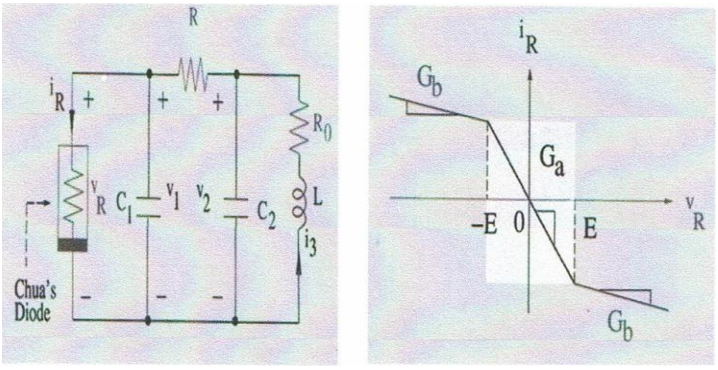

(a) ***(b)***

Fig.1 (a) Chua's circuit , (b) voltage-current characteristic of Chua's diode.

Let

$$\begin{cases} x_1 = v_1 \\ x_2 = v_2 \\ x_3 = i_3 \end{cases} \tag{19}$$

After simple transformations and by taking $R_0 = 0$ and $E = 1$, the system (17) can be written in its compact form as,

$$\begin{cases} \dot{x_1} = \alpha(x_2 - x_1 - g(x_1)) \\ \dot{x_2} = x_1 - x_2 + x_3 \\ \dot{x_3} = -\beta x_2 \end{cases} \tag{20}$$

with $g(x_1) = -G_b x_1 - \frac{1}{2}(G_a - G_b)(|x_1 + 1| - |x_1 - 1|)$

In spite of its extreme sensitivity to initial conditions, Chua's system (20) exhibits chaotic behavior when the parameters are

selected as α= 9,β=100/7, G_a =8/7 , G_b=5/7 and with initial conditions given by *($x_1(0);x_2(0);x_3(0)$)=(-1.6; 1; 1.6).*
The simulation results are shown in Fig.2 which displays the chaotic attractors of the Chua circuit.

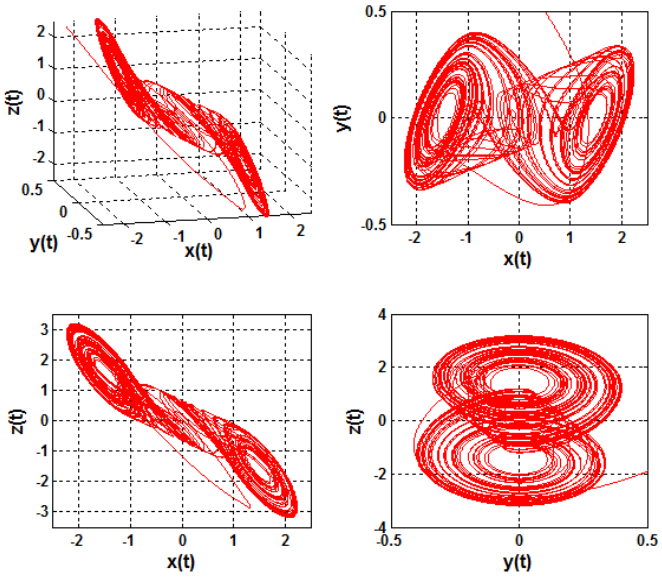

Fig.2 Chua chaotic attractors : (a) 3D attractor; (b)(c) and (d) 2D attractors with initial conditions ($x_1(0);x_2(0);x_3(0)$)=(-1.6; 1; 1.6).

To apply the hybrid dislocated synchronization (HDS) of two identical chaotic Chua systems, the master system is presented by system (20) and the slave system is taken as

$$\begin{cases} \dot{y}_1 = \alpha(y_2 - y_1 - g(y_1)) + u_1 \\ \dot{y}_2 = y_1 - y_2 - y_3 + u_2 \\ \dot{y}_3 = -\beta x_2 + u_3 \end{cases} \quad (21)$$

where $(u_1, u_2, u_3)^T$ is the vector controller.

B. Sensitivity to initial conditions (ICs) changes in Chua circuit.

To show the sensitivity to the changes in initial conditions (ICs) for Chua's chaotic system, we have plotted trajectories, shown in fig.4, of the master system (20) and the slave system (21) without controllers with the same initial conditions and with minimal changes. We have chosen four cases:

- $x_1(0);x_2(0);x_3(0)$= ($y_1(0);y_2(0);y_3(0)$)= (-1; 1; 1)
- $x_1(0);x_2(0);x_3(0)$= (-1; 1; 1) *and* ($y_1(0);y_2(0);y_3(0)$)= (-1.001; 1.001; 1.001)
- $x_1(0);x_2(0);x_3(0)$= (-1; 1; 1) *and* ($y_1(0);y_2(0);y_3(0)$)= (-1.01; 1.01; 1.01)
- $x_1(0);x_2(0);x_3(0)$= (-1; 1; 1) *and* ($y_1(0);y_2(0);y_3(0)$)= (-1.1; 1.1; 1.1).

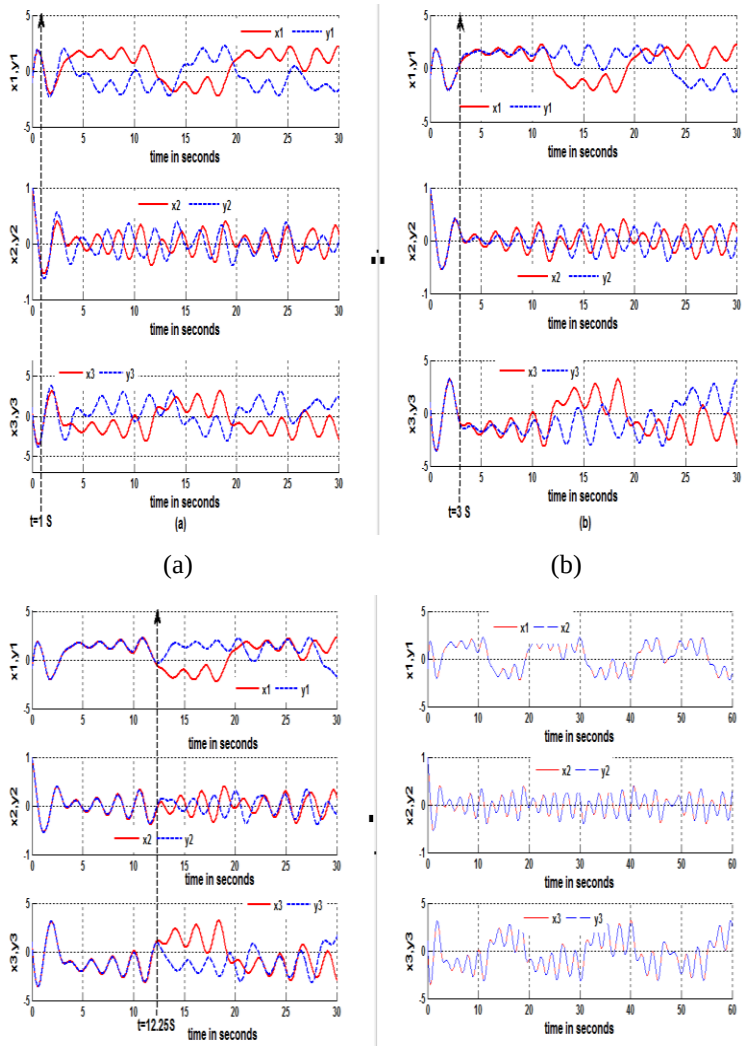

Fig.3 Temporal evolutions of master system and slave system trajectories without controllers with initial conditions as follow:
(a) *$x_1(0);x_2(0);x_3(0)$= (-1; 1; 1) and ($y_1(0);y_2(0);y_3(0)$)= (-1.1; 1.1; 1.1).*
(b) *$x_1(0);x_2(0);x_3(0)$= (-1; 1; 1) and ($y_1(0);y_2(0);y_3(0)$)= (-1.01; 1.01; 1.01).*
(c) *$x_1(0);x_2(0);x_3(0)$= (-1; 1; 1) and ($y_1(0);y_2(0);y_3(0)$)= (-1.001; 1.001; 1.001).*
(d) *$x_1(0);x_2(0);x_3(0)$= (-1; 1; 1) and ($y_1(0);y_2(0);y_3(0)$)= (-1; 1; 1).*

In fig.3, we notice that a minimal changes in the initial conditions leads to large divergences between the same trajectories. The TABLE I recapitulates the results of the simulation concerning the sensitivity to changes in the initial conditions.

TABLE I

Sensitivity to changes in Initial conditions for Chua's System

Rate of change in ICs	Time delay before the first divergence of trajectories (in seconds)
10 %	1
1 %	3
0. 1%	12.5
0	∞

In TABLE I, one can see that the decrease of the rate of change in the initial conditions leads to an increase in the time delay before the first divergence of trajectories.

C. The Hybrid Dislocated Synchronization (HDS) of Two Identical Chua's Systems

In fig.4 and fig.5 and with the help of MATLAB, we get the numerical results showing the temporal evolution of master system and slave system trajectories before and after adding controllers respectively. One can see, clearly, the hybrid dislocated synchronized trajectories of the master system (20) and the slave systems (21) displayed in fig.5.

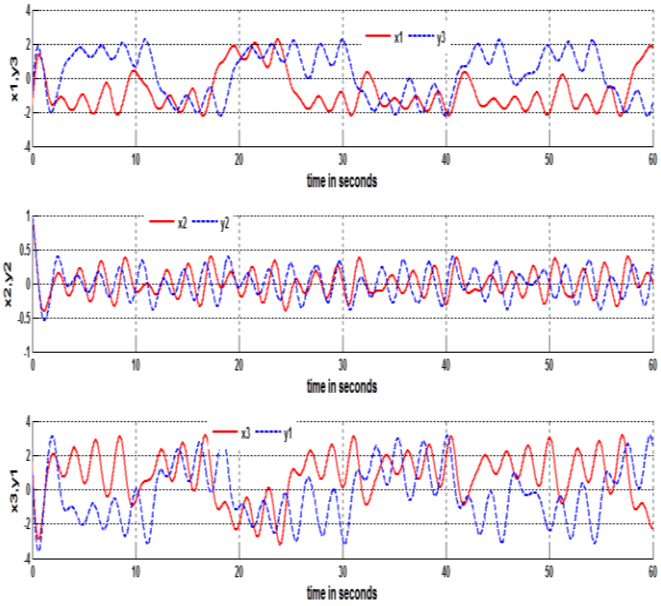

Fig.4 Temporal evolutions of master system and slave system trajectories without controllers

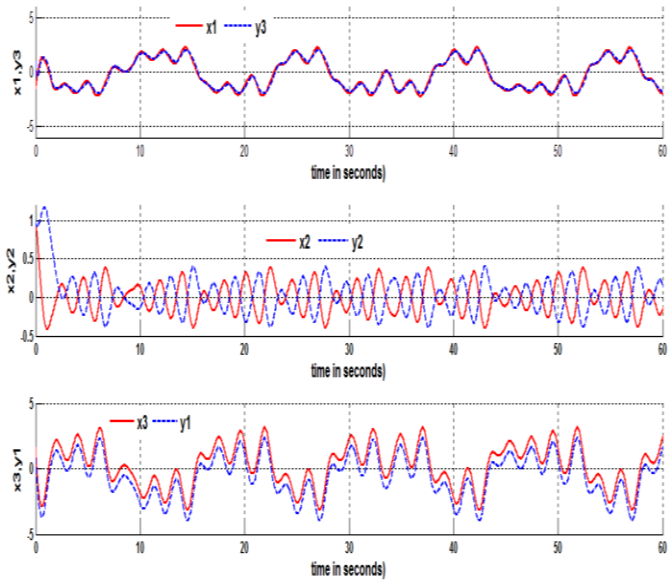

Fig.5 Temporal evolutions of master system and slave system trajectories after adding controllers

The synchronization errors between the master system and the slave system are defined for hybrid dislocated synchronization as in system (7) and according to our approach in Theorem 02, one can choose the matrix A as

$$A = \begin{pmatrix} -\alpha & \alpha & 0 \\ 1 & -1 & 1 \\ 0 & -\beta & 0 \end{pmatrix} \tag{22}$$

and the control matrix L is selected as

$$L = \begin{pmatrix} 0 & \alpha & 0 \\ 1 & 0 & 1 \\ 0 & -\beta & 0 \end{pmatrix} \tag{23}$$

We can simply show that $(A-L)^T + (A-L)$ is a negative definite matrix. Then, according to Theorem 2, the systems (20) and (21) are globally dislocated hybrid synchronized under the chosen controllers. The error functions can be written as

$$\begin{cases} \dot{e_1} = -\alpha e_1 \\ \dot{e_2} = -e_2 \\ \dot{e_3} = -2e_3 \end{cases} \tag{24}$$

Finally, fig.6 shows temporal evolution of synchronization errors .

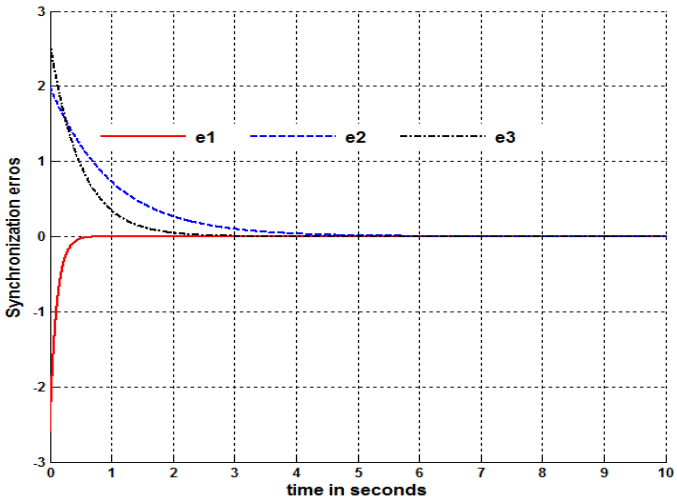

Fig.6 Temporal evolutions of synchronization errors e_1, e_2 and e_3 .

IV. Conclusion

In this paper, we present theoretical and simulation study results on a synchronization scheme named Hybrid Dislocated Synchronization (HDS) which can be executed between two identical systems of a large family of tridimensional autonomous continuous chaotic systems. As an example and to show the effectiveness of our approach, we use Chua's chaotic circuit to demonstrate the validity of the theoretical results. Using numerical simulations, we have showed the sensitivity to initials conditions changes of Chua's system and finally we have executed successfully the (HDS) synchronization between two identical Chua's chaotic systems. Our approach is rigorous because it's based, only, on two mathematical theorems presenting the necessary and sufficient conditions under which (HDS) synchronization can be achieved.

References

[1] Yamada, T. & Fujisaka, H., 1983. *Stability Theory of Synchronized Motion in Coupled-Oscillator Systems. II: The Mapping Approach*. Progress of Theoretical Physics, 70(5),pp.1240–1248. http://dx.doi.org/10.1143/ptp.70.1240.

[2] Fujisaka, H. & Yamada, T., 1983. *Stability Theory of Synchronized Motion in Coupled-Oscillator Systems*. Progress of Theoretical Physics, 69(1), pp.32–47.http://dx.doi.org/10.1143/ptp.69.32.

[3] Pecora, L.M. & Carroll, T.L., 1990. *Synchronization in chaotic systems.* Physical Review Letters, 64(8), pp.821–824. http://dx.doi.org/10.1103/physrevlett.64.821.

[4] Carroll, T.L. & Pecora, L.M., 1991. *Synchronizing chaotic circuits*. IEEE Transactions on Circuits and Systems, 38(4), pp.453–456. http://dx.doi.org/10.1109/31.75404.

[5] [5] Alligood, K.T., Sauer, T.D. & Yorke, J.A., 1997. *Chaos. Textbooks in Mathematical Sciences*,pp.105–147. http://dx.doi.org/10.1007/978-3-642-59281-2_3.

[6] Ott, E., 2002. *Chaos in Dynamical Systems*, http://dx.doi.org/10.1017/cbo9780511803260

[7] Wang, Y.-W. & Guan, Z.-H., 2006. *Generalized synchronization of continuous chaotic system.Chaos*, Solitons & Fractals, 27(1), pp.97–101. http://dx.doi.org/10.1016/j.chaos.2004.12.038.

[8] Ouannas, A., Azar, A. T., Ziar, T., & Radwan, A. G. (2017). *Generalized Synchronization of Different Dimensional Integer-Order and Fractional Order Chaotic Systems*. Studies in Computational Intelligence, 671–697. doi:10.1007/978-3-319-50249-6_23.

[9] Ge, Z.-M. & Chen, C.-C., 2004. *Phase synchronization of coupled chaotic multiple time scales systems*. Chaos, Solitons & Fractals, 20(3), pp.639–647. http://dx.doi.org/10.1016/j.chaos.2003.08.001

[10] Jia, Q., 2007. *Projective synchronization of a new hyperchaotic Lorenz system*. Physics Letters A, 370(1),pp.40–45. http://dx.doi.org/10.1016/j.physleta.2007.05.028

[11] Yan, J. & Li, C., 2006. *Generalized projective synchronization for the chaotic Lorenz system and the chaotic Chen system*. Journal of Shanghai University (English Edition), 10(4), pp.299–304. http://dx.doi.org/10.1007/s11741-006-0004-y

[12] Li, R., Xu, W. & Li, S., 2007. *Adaptive generalized projective synchronization in different chaotic systems based on parameter identification*. Physics Letters A, 367(3), pp.199–206. http://dx.doi.org/10.1016/j.physleta.2007.03.025.

[13] Sarasu, P. & Sundarapan, V., 2012. *Generalized Projective Synchronization of Two-Scroll Systems via Adaptive Control*. International Journal of Soft Computing, 7(4), pp.146–156. http://dx.doi.org/10.3923/ijscomp.2012.146.156.

[14] Ouannas, A., Azar, A.T. & Ziar, T., 2019. *Control of continuous-time chaotic (hyperchaotic) systems: F-M synchronisation*. International Journal of Automation and Control, 13(2), p.226. http://dx.doi.org/10.1504/ijaac.2019.098215.

[15] Vaidyanathan, S. & Sampath, S., 2012. *Anti-synchronization of four-wing chaotic systems via sliding mode control*. International Journal of Automation and Computing, 9(3), pp.274–279. http://dx.doi.org/10.1007/s11633-012-0644-2.

[16] Vaidyanathan, S. & Rajagopal, K., 2011. *Anti-synchronization of Li and T Chaotic Systems by Active Nonlinear Control*. Communications in Computer and Information Science, pp.175–184. http://dx.doi.org/10.1007/978-3-642-22555-0_19.

[17] Li, R., 2008. *A special full-state hybrid projective synchronization in symmetrical chaotic systems*. Applied Mathematics and Computation, 200(1), pp.321–329. http://dx.doi.org/10.1016/j.amc.2007.11.010.

[18] Rasappan, S. & Vaidyanathan, S., 2012. *Hybrid synchronization of n–scroll Chua and Lur'e chaotic systems via backstepping control* with novel feedback. Archives of Control Sciences, 22(3), pp.343–365. http://dx.doi.org/10.2478/v10170-011-0028-9.

[19] Vaidyanathan, S. & Sampath, S., 2012. *Hybrid Synchronization of Hyperchaotic Chen Systems via Sliding Mode Control*. Advances in Computer Science and Information Technology. Computer Science and Engineering, pp.257–266. http://dx.doi.org/10.1007/978-3-642-27308-7_27.

[20] Ouannas, A., Azar, A.T. & Ziar, T., 2020. *Fractional inverse full state hybrid projective synchronisation*. International Journal of Advanced Intelligence Paradigms, 17(3/4), p.279. http://dx.doi.org/10.1504/ijaip.2020.109511

[21] Murali, K. & Lakshmanan, M., 1998. *Secure communication using a compound signal from generalized synchronizable chaotic systems.* Physics Letters A, 241(6), pp.303–310. http://dx.doi.org/10.1016/s0375-9601(98)00159-5.

[22] Thangavel, P., Murali, K. & Lakshmanan, M., 1998. *Bifurcation and Controlling of Chaotic Delayed Cellular Neural Networks*. International Journal of Bifurcation and Chaos, 08(12), pp.2481–2492. http://dx.doi.org/10.1142/s021812749800200x

[23] Tao Yang & Chua, L.O., 1997. *Impulsive stabilization for control and synchronization of chaotic systems: theory and application to secure communication.* IEEE Transactions on Circuits and Systems I: Fundamental Theory and Applications, 44(10), pp.976–988. http://dx.doi.org/10.1109/81.633887.

[24] Ott, E., Grebogi, C. & Yorke, J.A., 1990. *Controlling chaos.* Physical Review Letters, 64(11),pp.1196–1199. http://dx.doi.org/10.1103/physrevlett.64.1196.

[25] Shi-Hua, C. et al., 2002. *Tracking control and synchronization of chaotic systems based upon sampled-data feedback*. Chinese Physics, 11(3), pp.233–237. http://dx.doi.org/10.1088/1009-1963/11/3/306

[26] Park, J.H. & Kwon, O.M., 2005. *A novel criterion for delayed feedback control of time-delay chaotic systems*. Chaos, Solitons &

Fractals, 23(2), pp.495–501. http://dx.doi.org/10.1016/j.chaos.2004.05.023.

[27] Vassiliadis, D., 1992. *A Method For Adaptive Control and Learning in Chaotic Systems.* Chaotic Dynamics, pp.211–219. http://dx.doi.org/10.1007/978-1-4615-3464-_19

[28] Adloo, H. et al., 2011. *Two Dimensional Sliding Mode Control*. Sliding Mode Control. http://dx.doi.org/10.5772/15590.

[29] Karthikeyan, R. & Sundarapandian, V., 2014. *Hybrid Chaos Synchronization of Four–Scroll Systems via Active Control*. Journal of Electrical Engineering, 65(2), pp.97–103. http://dx.doi.org/10.2478/jee-2014-0014.

[30] Lei, J., Dai, S. & Fan, Z., 2009. *Design of a backsteping Controller for a Class of High-Supersonic Missiles*. 2009 International Conference on Artificial Intelligence and Computational Intelligence. http://dx.doi.org/10.1109/aici.2009.50.

[31] Evgeny, K., 2015. *Circuit-Based Monitoring of High-Performance Semiconductor Manufacturing Processes*. A thesis submitted to the department of Engineering ,Macquarie University, Australia, for the degree of Doctor of Philosophy.

Efficient STATCOM based on hybrid sliding mode control-proportional integral control and 48-pulse converter

Hassen BELILA[1], Nasserdine BOUDJERDA[2], Ahsene BOUBAKIR[3], Imen BAHRI[4]
University of Oum El Bouaghi, Algeria (1), LER laboratory University of Jijel, Algeria (2), LAJ laboratory University of Jijel, Algeria (3), University of Paris-Saclay, France (4)

Abstract. *Flexible alternating current transmission systems (FACTS) evolved as a result of the development of power electronics and began to play a key role in improving the quality of Network power. The purpose of this work is to provide a control strategy of voltage and reactive power flow in one of the most used FACTS devices known as STATCOM. This strategy is based on a hybrid control (sliding mode control-classic PI control), in addition STATCOM uses a 48-pulse converter. The simulations proved the efficiency of the proposed system in both the control performance and harmonic distortion rate of the current injected into the grid.*

Keywords: STATCOM, Sliding Mode Control, reactive power compensation, 48-pulse converter, harmonics.

1. Introduction

The consumption of electrical energy is continually increasing as a result of industrialization and population increase. Thus, in order to achieve a balance between production and consumption, the number of power stations, lines, transformers, and other equipments in the power network must be increased, resulting in higher costs and environmental degradation [1].

The traditional means of electricity generation (thermal and nuclear power stations) are well adapted to the performance of electrical systems because their production is controllable, however, they use energy ressources with significant environmental disadvantages: Limited reserves, greenhouse gas emissions, and waste disposal, (particularly nuclear waste) [1], [2]. These energy and environmental concerns have pushed the evolution of electrical networks toward a vast integration of new unconventional and distributed electricity production sources, (particularly wind and photovoltaics PV), characterized by their reliance on climatic conditions (wind for aeolian and sunlight for PV) [2].

The current needs of consumers for high quality electricity require a highly efficient network. Many customers may be faced with major technical and economic problems as a result of poor energy quality due to the increasing sensitivity of the receivers and the process controls used. Disturbances such as voltage fluctuations, flashing, harmonics, or imbalances can prohibit devices from functioning properly and force certain industrial processes to shut down [3]–[7].

Conventional network control means such as electromechanical devices (transformer with adjustable load supports, phase-shifting transformers, serial or parallel compensators switched by circuit breakers, modification of production instructions, change in network topology, and action on generator excitation) may prove to be too slow and insufficient in the future to respond effectively to network disturbances, especially given the new constraints.

The rapid development of power electronics has given a significant impact on improving power grid operation by improving parameter control and introducing control devices based on advanced power electronics (GTO, IGBT), known as FACTS (Flexible Alternative Current Transmission Systems) [8].

The latest generation of FACTS systems is mostly composed of voltage (or current) converters based on modern static switches (GTO, IGBT), connected to capacitors as continuous voltage sources. These converters can be classified based on their network connection as shunt, series, or hybrid compensators, such as STATCOM (STATic COMpensator), SSSC (Static Synchronous Series Compensator), and UPFC (Unified Power Flow Controller) respectively.

The STATCOM is commonly used for reactive energy compensation and, as a result, voltage regulation at the bus bar to which it is linked. It generates a three-phase AC voltage synchronized with the voltage of the electrical grid from a DC voltage source. In practice, no active power is involved; only reactive power is exchanged between the STATCOM and the power grid, allowing for both power factor correction and compensation for falls and surges, hence enhancing the power quality of the network [8]–[10].

Extensive studies in recent years have revealed that the success of STATCOM is heavily dependent on the accuracy and robustness of the adopted control approach [11], [12].

Traditional PI controllers are generally simple to implement, however they are heavily affected by parameter variations and may suffer from stability issues; as a result, the authors of the reference [13] present an adaptive PI control of a STATCOM. In [14] and [15], the authors suggest a fuzzy logic control of a D-STATCOM (D-STATCOM: STATCOM coupled to a low voltage distribution network) and the results are compared with those of a standard PI control. However, it should be mentioned that this new technique has a long response time and a noisy stationary state (small oscillations). The authors of reference [16] used a D-STATCOM to adjust the output voltage of a hybrid power plant (eolian-diesel unit), and a sliding mode control was used. The authors of reference [17] attempt to improve the performance of a D-STATCOM connected to a low-voltage distribution network by selecting an appropriate DC-side reference of the D-STATCOM, this method reduces switching losses and current harmonics of the D-STATCOM without degrading its dynamics, a conventional PI control was used. The authors of reference [18] proposed a hybrid approach (SMC-PI) on a D-STATCOM to increase both static and dynamic performance over the usual PI configuration.

In the present work, we investigate the compensation of high voltage transmission lines by using a STATCOM system. Knowing that the control strategy is critical for good static and dynamic performance, we suggest a hybrid control method (sliding mode control–PI control) as we know the robustness and the dynamic performance of the sliding mode technique in general. In addition, we propose the use of a 48-pulse converter as an inverter for the STATCOM topology given its very low rate of harmonic distortion on the AC side.

2. Modeling of the grid connected STATCOM

The equivalent diagram of the STATCOM can be found in (Fig.1). Only the busbar of the common coupling point (CCP) is considered for the STATCOM modeling and the DC source is assumed to be constant (Fig.1.a). As a result, the equivalent circuit of Fig.1.b is an AC voltage source v_{sh} coupled to a

network node by the inductor L_{sh} of a coupling transformer and a resistor R_{sh} representing the transformer's ohmic losses and the inverter's switching losses [19]. The current i_{sh} is determined by the difference between the node voltage v_r and the STATCOM's adjustable voltage v_{sh} [20][21].

The amount of reactive power transferred between the STATCOM and the network is managed by the amplitude of the STATCOM voltage v_{sh}. This reactive energy is either injected into or removed from the network, allowing the bus bar voltage v_r to be regulated at a desired value [22].

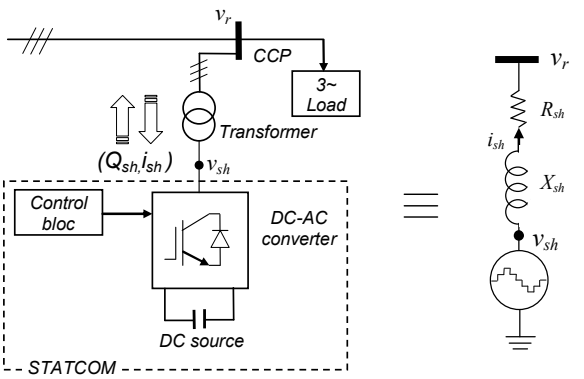

a. Bloc diagram b. Equivalent circuit

Fig.1. Equivalent diagram of a STATCOM

The application of Kirchhoff's laws on the equivalent circuit of Fig.1.b gives:

$$\begin{cases} v_{sha} - v_{ra} = R_{sh} i_{sha} + L_{sh} \dfrac{di_{sha}}{dt} \\ v_{shb} - v_{rb} = R_{sh} i_{shb} + L_{sh} \dfrac{di_{shb}}{dt} \\ v_{shc} - v_{rc} = R_{sh} i_{shc} + L_{sh} \dfrac{di_{shc}}{dt} \end{cases} \quad (1)$$

Where:

(v_{ra} , v_{rb} , v_{rc}): Three phase voltages at the CCP.

(v_{sha} , v_{shb} , v_{shc}): Three phase voltages at the output of the STATCOM.

(i_{sha} , i_{shb} , i_{shc}): Three phase shunt current of the STATCOM.

The well-known Park transformation allows the following transition from a balanced three phase system (a, b, c) to a rotating frame with only two orthogonal axes (d,q) [27]:

$$\begin{bmatrix} x_d \\ x_q \end{bmatrix} = P(\theta) \begin{bmatrix} x_a \\ x_b \\ x \end{bmatrix} \quad (2)$$

Where:

(x_a,x_b,x_c): Phase components of the three phase system (voltage, current …).

(x_d,x_q) : Park components.

θ : Angle between the phase axis *a* and the rotating axis *d*.

$P(\theta)$: Transformation matrix given as follow:

$$[P(\theta)] = \sqrt{\frac{2}{3}} \begin{bmatrix} \cos(\theta) & \cos(\theta - 2\pi/3) & \cos(\theta + 2\pi/3) \\ \sin(\theta) & \sin(\theta - 2\pi/3) & \sin(\theta + 2\pi/3) \end{bmatrix}$$

The inverse Park transformation allows the return to phase components (*a*, *b*, *c*) as follows:

$$\begin{bmatrix} x_a \\ x_b \\ x_c \end{bmatrix} = P(\theta)^{-1} . \begin{bmatrix} x_d \\ x_q \end{bmatrix} \quad (3)$$

$P(\theta)^{-1}$: Inverse transformation matrix.

Considering $\theta = 2\pi ft$ (f : frequency of the grid currents), the application of park transformation to equation (1) gives [23]:

$$\begin{cases} v_{shd} - v_{rd} = R_{sh} i_{shd} + L_{sh} \dfrac{di_{shd}}{dt} - \omega L_{sh} i_{shq} \\ v_{shq} - v_{rq} = R_{sh} i_{shq} + L_{sh} \dfrac{di_{shq}}{dt} + \omega L_{sh} i_{shd} \end{cases} \quad (4)$$

Then, we can write the following state equation of the STATCOM:

$$\begin{cases} \dot{x}_1 = \dfrac{d}{dt} i_{shd} = -\dfrac{R_{sh}}{L_{sh}} i_{shd} + \omega . i_{shq} - \dfrac{1}{L_{sh}} v_{rd} + \dfrac{1}{L_{sh}} u_1 \\ \dot{x}_2 = \dfrac{d}{dt} i_{shq} = -\dfrac{R_{sh}}{L_{sh}} i_{shq} - \omega . i_{shd} - \dfrac{1}{L_{sh}} v_{rq} + \dfrac{1}{L_{sh}} u_2 \end{cases} \quad (5)$$

Where:

$\begin{bmatrix} u_1 \\ u_2 \end{bmatrix} = \begin{bmatrix} v_{shd} \\ v_{shq} \end{bmatrix}$: Input vector of the system.

$\begin{bmatrix} x_1 \\ x_2 \end{bmatrix} = \begin{bmatrix} i_{shd} \\ i_{shq} \end{bmatrix}$: State variables of the system.

3. Proposed sliding mode control of the STATCOM

According to equation (5), the relative degrees of outputs $x_1 = i_{shd}$ and $x_2 = i_{shq}$ are unit, i.e. $r_1 = r_2 = 1$. To boost pursuit performance in steady state we picked the following integral type sliding surfaces [24]:

$$S_1 = \left(\frac{d}{dt} + \lambda_1 \right) \int_0^t e_1 \quad (6)$$

And,

$$S_2 = \left(\frac{d}{dt} + \lambda_2 \right) \int_0^t e_2 \quad (7)$$

Where:

$$e_1 = i_{shd}^* - i_{shd} \quad (8)$$

And,

$$e_2 = i_{shq}^* - i_{shq} \quad (9)$$

By inserting equations (8) and (9) into (6) and (7), respectively, we obtain the derivatives of the following sliding surfaces:

$$\dot{S}_1 = \dot{i}_{shq}^* - \dot{i}_{shq} + \lambda_1 . e_1 \quad (10)$$

And,

$$\dot{S}_2 = \dot{i}_{shq}^* - \dot{i}_{shq} + \lambda_2 . e_2 \quad (11)$$

Then, by inserting equations (5) into (10) and (11), we get:

$$\dot{S}_1 = \dot{i}^*_{shd} + \frac{R_{sh}}{L_{sh}} i_{shd} - \omega . i_{shq} + \frac{1}{L_{sh}} v_{rd} - \frac{1}{L_{sh}} u_1 + \lambda_1 . e_1 \quad (12)$$

And,

$$\dot{S}_2 = \dot{i}^*_{shq} + \frac{R_{sh}}{L_{sh}} i_{shq} + \omega . i_{shd} + \frac{1}{L_{sh}} v_{rq} - \frac{1}{L_{sh}} u_2 + \lambda_2 . e_2 \quad (13)$$

And, in order to check Lyapounov's stability criterion ($S_i . \dot{S}_i < 0$), we must have:

$$\dot{S}_1 = -\alpha_1 S_1 - \beta_1 \, sign(S_1) \quad (14)$$

And,

$$\dot{S}_2 = -\alpha_2 S_2 - \beta_2 sign(S_2) \quad (15)$$

Where α_1 , α_2 , β_1 , β_2 are design parameters chosen based on desired closed loop performance. They enable the designer to increase response speed and robustness vis-à-vis uncertainties and exogenous inputs.

Note: The greater and larger the numbers α_1 and α_2 , the faster the time of attractiveness towards the sliding surface; while low values β_1 and β_2 lower the oscillations.

By equating equations (12) with (14) and (13) with (15), we get:

$$\dot{i}^*_{shd} + \frac{R_{sh}}{L_{sh}} i_{shd} - \omega . i_{shq} + \frac{1}{L_{sh}} v_{rd} - \frac{1}{L_{sh}} u_1 + \lambda_1 . e_1 = -\alpha_1 S_1 - \beta_1 \, sign(S_1) \quad (16)$$

And,

$$\dot{i}^*_{shq} + \frac{R_{sh}}{L_{sh}} i_{shq} + \omega . i_{shd} + \frac{1}{L_{sh}} v_{rq} - \frac{1}{L_{sh}} u_2 + \lambda_2 . e_2 = -\alpha_2 S_2 - \beta_2 sign(S_2) \quad (17)$$

This allows us to find the following u_1 and u_2 command expressions:

$$u_1 = L_{sh} \dot{i}^*_{shd} + R_{sh} i_{shd} - L_{sh} \omega . i_{shq} + v_{rd} + L_{sh} \lambda_1 e_1 + \alpha_1 L_{sh} S_1 + \beta_1 L_{sh} \, sign(S_1) \quad (18)$$

And,

$$u_2 = L_{sh} \dot{i}^*_{shq} + R_{sh} i_{shq} + L_{sh} \omega . i_{shd} + v_{rq} + L_{sh} \lambda_2 e_2 + \alpha_2 L_{sh} S_2 + \beta_2 L_{sh} \, sign(S_2) \quad (19)$$

Taking into consideration:

$$u_1 = u_{eq1} + u_{c1} \quad (20)$$

And,

$$u_2 = u_{eq2} + u_{c2} \quad (21)$$

Finally, the following formula defines the command:

- The terms of the u_{eq1} and u_{eq2} equivalent commands, specified as follows:

$$u_{eq1} = L_{sh} \dot{i}^*_{shd} + R_{sh} i_{shd} - L_{sh} \omega . i_{shq} + v_{rd} + L_{sh} \lambda_1 e_1 \quad (22)$$

And,

$$u_{eq2} = L_{sh} \dot{i}^*_{shq} + R_{sh} i_{shq} + L_{sh} \omega . i_{shd} + v_{rq} + L_{sh} \lambda_2 e_2 \quad (23)$$

- Correction terms u_{c1} and u_{c2} :

$$u_{c1} = \alpha_1 L_{sh} S_1 + \beta_1 L_{sh} \, sign(S_1) \quad (24)$$

And,

$$u_{c2} = \alpha_2 L_{sh} S_2 + \beta_2 L_{sh} \, sign(S_2) \quad (25)$$

Finally, we propose in Figure 2, the bloc diagram of the hybrid SMC-PI strategy of the STATCOM based on an internal SMC control of two variables (i_{sd} and i_{sa}) and two external PI control loops for V_{dc} and v_r . This control strategy can be explained as follows:

- The two internal current control loops are achieved by a STATCOM-SMC control block.
- The continuous bus voltage control loop's role is to keep this voltage constant by controlling the active power transit between the PCC and the continuous bus. The reference voltage V^*_{dc} and measured voltage V_{dc} are the regulator's inputs, and the output is the direct component of the reference current i^*_{shd} (Fig. 2). This voltage is frequently controlled by a PI type regulator [25].
- The control of the reactive power exchange between the STATCOM and the power grid regulates the v_r voltage at the 'PCC' coupling point. As shown in Figure 2, a PI controller generates a reference signal for the STATCOM's reactive current component i^*_{shq} .

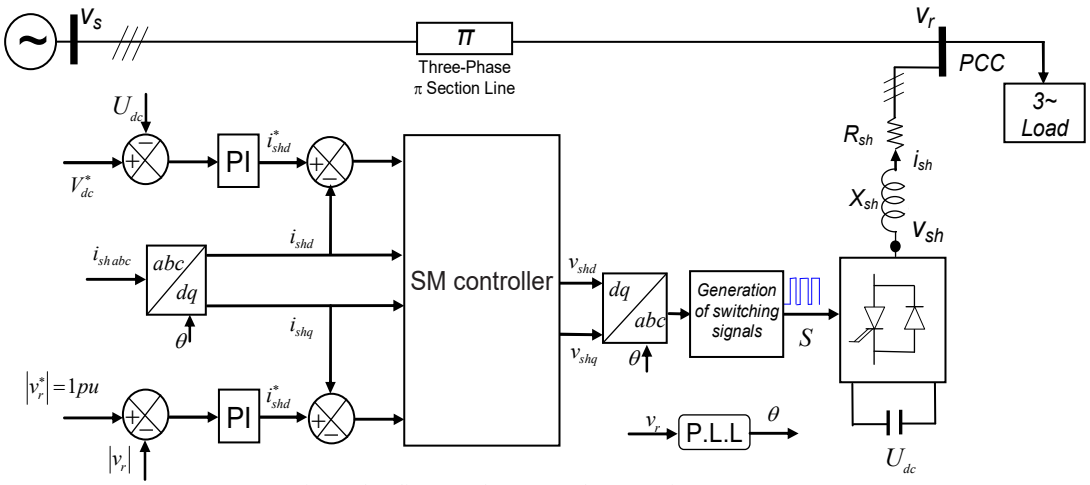

Fig.2. Bloc diagram of SM control strategy for STATCOM [24]

Because of its very low harmonic distortion content on the AC side, the 48-pulse converter can be used in high voltage and high power applications without the requirement for AC filters. This converter's consists of four identical three-level GTO converters (each requiring 12 control pulses) coupled together by four phase-shifting transformers, as shown in Figure 3 [26]. Transformers are specifically required in our application to raise the output voltage and adapt it to that of the network; they thus serve a dual purpose: they perform the phase shifts required to get multi-level voltage and they raise the voltage to match the very high voltage. In order to avoid very large number of switching operation, we use full-wave control which leeds to a minimum switching losses.

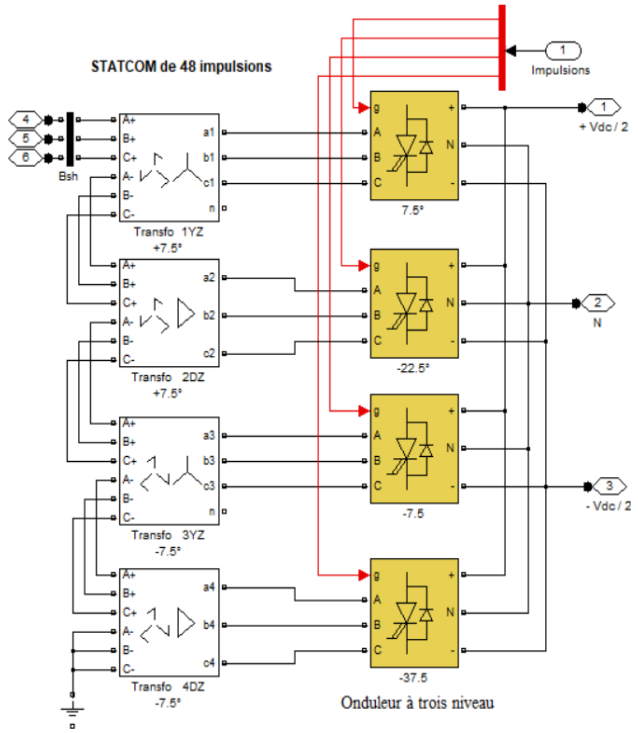

Fig.3. 48 pulse GTO voltage inverter

4. Simulations and results analysis

4.1. Simulations

Figure 4 presents a single-line diagram of the power network used to validate the operation of the proposed STATCOM.

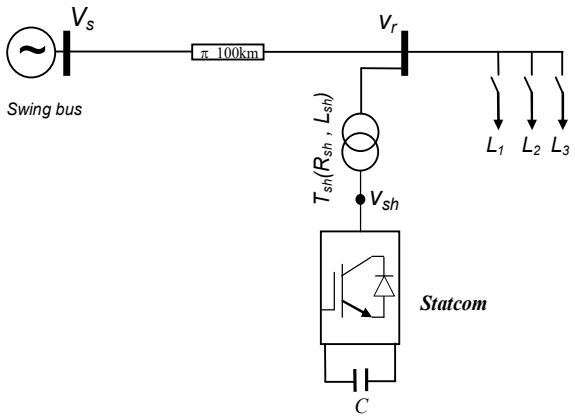

Fig.4. Single-line diagram of the studied network

The considered network is composed of a 400 KV reference generator and a transmission line modeled in π to supply a load (L1, L2, L3) at the set of bar '*r*'.
The T_{sh} transformer is used to reduce the voltage from 400 KV (network voltage) to 20 KV (STATCOM output voltage).

The simulations are carried out in a per unit system with base values of S_B = 1000 MVA and U_B = 400 kV, and the voltage of the generator busbar is V_S = 1.0 pu.
Three loads (L1, L2 and L3) are connected to the busbar " *r* " as shown in the following table:

Table 1. Load variation

Connection time(s)	0s to 0.5s	0.5 to 1s	1s to 1.5s	1.5s to 2s
Load	L1	L1+L2	L+L2+L3	L3

Where:
L1: inductive load , P1 = 1.0 pu and Q1 = 0.4 pu.
L2: inductive load , P2 = 0.5 pu, and Q2 = 0.4 pu.
L3: capacitive load , P3 = 0.3 pu, Q3c = 0.2 pu, Q3l = 0.01 pu

4.2. Results analysis

4.2.1 Network without STATCOM (STATCOM deconnected)

The voltage drop generated by the inductive load L2 at time t = 0.5 s is shown in Fig.5 at both the source and load bus bars V_s and V_r. At time t = 1 s, the capacitive load connection L3 naturally dampens this voltage drop. Finally, the disconnection of all inductive loads in the final transition at time t = 1.5 s resulted in a capacitive load flow and a surge at the two bus bars. Note t small influence of load fluctuations on the source bus bar.

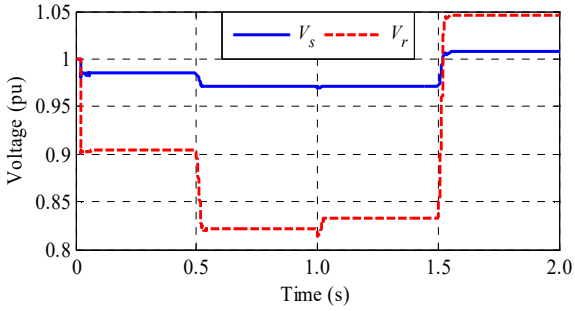

Fig.5. Source voltage v_s and load voltage v_r before compensation

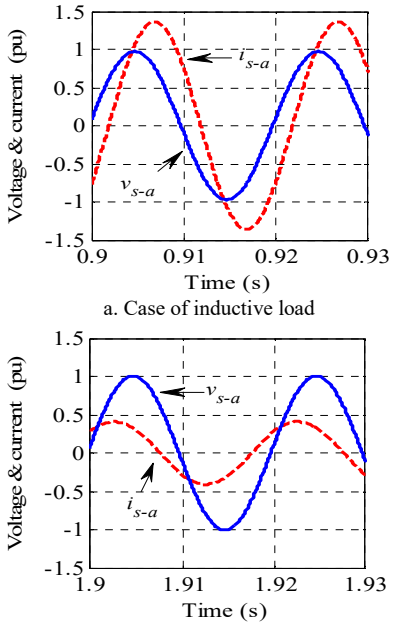

Fig.6. Grid voltage v_s and current i_s before compensation

The phase shift between the voltage and current of the source is shown in Fig.6, and it is evident that the voltage is ahead of the current, as shown in Fig.6.a in the case of inductive load. In the

case of a capacitive load, the current is ahead of the voltage, as shown in Fig.6.b.

4.2.2. Network with connected STATCOM

The STATCOM produces reactive current (i_{shq}>0) for inductive loads and absorbs reactive current (i_{shq}<0) for capacitive loads, as shown in Fig.7.

In inductive mode the STATCOM injects a quantity of reactive power $Q_{sh} \approx$ [0.45 0.91 0.76] pu in the three intervals to raise the voltage v_r to 1.0 pu, while in capacitive mode the STATCOM absorbs reactive energy from the network(Q_{sh}<0) to keep the voltage profile v_r constant, as shown in Fig.8.
We notice that the STATCOM consumes a very low amount of active power to compensate for losses in the power switches of the static converter (Fig.8).

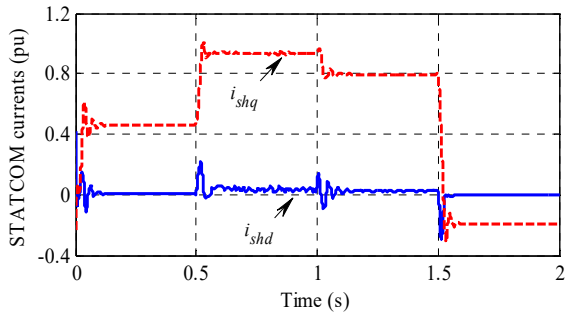

Fig.7. STATCOM currents i_{shd} and i_{shq}

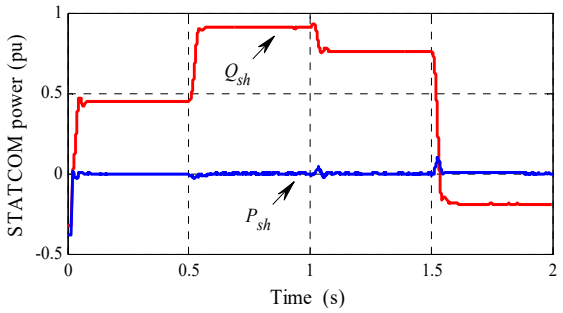

Fig.8. STATCOM Active and reactive power (P_{sh},Q_{sh})

The voltage of the load bus bar is well regulated at its nominal value, v_r = 1.0 pu, as shown in Fig.9. Furthermore, a favorable effect is also observed on the voltage v_s, which approaches its nominal value (Fig.9).

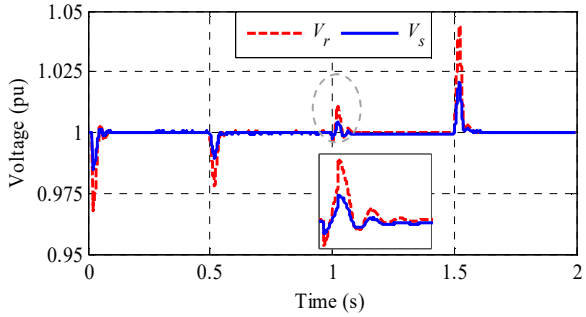

Fig.9. Source voltage v_s and load voltage v_r after SMC compensation

Figure 10 shows that the voltage v_s and the current i_s are in phase in steady state after compensation; indicating that there is no transit of reactive power between the source and the load after compensation.
Figure 11 displays the shapes and phase shift between the v_{sh} and v_r voltages after PI-SMC compensation; we note a zero phase shift (v_{sha} and v_{ra} are in phase). We can determine the capacitive mode of operation for (v_r < v_{sh}) and the inductive mode of operation for (v_r > v_{sh}). Furthermore, Fig.12 shows that i_{sh} current is forward quadrature to v_{sh} voltage for the capacitive mode and backward quadrature for the inductive mode, implying that only reactive energy is transferred between the STATCOM and the network. We notice the specific waveform of the output voltage of the 48-pulse converter which is very close to the sine wave.

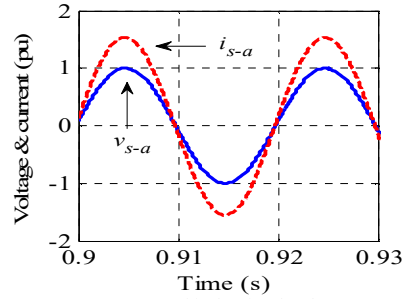

a. Case of inductive load

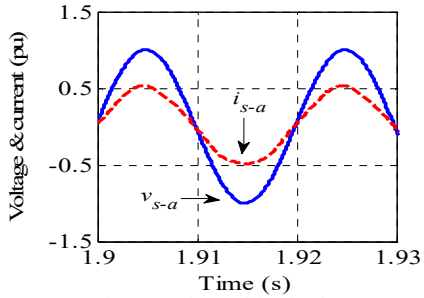

b. Case of capacitive load

Fig.10. Grid voltage v_s and current i_s after compensation

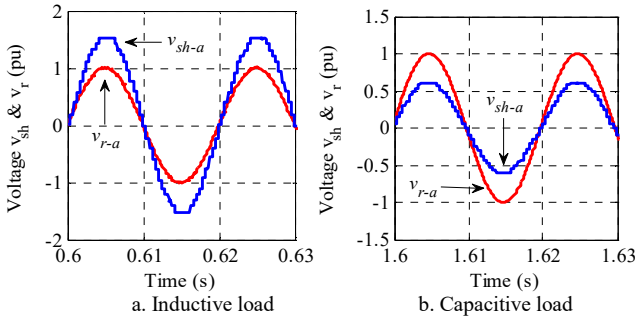

a. Inductive load b. Capacitive load

Fig.11. Grid voltage v_{sh-a} and v_{r-a} after compensation

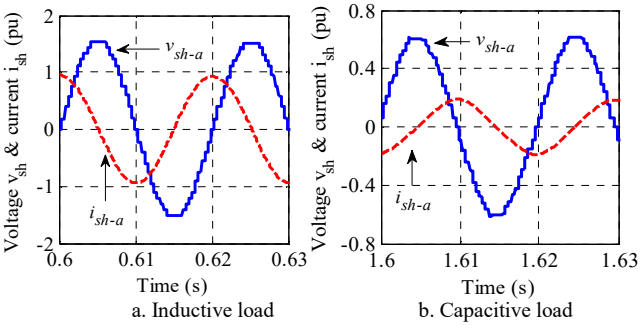

a. Inductive load b. Capacitive load

Fig.12. Grid voltage v_{sh-a} and current i_{sh-a} after compensation

Figure 13 shows the THD of v_{sh} voltage at the STATCOM output as well as the i_{sh} current injected into the network by the PI-SMC hybrid control. THD for voltage is 4.11 % and 0.90 % for current. These values are fully compliant with IEEE regulations, which focus only on the injected current by limiting its THD to 5% and the amplitude of each current harmonic to 3% [27].

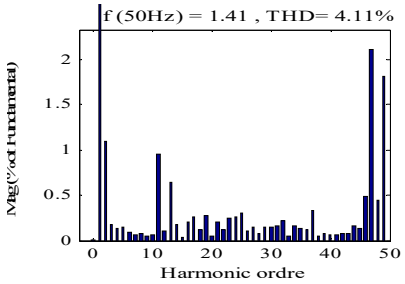

a. Harmonic spectrum of the $v_{sh\text{-}a}$

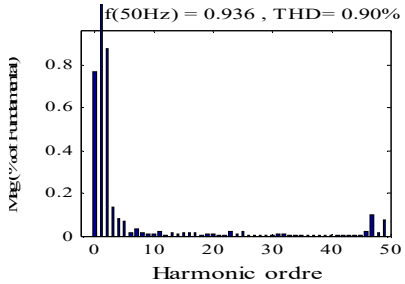

b. Harmonic spectrum of the $i_{sh\text{-}a}$

Fig. 13. Harmonic spectrum of the phase voltage $v_{sh\text{-}a}$ and current $i_{sh\text{-}a}$ at the STATCOM output

6. Conclusion

We began this paper by emphasizing the detrimental effect of reactive power transit on the load bus bar. Then we connected a STATCOM to this bar in order to adjust for reactive power and keep the voltage at its nominal value. In terms of compensation and enhanced energy quality, the adoption of hybrid control strategy (PI – SMC) has produced extremely excellent results. Indeed, the proposed innovative methodology ensures a very fast dynamic adjustment in the case of a rapid change in load and operates as a shock absorber, in addition to a better energy quality in a constant state. In addition the use of 48-pulse converter achieves an output voltage with very good shape while minimising the switching losses.

References

[1] B. Wu, Y. Lang, N. Zargari, and S. Kouro, "Power conversion and predictive control of wind energy conversion systems," in *John Wiley and sons Publication, IEEE Press*, 2011, p. 453.

[2] H. Bayem, "Apport des méthodes probabilistes aux études d ' intégration des énergies renouvelables aux systèmes électriques," Thèse de doctorat, Université Paris Sud - Paris XI, 2009.

[3] M. Moghbel, M. A. S. Masoum, A. Fereidouni, and S. Deilami, "Optimal sizing, siting and operation of custom power devices with STATCOM and APLC functions for real-time reactive power and network voltage quality control of smart grid," *IEEE Trans. Smart Grid*, vol. 9, no. 6, pp. 5564–5575, 2018, doi: 10.1109/TSG.2017.2690681.

[4] R. Moghe, D. Divan, D. Lewis, and J. Schatz, "Turning Distribution Feeders into STATCOMs," *IEEE Trans. Ind. Appl.*, vol. 53, no. 2, pp. 1372–1380, 2017, doi: 10.1109/TIA.2016.2634520.

[5] E. Kontos, G. Tsolaridis, R. Teodorescu, and P. Bauer, "High Order Voltage and Current Harmonic Mitigation Using the Modular Multilevel Converter STATCOM," *IEEE Access*, vol. 5, pp. 16684–16692, 2017, doi: 10.1109/ACCESS.2017.2749119.

[6] K. R. Padiyar, "Facts Controllers in Power Transmission Distribution," in *New age international publishers*, 2007, p. 548.

[7] L. Feola, R. Langella, I. Papic, and A. Testa, "Selective interharmonic compensation to improve statcom performance for light flicker mitigation," *IEEE Trans. Power Deliv.*, vol. 33, no. 5, pp. 2442–2451, 2018, doi: 10.1109/TPWRD.2018.2810333.

[8] K. K. Sen and M. L. Sen, "Introduction to FACTS Controllers: Theory, Modeling, and Applications," in *Wiley-IEEE Press*, 2009, p. 552.

[9] S. D. Mahajan, M. Murali, and T. B. Mali, "Comparative analysis of 6, 12 and 48 pulse T-STATCOM," *IEEE 7th Power India Int. Conf. PIICON*, 2016, doi: 10.1109/POWERI.2016.8077252.

[10] M. I. Mosaad, "Model reference adaptive control of STATCOM for grid integration of wind energy systems," *IET Electr. Power Appl.*, vol. 12, no. 5, pp. 605–613, 2018, doi: 10.1049/iet-epa.2017.0662.

[11] E. Tremblay, S. Atayde, and A. Chandra, "Comparative study of control strategies for the doubly fed induction generator in wind energy conversion systems: A DSP-based implementation approach," *IEEE Trans. Sustain. Energy*, vol. 2, no. 3, pp. 288–299, 2011, doi: 10.1109/TSTE.2011.2113381.

[12] G. Abad, J. Lopez, M. Rodriguez, L. Marroyo, and G. Iwanski, "Doubly Fed Induction Machine: Modeling and Control for Wind Energy Generation," in *Wiley-IEEE Press*, 2011, p. 625.

[13] Y. Xu and F. Li, "Adaptive PI control of STATCOM for voltage regulation," *IEEE Trans. Power Deliv.*, vol. 29, no. 3, pp. 1002–1011, 2014, doi: 10.1109/TPWRD.2013.2291576.

[14] S. K. Routray, N. Nayak, and P. K. Rout, "A Robust Fuzzy Sliding Mode Control Design for Current Source Inverter based STATCOM Application," *Procedia Technol.*, vol. 4, pp. 342–349, 2012, doi: 10.1016/j.protcy.2012.05.052.

[15] A. Ajami and N. Taheri, "A Hybrid Fuzzy/LQR Based Oscillation Damping Controller Using 3-level STATCOM," *Int. J. Comput. Electr. Eng.*, vol. 3, no. 2, pp. 184–189, 2011, doi: 10.7763/ijcee.2011.v3.312.

[16] H. Yunhao, S. Yuanyuan, Z. Han, and M. Yang, "Sliding mode reactive power control of isolated wind-disel hybrid power system based on STATCOM," *37th Chinese Control Conf. Jul. 2018, Wuhan, China*, pp. 8709–8714, 2018.

[17] S. Ziaeinejad and A. Mehrizi-Sani, "Design tradeoffs in selection of the DC-side voltage for a D-STATCOM," *IEEE Trans. Power Deliv.*, vol. 33, no. 6, pp. 3230–3232, 2018, doi: 10.1109/TPWRD.2017.2750422.

[18] F. Hamoud, M. L. Doumbia, and A. Cheriti, "Hybrid PI-Sliding Mode Control of a voltage source converter based STATCOM," *16th Int. Power Electron. Motion Control Conf. Expo. PEMC 2014*, pp. 661–666, 2014, doi: 10.1109/EPEPEMC.2014.6980571.

[19] S. K. Routray, N. Nayak, and P. K. Rout, "A Robust Fuzzy Sliding Mode Control Design for Current Source Inverter based STATCOM Application," *Procedia Technol.*, vol. 4, pp. 342–349, 2012, doi: 10.1016/j.protcy.2012.05.052.

[20] S. Gerbex, R. Cherkaoui, and A. J. Germond, "Optimal location of multi-type FACTS devices in a power system by means of genetic algorithms," *IEEE Trans. Power Syst.*, vol. 16, no. 3, pp. 537–544, 2001, doi: 10.1109/59.932292.

[21] N. Yorino, E. E. El-Araby, H. Sasaki, and S. Harada, "A new formulation for FACTS allocation for security enhancement against voltage collapse," *IEEE Trans. Power Syst.*, vol. 18, no. 1, pp. 3–10, 2003, doi: 10.1109/TPWRS.2002.804921.

[22] F. Shahnia, S. Rajakaruna, and A. Ghosh, "Static Compensators (STATCOMs) in Power Systems," in *Power Systems*, 2015.

[23] S. A. Touil, N. Boudjerda, A. Boubakir, and K. El Khamlichi Drissi, "A sliding mode control and artificial neural network based MPPT for a direct grid-connected photovoltaic source," *Asian J. Control*, vol. 21, no. 4, pp. 1892–1905, 2019, doi: 10.1002/asjc.2007.

[24] H. Belila, N. Boudjerda, A. BOUBAKIR, and I. BAHRI, "Improved STATCOM efficiency using a hybrid technique based on sliding mode control and proportional integral control," *Prz. Elektrotechniczny*, vol. 96, no. 10, pp. 156–162, 2020, doi: 10.15199/48.2020.10.29.

[25] M. Saeedifard, "Space Vector Modulation of Multi-Level and Multi-Module Converters for High Power Applications," Thèse de doctorat, Université de Toronto, 2008.

[26] C. A. C. Cavaliere, E. H. Watanabe, and M. Aredes, "Multi-pulse STATCOM operation under unbalanced voltages," *Proc. IEEE Power Eng. Soc. Transm. Distrib. Conf.*, vol. 1, no. c, pp. 567–572, 2002, doi: 10.1109/pesw.2002.985066.

[27] T. M. Blooming and D. J. Carnovale, "Application of IEEE STD 519-1992 harmonic limits," *Conf. Rec. 2006 Annu. Pulp Pap. Ind. Tech. Conf. IEEE*, pp. 1–9, 2006.

Control of reaction and thermo-acoustic instabilities of a combustion chamber

A.Debbah , A.Kerboua , R.Klaiaia

***Abstract*— This paper deals with the improvement of the control and the vanishing of the thermo-acoustic instability in gas-turbine engine combustors via a design of an active controller. The proposed design used a multi-objective genetic algorithm (MOGA) and multi-objective particle swarm optimization (MOPSO) to stabilize the unstable system from limit cycle with uncertain model. These parameters were chosen to minimize four objective functions: the mass fraction of the fuel produced, temperature control, flame fluctuation and the variation in the flow mass rate of input fuel. In addition, an improvement in suppression of the instability was achieved by coupling the combustor and the unsteady heat perturbations and thermos-acoustic models in simulation.**

Keywords—Combustion instabilities; Thermo-acoustic instability; Active control; Multi-objective optimization.

I. INTRODUCTION

Regardless of their configuration or application, all turbine engines will contain four main stages. These are the compressor, combustor, the turbine which generates mechanical work, and the exhaust generating thrust if required [1]. A large majority of research has concentrated on improving the efficiency of the compressor and exhaust stages. In recent years, recognition of global warming caused by greenhouse gases has pushed governmental organizations to restrict the allowed Carbon Monoxide and Carbon Dioxide ground emission levels in gas turbine engines, manufacturers have been able to comply with these requirements by constantly increasing the Operating Pressure Ratio (O.P.R.) of the engine. In addition to the major modifications to the compressor, this has allowed for a reduction in CO and CO2 emissions by reducing the amount of fuel burnt for a given thrust output in counterpart flame burning temperatures have increased because of the higher pressures at the combustor inlet [1]. It is expected that the O.P.R. will rise. The issue with increasing O.P.R., is that the induced higher flame temperature is responsible for an increase in Nitrogen Oxides; these refer to nitric oxide (NO) and nitrogen dioxide (NO2), both formed during combustion (NOx) emissions. Combustor instability suppression presents a challenging problem for controls design due primarily to the large dead time phase delay (of many hundreds of degrees or more) and noise in the combustion process. Besides large phase delay and noise, there are other characteristics of combustor instabilities, such as amplitude modulations and net random phase walks, which could play an important role in the control design [1]. A number of research efforts have attempted suppression of the thermo-acoustic instability through active control. The goal of these active control efforts was to reduce the energy concentrated at the instability frequency and to reduce the overall amplitude of the combustor pressure oscillations. Some active control concepts involved speaker actuation and others involved fuel modulation [1]. The last trends in control and stabilizing dynamic combustion systems demand the research, development and applications of advance control approaches based on the principles of optimality, robustness and intelligence. Proportional integral derivative (PID) and its derived configurations such as PI [2] or PD [3] control is the conventional most commonly used controller in the engine industry. The controller's popularity can be attributed to its functional simplicity, effectiveness over a wide range of operation conditions, and easier implementation using current micro-controller technology. To compensate time-delay and gain scheduling [4], modern model-based control approaches are developed using more dynamically coupled physical models. Linear-Quadratic-Gaussian (LQG) optimal control [5,6] is a power control means. However, it lacks the accurate linear state-space models of a practical engine combustor. This situation will be changed in the future, since new generations of state-space identification methods will be commercially available. More advanced methods such as fuzzy logic [7], neural network [8,9], robust (H∞, H2) [10–11], optimal (LQG), adaptive [12], predictive (hybrid) [13,14] control could also be applied to stabilize an unstable combustor. In general, there is a rich literature on robust sliding mode control [15,16,17]. The proposed robust design could be applied to design feedback controllers which are effective over a wide range of operating conditions and have great potential to apply in practice. There are some interests in the proposed optimized controller which can achieve fast response, good transient performance and robustness with respect to variations in combustor's parameters and modeled disturbances [18,19]. The paper is rganized as follows; the first section is a review on control of combustion in gas turbine process and the last research and future works. The second section presented the mathematical model. In section three, we explained optimized robust control, and section four discusses the simulation and the result that we got. Finally, the last section was dedicated to conclusion.

A.Debbah. is with Petrochemical and process engineering department, University of 20 Aout 1955-Skikda, Algeria. L2RCS Laboratory, Department of Electronics, University of Badji Mokhtar, Annaba, Algeria. (Phone .: + 213 0540654973 a.debbah@univ-skikda.dz.)

A.Kerboua. is with Petrochemical and process engineering department, University of 20 Aout 1955-Skikda, Algeria. (kerboua_adlen@yahoo.fr)

R.Klaiaia. is with electromechanical department, University of 20 Aout 1955-Skikda, Algeria. (ridaklaia@hotmail.com)

II. MATHEMATICAL MODEL

A simple combustor model is needed to incorporate into the overall fuel gas turbine system. The model must be able to simulate the temperature rise to the working fluid when it is

combusted. The model assumes the fuel input to the combustor to be methane. However, it is possible to burn the excess hydrogen straight.

A. The combustor model

The combustor model used was developed by Fannin [20]. It is called an "unsteady well stirred reactor" (WSR) model. It assumes methane (CH4) as the fuel and air as the oxidizer. The balanced combustion reaction is as follows:

$$CH_4 + 2(O_2 + 3.76N_2) \Longrightarrow CO_2 + 2H_2O + 7.52N_2 \quad (1)$$

A non-linear state space model can be constructed using conservation of species and energy in the control volume of the combustor. The conservation of species equations is based on the three species present inside the combustor. They are the fuel (methane), the oxidizer (air), and the products of combustion. The amount of species created in the control volume will be driven by the Arrhenius rate term for chemical kinetics of combustion. The conservation of species equations for the fuel and oxidizer are as follows:

$$\rho V \frac{dY_{fuel}(t)}{dt} = \dot{m}_{in} Y_{fuel,in}(t) - \dot{m}_{out} Y_{fuel}(t) + W_{fuel} \dot{\omega}_{fuel}(t) V \quad (2)$$

$$\rho V \frac{dY_{oxid}(t)}{dt} = \dot{m}_{in} Y_{oxid,in}(t) - \dot{m}_{out} Y_{oxid}(t) + MW_{fuel} \frac{Y_{oxid,in}(t)}{Y_{fuel,in}(t)} \dot{\omega}_{fuel}(t) V \quad (3)$$

$$\dot{\omega}_{fuel} = (-24.100 \frac{kmol}{kg*s}) \rho {Y_{fuel}}^{0.3} (0.233 Y_{oxid})^{1.3} e^{\frac{15.098}{R_u T(t)}} \quad (4)$$

ρ: Density inside combustor.

V: Volume of combustor

$\dot{m}_{in}$: Total mass flow rate into combustor.

$\dot{m}_{out}$: total mass flow rate out of combustor.

$Y_{fuel,in}(t)$, $Y_{oxid,in}$: mass fraction of fuel & oxidizer into combustor respectively.

MW_{fuel}: molecular weight of fuel (methane).

$\dot{\omega}_{fuel}$: Arrhenius rate term for consumption of species due to combustion.

Due to the definition of the mass fraction, the equation for the mass fraction of the products is simply

$$Y_{prod} = 1 - Y_{fuel} - Y_{oxid} \quad (5)$$

As stated above, the left-hand side of equation (6) represents the change in internal energy of the species inside the combustion chamber. In order to make this term and expression of temperature only (and not Yfuel, and Yoxid) it is assumed that the majority of the species inside the combustor are products (CO2, H2O, and N2), such that:

$$\rho V \frac{d}{dt} e(t)_{prod} \dot{m}_{in} \left(Y_{oxid,in} h_{oxid,in} + Y_{fuel,in} h_{fuel,in}\right) - \dot{m}_{out} \sum_{i=1}^{3} Y_i(t)\, h_{i,out}(t) \quad (6)$$

B. Thermo-acoustic model

The equivalence ratio is defined as the ratio of mass of fuel to mass of air, divided by the ratio of mass of fuel to mass of air in stoichiometric conditions. This can be written as:

$$\phi_r = \frac{m_{fuel}}{m_{air}} . \frac{m_{air,stoc}}{m_{fuel,stoc}} \quad (7)$$

In experimental rigs, the change in equivalence ratio is usually applied by modifying the quantity of fuel being injected m'_{fuel} , and the dispersion of imposed equivalence fluctuation and induced reduction in control authority must be taken into account. In our simulations however, it is easier to implement a change of mass of air $m'_{air}$and we assume a perfect actuation mechanism. According to eq. (7), both methods are analogous and therefore the simulations will only include velocity perturbations to the flame. The instabilities arise from the interactions between the combustor's oscillatory flows and heat release and the flow processes manifesting as large amplitude, organized oscillations of the combustor's flow field (comprising velocity, pressure temperature and the reactants) which generate disturbance that adds energy to the acoustic field when in phase with the pressure oscillations (Fig.1). A reduced-order behavioral model is used to represent the combustor instability. This model consists of the flame dynamics, acoustics, and saturation nonlinearity [21].

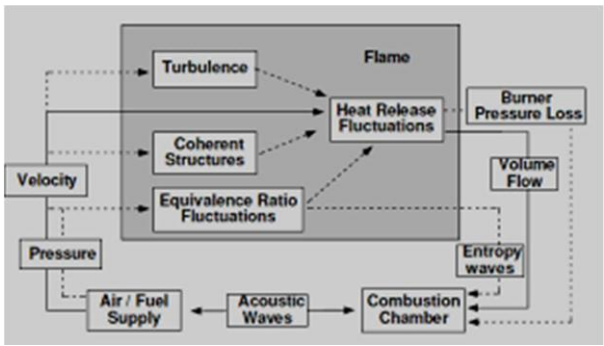

Figure. 1 Interactions between flow, acoustics and heat release in a Combustion system [21].

With the addition of noise, this instability is self-excited, that is, it requires no input via fuel injection modulation for sustained oscillations to take place. We chose the running parameters shown in Fig.2 to induce limit cycle saturation within the combustor.

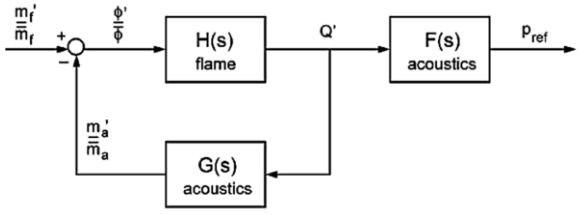

Figure. 2 Block diagram representation of a simple ducted flame combustor

We can write the block diagram representation of our combustor including only flame and acoustics modeling as shown in Fig.2, where $\dot{Q}$ represents the fluctuating flame heat

release ratio, $\frac{\acute{\phi}}{\bar{\phi}}$ is related to the air-fuel equivalence ratio, and $\frac{\acute{m_a}}{\bar{m}_a}$ is fractional air-mass flow fluctuation at the combustion zone. The open loop transfer function (OLTF) needed for control purposes is then from changes in fuel mass flow rate fluctuations $\acute{m}_f$, to the sensor of the acoustic pressure measured in the duct P_{ref}. The response of the pressure measurement, P_{ref}, to the heat release fluctuation, $\acute{Q}$, is modeled by an acoustic transfer function F(s), and the response of the fractional air mass flow fluctuation at the combustion zone, $\frac{\acute{m_a}(s)}{\bar{m}_a}$, to the heat release fluctuation, $\acute{Q}$, is modeled by G(s). Assuming a compact flame, the heat release fluctuation, $\acute{Q}$, is modeled by the relationship $\acute{Q}(s) = H(s)\frac{\acute{\phi}(s)}{\bar{\phi}}$ where H(s) is the flame model. The modified white noise is generated such that it mostly contains energy within the frequency range of interest, selected here as 30 Hz to 3000 Hz. The transfer function is then obtained by dividing the spectral transform of the output, $P_{ref}(s)$, by the spectral transform of the input $r(s) = \frac{\acute{m_f}(s)}{\bar{m_f}}$. For non-linear systems however, the system responds

at frequencies not just limited to the input frequency, and the gain and phase change applied by the system can depend on the frequency and amplitude of the input. Weakly non-linear systems, such as those modeled with flame describing function or the G Equation for example, also have an input dependent gain and phase shift, but their main output frequency will be the same as the input frequency (to first order, their response is essentially linear).

A set of finite-dimensional, low order, unstable systems is considered:

$$\frac{P_{ref}(s)}{r(s)} = \frac{(s^2+2c_z\omega_{z1}s+\omega_{z1}^2)(s^2+2c_z\omega_{z2}s+\omega_{z2}^2)}{(s^2+2c_{p1}\omega_{p1}s+\omega_{p1}^2)(s^2+2c_{p2}\omega_{p2}s+\omega_{p2}^2)} \quad (9)$$

$$\frac{V_c(s)}{r(s)} = \frac{1}{s+z_c} \quad (10)$$

With $\omega_{z1} = 150\,rad/s,\ \omega_{z2} = 250\,rad/s,\ \omega_{p1} = 200\,rad/s, \omega_{p2} = 500\,rad/s$, $c_{p1} = 0.02,\ c_{p2} = -0.02,\ z_c = 100\,rad/s, c_z = [-0.5,0.25]$.

III. ROBUST CONTROL DESIGN

Indeed, the bifurcation behavior of the combustor [23], and the non-linear behavior of the thermo-acoustic model whilst it is in limit cycle hinders the measurement of the underlying linearly unstable system which we wish to control [1]. Because of this, model obtained from limit cycle are noisy, and do not yield the gain and phase of the thermo-acoustic system. We have shown, however, that the phase information thus obtained can be accurately corrected to provide information for the linearly unstable system. The gain of the thermo-acoustic system remains unknown, and therefore the design of a plant based controller must allow for a sufficiently large phase and gain margin [22]. An alternative to plant based control lies with robust controllers were shown to perform well on systems with a moving acoustic discontinuity. They were able to stabilize the unstable system from limit cycle with uncertain model. Let us consider the combustor and the thermo-acoustic model (2,3,6,9,10) as a MIMO norm bounded form [24,29]:

$$\begin{aligned} \dot{x}(t) &= (A + \Delta A(t))x(t) + B(u(t) + \Delta_x(t)) \\ y(t) &= Cx(t) \end{aligned} \quad (11)$$

Where A and B are respectively the state and control matrix of the system, the state variables $x = (y_{fuel}, y_{oxid}, T, P_{ref}, V)$ belongs to R^5 and ΔA is the uncertainty in dynamic matrix. $x = (T, P_{ref})$ belongs to R^2 is a smooth measurable output vector. $u = (\overline{m}_f, m'_f)$ is the control vector.

A. Reformulating the problem to Equivalent sliding mode Control

Consider the following linear continuous sliding function [24-26]:

$$\sigma_x(t) = Sx(t) = B^T Px(t) \quad (12)$$

Where, $S \in R^{5x5}$, in the design of this control the SB is non-singular. From (6) and (7), the equivalent control law may be obtained as

$$u_{eq}(t) = -(SB)^{-1} SAx(t) \quad (13)$$

Where $S = B^T P$, and SB is non-singular. It should be remarked that the obtained control law contain some uncertain terms, which can be deduced from non-linear system, this can lead to a practical controller. The non-linear part of controller will be taken as [25]

$$u_{nl}(t) = -(SB)^{-1}(|SB|\delta_f + \varepsilon_0)sign(\sigma_x) \quad (14)$$

Where $|\Delta_x| \le \delta_f$ and ε_0 is a positive number. Select the Lyapunov function as given by [26]:

$$V_x = \frac{1}{2}\sigma_x^2 \qquad \dot{V}_x = \sigma_x \dot{\sigma}_x \quad (15)$$

From equations (13), (14) and (15) the following expressions are obtained:

$$\dot{\sigma}_x(t) = -(|SB|\delta_f + \varepsilon_0)sign(\sigma_x) + SB\Delta_x \quad (16)$$

$$\dot{V}_x(t) = -(|SB|\delta_f + \varepsilon_0)|\sigma_x| + \sigma_x SB\Delta_x \le -\varepsilon_0|\sigma_x| \quad (17)$$

As proved in [25,26,30], is asymptotically stable if $-\varepsilon_0|\sigma_x|$ is asymptotically stable for $\varepsilon_0 \ge 0$, with ΔA and Δ_x are bounded.

B. Auxiliary feedback and stability analysis

To solve this problem, the sliding mode controller will be designed with a feedback control as follows:

$$u(t) = -Kx(t) + \nu(t) = u_{eq}(t) + u_{nl}(t) \tag{18}$$

K is chosen to get a $\tilde{A} = A + \Delta A - BK = \bar{A} + \Delta A$ stable in closed loop. Selecting the Lyapunov function as:

$$\begin{aligned} \dot{V} &= 2x^T P\dot{x} = 2x^T(\tilde{A}x(t) + B(\nu + \Delta_x)) \\ &= 2x^T P\bar{A}x(t) + 2x^T P\Delta Ax(t) + 2x^T PB(\nu + \Delta_x) \\ &= 2x^T P(\bar{A} + \Delta A)x(t) + +2x^T PB(\nu + \Delta_x) \end{aligned} \tag{19}$$

For $t \geq t_0$, the sliding variable $\sigma_x(t) = B^T Px(t) = 0$ which implies $2x^T PB(\nu + \Delta_x) = 0$.

Theorem 1: The uncertain sliding dynamics in (19) is asymptotically stable in closed loop with a state feedback, for Lyapunov function candidate $V = x^T Px$, if there exist a symmetric matrix $P > 0$, satisfying the following LMI:

$$\begin{aligned} &\max \alpha \\ &subjected\ to\ (A + \Delta A - BK)Q + Q(A + \Delta A - BK)^T \\ &+ 2\alpha Q < 0 \\ &Q > 0 \\ &\alpha > 0 \end{aligned} \tag{20}$$

With $L = KQ$ and $Q = P^{-1}$. The closed loop system matrix has its eigen values in the strict left hand side of the line α, in complex s-plan.

C. Robust design

The equation (20) is non-linear matrix inequality, difficult to solve being non convex, can be solved by increasing α in order to shift the eigen value of $A + \Delta A - BK$ progressively toward stable plane. However, in order to make the controller more robust in face of the model uncertainties, and non-linearity, we will propose robust design [26-30].

The uncertain matrix $\Delta A = M\Delta(t)N$, where M and N are known, and $\Delta(t)$ is an unknown matrix satisfying $\Delta(t)^T \Delta(t) \leq I$ [24-26]. Note that this congruence transformation does not change the definiteness of $\Delta(t)$.

Theorem 2: The uncertain sliding dynamic in (20) can be robustly stabilized if there exists $Q^T > 0$, $K > 0$ and $\alpha > 0$ satisfying the following LMI:

$$\begin{bmatrix} AQ + QA^T - BKQ - Q^T K^T B^T + 2\alpha Q + \varepsilon_1 MM^T & NQ \\ Q^T N^T & -\varepsilon_1 I \end{bmatrix} < 0 \tag{21}$$

Proof: by replacing ΔA by $M\Delta(t)N$ in (20), it yields

$$\begin{aligned} &AQ + QA - BKQ - QBK + 2\alpha Q + M\Delta NQ \\ &+ Q^T N^T \Delta M^T < 0 \end{aligned} \tag{22}$$

With the assumption $\Delta(t)^T \Delta(t) \leq I \rightarrow \|\Delta(t)\| < I$, as given in [26-27], it follows that:

$$M\Delta NQ + Q^T N^T \Delta M^T \leq \varepsilon_1^{-1} MM^T + \varepsilon_1 NQQ^T N^T \tag{23}$$

With $\varepsilon_1 > 0$, the inequality (17) is satisfied if the following equation is satisfied:

$$\begin{aligned} &AQ + QA - BKQ - QBK + 2\alpha Q + \varepsilon_1^{-1} MM^T \\ &+ \varepsilon_1 NQQ^T N^T < 0 \end{aligned} \tag{24}$$

Using Schur complement, we can put (24) in the form (21) as desired. The proposed robust Sliding Mode Controller (SMC) can be constructed similar to the previous algorithm by replacing (19) by (20)[27].

D. Multi-objective optimization algorithms

A general approach to solve problems with multiple conflicting objectives is to find the set of acceptable solutions that provide tradeoffs among the conflicting objectives. The set of acceptable solutions contains non-dominated solutions, which are solutions that satisfied the condition that no other solutions exist that dominated it. attempts to directly generate multiple tradeoff solutions by considering all objectives simultaneously. It include non-Pareto-based approach, such as VEGA (vector evaluated genetic algorithm) by schaffer, and Pareto-based approach, such as MOGA (multi-objective GA) by Fonseca and Fleming , NSGA-II (non-dominated sorting GA) by Deb et al, NPGA (Niched Pareto GA) by Horn et al, SPEA (strength Pareto EA) by Zitzler and Thiele [31]. A weakness of non-Pareto-based approach is that it cannot generate compromise solutions and it is sensitive to the shape of the Pareto front. For Pareto-based method, it has advantages in that it can solve ill-posed problem, not susceptible to the shape of Pareto front, and it is highly efficient in generating multiple solutions in a single run. In addition, with the adoption of meta-heuristics (Nguyen and Kachitvichyanukul,, the efficiency, the search ability, and the flexibility for handling various models have been much improved. Hence, recent research interests focus more on the search of Pareto front for MO problems via meta-heuristics [31]. Nguyen and Kachitvichyanukul developed a Pareto based multi-objective particle swarm optimization (MOPSO) algorithm which takes advantage of PSO to search for multiple solutions in the multi-objective space. An Elite

archive is adopted to store the non-dominated solutions found so far and the guidance references for the swarm movement are selected from these non-dominated solutions to ensure that the swarm tends to move toward the direction of the Pareto front. Several ways to select reference particles to guide the particle movement are proposed as different movement strategies to diversify the movement of particles. MOPSO is tested using standard test functions and such real world problems as engineering design problem and portfolio optimization problem [32]. The experimental results showed robust solutions with high quality Pareto front and MOPSO outperforms NSGA-II. MOPSO was also applied successfully to solve multi-objective job shop scheduling problems as reported in Wisittipanich and Kachitvichyanukul. The idea of movement strategies is also extended as mutation strategies for multiple objective differential evolution (MODE) as reported in Wisittipanich and Kachitvichyanukul [31,33]. The aim Our strategy is to obtained a stable system using an active controller for the thermo-acoustic model so no heat losses and zero change in kinetic or potential energy, then the maximum flame temperature can be achieved by applying a multi-objective genetic algorithm (MOGA) [34,35] or multi-objective particle swarm optimization (MOPSO) [35] to optimized the parameters of the sliding mode control algorithm (SMC). These parameters were chosen to:

1st. Get system stable with maximum power, it means the error of temperature tend to zero at maximum set point, with the least possible amount of fuel.

2nd. The output can be improved by burning the mixture under turbulent conditions (Equivalence Ratio) and increasing the fuel conversion rate and reduce the NOx emission (Output fuel tend to zero).

3rd. Achieve satisfactory actuation, by consuming less power and the actuator's frequency response and its durability must match the frequency of combustion-driven oscillations, limiting the range of applications at very high frequency (control signal variation tends to zero).

$$
\begin{aligned}
&min \quad f_1(\delta_f,\varepsilon_0)=\int_0^{t_{op}}\sigma_x(\delta_f,\varepsilon_0)^2dt \\
&f_2(\delta_f,\varepsilon_0)=\int_0^{t_{op}}y_i(\delta_f,\varepsilon_0)^2dt, i=fuel,oxid \\
&f_3(\delta_f,\varepsilon_0)=\int_0^{t_{op}}\overline{m}_f(\delta_f,\varepsilon_0)^2dt \\
&f_4(\delta_f,\varepsilon_0)=\int_0^{t_{op}}m'_f(\delta_f,\varepsilon_0)^2dt \\
&subjected\ to\ \delta_f>0,\varepsilon_0>0,-(|SB|\delta_f+\varepsilon_0)k\sigma_x{}^2+\sigma_x SB\Delta_x<0
\end{aligned}
\qquad (26)
$$

We selected four objectives function: f1 Output error (temperature, acoustic pressure), f2 fuel conversion rate, f3 actuator energy, and f4 fuel fluctuation (equivalence ratio). The inequality constraint can be leads to feasible optimization

$-(|SB|\delta_f+\varepsilon_0)k\sigma_x{}^2+\sigma_x SB\Delta_x<-\varepsilon_0 k\sigma_x^2$ for $\varepsilon_0>0$

with $k\sigma_x^2$ is positive definite function [15],[19].

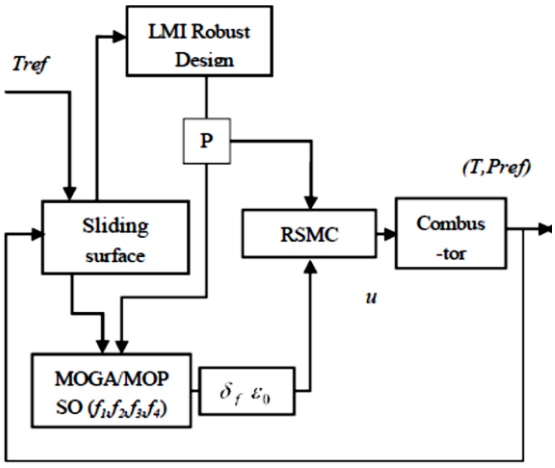

Figure 3. Block diagram of the proposed controller

IV. SIMULATION AND RESULTS

Then, with the flexibility of the GA and PSO algorithms, these numerical bounds can be used directly in an online optimization of decision variables δ_f , ε_0 .

TABLE 1. GA PARAMETERS USED IN SIMULATION

Parameter	Value
Population size	40
Generations	50
Type of selection	Roulette wheel
Type of crossover	Intermediate
Fitness function	Equation (26)
Constraints-handling methods	Penalty function
Type of mutation	Adapt feasible
Crossover Ration	0.8

TABLE 2. PSO PARAMETERS USED IN SIMULATION

Parameter	Value
Maximum iterations	50
Population size	40
Dimension	2
Value of K2	2.0
Maximum weight	0.90
Minimum weight	0.40
Fitness function	Equation (26)

By running the simulation of the thermos-acoustic and combustor models with the data provided [21] and [22], optimization algorithms provide the optimal values of decision variables as (MOGA $\delta_f=4$, $\varepsilon_0=5.3162$, MOPSO: $\delta_f=4{,}9010$, $\varepsilon_0=5.6516$). It should be noted that in this study, we focus on integrating the multi-objective meta-heuristic optimization (MOGA, MOPSO) in order guarantee the time performances and robustness

regarding model uncertainties; we aren't focused on the comparison between the performances of the both optimization strategies. The results found in the optimization are similar for the both strategies. In order to obtain realistic simulation a white noise is applied as an acoustic velocity perturbation at the upstream end of the duct.

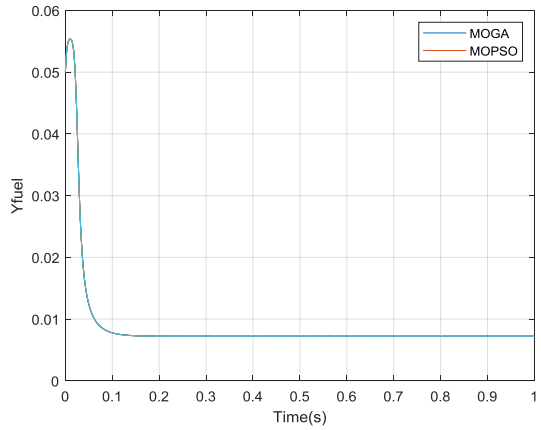

Figure 4. Fuel mass fraction inside combustor

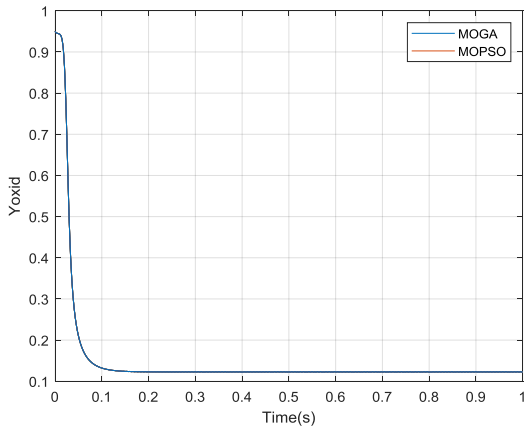

Figure 5. Oxider mass fraction inside combustor

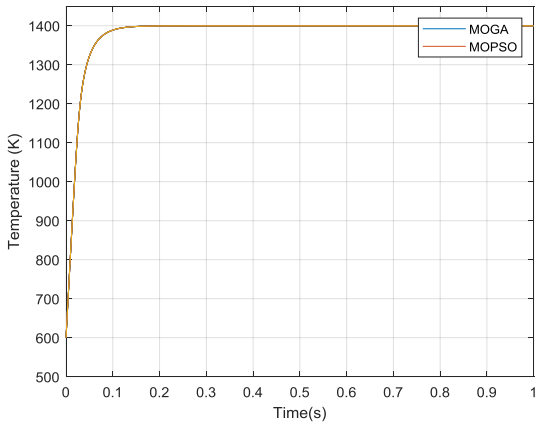

Figure 6. Output temperature of combustor

The modified white noise is generated such that it mostly contains energy within the frequency range of interest, selected here as 30 Hz to 3000 Hz, and 3 different amplitude are applied to check the reaction of the active control.

The mass fractions of the fuel and the oxidizer fall rapidly and eventually stabilize near zero. This result implies that nearly all of the fuel and the oxidizer are being converted to products, which is consistent with the ratio of the fuel and oxidizer, which was chosen to be close to the stoichiometric value. The value of the product mass fraction inside the combustor would be close to unit. This gives credence to the assumption that the exit fluid consists of mostly products of combustion. As can be observed from Fig.6, the combustor raises the temperature of the working fluid from 600K to approximately 1400 K. These results are consistent with the test data provided in [5].

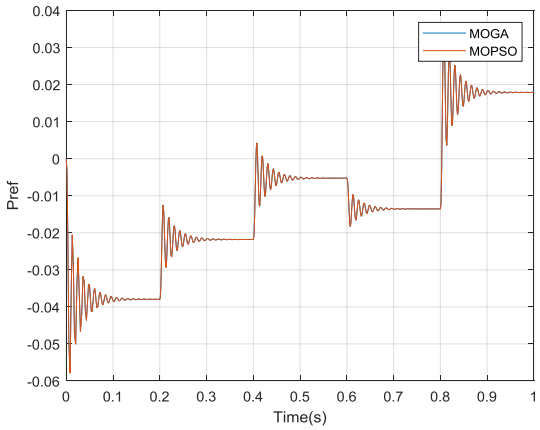

Figure 7. Output flame pressure

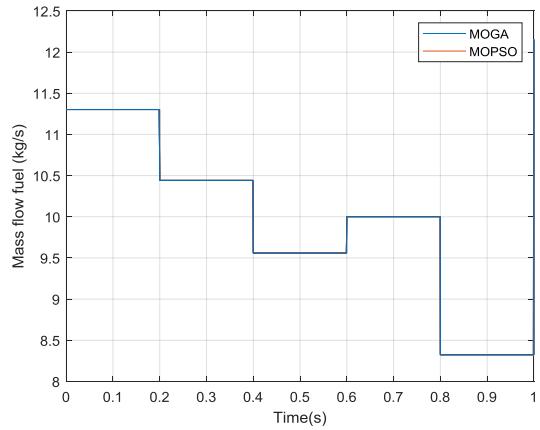

Figure 8. Fuel mass flow

As shown in Fig. 7, the pressure was stabilized due to the active controller. The actuation from the controller modifies the fuel mass flow rate as show in Fig.8 to obtain a stable flame. This result obtained due to the parameter of δ_f , ε_0 switching control optimized by MOSMO and MOGA under the four functions objectives that we mentioned before. Plus a stable flame due to the active controller.

V. CONCLUSION

Active control is able to stabilize combustor instabilities by interrupting the coupling between the temperature, mass

fraction and the thermo-acoustic model. Active robust controllers whose parameters optimized, offer an efficient means of maintaining control across a range of operating conditions. Robust sliding mode strategies are an attractive type of active controller as they do not require detailed prior system characterization nor on-line system identification. Instead, they utilize some general properties satisfied by a wide range of uncertain systems, and optimize according to Linear matrix inequality (LMI) based schemes. This approach was applied to a numerical model of an unstable combustion system. The modified pressure measurement resulted in the robust design being effective in cases where it was not when a single pressure measurement was used, demonstrating the success of the approach. The proposed control design method utilizes a meta-heuristic optimization added to LMI optimization algorithm, which incorporates a Pareto front to manage the compromise between objectives systems to stabilize an unstable and uncertain system

REFERENCES

[1] Dan Zhao , Zhengli Lu , He Zhao , X.Y Li , Bing Wang , Peijin Liu .A review of active control approaches in stabilizing combustion systems in aerospace industry, Journal of Progress in Aerospace Sciences, Vol 97, February 2018.

[2] N. Olgac, U. Zalluhoglu, A.S. Kammer, A new perspective in designing delayed feedback control for thermoacoustic instabilities (TAI), Combust. Sci. Tech. 187(5), pp.697–720, 2015.

[3] U. Zalluhoglu, N. Olgac, A.S. Kammer, Delayed feedback control laws for Rijke tube thermoacoustic instability, synthesis and experimental validation, IEEE Trans. Contr. syst. Technol. 24 (5) , pp.1861–1867, 2016.

[4] S. Kozak, State-of-the-art in control engineering, J. Electr. Syst. Inf. Technol. 1,pp. 1–9, 2014.

[5] S.J. Illingworth, A.S. Morgans, Adaptive feedback control of combustion instability in annular combustors, Combust. Sci. Tech. 182 (1), pp.143–164, 2010.

[6] S. Murugappan, S. Acharya, D.C. Allgood, S. Park, A. Annaswamy, A.F. Ghoniem, Optimal control of a swirl-stabilized spray combustor using system identification approach, Combust. Sci. Technol. 175(1) , pp.55–81, 2003.

[7] S. Menon, Y. Sun, Fuzzy Logic Control of Reheat Buzz, 1996,ttps://doi.org/10.2514/6. 1996-2759. AIAA Paper 96-2759

[8] R. Blonbou, A. Laverdant, S. Zaleski, P. Kuentzmann, Active adaptive combustion control using neural networks, Combust. Sci. Tech. 156 (1) pp. 25–47, 2000.

[9] E. Gutmark, K. J. Wilson, K. H. Yu, K. C. Schadow, Active control of a liquid fueldump/bluff-body combustor using pulsed fuel injection. AIAA-95–0809, https://doi.org/10.2514/6.1995-809.

[10] A.S.P. Niederberger, D. Fritsche, K. Boulouchos, L. Guzzella, Thermoacousticinstability suppression by gain-delay and Hinf controllers designed for secondaryfuel injection, IEEE Trans. Contr.Syst. Technol. 17 (5) , pp.1028–1042, 2009.

[11] Y.C. Chu, K. Glover, A.P. Dowling, Control of combustion oscillations via H loopshaping, mu-analysis and integral quadratic constraints, Automatica, 39 , pp.219–231, 2003.

[12] [12] X. Yuan, K. Glover, Model-based control of thermo-acoustic instabilities in partially premixed lean combustion – a design case study, Int. J. Contr. 86 (11), pp., 2052–2066, 2013.

[13] S.J. Illingworth, A.S. Morgans, Advances in feedback control of Rijke tube thermoacoustic instability, Int. J. Flow Contr. 2 (4),pp.197–218, 2011.

[14] G.P. Liu, S. Daley, Output-model-based predictive control of unstable combustionsystems using neural networks, Contr. Eng. Pract. 7 (5) , pp.591–600, 1999.

[15] T.C. Lieuwen, V. Yang, Combustion Instabilities in Gas Turbine Engines: Operational Experience, Fundamental Mechanisms, and Modeling, AIAA Inc.,USA, 2005.

[16] S. Candel, Combustion instabilities coupled by pressure waves and their active control, Proc. Combust. Inst., 24 (1) , pp.1277–1296, 1992.

[17] A.P. Dowling, A.S. Morgans, Feedback control of combustion oscillations, Annu.Rev. Fluid Mech. 37 (1–2) , pp.151–182, 2005.

[18] J. Rubio-hervas, M. Reyhanoglu, W. MacKunis, Observer-based sliding mode control of Rijke-type combustion instability, J. Low Freq. Noi. Vib. Act. Contr. 34(2) , pp. 207–217, 2015.

[19] X.Y. Li, D. Zhao, Feedback control of self-sustained nonlinear combustion oscillations, J. Eng. Gas Turbo. Pow. 138 (2016), 061505.

[20] C. Fannin. Linear Modeling and Analysis of Thermo-acoustic Instabilities in a Gas Turbine Combustor, PhD dissertation, Virginia Polytechnic Institute and State University, 2000.

[21] [21] C.M.A.Luzzato, Modelling and control of combustion instabilities with anchored laminar ducted flames, Phd Thesis, Department of Aeronautics, Imperial College London, August 2, 2015.

[22] Morgans, A. S., & Annaswamy, A. M. Adaptive Control of Combustion Instabilities for Combustion Systems with Right-Half Plane Zeros. Combustion Science and Technology, 180(9), pp.1549–1571, 2008.

[23] L.Acampora, E.Mancusia, F.S. Marrab, Bifurcation Analysis of Perfectly Stirred reactors with Large Reaction Mechanisms, chemical 43 (1), engineering transactions, 2015.

[24] A.Debbah, H.Kharfene and A.Kharboua, " Using Robust sliding mode controller to improving the aerodynamic performance of a gas turbine", The 4thinternational Seminar on new and renewable energies, Ghardaia-Algeria 24-25 October, 2016.

[25] Tsai C. and Wu H., "Robust passivity-based control of weakly minimum phase nonlinear uncertain systems: An application to manipulator," in 2009 7th Asian Control Conference, ASCC 2009, Hong Kong, China, pp. 919-924, 2009.

[26] A.Debbah, Hamid Kharfane, GA/PSO robust sliding mode control of aerodynamics in gas turbine, Acta Universitatis Sapientiae, Electrical and Mechanical Engineering,Vol 10(1), 2019.

[27] V.Q.Leu, H.H.Choi, and J.W.Jung, "LMI based sliding mode speed tracing control design for surface-mounted permanent magnet synchronous Motors",Journal of electrical engineering and technology ,Vol.7,No.4,pp.513-523, 2012.

[28] L. Der-Cherng, S. M. Ren, and C. Shih-Tse, "A Feedback linearization Design for Compressor's Surge Control," in Industrial Technology, 2008. ICIT 2008. IEEE International Conference on, pp. 1-6, 2008.

[29] S. Boyd, EL.Ghaoui, E. Feron , and V. Balakrishnan, Linear Matrix Inequalities in System and Control Theory. SIAM, Philadelphia, 1994.

[30] [30] Lui, J., “Intelligent Control Design and MATLAB Simulation”. Springer. Tsinghua University Press. Beijing, 2018.

[31] Juneja, M., and Nagar,S.K., “ Particle swarm optimization algorithm and its parameters: A review”, in Proc. of International Conference on Control. Computing Communication and Materials (ICCCCM), pp.1-5, 2016.

[32] Kramer,O., “A Review of Constraint-Handling Techniques for Evolution Strategies”, Journal of applied computational intelligence and soft computing, Vol.2010, pp.1-11, January, 2010.

[33] Deb, K., “An efficient constraint handling method for genetic algorithm. Computer methods in applied mechanics and engineering”, Journal of Computer Methods in applied Mechanics and engineering Elsevier, 186 (2-4), pp.311-338, June 2000.

[34] Khan, A.A., and Mir, R.N., “Optimization of Constrained Function Using Genetic Algorithm”, Journal of Computer Engineering and Intelligent System, Vol.8, No.2, pp. 11-15, 2017.

[35] Shieh, M.-D., Li, Y., & Yang, C.-C, Comparison of multi-objective evolutionary algorithms in hybrid Kansei engineering system for product form design. Advanced Engineering Informatics, 36, pp.31–42, 2018.

Contribution on modeling and control of a wind power system based on fuzzy

Djalal Baladji
Laboratory of Electronics and New Technologies University of Oum El Bouaghi.
Baladji .djalal @univ-oeb.dz
baladji.djalal@gmail.com

Pr.Kheireddine Lamamra
Laboratory of Electronics and New Technologies University of Oum El Bouaghi.
Lamamra.kheireddine@univ-oeb.dz
l_kheir@yahoo.fr

Abstract—In this work, we study the modeling and control of a wind energy conversion chain based on a Dual Power Asynchronous Machine. First, the mathematical model of the whole system under study is developed in d-q Park coordinates. Then, the proposed control strategy is designed based on a fuzzy logic control technique that gives good results. Finally, the results of the different simulations of the whole conversion chain, performed under MATLAB/Simulink environment, are presented.

Keywords— wind power, double asynchronous generator power supply (GADA) , fuzzy control, MPPT.

1 Introduction:

Nowadays, wind energy has become a viable solution for electricity generation as a complement to other energy sources. The wind power system studied converts the kinetic energy of the wind into mechanical energy, usually this energy is transformed into electrical energy by the generator which allows a variable speed production of electricity. This allows the wind resource to be better exploited for different climatic conditions (wind speed...).

In fact, the rotor captures the kinetic energy of the wind and transmits its rotation directly to the main shaft. The kinetic energy has been converted into mechanical energy. A fast motion is transmitted to the output shaft, which is connected to the generator, which converts the mechanical energy of the rotary motion into electrical energy, before injecting the produced energy into the grid [1], the generator is connected to power converters. The converter on the grid side controls the DC bus voltage and the power factor [2, 3]. In addition, the generator-side power converter controls the active and reactive power produced by the GADA [4]. This paper presents a method for controlling a Dual Power Asynchronous Generator, which provides a tool for recursive control law design based on fuzzy logic [5].

2 Wind turbine system :

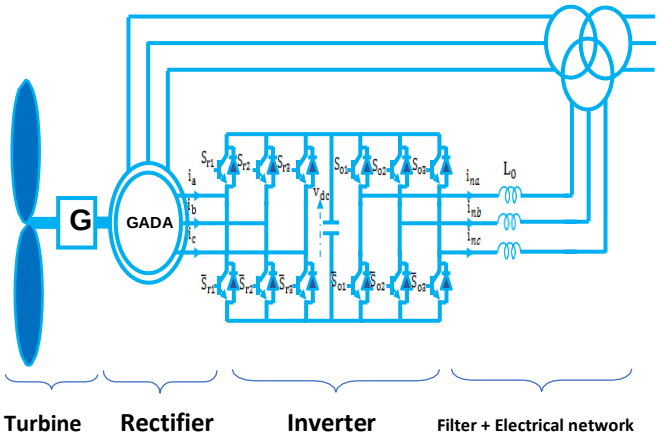

Figure 1: Architecture of a GADA-based wind power system

A. Modelling the 'Generator - DC/AC' combination

The modeling of the Double-fed asynchronous machine has already been the subject of numerous studies, the choice of a representation model, whether formal or derived from an identification, is always made according to the type of control to be carried out. The machine is supplied with voltage: the components of the control vector of the state equation will therefore be voltages. The different quantities will initially be expressed in their respective references (a, b, c). The first change of variable will allow expressing its voltages in the reference frame (d, q) [4]. Like any machine, the GADA can be represented by three stator windings and three rotor windings.

The voltage equation is written:

For the stator $v_s = [R_s][i_s] + \frac{d}{dt}[\varphi_s]$

with $v_{s=}[v_{sa} \quad v_{sb} \quad v_{sc}]^T$: Stator voltages

$i_{s=}[i_{sa} \quad i_{sb} \quad i_{sc}]^T$: Stator currents

$\varphi_{s=}[\varphi_{sa} \quad \varphi_{sb} \quad \varphi_{sc}]^T$: Stator flux

For the rotor: $v_r = [R_r][i_r] + \frac{d}{dt}[\varphi_r]$

with:

$v_{r=}[v_{ra} \quad v_{rb} \quad v_{rc}]^T$: Rotor voltages

$i_{r=}[i_{ra} \quad i_{rb} \quad i_{rc}]^T$: Rotor currents

$\varphi_{r=}[\varphi_{ra} \quad \varphi_{rb} \quad \varphi_{rc}]^T$: Rotor flux

The most appropriate model to study the dynamic behavior of the machine and the implementation of the control laws is a model expressed in PARK coordinates [6], The park model is the replacement of the stator windings (a,b,c) by equivalent windings (d,q). We can switch from one to the other reference point using a transition matrix. The change of variable to the voltage, current, and flux equations gives :

$$[i_{rdq}] = p(\theta)[i_{rabc}]$$
$$[v_{rdq}] = p(\theta)[v_{rabc}]$$
$$[\varphi_{rdq}] = p(\theta)[\varphi_{rabc}]$$

Hence, the stator and rotor voltage equations of the MADA are written:

$$v_{sd} = R_s i_{sd} + \frac{d}{dt}\varphi_{sd} - \varphi_{sq}\omega_s$$
$$v_{sq} = R_s i_{sq} + \frac{d}{dt}\varphi_{sq} - \varphi_{sd}\omega_s$$
$$v_{rd} = R_r i_{rd} + \frac{d}{dt}\varphi_{rd} - \varphi_{rq}\omega_r$$
$$v_{rq} = R_r i_{rq} + \frac{d}{dt}\varphi_{rq} - \varphi_{rd}\omega_r$$

In the following, we consider the vector $[i_{rd}\ i_{rq}\ \varphi_{sd}\ \varphi_{sq}\ \omega]^T$ *as the state vector and* $[v_{rd}\ v_{rq}]$ *as the control variables, hence the model of the overall system in state space is expressed in d-q coordinates as follows:*

$$\frac{d\,i_{rd}}{dt} = -\mu i_{rd} + \omega_r i_{rq}\,\alpha\frac{R_s}{L_s}\varphi_{sd} + \frac{1}{L_r\sigma}v_{rd} - \alpha v_{sd}$$
$$\frac{d\,i_{rq}}{dt} = -\mu i_{rq} - \omega_r i_{rq}\,\alpha p\omega\varphi_{sq} + \frac{1}{L_r\sigma}v_{rq} - \alpha v_{sq}$$

with:

$\mu = \frac{R_s}{L_r\sigma} + \frac{R_s M_{sr}^2}{L_r L_s^2\sigma}$ and $\alpha = \frac{M_{sr}}{L_r L_s\sigma}$

We have expressed the equations of the machine but there is also the electromagnetic torque. The latter can be derived from the expression of the co-energy obtained using a power balance

$$C_{em} = \frac{p\,M_{sr}}{L_s}\left(\varphi_{sq} i_{rd} - \varphi_{sd} i_{rq}\right)$$

And the relationship between torque and speed is written :

$$j\frac{d\omega}{dt} = C_{em} - C_r - f\omega$$

3 Application of fuzzy logic to MADA active and reactive power control

In this section, we will follow the steps shown in the Main Steps diagram when designing an RLF to design two Mamdani type fuzzy logic controllers for the current and power control loop, to improve the control performance, both controllers are of the same type, and have the same membership functions. The difference is only in the normalization gains. The general block diagram of the fuzzy logic control of MADA is given in fig (2).

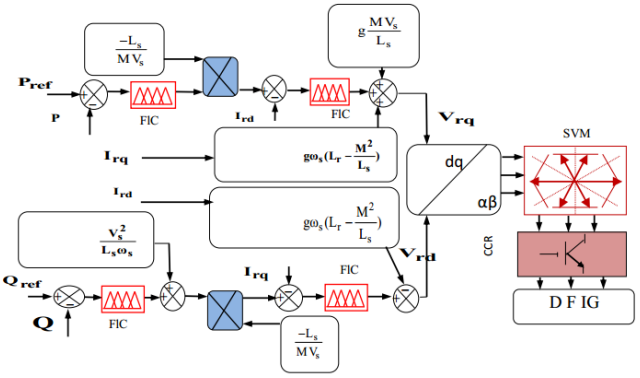

Figure 2: Block diagram for fuzzy logic control of MADA

4 Robustness study:

The simulation results reported in the following figures concern the control of the wind power conversion chain based on a double-fed variable-speed asynchronous machine, with the application of reference steps of active and reactive powers.

From the following figures, we can see that the measured active and reactive power quantities follow their reference values, and from these results, better tracking of the fuzzy controllers than the PI controllers.

For the robustness tests of the fuzzy controller control, we studied the influence of the variation of

the rotor resistance R_r and the inductance L_r on the control performance.

We simulated the system for a gradual increase of 150% in resistance and rotor inductance at time t=0.25, and a return to their initial values at t=0.35. The following figures show the results of the simulation test.

The simulation results show respectively that these parametric variations introduced at time t=0.25 have a slight influence on the performance of the control; in contrast to the PI controller which is influenced leading to destabilization.

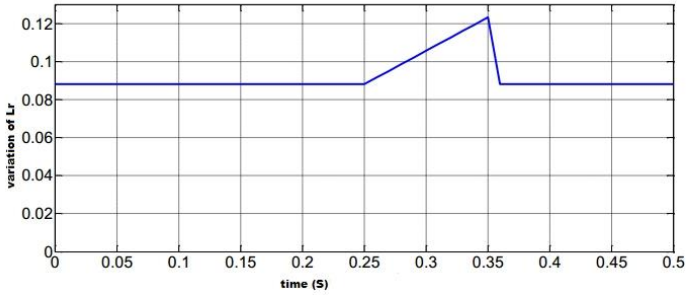

Figure 3 : Variation of rotor inductance

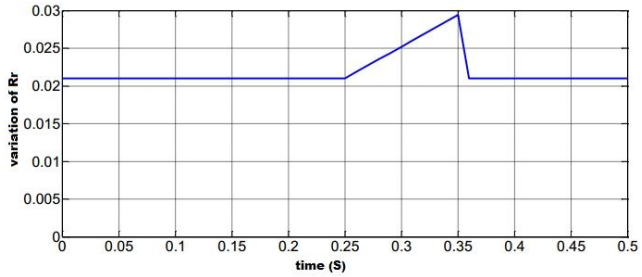

Figure 4: The disappearance of the rotor resistance

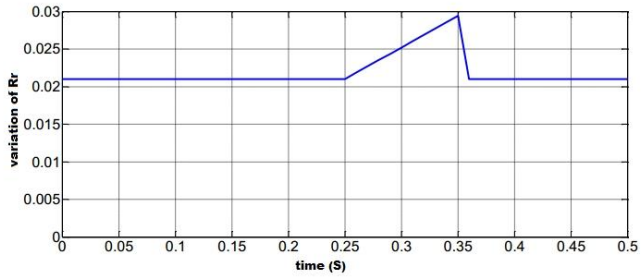

Figure 5: Active power with a fuzzy controller

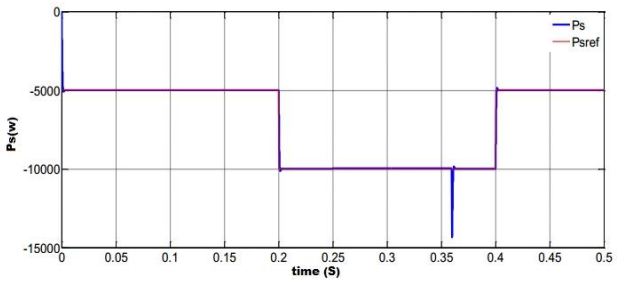

Figure 6: Active power with a fuzzy controller

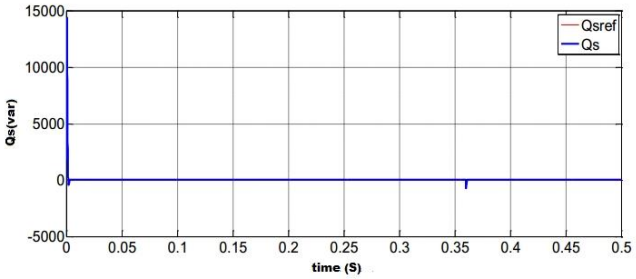

fig.6: Reactive power with a fuzzy controller

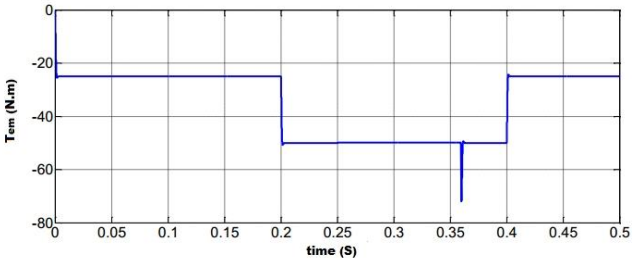

Figure 7: Electromagnetic torque with a fuzzy controller

5 Conclusion:

In this paper, the technique and basic notions of fuzzy logic were presented, and aspects of fuzzy logic control (FLC), as well as the design of a fuzzy controller, were introduced while justifying our choice of this type of control which lies in its ability to deal with the imprecise, the uncertain and the vague of its simplicity of design. A fuzzy controller-based simulation was carried out to perform speed control in place of the PI controller of a dual-fed asynchronous machine.

The simulation results obtained show that the FLC has a very satisfactory tracking performance, and has proven its efficiency, especially in parametric variations. The major problem in the design of the FLC is the choice of membership functions for the input and output variables.

References

[1] Karim Noussi, Abdelmajid Abouloifa, Hanane Katir, Ibtissam Lachkar, Fouad Giri, "Nonlinear control of grid-connected wind energy conversion system without mechanical variables measurements" *ijpeds.v12.i2.pp1139-1149*

[2] Ankamreddi Venkataramana, K.Narendrababu and D Ravi Kishore "Quasi Power Factor Correction for High Efficient AC/DC Converter" *nternational Journal for Modern Trends in Science and Technology, Learn. Syst., 7(05): 206-211, 2021*

[3] Kangaji, Ladislas and Abo-Al-Ez, Khaled M. and Orumwense, E.F.," Modelling and Performance Analysis of Grid Connected PMSG Based Tidal Generation System (July 26, 2021)". *AIUE Proceedings of the 2nd Energy and Human Habitat Conference 2021*.

[4] Khojet El Khil. S, 2006. Vector control of a doubly powered asynchronous machine (DPM). PhD thesis, Institut National Polytechnique de Toulouse.

[5] K. Noussi, A. Abouloifa, H. Katir and I. Lachkar, "Modeling and Control of a Wind Turbine Based On a Doubly Fed Induction Generator," 4th World Conference on Complex Systems (WCCS), *2019, pp. 1-5,*

[6] Alireza Rezvani, Majid Gandomkar, "Modeling and control of grid connected intelligent hybrid photovoltaic system using new hybrid fuzzy-neural method" *Solar Energy, Volume 127, 2016, Pages 1-18.*

[7] S. Boersma *and al*., "A tutorial on control-oriented modeling and control of wind farms," *2017 American Control Conference (ACC)*, 2017, pp. 1-18.

[8] Dana-Alexandra Ciupageanu, Linda Barelli and Gheorghe Lazaroiu "Real-time stochastic power management strategies in hybrid renewable energy systems: A review of key applications and perspectives" *Electric Power Systems Research, Volume 187,2020,*

[9] Christian Klemm and Peter Vennemann "Modeling and optimization of multi-energy systems in mixed-use districts: A review of existing methods and approaches" *Renewable and Sustainable Energy Reviews, Volume 135,2021*.

[10] Rushdi, Mostafa A. and Rushdi, Ahmad A. and Dief, Tarek N. and Halawa, Amr M. and Yoshida, Shigeo and Schmehl, Roland "Power Prediction of Airborne Wind Energy Systems Using Multivariate Machine Learning" *Energies,13,2020.*

[11] Mosavi, Amir and all "State of the Art of Machine Learning Models in Energy Systems, a Systematic Review" Energies,12,2019 .

[12] Yanfeng Liu, Sisi Yu, Ying Zhu, Dengjia Wang, Jiaping Liu "Modeling, planning, application and management of energy systems for isolated areas: A review" *Renewable and Sustainable Energy Reviews, Volume 82, Part 1, 2018, Pages 460-470.*

[13] Beibei Xu and all "Modeling a pumped storage hydropower integrated to a hybrid power system with solar-wind power and its stability analysis" *Applied Energy, Volume 248, 2019, Pages 446-462.*

[14] Chengshan Wang and all "Modeling and optimal operation of community integrated energy systems: A case study from China" *Applied Energy, Volume 230, 2018, Pages 1242-1254*

[15] X. Li and S. Wang, "A review on energy management, operation control and application methods for grid battery energy storage systems," *in* CSEE Journal of Power and Energy Systems, *2019.*

[16] X. Li and S. Wang, "A review on energy management, operation control and application methods for grid battery energy storage systems," *in* CSEE Journal of Power and Energy Systems, *2019.*

[17] K. Kumar, N. Ramesh Babu and K. R. Prabhu, "Design and Analysis of RBFN-Based Single MPPT Controller for Hybrid Solar and Wind Energy System," *in* IEEE Access, *vol. 5, pp. 15308-15317, 2017.*

[18] R. Anilkumar, G. Devriese and A. K. Srivastava, "Voltage and Reactive Power Control to Maximize the Energy Savings in Power Distribution System With Wind Energy," *in* IEEE Transactions on Industry Applications, *vol. 54, no. 1, pp. 656-664, Jan.-Feb. 2018.*

[19] Mohammad Mohammadi, Younes Noorollahi, "Behnam Mohammadi-ivatloo, Fuzzy-based scheduling of wind integrated multi-energy systems under multiple uncertainties" *Sustainable Energy Technologies and Assessments, Volume 37, 2020.*

[20] Prabodh Bajpai, Vaishalee Dash, "Hybrid renewable energy systems for power generation in stand-alone applications: A review*" Renewable and Sustainable Energy Reviews, Volume 16, Issue 5, 2012, Pages 2926-2939.*

[21] Aqeel Ahmed Bazmi, Gholamreza Zahedi "Sustainable energy systems: Role of optimization modeling techniques in power generation and supply—A review" *Renewable and Sustainable Energy Reviews, Volume 15, Issue 8, 2011, Pages 3480-3500*

[22] M. Aly, E. M. Ahmed and M. Shoyama, "Thermal and Reliability Assessment for Wind Energy Systems With DSTATCOM Functionality in Resilient Microgrids," in *IEEE Transactions on Sustainable Energy*, vol. 8, no. 3, pp. 953-965, July 2017.

[23] B. K. Bose, "Power Electronics, Smart Grid, and Renewable Energy Systems," *in* Proceedings of the IEEE.

Study and simulation of a photovoltaic solar panel connected to the electrical network

Mounira MEKKI[1], Djamila CHERIFI[2]

University of Oum El Bouaghi, Algeria (1), University of Saida, Algeria (2).

Abstract. *This work presents a photovoltaic generation system, and deals with the connection of a photovoltaic system to the three-phase electricity grid. This system injects solar energy into the grid as active power.*
This injection is carried out through a single-stage conversion system, consisting of a DC-DC converter (Boost) and an AC DC inverter.
MPPT controller is applied for point tracking of maximum power of PV system under normal lighting and temperature conditions.

Keywords: Photovoltaic system, DC-DC converter, DC-AC converter, MPPT, electrical network.

1. Introduction

Solar energy is a source of energy accessible to all (manufacturers, communities and individuals) .Thanks to it, it is possible to produce three types of energy: heat energy with solar thermal installations (heaters) solar water or solar air conditioning), electrical energy with photovoltaic solar installations and solar thermal concentration [1].
Photovoltaic electricity was first developed for stand-alone applications without connection to an electrical network, for example for telecommunications satellites or for isolated dwellings. It is now found in various power applications such as calculators, watches and other everyday objects. Indeed, this electricity produced by individual photovoltaic cells can supply various continuous loads without difficulty. More recently, with the emergence of photovoltaic installations connected to the distribution network, photovoltaics have undergone significant development as a means of producing electricity. This constant evolution has been made possible thanks to fundamental research carried out in the field of photovoltaic materials, but also by the progressive improvement of the devices for managing this energy carried out in parallel. Indeed, photovoltaic electricity is an intermittent energy source, non-linear in nature and dependent on many parameters such as irradiance and temperature. It was therefore necessary to adapt this source of energy to our mode of consumption, either by storing solar production in batteries or in any other means of storage under development, or by returning it to the public electricity grid [2].

2. Modeling of a photovoltaic cell

2.1 Real model with one diode

Regarding the behavior of an actual solar cell, two parasitic resistances are considered for a more accurate description. [3]

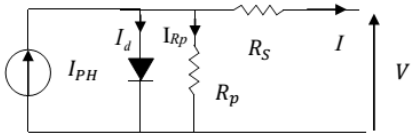

Fig 1. Diagram of the equivalent electrical circuit of a solar cell

$$I_{module} = I_{ph} - I_s\left[\exp\left(\frac{V_{module} + N_s.R_s.I}{N_s.n.V_T}\right) - 1\right] - \frac{V_{module} + N_s.R_s.I}{N_p.R_p}$$

2.2 Description of the BP 3160 module

The BP 3160 is a particularly successful 160W photovoltaic module. Multi-crystalline cells with anti-reflective coating ensure better absorption. A 3% tighter power tolerance guarantees a higher average power output. The BP 3160 has been specially designed for grid-connected applications, such as the roofs of large commercial buildings, small residential and power photovoltaic power plants. This module offers a first-rate quality-price ratio thanks to its 72 high-efficiency cells and its white Tedlar sheet.

2.1.1 Typical electrical characteristics of the BP 3160 module

Table II.1 summarizes the electrical characteristics of the PV module supplied by the manufacturer.

Parameters	Value
Maximum power	160[W]
Garanteed minimum power	155[W]
Voltage at maximum power	34,5[V]
Current at maximum power	4,55[A]
Short circuit current	4,8[A]
Open circuit voltage	44,2[V]

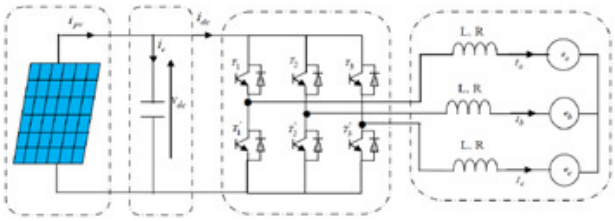

Fig 2. Overall simulation diagram of a photovoltaic module [4]

3. Results and discussions

3.1 Characteristics of the PV system

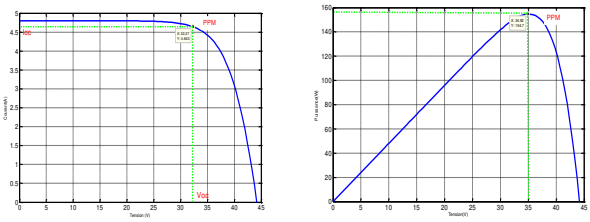

Fig 3. I(V) et P(V)

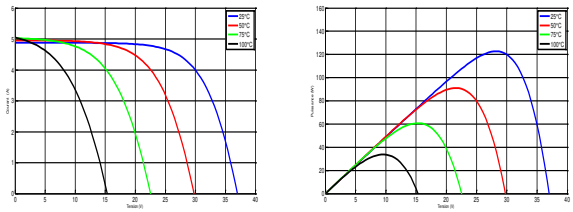

Fig 4. I (V) and P (V) under the influence of temperature

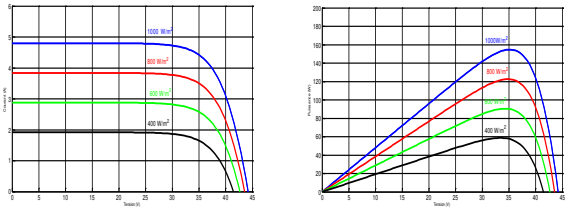

Fig 5. I (V) and P (V) under the influence of illumination

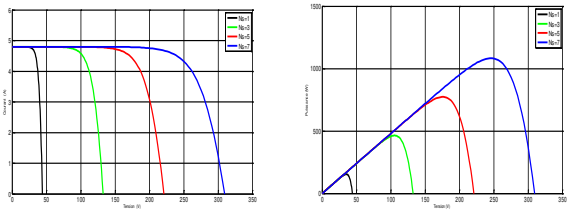

Fig 6. I (V) and P (V) of PV cells connected in series

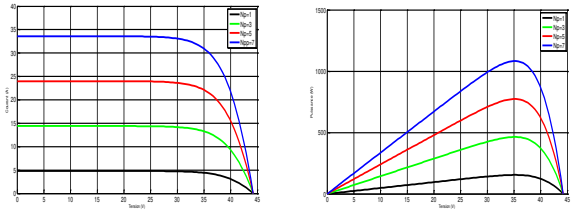

Fig 7. I (V) and P (V) of PV cells connected in parallel

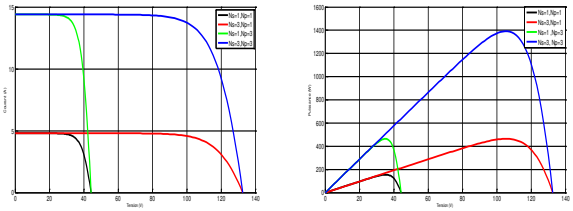

Fig 8. I (V) and P (V) of PV cells connected in mixed

3.2 Characteristics at the output of the boost chopper [5]:

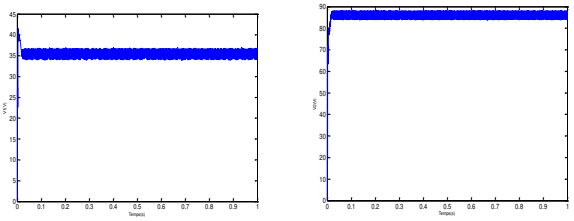

Fig.9 Voltage at the input and output of the chopper

3.3 Characteristics at the output of the inverter:

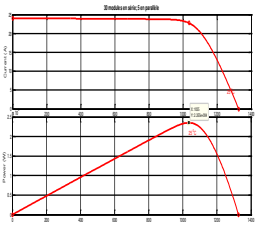

Fig 10. I(V) et P(V)

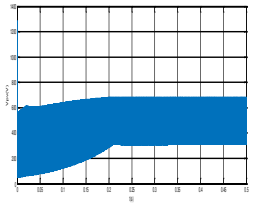

Fig 11. Vpv(t)

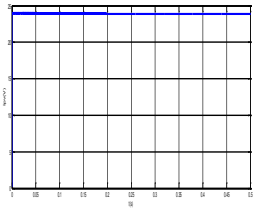

Fig 12. Ipv(t)

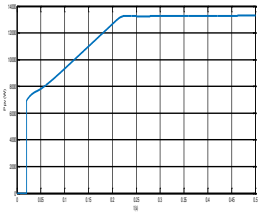

Fig 13. Ppv(t)

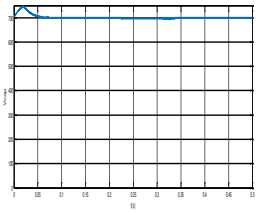

Fig 14. Vcap(t)

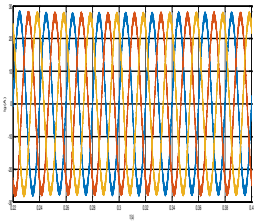

Fig 15. Ig(t)

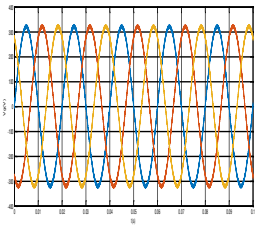

Fig 16. Vg(t)

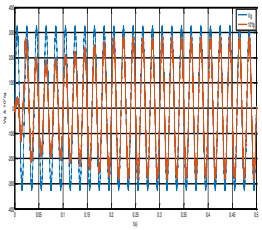

Fig 17. Phase shift between voltage and current

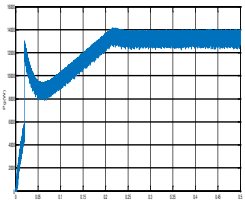

Fig 18. Pg(t)

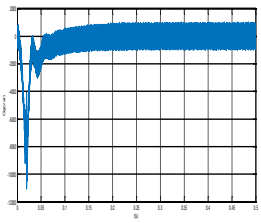

Fig 19. Pg(t)

The proposed system includes 30 modules in series and 5 modules in parallel. The simulation results obtained show that the voltage and current are amplified to reach 1035V and 23A, respectively. in which corresponds to a 5 times improvement in current over the output of a single panel and approximately 30 times in voltage as shown in “Fig. 10 ”

On the other hand, the supply voltage and current obtained from the PV modules reach respectively 600 V and 24 A, which corresponds to the maximum power supplied by the PV module, i.e. P = 1350W , as illustrated in the figures “Fig. 11, Fig.12 and Fig.13 ”. The proposed system is integrated directly into the grid, with the inverter supplying approximately 28 A to the grid (see “Fig. 15”). Note that the inverter reduces the input voltage considered as capacitor voltage (i.e. the output of the capacitor) by 700 V as shown in figure "Fig. 14 ”at approximately 320 V as shown in the figure“ Fig. 16 ”. The result obtained in “Fig.17 ”shows that the phase difference between the mains voltage and current is zero. In addition, the power injected into the grid is purely active, which means

6. Conclusion

Photovoltaic energy is gradually becoming a full-fledged energy source, increasingly required to produce electrical energy ranging from domestic to large power plants connected to the grid.

The modeling and control of a photovoltaic generator connected to the grid operating with a DC / DC converter (Chopper Boost) under the Matlab Simulink environment was presented. For the

photovoltaic system to operate at its maximum power, it must include an adaptation stage associated with an MPPT algorithm, several types of MPPT algorithms have been developed in the scientific literature. In our study, we used the "Perturb and Observe" (P&O) algorithm. The purpose of this configuration is of course to inject the active power produced by the photovoltaic generator into the grid while ensuring good quality of energy supplied to consumers.

In the last part we tried to perform a simulation under the Matlab Simulink environment of a photovoltaic plant connected to the electricity grid. We have presented the different transformations that take place in the chain from the photovoltaic generator which produces the direct current then passing the direct-alternating converter (the inverter) which is controlled by PWM and which has the function of transforming the energy of direct to alternating form to be able to supply alternating current loads.

The photovoltaic generator compensates on the one hand for losses in the inverter and on the other hand for losses in the overall circuit. If there is sufficient sunlight, the system can supply electrical energy to consumers and to the power grid.

References

[1] Laronde Rémi. "Essais Accélérés de Dégradation de Modules photovoltaïques". Thèse de doctorat. Institut National des Sciences Appliquées de Toulouse, 2009.

[2] Petibon Stéphane. "Nouvelles architectures distribuées de gestion et de conversion de l'énergie pour les applications photovoltaïques". Thèse de doctorat, Université de Toulouse, 2009.

[3] Boualem, Dendib , "Technique conventionnelles et avancée de poursuite MPPT pour des applications photovoltaïques : étude comparative" , Université Ferhat Abbes-Sétif Mémoire de Magister, Département d'électronique TS4/6338, 2007.

[4] V.Stéphane**.** "Systèmes photovoltaïques raccordes au réseau : Choix et Dimensionnement des étages de conversion. Thèse Doctorat Université de Grenoble 2010.

[5] M.Angel Cid Pastor.Conception et Réalisation de Modules Photovoltaiques Electroniques.Institut national des Sciences Appliquées de Toulouse , 2006.

Maximum Power Point Tracking for a PV System using Support Vector Machine

Bayarassou Houria
Laboratory of Electronics and New Technologies
Department of Electrical Engineering
University of Oum El Bouaghi Algéria
bayarassou.houria@univ-oeb.dz

Megri Abderrahim Fayçal
Laboratory of Electronics and New Technologies
Department of Electrical Engineering
University of Oum El Bouaghi Algéria
f.megri@univ-oeb.dz

Bennour Hachem
Laboratory of Electronics and New Technologies
Department of Electrical Engineering
University of Oum El Bouaghi Algéria
hachem.bennour@univ-oeb.dz

***Abstract*—Since the maximum power point (MPP) of a photovoltaic system changes with the changes in irradiation and temperature, an appropriate maximum power point tracking (MPPT) controller must be applied in the photovoltaic system.**

In this article, one of the powerful machine learning, support vector machine (SVM) is used as a predictive model, combining two traditional MPPT methods and the most commonly used: perturb and observation and incremental conductance to force photovoltaic systems to operate more efficiently In different weather conditions. The effectiveness of the proposed method is verified by Mathlab/Simulink simulation.

Keywords—PV system, maximum power point tracking (MPPT), support vector machine (SVM), Perturb and Observe (P&O), Incremental Conductance (INC).

I. INTRODUCTION

Energy production has become a crucial issue, as the need for energy has been increasing in recent years. Knowing that a large part of the world's energy consumption is covered by fossil sources (oil, natural gas, coal) that increase pollution [1-3].

Since then, renewable energies have become a hot topic. In this context, photovoltaic energy is one of the most important alternative energy sources. For this purpose, several methods called maximum power point tracking techniques (MPPT) have been developed and improved to obtain the maximum power and improve the efficiency of photovoltaic systems under varying atmospheric conditions (light and temperature) [4].

MPPT techniques are basically divided into three categories [5]:

Online MPPT: as perturbation and observation (P&O) and Incremental conductance (INC), which are widely used for their ease of implementation. These methods require instantaneous measurements of PV current, voltage, and power.

Off-line MPPT: which are machine learning techniques such as fuzzy logic control (FLC), artificial neuro-fuzzy inference systems (ANFIS) [6] and neural networks (ANN), these methods need existing data on the PV system. Offline methods have better efficiency than online methods. Nevertheless, offline MPPT techniques have some drawbacks such as high memory consumption.

Hybrid MPPT: which is the combination of online techniques and offline techniques, to have a better performance, like the cascade combination of ANN-P&O [7,8].

In this paper, one of the powerful machine learning techniques, which is SVM combined with online methods perturbation and observation (SVM-P&O) and Incremental of conductance, (SVM-INC) in order to ensure the continuation of the maximum power delivered by the photovoltaic array under the variation of the climatic conditions.

Our paper is organized as follows : The second section introduces the modeling of the solar panel and its characteristics as a function of temperature and irradiation. In the third section, we will explain the MPPT methods used, including P&O, INC, and SVM. The fourth part includes the use of Matlab/Simulink simulation tools to simulate the model. The fifth section shows the results and discussion, followed by a brief conclusion.

II. SOLAR CELL MODEL

In solar conversion, the equivalent electrical diagram of a photovoltaic PV cell shown in Fig.1 is the most used [9-14]. Where Iph is the photocurrent, assembled in parallel with a diode D, and Id is the current of the diode in the dark. Rp is the parallel resistance and Rs is the series resistance.

The following equation describes the current-voltage characteristics of the PV module [14,16]

$$I = Ipv - I0\left[\exp\left(\frac{V+RsI}{NsVtA}\right) - 1\right] - \frac{V+RsI}{Rp} \quad (1)$$

With $$Vt = KT/q \quad (2)$$

The generated photocurrent associated to the solar irradiation can be written by the next equation

$$Ipv = (Ipv,n + Ki\Delta T)\frac{G}{Gn} \quad (3)$$

Moreover, the diode saturation current I0 is strongly dependent on the temperature by the following equation

$$I_0 = \frac{Isc,n+Ki\Delta T}{\exp\left(\frac{Voc,n+Kv\Delta T}{NsVtA}\right)-1} \quad (4)$$

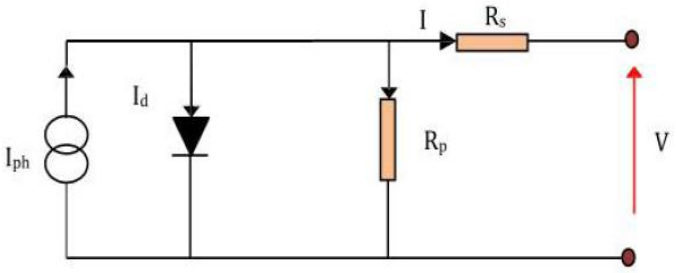

Fig. 1. Single diode equivalent model [17]

I , Ipv PV output current and Photovoltaic current
I0 Saturation current
V PV output voltage
Vt Thermal voltage
ΔT $\Delta T=T-T_n$ with T and T_n the actual and nominal temperature,K
G Irradiation, W/m^2
Gn Irradiation level for standard test condition
A Diode ideality factor,$1 \leq A \leq 1.5$
K Boltzman's constant, 1.380658×10^{-23} J/K
Rs Serial resistor
Rp Parallel resistor
Ns Cells connected in series
q Electron charge, $1.60217733 \times 10^{-19}$ **C**
Ki Current temperature coefficient
Kv Voltage temperature coefficient
Ipv,n Current generated in the conditions STC
Isc,n Nominal short-circuit current
Voc,n Nominal open circuit voltage

III. MPPT METHOD

A. *Support vector machine SVM*

Support vector machines (SVM)[18,19] is a classification and regression prediction tool [20] using supervised learning to maximize predictive accuracy [21].

SVMs have several promising features such as better empirical performance, which have made it gain popularity [22]. The goal of SVM is to find a classifier that can classify the data and separate them. This classifier is known as the hyperplane Fig. 2 [23]. The classification model predicts the outputs (responses) for the inputs that have not yet been seen from the existing inputs (predictors) and previous responses.

The separating hyperplane has the equation

$$w.X + b = 0 \quad (5)$$

to

Where w represents the normal vector of the hyperplane and X is the input vector.

The distance from a point to the plane is given by :

$$d(x) = \frac{|\mathrm{w}.\mathrm{X} + \mathrm{b}|}{|\mathrm{w}|} \quad (6)$$

The objective of SVMs is to find an optimal hyperplane that separates two classes with a maximum distance called the margin.

Let X1 and X2 be two points of different classes f(X1)= +1 and f(X2)= -1

Hence (w.X1)+b= +1 and (w.X2)+b= -1

Then (w.(X1-X2))+b=2

The margin is given by the following equation

$$M = \frac{(\mathrm{X1} - \mathrm{X2}).\mathrm{w}}{|\mathrm{w}|} \quad (7)$$

The maximizing is represented by the equation

$$maximum \qquad M = \frac{2}{|\mathrm{w}|} \quad (8)$$

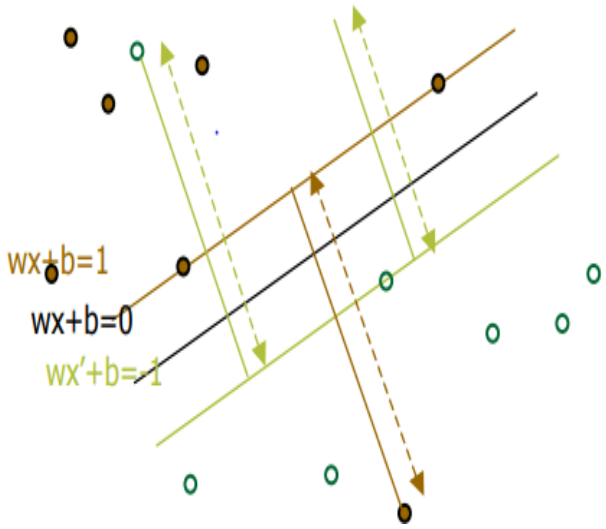

Fig. 2. Representation of Hyper planes [21]

The kernel is a set of mathematical functions that SVMs use, these functions take input data and transform it into the required form. There are different forms of kernel function that generate different SVM algorithms, and among the most used kernel functions are : Plynomial, linear, sigmoid, radial basis function (RBF), and exponential radial basis function (ERBF),...etc.

In this article we will test types of kernel function: RBF and ERBF, because they are perfectly suitable for modeling

nonlinear systems [24], which are represented by the following mathematical equations:

$$RBF: \quad K(u,v) = \exp\frac{-\|u-v\|^2}{2\sigma^2} \tag{9}$$

$$ERBF: \quad K(u,v) = \exp\frac{-\|u-v\|}{2\sigma^2} \tag{10}$$

Where σ^2 is the variance and our hyper-parameter, because it is important to choose the right value of to get occurate results.

Different levels of insolation (G) and temperature (T) with the previous PV current and voltage can be represented as input variables to build a model able to predict Vref and Iref.

B. Perturb and observe

It is a power feedback method and has become the most commonly used MPPT method due to its simplicity and ease of implementation [25]. As the name suggests, this method is based on the perturbation (increase or decrease) of the voltage Vref and the observation of its influence on the power, directly acting on the duty cycle of the DC/DC converter.

The observation of the power then allows a decision to be made about the next disturbance to be introduced, if the power increases, the disturbance will continue in the same direction, otherwise, the opposite [26].

The algorithm ensuring the P&O command is described in Fig.3 below :

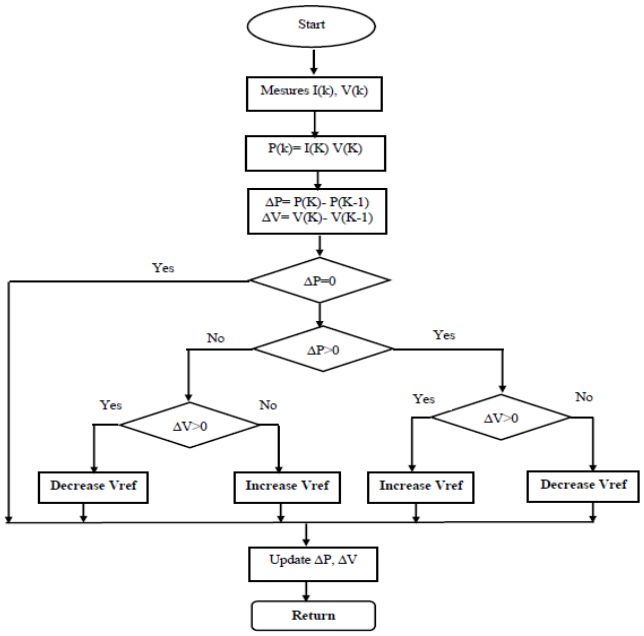

Fig. 3. The Flowchart of the P&O Method

C. Incremental Conductance

The Incremental Conductance method is based on the variation of power with voltage [27]. If the dp/dv derivative is zero it means that we are on MPP, if it is positive the operating point is to the left of the maximum, and when it is negative, we are on the right [28].

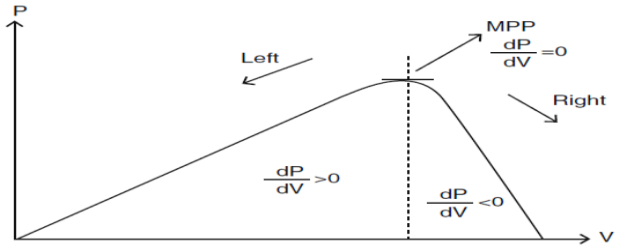

Fig. 4.Basic idea of incremental conductance method on a P-V curve of solar module

Knowing that $P=I.V$ (10)

Hence, P is the PV power, I is the PV current, V is the PV voltage.

The derivation of the product with respect to the voltage V gives the following relation

$$\frac{dP}{dV} = \frac{d(IV)}{dV} = I + V\frac{dI}{dV} = I + V\frac{\Delta I}{\Delta V} \tag{11}$$

Then the new conditions on the variation of conductance is as follows:

$$\frac{\Delta I}{\Delta V} = \frac{-I}{V} \quad at\ MPP \tag{12}$$

$$\frac{\Delta I}{\Delta V} > \frac{-I}{V} \quad left\ to\ MPP \tag{13}$$

$$\frac{\Delta I}{\Delta V} < \frac{-I}{V} \quad right\ to\ MPP \tag{14}$$

If the relation (12) is verified, then the MPP is reached no change of the voltage is necessary. If the relation (12) is false, the voltage is adjusted according to whether V is greater or less than Vmp.

Where Vmp is the maximum power point voltage.

The flow chart of incremental conductance MPPT is shown in Fig.5 :

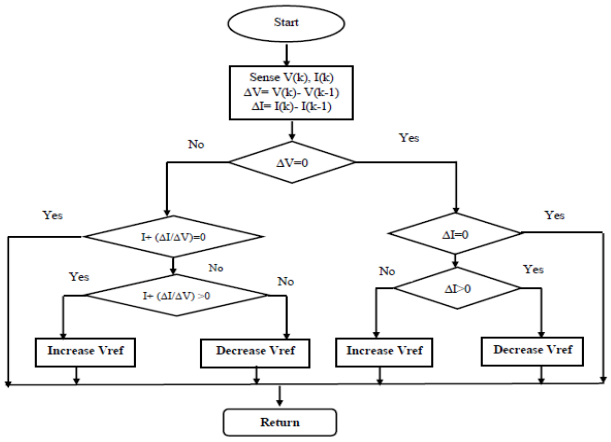

Fig. 5. The Flowchart of the INC Method

IV. Simulation Model

Matlab/Simulink software was used to verify and validate the effictivnesse of the proposed method SVM with P&O.

The system shown in Fig.6 consists of a PV model, MPPT technique, SVM predicting model using kernel function, PWM generator, Boost converter, and 50 Ohms load resistor. The switching frequency of the system is defined as 20KHZ.

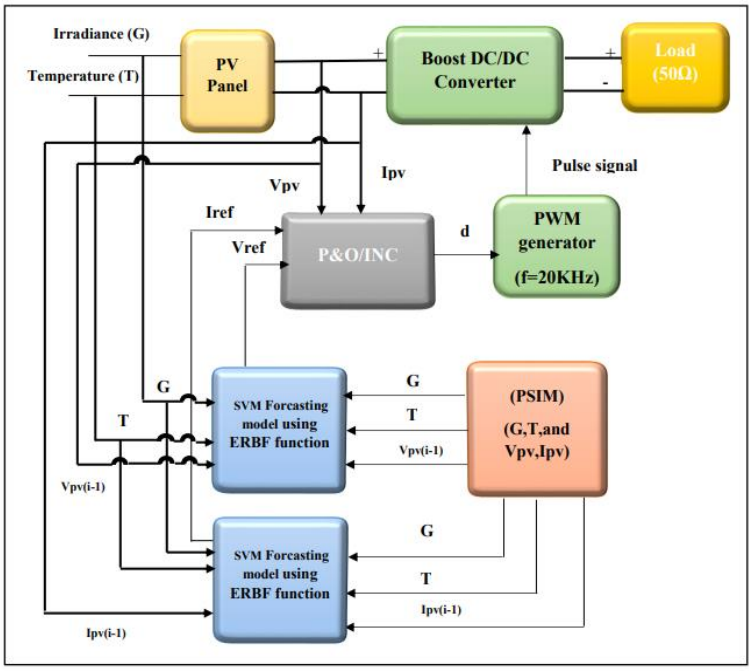

Fig. 6. Complete PV system designed using SVM with P&O and INC

A KYOCERA KV200GT PV module is adopted as PV power source whose specifications are quoted in Table I.

TABLE I. SPECIFICATION OF KC200GT PV PANEL [22]

Parameter	Value
Maximum current (Imp)	7.61A
Maximum voltage (Vmp)	26.3V
Maximum power (Pmax)	200.143W
Short circuit current (Isc)	8.21A
Open circuit voltage(Voc)	32.9V
Temperature coefficient of Isc (Ki)	3.18e-3A/K
Temperature coefficient of Voc (Kv)	-0.123V/K
Number of cells in series (Ns)	54
Diode ideality factor (A)	1.3
Series resistance (Rs)	0.221Ω
Shunt resistance (Rp)	415.405 Ω

Boost DC-DC converter shown in Fig.7. is utilized to step up the output voltage, compared to that delivered by the source [25], hence the name'boost'.it is used as a power conversion stage to mutch the source and load impedance.

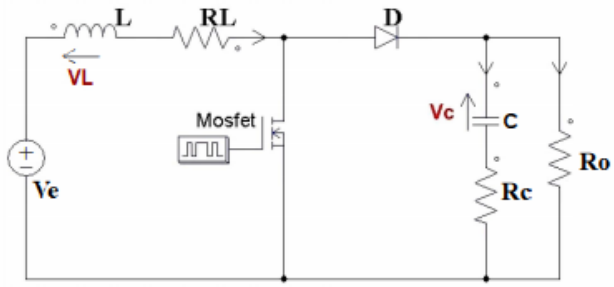

Fig. 7. Equivalent model of boost converter

Parameters used for the boost converter has the following specifications [16].

TABLE II. BOOST CONVERTER AND RESISTIVE LOAD PARAMETERS

Parameters	Value
Input Capacitor (Cin)	1×10-6 F
Inductor (L)	0.011 H
Output capacitor (Cout)	6×10 F
Load	50 Ω

To train and validate the SVM algorithm, we used 130 data set from PSIM which consists of three input solar irradiance (G), temperature (T), and previous PV voltage (previous PV current) as predictors and voltage reference Vref (current reference Iref) as the output response.

As we have mentioned before for the forecasting SVM model we have tested two types of kernel function the RBF kernel and the ERBF kernel, the test results are summarized in Table III which compares kernels with performance measures, including support vector (SV) and its % (SV%).

The result shows that the ERBF kernel is the most suitable for our datasets, as it has the minimum number of support vectors, the minimum percentage of support vectors compared to the RBF kernel.

Fig.8. illustrate predicted values (Vref, Iref) with RBF and ERBF kernel with datasets (Vpv(i-1), Ipv(i-1)), we can see that the optimum kernel is ERBF kernel, whose values are closer to the datasets.

TABLE III. COMPARING KERNELS WITH PERFORMANCE MEASURES FOR PV VOLTAGE AND PV CURRENT

Kernel Function	Voltage SV	Voltage SV%	Current SV	Current SV%
RBF	50	38.8	79	61.2
ERBF	28	21.7	71	55.0

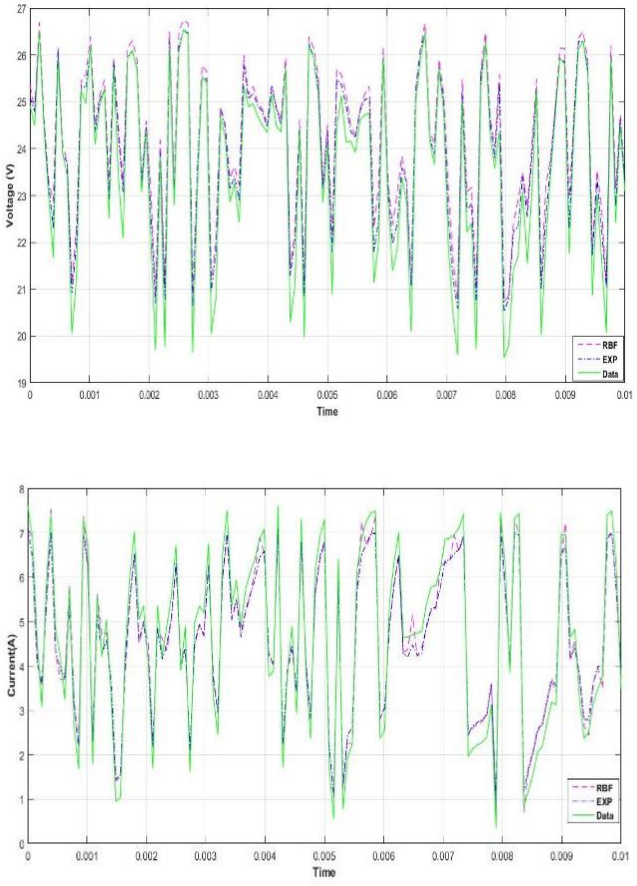

Fig. 8. Comparing predicted values (Vref, Iref) with RBF and ERBF kernel with datasets (Vpv, Ipv)

In order to obtain the optimal duty cycle d, we used two blocs of SVM with ERBF to build a model which can predict Iref and Vref and then passed to the P&O/ INC method, and finally processed to the boost DC-DC converter.

V. RESULTS AND DISCUSSION

TABLE IV and Fig (9-11) exemplify the tabularized and graphical results from the Matlab/Simulink simulation. The SVM-P&O and SVM-INC are compared to each other using PV and load efficiency under the different weather conditions (STC, PTC, and NOTC).

For the STC condition, results show that the SVM-INC had the best result with 99.50% PV efficiency and 96.65% load efficiency.

At PTC condition, also SVM-INC whose product the best results with 99.31% PV efficiency and 96.28% load efficiency.

For the NOTC condition, the SVM-P&O technique had the best result this time with 98.30% PV efficiency however, it underperformed with 95.45% load efficiency.

TABLE IV. SIMULATED RESULTS OF SVM-P&O AND SVM-INC

Weather conditions	Measurment	SVM-P&O	SVM-INC
1000W/m^2, 25°C (STC)	PV efficiency	98.50%	99.50%
	Load efficiency	96.62%	96.65%
1000W/m^2, 20°C (PTC)	PV efficiency	98.41%	99.31%
	Load efficiency	96.65%	96.28%
800W/m^2, 47.4°C (NOTC)	PV efficiency	98.3%	98.16%
	Load efficiency	95.45%	95.72%

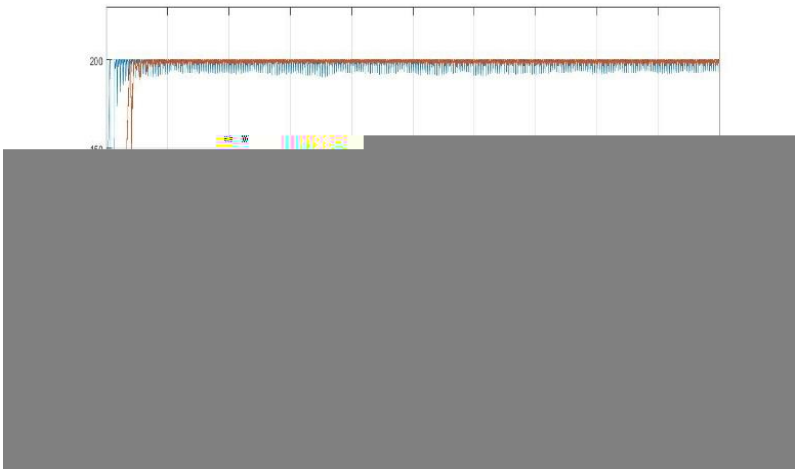

Fig. 9. KC200GT input power at STC

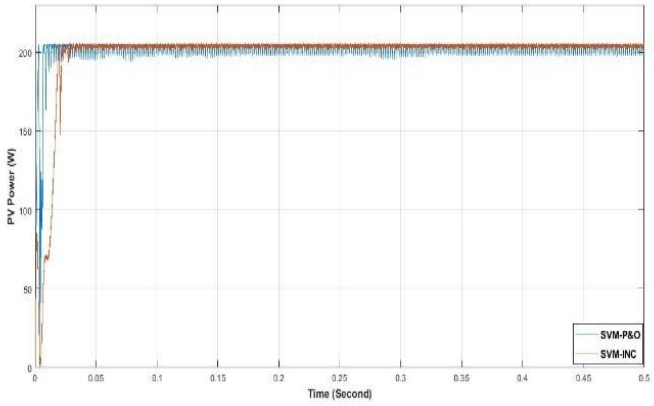

Fig. 10. KC200GT input power at PTC

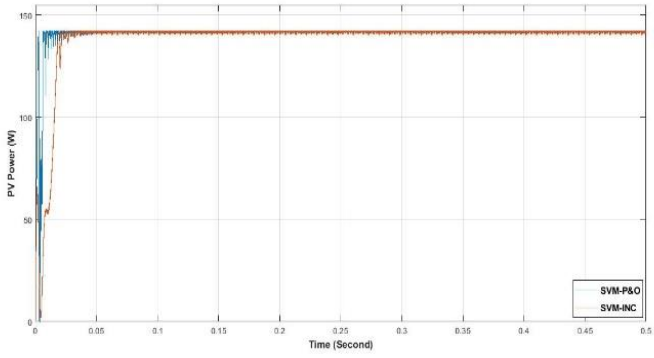

Fig. 11. KC200GT input power at NOTC

VI. Conclusion

This paper presents a combined SVM predicting model with conventional MPPT technique P&O and INC. First of all, we have tested two types of kernel function RBF and ERBF function for the SVM predicting model. Then after the selection of the optimal kernel function ERBF the SVM model predicts current and voltage reference using previous PV current and voltage to be after that the inputs of P&O and INC controller to track the maximum power point in the PV system. The obtained results indicate that the proposed technique can be used to extract the MPP under different weather conditions effectively.

References

[1] « Flexible global carbon pricing study: A new method to establish the international cooperation on reducing carbon emission », *IPEC, 2012 Conference on Power&Energy*, vol. 2012, nº 11, p. 300-304, 2012.

[2] P. F. Frack, P. Mercado, G. Sarriegui, et R. D. D. Doncker, « Renewable energy supply of refugee camps to decrease fuel consumption and CO2 emissions », *2015 IEEE 6th International Symposium on Power Electronics for Distributed Generation Systems (PEDG)*, 2015, doi: 10.1109/PEDG.2015.7223091.

[3] N. Aouchiche, « Conception d'une commande MPPT optimale à base d'intelligence artificielle d'un système photovoltaïque. », p. 108.

[4] « Les Cellules Photovoltaïques | PDF | Dopage (semi-conducteur) | Semi-conducteurs », *Scribd*. https://fr.scribd.com/document/365639018/Les-Cellules-Photovoltaiques (consulté le sept. 15, 2021).

[5] A. M. Farayola, A. N. Hasan, et A. Ali, « EFFICIENT PHOTOVOLTAIC MPPT SYSTEM USING COARSE GAUSSIAN SUPPORT VECTOR MACHINE AND ARTIFICIAL NEURAL NETWORK TECHNIQUES », p. 17.

[6] S. Ray, « A Comparative Study on Different MPPT Techniques Applied On Photovoltaic System », *International Journal of Advanced Research in Electrical, Electronics and Instrumentation Engineering*, vol. 04, p. 1249-1252, mars 2015, doi: 10.15662/ijareeie.2015.0403011.

[7] B. Pakkiraiah et G. D. Sukumar, « Research Survey on Various MPPT Performance Issues to Improve the Solar PV System Efficiency », *Journal of Solar Energy*, vol. 2016, p. e8012432, juill. 2016, doi: 10.1155/2016/8012432.

[8] H. J. El-Khozondar, R. J. El-Khozondar, K. Matter, et T. Suntio, « A review study of photovoltaic array maximum power tracking algorithms », *Renewables: Wind, Water, and Solar*, vol. 3, nº 1, p. 3, févr. 2016, doi: 10.1186/s40807-016-0022-8.

[9] VeeracharyM, « PSIM circuit-oriented simulator model for the nonlinear photovoltaic sources », *IEEE Transactions on Aerospace and Electronic Systems*, vol. 42, nº 2, p. 735-740, avr. 2006, doi: 10.1109/TAES.2006.1642586.

[10] A. Mohapatra, B. Nayak, et K. Mohanty, « Current based novel adaptive P&O MPPT algorithm for photovoltaic system considering sudden change in the irradiance », *2014 IEEE International Conference on Power Electronics, Drives and Energy Systems, PEDES 2014*, févr. 2015, doi: 10.1109/PEDES.2014.7042032.

[11] F. Masmoudi, F. Ben Salem, et N. Derbel, Single and double diode models for conventional mono-crystalline solar cell with extraction of internal parameters. 2016, p. 728.

[12] I. de la Parra, M. Muñoz, E. Lorenzo, M. García, J. Marcos, et F. Martínez-Moreno, « PV performance modelling: A review in the light of quality assurance for large PV plants », *Renewable and Sustainable Energy Reviews*, vol. 78, p. 780-797, 2017, doi: https://doi.org/10.1016/j.rser.2017.04.080.

[13] F. Mehmood, N. Ashraf, L. Alvarez, T. Malik, H. Qureshi, et T. Kamal, « Grid integrated photovoltaic system with fuzzy based maximum power point tracking control along with harmonic elimination », *Transactions on Emerging Telecommunications Technologies*, janv. 2020, doi: 10.1002/ett.3856.

[14] M. G. Villalva, J. R. Gazoli, et E. R. Filho, « MODELING AND CIRCUIT-BASED SIMULATION OF PHOTOVOLTAIC ARRAYS », p. 11, 2009.

[15] A. Loukriz, S. Messalti, et A. Harrag, « Design, simulation, and hardware implementation of novel optimum operating point tracker of PV system using adaptive step size », *Int J Adv Manuf Technol*, vol. 101, nº 5-8, p. 1671-1680, avr. 2019, doi: 10.1007/s00170-018-2977-7.

[16] S. Sumathi, L. Ashok Kumar, et P. Surekha, *Solar PV and Wind Energy Conversion Systems*. Cham: Springer International Publishing, 2015.

[17] Alonso C. Contribution à l'optimisation , la gestion et le traitement de l'énergie. Habilitation à diriger des travaux de recherches. Université PAUL SABATIER – TOULOUSE III, 2003.

[18] C. Cortes et V. Vapnik, « Support-vector networks », *Mach Learn*, vol. 20, nº 3, p. 273-297, sept. 1995, doi: 10.1007/BF00994018.

[19] D. Tomar et S. Agarwal, « A comparison on multi-class classification methods based on least squares twin support vector machine », *Know.-Based Syst.*, vol. 81, nº C, p. 131-147, juin 2015, doi: 10.1016/j.knosys.2015.02.009.

[20] M. E. Mavroforakis et S. Theodoridis, « A geometric approach to Support Vector Machine (SVM) classification », *IEEE Transactions on Neural Networks*, vol. 17, nº 3, p. 671-682, mai 2006, doi: 10.1109/TNN.2006.873281.

[21] V. Jakkula, « Tutorial on Support Vector Machine (SVM) », p. 13.

[22] H. Yang, S. Zhang, K. Deng, et P. Du, « Research into a Feature Selection Method for Hyperspectral Imagery Using PSO and SVM », *Journal of China University of Mining and Technology*, vol. 4, nº 17, p. 473-478, 2007, doi: 10.1016/S1006-1266(07)60128-X.

[23] M. Hasan et F. Boris, « SVM : Machines à Vecteurs de Support ou Séparateurs à Vastes Marges », p. 20.

[24] S. Iplikci, « Online trained support vector machines-based generalized predictive control of non-linear systems », *International Journal of Adaptive Control and Signal Processing*, vol. 20, p. 599-621, déc. 2006, doi: 10.1002/acs.919.

[25] K. L. Lian, J. H. Jhang, et I. S. Tian, « A Maximum Power Point Tracking Method Based on Perturb-and-Observe Combined With Particle Swarm Optimization », *IEEE J. Photovoltaics*, vol. 4, nº 2, p. 626-633, mars 2014, doi: 10.1109/JPHOTOV.2013.2297513.

[26] A. Loukriz, S. Messalti, et A. Harrag, « Design, simulation, and hardware implementation of novel optimum operating point tracker of PV system using adaptive step size », *Int J Adv Manuf Technol*, vol. 101, nº 5-8, p. 1671-1680, avr. 2019, doi: 10.1007/s00170-018-2977-7.

[27] S. Jain et V. Agarwal, « Comparison of the performance of maximum power point tracking schemes applied to single-stage grid-connected photovoltaic systems », Electric Power Applications, IET, vol. 1, p. 753-762, oct. 2007, doi: 10.1049/iet-epa:20060475.

[28] N. Aouchiche et M. S. A. Cheikh, « Poursuite du point de puissance maximale d'un système photovoltaïque par les méthodes de l'incrémentation », p. 14.

Comparison of Tow Methods P&O and Fuzzy Logic Controller For MPPT in The Photovoltaic System.

Khelaifa Fethi
Department of Electrical Engineering
Laboratory of Electronics and New Technologies-LENT-
Larbi Ben M'hidi University Oum El Bouaghi, Algeria.
fethi.khelaifa@univ-oeb.dz / khaliafa1994@gmail.com

Lamamra Kheireddine
Department of Electrical Engineering
Laboratory of Electronics and New Technologies-LENT-
Larbi Ben M'hidi University Oum El Bouaghi, Algeria.
Lamamra.Kheireddine@univ-oeb.dz / l_kheir@yahoo.fr . IEEE Member.

Toumi Djaafar
Faculty of Science and Technology
Echahid Hamma Lakhdar University
El Oued, Algeria.
toumidjaafar@gmail.com

***Abstract*— An important consideration in the use of the PV system is to operate the system near the maximum power point to increase the output efficiency of the PV panel. Maximum power point tracking (MPPT) techniques are used in PV applications to extract the maximum power that the PV panel can produce, which depends on different atmospheric conditions, namely solar insolation and temperature. In this paper, a new maximum power point tracker using fuzzy set theory is proposed to improve the energy conversion efficiency. A fuzzy algorithm based on linguistic rules describing the operator control strategy is applied to the boost converter control so that the maximum power point tracker linguistic variables implemented in the fuzzy logic controller were appropriately selected to modulate the DC-DC converter. The fuzzy logic controller offers advanced features such as fast response, good oscillation performance the results obtained are compared with the P&O technology.**

Keywords— PV system, Maximum power point tracking (MPPT), fuzzy logic. P&O.

I. INTRODUCTION

Photovoltaic energy source is one of the most popular energy sources that many researchers are working on because it is clean, pollution-free and endless and can meet our demand without disturbing the environment. To decrease the use of conventional energy, the PV source must be integrated into the grid through step-up converters. [1]

As the efficiency of the PV source is very less an important consideration in the use of PV system is to operate the system near the maximum power point in order to increase the output efficiency of the PV panel, [2] as the maximum power point depends on the temperature and irradiance which are non-linear in nature, a maximum power point tracking control system is used, which can maximize the output energy of the PV system and work effectively on the non-linear variations of the parameters such as temperature and irradiance. [3]

There are many MPPT algorithms such as perturbation and observation (P&O), incremental conductance, fractional short-circuit current, fractional open circuit-voltage, neural networks and fuzzy logic. Each has its own advantages and disadvantages. [4] This paper focuses on the comparison of fuzzy logic controller and perturbations and observations (P&O) for tracking the maximum power point which is influenced by the non-linear characteristics of the photovoltaic panel depends on variable environmental conditions such as temperature and solar energy radiation. [5]

The major problem with the existing solar power MPPT harvesting technologies is that, the efficiency of the solar power system is still very low and the PV system does not operate at its best efficiency corresponds to the nonlinear variations, [6] thus the fuzzy logic controller is designed and compared with P&O Technique for MPPT controller operation for efficient operation under nonlinear parameter variations. One of the most difficult parts is the design of the fuzzy logic rules to track the maximum power point and control the DC - DC converter.

II. CHARACTERISTICS OF THE PHOTOVOLTAIC SYSTEM

A. Mathematical model of the photovoltaic cell:

A photocell consists of a semiconductor material that absorbs light energy and converts it directly into an electric current. She based on the physical phenomenon called the "photoelectric effect", which consists of creating an electric impulse when the surface of this cell is exposed to light [7]. Figure 1 shows a simplified electrical diagram of a solar cell [8].

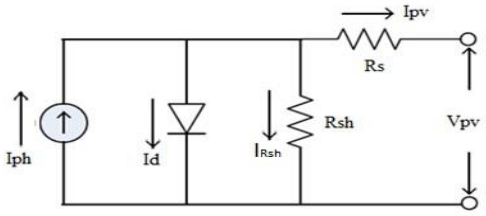

Figure.1. Solar cell diode model.

Kirchhoff's laws allow the writing of the following relationships:

$$I_p=I_d+I_{RP}+I_{RS} \quad (1)$$

The current in the diode is given by the following expression:

$$I_d=I_0\,[\exp\,(q\,(V+Rs)/mKT)-1] \quad (2)$$

The current flowing through the parallel resistance is given by:

$$I_{Rp}=V+I.R_s/R_p \quad (3)$$

From the equations above the expression of the total current is established:

$I = I_{pv} - I_0 [\exp (q*V+I*R_S/N_S*n*K*T)-1] - (V+I*R_S/R_P)$

(4)

Where:

I: is the current of the PV solar module.

Ipv: Photocurrent [A].

V: voltage at the terminals of the PV module [V].

I0: saturation current of the diode [A].

q: electron charge which is 1.602 * 10 ^ (-19) Coulomb.

Rs: series resistance of PV solar module (Ω).

Rp: parallel resistance of the PV module (Ω).

K: Boltzmann constant (J / K).

T: junction temperature [K].

Ns: number of cells in series and; n is the ideality factor of the diode.

The Matlab / Simulink model of the PV module is given in Fig.2.

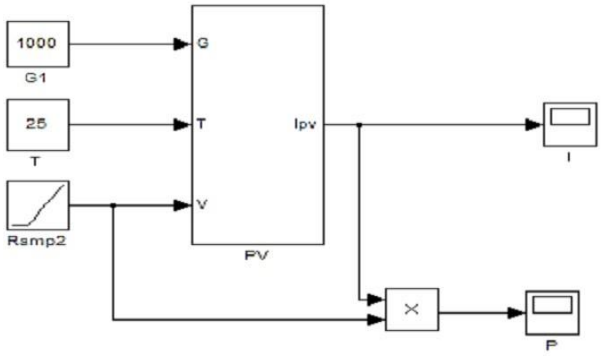

Figure.2. Presentation of the PV module in Matlab/Simulink.

B. the P&O Algorithm:

In this algorithm, a small error is introduced into the system due to the power of the module changes. [9] If the power change is positive the disturbance continues in that direction After the MPP point the power at the next instant decreases, then the disturbance reverses At the steady state, the algorithm oscillates around the peak point.

C. the Fuzzy Logic Controller:

The fuzzy system is composed of a knowledge-based rule system; the main part of FLC is the knowledge base composed of the If-Then rules. [10]

Fuzzy Logic is implemented to get the MPP operating voltage point faster with less overshoot and it can minimize the voltage fluctuation after the MPP recognition. [11] The control objective is to track the maximum power will therefore lead to efficient operation of the PV panel.

To design the FLC, the variables that represent the dynamic performance of the system should be chosen as input for the controller. The basic block diagram implemented in the fuzzy logic controller is shown in Figure.3.

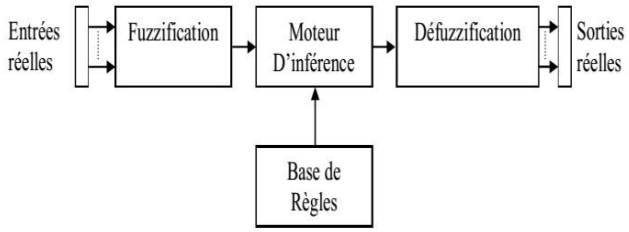

Figure.3. General diagram of a fuzzy command.

Fuzzy control is based on three main steps are:

a. Fuzzification

In the fuzzification step, the numerical input variables are calculated or converted into linguistic variables based on a subset called membership function. To translate the value of voltage change and power change, the fuzzy input "power change" and "voltage change" is designed with seven fuzzy variables called PB (Positive Big), PM (Positive Medium), NS (Negative Small), PS (Positive Small), ZE (Zero), NM (Negative Medium), and NB (Negative Large).The voltage change and power change are the input variables in the proposed system and the output of the fuzzy logic controller is the duty cycle change. [12].

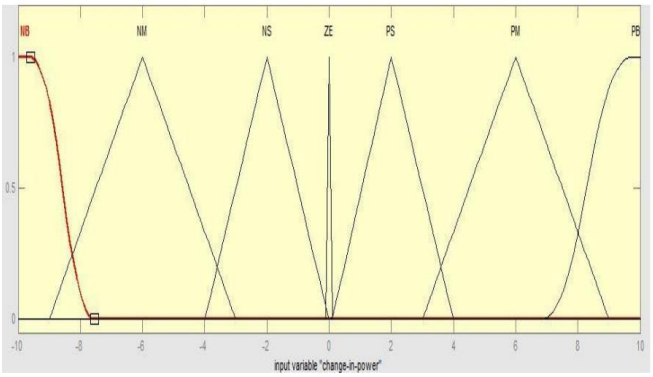

Figure.4.FLC voltage change input.

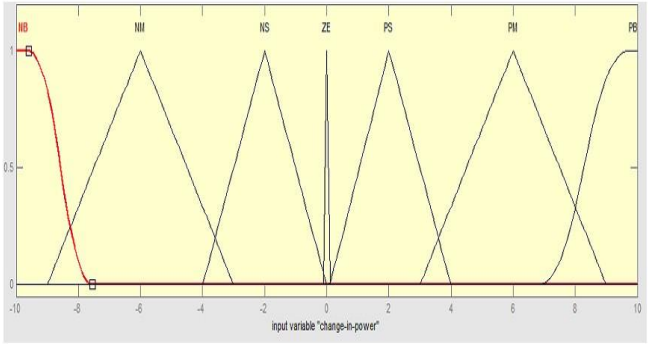

Figure.5.Input to the FLC as power change.

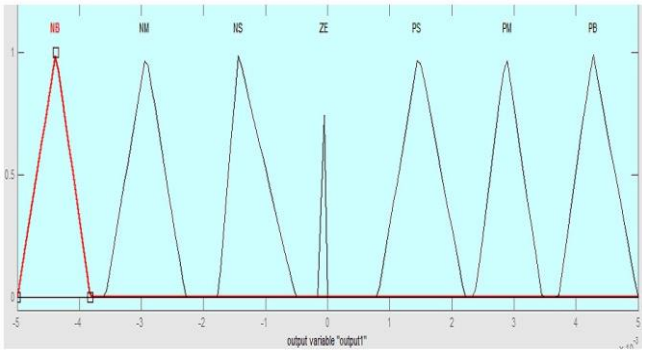

Figure.6.Output of the FLC as a change of cyclic ratio.

b. Inference system

The fuzzy rule algorithm collects a set of fuzzy control rules in a specific order, these rules are used to control a system to meet the desired performance requirements and they are designed based on the expert knowledge of the system under control. [13] The fuzzy inference of FLC is based on the Mamdanis method, which is associated with max-min composition.

c. defuzzification

The input for the defuzzification process is a fuzzy set and the output is a single number to be applied to the system, for the final desired output according to the system, a non-fuzzy value of control output is required, so a defuzzification step is mandatory.[14] The defuzzification method presenting in the proposed scheme.

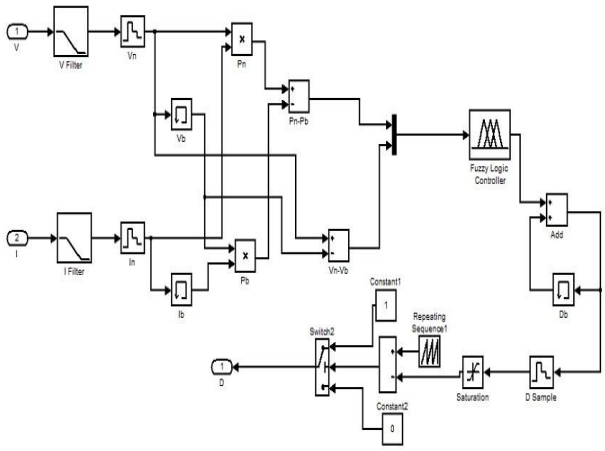

Figure.7.Model of the fuzzy logic controller.

III. RESULTS AND DISCUSSIONS

The power output of PV module and inverter with two different MPPT techniques is obtained in MATLB / Simulink at 400 W/m^2 irradiance and 250 C^o temperature. The simulation results show the implementation of fuzzy logic and P&O technique on tracking the maximum power point (Pm) is given in figure 8 (a), (b).

We note that the maximum power produced is accurate, stable and effective compared to the fuzzy logic technique compared to the P&O technique.

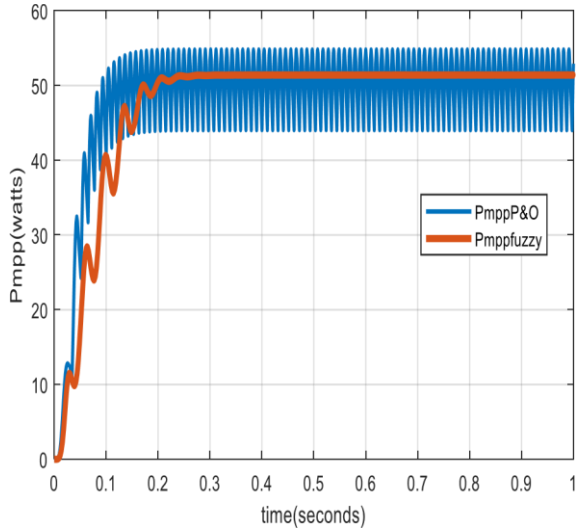

(a)

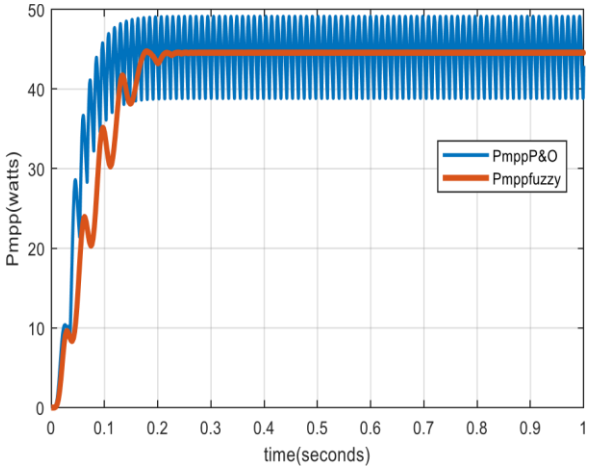

(b)

Figure.8.Maximum power (Pmpp) and power output (Po) of the proposed PV array.

The voltage variations in Vmpp and Vo for these converters are shown in the corresponding figure 9 (a) and (b).

We note that fuzzy logic controller gives us more stable results compared to the P&O technique.

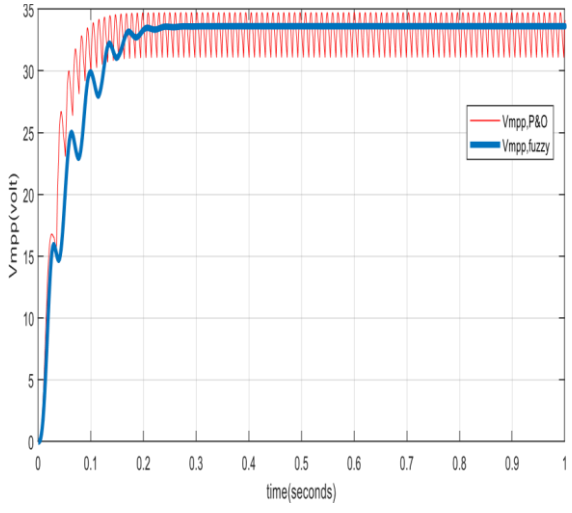

(a)

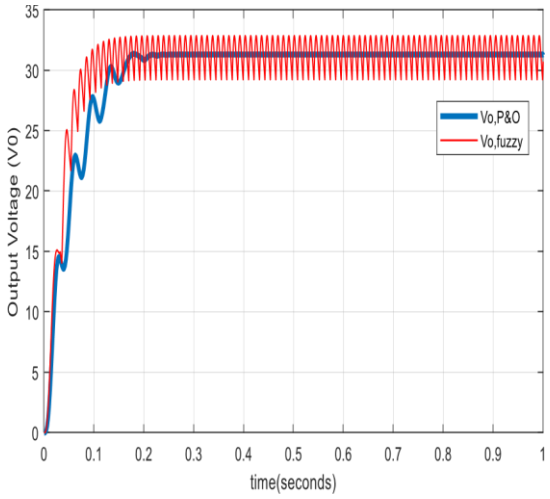

(b)

Figure.9.Output voltage (Vmpp) and output voltage (Vo) of the photovoltaic generator PV.

IV. Conclusion

In this paper, the V-I and P-V characteristics of the PV module are obtained using MATLAB / Simulink at a temperature of 250 ° C and an irradiance of 400 W/m2. The analysis of fuzzy logic controller and P&O based MPPT is done and the simulation results are presented. From the simulation results, the Fuzzy based MPPT tracks the power continuously with less fluctuations and also has less overshoot with fast tracking time compared to the P&O MPPT algorithm.

References

[1] Dunia, James, and Bakari MM Mwinyiwiwa. "Performance Comparison between ĆUK and SEPIC Converters for Maximum Power Point Tracking Using Incremental Conductance Technique in Solar Power Applications." world academy of science, engineering and technology International Journal of Electrical, Computer, Electronics and Communication Engineering Vol:7 No:12, 2013.

[2] A. Azouzoute, A.A. Merrouni, S. Touili, Overview of the integration of CSP as an alternative energy source in the MENA region, Energy Strategy Rev 29 (2020) 100493.

[3] Khelaifa .F, L. Kheireddine, S.Youcef "Modeling of partial shading in photovoltaic systems by MLP artificial neural networks ";The International Conference on Sustainable, Renewable Energy Systems and Applications (ICSRESA'19), December 4 – 5, 2019.

[4] A.H. Elsheikh, V.P. Katekar, O.L. Muskens, S.S. Deshmukh, M.A. Elaziz, S.M. Dabour, Utilization of LSTM neural network for water production forecasting of a stepped solar still with a corrugated absorber plate, Process Safety and Environmental Protection, 148 (2021) 273-282.

[5] Habbati Bellia, Ramdani Youcef and Moulay Fatima. "A detailed modeling of photovoltaic module using MATLAB." NRIAG Journal of Astronomy and Geophysics vol. 3, no. 1, 2014, pp.53-61.

[6] J. Ahmed and Z. Salam, "An Enhanced Adaptive P&O MPPT for Fast and Efficient Tracking Under Varying Environmental Conditions," *IEEE Trans. Sustain. Energy*, vol. 9, no. 3, pp. 1487–1496, 2018.

[7] M. Angel Cid Pastor, ''Conception et réalisation de modules photovoltaïques électroniques''. Thèse de doctorat, Institut National des Sciences Appliquées de Toulouse, septembre 2006.

[8] Hunan-Liang Tsai, Ci-Siang Tu and Yi-Jie Su, Member, IAENG "Development of Generalized Photovoltaic Model Using MATLAB/SIMULINK" Proceedings of the world congress on Engineering and Computer Science, October 22-24, 2008, San Francisco, USA.

[9] J. Prasanth Ram and N. Rajasekar, "A Novel Flower Pollination Based Global Maximum Power Point Method for Solar Maximum Power Point Tracking," *IEEE Trans. Power Electron.*, vol. 32, no. 11, pp. 8486–8499, 2017.

[10] Raedani, Ronn, and Moin Hanif. "Design, testing and comparison of P&O, IC and VSSIR MPPT techniques." In Renewable Energy Research and Application (ICRERA), 2014 International Conference on, pp. 322-330. IEEE, 2014.

[11] M.Zein Alabedin, E.F. El-Saadany, M.M.A. Salama, "Maximum Power Point Tracking for Photovoltaic System Using Fuzzy Logic and Artificial Neural Networks".

[12] M.A.S. Masoum, M.Sarvi, "A new fuzzy-based maximum power point tracker for photovoltaic applications", Iranian Journal of Electrical & Electronic Engineering, Vol.1, January 2005.

[13] N.Ammasai Gounden, Sabitha Ann Peter, Himaja Nallandula and S.Krithiga. "Fuzzy logic controller with MPPT using linecommuted inverter for three-phase grid-connected photovoltaic systems", Renewable Energy (ELSEVIER Journal), vol.34, pp. 909-915, July 2008.

[14] Y. Chaibi, A. Allouhi, M. Malvoni, M. Salhi, and R. Saadani, "Solar irradiance and temperature influence on the photovoltaic cell equivalent-circuit models," *Sol. Energy*, vol. 188, pp. 1102–1110, 2019.

Hybrid Control Using Fuzzy Sliding Mode Control of Doubly Fed Induction Machine

Abdelghafour HERIZI, Riyadh ROUABHI, Soufiane KRIM & Elkhier HACHI
LGE Research Laboratory, Department of Electrical Engineering, Faculty of Technology
University Mohamed Boudiaf of M'sila, BP 166 Ichbilia 28000, Algeria
abdelghafour.herizi@univ-msila.dz, riyadh.rouabhi@univ-msila.dz

***Abstract*— In this article, we present a new sliding mode control strategy applied to the doubly fed induction machine. The proposed control combines sliding mode and fuzzy logic to achieve robust control. This technique finds its strongest justification for the problem of using a nonlinear control law robust to the uncertainties of the model. The objective of this control is improved the outputs generated by the doubly fed induction machine supply decoupled by orientation of the stator flux. Finally, the performance of the system was tested and compared by simulation in terms of follow-up of instructions, and the robustness with respect to the parametric variations of this machine. The simulation results obtained clearly show the effectiveness of this control.**

Keywords*— doubly fed induction machine, sliding mode control, fuzzy logic, hybrid control, Stator flux orientation.

I. INTRODUCTION

For several years, sliding mode control (SMC) has remained one of the most studied areas of control in research. Indeed, the robustness and the simplicity which characterize it, are the essential reasons which often lead us to seek more on this technique.

The sliding mode control algorithm is classified in VSS (Variable Structure System) control systems. This technique is based on the principle that it is easier to control a 1st order system than it is to control an nth order system, whether linear or not. The principle of this type of system with variable structure consists in bringing, whatever the initial conditions, the point representative of the evolution of the system on a hyper surface of the phase space (representing a set of relations, static, between state variables). The surface considered is then designated as being the sliding or switching surface [1]. The resulting dynamic behavior, called the ideal sliding regime, is completely determined by the parameters and equations defining the surface. The advantage of obtaining such a behavior is twofold: on the one hand, there is a reduction in the order of the system, and on the other hand, the sliding regime insensitive to disturbances occurring in the same directions as the inputs.

The sliding mode control has largely proven its effectiveness through reported theoretical studies, its main fields of application are robotics and electric motors [2-7]. The advantage that such a control provides and which makes it so important is its robustness with respect to the perturbations and uncertainties of the model. However, these performances are obtained at the cost of certain disadvantages [8-10]:

- A chattering or chattering phenomenon caused by the discontinuous part of this control and which can have a harmful effect on the actuators;
- The system is subjected at all times to a high control in order to ensure its convergence to the desired state and this is not desirable.

Among the solutions proposed to these problems, mention may be made of limit-band sliding mode control which consists in replacing the switching function in the control by a saturation function.

In fact, this solution is only a special case of the fuzzy sliding mode control, hence the interest in using a control which combines fuzzy logic and sliding mode in order to obtain a robust and smooth control. The control proposed in this article is called the fuzzy sliding mode control. In order to test its efficiency and robustness, the latter is applied to the control of the doubly fed induction machine, taking into account its kinematic constraint and its dynamic model.

The article is structured as follows: First, a dynamic model of the doubly fed induction machine (DFIM) was proposed under Matlab/Simulink. Then, a sliding mode control strategy of the doubly fed induction machine which allows independent control of the output state variables. In the fourth section, we synthesize a sliding-fuzzy control law of DFIM. Finally, robustness tests of the machine control will be carried out, simulations will be presented.

II. MATHEMATICAL MODELLING OF DFIM

The dynamic model of DFIM in (d,q) reference, which includes both the electrical and mechanical dynamics, can be described by the matrix form as follows [11, 12]:

$$\dot{X} = AX + BU \tag{1}$$

Where:

$$X = [\varphi_{sd} \quad \varphi_{sq} \quad I_{rd} \quad I_{rq}]^T, U = [V_{sd} \quad V_{sq} \quad V_{rd} \quad V_{rq}]^T$$

$$[A] = \begin{bmatrix} -\frac{1}{T_s} & \omega_s & \frac{M}{T_s} & 0 \\ -\omega_s & -\frac{1}{T_s} & 0 & \frac{M}{T_s} \\ \alpha & -\beta\omega & -\delta & (\omega_s - \omega) \\ \beta\omega & \alpha & -(\omega_s - \omega) & -\delta \end{bmatrix} ;$$

$$[B] = \begin{bmatrix} 1 & 0 & 0 & 0 \\ 0 & 1 & 0 & 0 \\ -\frac{M}{\sigma L_s L_r} & 0 & \frac{1}{\sigma L_r} & 0 \\ 0 & -\frac{M}{\sigma L_s L_r} & 0 & \frac{1}{\sigma L_r} \end{bmatrix}$$

With: $\sigma = 1 - \frac{M^2}{L_r L_s}$; $T_r = \frac{L_r}{R_r}$; $T_s = \frac{L_s}{R_s}$; $\alpha = \frac{M}{\sigma L_r L_s T_s}$; $\beta = \frac{M}{\sigma L_r L_s}$; $\delta = \frac{1}{\sigma}\left(\frac{1}{T_r} + \frac{M^2}{L_s T_s L_r}\right)$

The mechanical equation is of the following form:

$$J\frac{d\Omega}{dt} = C_{em} - C_r - f\Omega \quad (2)$$

With:

C_{em} and C_r : the electromagnetic torque and the resisting torque (the mechanical load) ;

f and J : coefficient of friction and moment of inertia of the rotor shaft.

The electromagnetic torque is expressed as a function of currents and flows by:

$$C_{em} = P\frac{M}{L_s}\left(\varphi_{sq} I_{rd} - \varphi_{sd} I_{rq}\right) \quad (3)$$

With respectively:

I_{sd}, I_{sq}, I_{rd} and I_{rq} : Direct and quadratic stator and rotor currents of the two-phase system;

$\varphi_{sd}, \varphi_{sq}, \varphi_{rd}$ and φ_{rq} : Direct and quadrature stator and rotor flux of the two-phase system;

P: The number of pole pairs of the DFIM.

The examination of the expression of the torque of the machine shows that it results from a difference of two components in quadrature of the stator current and of the rotor flux which presents a complex coupling between the quantities of the machine. The control is that linked to the rotating field so that the axis (d) coincides with the desired direction of the flow, which can be rotor, stator, or air gap. Thus it is possible to orient the different flows of the machine [13, 14].

The principle of the orientation of the stator flux in the direct transformation of park is illustrated in figure 1.

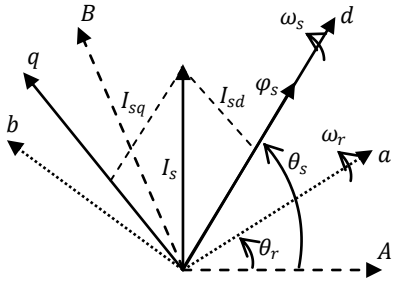

Fig. 1. Stator flux orientation on the d axis [11].

By choosing a (d, q) frame of reference linked to the rotating stator field and by aligning the stator flux vector with the d axis, this results in: $\varphi_{sd} = \varphi_s$ and $\varphi_{sq} = 0$.

If one supposes that the electrical network is stable, that leads to φ_s constant. In addition, the stator resistance can be neglected. Based on these considerations, we obtain: $V_{sd} = 0, V_{sq} = V_s$ and $V_{sq} = V_s/\omega_s$.

Adapting the above equations to the simplifying assumptions gives:

$$\begin{cases} I_{sd} = \frac{\varphi_s}{L_s} - \frac{M}{L_s} I_{rd} \\ I_{sq} = -\frac{M}{L_s} I_{rq} \end{cases} \quad (4)$$

$$\begin{cases} \varphi_{rd} = \left(L_r - \frac{M^2}{L_s}\right) I_{rd} + \frac{V_s M}{\omega_s L_s} \\ \varphi_{rq} = \left(L_r - \frac{M^2}{L_s}\right) I_{rd} \end{cases} \quad (5)$$

$$\begin{cases} V_{rd} = R_r I_{rd} + \sigma L_r \frac{dI_{rd}}{dt} + \frac{M}{L_s} V_{sd} \\ \qquad -(\omega_s - \omega)\sigma L_r I_{rq} \\ V_{rq} = \left(R_r + \frac{M^2}{L_s T_s}\right) I_{rq} + \sigma L_r \frac{dI_{rq}}{dt} + \frac{M}{L_s} V_{sq} \\ \qquad -\frac{M}{L_s}\omega\varphi_{sd} + (\omega_s - \omega)\sigma L_r I_{rd} \end{cases} \quad (6)$$

The Backstepping approach, which we will apply to the control of the DFIM, is based on the principle of the orientation of the stator flux.

The model of the machine, equation 1, in the reference (d, q) is given by:

$$\begin{cases} \dot{\varphi}_{sd} = \frac{M}{T_s} I_{rd} - \frac{1}{T_s}\varphi_{sd} + V_{sd} \\ \dot{\varphi}_{sq} = \frac{M}{T_s} I_{rq} - \omega_s \varphi_{sd} + V_{sq} \\ \dot{I}_{rd} = -\delta I_{rd} + (\omega_s - \omega) I_{rq} + \alpha\varphi_{sd} - \frac{M V_{sd}}{\sigma L_s L_r} + \frac{V_{rd}}{\sigma L_r} \\ \dot{I}_{rd} = -(\omega_s - \omega) I_{rd} - \delta I_{rq} + \beta\omega\varphi_{sd} - \frac{M V_{sq}}{\sigma L_s L_r} + \frac{V_{rq}}{\sigma L_r} \\ \dot{\Omega} = -\frac{1}{J}\left(P\frac{M}{L_s}\varphi_{sd} I_{rq} + f\Omega + C_r\right) \end{cases} \quad (7)$$

III. SLIDING MODE CONTROL

The primary concept of SMC is first to attract the states of the machine right into a certainly decided on region, after which to layout a control regulation with a view to usually hold the machine in that region [14]. In summary, a SMC is split into 3 parts:

A. *Choice of switching surface*

For a non-linear system presented in the following form:

$$\dot{X} = f(X,t) + g(X,t).u(X,t) \quad X \in R^n, u \in R \quad (8)$$

Where:

$f(X,t)$, $g(X,t)$ are continuous and unsure nonlinear functions, meant limited.

We take the shape of trendy equation given with the aid of using J.J.E Slotine to decide the sliding surface given with the aid of using [15]:

$$S(X) = \left(\frac{d}{dt} + \lambda\right)^{n-1} e \quad e = X^d - X \quad (9)$$

Where λ : positive coefficient; e : error on the signal to be adjusted; n : system order.

B. *Convergence condition*

The convergence situation is described with the aid of using the equation Lyapunov [16], it makes the region appealing and invariant.

$$S(X)\dot{S}(X) < 0 \quad (10)$$

C. Control calculation

The control set of rules is described with the aid of using the relation:

$$u = u^{eq} + u^{n} \tag{11}$$

Where:

u^{eq} : is the equal control vector, may be acquired with the aid of using thinking about the situation for the sliding regime;

u^{n} : is the switching part of the control (the correction factor).

In order to relieve the unwanted chattering phenomenon, J.J.E Slotine and W. Li proposed a method to lessen it, with the aid of using the "sign" function of the switching surface [15]. The switching a part of the control u^{n} is described with the aid of using:

$$u^{n} = k\ \mathrm{sign}\big(S(X)\big) \tag{12}$$

With k is the controller gain.

To obtain the sliding mode control of a doubly-fed induction machine, the surfaces are chosen according to the error between the reference input signal and the measured signals as follows [14]:

A. Speed regulation surface

For $n = 1$, the speed control manifold can be obtained from equation (22) as follow:

$$S(\Omega) = \Omega_{ref} - \Omega \tag{13}$$

The derivative of the surface is:

$$\dot{S}(\Omega) = \dot{\Omega}_{ref} - \dot{\Omega} \tag{14}$$

Substituting the expression (equation (7)) of $\dot{\Omega}$ in equation (14), we obtain:

$$\dot{S}(\Omega) = \dot{\Omega}_{ref} + \frac{1}{J}\left(\frac{p.M}{L_s}\varphi_{sd} I_{rq} + f\Omega + C_r\right) \tag{15}$$

We take:

$$I_{rq} = I_{rq}^{eq} + I_{rq}^{n} \tag{16}$$

The control appears clearly in the following equation:

$$\dot{S}(\Omega) = \dot{\Omega}_{ref} + \frac{1}{J}\left(\frac{p.M}{L_s}\varphi_{sd}\left(I_{rq}^{eq} + I_{rq}^{n}\right) + f\Omega + C_r\right) \tag{17}$$

During the sliding mode and in steady state, we have: $S(\Omega) = 0$, $\dot{S}(\Omega) = 0$ and $I_{rq}^{n} = 0$. The equation of the equivalent control becomes:

$$I_{rq}^{eq} = -\frac{J L_s}{pM\varphi_{sd}}\left(\dot{\Omega}_{ref} + \frac{f}{J}\Omega + \frac{C_r}{J}\right) \tag{18}$$

During the convergence mode, the condition $S(\Omega)\dot{S}(\Omega) < 0$ must be verified. By replacing the expression of the equivalent control in the expression of the derivative of the surface, we obtain:

$$\dot{S}(\Omega) = \frac{pM\varphi_{sd}}{J L_s} I_{rq}^{n} \tag{19}$$

We ask:

$$I_{rq}^{n} = k_{I_{rq}}.sat\big(S(\Omega)\big) \tag{20}$$

To check the condition of stability of the system, the constant $k_{I_{rq}}$ must be negative.

B. Stator flux regulation surface

The stator flux regulation surfaces, given by the following equations:

$$S(\varphi_{sd}) = \varphi_{sd}^{ref} - \varphi_{sd} \tag{21}$$

$$\dot{S}(\varphi_{sd}) = \dot{\varphi}_{sd}^{ref} - \dot{\varphi}_{sd} \tag{22}$$

We replace the expression of $\dot{\varphi}_{sd}$ from equation (7) in equation (22):

$$\dot{S}(\varphi_{sd}) = \dot{\varphi}_{sd}^{ref} - \left(V_{sd} + \frac{M}{T_s} I_{rd} - \frac{1}{T_s}\varphi_{sd}\right) \tag{23}$$

The control current I_{rd}^{ref} defined by:

$$I_{rd}^{ref} = I_{rd}^{eq} + I_{rd}^{n} \tag{24}$$

During the sliding mode and in the steady state, we have: $S(\varphi_{sd}) = 0$, $\dot{S}(\varphi_{sd}) = 0$ and $I_{rd}^{n} = 0$. Then the equivalent command is given by:

$$I_{rd}^{eq} = \frac{T_s}{M}\left(\dot{\varphi}_{sd}^{ref} - V_{sd} + \frac{1}{T_s}\varphi_{sd}\right) \tag{25}$$

By replacing the expression of the equivalent command in the expression of the derivative of the surface, we obtain:

$$\dot{S}(\varphi_{sd}) = -\frac{M}{T_s} I_{rd}^{n} \tag{26}$$

So, for the condition $S(\varphi_{sd}) \cdot \dot{S}(\varphi_{sd}) < 0$ to be verified, we take:

$$I_{rd}^{n} = k_{I_{rd}}.sat\big(S(\varphi_{sd})\big) \tag{27}$$

With: $k_{I_{rd}}$ positive constant.

C. Direct rotor current regulation surface with limitation

In order to limit all possible overshoots of the current I_{rd}, we add a current limiter defined by:

$$I_{rd}^{lim} = I_{rd}^{max}.sat(I_{rd}) \tag{28}$$

The forward stator current error is defined by:

$$e = I_{rd}^{lim} - I_{rd} \tag{29}$$

The expression of the direct stator current control surface is given by:

$$S(I_{rd}) = e = I_{rd}^{lim} - I_{rd} \tag{30}$$

The derivative of the surface is:

$$\dot{S}(I_{rd}) = \dot{I}_{rd}^{lim} - \dot{I}_{rd} \quad (31)$$

We replace the expression of $\dot{I}_{rd}$ from equation (7) in equation (31), we find:

$$\dot{S}(I_{rd}) = \dot{I}_{rd}^{lim} - \left(-\delta I_{rd} + (\omega_s - \omega) I_{rq} + \alpha\varphi_{sd} - \frac{M}{\sigma L_s L_r} V_{sd} + \frac{1}{\sigma L_r} V_{rd}\right) \quad (32)$$

The control reference voltage V_{rd}^{ref} is defined by:

$$V_{rd}^{ref} = V_{rd}^{eq} + V_{rd}^{n} \quad (33)$$

During the sliding mode and in the steady state, we have: $S(I_{rd}) = 0$, $\dot{S}(I_{rd}) = 0$ and $V_{rd}^{n} = 0$.

So, the equivalent command is given by:

$$V_{rd}^{eq} = \left(\dot{I}_{rd}^{lim} + \delta I_{rd} - (\omega_s - \omega) I_{rq} - \alpha\varphi_{sd} + \frac{M}{\sigma L_s L_r} V_{sd}\right) \sigma L_r \quad (34)$$

We replace the expression of the flow φ_{sd} (equation 4 with $I_{sd} = 0$), the expression (34) becomes:

$$V_{rd}^{eq} = \left(\dot{I}_{rd}^{lim} + \frac{1}{\sigma T_r} I_{rd} + \frac{M}{\sigma L_s L_r} V_{sd} - (\omega_s - \omega) I_{rq}\right) \sigma L_r \quad (35)$$

By replacing the expression of the equivalent control (equation 35) in the expression of the derivative of the surface, we obtain:

$$\dot{S}(I_{rd}) = -\frac{1}{\sigma L_r} V_{rd}^{n} \quad (36)$$

For the condition $S(I_{rd})\dot{S}(I_{rd}) < 0$ must be verified, we take:

$$V_{rd}^{n} = k_{V_{rd}} . sat\left(S(I_{rd})\right) \quad (37)$$

With: $k_{V_{rd}}$ positive constant.

D. *Quadrature rotor current regulation surface with limitation*

In order to limit all possible overshoots of the current I_{rq}, we add a current limiter defined by:

$$\mathrm{I_{rq}^{lim}} = \mathrm{I_{rq}^{max}} . \mathrm{sat}\left(\mathrm{I_{rq}}\right) \quad (38)$$

The equation for the quadrature stator current control can be obtained by:

$$\mathrm{S}\left(\mathrm{I_{rq}}\right) = \mathrm{I_{rq}^{lim}} - \mathrm{I_{rq}} \quad (39)$$

The derivative of the surface is:

$$\dot{S}\left(I_{rq}\right) = \dot{I}_{rq}^{lim} - \dot{I}_{rq} \quad (40)$$

We replace the expression of the current I_{rq} from equation (7) in equation (40):

$$\dot{S}\left(I_{rq}\right) = \dot{I}_{rq}^{lim} - \left(-(\omega_s - \omega) I_{rd} - \delta I_{rq} + \beta\omega\varphi_{sd} - \frac{M}{\sigma L_s L_r} V_{sq} + \frac{1}{\sigma L_r} V_{rq}\right) \quad (41)$$

The control reference voltage V_{rq}^{ref} is defined by:

$$V_{rq}^{ref} = V_{rq}^{eq} + V_{rq}^{n} \quad (42)$$

During the sliding mode and in steady state, we have: $S\left(I_{rq}\right) = 0, \dot{S}\left(I_{rq}\right) = 0$ and $V_{rq}^{n} = 0$.

So, the equivalent command is given by:

$$V_{rq}^{eq} = \left(\dot{I}_{rq}^{lim} + (\omega_s - \omega) I_{rd} + \delta I_{rq} - \beta\omega\varphi_{sd} + \frac{M}{\sigma L_s L_r} V_{sq}\right) \sigma L_r \quad (43)$$

By replacing the expression of the equivalent control in the expression of the derivative of the surface, we obtain:

$$\dot{S}\left(I_{rq}\right) = -\frac{1}{\sigma L_r} V_{rq}^{n} \quad (44)$$

For the condition $S\left(I_{rq}\right)\dot{S}\left(I_{rq}\right) < 0$ must be verified, we take:

$$V_{rq}^{n} = k_{V_{rq}} . sat\left(S\left(I_{rq}\right)\right) \quad (45)$$

With:

$k_{V_{rq}}$ positive constant.

IV. Fuzzy Sliding Mode Control

The predominant downside of sliding mode control is the excessive switching frequency (chattering). This phenomenon is unwanted due to the fact it could excite unmodeled excessive frequency modes withinside the controlled system.

To remedy this phenomenon, a control that will provide performance prediction even if the system model is not well known is needed. This control must also adapt to variations in parameters or external disturbances. These types of control are generally called "intelligent control", working primarily on the principles of fuzzy logic and genetic algorithms.

A. *Principle of fuzzy logic*

In conventional set theory, an element does or does not belong to a set, so the degree to which an element belongs to a set can only be zero or equal to unity. On the other hand in the theory of fuzzy sets, an element can more or less belong to a set, the degree of membership of an element to a fuzzy set can take any value included in the interval [0, 1].

B. *Structure of a fuzzy controller*

Unlike conventional tuning techniques, fuzzy logic tuning does not use specific or precise formulas or mathematical relationships. But, it manipulates inferences with several fuzzy rules based on AND, OR, THEN, … etc. Fuzzy operators, applied to linguistic variables [14, 17-19].

A fuzzy logic regulator consists of the following four parts: the basis of the rules, the fuzzification, the inference engine and the defuzzification.

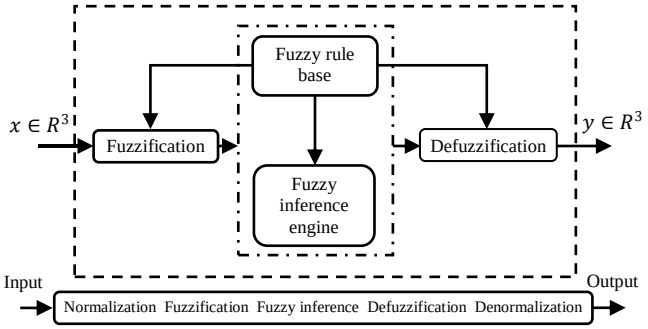

Fig. 2. General block diagram of a fuzzy controller [18].

C. *Development of a fuzzy regulator for the DFIM*

In what follows, the active and reactive power regulators are replaced by a sliding-fuzzy mode regulator to obtain robust high-performance regulation. An equivalent control part (SMC) and a fuzzy logic control (FLC) part are contained in this fuzzy sliding mode control (FSMC), figure (3), proposed by the following equation:

$$u_{FSMC} = u_{eq} + u_f \tag{46}$$

Where:

u_{eq} is the equivalent control which indicates the notion of the state trajectory along the sliding surface.

u_f is the fuzzy control (attractive), is a constant, which is set to satisfy the robustness requirement the mathematical development of this control is given in the previous section.

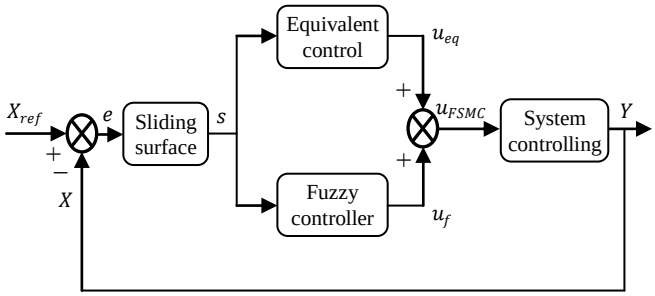

Fig. 3. Schematic of hybrid control slidnig-fuzzy.

The fuzzy controller developed in this work is by the following figure:

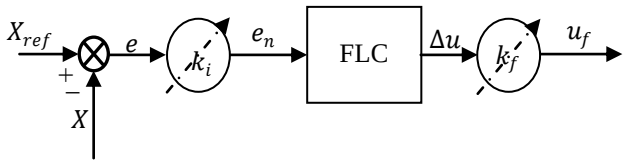

Fig. 4. Block diagram of a fuzzy controller.

In the figure above, the proposed fuzzy controller is composed by: A normalization factor k_i associated with the error (e) and k_f associated with the variation of the control Δu, fuzzification block of the error, fuzzy control rules, decide the control gains k_i according to the current operating state of the controlled system and a defuzzification block used to convert the fuzzy control variation to a digital value.

In the proposed controller (fuzzy logic system of the Mamdani type), we note that i1 is important to choose the values of k_i and k_f. A good choice and with a good distribution can guarantee a successful conception. On the other hand, a bad choice leads to long corrections in the following steps; it is often even necessary to redefine the ranges of values in order to avoid failure in the design. A good choice requires experience and knowledge of the system to be controlled.

Fuzzy rules can be written as shown in table I.

TABLE I. THE BASIS RULES OF THE FSMC.

Input	Negative Big	Negative Medium	Zero	Positive Medium	Positive Big
Output	Positive Big	Positive Medium	Zero	Negative Medium	Negative Big

The membership functions for input and output are shown in Figure (5) and Figure (6), respectively.

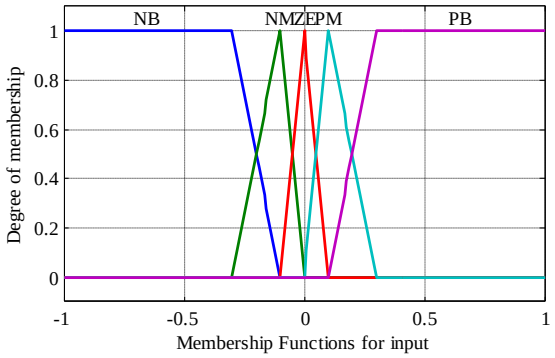

Fig. 5. Membership functions of input (e).

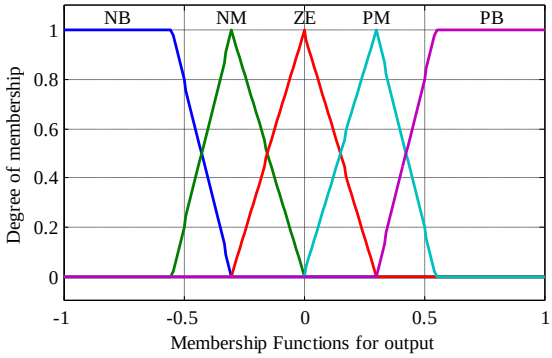

Fig. 6. Membership functions of output (u_f).

The block diagram of FSMC of a DFIM is illustrated by the figure below:

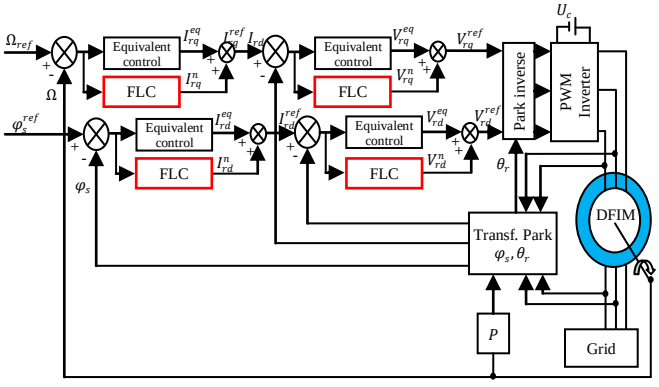

Fig. 7. Block diagram of the hybride sliding-fuzzy control of a DFIG.

V. RESULTS OBTAINED

The objective of this step is to control the doubly fed induction machine by fuzzy-sliding mode control. Different tests will be applied to show the performance of this control.

A. *Machine operation when varying the speed*

The simulation results during the variation of the speed are grouped together in figure 8. We notice the good continuation of the speed towards its new reference, the flow undergone a slight variation at the time of the speed change.

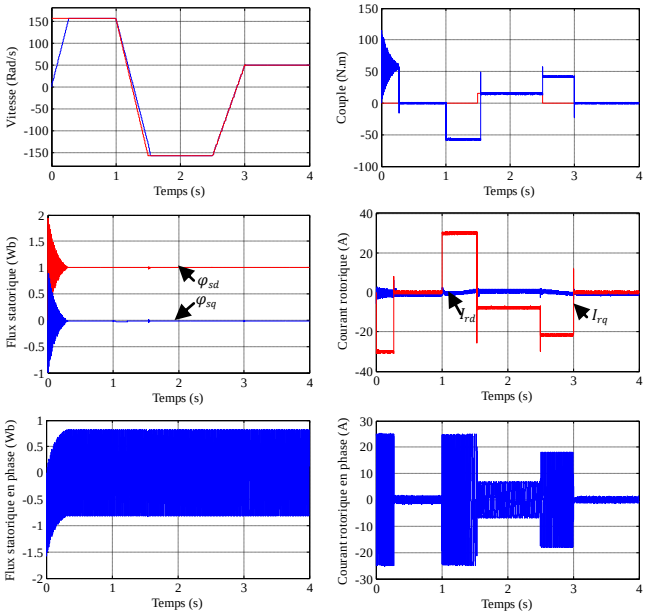

Fig. 8. Simulation results when varying the speed

B. *Operation of the machine during variation of the rotor resistance*

Figure (9) illustrates the dynamic responses of the machine, speed, torque, stator flux and rotor currents, during the variation of R_r by +100% of its nominal value between times t=1.5s and t=2.5s. We notice that no change in speed, torque and flow. Decoupling is still maintained.

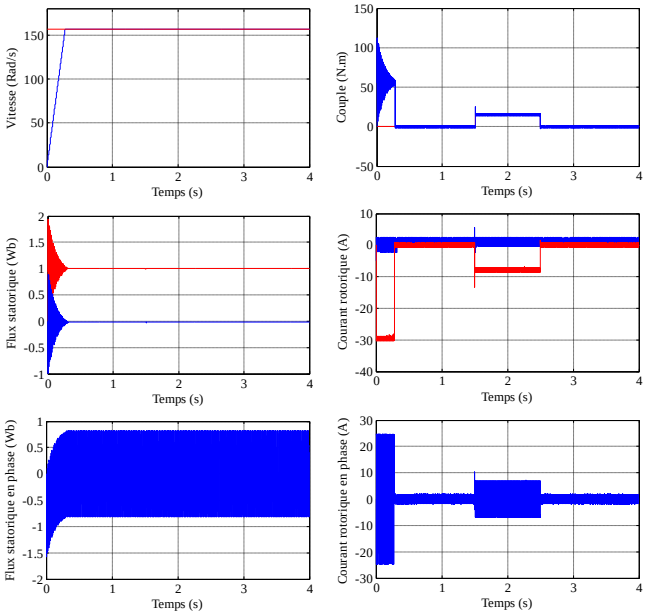

Fig. 9. Simulation results when varying the rotor resistance

C. *Machine operation during stator resistance variation*

The simulation results represented by figure (10) obtained for an increase in R_s of 100% of its nominal value. We can notice that no change in the speed variation and a small variation in the flow.

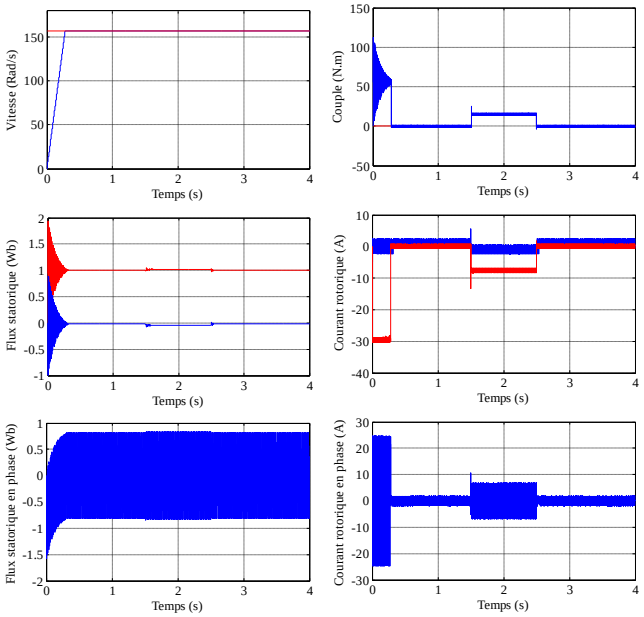

Fig. 10. Simulation results when changing stator resistance.

D. *Results interpretation*

The simulation results of the change in the speed setpoint show that the latter follows their reference well and we can see the improvement in response time. So, we can say that the hybrid fuzzy sliding control is effective (minimum chattering).

According to the results obtained during the variation of the rotor and stator resistances does not cause any undesirable effect at the level of all the dynamic responses, and this shows the robustness of the control used in the face of the parametric variation of the machine as well as the decoupling is always maintained between flux and torque.

VI. CONCLUSION

In this article, after having introduced the theory of sliding mode control, we presented a control law of the doubly fed induction machine using the technique of stator flux orientation.

In order to improve the responses generated by our engine, another control law also uses the sliding mode technique is proposed. This is the hybrid fuzzy sliding control.

Simulation results are better compared to vector control and sliding mode control. So we can say that the sliding-fuzzy command is robust to external disturbances and to parametric variations unlike the control by sliding mode.

REFERENCES

[1] A. Nasri, A. Hazzab, I.K. Bousserhane, S. Hadjiri and P. Sicard, "Two wheel speed robust sliding mode control for electrical vehicle drive", Serbian Journal of Electrical Engineering, vol. 5, no. 2, pp. 199-216, 2008.

[2] N. Derbel, J. Ghommam and Q. Zhu, "Applications of sliding mode control", Springer Science+Business Media Singapore, 2017.

[3] S. Li, X. Yu, L. Fridman, Z. Man and X. Wang, "Advances in variable structure systems and sliding mode control: theory and applications", Springer International Publishing AG, 2018.

[4] P.E. Vidal and M. Pietrzak-David, "Flux sliding mode control of a doubly fed induction machine", European Conference on Power Electronics and Applications, pp. 1-10, 2005.

[5] Y. Bekakra and D. ben attous, "A sliding mode speed and flux control of a doubly fed induction machine", International Conference on Electrical and Electronics Engineering, Bursa, pp. I-174-I-178, 2009.

[6] Z. Boudjema, R. Taleb, A. Yahdou and H. Kahal, "High order sliding mode control of a DFIM supplied by two power inverters", Journal of Electronic and Computer Engineering, vol. 8, no. 1, pp. 23-30, 2015.

[7] A. Saidi & F. Naceri, "Comparative study between sliding mode controller and fuzzy sliding mode controller in a speed control for doubly fed induction motor", 4th International Conference on Control Engineering & Infonnation Technology, Hammamet, Tunisia, 2016.

[8] A. Boucheta, I.K. Bousserhane, A. Hazzab, B. Mazari and M.K. Fellah, "Fuzzy-Sliding Mode Controller for Linear Induction Motor Control", Rev. Roum. Sci. Techn. – Électrotechn. Et Énerg., vol. 54, no. 4, pp. 405-414, 2009.

[9] I. Bendaas & F. Naceri, "A New Method to Minimize the Chattering Phenomenon in Sliding Mode Control Based on Intelligent Control for Induction Motor Drives", Serbian journal of electrical engineering, vol. 10, no. 2, pp. 231-246, 2013.

[10] A. Bouguerra, S. Zeghlache, K. Loukal and D. Saigaa, "Fault Tolerant Fuzzy Sliding Mode Controller of Brushless DC Motor (BLDC MOTOR)", the Mediterranean Journal of Measurement and Control, vol. 12, no. 2, pp.585-597, 2016.

[11] R. Rouabhi, R. Abdessemed, A. Chouder and A. Djerioui, "Power quality enhancement of grid connected doubly-fed induction generator using sliding mode control", International Review of Electrical Engineering, vol. 10, no. 2, pp. 266-276, 2015.

[12] A. Herizi, A. Bouguerra, S. Zeghlache and R. Rouabhi, "Backstepping control of a doubly-fed induction machine based on fuzzy controller", European Journal of Electrical Engineering, vol. 20, no. 5-6, pp. 645-657, 2018.

[13] F. Boumaraf, M. L. Bendaas, A. Rachid and B. Sebti, "Direct torque control of doubly fed induction machine", International Journal on Electrical Engineering and Informatics, vol. 7, no. 3, pp. 541-555, 2015.

[14] A. Herizi, "Amélioration des performances de la commande non linéaire robuste d'un moteur asynchrone à double alimentation "MADA"", Doct. Thesis, University of M'sila, Algeria, 2021.

[15] J.J.E. Slotine and W. Li, "Applied nonlinear control", Prence Hall, USA, 1998.

[16] P. Lopez and A.S. Nouri, "Théorie Elémentaire Et Pratique de La Commande Par Les Régimes Glissants", Springer, 2006.

[17] D. Ben Attous & Y. Bekakra, "Speed control of a doubly fed induction motor using fuzzy logic techniques", International Journal on Electrical Engineering and Informatics, vol 2, no. 3, pp 179-191, 2010.

[18] K. Loukal, L. Benalia and A. Bouguerra, "Speed control of a doubly fed induction motor based on fuzzy gain-adaptive IP", International Journal of Information Technology and Electrical Engineering, vol. 6, no. 3, pp. 43-50, 2017.

[19] A. Saidi and F. Naceri, "Comparative study between sliding mode controller and fuzzy sliding mode controller in a speed control for doubly fed induction motor", 4th International Conference on Control Engineering & Infonnation Technology, Hammamet, Tunisia, 2016.

Drone Hand Gesture Control

MEHIDI Mohammed
GEII Department, ENST
Algiers-Algeria
m_mehidi@enst.dz

Abstract— ***Human-machine interfaces are an important element in modern industry. Since man has become able to control several machines without any effort, this document presents a project which aims to firstly implement hand gesture movements. to control a quadcopter-type drone (AR DRONE 2.0) without using a control pad or a keyboard. Secondly developing an algorithm that makes the drone follow the hand of the user, and lastly, retrieve the information's about the path, speed, battery, and the Hight of the drone…***

Keywords— hand gesture,Hand Recognition,Drone , control ,mouvements,capture.

I. INTRODUCTION

The Gesture Recognition System has received a lot of attention in the past few years due to the diversity of its applications and the ability to interact with the machine efficiently through human-machine interaction. Hand and face gestures have become a second language that almost complements many speeches and is used in so many controls fields such as smart TVs and smartphones (screens shots using hand gestures).

our contribution is to implement gesture recognition for the control of the AR drone 2.0 type drone where we have set two criteria to be respected: the flexibility of movement and stability of the drone. 11 drone travel modes must be commanded also retrieving the trajectory followed by the drone.

The application was developed with the python language because it greatly facilitates the phase of communication with the drone.

The remainder of this paper is organized as follows. The first section gives an overview description of gesture recognition in general. The second section presents the used tools while working on this project with a brief explanation of each one of them. The third section describes the different gestures used to control the movement of the drone ensure a flexible drone movement and explaining the drone hand Follow algorithm while the last section concludes this work showing all results and discusses the possible future work.

II. GESTURE RECOGNITION

In this section, we will introduce the computer technology that allows analyzing a gesture captured by means of a computer camera to transcribe it under the form of data that can be used by a machine

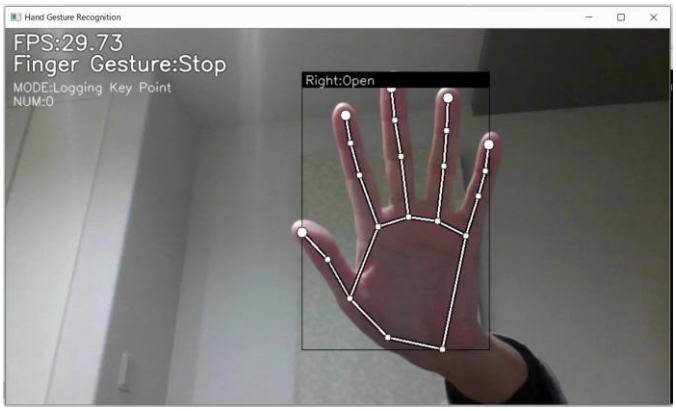

Fig. 1: Gesture recognition [1]

Gesture recognition refers to all the processes used to analyze a scene, i.e., the capture of gestures (for example using a camera or glove equipped with sensors), segmentation, assessment of poses, and interpretation strictly speaking. The following subsection presents the general structure of the gesture recognition described in [2], [3]; although the authors describe the process capture and interpretation of bodily (physical) gestures, their analysis highlights issues valid for any type of gesture, including hand and hand gestures

Pattern recognition is the information-saturated transfer stage of our world (visual, auditory,) towards the world of the machine. This process does not consist only to convert an analog information source into binary, it is a question of interpreting the source into exploitable.

III. THE USED TOOLS ON THE GESTURE CONTROL PROJECT

first of all, this project is based on a real-time concept, so we will explain this concept; A real-time application can be defined as a system whose behavior depends not only on the accuracy of the treatments performed but also on the time when the results of these treatments are produced [4]

The objectives to be achieved during the design:

- Predictable system.
- Logical determinism: the same input applied to the produced system.
- To have the same exit every time.
- Temporal determinism: time constraints are respected.
- Reliability: the system (software, hardware) meets availability constraints.

1. PyCharm development interface

PyCharm is an integrated development environment used to program in Python, it allows code analysis and contains a graphical debugger.

2. Python Libraries used:

✓ The NumPy library:

NumPy is a library for the Python programming language, intended for manipulating multidimensional matrices or arrays as well as functions mathematics operating on these tables.

Specifically, this free and open-source software library provides multiple functions allowing, in particular, to create a table directly from a file or from the opposite of saving an array in a file, and manipulating vectors, matrices, and polynomials.

NumPy is the base of SciPy, a grouping of Python libraries around computation scientists. [5]

✓ Open CV Library:

OpenCV (Open-Source Computer Vision Library) is an open-source computer vision and machine learning software library. OpenCV was built to provide a common infrastructure for computer vision applications and to accelerate the use of machine perception in commercial products. Being a BSD-licensed product, OpenCV makes it easy for businesses to utilize and modify the code. [6]

✓ MediaPipe Library

Media Pipe is a cross-platform framework for building multimodal applied machine learning pipelines MediaPipe is a framework for building multimodal (eg. video, audio, any time series data), cross-platform (i.e Android, iOS, web, edge devices) applied ML pipelines. With MediaPipe, a perception pipeline can be built as a graph of modular components, including, for instance, inference models (e.g., TensorFlow, TFLite) and media processing functions. [7]

✓ Parrot drone 2.0

The 2.0 model was introduced in May 2012, not only does it keep track of its position, but can be used to create 3D models of each movement, via the application of AR Drone. It can also store videos directly. With its 4 GB of built-in flash memory and can hold more hours of HD video. This drone has a high-density 1500 mAh battery. Currently, the AR Drone 2.0 is not capable of only five to 10 minutes of flight, even after a full charge

✓ Communication with AR Drone 2.0

Communication with the drone is done by following the following steps:

a) AR. Drone creates a WIFI network called adrone2_xxx 192.168.1.1

b) The client device connects to the network and requests an IP address from the DHCP server of the drone

c) The AR Drone DHCP server grants the client an IP address, which is 192.168.1.2

d) The client device can start sending requests to the IP address of the drone AR and its service ports

✓ Communication ports for controlling the drone

The communication ports used to control the AR Drone 2.0 are:

a) The control and configuration of the drone are done by sending commands to the UDP port "5556".

b) Navdata Information (Data Navigation) such as its status, position, speed, etc., are sent by the drone to its client on the UDP port "5554"

c) A video stream (Video Stream) is sent by the AR drone to the client device on the TCP port 5555.

After the detection of the user's hands, several algorithms were adopted to convert gestural movements into drone movements

Each point in the hand detected is marked with a number from 0 to 20, these numbers are stored in a list (a vector) to use in the acknowledgment. The points are linked together by lines to build the shape of the main in a virtual interface, the figure below shows the result.

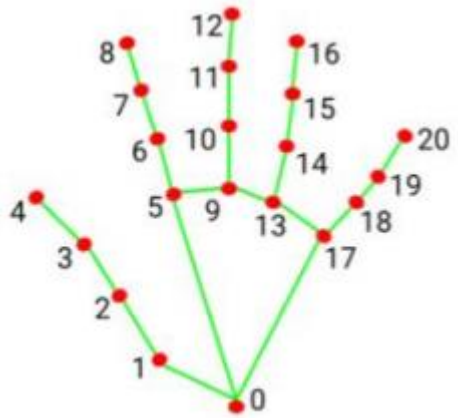

Fig. 2: Hand Landmarks [7]

0. WRIST
1. THUMB_CMC
2. THUMB_MCP
3. THUMB_IP
4. THUMB_TIP
5. INDEX_FINGER_MCP
6. INDEX_FINGER_PIP
7. INDEX_FINGER_DIP
8. INDEX_FINGER_TIP
9. MIDDLE_FINGER_MCP
10. MIDDLE_FINGER_PIP
11. MIDDLE_FINGER_DIP
12. MIDDLE_FINGER_TIP
13. RING_FINGER_MCP
14. RING_FINGER_PIP
15. RING_FINGER_DIP
16. RING_FINGER_TIP
17. PINKY_MCP
18. PINKY_PIP
19. PINKY_DIP
20. PINKY_TIP

Fig. 3: Landmarks names [7]

From these points, we define algorithms to recognize the gesture applied by the user and give the output corresponding to this gesture, each finger has been referenced by a Boolean variable that indicates whether it is raised or not, for example

- FingerOne (is up) = Ture,
- FingerOne (is down) = False

A Fingers table is defined and contains the state of each finger, from this table, the gesture applied by the user is indicated.

A small example of the Fingers vector is explained in this picture

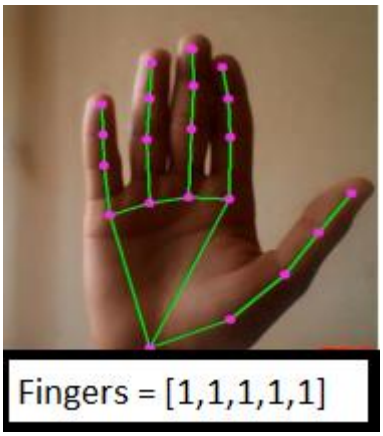

Fig. 4: gesture example

IV. THE DIFFERENT GESTURES USED TO CONTROL THE MOUVEMENT OF THE DRONE

To launch the drone (take-off), every five fingers must be raised means that the array fingers = [1,1,1,1,1], a Boolean variable "Fly" is defined to indicate that the drone is on the move. The following flowchart details the algorithm used.

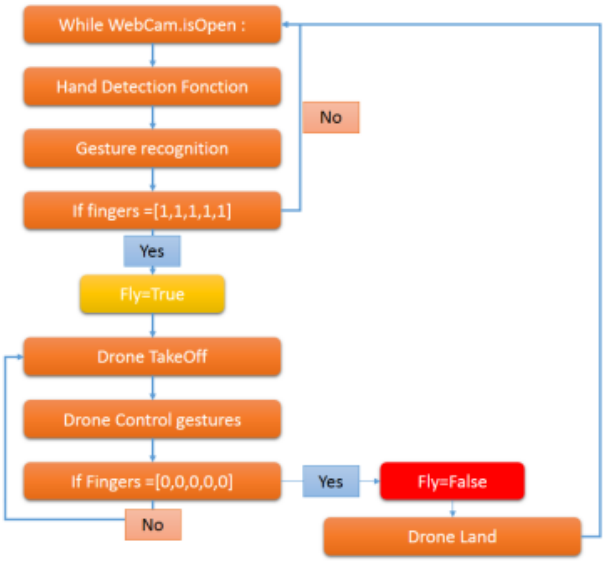

Fig. 4: organizational chart of drone launch algorithm

After the hands are detected, if the Fly variable is equal to 1, we move on to the execution of the other algorithms which depend on the applied gesture, Figure 5 shows an example execution of the take-off mode

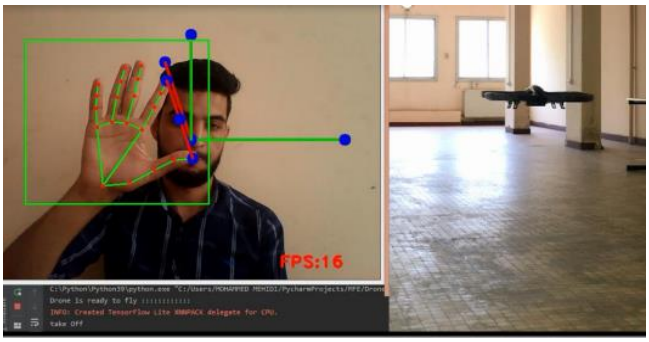

Fig. 5: an example execution of the take-off mode

Once in Take-off mode, a line is drawn between the thumb and forefinger (the line of command), modes.

1. First mode

This mode is used to control 4 movements of the drone and it is distinguished from the other mode by the three fingers (middle finger, ring finger, and little finger). When those fingers are up (fingers = [1,1,1,1,1]), the first mode is sectioned.

In this mode you can command the 4 movements (up / down / CW Rotation / CCW Rotation) depending on: the length, angle and inclination of the command line.

✓ The "up" command

the command line has an angle of 90 ° on the coordinate system and a control distance (between index finger and thumb) greater than 250, an example application is shown in figure 6:

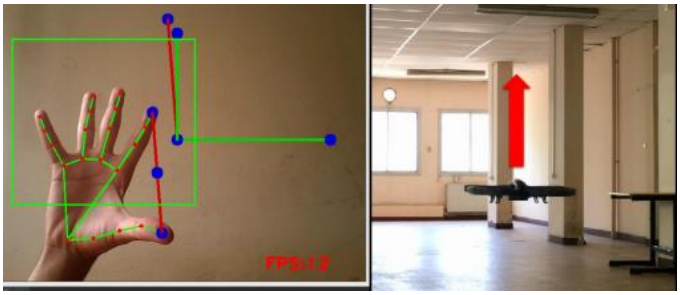

Fig. 6: the execution of the <<up>> command

✓ The "down" command

the command line has an angle of 90 ° on the reference and a control distance less than 65, an application example is shown in the figure 7

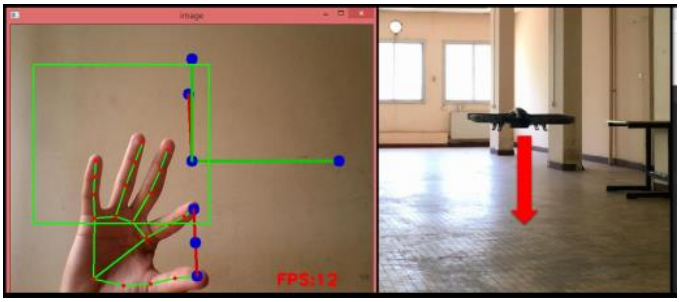

Fig. 7: the execution of the <<down>> command

✓ The "CW Rotation" command

The command line has an angle greater than 135 ° and a length greater than 170, the figure below illustrates the application of the command

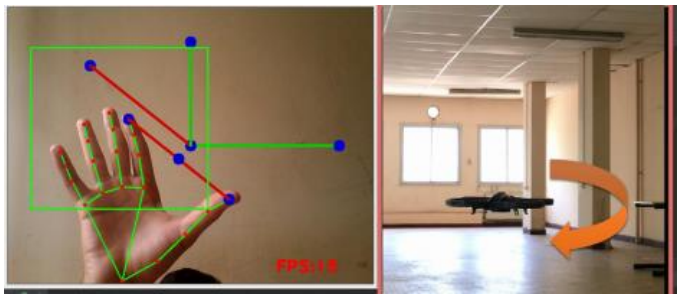

Fig. 8: the execution of the <<CW Rotation>> command

✓ The "CCW Rotation" command

The command line has an angle of less than 45 ° and a length greater than 170, Figure 9 illustrates the application of the command.

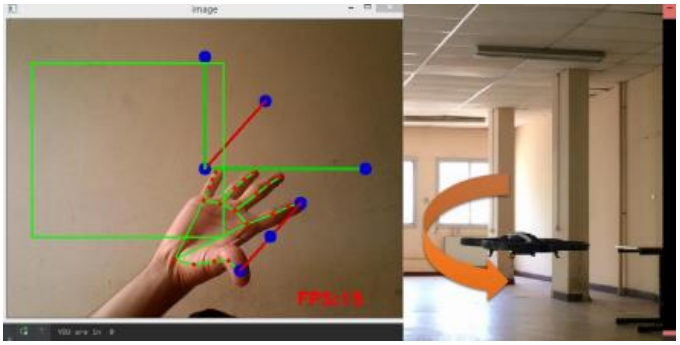

Fig. 9: the execution of the <<CCW Rotation>> command

2. Second Mode

In this mode, we are interested in the 4 remaining commands to control the drone movements. This mode is distinguished by the three fingers (middle finger, ring finger, and auricular close), the fingers vector, in this case, is equal to [1,1,0,0,0], therefore, the 4 movements (forward / backward / left shifting / right shifting) can be commanded depending on the length, angle, and inclinations of the command line.

✓ The "Forward" command

The command line has an angle of 90 ° on the reference and a control distance (between index finger and thumb) greater than 250, an example application is shown in figure 10:

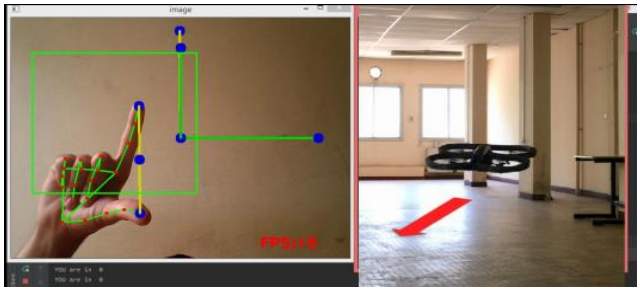

Fig. 10: the execution of the <<forward>> command

✓ The “Backward” command

The command line has an angle of 90 ° on the reference and a control distance of less than 65, an application example is shown in figure 11:

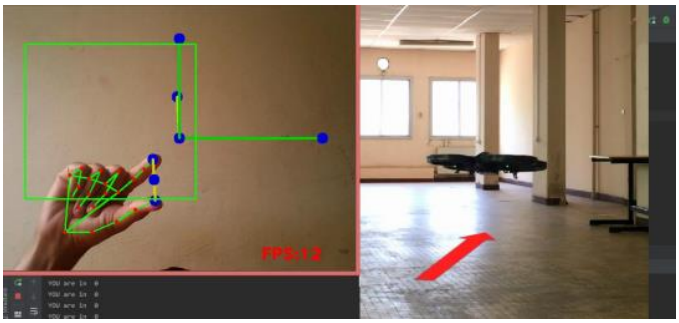

Fig. 11: the execution of the <<Backward>> command

✓ The "left shifting" command

The command line has an angle greater than 135 ° and a length greater than 170, the figure below illustrates the application of the command.

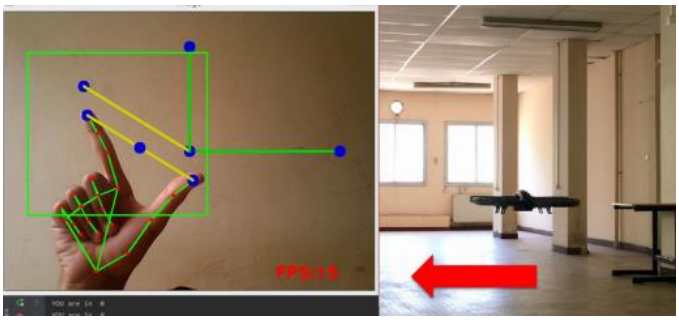

Fig. 12: the execution of the << left shifting >> command

✓ The "Right shifting" command

The command line has an angle of less than 45 ° and a length greater than 170, the figure below illustrates the application of the command

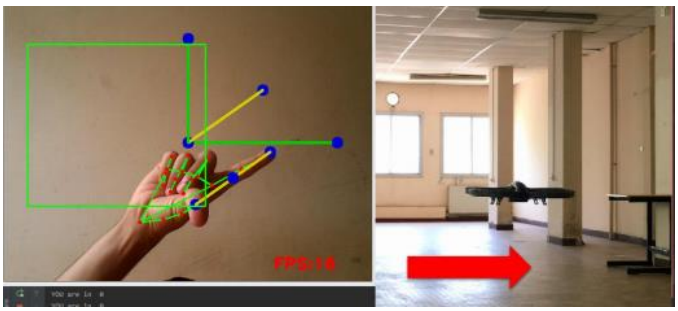

Fig. 13: the execution of the << Right shifting >> command

✓ The “Drone Hover” command

The two index and middle fingers are raised, and the distance between the two is less than 40, the figure below explains the situation

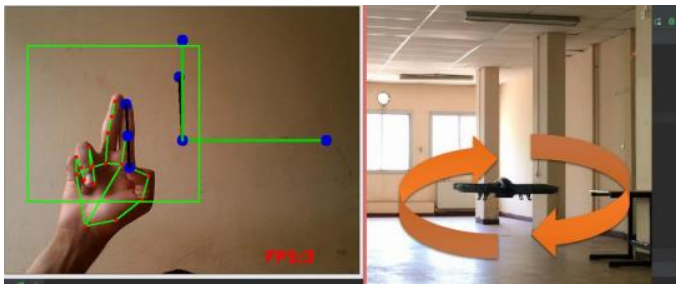

Fig. 14: the execution of the << Hover >> command

The flowchart below illustrates the two modes and the controls for each

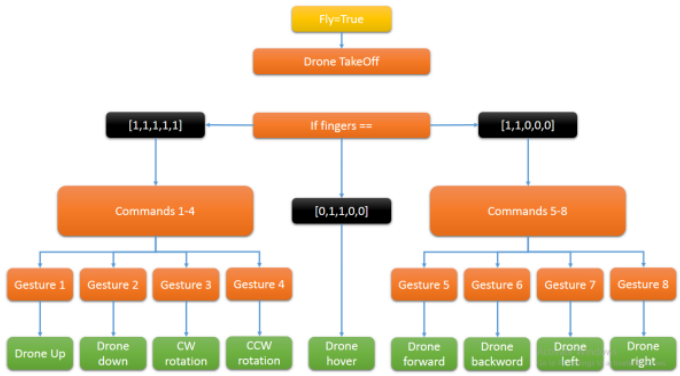

Fig. 15: organizational chart of the 2 mode of execution

IV.1. Retrieving the trajectory followed by the drone

When using the drone, it is necessary to recover the trajectory followed, for this we have defined an algorithm to have all the coordinates (x, y) of the drone in space and use them to draw a trajectory in a virtual interface. An example of a trajectory drawn when the drone moves to the left and afterward upwards is illustrated in figure 16:

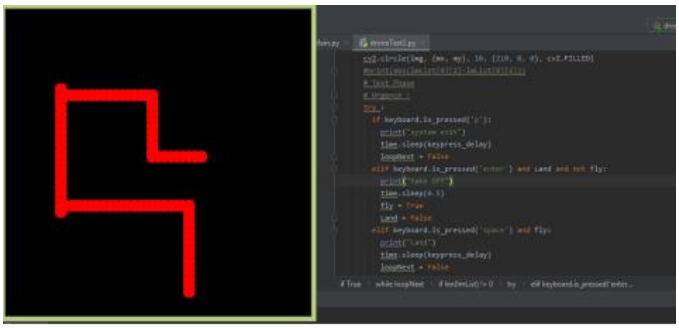

Fig. 16: Drone Draw path function result

V. THE DRONE FOLLOW HAND ALGORITHM

In this section, we have implemented an algorithm that allows the drone to follow the user's hand with the drone's front camera. The comfort zone is defined as being the area on which the drone is neither very close nor very far from the hand of the user

The figure below shows the result obtained when detecting the hand in mode Follow Hand:

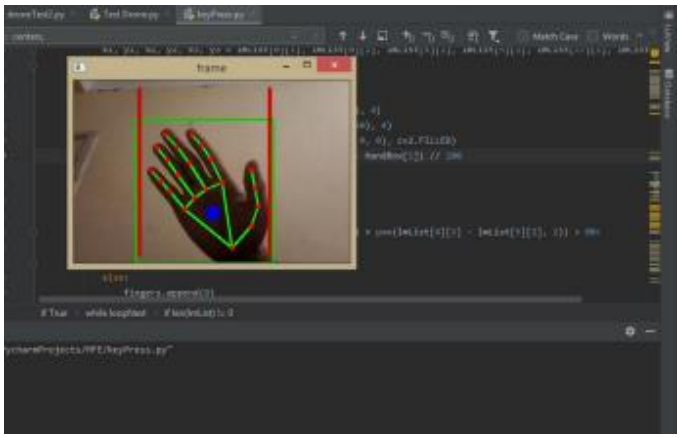

Fig. 17: Hand Detection in follow hand Algorithm

A circle is defined in the center of the hand is used to define the displacement longed for

If the diameter of this circle is very small, it means that the hand is far from the drone, therefore the drone must make a forward movement to reach the comfort zone, otherwise, if the diameter of the circle is very large, so the drone has to move back to reach the comfort zone, otherwise, the drone will stay in its position.

Now if the circle is located on the left side of the screen, then the drone should do a CW Rotation until you have the circle in the middle of the screen, the same for the case inverse, if the circle is located on the right side of the screen, then the drone must make a CCW Rotation

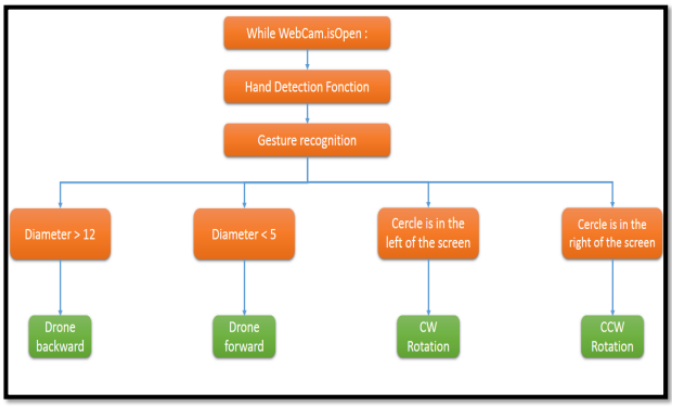

Fig. 18: organizational chart of Hand Detection in follow hand Algorithm

When testing this algorithm, it was found that when the hand is away from the drone, the detection is very bad this may be due to the quality of the drone camera. Through against for small distances, the code works perfectly. However, to do this, it is necessary to use flexibility coefficients and high-performance equipment to ensure the stability of the detection of hand movements

VI. CONCLUSION

In this chapter, we have presented an overview of the AR Drone 2.0, these features, and how to establish communication with this drone. We could control the AR Drone 2.0 by gestural movements, several algorithms have been implemented to have a flexible and stable operation. We also succeeded in recover the trajectory followed by the drone.

Finally, we were able to order the drone to follow the user's hand through the drone's front camera, but this presented its effectiveness for detection over short distances of the order of one to one and a half meters only, this is probably due to the quality of the front camera of the drone.

REFERENCES

[1]: hand gesture recognition Media pipe, GitHub, Retrieved from https://github.com/kinivi/hand-gesture-recognition-mediapipe last check 9/7/2021, 2:26 PM

[2]: Thomas B. Moeslund and Erik Granum. A survey of computer vision-based human motion capture. Comput. Vis. Image Underst., 81(3) :231–268, 2001.

[3]: Thomas B. Moeslund, Adrian Hilton, and Volker Kruger. A survey of advances in vision-based human

[4]:https://elearn.univtlemcen.dz/pluginfile.php/60327/mod_resource/content/2/Chapitre 1_Version_PDF.pdf last check 9/7/2021, 2:49 PM

[5]: «Scientific computing tools for Python — SciPy.org » on www.scipy.org (last check 9/7/2021).

[6]: About, OpenCV, Retrieved from https://opencv.org/about/ last check 9/7/2021, 2:54 PM

[7]: MediaPipe is a cross-platform framework for building multimodal applied machine learning pipelines, opensource. Google, Retrieved from https://google/projects/mediapipe last check check 9/7/2021, 2:59 PM

Contribution to induction motor control for electric traction based on intelligent techniques

Zairi Raid(1)**- Salmi Salah**(1)

(1) *Transport and Environment Engineering laboratory, University of the Mentouri brothers Constantine-1.*
E-Mails: raidzairi2901@gmail.com,

ABSTRACT— **The negative impact of CO2 emissions from diesel is forcing the electrification of rail systems to reduce gas emissions. In the case of electric traction the induction motor is considered in many applications as the best solution. This paper presents an intelligent strategy to improve the control performance of the asynchronous motor in a railway traction chain. The technique used to control this motor is IFOC because of its good suitability on the one hand its robustness, of which speed, torque and flux play an essential role in terms of the dynamic parameters of the system. The maximum torque and efficiency are obtained by controlling the speed by the conventional PI controller and that of fuzzy logic and neural network. The simulation results obtained by Matlab/Simulink show that the artificial intelligence ensures the best performance in terms of robustness, stability and fidelity during the sudden variation of the speed and torque.**

***KEY-WORDS*—Railway Traction Chain, IFOC, Artificial intelligence, machine, Simulation**

1 Introduction

Nowadays, the development in electric railway traction with induction motor operating at different frequencies, particularly with controlled voltage supply. Including powered voltage-controlled, has increased significantly owing to the technological evolution of static converters associated with control systems as well as signal processors which allow the real-time processing of complex control algorithms [1].

Induction motors (IM) are widely used as actuators for industrial applications due to their reliability, ruggedness and relatively low maintenance cost [2]. Again presence of inherent coupling effect between the torque and flux of an induction motor makes the control strategy nonlinear and motor's response becomes slow [3]. For this reason, many control techniques were developed to enable decoupling the torque and the flux, in order to control the torque and the flux independently, as in DC motors. Among these methods, we reference the IFOC established by Blaschke [4].

IFOC is commonly used with proportional-integral (PI) or proportional-integral-derivative (PID) controllers, however, in some cases, when the dynamics of the system changes with time or with operating conditions, the performance of the PI is decreased and the control quality is deteriorated (as the gains is fixed in all operating conditions). Fuzzy logic and neural networks are said to be intelligent, used to overcome the above drawbacks. This paper focused on a comparison between three control techniques for an induction motor, PI, fuzzy logic and neural network studied in numerical simulation software (Matlab/Simulink).

2 Induction motor modeling

The dynamics of the induction motor is complex because of the coupling between the stator and the rotor, especially when the coupling coefficients vary with the rotor position. In this model the real three-phase induction motor is replaced by a fictitious, but magnetically equivalent, two-phase machine, due to the Park transformation which allows the transition from a three-phase system (a, b, c) to a system (d, q, h), and certain simplifying assumptions [5].

The analytical study of an induction motor using Park's transformation requires the use of a reference frame that reduces the number of quantities that need to be known in order to simulate the operation of the machine. For this work, we have chosen the stator frame of reference because it is better suited to our study.

2.1 Voltage-fed Asynchronous Machine Model:

The model of the voltage-fed induction motor for a reference frame linked to the stator in a Park reference frame is given by the following electrical equations:

Stator :

$$\begin{cases} V_{sd} = R_s I_{sd} + \frac{d}{dt}\psi_{sd} & (1) \\ V_{sq} = R_s I_{sq} + \frac{d}{dt}\psi_{sq} & (2) \end{cases}$$

Rotor :

$$\begin{cases} V_{rd} = 0 = R_r I_{rd} + \frac{d}{dt}\psi_{rd} - \omega_r \psi_{rq} & (3) \\ V_{rq} = 0 = R_r I_{rq} + \frac{d}{dt}\psi_{rq} - \omega_r \psi_{rd} & (4) \end{cases}$$

Equations du flux :

Stator :

$$\begin{cases} \psi_{sd} = L_s I_{sd} + I_{rd} M & (5) \\ \psi_{sq} = L_s I_{sq} + I_{rq} M & (6) \end{cases}$$

Rotor :

$$\begin{cases} \psi_{rd} = L_r I_{rd} + I_{sd} M & (7) \\ \psi_{rq} = L_r I_{rq} + I_{sq} M & (8) \end{cases}$$

The equation of motion, linking the electrical and mechanical parts is written as follows:

$$j\frac{d\Omega_r}{dx} = T_e - T_r \qquad (9)$$

Torque equation :

$$T_e = \frac{PM}{L_r} .(\psi_{rd}. I_{sq} - \psi_{rq}. I_{sd}) \quad (10)$$

3 Rotor flux orientation control

The orientation of the stator flux and the air gap flux does not give good performance compared to the orientation of the rotor flux, which gives high torque but requires adaptation of the rotor parameters (which vary with temperature and frequency) [6].

In this case the rotor flux vector control that we implement is based on an orientation of the rotating frame of reference of axes (d, q) such that the d-axis is coincident with the direction of ψr. The flux ψ_r being oriented on the d-axis [7], Thus, the consequences ($\psi_r = \psi_{rd}, \psi_{rq} = 0$) are injected into the model equations to obtain the control and autopilot laws.

In this work, we will adopt an indirect control strategy by orientation of the rotor flow with position or speed sensor at the rotor, necessary to carry out the changes of coordinates.

Therefore, the motor is powered by a voltage inverter, and the control is operated using the pulse width modulation technique. In this case, the control variables are V_{sd} and V_{sq}.

State variables: i_{sd} , i_{sq} , ψ_{rd} et ψ_{rq}

Control variables: V_{sd} et V_{sq}

3.1 Rotor flux equation system

$$V_{sd} = \sigma L_s \frac{di_{sd}}{dt} + R_s i_{sd} - \omega_s \sigma L_s i_{sq} + \frac{M}{L_r} \frac{d}{dt} \psi_r \quad (11)$$

$$V_{sq} = \sigma L_s \frac{di_{sq}}{dt} + R_s i_{sq} + \omega_s \sigma L_s i_{sd} + \omega_s \frac{M}{L_r} \psi_r \quad (12)$$

$$\frac{d}{dt} \psi_r = \frac{M}{T_r} i_{sd} \quad (13)$$

$$T_e = \frac{PM}{L_r} \psi_r i_{sq} \quad (14)$$

$$\omega_r = \frac{M}{T_r} \frac{i_{sq}}{\psi_r} \quad (15)$$

$$j \frac{d\Omega_r}{dx} = T_e - T_r - f\Omega_r \quad (16)$$

For decoupling, we are interested in the compensation technique, which appears to be the simplest because it consists of adding decoupling terms on each of the axes, but with opposite signs.

4 Regulation

4.1 Application of regulator PI to the induction motor

In our work, we used the PI corrector of the proportional-integral action PI which is very widespread in the field of the control of the electric machines and its simplicity of implementation [5].Subsequently the simulation, the calculations of the coefficients (the gains) of the PI controller made by the method of pole compensation at the level of speed control as well as the stator currents (isd, isq), Unfortunately, the calculations did not give enough accuracy to put exact values, where we therefore had to adopt another method that works by the experimental, called the method of Nicole Ziegler. For this, the simulation is performed with the following parameters:

Table 1: Controller parameters used.

Regulator	Kp	Ki
Speed	200	0.5
current (d axis)	10	6000
current (q axis)	5.10	484.21

Fig. 1 present the block diagram of the simulation of an induction motor controlled by the IFOC technique and with the PI controller.

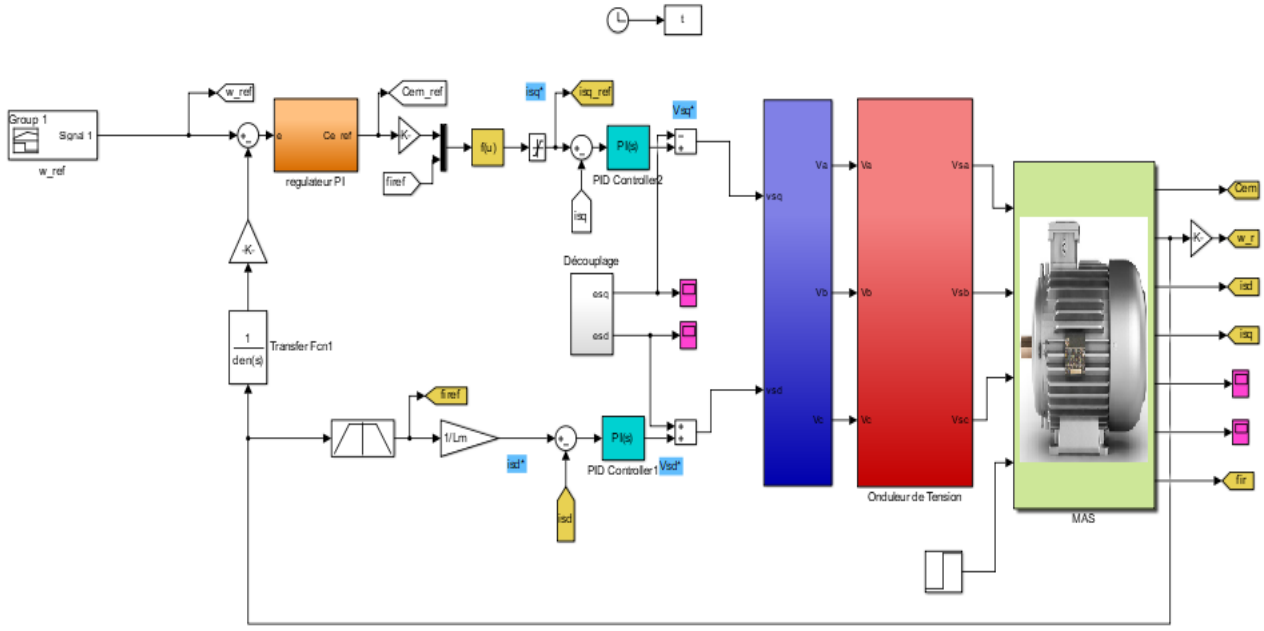

Fig. 1 Block diagram of an Induction motor controlled by the IFOC technique and with PI controller.

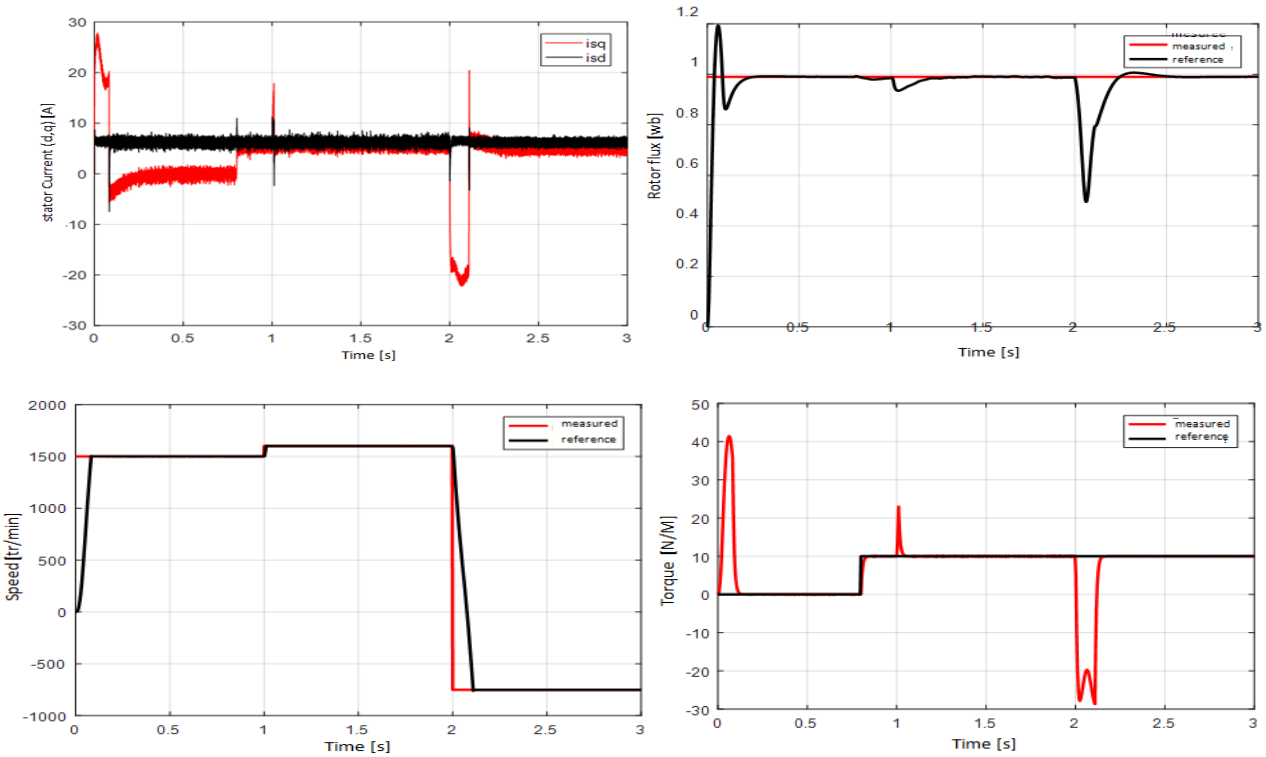

Fig. 2 Simulation results of vector control on a IM by the PI controller.

We note that the speed reached its nominal value with good dynamics and no static error. At the time of application, the load torque (Tr = 10 N.m) with a time (t = 0.8 s), the speed decreased, but it recovers again without static error. The rotor flux components show good flux control with successful decoupling, the torque is quickly controlled in the transient regime.

The emergence of the peaks and are not large in the stator phase currents and in the torque as well as in the rotor fluxes during the speed reversal and especially during the application of the load torque in the time (t = 0.8 s) with a load (Tr = 10 N.m).

4.2 Fuzzy logic speed control of the asynchronous machine

The distribution and especially the number of membership functions over the universe of discourse is very delicate because the computation time of the algorithm must be taken into account during the practical implementation.
For the input fuzzification phase We have selected the same triangular and trapezoidal membership functions for the input and output variables divided into five or seven symmetric and equidistant subsets Fig.3 and Fig.4. This choice allows an easy implementation and fuzzification step because it does not require a large computational time when evaluated in real time.

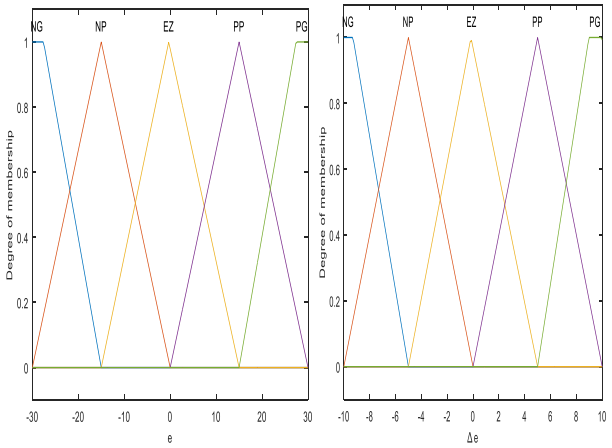

Fig. 3 Membership functions and universe of discourse for the input variables for (5*5) rules.

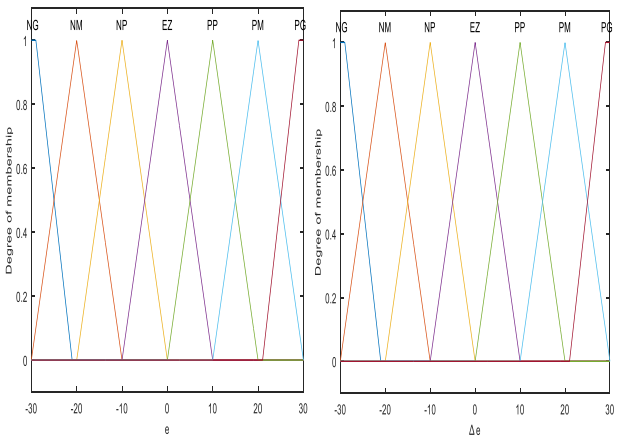

Fig. 4 Membership functions and universe of discourse for the input variables for (7*7) rules.

We have a closed-loop system of FLC regulated speed, we can establish the control rules, which link the output with the inputs, according to our basis on expertise. By offering the inputs of e and Δe which concerns the two cases (5*5) and (7*7) , there are five or seven fuzzy sets in two methods, this implies twenty-five or forty-nine successively possible combinations of these inputs, and thus twenty-five or forty-nine rules.

Table (2): Table of twenty-five rules.

e / Δe	NG	NP	EZ	PP	PG
NG	NG	NG	NG	NP	EZ
NP	NG	NG	NP	EZ	PP
EZ	NG	NP	EZ	PP	PG
PP	NP	EZ	PP	PG	PG
PG	EZ	PP	PG	PG	PG

Table (2): Table of forty-nine rules.

e / Δe	NG	NM	NP	EZ	PP	PM	PG
NG	NG	NG	NG	NG	NM	NP	EZ
NM	NG	NG	NG	NM	NP	EZ	PP
NP	NG	NG	NM	NP	EZ	PP	PM
EZ	NG	NM	NP	EZ	PP	PM	PG
PP	NM	NP	EZ	PP	PM	PG	PG
PM	NP	EZ	PP	PM	PG	PG	PG
PG	EZ	PP	PM	PG	PG	PG	PG

For defuzzification we use The centre of gravity method in order to see the variation of the reference electromagnetic torque. Where the strict value ΔC_e^* is taken from the geometric centre of the output fuzzy variable. Its discretized equation is given by:

$$\Delta C_e^* = \frac{\sum_{i=1}^{n} \Delta C_e(x_i)\mu\Delta C_e(x_i)}{\sum_{i=1}^{n} \mu\Delta C_e(x_i)} \quad (17)$$

For the simulation, we have carried out the results according to the regulation of the parameters of the corrector which are represented in table (3):

Table (3): FLC controller parameters used.

Regulator	K
Gain of the error "K_e"	0.013
Gain of the error derivative "$K_{\Delta e}$"	2e-05
Output gain "K_{Ce-ref}"	8900

For the regulation of i_{sd} and i_{sq} currents, it is the same as for the PI regulator.
Here is the block diagram of the simulation of an asynchronous machine controlled by the IFOC technique and with fuzzy logic controller.

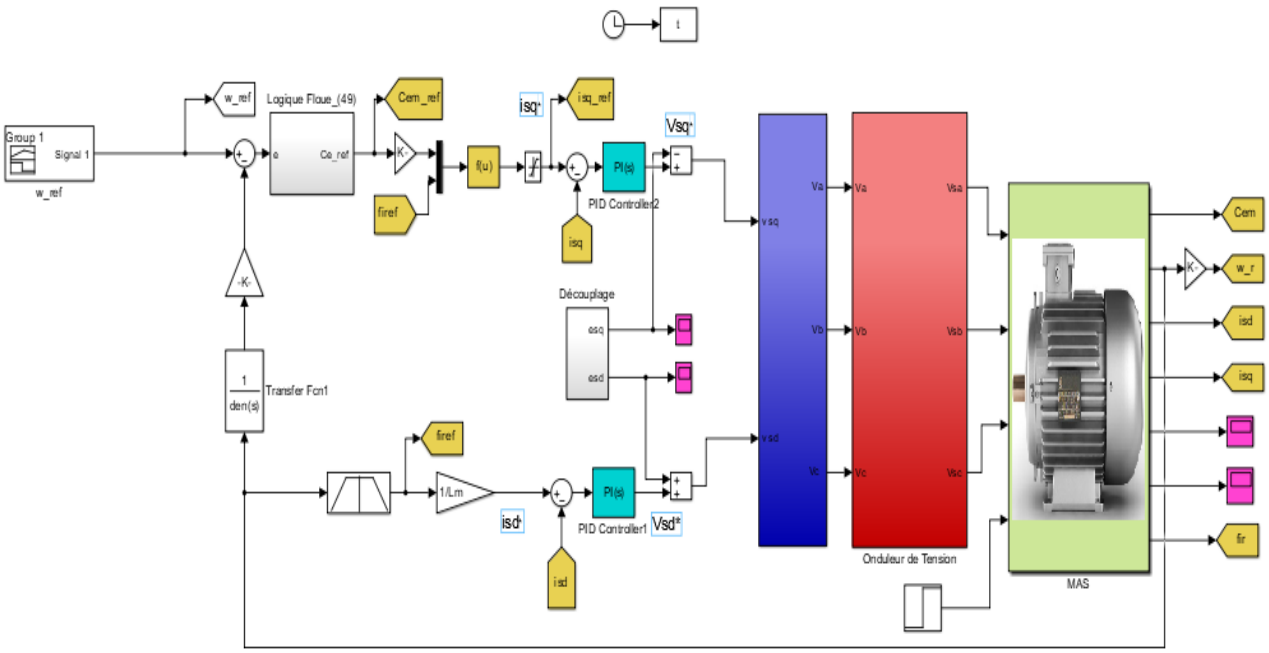

Fig. 5 Block diagram of the simulation of an induction motor controlled by the IFOC technique and with fuzzy logic controller.

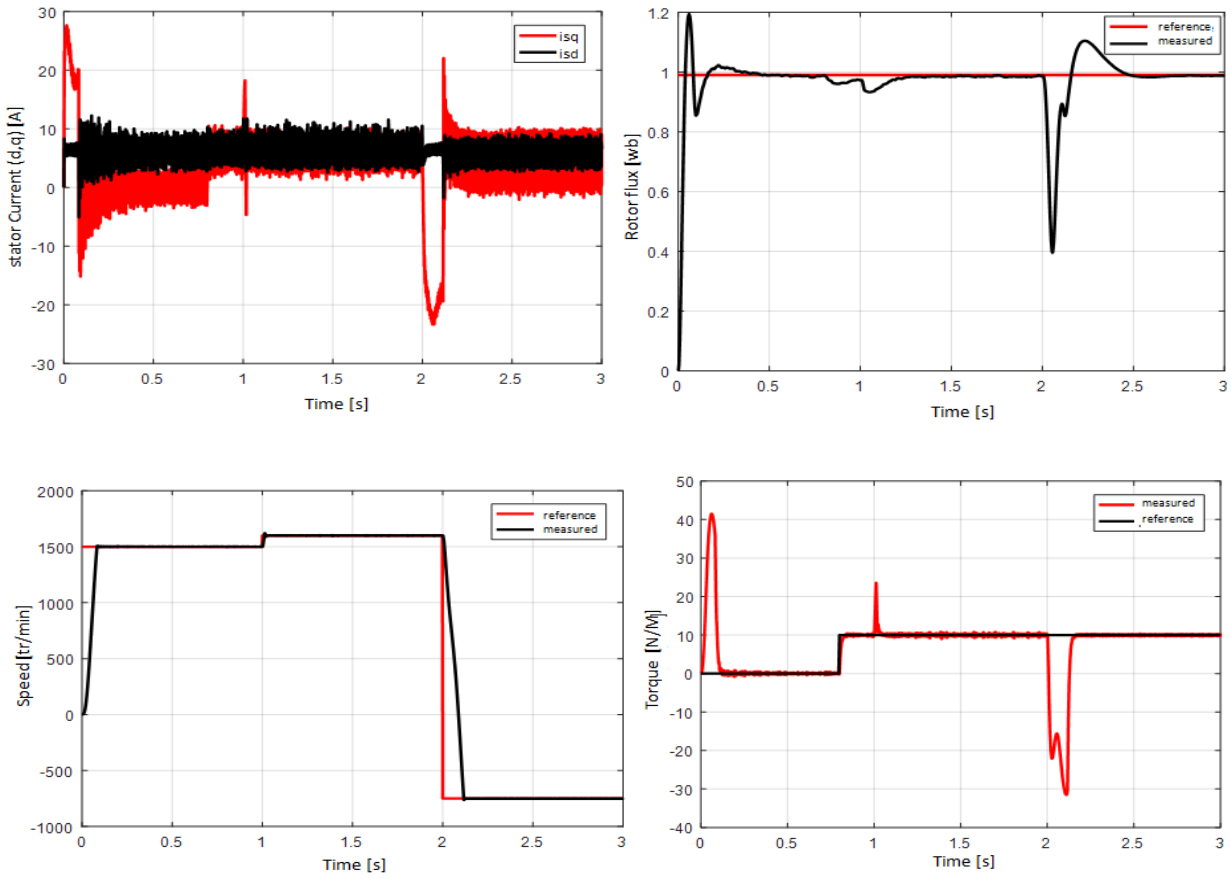

Fig. 6 Simulation results of the IFOC control of a IM by the FLC controller.

The simulation results obtained represent an improved dynamic response at the velocity level. The latter reaches its reference in a response time of 0.09s. On the other hand, the other dynamic responses evolve almost according to the same pattern. The control shows that it is insensitive to the application of the resistive load.

In these results, the decoupling between the electromagnetic torque and the flux during the application of the load (Tr = 10 N.m) over a period of (t = 0.8 s) is quickly rejected by the fuzzy speed controller. On the other hand, the ripples observed during the application of the load torque degraded the stability of the control.

The stator current curve is quasi sinusoidal, because the introduction of a load torque in (Tr = 10) N.m causes an increase in the current.

4.3 Application of neural networks to the induction motor:

4.3.1 Preparation of training data (input-output):

We have chosen the best results obtained when estimating the rotation speed of an IM regulated by fuzzy logic. Thus, 60001 samples per variable are available for the supervisor. After preparing the training base, 70% of the data were retained to be used for the supervised learning of the network, 15% for the validation of the network, and the remaining 15% were retained for the learning test.

4.3.2 Choice of neural network topology:

The choice of the neural network architecture is delicate, as there is no methodology for calculating the number of hidden layers or neurons per layer. We therefore worked by trial and error. Firstly, we opted for structures with a single hidden layer and a reduced number of neurons. Each time, the performance of the network is evaluated, and if the results are not acceptable, the number of neurons is gradually increased until the desired performance is obtained. For the activation functions, we used tangent-sigmoid functions (tansig, in Matlab) for the neurons of the hidden layers, and linear activation functions for the output of the network (purline).

4.3.3 Choice of the learning algorithm:

The last step is the choice of the learning algorithm. We have chosen the back-propagation error learning method. The algorithm chosen is the gradient descent (traingd). As regards the performance indices: the mean square error (mse) to be minimised, and the regression value R which measures the correlation between the outputs and the targets (desired outputs).

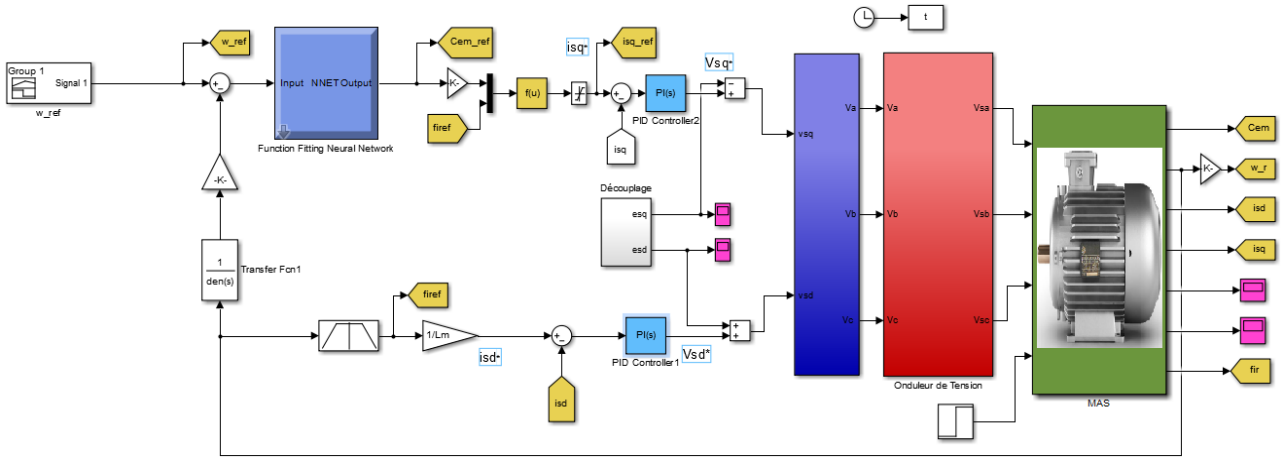

Fig. 7 Block diagram of the simulation of induction motor controlled by the IFOC technique and with neural network controller.

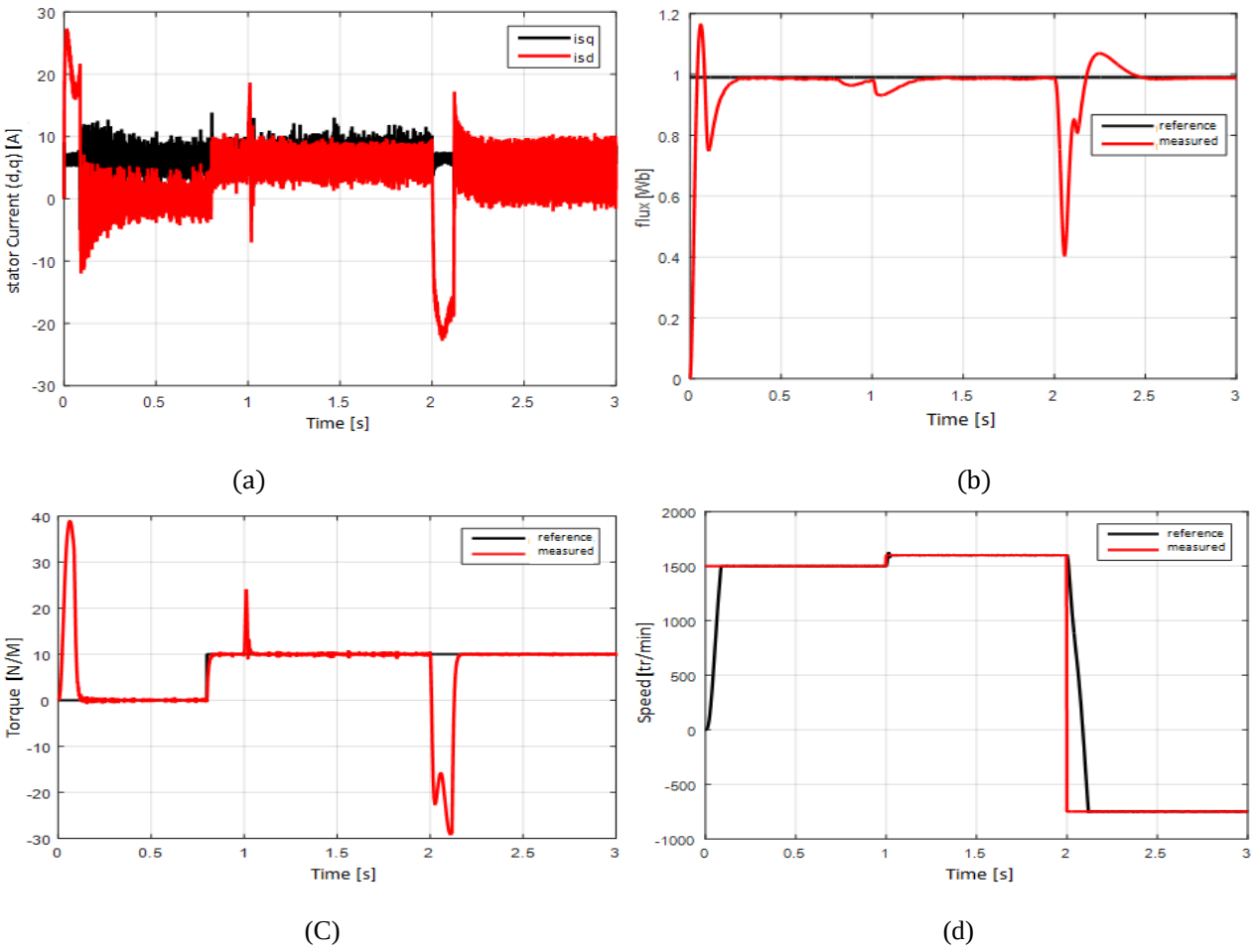

Fig. 8 (a, b, c and d). The IFOC control of an induction motor by neural network

hey all show the speed, torque, flux and stator current estimated by the ANN at no load or when applying a load. The speed behavior is presented in ***Fig. 8*** **(d),** when the load is equal to zero at t=0s and when applying a load of 10 N.m at t=0.8s the measured speed gradually reaches the reference speed (faster) and stabilizes at this reference value.

The electromagnetic torque curve illustrated in ***Fig. 8*****(c)** shows that a strong current demand between t=0s and t=0.1s (start-up) after which the torque quickly returns to its reference value. It takes the zero value as soon as the speed stabilizes.

In the initial conditions of the load i.e. t=0, the amplitudes of the currents are shown in ***Fig. 8*** **(a),** when the load is at t=0.8s the stator currents are instantaneously increased.

t can be seen that the flow ***Fig. 8 (***b) is slightly disturbed when the torque varies.

The most interesting conclusion of all the tests carried out is that the motor response and that estimated by the network are quite similar and that there is almost no error

in the steady state. This shows the ability of the model to generalize and adapt to situations not envisaged in the training phase.

4.3.4 Comparisons between regulators (PI, FLC, RNA)

Report on the results obtained in the previous section, concerning the control of the regulators (PI, FLC, and RNA). The results announced as follows:

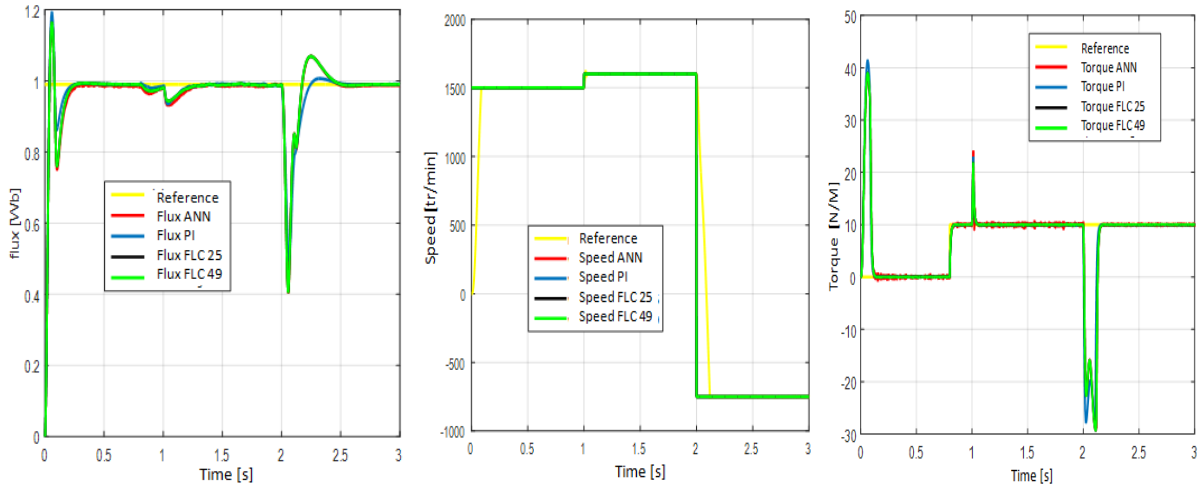

Fig. 9 Vector control results for all PI, FLC, and RNA controllers.

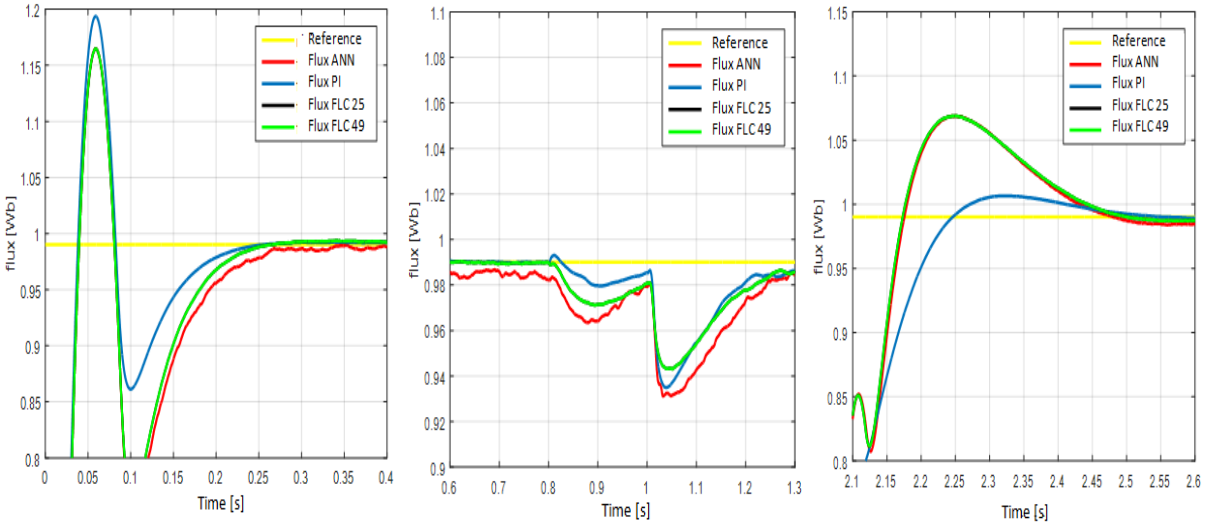

Fig. 10 Zoom of the flux for the different controllers.

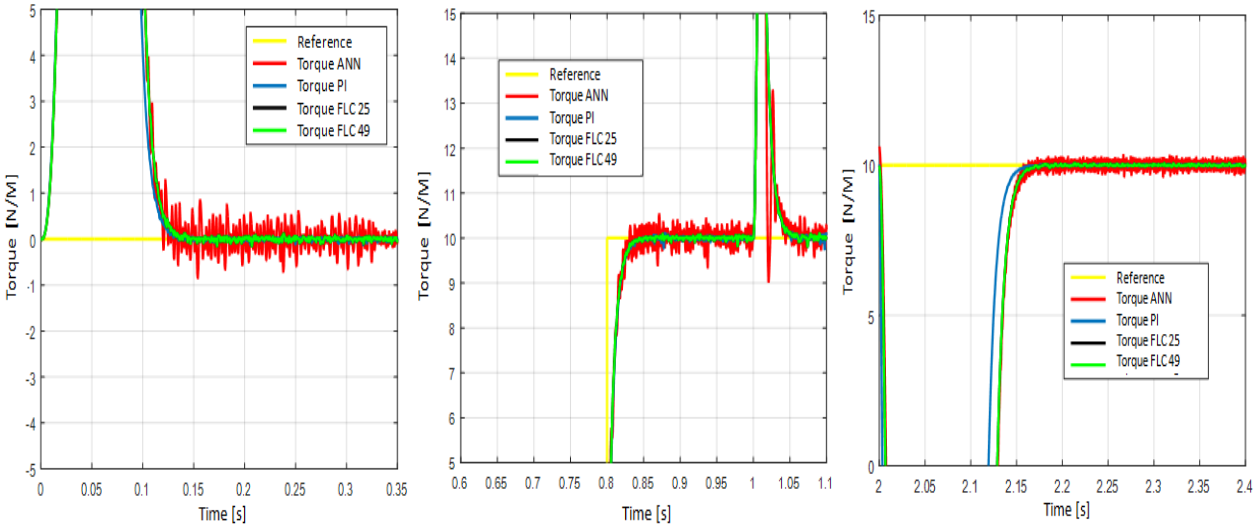

Fig. 11 Torque zoom for the different controllers

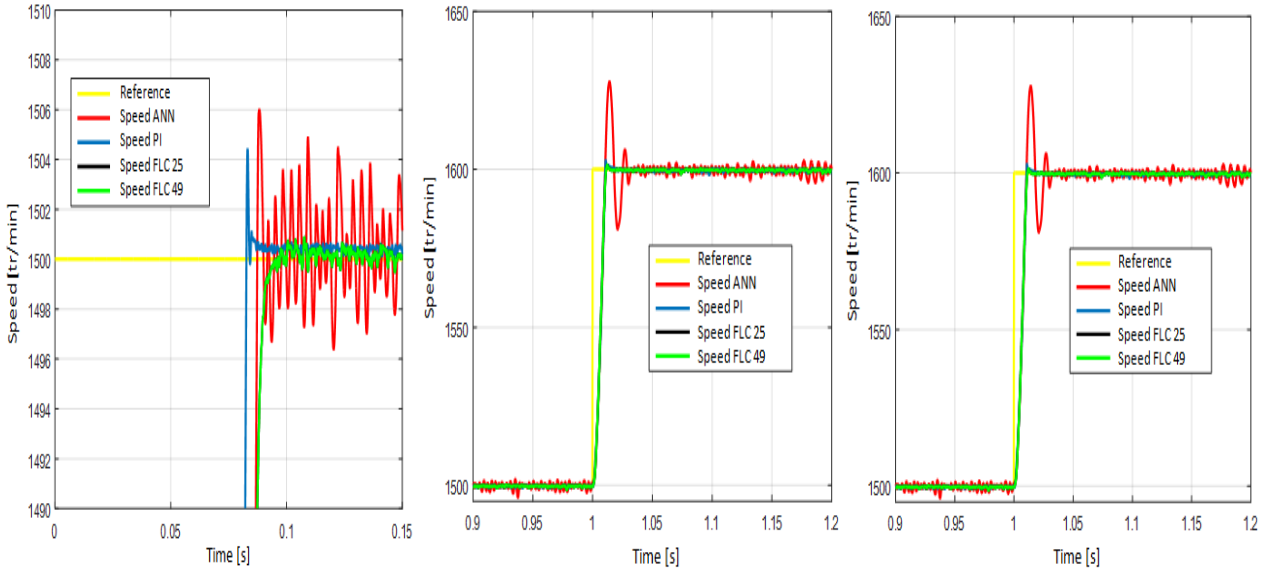

Fig. 12 Speed zoom for the different controllers.

After getting the MATLAB results, we can compare the controllers (classical PI, fuzzy controller, neural network) according to parameters to judge the best one. The comparison is done by the following table:

Table (4): Comparison between the different controllers

regulator	Proportional-Integral	Fuzzy Logic	Neuron Network
Response time	Faster than others (RN and FL)	Fast response and better than others (RN and PI)	Acceptable response compared to FL and better than PI
Performance	Acceptable performance	Acceptable performance	High performance
Robustness	Robust	Very robust	Less robust
Fidelity	Reliable	Very faithful and reliable	Faithful
Stability	Average stability	Very stable	Average stability
Defluxing	Acceptable deflection	Good deflection	Acceptable deflection

5 Conclusion

Despite the positive aspects that characterise the PI controller, it is difficult to master its role at times. The field of fuzzy logic control has become very important, thanks to its ability to process certain information, its importance lies in its high accuracy, fast dynamic response, stability, simplicity of design and implementation, and robustness to the variation of internal or external parameters. Artificial neural networks can be used to design digital controllers that can maintain high dynamic performance of the machine even with the problem of detuning, they are able to mimic the behaviour of any complex non-linear system.

6 References

[1]*SABATE, Victor. "Traction électrique ferroviaire: Convertisseurs et moteurs." Techniques de l'ingénieur. Génie électrique 12. D5502 (1998).*

[2]*Mohamadian M. , Nowicki E. , Ashrafzadeh F. , Chu A. , Sac hdeva R. , Evanik E. Un nouveau contrôleur de réseau neuronal et sa mise en œuvre DSP efficace pour les entraînements de moteurs à induction à commande vectorielle IEEE Trans. Ind. Appl. , 39 (6) (2003) , p. 1622 - 1629*

[3] *Rashid MH Power circuits électroniques, dispositifs et applications. ISBN: 978-81-317-0246-8.*

[4] *Blaschke, Felix. "The principle of field orientation as applied to the new transvector closed-loop control system for rotating-field machines," Siemens review, 1972.*

[5*] L Baghli, « Modélisation et Commande des Machines Asynchrone », Cours de Commande IUFM de Lorrain UHP, 03/04.*

[6] Grellet, Guy, and Guy Clerc. Actionneurs électriques. Éditions Eyrolles, 1997.

[7] Benoit, R. Bruno, F. Philippe, D. Jean paul, H. (2007). «*Commande vectorielle de la machine asynchrone - Désensibilisation et optimisation par la logique floue* », Edition TECHNIP 27 rue Ginoux, 75737 PARIS Cedex 15, FRANCE.

Stability enhancement of a Single Machine Infinite Bus system using H-infinity control

Abdeslem Khelloufi, Bilal Sari
DAC Laboratory, Department of Electrical Engineering
University of Setif 1
Setif, Algeria
abdeslem.khelloufi@univ-setif.dz
bilal.sari@univ-setif.dz

Seif Eddine Chouaba
DAC Laboratory
University of Setif 1
Setif, Algeria
seif.chouaba@univ-setif.dz

***Abstract*—This work presents a robust H_∞ output feedback control design of a Power System Stabilizer (PSS). This PSS is used to damp low-frequency oscillations in power systems over a wide range of operating conditions. The H_∞ control is employed in the Single-Machine connected to an Infinite Bus (SMIB) system using two weighting functions. The proposed stabilizer offers robust stability against different external disturbances and parameter uncertainties. A comparative simulation study shows a significantly enhancement and good performance of the proposed design compared to an IEEE conventional power system stabilizer.**

***Index Terms*—SMIB, Power System Stabilizer, H_∞ synthesis, Robust Control**

I. Introduction

The low-frequency oscillations are a challenge in the stability of power systems, which can lead to blackouts. These oscillations are divided into an inter-area mode, a torsional mode, and a local mode. Among the controllers used to damp low-frequency oscillations is power system stabilizers (PSS), which used to generate a supplementary damping torque signal through the excitation system [1], [2].

The conventional power system stabilizers are based on a lead-lag compensator. In the current IEEE standard [3], The types of power system stabilizers according to the number of inputs are classified in two categories: single-input like (PSS1A, PSS5C) and dual-input like (PSS2C, PSS3C, PSS4C, PSS6C, PSS7C). According to the working frequency bands,there are two types: single frequency band like (PSS1A, PSS2C,...), and multiple frequency bands like (PSS4C, PSS5C) which used to damp separate frequency bands (very low, low, intermediate, and high-frequency modes) [3]. In the literature, numerous methods have been developed to damp low-frequency oscillations. The sliding mode control (SMC) is presented in paper [4], pole placement techniques in [5], a farmland fertility algorithm (FFA) [6], a genetic algorithm [7], a Particle Swarm Optimization (PSO) [8], Bio-inspired Algorithms [9]. Therefore, artificial intelligence-based training and tuning techniques have been used to develop a PSS as a Deep Reinforcement Learning-Based method [10], adaptive neural networks approach [11], a fuzzy logic controller [12]. Furthermore, robust control theories have been employed in the design of robust power system stabilizers [13]. At the nominal operating conditions, the conventional power system stabilizer (CPSS) works efficiently, but its performance decreases if the operating point has changed [14]. In this case, the CPSS does not guarantee the power system robustness for different range of operating points. To solve the robustness problem, the robust control design guarantees stability under external disturbance or parametric uncertainties. In [15], the authors have been designed their PSS using the concept of Glover-McFarlane's loop shaping design. A Linear Matrix Inequalities (LMI) technique is used to synthesize a robust PSS usnig pole-placement [16]. Robust control methods based on H_2 and H_∞ Norm designed in [14] have been applied on an SMIB using three weighting functions. In this work, an H_∞ control approach has been developed on the SMIB using two weighting functions. This paper is organized as follows. Section II presents the description and mathematical model of the SMIB. Section III gives the control problem formulation. Section IV explains the proposed resolution and chosen weighting functions in the proposed design. Section V shows simulation results, in which a comparative study is performed between the proposed control strategy and the conventional CPSS. Finally, Section VI ends this paper and gives some concluding observations.

II. Plant Model

A SMIB system consists of a Single Machine connected to Infinite Bus through an external reactance X_e and an external resistance R_e, as shown in Fig.1.

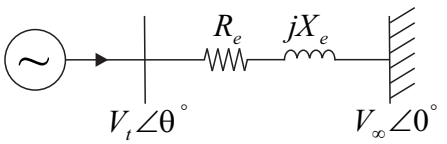

Fig. 1. Diagram of SMIB system.

The mathematical model of the synchronous machine is described by the equations given below [1]:

$$\dot{\omega} = \frac{\omega_s}{2H}[T_m - (E_q^{'} I_q + (X_q - X_d^{'}) I_d I_q) - D(\omega - \omega_s)] \quad (1)$$

$$\dot{\delta} = (\omega - \omega_s) \quad (2)$$

$$\dot{E}_q^{'} = \frac{1}{T_{do}^{'}}[E_q^{'} + (X_d - X_d^{'})I_d - E_{fd}] \quad (3)$$

$$\dot{E}_{fd}^{'} = \frac{1}{T_A}[-E_{fd} + K_A(V_{ref} - V_t)] \quad (4)$$

Where all the notations are given in the appendix.
The Heffron-Philips model scheme of the SMIB system is shown in Fig.2.

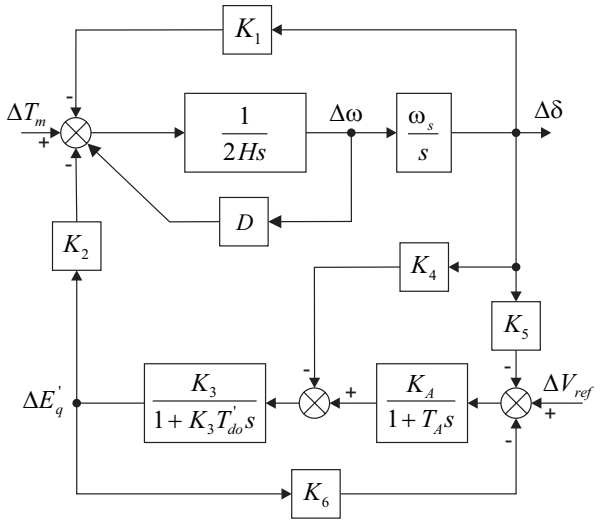

Fig. 2. Scheme of Heffron-Phillips model.

The linearized state-space model will be considered [17]:

$$\begin{aligned} \Delta\dot{x}(t) &= A\Delta x(t) + B_1\Delta w(t) + B_2\Delta u(t) \\ \Delta y(t) &= C\Delta x(t) \end{aligned} \quad (5)$$

The matrices A,B and C are defined as:

$$A = \begin{bmatrix} \frac{-1}{K_3T_{do}^{'}} & \frac{-K_4}{T_{do}^{'}} & 0 & \frac{1}{T_{do}^{'}} \\ 0 & 0 & \omega_s & 0 \\ \frac{-K_2}{2H} & \frac{-K_1}{2H} & \frac{-D\omega_s}{2H} & 0 \\ \frac{-K_AK_6}{T_A} & \frac{-K_AK_5}{T_A} & 0 & \frac{-1}{T_A} \end{bmatrix} \quad (6)$$

$$B = [B_1|B_2] = \begin{bmatrix} 0 & 0 & 0 \\ 0 & 0 & 0 \\ 0 & \frac{1}{2H} & 0 \\ \frac{K_A}{T_A} & 0 & \frac{K_A}{T_A} \end{bmatrix}, \quad (7)$$

$$C = \begin{bmatrix} 0 & 0 & 1 & 0 \end{bmatrix}, \quad (8)$$

where $\Delta x(t) = \begin{bmatrix} \Delta E_q^{'} & \Delta\delta & \Delta v & \Delta E_{fd} \end{bmatrix}^T$ is the state vector, $\Delta w(t) = \begin{bmatrix} \Delta V_{ref} & \Delta T_m \end{bmatrix}^T$ is a vector of the external inputs (External disturbances), the control signal of the power system stabilizer $\Delta u(t) = \Delta V_{pss}$ and the system output signal is $\Delta y = \Delta v$. The SMIB system data and the relationships of the model's K-constants are given in the appendices

III. Control Problem Formulation

The general configuration of the problem is illustrated in the Fig.3, where the augmented plant transfer matrix is $P(s)$, the robust controller is $K(s)$, the external inputs w are the reference voltage variation ΔV_{ref} and the mechanical torque variation ΔT_m, the measurement output y is the speed deviation, the control signal u is the output of H_∞ Power System Stabilizer (HPSS) and the external outputs z will be given in the next section.

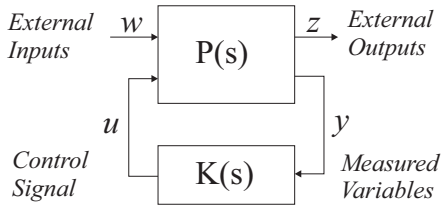

Fig. 3. Standard control configuration.

The open-loop transfer matrix from $\begin{bmatrix} z \\ y \end{bmatrix}$ to $\begin{bmatrix} w \\ u \end{bmatrix}$ is given as follows:

$$\begin{bmatrix} z \\ y \end{bmatrix} = \begin{bmatrix} P_{11}(s) & P_{12}(s) \\ P_{21}(s) & P_{22}(s), \end{bmatrix} \begin{bmatrix} w \\ u \end{bmatrix} \quad (9)$$

The linear Fractional Transformation (LFT) representation of the system in closed loop is given as follows:

$$T_{zw}(s) = P_{11}(s) + P_{12}(s)K(s)[I - P_{22}(s)K(s)]^{-1}P_{21}(s) \quad (10)$$

The H_∞ control problem is formulated as the minimisation of the H_∞ norm γ of the closed loop transfer matrix as follows:

$$||T_{zw}(s)||_\infty < \gamma \quad (11)$$

The state space representation of the standard problem configuration is given by the following form:

$$\begin{bmatrix} \dot{x} \\ z \\ y \end{bmatrix} = \begin{bmatrix} A & B_1 & B_2 \\ C_1 & D_{11} & D_{12} \\ C_2 & D_{21} & D_{22} \end{bmatrix} \begin{bmatrix} x \\ w \\ u \end{bmatrix} \quad (12)$$

where

$$B_1 = \begin{bmatrix} 0 & 0 \\ 0 & 0 \\ 0 & \frac{1}{2H} \\ \frac{K_A}{T_A} & 0 \end{bmatrix}, B_2 = \begin{bmatrix} 0 \\ 0 \\ 0 \\ \frac{K_A}{T_A} \end{bmatrix}, D_{11} = \begin{bmatrix} 1 & 0 \\ 0 & 0 \end{bmatrix},$$

$$C_1 = \begin{bmatrix} -K_6 & -K_5 & 0 & 0 \\ 0 & 0 & 0 & 0 \end{bmatrix}, D_{12} = \begin{bmatrix} 0 \\ 1 \end{bmatrix},$$

$$C_2 = \begin{bmatrix} 0 & 0 & 1 & 0 \end{bmatrix}, D_{21} = \begin{bmatrix} 0 & 0 \end{bmatrix}, D_{22} = \begin{bmatrix} 0 \end{bmatrix},$$

and A is defined in (6). One recalls that all the notations used in this state space model are given in the appendix.

IV. $H\infty$ Controller Resolution

It is necessary to include weighting functions $W_1(s)$ and $W_2(s)$ in the Plant to get some dynamical performances in an H_∞ problem. The Fig.4 illustrates the augmented plant with the weighting functions $W_1(s)$ and $W_2(s)$. The new considered external outputs are: z_1 and z_2, where z_1 is the speed deviation Δv connected to error weighting function W_1 ($z_1 = W_1(s)\Delta v$) and z_2 is the control output u connected to control weighting function W_2 ($z_2 = W_2(s)u$). The choice of these weighting functions is an essential step, an error weighting function W_1 is chosen to limit the speed deviation peak Δv. It is given by the following gain:

$$W_1(s) = \frac{1}{\Delta v_{max}} \tag{13}$$

The control weighting function $W_2(s)$ is used to accelerate the convergence of the HPSS output ΔV_{pss} to zero and therefore, the settling time of the speed deviation will be decreased. The weighting function $W_2(s)$ structure is given by the following equation:

$$W_2(s) = \frac{w_b}{s + w_b \cdot \epsilon} \tag{14}$$

Where w_b and ϵ are the tuning parameters. The following values satisfy the performance requirements for the considered nominal operating point ($P = 0.8p.u., Q = 0.4p.u.$ and $X_e = 0.2p.u.$):
$\Delta v_{max} = 10^{-3}$, $w_b = 62.5$ and $\epsilon = 10^{-4}$.
The resolution of H_∞ problem is carried out by using the LMI toolbox of Matlab. The found gamma is $\gamma = 21.288$. The obtained stabilizer HPSS can be put under the following form:

$$K(s) = \frac{a_1 s^4 + a_2 s^3 + a_3 s^2 + a_4 s + a_5}{b_0 s^5 + b_1 s^4 + b_2 s^3 + b_3 s^2 + b_4 s + b_5} \tag{15}$$

The numerical values of HPSS are given in the next table I:

TABLE I
THE HPSS DATA

Parameter	Value	Parameter	Value
a_1	$-8.72 \cdot 10^{-4}$	b_1	$8.605 \cdot 10^{-11}$
a_2	$-2.37 \cdot 10^{-3}$	b_2	$3.00 \cdot 10^{-7}$
a_3	$2.93 \cdot 10^{-1}$	b_3	$4.39 \cdot 10^{-4}$
a_4	2.94	b_4	$8.53 \cdot 10^{-2}$
a_5	$1.83 \cdot 10^{-2}$	b_5	$2.45 \cdot 10^{-8}$
b_0	$1 \cdot 10^{-14}$		

V. Simulation Results

To verify the effectiveness and the robustness of the proposed HPSS, several studies have been performed on the SMIB system at different operating points where the data of the system are given in the Appendix. Furthermore, a comparative study is carried out with a conventional CPSS. In fact, three different operating points have been considered with respect to the active power P, the reactive power Q, and the reactance of the transmission line X_e. A 5% step disturbance at the AVR voltage reference input is applied for the following tests:

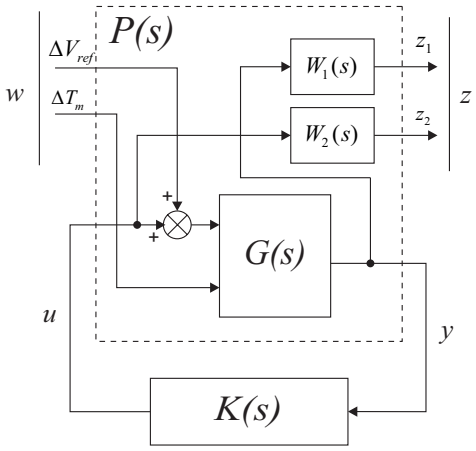

Fig. 4. Weighting functions augmentation of the system.

- 1^{st} Test (T1): $P = 0.8p.u, Q = 0.4p.u$ and $X_e = 0.2p.u.$
- 2^{nd} Test (T2): $P = 0.8p.u, Q = 0.0p.u$ and $X_e = 0.6p.u.$
- 3^{rd} Test (T3): $P = 1.0p.u, Q = 0.5p.u$ and $X_e = 0.7p.u.$

The Fig. 5, Fig. 6 and Fig. 7 present a system response using the conventional PSS (CPSS) and the proposed stabilizer (HPSS) to a 5% step disturbance at the AVR voltage reference input of the three tests (T1, T2 and T3).

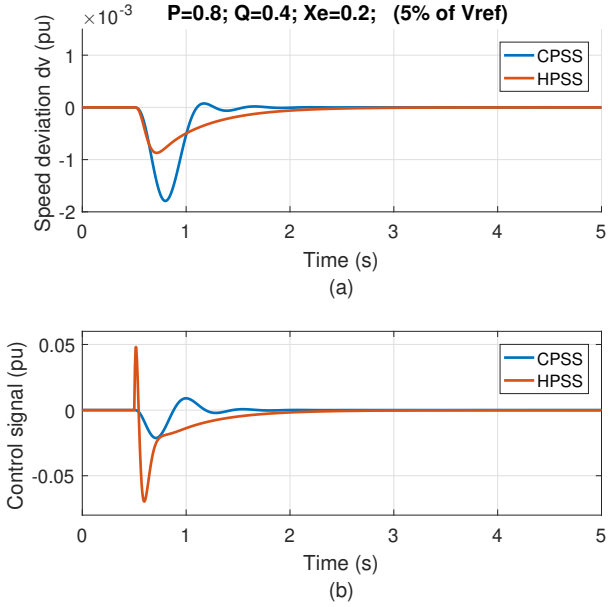

Fig. 5. SMIB response to a 5% step disturbance at the voltage reference input for the test (T1), ($P = 0.8, Q = 0.4$ and $X_e = 0.2$).

Comparing the simulation results obtained with the HPSS with a conventional CPSS shows that the proposed stabilizer achieves good robustness and performances. As can be observed in Fig.5, Fig.6 and Fig.7, the amplitude of the first oscillation of the proposed HPSS is less than the conventional CPSS in all the performed tests (T1, T2 and T3), where the conventional CPSS can not stabilize the system in the 2^{nd}

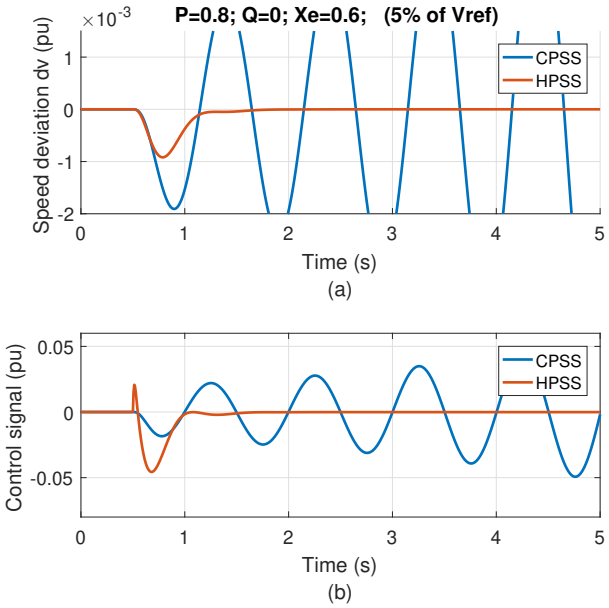

Fig. 6. SMIB response to a 5% step disturbance at the voltage reference input for the test (T2), ($P = 0.8, Q = 0.0$ and $X_e = 0.6$).

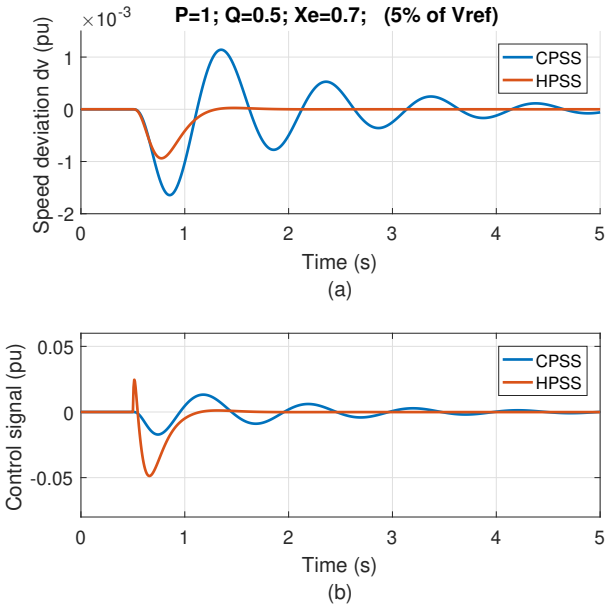

Fig. 7. SMIB response to a 5% step disturbance at the voltage reference input for the test (T3), ($P = 1.0, Q = 0.5$ and $X_e = 0.7$).

test and it has many oscillations in the 3^{rd} test. Moreover, the proposed HPSS has just one oscillation in all the performed tests. The settling times of the proposed HPSS are the least in both the 2^{nd} test and the 3^{rd} test. The control signal of the proposed design is in the range $-0.1 < V_{pss} < 0.1$ in all the tests as recommended by IEEE standard [3] which demonstrates the feasibility of the real implementation. The Table II shows a quantitative comparison of the proposed HPSS with a conventional CPSS. Where, the calculated parameter $\overline{y}_1$ represents the first oscillation amplitude of the system response, $\overline{y}_2$ is the amplitude of the second oscillation and t_s is the settling time for $|y| < 0.0001$. It is noted that the conventional CPSS gives a better settling time only in the first test compared to the proposed HPSS. However, with this CPSS, the stability is not preserved in the second test and the system became too slow in the third test. It is noted that the proposed HPSS has preserved the system stability for all three operating points. Furthermore, it is clear that the proposed HPSS has a better dynamical performance in terms of oscillations damping.

TABLE II
COMPARISON OF PERFORMANCE BETWEEN THE CONVENTIONAL PSS (CPSS) AND THE PROPOSED PSS (HPSS).

		1st Test	2nd Test	3rd Test
1^{st} amplitude	HPSS	$0.87 \cdot 10^{-3}$	$0.92 \cdot 10^{-3}$	$0.94 \cdot 10^{-3}$
$\bar{y}_1$ in p.u.	CPSS	$1.79 \cdot 10^{-3}$	Unstable	$1.64 \cdot 10^{-3}$
2^{nd} amplitude	HPSS	0.0	0.0	0.0
$\bar{y}_2$ in p.u.	CPSS	$0.75 \cdot 10^{-4}$	Unstable	$11.41 \cdot 10^{-4}$
Settling time	HPSS	1.26	0.64	0.67
t_s in s.	CPSS	0.57	Unstable	3.96

VI. CONCLUSION

This paper has presented a robust power system stabilizer design using H_∞ control to enhance the stability and robustness of the Single Machine connected to an Infinite Bus system (SMIB) against an external disturbance (Reference voltage variation ΔV_{ref} or mechanical torque variation ΔT_m). Three different unknown loads with several values of the external impedance X_e (represented by the three considered operating conditions) have been performed. The proposed HPSS controller has a simple architecture, simple weighting functions, good performance and good robustness compared to the conventional CPSS. The simulation results confirm the great benefit of the proposed HPSS compared to the conventional CPSS regarding the stability, the disturbance rejection, the speed deviation dynamical performances.

APPENDIX

A. The SMIB Equations

In this section, the relationships between the system parameters have been defined for a single machine connected to an infinite bus [18]. The values of the constants K_1 to K_6 are

defined as:

$$K_1 = \frac{X_q - X_d^{'}}{X_e + X_d^{'}} I_{q0} V_\infty sin\delta_0 + \frac{V_{q0} V_\infty cos\delta_0}{X_e + X_q}$$

$$K_2 = \frac{V_\infty}{X_e + X_d^{'}} sin\delta_0$$

$$K_3 = \frac{X_d^{'} + X_e}{X_d + X_e}$$

$$K_4 = \frac{X_d - X_d^{'}}{X_e + X_d^{'}} V_\infty sin\delta_0$$

$$K_5 = \frac{X_q}{X_e + X_q} \frac{e_{do}}{e_{to}} V_\infty cos\delta_0 - \frac{X_d^{'}}{X_e + X_d^{'}} \frac{e_{qo}}{e_{to}} V_\infty sin\delta_0$$

$$K_6 = \frac{X_e}{X_e + X_d^{'}} \frac{e_{q0}}{e_{to}}$$

where

P, Q	Active and reactive powers (p.u.)
D	Damping coefficient
H	Inertia constant (s)
ω	Rotor angular speed (rad/s)
ω_s	Synchronous rotor angular speed (rad/s)
δ	Power angle (rad)
δ_0	Initial Power angle (rad)
θ	Power angle (deg)
I_g	Generator current (p.u.)
I_d, I_q	d and q-axis components (p.u.) of the generator current
V_d, V_q	d and q-axis components (p.u.) of the generator voltage
K_A	AVR gain (p.u.)
T_A	AVR time constant (s)
R_e, X_e	Resistance and reactance of the transmission line (p.u.)
E_{fd}	Rotor field voltage (p.u.)
V_t	Terminal voltage (p.u.)
e_t	Initial terminal voltage (p.u.)
e_{d0}	Initial d-axis terminal voltage (p.u.)
e_{q0}	Initial q-axis terminal voltage (p.u.)
V_{ref}	Reference voltage (p.u.)
V_∞	Infinite bus voltage (p.u.)
T_m	Mechanical torque (p.u.)
T_e	Electrical torque (p.u.)
$E_q^{'}$	q-axis transient internal voltage (p.u.)
$T_{do}^{'}$	d-axis transient open circuit generator time constant (s)
X_d, X_q	generator d and q axis reactances (p.u.)
$X_d^{'}$	generator d-axis transient reactance (p.u.)

B. The SMIB Data

The numerical values of the SMIB parameters presented in Fig.1 are:

X_d	$X_d^{'}$	X_q	$T_{do}^{'}$	V_∞	H	ω_s	K_A	T_A
2.0	0.244	1.91	4.18	1.0	3.25	314.15	50.0	0.05
p.u	p.u	p.u	s	p.u	s	rad/s	p.u	s

C. The Convention power system stabilizer

The transfer function of the conventional power system stabilizer used in this paper is given as follows:

$$K_0(s) = K_s \frac{(s + T_1)^2}{(s + T_2)^2} \tag{16}$$

The conventional CPSS tuning parameters are obtained from [19].

REFERENCES

[1] P. Kundur, N. J. Balu, and M. G. Lauby, *Power system stability and control*. McGraw-hill New York, 1994, vol. 7.

[2] A. A. Sallam and O. P. Malik, *Power System Stability: Modelling, analysis and control*. Institution of Engineering and Technology, 2015.

[3] "IEEE Recommended Practice for Excitation System Models for Power System Stability Studies," *IEEE Std 421.5-2016 (Revision of IEEE Std 421.5-2005)*, pp. 1–207, Aug. 2016.

[4] K. Sreedivya, P. A. Jeyanthy, and D. Devaraj, "Design of power system stabilizer using sliding mode control technique for low frequency oscillations damping," in *2019 IEEE International Conference on Intelligent Techniques in Control, Optimization and Signal Processing (INCOS)*. IEEE, 2019, pp. 1–6.

[5] K. Kumara and A. Srinaivasan, "Design of pole placement power system stabilizer for SMIB-effect of operating conditions," in *2017 International Conference on Electrical, Electronics, Communication, Computer, and Optimization Techniques (ICEECCOT)*. IEEE, 2017, pp. 518–523.

[6] A. Sabo, N. I. Abdul Wahab, M. L. Othman, M. Z. A. Mohd Jaffar, and H. Beiranvand, "Optimal design of power system stabilizer for multimachine power system using farmland fertility algorithm," *International Transactions on Electrical Energy Systems*, p. e12657, 2020.

[7] M. Dubey, "Design of genetic algorithm based fuzzy logic power system stabilizers in multimachine power system," in *2008 Joint International Conference on Power System Technology and IEEE Power India Conference*. IEEE, 2008, pp. 1–6.

[8] D. Wang, N. Ma, M. Wei, and Y. Liu, "Parameters tuning of power system stabilizer PSS4B using hybrid particle swarm optimization algorithm," *International Transactions on Electrical Energy Systems*, vol. 28, no. 9, p. e2598, 2018.

[9] E. L. Miotto, P. B. de Araujo, E. de Vargas Fortes, B. R. Gamino, and L. F. B. Martins, "Coordinated tuning of the parameters of PSS and POD controllers using bioinspired algorithms," *IEEE Transactions on Industry Applications*, vol. 54, no. 4, pp. 3845–3857, 2018.

[10] G. Zhang, W. Hu, D. Cao, Q. Huang, J. Yi, Z. Chen, and F. Blaabjerg, "Deep reinforcement learning based approach for proportional resonance power system stabilizer to prevent ultra-low-frequency oscillations," *IEEE Transactions on Smart Grid*, 2020.

[11] S. Kamalasadan, G. D. Swann, and R. Yousefian, "A novel system-centric intelligent adaptive control architecture for power system stabilizer based on adaptive neural networks," *IEEE Systems Journal*, vol. 8, no. 4, pp. 1074–1085, 2013.

[12] M. Ramirez-Gonzalez and O. Malik, "Simplified fuzzy logic controller and its application as a power system stabilizer," in *2009 15th International Conference on Intelligent System Applications to Power Systems*. IEEE, 2009, pp. 1–6.

[13] K. Niimi, K. Yukita, T. Matsumura, and Y. Goto, "Verification of load frequency control using H_∞ control," in *2018 7th International Conference on Renewable Energy Research and Applications (ICRERA)*. IEEE, 2018, pp. 1174–1178.

[14] A. Sil, T. Gangopadhyay, S. Paul, and A. Maitra, "Design of robust power system stabilizer using H_∞ mixed sensitivity technique," in *2009 International Conference on Power Systems*. IEEE, 2009, pp. 1–4.

[15] S. Barik and A. T. Mathew, "Design and comparison of power system stabilizer by conventional and robust H_∞ loop shaping technique," in *2014 International Conference on Circuits, Power and Computing Technologies [ICCPCT-2014]*. IEEE, 2014, pp. 124–129.

[16] P. S. Rao and I. Sen, "Robust pole placement stabilizer design using linear matrix inequalities," *IEEE Transactions on Power Systems*, vol. 15, no. 1, pp. 313–319, 2000.

[17] P. Sauer, M. Pai, and J. Chow, *Power System Dynamics and Stability: With Synchrophasor Measurement and Power System Toolbox*. Wiley, 2017.

[18] F. P. Demello and C. Concordia, "Concepts of synchronous machine stability as affected by excitation control," *IEEE Transactions on power apparatus and systems*, vol. 88, no. 4, pp. 316–329, 1969.

[19] P. S. Rao and I. Sen, "Robust tuning of power system stabilizers using QFT," *IEEE transactions on control systems technology*, vol. 7, no. 4, pp. 478–486, 1999.

Effect of defective NPC Three level Inverter on speed artificial neural network control of Induction Motor

Mendaz Kheira
Department of electrical engineering, Belhadj Bouchaib University Ain Temouchent, IRECOM laboratory Sidi Bel Abbes, Algeria
Kheiram76@yahoo.com

Benhadda Yamina
Department of electrical engineering, Mohamed Boudiaf University, Oran, Algeria
benhadda_yamina@yahoo.fr

Attou Amine
Department of electrical engineering, Belhadj Bouchaib University Ain Temouchent, ICEPS laboratory Sidi Bel Abbes, Algeria
attouamine@yahoo.fr

Bounoua Houria
Department of electrical engineering, IRECOM laboratory Sidi Bel Abbes University, Algeria
hsemmach@yahoo.com

Abstract— this paper proposes an artificial neural network-based speed controller model of induction motor drives. The performance of traditional feedback controllers has been found to be insufficient for speed control of induction motors due to the nonlinear structure of the system, changing environmental conditions, and the effects of disturbances. This paper investigates the neural speed control of induction motor combined with three-level NPC inverter for accurate and fast speed control and on the other hand the effect of fault in three-level NPC inverter on neural speed control of induction motor. The faults presented in this work can be classified into switching faults of the three-level NPC inverter and their effects on the physical parameters of the induction motor. The simulation results are performed using Matlab/Simulink which clearly shows the robustness of this controller.

Keywords—Induction motor; neural network; NPC three level inverter; switch fault, robustness.

I. INTRODUCTION

Today, alternating current machines can replace the direct current machine in most variable speed applications. In particular, induction motor is considered the preferred actuator in constant speed applications. It offers some advantages compared to the DC motor, such as its ease of manufacture and maintenance.

The neural network (ANN) is widely used as a universal approximates in nonlinear mapping and uncertain nonlinear control problems. Neural control is very powerful tool capable of achieving very good results in the control of complex systems. It is preferred to use neural networks (ANN) for control when requirements for precision are high and system is not identified precisely or its parameters are changing [1]-[2].

In recent years, there has been an increasing demand for the use of multi-level converters in power electronics applications. The increase in the number of voltage levels in the converter output voltage leads to a satisfactory level of total harmonic distortion (THD) while reducing the stress in each switching component by reducing their supported voltages especially in high power applications. The common neutral point clamped (NPC) inverter is one of the most used multi-level topologies in industrial applications [16] because of the several advantages offered in terms of its reduced stress across the semiconductors, less harmonic content, and lower voltage distortion.

The speed sensorless vector control of induction motors driven by three-level neutral-point clamped (TL-NPC) inverters have become a research hotspot in the field of high-power, motor drive. At present, the high-voltage high-power motor drive device often adopts a three-level neutral-point clamped structure, which has the advantages of small loss, high efficiency, and small harmonics compared with a conventional two-level inverter.

The power electronics part is considered as the weakest component in the drive system and about 38% of the induction motor faults are due to switching faults. In this section the causes and effects of various switching faults in the induction motor performance are described. Switching faults may occur due to many reasons, which include electrical stress due to stored charge carriers, maximum reverse current, faulty base drive system, manufacturing defects, ageing on the capacitor, loose connections, abnormal transients, etc. It can result in reduced performance of the motor, increase in temperature that resulting an increase in stator current or may even result in shutdown of the motor [12]-[15].

Multilevel inverter offers interesting advantages such as possibility of operation in medium, high voltage and high power applications, providing a better voltage waveform with low total harmonic distortion for electric machine applications. However, the number of switches needed in the topology increases with the number of levels and, although the switches may be highly reliable, a system's fault probability will become increasing. An unbalanced voltage is generated

when a fault occurs which can produce permanent damage to the load or complete system failure [7]-[8].

This paper presents two studies: the first one is about the use of a neural speed controller for an induction motor combined with a variable speed drive which is a three-level NPC PWM inverter without application of fault. In this study, the principle of artificial neural network and three-level NPC PWM inverter are combined for better robustness, minimized ripples and higher operating performance. It is also found in this study that the neural network speed controller provides high efficiency and good resistance to speed reference variation.

The second study is to test the robustness of the neural speed controlled by applying a switching fault in the three-level NPC inverter and show there effect on physical parameters of the induction motor.

Result simulation using Matlab shows the effect of switching fault NPC three level inverter on physical parameters of the induction motor and show the performance and robustness given by neural speed controller.

II. MATHMATICAL MODEL OF INDUCTION MOTOR

The mathematical model of the induction motor is used for analyzing the dynamic behaviour of the motor. The change in the dynamic behavior of the motor affects the motor parameters such as speed, torque, resistance, flux analyzing the change in performance of the induction motor. Dynamic model of the induction motor is derived by transforming the three-phase quantities into two phases direct and quadrature axes quantities (Park transforms). Mathematical equation of the induction motor is given below (dq rotating) wish rewritten in rotation reference frame [12]:

$$\frac{d\Omega}{dt} = \frac{n_p L_m}{J L_r}\left(\varphi_{rd} I_{sq} - \varphi_{rq} I_{sd}\right) - \frac{1}{J} C_r - \frac{1}{J} f\Omega \quad (1)$$

$$\frac{dI_{sd}}{dt} = -\lambda\, I_{sd} + w_s I_{sq} + \frac{K}{\tau_r}\varphi_{rq} + w_r\, K\varphi_{rd} + \frac{1}{\sigma L_s} v_{sd} \quad (2)$$

$$\frac{dI_{sq}}{dt} = -w_s I_{sd} - \lambda\, I_{sq} - w_r\, K\varphi_{rd} - \frac{K}{\tau_r}\varphi_{rq} + \frac{1}{\sigma L_s} v_{sq} \quad (3)$$

$$\frac{d\varphi_{rd}}{dt} = \frac{L_m}{\tau_r} I_{sd} - \frac{1}{\tau_r}\varphi_{rd} + (w_s - w_r)\varphi_{rq} \quad (4)$$

$$\frac{d\varphi_{rq}}{dt} = \frac{L_m}{\tau_r} I_{sq} - (w_s - w_r)\varphi_{rd} - \frac{1}{\tau_r}\varphi_{rq} \quad (5)$$

With: $\tau_r = \frac{L_r}{R_r}$, $\sigma = 1 - \frac{L_m^2}{L_s\, L_r}$

σ: Scattering coefficient Blondel

$$landa = \lambda = \frac{1}{\tau_s\ \sigma} + \frac{1}{\tau_r}\left(\frac{1-\sigma}{\sigma}\right)$$

$$K = \frac{L_m}{\sigma L_s\ L_r}$$

III. SPEED ARTIFICIAL NEURAL CONTROL

The Artificial Neural Network (ANN) is widely used in many fields of technology application and scientific re-search. This technique can be used in cases of difficult problems that cannot be described by precise mathematical approaches where they are very complicated to manipulate [1]-[6]

The induction motor can be controlled using artificial intelligence techniques; however, Fig. 1 is depicting the control system based on artificial neural network. Mainly, two functions need to be performed in such control system, reference speed and musered speed.

However, ANN controller is required to be trained for reference speed and speed musered emulation. In this control paradigm, that, we got two inputs to ANNA in return, speed data may resource during working conditions of induction motor and feed into ANN for training purpose. [3]- [4]-[5]:

Number of layers is implemented depending on the real-world requirements, nodes are propagating in each layer, every node is performing a function on reception of data from the preceding node, so that, each node is yielding an output that differs from their input. Nodes are connected with each other by logical connections called neurons. [17]

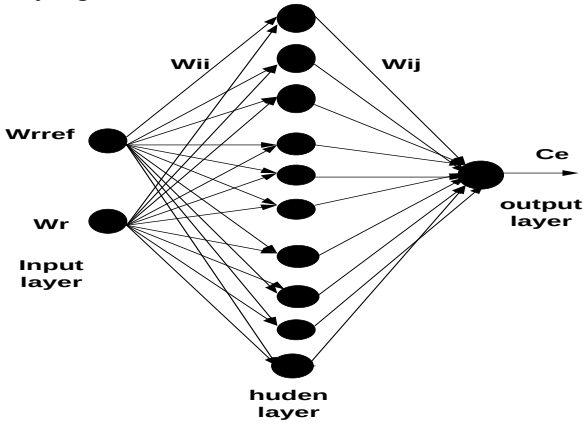

Fig. 1. Structure of ANN controller

The inputs to the network are sampled from the reference speed 'Wrref' and the musered speed 'Wr' data.

The network is trained with Levenberg-Marquardt back-propagation algorithm (LM) [14]. The structure of the neural network controller of speed was a neural network with one linear input node, 10 neurons in the hidden layer, and one neuron in the output layer [3]-[6]. The ANN algorithm is elaborated in the following steps:

Step 1: Firstly, reference speed and the musered speed are given as inputs to the network. The input vector matrix is given by [X] 2*1 with two inputs.

Step 2: Subsequently, the targets are chosen in order to attain the desired variables of the network. The target vector matrix is given by [t] 1*1 with one output.

Step 3: The weights and biases are then initialized and are updated corresponding to Levenberg–Marquardt optimization algorithm. The output vector matrix is given by [y] where [w] and [b] are the weights and biases row matrices, respectively.

Step 4: The ANN is trained by using the data provided in Step 1 and Step 2, respectively, and by fixing the goal

parameter to a minimum. The error data in the form of an error vector matrix (E) is generated to confirm that the desired convergence of the specified goal parameters or epochs during training has been met then training stops.

$$E = \frac{\sum_{i=1}^{n}(t_i - y_i)^2}{I} \quad (6)$$

Where "E" is the error data matrix obtained using a mean squared error as the objective function, "n" is the total number of outputs and "I" is the number of iterations.

Step 5: After the training the network, the optimized value of the steady state error as the output is yielded.

The structure of a developed ANN controller is 2, 10, 1, which means that the network has two neurons in the input layer, 10 neurons in the hidden layer and one neuron in the output layer. The fig.2 show model of layer of ANN in Matlab

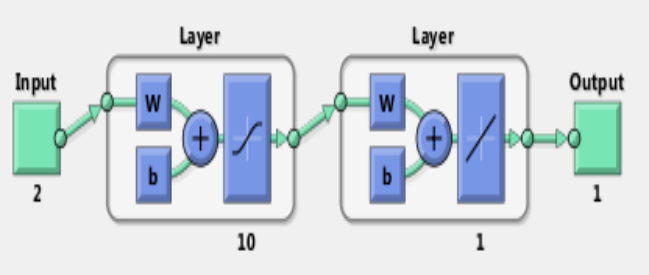

Fig. 2. Matlab model of layer1 and layer 2 off ANN controller

The Fig.3 shows the subsystem of Neural Network, It is a network with two layers: layer1 is the hidden layer and layer 2 is output layer.

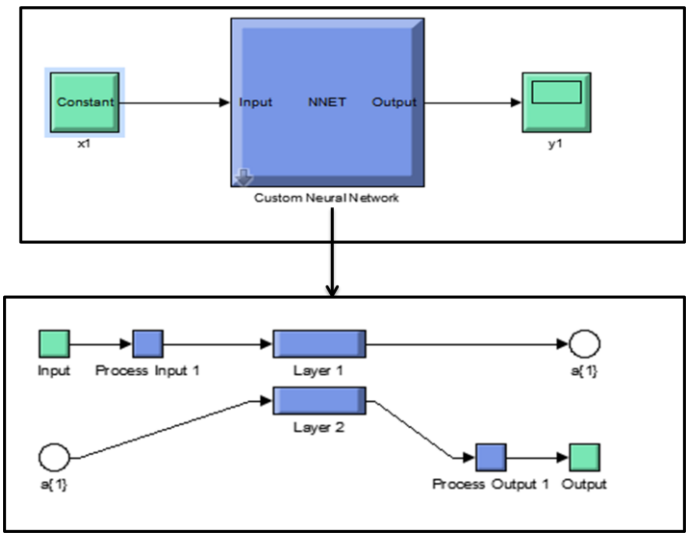

Fig. 3. Subsystem of layer1 and layer 2 off ANN controller

Fig.4 shows the command of induction motor using speed neural network control. It is a network with two neurons in the input layer, whose inputs are: reference speed W_{rref}, musered speed W_r while the output is the electromagnetic torque C_e.

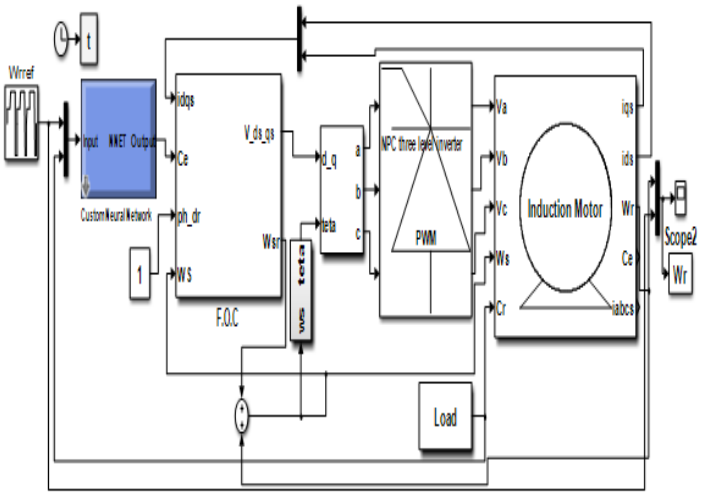

Fig. 4. Speed neural network control of induction motor associated with NPC three level inverter.

IV. NPC THREE LEVEL INVERTER STRUCTURE

A three-phase three-level NPC converter is shown in Figure4. The three phases have a common DC bus, divided by two capacitors into three levels. The voltage across each capacitor is $V_{DC}/2$; and the voltage stress across each switching device is limited to $V_{DC}/2$ through the clamping diodes. A three-level NPC converter is able to produce five levels of line to line voltage and three levels of phase voltage. This NPC converter reduces harmonics in both voltage and current output [7]-[8]-[16].

Inverter power switch faults are subdivided into short circuit and open circuit [13]-[14]-[19].

Short circuits, in most cases, that can lead to brutal damages on the switch itself or even on the drive. These faults usually cause the tripping of fuses and, in tolerant structures (conservative design), the turn-on of spare power switches [11] - [12].

Open-Switch Faults that have less immediate negative effect. However, the cumulative effect may lead to non-reversible degradations [9]-[10].

Open-Circuit Fault in K_1: To generate switching positive state, $K_1$and K_2 should be turned on, and positive currents will pass through these switching devices. While, when K_1fault occurs, another current path is formed, from $D_1$and K_2. Output current decreases to 0. When K_1 fault occurs, the switching positive state can't work as normal. [18]

Without application of fault the output voltage is equal to the reference value (200V) and the output current reaches to 1.4 A in the full-load condition, and all capacitors have the same voltage value (100 V). The voltage of capacitors is equal

to half of the DC-link voltage because of their serial connection.

Our study based on the application of three switches defected in three arms (K_1"first arms", K_7 "second arms" and K_{10}"third arms") to see the influence of this switch fault on physical parameter of squirrel cage motor by used of speed sliding and speed sliding neural controllers.

The Fig.5 shows the application of the switch fault K1, K7and K10 of three level NPC inverter.

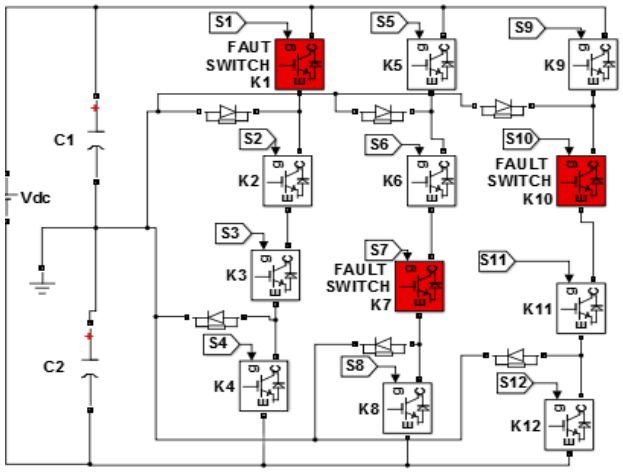

Fig. 5. NPC three level inverter with application of K_1,K_7, K_{10} switch fault

The Fig.7 show during the switch fault K1, K7and K10 at t= [0.2s 0.7s] the output filtering current decreases to 0.32A, the increase in switches faults defect on the current value which is observed by their reduction or cancellation.

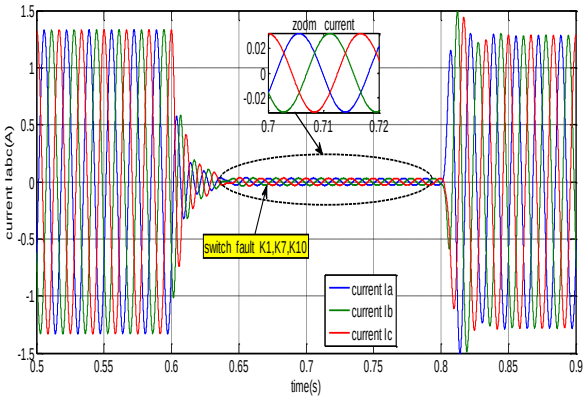

Fig. 6. Output current response of NPC three level inverter with application of K_1,K_7, K_{10} switch fault

The Fig.7 show simulation results of three levels NPC inverter outputs line-line voltages with three states. The system is operating normally before 0.6s. When the switch fault K_1, $K_7$and K_{10} occurs at t= [0.6s 08s], the output voltage of three level inverter NPC is distorted and the level of the output voltage is reduced.

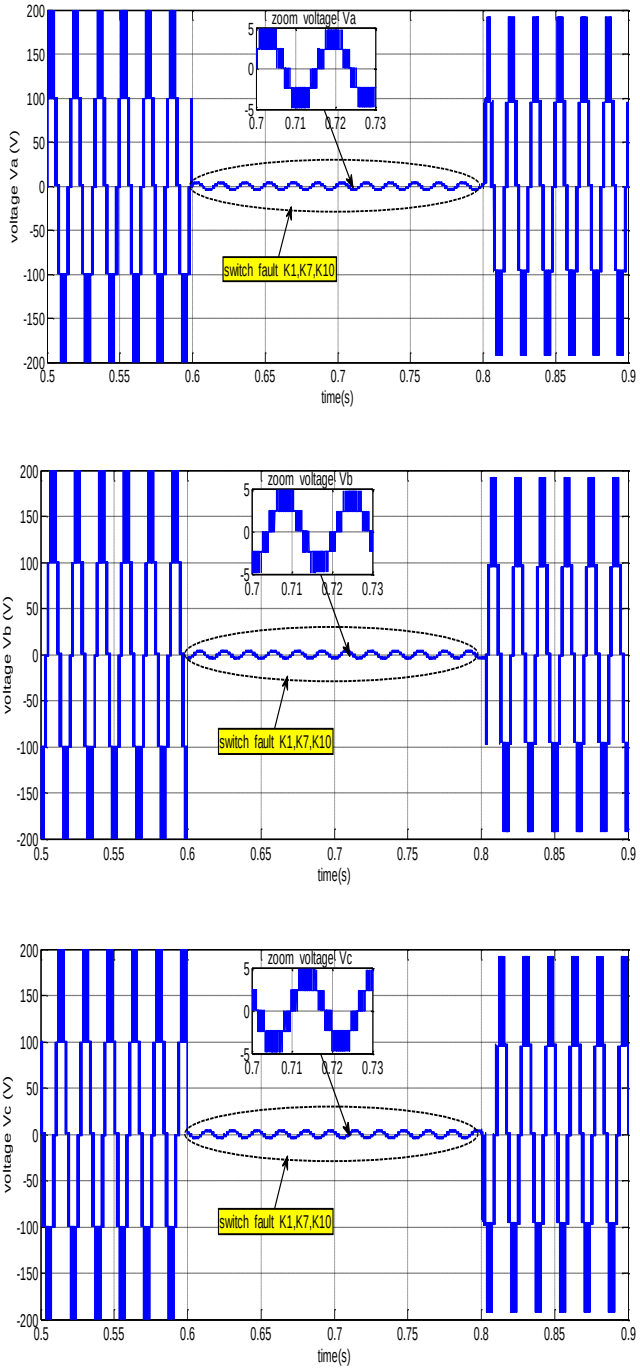

Fig. 7. Output voltaget response of NPC three level inverter with application of K_1,K_7, K_{10} switch fault

The Fig. 8 shows the filtered output voltage which is equal to the reference voltage before the fault (200v) but during the application of a switch fault K_1, K_7 and K_{10} notice a significant decrease in the output filtering voltage (5v).

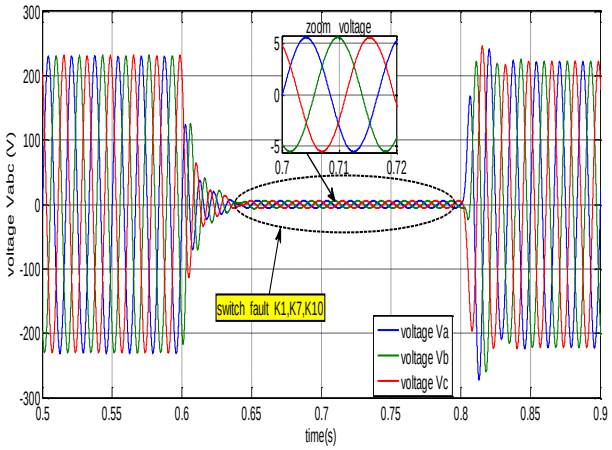

Fig. 8. Output voltage response of NPC three level inverter with application of K_1,K_7, K_{10} switch fault

V. SIMULATION RESULT

The results presents firstly the use of a neural speed controller for an induction motor combined with NPC three-level inverter without application of fault, and secondly the existence of this controller with the defects of switch fault.

The simulation results given by Fig.9 show that the speed artificial neural network control without application of switch fault is robust with respect to the variation of the reference speed, since the speed measured without fault track the reference speed at start up as at the reversal of direction of rotation, in a very satisfactory, it can be observed also that the measured speed does not influence by the application of load at time t=0.2s. Concerning the torque response, we can observe that it follows the load value, as we can notice the effect of the speed increase and the rotation direction reversal on their response. From these results, it can be concluded that the neural speed controller gives satisfactory results.

The application of switches fault K1, k7 and K10 at time t= [0.6s 0.8s] in the three-levels NPC inverter associated with the induction motor by the use of speed artificial neural network control, we can see that this type of defect causes a disturbed and unstable operation of the system due to the change in the mode of operation during the application of the defect.

During the application of defect K1, k7 and K10 of NPC three level inverter with application of speed artificial neural network control shows a very significant decrease in the speed, as it can also notice that the torque rate also have very strong undulations during a fault. We result that the presence of this type of inverter defect can damage other components and endanger the operation of the system.

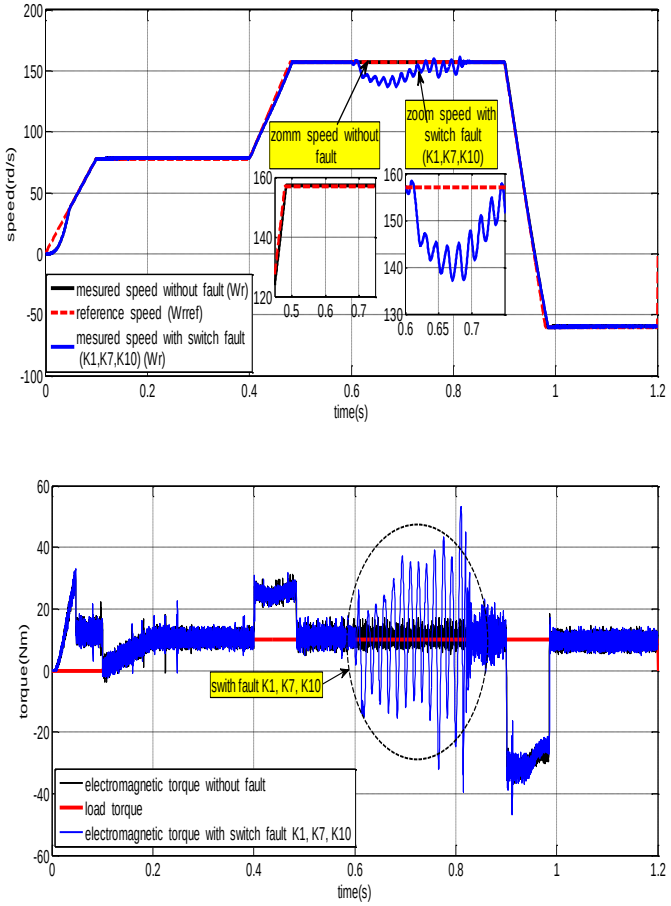

Fig. 9. Speed and torque response for speed artificial neural control with application of K_1,K_7, K_{10} switch fault of NPC three level inverter.

The Fig.10 shows that during the switches fault K_1, K_7, K_{10} at the time t= [0.6s 0.8s] we can see a strong increase in the rotor and stator current and huge imbalance is noticed in this two phase currents, where they magnitude reaching a very high value which leads to the degradation of the system and damaging of the motor.

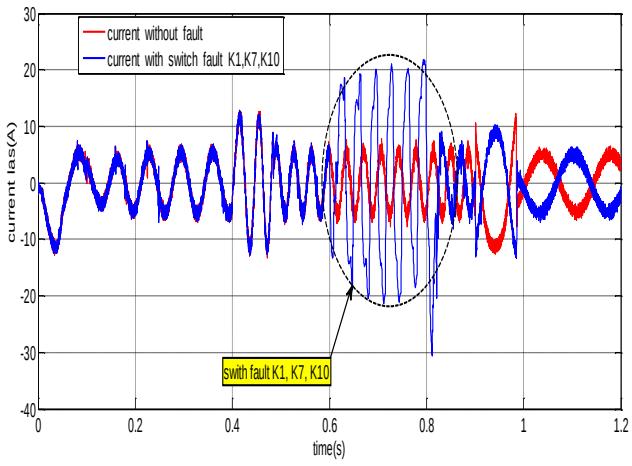

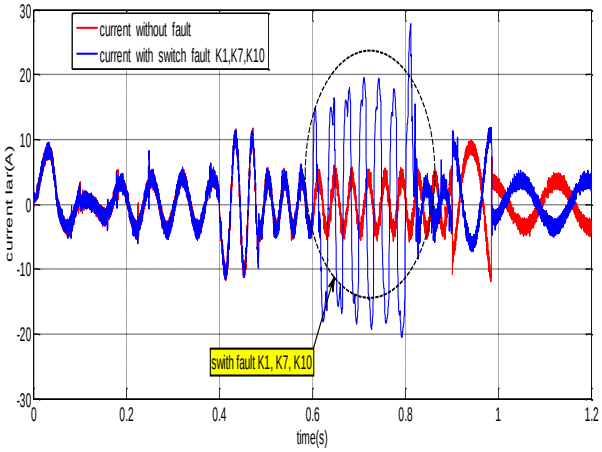

Fig. 10. stator and rotor current response for speed artificial neural control with application of K_1,K_7, K_{10} switch fault of NPC three level inverter.

VI. CONCLUSION

This work is presenting firstly a straight forward approach to synthesis the strength of artificial intelligence controller for induction motor speed control combined with NPC three levels inverter without fault. Results proved that ANN controller is drawing enhanced performance, is found quick and accurate in induction motor speed control, from the stability point of view, ANN controller is more reliable due to accurate and quick speed.

Concerning the second part that presented speed artificial neural network controller with the existence of switch fault for the NPC three levels inverter gives performance result. So the regulator enables us to have the influence of the existence of a defect on the physical parameters of the induction motor (speed, electromagnetic torque, stator and rotor currents) which is in the undulation and the oscillation which disturbed various signals. The simulation study indicates clearly the superior performance of controller speed neural network control. It appears from the response properties that it has a high performance in presence of defects.

It results that the proposed intelligent controller had a good dynamic stability without application of defective NPC three level inverter, as it gives satisfactory results with faults.

REFERENCES

[1] S. Altaf, M. S. Mehmood, M. Imran "Implementation of efficient artificial neural network data fusion classification technique for induction motor fault detection", Journal of Engineering Sciences, vol 5, No 2, pp. 16-21, 2018.

[2] M. M. Abdu, M. S. Moustafa, S. F. Saraya "Speed control of three phase induction motor using neural network", International Journal of Computer Science and Information Security, vol 16, No 5, pp. 259-272, 2018.

[3] J. L. Rashad, A. F. Hassan "Artificial neural estimator and controller for field oriented control of three IM", International Journal Intelligent Systems and Application, vol 11, No 6, pp. 40-48, 2019.

[4] M. H. Lazreg, A. Bentaallah "Sensorless speed control of double star induction machine with five level DTC exploiting neural network and extended Kalman filter", Iranian Journal of Electrical and Electronic Engineering, vol 15, No 1, pp. 142-150, 2019.

[5] S. Venkatesan, K. Premkumar, P. M .Vishnu "Speed control of permanent magnet synchronous motor using neural network model predictive control", Journal of Energy Systems, vol 4, No 2, pp. 71-87, 2020.

[6] P. Narongrit, S. W. Ming "Online Speed Estimation Using Artificial Neural Network for Speed Sensorless Direct Torque Control of Induction Motor based on Constant V/F Control Technique", Energies, vol 11, No 12, pp. 1-14, 2018.

[7] D. J. Vaghela, H. N. Chaudhar, D. A. Patel "Analysis and simulation of multi level inverter fed induction motor drive", International Journal Of Engineering Sciences & Research Technology, vol 3, No 4, pp. 1974-1978, 2014.

[8] S. Singh, A. Varshnry "Multilevel Topology in Three Level Inverter Fed Induction Motor Drive", International Journal of Advance Science and Technology, vol 29, No 10, pp. 8846-8853, 2020.

[9] E. Parimalasundar, S. N. Vanitha, "Identification of Open-switch and short-switch failure of multilevel inverters through DWT and ANN Approach using LabVIEW", Journal Electrical Engineering Technology, vol 10, No 6, pp. 2277-2287, 2015.

[10] S. S. Moosavi, A. Kazemi, H. A. Akbari "Comparison of various Open circuit fault detection methods in The IGBT based DC/AC inverter used in electrical vehicle", Engineering Failure Analysis, vol 96, pp. 223-235, 2019.

[11] R. B. Dhumale, S. D. Lokhande, N. D. Thombare "Fault detection and diagnosis of high speed switching devices in power inverter", International Journal of Research in Engineering and Technology, vol 4, No 2, pp. 253-257, 2015.

[12] T.G. Manjunath, A. Kusagur "Fault diagnosis and reconfiguration of multilevel inverter switch failure-A performance perspective", International Journal of Electrical and Computer Engineering, vol 6, No 6, pp. 2610-2620, 2016.

[13] L. Mao, H. L. Ying, Q. Liang, W. Chen, Q. Y. Guo " Fault detection of a proposed three-level inverter based on a weighted kernel principal component analysis", Journal of Power Electronics, vol 16, No 1, pp. 182-189, 2016.

[14] E.V. Sumy, N. Reema "effects of switching faults on induction motor drive system", International Research Journal of Engineering and Technology, vol 3, No 5, pp. 607-611, 2015.

[15] L. Peifei, S. Drid, L. Z. B. Ouyang "Nonlinear effects of three-level neutral-point clamped inverter on speed sensorless control of induction motor", Electronics, vol 8, No 402, pp. 2-14, 2019.

[16] S. E. Daoudi, L. Lazrak, M. A. Lafkih " Sliding mode approach applied to sensorless direct torque control of cage asynchronous motor via multi-level inverter", Protection and Control of Modern Power Systems, vol 5, No 13, pp. 1-10, 2020.

[17] O. Otkun" Sensorless Speed Control of Induction Motors with Artificial Neural Networks", Journal of Engineering and Tecnology, , vol 4, No 1, pp. 19-26, 2020.

[18] S. Cheng, J. Zhao1, C. Chen, Kaidi Li, W. Xun ,T. Yu1, Y.Yongsheng "An open-circuit fault-diagnosis method for inverters based on phase current", Transportation Safety and Environment, Vol. 2, No. 2, pp. 148–160,2020.

[19] N. R. Kedika, S. Pradabane "Fault-tolerant multi-level inverter topologies for open-end winding induction motor drive" , International Transaction Electrical Energy Systems, Vol. 30, No. 5, pp. 1–21,2020.

Reconfigurable Multirotor Control Using Fractional-Order $PI^{\lambda}D^{\mu}$ Controller in the Presence of Uncertain Geometric Parameters

Saddam Hocine Derrouaoui[1], Yasser Bouzid[1] and Mohamed Guiatni[1]

***Abstract*— In this work, and for the first time, a Fractional Order Proportional Integral Derivative (FOPID) controller tuned by Particle Swarm Optimization (PSO) algorithm, is investigated to control and stabilize the attitude and position of a reconfigurable multirotor in the presence of uncertain geometric parameters. Furthermore, the variation of the structure parameters makes the flight stability and control of this aerial vehicle very challenging tasks differently to the classical drone. Our proposed control architecture considers the variable dynamic of this structure and calculates these changes on-line in the control loop.**

***Index Terms*— Reconfigurable multirotor, uncertain geometric parameters, Fractional Order Proportional Integral Derivative (FOPID).**

I. Introduction

A. Related works and contribution

Nowadays, reconfigurable drones can adapt to different flight conditions, missions and environments, due to their adaptable and variable shapes, unlike the classic drones [1] [2]. Nevertheless, by consulting the open sources of the literature, we find that few control approaches have been exploited by researchers to stabilize and control this type of UAVs.

Despite the rapid advancement in the control of the flying systems, PID controllers are still the majority used control algorithm in aeronautics [3] [4] [5] [6], due to their simplicity [7] [8] [9].

A Fractional Order Proportional Integral Derivative (FOPID) controller [10] [11] [12], is a generalization of the classic PID controller, where it was first used by Podlubny [13] in order to enhance the performance of the systems controlled by PID.

In [14], the auhtors have used a control strategy based mainly on a PID to control a quadrotor that can rotate its body in flight. Researchers in reference [15] have focused on the problem of optimizing the energy of a quadrotor with rotating arms, where the drone orientations are controlled by PID controllers. Bucki et *al.* in paper [16], have stabilized the attitude of a reconfigurable quadrotor that can fold and unfold its arms in flight. In work [17], a conventional PID was used to control the attitude of a quadrotor with variable shape. In the series of references [18] [19], a classic PID has been applied in order to control and stabilize extendable arm drones. Authors in [20] have exploited a PID controller to stabilize a special reconfigurable UAV in attitude. In reference [21], a cascade PD was used to deal with the uncertainties problem of a quadcopter UAV. In paper [22], the trajectory optimization of a reconfigurable Unmanned aerial–aquatic vehicle was investigated. In order to stabilize and control a reconfigurable drone in flight, a conventional PID was applied in paper [23].

The principal contribution of this work is to propose a simple Fractional Order Proportional Integral Derivative (FOPID) controller to control and stabilize the attitude and position of a reconfigurable multirotor in the presence of uncertain geometric parameters. The five parameters of the FOPID controller are tuned by Particle Swarm Optimization (PSO) algorithm to select the optimal ones for each flight configuration. In addition, the majority variables parameters related to the geometric structure are calculated instantly in the control loop.

II. Multiorotor Modeling

In this part, we will briefly present the mathematical model that represents the dynamic of our reconfigurable multirotor, where the structural variations are taken into account [24] [25] [26].

The linear and the angular velocity vectors expressed in the mobile frame are represented respectively: $N^m = (u, v, w)^T \in \mathbb{R}^3$ and $P = (p, q, r) \in \mathbb{R}^3$.

The relation between the velocities and the external forces $\mathtt{F}^m = (f_x^m, f_y^m, f_z^m)^T \in \mathbb{R}^3$ and moments $\mathtt{T}^m = (\tau_x^m, \tau_y^m, \tau_z^m)^T \in \mathbb{R}^3$ is given by:

$$\begin{bmatrix} mI_{3\times3}(\alpha_i(t), \mathrm{d}_i(t)) & O_{3\times3} \\ O_{3\times3} & I_{3\times3}(\alpha_i(t), \mathrm{d}_i(t)) \end{bmatrix} \begin{bmatrix} \dot{N}^m \\ \dot{P} \end{bmatrix} + \begin{bmatrix} P \times mN^m \\ P \times I(\alpha_i(t), \mathrm{d}_i(t))P \end{bmatrix} = \begin{bmatrix} \mathtt{F}^m \\ \mathtt{T}^m \end{bmatrix} \quad (1)$$

III. Multirotor control

The reconfigurable multirotor is considered as a series of structures (configurations), where each one is presented by its own parameters.

The transfer functions $G_{ci}(s)$, which represent our FOPID controllers (see Figure 1) are appeared in Equation 2 as:

$$\begin{aligned} G_{ci}(s) &= \tfrac{U_i(s)}{E_i(s)} \\ &= K_{Pj}(\alpha_i(t), \mathrm{d}_i(t)) + K_{Ij}(\alpha_i(t), \mathrm{d}_i(t))\tfrac{1}{s^{\lambda_j}} \\ &+ K_{Dj}(\alpha_i(t), \mathrm{d}_i(t))s^{\mu_j} \end{aligned} \quad (2)$$

[1]Saddam Hocine Derrouaoui, Yasser Bouzid and Mohamed Guiatni are with Complex Systems Control & Simulators Laboratory (CSCSL), Ecole Militaire Polytechnique, Algiers, Algeria derrouaouish@gmail.com, yasseremp@gmail.com, mohamed.guiatni@gmail.com

where K_{Pj}, K_{Ij}, K_{Dj}, λ_j and μ_j are variable positive parameters related to each flight configuration. $E_i(s)$ is the error, and $U_i(s)$ is controller's output. j, i=1, .., 4.

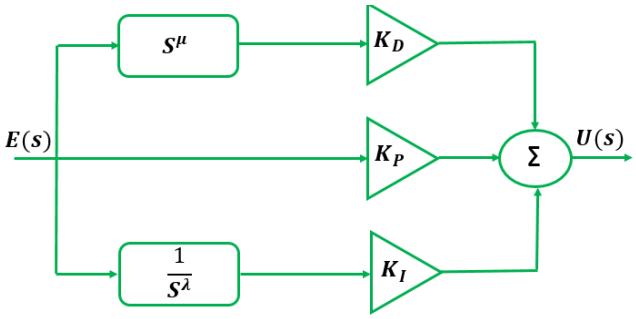

Fig. 1: FOPID block-diagram.

To assign the adequate controller gains for each structure, we have exploited a switching mechanism as shown in Figure 2. This mechanism works when it receives CoG, inertia, angles $\alpha_i(t)$ and lengths $\mathrm{d}_i(t)$ of the desired morphology to switch towards the appropriate gains.

The rotation and extension of the arms cause a variation of the arms by an angle α_i and by a distance d_i. These variations are sent to the switching mechanism block and to others blocks to update and calculate the structure parameters (see Figure 2).

The reference trajectories are provided by a Trajectory Generator Block (TGB) as shown in Figure 2. The attitude and translations of the drone are controlled by varying the position of the arms or by the angular speeds of the four rotors.

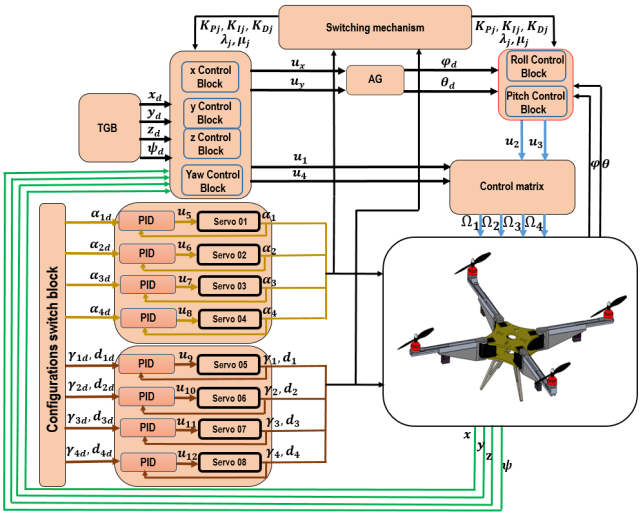

Fig. 2: Control architecture.

IV. Simulation Results

1) Simulation scenario: From the initial point, the multirotor begins to rise vertically with the "x" configuration to cross a vertically narrow space. After 10 seconds of flight, it changes its structure to "Y" and takes aerial photos for 10 seconds. Then, it changes its structure to "T", in order to reach the next point. Afterwards, it changes to the last morphology "H", to pass through a horizontally narrow space.

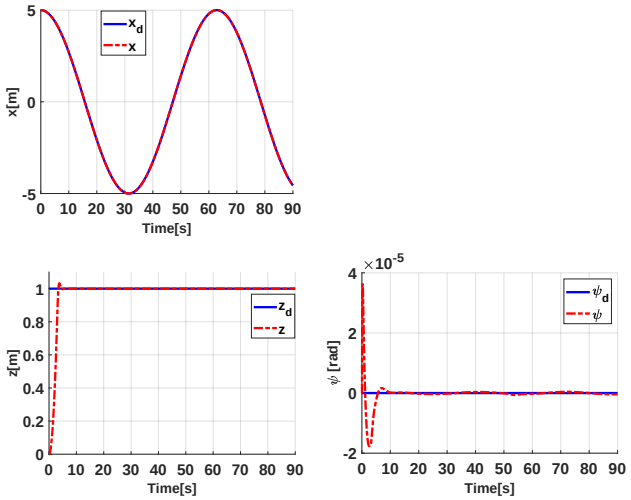

Fig. 3: Evolution of 3D trajectory.

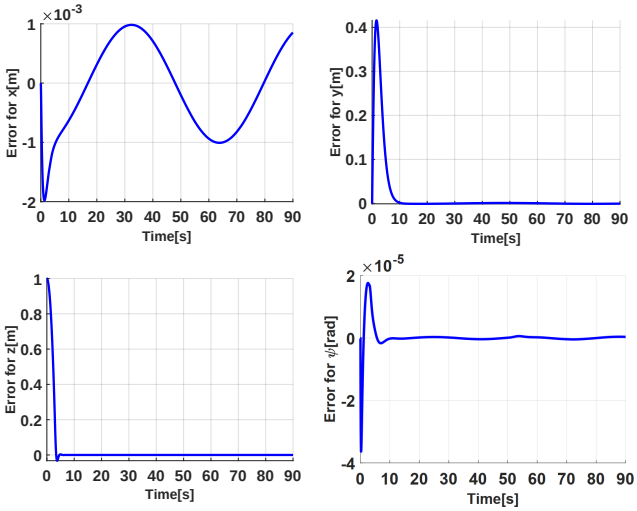

Fig. 4: Evolution of errors.

The parameters considered in simulation for the FOPID controllers are well selected using PSO algorithm (see Table I).

TABLE I: FOPID controller parameters of the five configurations.

	x	Y	T	YI	H
K_{Pj}	13.56	10.89	12.51	12.23	9.12
K_{Ij}	3.02	6.73	8.12	4.22	5.10
K_{Dj}	2.22	4.66	5.04	6.11	5.61
λ_j	0.18	0.78	0.33	0.15	0.11
μ_j	0.91	0.16	0.88	0.36	0.95

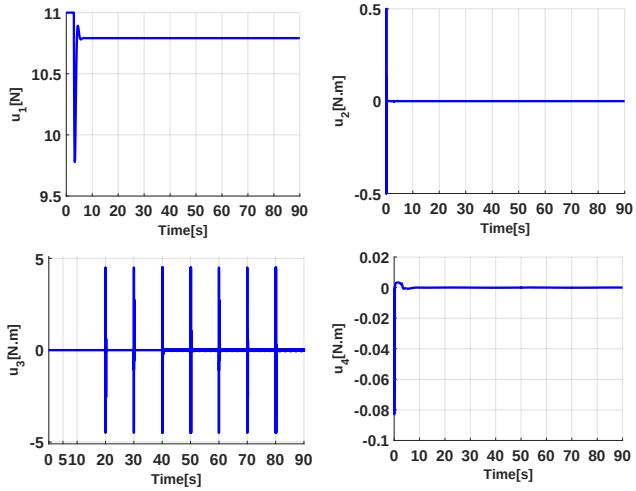

Fig. 5: Evolution of control signals.

A. *Interpretation of the simulation results*

From Figure 3, we note that the evolution curves of the x and y positions track the reference trajectories with some deviations, which is represented by their errors in Figure 4. Furthermore, the altitude z follows the desired trajectory z_d with a small overshoot of $0.04m$ at the start. It starts from $z = 0$ up to $1m$ (see Figure 3), where its error is canceled after 6 seconds (see Figure 4) and its control signal u_1 is at its maximum in the beginning before to stabilize around a constant value (see Figure 5).

The change of the control signal u_3 is due to the change of shape during flight and the trajectory y_d. For the yaw angle ψ, there is a very slight deviation in the system response as displayed in Figure 3. This is illustrated by the cancellation of the error in Figure 4 and by the very low values of the u_4 control in Figure 5.

The simulations carried out have shown that, the FOPID controller has given acceptable results in the face of uncertain geometric parameters of the reconfigurable multirotor.

V. Conclusion

In this paper, we have introduced a FOPID controller to stabilize and control the attitude and position of a reconfigurable multirotor in the presence of uncertain geometric parameters. This aerial vehicle changes its aerial configuration depending on the requirement tasks. Furthermore, the majority of variable parameters were calculated instantly in the control loop. From the simulation results, we can conclude that, the applied control strategy has achieved its objective.

References

[1] S. H. Derrouaoui, Y. Bouzid, M. Guiatni, and I. Dib, "A comprehensive review on reconfigurable drones: Classification, characteristics, design and control technologies," *Unmanned Systems*, pp. 1–27, 2021.

[2] S. H. Derrouaoui, Y. Bouzid, and M. Guiatni, "Pso based optimal gain scheduling backstepping flight controller design for a transformable quadrotor," *Journal of Intelligent & Robotic Systems*, vol. 102, no. 3, pp. 1–25, 2021.

[3] A. Rhouma, S. Hafsi, and K. Laabidi, "Stabilizing and robust fractional pid controller synthesis for uncertain first-order plus time-delay systems," *Mathematical Problems in Engineering*, vol. 2021, 2021.

[4] V. M. Babu, K. Das, and S. Kumar, "Designing of self tuning pid controller for ar drone quadrotor," in *2017 18th international conference on advanced robotics (ICAR)*. IEEE, 2017, pp. 167–172.

[5] A. Hermawan and M. Muliady, "Realisasi dan tuning pengontrolan pid drone fixed wing untuk pemetaan udara," *Jurnal Teknik Elektro dan Komputer TRIAC*, vol. 6, no. 2, pp. 27–33, 2019.

[6] S. Zouaoui, E. Mohamed, and B. Kouider, "Easy tracking of uav using pid controller," *Periodica Polytechnica Transportation Engineering*, vol. 47, no. 3, pp. 171–177, 2019.

[7] P. Chen, Y. Luo, Y. Peng, and Y. Chen, "Optimal robust fractional order piλd controller synthesis for first order plus time delay systems," *ISA transactions*, 2021.

[8] M. Elajrami, Z. Satla, and K. Bendine, "Drone control using the coupling of the pid controller and genetic algorithm," *Communications-Scientific letters of the University of Zilina*, vol. 23, no. 3, pp. C75–C82, 2021.

[9] L. Bauersfeld and G. Ducard, "Fused-pid control for tilt-rotor vtol aircraft," in *2020 28th Mediterranean Conference on Control and Automation (MED)*. IEEE, 2020, pp. 703–708.

[10] F. Padula and A. Visioli, "Optimal tuning rules for proportional-integral-derivative and fractional-order proportional-integral-derivative controllers for integral and unstable processes," *IET Control Theory & Applications*, vol. 6, no. 6, pp. 776–786, 2012.

[11] S. Zheng, X. Tang, and B. Song, "A graphical tuning method of fractional order proportional integral derivative controllers for interval fractional order plant," *Journal of Process Control*, vol. 24, no. 11, pp. 1691–1709, 2014.

[12] B. Khokhar, S. Dahiya, and K. S. Parmar, "A novel fractional order proportional integral derivative plus second-order derivative controller for load frequency control," *International Journal of Sustainable Energy*, vol. 40, no. 3, pp. 235–252, 2021.

[13] I. Podlubny, "Fractional-order systems and pi/sup/spl lambda//d/sup/spl mu//-controllers," *IEEE Transactions on automatic control*, vol. 44, no. 1, pp. 208–214, 1999.

[14] V. Riviere, A. Manecy, and S. Viollet, "Agile robotic fliers: A morphing-based approach," *soft robotics*, vol. 5, no. 5, pp. 541–553, 2018.

[15] H. Xiong, J. Hu, and X. Diao, "Optimize energy efficiency of quadrotors via arm rotation," *Journal of Dynamic Systems, Measurement, and Control*, vol. 141, no. 9, 2019.

[16] N. Bucki and M. W. Mueller, "Design and control of a passively morphing quadcopter," in *2019 International Conference on Robotics and Automation (ICRA)*. IEEE, 2019, pp. 9116–9122.

[17] Y. Kamil, D. Hazry, K. Wan, Z. M. Razlan, and S. AB, "Design a new model of unmanned aerial vehicle quadrotor using the variation in the length of the arm," in *The 2017 International Conference on Artificial Life and Robotics (ICAROB 2017)*, 2017, pp. 723 –726.

[18] T. Oktay and K. Oğuz, "Non simultaneous morphing system design for yaw motion in quadrotors," *Journal of Aviation*, vol. 3, no. 2, pp. 81–88, 2019.

[19] O. Köse and T. Oktay, "Non simultaneous morphing system desing for quadrotors," *Avrupa Bilim ve Teknoloji Dergisi*, no. 16, pp. 577–588, 2019.

[20] K. Patnaik, S. Mishra, Z. Chase, and W. Zhang, "Collision recovery control of a foldable quadrotor," *arXiv preprint arXiv:2105.12273*, 2021.

[21] S. Lee, D. K. Giri, and H. Son, "Modeling and control of quadrotor uav subject to variations in center of gravity and mass," in *2017 14th International Conference on Ubiquitous Robots and Ambient Intelligence (URAI)*. IEEE, 2017, pp. 85–90.

[22] X. Su, Y. Wu, F. Guo, J. Cui, and G. Yang, "Trajectory optimization of an unmanned aerial–aquatic rotorcraft navigating between air and water," *International Journal of Advanced Robotic Systems*, vol. 18, no. 2, p. 1729881421992258, 2021.

[23] O. Köse and T. OKTAY, "Non simultaneous morphing system desing for quadrotors," *Avrupa Bilim ve Teknoloji Dergisi*, no. 16, pp. 577–588, 2019.

[24] S. H. Derrouaoui, M. Guiatni, Y. Bouzid, I. Dib, and N. Moudjari, "Dynamic modeling of a transformable quadrotor," in *2020 International Conference on Unmanned Aircraft Systems (ICUAS)*. IEEE, 2020, pp. 1714–1719.

[25] S. H. Derrouaoui, Y. Bouzid, and M. Guiatni, "Towards a new design with generic modeling and adaptive control of a transformable quadrotor," *The Aeronautical Journal*, pp. 1–31.
[26] Derrouaoui, S. H., Bouzid, Y., & Guiatni, M., "Nonlinear robust control of a new reconfigurable unmanned aerial vehicle" *Robotics*, vol. 10, no. 2, p. 76, 2021.

Design, simulation, sizing and optimization of hybrid renewable energy systems PV/Wind/Battery using PSO algorithm

Walid BENSALMI
Electronics department
Constantine university 1
Constantine, Algeria
walidbensalmi1@gmail.com
ORCID: https://orcid.org/0000-0003-3708-233X

Ahmed BELHANI
Electronics department
Constantine university 1
Constantine, Algeria
ahmed.belhani@umc.edu.dz
ORCID: https://orcid.org/0000-0001-5595-9604?lang=en

***Abstract*— In this paper, an optimization model is presented to determine the best size of a hybrid energy system (HES), which consists of photovoltaic (PV), wind turbine (WT) and battery. For distant regions and also the smart cities, this system enables a clean and stable power source. In this context, this study explores the application of a simple and efficient Particle Swarm Optimization (PSO) algorithm. This algorithm aims to determine the optimal configure of system components to minimize cost and meet load demand. For this objective, all the components are modeled (PV, WT and battery) and the levelized cost of energy is defined as an objective function. The concept of loss of power supply probability (LPSP) should be considered in hybrid energy systems in order to have a reliable system. The research presented in this paper was conducted in Constantine, Algeria and may be applied to any similar regions throughout the world.**

Keywords - hybrid energy system (HES), photovoltaic (PV), wind turbine (WT), Particle Swarm Optimization (PSO).

I. INTRODUCTION

In recent years, the use of renewable energies has increased greatly due to the development of society and the economy and falling oil prices [1]. This development has led to more attention to environmental pollution. Renewable energy, as a clean energy source, can be used to replace fossil fuels, which pollute the environment and are a non-renewable resource, in order to provide enough electricity to meet people's daily needs and contribute to social development [2]. So it is clear that the future energy sustainability heavily depends on how the renewable energy problem is addressed to contribute in meeting the electrical power demand.

The most important challenge of the single renewable energy systems is their random environmental conditions (solar radiation and wind speed). As a solution, the combination of different energy sources such as wind and solar with battery storage improve the system efficiency and reliability [1]. However, due to the non-linear response of the system components and the dependence on environmental conditions and the random load profile, smart grid is used to tailor and incorporate these units so that electricity may be moved across the system as efficiently and affordably as feasible [1].

The particle swarm optimization technique was used in this work to optimize an off-grid hybrid energy system (HES) and produce better results for matching renewable energy generation with home load using HES, utilizing MATLAB. In hybrid systems, optimal size is an important issue, it is defined by determining the number of system components to minimize cost and meet local load demand. An optimization approach can be used to do this work.

In previous studies, different methods have been presented for sizing, modeling and feasibility evaluation of such systems, utilizing a mix of renewable energy sources to deliver power for various applications. These methods are based on traditional methods, artificial intelligence methods and hybrid methods. This makes the selection of a suitable sizing methodology, much more important [1]. The reference [1] encompasses review in detail the different configurations, criteria selection, sizing methodologies and control & energy management of hybrid energy systems. Gupta et al. [3] employed C++-based analytical tools to efficiently construct a low-cost village electrification system while the diesel generator maintains a consistent output. Analytical approaches use less time to acquire the needed size for a specific demand than Monte Carlo simulation. An iterative optimization method was used by Yang et al. [4] to optimize a hybrid energy system size, they used LPSP and Leveled Cost of Energy model to optimize power reliability and system cost. Koutroulis et al. [5] presented an optimal sizing of HES based on a genetic algorithm to select the optimal number of units (PV modules, wind turbines and batteries) with a minimum cost, subject to the satisfaction of the load demand. Askarzadeh and dos Santos Coelho [6] proposed an optimized sizing of a hybrid solar, wind and battery system through PSO algorithm, their objectives are the minimization of life cycle cost (LCC) subject to reliable supply to meet load demand. Sharma et al. [7] developed hybrid method that combines a genetic algorithm (GA) with a particle swarm optimization algorithm to build and optimize an off-grid hybrid energy system's cost. The results show that the HGAPSO algorithm outperforms the GA and PSO algorithms in terms of cost savings.

In this paper, a particle swarm optimization algorithm has been introduced to size a hybrid energy system combined of PV/wind/battery taking into account seasonal variations in the load profile with the measured solar and wind energy resources, the cost of components and the cost of maintenance.

II. MODELING OF HYBRID ENERGY SYSTEM

Prior to any phase of optimal sizing, it is critical to model the hybrid system. This system is a configuration of two or more renewable and even non-renewable energy. Fig. 1 shows a schematic of the proposed hybrid energy system, as can be seen it consists of a photovoltaic, a wind turbine generator, inverter and a battery storage. All components are connected to the DC bus, except the load. Solar and wind energy are converted into electricity via PV modules and wind turbines. When the amount of energy produced exceeds the amount required to power the load, the excess energy is supplied to the battery bank until it is fully charged. When the energy produced is insufficient to meet the load, the batteries release energy to help the PV modules in covering the load, depending on the battery's level of charge.

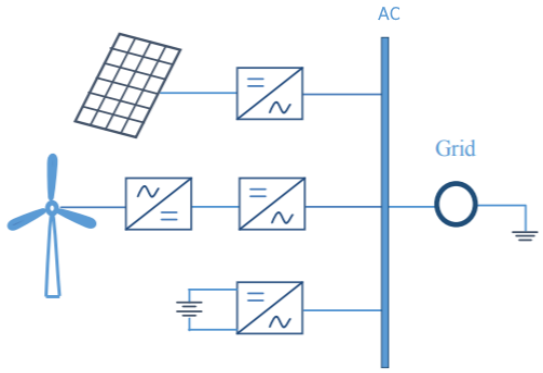

Fig. 1. Schematic drawing of the proposed system.

In the following subsections, a description of a general methodology for modeling a photovoltaic panel, wind turbine, and battery is described in detail.

A. Model of PV array

In order to present photovoltaic characteristics in operating conditions that differ from the standard test condition (1000W/m, 25C cell temperature), The solar radiation, the ambient temperature and manufacturer's data of the PV panels are used as model inputs to estimate the output energy generated for photovoltaic panel [8]. The output power of each PV system at time t, with respect to the solar radiation and the ambient temperature, can be obtained by the following formula [8]:

$$P_{pv}(t) = P_{rate_pv} \times \eta_{pv} \times \frac{S}{S_{ref}} \times [1 + K_t(T_c - T_{ref})] \qquad (1)$$

Where:

- $P_{pv}(t)$ (kW) : the output power of PV arrays.
- P_{rate_pv} (kW) : the rated power of the photovoltaic module.
- η_{pv}: the photovoltaic derating factor.
- S ($^{W}/_{m^2}$): solar radiation intensity.
- S_{ref} ($^{W}/_{m^2}$) : the incident radiation at standard test conditions ($S_{ref} = 1000\ ^{W}/_{m^2}$).
- K_t ($^{1}/_{C}$): the temperature coefficient of power $K_t = -3.7 \times 10^{-3}$ ($^{1}/_{C}$).
- T_{ref}: the photovoltaic module temperature under standard test conditions.
- T_c (C): the photovoltaic panel temperature.

The PV cell temperature (T_c) can be estimated as follows [9]:

$$T_c = T_a + S\left(\frac{NOCT - 20}{800}\right) \qquad (2)$$

Where:

- T_a (C): the ambient temperature.
- S ($^{W}/_{m^2}$): solar radiation intensity.
- $NOCT$: the nominal operating cell temperature.

If there are a number of photovoltaic panels then the total power is:

$$P_{T_{pv}}(t) = P_{pv}(t) \times N_{pv} \qquad (3)$$

Where:

- $P_{pv}(t)$ (kW) : the output power of PV arrays.
- N_{pv} : the numbers of PV arrays.

B. Model of wind turbine

The electrical power generated by wind turbines does not behave in the same way as the wind in terms of variation [8]. There are currently many models for estimating the output power of wind turbines, such as linear, quadratic model [10], and model using the Weibull distribution [11]. In this study, a quadratic model based on rated power is used to present the wind turbine hourly output power. The power generated by a wind turbine is determined by three main factors: the power output curve, wind speed data from the chosen location, and tower height [25]. Following are descriptions of three operational levels [6], as illustrated in Fig. 2 [12]:

a) The wind turbine will stop running when the wind speed is less than the cut-in value or exceeds the cut-off value (region 1, region 4).
b) When the cut-in value is exceeded, the power delivered by the generator increase proportional to the wind speed until reaching the rated speed of the wind turbine (region 2).
c) When the wind speed reaches the rated wind speed, the generator produces a constant output power (region 3).

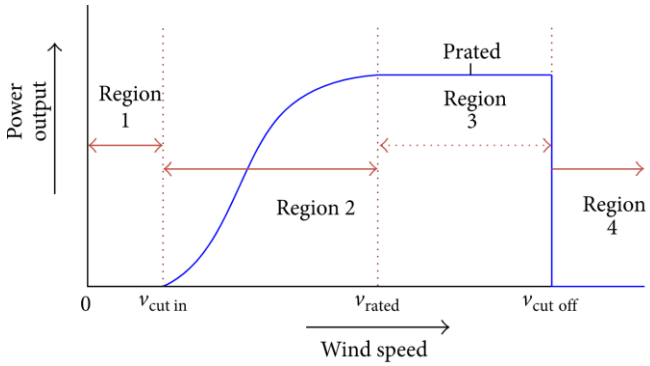

Fig. 2. Wind turbine output power characteristics [12].

The output power of wind turbine at time t is obtained as follows [13]:

$$P_{wt}(t) = \begin{cases} 0 & if \quad v \le V_i \ or \ v \ge V_o \\ P_r \dfrac{v - V_i}{V_r - V_i} & if \quad V_i < v < V_r \\ P_r & if \quad V_r < v < V_o \end{cases} \tag{4}$$

Where:

- $P_{wt}(t)$: the output power of wind turbine.
- v $(^{m}/_{s^2})$: the wind speed.
- V_i, V_o, V_r $(^{m}/_{s^2})$: cut-in speed, cut-off speed and rated speed respectively.
- P_r (kW): rated power.

The wind speed is usually available for standard height, so the measured data of average hourly wind speed must be converted to the corresponding value at the hub height, which is calculated according to [14]:

$$v = v_o \times \left(\frac{H}{H_o}\right)^{\propto} \tag{5}$$

Where:

- v $(^{m}/_{s^2})$: the wind speed at height H.
- v_o $(^{m}/_{s^2})$: the wind speed at height H_o.
- H (m): the desired height.
- H_o (m): the reference height.
- $\propto$: the roughness factor.

If there are a number of wind turbines then the total power is:

$$P_{T_{wt}}(t) = P_{wt}(t) \times N_{wt} \tag{6}$$

Where:

- $P_{wt}(t)$: the output power of wind turbine.
- N_{wt}: the numbers of wind turbines.

C. *Modeling of battery storage system*

A battery bank system, which is usually of the lead-acid type [6], is a fundamental component in all renewable energy systems. It is used to store the excess electrical energy to regulate system voltage and to meet demand 24 hours a day, because the renewable energy systems provide irregular output power due to variable meteorological environments [15]. The state of charge (SOC) of the battery depends on the output power of the PV panels, the wind turbines and the load and can be estimated as follows [16]:

1) Charging mode:

When the total output of the PV panels and wind turbine is more than the energy demand, the surplus power will be stored in the batteries. The battery energy can be described by [16]:

$$E_{BA}(t) = E_{BA}(t-1)(1-\sigma) + \left(E_{GA}(t) - \frac{E_L(t)}{\eta_{inv}}\right)\eta_{bc} \tag{7}$$

2) Discharging mode:

In this mode, the battery bank is used to supply the load. The energy will be extracted from the batteries, when power generation is insufficient to meet load demands. The battery energy can be obtained by [16]:

$$E_{BA}(t) = E_{BA}(t-1)(1-\sigma) - \left(\frac{E_L(t)}{\eta_{inv}} - E_{GA}(t)\right)/\eta_{bd} \tag{8}$$

Where:

- $E_{BA}(t)$: state of charge at time (t).
- $E_{BA}(t-1)$: state of charge at time (t-1).
- σ: hourly self-discharge rate.
- $E_{GA}(t)$ (kW): the total output power
- $E_L(t)$ (kW): the load demand.
- η_{bc}: the battery charging efficiency.
- η_{bd}: the battery discharging efficiency.
- η_{inv}: the inverter efficiency.

D. *Model of inverter*

The inverter converts the variable direct current output of a photovoltaic solar panel, the wind turbine and battery into alternating current. Because most electrical devices are supplied with AC power, an inverter is used before the load. The power that passes through the inverter to meet the demand is provided by [17]:

$$P_{in} = \frac{P_{ch}}{\eta_{inv}} \tag{9}$$

Where:

- P_{in} (kW): the power transiting the inverter.
- P_{ch} (kW): the hourly demand.
- η_{inv} $(\%)$: the inverter efficiency specified by the manufacturer.

III. FORMULATION OF THE OPTIMUM SIZING PROBLEM

The overall objective of this study is to show how to size system components to their optimal size. This is done by the minimization of the total annual cost (TAC) subject to some constraints.

A. *Objective function*

The purpose of the optimum design problem is the minimization of the total annual cost. The TAC can be divided into the annual capital cost (C_{Cap}) and the annual maintenance cost (C_{Man}). The optimization problem defined by [16]:

$$TAC = C_{Cap} + C_{Man} \tag{10}$$

The capital recovery factor (CRF), defined by Eq. (11), and is used to convert the initial capital cost to the annual capital cost [16].

$$CRF = \frac{j(1+j)^n}{(1+j)^n - 1} \quad (11)$$

Where:

- n: the lifetime of the system in years.
- j: the interest rate of the system.

Over the project's lifetime, some components need to be replaced several times. Only the batteries and inverter are assumed to be replaced in this study. Photovoltaic and wind turbine lifetimes are assumed to be 20 years. The battery bank is expected to be 5 years. Using the present worth factor for a single payment, we get [16]:

$$C_{Ba} = P_{Ba} \times \left(1 + \frac{1}{(1+i)^5} + \frac{1}{(1+i)^{10}} + \frac{1}{(1+i)^{15}}\right) \quad (12)$$

Where:

- C_{Ba}: the present worth of battery.
- P_{Ba}: the battery price.

Similarly, the lifetime of converter is expected to be 10 years. Using the present worth factor for a single payment, we get [16]:

$$C_{Conv/Inv} = P_{Conv/Inv} \times \left(1 + \frac{1}{(1+i)^{10}}\right) \quad (13)$$

Where:

- $C_{Conv/Inv}$: the present worth of converter/inverter components.
- $P_{Conv/Inv}$: the converter/inverter price.

Eq. (14) is obtained by dividing the capital cost into annual costs for the wind turbine, solar panels, converter/inverter, and battery [16].

$$C_{Cap} = CRF \times \begin{bmatrix} N_{wt} \times C_{wt} + N_{pv} \times C_{pv} + N_{Batt} \times C_{Batt} \\ + N_{Conv/Inv} \times C_{Conv/Inv} \end{bmatrix} \quad (14)$$

Where:

- C_{wt}: the unit cost of wind turbine.
- C_{pv}: the unit cost of PV panels.
- $N_{Conv/Inv}$: the number of converter/inverter systems.

The annual maintenance cost of the system is obtained by [13]:

$$C_{Man} = N_{Wind} \times C_{Mnt}^{Wind} + N_{Pv} \times C_{Mnt}^{PV} \quad (15)$$

Where:

- C_{Mnt}^{Wind} (kWh): the wind turbine's maintenance cost.
- C_{Mnt}^{PV} (kWh): the PV panel's maintenance cost.

The cost of battery maintenance is overlooked.

The levelized cost of energy (LCOE) in $/kWh is used to evaluate the economic performance of the hybrid system. The LCOE is calculated by the total annualized cost of the HES (TAC) and the total power load served ($E_L(t)$) [25].

$$LCOE = \frac{TAC}{\sum_{t=1}^{8760} E_L(t)} \quad (16)$$

B. Constraints

The above-mentioned objective function must be optimized in consideration of the constraints below.

1) Loss of power supply probability

The concept of loss of power supply probability (LPSP) should be considered in hybrid energy systems in order to have a reliable system. It is important to determine the combination PV/WT/Battery's minimum cost that yields the needed LPSP [18]. LPSP is defined by a value between 0 and 1 [19].The load will never be satisfied if the LPSP is 1, and the load will always be satisfied if the LPSP is 0 [19]. LPSP is calculated in the following equation, for a specified period, T (1 year in this study) [19]:

$$LPSP = \frac{\sum_{t=1}^{T} LPS(t)}{\sum_{t=1}^{T} E_L(t)} \quad (17)$$

Where LPS is the loss of power supply can be obtained by [19]:

$$LPS(t) = E_L(t) - (E_{GA}(t) + E_{BAtt}(t-1) - SOC_{min})\,\eta_{inv} \quad (18)$$

Fig. 3 indicates the calculation of LPSP at each hour during the year.

2) State of charge

At any time, the battery charging and discharging operation is constrained by the minimum and the maximum permissible level, the following equation should be satisfied [14]:

$$SOC_{min} \leq SOC(t) \leq SOC_{max} \quad (19)$$

Where:

- SOC_{min}: the minimum permissible level.
- SOC_{max}: the maximum permissible level.

The maximum permissible level of battery bank is given by [17]:

$$SOC_{max} = C_{bat} \times N_{bat} \quad (20)$$

The minimum permissible level of battery bank is given by [17]:

$$SOC_{min} = C_{bat} \times N_{bat}(1 - DOD) \quad (21)$$

Where:

- C_{bat}: the nominal capacity of each battery.
- N_{bat}: the total number of batteries.
- DOD : the maximum depth of discharge in percentage.

3) The decision variables

The decision variables are the number of PV arrays, wind turbines and battery. So the following constraints should be satisfied [20]:

$$\begin{aligned} N_{pv} &= integer\,, 0 \leq N_{pv} \leq N_{pv}^{max} \\ N_{wt} &= integer, 0 \leq N_{wt} \leq N_{wt}^{max} \\ N_{Batt} &= integer, 0 \leq N_{Batt} \leq N_{Batt}^{max} \end{aligned} \quad (22)$$

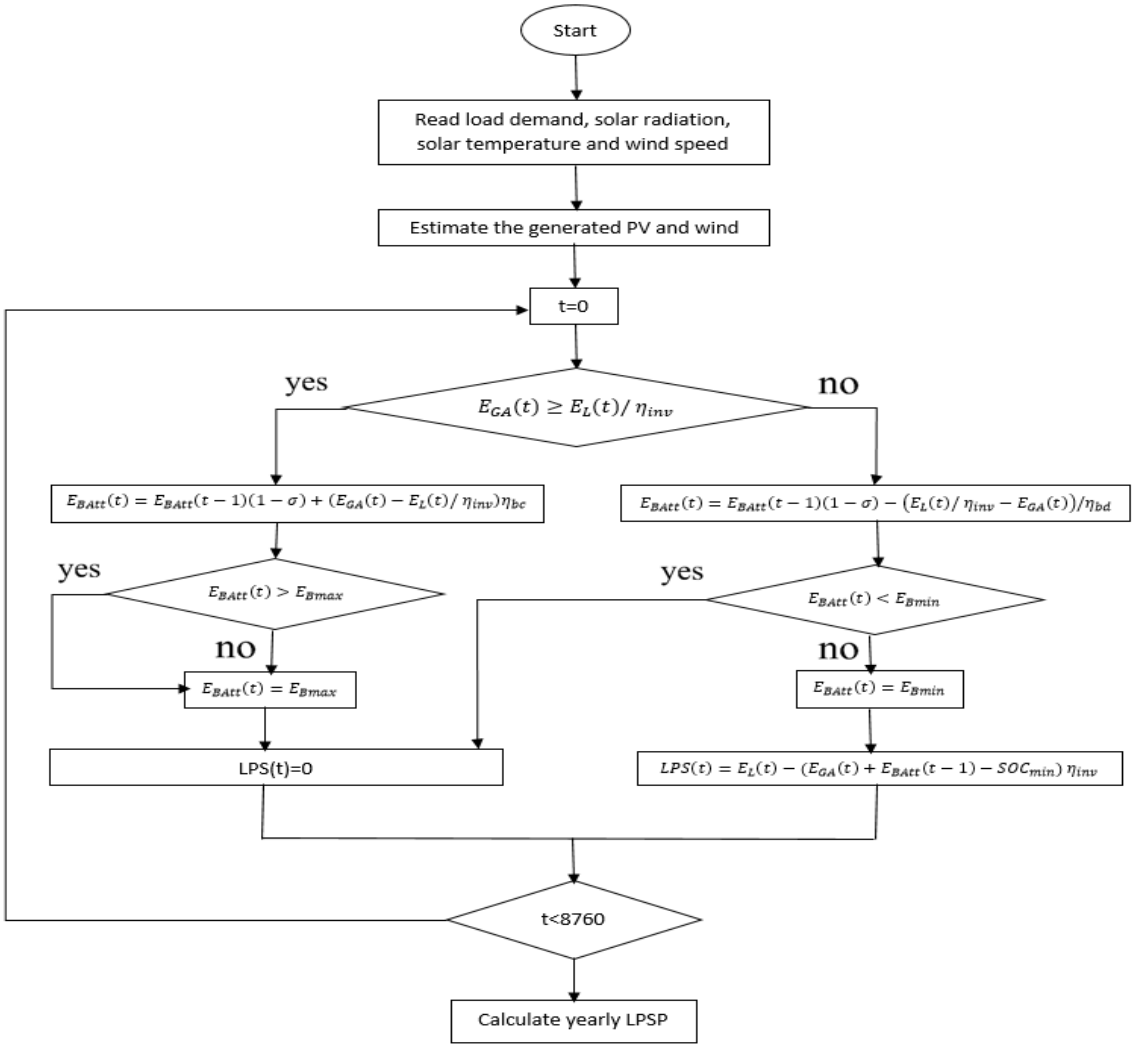

Fig. 3. The flowchart for the LPSP.

IV. PARTICLE SWARM OPTIMIZATION (PSO) ALGORITHM

The PSO algorithm is originally invented by Kennedy and Eberhart in 1995 [21]. It became one of the most used optimization algorithms because it has simple concept and can quickly find a reasonably good solution. This approach is based on the social behavior of birds, fish schools, and the swarm theory [22]. PSO is a metaheuristic algorithm which starts with a population of random solutions (particles) and attempt to discover the global solution of an optimization problem [6]. The algorithm of particle swarm optimization as used in this study is given in Fig. 4 [23].

In the PSO algorithm, each particle represents a possible solution, the optimization objective function evaluates these solutions to determine their fitness [24]. The number of solutions doubles in the next iteration until the best one is found. More particles in each iteration encourages the discovery of the best solution and reduces the number of optimization iterations. In PSO, each individual move around in the search space [24]. The local best values for each particle are obtained called $p_{best}$and the global best value among all particles is obtained called g_{best}. Each particle tries to modify its position and velocity according to its own experience and the experience of neighboring particles. Position and velocity of each particle can be modified by the following equations [24]:

$$v_i^{k+1} = w^k.v_i^k + c_1.r_1.\left(p_{best}^k - x_i^k\right) + .r_2.\left(g_{best}^k - x_i^k\right) \quad (23)$$

$$x_i^{k+1} = x_i^k + v_i^{k+1} \quad (24)$$

Where:

- i : the particle.
- k : the iteration.
- v_i^k : the particle velocity.
- x_i^k : the current position of each particle.
- c_1, c_2 : positive acceleration constants.
- r_1, r_2 : uniform randomly generated numbers.
- p_{best}^k : The local best values for each particle.
- g_{best}^k : the global best value among all particles.
- w^k : the inertia weight factor.

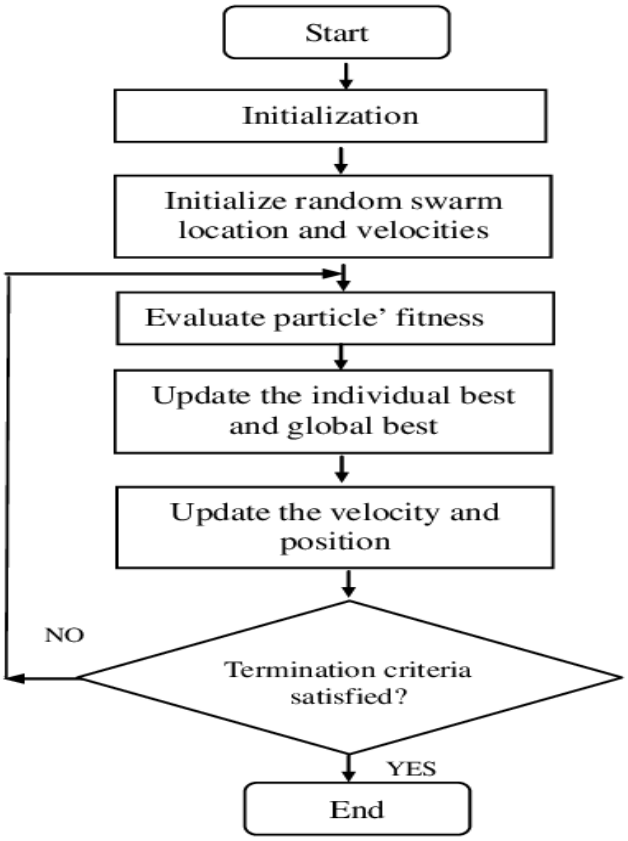

Fig. 4. Flow chart of PSO developed algorithm [23].

V. SIMULATION RESULTS AND DISCUSSION

In order to evaluate the performance of the heuristic techniques for optimum sizing of a real system, the meteorological data for the study area is obtained from Algeria, Constantine (latitude 36.3384, longitude 6.6199). This site represents the different climatic conditions considering seasonal variation. MATLAB software is used to code and execute the algorithm of optimization and run it on a PC with Intel I7-8550U CPU and 8 GB of RAM under Windows 7.

All the meteorological data has been taken from Nasa Power website during the year (8760 h). Fig. 5 shows a load profile well suited to the study area. It is considered the same for all days of the year. As shown in Fig. 6, the yearly solar irradiance, temperature and wind speed. According to the statistics, the solar radiation is highest in June and July and lowest in January. It can be seen that the change of temperature is most obvious in a year, with the maximum temperature in July and the lowest temperature in December. Wind speed data is also shown in Fig. 6, the average wind speed is 3.6 m/s, which can lead to generating electricity at night, unlike solar radiation.

The components of the studied system include the solar panel, the wind turbine, and a battery bank, the technical and economic specifications of which are detailed in Table 1.

Components	Description	
PV panel	Maximum power	270 W
	Cost	100 $
	Maintenance cost	2$
	Lifetime	25 years
Wind turbine	Nominal power	10000 W
	Cost	2500 $
	Maintenance cost	25 $
	Lifetime	20 years
	Cut in speed	2m/s
	Cut out speed	18m/s
	rated speed	10m/s
Battery lead-acid	Nominal capacity	200 Ah
	Maximum depth of discharge	50%
	Charge / discharge efficiency	80%
	Cost	350 $
	Maintenance cost	3.5 $
	Lifetime	5 years
DC/AC converter	Cost	900 $
	Maintenance cost	10.8 $
	Efficiency	92%
	Lifetime	10 years

Table 1: The parameters of the system components.

The parameters of the PSO algorithms are adjusted as follows:
Iteration max=100, number of particles=50, c1=1.5, c2=1, r1=1, r2=1, ω =1.5.

The aim of this study is to create a hybrid energy system that can provide continuous and reliable power to a load. The PSO algorithm try to find the optimum number of solar panels, wind turbines and battery. The minimum and maximum numbers of each component are set to 0 and 200 for the number of photovoltaic modules, from 0 to 10 for the number of wind turbines and from 0 to 50 for the number of batteries.

Table 2 summarizes the results of the PSO algorithms on the sizing problem (the optimum number of the components and the COE value) with different values of LPSP (0%, 0.2% and 10%). These are different levels of reliability, it is known as the maximum LPSP that may be used, and it is set by the user. We can see that reliability improvement (LPSP) increases the cost of the system so by decreasing LPSP from 10% to 0%, COE surged about 1.9 times, because reliability is expensive.

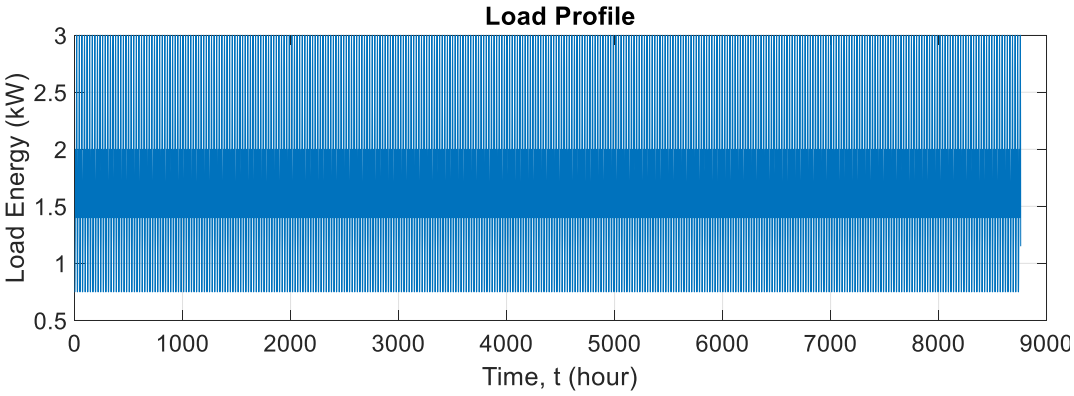

Fig. 5. Load profile of the study area during one year.

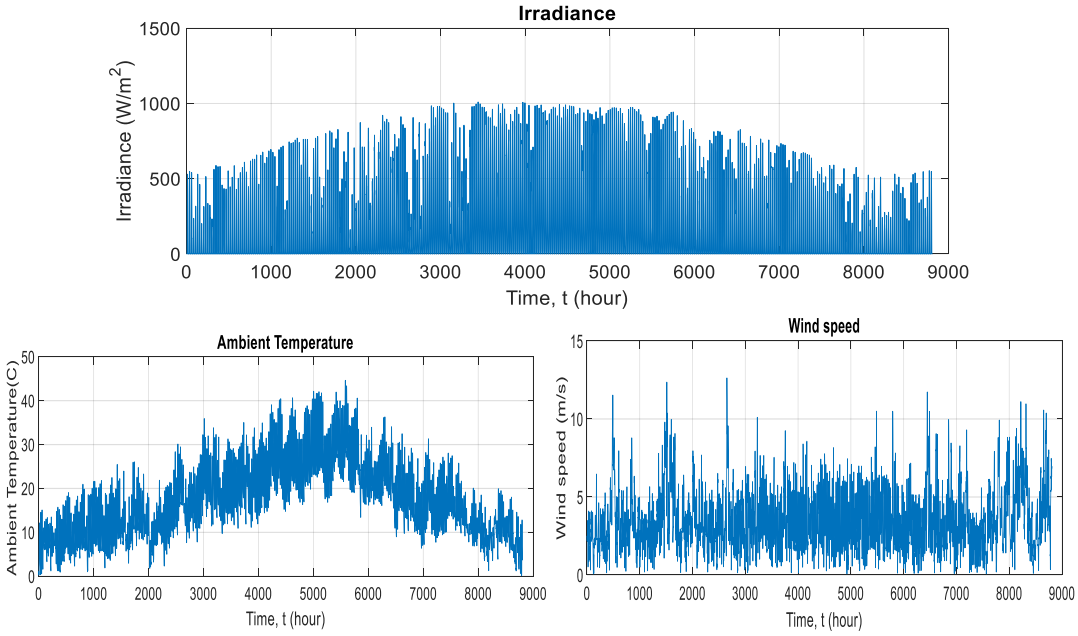

Fig. 6. The yearly meteorological data during one year.

LPSP (%)	N_{pv}	N_{wt}	N_{Batt}	COE ($/kWh)
0	35	3	12	1.18
0.2	26	2	10	0.88
1	18	1	9	0.62

Table 2: Comparison of the results obtained by the PSO algorithm with different value of LPSP

Fig. 7 & 8. Show the power generated by the PV panels and wind turbines in LPSP=0. We noticed that the power of PV is high in summer and low in winter unlike the power of wind turbines which is balanced with different seasons. This is the benefit of wind turbines in HES which can lead to generating electricity in winter and at night to help PV panels to contribute in meeting the electrical power demand.

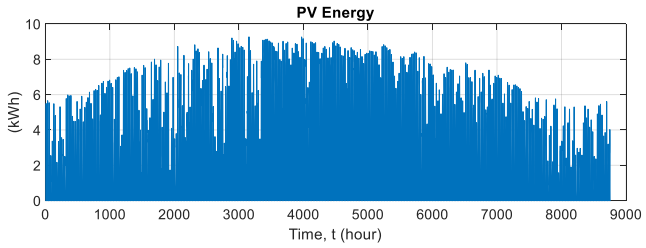

Fig. 7. Simulating intra-hourly PV energy fluctuations of the hybrid system in one year.

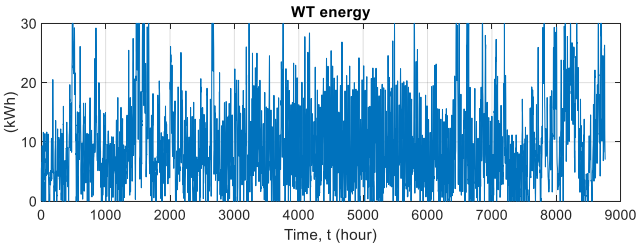

Fig. 8. Simulating intra-hourly WT energy fluctuations of the hybrid system in one year.

VI. CONCLUSION

This paper develops a methodology for optimum sizing of a hybrid renewable energy system consisting of PV, WT and battery utilizing PSO. The optimization objective was to minimize the system cost, subject to the satisfaction of the load demand. First, a description of a general methodology for modeling a photovoltaic panel,

wind turbine, and battery have been presented in detail. The proposed optimization technique was then exposed, along with the basic notion of PSO. Finally, a hybrid system was optimized using the PSO.

Simulation results reveal that the LCOE will decrease as the allowable LPSP increases from 0% to 2%. The lower LCOE indicates that if the LPSP is small and acceptable, the initial capital costs of a HES will be considerably reduced. Also the result show the value of wind turbines in HES which can lead to generating electricity in winter and at night to help PV panels to contribute in meeting the electrical power demand, this makes the number of batteries decrease. The techniques and analytical approaches utilized in this study can be applied to other hybrid systems as well.

VII. REFERENCES

[1] S. Upadhyay and M. P. Sharma, "A review on configurations, control and sizing methodologies of hybrid energy systems," *Renew. Sustain. Energy Rev.*, vol. 38, pp. 47–63, 2014.

[2] A. Makhsoos *et al.*, "Design, simulation and experimental evaluation of energy system for an unmanned surface vehicle," *Energy (Oxf.)*, vol. 148, pp. 362–372, 2018.

[3] A. Gupta, R. P. Saini, and M. P. Sharma, "Steady-state modelling of hybrid energy system for off grid electrification of cluster of villages," *Renew. Energy*, vol. 35, no. 2, pp. 520–535, 2010.

[4] H. Yang, L. Lu, and W. Zhou, "A novel optimization sizing model for hybrid solar-wind power generation system," *Sol. Energy*, vol. 81, no. 1, pp. 76–84, 2007.

[5] E. Koutroulis, D. Kolokotsa, A. Potirakis, and K. Kalaitzakis, "Methodology for optimal sizing of stand-alone photovoltaic/wind-generator systems using genetic algorithms," *Sol. Energy*, vol. 80, no. 9, pp. 1072–1088, 2006.

[6] A. Askarzadeh and L. dos Santos Coelho, "A novel framework for optimization of a grid independent hybrid renewable energy system: A case study of Iran," *Sol. Energy*, vol. 112, pp. 383–396, 2015.

[7] D. Sharma, P. Gaur, and A. P. Mittal, "Comparative analysis of hybrid GAPSO optimization technique with GA and PSO methods for cost optimization of an off-grid hybrid energy system," *Energy Technol. Policy*, vol. 1, no. 1, pp. 106–114, 2014.

[8] A. Ben Jemaa, N. Essounbouli, and A. Hamzaoui, "Optimum sizing of hybrid PV/Wind/battery installation using a fuzzy PSO," in *3rd International Symposium on Environmental Friendly Energies and Applications (EFEA)*, 2014, pp. 1–6.

[9] A. Chauhan and V. K. Dwivedi, "Optimal sizing of a stand-alone PV/wind/MHP/biomass based hybrid energy system using PSO algorithm," in *2017 6th International Conference on Computer Applications In Electrical Engineering-Recent Advances (CERA)*, 2017, pp. 7–12.

[10] R. Pallabazzer, "Evaluation of wind-generator potentiality," *Sol. Energy*, vol. 55, no. 1, pp. 49–59, 1995.

[11] Johnson, G.L, Wind energy systems, USA: Pertinance Hall, 1985.

[12] V. Sohoni, S. C. Gupta, and R. K. Nema, "A critical review on wind turbine power curve modelling techniques and their applications in wind based energy systems," *J. Energy*, vol. 2016, pp. 1–18, 2016.

[13] A. Maleki and A. Askarzadeh, "Comparative study of artificial intelligence techniques for sizing of a hydrogen-based stand-alone photovoltaic/wind hybrid system," *Int. J. Hydrogen Energy*, vol. 39, no. 19, pp. 9973–9984, 2014.

[14] F. A. Alturki, A. A. Al-Shamma'a, H. M. H. Farh, and K. AlSharabi, "Optimal sizing of autonomous hybrid energy system using supply-demand-based optimization algorithm," *Int. J. Energy Res.*, vol. 45, no. 1, pp. 605–625, 2021.

[15] A. Redouane, P. Acouetey, A. E. Hasnaoui, and I. E. Harraki, "Feasibility study of energy hybrid systems for villages of the southern Moroccan coastline," in *2018 6th International Renewable and Sustainable Energy Conference (IRSEC)*, 2018, pp. 1–6.

[16] A. Maleki, M. Ameri, and F. Keynia, "Scrutiny of multifarious particle swarm optimization for finding the optimal size of a PV/wind/battery hybrid system," *Renew. Energy*, vol. 80, pp. 552–563, 2015.

[17] F. Fodhil, A. Hamidat, and O. Nadjemi, "Potential, optimization and sensitivity analysis of photovoltaic-diesel-battery hybrid energy system for rural electrification in Algeria," *Energy (Oxf.)*, vol. 169, pp. 613–624, 2019.

[18] R. Ayop, N. M. Isa, and C. W. Tan, "Components sizing of photovoltaic stand-alone system based on loss of power supply probability," *Renew. Sustain. Energy Rev.*, vol. 81, pp. 2731–2743, 2018.

[19] A. Maleki and F. Pourfayaz, "Optimal sizing of autonomous hybrid photovoltaic/wind/battery power system with LPSP technology by using evolutionary algorithms," *Sol. Energy*, vol. 115, pp. 471–483, 2015.

[20] S. Sanajaoba and E. Fernandez, "Maiden application of Cuckoo Search algorithm for optimal sizing of a remote hybrid renewable energy System," *Renew. Energy*, vol. 96, pp. 1–10, 2016.

[21] KENNEDY and J, "Particle Swarm Optimization, Proceeding," *IEEE International Conference on Neural Networks, Piscataway, 1995*, pp. 1942–1948, 1995.

[22] A. J. Ardakani, F. F. Ardakani, and S. H. Hosseinian, "A novel approach for optimal chiller loading using particle swarm optimization," *Energy Build.*, vol. 40, no. 12, pp. 2177–2187, 2008.

[23] İ. B. Aydilek, "A hybrid firefly and particle swarm optimization algorithm for computationally expensive numerical problems," *Appl. Soft Comput.*, vol. 66, pp. 232–249, 2018.

[24] M. A. Mohamed, A. M. Eltamaly, and A. I. Alolah, "PSO-based smart grid application for sizing and optimization of hybrid renewable energy systems," *PLoS One*, vol. 11, no. 8, p. e0159702, 2016.

[25] X. Xu, W. Hu, D. Cao, Q. Huang, C. Chen, and Z. Chen, "Optimized sizing of a standalone PV-wind-hydropower station with pumped-storage installation hybrid energy system," *Renew. Energy*, vol. 147, pp. 1418–1431, 2020.

PERFORMANCE ENHANCING OF 3-PHASE UPQC USING FEEDBACK LINEARISATION BASED DPC TECHNIQUE FOR POWER QUALITY IMPROVEMENT

Dahdouh Adel[a,*], Mazouz Lakhdar[b], Brahim Elkhalil Youcefa [c]

[a,b,c] Applied Automation and Industrial Diagnostic Laboratory, Electrical Engineering Department.
Faculty of Science and Technology, Djelfa University, 17000 Djelfa, Algeria

Adel.dahdouh@univ-djelfa.dz, l.mazouz@univ-djelfa.dz, khalilyoucefa@gmail.com

Abstract

This paper presents the compensation principle using feedback linearization based DPC control strategies of the unified power quality conditioner, which aims at the integration of series-active and shunt-active power filters. In order to improve the performances of UPQC, a control method based on a feedback linearization based DPC controller combined with space vector modulation (SVM) is proposed. The purposes are to deliver compensation signals more quickly and accurately at varied load conditions and to eliminate voltage as well as current harmonics with good dynamic response. Extensive simulation results obtained by Matlab/Simulink for a passive load connected through an uncontrolled bridge rectifier validate the performance of the suggested control scheme. The comparison of these results with those obtained with a PI controller demonstrates the superiority of the proposed controller.

Keywords

Harmonic extraction, Power active filter, UPQC, Feedback linearization controller, DPC, Space vector modulation (SVM).

1. INTRODUCTION

In recent years, the increasing use of power electronic devices has led to the deterioration of power quality due to harmonic generations [1]. The terminology and the guidelines for power quality have been described in detail at IEEE-519 and IEC-555. According to these guidelines, the allowed total harmonic distortion should be less than 5% [2].

The aforementioned problems are partially solved with the help of passive filters [3-5]. However, this kind of filter cannot solve random variations in the load current waveform and voltage waveform. On the other hand, compensating devices such as Static Var Compensator (SVC), Parallel Active Filter (PAF), Series Active Filter (SAF), and hybrid filters are proposed to ensure power quality [6]. However, their capabilities are usually limited as they can only solve one or two power quality problems. Recent research has shown that the unified power quality conditioners (UPQCs), an integration of series and shunt active filters, can be utilized to solve most power quality problems simultaneously [7].

The UPQC can maintain the load end-voltage at the desired level and prevent incoming sags/swells in voltages [8]. In addition the UPQC can efficiently support the reactive power requirement of the load, and suppress the generated load harmonic currents, so that do not propagate back to the utility, which can cause voltage and current distortion to other consumers [9].

Different control approaches for the UPQC have been pro-posed. In [11] authors have applied a linear control using PI controller. The control of the UPQC connected to a Wind system by PI controller is proposed in [12]. An intelligent controller has been applied by [13] and [14]. A four wire topology of the UPQC controlled by PI has been studied in [15], [16] and [17].

The aim of this paper is twofold. Firstly, to design a feedback linearization based DPC controller combined with space vector modulation for the UPQC to enhance power quality. secondly, to compare the performances of the proposed controller with a PI controller to validate the proposed controller, through an extensive simulation results for a passive load connected through an uncontrolled bridge rectifier.

The rest of the paper is organized as follows: in section II, the control design of the UPQC is presented, while in section III, simulation results and their discussion are given, finally a conclusion of the present work is derived.

2. CONTROL DESIGN

2.1 Mathematical Model of UPQC

The differential equations describing the dynamic model of UPQC are defined in stationary α-β reference frame, as given in equations (1) and (2).

The parallel filter model is governed by the following equation.

$$\dot{x}_p = f_p(x_p) + g_p(x_p)u_p \tag{1}$$

where:

$$f_p(x_p) = \begin{bmatrix} -\frac{R_{fp}}{L_{fp}} x_{p1} \\ -\frac{R_{fp}}{L_{fp}} x_{p2} \end{bmatrix}, g_p(x_p) = \begin{bmatrix} \frac{1}{L_{fp}} & 0 \\ 0 & \frac{1}{L_{fp}} \end{bmatrix}, x_p = \begin{bmatrix} P_{fp} \\ Q_{fp} \end{bmatrix}, u_p = \begin{bmatrix} V_{fp\alpha} \\ V_{fp\beta} \end{bmatrix}$$

$$y_p = \begin{bmatrix} y_{p1} \\ y_{p2} \end{bmatrix} = \begin{bmatrix} h_{p1} \\ h_{p2} \end{bmatrix}$$

$V_{fp\alpha\beta}$, P_{fp} and Q_{fp} are the voltages and active and reactive powers of the shunt filter respectively.

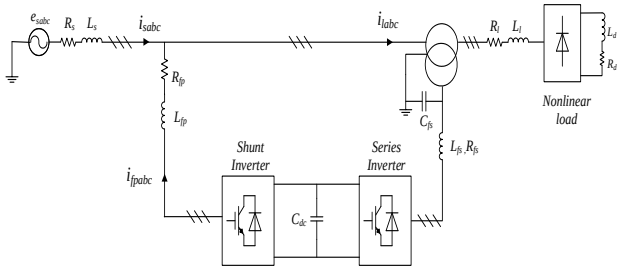

Figure. 1. Single-line scheme of the UPQC .

The series filter model is described by:

$$\dot{x}_s = f_s(x_s) + g_s(x_s)u_s \tag{2}$$

Where: $f_s(x_s) = \begin{bmatrix} \frac{1}{C_{fs}} x_{s1} \\ \frac{1}{C_{fs}} x_{s2} \end{bmatrix}$, $g_s(x_s) = \begin{bmatrix} \frac{1}{L_{fs}} & 0 \\ 0 & \frac{1}{L_{fs}} \end{bmatrix}$, $x_s = \begin{bmatrix} P_{fs} \\ Q_{fs} \end{bmatrix}$, $u_s = \begin{bmatrix} V_{fs\alpha} \\ V_{fs\beta} \end{bmatrix}$

$$y_s = \begin{bmatrix} y_{s1} \\ y_{s2} \end{bmatrix} = \begin{bmatrix} h_{s1} \\ h_{s2} \end{bmatrix}$$

$V_{fs\alpha\beta}$, P_{fs} and Q_{fs} are the voltages and active and reactive powers of the series filter respectively.

2.2 Harmonic extraction

Active filter depends greatly on the extraction method used to eliminate harmonics from the distorted waveforms [18], [19]. Hereafter, harmonics extraction methods are described.

2.2.1 Harmonic currents extraction using PQ theory

In this work the instantaneous power theory technique (PQ theory) is chosen as highlighted in Fig. 2.

Instantaneous active and reactive powers of the nonlinear load are calculated by:

$$\begin{bmatrix} P_l \\ Q_l \end{bmatrix} = \begin{bmatrix} v_{s\alpha} & v_{s\beta} \\ v_{s\beta} & -v_{s\alpha} \end{bmatrix} \begin{bmatrix} i_{l\alpha} \\ i_{l\beta} \end{bmatrix} \tag{3}$$

Where the instantaneous powers can be expressed as follows:

$$\begin{cases} P_l = \bar{P}_l + \tilde{P}_l \\ Q_l = \bar{Q}_l + \tilde{Q}_l \end{cases} \tag{4}$$

For harmonic and reactive power compensation, all of the reactive power ($\bar{Q}_l$ and $\tilde{Q}_l$ components) and harmonic component ($\tilde{P}_l$) of active power are selected as compensation power references and the compensation currents reference are calculated as (5).

$$\begin{bmatrix} i^*_{fp\alpha} \\ i^*_{fp\beta} \end{bmatrix} = \frac{1}{v^2_{s\alpha} + v^2_{s\beta}} \begin{bmatrix} v_{s\alpha} & v_{s\beta} \\ v_{s\beta} & -v_{s\alpha} \end{bmatrix} \begin{bmatrix} \tilde{P}_l \\ Q_l \end{bmatrix} \tag{5}$$

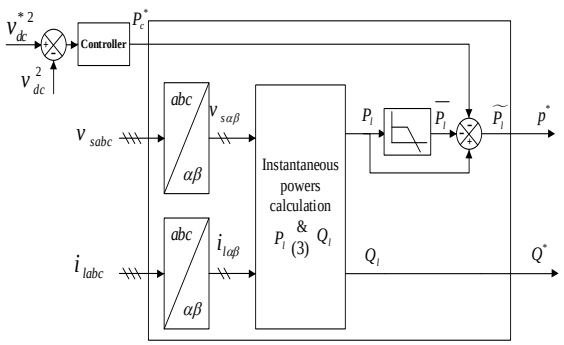

Figure. 2. Harmonic currents extraction scheme using PQ theory

On the other hand the signal P_c^* is used as an average real power, and is obtained from the DC voltage controller.

2.2.3 Harmonic voltages extraction using PQ-PLL theory

It consists of two parts, the first is to extract voltage harmonics, and it is similar to PQ theory for currents (Equation (6)).

$$\begin{bmatrix} \overline{v_{s\alpha}} \\ \overline{v_{s\beta}} \end{bmatrix} = \frac{1}{i^2_{l\alpha} + i^2_{l\beta}} \begin{bmatrix} i_{l\alpha} & i_{l\beta} \\ -i_{l\beta} & i_{l\alpha} \end{bmatrix} \begin{bmatrix} \overline{P_l} \\ \overline{Q_l} \end{bmatrix} \tag{6}$$

The second part is to calculate the voltage drop across the load as shown in Fig. 3.

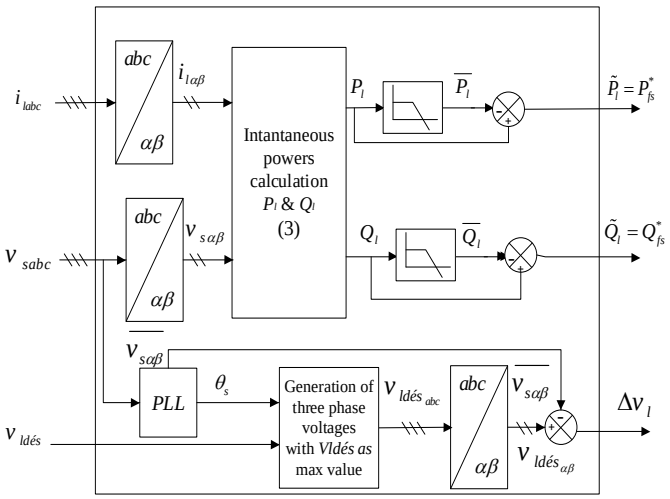

Figure. 3. Harmonic voltages extraction scheme using PQ-PLL theory .

2.3 Feedback Linearisation Controller (FLC) Synthesis

Consider the nonlinear system represented by:

$$\dot{x} = f(x) + \sum_{i=1}^{p} g_i(x)u_i \qquad i = 1, 2, ..., p$$
$$y_i = h_i(x) \tag{7}$$

where g(x) and f(x) are scalar functions.

The well-known method to form feedback linearization law of the previous system is shown in Fig. 4 [20]. The problem of finding the vector relative degree of the system (7) implies differentiation of each output signal until one of the input signals appear explicitly in the differentiation. For each output signal, we define r_j as the smallest integer such that at least one of the inputs appears in $y_j^{(r_j)}$ [9]:

$$y_j^{(r_j)} = L_f{}^{r_j} h(x) + \sum_{i=1}^{p} L_{gi}(L_f{}^{r_j - 1} h_j(x))u_i \quad j = 1, 2, ..., p \tag{8}$$

Where: $L_f h_j$ and $L_{gi}(L_f{}^{r_j - 1} h_j)$ stand for *Lie derivatives* of *h* with respect to *f* and *g*, respectively.

The global relative degree (*r*) is defined as the sum of all the relative degrees obtained using (8). It must be less than or equal to the order of the system: $r = \sum_{j=1}^{p} r_j \le n$

To find the expression of linearizing law *u* that allows making linear the relationship between inputs and outputs, the expression (8) can be written in its matrix form:

$$[y_1^{r_j} \ \ldots \ \ldots y_p^{r_p}]^t = \zeta(x) + D(x)u \tag{9}$$

Where:

$$\zeta(x) = \begin{pmatrix} L_f{}^{r_1} h_1(x) \\ L_f{}^{r_2} h_2(x) \\ \cdot \\ \cdot \\ \cdot \\ L_f{}^{r_p} h_p(x) \end{pmatrix} \tag{10}$$

And

$$D(x) = \begin{pmatrix} L_{g_1} L_f{}^{r_1-1} h_1 & L_{g_2} L_f{}^{r_1-1} h_1 & \ldots & L_{g_p} L_f{}^{r_1-1} h_1 \\ L_{g_1} L_f{}^{r_2-1} h_2 & L_{g_2} L_f{}^{r_2-1} h_2 & \ldots & L_{g_p} L_f{}^{r_2-1} h_2 \\ \cdot & \cdot & \ldots & \cdot \\ L_{g_1} L_f{}^{r_p-1} h_p & L_{g_2} L_f{}^{r_p-1} h_p & \ldots & L_{g_p} L_f{}^{r_p-1} h_p \end{pmatrix} \tag{11}$$

$D(x)$ is called the decoupling matrix system.
Assuming that D(x) is not singular, the linearizing control law has the following form [9]:

$$u = D(x)^{-1}(-\zeta(x) + v) \tag{12}$$

Notice that linearization would be possible only if the decoupling matrix D(x) is reversible. The block diagram of the linearized system is given in figure (4).

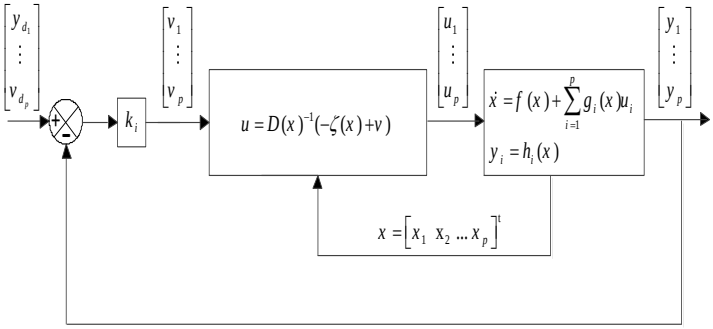

Figure. 4. Block diagram of linearized MIMO system.

2.3.1 DC voltage FLC synthesis

The synthesis of the DC voltage controller is based on the second subsystem. The derivative of the output $y=h = v_{dc}^2$ is given by:

$$\dot{y} = L_f h(x) + L_g h(x)u = \frac{2}{C_{dc}} P_{dc} \tag{13}$$

The control input P_{dc} appear in (15), so the relative degree is r =1. The relative degree of this output is equal to the order of subsystem 2, which corresponds clearly to an exact linearization [10].

Then the control law is obtained by:

$$P_{dc}^* = 2C_{dc}v \tag{14}$$

where: $\dot{y} = v$

For a problem of trajectory tracking defined by v_{dc}*(t), the term v is expressed by:

$$v = k_{dc}(v_{dc}^{*2} - v_{dc}^2) + \frac{dv_{dc}^{*2}}{dt} \tag{15}$$

Where, k_{dc} is a positive constant

2.3.2 Parallel powers FLC synthesis

Each output derivative is given by:

$$\dot{y}_j = L_f\ h(x) + \sum_{i=1}^{2} L_{gi}(L_f\ h_j(x))u_i \quad j = 1,2 \tag{16}$$

Then (16) can be written in matrix form as:

$$\begin{bmatrix} \dot{y}_1 \\ \dot{y}_2 \end{bmatrix} = \begin{bmatrix} -\frac{R_{fp}}{L_{fp}} x_{p1} \\ -\frac{R_{fp}}{L_{fp}} x_{p2} \end{bmatrix} + \begin{bmatrix} \frac{1}{L_{fp}} & 0 \\ 0 & \frac{1}{L_{fp}} \end{bmatrix} \begin{bmatrix} u_1 \\ u_2 \end{bmatrix} \tag{17}$$

The decoupling matrix determinant is different to zero, and then the control law is given as:

$$u = \begin{bmatrix} u_1 \\ u_2 \end{bmatrix} = D(x)^{-1}\left[-\zeta(x) + \begin{bmatrix} v_1 \\ v_2 \end{bmatrix}\right] \tag{18}$$

The application of the linearization law on the first subsystem leads to the following decoupled linear system:

$$\begin{bmatrix} \dot{y}_1 \\ \dot{y}_2 \end{bmatrix} = \begin{bmatrix} v_1 \\ v_2 \end{bmatrix} \tag{19}$$

The control law used for tracking is:

$$\begin{aligned} v_1 &= k_{p1}(P_{fp}^* - P_{fp}) + \frac{dP_{fp}^*}{dt} \\ v_2 &= k_{p2}(Q_{fp}^* - Q_{fp}) + \frac{dQ_{fp}^*}{dt} \end{aligned} \tag{20}$$

Where k_{p1} and k_{p2} are positive constants.

2.3.3 Series powers FLC synthesis

Each output derivative is given by:

$$\dot{y}_j = L_f\ h(x) + \sum_{i=1}^{2} L_{gi}(L_f\ h_j(x))u_i \quad j = 1,2 \tag{21}$$

Then (21) can be written in matrix form as:

$$\begin{bmatrix} \dot{y}_1 \\ \dot{y}_2 \end{bmatrix} = \begin{bmatrix} -\frac{R_{fs}}{L_{fs}} x_{s1} \\ -\frac{R_{fs}}{L_{fs}} x_{s2} \end{bmatrix} + \begin{bmatrix} \frac{1}{L_{fs}} & 0 \\ 0 & \frac{1}{L_{fs}} \end{bmatrix} \begin{bmatrix} u_1 \\ u_2 \end{bmatrix} \tag{22}$$

The decoupling matrix determinant is different to zero, and then the control law is given as:

$$u=\begin{bmatrix}u_1\\u_2\end{bmatrix}=D(x)^{-1}\left[-\zeta(x)+\begin{bmatrix}v_1\\v_2\end{bmatrix}\right] \tag{23}$$

The application of the linearization law on the first subsystem leads to the following decoupled linear system:

$$\begin{bmatrix}\dot{y}_1\\\dot{y}_2\end{bmatrix}=\begin{bmatrix}v_1\\v_2\end{bmatrix} \tag{24}$$

The control law used for tracking is:

$$\begin{aligned}v_1&=k_{s1}(P_{fs}^{*}-P_{fs})+\frac{dP_{fs}^{*}}{dt}\\v_2&=k_{s2}(Q_{fs}^{*}-Q_{fs})+\frac{dQ_{fs}^{*}}{dt}\end{aligned} \tag{25}$$

Where k_{s1} and k_{s2} are positive constants.

2.4 Space Vector Modulation

In this section, SVM technique is presented to produce PWM control signals (s_a, s_b and s_c) to the power switches of the inverter. SVM compensates the required volt-seconds using discrete switching states and their on-times. The space vector diagram of a three phase voltage source inverter is a hexagon (Fig. 5), consisting of six sectors. Every sector is an equilateral triangle of a height h =√3/2 [23]. For any given reference vector, the sector of operation is determined by using Eq (26).

$$S_i=\text{int}\left(\frac{\theta_s}{60}\right)+1 \tag{26}$$

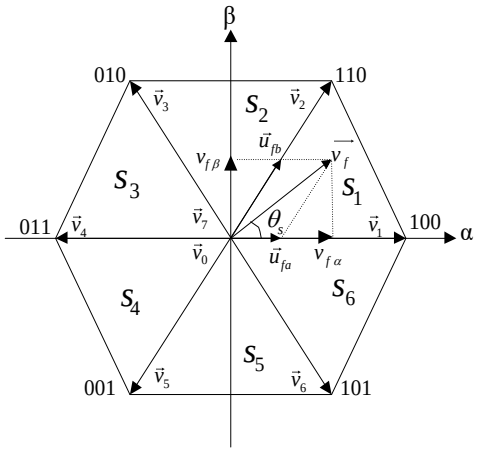

Figure. 5. Space vector diagram.

The on-time calculation is similar for all sectors. Volt-second equation is given by:

$$\vec{v_f}T_s=t_i\vec{v_i}+t_{i+1}\vec{v}_{i+1}+t_0\vec{v}_0 \tag{27}$$

where $T_s = 1/f_s$, with f_s is the switching frequency.
In the first sector,

$$\begin{cases}\vec{v_1}=\sqrt{\frac{2}{3}}v_{dc}\\\vec{v_2}=\sqrt{\frac{2}{3}}v_{dc}\left(\frac{1}{2}+j\,\frac{\sqrt{3}}{2}\right)\\\vec{v_0}=0\end{cases} \tag{28}$$

The reference vector can be also written as follows,

$$\vec{v_f}=v_{f\alpha}+jv_{f\beta} \tag{29}$$

From Equations (27, 28 and 29) one can find:

$$\begin{cases}v_{f\alpha}=\sqrt{\frac{2}{3}}v_{dc}\frac{t_1}{T_s}+\frac{1}{\sqrt{6}}v_{dc}\frac{t_2}{T_s}\\v_{f\beta}=\frac{1}{\sqrt{2}}v_{dc}\frac{t_2}{T_s}\end{cases} \tag{30}$$

From equation (30), ON times calculation are given below

$$\begin{cases}t_1=\frac{\sqrt{6}v_{f\alpha}-\sqrt{2}v_{f\beta}}{v_{dc}}T_s\\t_2=\frac{\sqrt{2}v_{f\beta}}{v_{dc}}T_s\\t_0=T_s-(t_1+t_2)\end{cases} \tag{31}$$

The choice of the null vector determines the SVM scheme. There are a few options: the null vector v_0 only, the null vector v_7 only, or a combination of the null vectors. A popular SVM technique is to alternate the null vector in each cycle and to reverse the sequence after each null vector as shown in Fig. 6. This will be referred to as the symmetric 7-segment technique [24].

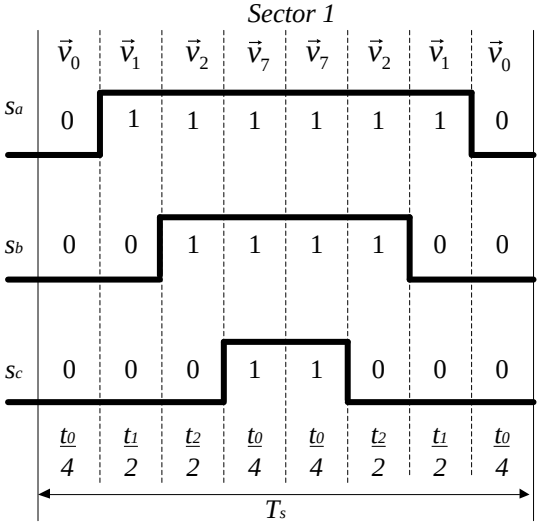

Figure. 6. 7-Segment Switching Sequence for V_{ref} in sector 1.

Finally, the basic operation of the proposed control method associated to a nonlinear load is summarize in Fig. 7. The switch control signals are derived from a Space Vector Modulator (SVM). Voltage references for the SVM are derived from the feedback linearization based DPC controllers. The references are computed by using the instantaneous PQ theory for currents and PQ-PLL for voltages. The compensation objective is to compensate harmonics in both voltage and current, reactive power compensation, and to regulate the DC bus during bidirectional active power exchange between the two active filters and the power system grid. Detailed description of different parts of UPQC is given hereafter.

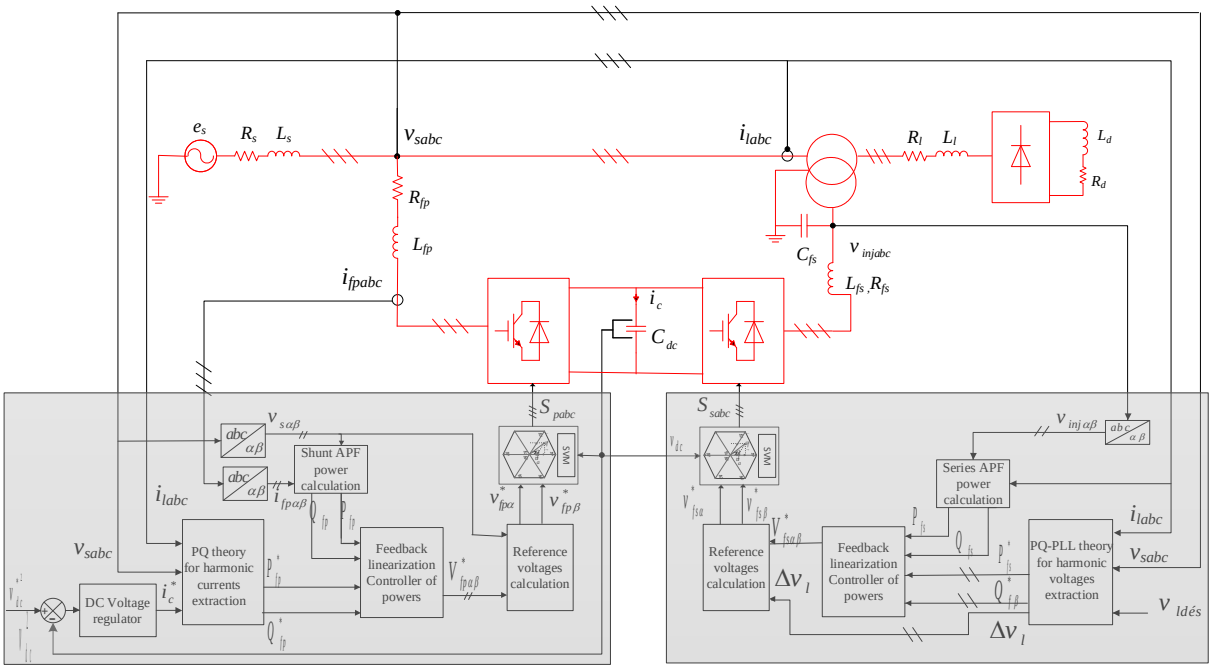

Figure. 7. Feedback linearization based DPC control scheme of the UPQC .

3. RESULTS AND DISCUSSION

Harmonic current and voltage filtering, reactive power compensation and performance of the UPQC with the proposed control have been examined in Matlab/Simulink environment, under nonlinear load variation and voltage sag. The parameters used in the present study are shown in Table I, while parameters and detailed study of linear control of the UPQC with PI controller is detailed in [25].

TABLE I
SYSTEM PARAMETERS

Parameter	value
RMS value of the source voltage	220 V
DC-link capacitor C_{dc}	8 mF
Source impedance Rs, Ls	3mΩ, 2.6 µH
Shunt filter impedance R_{fp}, L_{fp}	20 mΩ, 2.5 mH
Series filter impedance R_{fs}, L_{fs},C_{fs}	1.5 Ω, 3 mH, 0.1 mF
Line impedance R_l, L_l	10 mΩ, 0.3 µH
Diode rectifier load R_d , L_d	15 Ω, 2 mH
DC-link voltage reference	900 V
Switching frequency f_s	12 kHz
k_{p1}= k_{p2}	2100
k_{s1}= k_{s2}	1300
k_{dc}	250

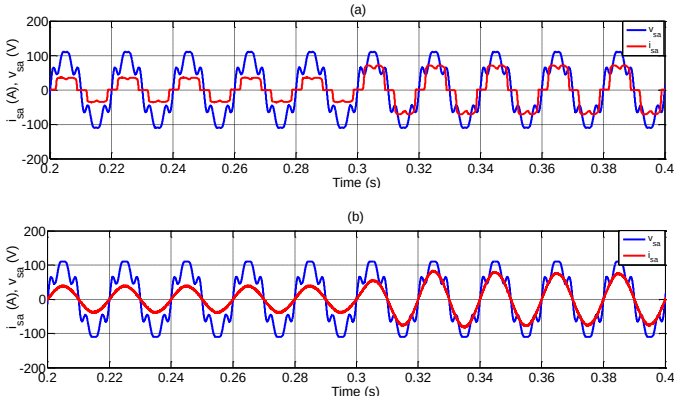

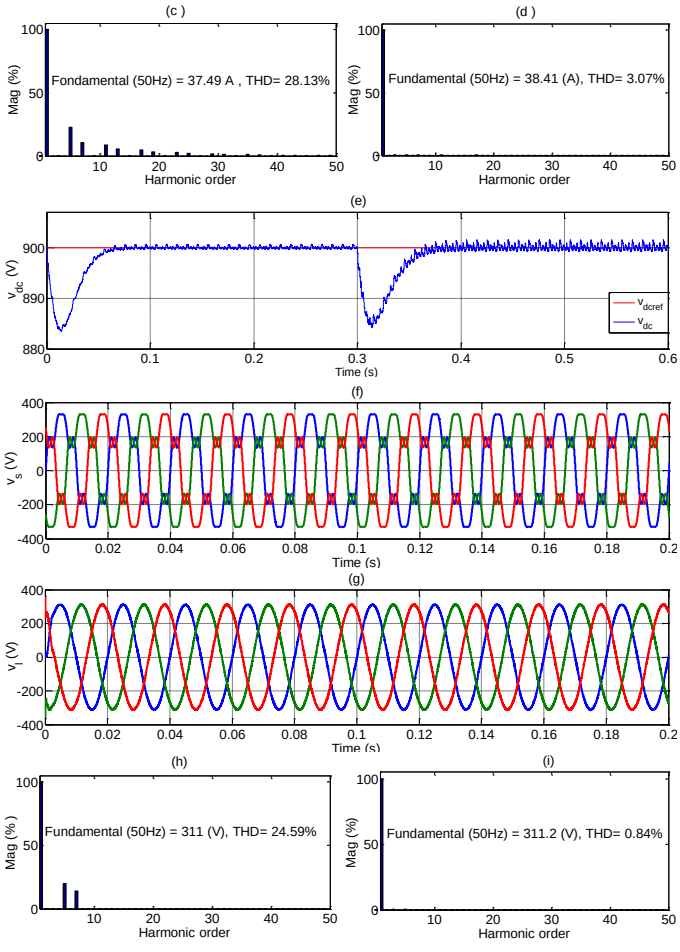

Fig. 7. Simulation results of the proposed controller. a): Source voltage and source current of a-phase before compensation, b): Source voltage and source current of a-phase after compensation, c): Harmonic spectrum of source current before compensation, d): Harmonic spectrum of source current after

compensation. e): DC-link voltage v_{dc}, f): Load voltage before compensation. g): Load voltage after compensation. h): Harmonic spectrum of load voltage before compensation, i): Harmonic spectrum of load voltage after compensation.

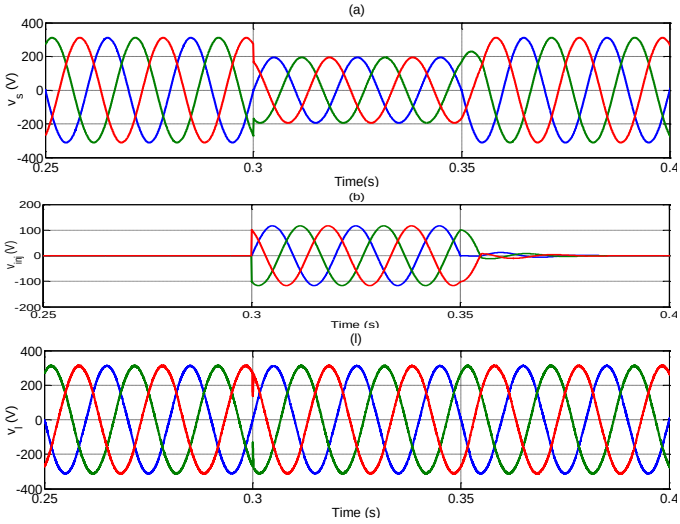

Fig. 8. Simulation results of the proposed sliding mode controller during a sag test. a): Source voltage during a sag. b): Injected voltage for compensating a sag. c): Load voltage during a sag after compensation.

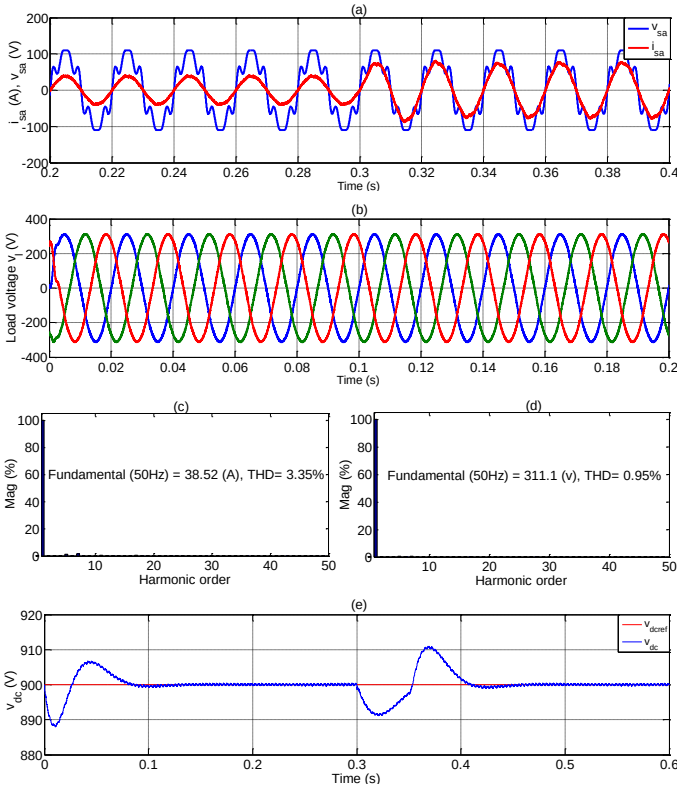

Fig. 9. Simulation results with PI controller. a): Source voltage and source current of a-phase before compensation, b): Load voltage after compensation. c): Harmonic spectrum of source current after compensation, d): Harmonic spectrum of load voltage after compensation. e): DC-link voltage v_{dc}.

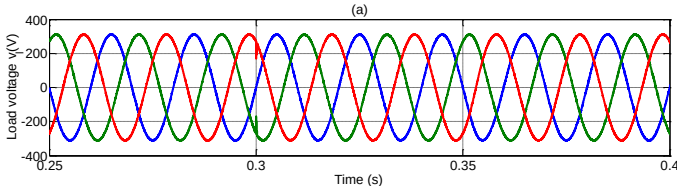

Fig. 10. Simulation results with PI controller during a sag test. a): Load voltage during a sag after compensation.

The dynamic behavior under a step change of the load at t = 0.3s is presented in Figs. 7.a and 7.b. It can be observed that the grid current become sinusoidal after the control application, and unity power factor operation is successfully achieved, even in this transient state.

In case of nonlinear control, the harmonic spectrums of AC grid current and load voltage before and after compensation are illustrated in Fig. 7.(c) and (d), for current, in Fig. 7.(h) and (i) for voltage. For linear control, the same spectrums are shown in Fig. 9.(c) and (d). It results that the UPQC decreases the total harmonic distortion (THD) in the grid currents from 28.13% to 3.35% with PI controller. However, with feedback linearization based DPC controller, the current THD is decreased down to 3.07%. Load voltage THD decreases from 24.59% to 0.95% with PI, while it is further decreases to 0.84% when feedback linearization based DPC controller is applied, which proves the effectiveness of the proposed nonlinear controller.

The UPQC was tested with sag in grid voltage, and the load voltage was again found very close to a sinusoidal voltage. So, the UPQC is able to produce the required compensating voltage components to keep constant load voltage.

The absence of an overshoot in DC voltage response during load change, low rise time and low THD, demonstrates the superiority of the feedback linearization based DPC controller compared to its counterpart traditional PI controller as illustrated in Table. II.

TABLE II
COMPARISON OF PI CONTROLLER WITH SLIDING MODE CONTROLLER

Factor	PI controller	FL-DPC controller
THDi (%)	3.35	3.07
THDv (%)	0.95	0.84
Charging of DC link (s)	0.11	0.08
Overshoot	+	-

4. CONCLUSION

In this paper a control design of the UPQC is carried out including its mathematical model, harmonic extraction methods for both currents and voltages. feedback linearization based DPC controller is derived to suppress currents and voltages harmonics. For the close power switches control, SVM approach has been used due to its benefits in term of fixed frequency of implementation. Simulation results show that in all the stages of system operation, the load side voltages and source side currents are very close to a sinusoidal shape. These results show clearly that UPQC controlled by feedback linearization based DPC offers much better performance compared to traditional controllers case.

REFERENCES

[1] Y. Lu, G. Xiao, X. Wang, F. Blaabjerg and D. Lu, “Control Strategy for Single-Phase Transformerless Three-Leg Unified Power Quality Conditioner Based on Space Vector Modulation”, IEEE Transactions on Power Electronics, vol. 31, no. 4, April 2016, pp. 2840-2849.

[2] R. M. Abdalaal and C. N. M. Ho, "Analysis and Validations of Modularized Distributed TL-UPQC Systems With Supervisory Remote Management System," in IEEE Transactions on Smart Grid, vol. 12, no. 3, pp. 2638-2651, May 2021, doi: 10.1109/TSG.2020.3044992.

[3] Jayanti Sarker, S.K. Goswami, “Optimal Location of Unified Power Quality Conditioner in Distribution System for Power Quality Improvement”, International Journal of Electrical Power & Energy Systems, Vol. 83, December 2016, pp. 309-324.

[4] N. Patnaik, A. K. Panda, “Performance analysis of a 3 phase 4 wire UPQC system based on PAC based SRF controller with real time digital simulation”, International Journal of Electrical Power & Energy Systems, Volume 74. January 2016, pp. 212-221.

[5] M. Anand and P. Kumar, "Fuzzy Controller based Topologies of NS-UPQC and B4-UPQC," 2020 IEEE International Conference on Advent Trends in Multidisciplinary Research and Innovation (ICATMRI), 2020, pp. 1-7, doi: 10.1109/ICATMRI51801.2020.9398396.

[6] Peng Li, Yuwei Li, Ziheng Yin, "Realization of UPQC H∞ coordinated control in Microgrid", International Journal of Electrical Power & Energy Systems, Vol. 65, February 2015, pp. 443-452.

[7] S. R. Arya, S. J. Alam and P. Ray, "Control algorithm based on limit cycle oscillator-FLL for UPQC-S with optimized PI gains," in CSEE Journal of Power and Energy Systems, vol. 6, no. 3, pp. 649-661, Sept. 2020, doi: 10.17775/CSEEJPES.2019.01030.

[8] DAHDOUH, ADEL, Barkat, Said, Aissa, Chouder,"A Combined Sliding Mode Space vector Modulation Control of the Shunt Active Power Filter Using Robust Harmonic Extraction Method A Combined Sliding Mode Space vector Modulation Control of the Shunt Active Power Filter Using Robust Harmonic Extraction Method". Algerian Journal of Signals and Systems. Vol. 1, 2016, pp. 37-46. 10.51485/ajss.v1i1.17.

[9] M. Bouzidi, A. Benaissa, S. Barkat, "Application of feedback linearization to the virtual flux direct power control of three-level three-phase shunt active power filter", International review of electrical engineering, Vol. 5, No. 3, pp.1128-1140, 2012..

[10] T. Koroglu, A. Tan, M. M. Savrun, M. U. Cuma, K. C. Bayindir and M. Tumay, "Implementation of a Novel Hybrid UPQC Topology Endowed With an Isolated Bidirectional DC–DC Converter at DC link," in IEEE Journal of Emerging and Selected Topics in Power Electronics, vol. 8, no. 3, pp. 2733-2746, Sept. 2020, doi: 10.1109/JESTPE.2019.2898369.

[11] R. H. Yang and J. X. Jin, "Unified Power Quality Conditioner With Advanced Dual Control for Performance Improvement of DFIG-Based Wind Farm," in IEEE Transactions on Sustainable Energy, vol. 12, no. 1, pp. 116-126, Jan. 2021, doi: 10.1109/TSTE.2020.2985161.

[12] S. Devassy and B. Singh, "Performance Analysis of Solar PV Array and Battery Integrated Unified Power Quality Conditioner for Microgrid Systems," in IEEE Transactions on Industrial Electronics, vol. 68, no. 5, pp. 4027-4035, May 2021, doi: 10.1109/TIE.2020.2984439.

[13] M. A. Mansor, K. Hasan, M. M. Othman, S. Z. B. M. Noor and I. Musirin, "Construction and Performance Investigation of Three-Phase Solar PV and Battery Energy Storage System Integrated UPQC," in IEEE Access, vol. 8, pp. 103511-103538, 2020, doi: 10.1109/ACCESS.2020.2997056.

[14] J. Yu, Y. Xu, Y. Li and Q. Liu, "An Inductive Hybrid UPQC for Power Quality Management in Premium-Power-Supply-Required Applications," in IEEE Access, vol. 8, pp. 113342-113354, 2020, doi: 10.1109/ACCESS.2020.2999355.

[15] Y. Harbouche, L. Khellache and R. Abdessemed, "UVTG Control Strategy for Three Phase Four Wire UPQC to Improve Power Quality", International Electrical Engineering Journal, vol. 6, No. 9, 2015, pp. 1988-1993.

[16] S. A. O. da Silva, L. B. G. Campanhol, G. M. Pelz and V. de Souza, "Comparative Performance Analysis Involving a Three-Phase UPQC Operating With Conventional and Dual/Inverted Power-Line Conditioning Strategies," in IEEE Transactions on Power Electronics, vol. 35, no. 11, pp. 11652-11665, Nov. 2020, doi: 10.1109/TPEL.2020.2985322..

[17] S. J. Alam and S. R. Arya, "Control of UPQC based on steady state linear Kalman filter for compensation of power quality problems," in Chinese Journal of Electrical Engineering, vol. 6, no. 2, pp. 52-65, June 2020, doi: 10.23919/CJEE.2020.000011.

[18] A. Ozdemir.and Z. Ozdemir., "Digital current control of a three-phase four-leg voltage source inverter by using p-q-r theory" Power Electronics, IET , Vol.7, No.3, March 2014, pp.527-539.

[19] L.S Czarnecki, "Constraints of instantaneous reactive power p-q theory" in Power Electronics, IET , vol.7, no.9, September 2014, pp.2201-2208.

[20] S. K. Dash and P. K. Ray, "A New PV-Open-UPQC Configuration for Voltage Sensitive Loads Utilizing Novel Adaptive Controllers," in IEEE Transactions on Industrial Informatics, vol. 17, no. 1, pp. 421-429, Jan. 2021, doi: 10.1109/TII.2020.2986308.

[21] R. Guzman, L.G Vicuna,J. Morales, M. Castilla, J. Matas,. "Sliding-Mode Control for a Three-Phase Unity Power Factor Rectifier Operating at Fixed Switching Frequency" in Power Electronics, IEEE Transactions on , vol.31, no.1, Jan. 2016, pp.758-769.

[22] A. Chebabhi, M.K Fellah and M.F Benkhoris "Sliding Mode Controller for Four Leg Shunt Active Power Filter to Eliminating Zero Sequence Current, Compensating Harmonics and Reactive Power with Fixed Switching Frequency ", Serbian Journal Of Electrical Engineering, Vol. 12, No. 02, june 2015, pp. 205- 218.

[23] K.Ramya and R.Prakash "Comparative Analysis of PWM Techniques for Three Level Diode Clamped Voltage Source Inverter", International Journal of Power Electronics and Drive System, Vol. 5, No. 01, July-2014, pp. 15- 23.

[24] J. Han, X. Li, Y. Jiang and S. Gong, "Three-Phase UPQC Topology Based on Quadruple-Active-Bridge," in IEEE Access, vol. 9, pp. 4049-4058, 2021, doi: 10.1109/ACCESS.2020.3047961.

[25] DAHDOUH, ADEL, Barkat, Said, Aissa, Chouder," SLIDING MODE BASED ON SPACE VECTOR MODULATION CONTROL OF THE UNIFIED POWER QUALITY CONDITIONER". Mediterranean Journal of Measurement and Control. Vol. 13, 2017, pp. 686-694.

BIOGRAPHIES

Adel Dahdouh received his License and Master degrees in Electrical Engineering from Mohamed Boudiaf University of M'sila, Algeria, in 2013 and 2015 respectively. Currently, he is a researcher in Applied Automation and Industrial Diagnostic of Djelfa (LAADI). His research interest includes control of power converters, power quality enhancement, micro-grids and energy management systems.

Lakhdar MAZOUZ, is an assistant lecturer and researcher at the department of Electrical Engineering, University of Djelfa Algeria. He received the licence degree on electrical engineering from the University of Laghouat, Algeria. He received PhD degree in 2017 from the Djillali Liabes University of Sidi Bel-Abbes (Algeria) and the Magister degree, from the same University in 2010. He is current research interests are: the VSC-HVDC link, the FACTS and the Offshore Wind Farms.

Brahim Elkhalil Youcefa received his License and Master degrees in Electrical Engineering from Mohamed Boudiaf University of M'sila, Algeria, in 2013 and 2015 respectively. He received PhD degree in 2020 from the Djillali Liabes University of Sidi Bel-Abbes (Algeria) His research interest includes control of power converters, power quality and modeling and control of renewable energy sources

Supervisory Control for a robot manipulators using fuzzy interval

Bennour Hachem
Laboratory of Electronics and New Technologies
Department of Electrical Engineering
University of Oum El Bouaghi, Algéria
Hachem.bennour@univ-oeb.dz

Megri Abderahim Faycal
Laboratory of Electronics and New Technologies
Department of Electrical Engineering
University of Oum El Bouaghi, Algéria
f.megri@univ-oeb.dz, f_megri@yahoo.fr

Bayarassou Houria
Laboratory of Electronics and New Technologies
Department of Electrical Engineering
University of Oum El Bouaghi, Algéria
Bayarassou.houria@univ-oeb.dz

***Abstract*—In this paper, we present a supervision approach to control a mobile robot that follows a moving target in a medium that contains obstacles. The mobile robot is controlled through three different controllers: attraction to a moving target, Overcome obstacles and get back on track and the supervision controller. The role of a supervisor is to coordinate interactions between other controllers according to the global Information of the system. The proposed hybrid controller was designed using fuzzy intervals that manages the combination of two controllers according to the mobile robot linear and angular velocities.**

Keywords*—Supervisor, aggregation operators, fuzzy intervals, mobile robot.

I. INTRODUCTION

Our goal in this work is to design a fuzzy supervisor that determines a weighting factor α, which gives the participation rate of each control signal then we apply it to the control of a moving robot that is controlled by two controllers: target tracking and obstacle avoiding[1]–[4].

Thus, an approach based on aggregation mechanisms (aggregation by fuzzy rules and aggregation by mathematical operators) is developed to develop the weighting factor α of the supervisor[5].

In this case, the supervisor's action consists of giving more weight to the obstacle avoidance controller in the event of an obstacle in the path. Then it gives more weight to the target tracking controller in the normal case [2], [6], [7].

In the summary of the supervisor, we base on the importance of the form of representation of objectives. For this, we propose a representation based on intervals (fuzzy and fuzzy intervals)[5], [8].

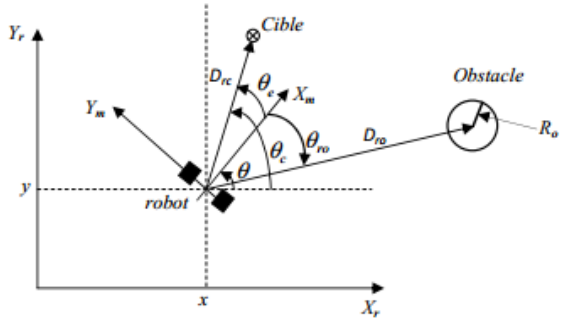

Figure 1graphic representation of a mobile robot with differential wheels

Finally, we compared the simulation results that we obtained by using the supervisor based on fuzzy intervals with the results obtained from the simulation using the Fuzzy supervisor [2].

II. MODEL SYSTEM

We represent by figure (1) a kinematic modeling of a mobile robot. Indeed, a mobile robot can be considered as an autonomous wheeled vehicle capable of performing missions in known or unknown environments[9].

Hence the following kinematic model:

$$dx / dt = \upsilon . \cos(\theta)$$

$$dy /dt = \upsilon . \sin(\theta)$$

$$d\theta /dt = \omega$$

Where θ, ν and ω are respectively the robot orientation, linear and angular velocities.

From Figure (1) We define the position errors as :

$e_x = (x_T - x) = D_{RT} \cos (\theta_{RT})$

$e_y = (y_T - y) = D_{RT} \sin (\theta_{RT})$

Where DRT corresponds to the current distance between the robot and the dynamic target T, which is expressed by

$D_{RT} = \sqrt{ex^2 + ey^2}$

Similarly, the current angle of the robot according to the target, noted θRT, is computed as :

$\theta_{RT} = \alpha \tan 2 (ey, ex)$

The angle error is given by

$\theta_e = (\theta_{RT} - \theta)$

III. FUZZY CONTROL DESIGN

A. *tracking contoller*

The fuzzy controller has two inputs: distance between the robot and the dynamic target (DRT) and the angle of the robot according to the target θRT .

Two output variables: linear velocity (ν) and angular velocity (ω).

For the first input and output, the distance (Drc), we define three membership functions characterizing the linguistic values (P: small, M: average, G: large) and five fuzzy sets for the second input and output, the orientation error (θe), (NG: large negative, NM: medium negative, N: zero, PM: medium positive, PG: large positive) . See figure (2).

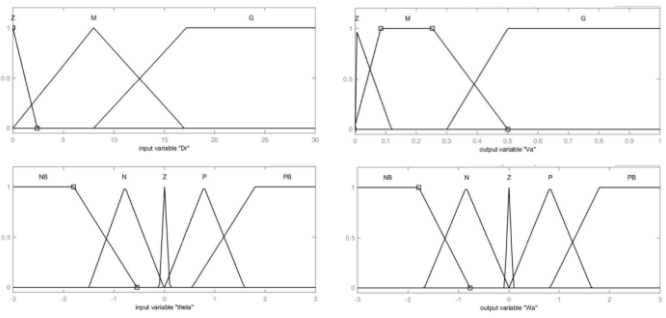

Figure 2membership function shapes of the FLCinput/output variables

Table (1) shows the decision table of the considered fuzzy controller.

Table 1 fuzzy rule sets of the attraction to the dynamic target flc

Θe / Drc	NG	NM	N	PM	PG
P	N/GG	N/GM	N/D	N/DM	N/DG
M	N/GG	M/GG	G/D	M/DG	N/DG
G	N/GG	M/GG	G/D	M/DG	N/DG

B. *obstacle avoidance controller*

The obstacle avoidance controller that we used has two input variables: distance and robot obstacle angle (Dro and θro) respectively, (see figure1), two output variables: linear and angular speed. The distribution of the discourse universes of these variables are shown below figure (3).

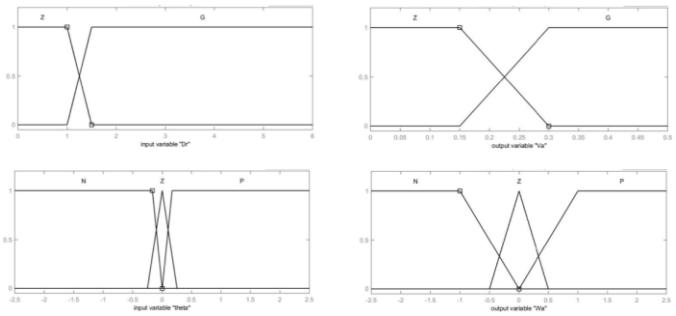

Figure 3 membership function of the FLC input/output variable

The rule base for this controller is generated according to the table (Tab 2).

TABLE 2 *fuzzy rules set of the obstacle avoidance FLC*

θro / Dro	N	Z	P
P	P/G	P/D	P/D
G	G/N	G/N	G/N

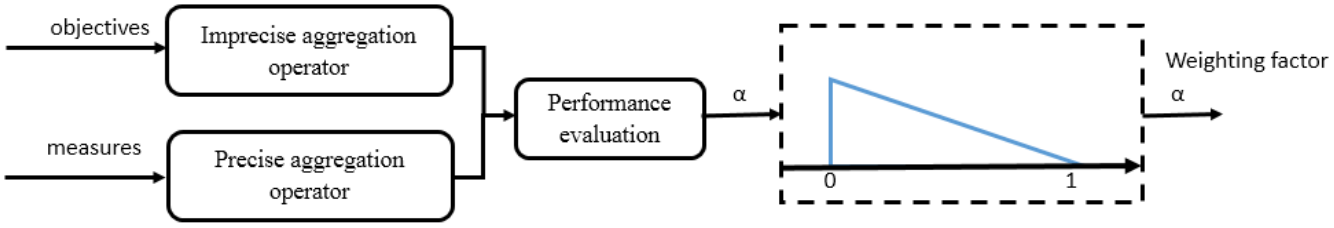

Figure 4 the supervision structure

C. *Supervision controller*

The supervision structure shown in figure (4) consists of coordinating the local controllers in order to reach a satisfactory compromise between the global objectives. The global objectives, denoted Pobj, are represented by fuzzy intervals.

1) *Objectives representation*

In this study, we used only triangular fuzzy intervals to represent the objectives. The tolerance intervals of the indicators are chosen as follows

Linear velocity (v) = p1 and angular velocity (ω) = p2.

$P_1^{obj}(\alpha) = [(P1obj(g)^-), (P_1^{obj}(g)^+)] = [(-1 + g), (1 - g)]$

$P_1^{obj}(\alpha) = [0\ 1\ 1\ 2]$.

$P_2^{obj}(\alpha) = [(P2obj(g)^-), (P_1^{obj}(g)^+)] = [(-1 + g), (1 - g)]$

$P_2^{obj}(\alpha) = [2\ 0\ 0\ 2]$.

Thus, an approach based on aggregation mechanisms (aggregation by fuzzy rules and aggregation by mathematical operators) will be developed to develop the supervisor's weighting factor alfa as shown in figure (4).

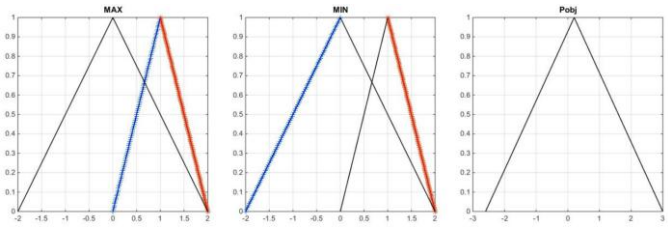

Figure 5 aggregated fuzzy intervals

To calculate the aggregate value of P1 and P2 we used the analytical expression of the MIN and MAX operators

$MIN(A,B)(z) = Sup_{z=min(x,y)} \min(A(x), B(y))$.

$MAX(A,B)(z) = Sup_{z=max(x,y)} \min(A(x), B(y))$.

IV. SIMULATION RESULTS

To perceive the effectiveness of the control scheme proposed in this paper. We have simulated it in matlab. This robot should

reach a dynamic target, moving on direct robot path. Or with sinusoidal movement

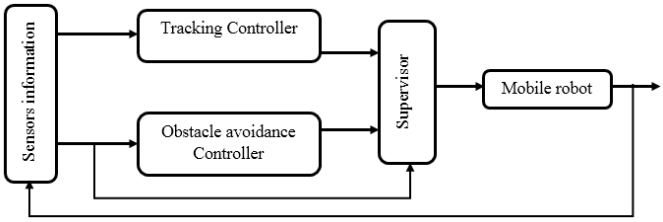

Figure 6 the proposed control sheme

We have compared the results obtained from simulations of control by fuzzy intervals with fuzzy controller Which has the same characteristics and settings as the fuzzy interval controller. The result was as shown in figures (7,8,9,10).

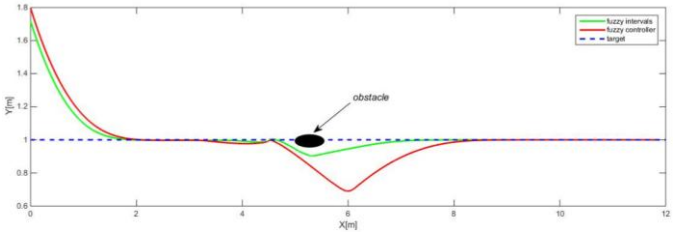

Figure 7avoiding an obstacle while tracking a direct robot path

The evolution of the fusion gain for fuzzy intervals and fuzzy controller

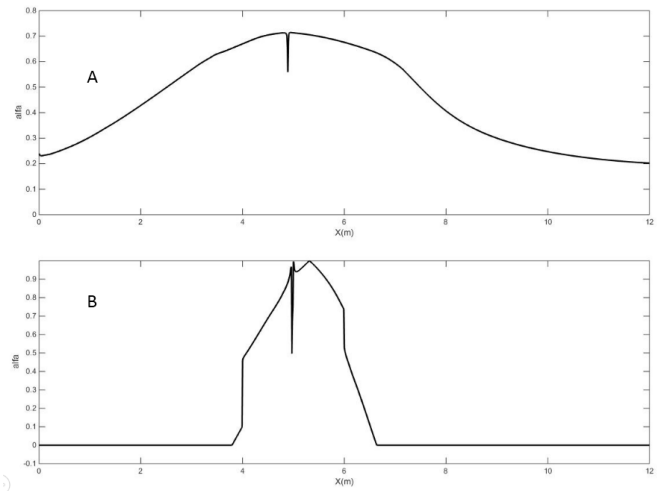

Figure 8 (A) fuzzy interval , (B) fuzzy controller

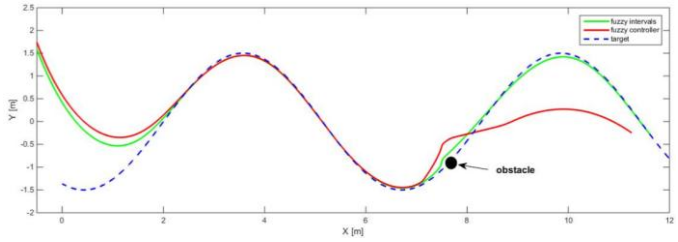

Figure 9 obstacle avoidance while tracking a sunusoidal movement

The evolution of the fusion gain for fuzzy intervals and fuzzy controller

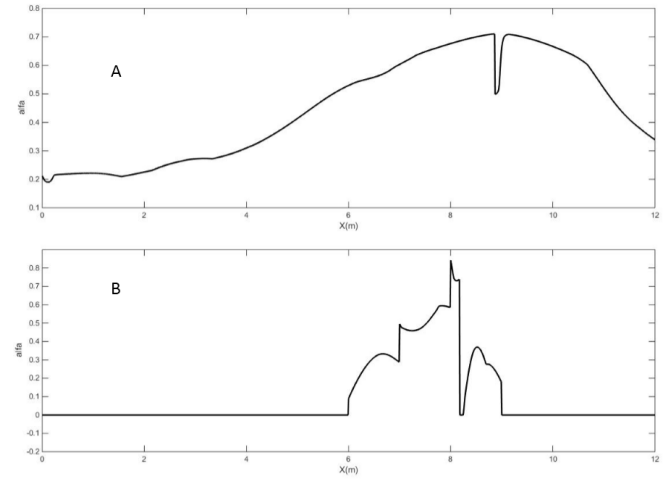

Figure 10 (A) fuzzy interval, (B) fuzzy controller

V. RESULTS INTERPRETATION

Overall, the trend of the different results illustrates comparable performance with that obtained with supervision based on fuzzy controller. However, the results obtained with the fuzzy intervals are more refined and more stable. This is in particular due to the replacement of free commutations by soft commutations through the representation by fuzzy intervals.

VI. CONCLUSION

In this work, we have developed a hybrid robust controller for a class of nonlinear and disturbed systems. The main idea is the use of a fuzzy supervisor to manage efficiently the action of two controllers, such that the system remains stable and robust despite the plant switching from one mode to a new one.

Furthermore, this structure allows us to take advantage of both controllers and to efficiently eliminate their drawbacks.

Simulation results showed the efficiency and the design simplicity of the proposed approach.

REFERENCES

[1] M. Taher, H. E. Ibrahim, S. Mahmoud, et E. Mostafa, Tracking of a Moving Target by Improved Potential Field Controller in Cluttered Environments. .

[2] M. Ider et B. Mendil, « Type-2 fuzzy logic control for a mobile robot tracking a moving target », Mediterr. J. Model. Simul., vol. 3, no 1, p. 057‑065, mars 2015.

[3] T.-H. S. Li, S.-J. Chang, et W. Tong, « Fuzzy target tracking control of autonomous mobile robots by using infrared sensors », IEEE Trans. Fuzzy Syst., vol. 12, no 4, p. 491‑501, août 2004, doi: 10.1109/TFUZZ.2004.832526.

[4] A. Al-Mayyahi et W. Wang, « Fuzzy inference approach for autonomous ground vehicle navigation in dynamic environment », in 2014 IEEE International Conference on Control System, Computing and Engineering (ICCSCE 2014), nov. 2014, p. 29 ‑ 34, doi: 10.1109/ICCSCE.2014.7072684.

[5] « MIN and MAX operators for trapezoidal fuzzy intervals | Emerald Insight ». https://www.emerald.com/insight/content/doi/10.1108/17563781011028541/full/html (consulté le sept. 17, 2021).

[6] « Synthesis of switching controllers: A fuzzy supervisor approach - ScienceDirect ». https://www.sciencedirect.com/science/article/abs/pii/S0362546X06000472 (consulté le sept. 17, 2021).

[7] R. A. Hilhorst, J. van Amerongen, P. Löhnberg, et H. J. A. F. Tulleken, « A supervisor for control of mode-switch processes », Automatica, vol. 30, no 8, p. 1319‑1331, août 1994, doi: 10.1016/0005-1098(94)90111-2.

[8] R. Boukezzoula, S. Galichet, et L. Foulloy, « MIN and MAX Operators for Fuzzy Intervals and Their Potential Use in Aggregation Operators », IEEE Trans. Fuzzy Syst., vol. 15, no 6, p. 1135‑1144, déc. 2007, doi: 10.1109/TFUZZ.2006.890685.

[9] P. K. Padhy, T. Sasaki, S. Nakamura, et H. Hashimoto, « Modeling and position control of mobile robot », in 2010 11th IEEE International Workshop on Advanced Motion Control (AMC), mars 2010, p. 100‑105, doi: 10.1109/AMC.2010.5464018.

Linear Quadratic-Based Computed-Torque Control of an Actuated Pendulum with Friction

Akram Ghediri
Laboratory of Electronics and New Technologies
Department of Electrical Engineering
University of Larbi Ben M'hidi
Oum El Bouaghi, Algeria
akramghediri@gmail.com, ghediri.akram@univ-oeb.dz

Kheireddine Lamamra
Laboratory of Electronics and New Technologies
Department of Electrical Engineering
University of Larbi Ben M'hidi
Oum El Bouaghi, Algeria
l_kheir@yahoo.fr, Lamamra.kheireddine@univ-oeb.dz

Abdelaziz Ait Kaki
Department of Electrical Engineering
University of Larbi Ben M'hidi
Oum El Bouaghi, Algeria
aitkakiabdelaziz1966@gmail.com, ait.kaki.abdelaziz@univ-oeb.dz

***Abstract*—Abstract—In this paper, the trajectory tracking control of an actuated pendulum with friction using LQ-based computed-torque controller is studied. The control scheme consists of feedback linearization loop to cancel nonlinear dynamics and LQ as outer-loop controller. The dynamic model is developed using Euler-Lagrange formulation and the stability behavior is analyzed for both open and closed-loop system. Simulation result show that LQ-based computed-torque controller is effective in terms of computing optimal feedback gains that minimize the position and velocity tracking errors.**

***Index Terms*—optimal control; linear quadratic regulator; computed-torque; stability; pendulum.**

I. Introduction

Robot manipulators are considered one of the most essential elements for industrial automation and manufacturing nowadays, where robots are required to perform various tasks such as welding, painting, packing, assembly applications and so on. Generally, those tasks require following a desired trajectory by robots with high precision and repeatability. However, tracking problems can be challenging, since robot manipulators consists of hard and coupled nonlinearities, and subjected to nonlinear dynamics [2] [6]. As a result it is difficult to design a robust controller that is capable of minimizing trajectory tracking errors and maintaining the energy cost as low as possible. [1] [3]

A common approach to deal with robot trajectory tracking problem is computed-torque control, where the exact dynamics can be used to cancel nonlinearities by transforming the nonlinear system to equivalent linear one. Then, linear control techniques can be implemented as outer-loop controllers such as Proportional-Integral-Derivative (PID) and linear Quadratic Regulators (LQR) [2] [7].

PID controller is a commonly used control feedback scheme for industrial applications, due to its simplicity and efficiency of dealing with vast real world control problems. PID controller involves three different parameters, namely, the proportional, integral and derivative gains, which must be tunned to meet the required performance. However, for some high demanding application, it's difficult to select the optimal PID gains that satisfy critical performance.In order to overcome this kind of problems, optimal controllers such as Linear-Quadratic Regulators can be implemented to achieve the best possible performance with respect to the given criteria. [4] [5] [8]

This paper is organized as follows. In section two, the dynamic equations of motion are developed for an actuated pendulum with friction system using Euler-Lagrange formulation, along with stability behavior analysis. In section Three, trajectory tracking problem is formulated and LQ Computed-Torque controller is developed for the given system. the simulation results of the proposed controller are presented in section four,. Finally, conclusions are given in the last section.

II. Mathematical Modeling

A. Dynamics

Consider an actuated pendulum with friction as shown in Fig. 1. The system consists of point-mass m, attached a rigid link of length L (assumed to be of negligible mass), which pivots about the origin $(0, 0)$ by an angle θ, under the effect of gravitational force mg, input torque τ, and viscous friction of a coefficient $b > 0$.

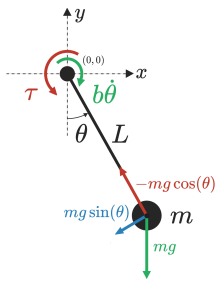

Fig. 1. Actuated pendulum with friction.

Position vector of the point-mass can be obtained as

$$\begin{bmatrix} x \\ y \end{bmatrix} = \begin{bmatrix} L\sin(\theta) \\ -L\cos(\theta) \end{bmatrix} \tag{1}$$

which can be differentiated with respect to time, and having velocity vector as

$$\begin{bmatrix} \dot{x} \\ \dot{y} \end{bmatrix} = \begin{bmatrix} L\cos(\theta) \\ L\sin(\theta) \end{bmatrix} \dot{\theta} \tag{2}$$

The Lagrangian $\mathcal{L}$ is defined to be the difference between the kinetic and potential energy $\mathcal{K}$ and $\mathcal{P}$, respectively, where

$$\mathcal{K} = \frac{1}{2}m(\dot{x}^2 + \dot{y}^2) = \frac{1}{2}mL^2\dot{\theta}^2 \tag{3}$$

$$\mathcal{P} = mg(L - y) = mgL\left[1 - \cos(\theta)\right] \tag{4}$$

Using the Lagrange-Eular formulation, the equation of motion can be written as

$$\begin{aligned} \tau &= \frac{d}{dt}\left(\frac{d\mathcal{L}}{d\dot{\theta}}\right) - \frac{d\mathcal{L}}{d\theta} + \tau_f \\ &= mL^2\ddot{\theta} + b\dot{\theta} + mgL\sin(\theta) \end{aligned} \tag{5}$$

or in state-space form as

$$\begin{aligned} \dot{x} &= f(x) + g(x)u \\ y &= h(x) = x \end{aligned} \tag{6}$$

where

$$\begin{aligned} &x = \begin{bmatrix} \theta & \dot{\theta} \end{bmatrix}^T, u = \tau, \\ &f(x) = \begin{bmatrix} f_1(x) \\ f_2(x) \end{bmatrix} = \begin{bmatrix} \dot{\theta} \\ -\frac{g}{L}\sin(\theta) - \frac{b}{mL^2}\dot{\theta} \end{bmatrix}, \\ &g(x) = \begin{bmatrix} g_1(x) \\ g_2(x) \end{bmatrix} = \begin{bmatrix} 0 \\ \frac{1}{mL^2} \end{bmatrix}. \end{aligned} \tag{7}$$

B. Stability analysis

To conclude the stability behavior of the system, we first find a set of states $\bar{x}$ (equilibrium points), that satisfy $\dot{x} = 0$ in the absence of an input (i.e. $u = 0$). Then, we linearize the system at $\bar{x}$, by deriving the Jacobian matrix from the dynamics and substituting x with $\bar{x}$. The equilibrium points of the system are easily seen to be

$$\bar{x} = (k\pi, 0), k \in \mathbb{Z} \tag{8}$$

and the Jacobian matrix can be obtained as

$$J = \begin{bmatrix} \frac{df_1}{dx_1} & \frac{df_1}{dx_2} \\ \frac{df_2}{dx_1} & \frac{df_2}{dx_2} \end{bmatrix} = \begin{bmatrix} 0 & 1 \\ -\frac{g}{L}\cos(\theta) & -\frac{b}{mL^2} \end{bmatrix} \tag{9}$$

Thus, the linearized model of the system at equilibrium points becomes

$$A = \begin{bmatrix} 0 & 1 \\ (-1)^{k+1}\frac{g}{L} & -\frac{b}{mL^2} \end{bmatrix} = \begin{bmatrix} 0 & 1 \\ -D & T \end{bmatrix} \tag{10}$$

where T and D represent the trace and determinant of the matrix A, respectively, which yields eigenvalues of the form

$$\lambda_{1,2} = \frac{T}{2} \pm \sqrt{\frac{T^2}{4} - D} \tag{11}$$

The system's stability behavior can be summarized as

- If $D < 0$, the eigenvalues are real and of opposite sign, and the phase portrait is a saddle (which is always unstable)
- If $0 < D < \frac{T^2}{4}$, the eigenvalues are real, distinct, and of the same sign, and the phase portrait is a node, stable if $T < 0$, unstable if $T > 0$
- If $0 < \frac{T^2}{4} < D$, the eigenvalues are neither real nor purely imaginary, and the phase portrait is a spiral, stable if $T < 0$, unstable if $T > 0$

The phase portrait of the system is shown in Fig. 2, assuming that $m = 0.1(kg)$, $L = 0.15(m)$, $g = 9.81(\frac{m}{s^2})$, and $b = 5 \times 10^{-3}(\frac{N.m.s}{rad})$.

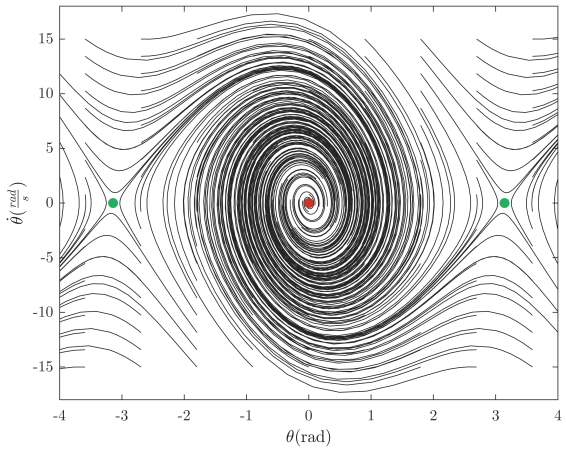

Fig. 2. Phase portrait of an actuated pendulum with friction.

III. Tracking Control Problem

The tracking control problem can be stated as follow: let θ_d, $\dot{\theta}_d$ and $\ddot{\theta}_d$ be a desired trajectory that the pendulum is required to follow. Compute an input u, so that the tracking errors $e = \theta_d - \theta$, $\dot{e} = \dot{\theta}_d - \dot{\theta}$ and $\ddot{e} = \ddot{\theta}_d - \ddot{\theta}$ converge to zero, with all involved signals remain bounded.

A. Computed-Torque Control

A common approach to deal with tracking control problems of robotic systems is computed-torque control (CTC), or inverse dynamics control as referred to in the robotics literature. This approach is based on feedback linearization, which involves using the exact inverse dynamics model to transform the nonlinear system to equivalent linear system, so that linear control techniques can be implemented. Computed-torque control input is straightforward driven from (5) as

$$\begin{aligned} u &= \alpha(x) + \beta(x)v \\ &= mgL\sin(\theta) + b\dot{\theta} + mL^2v \end{aligned} \tag{12}$$

where v is outer-loop control input. Substituting (12) in (6), yields equivalent open-loop linear system as

$$\begin{aligned} \dot{x} &= Ax + Bv \\ &= \begin{bmatrix} 0 & 1 \\ 0 & 0 \end{bmatrix}\begin{bmatrix} \theta \\ \dot{\theta} \end{bmatrix} + \begin{bmatrix} 0 \\ 1 \end{bmatrix} v \end{aligned} \tag{13}$$

We can easily verify that it has eigenvalues $\lambda_{1,2} = 0$, due to the pair of integral action (Brunovsky canonical form). Therefore, it can be stabilized by state feedback control law $v = -Kx$, on condition that the system is controllable from input v. The controlability matrix can be expressed as

$$\begin{bmatrix} B & AB \end{bmatrix} = \begin{bmatrix} 0 & 1 \\ 1 & 0 \end{bmatrix} \tag{14}$$

Having a full rank of $n = 2$, makes the system controllable from input v.

B. LQ Computed-Torque Control

Linear–quadratic regulator (LQR) is an optimal control technique, which provides high performance state-feedback gains in terms of stabilizing the closed-loop system at the origin or an operating point with low cost effort. Given the system in (13), the quadratic performance index for LQR is expressed as

$$J = \frac{1}{2}\int_0^\infty \left(Q_1\theta^2 + Q_2\dot{\theta}^2 + Rv^2\right) dt \tag{15}$$

where $Q_1, Q_2 \geq 0$ and $R > 0$ are parameters to be selected for meeting the required performance. Due to the form of A and B matrices, the solution of the Riccati equation is straightforward, which yields the optimal stabilizing feedback gains as

$$K_1 = \sqrt{\frac{Q_1}{R}}, K_2 = \sqrt{2K_1 + \frac{Q_2}{R}} \tag{16}$$

LQ can be implemented as outer-loop control in computer-torque scheme for the trajectory tracking problem. By selecting a control input

$$v = \ddot{\theta}_d + K_1 e + K_2 \dot{e} \tag{17}$$

and substituting in (13), the closed-loop error dynamics system can be written as

$$\begin{bmatrix} \dot{e} \\ \ddot{e} \end{bmatrix} = \begin{bmatrix} 0 & 1 \\ -K_1 & -K_2 \end{bmatrix} \begin{bmatrix} e \\ \dot{e} \end{bmatrix}. \tag{18}$$

with eigenvalues of the form

$$\lambda_{1,2} = -\frac{K_2}{2} \pm \sqrt{\frac{K_2^2}{4} - K_1} \tag{19}$$

Therefore, as long as K_1 and K_2 are strictly positive (implying that $Q_1 > 0$), the close-loop error dynamics system is asymptotically stable.

IV. Simulation and Results

This section demonstrates and discuss the performance of LQ-based computer-torque controller for the trajectory tracking problem. Physical parameters of the studied system are assumed to be $m = 0.1(kg)$, $L = 0.15(m)$, $g = 9.81(\frac{m}{s^2})$, and $b = 5 \times 10^{-3}(\frac{N.m.s}{rad})$. To test the effectiveness of the proposed controller, we have chosen two sets of parameter as $Q_1 = Q_2 = 20, R = 1$ and $Q_1 = Q_2 = 5, R = 10$, which yield equivalent feedback gains as $K = [4.72, 5.38]$ and $K = [0.71, 1.38]$, respectively. Finally, for the purpose of this work, the desired trajectory is chosen as

$$\theta_d = \frac{1}{10}\cos\left(\frac{\pi}{2}t\right), \dot{\theta}_d = -\frac{\pi}{20}\sin\left(\frac{\pi}{2}t\right), \ddot{\theta}_d = -\frac{\pi^2}{4}\theta_d.$$

The control scheme of LQ-based computed-torque is shown in Fig. 3. Using dedicated simulation software, yields the results shown in Fig. 4 and 5, which represent position and velocity trajectory tracking performance for different controller parameters, respectively.

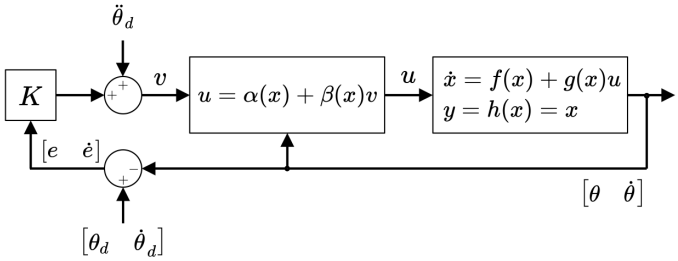

Fig. 3. LQ-based computed-torque control scheme.

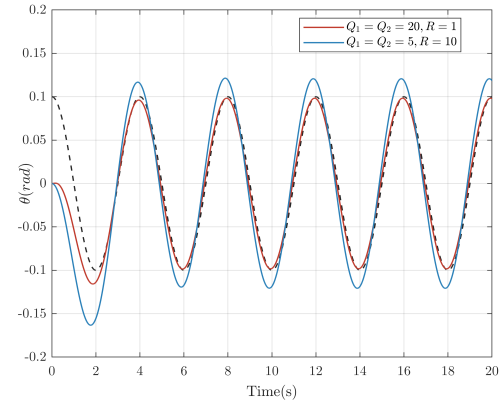

Fig. 4. Position tracking.

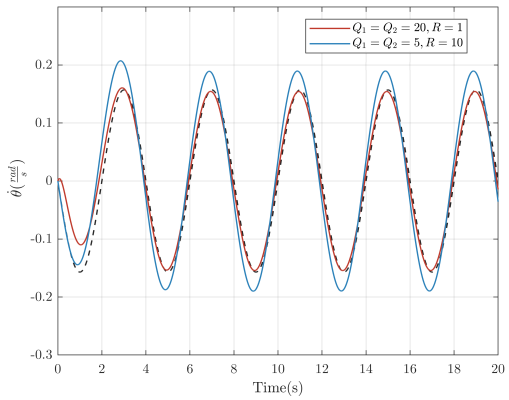

Fig. 5. Velocity tracking.

For $Q_1 = Q_2 = 20$ and $R = 1$, the closed-loop eigenvalues are real, distinct, and negative, which result in a relatively small steady-state tracking error with no overshooting for both the position and velocity. However, in case of $Q_1 = Q_2 = 5$ and $R = 10$, the closed-loop eigenvalues are complex with negative real parts, which result a small overshooting in both the position and velocity tracking performance.

V. Conclusions

In this paper, LQ-based computed-torque controller was presented for trajectory problem of an actuated pendulum with friction system. Simulation results show that the proposed controller is efficient in terms of minimizing tracking errors with considerations of different parameters. As future work for this control technique, LQ parameters will be tuned using deep reinforcement learning for computing optimal feedback gains that minimize both tracking errors and the applied torque.

References

[1] Khalil, W. and Dombre, E., 2004. Modeling, identification and control of robots. Butterworth-Heinemann.
[2] Lewis, F.L., Dawson, D.M. and Abdallah, C.T., 2003. Robot manipulator control: theory and practice. CRC Press
[3] Lynch, K.M. and Park, F.C., 2017. Modern Robotics Mechanics, Planning, and Control.
[4] Spong, M.W., Hutchinson, S. and Vidyasagar, M., 2020. Robot modeling and control. John Wiley & Sons.
[5] Middletone, R.H. and Goodwin, G.C., 1986, December. Adaptive computed torque control for rigid link manipulators. In 1986 25th IEEE Conference on Decision and Control (pp. 68-73). IEEE.
[6] Asada, H. and Slotine, J.J., 1986. Robot analysis and control. John Wiley & Sons.
[7] Willems, J.C., 1982. Linear systems: Thomas Kailath.
[8] Rastogi, E. and Prasad, L.B., 2015, December. Comparative performance analysis of PD/PID computed torque control, filtered error approximation based control and NN control for a robot manipulator. In 2015 IEEE UP Section Conference on Electrical Computer and Electronics (UPCON) (pp. 1-6). IEEE.

Torque Ripple Reduction of Induction Machine A Comparison between Two Approaches DTC-SVM

Lakhdar Djaghdali

Department of electrical Engineering, University of Msila, Algeria
djaghdali.lakhdar@univ-msila.dz

Abstract – The paper deals with a comparison between two DTC-SVM approaches: DSVM-DTC with a hysteresis controllers and MPDTC with a predictive controller. In DTC-SVM, the switching frequency is limited by the sampling frequency; its theoretical maximum value is half the sampling frequency. However, in reality the switching frequency is lower than this value, and thus, high flux and torque ripples occur compared with modulator-based control methods. In order to overcome this, an optimization problem is formulated and solved in real time. Thereby, apart from the regulation of the torque and the flux magnitude to their references, an additional control objective should be met: the minimization of the torque and flux ripple. To do so, the time point at which the switches of the inverter should change state is calculated. Following the formulation of both approaches, their implementation in the Matlab-Simulink environment has been treated. The transient behavior as well as the steady state features of the induction motor drive under both DTC-SVM approaches are compared and commented. The comparison is based on several criteria including: static and dynamic performance, structure and implementation complexity, and especially decoupling, torque and flux ripple. It has been found that the second approach MPDTC yields high dynamic performances in the whole speed range. These performances are characterized by a low torque ripple with a high capability to eliminate the demagnetization problem which penalizes the flux regulation at low speeds in the first DTC-SVM approach. However, the second DTC-SVM approach with a predictor controller requires much more CPU time than the first one.

Keywords - Induction motor, direct torque control, Predictive direct torque control, space vector modulation (SVM).

1. INTRODUCTION

Since direct torque control (DTC) was introduced in the mid-1980s by Takahashi and by Depenbrock, it has been widely used for induction machine drives [1], [2]. Besides its simplicity, DTC is able to produce fast torque and flux control. However, it is well known that DTC presents some disadvantages, such as the variable commutation frequency behavior of the inverter [3], and notable torque and flux ripples.

In recent years, many efforts have been made to improve the performance of DTC, especially by reducing the torque ripples and stator flux, and by fixing the inverter commutation frequency. Several studies investigated the possibility to associate space-vector modulation (SVM) techniques with DTC strategies in order to control the switching frequency [4], [5]. To overcome the aforementioned disadvantages for an IM drive, various methods have been presented in the literature. In [6] and [7], the matrix converter provides more voltage vectors modulation and hence, low torque and stator flux ripples can be achieved. However, in order to minimize these ripples and keep almost constant switching frequency, it is necessary to have an increasing number of power switches which lead to a reduced overall efficiency and a high cost. Second, the model predictive control (MPC) approach provides a possibility to determine the voltage vectors which result in the lowest torque and stator flux ripples [8]. However, this approach has the disadvantage that the control law complexity grows exponentially with the length of the prediction horizon. Third, the modified DTC scheme with a reference flux vector calculator (RFVC) for an IM drive is presented in [9], which achieves a good torque response regardless of the operating torque. However, the PWM switching frequency is relatively high compared to the other DTC approaches. Another modified method incorporates a space vector modulation (SVM) into the DTC structure. This DTC-SVM can regulate the torque and stator flux more accurately and moderately with fixed switching frequency. A variety of methods to calculate the voltage space vector reference have been presented in the literature [10]–[13]. As per author in [10], a discrete SVM technique with predefined switching instants and extended switching tables is described for the DTC strategy. Even if this scheme can operate with fixed switching frequency, it is only suitable for induction motor (IM) drives. In [11], the DTC-SVM including a proportional integral (PI) controller is presented to fulfill the reduced torque and flux ripple requirements. However, the torque and stator flux responses during low speed operations are not shown in detail. Also, the sliding mode control (SMC) method is suggested for the DTC-SVM of IM drives in [12]. Although this approach improves the static, dynamic, and sinusoidal tracking performances, and reduces the chattering of the sliding surface, only simulation results are provided as means of verification. In [14], the fuzzy control (FC) method for the DTC-SVM is presented to reduce the torque ripple. In this method, fast torque response and minimum torque ripples are the main advantages. However, many trials are required to properly select the membership function which guarantees the system stability. As mentioned above, each discussed method has its own benefits and limitations. In addition, the high nonlinearities of an IM have made it difficult to achieve the fast and stable control performance.

Recently, the nonlinear control technique based on the feedback linearization (FL) theory has been used for various applications in the area of power electronics and drives [15]. The main idea of the feedback linearization control (FLC) approach is to algebraically transform nonlinear system

dynamics into linear one so that linear control techniques can be applied. Furthermore, the control laws for nonlinear systems can be systematically established based on the FLC technique. These laws can be further verified in advance to accommodate the actual system model characteristics in real application. In [16] the adaptive neural fuzzy inference system method is based on fuzzy logic and artificial neural networks for decoupled stator flux and torque control. The stability will be affected by parameter variation and the system model must be known, as the system's dynamic performance and stability will be significantly affected by parameter variations.

Within these approaches, the paper devotes to a comparative study between the performances of two DTC-SVM: The comparison is based on several criteria including: static and dynamic performance, structure and implementation complexity, decoupling, torque and stator flux ripple.

This paper is organized in seven sections. The model of the induction machine is presented in the next section. The control method by DSVM – DTC and MPDTC will be discussed in section three and four. In the fifth and sixth sections, we present the technique of Space Vector Pulse Width Modulation (SVM) and we compare the simulation results. Finally, a general conclusion summarizes this work. The simulation results are obtained by using Matlab/Simulink.

2. MODEL OF THE INDUCTION MACHINE

Among the various types of models used to represent the induction machine, there is one that uses each of the stator currents, stator flux, and speed as state variables, voltages (V_{sd}, V_{sq}) as control variables. This model is presented in reference (d, q), related to the rotating field. This model is expressed by the following system of equations [17]:

$$\begin{cases} V_{ds} = R_s.I_{ds} + \frac{d\Phi_{ds}}{dt} - \omega_s.\Phi_{qs} \\ V_{qs} = R_s.I_{qs} + \frac{d\Phi_{qs}}{dt} + \omega_s.\Phi_{ds} \\ V_{dr} = 0 = R_r.I_{dr} + \frac{d\Phi_{dr}}{dt} - (\omega_s - p\Omega).\Phi_{qr} \\ V_{qr} = 0 = R_r.I_{qr} + \frac{d\Phi_{qr}}{dt} + (\omega_s - p\Omega).\Phi_{dr} \end{cases} \quad (1)$$

In addition, the components of the stator and rotor flux are expressed by:

$$\begin{cases} \Phi_{ds} = L_s.I_{ds} + L_m.I_{dr} \\ \Phi_{qs} = L_s.I_{qs} + L_m.I_{qr} \\ \Phi_{dr} = L_r.I_{dr} + L_m.I_{ds} \\ \Phi_{qr} = L_r.I_{qr} + L_m.I_{qs} \end{cases} \quad (2)$$

Moreover, the mechanical equation of the machine is given by :

$$j\frac{d\Omega}{dt} + f\Omega = T_e - T_r \quad (3)$$

The electromagnetic torque equation can be expressed in terms of stator currents and stator flux as follows:

$$T_e = P.(\Phi_{ds}.I_{qs} - \Phi_{qs}.I_{ds}) \quad (4)$$

3. DISCRETE SPACE VECTOR MODULATION FOR DIRECT TORQUE CONTROL DSVM-DTC

The command DSVM-DTC analyzes the problem of chattering introduced at the torque and flux in the classical DTC [18].The name DSVM stems from the fact that each sample period is divided into three equal time intervals so as to produce the technical Vector PWM. Thus, the voltage vectors number increase in an improvement of the trajectory of the flux vector and consequently a reduction of the corrugations. The control system uses predefined tables for each speed level complicating this approach [19].

3.1 Principle of command DSVM – DTC

3.1.1 Speed of the induced voltage

In this approach, there is an asymmetry in the behavior of the torque because of the induced voltage created by the speed under constant flux [19]. The DSVM calculates and uses this voltage to select a voltage vector. The range acceleration from Zero where the induced voltage is equal to the applied voltage vector is divided into three regions; low, medium and high.

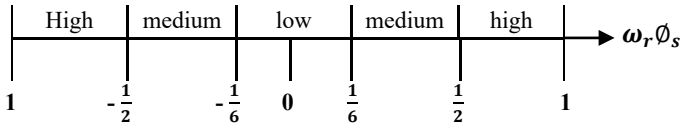

Figure 1. Voltage speed region [p.u]

The induced voltage is:

$\omega_r \begin{bmatrix} \emptyset_\alpha \\ \emptyset_\beta \end{bmatrix}$ its only value is the calculated voltage is used

$$\bar{V}_s = \omega_r \bar{\emptyset}_s \quad (5)$$

It is then compared to the regions.

3.1.2 Sector used in DSVM_DTC

The command DSVM_DTC uses twelve sectors instead of six; twelve sectors will be used for the high speed range. While the low and medium speed range only six sectors are used.

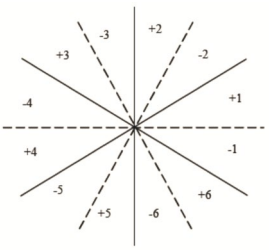

Figure 2. Sector of the ***DSVM- DTC***

3.1.3 Comparator hysteresis torque

The DSVM_DTC command can produce several voltage vectors if they are applied properly there will be less ripple in the torque and flux. To achieve this, one uses a hysteresis comparator to 5 levels instead of two for the torque.

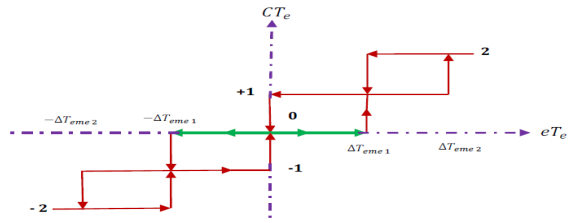

Figure 3. Torque hysteresis block

If the error of the torque is so small hysteresis is in state 0. In this case, a voltage vector is selected to maintain the torque at the current level. If hysteresis is capable +1 or - 1, the chosen vector must be means to hoist the couple in the small area. When hysteresis is capable +2 or - 2, the vector chosen to offset the error as soon as possible torque must be large enough, that is to say the same vector used in the conventional DTC.

3.1.4 Switching table

In this type of control the switching table has four input variables are the state of flux hysteresis, torque, sector number and the induced voltage by the speed (Figure 4). Since the command selects voltage vectors according to the induced voltage therefore each speed region using a corresponding switching table.

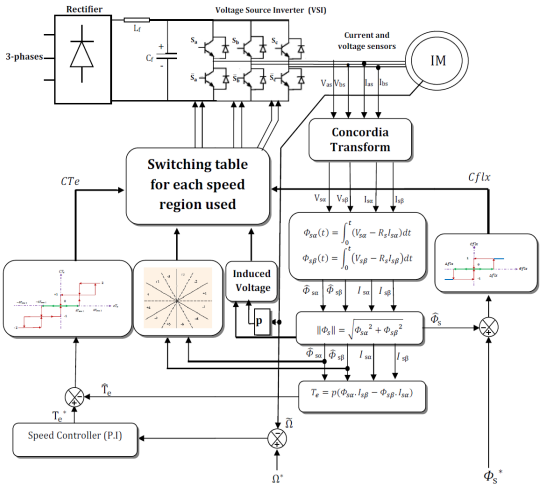

Figure 4. Block diagram of the general structure of the control **DSVM-DTC**

When the command runs in the high speed region two switching tables are used for each sector because of an asymmetry introduced by the induced voltage. Switching of the tables used in this case are also asymmetrical. For low and medium speed control one table is used for each sector. Thus different switching tables can be used depending on the direction of rotation.

3.1.5 Voltage inverter

In control DSVM_DTC each sample period is divided into three equal time intervals. In each interval is applied is an active vector is a zero vector. The inverter has to work three times the sampling frequency.
For example, U_{223} vector is synthesized by the application of U_{222} in the first two intervals, then U_{333}.

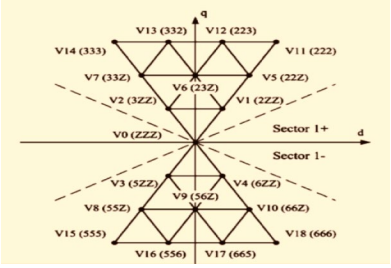

Figure 5. Vectors DSVM in sector (+ 1, -1)

3.1.6 Selecting tensions vectors

The induced voltage depends on the mechanical speed, when it increases; the voltage Vs applied to the machine also increases. The voltage vector $\overline{V}_s$ causes the flux $\overline{\emptyset}_s$ with an offset of $\frac{\pi}{2}$ so it is keyed on the axis $\beta^{\emptyset_s}$ the resulting vector that affects the couple is the component $V_\beta^{\emptyset_s}$ of the voltage vector delivered by the voltage inverter least $\overline{V}_s$ Therefore, the voltage vector V_s selection criterion is chosen as a reference. If $V_\beta^{\emptyset_s} \approx \overline{V}_s$ torque is maintained at its current state if $V_\beta^{\emptyset_s} > \overline{V}_s$ torque increases, and if $V_\beta^{\emptyset_s} < \overline{V}_s$ torque decreases.

a. Region at low speed

The voltage vector $\overline{V}_s$ is close to zero when it is in low-speed region. The switching vectors are chosen symmetrically around zero according to the low speed table. This switching table depends on the direction of motor rotation. If the estimated torque is close to the reference value, the hysteresis state of the torque is zero and therefore the voltage vector selected is zero. If the hysteresis torque state is +1 or -1, a moderate increase or decrease, respectively, is sought. The selection of the voltage vector is made between U_{200}, U_{300}, U_{500} and U_{600}. To increase the torque U_{200} and U_{600} stream must be chosen. While U_{300} and U_{500} are used to decrease the flux. When the gap between the reference torque and estimated is great that is to say CTe = +2 or -2, the command DSVM_DTC imposes an identical choice than the conventional DTC. Thus, U_{222} vectors U_{333}, U_{555} and U_{666} are selected to make up the gap as quickly as possible.

CTe / Cflx	-2	-1	0	1	2
-1	U_{555}	U_{500}	U_{000}	U_{300}	U_{333}
1	U_{666}	U_{600}	U_{000}	U_{200}	U_{222}

Table 1. Switching table for low positive speed, sector (+1,-1).

b. Region at medium speed

In the region of medium speed $V_n / 6 < |V_s| < V_n / 2$ the induced voltage begins to introduce an asymmetry in the behavior of the torque. For positive V_s and CTe = 0, the control DSVM_DTC considers the choice of U_{200} and U_{300},

since these vectors make $V_{\beta}^{\emptyset s}$ approximately equal to V_s while maintaining torque at its current level. The choice of the U_{200} imposes an increased flux while U_{300} allows a reduction of the flux. For CTe = -1 a slight decrease in torque, the voltage vector is selected U_{000}, because it is the only vector at this level can be chosen for the two cases of the gap of flux. For CTe = +1, U_{220} is selected when the flux should be increased and U_{330} when one wants a decrease. When CTe = 2 or - 2, the control DSVM_DTC exploits the principle of the conventional DTC control.

CTe / Cflx	-2	-1	0	1	2
-1	U_{555}	U_{000}	U_{300}	U_{330}	U_{333}
1	U_{666}	U_{000}	U_{200}	U_{220}	U_{222}

Table 2. Switching table for positive average speed, sector (+1,-1).

c. *Region at High speed*

In the high speed region,$|V_s| > V_n / 2$, each sector is divided into two and all available vectors are used. Thus, the induced voltage is reduced considerably. Suppose $\emptyset_s$ is in the sector -1 and if the torque is to be kept at zero, the U_{220} and U_{230} voltage vectors are selected based on the reference flux. To reduce torque (CTe = -1), the choice of the closest and lower tensions vectors $V_{\beta}^{\emptyset s}$ are U_{200} or U_{300}. To increase torque (CTe = 1), there are two possibilities, either the increase in the flux with the selection of tensions vectors U_{222} and U_{223}, or decreasing the flux with the choice of tension vectors U_{332} and U_{333}. When switching the error of torque from zero to one, we notice that there are several switches of the voltage vector in the switching tables thus reducing ripples in the stream (U_{230}, U_{220}, U_{332}, U_{222} for the sector-1). In the case where the hysteresis comparator of the torque CTe = + 2 or -2, the selected voltage vectors are maximum and identical to those of the medium and low speed.

CTe / Cflx	-2	-1	0	1	2
-1	U_{555}	U_{300}	U_{230}	U_{332}	U_{333}
1	U_{666}	U_{200}	U_{220}	U_{222}	U_{222}

Table 3. Switching table for high positive speed, sector -1.

CTe / Cflx	-2	-1	0	1	2
-1	U_{555}	U_{300}	U_{330}	U_{333}	U_{333}
1	U_{666}	U_{200}	U_{230}	U_{223}	U_{222}

Table 4. Switching table for high positive speed, sector +1.

4. PREDICTIVE DIRECT TORQUE CONTROL (MPDTC)

The Predictive control is a technique of advanced control automation. It aims to control complex industrial systems [20]. The basic principle of predictive control is taken into account, at the current time, the future behavior, through explicit use of a numerical model of the system in order to predict the output in the future, on a finite horizon [21].One of the advantages of predictive methods lies in the fact that for a pre-calculated set on a horizon, it is possible to exploit the information of predefined trajectories located in the future, given that the aim is to match the output of system with this set on a finite horizon [21] (figure.6).

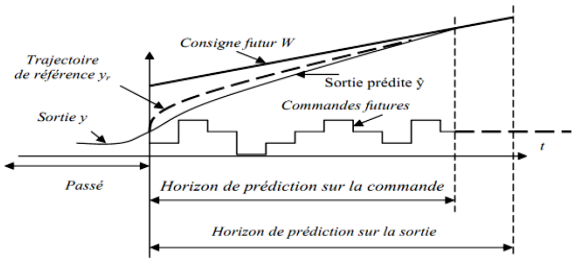

Figure.6 Time evolution of the finite horizon prediction

4.1 Formulation of The Model

All algorithms predictive control differs from each other by the model used to represent the process and the cost function to be minimized [23]. We will give for our formulation, the technique of the linearization input-output of the induction machine, in order to give a linearized model; module of the stator flux and the torque are uncoupled. The interest of such approach is to linearize the model of the machine and to obtain a homogeneous behavior whatever the point of operation.

We recall the system of the equations of the induction machine in the reference (α, β) which is given by:

$$\begin{cases} \frac{dI_{s\alpha}}{dt} = -\left(\frac{R_s}{\sigma L_s} + \frac{R_r}{\sigma L_r}\right) I_{s\alpha} - \omega_r I_{s\beta} + \frac{R_r}{\sigma L_r L_s}\phi_{s\alpha} + \frac{\omega_r}{\sigma L_s}\phi_{s\beta} + \frac{1}{\sigma L_s}V_{s\alpha} \\ \frac{dI_{s\beta}}{dt} = -\left(\frac{R_s}{\sigma L_s} + \frac{R_r}{\sigma L_r}\right) I_{s\beta} + \omega_r I_{s\alpha} + \frac{R_r}{\sigma L_r L_s}\phi_{s\beta} - \frac{\omega_r}{\sigma L_s}\phi_{s\alpha} + \frac{1}{\sigma L_s}V_{s\beta} \\ \frac{d\phi_{s\alpha}}{dt} = V_{s\alpha} - R_s I_{s\alpha} \\ \frac{d\phi_{s\beta}}{dt} = V_{s\beta} - R_s I_{s\beta} \end{cases}$$

… (6)

The generated torque can be expressed in terms of stator currents and stator flux as follows:

$$T_e = p\left(\phi_{s\alpha} I_{s\beta} - \phi_{s\beta} I_{s\alpha}\right) \quad (7)$$

The system of equations receives in the form suggested for the application of the linearization within the meaning of the input-output as follows:

$$\begin{cases} \dot{x} = f(x) + g_1(x)V_{s\alpha} + g_2(x)V_{s\beta} \\ y = h(x) \end{cases} \quad (8)$$

With:

$$f(x) = \begin{bmatrix} f_1(x) \\ f_2(x) \\ f_3(x) \\ f_4(x) \end{bmatrix} =$$

$$\begin{bmatrix} -\left(\frac{R_s}{\sigma L_s}+\frac{R_r}{\sigma L_r}\right)I_{s\alpha} - \omega_r I_{s\beta} + \frac{R_r}{\sigma L_r L_S}\phi_{s\alpha} + \frac{\omega_r}{\sigma L_S}\phi_{s\beta} \\ -\left(\frac{R_s}{\sigma L_s}+\frac{R_r}{\sigma L_r}\right)I_{s\beta} + \omega_r I_{s\alpha} + \frac{R_r}{\sigma L_r L_S}\phi_{s\beta} - \frac{\omega_r}{\sigma L_S}\phi_{s\alpha} \\ -R_s I_{s\alpha} \\ -R_s I_{s\beta} \end{bmatrix} \quad (9)$$

Where the vector of states x and the commands u are:

$$x = \left[I_{s\alpha}, I_{s\beta}, \phi_{s\alpha}, \phi_{s\beta}\right]^t, \quad u = [V_{s\alpha}, V_{s\beta}]^t$$

And: $g_1(x) = \left[\frac{1}{\sigma L_s}, 0, 1, 0\right]^t$, $g_2(x) = \left[0, \frac{1}{\sigma L_s}, 0, 1\right]^t$

4.2.1 Control Flux-Torque:

Our concern is to minimize the pulsations of the torque and the flux of the induction machine. For that, we chose the torque and the module of stator flux like variables to be controlled; thus the vector of output is given by the equation according to:

$$y = \begin{bmatrix} h_1 \\ h_2 \end{bmatrix} = \begin{bmatrix} T_e \\ |\emptyset_s|^2 \end{bmatrix} = \begin{bmatrix} p\left(\phi_{s\alpha} I_{s\beta} - \phi_{s\beta} I_{s\alpha}\right) \\ \phi_{s\alpha}^2 + \phi_{s\beta}^2 \end{bmatrix} \quad (10)$$

4.2.2 Input-Output Linearization:

The method of the input-output linearization is developed starting from the theories of the differential geometry [24]. It consists of using the derivative of Dregs to express the model of the machine in relation to input-output. To obtain the non-linear law of control, let us derive as much from time than it is necessary in order to reveal the entry u. The derivatives of the two outputs are given by:

$$\begin{aligned} \dot{y}_1 &= L_f h_1(x) + L_{g1} h_1(x) V_{s\alpha} + L_{g2} h_1(x) V_{s\beta} \\ &= \sum_{i=1}^{4} \frac{\partial h_1}{\partial x_i} f_i(x) + \sum_{i=1}^{4} \frac{\partial h_1}{\partial x_i} g_1(x) V_{s\alpha} + \\ &\quad \sum_{i=1}^{4} \frac{\partial h_1}{\partial x_i} g_2(x) V_{s\beta} \end{aligned} \quad (11)$$

With:

$$\begin{aligned} \boldsymbol{L_f h_1} &= -p\phi_{s\beta}\left[-\left(\frac{R_s}{\sigma L_s}+\frac{R_r}{\sigma L_r}\right)I_{s\alpha} - \omega_r I_{s\beta} + \frac{R_r}{\sigma L_r L_S}\phi_{s\alpha} + \frac{\omega_r}{\sigma L_S}\phi_{s\beta}\right] \\ &\quad + p\phi_{s\alpha}\left[-\left(\frac{R_s}{\sigma L_s}+\frac{R_r}{\sigma L_r}\right)I_{s\beta} + \omega_r I_{s\alpha} + \frac{R_r}{\sigma L_r L_S}\phi_{s\beta} - \frac{\omega_r}{\sigma L_S}\phi_{s\alpha}\right] \\ \boldsymbol{L_{g1} h_1} &= p\left(I_{s\beta} - \frac{1}{\sigma L_s}\phi_{s\beta}\right) \\ \boldsymbol{L_{g2} h_1} &= p\left(\frac{1}{\sigma L_s}\phi_{s\alpha} - I_{s\alpha}\right) \end{aligned} \quad (12)$$

$$\begin{aligned} \dot{y}_2 &= L_f h_2(x) + L_{g1} h_2(x) V_{s\alpha} + L_{g2} h_2(x) V_{s\beta} \\ &= \sum_{i=1}^{4} \frac{\partial h_2}{\partial x_i} f_i(x) + \sum_{i=1}^{4} \frac{\partial h_2}{\partial x_i} g_1(x) V_{s\alpha} + \\ &\quad \sum_{i=1}^{4} \frac{\partial h_2}{\partial x_i} g_2(x) V_{s\beta} \end{aligned} \quad (13)$$

With:

$$\begin{cases} \boldsymbol{L_f h_2} = -2R_s(\phi_{s\alpha} I_{s\alpha} - \phi_{s\beta} I_{s\beta}) \\ \boldsymbol{L_{g1} h_2} = 2\phi_{s\alpha} \\ \boldsymbol{L_{g2} h_2} = 2\phi_{s\beta} \end{cases} \quad (14)$$

4.2.3 Linearization of the System:

The matrix defining the relation between the inputs of the system and its derived outputs is given by the expression:

$$\begin{bmatrix} \dot{y}_1 \\ \dot{y}_2 \end{bmatrix} = A(x) + D(x) \begin{bmatrix} V_{S\alpha} \\ V_{S\beta} \end{bmatrix} \quad (15)$$

With: $A(x) = \begin{bmatrix} L_f h_1 \\ L_f h_2 \end{bmatrix}$;

$$D(x) = \begin{bmatrix} L_{g1} h_1 & L_{g2} h_1 \\ L_{g1} h_2 & L_{g2} h_2 \end{bmatrix}$$

$$= \begin{bmatrix} p(I_{s\beta} - \frac{1}{\sigma L_s}\phi_{s\beta}) & p(\frac{1}{\sigma L_s}\phi_{s\alpha} - I_{s\alpha}) \\ 2\phi_{s\alpha} & 2\phi_{s\beta} \end{bmatrix}$$

$D(x)$: Is decoupling Matrix.

$$\begin{aligned} \text{Det}[D(x)] &= p\left(I_{s\beta} - \frac{1}{\sigma L_s}\phi_{s\beta}\right).2\phi_{s\beta} - \\ &\quad p\left(\frac{1}{\sigma L_s}\phi_{s\alpha} - I_{s\alpha}\right).2\phi_{s\alpha} \end{aligned} \quad (16)$$

After simplification, we get:

$$\begin{aligned} \det[D(x)] &= 2p\left[\frac{-1}{\sigma L_s}\left({\phi_{s\beta}}^2 + {\phi_{s\alpha}}^2\right) + I_{s\beta}\phi_{s\beta} + \right. \\ &\quad \left. I_{s\alpha}\phi_{s\alpha}\right] \neq \mathbf{0} \end{aligned} \quad (17)$$

The determinant of the matrix D(x)is different from zero; therefore D(x)is a reversible matrix.

$$D^{-1}(x) = \frac{1}{2p\left[\frac{-1}{\sigma L_s}\left({\phi_{s\beta}}^2 + {\phi_{s\alpha}}^2\right) + I_{s\beta}\phi_{s\beta} + I_{s\alpha}\phi_{s\alpha}\right]} \begin{bmatrix} 2\phi_{s\beta} & -p(\frac{1}{\sigma L_s}\phi_{s\alpha} - I_{s\alpha}) \\ -2\phi_{s\alpha} & p(I_{s\beta} - \frac{1}{\sigma L_s}\phi_{s\beta}) \end{bmatrix}$$

... (18)

The linearization following input-output which is introduced for the system illustrated by (l'eq-8) is given by:

$$\begin{bmatrix} V_{s\alpha} \\ V_{s\beta} \end{bmatrix} = D^{-1}(x)\left[-A(x) + \begin{bmatrix} V_1 \\ V_2 \end{bmatrix}\right] \quad (19)$$

$V = \begin{bmatrix} V_1 \\ V_2 \end{bmatrix}$: represent the new vector of input.

The application of the law linearizing (l'eq-19) on the system (l'eq-15) led to two linear and uncoupled mono variable system:

$$\begin{cases} V_1 = \dot{h_1}(x) \\ V_2 = \dot{h_2}(x) \end{cases} \quad (20)$$

To ensure perfect regulation and track the desired signals of the flux and torque toward their reference, V_1 and V_2 are chosen as follows:

$$\begin{cases} V_1 = \left|\dot{\emptyset}_s\right|_{ref}^2 + k_1\left(|\emptyset_s|_{ref}^2 - |\emptyset_s|^2\right) \\ V_2 = \dot{T}_{e\,ref} + k_2\left(T_{e\,ref} - T_e\right) \end{cases} \quad (21)$$

Here, the subscript 'ref' denotes the reference value and (k_1, k_2) are constant design parameters to be determined in order to make the decoupled system in (Eq. 15) stable. The behavior of the linearized model is imposed by the pole placement method. The coefficients selected, such as $s + k_1$ and $s + k_2$, are the Hurwitz polynomials [25].

4.3 Criterion of Optimization:

We must find the future control sequence to apply on the system to reach the desired set point by following the reference trajectory. To do this, we just minimize a cost function which differs according to the methods, but generally this function contains the squared errors between the reference trajectory and the predictions of the prediction horizon and the variation of the control [21] [22]. This cost function is given as follows:

$$J = \sum_{j=N_1}^{N_2} [w(t+j) - \hat{y}(t+j)]^2 + \lambda \sum_{j=1}^{N_u} \Delta u(t+j-1)^2$$

…(22)

With:

w (t + j): Set point applied at time (t + j).

$\hat{y}(t+j)$: Output predicted time (t + j). Δu (t + j-1): Increment of control at the moment (t + j-1).

N_1: Minimum prediction horizon on the output.

N_2: Maximum prediction horizon on the output, with $N_2 \geq N_1$.

N_u : Horizon prediction on the order.

λ: Weighting factor on the order.

T_s: The period of sampling.

The definition of the quadratic criterion showed that the user must set four parameters. The choice of parameters is difficult because there is no empirical relationship to relate these parameters to conventional measures automatically.

The model linearized and uncoupled from the induction machine, so that it is established inside the predictive control, which is shown by (Figure. 7).

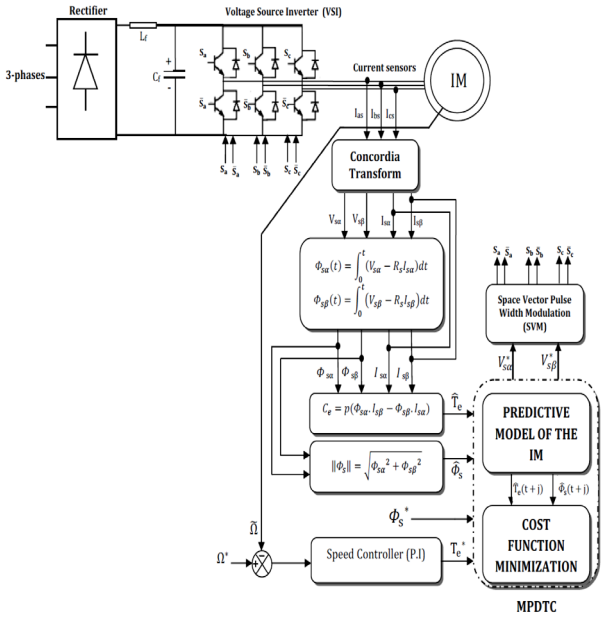

Figure 7. Diagram block of the predictive direct torque control

5. Space Vector Pulse Width Modulation

The SVM technique was first presented by a group of German researched in the second half of the 1980s [26]. Since then, a lot of work has been done on the theory and implementation of SVM techniques. SVM techniques have several advantages that are offering better DC bus utilization, lower torque ripple, lower Total Harmonic Distortion (THD) in the AC motor current, lower switching losses, and easier to implement in the digital systems. At each cycle period, a preview technique is used to obtain the voltage space vector required to exactly compensate the flux and torque errors. The torque ripple for this SVM-DTC is significantly improved and switching frequency is maintained constant. The voltage vectors, produced by a 3-phase PWM inverter, divide the space vector plane into six Sectors as shown in Figure (8.A).

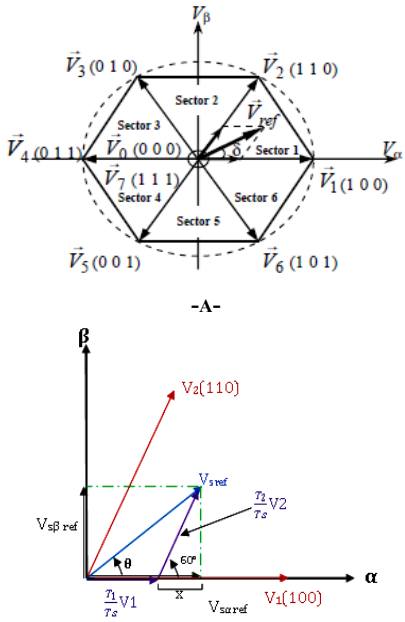

Figure 8. Switching States of SVM .Projection of the Reference Voltage Vector

SVM, based on the switching between two adjacent boundary active vectors and a zero vector during one switching period T_s, and for a given reference voltage vector in the first sector $(0 - \frac{\pi}{3})$ is shown in Figure (8.B). $\overline{V}_{s\,ref}$ is a synthesized voltage, space vector and its equation is given by:

$$\bar{V}_{s\,ref} T_s = \bar{V}_0 T_0 + \bar{V}_1 T_1 + \bar{V}_2 T_2 \quad (23)$$

$$T_s = T_0 + T_1 + T_2 \quad (24)$$

Where, T_0 , T_1 and T_2 is the work time of basic space voltage vectors $\overline{V}_0$, $\overline{V}_1$ and $\overline{V}_2$.

The determination of the Amount of times T_1 and T_2 given by mere projections is:

$$\begin{cases} V_{s\alpha\,ref} = \frac{T_1}{T_S}|\bar{V}_1| + x \\ V_{s\beta\,ref} = \frac{T_2}{T_S}|\bar{V}_2| \sin\left(\frac{\pi}{3}\right) \\ x = \frac{V_{s\beta\,ref}}{\mathrm{tg}(\frac{\pi}{3})} \end{cases} \Rightarrow$$

$$\begin{cases} T_1 = \frac{T_S}{2U_{dc}}\left(\sqrt{6}V_{s\alpha\,ref} - \sqrt{2}V_{s\beta\,ref}\right) \\ T_2 = \frac{T_S\sqrt{2}}{U_{dc}} V_{s\beta\,ref} \end{cases} \quad (25)$$

6. THE RESULTS OF SIMULATIONS

In this section, the effectiveness of the second approach for torque and flux control of an IM is verified by computer simulations. A series of tests were conducted to check the performance of the proposed system.

6.1 Influence Horizon of Prediction N_2

N_2 is varied to see its effect on performance. The following figures show the evolution of the output (torque and stator flux) for different values of N_2.

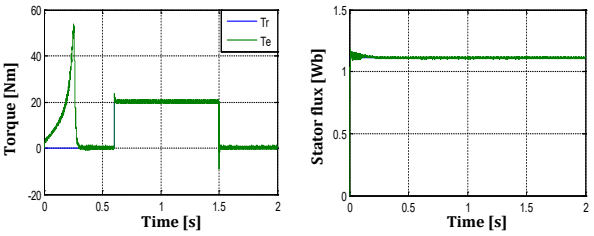

Figure.9 Evolution of the torque and stator flux magnitude for: N_1=1, **N_2=20**, N_u=1, λ=0.8, T_s=0.00001s.

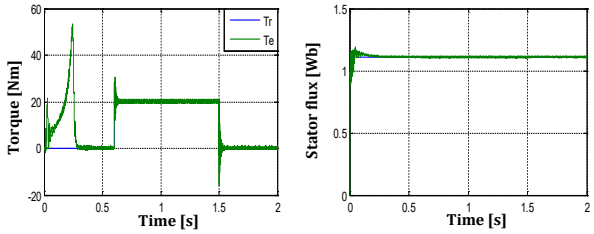

Figure.10 Evolution of the torque and stator flux magnitude for: N_1=1, **N_2=10**, N_u=1, λ=0.8, T_s=0.00001s.

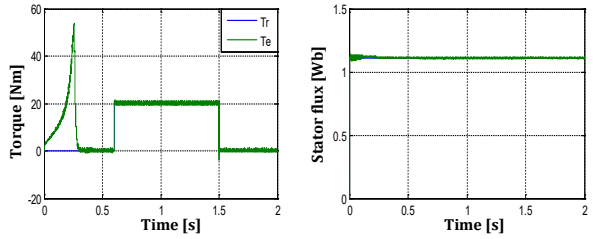

Figure.11 Evolution of the torque and stator flux magnitude for: N_1=1, **N_2=30**, N_u=1, λ=0.8, T_s=0.00001s.

6.2 Influence Weighting Coefficient λ

λ is varied to see its effect on performance. The following figures show the evolution of the output (torque and stator flux) for deferent values of λ:

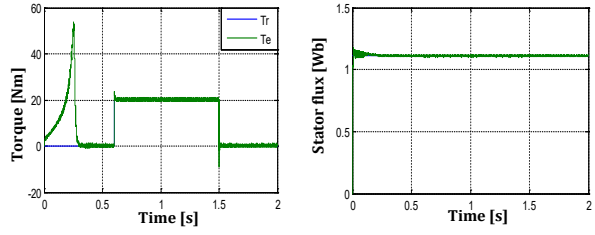

Figure.12 Evolution of the torque and stator flux magnitude for: N_1=1, N_2=20, N_u=1, **λ=0.8**, T_s=0.00001s.

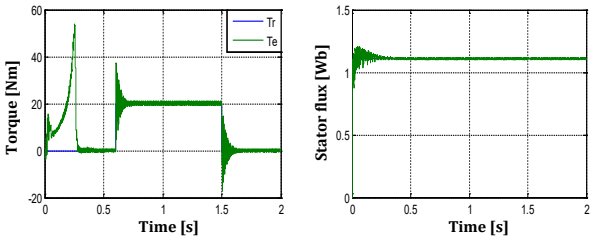

Figure. 13 Evolution of the torque and stator flux magnitude for**:** N_1=1, N_2=20, N_u=1, **λ=0.6**,T_s=0.00001s.

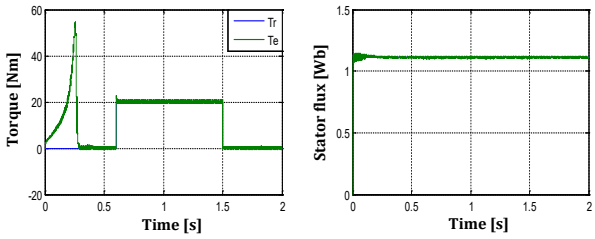

Figure. 14 Evolution of the torque and stator flux magnitude for**:** N_1=1, N_2=20, N_u=1, **λ=0.95**,T_s=0.00001s.

According to the results of the evolution of the output variables, we note that an increase in λ results in a reduction in the response time of the system and a reduction results in a large overshoot of the set point. Thus, a strong N_2 increase results slowly in answer the system, whereas a reduction results in a large overshoot of the set point especially on the level of flux.

Previous simulations call for several comments:

- We noted that the major drawback of predictive control is that the performance is greatly influenced by the choice of the synthesis parameters N_1, N_2, N_u, and ***λ*** therefore, a judicious choice of these parameters is necessary before the implementation of the simulation algorithm, to meet the desired performance.
- When there are actually values of the set point in the future, all of these informations are used between horizons of N_1 and N_2 so as to converge the predicted output to this set point.
- The coefficient λ is used to give more or less weight to the control relative to the output, so as to ensure the convergence when the starting system is a risk of instability.

6.3 Comparisons of simulations

In what follows, we consider the transient behavior of the induction motor under a reference speed. The results of two approaches are shown in Figures 15, 16 and 17.

Referring to figures (16) shows the speed response of MPDTC and DSVM-DTC controller. The MPDTC reacts faster than the DSVM-DTC when load torque is suddenly applied and removed.

Moreover, tracking performances were improved by the use of the MPDTC law, in comparison with those of DSVM-DTC. These properties make the new algorithm suitable for applications where high tracking accuracy is required in the presence of external disturbances.

Comparing figures (15), the second approach MPDTC

offers a notable reduction of the electromagnetic torque ripple compared to the first using hysteresis controllers.

Referring to figures (17) the magnitude of the stator flux is quickly established at its reference value, in both control techniques. The MPDTC has a visible reduction in oscillation amplitude of the modulus of the flux with respect to the DSVM-DTC. The dynamic component of the stator flux is not affected by the application of the load command. The MPDTC has as good of a dynamic response as the first approach.

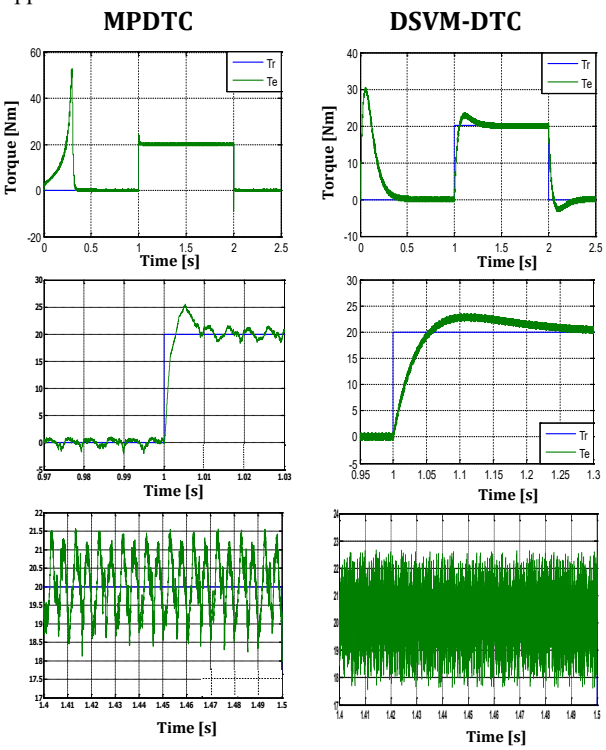

Figure.15 Comparison of the electromagnetic torque

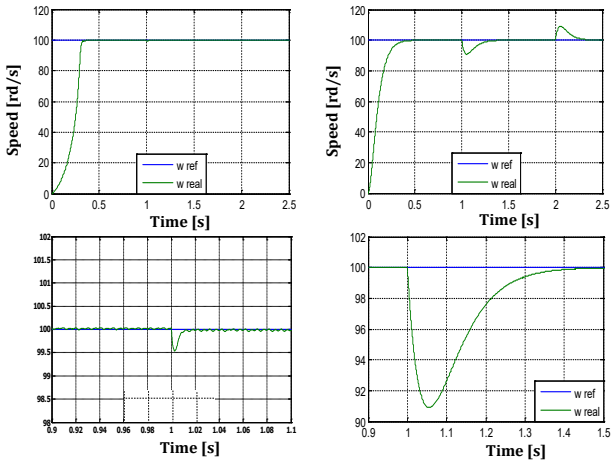

Figure. 16 Comparison the speed of rotation

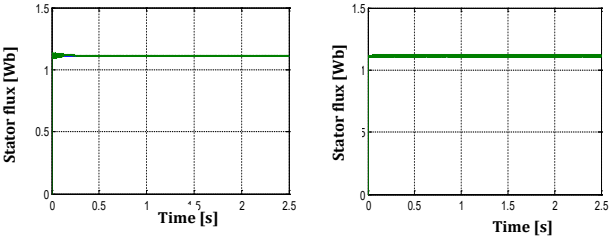

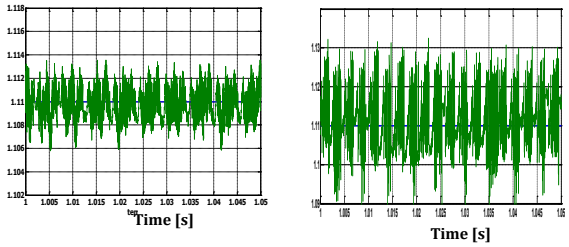

Figure.17 Comparison of the stator flux magnitude

(Table. 5) summarizes the results of the comparative study treated previously. In fact from this table, one can choose the approach to be used according to the needed objectives, the desired performances and the available means.

Control Approach	DSVM-DTC	MPDTC
Electromagnetic torque ripples	high	low
Stator flux ripples	high	low
Switching losses	high	low
rejection of disturbance	Bad	good
Algorithm complexity	medium	high
Commutation frequency	fixed	fixed
computing time	medium	high

Table 5. Comparison between Performances of the two DTC-SVM Approaches

Characteristics of the machine used for simulation:

parameter	*symbol*	*Value*
Number of pole pairs	p	2
Power	P_u	3 KW
Line voltage	U_n	380V
Line current	I_n	6.3A
Nominal frequency	f	50Hz
Mechanical rotor speed	N_n	1430 tr/mn
Electromagnetic torque	T_e	20Nm
Stator Resistance	R_s	3.36 Ω
Rotor Resistance	R_r	1.09 Ω
Stator cyclic inductance	L_s	0.256H
Mutual cyclic Inductance	L_m	0.236H
Rotor cyclic inductance	L_r	0.256H
Rotor inertia	j	$4{,}5.10^{-2}$Kg.m^2
Viscosity coefficient	f	$6{,}32.10^{-4}$N.m.s

7. CONCLUSION

This paper has been devoted to the comparison between the performance of the DSVM_DTC strategy with hysteresis controllers and those of a MPDTC with a predictive controller has been carried out considering simulation works. The transient behavior as well as the steady state features of the induction motor drive under both DTC-SVM approaches have been compared and commented. Simulation works have clearly shown that the second approach yields high dynamic performance in torque and

stator flux module with lower ripple, than the first one, as well as rejection disturbance at speed. However, the MPDTC with a predictive controller would inevitably require control systems with higher CPU frequencies in so far as their implementation schemes are more complicated than those of the first one.

REFERENCES

[1] I. Takahashi and T. Noguchi. A new quick-response and high-efficiency control strategy of an induction motor. IEEE Transaction industry Applications, IA-16: 820-827, Sept/Oct 1986.

[2] M.P. Kazmierkows and A.B. Kasprowicz. Improved direct torque and flux vector control of PWM inverter-fed induction motor drives. IEEE Transactions on industrial Electronics, 42(4): 344-350, August 1995.

[3] A. Yangui F. Ben Salem and A. Masmoudi. On the reduction of the commutation frequency in DTC : a comparative study. European Transactions on Electrical Power Engineering (ETEP), 15(6): 571-584, 2005.

[4] P. Chlebis P. Brandstetter and P. Palacky. Direct torque control of induction motor with direct calculation of voltage vector. Advances in Electrical and Computer Engineering Journal, 10(4): 17-22, 2010.

[5] A. Joseline Metilda R. Arunadevi, N. Ramesh and C. Sharmeela. Analysis of direct torque control using space vector modulation for three phase induction motor. Recent Research in Science and Technology, 3(7): 37-40, 2011.

[6] M. Borujeni, F.; Ardebili, M. "DTC-SVM control strategy for induction machine based on indirect matrix converter in flywheel energy storage system". Power Electronics, Drives Systems & Technologies Conference (PEDSTC), 2015 6th .Pages: 352 – 357.

[7] M. Farhad; Khaburi, D.A. " Torque ripple reduction in direct torque control of induction machines by use of all voltage vectors of matrix converters". Power Electronic & Drive Systems & Technologies Conference (PEDSTC), 2010 . Pages: 261 – 266.

[8] Y. Zhang ; H. Yang « Torque Ripple Reduction of Model Predictive Torque Control of Induction Motor Drives" Energy Conversion Congress and Exposition (ECCE), 2013. Pages: 1176 – 1183.

[9] Y. Inoue, S. Morimoto, and M. Sanada, "Examination and linearization of torque control system for direct torque controlled IPMSM," IEEE Trans. Ind. Appl., vol. 46, no. 1, pp. 159–166, Jan./Feb. 2010.

[10] C. Patel, R. P. P. A Day, A. Dey, R. Ramchand, K. Gopakumar, and M. P. Kazmierkowski. "Fast direct torque control of an open-end induction motor drive using 12-sided polygonal voltage space vectors," IEEE Trans. Power Electron., vol. 27, no. 1, pp. 400–410, Jan. 2012.

[11] Y. Kumsuwan. "Reduction of Torque Ripple In Direct Torque Control For Induction Motor Drives Using Decoupled Amplitude and Angle of Stator Flux Control". ECTI Trans On Electrical Eng, Electronics and Communication VOL 8, N° 2 august 2010. pp 187-196.

[12] D. Sun "Sliding Mode Direct Torque Control for Induction Motor with Robust Stator Flux Observer". Intelligent Computation Technology and Automation (ICICTA), 2010 International Conference, Year: 2010, Volume: 3, Pages: 348 – 351.

[13] S. Benaicha; F. Zidani; R.N. Said; M.S.N. Said. "A novel direct torque fuzzy control of SVM-inverter-fed induction motor drive". Power Engineering, Energy and Electrical Drives (POWERENG), 2013 Fourth International Conference. Year: 2013; Pages: 340 – 345.

[14] H. Li, Q. Mo, Z. Zhao. "Research on direct torque control of induction motor based on genetic algorithm and fuzzy adaptive PI controller", Measuring Technology and Mechatronics Automation, Vol. 3, pp. 46-49, 2010.

[15] W. Zhao, D. D. C. Lu, and V. G. Agelidis, "Current control of grid connected boost inverter with zero steady-state error," IEEE Trans. Power Electron., vol. 26, no. 10, pp. 2825–2834, Oct. 2011.

[16]T. Riad, B. Hocine, M. Salima, "New direct torque neuro-fuzzy control based SVM-three level inverter-fed induction motor", International Journal of Control, Automation, and Systems, Vol. 8, pp. 425-432, 2010.

[17] G. Grellet, G. Clerc, " Electric Actuators, Principle, Models, Order ". Electro Collection. Eyrolles Edition 2000.

[18] D. Casadei, G. Serra, and A. Tani. "Implementation of DTC algorithm for induction motors based on discrete space vector modulation". IEEE Trans. On Power Electronics, vol 15, N04, pp769-777, July 2001.

[19] Reddy, M.R.P.; Brahmaiah, B.; Reddy, T.B. "Discrete space vector modulation algorithm based vector controlled induction motor drives for reduced ripple". Power and Energy Systems Conference: Towards Sustainable Energy, 2014, Pages: 1 – 5.

[20] G. Papafotiou, J. Kley, K. G. Papadopoulos, P. Bohren, and M. Morari. "Model predictive direct torque control - part II: Implementation and experimental evaluation". IEEE Trans. Ind. Electron., 56(6):1906–1915, Jun. 2009.

[21] J. B. Rawlings and D. Q. Mayne. " Model predictive control: Theory and design ". Nob Hill Publ 2009.

[22] A. Zaki Diab , D. Kotin, V. Pankratov " Speed Control of Sensorless Induction Motor Drive Based On Model Predictive Control" XIV International Conference On Micro/Nanotechnologies And Electron Devices Edm. IEEE 2013.

[23] E.F. Camacho, C.Bordons, "Model Predictive Control", Springer-Verlag London, 2sd édition, 2003.

[24] A. Djermoune, P. Goureau. "Input-output decoupling of nonlinear control for an induction machine". Industrial Electronics, 1996. ISIE '96., Proceedings of the IEEE International Symposium Year: 1996, Volume: 2 Pages: 879 – 884.

[25] A. Isidori, Nonlinear Control Systems, 2nd ed., New York, Springer, 1989.

[26] L. Chen, K.L. Fang, and Z.F. Hu, "A scheme of fuzzy direct torque control for induction machine", Proceedings of the Fourth International Conference on Machine Learning and Cybernetics, Guangzhou, pp. 803-807, 2005.

Novel approach for a ladder network model of the transformer winding high-frequency parameters identification based on FRA data

Abdallah Chanane[1], Messaoud Belazzoug[1]

[1]Laboratoire des systèmes électriques et télécommande, Faculté de Technologie, Université Blida1, BP 270, route de Soumaa, Blida, Algeria.
chanane.abdallah@gmail.com,m_belazzoug@yahoo.fr
Corresponding author: chanane.abdallah@gmail.com
chanane.abdallah@univ-blida.dz

Abstract
The identification of the high-frequency ladder network model (LNM) parameters for the transformer winding is the way to confirm its actual condition. This paper aims to present the application of one of the latest approach algorithms, namely, Particle Swarm Optimization with Invasive Weed Optimization (PSO-IWO) method for the identification of the high frequency LNM parameters for the transformer winding. The physical realizability of the LNM is ensured and it is based on the frequency response analysis FRA data and some terminal measurements of a transformer winding. The results are agreement and indicate that the identified model, is superior in terms of representing the physical behavior of the transformer winding in high frequency.

Keywords
Identification, Transformer winding, Diagnosis, equivalent circuit, PSO-IWO

Introduction

Power transformer is one of the most expensive equipment in a power system. Transformers practice excessive faults during exploitation, and this disturb the quality and the continuity of service. For this motive, diagnosis is necessary. Several procedures have been developed for diagnosis such as vibration analysis [1], [2], transfer function (TF) [3], [4] and frequency response analysis (FRA) [5], [6].

The FRA is one of the best technique that can detect even the slightest changes in the transformer winding [7], [8]. Even so, pertaining FRA practice requires consistent interpretation methods including finite element modelling (FEM), mathematical models, analytical approaches, numerical indices and TF as reported in [6], [8], [9].

Nowadays, intelligent algorithms have been used to identify the LNM and to offer a global solution, such as genetic algorithm, particle swarm optimization, crow search and simulated annealing algorithms [10], [11] bacterial swarming [12], neural network [13], Grey Wolf [14] and bat algorithm [15]. In this paper, a novel approach is applied to identify the high-frequency parameters transformer winding using the PSO-IWO algorithm. The proposed algorithm uses the IWO method as a local search tool to improve the convergence and the characteristics of PSO in fast calculation. The proposed LNM is mutually coupled and physically realizable. Identification of the model parameters is presented and the results are validated through a case study of a transformer winding.

1. Proposed LNM

The transformer winding can be modeled by considering a mutually coupled LNM with N-section as shown in the Figure 1. The parameters of the LNM are defined as follows: N is the number of sections, r is the resistance per section, C_g is the capacitance to the ground per section, C_s is the series capacitance per section, L_s is the self-inductance and M_{1N} is the mutual inductances between different cells.

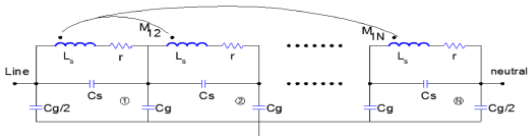

Fig. 1 *Equivalent circuit of a transformer winding*

- Capacitance matrix:

The total shunt capacitance (C_{geff}) and the ground capacitance per section (C_g) are, respectively, estimated according to the equations (1) and (2) [4], [14]:

$$C_{geff} = C_s . Q^2 / N \quad (1)$$

$$C_{gi} = C_g / N \quad (2)$$

Where: Q is the voltage distribution constant.

The equivalent capacitance of the LNM (C_{eq}) is estimated according to equation (3):

$$C_{eq} = \frac{C_{gi}}{2} + \frac{1}{\frac{1}{C_s} + \frac{1}{C_{gi} + \frac{1}{\frac{1}{C_s} + \cdots}}} \quad (3)$$

- Inductance matrix

One of the physical properties of the transformer winding is that the magnetic coupling decreases when the distance between the discs increases [4], [6]. Consequently, the self and the mutual inductances could be limited between two bounds (upper and lower bounds) as given in equations (4) and (5):

$$0.1\ L_{ij} < M_{ij} < 0.9\ L_{ij} \quad (4)$$

$$0.10M_{ij} < M_{ij+1} < 0.99M_{ij}\ ,\ i, j = 1\ \ldots.\text{where}, i \neq j$$

$$\text{and}\ \ L_{ij} > M_{12} > \ldots > M_{ij} \quad (5)$$

The total equivalent inductance of the model winding could be expressed as per equation (6):

$$L_{eq}(\text{estimated}) = NL_i + 2\sum_{i=1}^{N-1}(N-1)M_{i,i+1} \quad (6)$$

2. Proposed PSO-IWO method

2.1 PSO Algorithm

This algorithm is one of the stochastic algorithms [16]. By the way, novel concepts were developed such as the convergence rate and the selected parameters as reported in [17], [18], [19]. The position of the particle is calculated according to the individual's best and the group's best experience of the particle swarm. Each particle represents an achievable solution to the problem [18], [19].

2.2 IWO algorithm

The IWO is a stochastic algorithm inspired from the colonization of invasive weeds [20]. The algorithm starts randomly, then, members of the population produce seeds based on their comparative fitness in the population. The convergence rate and the selected parameters are reported in [20].

3.3 Hybrid PSO-IWO algorithm to identify the LNM

For a better solution quality, two algorithms are combined, in which, fully-guided movements for each iteration good exploration are ensured by PSO and IWO method respectively. This choice avoids some drawbacks such as being trapped in local optima or converging to global optima in a long time.

Reference value [4]	Frequency peaks (F_{Pi})						ΔF_{Pi}
	1st	2nd	3nd	4nd	5nd	6nd	
	40.48	142.58	249.42	346.41	414.34	473.73	
PSO-IWO	40.77	142.30	249.20	346.00	414.20	473.00	0.5917
CSA[11]	40.1	142.30	248.5	344.70	414.20	477.6	2.8100
Reference value [4]	Frequency Troughs(F_{Ti})						ΔF_{Pi}
	1st	2nd	3nd	4nd	5nd	-	
	105.19	224.79	334.44	410.09	472.42	-	
PSO-IWO	104.9	224.5	334.00	409.50	471.00	-	0.9830
CSA[11]	104.9	223.8	332.7	409.5	475.6	-	2.0400
$\Delta F_i = \frac{\sum \text{Reference values} - \sum \text{Estimated values}}{\sum \text{Reference values}} \text{x100}$							

Table. 2 Comparison of the reference and the estimated frequencies

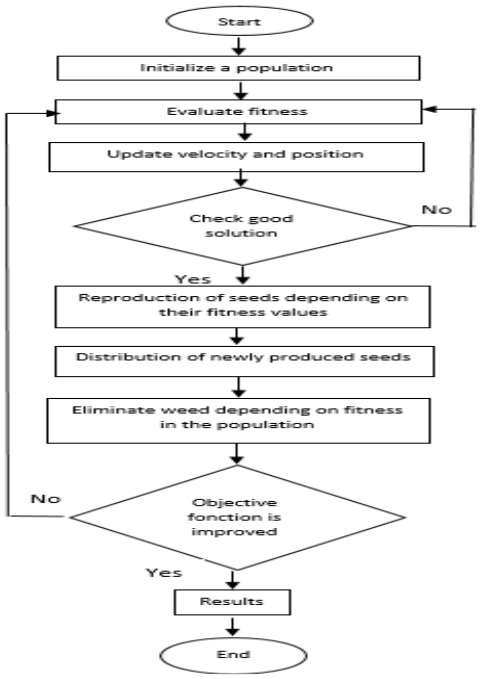

Fig. 2. *Flowchart of the PSO-IWO algorithm*

3. Implementation of the PSO-IWO to identify the LNM Parameters

FRA measurements were performed on the model of winding [4], in which the physical parameters are given as follow; the total inductance and effective capacitance were equal to 6.98mH and 5.6nF respectively. The total resistance was equal to 8Ω. An iterative algorithm was used to estimate the parameters of the involved electrical equivalent circuit. Finally, the FRA signature is obtained through the synthesized electrical equivalent circuit [4]. To identify the LNM of the transformer winding, the obtained results are compared to with those obtained by [11].

Parameters	Reference value (reprinted from [4])	PSO-IWO	CSA[11]	Deviation from the reference (%) $DEV = \frac{100}{N} \times \lvert\frac{Reference - identified}{Reference}\rvert$	
				PSO-IWO	CSA
Ls (mH)	0.4310	0.4310	0.4307	0.0	0.01
M1 (mH)	0.2392	0.2390	0.2390	0.013	0.138
M2 (mH)	0.1435	0.1430	0.1429	0.056	0.068
M3 (mH)	0.0947	0.0945	0.0949	0. 011	0.035
M4 (mH)	0.0612	0.0613	0.0610	0.026	0.053
M5 (mH)	0.0496	0.0497	0.0492	0.033	0.133
C_s (nF)	0.600	0.601	0.59	0.026	0.276
C_{eq}(nF)	0.8819	0.8824	0.8765	0.00	0.101
α	7.48	7.47	7.54	0.0223	0.021
L_{eq}(mH)	7.0385	7.0316	7.0292	0.0163	0.021

Table. 1 Comparison of the reference and the identified parameters of the LNM

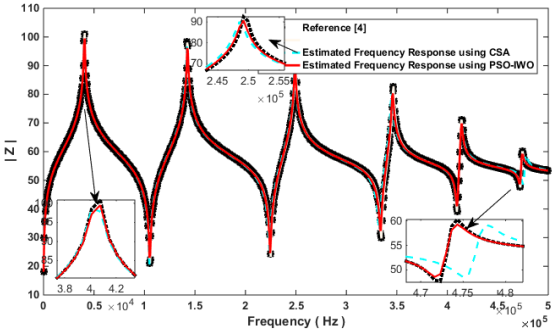

Fig. 3. *FRA curves of the model winding*

Discussion:

The proposed Ladder Network Model presents the physical behavior of the transformer winding. The proposed PSO-IWO method present serval advantages, mainly:

- The best exploration and exploitation search. Thereby, the global best solution always directed to a better position, as the algorithm proceeds.
- A luxurious, time-efficient and a flexible computation is verified, the effectiveness of PSO-IWO was tested by the Crow Search Algorithm.

conclusion

This paper has presented a novel approach based on PSO-IWO to identify the parameters of a Ladder Network Model of a transformer winding. The case study presented in previous sections suggest the capability of the PSO-IWO method for the construction of the LNM of a transformer winding. Through the case study, it has shown that the proposed PSO-IWO is good in terms of accuracy and effectiveness, since the proposed method is compared with other reported in the literature. The obtained results are very promising and prove the efficiency and the high solution quality.

Acknowledgment

The authors would like to thank the Directorate General for Scientific Research and Technological Development, Algeria (Direction Générale de la Recherche Scientifique et du Développement Technologique "DGRSDT", Algerie), for the resources provided for scientific research and development.

References

[1] Hong, K., Huang, H. and Zhou, J. (2015), "Winding condition assessment of power transformers based on vibration correlation", IEEE Transactions on Power Delivery, Vol. 30 No. 4, pp. 1735-1742.

[2] Seo, J., Ma, H. and Saha, T.K. (2017), "A joint vibration and arcing measurement system for online condition monitoring of onload tap changer of the power transformer", IEEE Transactions on Power Delivery, Vol. 32 No. 2, pp. 1031-1038.

[3] Mukherjee, P. and Satish, L. (2012), "Construction of equivalent circuit of a single and isolated transformer winding from FRA data using the ABC algorithm", IEEE Transactions on Power Delivery, Vol. 27 No. 2, pp. 963-970.

[4] Ragavan, K., Satish, L.: 'Localization of changes in a model winding based on terminal measurements: experimental study', *IEEE Trans. Power Deliv.*, 2007, **22**, (3), pp. 1557–1565

[5] Alsuhaibani, S., Khan, Y., Beroual, A. and Malik, N.H. (2016), "A review of frequency response analysis methods for power transformer diagnostics", Energies, Vol. 9 No. 11, p. 879

[6] Pramanik, S. and Satish, L. (2011), "Estimation of series capacitance of a transformer winding based on frequency-response data: an indirect measurement approach", IEEE Transactions on Power Delivery, Vol. 26 No. 4, pp. 2870-2878.

[7] Liu, Y., Ji, S., Yang, F., *et al.*: 'A study of the sweep frequency impedance method and its application in the detection of internal winding short circuit faults in power transformers', *IEEE Dielectr. Electr. Insul. Soc.*, 2015, **22**, (4), pp. 2046–2056

[8] Samimi, M., Tenbohlen, S.: 'FRA interpretation using numerical indices: state-of-the-art', *Electr. Power Energy Syst.*, 2017, **89**, pp. 115–125

[9] Liu, S., Liu, Y. A L. H. and Lin, F. (2016), "Diagnosis of transformer winding faults based on FEM simulation and on-site experiments", IEEE Transactions on Dielectrics and Electrical Insulation, Vol. 23 No. 6, pp. 3752-3760.

[10] Chanane, A., Bouchhida, O., Houassine, H.: 'Investigation of the transformer winding high-frequency parameters identification using particle swarm optimisation method', *IET Electr. Power Appl.*, 2016, **10**, (9), pp. 923–931

[11] Chanane, A., Houassine, H. and Bouchhida, O. (2019), "Enhanced modelling of the transformer winding high frequency parameters identification from measured frequency response analysis", IET Generation, Transmission and Distribution, Vol. 13 No. 8, pp. 1339-1345.

[12] Shintemirov, A., Tang, W. A T. W. and Wu, Q. (2010), "Improved modelling of power transformer winding using bacterial swarming algorithm and frequency response analysis", Electric Power Systems Research, Vol. 80 No. 9, pp. 1111-1120.

[13] Zambrano, G., Ferreira, A. and Caloba, L. (2006), "Power transformer equivalent circuit identification by artificial neural network using frequency response analysis", IEEE Power Engineering General Meeting, Montreal, Canada, No. 11, pp. 1-6.

[14] Abdallah Chanane, M. Belazzoug, ' On accuracy of a mutually coupled ladder network model high-frequency parameters identification for a transformer winding using gray wolf optimizer method', Computer Science Compel-the International Journal for Computation and Mathematics in Electrical and Electronic Engineering Vol. 40 No. 1, pp. 40-50.

[15] Sahnoune Chaouche, M., Houassine, H., Moulahoum, S., *et al.*: 'BA to construction of equivalent circuit of a transformer winding from frequency response analysis measurement', IET Electric Power Applications, vol-12, pp-728-736.

[16] Kennedy, J., Eberhart, R.C.: 'Particle swarm optimization'. Proc. IEEE Int. Conf. on Neural Networks IV, Perth, Australia, 1995, pp. 1942–1948

[17] Trelea, I.: 'The particle swarm optimization algorithm, convergence analysis and parameter selection', Inf. Process. Lett., 2003, **6**, (85), pp. 317–325

[18] Shi, Y., Eberhart, R.C.: 'Empirical study of particle swarm optimization'. Proc. of the Congress on Evolutionary Computation, Washington D.C., USA, 1999, pp. 1945–1950

[19] Clerc, M., Kennedy, J.: 'The particle swarm explosion, stability, and
convergence in a multidimensional complex space', IEEE Trans. Evol.Comput., 2002, **6**, pp. 58–73

[20] Mehrabian, A.R., Lucas, C.:' A novel Numerical Optimization Algorithm Inspired from Weed Colonization', Ecological Informatics, 2006,(1), pp. 355-366.

Micro and nanoelectronics

NOVEL DESIGN OF PHOTONIC CRYSTAL STRUCTURE BASED ON A COUPLED MICROCAVITY-WAVEGUIDES FOR ALL-OPTICAL AND LOGIC GATES

[1]Roumaissa DERDOUR, [2]Mohamed Redha LEBBAL, [1]Souheil MOUETSI, [3]Abdesselam HOCINI, [1]Boumediene SADOUN.

[1] Laboratory of Electronics and New Technology (LENT), Department of Electrical Engineering,
University of Oum El Bouaghi, Ain Beida, 04201, Algeria
Corresponding author: maroma18@yahoo.fr

[2] Department of Electronics Faculty of Engineering Mentouri University Constantine1. Algeria

[3]Laboratory of signals and systems Analyze Department of Electronics. University of Mohamed Boudiaf Msila, Alegria.

ABSTRACT:

In this study, the transmission of the all-optical AND logic gate using a structure connected with a triangular photonic crystal lattice is improved. The proposed logic gate consists of a photonic crystal nano-resonator formed by changing the size of the air holes. In addition to the simplicity, the response time is very short and the designed nano-resonator increases the bit rate of the logic gate. The two-dimensional finite difference time domain (2D-FDTD) method is used to simulate the structure, the transmission obtained is about 98% with very negligible losses. The proposed photonic crystal AND logic gate are widely used in future integrated optical microelectronics.

Keywords: *logic gates, photonic crystals, optical integrated circuits. Interferences effect, resonant cavities*

INTRODUCTION:

Photonic crystals (PhCs) are the best platforms for designing all optical devices suitable for all optical integrated circuits. The periodic distribution of refractive index in these artificial structures results in a forbidden wavelength region for propagation of light; this forbidden wavelength region is called photonic band gap (PBG) [1-2]. By use of PBG, we can control the behavior of light inside PhCs in very small spaces. For this reason, designing ultra-compact devices based on PhC suitable for optical integrated circuits is feasible. Optical reflectors [3]. Optical band rejection filters [4] are some examples of proposed devices using PBG property of PhCs.

Optical logic devices play important roles in optical calculation and high-speed information processing [5]. In addition, the need of all-optical logic designs increases day by day to cope up with the demand of high-speed telecommunication networking and computing systems. [6]. Lack of the need of Optical-Electrical-Optical (O-E-O) conversion as well as the data processing in optical means [7]. All-optical logic gates are major unit of all-optical signal processing and optical communication [8]. Both of these need a lot of complex combination of all-optical logic gates. Every all-optical logic gate needs to be operated fast and functional as a critical and essential part of bigger structure [9]. Furthermore, we can improve the entire system to work faster and more reliable by optimizing an all-optical logic gate. [10] All-optical logic gates can be based on semiconductor optical amplifiers [11], quantum-dot semiconductor optical amplifiers [12.13], and photonic crystals [14].

Many structures have been proposed to introduce all-optical photonic crystal logic gates [15-16]. New structures for all-optical photonic crystal logic gates have been increasingly optimized [17-18]. In addition, different structures have been reported for logic gates to obtain high contrast ratios in all-optical photonic crystal logic gates [19.20.21]. Mohebzadeh and Olyaee reported a novel structure for photonic crystal NOT and XOR logic gates with high contrast ratio [19]. In their study, the contrast ratios of 20.53 dB and 19.95 dB were obtained for NOT and XOR logic gates, respectively, at the wavelength of 1550 nm. In addition, the XOR and XNOR logic gates were reported based on the Fano resonance in a plasmonic ring resonator with a contrast ratio of about 23 dB [21]. Muthu and al are recently reported XOR/OR logic gates with a response time of 120 fs [22]. More recently, an ultra-compressed structure has been reported for XOR/NOT/OR logic gates with a response time around 100 femtoseconds [23].

Another particularity of these structures is the Multifunctionality of this logic gate, which simultaneously provides a logic multiplexer and an AND logic gate using a 2D photonic crystal structure [24]. Kumar and Medhekar designed and simulated all-optical photonic crystal NOR and NAND gates using silicon rods in air [25]. In

this structure, we design a logic gate to provide the AND logic gate function. The AND gate is formed by the Y junction and two microcavities with a triangular array of silicon air holes. The two holes were located in the right waveguide. Their size was changed in order to optimize the transmitted power and to reduce the losses. To validate our results numerically, we use a finite-difference time-domain method (FDTD-2D) to simulate the wave propagation inside the Y-junction in a two-dimensional photonic crystal. The studied device is widely used in future integrated optical microelectronics.

DESIGN AND STRUCTURE:

The photonic crystal structure used in the design is a triangular array photonic crystal of air holes in a silicon substrate. The refractive index of silicon 3.42. The hole radius is chosen as r = 0.4*a, where (a) is the lattice constant and (r) is the radius of the air holes were chosen for a triangular lattice in order to obtain a photonic band gap (PBG) around 1.55 µm existing for telecommunication wavelengths. This crystal is illuminated by a Gaussian wave under normal incidence with a transverse electrically polarized (TE) mode. The length of the photonic crystal is 19*a and the time step is chosen to be 0.01. Note that it may be necessary to reduce the time step below the stability limit when simulating the materials.

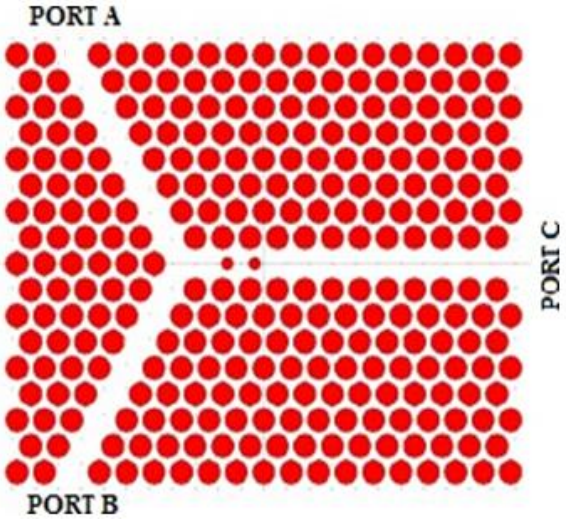

Figure 1: Design of the optimized All-optical AND logic gate

We chose this structure because triangular array can have large band gaps and silicon is expected to be a good platform for integrated photonic circuits and ultra-compact optical devices. [26, 27]. Figure 2 shows the band gap diagram who is obtained using the FDTD method. The band gap means that light in this range is not allowed to pass through the photonic crystal structure [28]. This band diagram and the primary photonic crystal structure are shown in Fig. 2. For this structure, in TE mode, there is a band gap between 0.293 a/λ and 0.428 a/λ, which is equivalent to the wavelength range of 1269 nm to 1890 nm. In our simulation, the wavelength 1550 nm is used.

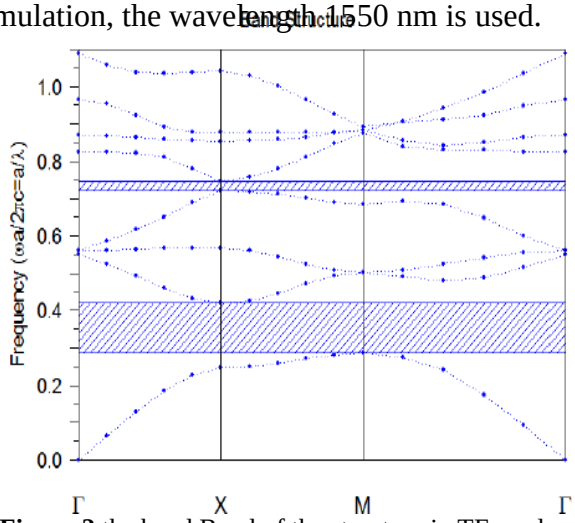

Figure.2 the band Band of the structure in TE mode.

RESULTS AND DISCUSSION:

In theory the AND gate is a device whose output is logical (1) if both inputs are logical (1). The logical AND function of two variables is represented either by writing a point between the two variables, or by writing the adjacent letters without a point. For example X. Y = Z or XY = Z reads, "X AND Y is equal to Z". The AND gate symbol and its timing diagram are shown in Figures (3-a) and (3-b) respectively, with two inputs marked A and B and one output marked X [29].

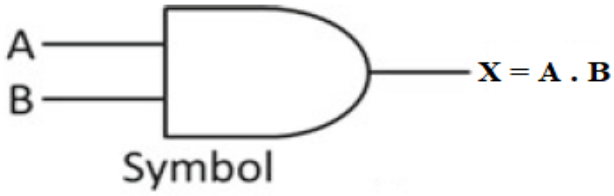

Figure 3-a: symbol of the AND logic gate.

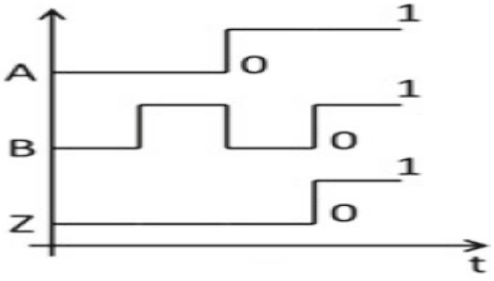

Figure 3-b: Timing Diagram

A continuous light source is used to verify the correct operation of the logic gate. This source is located in ports A and B. at port C a time monitor is provided to receive the light output. According to the truth table, the operation of the logic gate has been studied in three modes.

TABLE1 :

Port A	Port B	Port C	Logical output
0	0	0	0
0	1	0.015	0
1	0	0.015	0
1	1	0.982	1

Table1: The truth table for AND logic gate, where the output signal is as a function of input power Pi

In the first mode, the source on port A is active and the source on port B is inactive. In this case, most of the light is captured in the microcavities and a very small part of the light reaches the output port. The corresponding electromagnetic field is shown in Figure 4.a; the ratio of the received optical power to the input power in the proposed logic gate is 0.015, which is considered equal to the logic level of “zero”.

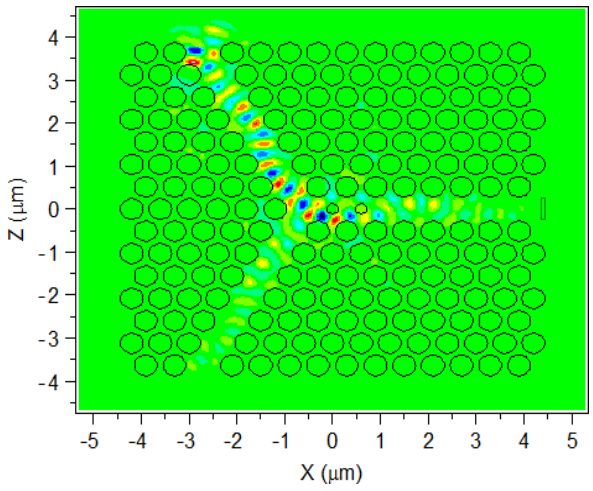

Figure 4.a: the electromagnetic field in the structure when A=1 and B=0

In the second mode, the light source on port B is active and the other light source is inactive. The function of the logic gate presented by the electromagnetic field representation is shown in Figure 4.b. The output power is 0.015. This optical power is equal to the logic level of “zero”.

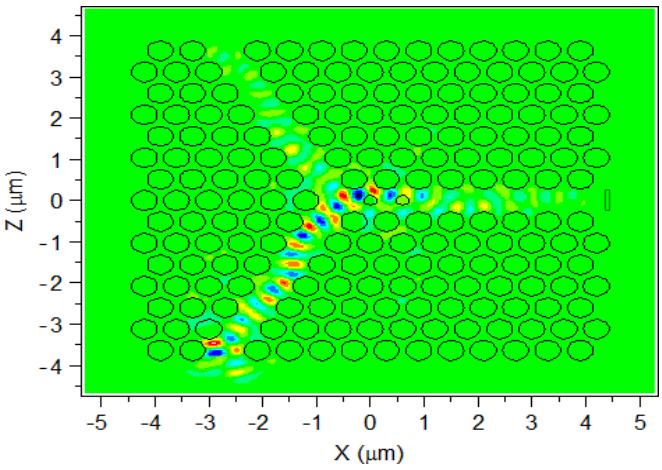

Figure 4.b: the electromagnetic field in the structure when A=0 and B=1

In the third mode, both optical sources are active. This means that from both ports A and B, light reaches the microcavities with high optical power. The two lights are merged in the microcavities and the high power light reaches the output port.

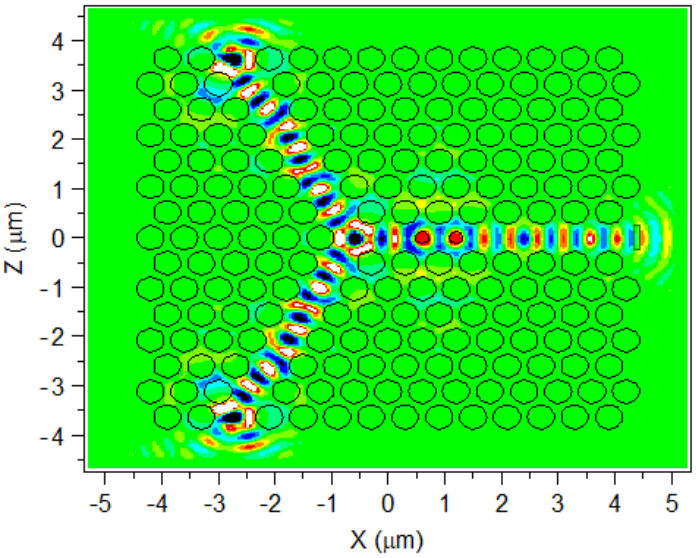

Figure 4.c: the electromagnetic field in the structure when A=1 and B=1.

Figure 4.c, shows the electromagnetic field of the logic gate in this state. The ratio of output power to input power is 2.9. This value is considered equal to logic level "one".

Figure 5 shows the power transfer diagram when both input ports are set to 1.

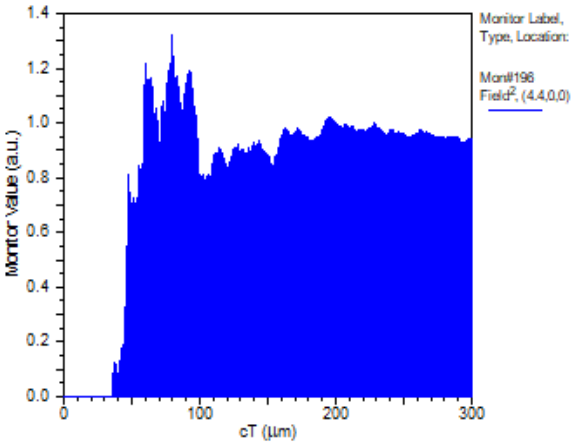

Figure 5: the power transfer diagram in the proposed AND logic gate

The contrast ratio can be calculated by the logic levels "one" and "zero" of the output power as

$$CR = 10\ log\ \frac{PL}{PH}$$

Where P_L and P_H are the lowest optical power at logic level "one" and the highest value of output power at logic level "zero [30].

Table 2 shows the comparison of the proposed structure with other similar structures proposed in previous works. The performance of the proposed logic gate is compared with four similar logic gates, it is very clear that our structure has much more compact dimensions compared to the other structures and that the use of microcavities allows to amplify the transmission in the output port. The performance of this structure is optimal in terms of contrast ratio.

TABLE2 :

Power intensity (µm)		Contrast ratio (dB)	Lattice type
REF [31]	33%	6.93	Square
REF [32]	36%	13.93	Square
REF [33]	73%	9.29	Square
REF [34]	80%	11.03	Square
THIS WORK	98%	22.98	Hexagonal

Table2: The comparison of the results of the proposed structure with other structures

The contrast ratio for the proposed photonic crystal AND logic gate is 23 dB

CONCLUSION

In this paper, a new connected structure is proposed and demonstrated by simulation in the telecommunication wavelength range (1.55 µm). Our structure is very compact with low power consumption and simplicity of operation compared to other compound structures logic gates. For the proposed all-optical AND logic gate the transmission is amplified and the contrast ratio (22.98 dB) is very satisfactory compared to other structures studied. The two-dimensional finite difference method (2D-FDTD) demonstrates the optical performance of the proposed structure and its dispersion diagram is presented using the PWE method. The studied structure provides a basis for the optimal design of the integrated circuit and has an important application perspective in all fields.

ACKNOWLEDGMENT:

This work was partially supported by general direction for scientific research and technological development, DGRSDT.

REFERENCES:

[1] Mir Hamid Rezaei, Abbas Zarifkar, Mehdi Miri, Ultra-compact electro-optical graphene-based plasmonic multi- logic gate with high extinction ratio, Optical Materials 84 (2018) 572–578

[2] Mahesh V Sonth, Savita Soma, Sanjaykumar C Gowre, “Investigation of light behavior of all optical full adders in twodimensional photonic crystals”, Microwave and Optical Technology Letters · November 2020

[3] Su Wei, Xinyu Wang, Zhen Geng, Yan Liu, A simple graphene nanoribbon structure-based terahertz all-optical logic gates with fano resonance, Optical Materials 97 (2019) 109401

[4] WANG Min, CHEN Jin-yong, WANG Gang, GAO Feng, SUN Kang, and XU Miao-zhong, “High resolution remote sensing image ship target detection technology based on deep learning”, Optoelectronics Letters, Vol.15 No.5, 1 September 2019

[5] Zhoufeng Ying,Zheng Zhao,Chenghao Feng,Rohan Mital,Shounak Dhar,David Z. Pan,Richard Soref And Ray T. Chen,"Automated Logic Synthesis For Electro-Optic Logic Based Integrated Optical Computing",Optics Express 28002.Vol. 26(2018)

[6] Vakhtang Jandier,Ramaz khomeriki and Daniel Erni,"Realization of true all-optical AND logic gate based on nonlinear coupled air-hole type photonic crystal waveguides",optics express 19845,Vol. 26 (2018)

[7] F. Mehdizadeh, M. Soroosh, H. Alipour-Banaei, E. Farshidi, “Ultra-fast analog-to-digital converter based on a nonlinear triplexer and an optical coder with a photonic crystal structure”, Applied Optics 56, 1799–1806 (2017).

[8] L.HE, W.X.Zhang and X.D.Z Hang, "Topological all-optical logic gates based on two-dimensional photonic crystals", optics express 25841,Vol. 27 No 18/2 (2019).

[9] Fengjiang Zhuan g, Qihe Shu, Dongmei Gong, gez hang, “Optical bistability in diode-end-pumped dual- wavelength

Yb:YAG laser for all-optical switching", Optical Materials Volume 107, September 2020,110146

[10] Leilei Shi Qianqian, Wang Jing, Luo Tao Zhu, "In-fiber wavelength-selective reflector based on Y-junction coupled whispering gallery mode resonator", Optical Materials , Vol. 12, No. 4, 191-195 (2018).

[11] Ding, Xuan; Wu, Gui-ling; Zuo, Fa-xing; Chen, Jian-ping . Bidirectional optical amplifier for time transfer using bidirectional WDM transmission. Optoelectronics Letters, 15(6), 401–405(2019)

[12] L.HE, H.Y.Ji,Y.J. Wang and X.D.Zhang, "Topologically protected beam splitters and logic gates based on two-dimensional silicon photonic crystal slabs",optics express 34015,Vol. 28, No. 23 / 9 (2020).

[13] Jia-wei Shen, Bo Zhu, Fang-ren Hu ,Si-jia Chen. A novel chromatic dispersion monitoring method for 1 024 QAM fiber-optic system based on asynchronous amplitude sampling. Optoelectronics Letters, 13(3), 221–224. (2017)

[14] Mahsa Salmani, Armaghan Eshaghi,Enxiao Luan,"Photonic computing to accelerate data processing in wireless communications", optics express 22299,Vol. 29, No. 14 / 5 (2021).

[15] A. Mohebzadeh-Bahabady, S. Olyaee, All-optical NOT and XOR logic gates using photonic crystal nano-resonator and based on an interference effect. IET Optoelectron. 12(4), 191–195 (2018)

[16] M. Pirzadi, A. Mir, D. Bodaghi, Realization of ultra-accurate and compact all-optical photonic crystal OR logic gate. IEEE Photon. Technol. Lett. 28(21), 2387–2390 (2016)

[17] F. Parandin, M.R. Malmir, M. Naseri, A. Zahedi, Reconfigurable all-optical NOT, XOR, and NOR logic gates based on two dimensional photonic crystals. Superlattices Microstruct. 113, 737–744 (2018)

[18] L. He, H. Ji, Y. Wang, X. Zhang, Topologically protected beam splitters and logic gates based on two-dimensional silicon photonic crystal slabs. Opt. Express 28(23), 34015–34023 (2020)

[19] E.H. Shaik, N. Rangaswamy, Realization of XNOR logic function with all-optical high contrast XOR and NOT gates. Opto-Electron. Rev. 26(1), 63–72 (2018)

[20] A. Mohebzadeh-Bahabady, S. Olyaee, Designing low power and high contrast ratio all-optical NOT logic gate for using in optical integrated circuits. Opt. Quant. Electron. 51(1), 1–13 (2019)
[21] M. Moradi, M. Danaie, A.A. Orouji, Design of all-optical XOR and XNOR logic gates based on Fano resonance in plasmonic ring resonators. Opt. Quant. Electron. 51(5), 1–18 (2019)

[22] K.E. Muthu, S. Selvendran, V. Keerthana, K. Murugalakshmi, A.S. Raja, Design and analysis of a reconfigurable XOR/OR logic gate using 2D photonic crystals with low latency. Opt. Quant. Electron. 52(10), 1–9 (2020)

[23] S.E. Kordi, R. Yousefi, S.S. Ghoreishi, H. Adrang, All-optical OR,NOT and XOR gates based on linear photonic crystal with high port-to-port isolation. Appl. Phys. B 126(10), 1–9 (2020)

[24] A. Farmani, A. Mir, M. Irannejad, 2D-FDTD simulation of ultracompact multifunctional logic gates with nonlinear photonic crystal. JOSA B 36(4), 811–818 (2019)

[25] A. Kumar, S. Medhekar, All optical NOR and NAND gates using four circular cavities created in 2D nonlinear photonic crystal. Opt. Laser Technol. 123, 105910 (2020)

[26] S. Naghizade, H. Saghaei, A novel design of all-optical full-adder using nonlinear X-shaped photonic crystal resonators. Opt. Quant. Electron. 53(3), 113 (2021)

[27] Vakhtang Jandieri,Ramaz Khomeriki,Tornike Onoprishvili,Douglas H. Werner,Jamal Berakdar And Daniel Erni,"Functional All-Optical Logic Gates For True Time-Domain Signal Processing In Nonlinear Photonic Crystal Waveguides",Optics Express 18317,Vol. 28, No. 12 / 8 (2020)

[28] N. Abirami, K.S. Joseph Wilson, "Investigation on photonic band gap of a magneto photonic crystal", optik, international journal for light and electron optics, 208.164092 (2019).

[29] Swarnakar S, Kumar S, Sharma S. Performance analysis of alloptical full-adder based on two-dimensional photonic crystals.J Comput Electron. 2018;17(3):1124-1134.

[30] Janyani, Vijay; Singh, Ghanshyam; Tiwari, Manish; D'alessandro, Antonio (2020). Optical And Wireless Technologies Volume 546 (Proceedings Of Owt 2018). High Contrast Ratio Based All-Optical Or And Nor Plasmonic Logic Gate Operating At E Band. , 10.1007/978-981-13-6159-3(Chapter 35), 325–332

[31] P. Andalib, N. Granpayeh, All-optical ultracompact photonic crystal AND gate based on nonlinear ring resonators. JOSA B 26(1), 10–16 (2009). DOI: 10.1364/JOSAB.26.000010

[32] A. Kumar, S. Medhekar, All optical NOR and NAND gates using four circular cavities created in 2D nonlinear photonic crystal. Opt. Laser Technol. 123, 105910 (2020)

[33] S. Rebhi, M. Najjar, A new design of a photonic crystal ring resonator based on Kerr effect for all-optical logic gates. Opt. Quant. Electron. 50(10), 1–17 (2018). doi.org/10.1007/s11082-018-1628-4

[34] Ehsan Veisi, Mahmood Seifoori, Saeed Oluaee, "A novel design of all-optical high speed and ultra-compact photonic crystal AND logic gate based on the Kerr effect", Applied Physics B (2021) 127:70

.

Incorporation of CdS nanoparticles on mesoporous silicon substrate as application for detection systems.

Fatima Saker
Laboratoire des Matériaux et Structure des Systèmes Electromécaniques et leur Fiabilité LMSSEF
Larbi Ben M'hidi Univercity
Oum El Bouaghi, Algeria
sfphysique@hotmail.fr

Louardi Remache
Laboratoire des Matériaux et Structure des Systèmes Electromécaniques et leur Fiabilité LMSSEF
Larbi Ben M'hidi Univercity
Oum El Bouaghi, Algeria
rlouardi@yahoo.fr

Abdellah Rahmani
Laboratoire des Matériaux et Structure des Systèmes Electromécaniques et leur Fiabilité LMSSEF
Larbi Ben M'hidi Univercity
Oum El Bouaghi, Algeria
https://orcid.org/0000-0001-7883-4759

Hassiba Moualkia
Laboratoire des Matériaux et Structure des Systèmes Electromécaniques et leur Fiabilité LMSSEF
Larbi Ben M'hidi Univercity
Oum El Bouaghi, Algeria
moualkia@yahoo.fr

Abstract—**in this study CdS nanoparticles were successfully deposited by chemical bath deposition (CBD) on the porous silicon (Psi) and glass substrates. In order to prepare porous silicon, an electrochemical etching method was carried out using p-type Si (100) at various current densities with fixed time (5 min). Crystallographic structure of prepared samples was analyzed with X-ray diffraction (XRD), The surface morphology of films was obtained by scanning electron microscopy (SEM). Results demonstrated that the morphology of the deposited materials was influenced by the porosityof the PSi substrate. The crystallite size determined by the Debye-Scherrer equation and the smallest value was 13.96 nm from CdS/PSi anodized using the current density of 60 mA/cm^2.SEM results confirms the shows the porous CdS thin films morphology. The optical properties of nanostructure CdS thin films were obtained by using UV-visible. TheCdS shows a band gap(E_g=2.3 eV)valueobtained by transmittancespectrum. The high surface area of CdS/PSi structures could be helpful for making highly sensitive photodetectors.**

Keywords—Porous silicon(PSi),CdS,nanoparticles, photodetector.

I.INTRODUCTION

Cadmium sulfide CdS has a direct band gap semiconductor of 2.42 eV at room temperature. And is one of the most important II-VI semiconductors used in the electronic and optoelectronic field [1].

CdSthin films can be deposited by different deposition techniques such as spray pyrolysis, thermal evaporation, chemical bath deposition, pulsed laser deposition, dip coating etc[1-5].Among these methods, the chemical bath deposition (CBD) is very simple and inexpensive method, it can be used to produce large area homogeneous films.

On the other hand, porous silicon has become a promising material for detection applications because of many reasons: its morphology, large specific surface area, low energy consumption, and its compatibility with silicon-based technologies[6-7]. In addition, the various morphological and structural properties of this material can be produced in a localized manner by a low-cost electrochemical process which can be integrated with microtechnological processes on silicon[6]. The sensitivity of PSi depends on the morphological characteristics of pores, including pore diameter,uniformity, surface smoothness and layer thickness [8]. Furthermore, its large specific surface area makes it more reactive than bulk silicon, which allows it to adapt to a large number of environmental and biochemical detection systems[9-10]. Many studies have been reported on improving the performance of porous silicon-based detectors[6-11]. specially to manufacture high-performance photo-detectors[6].Another more attractive way, that which consists in introducing nanoparticles of materials in the PSi matrix, this process makes it possible to improve the electrical properties of the elaborated layers and to manufacture sensors having higher and faster response[12].In this context, several materials can be incorporated into the PSi matrix like: ZnO, ZnS, TiO_2 ...and others more[13-14].

Several studies have been reported on the incorporation of nanoparticles into the matrix of PSi, and among the materials that can be integrated into the matrix of porous silicon, CdSe, CdS, ZnS, ZnO etc. S.A.Hasoon&al also made studies on fabrication of nanostructure CdS thin films deposited by vacuum thermal evaporation technique on PSi matrix[5]. Sara.T &al are fabricated CuS /PSi heterojunction photodetector using chemical spray pyrolysis route[4]. Khashan described the improvement of PSi photo-detectors when they are incorporated with ZnO nanoparticles prepared by a chemical method[15].N.F.Habubi described the response improvement of PSi photo-detectors when they are incorporated with CdSe nanoparticles prepared by laser ablation[16].

Yong Li & al [1]have studies the electronic properties of CdS/Si nano-heterostructure prepared by CBD on the silicon nanoporous pillar array.

This work aims to study the incorporation of CdSnanoparticles on the PSi matrix by using the chemical bath deposition (CBD)method. The effect of the PSi

substrate on the structural, morphological and optical properties of the CdS layers was investigated by comparing to the CdS/Glass structure.

II. EXPERIMENTAL METHOD

Preparation of PS matrix

The PSi layers were prepared by anodizing of p-type Boron doped(100) oriented monocrystalline silicon(C.Si) wafer , with resistivity0.015-0018 Ωcm and thickness of 250-300µm in hydrofluoric acid and ethanol with platinum electrode as cathode. The electrolyte was prepared by mixing HF with concentration (40%) and ethanol (C_2H_5OH99.98%) with the ratio of 1:1 by volume using a single-cell connected with keithley model 4200. The porous layers were prepared at various current densities of (30 and 60) mA/cm^{2}during5 min at room temperature where the porosity of PSi was 35% and 55% respectively
Finally, the samples were taken out and washed with ethanol and dried by hair dryer. The silicon wafers were cleaned in HF 2 % before the anodization process.

Incorporation of CdS nanoparticles

CdS thin films were deposited on the PSi and on glass using a CBD method. The used solution was a mixture of cadmium sulfate ($CdSO_4$), Ammonia (NH_4OH),Thiourea **(**$CS(NH_2)_2$and Deionized water (DI H_2O), where it was placed into the bath fixed at 50°C, next NH_4OH, $CdSO_4$ and**(**$CS(NH_2)_2$ were added to the (DI H_2O) for 60 min with a magnetic agitation to homogenize the mixture. The samples were taken out and washed thoroughly with de-ionization water and dried by hair dryer. As-grown CdS thin films were homogeneous, yellowish, and with good adherence to glass and PSi.

In this study, we have three samples: CdS nanoparticules deposited on glass (CdS/glass) and on porous silicon fabricated at 30mA/cm^2 (CdS30) and 60 mA/cm^2 (CdS60)during 5 min. The crystallographic structure of the prepared samples was analyzed with X-ray diffraction (XRD) using ARL-EQUINOX 100 X-ray diffractometer (CuKα1 radiation, 40 mA, 40KV) in the range of (10-90 deg).Optical transmittance and surface morphology of the CdS nanoparticles were investigated by means of a UV–visible spectrophotometer Jacso V-30 and (TESCAN VEGA3) scanning electron microscopy (SEM) .

III. RESULT AND DISCUSSION

III.1 Structural characterizations:

Fig.1 illustrates the XRD patterns of CdS nanoparticles deposited on glass and porous silicon substrates.
The X-ray diffraction (XRD) analysis indicates that CdS/glass and CdS/PSi thin films showed the cubic crystalline phase.
CdS/glass have showed peak at 26.6°corresponding to the (111) and small peaks at 29.9°, 44.2° and 52.4°corresponding to the (200), (220) and (311) orientations of CdS according to (COD ID:900108).
The patterns of CdS/SiP contain several diffraction peaks at 26.6°,29.9°,44.1°,51.7°corresponding to (111), (200), (220),(311), plane, respectively, belonging to the CdS cubic phase. When the peaks at 32.2° and 55.1 ° are corresponding to (111), (202) of CdO cubic phase according to (COD ID: 1011051).
The appearance of CdO can be explained by the oxidation of the CdS films at the levels of the silicon pores.
the layers deposited on PSi are more intense (almost x 4) compared to that deposited on glass, which shows the improvement of the CdS layers crystallization using porous silicon substrates. This amelioration is due to the good crystallization of the PSi substrates, on the other hand, the glass substrate is amorphous, which allows us to confirm the effect of the substrate type on the deposited layer of CdS. The structure obtained for samples CdS30 and CdS60 is similar to the results of other studies[17-18], which is maybe the structure of mixed phase that starts from the cubic and tends towards the hexagonal phase via annealing. This structure maybe becomes a hexagonal phase after annealing.

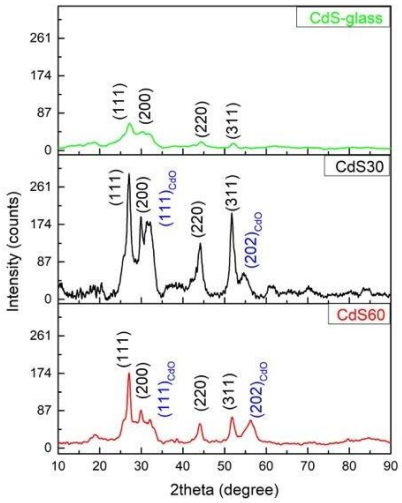

Fig. 1. XRD spectra of CdS nanoparticles deposited on glass and on porous silicon.

The grain size D is calculated using Debye Scherer's formula[19]:

$$D = \frac{K.\lambda}{\beta.\cos\theta} (1)$$

Where:
D: the grain size.
β : the full width at half maximum (FWHM in radians) of thepeak corrected for instrumental broadening
θ: the position of the diffraction peak considered.
K: Scherer constant, this value is taken as 0.9 for the calculations
λ: the wavelength of the X-ray.
The distances are expressed in [Å] and the angles in radians. the strain values ε can be calculated using the following formula [5]:

$$\varepsilon = \frac{\beta\cos\theta}{4} (2)$$

The dislocation density δ is deduced using the relation of Williamson and Smallman's [20]:

$$\delta = \frac{1}{D^2} (3)$$

In the table 1 we listed the XRD data and results for CdS/glass and CdS/Psi.

The calculated particle size showed that it was related to the nature of the substrate, as it took a lower value when replacing the glass substrate with the porous silicon substrate. It was also affected by the porosity ofthe porous silicon substrate, where we noticed that the crystallite size decreases when the porosity increases.

TABLE I. structural parameters of CdS nanoparticles deposited on glass and porous silicon substrates

templates	CdS/glass			CdS/PSi					
				CdS30			*CdS60*		
hkl	111			111	202	311	111	202	311
2 θ(°)	26.635			26.679	44.171	51.734	27.095	44.055	5.838
2 θ(°)REF	26.445			26.445	43.866	51.951	26.445	43.866	51.951
Δθ(°)	0.190			0.234	0.305	0.217	0.650	0.189	0.113
FWHM(°)	0.177			0.295	0.413	0.295	0.472	0.708	0.708
Crystallite size D (nm)	46.113			27.671	20.753	29.921	17.309	12.101	12.472
D_{midum} (nm)	46.116			26.115			13.960		
$d_{spacing}$(nm)	0.335	0.204	0.174	0.335	0.204	0.176	0.332	0.206	0.176
d(nm)REF	0.337	0.206	0.176	0.337	0.176	0.176	0.337	0.176	0.176
(δ)x10^{-3}(nm^{-2})	1.518			1.466			5.131		
(ε)x10^{-3}	0.751	2.860	1.847	1.252	1.669	1.158	2.001	2.863	2.778

III.2 Morphological study:
Figure 2 shows the SEM images of CdS thin films deposited on the PSi substrates from two different porosities (35% and 55%)
It can be seen that the structure consists of nanosheets with a vertical orientation, overlapped between them creating a porous morphology. The pores created have a polygonal shape, they are randomly distributed on the surface. The CdS60 has higher pore numbers than the other substrate; this result may be due to the porosity of CdS60, which is higher thanCdS30. We can distinguish clusters of round particles with a diameter from 300 nm to 400 nm on the walls of the pores.
This porous morphology makes the CdS / PSi structure a good candidate for detection systems (Photo-detection and gas sensors), because of the large specific surface area.

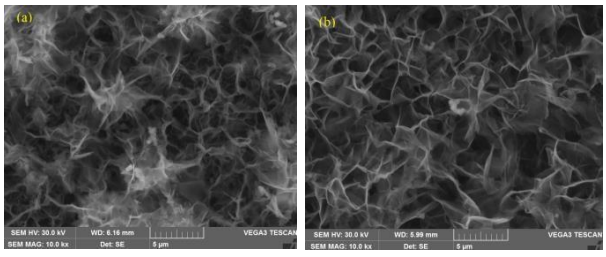

Fig.2. SEM image of CdS thin films deposited on the porous silicon: (a) CdS30, (b) CdS60.

III.3 Optical study:
Figure 3 shows the transmittance as a function of the wavelength for the CdS thin film deposited on glass.
In the wavelength range between 500 and 1000 nm, the transmittance varies between 25 and 55%.Theweak transmittance of the deposited film may be due tothe roughness surface because of the cluster's morphology of the CdS thin films.

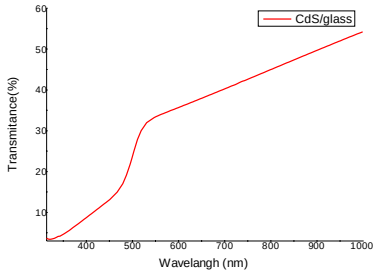

Fig.2. optical transmittance spectrum of CdS nanoparticles

The relation between the energy of the photon andtheoptical absorption coefficient (α) For direct transitions is expressed by the following relation [21], [22]:

$$A(h\nu)= A(h\nu- E_g)^{1/2} \quad (4)$$

Where:
A: constant
Eg: the optical gap [eV]
hν : the energy of a photon.
By scanning the entire energy domain, we have plotted $(\alpha h\nu)^2$ as a function of the energy of the photon E = hν (knowing that: $h\nu\ (eV) = \frac{hc}{\lambda} = \frac{12400}{\lambda(A°)}$ and extend the linear part of $(\alpha h\nu)^2$ up to the x-axis, we obtain the value of Eg (fig.4.)

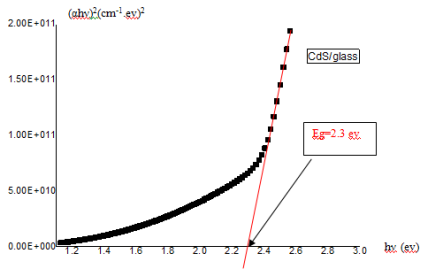

Fig. 4. Determination of the energy gap by extrapolation from the variation of $(\alpha h\nu)^2$ as a function of hν for a thin film of CdS

Fig.4 shows the optical band gap (E_g) of the CdS nanoparticles value for the simple CdS/glass
The value obtained of the energy band gap for the thin film of CdS deposited on glass is 2.3 eV.This value corresponds to what has been found by others[1].

CONCLUSION

Porous silicon layers were fabricated by the electrochemical etching method. CdS nanoparticles were deposited by chemical bath deposition. The XRD spectrum indicated that the CdS thin films have a cubic crystalline phase. The influence of porosity on the CdS nanoparticles properties, including structural and morphological properties, was investigated. CdS60 had the smallest value of particle size,it was around 13.9 nm. The value of the energy band gap of CdS was 2.3 eV.

REFERENCES

[1] Y. Li *et al.*, "Characterization of electronic structures from CdS/Si nanoheterostructure array based on silicon nanoporous pillar array,"*Materials Research Bulletin*, vol. 74, pp. 507–510, Feb. 2016, doi: 10.1016/j.materresbull.2015.11.023.

[2] N. P. Huse, A. S. Dive, K. P. Gattu, and R. Sharma, "An experimental and theoretical study on soft chemically grown CuS thin film for photosensor application,"*Materials Science in Semiconductor Processing*, vol. 67, pp. 62–68, Aug. 2017, doi: 10.1016/j.mssp.2017.05.010.

[3] S. Yadav and P. K. Bajpai, "Effect of Substrate on CuS/PVA Nanocomposite Thin Films Deposited on Glass and Silicon Substrate,"*SNL*, vol. 08, no. 02, pp. 9–19, 2018, doi: 10.4236/snl.2018.82002.

[4] S. T. Kassim, H. A. Hadi, and R. A. Ismail, "Fabrication and characterization of high photosensitivity CuS/porous silicon heterojunction photodetector,"*Optik*, vol. 221, p. 165339, Nov. 2020, doi: 10.1016/j.ijleo.2020.165339.

[5] S. A. Hasoon, I. M. Ibrahim, R. M. Al-Haddad, and S. S. Mahmood, "Fabrication of nanostructure CdS thin film on nanocrystalline porous silicon,"*International Journal of Current Engineering and Technology*, vol. 4, no. 2, pp. 594–601, 2014.

[6] N. Naderi and M. R. Hashim, "Effect of Surface Morphology on Electrical Properties of Electrochemically-Etched Porous Silicon Photodetectors,"*Int. J. Electrochem. Sci.*, vol. 7, p. 7, 2012.

[7] N. Ghellai, A. Chiali, N. E. Chabane-Sari, and N. Gabouze, "Etude et réalisation de capteurs de gaz à base de silicium poreux,"*Synthèse: Revue des Sciences et de la Technologie*, vol. 23, pp. 40–47, 2011.

[8] T. Jalkanen*et al.*, "Fabrication of porous silicon based humidity sensing elements on paper,"*Journal of Sensors*, vol. 2015, 2015.

[9] J. M. Buriak, "Organometallic Chemistry on Silicon and Germanium Surfaces,"*Chem. Rev.*, vol. 102, no. 5, pp. 1271–1308, May 2002, doi: 10.1021/cr000064s.

[10] A. Jane, R. Dronov, A. Hodges, and N. H. Voelcker, "Porous silicon biosensors on the advance,"*Trends in Biotechnology*, vol. 27, no. 4, pp. 230–239, Apr. 2009, doi: 10.1016/j.tibtech.2008.12.004.

[11] T. Jalkanen*et al.*, "Fabrication of Porous Silicon Based Humidity Sensing Elements on Paper,"*Journal of Sensors*, vol. 2015, pp. 1–10, 2015, doi: 10.1155/2015/927396.

[12] A. Rahmani, L. Remache, M. Guendouz, M. s. Aida, and Z. Hebboul, "Impact of the meso-PSi substrate on ZnO thin films deposited by spray pyrolysis technique for UV photodetectors,"*Appl. Phys. A*, vol. 127, no. 5, p. 396, May 2021, doi: 10.1007/s00339-021-04548-z.

[13] C.-M. Chou, H.-T. Cho, V. K. S. Hsiao, K.-T. Yong, and W.-C. Law, "Quantum dot-doped porous silicon metal–semiconductor metal photodetector,"*Nanoscale Res Lett*, vol. 7, no. 1, p. 291, Jun. 2012, doi: 10.1186/1556-276X-7-291.

[14] B. Meier, L. Egermann, S. Voigt, M. Stanel, H. Kempa, and A. C. Huebler, "Drift in the resistance of poly(3,4-ethylenedioxythiophene):poly(styrenesulfonate) printed films during thermal cycling,"*Thin Solid Films*, vol. 519, no. 19, pp. 6610–6612, Jul. 2011, doi: 10.1016/j.tsf.2011.04.225.

[15] K. S. Khashan, "OPTOELECTRONIC PROPERTIES OF ZnO NANOPARTICLES DEPOSITION ON POROUS SILICON,"*Int. J. Mod. Phys. B*, vol. 25, no. 02, pp. 277–282, Jan. 2011, doi: 10.1142/S0217979211054744.

[16] N. F. Habubi, R. A. Ismail, A. N. Abd, and W. K. Hamoudi, "Improved photoresponse of porous silicon photodetectors by embedding CdSe nanoparticles,"*IJPAP*, pp. 562–569, 2003.

[17] S. E. Haque, B. Ramdas, N. Padmavathy, and A. Sheela, "Facile one-pot low-temperature solid-state approach towards phase transformation of nanoCdS,"*Micro & Nano Letters*, vol. 9, no. 10, pp. 731–735, Oct. 2014, doi: 10.1049/mnl.2014.0167.

[18] J. Zhu *et al.*, "Highly efficient wurtzite/zinc blende CdS visible light photocatalyst with high charge separation efficiency and stability,"*J. Chem. Phys.*, vol. 152, no. 24, p. 244703, Jun. 2020, doi: 10.1063/5.0011132.

[19] V. G. Nair, R. Jayakrishnan, J. John, J. A. Salam, A. M. Anand, and A. Raj, "Anomalous photoconductivity in chemical spray pyrolysis deposited nano-crystalline ZnO thin films,"*Materials Chemistry and Physics*, vol. 247, p. 122849, Jun. 2020, doi: 10.1016/j.matchemphys.2020.122849.

[20] D. Komaraiah, E. Radha, Y. Vijayakumar, J. Sivakumar, M. V. R. Reddy, and R. Sayanna, "Optical, Structural and Morphological Properties of Photocatalytic ZnO Thin Films Deposited by Pray Pyrolysis Technique,"*Modern Research in Catalysis*, vol. 5, no. 4, Art. no. 4, Sep. 2016, doi: 10.4236/mrc.2016.54011.

[21] T. Güngör and H. Tolunay, "Drift mobility measurements in a-SiNx:H,"*Journal of Non-Crystalline Solids*, vol. 282, no. 2–3, pp. 197–202, Apr. 2001, doi: 10.1016/S0022-3093(01)00340-4.

[22] T. Gungor, "Ph. D. Thesis,"Hacettepe University, Department of Physics Engeneering, 2001.

Optical filters based on one dimensional dielectric photonic crystal defected by Magnetized cold plasma

Chouaib Chettah
Department of Petrochemical, University 20 August 1955-Skikda.
Hyperfrequency and Semiconductor Laboratory, University Frères Mentouri-Constantine1.
Constantine, Algeria.
chettah_chouaib@yahoo.fr &
c.chettah@univ-skikda.dz

Khaled Chettah
Department of Physics, University Frères Mentouri Constantine 1.
Research center in industrial technologies CRTI, Cheraga, Algiers.
Constantine, Algeria.
khaledphys25@gmail.com

Ouarda Barkat
Department of Electronics, University Frères Mentouri Constantine 1.
Electromagnetism and Telecommunications Laboratory, University Frères Mentouri Constantine 1.
Constantine, Algeria.
barkatwarda@yahoo.fr

***Abstract*— In this paper, a new analysis of optical selective filters containing one dimensional photonic crystal (1D-PC), magnetized cold plasma and dielectric materials are investigated using transfer matrix method. The effects of defective layers on transmission spectrum, the peak position and PBG are investigated as the function of the magnetic field and incidence angle.. It is found that the peak frequencies and the PBG are affected significantly by the magnetic field applied and number of defectives layers. Also, it is demonstrated that the plasma electron density of magnetized cold plasma layer has a significant effect on the transmission spectrum. Results obtained confirmed that it is possible to make a model of a highly selective tunable filter using photonic one dimensional plasma dielectric photonic crystal.**

Keywords*— *Transmission, Photonic Crystals, Magnetized cold plasma, Photonic Band Gap, Defectives layers

I. INTRODUCTION

Advances in plasma photonic crystal technology were encouraging in the realization of the optical filter [1-5]. It is an artificially periodic lattice composed of an alternation of thin non-magnetized or magnetized plasmas and dielectric materials. It is well known that non-magnetized plasma can be characterized by a complex frequency dependent permittivity medium. If an external magnetic field is introduced into plasma and low temperature photonic crystals, a new type of plasma photonic crystals called magnetized cold plasma photonic crystals (MCP-PCs) can be obtained [6-10].

MCP-PCs have attracted a lot of attention due to : their unique electromagnetic properties such as the ease of use of the external magnetic field, their magneto-optical effects based on the properties of PBGs and the ability to control the electron density of the plasma. Several studies suggest that MCP-PCs are emerging as new hot spots in photon engineering due to better control of the external magnetic field on PBGs. In this work, we study and analyze the transmittance as a function of the frequency of the one-dimensional periodic structure of the layers of indium arsenide (InAs) and silicon dioxide (SiO_2) [11,12] with a defective layer of Cold magnetized plasma (MCP) using the transfer matrix method (TMM) Fig.1. The optical constant of the MCP material is adjusted with varying parameters of the plasma. Therefore, we calculate the change in the transmittance of the structure with a defective MCP layer as a function of the angle of incidence, the electron density magnetic field and the thicknesses of the InAs and SiO_2 materials.

In addition, we calculate and compare the transmittance of the structures considered with one and two defective MCP layers. The frequency-dependent transmittance of the considered periodic multilayer structures is analyzed by inserting an MCP plasma layer in the symmetrical structure, for potential application in a tunable multichannel filter in the microwave region.

II. PROBLEM AND THEORY

Consider a one-dimensional photonic crystal structure (1D-PC), which is a periodic structure composed of a multilayer stack. This structure is symmetric in the form $(D_1D_2)^{N/2}$ P $(D_2D_1)^{N/2}$ immersed in free space, shown in Fig.1. There are *N* stacks where each *N/2* period or stack composed of dielectrics mediums indexed (D_1, D_2) and a magnetized cold plasma layer (MCP) layer indexed *P*. Each layer has a thickness d_l, and refractive index n_l. In order to find the formulation of the structure, we assumed that the incident electromagnetic wave from air to the dielectric and plasma layer, the layers are on the *x-y* plane and the *z* direction is normal to layer interface.

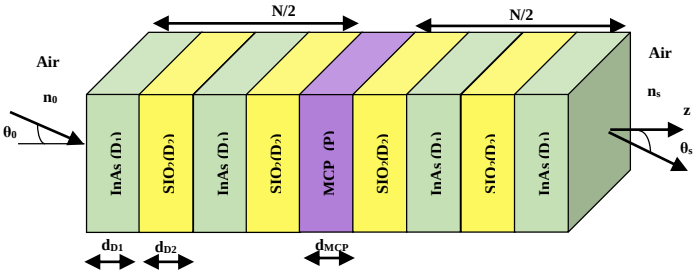

Fig. 1. Schematic representation of the 1D-PC Dielectric-Dielectric defected by MCP material

The refractive index profile of magnetized cold plasma *P* and Dielectric mediums (D_1, D_2) can be given as:

$$\begin{cases} n_{D1} = n_{InAs} = \sqrt{\varepsilon_{D1}} \\ n_{D2} = n_{SiO2} = \sqrt{\varepsilon_{D2}} \\ n_P = n_{MCP} = \sqrt{\varepsilon_P} \end{cases} \quad (1)$$

where ε_P, ε_{D1}, ε_{D2}, n_P, n_{D1}, n_{D2} denote respectively the relatives permittivity and refractive indices of *P*, D_1, D_2 mediums.

From the two fluid models, the complex permittivity of MCP layer *P* is a function of frequency ω and static magnetic field $\tilde{B}$ and can be expressed as [13]:

$$\varepsilon_P(\omega) = 1 - \frac{\omega_{pe}^2}{\omega^2\left(1 - i\frac{\gamma}{\omega} \pm \frac{\omega_{le}}{\omega}\right)} \quad (2)$$

where ω, γ, ω_{pe} and ω_{le} are the angular frequency, the effective collision frequency, plasma and gyro-frequency, respectively. ω_{pe} and ω_{le} are given by:

$$\omega_{pe} = \sqrt{n_e e^2 / m\varepsilon_0} \quad (3)$$

$$\omega_{le} = e\tilde{B}/m \quad (4)$$

where *e*, *m*, n_e and ε_0 are the electronic charge, the electronic mass, the electron density and the free-space permittivity, respectively.

In Eq. (2), the sign (±) in ω_{le} corresponds to the application of a positive or negative external magnetic field, in other words, the static magnetic field is applied in a *d*+*z* or *d*-*z* direction [13].

Based on Maxwell's equations and Boundary conditions, using the boundary conditions and the condition of continuity of *E* and *H* fields we can find out the relationship between the fields (1D-PC) structure consisting of *l* layer, this relation is already exposed by [14-15]:

$$\begin{bmatrix} E_1 \\ H_1 \end{bmatrix} = M_1 M_2 \dots\dots M_N \dots\dots M_{2N} \begin{bmatrix} E_l \\ H_l \end{bmatrix} \quad (5)$$

The matrix M_{l-1} of the l^{th} layer can be written in the form:

$$M_{(l-1)} = \begin{bmatrix} \cos(\delta_{(l-1)}) & i\,\gamma_{(l-1)}\sin(\delta_{(l-1)}) \\ i\,\gamma_{(l-1)}^{-1}\sin(\delta_{(l-1)}) & \cos(\delta_{(l-1)}) \end{bmatrix} \quad (6)$$

$\delta_{(l-1)}$ and $\gamma_{(l-1)}$ being the matrix parameters as a function of the incident angle of light, the optical constants and the thickness of the layer are expressed as:

$$\delta_{(l-1)} = k_{(l-1)}.d_{(l-1)}.\cos\theta_{(l-1)} \quad (7)$$

$$\gamma_{(l-1)} = \begin{cases} \frac{\eta_{(l-1)}}{\cos\theta_{(l-1)}} & \text{TE mode} \\ \eta_{(l-1)}\cos\theta_{(l-1)} & \text{TM mode} \end{cases} \quad (8)$$

where the wave numbers and intrinsic impedances are:

$$k_l = \omega\sqrt{\varepsilon_0\mu_0\varepsilon_l\mu_l} \quad (9)$$

$$\eta_l = \frac{k_l}{\omega\varepsilon_l\varepsilon_0} = \sqrt{\frac{\mu_0\mu_l}{\varepsilon_0\varepsilon_l}} \quad (10)$$

where ε_0, μ_0, ε_l and μ_l are the free space permittivity, free space permeability, relative permittivity, and relative permeability ($\mu_l = 1$),respectively.

Considering the transmission matrix of each layer, we can obtain the transmission matrix of the entire structure. For *l* number of multilayer's; the corresponding transfer matrix can be defined as a product of matrices, and is obtained from the symmetric PBG structure,

$$M = \prod_{k=1}^{(2N)} M_k = \begin{bmatrix} m_{11} & m_{12} \\ m_{21} & m_{22} \end{bmatrix} \quad (11)$$

The product of matrices of (1D-PC) structure with defect layer can be then written as follows [16]:

$$M = \prod_{k=1}^{(2N+1)} M_k = (M_{D1}M_{D2})^N M_P (M_{D2}M_{D1})^{(2N+1)} = \begin{bmatrix} m_{11} & m_{12} \\ m_{21} & m_{22} \end{bmatrix} \quad (12)$$

where M_{D1}, M_{D2} and M_P are the transfer matrixes of the Dielectric and the defect MCP layer. m_{11}, m_{12}, m_{21} and m_{22} are the complex numbers.

The transmittance *t* and reflectance *r* are defined as the ratios of the fluxes of the transmitted and reflected waves, respectively, to the flux of the incident wave. After a few derivations, the total reflection and transmission coefficients are given by [17]:

$$r = \frac{(m_{11} + p_s^{-1}m_{12})p_0^{-1} - (m_{21} + p_s^{-1}m_{22})}{(m_{11} + p_s^{-1}m_{12})p_0^{-1} + (m_{21} + p_s^{-1}m_{22})} \quad (13)$$

$$t = \frac{2.p_0^{-1}}{(m_{11} + p_s^{-1}m_{12})p_i^{-1} + (m_{21} + p_s^{-1}m_{22})} \quad (14)$$

Here p_0 and p_s are the first and last medium of the structure which are given by:

$$p_s^{-1} = \begin{cases} \frac{\eta_s\cos\theta_s}{Z_0} & \text{TE mode} \\ \frac{\eta_s}{Z_0\cos\theta_s} & \text{TM mode} \end{cases} \quad (15)$$

$$p_0^{-1} = \begin{cases} \frac{\eta_0\cos\theta_0}{Z_0} & \text{TE mode} \\ \frac{\eta_0}{Z_0\cos\theta_i} & \text{TM mode} \end{cases} \quad (16)$$

where $Z_0 = \sqrt{\mu_0/\varepsilon_0}$

III. NUMERICAL RESULTS

A. The transmittance of the defective asymmetric & symmetrical structure

To analyze the structure based on InAs/SiO_2 in symmetric and asymmetric by the TMM method, we plotted the transmittance spectrum in Fig.2, using the parameters shown in TABLE I.

TABLE I. THE PARAMETERS OF THE MATERIALS USED [13, 18].

Layer	ε	μ	d [mm]	B [T]	n_e [m^{-3}]	γ [Hz]
InAs	3.3842	1.0	3.1	-	-	-
SiO_2	1.4672	1.0	7.4	-	-	-
MCP	-	1.0	-	0.4	10^{18}	10^7

The transmittance of the asymmetric structure $(InAs/SiO_2)^2$ MCP $(InAs/SiO_2)^2$, shows a large difference as shown in Fig.2a. Likewise, the transmittance of the symmetrical structure $(InAs/SiO_2)^2$ MCP $(SiO_2/InAs)^2$ is analyzed which shows, that the band gap is divided into two bands due to the symmetrical arrangement Fig.2b.

The bandwidth of the defective symmetrical structure increases relative to the asymmetric structure due to the existing defect mode. The transmission fault peak of the symmetrical structure is used in many applications such as filters and laser resonators.

Next, we focus on the study of the symmetrical structure with an MCP plasma defect layer and with the variation of the angle of incidence and parameters of the plasma. As we know that the optical property of the material changes by changing the refractive index of the material as well as the angle of incidence.

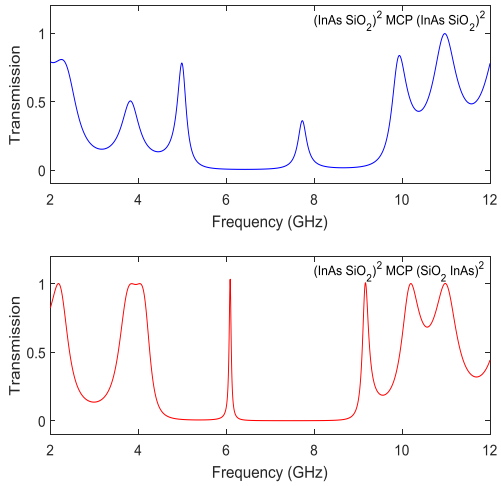

Fig. 2. Transmission spectra as a function of frequency; a) Asymmetric periodic structure, b) Symmetric periodic structure.

B. Effect of varying the angle of incidence

The variation of the angle of incidence plays a large role in the variations of the optical properties of the defective periodic structure considered. Therefore, the transmittance of 1D-PC symmetrical of $InAs/SiO_2$ with a MCP defect is analyzed as a function of the variation of the angle of incidence $\theta=0$, $\theta=\pi/6$, $\theta=\pi/4$ and $\theta=\pi/3$ Fig.3.

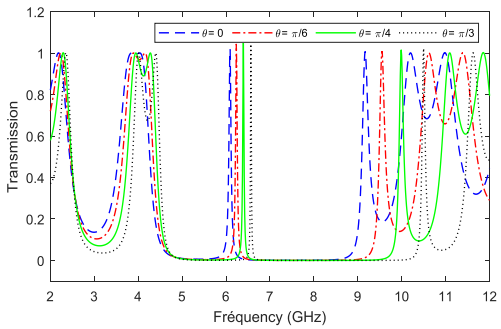

Fig. 3. Transmission spectra of the symmetric 1D-PC structure as a function of frequency for different values of incidence angle.

Fig3 and TABLE II show that the faulty transmission peaks and the forbidden bands are shifted to the higher frequency to increase the value of the angles of incidence and thus form a multiband filter, due to the composite behavior of the dielectric material and plasma. The transmittance shows that the large transmittance shift is obtained for a large value of the angle of incidence $\theta = \pi / 3$.

TABLE II. THE RESONANCE PEAKS AND THE WIDTHS OF THE PBG S OF THE TRANSMISSION OF THE SYMMETRICAL 1D-PC STRUCTURE, FOR THE TE MODE.

θ	**0**	**π/6**	**π/4**	**π/3**
fr [Ghz]	6.096	6.231	6.396	6.562
PBG [Ghz]	5.165	5.361	5.691	6.084

These results can be compared to a 1D-PC structure composed of Dielectric-superconductor with and without the defect layer [19], and analyzed the defect peak which is shifted to a higher frequency when the angle θ. The incidence is increasing, but the multichannel behavior has not materialized. Therefore, we have proposed very simple $InAs/SiO_2$ adhesive materials with an MCP defect layer and a period N=4, model easy to achieve [11, 12].

Our transmittance calculations of a one-dimensional symmetrical structure of Indium Arsenide (InAs), Silicon Dioxide (SiO_2) with an MCP plasma defect layer were better, for multi-channel filter applications having tenability property.

C. Effect of variation of plasma electron density

Electron density can change the frequency of plasma (MCP) and plays a big role in changing its refractive index. In Fig4, we analyze the frequency-dependent transmittance of the periodic multilayer structure of indium arsenide and silicon dioxide with a MCP defect layer, for different values of the electron density.

The transmittance is shifted to low frequencies as the electron density increases due to the decrease in the refractive index value of the plasma. Likewise, the transmission peak is slightly high and shifted towards low frequencies as the electron density increases and the optical constant of the plasma material changes TABLE III. Therefore, the electrical permittivity of the MCP plasma material changes due to the electron density. The results obtained from the transmittance appear as a tunable multichannel filter in the microwave region.

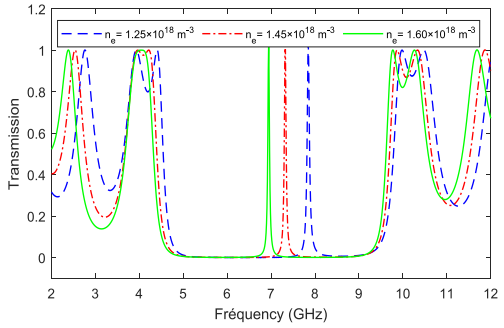

Fig. 4. Transmission spectra as a function of the frequency of the symmetric 1D-PC periodic structure for different values of the electron density of the plasma.

TABLE III. THE RESONANCE PEAKS AND THE TRANSMISSION PBGS FOR DIFFERENT VALUES OF THE ELECTRON DENSITY OF THE PLASMA.

n_e [m^{-3}]	1.25×10^{18}	1.45×10^{18}	1.60×10^{18}
fr [Ghz]	7.853	7.327	6.937
PBG [Ghz]	5.591	5.646	5.586

D. Effect of magnetic field

The electrical permittivity of MCP plasma can change by the external magnetic field because the gyroscopic frequency depends on the magnetic field. The external magnetic field changes the refractive index of the MCP plasma.

This means that the transmittance of the periodic structure containing plasma also varies with the magnetic field in MCP plasma. We have studied the transmittance of the periodic structure of InAs/SiO_2 with a defective layer of MCP plasma as a function of the variation of the applied external magnetic field, B = 0.1T, B = 0.2T, B = 0.3T, this is shown in Fig. 5. The transmittance as a function of the frequency and the variation of the external magnetic field was analyzed. The transmission peak has shifted to the higher frequency due to the effect of the MCP material at optical constant TABLE IV. As the magnetic field increases, each band is shifted to the highest frequency corresponding to the value of the magnetic field. This shows that the tunable multichannel filter is obtained by an external magnetic field for microwave devices.

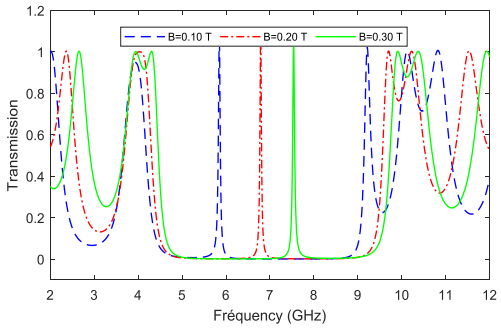

Fig. 5. Transmission spectra as a function of frequency of the symmetric 1D-PC periodic structure for different values of the magnetic field.

These results also compare a new tunable filter comprising a fault mode of the TE wave of a one-dimensional photonic crystal doped with a magnetized plasma and the transmission spectra of the periodic structure of dielectric (SiO_2) and dielectric (air) materials. The transmittance spectra as a function of the frequency are analyzed with MCP plasma defect on the variation of the magnetic field, the density of the plasma and the electron density, their interest is in the tunable filter [20].

TABLE IV. THE RESONANCE PEAKS AND PBG S OF THE TRANSMISSION FOR DIFFERENT VALUES OF THE MAGNETIC FIELD.

B	1.0	2.0	3.0
fr [Ghz]	5.841	6.787	7.538
PBG [Ghz]	5.21	5.586	5.661

E. Resonant structures and the quality factor Q

In Fig6, we have reported the variation of the transmission spectra as a function of the frequency of a symmetrically shaped 1D-PC structure, the aim of which is to study the relationship between the number of fault layers and the fault modes.

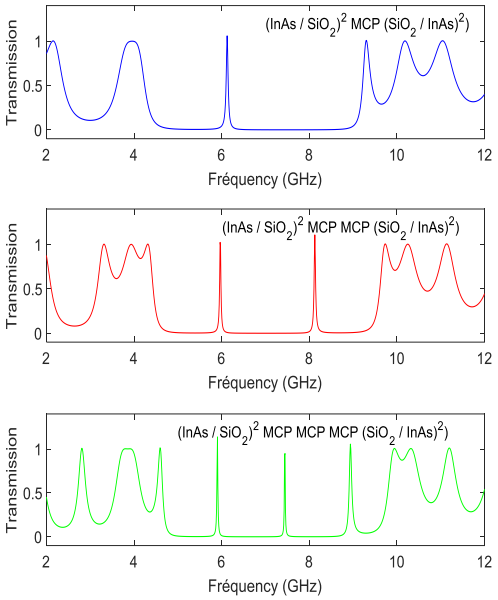

Fig. 6. Transmission spectra as a function of the frequency of the symmetric 1D-PC periodic structure for deferent numbers of defect layers, (θ = 0, TE mode, $\gamma = 1.0\times10^7$, $n_e = 1.0\times10^{18}$, B = 0.30 T); (dInAs = 3.1mm, $dSiO_2$ = 7.4mm, dMCP = 12.0mm); (nInAs = 3.3842, $nSiO_2$ = 1.4672).

TABLE V. RESONANT FREQUENCY AND QUALITY FACTOR Q FOR DIFFERENT CONFIGURATIONS.

Configuration	**Peaks**	**f_r**	**Q**
$(InAs\text{-}SiO_2)^2$ MCP $(SiO_2\text{- }InAs)^2$	1st Peak	6.126	1531.5
$(InAs\text{-}SiO_2)^2$ MCP MCP $(SiO_2\text{- }InAs)^2$	1st Peak	5.976	181.1
	2nd Peak	8.123	203.1
$(InAs\text{-}SiO_2)^2$ MCP MCP MCP $(SiO_2\text{-}InAs)^2$	1st Peak	5.901	85.5
	2nd Peak	7.447	354.6
	3rd Peak	8.934	124.1

Our results imply that the number of defects can be increased by adding defective layers in the 1D-PC structure of the symmetric shape, and for the filter to be more selective, we choose the first configuration or Q = 1531.5 Table V.

IV. CONCLUSION

In this work, a new design and analysis of one-dimensional defective photonic crystal structure, containing the magnetized cold plasma and Dielectric layer are presented. Theoretical results in terms of the transmission spectra for the various (1D-PCs) configurations were presented, and theoretically investigated by the transfer matrix method (TMM). Current simulations show that the width of the photonic band gap can be adjusted by modifying the magnetic field. In case of fixed the MCP layer's thickness, also magnetic field could increase the width of the phonic band gap. The number of the defect modes can be controlled by adjusting the number of defect layers in the structure. Therefore, the proposed structure configurations may be of potential use and interest in many applications such as optical communication selective filters.

RÉFÉRENCES

[1] B. Guo, "Photonic band gap structures of obliquely incident electromagnetic wave propagation in a one-dimension absorptive plasma photonic crystal," vol. 16, no. 4, p. 043508, 2009.

[2] H. Hojo and A. Mase, «Electromagnetic-wave transmittance characteristics in one-dimensional plasma photonic crystals," vol. 8, p. 477-479, 2009.

[3] W. Fan and L. Dong, «Tunable one-dimensional plasma photonic crystals in dielectric barrier discharge," vol. 17, no. 7, p. 073506, 2010.

[4] L. Qi, "The absorbing properties of one-dimensional plasma photonic crystals," vol. 82, no. 1, 2016.

[5] M. M. Abadla et al., "Properties of ternary photonic crystal consisting of dielectric/plasma/dielectric as a lattice period," vol. 185, p. 784-793, 2019.

[6] L. Qi, Z. Yang and T. Fu, "Defect modes in one-dimensional magnetized plasma photonic crystals with a dielectric defect layer," vol. 19, no. 1, p. 012509, 2012.

[7] Aly, A. H., Elsayed, H. A., Ameen, A. A., & Mohamed, S. H. "Tunable properties of one-dimensional photonic crystals that incorporate a defect layer of a magnetized plasma," vol. 31, no. 31, p. 1750239, 2017.

[8] T.-W. Chang, J.-R. C. Chien and C.-J. Wu, "Magnetic-field tunable multichannel filter in a plasma photonic crystal at microwave frequencies," vol. 55, no. 4, p. 943-946, 2016.

[9] A. Aghajamali, "Transmittance properties in a magnetized cold plasma–superconductor periodic multilayer," vol. 55, no. 23, p. 6336-6340, 2016.

[10] Chettah, C., Barkat, O. & Chaabi, A. Tunable Properties of Optical Selective Filters Based on One-Dimensional Plasma Superconductor Photonic Crystal. J Supercond Nov Magn (2021). https://doi.org/10.1007/s10948-021-05891-1

[11] Parm, I. O., Roh, Y., Hong, B., Park, C. S., & Yi, J., "The improvement of the SiO_2/InAs interface properties with the aid of fast electron irradiation in a direct current sputter deposition system," vol. 172, no. 3-4, p. 295-300, 2001.

[12] N. Valisheva et al., "Electrical properties of InAs-SiO_2-In 2 O 3 MIS structures with a modified interface," vol. 38, no. 2, p. 87-94, 2009.

[13] H. G. Booker, Cold Plasma Waves (Springer-Verlag, 1984), pp. 23–25.

[14] Scotognella, F.:Four-material one dimensional photonic crystals. Elsevier, Optical Materials. 34, 1610-1613 (2012)

[15] Oraizi H., Abdolali, A.:Several theorems for reflection and transmission coefficients of plane wave incidence on planar multilayer metamaterial structures. IET Microw. Antennas Propag. 4, 1870–1879(2010)

[16] Aly, A. H., Sabra, W., Abdel-Rahman, E.: Investigation of the transmittance in superconducting photonic crystal. Progress in Electromagnetics Research Symposium Proceedings, KL, MALAYSIA, March 27-30 (2012)

[17] Wu, C.-J. : Transmission and Reflection in a Periodic Superconductor/Dielectric Film Multilayer Structure. Journal of Electromagnetic Waves and Applications. 19, 1991–1996 (2005)

[18] D. E. Aspnes and A. Studna, "Dielectric functions and optical parameters of si, ge, gap, gaas, gasb, inp, inas, and insb from 1.5 to 6.0 ev," vol. 27, no. 2, p. 985, 1983.

[19] B. Mamri and O. Barkat, "Design of a Selective Filter Based on One-dimensional Superconductor Photonic Crystal," vol. 32, no. 11, p. 3397-3405, 2019.

[20] Kong, X., Liu, S., Zhang, H., & Li, C., "A novel tunable filter featuring defect mode of the TE wave from one-dimensional photonic crystals doped by magnetized plasma," vol. 17, no. 10, p. 103506, 2010.

Structure of the proposed RI biosensor (sensor with two functions)

Abderraouf HOCINI[1,*], Assia DAAS[1], Abdesselam HOCINI[2], Souheil MOUETSI[1]

[1] Department of Electrical Engineering, Faculty of Sciences and Applied Sciences,Pole Ain Beida, University of Oum El Bouaghi, 04201. Algeria.
[2] Laboratoire d'Analyse des Signaux et Systèmes, Department of Electronics, University of M'Sila BP.166, Route Ichebilia, M'Sila, 28000, Algeria.

*Email: raoufho28@gmail.com hocini.abderraouf@univ-oeb.dz

Abstract. Photonic sensors, in light of proposed structures comprised of rhombus–molded gaps matched with two waveguides, have been developed as another enthusiasm for specialists in science and technology. In this paper, it has been demonstrated that by utilizing the rhombus–formed openings examination, they got outcomes which are brilliant inside the depression locale. Consequently, the quality factor (Q) and the affectability (S) can be essentially improved for the proposed structure. This investigation are performed by reproduction utilizing limited contrast time area (FDTD). Different affectability are acquired as 565.38 nm/RIU and quality factor as high as 2.61×10^{5}have been accomplished, deducing in a location breaking points 1.03×10^{-6}. This blend angle gives the proposed structure an extra exhibition as a component to play out a name free biosensing for the biomedical visualization.

1. Introduction

Optical sensors, that offer prompt revelation and measurement of organic investigation, have pulled in an extraordinary consideration owing to their promising highlights, for example, security in a burnable and hazardous environment, assurance from electromagnetic impedances, snappy reaction and the separated web based detecting capacity. Photonic gems (PhC) are occasional dielectric components with the capacity to screen and control light age and stream. The periodicity can be shaped by embedded and punctured openings in a dielectric component, making a photonic band hole (PBG) area [1–2]. PhC have been utilized in few applications, as in twist waveguides, channels, sensitizers, lasers, amplifiers, and resonators. Among those optical innovations, receptive photonic precious stone (PhC) built sensors have gotten a lot of consideration because of their microcosmic size, their high affectability, negligible model preparing denied of fluorescence classifying and the chance of participate in MEMS (Micro Electro-Mechanical Systems) [3]. More often than not, it is about physical and compound/biochemical challenges, the PhC sensors offer an incredibly solid narrow mindedness inside the substance to be broke down, because of the effect of the photonic taboo band [4].The light can be packed in an extremely little volume, communicating with a colossal fluid light [5]. This wonder leaves the sensors to be very sensitive to minor refractive list (IR) factors that are shaped by the natural medium, with limits on the dividers of the PhC test. The examination is completed continuously and doesn't require the utilization of markers (bio-location without name). The acquired discoveries can be improved via doing advancements in the sensor frameworks, for instance a warmth balance, the movement of the coupling and the topological streamlining of the geometry (shape, opening size, thickness and Si level). At this premise, an assortment of IR sensor proposition have been broken down and acknowledged by means of various sorts of PhC structures, for example, smaller scale depressions [6-7-8], waveguides [9-10], Slotted waveguides [11-12-13-14], hetero-structures [15], from which critical advancements in detecting stages have been arranged. A large portion of these arranged sensors work as a solitary thought or sensor and the quantity of brands that can be veiled on one event is very

little. So, as to ease this lack, the fundamental thought is to build up a framework to permit blending a few research thoughts on a colossal substrate. That is the reason PhC-based sensors have been imagined and tried. A few photonic gem topologies have been proposed in the writing for structure of biosensors, contrasted and photonic precious stone smaller scale hole which has more deformity modes and optical restriction impact. So, as to improve the affectability of photonic precious stone miniaturized scale hole sensor, it is important to propose a sensor structure with colossal optical confinement impact [16-17-18-19].

In this paper, we depict the system and the reproduction procedure of the proposed PhC biosensor that is speculatively utilized for evaluating the glucose's focus. Considering the silicon-on-encasing (SOI) innovation, the planned structure is molded by two waveguides with ring-formed openings pit framework. The detecting standard depends on the move of reverberation frequency λ0, which occurs because of the adjustment in RI of the sensor when the PhC's air gaps are involved by a homogenous demonized water (n = 1.33) or other fluid (distilled water n = 1.3147, methanol n = 1.316, acetone n = 1.3445, isopropyl alcohol n = 1.363 [20]).For the glucose recognition, it has been affirmed that the resounding frequency design changes its unearthly position following a direct demonstration when the glucose fixation somewhere in the range of 0% and 60% is applied. The properties of the sensor are reproduced utilizing the limited distinction time-space (FDTD) calculation (RSoft CAD). In theory and statistics, light concentration in photonic crystals is estimated by resolving Maxwell's calculations in a varied dielectric medium, stated in equations (1)and (2); E and H are the electric and magnetic field intensities.

$$\nabla\times E(r,t)=-\frac{\partial}{\partial t}\left[\mu_0.H(r,t)\right] \quad (1)$$

$$\nabla\times H(r,t)=-\frac{\partial}{\partial t}\left[\varepsilon.\varepsilon_0(r).E(r,t)\right] \quad (2)$$

μ is the permeability which equals to μ0 as the measured material is non-magnetic,
ε :symbolizes the permittivity which is habitually written as $\varepsilon=\varepsilon_0.\varepsilon(r)$, where ε_0 is the permittivity of vacuum and ε(r) is the relative permittivity of the material.

Equation (3) is obtained by solving Equation (1) and inserting it into the time derivative of Equation (2):

$$\nabla\times\left[\frac{1}{\varepsilon(r)}\nabla\times H(r,t)\right]=-\frac{\partial^2}{\partial t}\left[\mu_0.H(r,t)\right] \quad (3)$$

Assuming harmonic time dependence for the magnetic field with angular frequency ω.
$H(r, t) = H(r)\, e^{-i\omega t}$, we obtain the master equation for the magnetic field:

$$\nabla\times\left[\frac{1}{\varepsilon(\vec{r})}\nabla\times H(\vec{r})\right]=\left(\frac{\omega}{c}\right)^2 H(\vec{r}) \quad (4)$$

The spatial and temporal steps are related through this equation:

$$\Delta t\leq\frac{1}{c}\left(\Delta x^{-2}+\Delta y^{-2}\right)^{1/2} \quad (5)$$

Where c is the speed of light in vacuum,
Δx and Δy are spatial stages in the *x*and *y*directions, respectively.

In order to terminate the computational field, the perfectly matched layers (PMLs) are employed [21].

2. Materials and theoretical model

The proposed plan depends on a 2D-PhC structure. It comprises of a periodical triangular grid of air-expanded gaps punctured in a silicon (Si) piece (refractive list n_{si}=3.45).The range of the air openings is r=0.38a, with a cross section steady a=550 nm, the thickness of the PhC chunk is set as h=230 nm. The Silicon dioxide (SiO_2) layer with a thickness of 1500 nm and low refractive record is utilized as a supporting layer to the high filed Silicon based chunk, to keep light to the pit center, forestalling optical misfortunes in the lower substrate, and the light detainment in the vertical course is then protected by full interior reflection. So as to

diminish the computational time which may happen in 3D structures, the PhC is changed into a 2D framework with the dielectric medium having the viable refractive file of 2.868, which relates to the powerful file of the focal guided TE mode. For the accompanied numerical reenactments, we have applied the powerful file approach given in [22], in blend with two different techniques specifically the 2D-PWE and the 2D-FDTD from the RSoftprogramming bundle. The dispersal properties of the deliberate PhC structure have been investigated utilizing the 2D-PWE technique in Band SOLVE programming. For the TE polarization, the photonic band hole (PBG) covers the scope of ω_1=0.278(a/λ) to ω_2=0.4 (a/λ) comparing to the wide frequency goes of1323.7>λ>1908.1 nm.

Subsequently, the viable working frequency extend is adequate to satisfy the detecting need, where the full mode creates a wide frequency move. Figure 1 shows the schematic of the planned biosensor. This last comprises of two waveguide couplers and one cavity. The two waveguides are acquired by expelling one column of air-expanded gaps in the x course, to couple light source in and out the Silicon section punctured ring-molded gaps PhC depression.

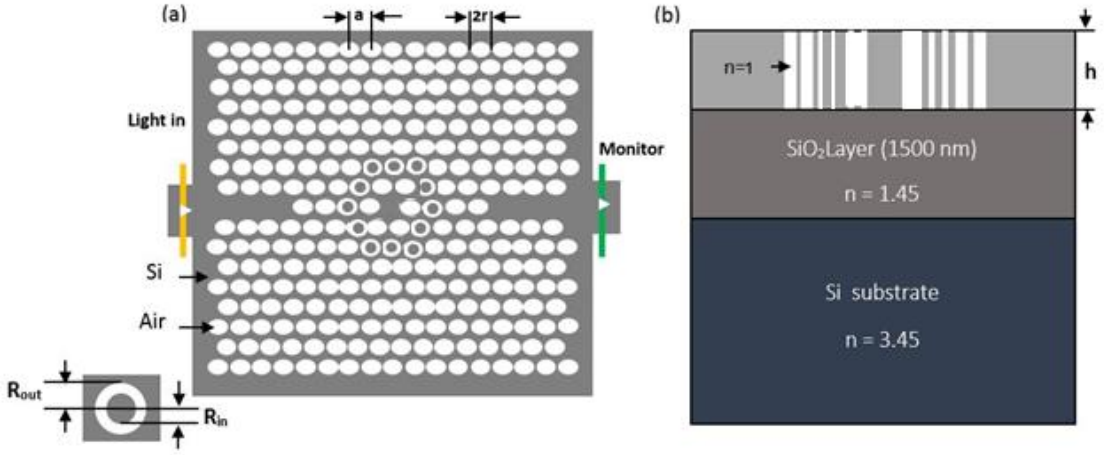

Figure 1. (a) Schematic diagram of the proposed rhombus-shaped photonic crystalcavity coupled to an input and output the PC waveguides.
(b)Schematic side and sectional view of the proposed PC biosensor structure in SOI substrate.

It is important to note that the ring-formed gaps arrangement doesn't just give greater adaptability as far as planning new structures in correlation with to roundabout molded ones, but also to improve the optical field containment, thus light-liquid cooperation inside the ring of low-dielectric material territory [23-24].

The ring-formed gap parameters are characterized by their internal and external range Rin=121nm (0.22a) and Rout=247.5 nm (0.45a) individually.In this manner the ringed air-expanded district is given by Rout−Rin=126.5 nm. The entire depression framework is isolated from the info and yield waveguides by three PhC gaps.

Two-dimensional limited contrast time-area (2D-FDTD) technique is utilized to gauge the structure's usefulness, considering the Perfect Matched Layers (PML) conditions in computations, to guarantee no back appearance in the broke down locale's breaking point.

In reproduction process, a TE energized Gaussian optical heartbeat, covering the entire recurrence scope of intrigue, is propelled at the information port to energize the hole modes. A force screen was put toward the finish of the yield waveguide to gauge the transmitted sign, and to improve the reproduction's precision, FDTD investigation is completed with a lattice size of0.01 nm.

3. Sensing properties of the designed structure

So, for showing the working head of the PhC pit based RI biosensor, a progression of FDTD reproductions have been led. The starter detecting examination is finished by assuming the neighborhood penetration of de-ionized (DI) water in the hole detecting zone, this compares to the change in refractive file (RI) of the ring molded gaps from 1.33 (DI-water) to 1.332305450 of (0 g/l to 60 g/l).

The relation between both the glucose's RI n and concentration C, can be expressed as follows [25]:

$$n = 0.00011889.C + 1.33230545 \quad (6)$$

For a neighborhood invasion, an exact system dependent on small scale penetration innovation by means of empty submicron size pipettes has been tentatively shown in [26]. This strategy permits to control a fluid affidavit inside an ideal PhC gap, and not influencing the nearby ones.

For assessing the usefulness of the structure, for instance fluid, should be in contact with the sensor, and the reproduction is done by changing the RI of the gaps from 1.3147 (refined water) to 1.363 (isopropyl liquor). This prompts a move in the yield transmission range that relates to an adjustment in the RI.

Figure 2, the quality factor, sensitivity and transmission spectrum of resonant mode will change with N .

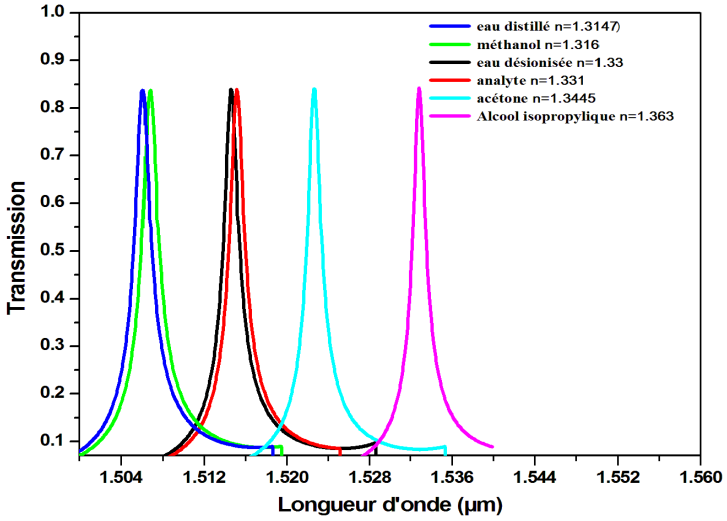

Figure 2. Transmission spectra.

Normalized transmission spectrum of the PC cavity as a function of wavelength is also illustrated in figure 2. According to changing the RI of the gaps from 1.3147 (refined water) to 1.363 (isopropyl liquor). we can find that the normalized transmittance remains the same and can reach to 84.5. It can be seen in this figure that when the number of functionalized holes increases, the resonant wavelength shifts to ward larger amounts. Figure 2is in their lower values, which can explain the choice of the local infiltration instead of the total infiltration.

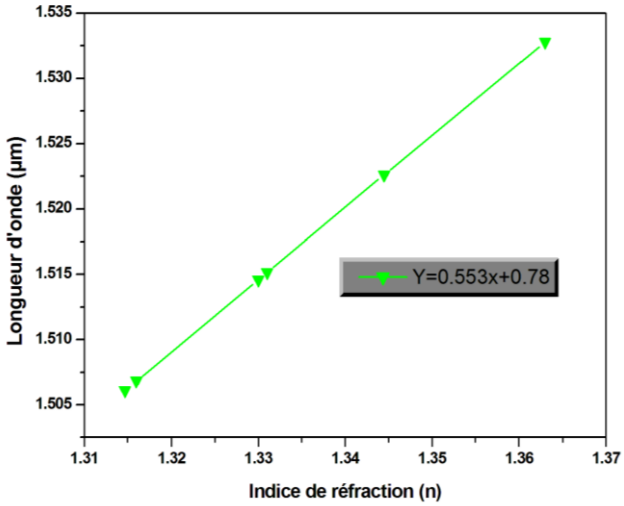

Figure 3. Resonant wavelength shift as a function of the RI n.

From figure 3, and if we assume that the relationship between the resonance shift and the refractive index is approximately linear,equation7 describes the resonance displacement for a given liquid index to predict the resonant frequency after a linear fit of the simulation data:

$$Y[\mu m] = (0.553.x + 0.78)[\mu m] \quad (7)$$

The quality factor of the proposed structures are calculated for different refractive indices as shown in the following figure:

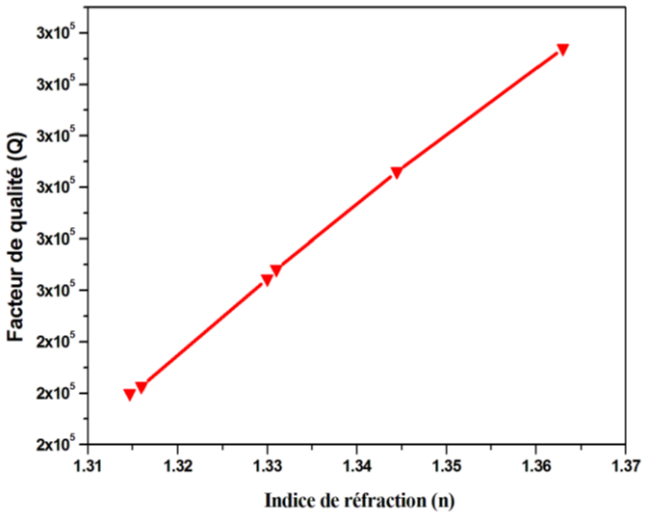

Figure 4. the Q factor variations according to the change of RI.

Note in the figure above that the quality factor Q increases with the increase in the refractive index.

Table 1. Biosensor sensitivity optimized for different liquids

Liquide	Indice de réfraction	Sensitivity (nm/RIU)	Δn(RIU)
L'eau distillée	1.3147	554.9	0.0153
Méthanol	1.316	554.29	0.014
L'eau déionisée	1.33	-	n_0
Analyte	1.331	550	0.001
Acétone	1.3445	553.1	0.0145
Alcool isopropylique	1.363	551.52	0.033

Table 2. Comparison of performance's parameters of the proposed biosensor with various similar PC-based designs.

Références	Type du capteur	Sensibilité (nm/RIU)	Δn
[22]2008	biocapteur RI formé de deux guides d'ondes et une microcavité	330	0,001
[23]2011	Capteurs RI à base de guide d'onde à CP	240	-
[24]2011	Capteurs RI à base de guide d'onde à CP	200	0,0014
[25]2012	Capteurs à base de cavité L3 à CP	35	0,038
[26]2013	Biocapteurs RI à base de guided'onde à CP	260	0,001
[27]2015	biocapteur RI formé de deux guides d'ondes et une microcavité	425	0,001
[28]2017	biocapteur RI formé de deux guides d'ondes et une microcavité		
Notre travail 2020	Design of high sensitive glucose concentration sensor based on ring-shaped holes photonic crystal cavity	550	0,001

The spectral response of the cavity as a function of changes in the refractive index, corresponding to the infiltration of the aqueous solution with the seven cases of glucose concentration is shown in the following figure:

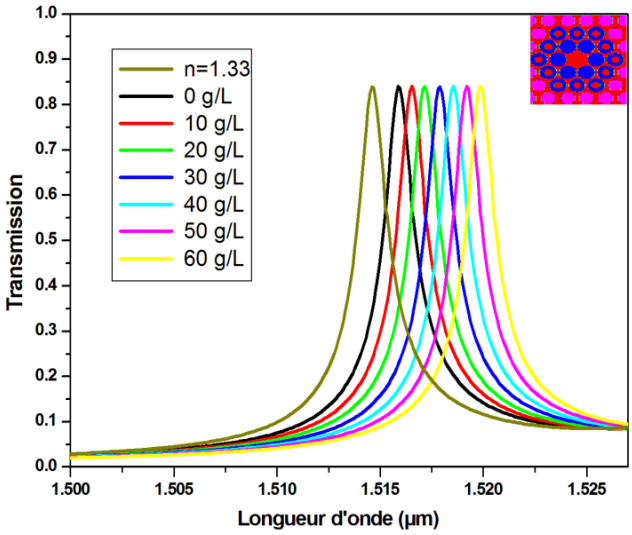

Figure 4. Normalized transmission spectrum of the PC microcavity as a function of wavelength .

The resonance peak located at 1514.6 nm ($a / \lambda = 0.363$) is identified as a reference mode corresponding to 0 g/l of glucose concentration. It should be noted that as the glucose concentration increases, the cavity mode shifts in response to the increase in refractive index from 1.33230545 to 1.33943885.

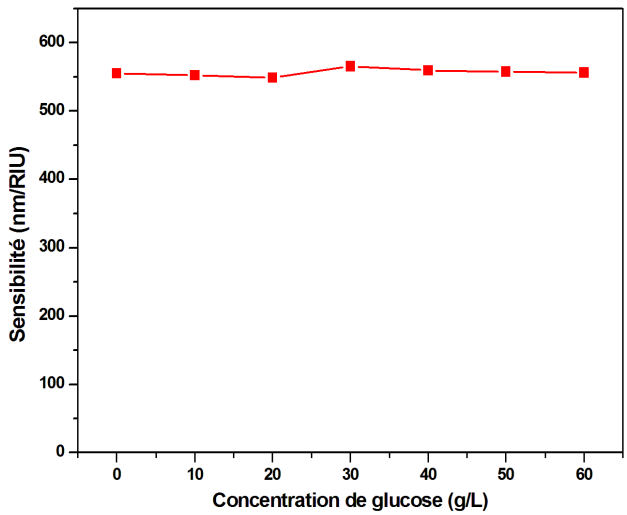

Figure 5. The S variations according to the change of the glucose concentration.

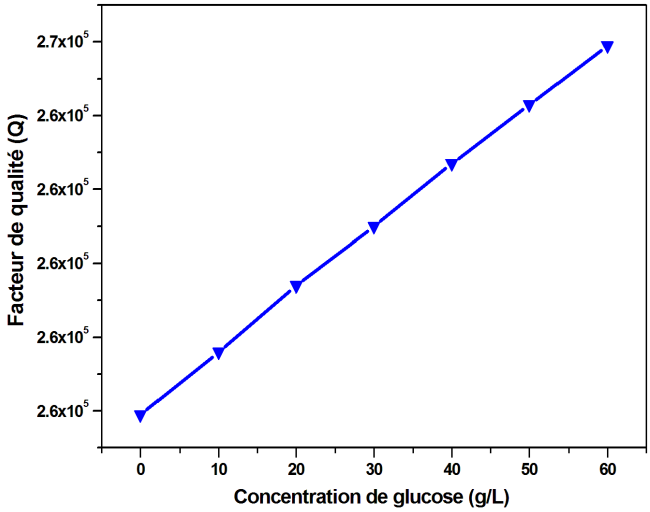

Figure 6. The Q factor variations according to the change of the glucose concentration.

As shown in figures (5 and 6), the sensitivity and the quality factor increase by increasing the glucose concentration (0 g/l - 60 g/l).

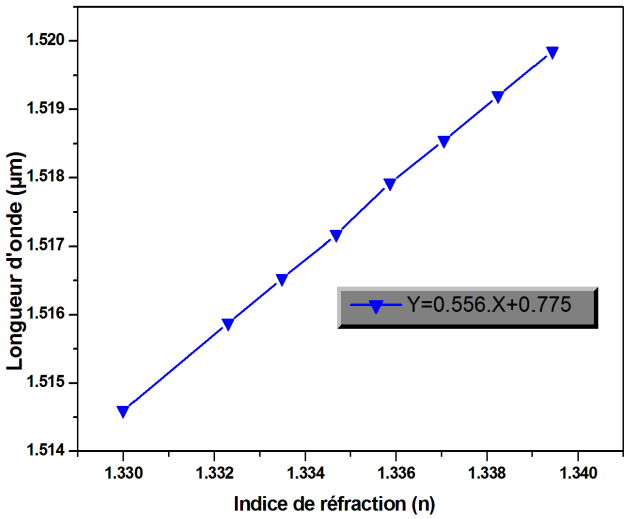

Figure 7. Resonant wavelength shift as a function of the RI n.

From figure 7, and if we assume that the relationship between the resonance shift and the refractive index is approximately linear, equation 8 describes the resonance displacement for a given liquid index to predict the resonant frequency after a linear fit of the simulation data:

$$Y[\mu m] = (0.556.x + 0.775)[\mu m] \quad (8)$$

Table 3. Comparison of performance's parameters of the proposed biosensor with various similar PC-based designs.

Référence	Structure de détection	S(nm/RIU)	Q	DL(RIU)
[22] 2008	Biocapteur formé par deux guides d'ondes et unemicrocavité.	330	$3{,}82\times10^{3}$	_
[30] 2017	Biocapteur constitué d'une nanocavité de type H2 et d'un guide d'onde W1à large bande.	131,70	$2{,}96\times10^{3}$	_
[22] 2008	Capteur à base de cavité à fente annulaire couplée à desguides d'ondes d'entrée et de sortie.	160	10^{7}	$8{,}75\times10^{-5}$
[29] 2014	Capteur constitué d'une cavité résonnante en forme d'anneau couplée à des guides d'ondes d'entrée et de sortie.	330	$8{,}2\times10^{6}$	$1{,}24\times10^{-5}$
[28] 2012	Capteur consistant en une cavité en anneau couplée à unguide d'onde optofluidique à lumière lente.	293	950	_
[31] 2017	Biocapteur basé sur un couplage d'une cavité de trous enforme d'anneau et de deux guides d'ondes d'entrée et desortie	462,61	$1{,}112\times10^{5}$	$3{,}03\times10^{-6}$
Dans ce travail 2021	Biocapteur basé sur un couplage d'une cavité de trous en forme losange et de deux guides d'ondes d'entrée et de sortie	520,5	$3{,}247\times10^{6}$	$8{,}99\times10^{-7}$
	Structure avec deux fonctions	**565,38**	$\mathbf{2{,}610\times10^{5}}$	$\mathbf{1{,}03\times10^{-6}}$

4. Conclusions

This work presents a new design for a PC-based cavity. The device structure consisted of two waveguides (input and output) in a 2-D-PC-Si-based layer, with a triangular lattice rhombus-shaped air holes. For the PC-based rhombus-shaped holes PC-RSH cavity, it has been demonstrated that a change in the RI of the rhombus contents corresponds to an increase in the glucose's concentration analyte. The variation in this latter is analyzed by using the FDTD method embedded in the commercial simulator RSoft. Various sensitivities of 565.38 nm/RIU and quality factor as high as 2.61×105have been accomplished, deducing in a location breaking points 1.03×10^{-6}. have been attained, respectively. Our proposed design with its four basic Structure of the proposed RI biosensor (sensor with two functions) can be implemented and used in many applications in the detection process of organisms and is a potential candidate for nanoscale sensors and so on.

5. References

[1]. Liedberg B, Lundström Iand Stenberg E 1993 *Sensors and Actuators B. Chemical*.*J*.**11**6372

[2]. HeidemanRG,Lambeck PV 1999*Sens. Actuators B Chem*.*J*.**61**100127

[3]. Scherer A, Painter O, Vuckovic J, Loncar MandYoshie T. 2002 *IEEE Transactions On Nanotechnology*.*J*.**8** 411.

[4]. Mortensen N A, Xiao Sand Pedersen J 2007 *Microfluidics and Nanofluidics*. *J*.**4** 117127

[5]. Caër C,Serna-Otálvaro S F,Zhang W,Le Roux XandCassan E2014*Opt. Lett.J.***39**57925794
[6]. Benmerkhi A,Bouchemat MandBouchemat T 2016*Optik. J.***127**56825687
[7]. Hocini A,Moukhtari R,Khedrouche D,Kahlouche AandZamani M2017 *Opt. Commun.J.***384**111117
[8]. Dutta H S,Pal S,2013*Opt. Quantum Electron. J.***45** 907917
[9]. Bougriou F,Bouchemat T,Bouchemat MandParaire N2013*Eur. Phys.Appl. Phys.J.***62**11201
[10]. Zhang Y,Zhao Y,Wang Q2013*Sens. Actuators BChem.J.***184**179188
[11]. Lai W C,Chakravarty S,Wang X,Lin CandChen RT.2011*Opt. Lett. J.***36**984986
[12]. Harhouz A,Hocini A2015*Electromagn. Wave Appl. J.* **29** 659667
[13]. Hocini A,Harhouz A2016 *Nanophotonics. J.***10** 016007016010
[14]. Di Falco A,O'Faolain LandKrauss TF.2009*Appl.Phys. Lett. J.* **94**06350310635033
[15]. Säynätjoki A,Mulot M,Vynck K,Cassagne D,Ahopelto JandLipsanen H. 2008 *Nanostruct. Fundam. Appl. J.* **6** 4246
[16]. Qiu M2002*Appl.Phys. Lett.J.* **81**1163
[17]. Kafesaki M,Soukoulis CMandAgio M.2002 *applied physics. J.***96** 40334038
[18]. Dutta H S,Goyal A K,Pal S2014 *Nanophotonics.J.***8** 083088083088
[19]. RigamontiG,Bello V,MerloS 2018*Sensors . J.***18**603
[20]. Yeh YL2008 *Opt. Lasers Eng. J.* **46** 667670
[21]. Dorfner DF,Hurlimann T,ZabelT,Frandsen LH,AbstreiterGandFinley JJ2008*Appl.Phys. Lett. J.***93**. 181103181106
[22]. Faraon A,Englund D,Fushman I,Vučković J,Stolz NandPetroff P2007*Appl.Phys. Lett.J.***90**213110213113
[23]. Loncar M,Scherer A2004*Optical Microcavities*(World Scientific Publishing)
[24]. Zhou J,Tian H,Yang D,Liu Q and Ji Y 2014 *Opt. Commun.J.* **330**175183
[25]. Benmerkhi A,Bouchemat M andBouchemat T 2016 *Photonics Nanostruct.J.***20**717
[26]. Huang L,Tian H,Zhou J,Liu Q,Zhang P andJi Y2015*Opt. Commun.J.***335**7377
[27]. Arafa S,Bouchemat M,Bouchemat T,Benmerkhi A andHocini A2017*Opt. Commun.J.***384**93100
[28]. Benelarbi D, Bouchemat T and BouchematM2017*Opt Quant Electron.J.* **49** 347
[29]. Arafa S,Bouchemat M,Bouchemat TandBenmerkhiA2017*Optik.J.***131**4957
[30]. White I M,Fan X 2008*Opt. Express .J.***16**10201028
[31]. Dominguez-Juarez J L,Kozyreff GandMartorell J2011*Nat. Commun.J.***2** 18

A Low-Power and High Sensibility of the Smart CMOS(Si and 4H-SiC) Temperature Sensor in 130nm Technology

Mourad HEBALI
Department of Electrotechnical, University Mustapha STAMBOULI of Mascara, 29000 Mascara, Algeria.
Laboratory CaSiCCe, ENP Oran-MA, 31000 Oran, Algeria.
mourad.hebali@univ-mascara.dz

Hocine Abdelhak AZZEDDINE
Department of Electrotechnical, University Mustapha STAMBOULI of Mascara, 29000 Mascara, Algeria.

Menaouer BENNAOUM
Department of Electrotechnical, University Mustapha STAMBOULI of Mascara, 29000 Mascara, Algeria.

Benaoumeur IBARI
Department of Electrotechnical, University Mustapha STAMBOULI of Mascara, 29000 Mascara, Algeria.

Abstract— **One of the many applications of CMOS technology is the design the temperature sensors. In this paper, the electrical performance of smart CMOS(Si and 4H-SiC) temperature sensor in 130 nm technology have been studied using OrCAD PSpice software. The proposed CMOS circuit is developed to provide the first smart temperature sensor based on two different semiconductor technologies (Si and 4H-SiC) integrated on the same chip. These technologies are activated separately according to the temperature range (Low and High). The study of this smart sensor have shown that they operate under a low voltage less than 0.8 V and ultra low power of order nW. In addition, it is characterized by high sensitivity and good linearity across a temperature range from -120°C to 500°C. It is expected that the use of Si and 4H-SiC technologies for both temperature ranges (low and high) respectively will increase the life of this sensor.**

Keywords—Si; 4H-SiC; Temperature; Smart Sensor; CMOS

I. INTRODUCTION

Naturally, all semiconductors physical parameters are related to temperature change. That's why all designs and feasibility studies of semiconductor devices have to take into account normal working temperature range [1]. For this, temperature sensors play an important role in many measurement and in different fields of electrical engineering [2]. With the fast evolution of science and technology, the need of high performance, High and fast processing, low power consumption and small chip. Furthermore, high accuracy is required for the temperature sensors [3]. For this, the smart temperature sensor was invented in recent years [4]. So that it is considered an integrated system that consists of a temperature sensor, processor and interface electronics [5]. The linearity, sensitivity, temperature range and low power consumption are among the most important characteristics of the sensor [2].

The MOS transistors in Silicon technology have been shown to be more optimal for CMOS circuit design due to the improved subthreshold slope and the reduced leakage current compared to bulk CMOS [6]. In addition, many semiconductors have been proposed to replace Si technology, among these materials Silicon Carbide (SiC) (3C-SiC, 4H-SiC and 6H-SiC), this is due to their distinctive properties such as wide bandgap, high saturation velocity of electrons and high thermal conductivity [7].

In this paper, we will study the electrical behavior of smart CMOS(Si and 4H-SiC) temperature sensor in 130 nm technology. Based on the MOSFETs transistors in Si and 4H-SiC technologies by BSIM3v3 Model [6-7], we propose a new smart temperature sensor design integrated these technologies in a one-chip. Then we simulate this smart sensor with a supply voltage of 0.8V and in the temperature range – 120 to 500 °C.

II. SMART CMOS TEMPERATURE SENSOR DESCRIPTION

A block diagram of the proposed smart CMOS(Si and 4H-SiC) temperature sensor is shown in Fig. 1. Each block is a sub-circuit of overall circuit of sensor. Current source sub-circuit (transistors M1 to M5 in Fig. 2) is a self-biasing circuit which generates a current independent of bias voltage. Two temperature variation sub-circuits, these sub-circuits consist of three pairs of transistors (transistors M6 to M14 and transistors M15 to M23 for the Si and 4H-SiC technologies respectively) operating in sub-threshold region and connected in series as shown in Figure 2. They are directly biased with current mirror formed by PMOSi transistors. In this circuit, output voltage is proportional to temperature change if MOSi and MOS(4H-SiC) transistors drain current I_D varies exponentially with gate-source voltage V_{GS} (Eq.3). Calibration sub-circuit is two NMOSi transistors (M_{Cal1} and M_{Cal2}) point used to calibrate temperature sensor from a reference voltage (voltage calibration V_{Cal}).

Control sub-circuit is a programmable logic circuit which allows one of two temperature variation sub-circuits to be activated by the switches (Φ and $\overline{\Phi}$ of Fig.1, transistors MOSFETs MSw(Si) and MSw(4H-SiC) of Fig.2), because these switches are connected between the temperature variation sub-circuits and the current source sub-circuit and the calibration sub-circuit.

The circuit operation can be understood from the block diagram of Fig. 1 and the simulation circuit of Fig.2. When the temperature is below 140°C (low temperature range), the output of the control sub-circuit is set to a logic "1 0" which turns the switch (Φ) on for the temperature variation sub-circuit in Si technology. When the temperature becomes over 140°C (high temperature range), the output of the control sub-circuit is switched and turns on the second switch ($\bar{\Phi}$) of the temperature variation sub-circuit in 4H-SiC technology.

The drain current in sub-threshold region of a MOSFET is given by Eq.1 [8]:

$$I_D = KI_0 \exp\left(\frac{V_{GS}-V_{Th}}{nV_T}\right).\left(1-\exp\left(\frac{-V_{DS}}{V_T}\right)\right) \quad (1)$$

Where:

$$I_0 = \mu_{eff}\sqrt{\frac{q\varepsilon_{SiGe}N_{ch}}{2\Phi_s}}{V_T}^2 = \mu_{eff}C_{ox}(\eta-1){V_T}^2 \quad (2)$$

V_T: Is thermal voltage,
K :Is geometric channel report
η :Is sub-threshold coefficient.

When V_{DS} is very low, the drain current I_D becomes almost independent of V_{DS} and given by:

$$I_D = KI_0 \exp\left(\frac{V_{GS}-V_{Th}}{nV_T}\right) \quad (3)$$

The output voltage V_{Out} of this smart CMOS(Si and 4H-SiC) temperature sensor can be expressed as :

$$V_{Out} = \begin{cases} \left(\frac{\eta_{Si}K_B}{q}\ln(6)\right)T + \Delta V_{Th-Si} & T < 140°C \\ \left(\frac{\eta_{4H-SiC}K_B}{q}\ln(6)\right)T + \Delta V_{Th(4H-SiC)} & T > 140°C \end{cases} \quad (4)$$

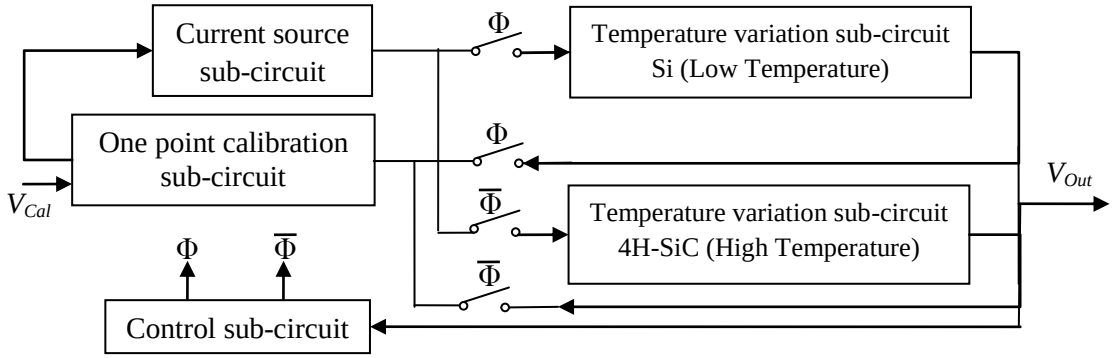

Fig.1. Block diagram of the proposed smart CMOS(Si and 4H-SiC) temperature sensor.

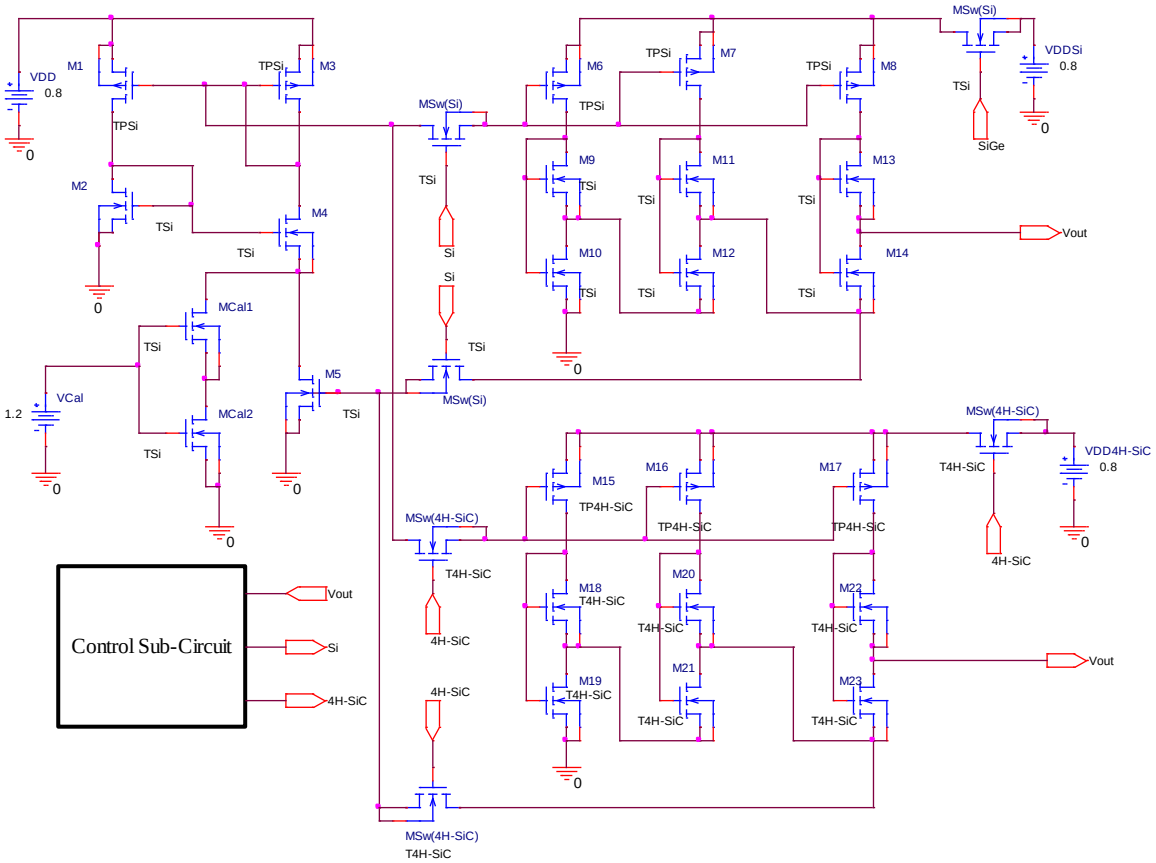

Fig.2. Smart CMOS(Si and 4H-SiC) temperature sensor simulation circuit.

III. RESULTS AND DISCUSSION

Fig.3. shows smart CMOS(Si and 4H-SiC) temperature sensor's output voltage simulation results as a function of temperature for both operating modes. As shown, sensor's output voltage V_{Out} is a linear function of temperature in different temperature ranges (Low and High) as expected from Eq. (4). The results obtained clearly show that the smart CMOS(Si and 4H-SiC) temperature sensor in 130nm technology works correctly according to the circuit operation proposed in this study.

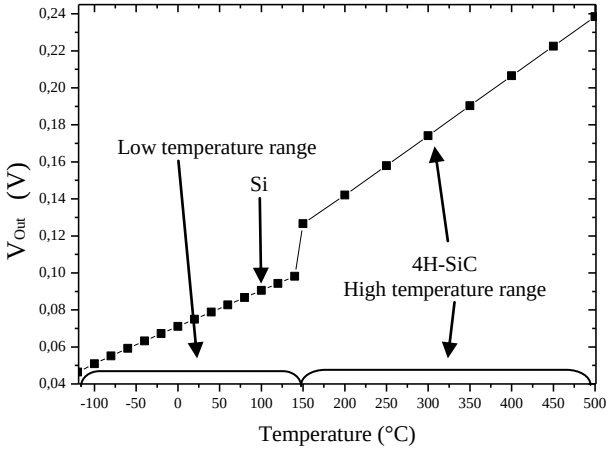

Fig.3. V_{Out} of smart CMOS(Si and 4H-SiC) temperature sensor.

The evolution of the output voltage V_{Out} as a function of the temperature in Fig.1 shows that this study achieves the good linearity of the smart CMOS(Si and 4H-SiC) temperature sensor in the both temperature ranges. The slope of this smart sensor is dependent on the threshold coefficient (η) in both temperature ranges (low and high) which distinguishes each type of semiconductor. This makes this smart sensor characterized by high sensitivity despite the high temperature, due to the transition from temperature variation sub-circuit in Si to temperature variation sub-circuit in 4H-SiC, which correspond to the two temperature ranges low and high respectively as shown in Table I. The different properties illustrated in Table I show that the smart sensor is characterized by an ultra low power due to the circuit of this smart sensor operates in sub-threshold region and that the transistors of this sensor proved their worth in the low power [6-7]. The transition between the two temperature variation sub-circuits according to the temperature allows for an increase in the life of this smart sensor. The results show that the smart CMOS(Si and 4H-SiC) sensor in 130nm technology is characterized by high electrical performace in a large temperature range.

TABLE I. PROPERTIES OF THE SMART CMOS(Si and 4H-SiC) TEMPERATURE SENSOR.

Mode switches Parameters	**$\Phi = 1$ and $\bar{\Phi} = 0$**	**$\Phi = 0$ and $\bar{\Phi} = 1$**
Material	Si	4H-SiC
Sensitivity (mV/°C)	0.31919	0.3619
Consumption (nW)	39.1552 (at 120°C)	
Ranges (I and II) °C	-120 −140	140 −500
Range (°C)	-120 − 500°C	
Bias voltage (V)	0.8	
CMOS Technology (nm)	130	

IV. CONCLUSION

In this work, we investigated the integration of two semiconductors technologies (Si and 4H-SiC) in a CMOS smart temperature sensor. By studying a new smart CMOS(Si and 4H-SiC) temperature sensor in 130nm technology under Pspice BSIM3v3. Output voltage was found to change linearly with temperature. When powered with supply voltage 0.8 V, the smart temperature sensor has low power consumption. It has also been demonstrated that this smart sensor can be used in two temperature ranges with two different semiconductors technologies.

V. REFERENCES

[1] Mourad Hebali, Djilali Berbara, Mohammed Benzohra, Djilali Chalabi, Abdelkader Saïdane, and Menaouer Bennaoum,"CMOSi1-xGex 130 nm High Sensitivity Ultra-Low Power Temperature Sensor", Sensor Letters, Vo.15, Number 4, (2017), pp. 328–332(5).

[2] R.A. Bianchi, F. Vinci Dos Santos, J.M. Karam, B. Courtois, F. Pressecq, S. Siffiet, "CMOS-compatible smart temperature sensors", Microelectronics Journal 29 (1998) 627-636.

[3] Poki Chen, Mon-Chau Shie, Zhi-Yuan Zheng, Zi-Fan Zheng, and Chun-Yan Chu, "A Fully Digital Time-Domain Smart Temperature Sensor Realized With 140 FPGA Logic Elements", IEEE TRANSACTIONS ON CIRCUITS AND SYSTEMS—I: REGULAR PAPERS, VOL. 54, NO. 12, DECEMBER 2007.

[4] Chun-Chi Chen and Zong-Yi Guo, "A CMOS Smart Temperature Sensor with One Homogeneous Delay Line and Curvature Compensation", 30th Eurosensors Conference, EUROSENSORS 2016, ELSVEVIER, Procedia Engineering 168 (2016) 1755 – 1758.

[5] K.A.A. Makinwa, "Smart temperature sensors in standard CMOS" Elsevier, Procedia Engineering, Proc. Eurosensors XXIV, September 5-8, 2010, Linz, Austria.

[6] Mourad Hebali, Menaouer Bennaoum, Mohammed Benzohra, Djilali Chalabi and Abdelkader Saïdane, "BSIM3v3 Characterization and Simulation of MOS $Si_{1-x}Ge_x$ Transistors with 130 nm Submicron Technology" Journal Nano-and Electronic Physics, Vo.11, Issue 4, 2019, pp.04021(1-6).

[7] Mourad Hebali, Djilali Berbara, Mohammed Benzohra, Djilali Chalabi, Abdelkader Saïdane, and Abdelkader Baghdad Bey "MOSiC (3C, 4H and 6H) Transistors 130nm by BSIM3v3 Model in Low Voltage and Low Power" Journal of Engineering Science and Technology Review (JESTR) , Vo.10, No. 5, (2017),pp. 195–198.

[8] Yu-Shiang Lin, Dennis Sylvester, and David Blaauw , IEEE Custom Integrated Circuits Conference (CICC), 507 (2008).

Effects of Boron diffusion on Titanium silicide formation

Karboua Houcine
Electronics Department
Faculty of Enginner Sciences
Batna 2 University
05000 Batna Algeria
Email: khoucine4@yahoo.fr

M'hamed Boulakroune
Laboratory of Electrical Engineering
Polytechnic Electrical and Automatic
Department National Polytechnic School
of Constantine, 25000 Constantine,
Algeria
Email:boulakroune.mhamed@yahoo.fr

Fortaki Tarek
Electronics Department
Faculty of Enginner Sciences
Batna 2 University
05000 Batna Algeria
Email: t_fortaki@yahoo.fr

***Abstract*—Secondary ion mass spectrometry (SIMS) has been used to investigate Boron diffusion in Titanium silicide layers for several annealing conditions of duration and temperature. Experimental profiles were simulated using a model based on the famous Fick's laws and the effect accompanying boron diffusion during silicidation like segregation and clustering. The comparison between simulation results and those of the literature in the same annealing conditions shows a good agreement between our results and those of other works. This explains that boron diffusion in titanium silicide depends on segregation, clustering and the solid solubility exceeds.**

Keywords—SIMS, Titanium Silicide, Boron, simulation, diffusion.

I. INTRODUCTION

Currently, using Titanium silicide as contact and interconnection in the industry of CMOS technology faces a difficult trade-off between thickness and sheet resistance. The contact junction depth must still scale with gate length. To avoid high contact resistance and high contact leakage, no more than half the contact junction depth can be consumed in the formation of the silicide. Therefore, the silicide must become progressively thinner to accommodate the more shallow contact junction for scaled contacts [1].

In this work, we present an attractive candidate the Titanium silicide with each interesting characteristics: low resistivity, low silicide formation temperature and good thermal stability [2]-[3].For our samples Titanium silicide boron doped we used a serial of heat treatment with RTA and STA.The rapid heating is an attractive method to reduce thermal budget and shallow junction [4]. Indeed J. Du et al [3] show that the conductivity of the thin films increases with the increase in the content of $TiSi_2$ crystalline phase.

Secondary Ion Mass Spectrometry (SIMS) technique was used to investigate boron diffusion in the Titanium silicide layer before and after annealing. However, it is necessary to simulate the resulting profile in order to understand the effects of boron on silicidation and to predict accurately the dopants shapes in any annealing conditions. It is know that the effect of silicidation is the induction of segregation of dopants. This is an important factor for governing transport and contact resistance of MOSFET devices [5]. This paper presents a comparison between experimentation and simulation of boron diffusion in Titanium silicide formation. The SIMS profiles were obtained by analysis different structures of boron in Ti/Si structure in different operative conditions using a Cameca-*Ims3f* instrument at oblique incidence. The simulation is founded on numerical model based on the Fick's law and the effects of dopants segregation and accumulation before and after annealing. This leads to simulate boron diffusion in Titanium silicide and to obtain several parameters which control the phase's evolution of this kind of silicide..

II. EXPERIMENTAL PROCEDURE

In order to obtain concrete results we used a serial of heating treatments short and rapid annealing and several temperature values to understand much more the effect of boron diffusion on silicidation.

TABLE I. DESCRIPTION OF THE ANNEALING CONDITIONS

Samples	Conditions	
	Temperature (°C)	*Duration (min)*
1	710	3
2	710	7
3	710	9
4	680	11
5	680	20
6	680	25

III. NUMERICAL METHOD AND MODELING

Diffusion is a physical phenomenon controlled by the famous Fick's laws and characterized by the tendency of doping species to spreading out. Ionic implantation is the most famous process used to introduce the doping species in the microelectronic industry. In very high doping level, the limits of solid solubility in silicon can be reached and have atoms trapped in interstitial and lacunars sites. This phenomenon will be modeled using the SIMS profile and simulation of the diffusion evolution according to different annealing parameters, i.e., temperatures and durations.

A. The Proposed Model

In the few last years there was a renew interest to control the dopants segregation in the silicide as the devices sizes reducing [5]-[6]-[7]. To understand the diffusion mechanism accompanying silicidation phenomenon, in this work, we present a new study based on real SIMS profiles obtained in different conditions, i.e., various temperature and heat duration.

Starting with the calculation of the solid solubility limit, whichexpressed by the following estimated equation given by Solmi et al [8]:

$$C_{Sol}=9{,}25.10^{22}\exp\left(\frac{0{,}73}{K_B.T}\right), \quad (1)$$

With KB: Boltzmann's constant (J/°K) and T: annealingtemperature in Kelvin.

With the high doping concentration, solid solubility level can easily exceeded and the damage created by the ionic implantation leads to many phenomena like segregation, cluster formation and dopants trapping.

The proposed model based on the famous Fick's law with a combination of different equation traducing dopants segregation, clustering formation and trapping.

$$\vec{F}_b = -D_b\frac{\partial C_b(x,t)}{\partial x}, \quad (2)$$

In transitory mode, we have:

$$\frac{\partial C_b(x,t)}{\partial t} = -\frac{\partial F_b}{\partial x}, \quad (3)$$

C b: concentration of an impurity " B ".
Fb: flow of an impurity "B".
Db: the diffusion Coefficient.

The combination on the equation (2) and (3) we have the third Fick's law:

$$\frac{\partial C_b(x,t)}{\partial t} = -D_b\frac{\partial^2 C_b(x,t)}{\partial x^2}, \quad (4)$$

Generally, the vacancy diffusion is dominating, and the diffusion coefficient becomes proportional to the vacancy density [9].

The concentration of the ionized impurity C_b^* and the total impurity concentration Cb, were linked by $C_b^* = \alpha C_b$ α: activation level of the doping agent
(0 ≤α≤ 1).
α = 1: toutes les impuretés sont ionisées.
α = 0: les impuretés sont totalement inactives.
Therefore, we will have:

$$S_B = \frac{1}{1+2m^2\left(\frac{\alpha_B C_B}{C_{sol}}\right)^{2m-1}}, \quad (5)$$

It is noticed that the trapping factor is directly related to the concentration C, by α, the size of the clusters m, and concentration of significant balance of a beginning of clusters formation C_{sol}. This factor reduces the diffusion coefficient considerably in high doping level.

Gaps influences (β): There are several types of diffusion (vacancy, interstitial ...), usually vacancy diffusionis the dominant phenomenon, and the diffusion coefficient becomes proportional to the vacancy density [9].

$$D=D_i^0V^0+D_i^-V^-+D_i^+V^++D_i^{-2}V^{-2}+..., \quad (6)$$

With: $D_i^0, D_i^-, D_i^+, D_i^{-2}$: intrinsic diffusivity.
V^0, V^-, V^+, V^{-2} : Standard gaps concentrations.

The effect of gaps occurs by the presence of a deficient state of multiply charged impurities, where the diffusion is assumed to be performed by the interaction of set of diffusers [10].

At the thermodynamic equilibrium, a number of deficiencies still exist, because the energy is increased by the presence of a disorder in the structure. The probability that we have a vacant site is given by the Boltzmann equation [11]:

$$p=\exp\left(-\frac{E_V}{K_BT}\right), \quad (7)$$

EV: is the required energy to bring an atom of a busy site that is a neighboring site; it depends on the position of the Fermi level Ef.

$$\frac{C_l}{C\text{-}C_l}=\exp\left(-\frac{E_V}{K_BT}\right), \quad (8)$$

C is the total concentration of atoms; C_L is the concentration of vacancy. The vacancy density for a given state of charge depends on the temperature; it is given by [12]:

$$C_L=C_i\exp\left(\frac{E_f\text{-}E_i}{K_BT}\right), \quad (9)$$

Ci: is the intrinsic vacancy concentration, E_f: the intrinsic Fermi level.

From the third Fick's law, we have:

$$\frac{\partial C_b}{\partial t}=-\frac{\partial}{\partial x}\left[-D_i\frac{1+\beta f_b}{1+\beta}\left(\left(1+\frac{\alpha C_b}{\sqrt{(\alpha C_b)^2+4n_i^2}}\right)\frac{\partial C_b}{\partial x}\right)S_B\right], \quad (10)$$

$$f_b=\frac{p}{n_i}=\frac{2n_i}{\sqrt{(\alpha C_b)^2+4n_i^2}-(\alpha C_b)}$$

B. Initial conditions

Equation (10) represents the general expression of the proposed model. To solve problem with a partial differential equation, we have used a numerical method which is the finite differences. The initial and the limit conditions are determined from Fig. 1which shows a good adjustment between SIMS profile and the simulated one used as initial conditions. According to the study done by Solmi et al [8], we have used a combination of two half Gaussian function with various experimental parameters,

$$N=C_P\exp\left[-\frac{(X\text{-}R_P)^2}{2\Delta R_P^2}\right], \quad (11)$$

N is the concentration (at/cm3)
Cp isthe ion implantation dose, Rp is the projected Range, and ΔRp the standard deviation [13].

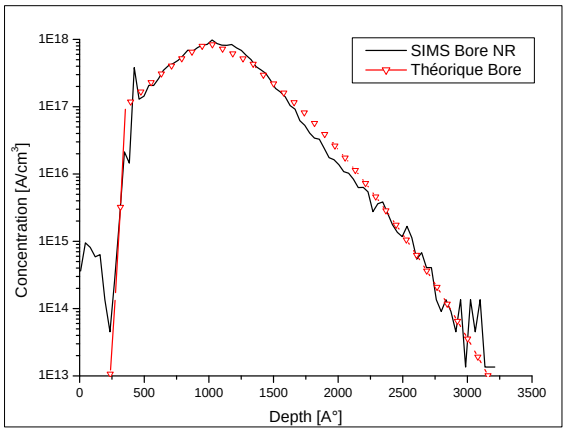

Fig. 1. Theoretical and experimental SIMS Boron profile Before annealing

IV. RESULTS AND DISCUSSION

A. *Simulation Of SIMS Profiles*

Figure 2 presents real SIMS profiles of boron in TiSi2structureand the simulation in different annealing conditions (various values of temperature and duration). It show a great agreement between simulation and SIMS profiles.

We can notice two different gaits: the double slope and a Gaussian shape :

The shape of Boron profile after annealing depends on several factors:

Peaks boron in the silicide film and a much larger out diffusion length. This may be caused by the higher boron diffusivity in both materials.

Silicidation inducessegregation ofdopant, so the boron distribution is not uniform.

The defects in the metal.

From R.Beyrs [14] in the high doping case we have the formation of some precipitates like the TiB wich induces a fence to silicon diffusion so it can stop the moving from C49 to C54 phases.

According to these details, the diffusion of boron in titanium silicide depends on several phenomena:

- Dopants segregation clustering and the vacancies.
- The solid solubility exceedance.

a

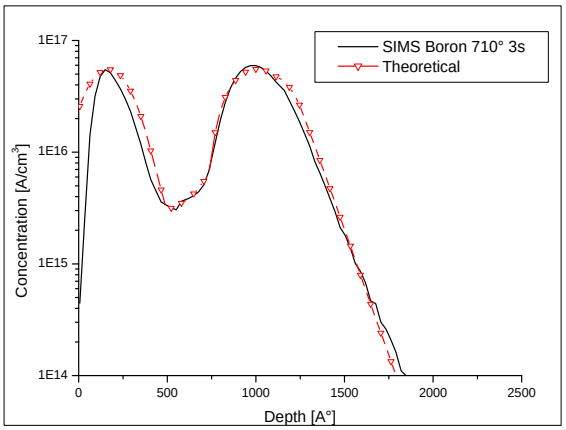

b

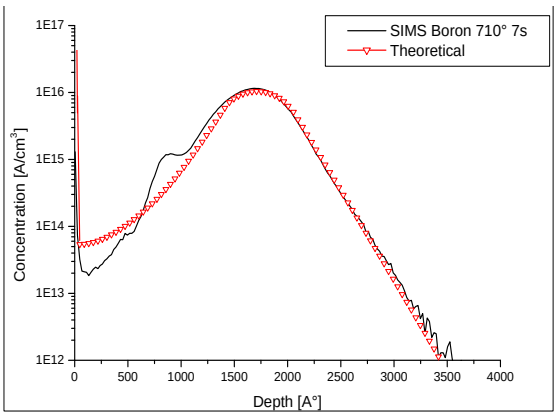

c

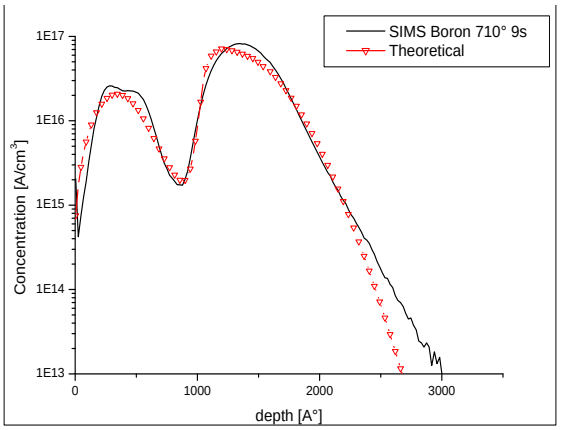

d

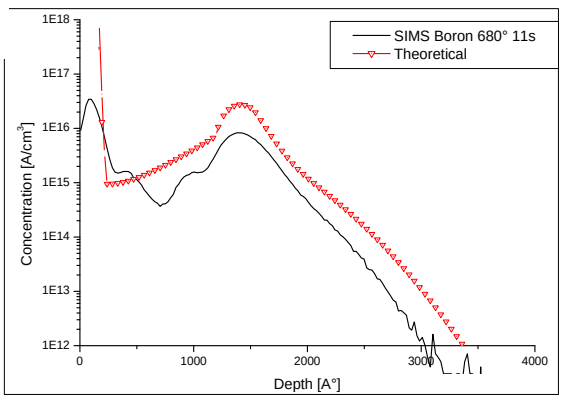

e

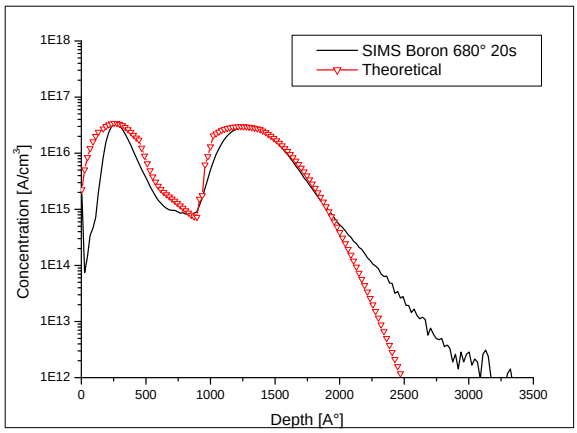

f

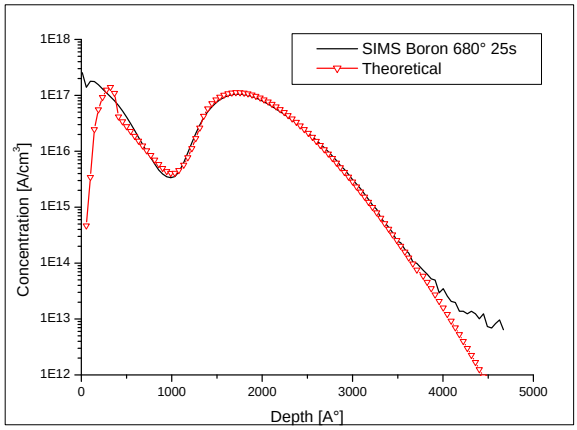

Fig.. 2. Simulation of SIMS profiles: (a), annealing 710°C, 3s (b), annealing 710°C, 7s (c),annealing 710°C, 9s (d), annealing 710°C, 11s (e), annealing 710° C, 20s (f), annealing 710°C, 25s.

According to the work of R. Pretorius [16] the diffusion coefficient of the boron in TiSi2 is around 10-13 cm2/s at 600°C so it's close to our result obtained at 680°C

- β Was chosen to equal 0.11, Girault et al [14] advice to take β : 0.1 to 0.3.

- The fraction of activated dopants α is about 20% in the majority of samples and Zhao et al [17] shows that αmust be higher than 18%.

TABLE II. SIMULATION RESULTS

Samples	Conditions		
	Temperature (°C)	***Duration (min)***	***Diffusion coefficient Cm^2/s***
1	710	3	$1{,}3344.10^{-12}$
2	710	7	$3{,}7308.10^{-11}$
3	710	9	$1{,}7522.10^{-12}$
4	680	11	$3{,}8197.10^{-12}$
5	680	20	$7{,}7311.10^{-12}$
6	680	25	$6{,}0164.10^{-12}$

CONCLUSION

Secondary ions mass spectrometry technique have been used to investigate Boron diffusion during silicidation for several annealing duration and temperature. The simulation is based on numerical method which is finite differences. It is shown a great agreement between simulation and experimentation. This accordance led to determine several parameters, which explain the comportment of boron in $TiSi_2$ structure during different phases of silicidation. In particular, the shape of boron distribution profilein titanium silicide depends on several structural factors as well as annealing conditions, i.e. segregation, presence of defects, the solid solubility, exceedance, etc.

REFERENCES

[1] W. Chien-Ting,Y.J Lee, F.K. Hsueh, P.J. Sung, T.C. Cho,M.I. Current, T.S. Chaoc *J. of Solid State, Science and Technology*.3, 122 (2014).
[2] S. Lia, C. Zhoub, S. Rajua, M. Chana,*Diamond & Related Materials*.39, 43 (2017).
[3] J. Du, P. Du, M. Xu, P. Hao, Y. Huang, G. Han, C. Song, W. Weng,J. Wang, G. Shen.*J. Appl. Phys*. 101 (2007).
[4] M. Hasumi, T. Nakamura, S. Yoshidomi, T. Sameshima, Jpn. J. Appl. Phys.53, 184 (2014).
[5] A. Kumar, M. Law,*IEEE*.4, 13 (2013).
[6] C. Urban, Q.T Zhao, C. Sandow, M. Muller, U. Breuer, S. Mantl, *ULIS 2008 International Conference on integration of silicon*. 12, 14 (2008).
[7] M. Zhang, J. Knoch, Q.T. Zhao, S. Lenk, U. Breuer, S. Mantl, *Solid-State Device Research Conference*. 12, 16 (2005).
[8] S. Solmi, F. Baruffaldi, R. Canteri,*J. Appl. Phys*.69, 2135 (1991).
[9] C.P. Ho, J.D. Plummer, S.E. Hansen, R.W. Dutton, *IEEE* 30, 11 (1983).
[10] R.B. Fair,Impuritydopingprocess in silicon(Ed. by. F.F. Y. WangNorth-Holland Amsterdam:1981).
[11] C. Kittel, Physique de l'état solide. 5ème édition (ed.by.wiley edition:1983).
[12] S. M. SZE, Physics of semiconductor devices2nd Edition (Ed. By. John Wiley and Sons: New York:1981).
[13] R.W. Cahn, P. Haasen, E.J. Kramer, *Materials Science and Technology*. 4, 254 (1991).
[14] G. Giroult, A. Nouailhat M. Gouneau, *J. Appl. Phys*.67, 515 (1990).
[15] R. Beyers, R Sinclair, J. Appl. Phys. 57, 12 (1985).
[16] R. pretorius, *J.Appl phys*.81, 5 (1997).
[17] Z. Zhao, N.D. Theodore, N. Rajitha. P. Vemuri, S. Das, W.Lu, S.S. Lau, and T.L. Alford, *Applied Physics Letters*.103, 192103(2013).

Magneto-optical properties of magnetic photonic crystal fiber of Cerium substituted yttrium iron garnet medium (Ce -YIG) filled with magnetic fluid Fe3O4

GHALEM Salim[1]
Department of Electronics, Laboratory L.M.I
University of Constantine 1
Constantine, ALGERIA

LEBBAL Mohamed Redha
Department of Electronics, Laboratory L.M.I
University of Constantine 1
Constantine, ALGERIA

BOUCHEMAT Mohamed
Department of Electronics, Laboratory L.M.I
University of Constantine 1
Constantine, ALGERIA

BOUMAZA Touria [1]
Department of Electronics, Laboratory L.M.I
University of Constantine 1
Constantine, ALGERI

***Abstract*— In this work, we propose a photonic crystal fiber based on magneto-photonic crystal (MPC), formed by a triangular ring of circular air holes filled with magnetic fluid (MF) based on magnetic nanoparticle Fe3O4, in a Cerium substituted yttrium iron garnet medium (Ce -YIG), in this fiber, we have theoretically studied the conversion mode, reported and studied the effect of some parameters such as the radius and using a beam propagation method (BPM) in two dimensions. In our proposed structure the maximum conversion modes ratio equal to 98% with low coupling length Lc=15µm is obtained for gyrotropy g=0.35 and Faraday Rotation FR=1900 × 10^4 deg⁄cm.**

Keywords— magneto-photonic crystal fiber, Photonic crystals, optical isolator, mode conversion TE-TM.

.

I. INTRODUCTION

This PCF is a kind of fiber based on the properties of photonic crystal, whose significant difference from traditional fiber is the introduction of periodic air-hole structures into the cross section of the fiber. If the refractive index of the core area is higher than the average refractive index of air hole cladding, its guiding mechanism is total internal reflection and it is classified as index guiding fiber. If the refractive index of the core area is lower than the average refractive index of air-hole cladding.

When magneto-optic materials and photonic crystals are combined, new components based on magneto-photonic crystals emerge to exalt the non-reciprocal effects of propagation, during the past few years, some research efforts have been devoted to the investigation of magneto-optical effects in photonic crystals composed of magneto-optical materials [1].

II. MAGNETO-OPTICAL FARADAY EFFECT

The non-reciprocal optical effect of Faraday rotation (FR) is widely exploited in optical isolators, optical circulators and some other magneto-optical (MO) devices [2]. The improvement of Faraday rotation (FR) to reduce the size and cost of magneto-optical devices has been of great interest among researchers [3–6]. As is known, the first design concept of an integrated isolator was based on a non-reciprocal TE - TM mode conversion. In fact, most proposals for waveguide type are based on this [7], [8]. Rare earth elements, such as bismuth and cerium, have been found to increase RF without significantly increasing absorption [9, 10].

It is well-known that the FR effect is caused by a periodic power transfer between the transverse components Ex and Ey [11].

In an isotropic material, three diagonal elements are identical and, in the presence of a magnetic field along the Z axis, there is a non-diagonal element ε, which couples the x and y components of the optical E field [12, 13, 14].

$$\varepsilon = \begin{bmatrix} \varepsilon_{xx} & -\varepsilon_{yx} & 0 \\ \varepsilon_{xy} & \varepsilon_{yy} & 0 \\ 0 & 0 & \varepsilon_{zz} \end{bmatrix}$$

(1)

Where ε represents the diagonal elements of dielectric tensor ε_{xx}, $\varepsilon_{yy}$and ε_{zz}.

Where the magnetooptic permittivity parameters εxx= εyy= εzzare real. In our case, these parametersare given as follows: $\varepsilon = \varepsilon_{xx} = \varepsilon_{yy} = \varepsilon_{zz}$ (2)

The gyrotropy parameter (g), which is responsible for the MO effect, is proportional to Hext in a first approximation, according to the relation: g = ε0χ Hext, (3)

Where ε0 is the permittivity in vacuum and χ is the MO susceptibility in the magnetic field Hext. In absence of Hext, the polarization state of the light wave passing through the wave guide does not change.

However, the complex refractive index of magneto optical matrix is given by N = n + ik, where n is the real partof complex refractive index for diagonal tensor elements and k is the imaginary part of complex refractive index.The complex dielectric permittivity of diagonal elements is given by:

$(n + iK)^2 = \varepsilon$, (4).

The real and the imaginary parts of dielectric tensor aregiven by:

$$\begin{cases} \varepsilon' = n^2 - K^2, \\ \varepsilon'' = 2nK, \end{cases} \quad (5)$$

Where K is called the coefficient of extinction and it'sgiven by:

$K = \frac{\propto\lambda}{4\pi}$ (6)

Where λ is the free space wavelength and α (cm-1) represents the losses inside the matrix, it is linked to intrinsicabsorption of magneto-optical matrix.The specific formula of FR in Deg/cm is given by

$$\boldsymbol{\theta F} = \frac{\pi Re(\varepsilon_{mo})}{n\lambda} \quad (7)$$

Where n and λ are the refractive index and the wavelength, respectively. Thenon-diagonal term of permittivity tensor can call by the gyrotropy parameter g (εmo = g). This tensor is very often used to study the MO effects, this off diagonal terms lead to a coupling between the TE and TM modes.

Assuming that the incident mode is the transverse magnetic (TM), the conversion output R(z) is defined as the intensity ratio of the TE mode at the distance z on the intensity of the TM mode at the start (z = 0):

$$R(z) = \frac{I_{TE(z)}}{I_{TM(0)}} \quad (3)$$

It can be written then:

$$R(z) = \frac{{\theta_F}^2}{{\theta_F}^2 + (\Delta\beta/2)^2} \sin^2\left[\left({\theta_F}^2 + \left(\frac{\Delta\beta}{2}\right)^2\right)^{\frac{1}{2}} z\right] \quad (4)$$

Here we see that the TE-TM mode conversion is affected by the faraday rotation $\theta_F \left(\frac{deg}{cm}\right)$ of the materiel and the phase mismatch $\Delta\beta \left(\frac{deg}{cm}\right)$, When

$\Delta\beta = \beta TE - \beta TM = (NTE - NTM)(2\pi/\lambda) = \Delta N(2\pi/\lambda)$ (5)

with NTE and NTM are the effective indexes of the TE and TM modes, respectively, and β is the propagation constant.

In practice, for an efficient mode conversion, the difference between the refractive index TE and TM need to be low as possible. It was obtained for a distance named the couplinglength. When Δβ is not zero, the mode conversion efficiency is limited to value RM obtained at the end of a length of coupling LC, and can be expressed as relation [15]:

$$L_C = \frac{\pi}{(4{\theta_F}^2 + \Delta\beta^2)^{1/2}} \quad (6)$$

$$R_m = \frac{{\theta_F}^2}{{\theta_F}^2 + (\Delta\beta/2)^2} \quad (7)$$

One of the most useful properties of CeYIG is the rotation faraday FR which makes it appropriate for the manufacture non-reciprocal devices based on MPC. [16, 17]. Various geometries of waveguides in a PC structure with containing magneto-optic were presented recently, such as the waveguides in a PC structure with triangular and square lattice reported by DEGHDAK et al [18,19] and KAHLOUCHE et al [20,21], and OTMANI et al [22],MounirBouras et al [23], which consists of improvement FRE , and low coupling length.

III. SIMULATION RESULTS AND DISCUSSIONS

As shown in Figure. 1, the XY cross-section of the MPCF has the following variable parameters: nCe YIG = 2.21, nFe3O4 = 1.4102, Λ = 2.52 µm, d = 2.16 µm, where n, Λ and d, are refractive index, period and hole diameter, respectively. Moreover, the refractive indexes of the MF can be changed with the applied external magnetic field, H [24], such as, at H = 89.9 Oe, nFe3O4 = 1.4635 and at H = 271Oe, nFe3O4 = 1.4670.

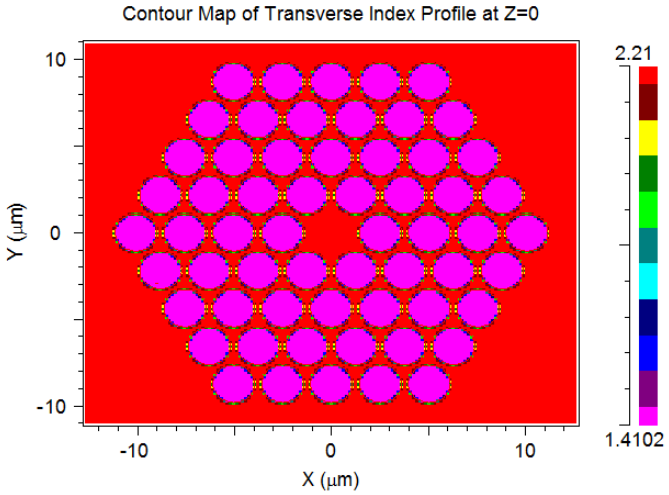

Figure 1 . Index profile of the PCF structure

IV. MODE CONVERSION:

The analysis done in this study has been concentrated on the TE polarization, for which the 2D MPCF. In Figures 2.a and b, the E-field distribution reported inside the fiber and the power run through the fiber (MPCF), the figure 2.a) represents a mode coupling into the MPCF for g=0 there no coupling between the mode. On the contrary, in figure 2.b) once the gyrotropy parameter (g) increases inside 2D magneto-photonic crystal fiber MPCF, so the modes start to couple between them, it starts coupling at value of g=0.11, The Figure 2.b) shows the E-field distribution and the mode conversion obtained with a BeamPROP (BPM) in the case of MO material Cerium-substituted yttrium iron garnet (Ce-YIG) g = 0.27.

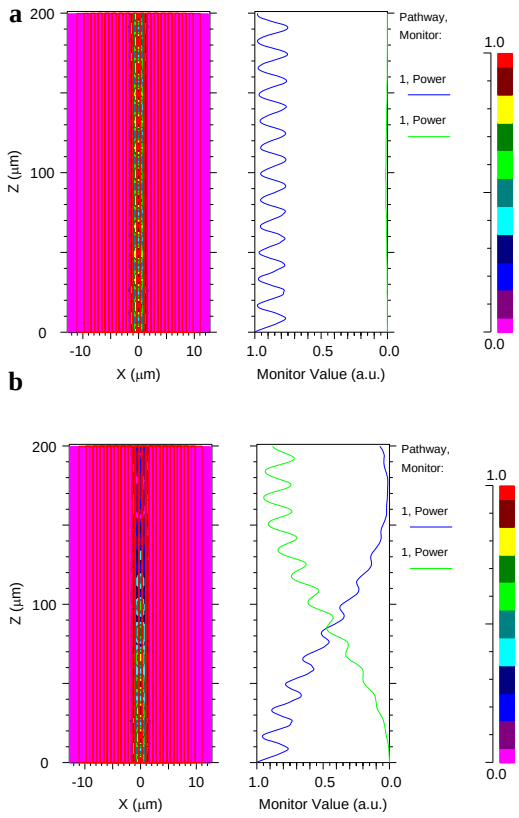

Figure. 2. a) Mode conversion in an isotropic PCF,

b) Mode conversion in 2D magneto-photonic crystal fiber MPCF (g=0,25).

V. THE EFFECT OF RADUIS R ON THE OUTPUT CONVERSION RM:

To examine the effect of the radius of the air holes r on the output conversion Rm, the radius of air holes r is set for different values. Figure 6 a) display variation of conversion output as function radius of air holes r, in this graph show that the modes coupling increase when r increases, with gyrotropy parameter g=0,11 that the coupling is strong between modes, the effect of radius r is proportional on the coupling efficiency, if the is small (r= 1.2 µm) the yield is also small but when it increases, the performance of the conversion increases, thus these results show that the field intensity increases proportionally depending on the radius r. Figure 6.b) shows the output conversion of power Rm for gyrotropy parameter g=0,11,radius r=2.16, Rm increases with the increase of r, such with r=1,20 µm the output is 60% and reached 98% with r=2.16µm.

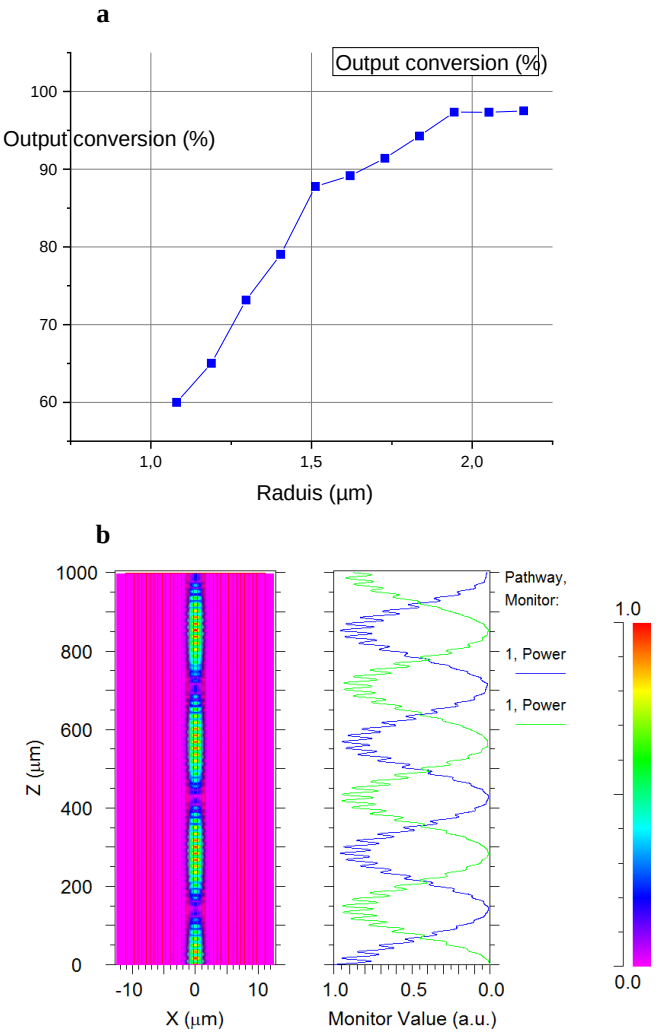

Figure 5. Variations of the power conversion as functions as thickness T, (a=0.73) μm, gyrotropy parameter g=0.45, radius r=0.3a.

VI. THE EFFECT OF GYROTROPY G ON COUPLING MODE:

Figure 3 represents a mode coupling in an MPC fiber, for gyrotropy parameter g = 0,06, g=0,08, and g = 0,1. In this figure, when the non-diagonal terms in the permittivity tensor are zero, the modes are separated; by the existence of these terms induce a coupling mode, which increase proportionally with the increase of these terms, thus a study of the effect of g on mode conversion Faraday rotation is taken in figure.3.

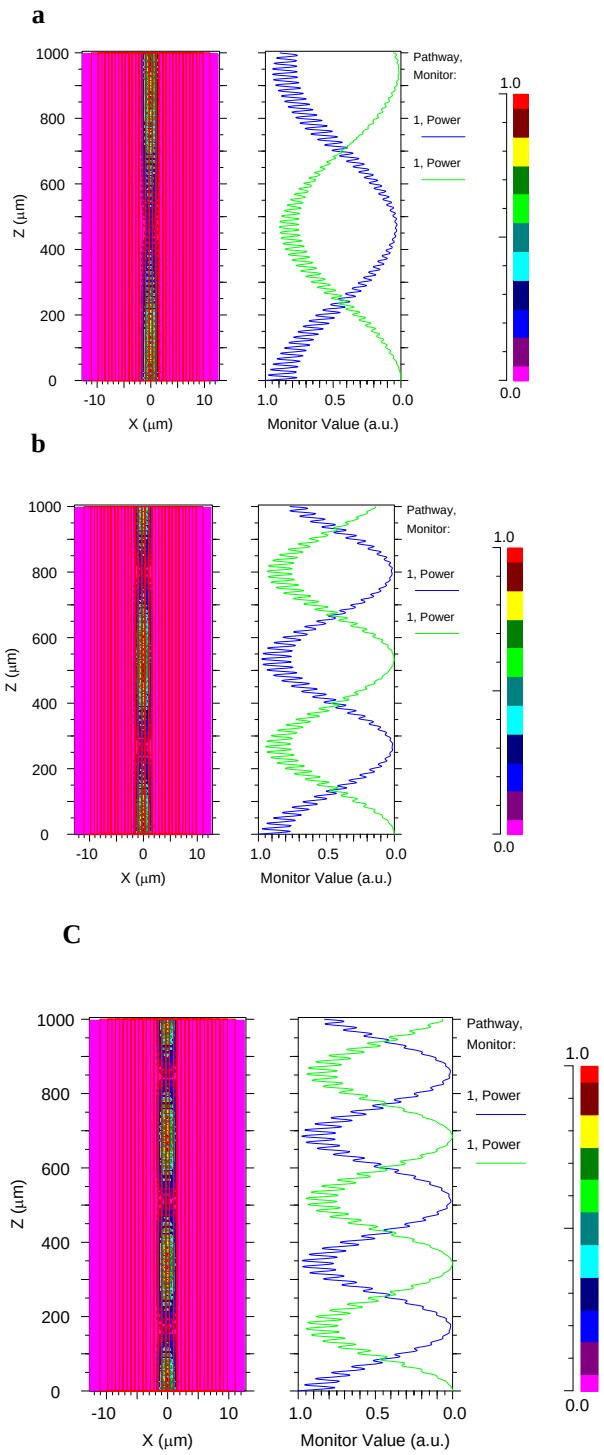

Figure 3- Mode conversion in an MPC Fiber formed by a triangular lattice of air holes: (a) g = 0,06, (b) g =0,08, and,(c) g = 0,1.

VII. THE EFFECT OF GYROTROPY(G) AND RADIUS R ON THE FARADAY ROTATION FR:

Figure 4 a) shows the influence of gyrotropy parameter (g) on Faraday rotation (FR). The existence of the off-diagonal parameters in ε allows the coupling between the TE and TM modes in a periodic way, and the variation of these parameters influences much more on the conversion.

An increase in FR is observed with the increase of gyrotropy parameter (g): for g = 0,1, the value of FR is 600 × 104deg⁄cm and for g = 0,3, FR reaches 1900 × 104deg⁄cm,

In the figure 4 b), we represent the variation of faraday rotation according to the gyrotropy (g) and radius r, in fact, the faraday rotation remains constant as long as the value radius r varies, such as, it is equal to 0,6 104 approximately. Then the radius r values do not influence on the rotation faraday in this structure.

a

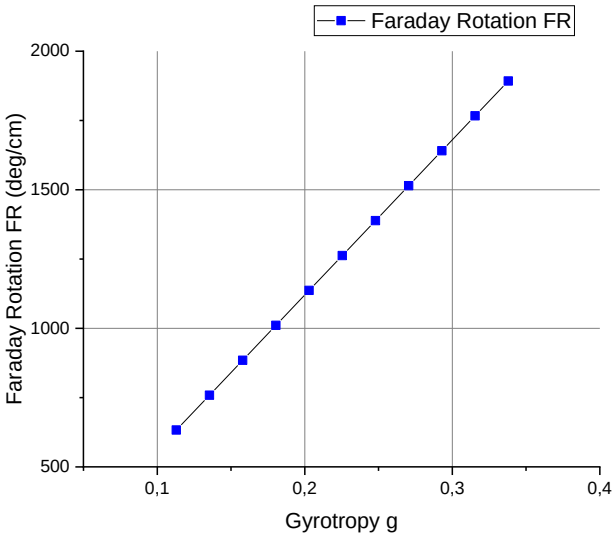

a

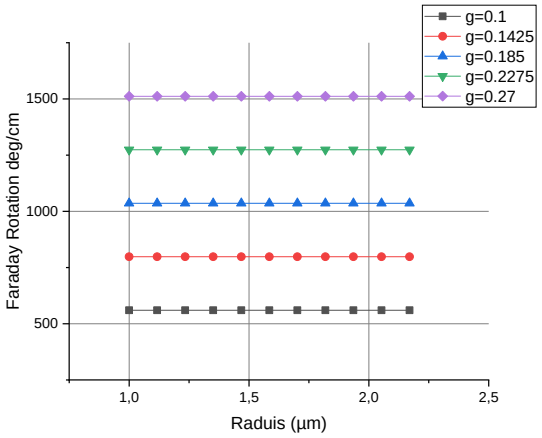

Figure 4 a) variation faraday rotation (FR) versus gyrotropy parameter (g)

b) Influence of the radius of air holes on the Faraday rotation FR with different value of gyrotropy parameter g at λ = 1.55 μm,

VIII. THE EFFECT OF GYROTROPY (G) ON COUPLING LENGTH LC

The existence of the off-diagonal parameters in ε allows the coupling between the TE and TM modes in a periodic way, and the variation of these parameters influences much more on. In figure 5 we see that the coupling length decreases with the increase of the gyrotropy such as, in g=0.12, the coupling length Lc =140μm, if g increases to g=0.34 the coupling length decrease to Lc=15μm)

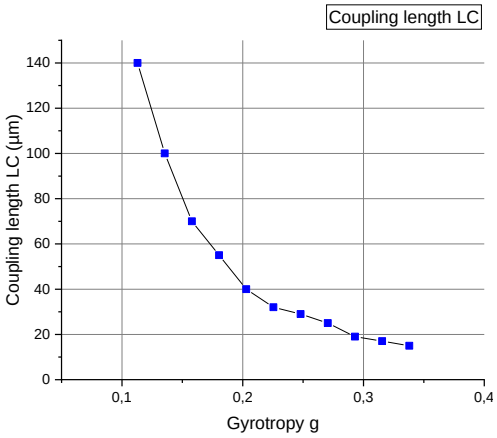

Figure(5)Variationcoupling length (LC) versus gyrotropy parameter (g) .

IX. CONCLUSION

During the last two decades, the simulation and technical modeling of magneto photonic fiber MPCF have been considerably developed. this work, presented a study of our proposed MPCF, filled with magnetic fluid (MF) based on magnetic nanoparticle Fe3O4 (1.4102), in a Cerium substituted yttrium iron garnet medium Ce-YIG (n = 2,21), arranged on a triangular lattice constant a =2.52 µm, embedded in Ce-YIG (n = 2,21), grown on a silica SiO2 substrate(n=1,45).

We have optimized our proposed structure based on Ce:YIG/Fe3O4 at the telecommunications wavelength λt = 1,55 µm, for an optimal radius r = 2.16µm.

We have studied also the improvement of the conversion efficiency of the polarization modes in this fiber. A conversion rate of 98% is observed for the optimized geometrical structure.

The results show that the radius variation is proportional to the modes conversion efficiency and when the gyrotropy parameter g increases to 0.3, the FR increases and the coupling length can decrease to 15µm. These simulation results represent an important step in the design of magneto optical devices, which are useful for fabricating MPhCs isolator with decreasing propagation losses and low size, to integrate it with other optical functionality.

Acknowledgments

This work was supported in part by the Algerian Ministry of Higher Education and Scientific Research through the PRFU project (grant no. A10N01UN250120180005) of the Department of Electronics, Laboratory L.M.I., Frères MentouriConstantine-1 University, would also like to thank all the members of Laboratory LMI.

[1] Qiong Wang, Zhengbiao Ouyang,* And Qiang Liu ‘Multiport Photonic Crystal Circulators Created By Cascading Magneto-Optical Cavities’Vol. 28, No. 4 / April 2011 / J. Opt. Soc. Am. B.

[2] W. Wang, M. Gu, and G. Liu, “Quantum theory of nonlinear and reciprocal properties of magneto-optical effects in paramagnetic media under a high magnetic field,” Phys. Rev. B, vol.72, p. 014415, 2005.

[3] Kato H, Matsushita T, Takayama A, Egawa M, Nishimura K and Inoue M 2003 Theoretical analysis of optical and magneto-optical properties of one-dimensional magneto photonic crystals *Appl. Phys. Lett.* 93 3906.

[4] Kahl S and Grishin A M 2004 Enhanced Faraday rotation in all-garnet magneto-optical photonic crystal *Appl. Phys. Lett.* 84 1438.

[5] Kato H and Inoue M 2002 Reflection-mode operation of onedimensional magnetophotonic crystals for use in film-based magneto-optical isolator devices *Appl. Phys. Lett.* 91 7017.

[6] Li R and Levy M 2005 Bragg grating magnetic photonic crystal waveguides *Appl. Phys. Lett.* 86 251102

[7] H. Hemme, H. Dotsch, and H. P. Menzler, “Optical isolator based on mode conversion in magnetic garnet films,” Appl. Opt., vol. 26, pp. 3811-3817, 1987.

[8] K. Ando, “Waveguide optical isolator: a new design,” Appl. Opt., vol. 30, pp. 1080-1084, 1991.

[9] Magdenko L, Popova E, Vanwolleghem M, Pang C, Fortuna F, Maroutian T, Beauvillain P, Keller N and Dagens B 2010 Wafer-scale fabrication of magneto-photonic structures in bismuth iron garnet thin film *Electron. Eng. Lett.* 87 2437–42

[10] Park M B and Cho N H 2001 Structural and magnetic characteristics of yttrium iron garnet (YIG, ceYIG) films prepared by RF magnetron sputtering techniques *J. Magn. Mater.* 231 253

[11] L. D. S. Alcantara, F. L. Teixeira, A. C. César, and B. H .V. Borges, “New full-vectorial fd-bpm scheme: application to the analysis of magnetooptic and nonlinear saturable media,” Lightwave Technol., vol. 23, no. 8, p. 2579, 2005.

[12] Shanhui Fan And Zheng Wang An Ultra-Compact Circulator Using Two-Dimensional Magnetooptical Photonic Crystals’J. Magn. Soc. Jpn, 30, 641-645 (2006).

[13] Z. Wang, S. Fan ‘Magneto-Optical Defects in Two-Dimensional Photonic Crystals’Appl. Phys. B81, 369–375 (2005)

[14] ZhengWanga, Shanhui Fan ‘Magneto-Optical Circulator In Two-Dimensional Photonic Crystals’Proc. Of Spie Vol. 6128 61280d-1.

[15] HadiAmata, Franc¸ois Royer, FadiChoueikani, DamienJamon, Franc¸oisParsy, Jean-Emmanuel Broquin, Sophie Neveu, and Jean Jacques Rousseau ‘’ Hybrid magneto-optical mode converter made with a magnetic nanoparticles-doped SiO2/ZrO2 layer coated on an ion-exchanged glass waveguide’’ applied physics letters 99, 251108 (2011)

[16] Ali Esmaieli, Rahim Ghayour‘Magneto-Optical Photonic Crystal 1×3 Switchable Power Divider’Photonics and Nanostructures – Fundamentals and Applications 10 (2012) 131–139.

[17] Mehmet C. Onbasli,*, LukášBeran,*, Martin Zahradník, Miroslav Kučera, Roman Antoš, Jan Mistrík, Gerald F. Dionne, Martin Veis& Caroline A. Ross ‘ Optical and magneto-optical behavior of Cerium Yttrium Iron Garnet thin films at wavelengths of 200–1770 nm ’ Scientific RepoRts 2016.

[18] RachidDeghdak, Mohamed Bouchemat, MahieddineLahoubi, ShengliPu, TourayaBouchemat, Hamza Otmani ‘Sensitive Magnetic Field Sensor Using 2d Magnetic Photonic Crystal Slab Waveguide Based On Big/GGG Structure’ J Comput Electron- Springer Science+Business Media New York 2017.

[19] R. Deghdak, M. Bouchemat, T. Bouchemat, M. Lahoubi, H. Otmani’Optimized Complete Photonic Band Gap In Magneto-Photonic Crystal Slab’ Nanoscience And Nanotechnology 2016, 6(1a): 39-42.

[20] A. Kahlouche*, A. Hocini, D. Khedrouche‘Mode Conversion In 2d Magneto Photonic Crystals Made Of Sio2/Zro2 Matrix Doped With Magnetic Nanoparticles’Vol. 127 (2015) ActaPhysicaPolonica A No. 4.

[21] Ahmed Kahlouche*, AbdesselamHocini, DjamelKhedrouche ” Mode Conversion In Two- Dimensional Magneto-Photonic Crystal Waveguide Made By Fully Compatible Optical Sol-Gel Matrix’OpticaApplicata, Vol. Xlvi, No. 4, 2016

[22] Hamza Otmani, MahieddineLahoubi, ShengliPu, Mohamed Bouchemat, TourayaBouchemat,Yongliang Zhao, RachidDeghdak, “Simulation Of Magneto-Optical Properties Of Magnetic Photonic Crystal Waveguides,”J. Nanophoton. 13(2), 026002 (2019).

[23] MounirBouras, AbdessalemHocini ‘Mode conversion in magneto-optic rib waveguide made by silica matrix doped with magnetic nanoparticles’ Optics Communications 363 (2016) 138–144

[24] J. Chen, X. Chen, S. Pu, Z. Di, and Y. Xia, “Realization of optical limiting with a magnetic fluid film,” Opt. Commun. 276, 268–271 (2007).

Optical and Structural Properties of Copper Doped Zinc Oxide thin films Prepared Via Spray Pyrolysis Method.

M. TOUATI TLIBA [a, b] , B. Benhaoua [a,b]

[a] Lab. VTRS, Faculty of Science & Technology, Univ. El-Oued, El-Oued 39000, Algeria

[b] Unité de Developpement des Energies Renouvelabes dans les Zones Arides, El oued 39000, Algeria

[c] *Centre National de Recherche en Sciences des Materiaux Tunisie*

Abstract

Un doped and copper doped ZnO (0-5 wt.%) were synthesized by spray pyrolysis technique (homemade) annealed at 375°C. Zinc acetate and copper chloride were used as sources precursor of ZnO and Cu doping, respectively. Optical and structural properties of elaborated thin films were examined by using UV-visible and X-ray diffraction. The optical study indicate that the average transmittance of all samples was more than 81% in the visible region and become more transparent after doping. Optical gap energy was observed to vary between 3.25 - 3.28eV. The structural analysis showed formation a hexagonal wurtzite structure ZnO with a strong (002) preferred orientation except (for 0.0 and 1.5 wt%), while the crystallite size is estimated 23 to 29nm for 0-5wt.% Cu doped ZnO thin films.

Key words : Thin films ; Cu doped ZnO ; Spray pyrolysis ; X-ray diffraction .

1. Introduction

Zinc oxide (ZnO) is one of the most important semiconductor materials , which has attracted a lot of scientific attention due to its several applications such as, light emitting diodes [1], gas sensors [2], solar cells [3] transparent conducting contacts [4], energy storage devices [5], electronic devices [6], liquid crystal displays [7], photo detection [8]. It has wide band gap (3.3 eV) with a large exciton binding energy (60 meV) at room temperature [9, 10] and own the property of transparent conducting oxides (TCO) which are widely used in various transparent electronics applications [11]. As thin films ZnO can be deposited by several techniques such as chemical precipitation method [12], sol-gel [13], chemical bath deposition (CBD) [14], Co-precipitation [15] and spray pyrolysis [16]. Among these methods, more focuses, particularly, on the spray pyrolysis technique because of its advantages such as simplicity, safety and low cost of the equipments for thin films deposition. Use of moving nozzle coupled with spray pyrolysis was proced on glass substrate leading to relatively homogeneous composition and fine microstructure with high quality [17]. Also possibilities

of large-scale area deposition, low temperature processing and direct control of film thickness are feasible. Doped ZnO with little amount of several elements was an attracted subject for researchers. It is well known that doping with aluminum was to obtain a conducting transparent ZnO [18]; whereas doping with Cooper, in pervious study [13], was to ameliorate the sensitivity for the gas detection trough the augmentation of the specific reactive surface. As well, Mn doping regarded as an ideal material for short wavelength magneto-optical applications due to its the thermal solubility of Mn into the ZnO and large band gap [19]. While, doped Lanthanum, it enhances in the removal of the ions copper from water solutions [17], etc…

The aim of this work is to focus more on Cu doping effect, in the range of concentration (0-5 Wt. %) in the sprayed solution, on optical, structural and morphological properties of synthesized ZnO via a spray pyrolysis technique with moving nozzle [17]. Outcome of Cu doping concentration stepped as (0.0, 0.5, 1.5, 2.0 and 5.0wt. %) on optical, structural and of ZnO thin films deposited onto glass substrate at temperature up to 375°C will be investigated. All elaborated samples of Cu doped ZnO thin films and undoped were characterized using UV-visible spectroscopy, X-ray diffraction (XRD) and scanning electron microscopy (SEM) techniques, respectively.

2. Experimental methods

2.1. Synthesis of thin films ZnO

In this study, 0-5wt% Cu doped ZnO thin films were prepared via spray pyrolysis technique. For the preparation of thin films, zinc acetate dehydrate (Zn $(CH_3COO)_2$, $2H_2O$) and copper chloride ($CuCl_2$,$7H_2O$) were used as sources for ZnO and Cu dopant, respectively. First of all, zinc acetate dehydrate (0.5 M) were prepare by dissolving zinc acetate amount of 2.19 g in 20 ml double distiller water and methanol solution in a volume ratio (1/2:1/2). Some drops of acetic acid (CH_3COOH) were added into solutions as stabilizer and the mixture stirred on magnetic for 90min at 50 C° under vigorous stirring till getting a clear and homogeneous colorless solutions. For Cu doped ZnO, the molar percentages doping of Cu/Zn (0.5-5 wt.%) were added to the initial above solutions with kept in magnetic stirrer for the same time and temperature (90 min at 50 C°) until become a clear and homogeneous bleu solutions too. All our thin films samples deposited on heated 375C°glass slides (ref: 217102) during 12 min with a spray rate of the solution about 5mL/min with keeping distance nozzle-substrate equal 5 cm.

2.3. Characterization Techniques

The optical transmittance spectra of all samples were measured using a UV-Visible spectrophotometer (Shimadzu, Model 1800) in the region of 300-900 nm. X-ray diffraction of all thin films recorded using (XRD) with CuKα radiation (λ=1.5418 Å).

3-Results and discussion

3.1 Optical analysis

Fig.1 illustrates the optical transmittance spectra of thin films for different concentrations doping (0, 0.5, 1.5, 2 and 5 wt%) measured in range 300-900 nm. All the samples have transmittance of about (81-91%) in the wavelength range higher than 400nm, transmittance values after doping are greater than undoped value, this increase is may be assigned to high-quality of the thin films with feeble absorption losses or scattering [20]. as reveled by the feeble Urbach energy see table 1 and also based on calculated dislocation ($\delta=1/D^2$) which means the number of (lines/m^2) on the surface of the samples. It reveals that the doped sample at 2 wt% has the minimum value, then has a minimum scattering. Transmittance values are mentioned in Table 1. While at region wavelength lower 400 nm, an abrupt fall of the transmittance, for all the thin films, can be seen, exhibiting the onset fundamental absorption due to the transition between the valence band and conduction one. The energy band gap was calculated using well know Tauc equation:

$$(\alpha h\upsilon)^2 = B(h\upsilon - E_g)$$

where E_g and $h\upsilon$ are the band gap and the photon energy, respectively; α is the absorption coefficient and B is a constant. The variation of $(\alpha h\upsilon)^2$ plot as a function of ($h\upsilon$) is shown in Fig.2. The optical band gap E_g of all the samples are obtained by extrapolating the linear part of the $(\alpha h\upsilon)^2$ vs ($h\upsilon$) to the energy axis at $(\alpha h\upsilon)^2 = 0$. Fig. 2 displays the deduction of E_g values which are found to be about (3.25-3.28 eV) as listed in Table1. A decreasing in the optical band gap for the Cu doped samples compared to the undoped one (3.275eV) in the cases of (0.5, 1.5 and 2 wt. % of Cu) then increase for 5wt. % Cu doping. Such reduce may be caused by sp-d exchange interactions between the band electrons of ZnO as well as the localized d-electrons of Cu^{+2} ions substituting Zn^{+2} ions [21 , 22-25]. On the other hand, the decrease in the band gap by Cu doping is moreover attributed to the strong p-d mixing of O and Cu [26]. Whereas the increase from 3.268 to 3.284 eV in the case for 5Cu%. This increase in the value of E_g may originated from Burstein-Moss effect .

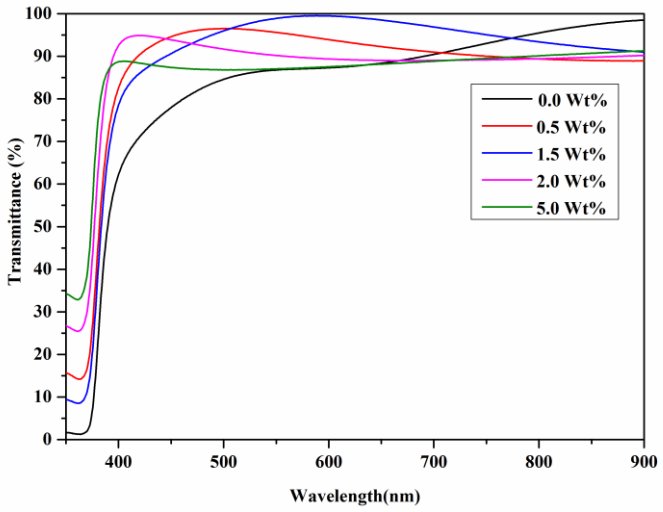

Fig.1. Transmittance spectra of ZnO thin films with different concentration (0-5wt%)

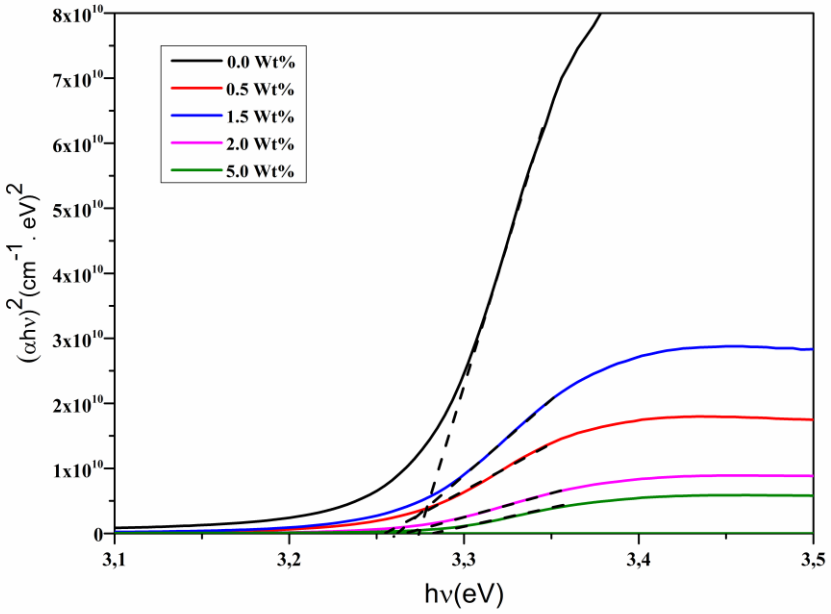

Fig.2. Plot of $(\alpha h\upsilon)^2$ versus $(h\upsilon)$ for the band gap determination for different concentration (0-5wt%).

We have used the band tail energy E_u, which characterizes the disorder defects in thin films, the band tail energy was calculated using the well know following relation:

$$\alpha = \alpha_0 \exp(h\upsilon / E_u)$$

where α is the absorption coefficient, α_0 is constant; $h\upsilon$ and E_u are photon energy and Urbach energy respectively. The Urbach energy was determined from the inverse of slop of *ln(a)* versus ($h\upsilon$), as depicted in Fig. 3. The found Urbach energy values varied between (88-104 meV), which are feeble values indicating the feeble disorder defects in thin films product. Compared between each other the Cu doped ZnO samples reveal high transmittance in the case of 2wt. % Cu doping which may be due to the less disorder in the product as illustrated in table 2.

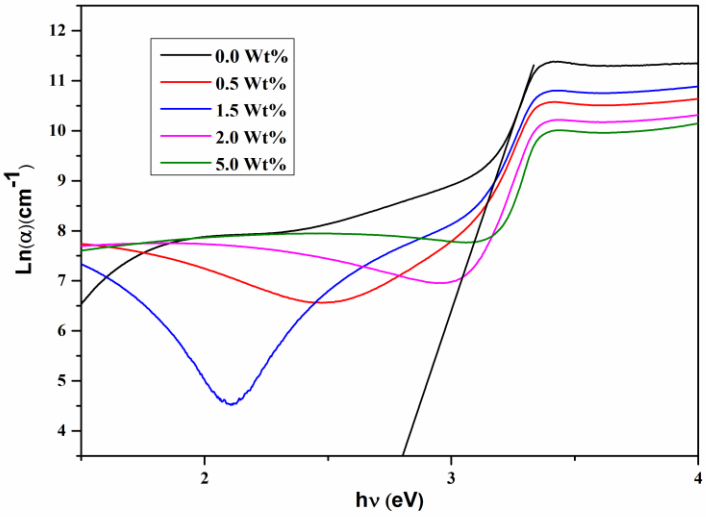

Fig.3. Plot of ($ln\alpha$) versus ($h\nu$) for the Urbach energy determination for different concentration (0-5wt%).

Table 2. Optical parameters for ZnO:Cu thin films.

Cu/Zn (wt%)	T%	E_g(eV)	E_u(meV)	δ (10^{+15}line/m^2)
0.0	81.25	3.275	88.58	1.76
0.5	86.12	3.259	104.70	1.37
1.5	85.04	3.262	104.15	1.47
2.0	91.71	3.268	89.68	1.11
5.0	89.86	3.284	95.69	1.42

3.2 Structural analysis

Fig.4 shows the XRD patterns of (0-5wt%) Cu doped ZnO. The obtained diffraction peaks obviously exhibits the crystalline nature of ZnO with peaks corresponding to (100), (002), (101), (110) and (103) which are in good according with the standard Join Committee Powder Diffraction JCPDS (Card No. 36-1451, space group $p6_3mc$) corresponding to hexagonal wurtzite structure of ZnO . As growth direction, *c*-axis (002) plane in all the thin films except ones (for 0.0 and 1.5 wt%) is the preferred. Comparing with undoped sample, one can detect from the XRD spectra that a small shift of the peaks towards the greater values of 2θ angles with (2 and 5 wt.%) Cu doped ZnO conforming the substitution of Zn^{2+} by Cu^{2+} in the lattice as seen in insert of Fig. 4. There are no additional or any peaks corresponding to copper. The averages size crystallite at (002) peaks were evaluated using Debye Sherrer's formula:

$$G = \frac{0.9\lambda}{\beta \cos\theta}$$

where λ, β and θ are the wavelength of X-ray, the full width at half maximum (*FWHM*) and the Bragg's angle of (*hkl*) reflections, respectively. The crystallite size of all thin films ZnO was averaged between (23-29 nm). After doping this average gradually increases with doping compared to the undoped ZnO. The maximum crystallite size was obtained with 2% wt Cu/Zn doping then decreases. For further information, the lattice parameter *c* is estimated using the following relations:

$$2d_{hkl}\sin\theta = n\lambda$$

and

$$\frac{1}{d^2{}_{hkl}} = \frac{4}{3}\left(\frac{h^2+hk+k^2}{a^2}\right)+\frac{l^2}{c^2}$$

where *n* is the order of diffraction, d_{hkl} is the plane spacing and *hkl* are the Miller indices of the planes. Compared to undoped sample, there is slight decreasing in the lattice parameter *c* of ZnO matrix for (2 and 5 wt% doping) which can be attributed to replacement of Zn^{+2} by Cu^{+2} having ionic radius (0.73Å) into ZnO crystal lattice. The later is a less than Zn^{+2} ionic radius (0.74 Å) leading to a decrease in the *d* inter spacing and unit cell. All those structural parameters of ZnO thin films are tabulated in Table 2

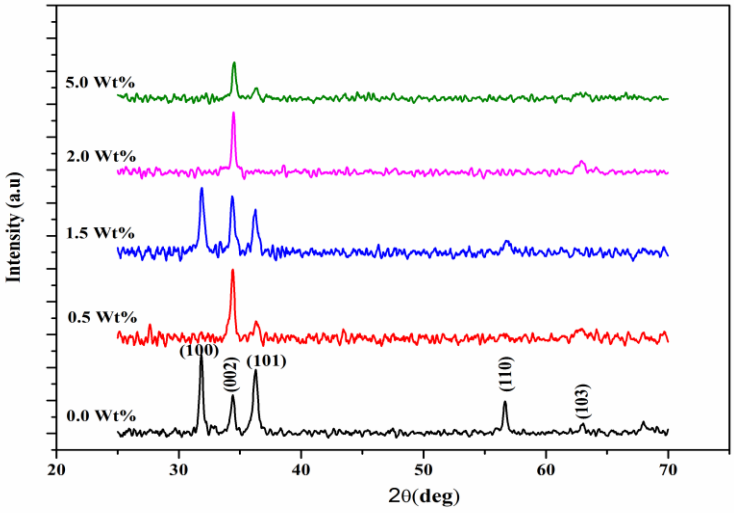

Fig. 4. X-ray diffraction pattern of ZnO thin films with different Cu concentration (0-5wt%), insert represents the shift of θ.

Table 2. Structural parameters for (0-5wt%) Cu doped ZnO thin films (c_0 is taken from JCPDS (Card No. 36-1451, space group $p6_3mc$))

Samples wt%Cu doping	2θ	Lattice parameters(Å)		Calculated d(Å)	Average grain size (nm)
		c	$\Delta c=c-c_0$		
0.0	34.424	5.2089	0.0029	2.6045	23.82
0.5	34.417	5.2099	0.0039	2.6049	26.98
1.5	34.406	5.2117	0.0057	2.6058	26.02
2.0	34.488	5.1996	-0.0064	2.5998	29.99
5.0	34.538	5.1923	-0.0137	2.5961	26.54

4. Conclusion

In summary, undoped (ZnO) and copper doped ZnO thin films were deposited by spray pyrolysis technique with moving nozzle (homemade) onto glass substrate heated at 375°C. The optical study reveals that the average transmittance of all samples was more than 81% in the visible region, and becomes more transparent with Cu doping. Also optical gap energy predicted to be in 3.25-3.28eV range. XRD study indicated that all thin films are crystallized in a hexagonal wurtzite structure with a strong *(002)* preferred orientation except (for 0.0 and 1.5 wt%). A maximum value of crystallite size *G*=29 nm is attained with 2wt.% doping. As a result, Cu is a good doping quality for transparent ZnO thin films amelioration which may be widely applied in optoelectronic devices, etc.

References:

[1] A. Djurišić, A.M.C. Ng, X. Chen, ZnO nanostructures for optoelectronics: material properties and device applications, Progress in quantum electronics, 34 (2010) 191-259.
[2] V. Galstyan, E. Comini, C. Baratto, G. Faglia, G. Sberveglieri, Nanostructured ZnO chemical gas sensors, Ceramics International, 41 (2015) 14239-14244.
[3] S.-Y. Lee, T. Hwang, S. Lee, W. Lee, B. Lee, J. Kim, S. Kim, H. Lee, H.-M. Lee, B. Park, Nanoroughness control of Al-Doped ZnO for high efficiency Si thin-film solar cells, Current Applied Physics, 15 (2015) 1353-1357.
[4] J.-H. Lee, K.-H. Ko, B.-O. Park, Electrical and optical properties of ZnO transparent conducting films by the sol–gel method, Journal of crystal growth, 247 (2003) 119-125.
[5] S. Kim, H. Moon, D. Gupta, S. Yoo, Y.-K. Choi, Resistive switching characteristics of sol–gel zinc oxide films for flexible memory applications, Electron Devices, IEEE Transactions on, 56 (2009) 696-699.
[6] R. Yousefi, B. Kamaluddin, P. Room-temperature, spectra indicate that they have a potential application as properties of ZnO nanobelts, Appl. Surf. Sci, 255 (2009) 9376-9380.
[7] N. Yamamoto, H. Makino, S. Osone, A. Ujihara, T. Ito, H. Hokari, T. Maruyama, T. Yamamoto, Development of Ga-doped ZnO transparent electrodes for liquid crystal display panels, Thin Solid Films, 520 (2012) 4131-4138.
[8] G.M. Ali, P. Chakrabarti, ZnO-based interdigitated MSM and MISIM ultraviolet photodetectors, Journal of Physics D: Applied Physics, 43 (2010) 415103.
[9] K. Raja, P. Ramesh, D. Geetha, Synthesis, structural and optical properties of ZnO and Ni-doped ZnO hexagonal nanorods by Co-precipitation method, Spectrochimica Acta Part A: Molecular and Biomolecular Spectroscopy, 120 (2014) 19-24.

[10] S. Fabbiyola, L.J. Kennedy, U. Aruldoss, M. Bououdina, A. Dakhel, J. JudithVijaya, Synthesis of Co-doped ZnO nanoparticles via co-precipitation: Structural, optical and magnetic properties, Powder Technology, 286 (2015) 757-765.
[11] G.E. Fernandes, D.-J. Lee, J.H. Kim, K.-B. Kim, J. Xu, Infrared and microwave shielding of transparent Al-doped ZnO superlattice grown via atomic layer deposition, Journal of Materials Science, 48 (2013) 2536-2542.
[12] M. Arshad, M.M. Ansari, A.S. Ahmed, P. Tripathi, S. Ashraf, A. Naqvi, A. Azam, Band gap engineering and enhanced photoluminescence of Mg doped ZnO nanoparticles synthesized by wet chemical route, Journal of Luminescence, 161 (2015) 275-280.
[13] C. Boukaous, B. Benhaoua, A. Telia, S. Ghanem, Effect of copper doping sol-gel ZnO thin films: physical properties and sensitivity to ethanol vapor, Materials Research Express, 4 (2017) 105024.
[14] A. Abdulrahman, STUDY THE OPTICAL PROPERTIES OF THE VARIOUS DEPOSITION SOLUTIONS OF ZnO NANORODS GROWN ON GLASS SUBSTRATE USING CHEMICAL BATH DEPOSITION TECHNIQUE, Journal of Ovonic Research Vol, 16 (2020) 181-188.
[15] Z. Fang, Y. Tan, H. Gong, C. Zhen, Z. He, Y. Wang, Transparent conductive Tb-doped ZnO films prepared by rf reactive magnetron sputtering, Materials Letters, 59 (2005) 2611-2614.
[16] M. Salah, S. Azizi, A. Boukhachem, C. Khaldi, M. Amlouk, J. Lamloumi, Effects of lithium doping on: microstructure, morphology, nanomechanical properties and corrosion behaviour of ZnO thin films grown by spray pyrolysis technique, Journal of Materials Science: Materials in Electronics, 30 (2019) 1767-1785.
[17] M. Tliba, A. Benhaoua, R. Gheriani, B. Benhaoua, A. Rahal, C. Boukaous, A. Tliba, La-DOPED ZNO THIN FILMS PREPARED BY SPRAY PYROLYSIS WITHMOVING NOZZLE: STUDY OF PHYSICAL PROPERTIES AND ADSORPTION ABILITY OF THE COPPER, DIGEST JOURNAL OF NANOMATERIALS AND BIOSTRUCTURES, 13 (2018) 991-1002.
[18] B. Benhaoua, A. Rahal, S. Benramache, The structural, optical and electrical properties of nanocrystalline ZnO: Al thin films, Superlattices and Microstructures, 68 (2014) 38-47.
[19] C. Bates, W. White, R. Roy, The solubility of transition metal oxides in zinc oxide and the reflectance spectra of Mn2+ and Fe2+ in tetrahedral fields, Journal of Inorganic and Nuclear Chemistry, 28 (1966) 397-405.
[20] R. Baghdad, B. Kharroubi, A. Abdiche, M. Bousmaha, M. Bezzerrouk, A. Zeinert, M. El Marssi, K. Zellama, Mn doped ZnO nanostructured thin films prepared by ultrasonic spray pyrolysis method, Superlattices and Microstructures, 52 (2012) 711-721.
[21] R. Elilarassi, G. Chandrasekaran, Synthesis and optical properties of Ni-doped zinc oxide nanoparticles for optoelectronic applications, Optoelectronics letters, 6 (2010) 6-10.
[22] K.J. Kim, Y.R. Park, Spectroscopic ellipsometry study of optical transitions in Zn 1− x Co x O alloys, Applied Physics Letters, 81 (2002) 1420-1422.
[23] J. Diouri, J. Lascaray, M. El Amrani, Effect of the magnetic order on the optical-absorption edge in Cd 1− x Mn x Te, Physical Review B, 31 (1985) 7995.
[24] M. Ferhat, A. Zaoui, R. Ahuja, Magnetism and band gap narrowing in Cu-doped ZnO, Applied Physics Letters, 94 (2009) 142502.
[25] E. Burstein, Anomalous optical absorption limit in InSb, Physical Review, 93 (1954) 632.
[26] H.F. McMurdie, M.C. Morris, E.H. Evans, B. Paretzkin, W. Wong-Ng, L. Ettlinger, C.R. Hubbard, Standard X-ray diffraction powder patterns from the JCPDS research associateship, Powder Diffraction, 1 (1986) 64-77.

Structural stability, electronic, and mechanical properties of new stable phases for the ternary alloy $Mg_xCd_{1-x}O$

Nor El Houda DJEZZAR*, Kouider DRISS-KHODJA, and Bouhalouane Amrani

Materials theory and simulation laboratory, Oran1 University Ahmed Ben Bella, Oran, Algeria

* djezzar.norelhouda@edu.univ-oran1.dz

Abstract

With the development of technology, finding new crystallographic phases with remarkable properties and that are easy to be elaborated experimentally is highly recommended. The II-VI semiconductors are very interesting materials for various applications due to the possibility to preselect and control their physical properties; which can be realized by varying the atomic concentration to form alloys. Herein, density functional theory (DFT) calculation has been performed for the alloy $Mg_xCd_{1-x}O$ to investigate the thermodynamic, dynamical, and local stability of $MgCdO_2$ for 50% of concentration and $MgCd_3O_4$ for 25%. $MgCdO_2$ is stable in a tetragonal phase whereas, the $MgCd_3O_4$ is not stable in the same cubic phase predicted for 75% (Pm-3m) in the previous work, instead, it is stable in another cubic phase (P-43m). the elastic constants and mechanical properties predict that adding Mg atoms to the alloy enhance the resistance of the material.

Keywords

$Mg_xCd_{1-x}O$, II-VI semiconductors, structural stability, mechanical properties.

Introduction:

Wide band gap II-VI semiconductors alloys are very interesting candidates for high performance optoelectronic devices in the blue and ultraviolet electromagnetic regions, such as light emitting diodes (LEDs) and laser diodes [1]–[4]. Despite the important properties of this type of semiconductors, the modulation of some of it is necessary. Among the options to control and modulate a property of a material is to form alloys, which can be stable in different possible phases.

In recent years, after all the achievements realized by researchers in the condensed matter field, using density functional theory (DFT); the experimenters are far from keeping pace with this development due to a lot of difficulties to calibrate the experimental parameters. Finding new stable phases may not only improve the properties of a system but also might facilitate its experimental study.

This work is an extension of our latest paper on the ternary alloy $Mg_xCd_{1-x}O$ studied in a new possible phase, wherein only the stability of Mg_3CdO_4 that refers to an atomic fraction of 75% was investigated along with its mechanical and optoelectronic properties [5]. In this paper, MgCdO2 for 50 % of concentration and $MgCd_3O_4$ for 25 % were studied for other phases in which the structural stability, and mechanical properties were discussed.

Computational details:

Based on Density functional theory (DFT) [6], the calculation was carried out by solving iteratively the Kohn-Sham equation as implemented in Wien2k and Quantum ESPRESSO simulation package codes [7], [8]. The exchange correlation potentials are treated using the generalized gradient approximation (GGA) in the form of Perdew, Burke and Ernzerhof (PBE) functional [9]. The electronic properties were calculated using Wien2k and improved with modified Becke-Johnson exchange potential by Tran and Blaha (TB-mbj-GGA) correction [10]. For x= 0.25, the material crystallizes in P-43m cubic space group; on the other hand, for x= 0.50 it crystallizes

in a tetragonal phase P4/mmm. For the Full-Potential Linearized Augmented Planewave Method (FPLAPW) [11], The muffin-tin radii for Mg, Cd and O are 2.03, 2.18 and 1.87 Bohr, respectively. The cut-off energy and the plane wave cut-off $RMT \times k_{max}$ were set by default. Further, the pseudo-potential plane wave method (PW-PP) using Ultrasoft pseudo-potential (USPP) [12] was used to describe the ion-electron interaction, with cutoff energies of 60 Ry and 600 Ry for the wave functions and the charge density respectively. The Brillouin zone was sampled with k-points meshes 11×11×11 based on the method of Monkhorst-pack (MP) [13] for the cubic structure and of 12×12×9 for the tetragonal structure. The self-consistent total energy calculation was set up to converge toward 10^{-4} Ry. The phonon properties are calculated using the density functional perturbation theory (DFTP) [14]. A 4×4×4 and 4×4×3 *q*-points MP meshes have been adopted for a cubic and tetragonal systems respectively.

Results and discussion

The analysis of possible phases of II-VI semiconductors ternary alloys from the material project database [15], led us to identify three new phases for $Mg_xCd_{1-x}O$ compound. In the previous work, the stability of Mg_3CdO_4 (i.e., x=0.75, cubic phase, Pm-3m space group) is confirmed together with its optoelectronic and mechanical properties [5]. The table 1 illustrate the structural parameters of the studied system. As shown in table 1, the parameters for MgO and CdO are in a good agreement with experimental results. The formation enthalpy for ternary alloy $A_xB_{1-x}C$ is defined by equation 1, as:

$$\Delta H = E(A_xB_{1-x}C)\text{-}x\ E(A) - (1\text{-}x)\ E(B)\ \text{-}E(C) / y \qquad \text{(eq.1)}$$

Where $E(A_xB_{1-x}C)$ is the total energy of the alloy at composition x. E(A), E(B) and, E(C) are the total energies of elements that form the alloy optimized in their bulk structure, and y is the number of atoms of the compound. The calculated ΔH (x=0.25) and, ΔH (x=0.50) are -1.36 eV/atm and -1.78 eV/atm respectively; indicating that this alloy may be thermodynamically stable.

The elastic constants are depicted in table 2, representing a local stability according to Born stability criteria [16], given by equation 2 and 3 for cubic and tetragonal systems respectively. Further, the phonon dispersion spectrums were calculated and represented in figure 2. the results show no imaginary frequencies for the phases $MgCd_3O_4$ (P-43m), $MgCdO_2$ (P/mmm) and for, Mg_3CdO_4 (Pm-3m) it has been reported previously [5], indicating a dynamic stability of the system in the studied new phases. It is Noteworthy, that $MgCd_3O_4$ is not stable in Pm-3m space group and we have not tested the stability of Mg_3CdO_4 in the space group P-43m.

$$C_{11}+2C_{12}>0,\ C_{11}-C_{12}>0,\ C_{44}>0 \qquad \text{(eq.2)}$$

$$C_{11}>|C_{12}|,\ 2C_{13}^2<C_{33}(C_{11}+C_{12}),\ C_{44}>0,\ C_{66}>0 \qquad \text{(eq.3)}$$

Beside the structural stability, understanding the elastic properties can predict the behavior of materials (i.e. stiffness, ductile or brittle behavior…), during elaboration under experimental conditions. Moreover, the lattice mismatch between the substrate and the deposited semi-conductor as a thin film can evince stresses on it and affect its properties. The Cadmium Oxide (CdO) is fragile compared with Magnesium Oxide (MgO); therefore, the addition of Mg atoms to CdO can improve its resistance against tensile or attraction and shear deformations. As it can be seen, for 25 % of Mg we observe a slight decrease of the elastic constants. Otherwise, for the rest of the atomic fraction; the stiffness viz the elastic constants increase and the results are listed in table 2. The elastic properties such as Bulk modulus B, shear modulus G, Young's modulus E and Poison's ratio υ, can be estimated using the Voigt-Reuss-Hill approximation [17], based on the elastic constants. These properties are calculated and listed in table 3. The bulk modulus concerns the resistance of the material against volume change, Shear modulus G measures the stiffness against shear deformation, and Young's modulus E, represents the ability of a material to deform elastically. The figure 3.a and 3.b, represent the variation of elastic properties and Pugh's ratio with respect to atomic fraction respectively. These quantities increase with the atomic fraction except for 25 % (see figure 3.a),

indicating that Mg atoms arise the stiffness of this alloy, against the deformation. Another important parameter is Pugh's ratio (ratio between bulk and shear modulus B/G), which describe the behavior of a deformed material. This ratio is related to the transition between brittle and ductile character of a solid and it was observed by Pugh in 1954 [18]. The critical value found by Pugh is 1.75. The ratio B/G reflects the hardness of a material. The smaller the ratio B/G is, the bigger the hardness of the material which is classified as brittle and therefore it can change easily its volume. On the other hand, material with a greater B/G is ductile and can be easily distorted. Pugh's ratio indicate that the alloy becomes brittle by adding Mg atoms.

Conclusion

The purpose of this paper, is to find alternatives for the well-known structures of the system $Mg_xCd_{1-x}O$, to modulate its properties and even to widen the elaboration possibilities for the experimental field. Based on density functional theory calculation, the phases $MgCd_3O_4$, $MgCdO_2$, and Mg_3CdO_4 are thermodynamically, locally and dynamically stable. The elastic constants and properties show that adding Mg atoms to the binary compound CdO to form the alloy $Mg_xCd_{1-x}O_4$ can improve its resistance against tensile or attraction and shear deformations, as a result the material becomes brittle

References

[1] M. Houssa, E. Scalise, K. Sankaran, G. Pourtois, V. V. Afanas 'Electronic properties of hydrogenated silicene and germanene', Applied Physics Letters: Vol 98, No 22, doi: https://doi.org/10.1063/1.3595682
[2] A. Datta, J. Fiala, P. Becla, and S. Motakef, 'Stable room-temperature thallium bromide semiconductor radiation detectors', APL Materials, vol. 5, no. 10, p. 106109, Oct. 2017, doi: 10.1063/1.5001181.
[3] H. M. Ng, State-of-the-Art Program on Compound Semiconductors XLI and Nitride and Wide Bandgap Semiconductors for Sensors, Photonics and Electronics V: Proceedings of the International Symposia. The Electrochemical Society, 2004.
[4] B. Nourozi, A. Aminian, N. Fili, Y. Zangeneh, A. Boochani, and P. Darabi, 'The electronic and optical properties of MgO mono-layer: Based on GGA-mBJ', Results in Physics, vol. 12, pp. 2038–2043, Mar. 2019, doi: 10.1016/j.rinp.2019.02.054.
[5] N. E. H. Djezzar, K. Driss-Khodja, and B. Amrani, 'Exploring dynamical, mechanical and optoelectronic properties of cubic Mg3CdO4: First-principle study', Materials Today Communications, vol. 26, p. 102106, Mar. 2021, doi: 10.1016/j.mtcomm.2021.102106.
[6] W. Kohn and L. J. Sham, 'Self-Consistent Equations Including Exchange and Correlation Effects', Phys. Rev. 140, A1133 (1965), doi: https://doi.org/10.1103/PhysRev.140.A1133.
[7] P. Blaha, K. Schwarz, G. K. Madsen, D. Kvasnicka, and J. Luitz, 'wien2k', An augmented plane wave+ local orbitals program for calculating crystal properties, vol. 60, 2001.
[8] Paolo Giannozzi et al., 'QUANTUM ESPRESSO: a modular and open-source software project for quantum simulations of materials', J. Phys.: Condens. Matter, 2009
[9] P. Perdew, 'Generalized gradient approximations for exchange and correlation: A look backward and forward', p. 6.
[10] D. Koller, F. Tran, and P. Blaha, 'Improving the modified Becke-Johnson exchange potential', Phys. Rev. B, vol. 85, no. 15, p. 155109, Apr. 2012, doi: 10.1103/PhysRevB.85.155109.
[11] O. K. Andersen, 'Linear methods in band theory', Phys. Rev. B, vol. 12, no. 8, pp. 3060–3083, Oct. 1975, doi: 10.1103/PhysRevB.12.3060.
[12] D. Vanderbilt, 'Soft self-consistent pseudopotentials in a generalized eigenvalue formalism', Phys. Rev. B, vol. 41, no. 11, pp. 7892–7895, Apr. 1990, doi: 10.1103/PhysRevB.41.7892.
[13] 'Phys. Rev. B 13, 5188 (1976) - Special points for Brillouin-zone integrations.
[14] S. Baroni, S. de Gironcoli, A. Dal Corso, and P. Giannozzi, 'Phonons and related crystal properties from density-functional perturbation theory', Rev. Mod. Phys., vol. 73, no. 2, pp. 515–562, Jul. 2001, doi: 10.1103/RevModPhys.73.515.
[15] A. Jain et al., 'Commentary: The Materials Project: A materials genome approach to accelerating materials innovation', APL Materials, vol. 1, no. 1, p. 011002, Jul. 2013, doi: 10.1063/1.4812323.
[16] F. Mouhat and F.-X. Coudert, 'Necessary and sufficient elastic stability conditions in various crystal systems', Phys. Rev. B, vol. 90, no. 22, p. 224104, Dec. 2014, doi: 10.1103/PhysRevB.90.224104.
[17] R. Hill, 'The Elastic Behaviour of a Crystalline Aggregate', Proc. Phys. Soc. A, vol. 65, no. 5, pp. 349–354, May 1952, doi: 10.1088/0370-1298/65/5/307.
[18] 'XCII. Relations between the elastic moduli and the plastic properties of polycrystalline pure metals: The London, Edinburgh, and Dublin Philosophical Magazine and Journal of Science: Vol 45, No 367'.
[19] A. Schleife, F. Fuchs, J. Furthmüller, and F. Bechstedt, 'First-principles study of ground- and excited-state properties of MgO , ZnO , and CdO polymorphs', Phys. Rev. B, vol. 73, no. 24, p. 245212, Jun. 2006, doi: 10.1103/PhysRevB.73.245212.

[20] D. Alfè, 'Melting Curve of MgO from First-Principles Simulations', Phys. Rev. Lett., vol. 94, no. 23, p. 235701, Jun. 2005, doi: 10.1103/PhysRevLett.94.235701.
[21] R. J. Guerrero-Moreno and N. Takeuchi, 'First principles calculations of the ground-state properties and structural phase transformation in CdO', Phys. Rev. B, vol. 66, no. 20, p. 205205, Nov. 2002, doi: 10.1103/PhysRevB.66.205205.
[22] A. J. Cinthia, G. S. Priyanga, R. Rajeswarapalanichamy, and K. Iyakutti, 'Structural, electronic and mechanical properties of alkaline earth metal oxides MO (M=Be, Mg, Ca, Sr, Ba)', Journal of Physics and Chemistry of Solids, vol. 79, pp. 23–42, Apr. 2015, doi: 10.1016/j.jpcs.2014.10.021.
[23] A. JemmyCinthia, G. Sudhapriyang, R. Rajeswarapalanichamy, and M. Santhosh, 'Structural, Electronic and Elastic Properties of ZnO and CdO: A First-Principles Study', Procedia Materials Science, vol. 5, pp. 1034–1042, 2014, doi: 10.1016/j.mspro.2014.07.394.
[24] U. Bhandari, C. O. Bamba, Y. Malozovsky, S. Franklin, D. Bagayoko, 'Predictions of Electronic, Transport, and Structural Properties of Magnesium Sulfide (MgS) in the Rocksalt Structure'. Journal of Modern Physics, Vol.09 No.09(2018)
[25] B.B. Karki, L. Stixrude, S.J. Clark, M.C. Warren, G.J. Ackland and J. Crain,'Structure and elasticity of MgO at high pressure', American Mineralogist, 2015, doi: https://doi.org/10.2138/am-1997-1-207
[26] F. Peng, D. Chen, H. Fu, and X. Cheng, 'Phase transition and elasticity of CdO under pressure', phys. stat. sol. (b), vol. 246, no. 1, pp. 71–76, Jan. 2009, doi: 10.1002/pssb.200844332.
[27] Edward D Palik; Gorachand Ghosh 'Handbook of optical constants of solids', 1998.

Table Captions

Table 1: Calculated structural parameters, bulk modulus B, bulk modulus first derivative with respect to pressure B', for the alloy composition.

Table 2: Calculated elastic constants Cij for $Mg_xCd_{1-x}O$ alloy (x=0,0.25,0.50,0.75 and 1)

Table 3: Calculated bulk modulus B, Young's modulus E, shear modulus G, Poisson's ratio ν and B/G.

Figure Captions

Figure 1: Crystal structures of $Mg_xCd_{1-x}O$ alloy. (a) CdO, (b) MgO, (c) $MgCd_3O_4$, (d) $MgCdO_2$, I Mg_3CdO_4.

Figure 2: Phonon band structure and phonon density of states (PDOS) of (a) $MgCd_3O_4$ and, (b) $MgCdO_2$.

Figure 3: Calculated (a) elastic properties (b) Pugh's ratio, with respect to the atomic fraction of Mg.

Table 1

Atomic fraction **x (%)**	**Structural formula**	**Space group**	**a (Å)**	**c (Å)**	**B (Gpa)**	**B'**
0	**CdO**	**Fm-3m**	4.7706 [a]	-	128.1663 [a]	4.7580 [a]
			4.7774 [b]		125.6225 [b]	4.8920 [b]
			4.7700 [c]		147.0000 [c]	4.2000 [c]
			4.7700 [e]		130.0000 [e]	4.1000 [e]
			4.7790 [h]		141.0000 [h]	4.0000 [h]
25	**$MgCd_3O_4$**	**P-43m**	5.0610 [a]	-	96.3165 [a]	4.7543 [a]
			5.0064 [b]		96.9986 [b]	4.5030 [b]
50	**$MgCdO_2$**	**P4/mmm**	3.2358 [a]	4.5775 [a]	138.2876 [a]	4.8264 [a]
			3.2402 [b]	4.5797 [b]	134.8346 [b]	4.5380 [b]
75	**Mg_3CdO_4**	**Pm-3m**	4.4457 [a]	-	142.2620 [a]	4.4960 [a]
			4.4442 [b]		141.3254 [b]	4.392 [b]
100	**MgO**	**Fm-3m**	4.2584 [a]	-	149.2165 [a]	4.1323 [a]
			4.2541 [b]		149.2977 [b]	4.0230 [b]
			4.2540 [c]		148.6000 [c]	4.3000 [c]
			4.2130 [d]		160.0000 [d]	-
			4.2410 [k]		167.0000 [k]	4.0000 [k]

[a] Wien2k (present work); [b] Quantum Espresso (present work); [c] Reference [19]; [d] Reference [20] ; [e] Reference [21] ;[k] Reference [22] ; [h] Reference [23]

Table 2

x (%)	Formule structurale	Space group	C11(Gpa)	C12(Gpa)	C44(Gpa)	C13(Gpa)	C33(Gpa)	C66(Gpa)
0	CdO	Fm-3m	185.5429 [a] 177.5764 [b] 207.8000 [f] 183.9900 [i]	101.8226 [a] 102.3213 [b] 106.3000 [f] 96.0100 [i]	51.4961 [a] 47.6761 [b] 54.9000 [f] 45.7800 [i]	-	-	-
25	$MgCd_3O_4$	P-43m	103.9901 [a] 116.0914 [b]	72.3860 [a] 89.14168 [b]	41.4389 [a] 39.5041 [b]	-	-	-
50	$MgCdO_2$	P4/mmm	235.9515 [a] 230.7819 [b]	84.9635 [a] 74.2087 [b]	70.2718 [a] 71.9990 [b]	96.6058 [a] 97.0285 [b]	209.9226 [a] 211.8841 [b]	47.7310 [a] 52.8634 [b]
75	Mg_3CdO_4	Pm-3m	248.844 [a] 226.3066 [b]	111.838 [a] 101.6665 [b]	102.618 [a] 96.9935 [b]	-	-	-
100	MgO	Fm-3m	285.2970 [a] 273.8164 [b] 291.0000 [g] 297.0000 [k]	82.8500 [a] 89.3129 [b] 91.0000 [g] 99.6000 [k]	147.1126 [a] 141.9353 [b] 139.0000 [g] 151.9000 [k]	-	-	-

[a] Wien2k (present work); [b] Quantum Espresso (present work); [f] Reference [24] ; [g] Reference [25]; [i] Reference [26]; [k]Reference [22]

Table 3

x (%)	Structural formula	Space group	B (Gpa)	E (Gpa)	G (Gpa)	υ	A	B/G
0	CdO	Fm-3m	129.7290 [a] 127.4063 [b]	126.7540 [a] 116.8403 [b]	47.3970 [a] 43.3657 [b]	0.3370 [a] 0.3471 [b]	1.2302 [a] 1.2671 [b]	2.7370 [a] 2.9379 [b]
25	$MgCd_3O_4$	P-43m	82.9207 [a] 98.1249 [b]	75.8028 [a] 70.7889 [b]	28.1573 [a] 25.6887 [b]	0.3461 [a] 0.3778 [b]	2.6224 [a] 2.9317 [b]	2.9449 [a] 3.8198 [b]
50	$MgCdO_2$	P4/mmm	137.5090 [a] 134.4371 [b]	165.5060 [a] 169.3200 [b]	63.6860 [a] 65.6246 [b]	0.2990 [a] 0.2900 [b]	1.1125 [a] 1.1584 [b]	2.1592 [a] 2.0486 [b]
75	Mg_3CdO_4	Pm-3m	142.2620 [a] 143.2132 [b]	220.9990 [a] 204.9288 [b]	87.2720 [a] 81.2305 [b]	0.2660 [a] 0.2614 [b]	1.4980 [a] 1.5564 [b]	1.8048 [a] 1.7630 [b]
100	MgO	Fm-3m	150.332 [a] 150.8141 [b] 155.0000 [h] 165.5000 [k]	296.632 [a] 283.4230 [b] 249.0000 [h] 305.0000 [k]	126.643 [a] 119.4200 [b] 155.0000 [h] 127.9000 [k]	0.1710 [a] 0.1866 [b] 0.1800 [h] 0.2520 [k]	1.4533 [a] 1.5386 [b] - 0.7600 [k]	1.1870 [a] 1.2629 [b] - -

[a] Wien2k (present work); [b] Quauntum Espresso (present work); [h] Reference [27];[k] Reference [22];[f] Reference [23]

Figure 1

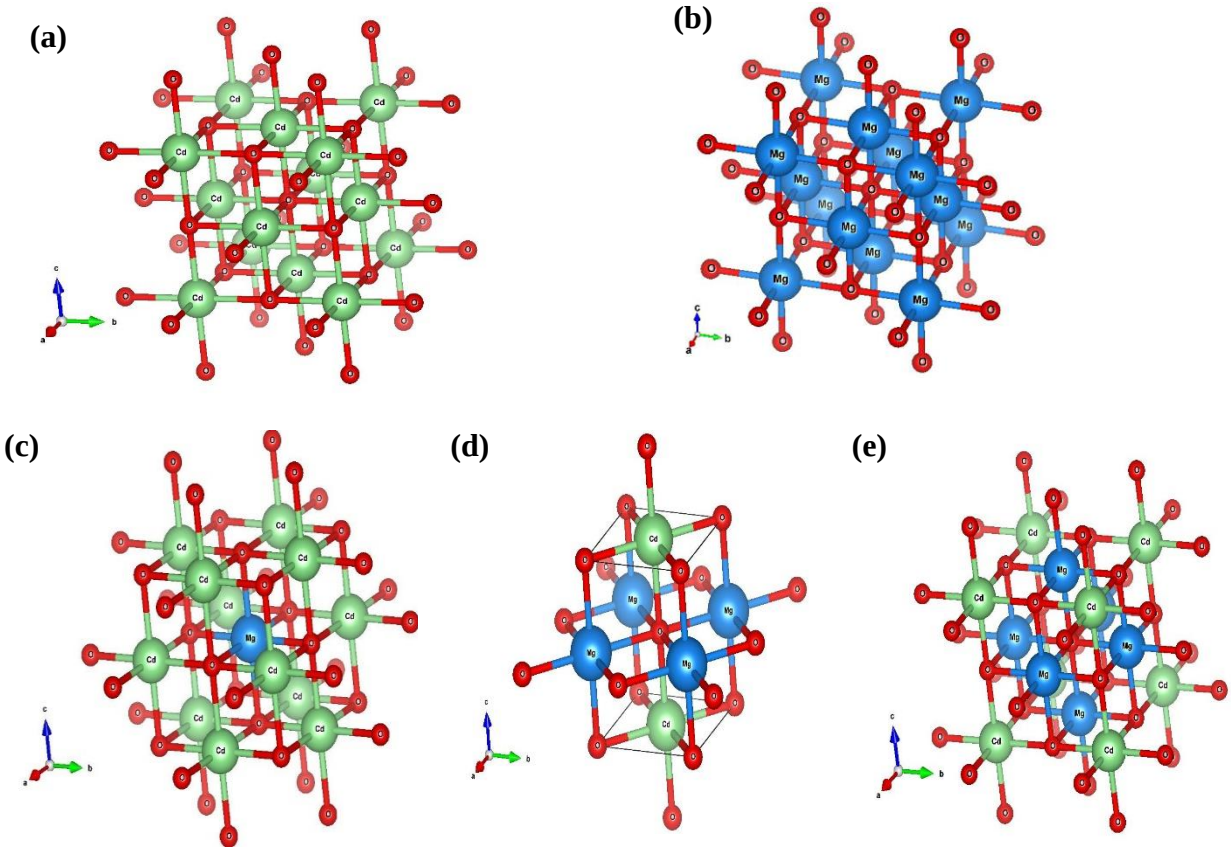

Figure 2

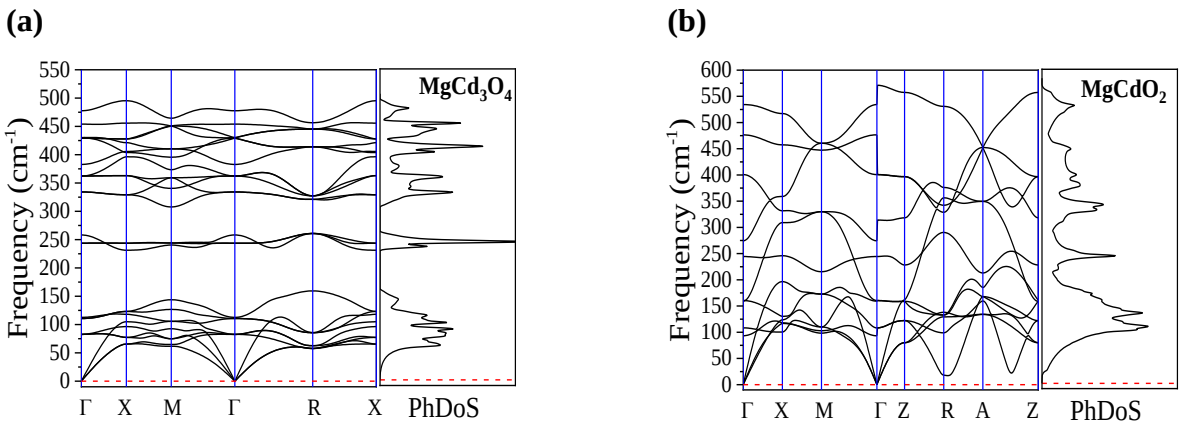

Figure 3

(a)

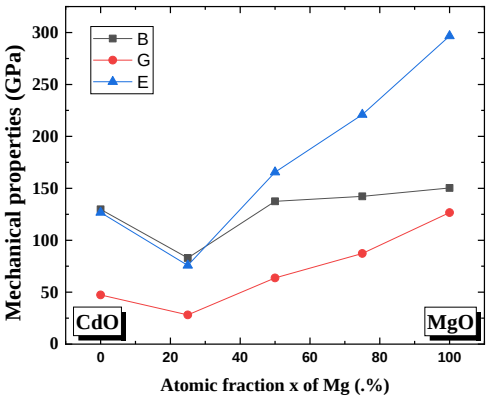
B
G
E
Mechanical properties (GPa)
300
250
200
150
100
50
0
CdO
MgO
0
20
40
60
80
100
Atomic fraction x of Mg (.%)

(b)

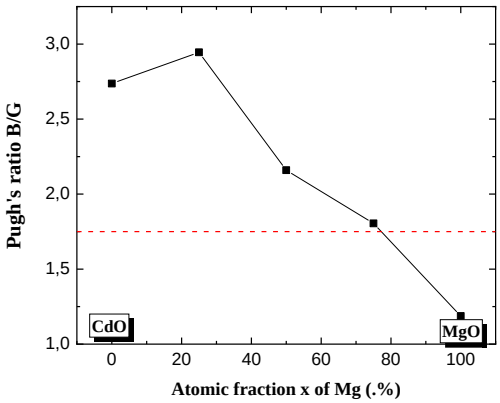
Pugh's ratio B/G
3,0
2,5
2,0
1,5
1,0
CdO
MgO
0
20
40
60
80
100
Atomic fraction x of Mg (.%)

A new Design of High-sensitive Photonic Crystal Biosensor Based on Ring-shape Holes for Detecting Glucose Concentration

Assia Daas, Souheil Mouetsi, Abderraouf Hocini
Laboratory of Electronics and New Technology (LENT), Department of electrical engineering, Faculty of sciences and applied sciences, University of Larbi Ben M'hidi, B.P.358, Oum el Bouaghi, Ain Beida, 04201, Algeria
Email: assiadaas@yahoo.fr

Abdesselam Hocini
Signal and Systems Analysis Laboratory, Department of Electronics, University of M'Sila BP.166, Route Ichebilia, M'Sila, 28000, Algeria

Fateh Lariouri
Department of Electronics, Faculty of Engineering Mentouri University Constantine 1 Algeria

Abstract **- In this work an optical sensors has been designed and studied with different parameters to select the best result of Q factor and sensitivity; for that, we choose a 2D photonic crystal (PhC). The refractive index (RI) sensor is formed by a point-defect resonant cavity in the quasi-sandwiched waveguide with a hexagonal lattice of air holes. The properties of the sensor are simulated using a couple of two methods finite-difference time-domain method (FDTD) and the plane wave method (PWE). The calculation results show that a change in ambient RI is apparent; the sensitivity of the sensor is achieved.**

The objective of our research was primarily modeling and optimization geometry of a first coupling path between a waveguide and a ring resonator with base of photonic crystals in order to improve the coupling properties in this structure.

It is in this context that we have exploited all the parameters already developed for improve the biodetection properties in a photonic crystal-based structure.

The role of our design is to sens small RI changes for detecting glucose concentration using resonant microcavity (RMC).

Index Terms -Biosensors, Cavity, Photonic crystals, Sensitivity, Quality factor, Resonance. FDTD, PWE.

I. INTRODUCTION

The simple, rapid and efficient detection of chemical or biological molecules has become a major challenge for the health, environment, agriculture, or even agro-food sectors, with increasingly demanding requirements. These have spawned the emergence of new technological solutions. In particular, on-chip integrated optical devices offer great potential for the development of transducers.

Generic, compatible with parallel detection, without markers of a wide variety of biomolecules and over a spectral range that can be adjusted from visible to infrared where absorption of many materials and biological noise are greatly reduced.

Their properties are mainly linked to the existence of forbidden bands which prevent the propagation of waves whatever the direction of the incident wave. These forbidden bands are used to create localized modes which confine optical energy. By introducing a defect (point or linear or both) into these structures, the periodicity and therefore the continuity of the Photonique Bande Gap (PBG) is broken and the propagation of light can be localized in the region of the defect.

The application of these photonic crystals as sensors constitutes a field of research which seems to be very promising due to their extreme miniaturization (0.1 mm^2 of detection surface), their high spectral sensitivity and the possibility of integrating them into MEMS. (Micro-Electro-Mechanical-Systems) The design of new photonic devices aimed at applications in various sectors of industry and high technologies, such as telecommunications (CP fibers), optoelectronics (lasers, photo detectors) and more recently bio-detection.

The detection phenomena are based on the high sensitivity of the localized modes appearing in the transmission spectra of photonic crystals via the variation of the refractive index of the analyte.

Two-dimensional microcavity photonic crystal sensors have both theoretically and experimentally demonstrated their ability to detect biochemical elements. Other authors have also proposed optical biosensors based on a CP waveguide. The sensors based on photonic crystal waveguides coupled with resonant cavities have many advantages such as compactness, high sensitivity, easy expansion to multi-channel sensors, various material choices and parallel measurement capability Recently, they have proved their aptitude for both theoretical and experimental detection, the latter is done by measuring the shift of the resonant wavelength in the transmission spectrum as a function of the change in the refractive index. .

Human health depends first and foremost on continuous biological monitoring. For this, the doctor is based on analyzes, most often blood, seeking to detect the presence but also to quantify biomolecules specific to diseases. These biomolecules are often either DNA that reveals genetic abnormalities or proteins, markers of disease. The most significant example concerns early diagnosis.

The more the bio detection will be sensitive, the more we detect a low concentration of these molecules and the more the probability of survival of the patient will be increased.

The uses of optical techniques in the context of bimolecular analyzes are very numerous. In this part, we present an overview of the different geometries of optical sensors used to measure refractive index variations for sensing applications, as well as a brief state of the art of their performance. The three most common configurations are: surface plasmon resonance (SPR) sensors, interferometry sensors and optical ring resonator sensors.

II. THEORETECAL AND DESIGN OF PROPOSED BIOSENSOR

In recent years, optical sensors which provide instantaneous detection and quantification of biological analytes have emerged of great interest, due to their promising characteristics such as: safety in flammable and explosive environment, immunity to electromagnetic interference, the rapidity of response and the ability to detect at a distance. Rapid advances in photonic technologies have dramatically improved detection performance, particularly in the areas of light-analyte interaction and device miniaturization. This has led to considerable improvements in the sensitivity and limit of detection (LD) of the sensor [1].

The principle of optical detection without label-free markers is based on the change one of the properties of light when it is in contact with the element of interest [2].

There are different detection methods for this, such as those exploiting the effects of changes in refractive index, absorbance property or non-linearity. Subsequently, we are only interested in detection based on the change of refractive index.

We have here a biosensor which has the ability to detect the glucose concentration [3].so an analysis has been performed to determine the parameters of the biosensor while the detection of glucose concentration in both normal and presence of glucose state, either with water or others aqueous solutions .

It formed by two-quasi waveguide and a ring cavity between their and the three are connected with a two punctual defect hole. So our coupling cavity-casiguids Phcs biosensor design is made using a hexagonal lattice of air holes with a refractive index Ri = 1) and radius of r=0.38a (a is the period and equal to 550 nm) these holes are implanted in silicon (Si) slab (background) with Ri=3.45; her thickness is 200nm . the radius of two defect air hole is R_d=0.3a

The purpose of using casi-guide is to pair the light in and out the cavity. And for a ring-shape holes is attend the maximum of confinement.

The number of holes is 17 × 17, size of the structure is 92.65 µm2, The silicon dioxide (SiO_2) layer with Ri of 1.45 (low index) and a thickness of 1500 nm is used as support of silicon slab (high index) this is what give us a big imprisonment of light in the vertical direction which safeguarded by full internal reflection, so optical losses are preventing accordingly thus the confinement in the cavity is enhanced. The values of radius' are Rin = 0.22a = 121 nm and Rout = 0.45a= 247.5 nm, respectively.

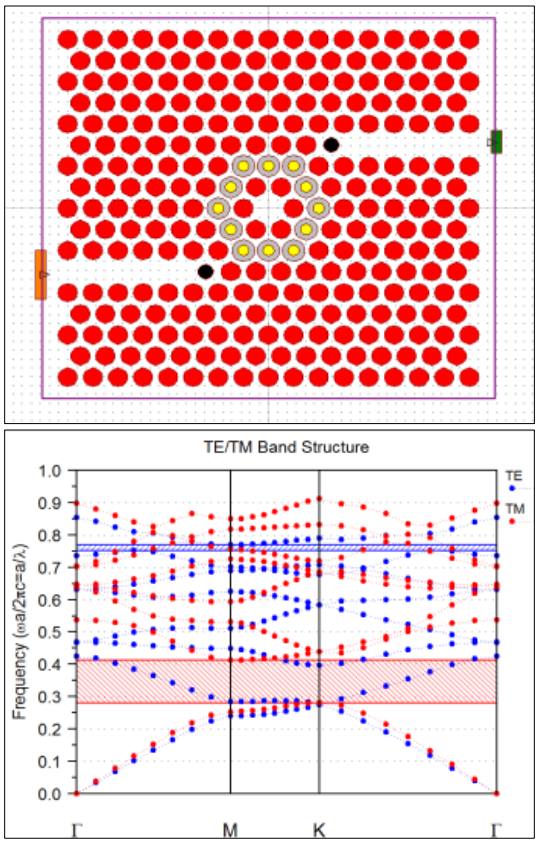

Fig. 1 Wavelength for the refractive index 1.33 glucose in the solution (C = 0 %).

Thus, the ringed air region is given as: Rout – Rin =126.5 nm. The Si is a good candidate for PhC applications and the number of holes is 27.

Concerning the fabrication process of such structure lies in the ring's manufacture, which is composed of dielectric rods emerged in air holes. Säynätjoki et al. [4] demonstrated that a thin rin beam lithography.

To decrease the computational calculations that may occur in two-dimensional (2-D) structures, in dielectric medium having the effective RI of 2.868, which corresponds to the effective index of the central guided TM polarization mode in a 230 nm thick Si slab on SiO2 at wavelength of 1550 nm. [5]

For the following numerical simulations, we applied the effective index approach given in references [6] and [7] . The dispersal properties of the systematic PhC structure have been analysed using the 2-D-PWE and FDTD method of Rsoft software[8].

For the TM polarization, The PBG of the fundamental structure without any defects calculated using PWE is depicted in Fig. 1. The basic structure has PBG for TM mode which is indicated by red region. As shown in Fig. 1, the normalized frequency is observed from ω1=0.279to ω2=0.409, where λ is the vacuum wavelength, which is sufficiently wide for sensing region.

We have λ=a/ ω so the broad so the PBG extends from wavelength range is 1334 nm < λ < 1971 nm.

III. ANALYSES AND DISCUSSION

The biosensor is used to detect the glucose concentration over a range from 0 g/L to 60 g/L. The sensing principle is based on the change of the refractive index (RI) of the functionalized holes when the glucose concentration(C) varies and this is expression of them relation [8]:

$$n = 1.33230545 + 0.00011889\ C \quad (1)$$

Where n is the refractive index and C the glucose concentration in g/L.

The different sensitivity and quality factor are with known glucose concentrations, displayed in table 1.

A Gaussian input light signal with a central wavelength of 1.55 in the glucose solution (C = 0 %). is launched into the input port of the inline quasi waveguide. The power monitor is placed at the end of the output port. The sensing mechanism is to detect the resonance wavelength, which is caused by the change of RI of the hole [10].

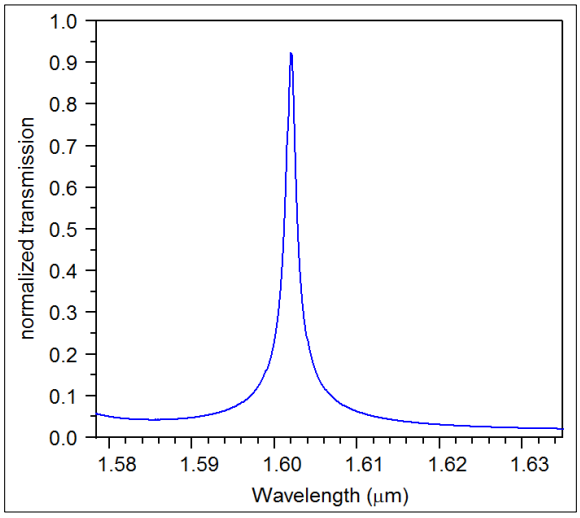

Fig.2: Wavelength for the refractive index 1.33 glucose in the solution (C = 0 %).

Figure 2 show resonant cavity radius by decreasing RC radius to Rin < 2 μm can be concluded that detection of the sensor for different samples can be done both by using the wavelength of the resonator and the transmissions power.

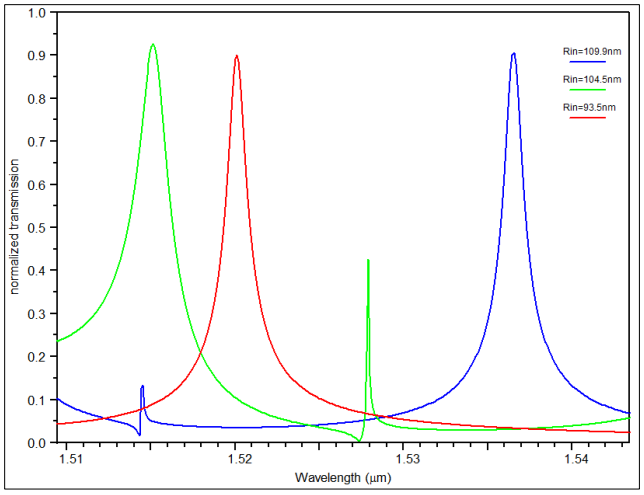

Fig. 3: The resonance wavelength for difference value of Rin.

Fig.4 represents the resonant wavelength for in different concentration of glucose. Table I shows the sensitivity and the quality factor, Fig. 5, 6 represents the resonant wavelength in different medium, TABLEII and first graph illustrate the result.

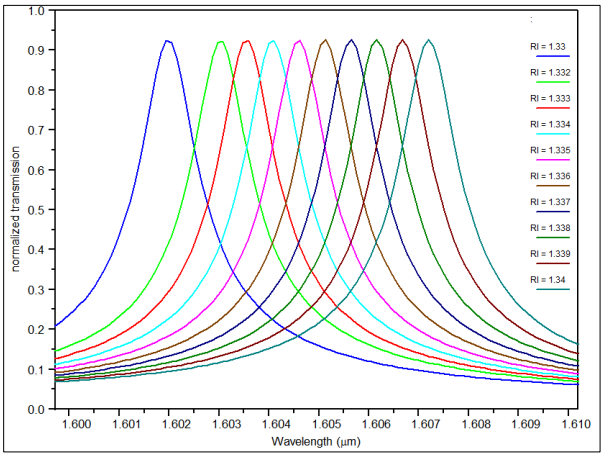

Fig. 4: Transmission spectrum in different concentration of glucose.

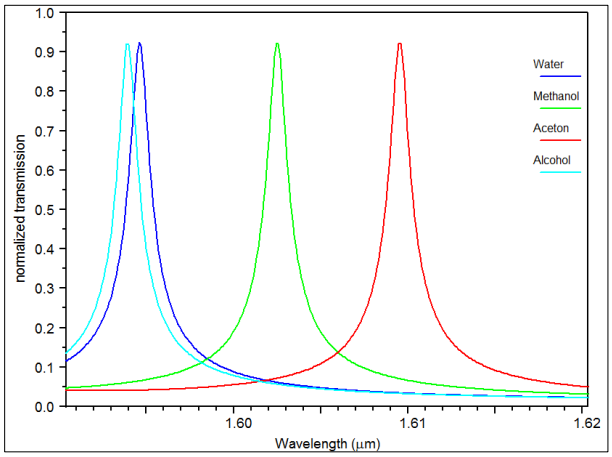

Fig. 5: Resonant wavelength for in different precises medium.

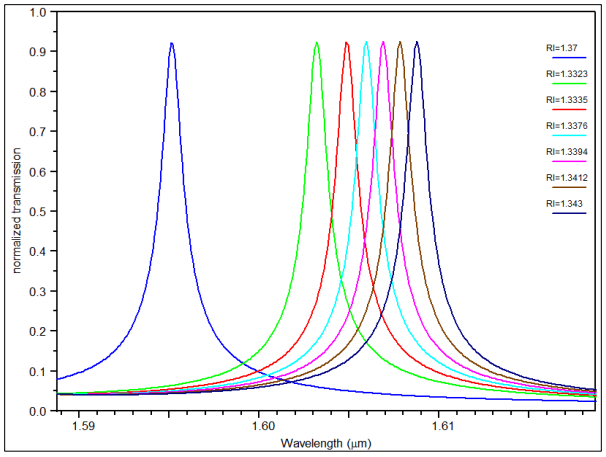

Fig. 6: Resonant wavelength for in different random medium.

Avital parameter in evaluating the performance of the designed sensor is the sensitivity (S) unit of nm/RIU which is defined as:

$$S=\Delta\lambda/\Delta n \quad (2)$$

λ_0: The resonance frequency which is the output signal [11].
$\Delta\lambda$: The difference between the resonant frequencies of the two successive output signals and Δn is the change in the RI.
$\Delta\lambda$ is the difference of two RI value.
S is measured in terms of another quantity used to describe the sensing capability of a sensor is quality factor.
(Q) is defined as the ratio of stored and losses energy.

$$Q=\lambda_0/\Delta\lambda \quad (3)$$

$\Delta\lambda$ is the full width at half maximum of the output signal [12,13].

Table 1
Sensor parameters changes for various value of glucose concentration

C(g/l)	Refractive index RI	wavelength λ (nm)	Q factor	sensitivity S (nm/RIU)
0	1.33	1602.0		
0	1.332	1603.1	890.611	500.000
0.10	1.333	1603.6	844.000	500.000
0.20	1.334	1604.1	891.167	500.000
0.30	1.335	1604.6	891.444	500.000
0.35	1.336	1605.1	891.722	600.000
0.40	1.337	1605.7	845.105	500.000
0.50	1.338	1606.2	892.333	500.000
0.60	1.339	1606.7	892.611	500.000
0.70	1.34	1607.2		

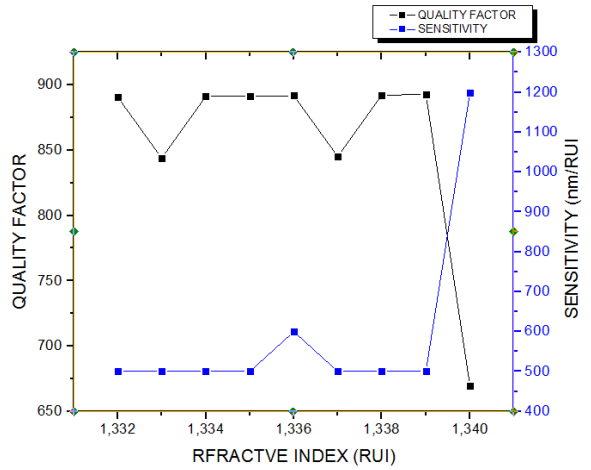

Fig. 8: variation of quality factor and sensitivity with difference values of RI.

From Fig. 8 conclude that sensitivity and quality factor are inversely proportional so it difficult to best result for both.

TABLE II. Sensor parameters changes in various mediums

Refractive index RI	wavelength λ (nm)	Q factor	sensitivity S (nm/RIU)
1.33	1602		
1.316	1594.6	938.000	526.667
1.331	1602.5	890.278	6851.852
1.3445	1695	190.449	3392.617
1.3147	1593.9		

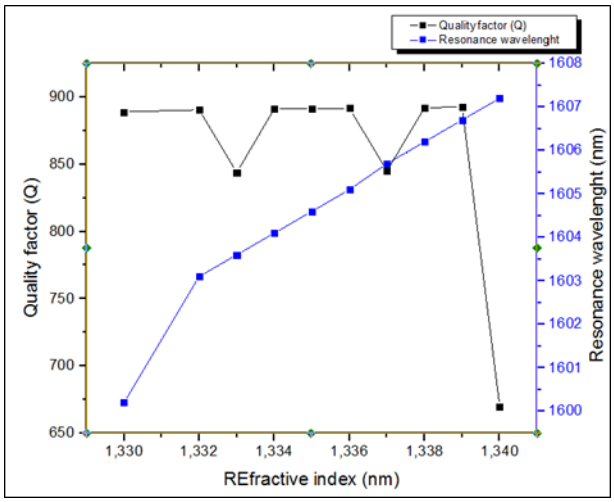

Fig. 9: variation of quality factor and resonance wavelength with difference solutions

From Fig. 9: we assume that the refractive index is directly proportional with the resonance wavelength almost in quasi-linearly way and inversely proportional with quality factor in a random way, so the transmission is decrease when refractive index increase.

It realized from last figure that the resonant wavelength varies linearly with the measurements of the different concentration of glucose.

In order to observe the effect of the inner radius (rin) of the cavity holes on the resonant wavelength for C = 0 %g/L, we vary the inner radius from 0.11a to 0.22a. Figure 3 show that resonant mode is influenced by the change of rin, and we find that 0.22a is the high transmission.

In order to analyze the parameters of our design a, we change the RI of the air hole's extern rings from 1.33 to 1.34 according to equation (1). Fig. 4 illustrates that the resonance peak located at 1604,1 nm the spectrum of transmission obtained when glucose concentration varying from 0 g/l to 60 g/l. It is inferred from this figure that the resonant wavelength increases with increasing RI. The best result is S=600 and Q=891.7.

In order to identify if our biosensor could be operated as an optofluidic biosensor for detecting the glucose concentration in aqueous solution; as we see in Fig. 5 and TABLE II we infer that the resonant wavelength increases with increasing RI. And the value of sensitivity and quality factor increase by contribution to our biosensors.

From the FDTD results, the designed structure sensitivity is equal to 600 nm/RIU and the quality factor reaches 892 in the RI range of 1.33 to 1.34.

The sensibility of the presented biosensor is better than that of some previous structures proposed in recent articles for detecting the glucose concentration [5,6,14]. The comparison of the existing sensing structures is displayed in TABLE III.

But the quality factor which calculated with a theoretical method has a low value and it is justified by the fact that the study is on a low concentration of glucose this is what make a big dissipation of power while the sensing system work.

TABLE III. Comparison of our results with some recent works

Reference	Sensing structure	S (nm/RIU)	Q
[5]	Ring shaped holes	422	8.99×10^{-7}
[6]	Ring cavity and holes	462,61	1.112×10^{5}
[14]	A ring cavity and holes with waveguide	462	1.11×10^{5}
This work	A ring ship with two waveguide	600	800

IV. CONCLUSION

In this work we have presented a proposal design for 2D ring cavity hexagonal and a ring air holes drilled in SI slab, this biosensor is intended for detecting low glucose concentration in an aqueous solution. The detection parameters and spectral position of the resonante mode were determined by adjusting the inner radius of the ring holes as well as the RI. The result of our simulation shows that a change of RI gives us a good sensitivity which achieved 600nm/RUI.

V. REFERENCE

[1]. R. Peltomaa, B. Glahn-Martínez, E. Benito-Peña, and M. Moreno-Bondi, "Optical Biosensors for Label-Free Detection of Small Molecules", Sensors, vol. 18(12), 4126, 2018.
[2]. Riikka Peltomaa, Bettina Glahn-Martínez, Elena Benito-Peña and María C. Moreno-Bondi, "Optical Biosensors for Label-Free Detection of Small Molecules".
[3]. D. Zecca, "Label-free photonic crystal technology for immunosensing applications", PhD Thesis, Doctoral Program in Electronic Devices, Politecnico di Torino, April 2016.
[4]. A. Ivinskaya, "Finite-Difference Frequency-Domain Method in Nanophotonics", PhD Thesis, Technical University of Denmark, 2011.
[5]. A. Hocini, S. Mouetsi, and A. Hocini, "Design of high-sensitive glucose concentration sensor based on ring-shaped holes photonic crystal cavity", Journal of Nanophotonics, vol. 14(1), 2020.
[6]. S. Arafa, M.Bouchemat, T.Bouchemat, and A.Benmerkhi, "High sensitive optofluidic sensor array based on ring-shaped holes photonic crystal H0-cavity", Optik, vol. 131, pp. 49–57, 2017.
[7]. A. Harhouz, and A. Hocini, "Design of high-sensitive biosensor based on cavity waveguides coupling in 2D photonic crystal," Journal of Electromagnetic -Waves and Applications, vol. 29(5), pp. 659–667, 2015.
[8]. F. Lacour, "propagation de la lumière dans les nanostructures et cristaux photoniques planaires associés aux guides d'onde : fabrication et caractérisation", PhD Thesis, Université de Franche-Comté, 2005.
[9]. A. Säynätjoki, M. Mulot, K. Vynck, D. Cassagne, J. Ahopelto, and H. Lipsanen, "Properties, applications and fabrication of photonic crystals with ring-shaped holes in silicon-on-insulator", Photonics and Nanostructures - Fundamentals and Applications, vol. 6(1), pp. 42–46, 2008.
[10]. A. Harhouz, and A. Hocini, "Design of high-sensitive biosensor based on cavity-waveguides coupling in 2D photonic crystal," Journal of Electromagnetic -Waves and Applications, vol. 29(5), pp. 659–667, 2015.
[11]. M. Qiu, "Effective index method for heterostructure-slab-waveguide-based two-dimensional photonic crystal," Appl. Phys. Lett, vol. 81, pp. 1163-1165, 2002.
[12]. M. H. Sani, and S. Khosroabadi, "A novel design and analysis of high-sensitivity biosensor based on nano-cavity for detection of blood component, diabetes, cancer and glucose concentration," IEEE Sensors Journal, 1–1, 2020.
[13]. A. Labbani, and B. Tebboub, "New Biosensor Design Based on Photonic Crystal Core-shell Rods Defects for Detecting Glucose Concentration," Journal of Nano and Electronic Physics, vol. 12(1), 2020.
[14]. F. Hosseinibalam, S. Hassanzadeh, A. Ebnali-Heidari, and C. Karnutsch, "Design of an optofluidic biosensor using the slow-light effect in photonic crystal structure," Applied Optics, vol. 51(5), pp. 568-576, 2012.

Electrochemical Synthesis of p-Cu_2O Thin Films on ITO-coated glass substrates for Photovoltaic Solar Cells

Rafiaa KIHAL*[1,2], Hassiba RAHAL[1,3] Samia RAHAL[4], Abed Mohamed AFFOUNE[1]

[1]*Laboratoire d'Analyses Industrielles et Génie des Matériaux, Département de Génie des Procédés, Faculté des Sciences et de la Technologie, Université 8 Mai 1945 Guelma, BP 401, Guelma 24000, Algeria.*

[2]*Université Abbes Laghrour Khenchela, BP 1252 Rue de Batna, Khenchela 40004, Algeria.*

[3]*Université 20 Août 1955 Skikda, BP 26 Route El-Hadaiek 21000, Algeria.*

[4] *Laboratoire d'Etude des Surfaces et Interfaces de la Matière Solide LESIMS, Département de Physique, Faculté des Sciences, Badji Mokhtar Université, Annaba, Algeria*

Emails: r_kihal@yahoo.fr, rahalhassiba03@gmail.com, rahalsamia98@yahoo.fr, afoune2@yahoo.fr

Abstract— **Cuprous oxide (Cu_2O) thin films have been prepared on ITO-coated glass substrates by electrodeposition technique from an aqueous solution containing copper acetate and sodium thiosulfate. Electrochemical kinetics of Cu_2O films were investigated by cyclic voltammetry. The obtained films were characterized by X-ray diffraction (XRD), scanning electron microscopy (SEM), UV/Vis spectroscopy and electrical measurements. The X-ray diffraction results indicated that the synthesized Cu_2O thin films had a good crystalline of deposited Cu_2O thin films with a pure cubic structure. Morphological study showed a better compactness structure composed of pyramid shape. Optical band gap was found to be 2.103 eV. Electrical properties of Cu_2O films showed a p-type semiconductor with low electrical resistivity of 100 Ω cm, carrier concentration of 3.62×10^{15} $cm^{-3}$and mobility of 17.24 cm^2 $V^{-1}s^{-1}$.**

Keywords—**Thin film, semiconductor, Cu_2O, electrodeposition, solar cells.**

I. INTRODUCTION

Cuprous oxide (Cu_2O) film is one of the most important members of metal oxide semiconductor because of its suitable band gap and high absorption coefficient in the visible region. In addition with good optical and electrical properties the material has several advantages such as availability and abundance of the starting materials, non-toxic nature and low production cost [1]. These films have been used in the potential application areas such as gaz sensors [2], solar cells application [3], photocatalysis [4], thin film homo-junction solar cells [5], photoelectrodes for solar water splitting [6,7] and working electrode in the application of photoelectrochemical solar cell (PESC) [8].

Electrodeposition technique is one of the most several methods are usually used to prepare Cu_2O thin films. It presents many advantages such as simplicity, low equipment cost, the possibility of preparing large area thin films and the control of the film thickness [6, 9]. Cu_2O films are usually electrodeposited from copper precursor solutions, such as copper nitrate, copper sulfate and copper acetate. Many researchers have used various additives in electrolytic bath in order to improve the quality of the deposited films such as uniformity, adhesion and crystallinity [1, 6, 9].

In this work, we report the preparation of Cu_2O thin films by electrodeposition technique in a solution of copper acetate and sodium thiosulfate at pH 11. Electrodeposited of Cu_2O thin films were investigated X-ray diffraction (XRD), scanning electron microscopy (SEM), optical spectroscopy, and electrical measurements.

II. EXPERIMENTAL DETAILS

A. Reagents

All chemical reagents used in the present work were of analytical grade. Copper acetate monohydrate ($Cu(C_2H_3O_2)_2.H_2O$, 98%, Sigma Aldrich) was used as copper source. Sodium acetate trihydrate ($CH_3COONa.3H_2O$, 99%, Sigma Aldrich) and sodium sulfate (Na_2SO_4, 99%, Sigma Aldrich) were used as a supporting electrolyte. However, sodium thiosulfate pentahydrate ($Na_2S_2O_3.5H_2O$, 99.5%, Sigma Aldrich) was used as an additive. All the aqueous solutions were prepared using distilled water.

B. *Preparation and characterization techniques of Cu_2O thin films*

Electrodeposition of Cu_2O thin films was carried out using a three electrode electrochemical cell with a platinum (Pt) wire as a counter electrode, indium tin oxide (ITO)-coated glass (8-10 Ω/square, Sigma Aldrich) substrate was used as working electrode. A saturated calomel electrode (SCE) was used in all experiments as a reference electrode. Before the deposition, the substrates were cleaned ultrasonically in acetone, ethanol and then rinsed in distilled water. Cuprous oxide thin films were electrodeposited in an aqueous solution of 0.01 M $Cu(C_2H_3O_2)_2.H_2O$, 0.1 M $CH_3COONa.3H_2O$ and 1.2 mM $Na_2S_2O_3.5H_2O$ at 60 °C. pH solution was adjusted to 11 using potassium hydroxide (KOH). Sodium thiosulfate is used to stabilize Cu^{2+} ions in the solution [10-12].

Cyclic voltammetry study was carried out using Princeton Applied Research Model 273 A Potentiostat/Galvanostat, coupled to a personal computer with Power Suite software for data acquisition and potential control. Thin films of cuprous oxide were electrodeposited for 30 minutes and dried in air at 100°C.

The crystalline phase of Cu_2O thin films was investigated by X-ray diffraction using a Bruker Discover D8 Diffractometer with CuK_α radiation (λ = 1.5406 Å). Scanning electron microscopy images was performed using a VEGA3 TESCAN scanning electron microscope operating at 20 kV accelerating voltage. Optical transmittance of thin films was measured by a Perkin Elmer Lambda 950 UV–vis-NIR spectrometer. Electrical properties of deposited Cu_2O films were determined by a HMS 3000 Hall measurement system at room temperature. Ag-paste was used at the corners of films to make four good contacts with probes. Thickness of the films was measured using a Dektak stylus profilometer.

III. Results and Discussion

A. *Electrochemical study*

Fig. 1 shows the cyclic voltammogram of the solutions containing 0.01 M copper acetate and 0.1 M sodium acetate and 1.2 mM sodium thiosulfate for pH 11 and at T = 60 °C . The potential sweep was ranged from 0.3 to -2.0 V with a scan rate of 50 mV s^{-1}.

From this Fig., we recorded two cathodic peaks. The first peak situated at -0.58 V, which attributed to the reduction of Cu^{2+} to Cu^{+} where water converted to hydroxide ions molecule. The hydroxide ions react with Cu^{+} in the solution to form Cu_2O film on the substrate according to the following reactions [13, 14]:

$$Cu^{2+} + e^{-} \longrightarrow Cu^{+} \quad (1)$$

$$2Cu^{+} + 2OH^{-} \longrightarrow Cu_2O + H_2O \quad (2)$$

The second cathodic peak is observed at -1.33 V which can be mainly ascribed to the deposition of metallic copper with release of hydrogen (Eq. (3, 4)).

$$Cu^{2+} + 2e^{-} \longrightarrow Cu \quad (3)$$

$$2H^{+} + 2e^{-} \longrightarrow H_2 \quad (4)$$

Similar cathodic peaks are reported in the literature [15-18], but the present cathodic peaks are shifted to negative potentials if compared with literature.

During reverse scan, an anodic peak is observed at 0.29 V corresponding to the oxidation of metallic copper [14,15], indicating the only formation of Cu_2O on ITO-coated glass substrate which is confirmed below by XRD analysis.

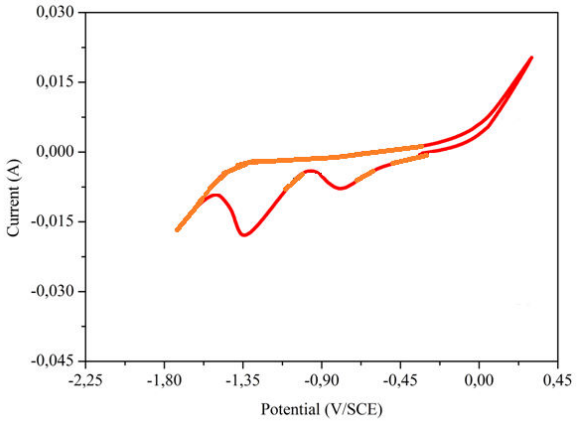

Fig.1. Cyclic voltammogram of the solution containing 0.01 M $Cu(C_2H_3O_2)_2.H_2O$ and 0.1 M $CH_3COONa.3H_2O$ at pH 11. The potential scanning rate was 50 mV/s.

B. *XRD Analysis*

Thickness of Cu_2O films was measured by Dektak stylus profilometer and was found to be 368 nm. Fig. 2 shows the XRD pattern for a Cu_2O thin film deposited onto ITO-coated glass substrates at -0.58V and at 60 °C. From this figure, all the diffraction peaks of Cu_2O films correspond to the peaks of cubic phase of standard Cu_2O (JCPDS card no: 05-0667) [19]. X-ray diffraction patterns show that the intensity of the (311) diffraction peak is higher when compared with the other peaks (111) and (200), indicating preferential orientation along the c-axis. No impurities such as cupric oxides are found in the XRD pattern besides the substrate. The presence of several peaks in the diffraction pattern is indicative of polycrystalline nature of the film.

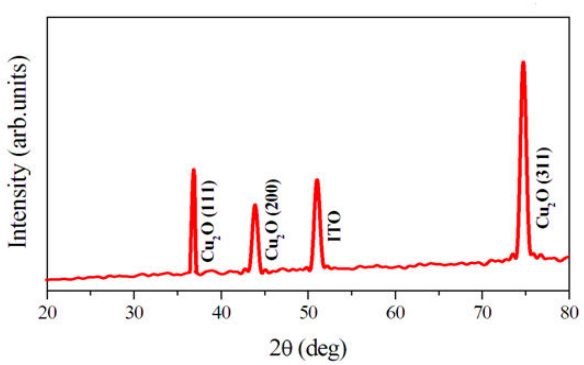

Fig. 2. X–ray diffraction of the Cu_2O thin films deposited onto ITO–coated glass substrates

The calculated value of the lattice constant parameters of Cu_2O films is 4.213 Å. which were slightly different than that of standard Cu_2O (JCPDS 05-0667, $a = b = c = 4.269$ Å) [20, 21].

The crystallite size (D) of Cu_2O thin films was calculated from the major diffraction peaks using the Scherrer's formula (Eq. (5)) [3]:

$$D = 0{,}89\lambda/\beta \cos\theta \quad (5)$$

Where λ is the wavelength of the incident beam (1.5406 Å), β is the full width at half maximum and θ is the Bragg's angle in rad. The average crystallite size of deposited Cu_2O is found to be 28.93 nm.

C. SEM analysis

The surface morphologie of Cu_2O films deposited onto ITO–coated glass substrates obtained is shown in Fig. 3. Micrograph of deposited Cu_2O film showed a better compactness structure composed of pyramid shape. This shape is also observed when Cu_2O thin films deposited onto various substrates by different copper salt solution [22, 23], which is consistent with XRD results.

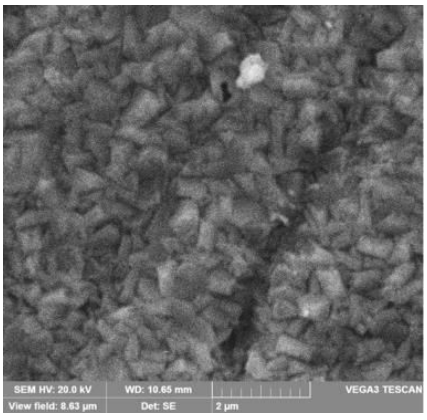

Fig. 3. SEM image of Cu_2O films deposited onto ITO–coated glass substrates

D. Optical properties

The optical transmittance spectrum of deposited Cu_2O thin films in the wavelength range from 400 to 1100 nm taken at room temperature is shown in Fig. 4. It was shown that the film present a high optical transmission (>70%) in the visible wavelength range, which confirms the good optical quality of the electrodeposited Cu_2O thin films. The absorption coefficient (α) was determined in the order of $>10^4$ cm^{-1}.

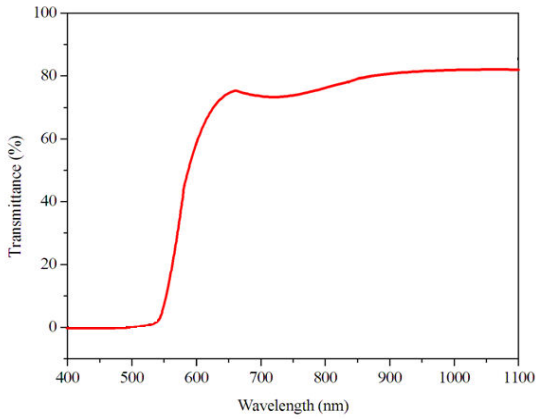

Fig. 4. Transmittance spectrum of Cu_2O thin films deposited onto ITO–coated glass substrates

Fig. 5 shows the plot of $(\alpha h\nu)^2$ versus photon energy $(h\nu)$ of Cu_2O thin films. It has been observed that the plots of $(\alpha h\nu)^2$ versus $(h\nu)$ are linear over a wide range of photon energies indicating the direct type of transitions. The optical band gap of the films was determined using Tauc's formula (Eq. (6)) [24]:

$$(\alpha h\nu)^2 = A\left(h\nu - E_g\right) \quad (6)$$

Where α is absorption coefficient, h is Planck's constant, ν is photon energy, A is a constant and E_g is the direct transition band gap. The optical band gap value was determined by extrapolating the linear portion of the plot of $(\alpha h\nu)^2$ versus photon energy $(h\nu)$, which is illustrated in Fig. 5. The band gap of Cu_2O thin films was estimated to be 2.067 eV. This value is in good agreement with the reported values of band gap of Cu_2O thin films [19, 25]. The obtained optical results make Cu_2O film as a promising semiconductor material for use in photovoltaic solar cells applications.

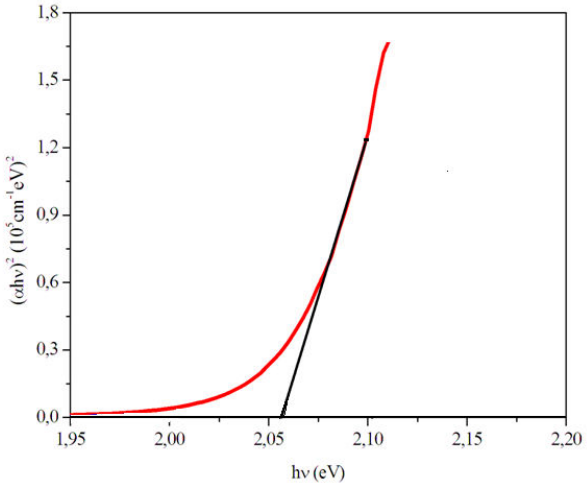

Fig. 5. Plot of $(\alpha h\nu)^2$ versus hν of Cu_2O thin films

E. Electrical properties

Electrical properties of Cu_2O films were examined by Hall Effect measurements at room temperature. Cu_2O films showed a p-type electrical conductivity with carrier concentration of 3.62×10^{15} cm^{-3}, mobility of 17.24 cm^2 $V^{-1}s^{-1}$ and a low electrical resistivity of 100 Ω cm. These values are in agreement with the results reported by others [26, 27].

IV. CONCLUSIONS

Cuprous oxide (Cu_2O) thin films have been successfully electrodeposited onto ITO-coated glass substrates from aqueous copper acetate solutions with addition of sodium thiosulfate at 60 °C. The X-ray diffraction results indicated that the synthesized Cu_2O thin films had a good crystalline of deposited Cu_2O thin films with a pure cubic structure. The surface morphology of obtained films showed a better compactness structure composed of pyramid shape. Optical properties of Cu_2O thin films revealed a high optical transmission (>70%) and high absorption coefficient ($\alpha>10^4$ cm^{-1}) in visible region. The optical band gap was estimated to be 2.067 eV. Hall Effect measurements indicated that the deposited cuprous oxide had a cathodic photocurrent indicating p-type semiconductor with carrier concentration of 3.62×10^{15} cm^{-3}, mobility of 17.24 cm^2 $V^{-1}s^{-1}$ and a low electrical resistivity of 100 Ω cm. The obtained Cu_2O thin films with suitable properties could be promising material for use in various applications such as photovoltaic solar cells.

ACKNOWLEDGMENT

The financial support of the Algerian Ministry of Higher Education and Scientific Research, Algeria (CNEPRU project number: J0101520090018) is greatly acknowledged.

REFERENCES

[1] R. Oommen, U. Rajalakshmi, Sanjeeviraja, "Characteristics of electron beam evaporated and electrodeposited Cu_2O thin films-comparative study", Int. J. Electrochem. Sci., vol.7, pp.8288-8298, 2012.

[2] P. A. Praveen Janantha, L. N. L. Perera, K. M. D. C. Jayathilaka, J. K. D. S. Jayanetti, D. P. Dissanayaka. W. P. Siripala, "Use of Cu_2O microcrystalline thin film semiconductors for gas sensing", Proc. Tech. Sess. Inst. Phys– Sri Lanka, vol. 25, pp.70-76, 2009.

[3] N. Soundaram, R. Chandramohan, S. Valanarasu, R. Thomas. A. Kathalingam, "Studies on silar deposited Cu_2O and ZnO films for solar cell application", J. Mater. Sci.-Mater. Electron., vol. 26 (7), pp. 5030-5036, 2015

[4] J. Dong, H. Xu, F. Zhang, Ch. Chen, L. Liu, G. T. Wu, "Synergistic effect over photocatalytic active Cu_2O thin films and their morphological and orientational transformation under visible light irradiation", Appl. Catal., A, vol. 470, pp. 294-302, 2014.

[5] R. P. Wijesundera, L. K. A. D. D. S. Gunawardhana, W. Siripala, "Electrodeposited Cu_2O homojunction solar cells: Fabrication of a cell of high short circuit photocurrent", Sol. Energy Mater. Sol. Cells, vol. 157, pp. 881-886, 2016.

[6] Q. Ma, J. P. Hofmann, A. Litke, E. J. M. Hensen, "Cu_2O photoelectrodes for solar water splitting: tuning photoelectrochemical performance by controlled faceting", Sol. Energy Mater. Sol. Cells, vol. 141, pp. 178-186, 2015.

[7] Zh. Zhang, P. Wang, "Highly stable copper oxide composite as an effective photocathode for water splitting via a facile electrochemical synthesis strategy", J. Mater. Chem.,vol. 22, pp.2456-2464, 2012.

[8] D. S. C. Halin, I. A. Talib, A. R. Daud, M. A. A. Hamid, "Characterizations of cuprous oxide thin films prepared by sol-gel spin coating technique with different additives for the photoelectrochemical solar cell". Int. J. Photoenergy, vol. 2014, pp. 1-6, 2014.

[9] H Rahal, R Kihal, AM Affoune, S Rahal, "Electrodeposition and characterization of Cu_2O thin films using sodium thiosulfate as an additive for photovoltaic solar cells", Chinese J. Chem.Eng., vol. 26, pp.421-427, 2018.

[10] S. S. Nikam, M. P. Suryawanshi, S. M. Bhosale, M. A. Gaikwad, P. A. Shinde, A. V. Moholkar, "Cu_2O thin films prepared using modified successive ionic layer adsorption and reaction method and their use in photoelectrochemical solar cells", J. Mater. Sci.-Mater. Electron., vol. 27 (2), pp.1897-1900, 2016.

[11] S. S. Oluyamo, Nyagba, S. Mbafan, Ojo, S. Ambrose, "Optical properties of copper (I) oxide thin films synthesized by silar technique", J. Appl. Phys, vol. 6 (3), pp. 102-105, 2014.

[12] A.T. Ravichandran, K. Dhanabalan, R. Chandramohan, A. Vasuhi, P. Parameswaran, "Optical properties of modified-silar grown copper oxide nanocrystalline thin films", Int. J. Inf. Res. Rev., vol. 1 (1) , pp. 007-011, 2014.

[13] A. El-Shaer, A. R. Abdelwahed, A. Tawfik, M. Mossad, D. Hemada, Effect of deposition parameters on electrodeposited cuprous oxide thin films, Int. J. Emerg. Technol. Adv. Eng., vol. 4 (12), pp. 595-602, 2014.

[14] G. Riveros, A. Garmendia, D. Ramirez, M. Tejos, P. Grez, H. Gomez, E. A. Dalchiele, Study of the electrodeposition of Cu_2O thin films from DMSO solution, J. Electrochem. Soc., vol. 160 (1), pp. D28-D33, 2013.

[15] S. Laidoudi, A. Y. Bioud, A. Azizi, G. Schmerber, J. Bartringer, S. Barre, A. Dinia, Growth and characterization of electrodeposited Cu_2O thin films, Semicond. Sci. Technol, vol. 28 (11), pp. 115005-115011, 2013.

[16] A. El-Shaer, M. T. Y. Tadros, M. A. Khalifa, Fabrication of homojunction cuprous oxide solar cell by electrodeposition method, Nat. Sci., vol. 13 (5), pp.1-9, 2015.

[17] P. Grez, F. Herrera, G. Riveros, A. Ramirez, R. Henriquez, E. Dalchiele, R. Schrebler, Morphological, structural, and photoelectrochemical characterization of n-type Cu_2O thin films obtained by electrodeposition, Phys. Status Solidi A, vol. 209 (12), pp. 2470-2475, 2012

[18] A. S. M. Hanif, F. Mohamad, R. Z. Zakaria, Cyclic voltammetry measurement for n-type Cu_2O thin film using copper acetate-based solution, J. Eng. Appl. Sci., vol.10 (19), pp. 8562-8568, 2015.

[19] P. Grez, F. Herrera, G. Riveros, A. Ramirez, R. Henriquez, E. Dalchiele, R. Schrebler, "Morphological, structural, and photoelectrochemical characterization of n-type Cu_2O thin films obtained by electrodeposition", Phys. Status Solidi A, vol. 209 (12), pp. 2470-2475, 20.12.

[20] Z. C. Orel, A. Anzlovar, G. Drazic, M. Zigon, "Cuprous oxide nanowires prepared by an additive-free polyol process", Cryst. Growth Des., vol. 7 (2), pp. 453-458, 2007.

[21] M. A. Amrani, V. V. S. S. Srikanth, N. K. Labhsetwar, A. S. Al-Fatesh, H. Shaikh, "Phoenix dactylifera mediated green synthesis of Cu_2O particles for arsenite uptake from water", Sci. Technol. Adv. Mater., vol. 17 (1), pp.760-768, 2016.

[22] Y. Yang, Y. Li, M. Pritzker, "Control of Cu_2O film morphology using potentiostatic pulsed electrodeposition", Electrochim. Acta, vol. 213, pp. 225-235, 2016.

[23] C. Wang, J. Xu, S. Shi, Y. Zhang, Z. Liu, X. Zhang, S. Yin, L. Li, "The structural, optical and photoelectrical properties of Cu_2O films electrodeposited in different pH", RSC Adv., vol. 6, pp. 4271-5140, 2015.

[24] R. Kihal, H. Rahal, AM. Affoune, M. Ghers, "Electrodeposition of SnS Thin film Solar Cells in the Presence of Sodium Citrate", J. Electro. Sc. Tech. vol. 3 (8), pp. 206-2014, 2017.

[25] A. El-Shaer, A. R. Abdelwahed, M. M. Mosaad, A. Tawfik, D. Hemada, "Effect of pH on conductivity of electrodeposited cuprous oxide thin films", Nat. Sci., vol. 13 (3), pp.1-5, 2015.

[26] Y. Abdu, A.O. Musa, T. H. Darma, "Electroless deposition and electrical characterization of n-Cu_2O LAYER. " J. Pure. Appl. Sci., vol. 5 (2), pp.1-10, 2012.

[27] T. Jiang, T. Xie, W. Yang, L. Chen, H. Fan, D. Wang, "Photoelectrochemical and photovoltaic properties of p-n Cu_2O homojunction films and their photocatalytic performance", J. Phys. Chem. C, vol. 117, pp. 4619-4624, 2013.

Effects of doping profile and temperature on the solar cell performances

Asma Benchiheb
Faculté de médecine, Université de Constantine 3, Algérie
Laboratoire des Microsystèmes et Instrumentation. Département d'Electronique, Constantine 1,
asmabenchiheb@yahoo.fr

Nedjoua Benchiheb
Ecole National Supérieur d'hydraulique, Blida
nedjouabenchiheb@yahoo.fr

Yasmina Saidi
Département de Physique, Université de Constantine 1, Algérie
saidiyas09@yahoo.fr

Farida Hobar
Département d'électronique, Universit d' Oum El Bouaghi
Laboratoire des Microsystèmes et Instrumentation. Département d'Electronique, Constantine 1
hobarfarida@yahoo.fr

***Abstract*—In this paper, an optimization of the structure of a silicon solar cell is presented. This study takes into account the effects of temperature and doping level of each region of the device. As the simulation with the COMSOL software allowed us to demonstrate the link between the technological structure of an N + NP type solar cell and the various characteristics and parameters obtained at the output when it is subjected to a polarization. Thus, we considered different doping levels and thicknesses of the N + layer. It has been observed that the effects of temperature are negligible for low doping levels of the N + layer. However, in heavy doping, the benefit of reducing its thickness below 0.018 µm is demonstrated, especially for the high temperature operating range. Concerning the base, we observed that its thickness must be maintained in the order of 100 µm.**

Keywords—Solar Cell, optimization, temperature

I. INTRODUCTION

Currently, the efficiency of solar cells is in the order of 20% to 30%. In order to improve it, various solutions have been provided such as, for example, the use of multi-junctions [1,2]. However, the disadvantage of this solution is its relatively high price compared to that of uni-junction cells technologies.

To improve the efficiency of solar cells in the production of electricity, several models based on the techniques of emitter region optimizing [3-5] are proposed. Therefore, this quest made it possible to achieve great breakthroughs in the emitters design philosophy as well as to lead to solar cells exhibiting increasingly interesting yields, especially among those which are based on the use of silicon in their production.

In this paper, we present an optimization of silicon solar cell structure taking into consideration the operating

II. THE STUDIED STRUCTURE

The general structure and doping profile of the silicon solar cell studied are presented on Fig. 1 and table I. This one consists of three layers :

- One P-type layer forming the substrate and doped with boron.
- One phosphorus doped N-type layer with a Gaussian profile
- One layer of N + type also doped with phosphorus and a Gaussian profile.

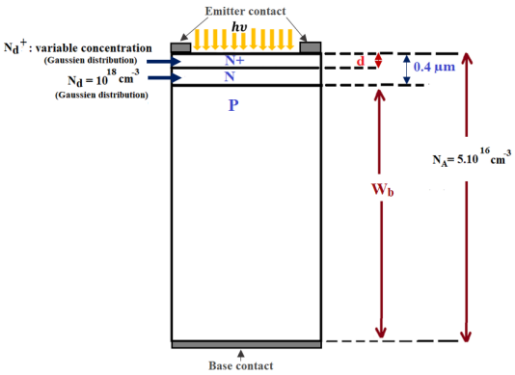

(a)

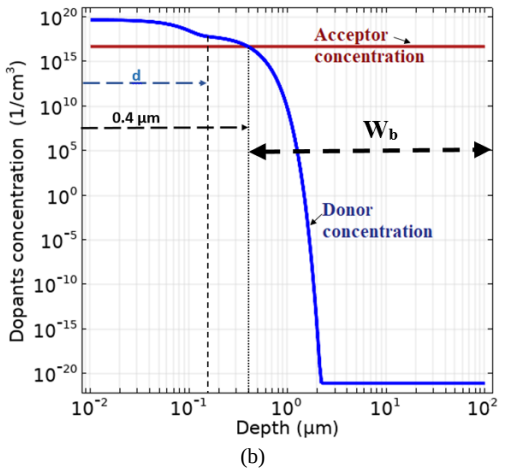

(b)

Fig.1. Structure of the silicon solar : a) general structure, b) doping profile

TABLE I. PHYSICAL PARAMETERS VALUES

Solar cell parameter	n-p (conventional)	n^+- n -p
Surface concentration	N_d=1. 10^{18}cm^{-3}	N_d^+ is variable
Emitter doping profile	Gaussian W_{Nd} = 0.4 µm	Gaussian on Gaussian W_{Nd+} = d
Base doping concentration **Base thickness**	Na= 5. 10^{16}cm^{-3} W_b	

III. DESCRIPTION OF NUMERICAL MODEL

The equations governing the transport phenomena in the solar cell are [6]:

$$div \cdot (\varepsilon \cdot \overrightarrow{gradV}) = -\rho \quad (1)$$

$$g_n - r_n = -\frac{1}{q} \cdot \vec{\nabla} \overrightarrow{J_n} \quad (2)$$

$$g_p - r_p = \frac{1}{q} \cdot \vec{\nabla} \overrightarrow{J_p} \quad (3)$$

$$\overrightarrow{J_n} = q \cdot n \cdot \mu_n \cdot \vec{E} + q \cdot D_n \cdot \vec{\nabla} n \quad (4)$$

$$\overrightarrow{J_p} = q \cdot p \cdot \mu_p \cdot \vec{E} - q \cdot D_p \cdot \vec{\nabla} p \quad (5)$$

With

- ρ : The charges density;
- **ε** : Material permittivity
- $J_{n,p}$: Current density for electrons, holes;
- $D_{n,p}$: Diffusion constant for electrons, holes
- $\mu_{n,p}$: Mobility of electrons, holes;
- KB : Boltzmann constant
- T : The temperature
- $r_{n,p}$: recombination term for electrons, holes
- $g_{n,p}$: photo generation term for electrons, holes

The recombination term $r_{n,p}$ takes into account Schockley-Read-Hall (SHR) type recombination and Auger effect [6-8].

Under illumination, the photo generation rate for each wavelength λ is calculated by the equation [9]:

$$G(\lambda \cdot x) = \alpha(\lambda) \cdot I_o(\lambda) \cdot e^{-\alpha(\lambda) \cdot x} \quad (6)$$

Where I_o (λ) is the intensity of photons at the cell surface (x = 0), I_o (λ,x) the intensity of photons at point x and α(λ) the absorption coefficient at λ wavelength.

The total photo generation rate is the integral of G (x) over all wavelengths forming the solar spectrum

IV. RESULTS AND DISCUSIONS

Fig.2 and Fig. 3 show respectively the variations of the light-generated current density (or photocurrent density), ΔJ_{ph1}, and the Variation of the increase in the conversion efficiency, $\Delta\eta_1$, as functions of the thickness d, for different surface doping levels and temperatures.

$\Delta J_{ph1}=J_{ph}-J_{ph0}$ and $\Delta\eta_1=\eta-\eta 0$ where J_{ph} and η are respectively the n^+- n –p light-generated current density and the conversion efficiency and J_{ph0} the light-generated current density without the N+ layer i.e with a 0.4 µm type N emitter and a metal contact directly taken on this layer. For this case, Wb is set to 100 µm

Fig. 2 demonstrates that overall, the increase in the surface doping of the N + region induces a growth of the photocurrent. However, for a given value of this surface doping and over a small thickness d (d <d_o), first, we observe an increase in the photocurrent but from a certain limit of d_o, this one decreases. Thus, for a surface doping less than 5.10^{19} cm^{-3}, d_o is in the order of 0.08 µm but for surface doping greater than 5.10^{19} cm^{-3}, d_o is in the order of 0.03 µm.

Regarding the effects of temperature, its influence is not remarkable until the surface doping level exceeds 10^{19}cm^{-3}. Indeed, from this limit, an increase in temperature induces a decrease in the photocurrent. In addition, this phenomenon is even more accentuated when the thickness of the layer N +, d, increases.

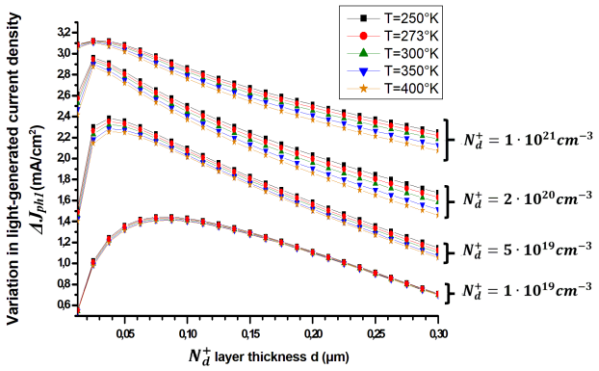

Fig.2. Variation of the increase in the light-generated current density with a high-low junction emitter versus n+-layer thickness for different surface doping concentration N_d^+ and temperatures.

Regarding the conversion efficiency, Fig.3 shows that, like the case of photocurrent, the influence of temperature is small when the doping level of the order of 10^{19} cm^{-3} (or less).

However, for average doping surface concentration (5.10^{19}cm^{-3}≤ Nd <2.10^{21} cm^{-3}), the increase in temperature leads to a decrease in the $\Delta\eta$ for thicknesses d in the order of 0.03 µm but for greater thicknesses (d> 0.1 µm), the variation of this factor is very small.

For high doping levels of the order of 10^{21} cm^{-3}, a net decrease in the variation of the conversion efficiency is observed for thicknesses d in order of 0.018 µm. This factor stabilizes when d exceeds 0.15um.

Thus, at high temperature and doping levels, the thickness of the layer must be kept low to ensure good performance.

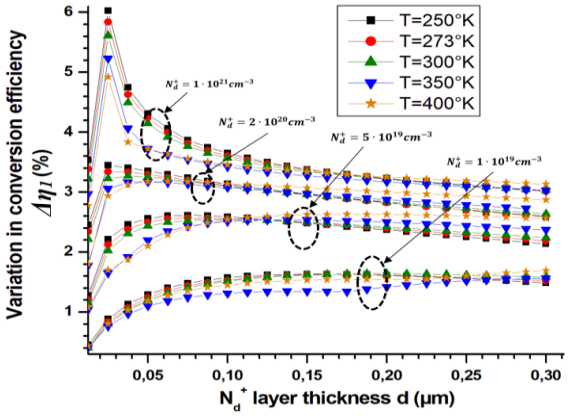

Fig.3. Variation of the increase in the conversion efficiency with a high-low junction emitter versus n+-layer thickness for different surface doping concentration N_d^+ and temperature.

In order to study the influence of the base thickness, W_b, on the cell current and its efficiency, we consider Nd + = $2.10^{20}cm^{-3}$, d= 0.02µm but with W_b variable. We also put : $\Delta\eta_2=\eta-\eta_0$ and $\Delta J_{ph2}=J_{ph}-J_{ph0}$ where $\eta_0=\eta$ (for Wb=0.1µm) and $J_{ph0} = J_{ph}$(for Wb=0.1µm)

Fig. 4, 5 and 6 show that the variations of the current and the efficiency as well as the open circuit voltage of the cell increase rapidly with the thickness as long as W_b <= 100µm. These effects are due to photo generation phenomena of electron-hole pairs which occur more and more as the base widens. However, when W_b exceeds 100µm, these growths slow down to become almost constant because in this case, less light manages to cross the thick base thus limiting the photo-generation.
Regarding the effects of temperature, the variation of the latter does not have much influence on the photo-current. However, its increase induces a decrease in the open-circuit voltage. This explains the decrease in the variation in injection efficiency with temperature.
From these curves, we can deduce that for a good optimization of the structure, the thickness of the base must be chosen in the order of 100 µm.

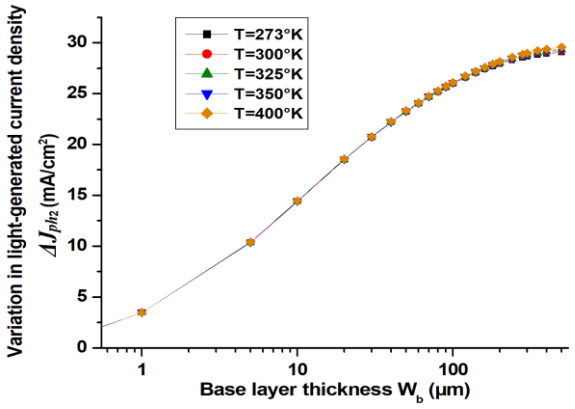

Fig.4. Variation of the increase in the light-generated current density with a high-low junction emitter versus base thickness Wb and temperature.

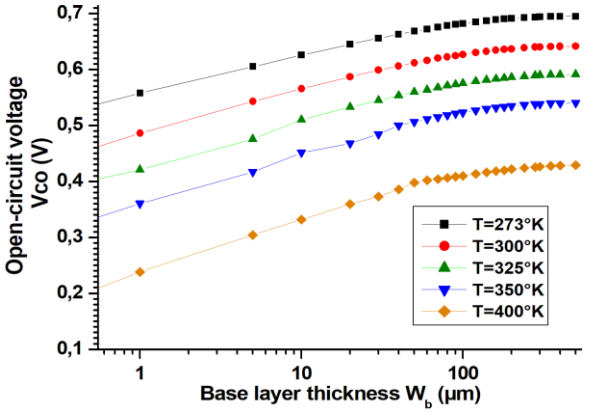

Fig.5. Open-cicuit voltage versus base thickness Wb and temperature.

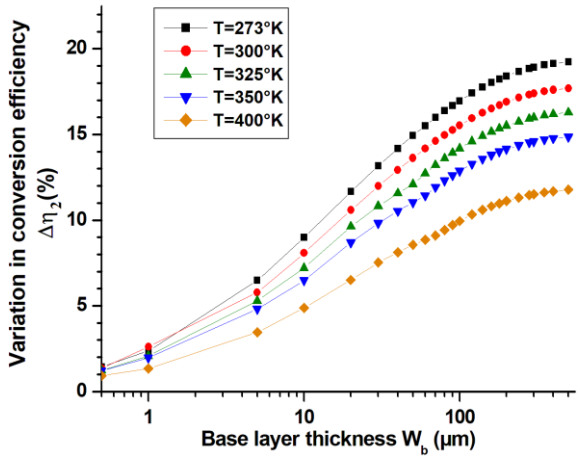

Fig.6. Variation of the increase in the conversion efficiency with a high-low junction emitter versus base thickness Wb and temperature.

V. Conclusion

In order to optimize the solar cell structure, the study of its electrical behaviour shows that the thickness of the base must be in the order of 100 µm. Regarding the emitter region, for high temperature operation, the thickness of the N + region must be kept very low (of the order of 0.018 µm) for high doping levels exceeding 10^{21} cm^{-3}. However, for regions of average doping surface concentration ($5.10^{19}cm^{-3} \leq N_d^+ < 2.10^{21}$ cm^{-3}), the thickness must be of the order of 0.3 µm. For low level doping ($N_d^+ < 5.10^{19}$ cm^{-3}), the temperature variation does not have much effect.

References

[1] A. Mumtaz M. Milanova, I. Sandall, K. Cheetham, Z. Cao, M. Cao, G. Piana, N. Fleck,L., Phillipsl., "GaAsSbN for Multi-Junction Solar Cells," 2020 47th IEEE Photovoltaic Specialists Conference (PVSC), 2020, pp. 1799-1803.

[2] A. Verma and A. Pethe, "Modelling and Analysis of Multi-Junction Photovoltaic Cells," 2020 IEEE 17th India Council International Conference (INDICON), 2020, pp. 1-6.

[3] M. Shadab Siddiqui, B. K. Pant, A. K. Saxena, Shivangi and S. Chandril, "An analysis of Passivated emitter and rear contact (PERC) cell and module," 2019 IEEE 46th Photovoltaic Specialists Conference (PVSC), 2019, pp. 0334-0338.

[4] S. Kim, H. Park, D. Phong Pham, Y. Kim S. Kim E.C. Cho Y. Cho, " Design of front emitter layer for improving efficiency in silicon heterojunction solar cells via numerical calculations," Optik, 2021, vol. 235, pp. 1-9.

[5] B.K. Ghosh, A. M. Khairul, A. Afishah, I. Saad, A. I. A. Rani and S. K. Ghosh, "Analysis of emitter layer diverse effects on electrical performance for prospective Si hybrid solar cell," 5th IET

International Conference on Clean Energy and Technology (CEAT2018), 2018, pp. 1-4

[6] A. Benchiheb, F. Hobar, " Modelling of the active defects influence on the electrical characteristics of an SiGe-HBT," Elsevier, ChineseJournal of Physics, 2017, vol. 55 pp. 1453-1465.

[7] Silvaco, Atlas User's Manual-Device simulation software. Santa Clara, CA,2010, Ch. 3.

[8] S. M. Sze, " Physics of semiconductor devices ", 2nd ed., John Wiley & Sons, 1981.

[9] A.K. Singh, J. Tiwari, A. Yadav, R.K. Jha, " Analysis of Si/SiGe heterostructure solar cell", Journal of energy, vol. 2014 pp. 1-7.

Systematic Study of Structural and Magneto-Electronic Properties of $Sr_{1-x}Ti_xS$ Alloys for Spintronic Applications

Elaggoune Warda
Département des sciences de la matière
Université de 08 Mai 1945
BP 401, Guelma 24000, Algeria
welaggoune@gmail.com

Meddour Athmane
Département des sciences de la matière
Université de 08 Mai 1945
BP 401, Guelma 24000, Algeria
a_meddour@yahoo.fr

Abstract **– In this work, the structural and the magneto-electronic properties of the $Sr_{1-x}Ti_xS$ compounds at dopant concentration x=0.25, 0.50, and 0.75 in the rock-salt ferromagnetic phase are studied using first-principles calculations based on density functional theory. The structural properties of the three compounds calculated indicate promising findings. The electronic band profiles, the density of states plots, and the integral magnetic moment validate the half-metallic feature only at x=0.25. As a result, the Sr0.75Ti0.25S compound is the most promising spintronic material in the series.**

Keywords **–** ***Structural properties, magneto-electronic properties, strontium chalcogenide, DFT, spintronic applications.***

I. INTRODUCTION

In recent years, the diluted magnetic semiconductors (DMSs) obtained by doping classical semiconductors with small fraction of transition metal atoms have attracted both scientific and technological interest, because, they exhibit half-metallic ferromagnetism which is a key ingredients for the future high-performance spintronic devices [1]. The semiconductor SrS from group II-IV elements has attracted more attention due to its wide band gap and its excellent properties. Because pure semiconductors are not appropriate for producing operational devices, these elements are doped with impurity atoms to improve their operating qualities. Diluted magnetic semiconductor (DMS) compounds based on II-IV are the perfect material for producing all spin-based semiconductor devices. There have been various efforts over recent decades towards ferromagnetic semiconductor synthesis [2-4]. In diluted magnetic semiconductors, the uniqueness of ferromagnetic and semiconducting behaviors is the consequence of a number of extraordinary and significant basic characteristics of atoms that carry an extra-magnetic moment. This result is consistent with that of Dietl [5]. A further essential element of DMSs is the tracking of the different physical characteristics, including the energy band gap, by changing the dopant of magnetic ions [6]. In this respect, we have computed, for three distinct concentrations x=0.25, 0.50 and 0.75, the structural, electronic and magnetic characteristics of the Ti-doped SrS compound. Our purpose is to monitor the compound's half-metallic conduct by changing the dopant concentration and to perform profound studies using the first-principle full-potential linearized augmented plane-waves (FP-LAPW) method with the generalized gradient approximation of Perdew-Burk- Ernzerhof for solids (GGA-PBEsol) [7]. It is worth to mention that there is no theoretical or experimental evidence on the three compounds with this approximation are available, thus our results are only predictions.

II. METHOD OF CALCULATION

The calculations of the structural, electronic and magnetic properties of $Sr_{1-x}Ti_xS$ Compounds were carried out following density functional theory as implemented in Wien2k code [8]. In order to generate the three 25%, 50%, and 75% concentrations of Ti, a standard cubic supercell of (1×1×1) which containing eight atoms in the rock-salt phase was constructed. The Brillouin zone was sampled in 8×8×8 Monk horst-Pack grid. The wave functions in the interstitial region were expanded up to $R_{mt}K_{max}$ = 8.0 (where K_{max} is the magnitude of the largest K vector in the plane wave and R_{mt} is the average radius of the muffin-tin spheres). The partial waves inside the atomic sphere had a maximum value of l_{max} = 10. The charge density, on the other hand, was set at G_{max} = 14 $a.u.^{-1}$.

III. RESULTS AND DISCUSSION

3.1 Structural parameters

The structural optimization of $Sr_{1-x}Ti_xS$ compounds with x=0.25, 0.50, and 0.75 was carried out in the neighborhood of the parent SrS semiconductor's lattice parameter. In the rock-salt structure, one, two, and three Sr cation atoms are substituted by one, two, and three Ti dopant atoms in 1×1×1 supercell to reach 0.25, 0.50, and 0.75 concentrations, respectively. The obtained structures are optimized through calculating their total energies as a function of the reduced volume. The results are fitted into Birch-Murnaghan equation of state [9] to define the lattice parameter and the bulk modulus for the doped systems. The simulated results are listed in Table 1.

Table 1
Computed values of lattice parameter a (Å) and bulk modulus B (GPa) for $Sr_{1-x}Ti_xS$ (x=0.25, 0.50, and 0.75)

Compound	a (Å)	B (GPa)
$Sr_{0.75}Ti_{0.25}S$	5.763	59.306
$Sr_{0.50}Ti_{0.50}S$	5.537	71.909
$Sr_{0.25}Ti_{0.75}S$	5.227	82.073

It can be seen from Table 1 that the lattice constant of the doped systems decreases and the bulk modulus increases with increasing Ti content. This is due to the fact that the ionic radius of Ti is smaller than that of Sr atom.

3.2 Electronic band structures and densities of states

We have utilized the optimized lattice parameters of the compounds to study the electronic band structures and densities of states. Spin resolved energy band gap structures for the two-spin channels direction along with high symmetry points in first Brillouin zone for $Sr_{1-x}Ti_xS$ at different concentrations 0.25, 0.50 and 0.75 are illustrated in the Fig.1, respectively.

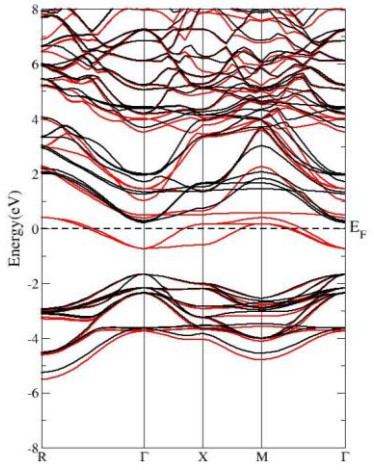

a)

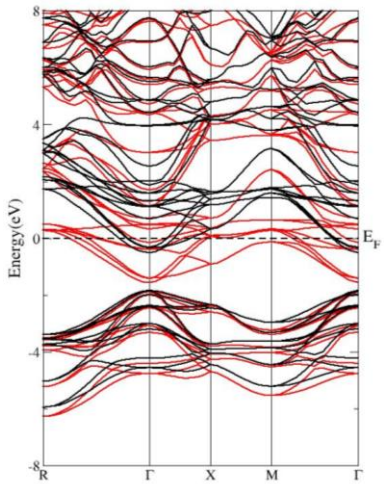

b)

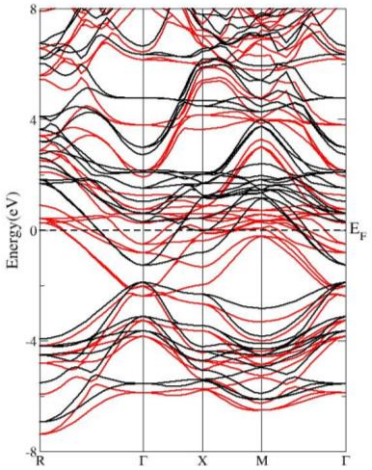

c)

Fig. 1 Electronic band structures of $Sr_{1-x}Ti_xS$ at a) x=0.25, b) x=0.50, and c) x=0.75 (Red color: spin up, Black color: spin down).

From the profiles of band structures, it is evident for the $Sr_{1-x}Ti_xS$ at x=0.25 that in majority spin channel, the band gap crosses the Fermi level (E_F) and therefore exhibits metallic character, but the minority spin channel does not pass the Fermi level and hence shows semiconductor feature. This indicates that this material is half-metallic ferromagnetic. On increasing the concentration over 25%, the HMF character disappear and the nature turn to be metallic for both the compounds $Sr_{0.50}Ti_{0.50}S$ and $Sr_{0.25}Ti_{0.75}S$.

The energy band gap E_g exists in minority spin channel has the direct nature, in which the valence band maxima (MVB) and the conduction band minima (MCB) occur at Γ point. Recalling that the occurrence of the half-metallic G_{HM} gap is a remarkable feature of the investigated DMS compounds.
The estimations of minority spin channel E_g (eV) and G_{HM} (eV) for $Sr_{1-x}TixS$ are listed in Table 2.

Table 2
Calculated band gap E_g (eV) and half-metallic band gap G_{HM} (eV) for $Sr_{0.75}Ti_{0.25}S$ compound.

Compound	E_g (eV)	G_{HM} (eV)
$Sr_{0.75}Ti_{0.25}S$	1.892	0.215
$Sr_{0.50}Ti_{0.50}S$	-	-
$Sr_{0.25}Ti_{0.75}S$	-	-

We may deduce from this table that only the $Sr_{0.75}Ti_{0.25}S$ compound is capable of generating completely spin-polarized current owing to feasible excitation and is thus responsible for improving the efficiency of spin-based devices.
The plots of spin-polarized total (TDOS) and partial (PDOS) densities of states for the $Sr_{0.75}Ti_{0.25}S$, $Sr_{0.50}Ti_{0.50}S$, and $Sr_{0.25}Ti_{0.75}S$ ferromagnetic compounds are displayed in Fig.2.

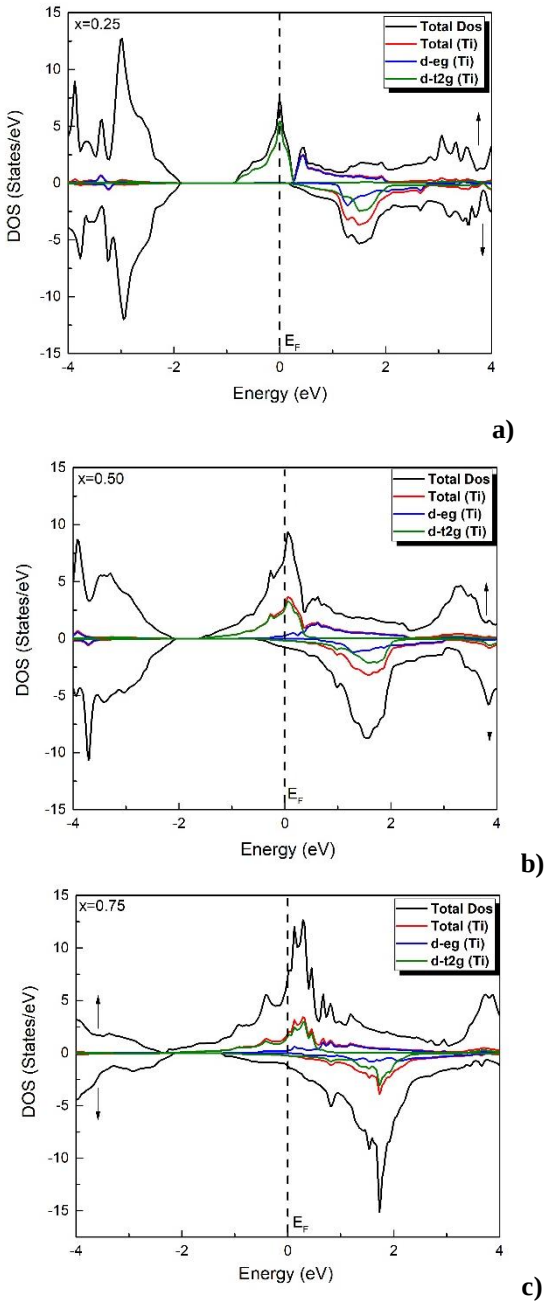

Fig. 2 Total and partial densities of states of $Sr_{1-x}Ti_xS$ at a) x=0.25, b) x=0.50, and c) x=0.75

For the $Sr_{0.75}Ti_{0.25}S$, the observed total and partial densities of states (DOS) reveal the half-metallic behavior, which is produced by metallic majority spin and semiconducting minority spin, culminating in 100% spin polarization at Fermi level. Both $Sr_{0.50}Ti_{0.50}S$ and $Sr_{0.25}Ti_{0.75}S$ have a metallic character due to the existence of 3d-Ti and 3p-S states at the Fermi level E_F. The findings of the band structures are confirmed by these studies.

The e_g states have a greater energy than the t_{2g} states, indicating that the Ti ions are located in an octahedral environment.

3.3 Magnetic properties

The computed values of total and local magnetic moments per Ti atom for $Sr_{1-x}Ti_xS$ (x=0.25, 0.50, and 0.75) are collected in Table 3.

Table 3
Computed total and local magnetic moments (μ_B) per Ti atom for $Sr_{1-x}Ti_xS$ (x=0.25, 0.50, and 0.75)

Compound	Total	Sr	S	Ti
$Sr_{0.75}Ti_{0.25}S$	2	0.006	-0.012	1.583
$Sr_{0.50}Ti_{0.50}S$	1.93	0.019	-0.005	1.527
$Sr_{0.25}Ti_{0.75}S$	1.87	0.050	0.042	1.455

The p-d hybridization (between 3d-Ti and p-S) creates the overall magnetic momentum of (Ti) atoms. A small locally-based magnetic moment was previously produced on the site Sr and the chalcogenide element S. A typical behavior of half-metallic ferromagnetism is the integral value of 2 μ_B on $Sr_{0.75}Ti_{0.25}S$. The positive and negative signs of the local magnetic moment values demonstrate the ferromagnetic and the antiferromagnetic interaction between Sr-Ti and S-Ti, respectively.

IV. CONCLUSION

In this paper, we have studied the structural, electronic and magnetic properties of $Sr_{1-x}Ti_xS$ compound at x=0.25, 0.50 and 0.75 concentrations by means of first principles calculations. Our calculated electronic structures predict the half metallicity with direct band gap for the Ti doped SrS at x=0.25. We expect the metallic nature for both concentrations x=0.50 and 0.75. We have found that the ferromagnetism is stabilized by the p-d hybridization. The negative sign in local magnetic moment of S atoms demonstrates that induced magnetic polarizations of S atoms are anti parallel to Ti atom. As a result of these findings, the $Sr_{0.75}Ti_{0.25}S$ is the ideal material for spintronic applications.

REFRENCES

[1] R. Pandey, S. Sivaraman, « Spectroscopic properties of defects in alkaline earth sulfides», J. Phys. Chem. Solids., Vol. 52, pp. 211, 1991
[2] H. Ohno, « Making nonmagnetic semiconductors ferromagnetic», Science, Vol 281, pp. 951, 1998
[3] F. Matsukura, H. Ohno, T. Dietl, Handbook of Magnetic Materials, in: K. H. J. Buschow (Ed.), North-Holland, Amsterdam 14 (2002) 1–87.
[4] S.A. Wolf, A.Y. Chtchelkanova, D.M. Treger, « Spintronics- A retrospective and perspective », IBM J. Res. Dev., Vol 50, pp. 101, 2006
[5] T. Dietl, « Ferromagnetic semiconductors », Semicond. Sci. Technol., Vol. 17, n°4, pp. 377, 2002

[6] Y. D. Reddy, B.K. Reddy, D. S. Reddy, D.R. Reddy, « Optical and electrical studies of vapor phase grown $Cd_{1-x}Co_xTe$ crystals », J. Spectrochim. Acta Part. A., Vol. 70, pp. 934–938, 2008
[7] J.P. Perdew, A. Ruzsinszky, G.I. Csonka, O.A. Vydrov, G.E. Scuseria, L.A. Constantin, X. Zhou, K. Burke, «Restoring the density-gradient expansion for exchange in solids and surfaces», Phys. Rev. Lett., Vol 100, pp. 136406, 2008
[8] P. Blaha, K. Schwarz, G.K.H. Madsen, D. Kvasnicka, J. Luitz, WIEN2K Vienna University of Technology, Austria, 2001
[9] F. Birch, « Finite strain isotherm and velocities for single-crystal and polycrystalline NaCl at high pressures and 300°K », J. Geophys. Res. Solid Earth., Vol. 83, pp.1257, 1978

Investigation of structural and optical properties of mixed phase nanoparticles titania synthesized by simple sol gel process

Rezika Zedek, Hatem Djedjiga, Mohamed Megherbi, Mohammed *Said Belkaid*

Laboratory of Advanced Technologies of Electrical Engineering (LATAGE), Faculty of Electrical Engineering and Computer science, Mouloud Mammeri University(UMMTO), BP 17 RP, 15000 *Tizi-Ouzou, Algeria*

rezika.zedek2010@yahoo.fr

Abstract

The purpose of this study is to calculate the band gap value of mixture phases of TiO_2 nanoparticless. The direct and indirect band gap of the samples can be estimated from measurements data of diffuse reflectance spectrascopy. Iron-doped titanium dioxide (TiO_2) nanoparticles were prepared via a facile and economical sol gel procedure. The prepared samples were characterized using X-ray diffraction (XRD) and UV-Vis diffuse reflectance spectroscopy. The obtained results by DRX displayed that samples annealed at 550 °C for 3h crystallized into mixture phases. The optical properties were investigated by UV-vis diffuse reflectance spectra (DRS). Using the DRS data, direct and indirect bandgap of the samples was determined by applying the Kubelka–Munk (K-M) equation. Graphics representations were used to calculate Eg: F(R) versus hv, F(R) versus λ, $(F(R)\ h\nu)^{\wedge n}$ versus hv with n = ½ for an indirect allowed transition and n = 2 for a direct allowed transition). Moreover the UV-Vis light-diffuse reflectance spectroscopy analysis depicted that the absorption region of Fe-doped TiO_2 was shifted to the visible-light range, which was attributed to incorporation of iron into the TiO_2 lattice during chemical reaction.

Keywords Titanium Dioxide, Mixture Phases, Kubelka–Munk Function, Absorbance Spectra, Direct and Indirect Band Gap Energy.

1. Introduction

Nanocrystalline transition metal oxide (TiO_2) is functional in a large range of industrial applications that include photocatalysis [1], solar cell [2-4], pigments and gas sensors [5]. It is the most extensively used oxide in some applications owing to its abundance [6], low cost, high efficiency, stability, nontoxicity and excellent biocompatibility [7-10]. The chemical and physical properties of nanomaterial are strongly influenced by the size crystallite, shape and crystalline phases. Recently, extensive researches have been conducted on the fabrication and characterization of TiO_2 nanoparticles because of their novel properties in large field application. TiO_2 has three kinds of phases, anatase (tetragonal), rutile (tetragonal), and brookite (orthorhombic) [11]. Gupta and Tripathi

signaled that the brookite is the rarest of the natural TiO_2 polymorphs and is the most difficult phase to prepare in the laboratory. Additionally, the different crystallographic orientations of the same material may exhibit different activities. For instance, from the catalytic viewpoint, anatase and rutile are the most important phase. On the other hand, TiO_2 is practically no moving in visible light due to its wide band gap energy, the anatase phase has a band gap of 3.2 eV (385 nm), while the rutile phase has a smaller band gap of 3.0 eV (410 nm) [12, 4]. Additionally, the anatase can show a photocatalytic activity only under UV light irradiation, while UV light accounts for only a small fraction (~5%) of the solar energy [13]. Therefore, band gap engineering by possible modification of materials is one of the moving investigate. Paul et Choudhury [14] demonstrated that pure anatase and rutile phase have band gap in the UV region, whereas a mixture of these phases has lower band gap and corresponds to the visible region. They indicate that the mixed phase nanocristalline titania exhibit superior photocatalytic activity, this is due to the synergitic effect of mixed phases [14]. Biswajit et Amarjyoti [15] reported that the crystalline anatase and pure rutile TiO_2 have band gap in UV region with short carrier lifetime, in contrast the mixture of these phases have lower band gap and longer decay time. Additionnally they displayed that in mixed phase TiO_2 the charge carriers are separated due to the transfer of electrons from anatase to rutile. Hurum et al [16] indicated that the presence of rutile phase extends the photoactive response to the visible region, harvesting more light, and stabilization of charge separation by electron transfer from rutile to anatase trapping sites slows down the recombination. Yamada et al [17] reported that the anatase phase has an indirect band gap, the conduction band electron and valence band hole will be in different position in the Brillouin zone, whereas the rutile phase has a direct band gap. In principal the band gap energy depends strongly the structure crystals. The mixture of TiO_2 NPs has

reduced band gap because of the presence of interface defects and due to the different alignment of the band states in anatase and rutile. Recently, Biswajit et Amarjyoti, Baiju et al [32,18] reported that the anatase-rutile mixture phase is found to have a magical effect on the charge transfer process, and longer carrier lifetime, whereas a short lifetime is reported when rutile content increases. Su et al. [19] reported that a mixture of 60 % anatase and 40 % rutile mixed phase TiO_2 exhibit better photoactivity than individual anatase or rutile polymorphs.

Diverse method have been introduced to prepare metal ion-doped TiO_2 nanoparticles are the hydrothermal method [20], sol-gel method [21-23], thermal hydrolysis [24],wet chemical synthesis and anodic- oxidation [25-26]. Among these methods, the sol–gel method represents several advantages over other methods are reported in literature.
In this present investigation, titania nanoparticles were developed by standard sol gel process and were characterized using XRD and UV-Vis diffuse reflectance spectroscopy. The principal goal of this paper is to determine an important direct and indirect optical band gap of mixture phases using Kabelka-Munk method.

2. Experimental part

2.1. Preparation of Undoped and Doped TiO_2 Nanoparticles

The experimental process for the synthesis of pure and Fe-doped TiO_2 nanoparticles was prepared by dissolving TTIP into ethanol under vigorous magnetic stirring for 1 hour at temperature of 70°C and followed by adding 2ml EG used as stabillizer. For a doping process, appropriate amount of iron sulfate hyperahydrate ($FeSO_4.7H_2O$) was added and stirred until a homogeneous solution precursor was obtained. The solution was dried at 70 °C for 3 hours, and then air cooled to room temperature. The samples powders were collected by suction filtration and washed by deionized water (about 60ml). The dried gel was grinded using a motar and calcined in a muffle furnace at 550◦C for 3 h. The samples of Fe doped and undoped TiO_2 nanoparticles were obtained by Sol Gel technique. Synthesis procedure for iron doped TiO_2 is schematically shown in Fig.1

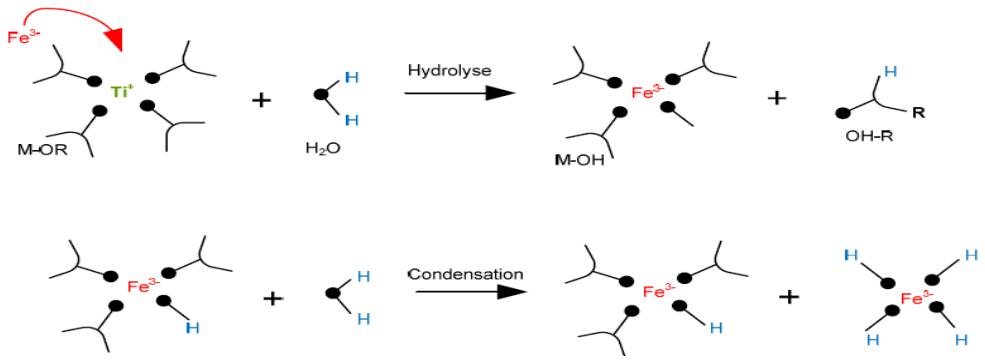

Fig. 1.Synthesis of Fe doped TiO_2 by Sol-Gel method.

2.2. Band gap energy

The band gap energy (Eg) is an essential parameter in semiconductor physics. The band gap is indicated by the region of strong absorption. Tauc proposed a method to estimate the optical band gap energy using data absorption spectra [27]. Subsequently, this method was developed by Davis and Mott [28]. In the Tauc method, the density of states is assumed to be parabolic, so that it can be linearized by a square-root function. In a simplified way, Eg is evaluated from the plot obtained between the highest valence band edge and the lowest conduction band edge. Electrons in a solid Occupy allowed energy bands separated by forbidden energy gaps. Two types of band-to-band transitions are suggested:

- Direct transitions (n = 2) when the participation of a phonon is not required to conserve momentum Fig.2 (a).
- Indirect transitions (n = 1/2) when at least one phonon participates in the absorption or emission of a phonon in order to conserve momentum Fig.2 (b).

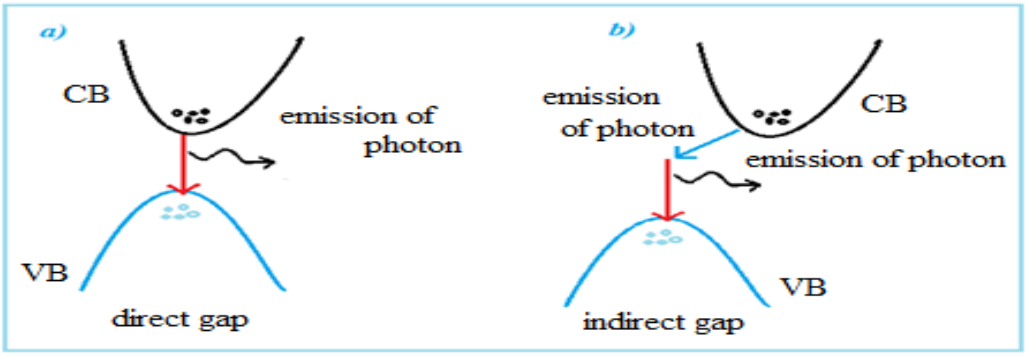

Fig. 2. Simplified representation of the band transition: (a) Direct gap, (b) Indirect gap

2.3. Measurements.

X-Ray diffraction (XRD) analysis was performed using a Bruker D8 Advanced two-circle Diffractometer with Cu-Kα (λ = 1.54021 Å) °) equiped with a Ge(111) monochromator and a Lynx Eye detector with an accelerating voltage of 40 kV and current of 40 mA (A) and scan speed 6°.min^{-} over the range of 2θ from 20 °C to 80°C and UV–vis diffuse reflectance spectroscopy was collected from ranging 200-800 nm with a resolution of 1.0 nm. The spectra were used to determine the optical proprieties

3. Result and discussion

➢ Phase identification by DRX

X-Ray Diffraction (XRD) analysis was carried out on TiO_2 NPs prepared by simple sol gel process.

The X-ray diffraction pattern of the prepared titania nanoparticles annealing at 550 °C for 3 h is depicted in Fig.3. Before annealing, the samples show the amorphous structure as shown in Fig.3a). This structure was converted into a crystalline structure after annealing as shown in Fig.3(b) and Fig.3(c). The results reveal the presence of mixture (anatase and rutile) phases with (101) and (110) main crystallographic orientations respectively. Angles corresponding to anatase are at 25.39, 37.91, 48.25, 62.7, 70.2 and 75.09, with peaks (101), (004), (200), (204), (220) and (215), respectively (ICSD no. 96-900-8214). While rutile phases 27.61, 36.25, 41, 32 and 56.69 are indicated as the (110), (101), (111) and (220) planes respectively.

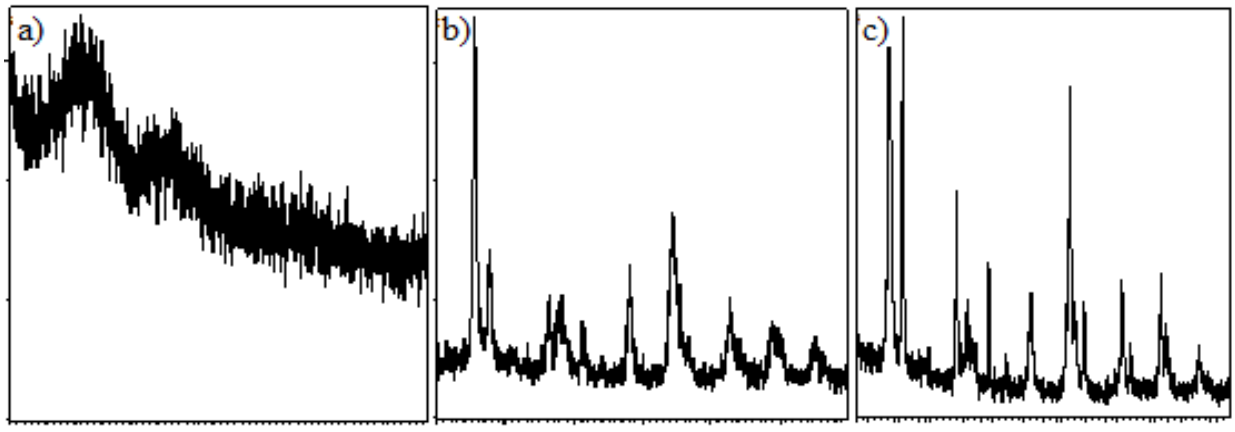

Fig 3. The XRD patterns of a) amorphous structure (before annealing) b) and c) of undoped and Fe-doped TiO_2 nanoparticles (after annealing at 550°C for 3h).

For TiO_2 NPs crystal system, the lattice parameters (a=b≠c) were estimated from 2θ values of XRD pattern using Bragg's law (Table 1). The lattice constants do not change with the presence of Fe

doping in the crystal TiO_2. The results of lattice parameters of pure and Fe^{3+}-doped-TiO_2 are presented in **Table 1**.

Table 1: lattice parameters of pure and Fe doped TiO_2 nanoparticles

Samples	Un-doped TiO_2	Fe-doped TiO_2
Anatase (2θ)	25.39(101) 48.25(200)	25.39(101) 48.22 (200)
Rutile (2θ)	27.50(110) 36.20(101)	27.52(110) 36.19(101)
Lattice parameters a=b ≠c(A°)(Bragg's law)	Anatase; a=b=3.55, c=9.00 Rutile; a=b=4.31, c=2.78	Anatase; a=b=3.56, c=8.96 Rutile; a=b=4.27, c=2.77

The mass fractions of the samples is calculated by the following formula **[30]** and presented in **Table 2**.

$$fr = \frac{Ir}{0.886\,Ia + Ir} \quad \text{..... (1)}$$

$$fa = \frac{0.886\,Ia}{0.886\,Ia + Ir} \quad \text{..... (2)}$$

Where fr and fa represent the weight percent of rutile TiO_2 and anatase TiO_2, respectively. I_a and I_r integrated diffraction intensities of the most intense anatase (101) and rutile (110) peaks, respectively. The parameters calculated using Eqs. **(1)** and **(2)** are depicted in **Table 2**

	(101) Anatase phase (%)	(110)Rutile phase (%)
Pure TiO_2	(25.39)81.86	(27.50)18.13
Fe-TiO_2	(25.39)18.42	(27.50)81.88

Table 2: the mass fractions of rutile and anatase phases in the samples

➢ Optical study by DRS

Data measurements of diffuse reflectance spectroscopy (DRS) have been performed to analyze the optical properties of undoped and Fe-doped TiO_2 NPs. The diffuse reflectance spectroscopy DRS is one of the most employed technique for the determination of the optical parameters such as absorbance spectra, bandgap direct and indirect of the material. The main goal of this part is to evaluate the result of the UV–vis diffuse reflectance spectroscopy, the application of the Kubelka–Munk theory and Tauc plot equation for the estimation of the optical bandgap direct and indirect of mixture TiO_2 NPs. The UV–vis absorption spectral of doped and TiO_2 pristine is carried out in diffuse reflectance mode (DRS). The reflectance of the samples is converted to absorbance by Kubelka–Munk function noted F(R) and given by **[29]**

$$F(R) = \frac{K}{S} = \frac{(1-R)^2}{2R} \quad \text{.....(3)}$$

Where F(R) is known Kabelka-Munk function, K is the molar absorption coefficient, S is scattering factor and R is the reflectance of TiO_2 NPs and is equal to:

$$\%R = \frac{R}{100} \quad \text{.....(4)}$$

The estimation of the band gap energy of the mixture phases by applying the Kubelka–Munk (F(R)) has been reported by Kubelka P **[31].** They have also signaled that the calculation of band gap value for TiO_2 by directly plotting F(R) against **hv** or **λ**. The absoption spectra of TiO_2 NPs are shown in **Fig. 4**. The optical band gap of undoped and doped TiO_2 were estimated around 440 nm (2.81eV) and 489.6nm (2.53 eV) by ploting F(R) versus photon energy hv. In all the cases, the optical edge or gap was inferred by linear extrapolation of the absorbance from the high slope region obtained from the spectra.

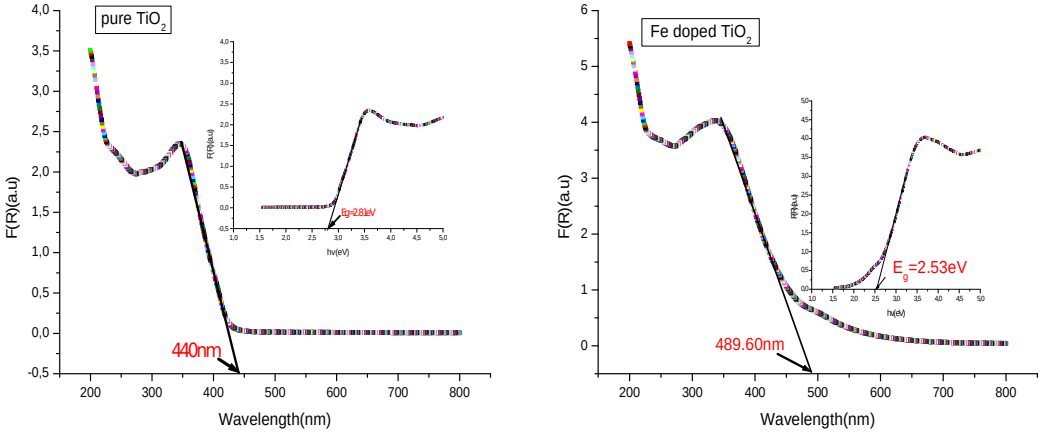

Fig. 4. Absorption spectra of undoped and doped TiO_2NPs

The Kubelka–Munk function can be modified by multiplying the F(R) by the incident photon energy (hv), using the corresponding coefficient (**n**) associated with an electronic transition as follows;

¿

Where h is the Planck's constant (J.s) and v is the light frequency (s^{-1}). The value of exponent n represents the nature of electronic transition from valence band to conduction band.

The **Figure 5** shows the determination of the direct band gap of the samples by plotting $[F(R)h\upsilon]^n$ (n=2 for direct band gap) vs energy ($h\upsilon$). The line drawn at the linear part of $[F(R)h\upsilon]^2$ at $h\upsilon$=0 gives the value of band gap. The band gap values of the samples are inserted in **Table3**.

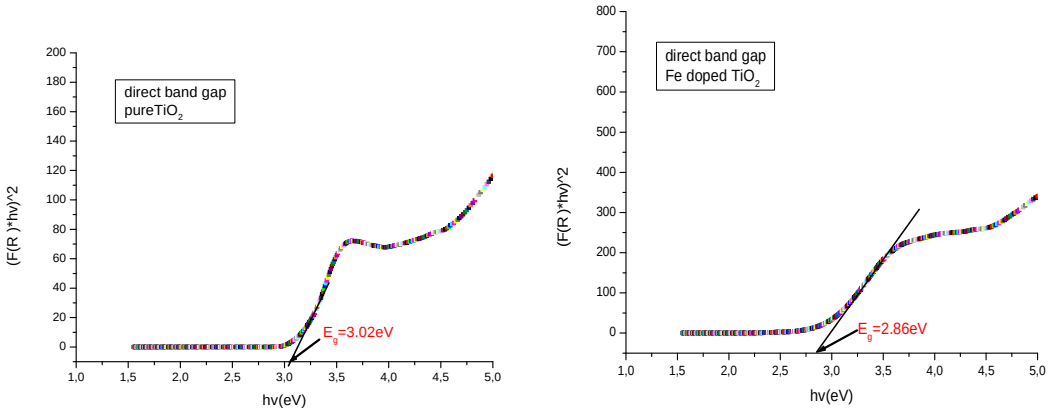

Fig. 5 shows the determination of the direct band gap for **a)** of pristine and **b)** doped TiO_2NPs by plotting $[F(R)h\upsilon]^{\wedge 2}$

The **Figure. 6** shows the determination of the indirect band gap of TiO_2 by plotting $[F(R)h\upsilon]^n$ (n=1/2 for indirect band gap) vs. energy ($h\upsilon$). The line drawn at the linear part of $[F(R)h\upsilon]^{1/2}$ at $h\upsilon$=0 gives the value of band gap. The values of the band gap of the samples are inserted in **Table3**.

Our results show that the band gap values estimated for the indirect transition are in agreement with the values obtained with the plotting absorption against wavelength, which confirme that the mixed phase samples exhibit an indirect electronic transition (indirect band gap. Obtained results are in accordance with Jin et Su results **[30, 19].**

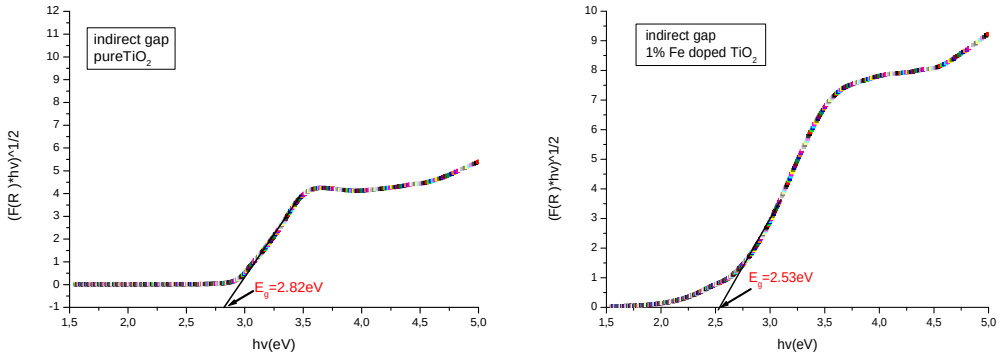

Fig. 6 Graphical representation of modified Kubelka–Munk function for **a)** undoped and **b)** doped TiO_2 by plotting $[F(R)hu]^{\wedge 1/2}$ versus hv

Table 3. Different values of Band gap energy estimated for pristine and Fe doped TiO_2 samples.

Samples	(F(R)hv)^2 (eV)	(F(R)hv)^1/2 (eV)	F(R) versus hv (eV)	F(R) versus λ (nm)
Pure TiO_2	3.02	2.82	2.81	440 (2.81eV)
Fe-TiO_2	2.86	2.53	2.53	489.60 (2.53eV)

4. Conclusion

In this paper, we have described the both band gap of nanocrystalline TiO_2 prepared by sol gel technique. A Comparison was made for optical property of pure and Fe doped TiO_2 NPs. Based on characterization results, all the produced samples are mixture phases and has lower indirect band gap, which corresponds to the visible region. We can conclude that sol gel, as a reproducible technique, is well adapted for the elaboration of high-quality of TiO_2 NPs with interesting structural and optical properties for photovoltaic application.

References

[1] Ao CH, Lee SC, Mak CL, Chan LY (2003) Photodegradation of volatile organic compounds (VOCs) and NO for indoor air purification using TiO_2: promotion versus inhibition effect of NO. Appl Catal B-Environ 42:119–129

[2] O'Regan B, Gratzel M (1991) A low-cost, high-efficiency solar cell based on dyesensitized colloidal TiO_2 films. Nature 353: 737–739.

[3] Sclafani A, Herrmann, J (1996) Comparison of the photoelectronic and photocatalytic activities of various anatase and rutile forms of titania in pure liquid organic phases and in aqueous solutions. J Phys Chem 100: 13655–13661.

[4] Munir S, Shah SM, Hussain H, khan RA (2016) Effect of carrier concentration on the optical band gap of TiO2 nanoparticles. Materials and Design 92 : 64–72

[5] Davis EA, Mott NF (1970) Conduction in non-crystalline systems V. Conductivity, optical absorption and photoconductivity in amorphous semiconductors. Philosophical Magazine 22: 0903– 0922.

[6] Nyankson E, Agyei-Tuffour B, Asare J Annan JE, Rwenyagila ER, Konadu DS, Yaya A, Dodoo-Arhin D (2013) Nanostructured TiO_2 and their energy applications -a review. J Engineering and Applied Sciences 8: 871-886.

[7] Zhang D, Chen J, Deng P Wang X, Li Y, Wen T, Li Y, Xiang Q, Liao Y (2019) Hydrogen evolution promotion of Au-nanoparticles- decorated TiO_2 nanotube arrays prepared by dip-loading approach. J American. Ceramic Society 102: 5873−5880.

[8] He Z, Kim C, Lin L, Jeon TH, Lin S, Wang X, Choi W (2017) Formation of heterostructures via direct growth CN on h-BN porous nanosheets for metal-free photocatalysis. Nano Energy 42: 58− 68.

[9] Pelaez M, Nolan NT, Pillai SC, Seery MK, Falaras P, Kontos AG Dunlop PSM, Hamilton JWJ, Byrne JA, O'Sheaf K, Entezari MH, Dionysiou DD (2012) A review on the visible light active titanium dioxide photocatalysts for environmental applications. Applied Catalysis B 125: 331–349.

[10] Chen H, Nanayakkara CE, Grassian VH (2012) Titanium Dioxide Photocatalysis in Atmospheric Chemistry. Chem. Rev 112: 5919–5948.

[11] Nyankson E, Agyei-Tuffour B, Asare J Annan JE, Rwenyagila ER, Konadu DS, Yaya A,

Dodoo-Arhin D (2013) Nanostructured TiO_2 and their energy applications -a review. J Engineering and Applied Sciences 8: 871-886.

[12] Munir S, Dionysiou DD, Khan SB, Shah SM, Adhikari B, Shah A (2015) Development of photocatalysts for selective and efficient organic transformations, J. Photochem. Photobiol. B 148: 209–222

[13] Liu X, Li Y, Deng D, Chen N, Xing X, Wang Y (2016) A one-step nonaqueous sol–gel route to mixed-phase TiO_2 with enhanced photocatalytic degradation of Rhodamine B under visible light. Cryst Eng Comm 18: 1964–1975.

[14] Paul S, Choudhury A (2014) Investigation of the optical property and photocatalytic activity of mixed phase nanocrystalline titania. Appl Nanosci 4: 839–847.

[15] Biswaji C, Bikash B, Amarjyoti C (2012) Extending Photocatalytic Activity of TiO_2 Nanoparticles to Visible Region of Illumination by Doping of Cerium. Photochemistry and Photobiology 88: 257-264.

[16] Hurum DC, Agrios AG, Gray KA, Rajh T, Thurnauer C (2003) Explaining the enhanced photocatalytic activity of degussa P25 mixed-phase TiO_2 using EPR. J Phys Chem B 107: 4545–4549

[17] Yamada Y, Kanemitsu, Y (2012) Determination of electron and hole lifetimes of rutile and nanatase TiO_2 single crystals. Appl Phys Lett 101: 133907.

[18] Baiju KV, Zachariah A, Shukla S, Biju S, Reddy MLP, Warrier KGK, (2009) Correlating photoluminescence and photocatalytic activity of mixed-phase nanocrystalline titania, Catal Lett. 130: 130–136.

[19] Su R, Ralf B, Lasse SR, Vang T, Michael S, Bjorn E, Anders P, Flemming B (2011) How the Anatase-to-Rutile Ratio Influences the Photoreactivity of TiO_2. J Phys Chem C 115: 24287–24292

[20] Zhu J, Zheng W, He B, Zhang J, Anpo M (2004) Characterization of Fe–TiO_2 photocatalysts synthesized by hydrothermal method and their photocatalytic reactivity for photodegradation of XRG dye diluted in water. J Mol Catal A 216: 35-43.

[21] Zhang YH, Reller A (2001) Nanocrystalline iron-doped mesoporoustitania and its phase transition. J Mater Chem 11: 2537-2541.

[22] Mokhtarimehr M, Akbar E, Mahmoud P (2013) Self-cleaning properties of Vanadium Doped TiO_2 sol-gel derived thin films. New J Glass Ceram 3: 34147-34150.

[23] Su C, Hong BY, Tseng CM (2004) Sol–gel preparation and photocatalysis of titanium dioxide. CatalysisToday 96: 119-126.

[24] Hirano M, Joji T, Inagaki M, Iwata H (2004) Direct formation of iron (III)-doped titanium oxide (Anatase) by thermal hydrolysis and its structural property. J Am Ceram Soc 87: 35-41

[25] D. Khudhair, A. Bhatti, Y. Li, H. Amani Hamedani, H. Garmestani, P. Hodgson, and S. Nahavandi, Mater. Sci. Eng. C 59, 1125 (2016).

[26] Y. Zhang, D. Yu, M. Gao, D. Li, Y. Song, R. Jin, W. Ma, and X. Zhu, Electrochim. Acta 160, 33 (2015).

[27] Tauc J, Grigorovici R, Vancu A (1966) Optical Properties and Electronic Structure of Amorphous Germanium. *Phys. Status Solidi B 15*: 627– 637.

[28] Mohammadnezhad F, Kampouri S, Wolff SK, Xu Y, Feyzi M, Lee JH, Ji X, Stylianou KC (2021)Tuning the Optoelectronic Properties of Hybrid Functionalized MIL-125-NH_2 for Photocatalytic Hydrogen Evolution. ACS Applied Materials &Interfaces *13:* 5044-5051 .

[29] Rosendo L and Ricardo G (2012) Band-gap energy estimation from diffuse reflectance measurements on sol–gel and commercial TiO2: a comparative study. J Sol-Gel Sci Technol 61: 1–7.

[30] Jing H, Yi-en D, Yang B, Jing A, Xuemei C, Yongqiang C, Pengfei W, Xiaojing Yang Y, Qi F (2019) Facile Formation of Anatase/Rutile TiO_2 Nanocomposites with Enhanced Photocatalytic Activity. J Molecules 24: 2996.

[31] Kasidid Y, Marcin K, Wojciech M TiO_2 with Tunable Anatase-to-Rutile Nanoparticles Ratios: How Does the Photoactivity Depend on the Phase Composition and the Nature of Photocatalytic Reaction", *ACS Applied Nano Materials***,** *4:* 633-643.

[32] Biswajit CAmarjyoti C (2013) Oxygen defect dependent variation of band gap, Urbach energy and luminescence property of anatase, anatase-rutile mixed phase and of rutile phases of TiO_2 nanoparticles", Physica E, 2013.

Pressure effect on structural, electronic and magnetic properties of the *M*As (*M* = Cr, Mn) binary compounds: A first-principles study

Ahlem kolli
Department of Physics, Faculty of Science, University Ferhat Abbas Setif 1
Laboratory of Surfaces and Interfaces Studies of Solid Materials (L.E.S.I.M.S)
Setif, Algeria
ahlem.kolli@univ-setif.dz

Nacir Guechi
Department of Medicine, Faculty of Medicine, University Ferhat Abbas Setif 1
Laboratory of Surfaces and Interfaces Studies of Solid Materials (L.E.S.I.M.S)
Setif, Algeria
nacir_guechi@yahoo.fr

***Abstract*—In this work, we have studied the structural, electronic and magnetic properties of the *M*As (*M* = Cr, Mn) binary compounds in the zinc blende phase, under hydrostatic pressure using ab initio calculations. The spin polarized calculations were performed using the Pseudo-Potential Plane Wave (PP-PW) method based on the Density Functional Theory (DFT) as implemented in the CASTEP code. The exchange correlation effect was treated using the GGA-PBE approximation. Geometric optimizations were performed for a pressure range between -8.5 and 30GPa. The calculated equilibrium lattice constant (*a*) for both compounds agrees very well with the available theoretical and experimental reports. According to the bulk modulus (*B*) values, the CrAs compound with *B* = 64.53 GPa is more resistant to volume changes than the MnAs compound with *B* = 45.98 GPa. The electronic populations, energy band structures and density of states were calculated to determine the magneto-electronic properties. Analysis of the obtained results shows that these compounds exhibit a half-metallic ferromagnetic behavior with a band gap in the minority spin states resulting from the *p-d* hybridization. The total magnetic moment of *M*As compounds comes mainly from the incomplete *d*-orbital of the Cr (Mn) atoms, and it is almost equal to an integer values of 3 μ_B (4 μ_B) per unit cell which is consistent with the Slater-Pauling rule. the half-metallicity in the studied compounds is generally maintained over a wide pressure range. These results would help in incorporating *M*As (*M* = Cr, Mn) compounds in spintronic devices.**

***Keywords*—DFT, PP-PW, CrAs, MnAs, half-metallicity**

I. INTRODUCTION

Half-metallic ferromagnets (HMFs) have the potential to play an important role in the continued development of spintronics, which uses electron spins to obtain, transport and process information [1]. The behavior of the HMFs was firstly predicted by de Groot et al. [2] in 1983 based on first-principle calculations for C1b-type Heusler alloys NiMnSb and PtMnSb. These materials behave as metals for one direction of spin and as semiconductors for the other direction of spin, leading to a full spin polarization (100%) at the Fermi level (E_F). Half-metallic ferromagnets have attracted much attention because of their high Curie temperature (T_C) and large half-metallic band gap [3], among these compounds, MnAs and CrAs.

The transition metal arsenides CrAs and MnAs are part of the large family of transition metal pnictides with a general formula TMX (TM = transition metal, X = P, As, Sb), Which crystallize in several phases depending on the temperature and pressure. At ambient conditions, CrAs crystallizes in MnP-type orthorhombic crystal structure [4], whereas MnAs adopts the hexagonal NiAs-type structure [5]. CrAs, and MnAs in the Wurtzite (WZ) or zinc-blende (ZB) structures have received particular attention because of compatibility with current III–V or II–VI semiconductors technology. Since 2000, Akinaga et al. [6] were found the possibility to fabricate zinc-blende type CrAs using molecular beam epitaxy (MBE) on a GaAs (001) substrate and found ferromagnetism behavior at room temperature with Curie temperature (T_C) higher than 400 K, which is in good agreement with theoretical predictions using Monte Carlo simulation and mean field theory [7]. Moreover, ZB-CrAs compound was found experimentally to exhibit a half-metallic ferromagnetic structure with a magnetic moment of 3 μ_B [6], These results agree well with the theoretical reports [8, 9]. Recently the growth of ZB-MnAs thin films on GaAs [10, 11] and InP [12] substrates by MBE has been reported. On the other hand, Han et all. [13] have studied the electronic and magnetic properties of the bulk, (001) surfaces and (001) interfaces for zinc blende MnAs by means of the full-potential linearized augmented plane-wave (FPLAPW) method from the first-principle calculations. They predicted that the zinc blende MnAs is a nearly half-metallic ferromagnet with 4.00 μ_B magnetic moment.

The investigation of the pressure effect on materials properties has attracted much attention. In fact, pressure serves as a versatile tool in materials research. In the current work, we present the results of structural, electronic and magnetic properties of the of the *M*As (*M* = Cr, Mn) binary compounds in the zinc blende phase using the first-principle calculations. We also discuss the half-metallic stability under hydrostatic pressure.

II. COMPUTATIONAL DETAILS

We have performed the first-principle calculations using the pseudo-potential plane-wave method based on density functional theory (DFT) [14] as implemented in the Cambridge Serial Total-Energy Package (CASTEP) [15], to study the structural and magneto-electronic properties of the *M*As (*M* = Cr, Mn) binary compounds in the zinc blende phase. The exchange-correlation potential and the interaction between the atomic core and the valence electrons were described using the Perdew–Burke–Ernzerhof (PBE) functional within the generalized gradient approximation (GGA) [16] and the ultrasoft pseudo potential [17]. The considered valence states are: Cr: $4s^1\ 3d^5$; Mn: $4s^2\ 3d^5$; As: $3d^{10}\ 4s^2\ 4p^3$. A plane-wave cut-off energy of 380 eV and a 10 × 10 × 10 k-points in the Brillouin zone were applied for the geometry optimization, we have selected 30 × 30 × 30 k-points to catlculate the density of states. The self-consistent field tolerance was set as a total energy difference smaller

than 5×10^{-6} eV/atom, the maximum force was less than 0.01 eV/Å the maximum stress was smaller than 0.02 GPa and the displacement of atoms was less than 5×10^{-4}Å.

III. Results and Discussion

The *M*As (*M* = Cr, Mn) binary compounds crystallize in The zinc-blende structure which is similar to that of ZnS, possesses a cubic lattice in the space group $F\bar{4}3\,m$, No. 216 with two atoms in the primitive unit cell (Fig. 1- b). The atomic positions are as follows [18] : *M* at (0, 0, 0) in Wyckoff coordinates and (1/4, 1/4, 1/4) occupied by the As atom (Fig. 1-a).

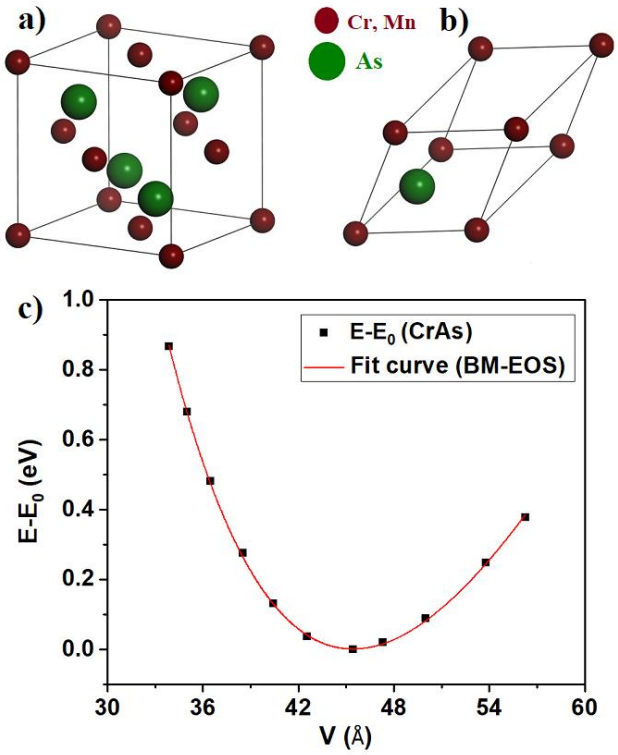

Fig. 1. a) Crystal structure of *M*As (*M* = Cr, Mn) compounds ; b) its corresponding primitive unit cell ; c) Calculated energy as a function of volume of CrAs compound (MnAs have the same curve).

In order to obtain the ground-state parameters, such as the lowest total energy per unit cell (E_0), equilibrium lattice constant (a_0), equilibrium volume (V_0), the bulk modulus (B_0) and its derivative (B'=dB/dP), a geometry optimization was performed by computing the total energy of the unit cell at each fixed pressure. The calculated total energy of CrAs compound using GGA-PBE versus unit-cell volume has been fitted to the Birch-Murnaghan (BM) equation of state (EOS) (1) [19] and is displayed in Fig. 1-c.

$$E(V) = E_0 + \left(\frac{9}{16}\right) BV_0 \left(\left(B'-4\right)\left(\frac{V}{V_0}\right)^{\frac{-2}{3}} - B' + 6 \right) \left(\left(\frac{V}{V_0}\right)^{\frac{-2}{3}} - 1 \right)^2 \quad (1)$$

According to the bulk modulus (B) values listed in Table I, the CrAs compound with B = 64.53 GPa is more resistant to volume changes than the MnAs compound with B = 45.98 GPa. It is important to note that the obtained results agree very well with the available experimental and theoretical data.

The spin-polarized band structures of *M*As (*M* = Cr, Mn) compounds at different pressures -8.5, 0 and 30 GPa, in the energy range from -4 to 4 eV are given in Fig. 2. At -8.5 and 0GPa, it is clearly seen that the majority spin channel (spin up) exhibits a metallic behavior in which the electronic states belonging to the valence band cross the Fermi level (set at 0 eV), while the minority spin channel (spin down) show a semiconducting nature with an indirect gap of 2.334 and 2.034 eV (1.893 and 1.753 eV) For CrAs (MnAs) compounds at -8.5 and 0 GPa respectively. At these pressures, both compounds can be considered as a perfect half-metallic.

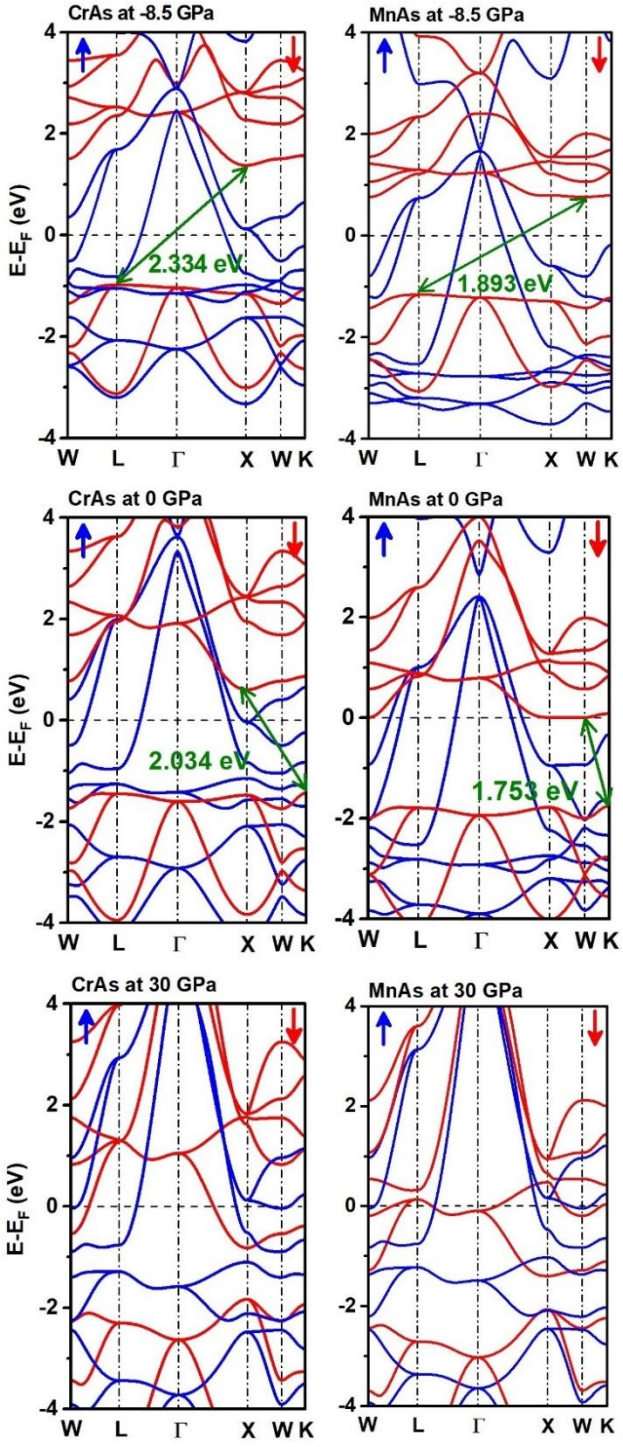

Fig. 2. Band structures for *M*As (*M* = Cr, Mn) compounds at pressures -8.5, 0 and 30 GPa (blue line: spin-up; the red line: spin-down).

However, the compounds at 30 GPa behave totally different, for which the spin majority and the spin minority states exhibit metallic natures.

TABLEI. The calculated lowest total energy per unit cell, E_0 (eV), lattice constant, a_0 (Å), volume, V_0 (Å^3), bulk modulus, B_0 (GPa) and its derivative B' for the MAs (M = Cr, Mn).

	E_0	a_0	V_0	B_0	B'
CrAs	-2639.7	5.663	181,69	64,53	3,13
Expt. [20]		5.637			
Calc. [7]		5.658		67.60	
MnAs	-825.9	5,720	187,16	45,98	1.76
Expt. [21]		5,689			
Calc. [13]		5.743			

The variations of the valence band maximum (VBM) and conduction band minimum (CBM) as functions of hydrostatic pressure from -8.5 to 30 GPa for the spin minority states are shown in Fig. 3. The half-metallic properties of the MAs (M = Cr, Mn) compounds are maintained in the shaded regions.

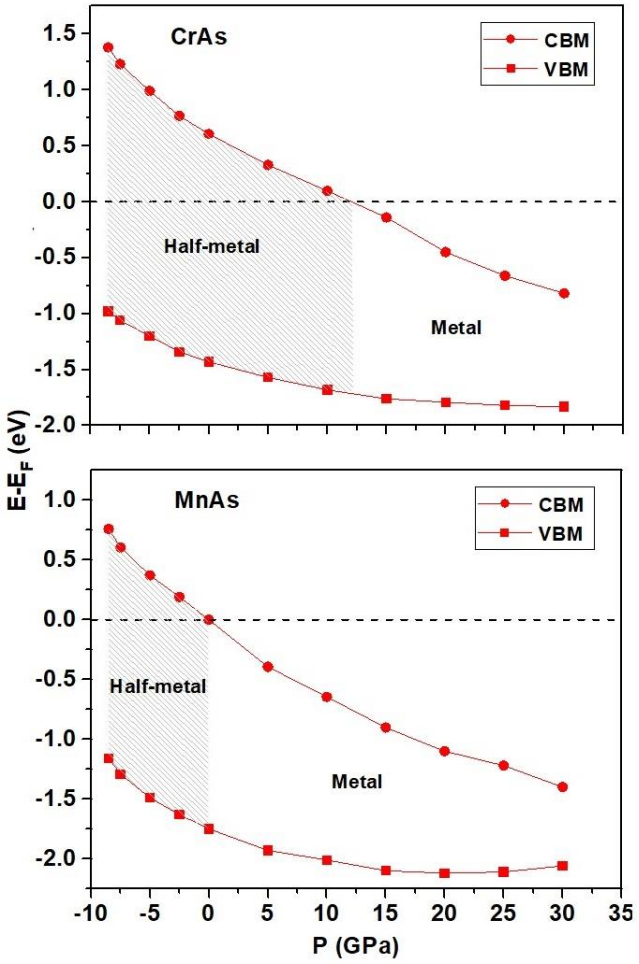

Fig. 3. Valence band maximum (VBM) and conduction band minimum (CBM) of MAs (M = Cr, Mn) compounds as functions of the hydrostatic pressure.

Increasing the pressure, the VBM and CBM show decreasing trend. For the CrAs and MnAs compounds, the half-metallic regions are -8.50 – 12.17 GPa, -8.5 – 0 GPa, respectively. When CBM crosses the Fermi level, their properties change from the half-metallic character to metallic character. from Fig. 3, we can also see that the half-metallic regions of CrAs compound is more important than that of the MnAs compound.

Further, we investigate with more details the electronic structure of MAs (M = Cr, Mn) compounds at zero pressure by calculating their total and partial density of states (TDOS and PDOS) in the energy range from -12 to 4 eV, presented in Fig. 4. It is clear to see that the most important contribution around the Fermi level comes essentially from contributions of Cr-3d (Mn-3d) states of CrAs (MnAs) compounds, whereas the contribution of 4p states belonging to As atom is small. The lower valence band with energy below −9 eV is due to 4s states of As atom. On the other hand, a clear gap in the minority spin channel is observed for MAs (M = Cr, Mn)

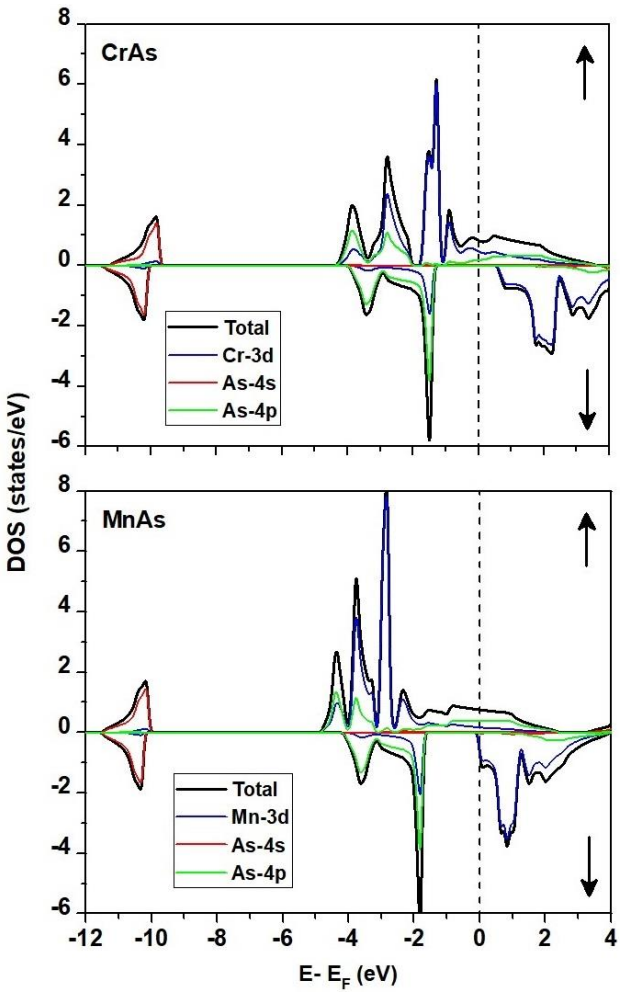

Fig. 4. Total and partial density of states (TDOS and PDOS) at zero pressure.

compounds, the origin of the gap is the sequence of the strong hybridization between the d states around the Fermi level of the transition metal atoms Cr or Mn and the p states of As atom. The calculation of the density of state at zero pressure shows that CrAs and MnAs have a half metallic behavior. These results confirm wath was obtained by studying the band structures and agree very well with theoretical reports [7, 13].

The total and atomic magnetic moments of the *M*As (*M* = Cr, Mn) compounds as a function of the pressure are shown in Fig. 5. In the half-metallic regions, the total magnetic moment is maintained at an integer values of 3 μ_B (4 μ_B) per unit cell for CrAs (MnAs) compounds and obeys to the "$M_t=Z_t$ -8" Slater-Pauling rule [22], where M_t is the total magnetic moment and Z_t is the total number of valence electrons in the unit cell, which is equal to 11 (12) electrons for CrAs (MnAs) compounds. The atomic magnetic moment of Cr, Mn atoms and total magnetic moment decrease, whereas that of As atom increases with increase in pressure, leading to the transition from the half-metallic character to metallic character at pressures greater than 12.17 GPa (0 GPa) for CrAs (MnAs) compounds. As seen in Fig. 5 the main contribution to the total magnetic moment is due to the incomplete *d*-orbital of the Cr or Mn atoms, while the magnetic moment on the As atom is quite small.

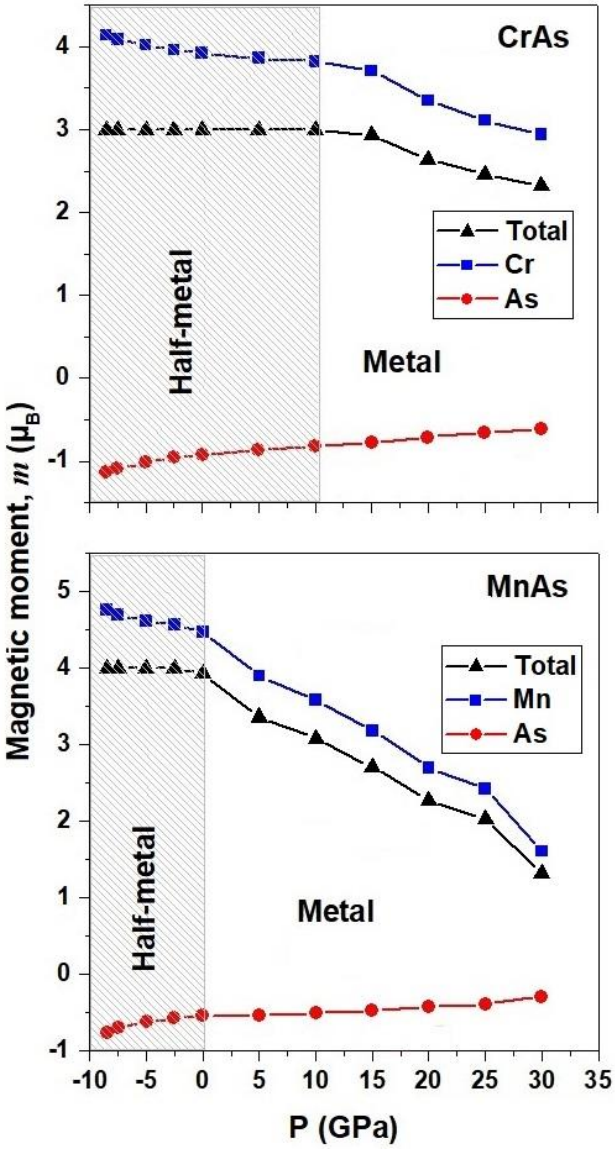

Fig. 5. Variation of the Total and atomic magnetic moments as functions of the hydrostatic pressure.

In Fig. 6, we display the pressure effect on the spin polarization (P) of *M*As (*M* = Cr, Mn) compounds defined by the formula [23] :

$$P = \frac{N\uparrow(E_F) - N\downarrow(E_F)}{N\uparrow(E_F) + N\downarrow(E_F)} \times 100 \quad (2)$$

Where $N\uparrow(E_F)$ and $N\downarrow(E_F)$ are the density of state at Fermi level (E_F) in the case of spin-up and spin-down, respectively.

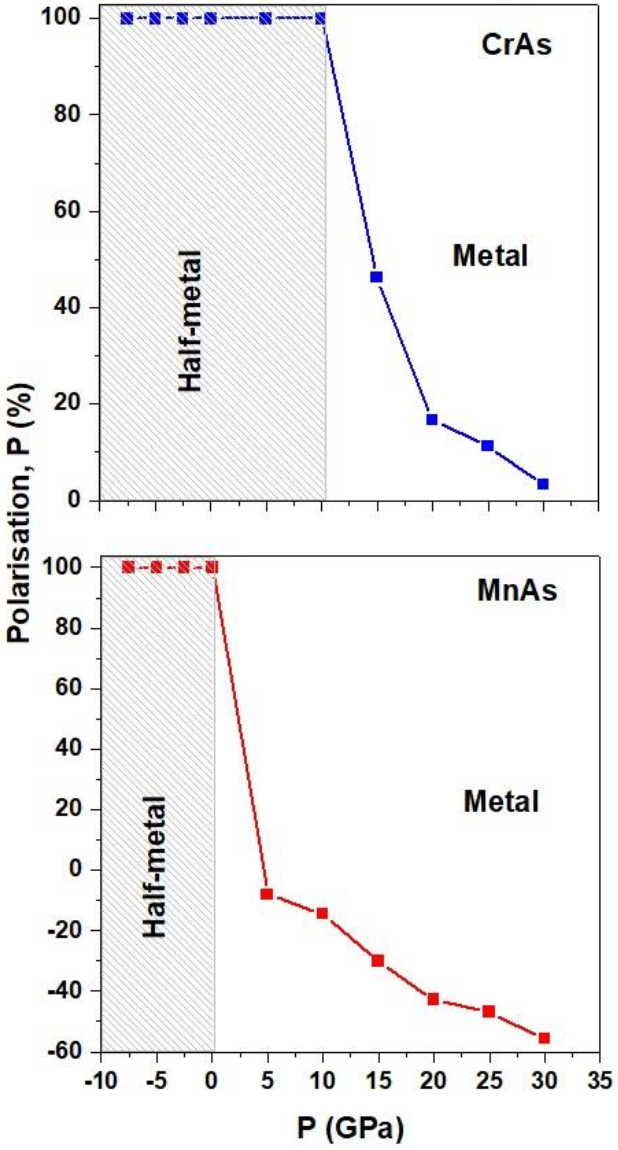

Fig. 6. Variation of the spin polarization (P) as functions of the hydrostatic pressure.

We find that the spin polarization for both compounds in the half-metallic regions is about 100%, which confirm that electrons can participate in conduction in just one spin channel. When the pressure is greater than 12.17 GPa (0 GPa) for CrAs (MnAs) compounds, the spin polarization exhibits a large deviation and rapidly decreases, Thus the compounds acquire a metallic behaviour.

IV. CONCLUSION

In summary, the effect of hydrostatic pressure on the structural, electronic and magnetic properties of the *M*As (*M* = Cr, Mn) compounds with zinc blende structure have been investigated using the (PP-PW) method with the GGA-PBE approximation based on DFT. The structural calculation

reveals that, the CrAs compound is more resistant to volume changes than the MnAs compound. On the other hand, our structural parameters agree very well with the theoretical and experimental data. From the electronic band structure and density of states (DOS) calculations, the CrAs (MnAs) compounds are found to be half-metallic ferromagnets with an indirect gap in the minority spin channel equal to 2.034 eV (1.753 eV) at zero pressure. However, the energy gap mades mainly by hybridization between the *p* states of As and *d* states of Cr or Mn. From the magnetic properties calculation, the results show that the CrAs (MnAs) compounds have an integral magnetic moment 3 μ_B (4 μ_B) per unit cell, which are following the "M_t=Z_t -8" Slater–Pauling rule. The hydrostatic pressure has important effect on the electronic and magnetic properties, resulting in a significant transition from a half-metallic ferromagnetic behavior with 100% spin polarization to metallic behavior for both compounds. The CrAs and MnAs compound have an excellent half-metallic ferromagnetic with high polarization in wide pressure range and represent a good candidate for spintronic applications and other applications.

ACKNOWLEDGMENT

Technical supports from the (L.E.S.I.M.S) Laboratory, University Ferhat Abbas Setif 1, Setif, Algeria, are gratefully acknowledged.

REFERENCES

[1] W. E. Pickett and J. S. Moodera, "Half metallic magnets," Phys. Today., vol. 54, pp. 39-45, 2001.

[2] R.A. De Groot, F.M. Mueller, P.G. Van Engen and K.H.J. Buschow, "New class of materials : half-metallic ferromagnets," Phys. Rev. Lett., vol. 50, pp. 2024, 1983.

[3] T. Graf, C. Felser and S. S. P. Parkin, "Simple rules for the understanding of Heusler compounds," Prog. Solid State Chem., vol. 39, pp. 1-50, 2011.

[4] H. Boller, and A. Kallel, "First order crystallographic and magnetic phase transition in CrAs," Solid State Commun., vol. 9, pp. 1699-1706, 1971.

[5] S. Sanvito and N. A. Hill, "Ground state of half-metallic zinc-blende MnAs," Phys. Rev. B., vol. 62, pp. 15553, 2000.

[6] H. Akinaga, T. Manago, M. Shirai, "Material design of half-metallic zinc-blende CrAs and the synthesis by molecular-beam epitaxy, " J. Appl. Phys. Japan., vol. 39, pp. L 1118–L 1120. 2000.

[7] A. Azouaoui, N. Benzakour, A. Hourmatallah and K. Bouslykhane, "Structural, magnetic properties and phase stability of CrAs in the zinc-blende structure : Investigated by first principle calculations and Monte Carlo simulation," Solid State Commun., vol. 323, pp. 114101, 2021.

[8] B. Sanyal, L. Bergqvist, O. Eriksson, "Ferromagnetic materials in the zinc-blende structure," Phys. Rev. B., vol. 68, pp. 054417, 2003.

[9] I. Galanakis, "Surface half-metallicity of CrAs in the zinc-blende structure," Phys. Rev. B., vol. 66, pp. 012406, 2002.

[10] K. Ono, J. Okabayashi, M. Mizuguchi, M. Oshima, A. Fujimori, and H. Akinaga, "Fabrication, magnetic properties, and electronic structures of nanoscale zinc-blende MnAs dots," J. Appl. Phys., vol. 91, pp. 8088-8092, 2002.

[11] T. W. Kim, H. C. Jeon, T. W. Kang, H. S. Lee, J. Y. Lee and S. Jin, "Microstructural and magnetic properties of zinc-blende MnAs films with half metallic characteristics grown on GaAs (100) substrates," Appl. Phys. Lett., vol. 88, pp.021915, 2006.

[12] H. Oomae, S. Trizawa, Y. Jinbo, H. Toyota, T. Kambayashi and N. Uchitomi, "Studies of zinc-blende type MnAs thin films grown on InP (001) substrates by XRD," J. Cryst. Growth., vol. 378, pp. 410-414, 2013.

[13] H. Han, T. Feng, C. Zhang, Z. Feng, M. Li, and K. L. Yao, "The stability and half-metallicity of (001) surface and (001) interface based on zinc blende MnAs," Phys. B : Condens. Matter., vol. 539, pp. 61-65, 2018.

[14] M. C. Payne, M. P. Teter, D. C. Allan, T. A. Arias, J.D. Joannopoulos, "Iterative minimization techniques for ab initio total-energy calculations: molecular dynamics and conjugate gradients," Rev. Mod. Phys., vol. 64, pp. 1045–1097, 1992.

[15] M.D. Segall, P. J. Lindan, M.A. Probert, C.J. Pickard, P.J. Hasnip, S.J. Clark and M.C. Payne, "Firstprinciples simulation: ideas, illustrations and the CASTEP code," J. Phys.: Condens. Matter., vol. 14, pp. 2717, 2002.

[16] J.P. Perdew, K. Burke, M. Ernzerhof, "Generalized gradient approximation made simple," Phys. Rev. Lett., vol.77, pp. 3865–3868, 1996.

[17] D. Vanderbilt, "Soft self-consistent pseudopotentials in a generalized eigenvalue formalism," Phys. Rev. B., vol. 41, pp. 7892–7895. 1990.

[18] I. Galanakis, "Surface half-metallicity of CrAs in the zinc-blende structure," Phys. Rev. B., vol. 66, pp. 012406, 2002.

[19] F. Birch, "The effect of pressure upon the elastic parameters of isotropic solids, according to Murnaghan's theory of finite strain," J. Appl. Phys., vol. 9, pp. 279-288, 1938.

[20] V. H. Etgens, P. C. De Camargo, M. Eddrief, R. Mattana, J. M. George and Y. Garreau, "Structure of ferromagnetic CrAs epilayers grown on GaAs (001)," Phys. Rev. Lett., vol. 92, pp. 167205, 2004.

[21] H. C. Jeon, T. W. Kang, S. U. Yuldashev, T. W. Kim and S. Jin, "Magnetotransport properties of zinc-blende-structured MnAs films with half-metallic characteristics," Appl. Phys. Lett., vol. 89, pp. 112517, 2006.

[22] I. Galanakis and P. Mavropoulos, "Zinc-blende compounds of transition elements with N, P, As, Sb, S, Se, and Te as half-metallic systems," Phys. Rev. B., vol. 67, pp. 104417, 2003.

[23] R. J. Soulen, J. M. Byers, M. S. Osofsky, B. Nadgorny, T. Ambrose, S. F. Cheng, ... and J. M. D. Coey, "Measuring the spin polarization of a metal with a superconducting point contact," science., vol. 282, pp. 85-88, 1998.

Theoretical Investigation of Properties of Semiconductors Materials Based Rare Earth

Asma KADRI
Department of engineering physics
University of Science and Technology of Oran -USTO- Mohamed Boudiaf
Oran, Algeria
asma.kadri@univ-usto.dz

Soumia BAHLOULI
Department of engineering physics
University of Science and Technology of Oran -USTO- Mohamed Boudiaf
Oran, Algeria
bsoumia56@yahoo.fr

Said HIADSI
Department of engineering physics
University of Science and Technology of Oran -USTO- Mohamed Boudiaf
Oran, Algeria

Mokhtar ELCHIKH
Department of engineering physics
University of Science and Technology of Oran -USTO- Mohamed Boudiaf
Oran, Algeria
m.elchikh@gmail.com

***Abstract*— In this work we present the structural, electronic, elastic and magnetic properties of semiconductors based rare earth nitrides ReN (Re=Sc, Y, Gd) in the three crystals cubic structures NaCl (B1), CsCl (B2), and ZB (B3), the properties have been determined by the first principle calculations based of the density function theory (DFT), using the WIEN2k simulation package. We have concluded that the rare earth nitrides ReN with (Re= Sc, Y, Gd) are semiconductors nature for the three compounds with direct bandgap 2.721eV for ScN, 3.044 eV for YN and 1.07eV for GdN compounds, at the normal conditions the rare earth nitrides are stable in the B1 structures, the results of magnetic properties showed that the two rare earth nitrides ScN and YN are nonmagnetic nature, in addition the GdN behave as ferromagnetic compound in rocksalt phase. The calculation of elastic constants proved that the compounds are mechanically stable. Our findings are in good agreement with the other experiments and theories results available.**

Keywords— The density function theory (DFT), WIEN2k, rare earth nitrides, ferromagnetic, semiconductors.

I. INTRODUCTION

Today, the world is broadly interested in studying the rare earth nitride materials because their important physical properties. The hardness of most rare earth nitrides are usually unstable at ambient conditions [1], therefore, we employed the theoretical calculation represented by the first principle technique for discover more properties about the rare earth nitrides. The goal of the present work is using the ab initio calculation to reveal more information and details of rare earth nitrides ReN with (Re=Sc, Y, Gd) properties.

II. THEORETICAL STUDY

These calculations have been performed using the full-potential (linearized) augmented plane wave (lapw+local orbital) [2,3] approach to the density functional theory [4] implemented in WIEN2k code [5], within the Generalized Gradient Approximation through Perdew-Burek-Eneerhof (GGA-PBE), which is used for treatment the electronic exchange-correlation energy function [6].

III. RESULTS AND DISCUSSIONS:

A. Structural properties:

The lattice constants, the bulk modulus B and its first derivative B' are calculated by minimizing the total energy of crystal at different values of the volume fitted to the Murnaghan equation state (EOS) [7], all these parameters are in the table 1.

The structural stability of the thre semiconductors compounds of rare earth nitride is analyzed among the three considered NaCl (B1), CsCl (B2), and ZB (B3) (figure 2.3.4) and it observed that B1 structure is the most stable for the three cubic structures at the ambient conditions.

Fig. 1. Unit cell of different cubic phases of rare earth nitrides ScN, YN and GdN compounds, the blue circle represent the Sc, Y or Gd atoms and red one represent the N atom.

At the ambient conditions it can be observed from the table and the figures that the rock salt phase is the most stable for the three semiconductors based rare earth nitrides as the total energy is minimum for B1 phase.

The lattice parameter a of ScN is computed as 4.5203 Å in B1 structure which is good agreement with the other theoretical and experimental results, 2.79 Å for the B2 structure which is 0.71% less than the theoretical result and 0.61 higher than the theoretical result in B3 structure with lattice parameter 4.91Å.

The present values of lattice parameter of YN compound in the B1 structure is about 0.71% higher than the experimental result, and 3.00Å, 5.8262Å for B2 and B3 respectively which are good agreement with other results.

The lattice parameter is calculated in rocksalt structure, Cesium chloride and Zinc Blend structures for the GdN compound and is in good accord with other results in the all cubic phases.

TABLE. 1. Calculated lattice parameter a (Å), equilibrium volume V (Å3), bulk modulus B (GPa), Shear modulus B'(GPa), total energy E (eV) of rare earth nitrides compounds Sc, YN and GdN.

		B1	B2	B3
ScN	*a (Å)*	4.5203 4.50[8] (theo) 4.5018[9] (exp)	2.79 2.81[10] (theo)	4.91 4.88[10] (theo)
	V (Å³)	23.086	21.71	29.596
	B (Gpa)	200.223	182.3277	148.467
	B' (Gpa)	4.1232	3.9281	4.8297
	E (eV)	-22289.1502	-22287.5170	-22288.9849
YN	*a (Å)*	4.912 4.93[11] (theo) 4.877 [12] (exp)	3.00 3.01[11] (theo)	5.2862 5.28[11] (theo)
	V (Å³)	29.628	27	36.929
	B (Gpa)	158.9976	147.0926	113.4592
	B' (Gpa)	4.2336	4.4647	4.0139
	E (eV)	-93623.3400	-93621.4560	-93622.8492
GdN	*a (Å)*	4.99 4.98[13] (theo) 4.99[14] (exp)	3.0389 3.025[13] (theo)	5.3486 5.3[13] (theo)
	V (Å³)	31.062	28.063	38.252
	B (Gpa)	148.703	141.0569	108.2775
	B' (Gpa)	4.2372	6.6354	3.988
	E (eV)	-308452.2825	-308450.6526	-308451.9328

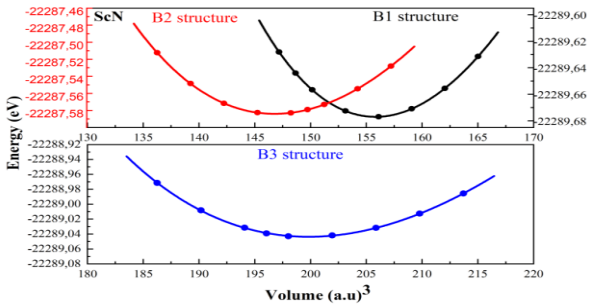

Fig. 2. Total energy (in eV) versus reduced volume for the three cubic phases of rare earth nitride ScN.

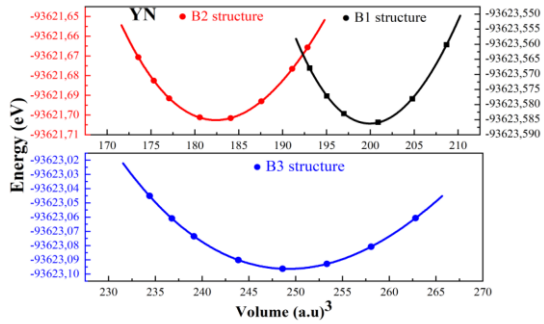

Fig. 3. Total energy (in eV) versus reduced volume for the three cubic phases of rare earth nitride YN.

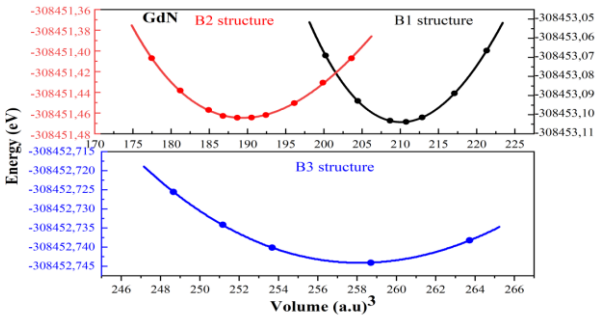

Fig. 4. Total energy (in eV) versus reduced volume for the three cubic phases of rare earth nitride GdN.

B. Magnetic properties:

The moment magnetic of the rare earth nitrides ReN (Re=Sc, Y and Gd) in the stable B1 structure is cheeked by studying the ferromagnetic (FM) and non-magnetic (NM) states by fitting the Munagan equation of state EOS of the total energy with relative volume.

The Figures 5 represent the total energy relative volume without and with spin polarization in B1 structure for rare earth nitrides compounds ReN (Re=Sc, Y, Gd). It observed that the compounds ScN, YN and GdN are stable in the nonmagnetic (NM) state at normal pressure, and for GdN, it can be seen that is more stable at the ferromagnetic (FM) state.

The table 2 represents the total and partial magnetic moment in Bohr magneton μ_B for the rare earth nitride GdN, the present work is good agreement with the other experimental and theatrical results.

TABLE. 1. Moment magnetic of rare earth nitride GdN in NaCl structure.

GdN		
μ_B (tot)	**μ_B (Gd)**	**μ_B (N)**
7.00	6.953	-0.0939

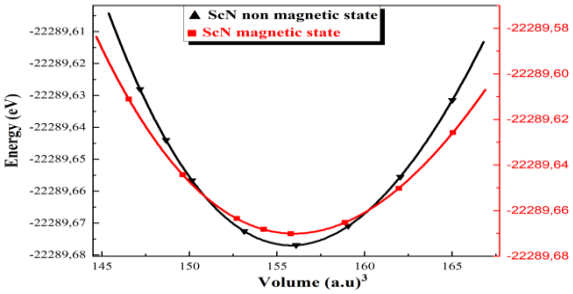

Fig. 5. Total energy versus relative volume in ferromagnetic (FM) and non-magnetic (NM)states of rare earth ScN.

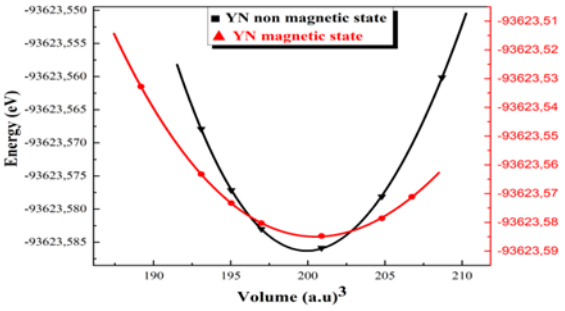

Fig. 6. Total energy versus relative volume in ferromagnetic (FM) and non-magnetic (NM)states of rare earth YN.

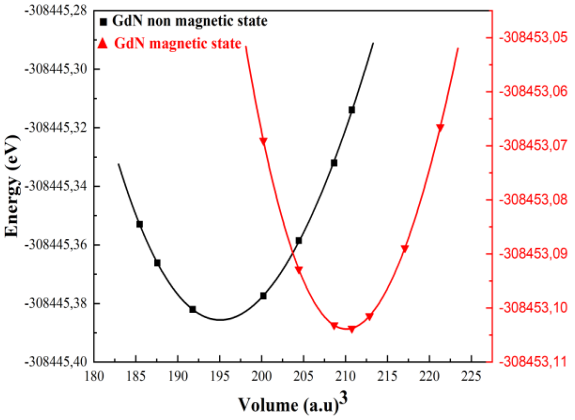

Fig. 7. Total energy versus relative volume in ferromagnetic (FM) and non-magnetic (NM)states of rare earth GdN.

C. *Electronic properties*

The electronic band structure of the rare earth nitride ReN (Re=Sc,Y, Gd) in NaCl structure are given in the figure 8,9,10 the Fermi level is located at zero energy.

It can be seen from the figure 5 (ScN compound) that band gap exists for the structures B1, there two bandgab direct 2.721 eV and 1.2 eV at Γ and X respectively, also there is a smaller indirect Γ-X bandgap with the Fermi level, about the YN compound we can observed the are two direct band gab 3.044 eV at Γ and 0.78 eV at X, also there is indirect Γ-X bandgap 0.23 eV.

In the GdN compound we can see there is no bandgap in the spin-up state and there is direct bandgap at X with 1.07 eV at X and indirect bandgap 1.09 ev at Γ-X.

From our work we can concluded that all the rare earth nitrides ReN with Re=Sc, Y, Gd are semiconductors nature, our results are close in agreement with the other results.

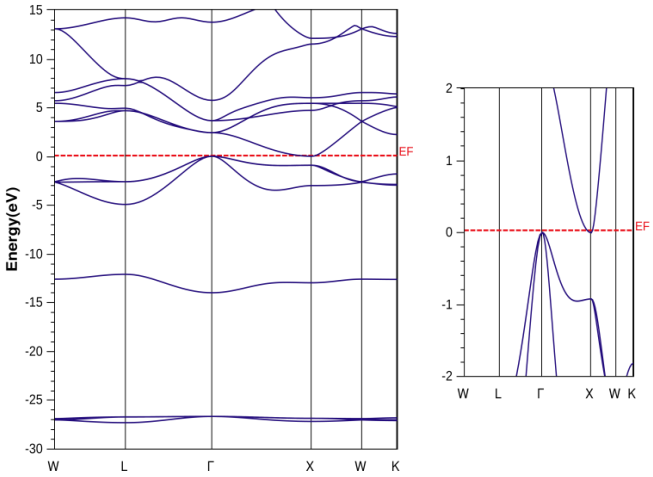

Fig. 8. Band structure of ScN in NaCl structure.

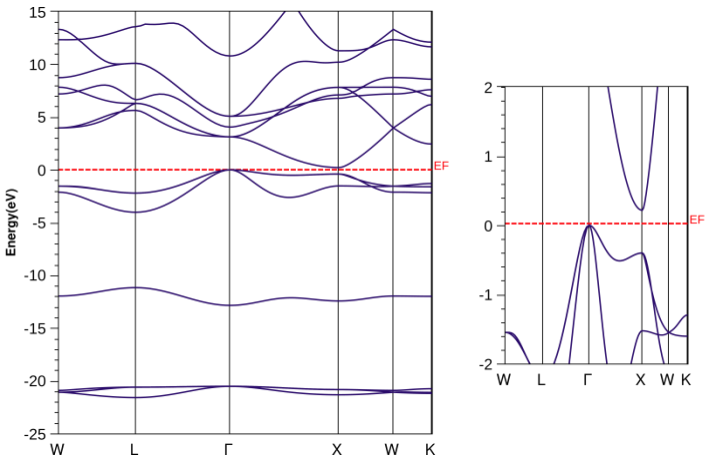

Fig. 9.Band structure of YN in NaCl structure.

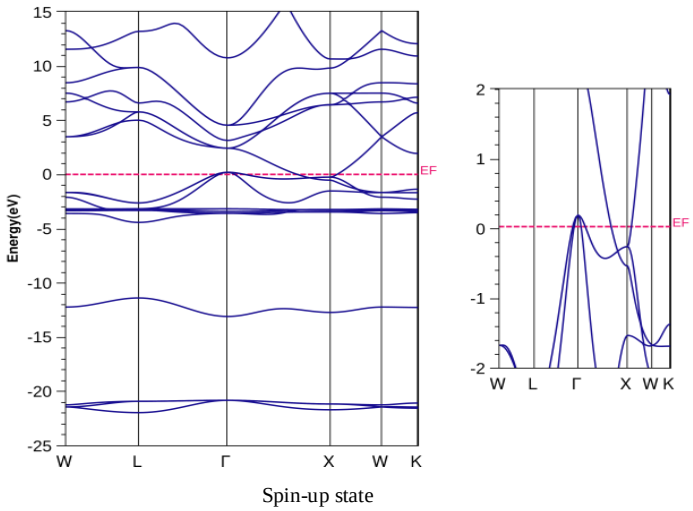

Spin-up state

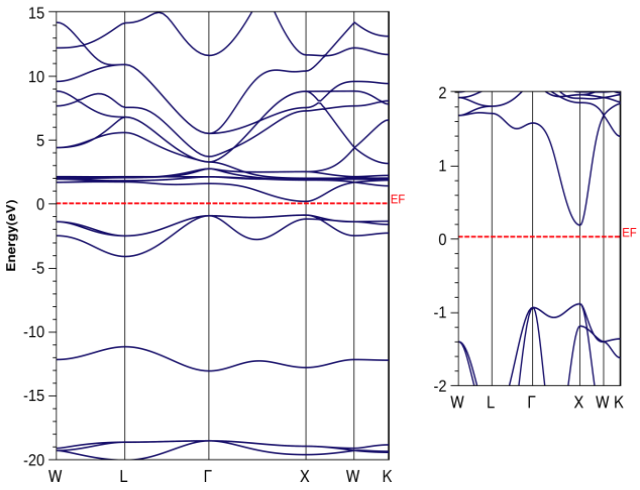

Spin-down state

Fig. 10. Band structure of GdN in NaCl structure for two states spin-up and spin-down.

D. Elastic properties:

The elastic constants of solids provide a link between the mechanical and dynamical behaviors of crystals, and give important information concerning the nature of the forces operating in solids. In particular, they provide information on the stability and stiffness of materials.

All cubic crystals have three independent elastic constants C_{11}, C_{12} and C_{44}, for the stability of cubic structure, the three elastic constants C_{11}, C_{12}, C_{44} should satisfy the Born-Huang [15] stability criteria:

$$C_{44} > 0, (C_{11}+2C_{11}) > 0, (C_{11}-C_{12}) > 0$$

The computed values of the elastic constants (C_{11}, C_{12}, C_{44}), bulk modulus B (GPa), Shear modulus B' (Gpa), Young's modulus E (GPa) and Poisson's ratio ν of the semiconductors based rare earth nitrides ReN (Re=Sc, Y, Gd) in the stable NaCl structure are listed in table 3.

It can be seen from the table 4 the elastic constants satisfy the Born-Huang criteria, we concluded that the rare earth nitrides ReN (Re=Sc, Y, Gd) are mechanically stable in normal pressure. The calculated elastic constants of rare earth nitrides ScN, YN and GdN are in close agreement with other theatrical and experimental results.

TABLE. 2. Calculated elastic constants C_{11}, C_{11}, C_{44} (GPa), bulk modulus B(GPa), Shear modulus B'(Gpa), Young's modulus E (GPa), Poisson's ratio ν, for rare earth nitrides ReN (Re=Sc, Y, Gd) in B1 structure

	ScN	**YN**	**GdN**
C_{11} (Gpa)	393.5978	327.0120	289.5688
C_{22} (Gpa)	104.0286	81.1886	78.5077
C_{44} (Gpa)	165.8863	125.0446	106.2940
B (Gpa)	200.551	163.129	148.861
B' (Gpa)	157.096	124.186	105.987
E (Gpa)	373.709	297.152	256.973
υ	0.189	0.196	0.212

.

E. Conclusion :

In conclusion, the structural, electronic, magnetic and elastic properties of rare earth nitride ReN (Re=Sc, Y, Gd) are analysed by the ab initio calculations using GGA-PBE approximation implemented in WIEN2K code with three cubic possible structures Rocksalt B1 , Caesium chlorides B2 and Zinc Blende B3.

ScN, YN and GdN compounds exhibit a semiconctor nature, the three rare earth nitrides ScN, YN and GdN are found that to be stable structurally and mechanically in NaCl (B1) phase at normal pressure. For the magnetic properties we was concluded the two compounds ScN and YN behave as non-magnetic compounds, on the contrary, the GdN compound is stable at ferromagnetic state.

The calculated results are in good agreement with the available results.

REFERENCES

[1] J. Yang, F. Gao, H. Wang, H. Gou, X., Z. Li, Materials Chemistry and Physics 119 499–504, 2010.

[2] E. Sjöstedt, L. Nordsrön, D. J. Singh, solid state communication 114, 15, 2000.

[3] G. K. H. Madsen, P. Blaha, K. Schwarz, E. Sjöstedt, L. Nordsrön, Phys. Rev B 64, 195134, 2001.

[4] W. Kohn, L. J. Sham, Phys. Rev. 140, A1133, 1965.

[5] P. Blaha, K. Schwarz, G. K.H. Madsen, D. Kvasnicka, and J. Luitz, "WIEN2k, an augmented plane wave ++ local orbitals program for calculating crystal properties," Karlheinz Schwarz, Techn. Universität Wien, Austria, ISBN 3-9501031-1-2, 2001.

[6] J. P. Perdew, K. Burke, M. Ernezerhof, Phys. Rev. Lett. 77, 3865, 1996.

[7] F.D. Murnaghan, Proc. Natl, Acad. Sci. USA 3 , 5390, 1994.

[8] C. Stampfl, W. Mannstadr, R. Asahi, A. J. Freeman, phys Rev B, volume 63, 155106, 2001.

[9] W. Lengauer, Journal of dolid state chemistry 76,4151,1988.

[10] N. Takeuchi, Phys Rev B, volume 65, 045204, 2002.

[11] L. Mancera, J. A. Rodriguez, N. Takeuchi, Journal phys : condens. Matter 15,3265-2633, 2003.

[12] P. Villars, L. D. Calvert, Pearson's Handbook pf cristallographie Data for Intermettalic phases American society for metals park, OF, 1985.

[13] R. M. Shabara, S. Z. Yahia, S. H. Aly, Results in phys 1, 30-35, 2011.

[14] W. Klemm, G. Z. Winkelmann, Among. Allg. Chem. 288-87, 1956.

[15] M. Born, K. Huang, Dynamical theory of crystal lattices, Clarendon, Oxford, 1956.

Influence of temperature and pressure on the atoms ejected path during thin films deposition

S.C.REFAS [1], A.BOUAZZA [2], Y.BELHADJI [3], R.OTHMANI [4]

L2GEGI Laboratory, University of Ibn Khaldoun Tiaret, Algeria

Email: Salah@univ-tiaret.dz

Abstract: The simulation with Monte-Carlo codes represented the efficiency tools which helps knowing the phenomena that occur inside the vacuum chamber for sputtering process. In this work, the impact of temperature and pressure parameters on the surface structure of thin films are studied in 3D form with the magnetron sputtering technique. Inside a vacuum chamber a 10^5 particles of Argon (Ar) gas are injected, the target contained the semi-conductor silicon (Si), and the substrate is placed with a variable distance from the target .The results obtained in this work show that a high temperature, pressure and a long distance between the target and substrate can negatively affects the path of the atoms ejected away from the target which will cause a decrease in the number of atom arriving on the substrate.

Keywords: thin films, sputtering, vacuum chamber, Monte Carlo codes.

1. Introduction

Thin film has become an essential part of human life, so it is difficult to find a field of activity where it does not exist [1-4], the semiconductor silicon dominate the industry due to the efficient performance it provides and its reasonable price, low-mass thin-film solar cells can be integrated into modern compact optoelectronic microcircuits and Si-based devices and can therefore be used in the aerospace industry [5]. There are several technologies that can be used for the production and disposition of thin films, among them the technique of sputtering, the properties of the films deposited by the sputtering technique depend on the material the gas used for discharge and deposition parameters such as pressure, target distance, temperature, substrate polarization and chemical composition[6-8], One of the most used programs to simulate the sputtering process is SRIM and SIMTRA program which is based on Monte Carlo simulations, these two programs are used to study the entire sputtering process and they allow to study all the steps that the ejected particles face in order to create the thin layer[9,12].

On this work the influence of temperature and high pressure on the path of the atoms ejected was studied with a variation of the distance between target and substrate using the semi-conductors silicon, first SRIM is used to calculate the energy and the direction of the particles that are sputtered away from the targets (Si). The transport of these species toward the substrate is then handled by the SIMTRA code with a temperature and high pressure variation, the objective of this work is to deduce the best possible regulation inside the vacuum chamber to achieve the highest number of atoms arrived on substrate, all the results found will be represented in a three-dimensional curves using Origin software. Our goal is to participate on the technology development of thin film and to offer a result that will allow us to solve several problems on the formation of cells and thin films.

2. Simulation method

Simulation of film growth on time scales of seconds or minutes is possible with the Kinetic Monte Carlo Algorithms [13,14], this approach can be used to model different surface processes such as nucleation, growth, post-deposition structural modification of films [15,16].

The kinetic energy and the number of atoms arrived at the substrate location are calculated by SRIM and SIMSTRA, first the energy and the direction of the particles that are sputtered away from the target are calculated by using SRIM software, in our work we started with SRIM [16-20], we applied a 10^5 ions of argon on the Silicon (Si) with an energy value of 100kev and an angular incidence of 85 degree, the result was saved on a file then used on SIMTRA.

The transport of these species to the substrate is then covered by the SIMTRA code[12],taking into account all collisions occurring in the gas phase, first we have created a vacuum chamber which has dimension of 30cm×30cm×50cm (as shown in Fig.1), a distance of 14cm and 20cm between target and substrate was taken, the magnetron used has a circle shape target with a radius of 2cm and the substrate also has the same shape with a radius of 6cm, we did a temperature and pressure variation on the semiconductor Silicon (Si) on two different distance 14cm and 20cm, the objective is to deduce the influence of temperature and high pressure on the atoms arriving on the substrate and to see also the thickness of the thin-films built, after all this configuration we can start the simulation this model will calculate the ejection of sputtered atoms on our target and gives the number of particle arriving on the substrate, the results will be saved on data files and will be presented by 3D curves.

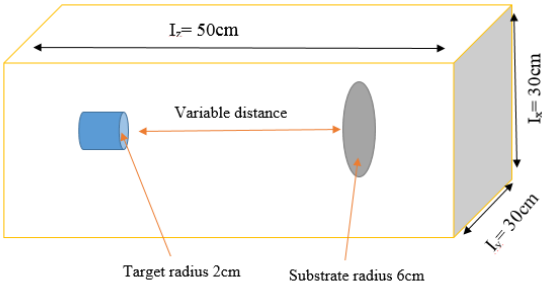

Fig. 1. Model used on the simulation

3. Results and discussion

3.1 Influence of temperature and high pressure on the atoms ejected path

3.1.1 Variation of temperature with fixed pressure on 14cm distance

The following figure represents the path and number of atoms sputtered and arrived on the substrate, three different temperature (300K, 500K and 800K) are used with a pressure value of 0.5 Pa inside the vacuum chamber, the target (Si) is being bombarded by Argon ions.

The choice of these temperatures gives us three cases to study inside the vacuum chamber which are warm, hot and extremely hot, the result will help us to make a comparison between them to see how the atoms ejected will act on every case.

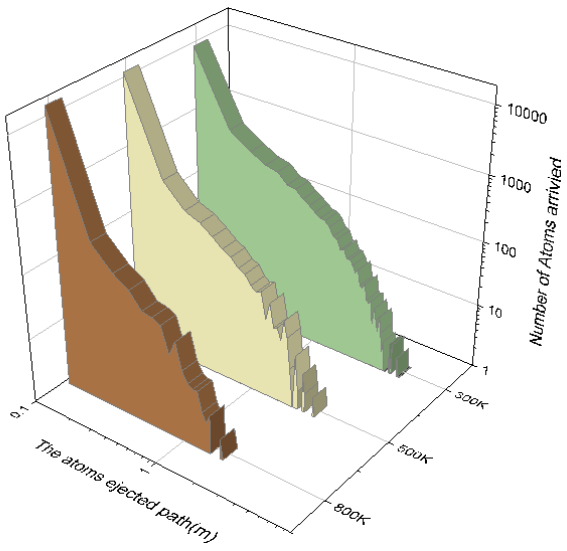

Fig. 2. Number of Si atoms arrived as function of the path using three different temperatures T= [300K, 500K, 800K] on 14cm distance

As shown in the figures above, the number of atoms arrived on the substrate are different on each temperature, when we applied a temperature of 300k the number of atoms arrived reached a value of 10K, every time we raise the temperature the ejected atoms cross the substrate with less distance.

The increase in temperature will create heat inside the vacuum chamber that will give a high mobility to the particles, the argon ions will bombard the target with great energy and the atoms ejected will get a great kinetic energy that will help them to reach the substrate faster.

It is also necessary to know that the excessive increase of temperature can cause damage to the materials used, before choosing the temperature it is necessary to do research on their ability to resist temperature.

3.1.2Variation of pressure with a fixed temperature on 14cm distance

For this time we will use three deferent pressure P= [0.5Pa, 3PA, 6Pa] and a temperature of 300k will be applied inside the chamber, the same gas and material will be used to bombard our target.

We chose these three different pressures which are normal pressure, high and extreme high to create a comparison between them that will help us to see how the atoms ejected will act on every case, the results are presented on the following figures:

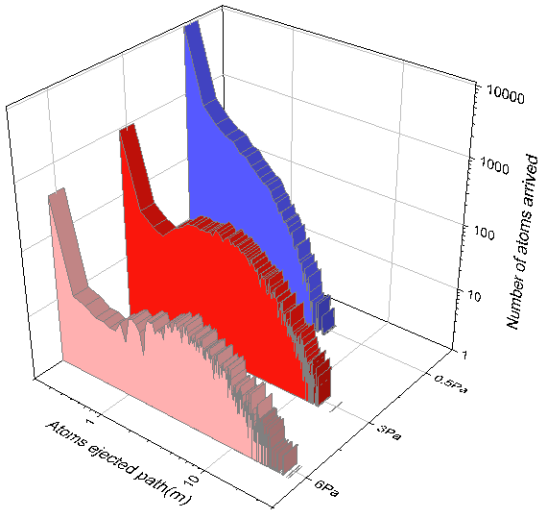

Fig. 3. Number of Si atoms arrived as function of the path using three different pressures P= [0.5Pa, 3Pa, 6PA] on 14cm distance

Pressure has a very big influence on the number of atoms, when we apply a pressure of 0. 5Pa we get a value of 10K for the target Si, after applying a pressure of 2Pa and 5Pa, there is a very large decrease in the number of atoms reaching the substrate and we notice that the atoms ejected will arrive into the substrate with higher path.

When we rise the pressure inside the vacuum chamber it will create a very large number of collisions and a large decrease in particle mobility, the ejected atoms will face a difficult path to reach the substrate, the atoms collide with the argon ions which will decrease their kinetic energy and they will not be able to reach the substrate.

3.1.3Variation of temperature with fixed pressure on 20cm distance

The same procedure will be carried out except for this case we have changed the distance between target and substrate

from 14cm into 20cm, the temperatures used are the same T=[300K, 500K, 800K], results are shown on the following curves

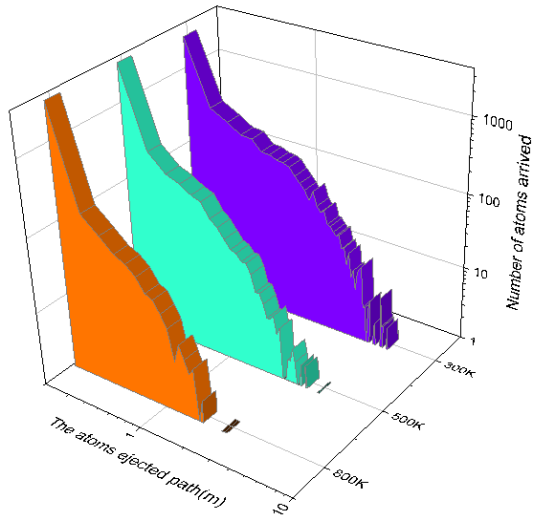

Fig. 4. Number of Si atoms arrived as function of the path using three different temperatures T= [300K, 500K, 800K] on 20cm distance

Changing the distance from 14cm to 20cm will result into a large decrease to the number of atoms arrived on the substrate, an applied temperature of 300k gives 3K of atom ejected on the material Si.

Widening the distance will cause several problems, a large amount of atoms ejected will not survive and won't be able reach the substrate.

3.1.4Variation of pressure with a fixed temperature on 20cm distance

This time we used the vacuum chamber with 20 cm distance between the target and substrate and a pressure variations P= [0.5Pa, 3Pa, 6Pa].

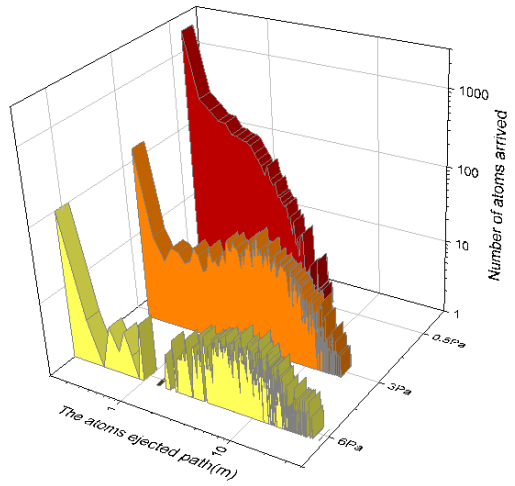

Fig. 5. Number of Si atoms arrived as function of the path using three different pressures P= [0.5Pa, 3Pa, 6PA] on 20cm distance

As shown on the above figures, the application of 20 cm distance inside the vacuum chamber gives the same result except that the atom arrived in the substrate has greatly diminished, it will create a thin layer less thick and with low quality.

5. Conclusion

The choice of deposition process is dependent upon several factors with the help of SIMTRA software we have studied the influence of temperature and high pressure on the magnetron sputtering, using a Monte Carlo code we have simulated several cases using silicon as a target, variations in temperature and pressure and distance between target and substrate have given the following important information about the disposition of thin films.

The temperature increase gives kinetic energy to the particle which increases their mobility inside the chamber, the atoms ejected will travel a shorter distance because they will face less collision.

On the other hand the increase of pressure will decrease the kinetic energy of the particles which will create several collision so the ejected particles will have a hard path to reach the substrate.

Finally we have shown that widening the distance will cause several problems, a large amount of atoms ejected will not survive and won't reach the substrate.

References

[1] A. Bouazza and A. Settaouti, "Monte Carlo simulation of the influence of pressure and target-substrate distance on the sputtering process for metal and semiconductor layers," Mod. Phys. Lett. B, vol. 30, no. 20, pp. 1–18, 2016, doi: 10.1142/S0217984916502535.

[2] A. Bouazza and A. Settaouti, "Understanding the contribution of energy and angular distribution in the morphology of thin films using Monte Carlo simulation," Monte Carlo Methods Appl, 2018, doi: 10.1515/mcma-2016.

[3] A. Bouazza and A. Settaouti, "Study and simulation of the sputtering process of material layers in plasma," Monte Carlo Methods Appl., vol. 22, no. 2, pp. 149–159, 2016, doi: 10.1515/mcma-2016-0106.

[4] A. Drize and A. Settaouti, "Three-dimensional Monte Carlo simulations of materials on the physical deposition process," Mod. Phys. Lett. B, vol. 31, no. 24, 2017, doi: 10.1142/S0217984917501652.

[5] A. L. Stepanov, V. V. Vorobev, A. M. Rogov, V. I. Nuzhdin, and V. F. Valeev, "Sputtering of silicon surface by silver-ion implantation," Nucl. Instruments Methods Phys. Res. Sect. B Beam Interact. with Mater. Atoms, vol. 457, no. May, pp. 1–3, 2019, doi: 10.1016/j.nimb.2019.07.020.

[6] N. Nedfors et al., "The influence of pressure and magnetic field on the deposition of epitaxial TiBx thin films from DC magnetron sputtering," Vacuum, vol. 177, no. December 2019, p. 109355, 2020, doi: 10.1016/j.vacuum.2020.109355.

[7] C. Oh et al., "Influence of oxygen partial pressure in In-Sn-Ga-O thin-film transistors at a low

temperature," J. Alloys Compd., vol. 805, pp. 211–217, 2019, doi: 10.1016/j.jallcom.2019.07.091.

[8] C. G. Granqvist, "Preparation of thin films and nanostructured coatings for clean tech applications: A primer," Sol. Energy Mater. Sol. Cells, vol. 99, pp. 166–175, 2012, doi: 10.1016/j.solmat.2011.11.048.

[9] J. Wang, M. B. Toloczko, N. Bailey, F. A. Garner, J. Gigax, and L. Shao, "Modification of SRIM-calculated dose and injected ion profiles due to sputtering, injected ion buildup and void swelling," Nucl. Instruments Methods Phys. Res. Sect. B Beam Interact. with Mater. Atoms, vol. 387, pp. 20–28, 2016, doi: 10.1016/j.nimb.2016.09.015.

[10] J. O. Achenbach, S. Mráz, D. Primetzhofer, and J. M. Schneider, "Correlative experimental and theoretical investigation of the angle-resolved composition evolution of thin films sputtered from a compound Mo2BC target," Coatings, vol. 9, no. 3, 2019, doi: 10.3390/COATINGS9030206.

[11] G. Abadias, F. Anğay, R. Mareus, and C. Mastail, "Texture and stress evolution in HfN films sputter-deposited at oblique angles," Coatings, vol. 9, no. 11, 2019, doi: 10.3390/coatings9110712.

[12] R. Mareus, C. Mastail, F. Anğay, N. Brunetière, and G. Abadias, "Study of columnar growth, texture development and wettability of reactively sputter-deposited TiN, ZrN and HfN thin films at glancing angle incidence," Surf. Coatings Technol., vol. 399, p. 126130, 2020, doi: 10.1016/j.surfcoat.2020.126130.

[13] G. Hobler, R. M. Bradley, and H. M. Urbassek, "Probing the limitations of Sigmund's model of spatially resolved sputtering using Monte Carlo simulations," Phys. Rev. B, vol. 93, no. 20, pp. 1–17, 2016, doi: 10.1103/PhysRevB.93.205443.

[14] H. Hofsäss, K. Zhang, and A. Mutzke, "Simulation of ion beam sputtering with SDTrimSP, TRIDYN and SRIM," Appl. Surf. Sci., vol. 310, pp. 134–141, 2014, doi: 10.1016/j.apsusc.2014.03.152.

[15] T. Smy et al., "Three-dimensional simulation of film microstructure produced by glancing angle deposition," J. Vac. Sci. Technol. A Vacuum, Surfaces, Film., vol. 18, no. 5, p. 2507, 2000, doi: 10.1116/1.1286394.

[16] P. Meakin and J. Krug, "Three-dimensional ballistic deposition at oblique incidence," Phys. Rev. A, vol. 46, no. 6, pp. 3390–3399, 1992, doi: 10.1103/PhysRevA.46.3390.

[17] A. Siad, A. Besnard, C. Nouveau, and P. Jacquet, "Critical angles in DC magnetron glad thin films," Vacuum, vol. 131, pp. 305–311, 2016, doi: 10.1016/j.vacuum.2016.07.012.

[18] J. F. Ziegler, M. D. Ziegler, and J. P. Biersack, "SRIM - The stopping and range of ions in matter (2010)," Nucl. Instruments Methods Phys. Res. Sect. B Beam Interact. with Mater. Atoms, vol. 268, no. 11–12, pp. 1818–1823, 2010, doi: 10.1016/j.nimb.2010.02.091.

[19] A. Baptista, F. Silva, J. Porteiro, J. Míguez, and G. Pinto, "Sputtering physical vapour deposition (PVD) coatings: A critical review on process improvement andmarket trend demands," Coatings, vol. 8, no. 11, 2018, doi: 10.3390/COATINGS8110402.

[20] H. C. Barshilia, A. Ananth, J. Khan, and G. Srinivas, "Ar + H 2 plasma etching for improved adhesion of PVD coatings on steel substrates," Vacuum, vol. 86, no. 8, pp. 1165–1173, 2012, doi: 10.1016/j.vacuum.2011.10.028.

A high-sensitivity biosensor based on metal–insulator–metal and rectangular resonator for biochemical detection

Hocine Bahri
Laboratory of Electronics and New Technologies (LENT),
University Oum El Bouaghi. Algeria
bahri.hocine@univ-oeb.dz

Souheil Mouetsi
Laboratory of Electronics and New Technologies (LENT), University Oum El Bouaghi.Algeria
s.mouetsi@univ-oeb.dz

Abdsselam Hocini
Laboratoire d'Analyse des Signaux et Systèmes, Département of Electronics
Univers- city of M'Sila, BP.166, Route Ichebilia, M'sila, 28000 Algeria

Sven Ingebrandt
Institute of Materials in Electrical Engineering 1, RWTH Aachen University, Sommerfeldstraße 24, D-52074 Aachen, Germany
ingebrandt@iwe1.rwth-aachen.de

Vivek Pachauri
Institute of Materials in Electrical Engineering 1, RWTH Aachen University, Sommerfeldstraße 24, D-52074 Aachen, Germany
pachauri@iwe1.rwth-aachen.de

Hocine Ben Slah
Laboratoire d'Analyse des Signaux e Systèmes, Département of Electronics
Univers- city of M'Sila, BP.166, Rou Ichebilia, M'sila, 28000 Algeria
University yahia fares médéa, Algeria

***Abstract*—Herein, a refractive index sensing based on a novel design of rectangular cavity couple with defect nanorod (RCDN), using metal-insulator-metal (MIM) waveguide is suggested for biochemical application. Herein, the optimized cavity design can provide the best sensing performance. In this work, we have numerically simulated with Finite-Difference-Time-Domain (FDTD) method, by varying small change in the geometric parameter we can bring a significant shift in the sensitivity of the device, also we can manipulate the resonance wavelength. The high sensitivity of the biosensor is 2035 nm/RIU. This device can be utilized in the on-chip detection of biochemical such glucose in water and cancer cells with high sensitivity.**

Keywords— Refractive Index (RI), Metal-insulator-metal (MIM), Near-infrared (NIR) and mid-infrared (MIR), Finite-Difference-Time-Domain (FDTD), biosensor

I. INTRODUCTION

Surface plasmon polaritons (SPPs) is an electromagnetic excitation that propagates along with the interface between a metal and a dielectric medium and whose amplitude decays exponentially with increasing distance into each medium from the interface[1] . Exhibit interesting and valuable properties such as energy asymptote in dispersion curves, resonant modes, field localization and enhancement, high sensitivity, and subwavelength confinement[2]. potential properties of SPPs are acknowledged to have a fast (rapid response), cost-effective, low-regent-consumption, easy-of-use (label-free), SPPs have the ability to field confinement, focus and channel light in subwavelength scale metallic structure to increase the photo lifetime, which enhance the near field of light-mater leading to high sensitivities (surface and bulk) to the slight change of the refractive index (RI) by dictating the evanescent tail of the SPP. Therefore, the SPP has a potential in medical diagnostics and environmental monitoring as RNA[3], DNA[4], protein [5], viruses [6], glucose concentration[7].Furher, surface plasmon resonance (SPR) has the ability of a high degree of integration, miniaturization, overcoming the diffraction limits, and localization of light in subwavelength regions, SPR has attracted attention in the scientific community and studied experimentally and theoretically the potential to guide, concentrate, and scatter light at the nanoscale[8].

one of the interesting plasmonic structures as MIM metal-insulator-metal (MIM), has more transmission loss(it can be neglected in nano-scale[9] and supports the propagation of SPP. Thus, was used for many fields as a sensors[10], filters[11], demultiplexers[12] , switches[10], and splitters[13]. Over the past few years, a several unique cavity designs used to improve the sensing performance of the plasmonic sensors based on the MIM waveguide such a disk resonators [8], double cavities [10], hexagonal cavities [14], rectangular resonators [15], nanorods [16]. many researchers is trying to increasing the sensitivity and improving the transmission spectrum by choosing a unique and thoughtful structures dimensions based on previous research papers. As a result, the optical biosensor on-chip with a tiny and sharp geometric feature using a plasmonic waveguide has been explored extensively

In this paper, a design based on a rectangular cavity couple with defect nanorod (RCDN) investigated for plasmonic biosensor using the Finite-Difference-Time-Domain (FDTD) method. The interaction of the RCDN create the transmission peaks. By varying the geometric parameters of the structure we control and manipulate the resonance wavelengths. Further We investigated this proposed sensor into sensing for different diseases, by using their unique refractive indies. Thus, the resonance wavelength is shifting, and this information allows us to calculate the sensitivity. The resonance wavelength increases almost linearly with RI content. Our proposed sensor can provide a sensitivity of 2035 nm⁄RIU with wavelength resolution reaching 3.84×10^{-6} RIU^{-1}, which can help discover broad applications in the plasmonics Nano sensing domain.

II. THEORY AND SIMULATION

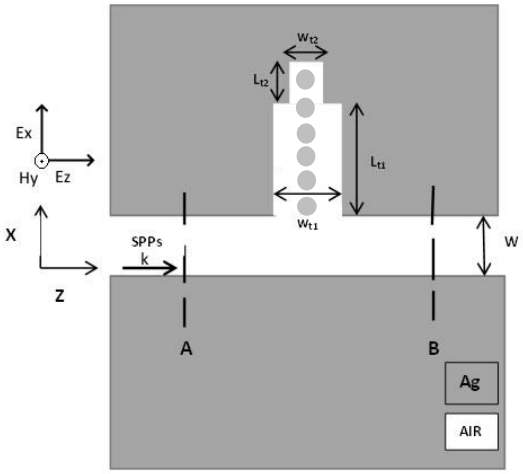

Fig **1(a)** a MIM waveguide structure are illustrated

In Fig **1(a)** a MIM waveguide structure are illustrated, which proposed a highly refractive index RI sensor composed of a straight waveguide couple with a ring of racetrack cavity and circular defect (hereafter represented as RRCCD). the device performance is compared with a other sensor design cavity and the RSOFT CAD software is used to calculate the transmission characteristics. Using a waveguide width as W =50nm coupled. All the structure parameters *D= 35nm , r = 15nm , Lt_1=175nm, Lt_2=75nm, Wt_1=50nm and Wt_2=30nm.*

Furthermore, a detects incident light from the source and B detects received light at the waveguide's output to detect transmittance as T= A/B, the input light waves emitted from A partly reflected, partly coupled into DRT, and then transmitted out along the power monitors' output B. The silver layer and the dielectric (air) material are represented by the gray and white areas, respectively. By trapping incident light waves, the use of Ag as a metal in the MIM structure improves absorption. As a result, more SPRs are generated with the smallest damping constant, which is the best performing choice at optical frequency. Furthermore, the Ag provides a framework in which the fluid test substance can be used. The Drude-Lorentz model gives the designated channel, The relative dielectric constant of silver [17]:

$$\varepsilon_m = \varepsilon_\infty - \frac{\omega_p^2}{\omega^2 - i\omega\gamma'} \quad (1)$$

(1)

Here, ε_∞, γ, and ωp are the dielectric constant at the infinite frequency, the electron collision frequency, the bulk plasma frequency, respectively. The parameters

are set to be ε_∞=3.7, ωp=9.1 eV, γ = 0,018 eV. During the FDTD simulations since the wavelength of the incident light is greater than the waveguide's width, only a single propagation mode TM_0 can exist in the structure, The TM mode dispersion equation of this case can be described by[18]:

$$\varepsilon_d \sqrt{n_{ef}^2 - \varepsilon_m} + \varepsilon_m \sqrt{n_{ef}^2 - \varepsilon_d}\, tanh\left(\frac{W\pi\sqrt{n_{ef}^2 - \varepsilon_m}}{\lambda}\right) = 0 \quad (2)$$

where ε_d is the permittivity of the dielectric, ε_m is the permittivity of the metal, n_{ef} is the effective refractive index, W is the width of the straight waveguide and λ is the wavelength of the incident light. We get the frequency dependent ε_m from (1), and ε_d can be defined by $\varepsilon_d = n^2$ where n is the refractive index of the dielectric. Therefore, A TM-polarized plane wave throws the MIM structure, the incident light will be coupled into the waveguide, and SPP waves are formed on the two metal interfaces. Ref19 gives the dispersion relation of the fundamental TM model in plasmonic waveguide structure, and the resonance wavelength of the ring resonator can be approximated by the following:

$$\lambda_m = \frac{2Re(\eta_{eff})L_{eff}}{m}, \quad m=1,2,3.. \quad (3)$$

$Re(\eta_{eff})$ is the real part of the effective refractive index of the SPP, L_{eff} is the effective resonance length.

III. NUMERICAL RESULTS AND DISCUSSION

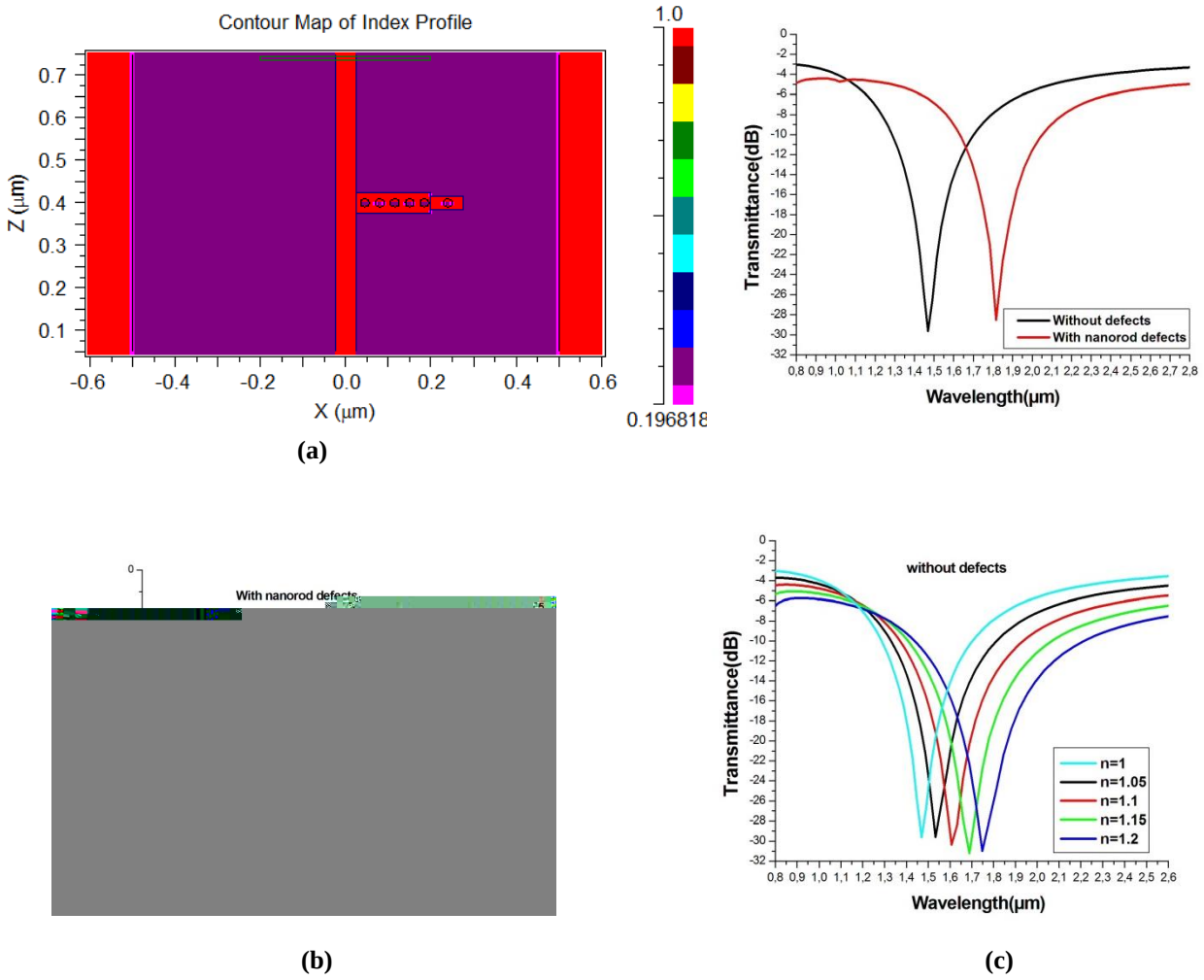

Fig 2. The MIM plasmonic structure with nanorod defects (a), Transmittance spectrum of the proposed plasmonic MIM waveguide (**b**) without defects and with metal nanorod defects. Transmittance spectra of the proposed MIM sensor (**c**) without and (**d**) with metal nanorod defects in cavity filled with different refractive index (RI) in the active region of the sensor and D=35nm, r = 15nm , Lt_1=175nm, Lt_2=75nm, Wt_1=50nm and Wt_2=30nm.

A two-dimensional FDTD method is used, with the grid sizes in the x and z directions as Δx = Δz = 3nm, and the time step, derived by Courant condition is $\Delta t = 0.95 = c\sqrt{(\Delta x)^2 + (\Delta z)^2}$ to ensure that all the outside waves are emitted, we use a perfect match layer (PML) as an absorbing boundary condition for the computational window's boundaries. The first step, filling the insulator with nothing, means that the insulator is the air (n=1) as shown in Fig. 2(b), we achieve one sharp peak with high transmission at a wavelength without defects λres =1.4687 µm, and with nanorod defects λres =1.8185 µm. Next, In Fig. 2(c,d), the transmission spectrum has been studied versus the wavelength for different refractive index RI ranges from n=1 to 1.2 with a step of 0.05 for both structures, while the other parameters remain unchanged. In Fig. 2(d) the resonance wavelength shifts as we increase the RI, this redshift phenomenon due to the proportional relationship between the Re(neff) and the wavelength λm according to Eq (2). a change in the resonant wavelength Δλ provides information about the refractive index shift Δn. To this, it is common practice to establish the most essential characteristics to characterize its performance, with the values of these parameters recommended to be considerably higher for biosensor devices, such as the spectrum sensitivity of such sensors, defined as S = Δλ/Δn[19]. For this structure, the sensitivity is S(without defect) = 1398nm/RIU, and S(defect nanorod) = 2035nm/RIU.

To get a better understanding of the mechanism of the inner magnetic field. Therefore, the Fig. **3** illustrate the magnetic field pattern of |Hy| at the wavelength of the peak, as we can notice an intense energy distribution can be observed inside the cavities and nothing in the output waveguide, however, off the resonance wavelength of the peak, the robust energy can be observed in the output, which conforms with the result we obtained in Fig **2 (b)**.

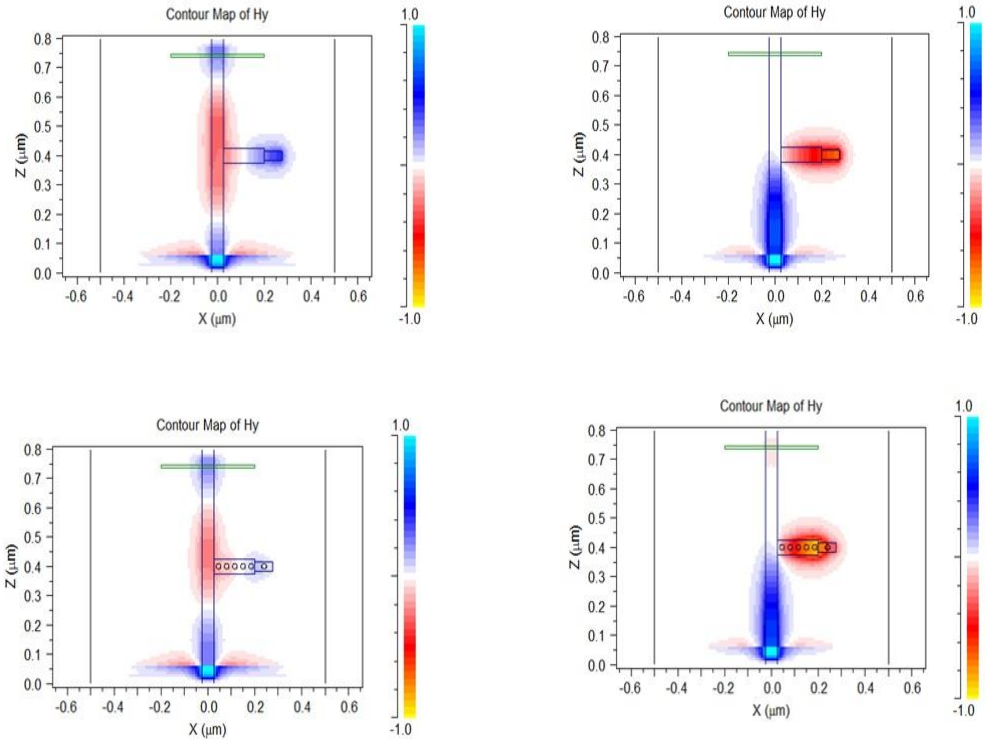

Fig. 3 Magnetic-filed patterns of the MIM plasmonic structure without defects (at λ = 1µm (a), λ_{res} =1.4687 µm (b)) and with nanorod defects (at λ = 1µm (c), λ_{res} =1.8185 µm(d))

Second by varying the RI from 1 to 1.2 with a step of 0.05 we studied the resonance wavelengths versus the refractive index for different r as it show in Fig 4(b). due to the proportional relationship between the Re(neff) and the wavelength λm according to Eq (3).

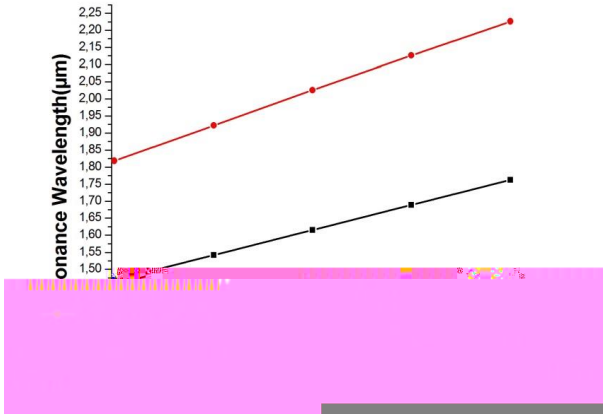

Fig. 4 Resonant wavelengths versus the refractive index (RI) without defects and with metal nanorod defects in cavity

We also carried out research on the performance of the geometry parameters to explain our choices for this structure. First, we studied the radius (r) of the circular cavity. To ensure the fabrication's feasibility, by varying r from 5 to 20 nm with a step of 5 nm, we noticed a shift occurring in the resonant peak, as shown in Fig 4 (a). Furthermore, as we increase the radius r=5nm in Fig 4 (c), we achieve a sensitivity as S=1402nm/RIU and for r=10nm and r=15nm we obtained a sensitivity reach to S=2392nm/RIU and S=2035nm/RIU, respectively.

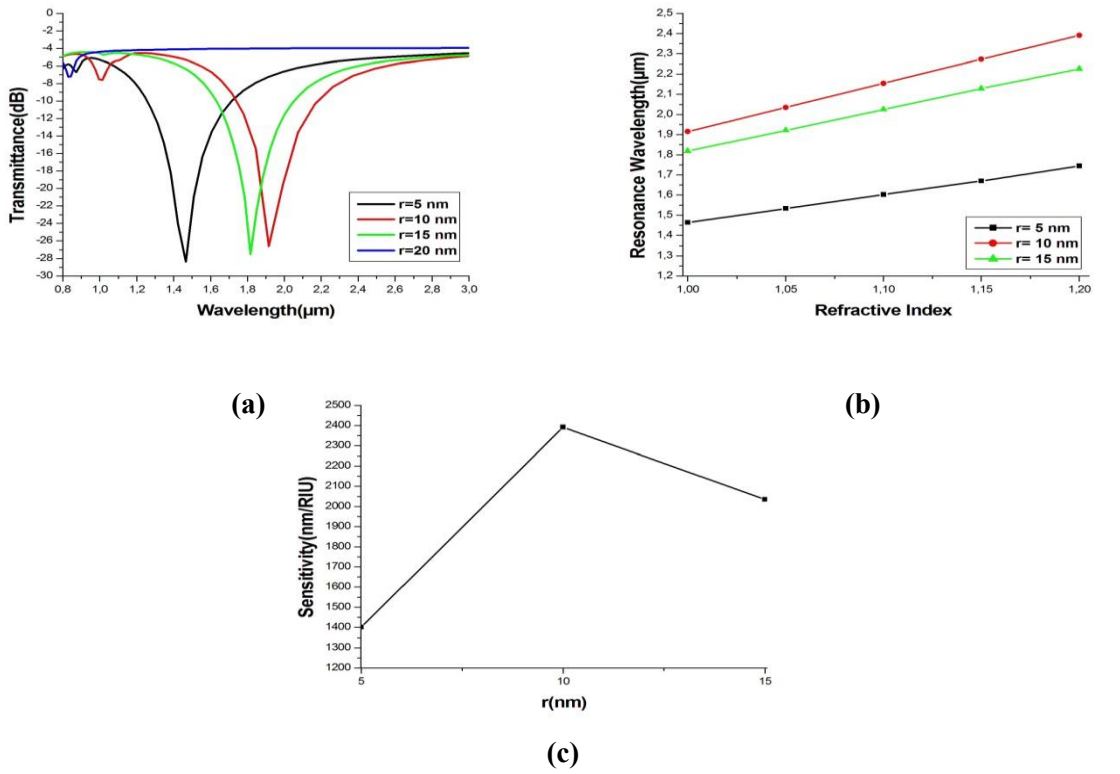

Fig. 5 Sensing properties as functions of r. (a) Transmission spectra of index 1 for r varying from 5 to 20 nm. (b) The resonance wavelengths versus the refractive index for different r. (c) Sensitivities of the plasmonic sensors for r varying from 0 to 15 nm.

IV. The Biomedical Applications of the Proposed Plasmonic Sensor

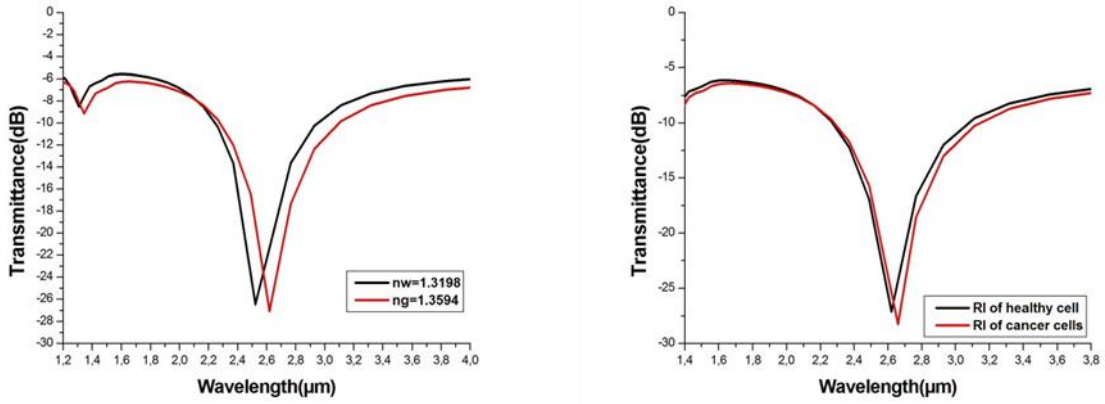

Fig. 6 (a) the peak of the transmission spectra versus the resonance wavelength for refractive index of the water nw=1.3198 and 25% solution of glucose in water as ng=1.3594. (b) The transmission spectrum versus the resonance wavelength for different refractive index of the cancer cells (1.37) and the healthy cells (1.353).

The following section use the sharper peak that occupies a narrower bandwidth in mid-IR from the previous result, as illustrated in Fig. 6. The mid-IR range is particularly well-suited for biosensing as it encompasses the molecular

vibrations that uniquely identify the biochemical building blocks of life, such as proteins, lipids, and DNA[20]. In addition, engineered mid-IR substrates with extremely high field enhancements at distinct resonance wavelengths enable the ultrasensitive IR detection of small amounts of biomolecules.

The proposed plasmonic sensor in biomedicals applications has been studied. Using a 25% glucose solution in water alters the refractive index of water from nw = 1.3198 to ng = 1.3594, as Fig. **6(a)** shows that we obtained a narrow, sharp peak with high transmission at the mid-IR range. A shift occurs as we change the RI of the surrounding medium, to study the RI of cancer[21] n=1.370, which is higher than the RI of the healthy cells (1.353) as depicted in Fig. **5(b)**, with a high sensitivity. All the results of the simulation have been summarized in **Table 2**.

Table. 2 Summary the result of the simulation

The test material	Refractive index	S (nm/RIU)
25% solution of glucose in water	nw = 1.3198, ng = 1.3594	2315
Cancer cells	n1 = 1.353, n2 = 1.370	2290

V. CONCLUSION

We have investigated a sample and new design of adjustable plasmonic nanostructures with high potential for biosensing applications in the near-IR and mid-IR bands. A rectangle and a defective Nanorod cavity are used in the proposed refractive index sensor. Furthermore, we investigated this structure for a variety of biological applications (detecting glucose, cancer, etc.). All the results of this structure show high sensitivities as 2035 nm/RIU and transmission spectra. This structure can pave the plasmonic biosensor. This structure may pave the way for a plasmonic biosensor. This sensor has a large potential in biosensing and optical on-chip nano-sensors due to its high sensitivity, simple configuration, and compact structure; relatively easy fabrication, simple configuration, and compact structure.

REFERENCES

[1] R. H. Ritchie, “Plasma losses by fast electrons in thin films Phys,” *Phys. Rev.*, pp. 874–881, 1957.

[2] P. Berini, “Loss Compensation andAmplification of SurfacePlasmon Polaritons,” *Act. Plasmon. Tuneable Plasmonic Metamaterials*, vol. 5, pp. 153–170, 2013.

[3] X. Ding, Y. Yan, S. Li, Y. Zhang, and W. Cheng, “Analytica Chimica Acta Surface plasmon resonance biosensor for highly sensitive detection of microRNA based on DNA super-sandwich assemblies and streptavidin signal ampli fi cation,” *Anal. Chim. Acta*, 2015, doi: 10.1016/j.aca.2015.03.021.

[4] S. Filion-côté *et al.*, “Design and analysis of a spectro-angular surface plasmon resonance biosensor operating in the visible spectrum Design and analysis of a spectro-angular surface plasmon resonance biosensor operating in the visible spectrum,” vol. 093107, 2014, doi: 10.1063/1.4894655.

[5] G. T. Victor J. Hruby, “affinitiesPlasmon-waveguide resonance (PWR) spectroscopy for directlyviewing rates of GPCR/G-protein interactions and quantifyingaffinities,” vol. 7, no. 5, pp. 507–514, 2008.

[6] M. Soler, X. Li, A. Belushkin, F. Yesilkoy, and H. Altug, “Towards a point-of-care nanoplasmonic biosensor for rapid and multiplexed detection of pathogenic infections ,” in *Plasmonics in Biology and Medicine XV*, 2018, vol. 10509, pp. 88–96, [Online]. Available: https://doi.org/10.1117/12.2289752.

[7] A. H. E. Konstantinos Aidinis, Kiyanoush Goudarzi, “Optical sensor based on two-dimensional photonic crystals for measuring glucose in urine,” *Opt. Eng.*, vol. 59, no. 5, p. 057104, 2020.

[8] M. R. Rakhshani, A. Tavousi, and M. A. Mansouri-Birjandi, “Design of a plasmonic sensor based on a square array of nanorods and two slot cavities with a high figure of merit for glucose concentration monitoring,” *Appl. Opt.*, vol. 57, no. 27, p. 7798, 2018, doi: 10.1364/ao.57.007798.

[9] E. Han, Z. Liu, L. Forsberg, “Ultra-compact directional couplers and Mach-Zehnder interferometers employing surface plasmon polaritons,” *Opt. Commun*, vol. 25, pp. 690–69, 2006.

[10] H. Ben salah, A. Hocini, M. N. Temmar, and D. Khedrouche, “Design of mid infrared high sensitive metal-insulator-metal plasmonic sensor,” *Chinese J.*

Phys., vol. 61, pp. 86–97, 2019, doi: 10.1016/j.cjph.2019.07.006.

[11] A. Hocini, H. Ben salah, D. Khedrouche, and N. Melouki, "A high-sensitive sensor and band-stop filter based on intersected double ring resonators in metal–insulator–metal structure," *Opt. Quantum Electron.*, vol. 52, no. 7, pp. 1–10, 2020, doi: 10.1007/s11082-020-02446-x.

[12] Shiva Khani, Mohammad Danaie, Pejman Rezaei, "Double and triple-wavelength plasmonic demultiplexers based on improved circular nanodisk resonators," *Opt. Eng.*, vol. 57, no. 10, p. 107102, 2018.

[13] R. Negahdari, E. Rafiee, and F. Emami, "Realization of all-optical plasmonic MIM split square ring resonator switch," *Opt. Quantum Electron.*, vol. 51, no. 7, 2019, doi: 10.1007/s11082-019-1924-7.

[14] M. Nejat and N. Nozhat, "Multi-band MIM refractive index biosensor based on Ag-air grating with equivalent circuit and T-matrix methods in near-infrared region," *Sci. Rep.*, vol. 10, no. 1, pp. 1–12, 2020, doi: 10.1038/s41598-020-63459-w.

[15] M. Rahmatiyar and M. Afsahi, "Design of a Refractive Index Plasmonic Sensor Based on a Ring Resonator Coupled to a MIM Waveguide Containing Tapered Defects," 2020.

[16] C. T. C. Chao *et al.*, "Highly sensitive and tunable plasmonic sensor based on a nanoring resonator with silver nanorods," *Nanomaterials*, vol. 10, no. 7, pp. 1–14, 2020, doi: 10.3390/nano10071399.

[17] S. G. T.W. Lee, "Subwavelength light bending by metal slit structures," *Opt. Express*, no. 13, pp. 9652–9659, 2015.

[18] J. A. Dionne, L. A. Sweatlock, H. A. Atwater, and A. Polman, "Plasmon slot waveguides: Towards chip-scale propagation with subwavelength-scale localization," *Phys. Rev. B - Condens. Matter Mater. Phys.*, vol. 73, no. 3, p. 035407, 2006, doi: 10.1103/PhysRevB.73.035407.

[19] M. Reza and M. A. Mansouri-birjandi, "A high-sensitivity sensor based on three-dimensional metal – insulator – metal racetrack resonator and application for hemoglobin detection," *Photonics Nanostructures - Fundam. Appl.*, vol. 32, no. January, pp. 28–34, 2018, doi: 10.1016/j.photonics.2018.08.002.

[20] D. Rodrigo *et al.*, "Mid-infrared plasmonic biosensing with graphene," *Science (80-.).*, vol. 349, no. 6244, pp. 165–168, 2015, doi: 10.1126/science.aab2051.

[21] P. Y. Liu *et al.*, "Cell refractive index for cell biology and disease diagnosis: past, present and future," *Lab Chip*, vol. 16, no. 4, pp. 634–644, 2016.

Influence of Synthesis Conditions and Al doping, on structural and optical properties of ZnO:SnO_2 thin film

S. Benkara, N. Seghairi, S. Bouabida and H. Ghamri

Laboratory of Active Components and Materials,
Larbi Ben M'hidi University, Oum El Bouaghi, Algeria
sali_benkara@yahoo.fr

***Abstract*— Zn/Sn nanocomposite deposited on glace substrate by sol gel dip-coating technic, using Zinc acetate and tin chloride as precursors and aluminium chloride as dopping source, absolute ethanol and monoethanolamine (MEA) were used as the solvent and stabilizer, respectively. The quantity of tin in the solution was 0; 25; and 40 at.% Sn, and of aluminium was 0; 0,5; 2; and 4 at.% Al. The films are deposited at two dipping speeds: 100 mm/min and 50 mm/min, and used two dipping cycles: 10 and 5.**

The structure, optical properties and morphology of nanofilms and the influence of experimental parameters as withdrawal speed and dipping cycles on deposition of ZnO films were studied using X-Ray Diffraction (XRD), UV–vis spectroscopy and optical microscope. The crystalline phase determination from XRD confirmed that the films are composed of hexagonal wurtzite ZnO and tetragonal rutile SnO_2 without compound impurities. The doping and dipping speed and cycles effect on optical bandgap is estimated by transmittance spectra.

I. Introduction

Coupling two semiconductors with different band gap widths have attracted considerable attention, because this way allows to assemble the best properties of the two oxides and obtain unique properties not exixted in single semiconductor.

ZnO-based composites have shown excellent optoelectronic properties due to the electronic coupling between ZnO and other oxide phases [1-3]. ZnO-SnO_2 nanocomposite has been widely studied. J.-C. Li et al. [4] have obseved in their ZnO-SnO_2 nanocomposite an enhancement in the conductivity, A. Hamrouni et al. [5] found that the photoefficiency of the ZnO–SnO_2 samples was superior to that of pure ZnO or SnO_2. Highly transparent ZnO–SnO_2 thin films were prepared by team of D.Y. Torres Martínez et al. [6] and shown an improuvement in photocatalytic activity.

To obtain high quality ZnO-SnO_2 nanocomposite films, a various synthesis can be used as Physical Vapor Deposition (PVD), Chemical Vapor Deposition (CVD) [7] and magnetron sputtering [8], these methods require sophisticated and expensive equipment; very high vacuum, high temperature, etc. Sol- gel technic has been successfully used in preparation of thin flms, given its advantages as simplicity, safety, low cost of the apparatus, easily control, which the films thickness can be easily controlled by number of coating layers [9].

This paper demonstrates the preparation of ZnO-SnO nanocomposite films doped with aluminuim varied at 0.5 at%, 2.0 at% and 4 at% by sol gel dip coating. The effect of Al doping concentrations, withdrawal speed and number of dipping on the crystallinity, surface morphology, optical, and transparency of deposited Al doped ZnO-SnO_2 thin films have been studied in detail.

II. Experimental Details

Tree solutions were prepered by sol gel dip coating method. Solution 1 present by Al-doped ZnO thin films was obtained by mixing Zinc acetate (Zn $(CH_3COO)_2$) and aluminium chloride ($AlCl_3$), using 1 and 3 % Al-doping concentration, were dissolved in a mixture of ethanol and MEA solution at room temperature. The molar ratio of MEA to zinc acetate was maintained at 1.0 and the concentration of zinc acetate was 0.1 M. The solutions was stirred at 60°C for 2 h to yield a clear and homogeneous solution.

The synthesis of the ZnO–SnO_2 (Solution 2) represented in adding a 0.1 M ethanol solution of $Zn(CH_3COO)_2{\cdot}2H_2O$, previously prepared at 60 °C under vigorous stirring, to solution of $SnCl_2{\cdot}2H_2O$. The amount of $SnCl_2{\cdot}2H_2O$ solution was opportunely determined in order to obtain thin films with molar ratio ZnO/SnO_2 equal to 1/0.25 and 1/0.4.

Solution 3 obatained from solution 2 which doped by 2% Al. Then the same conditions are followed.

Prior to deposition, glass substrates were cleaned with acetone, ethanol, and distilled water. The substrates were dipped into the prepared solutions and withdrawn at a constant speed of 100 and, 50 mm/min, respectively.

After each dip-coating process, all films were pre-heated at 200 °C for 10 min in a furnace prior to evaporating the solvent and organic residuals. To obtain the desired film thickness, this coating/drying procedure was repeated for ten and five times and finally the resulting thin films were annealed at 500 °C in air for 1 h.

The X Ray Diffraction curvs were obtained with X Ray diffractometer (ARL) Equinox 100, using Cu K_α radiation (Cu K_α = 0.15406). The UV measurements were carried out at room temperature using Jasko V-750 visible spectrophotometer (JASCO International Co. Ltd., Tokyo, Japan). Morphological structure of the samples were obtained using Optical Microscope (OM) euromex CMEX5000 (ME2660 and 2665).

S. BENKARA is with Electrical Engineering Department, Larbi Ben M'hidi University, Oum El Bouaghi, Algeria. And Laboratory of Active Components and Materials, Larbi Ben M'hidi University, Oum El Bouaghi, Algeria; (e-mail: sali_benkara@yahoo.fr).
N. Seghairi, was with Physic Department, Larbi Ben M'hidi University, Oum El Bouaghi (e-mail: nassima.seghairi@yahoo.fr).
S. Bouabida is with Electrical Engineering Department, Larbi Ben M'hidi University, Oum El Bouaghi (e-mail: bouabida.seddik@univ-oeb.dz).
H. Ghamri is with Physic Department, Hadj Lakhdar University, Batna1, Batna, Algeria; (e-mail: ghamri_houda@yahoo.fr).

III. RESULTS AND DISCUSION

XRD patterns of the undoped, Al-doped ZnO and Al doped Zn/Sn films are shown in Figure 1. Diffraction peaks are observed at 31.8°, 34.5°, 36.0°, and 56.5° in the undoped and Al-doped ZnO films (figure 1(a) and (b)), which can be indexed as diffractions of (100), (002), (101), and (110) planes of wurtzite structured ZnO.
while in the figure 1 (c), the peaks can be indexed as a mixture of the hexagonal wurtzite ZnO and tetragonal rutile SnO_2 according to standard SnO_2 cards.
It can be observed in curvs of doped ZnO, the intensity of (0 0 2) increases which confirmed the improvement in preferential orientation growth along (0 0 2) direction.
ZnO phase peaks are clearly sharp and intense due to its lower crystallization temperature than SnO_2. [10,11]

The average grain sizes of the various samples were determined by using the diffraction peaks (0 0 2) for ZnO and (1 1 0) for SnO_2. The valeus obtained of undoped ZnO, 2% Al doped ZnO and 2% Al doped Zn/Sn are respectively: 21.66 nm; 19.74 nm and 15,43 nm.

The crystallinity degree of the films decreased with dopping and much more for nanocomposite Al doped Zn/Sn. This is in agreement twith previous results obtained for coupled ZnO/SnO_2 [12,13].
In most studies, the mean sizes of ZnO and SnO_2 were larger in the single oxides than in the mixed ZnO–SnO_2 samples. Mixing two different oxides usually limits the growth of both. [12,14]
The addition of SnO_2 caused a reduction of the main crystallite size of ZnO according to results obtained in literature [12,14, 15].

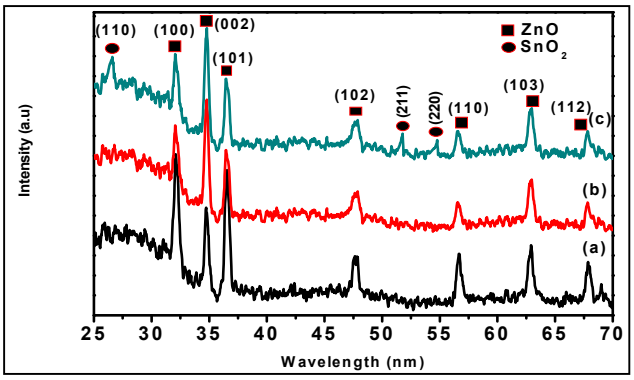

Figure 1. XRD patterns of (a) undoped ZnO; (b) 2% Al doped ZnO; (c) 2% Al doped Sn/Zn nanocomposite.

The optical transmission of Al doped Zn/Sn prepared with different doping percentage of Al are plotted in figure 2. The films show transmittance more than 95% in the visible region. It can be seen from these curves that the increase in the aluminum content decreases the transmission in the visible range.

The decrease in transmission at higher doping concentrations of Al can be attributed to the increased scattering of photons by crystal defects created by doping. [16,17].

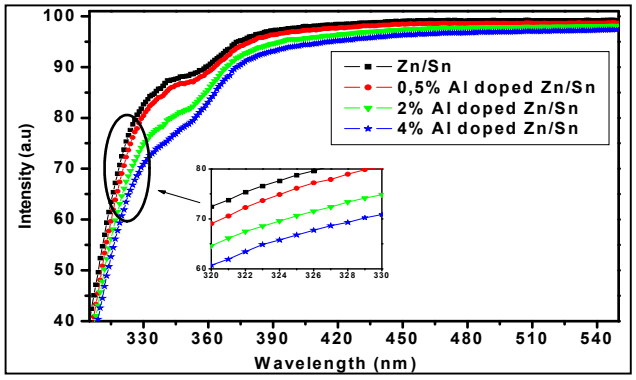

Figure 2. Transmittance curvs of Sn/Zn nanocomposite at different Al concentration.

Optical gap (Eg) is determined by tansmittance derivative and calculates from the following relationship: [18]

$$E_g = \frac{1243}{\lambda_{max}}$$

Where λ_{max} corresponds to the maximum value of the derivative.
The values of the band-gap energy with different doping concentrations are shown in figure 3.

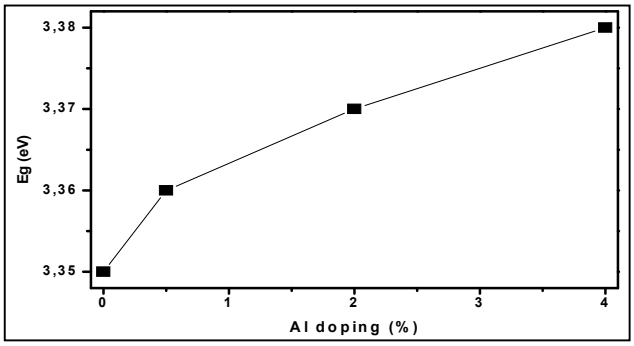

Figure 3. Eg variation versus the Al-doping concentration.

Fig. 4 shows spectra transmittance of Zn/Sn nanocomposite (40% Sn) deposited at dip-coating speed of 100 and 50 mm/min.

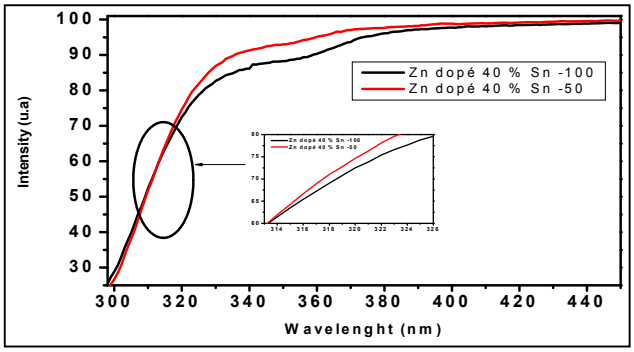

Figure 4. Transmittance curv of Sn(40%)/ ZnO nanocomposite at different dip-coating speeds

The films were transparent with an average optical transmittance greater than 95% in the visible spectral region.

The maximum transmittance is correspond to lower withdrawl speed (50 mm/min). Acording to S.M. Salaken et al. [19], the decrease in transmittance may be due to the increase in diffusion caused by the increase in grain boundary density in porous films.
Similarly, using the above formula, we determined the values of optical gap Zn/Sn layers prepared at the different withdrawal rates, we find 3,35 eV and 3,34 eV respectively correspond to the speed 100 and 50 mm/min. Eg values increase with the speed, the same behavior is seen by S. Aydemir. [20].

Fig. 5 shows the transmittance spectra of Zn/Sn nanocomposite (25% Sn) prepared at different number of dipping: 5 and 10. The film with 5 cycles shows higher transmittance reaches 95% at 380 nm wave length. From these spectra, it is obvious that the transparency varies with the thickness of thin layers which is controlled by the number and time of dipping.

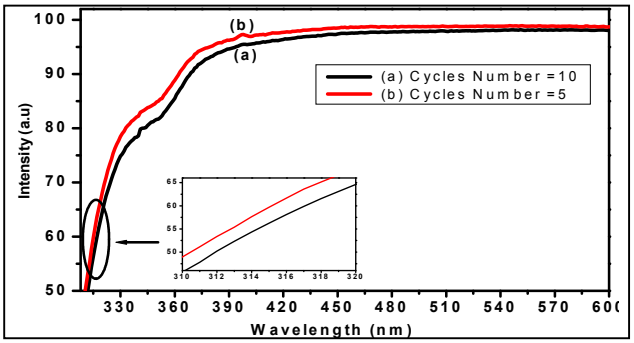

Figure 5. Transmittance curv of Sn(25%)/2% Al doped ZnO nanocomposite at different dipping cycles.

Fig. 6 shows the optical microscope images of Sn(40%)/ZnO nanocomposite deposited at different dipcoating speed.

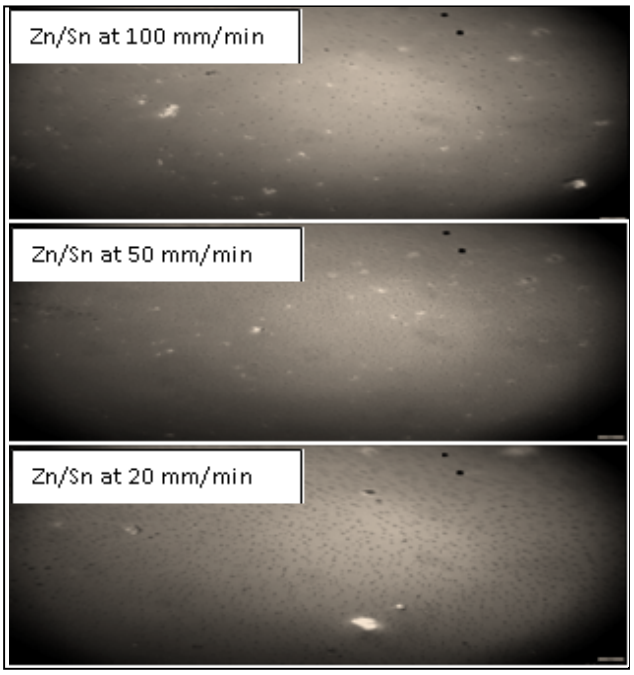

Figure 6. OM images of Sn(40%) doped ZnO nanocomposite at different dip coating speed.

These images revealed that the surface of all samples is homogeneous, and contains pores.

IV. Conclusion

Al-doped ZnO and Al doped Zn/Sn films are prepared by sol–gel dip coating technique at varying doping concentration, withdrawal speed of substrate and dipping cycles.
The films were dipped five and ten times, withdrawn at speeds of 100 and 50 mm/min and calcined at 500 °C in air for 1 hour.
The films were found to be highly c-axis oriented. The transmittance was decreased in the visible region with increase of Al doping and withdrawal speed. The decrease in transmission at higher doping concentrations of Al can be attributed to the increase in diffusion caused by the increase in grain boundary density in porous films.
The influence of Al doping and experimental parameters represented by dip-coating speed and dipping cycles on *Eg* was investigated. Their values were about 3.35–3.38 eV as Al dopant varied from 0,0 % to 4 % , and Eg decreased from 3,35 eV to 3,34 eV at withdrawal speed of 100 and 50 mm/min, respectively.

Acknowledgment

This work was supported by Active Components and Materials Laboratory, University of Oum El Bouaghi, Algeria. The authors are grateful to A. Djerman and G Nadia of Oum El Bouaghi University, Algeria, for their help and using the X-ray diffraction

References

[1] S. Chen, W. Zhao, S. Zhang, “Preparation, characterization and activity evaluation of p-n junction photocatalyst p-ZnO/n-TiO_2”, Applied Surface Science, vol. 255 (5), pp. 2478-2484, 2008.W.-K. Chen, Linear Networks *and Systems* (Book style). Belmont, CA: Wadsworth, 1993, pp. 123–135.

[2] B. Subash, B. Krishnakumar, V. Pandiyan, “An efficient nanostructured Ag_2S–ZnO for degradation of Acid Black 1 dye under day light illumination”, Separation and Purification Technology, vol. 96, pp. 204–213, 2012.

[3] J. Type. k, N. Guskos, G. Zolnierkiewicz, D. Sibera and U. Narkiewicz, “Magnetometric study of ZnO/CoO nanocomposites”, Rev. Adv. Mater. Sci. vol. 57, pp. 11-25, 2018.

[4] J-C Li, X-Y. Hou, Q. Cao, “Effect of Zn/Sn ratio on structure and properties of ZnO–SnO_2 nanocomposite films”, Journal of Alloys and Compounds, vol. 611, pp. 219–224, 2014.

[5] A. Hamrouni, N. Moussa, F. Parrino, A. Di Paola, A. Houas, L. Palmisano, “Sol–gel synthesis and photocatalytic activity of ZnO–SnO_2 nanocomposites”, Journal of Molecular Catalysis A: Chemical, vol. 390, pp. 133–141, 2014.

[6] D.Y. Torres Martinez, R. Castanedo Perez, G. Torres Delgado, O. Zelaya Angel, “Structural, morphological, optical and photocatalytic characterization of ZnO–SnO_2 thin films prepared by the sol–gel technique”, Journal of Photochemistry and Photobiology A: Chemistry, vol. 235, pp. 49–55, 2012.

[7] Q. Kuang, Z.Y. Jiang, Z.X. Xie, S.C. Lin, Z.W. Lin, S.Y. Xie, R.B. Huang, L.S. Zheng, “Tailoring the optical property by a three-

dimensional epitaxial heterostructure: a case of ZnO/SnO_2", J. Am. Chem. Soc. Vol. 127, pp. 11777–11784, 2005.

[8] K. Satoh, Y. Kakehi, A. Okamoto, S. Murakami, K. Moriwaki , T. Yotsuya, "Electrical and optical properties of Al-doped ZnO–SnO_2 thin films deposited by RF magnetron sputtering", Thin Solid Films, Volume 516, Issue 17**, pp.** 5814-5817**,** 1 July 2008.

[9] P. Chesler , C. Hornoiu, S. Mihaiu, C. Vladut, "Nanostructured SnO2–ZnO composite gas sensors for selective detection of carbon monoxide", Beilstein J. Nanotechnol., vol. 7, p. 2045–20566, 2016.

[10] G. Torres-Delgado, C.I. Zu˜niga-Romero, S.A. Mayen-Hernandez, R. Castanedo-Perez, O. Zelaya-Angel, "Optical and structural properties of the sol gel prepared ZnO thin films and their effect on the photocatalytic activity", Sol. Energy Mater. Sol. Cells, vol. 93 pp. 55–59, 2009.

[11] M. Zhang, T. An, X. Xu, C. Wang, G. Shen, J. Fu, "Preparation and photocatalytic properties of a nanometer ZnO–SnO_2 coupled oxide", Appl. Catal. A, vol. 260, pp. 215–222, 2004.

[12] C. Wang, X. Wang, B. Xu, J. Zhao, B. Mai, P. Peng, G. Sheng, J. Fu, J. Photochem.Photobiol. A: Chem. Vol. 168, pp. 47–52, 2004.

[13] C.-C. Lin, Y.-J. Chiang, J. Chem. Eng. 181–182, pp. 196–205, 2012.

[14] C. Wang, J. Zhao, X. Wang, B. Mai, G. Sheng, P. Peng, J. Fu, Appl. Catal. B: Environ. Vol. 39, pp. 269–279, 2002.

[15] A. Hamrouni, H. Lachheb, A. Houas, Mater. Sci. Eng. B, vol. 178, pp. 1371–1379, 2013.

[16] C.M. Muiva, Y. S. Sathiaraj, K. Maabong, "Effect of doping concentration on the properties of aluminum doped zinc oxide thin films prepared by spray pyrolysis for transparent electrode applications", Ceramic International, vol. 37, pp. 555-560, 2011.

[17] L.H. Kathwate, G. Umadevi, P.M. Kulal, P. Nagaraju, D.P. Dubald, A.K. Nanjundan,V.D. "Ammonia gas sensing properties of Al doped ZnO thin films", Sensors and Actuators A, vol. 313, pp. 112193, 2020.

[18] L. C. Klein. "Sol-Gel technology for thin films, fibers, preforms, electronics, and specialityshapes", Noyes Publications, 1988.

[19] S.M. Salaken, E. Farzana, and J. Podder, "Effect of Fe-doping on the structural and optical properties of ZnO thin films prepared by spray pyrolysis", J. Semicond. Vol. 34, pp. 7, 2013.

[20] Sinem Aydemir, "Fabrication and properties of zinc oxide thin film prepared by sol-gel dip coating method", Materials Science-Poland, vol. 33(3), pp. 515-520, 2015.

Tin disulphide properties optimisation for solar cells applications

KAMLI Kenza
Department of physics, Faculty of Sciences..
University 20 Août 1955.
Skikda, Algeria.
kenza_kamli@yahoo.fr, k.kamli@univ-skikda.dz

HADEF Zakaria
Department of physics, Faculty of Sciences..
University 20 Août 1955.
Skikda, Algeria.
zaki_hd2013@yahoo.fr, z.hadef@univ-skikda.dz

***Abstract*—Tin disulphide semiconductors are used in various applications and specifically in solar cells. They are relatively inexpensive compared to other thin films used in the photovoltaic technology. Tin disulphide thin film has been promisingly proposed for this field application as buffer or window layer. In this work, we study the effect of deposition time on the structural, morphological and optical properties of tin disulphide thin films deposited on glass substrates using spray pyrolysis technique. The phase of SnS_2 are identified using X-Ray diffraction. A single phase without impurities is observed for the elaborated samples. The optical analyses show that the film prepared at 65 min present the highest transmittance in the visible region. The obtained results confirm that SnS_2 thin films can be good candidates for solar cells devices. These results are of great importance in the prediction of the good application of SnS_2 thin films in solar cells.**

Keywords— Tin disulphide, Spray pyrolisis, Characterization techniques, Sollar cells.

I. INTRODUCTION

Considerable attention has been paid for the last few decades to the binary compounds based on the Sn–S system, due to their excellent properties and the high potential use in optoelectronic devices [1–4]. In particular tin disulfide (SnS_2) was considered as one of very interesting tin sulfides semiconductors. SnS_2 has been known for its potential applications in solar cells as well as electrical switchings [5]. Also SnS_2 belongs to IV–VI group of semiconductor compound with hexagonal crystal structure (a= 0.3648 nm, c= 0.5899 nm) [6]. It has a wide band gap energy (2.88 eV) [7], and n-type electrical conductivity with magnitude depending on the preparation methods.

Thin films of SnS_2 compound has been prepared by different technologies deposition techniques. Such as, chemical bath deposition [8], vacuum thermal evaporation [9], close-spaced sublimation [10], successive ionic layer adsorption and reaction (SILAR) [11], spray pyrolysis [12].

In this paper we report a chemical method called ultrasonic spray, for the deposition of SnS_2 thin films at 350 °C onto ordinary glass substrates. Spray deposition is well established and widely used technique for thin film processing. It is a chemical vapour deposition that has been succefully used for the deposition of various materials.

The effect of deposition time parameter on the films properties and their characterization by X-ray diffraction, chemical analysis, and optical techniques are also reported.

II. EXPERIMENTAL DETAILS

Tin disulfide thin films were prepared by spraying an alcoholic solution containing tin chloride IV ($SnCl_4(2H_2O)$) and thiourea $CS(NH_2)_2$ on glass substrates using spray pyrolysis process. Substrates were degreased in successive rinses with acetone, ethanol, and distilled water. Then, the total solution was sprayed on heated substrates at 350 °C with a molarity equal to 0.08 mol/l. A set of samples was obtained by changing the deposition time 25, 45 and 65 in atmospheric pressure.

The films were characterized by means of structural, morphological, and optical methods. The X ray diffraction studies were carried out using a D8 ADVANCED BRUKER diffractometer using a Cu Kα radiation (λ=1.5405 Å) in range of 10-85°, the crystallite size were estimated to study the effect of the molar concentration. The surface morphology of the films was observed using a JEOL, model JSM 6301F Scanning Microscopy by field effect. The surface morphological studies were done with the SEM photographs taken with JEOL model JSM6400 scanning microscope. To have an idea about the surface elemental composition of the film, energy dispersive analysis by X-rays (EDAX) was carried out using EDX spectrometer related to the SEM used before.

III. RESULTS AND DISCUSSION

A. Structural characteristics

The XRD profile of the ultrasonic sprayed SnS_2 thin films on glass substrates is shown in Fig. 1. The prominent Bragg reflection occurring at about $2\theta \approx 32.98°$ along with many other weak peaks confirms the polycrystalline nature of the films. In all cases we found that (101) is the preferred orientation, so we can say that all SnS_2 thin films are in hexagonal crystallographic phase (JCPDS 31-1399), with the c-axis perpendicular to the substrate.

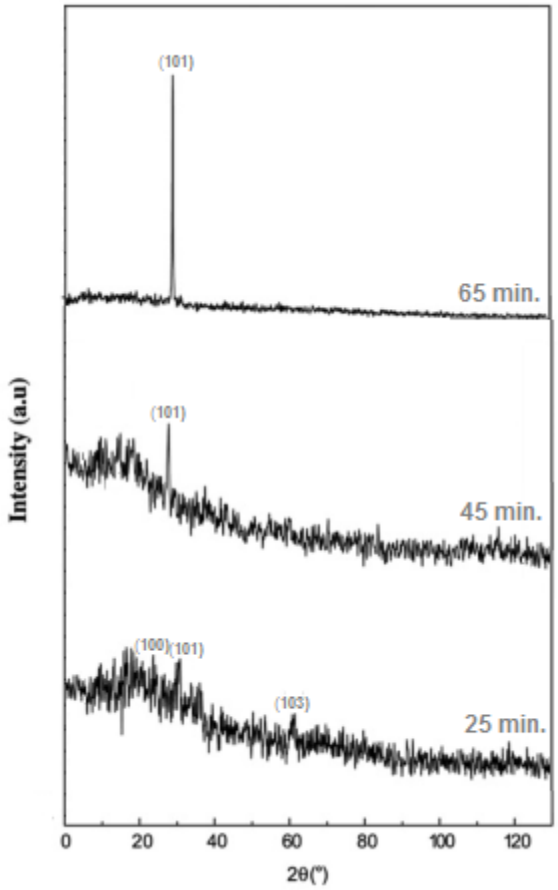

Fig. 1. X-ray diffraction pattern of SnS_2 thin films at different deposition time.

The average crystallite sizes of the films deposited with different molarities have been calculated using the Scherrer's formula:

$$D = \frac{0.9\lambda}{\beta \cos\theta}$$

Where λ, θ and β are X-ray wavelength, the Bragg's diffraction angle and the full width at half maxima of the peak corresponding to the θ value, respectively.

Crystallite size for samples obtained at different deposition times is shown in fig.2. It can be observed that the grain size increase with deposition time increasing of sprayed precursor solution from 9.46 nm to 13.5 nm. This later proves the crystallinity amelioration.

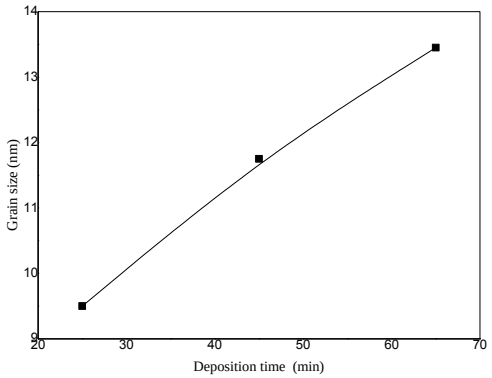

Fig. 2. Variation of crystallite size with different deposition time.

B. Morphological characteristics

The Fig. 3 shows typical SEM images and EDAX spectra of films deposited at the three studied deposition time and at substrate temperature 350 °C. Microscopic examination reveals that the obtained deposits are uniform and compact with good coverage to the substrate basis. As can be seen, the films morphology depends strongly on the deposition time. Film deposited at 65 min has a continuous and dense structure with a very smooth surface morphology as reveals Fig. 3.

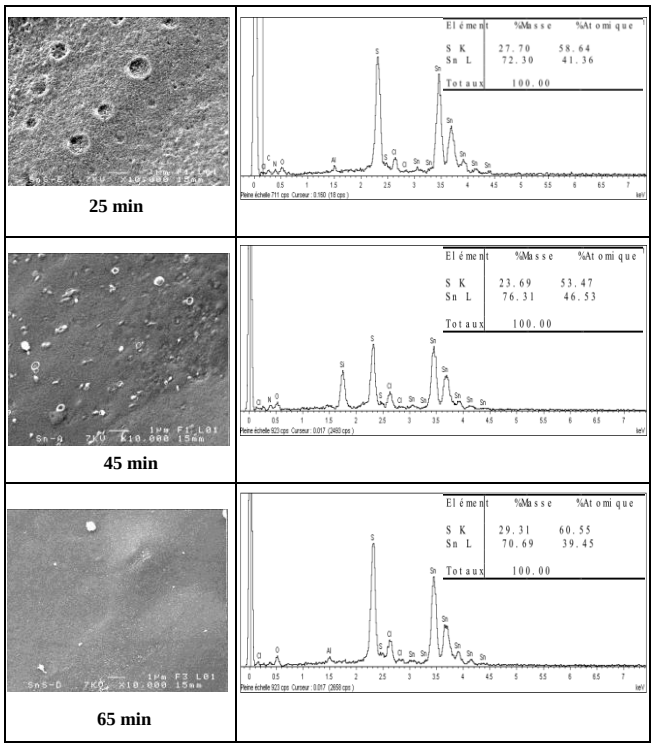

Fig. 3. SEM images and EDX spectra of SnS_2 thin films.

The EDX spectra of the SnS_2 films recorded in Fig. 3 shows the atomic and weight percentages of the elements present in the films and assure the chemical composition of SnS_2. As can be seen, atomic ratio for the samples increases with deposition time increasing. Also it can be noted, that the formed film at 65 min contain S and Sn with almost 39% and 61% ratio, respectively, which is the most near stoichiometric ratio for SnS_2 composition. In addition the presence of Cl is due to the used precursor, and those of O, N is due to the air.

C. Optical characteristics

Fig. 4 shows the optical transmittance curves as a function of the wavelength for the SnS_2 films deposited at 330°C with different molar concentrations.

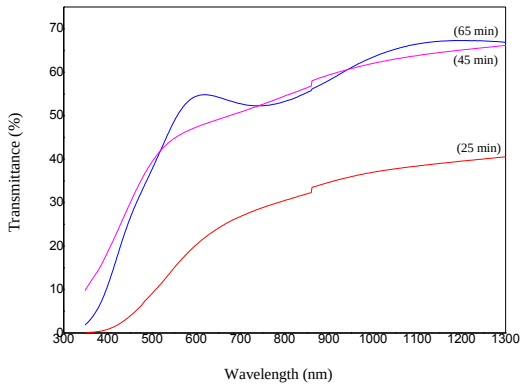

Fig. 4. UV-visible transmittance spectrum of SnS_2 thin films deposited at 350 °C at different deposition time.

As can be seen the optical transmittance increase with the molarity increasing. The fall of transmittance between 300 nm and 400 nm shows that the films absorb the light ultra violet. Furthermore, film deposited at 65 min exhibits interference fringe in the transmittance spectrum and a high transparency than the other films. This is due to the smooth surface of the former. It is well known that rough surface causes the light scattering resulting in transmittance reduction. This explains the low transmittance measured in films deposited at lowest deposition time.

IV. CONCLUSIONS

In the present work we have studied the influence of solution properties on SnS_2 thin films deposition by spray pyrolysis. Four molar concentrations were investigated. X-ray diffraction analysis reveals a polycrystalline nature (hexagonal phase) for all the films deposited at Ts = 330 °C. It was observed that the grain size is varied between ~ 14 and 9.5 nm. The morphological studies using SEM showed that the films are uniform and compact with good coverage to the substrate basis. EDS results confirm the presence of Sn and S. The optical characterization showed that the films transparent increase with molar concentration increasing. From these values we have suggested that the film deposited at 0.08 mol/l can be a potential candidate as an optical window in solar cells.

REFERENCES

[1] G. Valiukonics, D.A. Guseinova, G. Krivaite, A. Sileica, Phys. Status Solidi, B Basic Res. 135 (1990) 299.

[2] M.T.S. Nair, P.K. Fair, J. Phys. D: Appl. Phys. 24 (1991) 83.

[3] A. Ortiz, J.C. Alonso, M. Garcı´a, J. Toriz, Semicond. Sci. Technol. 11 (1996) 243.

[4] S. Lo ´pez, A. Ortiz, Semicond. Sci. Technol. 9 (1994) 1.

[5] R. Bissessur, D. Schipper, Materials Letters 62 (2008) 1638–1641.

[6] A. Chakrabarti, J. Lu, A. M. McNamara, L. M. Kuta, S. M. Stanley, Z. Xiao, J. A. Maguire, N. S. Hosmane, Inorganica Chimica Acta 374 (2011) 627–631.

[7] F. Tan, S. Qu, X. Zeng, C. Zhang, M. Shi, Z. Wang, L. Jin, Y. Bi, J. Cao, Z. Wang, Y. Hou, F. Teng, Z. Feng, Solid State Communications 150 (2010) 58–61.

[8] K.T. Ramakrishna Reddy, G. Sreedevi, K. Ramya and R.W. Miles. Energy Procedia 15 (2012) 340 – 346

[9] Chengwu Shi, Zhu Chen, Gaoyang Shi, Renjie Sun, Xiaoping Zhan, Xinjie Shen, Thin Solid Films 520 (2012) 4898–4901

[10] Chengwu Shi, Pengfei Yang, Min Yao, Xiaoyan Dai, Zhu ChenThin, Solid Films 534 (2013) 28–31

[11] N.G. Deshpande, A.A. Sagade, Y.G. Gudage, C.D. Lokhande, Ramphal Sharma, Journal of Alloys and Compounds 436 (2007) 421–426

[12] O.A. Yassin, A.A. Abdelaziz, A.Y. Jaber. Materials Science in Semiconductor Processing 38 (2015) 81–86

All optical gate based on photonic crystal ring resonator

Lila MOKHTARI,hadjira BADAOUI,
Mehadji ABRI

STIC Laboratory, Faculty of Technology,
University of Tlemcen, Algeria.

l_benseddik2003@yahoo.fr, elnbh@yahoo.fr,
abrim2002@yahoo.fr

Rahmi bachir, Lallam Farah
Moungar Abdelbasset.

STIC Laboratory, Faculty of Technology,
University of Tlemcen, Algeria.

fa.lallam72@gmail.com,ambassit@gmail.com.bachirrahmi39@gmail.com

Abstract: The aim of this paper was to propose and design a photonic crystal drop filter based on ring resonators and study its properties numerically. This structure is constituted in a two-dimensional square lattice. The resonant wavelengths of the PCRR proposed are λ = 1.553 µm, the extraction efficiency exceeds 99% with a quality factor of 5177. To study the all-optical OR and XOR logic gate function, we calculated the electric field distribution of the 2D photonic crystal for the 1.553 µm signal light.

Key words: photonic crystals ; filter ; ring resonators ; logic gates ; OR ; XOR .

1. Introduction

PCs are periodic optical nanostructures composed of two different materials with low and high dielectric constant [1-2]. As a result of this periodicity, it owns photonic band gap (PBG), where the transmission of light in certain frequency range is absolutely zero [3]. Depending on the geometry of the structure, PCs can be divided into three broad categories, namely one-dimensional (1D), two-dimensional (2D) and three- dimensional (3D) structures. 2D PCs due to their complete PBG and ease of design and fabrication attract more attention than 1D structures [4].

In this study, we propose a new design of PCRR based on square photonic crystal ring resonator with flower shaped. The COMSOL Multiphysics based on the finite element method FEM is used for simulate the distribution and transmission of electromagnetic wave. In our design, 100% dropping efficiency with quality factor of 5177 is achievable at wavelength λ=1.553 µm, which is a satisfactory result in comparison with other T-shaped channel drop filters based on photonic crystal ring resonators.

Optical logic gates are essential components required for optical signal processing and optical communication networks Saidani [5] proposed a multifunctional logic gate in a 2D PCs waveguide structure using multimode interference concept. By switching optical signal to different input waveguides, different functions such as XOR, OR, NOR and NOT gates have been obtained. An all optical NOR gate have been proposed by Isfahani [11]. We used the PCRR presented to realize the gate logic for OR and XOR function, there are presented by studying the electric distribution of the 2D photonic crystal for the 1.553 µm signal light.

2. Structural characteristics

2.1. Band gap structure

To determine the physical parameters of the filter, it is necessary to calculate the band gap diagram of the design. This last is traced using the plane wave expansion method PWE under COMSOL Multiphysics software [7]. The dielectric rod radius r=0.188×a, and background constant are taken a=0.64 µm. As shown in Fig.1, the PCs structure supports a photonic band gap in the region $0<wa/2\,\pi c<0.455$, $0.525<wa/2\,\pi c<0.545$ and $0.675<wa/2\pi c<0.750$ for TE mode.

The resonant frequency is chosen such that there will not be a propagative mode in a photonic structure without defect as shown in Fig. 1. At the wavelength 1.553 µm ($wa/2\pi c$=0.412), we observe the absence of modes in these regions. The electric field is reflected back because of the existence of the PBG as show in Fig. 1.

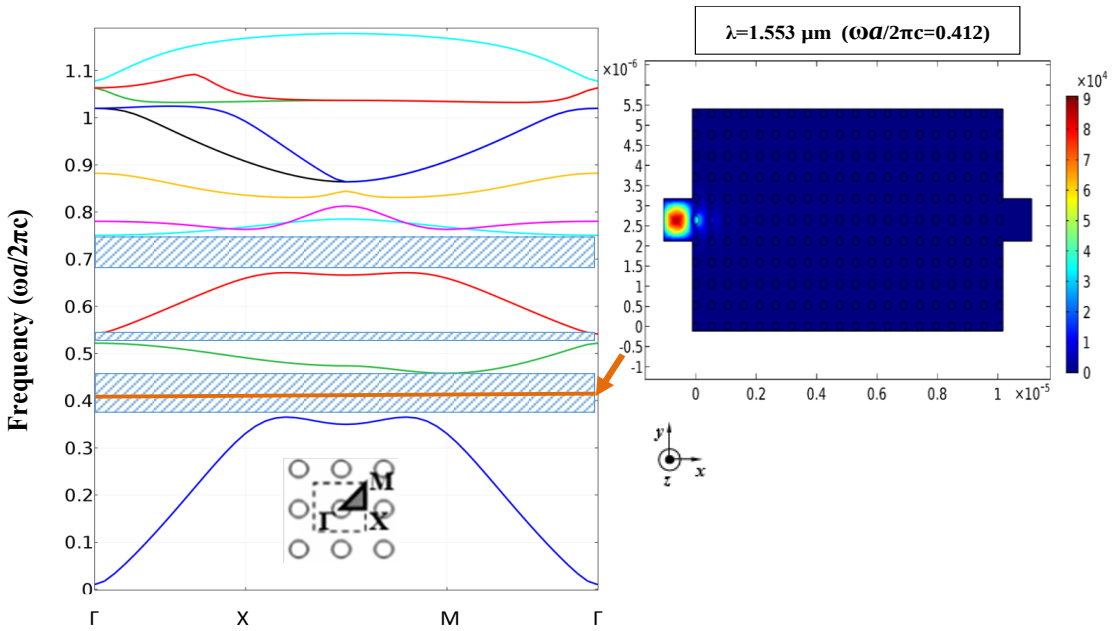

Figure 1. Schematic of photonic band gap.

2.2. Field formulation

Use the Helmholtz field eaqution and starting from the frequency-domain governing equation:

$$\nabla \times (\mu^{-1}\nabla \times \mathbf{E}) - \omega^2 \varepsilon_c \mathbf{E} = \mathbf{0} \quad (1)$$

The total electric field, E, can be decomposed into two components:

$$E = E_{total} = E_{background} + E_{relative} \quad (2)$$

In mode analysis and the boundary mode analysis COMSOL Multiphysics solve equation (1), the electric field in spectral domain is given by:

$$\mathbf{E}(\mathbf{r},t) = \mathrm{Re}(\tilde{\mathbf{E}}(\mathbf{r}_T)e^{j\omega t - j\beta z}) = \mathrm{Re}(\tilde{\mathbf{E}}(\mathbf{r})e^{j} \quad (3)$$

The spatial parameter, $\alpha = \delta z + j\beta$

- β : Propagation constant
- δz : Attenuation constant

Use the scattering boundary conditionto make a boundary transparent for a scattered wave. The boundary condition is also transparent for an incoming plane wave.

$$\mathbf{E} = \mathbf{E}_{sc} e^{-jk(\mathbf{n}\cdot\mathbf{r})} + \mathbf{E}_0 e^{-jk(\mathbf{k}\cdot\mathbf{r})} \quad \text{Plane}$$

(4)

2.3. Design of the channel drop filter

In this study, the structure of the two-dimensional photonic crystal considered is formed by a square lattice of dielectric cylindrical rods of GaAs embedded in an air background. The numerical simulations are based on finite element method exploiting the commercial software COMSOL. Rods have a refractive index value of n=3.28, and a radius of r=0.188×a, a=640 nm being the lattice of the photonic crystal structure which is defined as the distance between centers of two adjacent rods, and a resolution of 20 rods horizontally and 20 rods vertically. Fig.2 shows the schematic structure of a Channel-Drop Filter CDF based on a PCRR. In this structure the ring resonator is created by removing a 7 × 7 square of dielectric rods and then replacing it with four flowers with height holes each separated by a hole the radii r_1=0.2356×a. In this study the used mesh is non-uniform and the type of sequence used is physics-controlled mesh with scattering boundary condition.

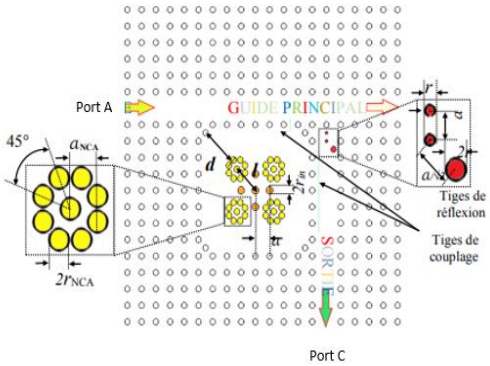

(a)

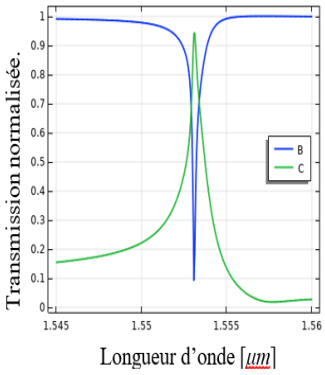

(b)

Fig. 2. (a) Single ring PCRR. (b) Normalized transmission spectra at two output ports B and C for PCRR. The designing parameters of the proposed NRC-QSRR *:* a= 640 nm, r=120.32 nm, r_{in} = 151.3 nm, a_{NRC}=551.36 nm, r_{NRC} =130.34nm, d= 1608.36 nm, l= 1169.61 nm.

The optical waves enter the structure through port 1 and exit through port 2, but during resonance, the optical wavelengths wil**l be transferred to the drop guide via the resonant ring and exit through port 3. At the resonance wavelength **λ = 1.553 μm**, the extraction efficiency exceeds 99% with a quality factor of 1411.

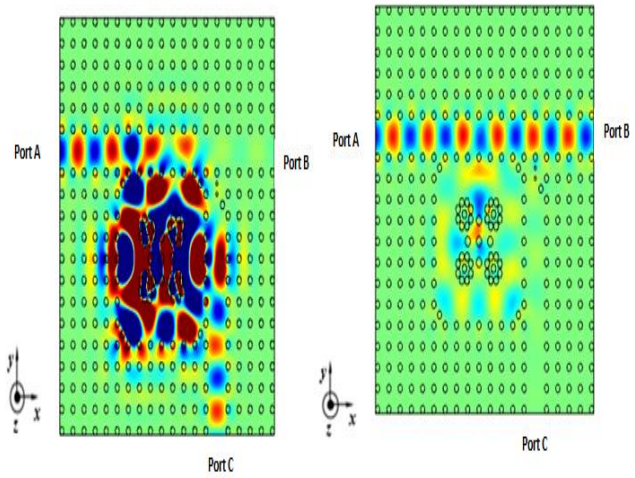

Fig.3. Electric field pattern of the ring resonator at a) λ = 1.553 μm (the resonant wavelength). b) λ = 1.556 μm (the off-resonance)

The electromagnetic wave transverse component Ez is presented around the wavelengths λ=1.553 μm and λ=1.556 μm where the positive pulses are in red and the negative pulses are in blue.

3.2. OR gate

The proposed OR gate structure is formed from two waveguides and two ring resonators with a resolution of 38 rods horizontally and 23 rods vertically. Two symmetrical optical waveguides AY and BY were formed along the *Γ–M* direction by removing two rows of GaAs rods, and put two ring resonators between them. The refractive index, radius and lattice constant of the structure are the same as the PRCC structure. The final schematic of our proposed OR gate structure is shown Fig.4.

The all-optical OR logic gate operation is presented by studying the electric field distribution of the 2D photonic crystal for the 1.553 μm signal light, and the calculated results are shown in Fig.4. If a signal is injected into input port A, then the

signal light can transmit through the optical waveguide AY and be output from port Y, as shown in Fig.4 (b). If a single beam is injected into input port B, then the signal light can transmit through the optical waveguide BY and be output from port Y, as shown in Fig.4 (c). If two beams are injected into input ports A and B simultaneously, then the signal light can transmit through optical waveguides AY and BY, as shown in Fig4. (d). Thus, an all-optical OR logic gate can be achieved very easily.

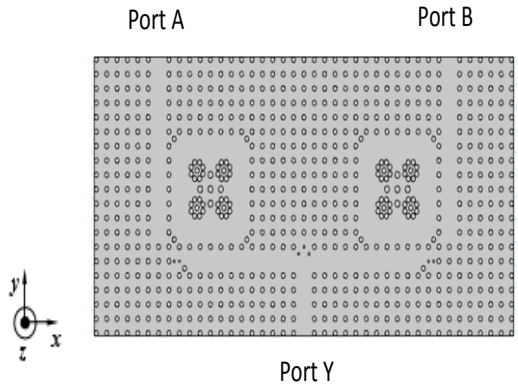

(1)

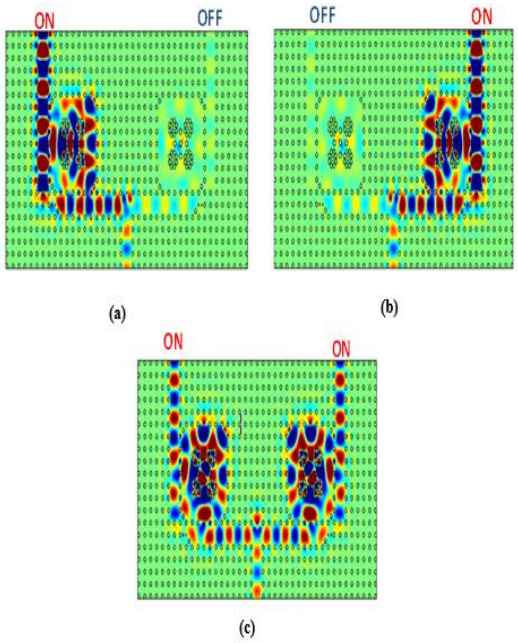

Fig.4 (A) OR gate structure. (a) 1 OR 0 = 1. (b) 0 OR 1 = 1. (c) 1 OR 1 = 1. The OR gate structure parameters are set such as: n=3.28, r=0.188×a and a=640 nm.

3.3. XOR gate

To study the all-optical XOR logic gate function, the same structure of OR gate 2D photonic structure is used adding one column of rods after the first ring resonator and is presented in Fig.5. The optical XOR logic gate operation is presented by studying the electric field distribution of the 2D PCRR device for a particular wavelength λ=1.553 μm**.**

First, we insert a signal light into only port A of the input waveguide. A large part of this signal travels to the port Y through the ring resonator waveguide. This is identified as the logic phenomenon “1 XOR 0 gives 1” and it is shown in Fig.5 (b).

The similar situation occurs, when the signal is incident to the B port only, and we get output as 1.This corresponds of the logic operation “0 XOR 1 gives1” as shown in Fig.5 (c).

When the signals given to the input ports A and B simultaneously, there occurs a phase difference between these two signals due to path difference, and we get a destructive interference. As a result of this, there is approximately zero output at the port Y. This corresponds to the logic operation “1 XOR 1 gives 0” as shown in Fig. 5 (d).

When the both input signals are same (“0”, “0” or “1”, “1”) the output of XOR gate is zero “0” and both are different (“0”, “1” or “1”, “0”) the output is one “1”.)

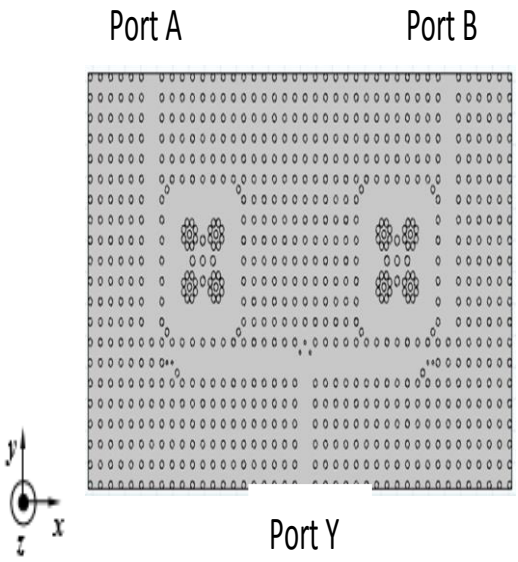

(A)

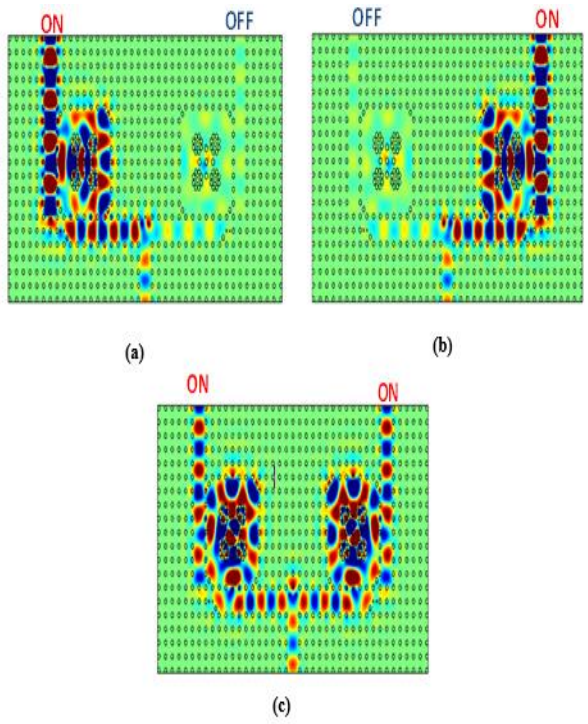

Fig. 6 (A) XOR gate structure. (a)1 XOR 0 = 1. (b) 0 XOR 1 = 1. (c) 1XOR 1 = 0. The XOR gate structure parameters are set such as: n=3.28, r=0.188×a and a=640 nm.

4. Conclusion

In this article, photonic crystal ring resonator based Channel-Drop Filter is designed and investigated. First we designed a flower shaped PCRR based on only one photonic crystal ring resonator. By combining two ring resonators, we proposed OR and XOR gates operating with TE mode optical signals.. Photonic crystal manufacturing is one of the main inconvenient that can be confronted where is expensive in production. Sub 100 nm dimensions need generally employing of high resolution electron beam lithography (EBL).

References

[1] S.H. Kim, H.Y. Ryu, H.G. Park, G.H. Kim, Y.S. Choi, Y.H. Lee, 'Two-dimensional photonic crystal hexagonal waveguide ring laser', Appl. Phys. Lett. 81 PP.2499–2501, 2002.

[2] V. Dinesh Kumar, T. Srinivas, A. Selvarajan,' Investigation of ring resonators in photonic crystal circuits', Photon. Nanostruct. 2 pp.199–206, 2004.

[3] Z. Qiang, W. Zhou, R.A. Soref, Optical add-drop filters based on photonic crystal ring resonators, Opt. Express 15 pp.1823–1831, 2007.

[4] S. Robinson, R. Nakkeeran, 'Investigation on two dimensional photonic crystal resonant cavity based band pass filter', Optik, Volume 123, pp.451–457, 2012.

[5] H.Alipour Banaeia, S.Seraj mohammadib,F.Mehdizadehc,Alloptical NOR and NAND gate based on nonlinear photonic crystal ring resonators,Optik Volume 125 pp.5701–5704, 2014.

[6] Mahmoud M Y, Bassou G, Taalbi A, Chekroun Z M. Optical channel drop filter based on photonic crystal ring resonators. Optics communications 2012; 285:368-372.

[7] M. A. M. Birjandi, and M. R. Rakhshani, " Anew design of tunable four-port wavelength demultiplexer by photonic crystal ring resonators" Optik (2013), http://dx.doi.org/10.1016/j.ijleo.2013.04.128.

[8] L. Mokhtari, H. A. Badaoui, M. Abri, M. Abdelbasset, F. Lallam, and B. Rahmi, "Proposal of a New Efficient or/Xor Logic Gates and All-Optical Nonlinear Switch in 2D Photonic Crystal Lattices," Progress In Electromagnetics Research C, Vol. 106, 187-197, 2020. doi:10.2528/PIERC20051501 http://www.jpier.org/pierc/pier.php?paper=20051501 (scopus)

[8] Saidani N, Belhadj W, Abdel Malek F. 'Novel all-optical logic gates based photonic crystal waveguide using self imaging phenomena'. Optical Quantum Electron 47:1829–46, 2015.

[9] Isfahani BM, AhamdiTameh T, Granpayeh N, Javan AM.' All optical NOR gate based on nonlinear photonic crystal microring resonators'. Optical Society of America, volume 26,pp.1097–102,May 2009.

[10] Moungar A, Badaoui H, Abri M, '16-Channels Wavelength Efficient Demultiplexing around

1.31/1.55 μm in 2D Photonic Crystal Slab', Optik (2019), https://doi.org/10.1016/j.ijleo.2019.04.032

Thin solid films
Structural, electrical and optical properties of Fe-doped CuO deposited by spray pyrolysis technique

[1]Daira Radouane, [1]Zerouali Madiha, [1]Boudjema Bouzid

[1]*Department of physics, University August 20, 1955 of skikda, Road of El Haddeik LP 26, Physico Chemistry of Surfaces and interfaces Research Laboratory of Skikda (LRPCSI), Algeria*
(*corresponding author*: *daira_radouane@yahoo.fr*).

Abstract:

Our work consists in depositing the copper oxide Fe doped CuO films by spray obtained from the solution of copper chloride $CuCl_2$ and $FeCl_2$ with a percentage of 2, 4; 6 and 8%, on glass substrates at a temperature of 350^0c. The thin films obtained are characterized by X-ray diffraction, visible UV spectroscopy and the four-point technique.

With X-ray diffraction, high peak intensity is obtained for the preferential orientations of (002) and (111), this intensity increases as the doping rate increases and gives us a more crystalline structure for a doping rate of 8%, also a grain size were estimated. The transmission of our films varies between 55% and 75% with a high absorption in the visible domain, the resistivity of our films increase with the increase of doping rate and the gap energy varies between 4.00 and 1.47 eV.

Keywords: CuO, Fe doped CuO, spray ultrasonic, XRD, optical proprieties, electrical resistivity.

.

I. INTRODUCTION:

Copper oxide CuO is a semiconductor material that is part of the transparent and conductive oxides (TCO), it has interesting electronic, electrical and optical properties for optoelectronic applications especially in the photovoltaic field. The band energy gap is of direct nature, the value of its optical gap is around 2.1 eV [1].

Copper oxides are used in several areas such as: gas sensors [2-6], solar cells [7-9] and light-emitting diodes[10].

The CuO films can be developed by several techniques such as: cathodic spray, laser ablation [11] and vacuum evaporation [12], chemical vapour deposition [12], sol-gel [13] and pyrolysis spray method [14, 15].

Our job is to obtain thin films of Fe doped CuO by spray spray. Our glass substrates are heated to a temperature of 350^0C, the solution used in our work is copper chloride $CuCl_2$ molarity of 0.1M as precursor and Fer chloride $feCl_2$ molarity of 0.1 M as dopant.

The study of the physical properties of our films was carried out according to the growth of the grain size and optical gap being that the copper oxide is one of the TCO used (transparent and conductive oxides), the growth rate corresponding to optimal resistivity will be sought.

II. Experimental procedure:

Fe-doped CuO copper oxide films were obtained from $CuCl_2$ copper chloride and fer chloride with a molarity of 0.1 M, our 1*1 cm^2 glass substrates were heated to a temperature of 350^0 C, These films are deposited by continuous spray for different doping rates.

The crystalline structure was evaluated using a PhilipsX'Pert diffractometer with radiation (λ = 1.54 A^0), which scans between 30^0 and 70^0. The optical transmission spectra were recorded with UV-Visible in the wavelength range 400-1000 nm. Electrical resistivity was measured with the four points.

III. Results and discussion:

III.1. Thickness measurement:

The thickness is measured using the surface profilometer, our calculated thickness is 762 nm.

III.2. Structural properties XRD:

The comparison of the data with the references of the JCPDS file (card N=° 45-0937) confirmed the cassiterite structure (monoclinic structure) of our films. The CuO phase was obtained around 2θ= 36.43^0, 38.51^0, 42.5^0, 47.33^0, 56.58^0, 60.77^0, and 64.13^0, which corresponds respectively to plans (002), (111), (-202), (020), (202), (-113), and (-311). (Figure 1).

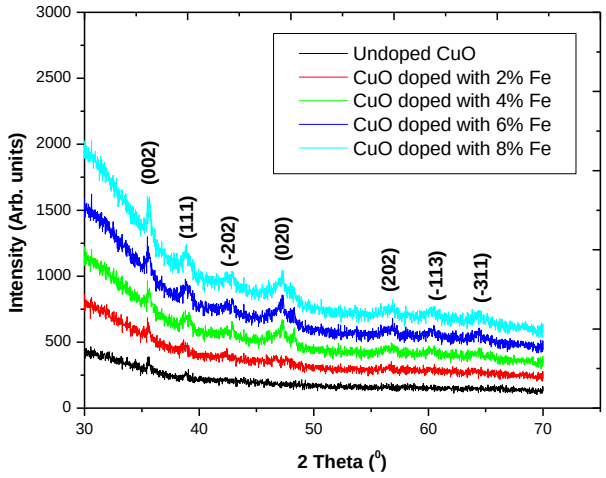

Fig 1. XRD patterns of Fe doped CuO thin films deposited using different doping rate.

The diffraction spectra show that our material has a poly crystalline structure. In all these films there are two preferential directions in the directions (002) and (111) the latter which is the most intense. The intensity of these two peaks increases with the increase in doping rate (Figure 2). A careful analysis of the diffraction patterns shows that there is no trace of iron related phase for all Fe-doped CuO compositions. This indicates that Fe ions were

successfully doped into the lattice of Cu sites without affecting the crystal structure of the parent CuO matrix.

The grain size of the most intense orientation (002) and the internal stress are calculated using the following formulas [16-17]:

$$D = \frac{0.9\lambda}{w.cos\theta}$$

$$\varepsilon = \frac{w.cos\theta}{4}$$

λ: is the wavelength of the incident X-ray beam. w: is the width halfway up the diffraction line. In Figure 3 we notice that average crystallite size decreases with increasing in Fe doping ratio indicating a small deterioration in the films'crystallinity.

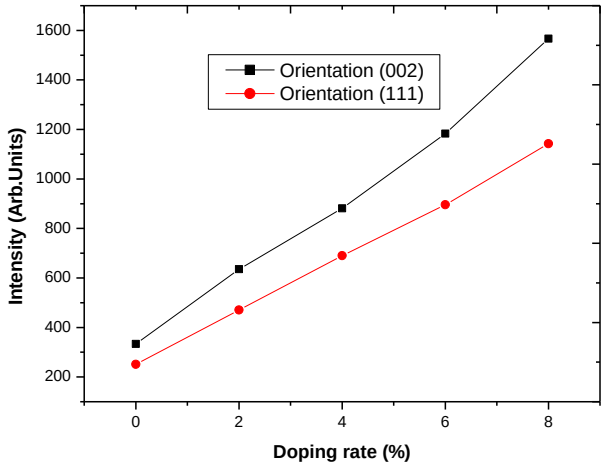

Fig.2. Variation of the (002) and (111) oriented crystallite size as a function of the doping rate

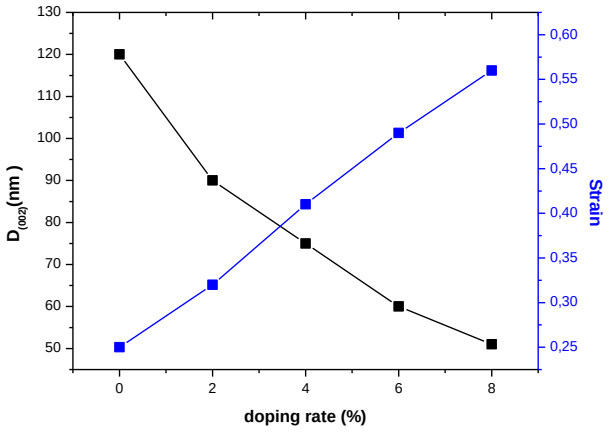

Fig.3. Variation crystallite size and the crystal strain as a function of the doping rate.

III.4. Optical properties:

Figure 4 shows the optical spectrum transmittance of the Fe doped copper oxide films between 400 and 1000 nm.

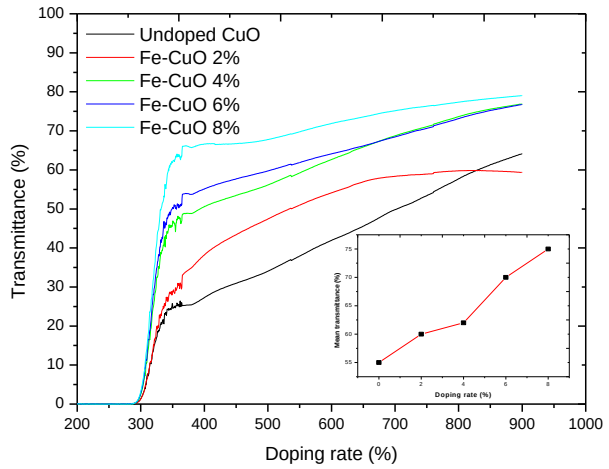

Fig.4. UV–visible transmittance spectra of the deposited Fe doped CuO thin films. (Inset: Variation of means transmittance as a function of the doping rate).

In the spectra of our films we distinguish two regions, a region of high transmission between 800 and 1000 nm, the transmission factor varies

between 55% and 75%. And another region in the visible high absorption from which the absorption coefficient α is calculated from the formula of Beer Lambert [18-19] :

$$T = e^{-\alpha d} \rightarrow \alpha = -\frac{1}{d} lnT$$

With: α is the coefficient of absorption and d the thickness of our films.

The gap energy will be calculated from the relationship [20-21]:

$$(\alpha h\vartheta)^2 = A * (h\vartheta - E_g)$$

A: is a reflectant constant of degree of disorder of the amorphous solid structure, α: is the absorption coefficient (dependent on wavelength), and E is gap energy in eV. We represent the gap energy as a function of the doping rate (Figure 5). The results revealed that with increase in Fe doping amount, an increase in the transmittance was observed, it is around 75 % in the visible wavelength zone.

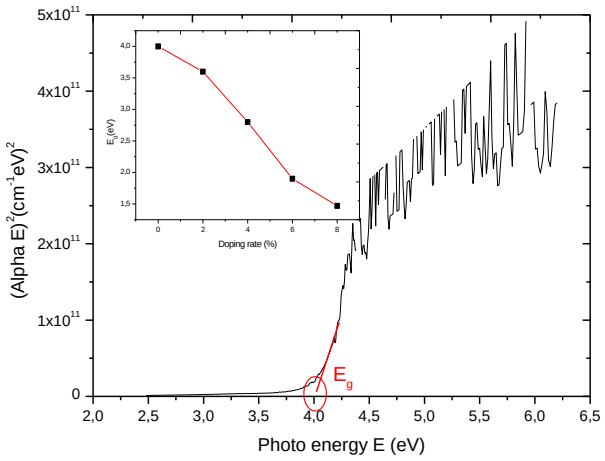

Fig.5. Plot of $(\alpha E)^2$ as a function of the photon energy *E*. (Inset: Variation of the band gap energy *Eg* as a function of the doping rate).

III.5. Electrical properties:

The resistance of our obtained films is measured by the four points. The value of the resistivity ρ is related to the measurement of the ratio $\frac{\Delta V}{I}$, according to the expression [22-26] :

$$\rho = \frac{\Delta V}{I} \frac{\pi\, d}{ln2} = R_s . d$$

Where: d: film thickness of the material, Rs: surface resistance.

In Figure 6 we note that the resistivity of our films increases with the increase of the doping rate, this evaluation could be attributed to the increase of grain boundaries (Figure 6).

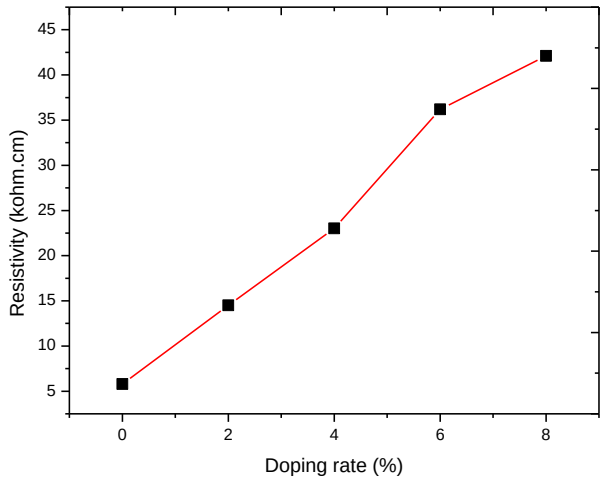

Fig.6. Resistivity of the deposited films Fe doped CuO

IV. Conclusion :

In this work, the Fe doped CuO thin films deposited with copper chloride were synthesized using a spray pyrolysis technique. We studied the influence of doping rate of Fe on the physical properties of our films, XRD results revealed that the prepared films had a polycrystalline nature. The incorporation of Fe did not change the monoclinic structure of CuO. The optical transmittance for the samples was below 75 %. The absorption band decrease with increasing in doping rate. The resistivity measurements show that the resistivity increases with increasing Fe concentration.

References

[1] B. Balamurugan, B.R. Mehta, "Optical and Structural Properties of Nanocrystalline Copper Oxide Thin Films Prepared by Activated Reactive Evaporation", Thin Solid Films, Vol. 396 ,pp. (90-96), (2001).
[2] R. Lange, "Photoelements and their Applications", Reinhold Publishing Co, New York ,(1939).
[3]. S. Seung-Deok, J. Yun-Ho, L. Seung-Hun, S. Hyun-Woo, K. Dong Wan, Nano scale Res. Lett. 6, 2 (2011).
[4]. Y. Jiang, S. Decker, C. Mohs, K. J. Klabunde, J. Catal. 180, 24 (1998).
[5] A. Chowdhuri, V. Gupta, K. Sreenivas, R. Kumar, S. Mozumdar, P.K. Patanjali, Appl. Phys. Lett. 84 (2004) 1180–1182.
[6] N. D. Hoa, S. Y. An, N. D. Dung, N. V. Quy, D. Kim," Synthesis of p-type Semiconducting Cupric Oxide Thin Films and Their Application to hydrogen detection", Sensors and Actuators B: Chemical,Vol.146,No.1, pp.(239-244),(2010).
[7] E. R. Kari, K. S. Brown, Choi, Electrochemical synthesis and characterization of transparent nanocrystalline Cu_2O films and their conversion to CuO films, Chem. Commun. (2006) 3311–3313.
[8] T. Maruyama, Copper oxide thin films prepared from copper dipivaloylmethanate and oxygen by chemical vapor deposition, Jpn. J. Appl. Phys. 37(1998) 4099–4102.
[9] A. Y. Oral, E. Mensur, M. H. Aslan, E. Basaran,MaterChemPhys, 83(1), 140 (2004).
[10] J. H. Benjamin, K. Nikolai, L. Ganhua, L. I. -Khan, C. Junhong, Z. Xin, Transport, analyte detection and optoelectronic response of p-type CuO nanowires, J. Phys. Chem. C 114 (2010) 2440–2447.
[11] K. Santra, C.K. Sarkar, M.K. Mukherjee and B. Ghosh, *Thin Solid Films*, 213(1992) 226
[12] A. Chen, H. Long, G. Yang, P. Lu, Vacuum 83 (2009) 927.
[13] J. Chen, F. Zhang, J. Wang, G. Zhang, B. Miao, X. Fan, J. Alloys Compd. 454 (2008) 268.
[14] B.Boudjema**,** R.Daira**,** A. Kabir, R. Djebien 'Physico-Chemical Properties of CuO Thin Films

Deposited by Spray Pyrolysis', Materials Sciences forum Vol 895, 2017, 33-36.
[15] R.Daira**,** A. Kabir, B.Boudjema**,** C. Sedreati 'Structural and optical tranmittance analysis of CuO thin film deposited by the spray pyrolysis method', Solid State Sciences, Vol 104, 2020, 106254.
[16] A. Hoseini Mashhad-toroghi, N. Shahtahmasebia , E. Azhira , P. Madahia, M. Mashreghi ," Deposition of Copper Oxide Nanostructured Thin films and Study of The Influence of Fe^{+3} Doped on the Structural, Optical and Antibacterial Properties of CuO Thin Films" ,Proceedings of the 4th International Conference on Nanostructures (ICNS4) , P.P.(852-854), (2012).
[17] D. P. Volanti, D. Keyson, L.S. Cavalcante, A.Z. Sim~oes, M.R. Joya, E.Longo, J. A. Varela, P. S. Pizani, A. G. Souza, J. Alloys Compd. 459, 2008.
[18] T. Yu, C.H. Sow, A. Gantimahapatruni, F.C. Cheong, Y. Zhu, K.C.Chin, X. Xu, C.T. Lim, Z. Shen, J.T.L. Thong, A.T.S. Wee ,Nanotechnology 16,1238, 2005.
[19] B. Dennis, Elements of X-Ray Diffraction, third ed., Prentice-Hall International, Upper Saddle River, N.J, London, 2000.
[20] T. Ziad. Khodair, H. Ali. Adwan, H. Noora.Shallal, Effect of Aluminum Doping on Structural Properties of CuO Thin Films Prepared by Chemical Spray Pyrolysis (CSP) Technique, diyala journal for pure sciences, 13, pp. 198-208, 2017.
[21] J.I. Pankove, Optical Processing in Semiconductors, Dover, New York, 1971.
[22] A. Moumen, B. Hartiti, E. Comini, Z. El khalidi, H.M.M. Arachchige, S. Fadili, P. Thevenin, Superlattice. Microst. 127 (2019) 2.
[23] A.T. Ravichandran, K. Dhanabalan, S. Valanarasu, A. Vasuhi, A. Kathalingam, J. Mater. Sci. Mater. Electron. 26 (2015) 921.
[24] D.M. Jundale, P.B. Joshi, Shashwati Sen, V.B. Patil, J. Mater. Sci. Mater. Electron. 23 (2012) 1492.
[25] R.Daira**,** B.boudjema, 'Application of laser technique for the calculating the speckle size and object incidence angle', Journal of intense pulsed lasers and applications in advanced physics, Vol. 5, No. 1, (2015), p. 1- 4.
[26] R.Daira**,** B.boudjema, M.Mordjaoui, M.Mezéri 'Electrical properties of metallophtha- locyanine thin films', Journal of optoelectronics and advanced materials – rapid communications, Vol 5, No 2, (2011) p. 167 –171.

Design and Analyze of a Monolithic Square Spiral Planar Micro-Transformer

Benhadda Yamina
Department of Electrical Engineering
University of Science and Technology
Oran, Algeria
benhadda_yamina@yahoo.fr

Derkaoui Mokhtaria
National Institute of Telecommunication
Oran, Algeria
mderkaoui@inttic.dz

Mendaz Kheira
Department of Electrical Engineering
University of Centre Belhadj Bouchaib
Ain Temouchent, Algeria
kheiramendez@gmail.com

Kharbouch Hayet
Department of Electrical Engineering
University of Science and Technology
Oran, Algeria
hayet.kharbouch@gmail.com

***Abstract*—The integration of electrical components has been the subject of many researches. In this paper, we design and analyze a monolithic square spiral planar micro-transformer integrated in a converter Flyback.**
Firstly, the geometrical and electrical parameters are presented. Secondly, the efficiency of Flyback is calculated to verify the performance of the converter. The final part of this paper shows the thermal modeling, using the finite element method that allowed us to determine the operating temperature in the materials of this component.

***Keywords*—** monolithic square spiral planar micro-transformer, converter flyback, thermal

I. INTRODUCTION

Several studies demonstrated the feasibility of integrated inductors on Silicon substrates, huge research efforts have been dedicated to their analysis, design, modeling and optimization [1-4]. As a result of these efforts, the inductor performance has been noticeably improved. Conversely, integrated transformers still remain strange components and are rarely used.
In this paper we will design and analyze the integrated or monolithic micro-transformer integrated in converter Flyback. This component is the coupling of two square inductor results. The finite element method has allowed us to see the evolution of the temperature in the different parts that make up the micro-transformer in 3D.

II. PRESENTATION OF THE FLYBACK CONVERTER

We have chosen a Flyback converter (figure 1) because it is composed of a transformer. The principle of operation of the Flyback is based on the energy transfer from primary to secondary through a transformer.

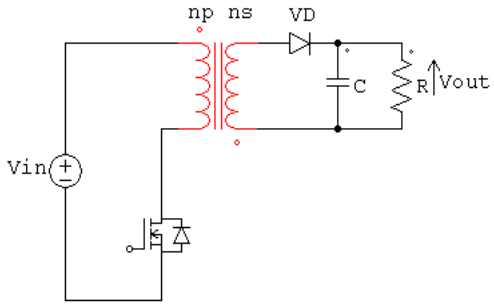

Fig. 1. Schematic of Flyback converter

The main specifications is presented in table I

TABLE I. MAIN SPECIFICATION

Parameters	Values
Input Voltage [V_{in}] (V)	14
Output voltage [V_{out}] (V)	12
Output power [P_{out}] (W)	5
Duty cycle [α] 0.5	0.5
Operation Frequency (MHz)	100

III. DIMENSIONING OF THE MICRO-TRANSFORMER

Dimensioning of the planar Micro-Transformer requires sizing the magnetic circuit and the geometrical parameters of two wading of our component, primary and secondary [5-6].
Turn ratio

$$m = \frac{\alpha}{\alpha - 1}\frac{V_{out}}{V_{in}} = 0.85 \qquad (1)$$

The primary inductance L_p is given by relation (2)

$$L_p = \frac{V_{in}^2 \alpha^2}{2 f P_{out}} \qquad (2)$$

The operation of passive transformer is based on the mutual coupling between two or more conductors, or more currently, inductors. An example of an integrated implementation it is shown in figure 2 where two inductors are intertwined in order to favor their mutual coupling.

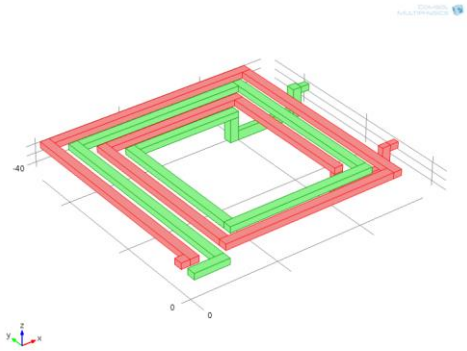

(a)

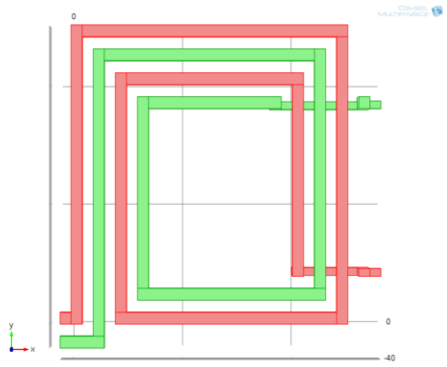

(b)

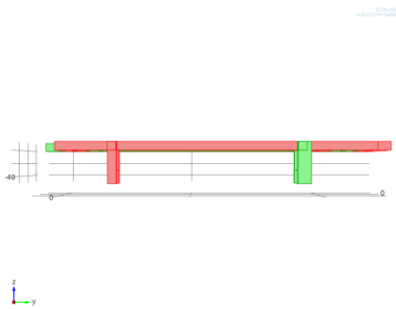

(c)

Fig. 2. Integrated planar micro-transformer , (a) general view, (b) view dessu, (c) front view

Primary and secondary turns' numbers are calculated by Mohan's [7-8] formula (3). The coefficients k_1 and k_2 are defined for each geometry. For a square micro coil spiral, k_1=2.34 and k_2=2.75.

$$n_p = \sqrt{\frac{L_p(1+k_2\rho)}{K_1\mu_0 d_{avg}}} \quad (3)$$

$$n_s = m.n_p \quad (4)$$

Where, we define the average diameter as $d_{avg} = (d_{out} + d_{in})/2$. A_m the factor's form defined as $A_m = d_{out} - d_{in} / d_{out} + d_{in}$.

We have taken the same spacing for both the primary and secondary windings, $w_p = w_s$:

$$w_p = w_s = \frac{[d_{out} - d_{in} - 2s_s(n_s - 1)]}{2n_s} \quad (5)$$

The primary and secondary spacing between conductors is expressed as follows

$$s_p = \frac{d_{out} - d_{in} - 2w_p n_p}{2(n_p - 1)} \quad (6)$$

$$s_s = \frac{d_{out} - d_{in} - 2w_s n_s}{2(n_s - 1)} \quad (7)$$

The primary and secondary length of the trace is expressed as follows

$$l_p = 4n_p[d_{out} - (n_p - 1)s_p - n_p w_p] - s_p \quad (8)$$

$$l_s = 4n_s[d_{out} - (n_s - 1)s_s - n_s w_s] - s_s \quad (9)$$

The skin thickness is defined as [9]

$$\delta = \sqrt{\frac{\rho}{\pi\mu f}} \quad (10)$$

Where ρ represent the resistivity of the conductor, $\rho = 1.7\ 10^{-8}\Omega m$ and μ its magnetic permeability. So that the current flows in the entire conductor, it is necessary that one of the following conditions is filled, $w \le 2\delta$ or $t \le 2\delta$.

Table II contains the specifications and the design results of the integrated micro-transformer.

Table II. Design results of the integrated micro-transformer

Parameter	Value
Outer diameter: d_{out}	500 µm
Inner diameter: d_{in}	450 µm
Primary turns: n_p	1.75
Secondary turns: n_s	1.25
Thickness of winding: t	13 µm
Width of primary winding: w_p	20 µm
Width of secondary winding: w_s	20 µm
Inter-spacing of primary winding: s_p	4.2 µm
Inter-spacing of secondary winding: s_s	6. 5 µm
Length of primary winding: l_p	3.2 µm
Length of secondary winding: l_s	2.8 µm

IV. ELECTRICAL MODEL

An accurate planar micro-transformer model is desired for circuit design (figure 3).

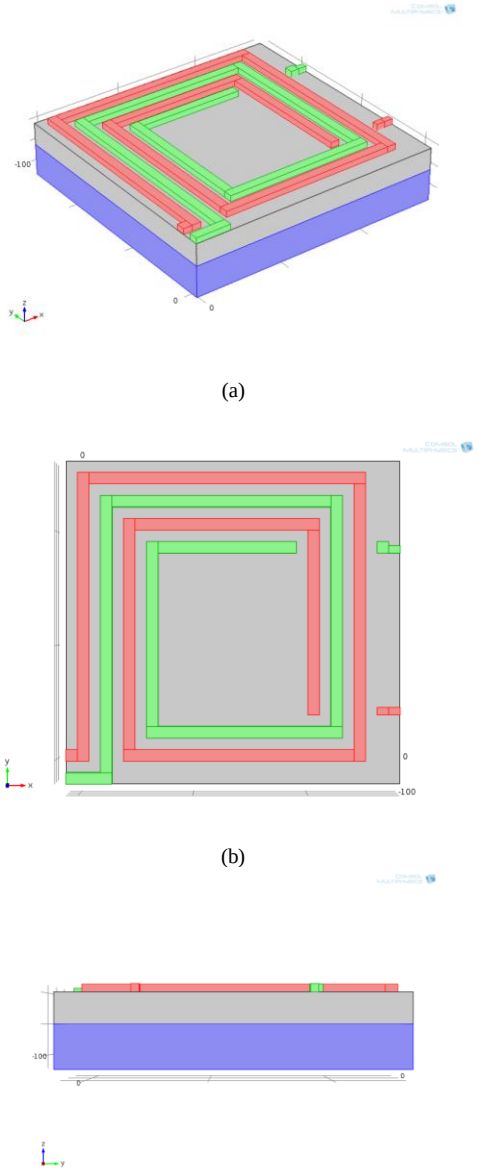

(a)

(b)

(c)

Fig. 3. Geometry of integrated micro-transformer on substrate on substrate, (a) general view, (b) view dessu, (c) front view

The equivalent electrical model of an integrated planar micro-transformer [10] is shown in Figure 4.

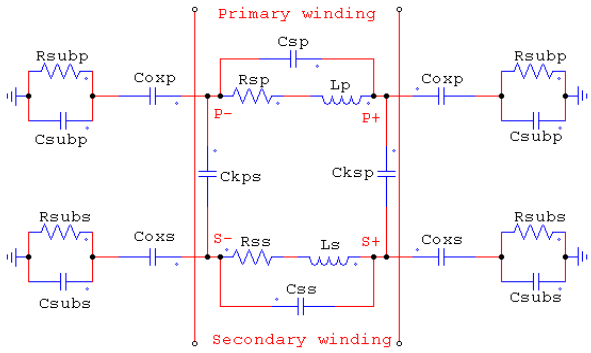

Fig. 4. Equivalent circuit of an integrated planar micro-transformer

1. Serial resistance R_{sp} and R_{ss} of the primary and secondary

$$R_{sp} = \frac{\rho_{cu} l_p}{w_p t} \quad (11)$$

$$R_{ss} = \frac{\rho_{cu} l_s}{w_s t} \quad (12)$$

2. Serial resistance R_{sACp} and R_{sACs} of the primary and secondary

$$R_{sACp} = \frac{\rho_{cu} l_p}{w_p t_{eff}} \quad (13)$$

$$R_{sACs} = \frac{\rho_{cu} l_s}{w_s t_{eff}} \quad (14)$$

t_{eff} : is given by the expression; $t_{eff} = \delta(1 - e^{-(t/\delta)})$

3. Coupling capacitance C_{sp} and C_{ss} of the primary and secondary

$$C_{sp} = \frac{1}{2} \varepsilon_0 \varepsilon_{ox} \frac{t_p l_p}{s_p} \quad (15)$$

$$C_{ss} = \frac{1}{2} \varepsilon_0 \varepsilon_{ox} \frac{t_s l_s}{s_s} \quad (16)$$

Where, ε_0 is the permittivity of free space, $\varepsilon_0 = 8.854187.10^{-12} Mm^{-1}$.

4. Coupling capacitance C_{kps} between the primary and secondary, coupling capacitance C_{ksp} between the secondary and primary

$$C_{kps} = \varepsilon_0 \varepsilon_{ox} \frac{w l_p}{t_{ox}} \quad (17)$$

$$C_{ksp} = \varepsilon_0 \varepsilon_{ox} \frac{w l_s}{t_{ox}} \quad (18)$$

5. Oxide capacitance C_{oxp} and C_{oxs} of the primary and secondary

$$C_{oxp} = \frac{1}{2} l_p w_p \left(\frac{\varepsilon_0 \varepsilon_{ox}}{t_{ox}} \right) \quad (19)$$

$$C_{oxs} = \frac{1}{2} l_s w_s \left(\frac{\varepsilon_0 \varepsilon_{ox}}{t_{ox}} \right) \quad (20)$$

6. Resistances R_{subp} and R_{subs} associated to the silicon substrate of the primary and secondary

$$R_{subp} = 2\rho_{sub}\frac{t_{sub}}{l_p w_p} \quad (21)$$

$$R_{subs} = 2\rho_{sub}\frac{t_{sub}}{l_s w_s} \quad (22)$$

7. Capacitance C_{subp} and C_{subs} associated to the silicon substrate of the primary and secondary

$$C_{subp} = \tfrac{1}{2}\varepsilon_0\varepsilon_{sub}\frac{l_p w_p}{t_{sub}} \quad (23)$$

$$C_{subs} = \tfrac{1}{2}\varepsilon_0\varepsilon_{sub}\frac{l_p w_p}{t_{sub}} \quad (24)$$

Table III shows the electrical parameters calculated.

TABLE III. ELECTRICAL PARAMETERS RESULTS

Electrical parameters	Values
Primary inductance: L_p	49 nH
Secondary inductance: L_s	36 nH
Primary serial resistance: R_{sp}	0.21 Ω
Secondary serial resistance: R_{ss}	0.18 Ω
Primary serial resistance: R_{sACp}	0.48 Ω
Secondary serial resistance: R_{sACs}	0.42 Ω
Primary resistance of silicon substrate: R_{subp}	0.10 Ω
Secondary resistance of silicon substrate: R_{subs}	0.11 Ω
Primary coupling capacitance: C_{sp}	346.59 pF
Secondary coupling capacitance: C_{ss}	191.86 pF
Coupling capacitance between the primary and secondary: C_{kps}	44.83 pF
Coupling capacitance between the secondary and primary: C_{ksp}	38. 79 pF
Primary oxide capacitance: C_{oxp}	44.83 pF
Secondary oxide capacitance: C_{oxs}	38.79 pF
Primary capacitance of silicon substrate C_{subp}	38.79 pF
Secondary capacitance of silicon substrate : C_{subs}	33.56 pF
Quality factor Q_p	43.94
Quality factor Q_s	37.33

The quality factor is defined as the ratio between the magnetic power stored and the power dissipated in the component (29), (30). Thus, the higher the quality factor, the smaller the power lost in the component [11].

$$Q_p = \frac{\omega \mathrm{L_p}}{\mathrm{R_p}} \quad (25)$$

$$Q_s = \frac{\omega \mathrm{L_s}}{\mathrm{R_s}} \quad (26)$$

Figure 5 shows the evolution of the quality factor as a function of frequency for the primary and secondary winding.

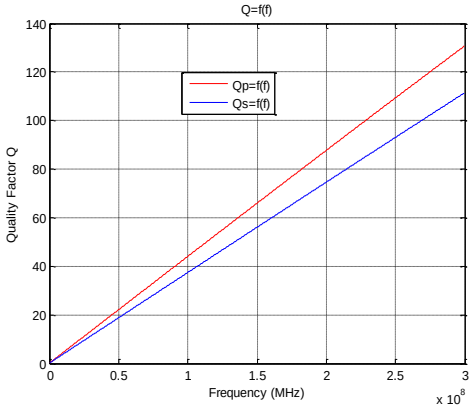

Fig. 5. Quality factor of the primary and secondary windings versus frequency

V. THE EFFICIENCY OF FLYBACK CONVERTER

The efficiency is calculated to see the performance of our Flyback converter [12-13].

$$\eta = \frac{P_{out} - P_{in}}{P_{out}} \quad (27)$$

$$P_{in} = P_j + P_f + P_{ed} \quad (28)$$

Transformer losses arise from [14-16]:

Winding joule losses: Current flowing through a winding's conductor causes joule heating. As frequency increases, skin effect and proximity effect causes the winding's resistance and, hence, losses to increase.

$$P_j = (R_{sp} + m^2 R_{ss}) I_{out}^2 \quad (29)$$

Hysteresis losses: Each time the magnetic field is reversed, a small amount of energy is lost due to hysteresis within the core.

$$P_f = m f^{\alpha} B_{\max}^{\beta} V \quad (30)$$

Where m, α *and* β are the coefficients depending on the size of the material. V is the volume of magnetic core.

Eddy current losses also called Foucault currents: Ferromagnetic materials are also good conductors and a core made from such a material also constitutes a single short-circuited turn throughout its entire length. Eddy currents therefore circulate within the core in a plane normal to the

flux, and are responsible for resistive heating of the core material.

$$P_{ed} = C\frac{f^2 B^2}{\rho} \qquad (31)$$

Where C and ρ are the coefficients depending on the size of the material.
The efficiency found is around 71%.

VI. THERMAL EFFECT IN A PLANAR MICRO-TRANSFORMER

In this section, we present the temperature distribution in our integrated micro-transformer, based on the finite element method [17-20].
This distribution is obtained by solving the equation (32) of heat taking into account certain boundary conditions.

$$\rho.C_p \frac{\partial T}{\partial t} - \nabla(k\nabla T) = q \ (32)$$

For an integrated micro-transformer in the air, the heat source can be expressed as (33)

$$q = \frac{P_{in}}{V} \qquad (33)$$

Where, V is the volume of our planar micro-transformer .
Geometry of this study is created in 3D space dimension. Our component consists of four domains. The domain of air surrounding our planar micro-transformer. The copper is the conductor material, the substrate is in ferrite, and the dielectric is in oxide.

In figure 6, we observe the temperature distribution in the planar micro-transformer on substrate. We see from these figures that the temperature is about 37 °C.

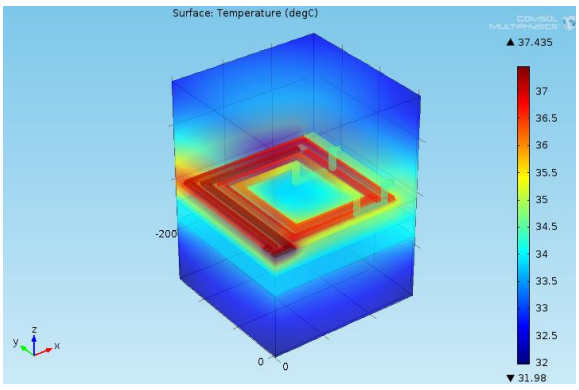

(a)

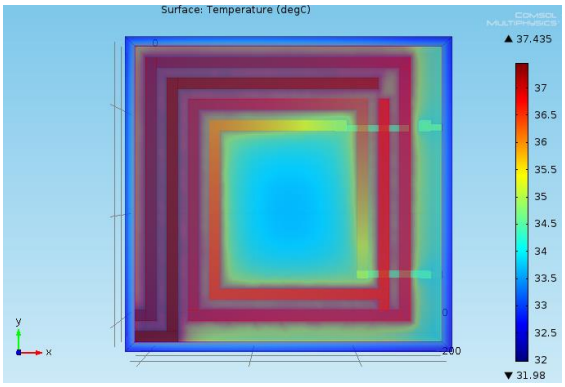

(b)

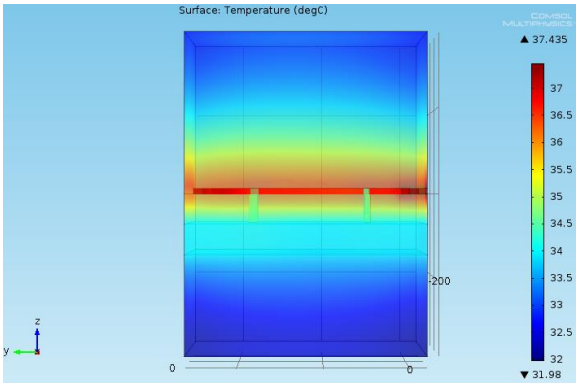

(c)

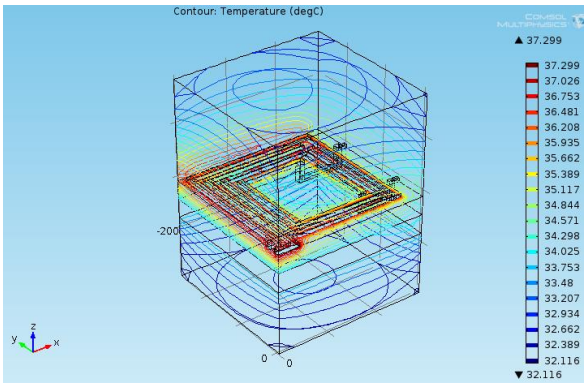

(d)

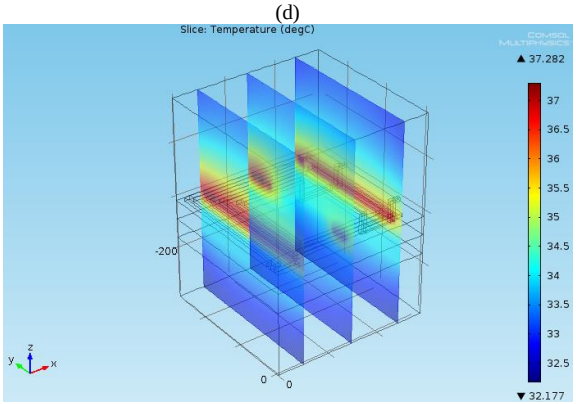

(e)

Fig. 6. Temperature distribution in the planar micro-transformer on substrate, (a) on general, (b) on dessu, (c) on front, (d) on contour, (e) on scile

VII. CONCLUSION

In this paper, design and analyze of a monolithic square spiral planar micro-transformer for its integration in a micro-converter has presented.

Higher efficiency of DC-DC Flyback using equivalent model parameters of transformer was obtained. The converter with the integrated transformer shows maximum efficiency of 71% for an output power 5 W.

We have visualized the thermal phenomenon in planar micro-transformer based on finite element method.

The simulation results show that an integrated planar micro transformer realized with substrate allows canalizing the magnetic field in the component. We conclude that the substrate losses can be minimized. It is also shown that the substrate of the monolithic component reduces losses also decreases the temperature.

ACKNOWLEDGMENT

Yamina Benhadda was born in Algeria in 1982. She obtained his Magister degree in plasma and electrical discharge at Mohamed Boudiaf University of Oran in 2010. She obtained his Doctorate degree in electrical engineering at Mohamed Boudiaf University of Sciences and Technology of Oran in 2016. In 2017, she became a full professor in this University. His research interests include the design and modeling of on-chip passive components, and the design of RF and millimeter-wave integrated circuits in silicon technologies. She is a member of research team of LEPA laboratory.

Mokhtaria Derkaoui is an associate professor, a PhD in electrical engineering and a young researcher in microelectronics from the University of Sciences and Technologies of Oran USTO, Algeria. She actually teaches modules in digital electronics and optoelectronics at the National Institute of Telecommunication & ICT of Oran INTTIC, Algeria. She is a member of research team of LEPA and LARATIC laboratories since 2010 and 2015 respectively.

Kheira Mendaz was born in Ain Temouchent (Algeria), on December 5, 1976. She graduated the University centre Belhadj Bouchaib, Electrical Engineering Department in Ain Temouchent (Algeria), in 2015. She received the Ph.D degrees in electrical engineering from Sidi Bel Abbes University, (Algeria), in 2015. She is Doctor at the University centre Belhadj Bouchaib, Electrical Engineering Department in Ain Temouchent (Algeria). His research interests concern: power electronics, electric machines, and EMC in power converter.

Hayet Kharbouch was born in Oran, Algeria. He received his PhD in 2018 from Mohamed Boudiaf University of Sciences and Technology of Oran.

REFERENCES

[1] M. Kim, F. Herrault, J. Kim and M. G. Allen, Monolithically-fabricated laminated inductors with electrodeposited silver windings, IEEE International Conference on Micro Electro Mechanical Systems (MEMS), pp. 873-876, Jan. 2013.

[2] J. Kim, J-. k. Kim, M. Kim, F. Herrault, M. G. Allen, Microfabrication of totoidal inductors integrated with nanolaminated ferromagnetic metallic cores, Journal of Micromechnics and Microengineering, 23(11), Nov. 2013.

[3] J. Kim, M. Kim, F. Herrault, J. Y. Park, and M. G. Allen, Electrodeposited nanolaminated CoNiFe cores for ultracompact DC-DC power conversion, IEEE Transactions on Power Electronics, 30(9), pp. 5078-5087, Sep. 2015.

[4] D. D. Yaya, M. B. Bechir, M. K. Youssouf, M. Soultan, F. Kahlouche, S. Capraro, A. Siblini, J. P. Chatelon and J. J. Rousseau, Characterization of integrated inductors with one and two YIG layers for low-power converters (1W), published by EDP Sciences, 2014.

[5] M. Derkaoui, A. Hamid, T. Lebey, R. Melati, Design and modeling of an integrated microtransformer in a flyback converter, Telkomnika, 11(4), pp. 669-682, 2013.

[6] S. Osmanaj, E. Nasufi, Design of an integrated planar inductor using accurate expressions for planar spiral inductances, IEEE Journal of Solid-State Circuits, 34(10), pp. 1419-1424, 1999.

[8] J. M. Wright, D. W. Lee, A. Mohan, A. Papou, P. Smeys, and S. X. Wang, Analysis of integrated solenoid inductor with closed magnetic core, IEEE Transactions on Magnetics, 46(6), pp. 2387-2390, Jun. 2010.

[9] C. R. Sullivan, D. V. Harburg, J. Qiu, C. G. Levey, and D. Yao, Integrating magnetic for on-chip power: a perspective, IEEE Transactions on Power Electronics, 28(9), pp. 4342-4353, Sep. 2013.

[10] H. Gan, On-chip transformer modeling, characterization, and applications in power and low noise amplifiers, These of Stanford University, March 2006.

[11] H. Yun, J. M. Kikkawa, J. Kim,T. Paik, C. R. Kagan, L. Meng, M. G. Allen, P. S. Jo, and C. B. Murray, Fabrication via a solution based process, Journal of Applied Physics 119, pp. 113901_1-113901_9, 2016.

[12] I. Aoki, Distributed active transformer-a new power-combining and impedance-transformation technique, IEEE Transactions on Microwave Theory and Techniques, 50(1), pp. 316-331, January 2002.

[13] I. Aoki, Fully integrated CMOS power amplifier design using the distributed active-transformer architecture, IEEE Journal of Solid-State Circuits, 37(3), pp. 371-383, March 2002.

[14] J. Muhlethaler, J. Biela, J. W. Kolar, and A. Ecklebe, Improved core-loss calculation for magnetic components employed in power electronic systems, IEEE Transactions on Power Electronics, 27(2), pp. 964-973, Feb 2012.

[15] P. Viarouge, J. C. Fagundes, E. Tourkhani, H. Le-Huy, Comportement thermique et conception des composants magnétiques dans les convertisseurs statiques de fréquence élevée, IEEE, pp. 582-585, 1995.

[16] C. Feeney, N. Wang, and S. C. O'Mathuna, A 20-MHz 1.8-W DC-DC converter with parallel microinductors and improved light-load efficiency, IEEE Transactions on Power Electronics, 30(2), pp. 771-779, Jan 2015.

[17] Y. Benhadda, A. Hamid, T. Lebey, M. Derkaoui, Design and modeling of an integrated inductor in a buck converter DC-DC, Journal of Nano and Electronic Physics, 7(2), pp. 2006 (6pp), 2015.

[18] A. Allaoui, A. Hamid, P. Spiterri, V. bley, T. Lebey, Thermal modeling of an integrated inductor in a micro-converter, Journal of Low Power Electronics, 11(1), pp. 63-73, 2015.

[19] Y. Benhadda, A. Hamid, T. Lebey, A. Allaoui, M. Derkaoui, R. Melati, Thermal behavior of an integrated square spiral micro coil, Telkomnika, 14(2), pp. 669-682, 2015.

[20] Y. Benhadda, A. Hamid, T. Lebey, Dimensioning and Modeling of a Circular Inductor Integrated in a Boost Converter, Journal of Nano and Electronic Physics, 8(4), 04039 (5pp), 2016.

ICEAINT

THE 1ST INTERNATIONAL CONFERENCE ON ELECTRONICS ARTIFICIAL INTELLIGENCE AND NEW TECHNOLOGIES

ISBN: 978-9931-9728-1-5